NANOSTRUCTURES: PHYSICS AND TECHNOLOGY

14th International Symposium

St Petersburg, Russia, June 26–30, 2006

Co-Chairs
Zh. Alferov
L. Esaki

PROCEEDINGS

Ioffe Institute
St Petersburg, 2006

Published by
Ioffe Physico-Technical Institute
26 Politekhnicheskaya, St Petersburg 194021, Russia
http://www.ioffe.ru/

Publishing license ΛP No 040971 of June 16, 1999.

ISBN 5-93634-019-8

The International Symposium "Nanostructures: Physics and Technology" is held annually since 1993. The first Symposium was initiated by Prof. Zh. Alferov and Prof. L. Esaki who are its permanent co-chairs. More detailed information on the Symposium is presented on the World Wide Web **http://www.ioffe.ru/NANO2006/**

The Proceedings include extended abstracts of invited talks and contributed papers to be presented at the Symposium. By tradition this book is published before the beginning of the meeting.

The volume was composed at the Information Services and Publishing Department of St Petersburg Physico-Technical Centre of RAS for Research and Education from electronic files submitted by the authors. When necessary these files were converted into the Symposium style without any text revisions. Only minor technical corrections were made by the composers.

Design and layout: N. Vsesvetskii
Desk editor: L. Solovyova

Information Services and Publishing Department
St Petersburg Physico-Technical Centre of RAS for Research and Education
8, bld. 3 Khlopina, St Petersburg 195220, Russia
Phones: (812) 534-58-58
Fax: (812) 534-58-50
E-mail: nano@mail.ioffe.ru

Printed in Russian Federation

The Symposium is held under the auspices of
the Russian Academy of Sciences

Organizers

Scientific Engineering Centre for Microelectronics at the Ioffe Institute
Ioffe Physico-Technical Institute
St Petersburg Physico-Technical Centre of RAS for Research and Education

in association with

the institutions of the Russian Academy of Sciences
Division of Physical Sciences
St Petersburg Scientific Centre

Acknowledgments

The Organizers gratefully acknowledge the following
for their contribution to the success of the Symposium:
Russian Academy of Sciences
Russian Foundation for Basic Research
St Petersburg Scientific Centre
AIXTRON AG, Germany
JSC "Svetlana-Optoelectronics", Russia
"ATC—Semiconductor technologies & Equipment" (SemiTEq), Russia

Location and Date

Symposium is held in St Petersburg, June 26–30, 2006.

Advisory Committee

G. Abstreiter (*Germany*)
Zh. Alferov (*Russia*)
Y. Arakawa (*Japan*)
A. Aseev (*Russia*)
G. Bastard (*France*)
D. Bimberg (*Germany*)
L. Eaves (*United Kingdom*)
L. Esaki (*Japan*)
S. Gaponov (*Russia*)
E. Gornik (*Austria*)
Yu. Gulyaev (*Russia*)
N. Holonyak Jr. (*USA*)
L. Keldysh (*Russia*)
G. Landwehr (*Germany*)
J. Merz (*USA*)
M. Shur (*USA*)
M. Skolnick (*United Kingdom*)
R. Suris (*Russia*)

Programme Committee

R. Suris, Chair (*St Petersburg, Russia*)
V. Evtikhiev, Secretary (*St Petersburg, Russia*)
A. Andronov (*Nizhny Novgorod, Russia*)
N. Bert (*St Petersburg, Russia*)
C. Chang-Hasnain (*Berkeley, USA*)
A. Chaplik (*Novosibirsk, Russia*)
V. Dneprovskii (*Moscow, Russia*)
V. Dubrovskii (*St Petersburg, Russia*)
A. Gippius (*Moscow, Russia*)
S. Gurevich (*St Petersburg, Russia*)
S. Ivanov (*St Petersburg, Russia*)
P. Kop'ev (*St Petersburg, Russia*)
Z. Krasil'nik (*Nizhny Novgorod, Russia*)
V. Kulakovskii (*Chernogolovka, Russia*)
M. Kupriyanov (*Moscow, Russia*)
X. Marie (*Toulouse, France*)
I. Merkulov (*St Petersburg, Russia*)
V. Panov (*Moscow, Russia*)
O. Pchelyakov (*Novosibirsk, Russia*)
E. Poltoratskii (*Moscow, Russia*)
H. Sakaki (*Tokyo, Japan*)
N. Sibel'din (*Moscow, Russia*)
M. Stutzmann (*Garching, Germany*)
V. Timofeev (*Chernogolovka, Russia*)
V. Volkov (*Moscow, Russia*)
L. Vorobjev (*St Petersburg, Russia*)

Organizing Committee

M. Mizerov, Chair (*Centre for Microelectronics*)
D. Donskoy (*St Petersburg Scientific Centre*)
G. Mikhailov (*St Petersburg*)
N. Sibel'din (*Lebedev Physical Institute*)
E. Solovyova (*St Petersburg Physico-Technical Centre of RAS for Research and Education*)
V. Zayats (*Division of Physical Sciences*)

Award Committee

Zh. Alferov, Chair (*Russia*)
F. Beltram (*Italy*)
P. Bhattacharya (*USA*)
L. Esaki (*Japan*)
F. Glas (*France*)
M. Heuken (*Germany*)
E. Kapon (*Switzerland*)
L. Keldysh (*Russia*)
R. Suris (*Russia*)
V. Timofeev (*Russia*)

Contents

Opening Plenary Session

OPS.02pl *W. Seifert*
Growth-related aspects of nanowire fabrication 1

OPS.03pl *P. Bhattacharya*, Z. Mi, J. Yang and S. Fathpour
Tunnel injection quantum dot lasers on GaAs, InP, and silicon 4

Lasers and Optoelectronic Devices

LOED.02o *L. V. Asryan*
Optical power of a quantum dot laser 7

LOED.03o *S. A. Blokhin*, N. A. Maleev, A. G. Kuzmenkov, A. V. Sakharov, M. M. Kulagina, Yu. M. Shernyakov, I. I. Novikov, M. V. Maximov, V. M. Ustinov, A. R. Kovsh, S. S. Mikhrin, N. N. Ledentsov, G. Lin and J. Y. Chi
High-performance vertical-cavity surface-emitting lasers based on sub-monolayer InGaAs quantum dots 9

LOED.04o F. Xie, D. Smith and *A. Belyanin*
Nonlinear quantum cascade lasers: physics and applications 11

LOED.05o C. A. Evans, V. D. Jovanović, D. Indjin, Z. Ikonić and *P. Harrison*
Thermal effects in quantum cascade lasers 13

LOED.06p *N. V. Kryzhanovskaya*, A. G. Gladyshev, N. A. Maleev, A. G. Kuzmenkov, A. E. Zhukov, S. A. Blokhin, A. M. Nadtochy, E. M. Arakcheeva, E. M. Tanklevskaya, A. P. Vasil'ev, E. S. Semenova, M. V. Maximov, V. M. Ustinov, E. Stock, D. Bimberg and N. N. Ledentsov
Lasing characteristics of microdisks with In(Ga)As quantum dots in temperature diapason from 5 to 300 K 15

LOED.07p *K. V. Marem'yanin*, A. A. Biryukov, S. M. Nekorkin, B. N. Zvonkov, V. Ya. Aleshkin, A. A. Dubinov, V. I. Gavrilenko, S. V. Morozov, A. A. Belyanin, V. V. Kocharovsky and Vl. V. Kocharovsky
Interband cascade lasers with tunnel junction demonstrate dual-wavelength generation 17

LOED.08p *Yu. A. Morozov*, M. Pessa, T. Leinonen, A. Härkönen and M. Yu. Morozov
Two-color vertical external-cavity surface-emitting laser 19

LOED.09p *V. V. Nikolaev*, N. S. Averkiev, A. E. Gubenko, A. R. Kovsh and E. L. Portnoi
Influence of Stark and Stokes shifts on operation of bistable QD lasers 21

LOED.10p *V. Yu. Panevin*, B. Eichenberg, V. A. Shalygin, L. E. Vorobjev, D. A. Firsov, E. M. Araktcheeva, N. V. Kryzhanovskaya, A. G. Gladyshev, A. E. Zhukov, V. M. Ustinov, S. Hanna and A. Seilmeier
Interband photoluminescence in stepped and tunnel-coupled quantum wells 23

LOED.11p *G. S. Sokolovskii*, I. I. Novikov, M. V. Maximov, A. E. Zhukov, A. G. Deryagin, V. I. Kuchinskii, V. M. Ustinov, W. Sibbett, M. A. Cataluna and E. U. Rafailov
Anomalous dynamics of the two-state lasing quantum dot laser diodes 25

LOED.12p *M. M. Zverev*, D. V. Peregoudov, E. V. Zdanova, N. A. Gamov, V. B. Studionov, S. V. Ivanov, S. V. Sorokin, I. V. Sedova, P. S. Kop'ev and Le Si Dang
Distribution of the non-equilibrium carriers in ZnSe-based electron beam pumped heterostructures 27

Spin Related Phenomena in Nanostructures

SRPN.01o V. A. Shalygin, Ch. Hoffmann, *S. N. Danilov*, S. A. Tarasenko, E. L. Ivchenko, V. V. Bel'kov, D. Schuh, W. Wegscheider and S. D. Ganichev
Circular photon drag effect 29

SRPN.02o *R. V. Cherbunin*, I. A. Yugova, I. V. Ignatiev, I. Ya. Gerlovin, A. Greilich, M. Syperek, L. Fokina, D. R. Yakovlev, Yu. P. Efimov, S. A. Eliseev and M. Bayer
Long-lived spin coherence of electrons in GaAs quantum wells 31

SRPN.03i E. Eble, *O. Krebs*, A. Lemaître, K. Kowalik, A. Kudelski, B. Urbaszek, X. Marie, T. Amand and P. Voisin
Spin physics in charge-controlled InAs-GaAs single quantum dots: optical pumping and hyperfine interaction 33

SRPN.04i *L. Besombes*, Y. Léger, L. Maingault, D. Ferrand and H. Mariette
Spin properties of charge tunable single Mn-doped quantum dot 36

SRPN.05o *D. R. Yakovlev*, A. Greilich, R. Oulton, E. A. Zhukov, I. A. Yugova, M. Bayer, A. Shabaev, Al. L. Efros, I. A. Merkulov, V. Stavarache, D. Reuter and A. Wieck
Optical generation of electron spin coherence in singly charged (In,Ga)As/GaAs quantum dots 37

SRPN.06i *S. A. Crooker*, M. Furis, X. Lou, C. Adelmann, D. L. Smith, C. J. Palmstrøm and P. A. Crowell
Imaging electrical spin injection and spin flow in ferromagnet-semiconductor devices 39

SRPN.07o S. D. Ganichev, V. V. Bel'kov, S. A. Tarasenko, S. N. Danilov, *S. Giglberger*, Ch. Hoffmann, E. L. Ivchenko, D. Weiss, C. Gerl, D. Schuh, W. Wegscheider and W. Prettl
Manifestation of pure spin currents induced by spin dependent scattering processes 42

SRPN.08o *M. M. Glazov* and L. E. Golub
Interplay of Rashba and Dresselhaus spin splittings in 2D weak localization . . . 43

SRPN.09o T. Nguyen-Quang, *J.-M. Jancu* and P. Voisin
Evanescent states in cubic semiconductors with inversion asymmetry and spin-orbit interaction . . . 45

SRPN.10p *P. S. Alekseev*, V. M. Chistyakov and I. N. Yassievich
Theory of spin detector and injector based on spin-dependent resonant tunneling . . . 47

SRPN.11p *V. Ya. Demikhovskii* and D. V. Khomitsky
Energy bands and spin polarization in 2DEG with spin-orbit coupling subject to periodic potential . . . 49

SRPN.12p *M. V. Dorokhin*, V. D. Kulakovskii, S. V. Zaitsev, V. Ya. Aleshkin, N. V. Baidus', Yu. A. Danilov, P. B. Demina, E. A. Uskova and B. N. Zvonkov
Circularly-polarized electroluminescence from InGaAs/GaAs quantum well heterostructures with ferromagnetic Schottky contact . . . 51

SRPN.13p N. S. Averkiev, V. N. Bogomolov, V. A. Berezovets, K. S. Romanov and *I. I. Farbstein*
Spin-dependent phenomena in new nanoobject — 2d layer on the internal interface Te-SiO_2 . . . 53

SRPN.14p *V. N. Gridnev*
Spin relaxation in a ferromagnet/semiconductor hybrid structure . . . 55

SRPN.15p I. S. Lyubinskiy, A. P. Dmitriev and *V. Yu. Kachorovskii*
Spin dynamics in the regime of hopping conductivity . . . 57

SRPN.16p *V. K. Kalevich*, E. L. Ivchenko, M. M. Afanasiev, A. Yu. Egorov, A. Yu. Shiryaev, V. M. Ustinov, B. Pal and Y. Masumoto
Optical pumping and spin-dependent recombination in GaAsN alloys . . . 59

SRPN.17p *A. V. Larionov*, V. E. Bisti, M. Bayer, J. Hvam and K. Soerensen
Control of spin relaxation in GaAs/AlGaAs coupled quantum wells by means of electric field . . . 61

SRPN.18p *M. O. Nestoklon*, L. E. Golub and E. L. Ivchenko
Spin splitting in SiGe/Si heterostructures . . . 63

SRPN.19p I. A. Yugova, A. Greilich, I. V. Ignatiev, *V. A. Nicoluk*, D. R. Yakovlev, M. Bayer, V. Stavarache, D. Reuter and A. Wieck
Fine structure and spin dynamics in InGaAs quantum wells . . . 65

SRPN.20p I. Sänger, B. Kaminski, D. R. Yakovlev, R. V. Pisarev, *V. V. Pavlov*, M. Bayer, G. Karczewski, T. Wojtowicz and J. Kossut
Spin and orbital quantization of electronic states as origins of second harmonic generation in semiconductors . . . 67

SRPN.21p *A. V. Scherbakov*, A. V. Akimov, D. R. Yakovlev, I. A. Merkulov, M. Bayer, A. Waag and L. W. Molenkamp
Multiple spin transfer from a polarized hole to Mn ions in (Zn,Mn)Se/(Zn,Be)Se quantum wells . . . 69

SRPN.22p *S. A. Tarasenko*
Optical orientation of electron spins by linearly polarized light in quantum well structures . . . 71

SRPN.23p *S. Yu. Verbin*, Bipul Pal, M. Ikezawa, I. V. Ignatiev and Y. Masumoto
Nuclear spin fluctuations in InP QDs . . . 73

SRPN.24p *W. Weber*, S. D. Ganichev, Z. D. Kvon, V. V. Bel'kov, L. E. Golub, S. N. Danilov, S. Seidl, D. Weiss, W. Prettl, Hyun-Ick Cho and Jung-Hee Lee
Demonstration of Rashba spin splitting in GaN-based heterostructures . . . 75

SRPN.25p *M. V. Yakunin*, Yu. G. Arapov, V. N. Neverov, S. M. Podgornyh, N. G. Shelushinina, G. I. Harus, B. N. Zvonkov and E. A. Uskova
Spin effects in stereoscopic pictures of the n-$In_xGa_{1-x}As$/GaAs double quantum well magnetoresistance dependencies on the perpendicular and parallel field components . . . 77

Nanostructure Technology

NT.01i *F. Glas* and G. Patriarche
Strain relaxation for controlled nanostructure geometry: from growth-organizing dislocation networks to nanowhiskers 79

NT.03o *Yu. V. Nastaushev*, S. N. Svitasheva, L. V. Sokolov, P. Werner, N. D. Zakharov, T. A. Gavrilova, O. V. Naumova and A. L. Aseev
Tall silicon nanopillars characterization by SEM, IV and SE techniques . . . 82

NT.04o *N. V. Sibirev*, V. G. Dubrovskii, R. A. Suris, G. E. Cirlin, I. P. Soshnikov, V. Gorbenko, M. Tchernycheva, J. C. Harmand and V. M. Ustinov
Theoretical analysis of nanowire growth by MBE and CVD techniques . . . 84

NT.06i *V. Ya. Prinz*
Molecularly thin semiconductor and metal shells: from nanotubes to nanocorrugated quantum systems . . . 86

NT.07o G. Luo, *I. Maximov*, S. Ghatnekar-Nilsson, D. Adolph, M. Graczyk, P. Carlberg, D. Hessman, T. Zhu, Z. F. Liu, H. Q. Xu and L. Montelius
Nanoimprint and reactive ion etching for fabrication of Si/SiO_2 NEMS structures . . . 89

NT.08o *J. Sadowski*, J. Z. Domagałai, V. Osinniyi, J. Kanski, M. Adell, L. Ilver, C. Hernandez, F. Terki, S. Charar and D. Maude
High ferromagnetic phase transition temperatures of thin GaMnAs layers annealed under arsenic capping . . . 91

NT.09p *G. V. Benemanskaya*, G. E. Frank-Kamenetskaya, V. S. Vikhnin and S. N. Timoshnev
Self-organizating chain-like nanostructures created by Cs and Ba adatoms on GaN(0001) n-type surface 93

NT.10p *A. M. Boiko* and R. A. Suris
The role of one-dimensional diffusion in a growth model of the surface of a Kossel's crystal 95

NT.11p *A. D. Bouravleuv*, K. Minami, T. Ishibashi and K. Sato
MnP and Ge self-assembled nanowhiskers on InP(001) 96

NT.12p *G. Comtet*, R. Bernard, E. Boer-Duchemin, G. Dujardin, A. J. Mayne and V. Huc
STM and AFM imaging and manipulation of individual CdSe nanorods 98

NT.13p *V. G. Dubrovskii*, G. E. Cirlin, Yu. G. Musikhin, A. A. Tonkikh, Yu. B. Samsonenko, N. K. Polyakov, S. V. Sorokin, I. V. Sedova, A. A. Sitnikova, S. V. Ivanov and V. M. Ustinov
Kinetic origin of III–V and II–VI quantum dot formation 99

NT.14p *A. V. Dvurechenskii*, N. P. Stepina, V. A. Armbrister, V. G. Kesler, P. L. Novikov, Zh. V. Smagina, A. K. Gutakovskii and V. N. Brudnyi
Homogeneous arrays of Ge nanocrystals grown by pulsed ion-beam nucleation during deposition on dielectric 101

NT.15p *A. V. Kopylov*, A. V. Prinz and V. Ya. Prinz
Novel type of quantum dots based on bell-shaped nanoshells: modeling, fabrication, and properties 103

NT.16p *A. G. Kuzmenkov*, S. A. Blokhin, N. A. Maleev, A. P. Vasil'ev, A. E. Zhukov and V. M. Ustinov
Optimal composition of microcavity structures with selectively oxidized apertures and DBRs 105

NT.18p *E. V. Naumova*, V. Ya. Prinz, S. V. Golod and V. S. Seleznev
Novel continuous regular 3D micro- and nanoshell systems design, fabrication, study and possible applications 107

NT.19p *A. I. Oreshkin*, I. V. Radchenko, S. I. Oreshkin, S. V. Savinov, N. S. Maslova and V. I. Panov
Initial stage of Ag adsorption on Si(110) surface 109

NT.20p *S. Shapoval*, A. Kovalchuk, V. Sirotkin, V. Zemlyakov, V. Krasnik, K. Dudinov, V. Lundin, E. Zavarin, A. Sakharov, A. Tsatsulnikov and V. Ustinov
Passivation of an $Al_xGa_{1-x}N$/GaN heterostructure by a nano-crystalline GaN layer deposited under electron cyclotron resonance plasma conditions 111

NT.21p I. G. Neizvestny, *N. L. Shwartz*, S. A. Teys, A. V. Vershinin, Z. Sh. Yanovitskaya and A. V. Zverev
Examination of 3 BL step structure on Si(557) by Tersoff potential 113

NT.22p *S. V. Sorokin*, I. V. Sedova, A. N. Semenov, T. V. L'vova, O. G. Lyublinskaya, V. A. Solov'ev, A. A. Usikova and S. V. Ivanov
Hybrid AlGaAsSb/InAsSb/CdSeTe heterostructures lattice-matched to GaSb for mid-IR applications 115

NT.23p *M. Tchernycheva*, J. C. Harmand, G. Patriarche, L. Travers and G. Cirlin
Growth and characterization of GaAs and InAs nanowires by molecular beam epitaxy 117

NT.24p *Yu. S. Yukecheva*, A. B. Vorob'ev, V. Ya. Prinz, V. V. Preobrazhenskii, M. A. Putyato and A. K. Gutakovsky
Fabrication of InGaAs/InAsSb micro- and submicrotubes with two-dimensional electron gas on Al_2O_3(0001) and GaSb(100)substrates 119

Quantum Wells and Quantum Dots

QWQD.01o *R. Seguin*, A. Schliwa, S. Rodt, K. Pötschke, U. W. Pohl and D. Bimberg
Systematic size-dependence of anisotropic exchange interaction in InAs/GaAs quantum dots 121

QWQD.02o *A. M. Mintairov*, J. L. Merz, D. S. Sizov, V. S. Sizov, V. V. Lundin, E. E. Zavarin, A. F. Tsatsul'nikov, A. S. Vlasov and N. N. Ledentsov
Single versus ensemble quantum dot emission in near-field spectra of InGaN QWs 123

QWQD.03o M. Geller, *A. Marent*, A. P. Vasil'ev, E. S. Semenova, A. E. Zhukov, V. M. Ustinov and D. Bimberg
5 ms storage time at room temperature in InGaAs quantum dots 125

QWQD.04o *E. V. Tsiper*
Computer simulation of resonant tunneling through quantum antidot in the fractional quantum Hall regime: evidence of fractional quantization of electric charge 127

QWQD.05o R. Oulton, R. V. Cherbunin, A. Greilich, *I. V. Ignatiev*, D. R. Yakovlev and M. Bayer
Hyperfine interaction in InGaAs QDs 129

QWQD.06o *T. M. Burbaev*, V. A. Kurbatov, M. M. Rzaev, N. N. Sibeldin, V. A. Tsvetkov and F. Schäffler
Electron-hole liquid in SiGe potential wells of nanostructures Si/SiGe/Si 132

QWQD.07o I. I. Dobinde, *A. N. Santalov*, E. A. Zhukov and V. S. Dneprovskii
The slowing down of intraband relaxation of CdSe/ZnS quantum dots at high density of the excited carriers 134

QWQD.08p P. V. Petrov, Yu. L. Ivanov, K. S. Romanov, A. A. Tonkikh and *N. S. Averkiev*
Fine structure of A^+ centers in GaAs/AlGaAs quantum wells 136

QWQD.09p *M. V. Entin* and L. I. Magarill
Photocurrent in nanostructures with asymmetric antidots 138

QWQD.10p N. Vukmirović, Z. Ikonić, D. Indjin and *P. Harrison*
The use of hexagonal symmetry for the calculation of single-particle states in III-nitride quantum dots 140

QWQD.11p V. S. Dneprovskii, D. A. Kabanin, *V. L. Lyaskovskii*, T. Wumaier and E. A. Zhukov
Nonlinear absorption and refraction of CdSe/ZnS quantum dots at two-photon resonant excitation 142

QWQD.12p *S. T. Pavlov*, I. G. Lang and L. I. Korovin
Resonant light scattering on quantum dots of any forms and sizes . . . 144
QWQD.13p *A. V. Platonov*, T. Kiessling, G. V. Astakhov, T. Slobodskyy, S. Mahapatra, W. Ossau, G. Schmidt, K. Brunner and L. W. Molenkamp
Anomalous in-plane magneto-optical anisotropy of self-assembled quantum dots . . . 146
QWQD.14p *Ricardo Ramírez*, José Rogan, Griselda García, Claudia Loyola, W. Orellana and Miguel Kiwi
Energy global minima of nanocluster structures . . . 148
QWQD.15p *V. G. Talalaev*, J. W. Tomm, N. D. Zakharov, P. Werner, U. Gösele, B. V. Novikov, A. S. Sokolov, A. Winzer, G. Gobsch, G. E. Cirlin and A. A. Tonkikh
Biasing of stacked InAs quantum dot array: tuning of inter-dot resonance and control of electron-hole alignment . . . 150
QWQD.16p A. Marent, M. Geller, *V. I. Zubkov*, I. S. Shulgunova, A. V. Solomonov and D. Bimberg
Carrier capture into self-organized InGaAs quantum dots . . . 152

Nanostructure Characterization

NC.02o *A. I. Oreshkin*, S. I. Oreshkin, I. V. Radchenko, S. V. Savinov, N. S. Maslova, D. A. Muzychenko, V. N. Mancevich and V. I. Panov
$1/f^{\alpha}$ tunneling current noise characteristics in the vicinity of individual impurity atoms on clean InAs(110) surface . . . 154
NC.03o *O. V. Kononenko*, G. N. Panin, S. V. Dubonos, I. I. Khodos, T. W. Kang and A. N. Baranov
Electrical, optical and structural characterizations of individual ZnO nanorods . . . 156
NC.04p A. Yu. Egorov, V. K. Kalevich, *M. M. Afanasiev*, A. Yu. Shiryaev, V. M. Ustinov, M. Ikezawa and Y. Masumoto
Optical study of band gap dependence on nitrogen content in GaAsN thin layers . . . 158
NC.05p *A. V. Ankudinov*, K. S. Ladutenko, A. N. Baranov, M. G. Rastegaeva, V. P. Evtikhiev and A. N. Titkov
Quantitative study of carriers leakage in operating semiconductor laser diodes by means of scanning Kelvin probe microscopy . . . 160
NC.07p *G. E. Frank-Kamenetskaya*, G. V. Benemanskaya and A. K. Kryzanivskii
Nanoclusters and domains on GaAs(100) surface in the transition from As-rich to Ga-rich . . . 162
NC.08p *L. V. Gavrilenko*, V. Ya. Aleshkin, A. V. Antonov and V. I. Gavrilenko
Fano resonances in photocurrent spectra of semiconductors and quantum well heterostructures doped with shallow donors . . . 164
NC.09p *V. I. Gavrilenko*, V. Ya. Aleshkin, D. V. Kozlov, S. V. Morozov, N. V. Zakrevskii, B. N. Zvonkov, A. V. Filippov, I. M. Markevtsev, A. N. Moiseenko, V. V. Platonov, V. D. Selemir, O. M. Tatsenko, S. Hansel and M. von Ortenberg
Magnetoabsorption study of InGaAs QW heterostructures in megagauss magnetic fields . . . 166
NC.10p *A. G. Gladyshev*, V. G. Tikhomirov, N. A. Maleev, N. V. Kryzhanovskaya, V. S. Mikhrin, A. P. Vasil'ev, A. E. Zhukov, M. V. Maximov and V. M. Ustinov
Nondestructive characterization of pHEMT epitaxial structures based on line-shape model for room temperature photoluminescence spectra . . . 168
NC.11p *E. B. Gorokhov*, V. A. Volodin, D. V. Marin, A. G. Cherkov, A. G. Borisov and S. V. Golod
Study of optical properties of Ge nanoclusters in dielectric films using scanning ellipsometry . . . 170
NC.12p *A. V. Ikonnikov*, Yu. B. Vasilyev, S. S. Krishtopenko, V. Ya. Aleshkin, V. I. Gavrilenko, M. L. Sadowski, W. Knap, Yu. G. Sadofyev, S. R. Johnson and Y.-H.Zhang
Cyclotron resonance study of InAs/AlSb QW heterostructures in quantizing magnetic fields . . . 172
NC.13p *J.-M. Jancu*, G. C. La Rocca and P. Voisin
Inversion asymmetry and spin-orbit coupling in III–V semiconductors . . . 174
NC.14p *P. Christol*, Y. Cuminal, J. B. Rodriguez, A. Joullié, V. K. Kononenko, A. A. Afonenko and D. V. Ushakov
Electrical and optical properties of InAs/InSb/GaSb superlattices for mid-infrared applications . . . 176
NC.15p *R. N. Kyutt*, A. G. Banshchikov, A. K. Kaveev, N. S. Sokolov, T. Eguchi, Y. Ohtake, M. Tabuchi and Y. Takeda
High resolution X-ray diffraction characterization of MnF_2 epitaxial films with metastable orthorhombic phase . . . 178
NC.16p *M. P. Mikhailova*, K. D. Moiseev, T. I. Voronina, T. S. Lagunova, A. F. Lipaev and Yu. P. Yakovlev
Interface roughness scattering in type II broken-gap GaInAsSb/InAs single heterostructures . . . 180
NC.17p V. V. Shnitov, *V. M. Mikoushkin*, Yu. S. Gordeev, S. Yu. Nikonov, O. V. Boltalina and I. V. Goldt
Plasmon spectrum of $C_{60}F_{18}$ and its transformation under electron irradiation . . . 182
NC.18p *O. S. Komkov*, A. N. Pikhtin and K. V. Bazarov
Optical transitions probability controlled by external electric field in InGaAs/GaAs quantum wells . . . 184
NC.19p *V. I. Sankin*, P. P. Shkrebiy and R. Yakimova
Discovering of Wannier–Stark ladder effect in 4H-SiC natural superlattice p–n junctions . . . 186
NC.20p *S. V. Savinov*, P. I. Arseev, N. S. Maslova, V. I. Panov and C. Van Haesendonck
Bias dependent shift of (2×1) reconstruction surface atomic structures on Ge(111) surface measured by LT STM . . . 188
NC.21p *S. M. Suturin*, N. S. Sokolov, R. N. Kyutt, V. P. Ulin, O. Sakata, K. Sumetani, J. Harada, K. M. Pavlov, Y. Takeda, M. Tabuchi and T. Shimura
X-ray diffraction studies of initial stages of CaF_2/Si(001) growth at high temperatures . . . 190
NC.22p D. M. Bauman, N. M. Shmidt, P. S. Vergeles, *E. B. Yakimov* and B. S. Yavich
Carrier distribution in MQW InGaN/GaN LED structures . . . 192

Excitons in Nanostructures

EN.01o *I. V. Ponomarev*, E. A. Stinaff, M. Scheibner, A. Bracker, M. F. Doty, M. E. Ware, D. Gammon, T. L. Reinecke and V. L. Korenev
Theory of spin states in excitonic quantum dot molecules . . . 194

EN.02o A. Reznitsky, A. Klochikhin, *S. Permogorov*, L. Tenishev, E. Tsitsishvili, R. v. Baltz, H. Kalt and C. Klingshirn
Effect of multiphonon processes on the spin relaxation of excitons localized in semiconductor quantum dots . . . 196

EN.03o *S. V. Goupalov*, B. C. Satishkumar and S. K. Doorn
Direct comparison of Raman intensities from carbon nanotubes under different resonant excitations: Role of exciton decay . . . 198

EN.04o *A. B. Dzyubenko*, D. A. Cosma, T. D. Kelly II, A. R. Todd and A. Yu. Sivachenko
Optics of charged excitons in quantum wells: free versus donor-bound complexes . . . 200

EN.05p *V. F. Agekyan*, I. Akai, N. G. Filosofov, T. Karasawa, G. Karczewski, A. Yu. Serov and N. N. Vassiliev
Exciton and Mn^{2+} intracenter luminescence in ZnMnTe/ZnMgTe heterostructures under high optical excitation . . . 202

EN.07p *V. I. Sugakov* and A. A. Chernyuk
Exciton condensed phase structures in semiconductor quantum wells outside the laser spot . . . 204

EN.08p *S. V. Zaitsev*, M. K. Welsch, A. Forchel, C. R. Becker, L. W. Molenkamp and G. Bacher
Strong coupling, direct and indirect excitons in artificial semimagnetic Cd(Mn,Mg)Te quantum dot molecule . . . 206

EN.09p *M. Fehr*, D. Andronikov, V. Kochereshko, A. Platonov, S. A. Crooker, T. Barrick and G. Karczewski
Temperature effects on exciton and trion states in CdTe quantum well structures . . . 208

Transport in Nanostructures

TN.02o *M. L. Polianski*
Theory of nonlinear conductance fluctuations in quantum dots . . . 210

TN.03o *M. V. Budantsev*, A. G. Pogosov, A. E. Plotnikov, A. K. Bakarov, A. I. Toropov and J. C. Portal
Observation of quantum Hall ferromagnetic state in nanostructured quantum wire . . . 212

TN.04o A. A. Andronov, *D. I. Zinchenko*, E. P. Dodin, Yu. N. Nozdrin, A. Yu. Klimov, V. V. Rogov, A. A. Marmalyuk and A. A. Padalitsa
Electron transport in semiconductor superlattices with narrow minigaps . . . 214

TN.05o V. L. Gurtovoi, S. V. Dubonos, A. V. Nikulov, N. N. Osipov and *V. A. Tulin*
Quantum oscillations of the rectified voltage and the critical current of asymmetric mesoscopic superconducting loops . . . 216

TN.06o *S. Rumyantsev*, A. Vijayaraghavan, S. Kar, A. Khanna, C. Soldano, N. Pala, R. Vajtai, O. Nalamasu, M. Shur and P. Ajayan
Effect of atmospheric pressure on conductance fluctuations in single-wall carbon nanotubes . . . 218

TN.08p *M. M. Mahmoodian* and M. V. Entin
Theory of one-dimensional double-barrier quantum pump in two-frequency signal regime . . . 220

TN.09p *V. A. Margulis* and I. A. Kokurin
Acoustoelectric current in 3D ballistic microconstriction . . . 222

TN.10p *I. V. Rozhansky* and N. S. Averkiev
Role of fluctuations in carrier transfer quantum processes in semiconductor heterostructures . . . 224

TN.11p *I. P. Zvyagin*
Fixed range hopping regime for ac conduction over weakly localized states . . . 226

Nanostructure Devices

ND.01o *D. B. Suyatin*, D. Wallin, L. E. Froberg, L. S. Karlsson, I. Maximov, L. R. Wallenberg, H. Q. Xu and L. Samuelson
Fabrication and electron transport study of three-terminal InAs nanowire junctions . . . 228

ND.02o *A. G. Pogosov*, M. V. Budantsev, R. A. Lavrov, A. Ye. Plotnikov, A. K. Bakarov, A. I. Toropov and J. C. Portal
Suspended single-electron Coulomb blockade transistor . . . 230

ND.03o *A. Khitun*, M. Bao, J.-Y. Lee, K. Galatsis and K. L. Wang
Spin-wave based logic devices . . . 232

ND.04o *M. Tchernycheva*, L. Nevou, L. Doyennette, F. H. Julien, A. Lupu, E. Warde, F. Guillot, E. Monroy, A. Vardi and G. Bahir
Unipolar optoelectronics using group III-nitride quantum wells and quantum dots . . . 234

ND.05o V. A. Krupenin, D. E. Presnov, *V. S. Vlasenko*, N. N. Afanasiev and D. N. Erkhov
Single-electron transistor based on highly doped silicon-on-insulator . . . 236

ND.06p *Chia-Fu Chang*, Yi-Ci Chan and Zou-ni Wan
Dependency microscopic morphological compensation for phase-separated composite film . . . 238

ND.07p A. A. Burlakov, V. L. Gurtovoi, *S. V. Dubonos*, A. V. Nikulov and V. A. Tulin
Multiple and single measurements of a mesoscopic quantum system with two permitted states . . . 240

ND.08p *A. A. Greshnov*, D. M. Bauman, B. Y. Ber, A. E. Chernyakov, A. P. Kovarskyi, A. M. Kovtunovich, N. M. Shmidt, B. S. Yavich and A. L. Zakgeim
Comparative study of efficiency of InGaN/GaN MQW light-emitting diodes with different nanostructural arrangement . . . 242

ND.09p *Cheol-Koo Hahn*, Dong Ho Kim, Cheong Hyun Roh, Hong Joo Song, Yeon-Shik Choi, Hoon Kim and Tae Geun Kim
Fabrication and characteristic investigation of resonant-cavity separate absorption and multiplication (RC-SAM) avalanche photodetector . . . 244

ND.11p *D. M. Krasovitskiy*, A. N. Alekseev, S. B Aleksandrov, A. E. Byrnaz, V. P. Chaly, M. V. Pavlenko, S. I. Petrov, Yu. V. Pogorelsky, A. P. Shkurko, I. A. Sokolov, M. A. Sokolov, M. V. Stepanov, A. G. Tkachenko, L. E. Velikovskiy, I. E. Velikovskiy and A. N. Pikhtin
Multilayer AlN/AlGaN/GaN/AlGaN heterostructures with quantum well channel for high power microwave field effect transistors . . . 246

ND.12p J. S. Roberts, Yu. P. Yashin, *Yu. A. Mamaev*, L. G. Gerchikov, T. Maruyama, D.-A. Luh and J. E. Clendenin
Resonance enhancement of spin-polarized electron emission from strain-compensated AlInGaAs-GaAsP superlattices . 248

ND.13p V. A. Tkachenko, *D. V. Sheglov*, Z. D. Kvon, E. B. Olshanetsky, A. V. Latyshev, A. I. Toropov, O. A. Tkachenko, J. C. Portal and A. L. Aseev
Smallest Aharonov–Bohm interferometer, fabricated by local anodic oxidation . . . 250

ND.14p *I. A. Shelykh*, N. G. Galkin and N. T. Bagraev
Gate-controlled spin filter and quantum splitter . . . 252

ND.15p *K. E. Spirin*, S. V. Morozov, V. I. Gavrilenko, Y. Kawaguchi and S. Komiyama
Evolution of the photoresponse time of GaAs/AlGaAs QHE device . . . 254

ND.16p *A. S. Vedeneev* and M. A. Feklisov
Quantum point contacts in inversion p-channel Si-MOS mesoscopic structures: Non-linear conductance and percolation path locality . . . 256

Nanostructures and Life Sciences

NLS.01i *D. Kovalev*
Silicon nanocrystals: photosensitizers for oxygen molecules . . . 258

NLS.02o *B. Bairamov*, V. Toporov, F. Bayramov, M. Petukhov, E. A. Glazunov, B. Shchegolev, G. Irmer, Y. Li, D. Ramadurai, P. Shi, M. Dutta and M. A. Stroscio
Functionalization of semiconductor quantum dots with biomedical structures for biophotonics applications . . . 259

NLS.03o *G. E. Cirlin*, A. A. Evstrapov, A. L. Bulyanitsa, V. G. Dubrovkii, I. P. Soshnikov, A. A. Tonkikh, Yu. B. Samsonenko, N. K. Polyakov, N. V. Sibirev and V. M. Ustinov
GaAs nanowhiskers: MBE growth optimization and observation of space-ordered biological structures . . . 261

NLS.04p T. V. Torchynska, A. Diaz Cano, S. Ostapenko, *Yu. V. Vorobiev*, S. Jimenez-Sandoval, J. Gonzalez-Hernandez and T. Zhukov
Raman study of bio-conjugated CdSe/ZnS core-shell quantum dots . . . 263

NLS.05p *G. G. Zegrya*, N. L. Bazhenov and K. D. Mynbaev
Interaction of isolated semiconductor quantum dots with charged amino acids . . . 265

Wide Band Gap Nanostructures

WBGN.01o A. N. Litvinov, *A. S. Gurevich*, V. P. Kochereshko, A. V. Platonov, B. A. Zyakin, A. Waag and G. Landwehr
Effective radiative recombination of electron and hole Tamm-like interface states in ZnSe/BeTe heterostructures . . . 267

WBGN.02o *T. Kiessling*, A. V. Platonov, G. V. Astakhov, S. Mahapatra, T. Sloboskyy, W. Ossau, G. Schmidt, K. Brunner and L. W. Molenkamp
Phonon replica fine structure in CdSe/ZnSe quantum dots . . . 269

WBGN.03o *D. S. Sizov*, W. V. Lundin, E. E. Zavarin, V. S. Sizov, A. F. Tsatsul'nikov, A. M. Mintairov, R. A. Suris, N. N. Ledentsov and J. Merz
Nonequilibrium carrier statistics in deep InGaN quantum dots . . . 271

WBGN.04p *V. Yu. Davydov*, A. A. Klochikhin, A. V. Sakharov, E. E. Zavarin, M. A. Sinitsyn, A. N. Smirnov, A. P. Skvortsov, M. A. Yagovkina, Hai Lu and William J. Schaff
The band gap composition dependence of InGaN alloys . . . 273

WBGN.05p *A. A. Klochikhin*, V. Yu. Davydov, V. V. Emtsev, A. N. Smirnov, C.-H. Shen, H.-Y. Chen and S. Gwo
Effect of the band bending on the optical spectra of thin epilayers and nano-size samples of n-InN . . . 275

WBGN.06p *P. S. Kop'ev*, V. N. Jmerik, A. M. Mizerov, T. V. Shubina, S. B. Listoshin, M. G. Tkachman, A. A. Sitnikova, R. V. Zolatareva, Ya. Domracheva, M. Yagovkina, M. V. Zamoryanskaya, Min-Ho Kim, Masayoshi Koike, Bum-Joon Kim and S. V. Ivanov
InGaN layers and InGaN/GaN quantum wells with intense room-temperature photoluminescence in a visible spectral range . . . 277

WBGN.07p *M. B. Smirnov*, V. Yu. Davydov and A. N. Smirnov
Lattice dynamics and Raman spectra of InGaN alloys and InN/GaN superlattices . . . 279

WBGN.08p *S. O. Usov*, A. F. Tsatsulnikov, V. V. Lundin, A. V. Sakharov, E. E. Zavarin, D. S. Sizov, Yu. G. Musikhin, N. A. Bert, E. M. Arakcheeva and N. N. Ledentsov
Investigations of a local indium composition in an ultrathin InGaN layers . . . 281

WBGN.09p *S. V. Zaitsev*, A. A. Maksimov, I. I. Tartakovskii, D. R. Yakovlev and A. Waag
Radiative and non-radiative recombination and peculiarities of photoluminescence kinetics in type-II ZnSe/BeTe superlattices . . . 283

Microcavity and Photonic Crystals

MPC.01o *V. D. Kulakovskii*, G. Sek, C. Hofmann, M. N. Makhonin, R. Krebs, A. Loeffler, J. P. Reithmaier, M. Kamp, L. V. Keldysh, T. L. Reinecke and A. Forchel
Effect of cavity mode excitation on emission spectra from pillar microcavity with quantum dots in the active layer . . . 285

MPC.02o *A. V. Baryshev*, R. Fujikawa, A. B. Khanikaev, H. Uchida and M. Inoue
Evidence of a collapse of the TM photonic stop bands in high-contrast photonic crystals . . . 287

MPC.03o *K. A. Atlasov*, K. F. Karlsson, E. Deichsel, B. Dwir, A. Rudra and E. Kapon
Membrane photonic crystal defect cavities for quantum wire lasers and 1D polariton . . . 289

MPC.04o *T. V. Teperik*, V. V. Popov, Yu. A. Avetisyan, F. J. García de Abajo, T. Kelf, Y. Sugawara and J. J. Baumberg
Photonic properties of a nanoporous metal: Rayleigh anomalies versus Mie plasmons . . . 291

MPC.05p *A. A. Dukin* , N. A. Feoktistov, A. V. Medvedev, A. B. Pevtsov, A. V. Sel'kin and V. G. Golubev
Polarization dependent stop-band collapse in 1D photonic crystal . . . 293

MPC.06p *A. A. Fedyanin*, O. A. Aktsipetrov, D. A. Kurdyukov, V. G. Golubev and M. Inoue
Second-harmonic generation spectroscopy of 3D gallium nitride photonic crystals . . . 295

MPC.07p *S. S. Gavrilov*, N. A. Gippius, V. D. Kulakovskii and S. G. Tikhodeev
Collective threshold phenomena in microcavity exciton polariton system . . . 297

MPC.08p *M. A. Kaliteevski*, V. V. Nikolaev, D. M. Beggs, S. Brand and R. A. Abram
Stability of the photonic band-gap in the presence of disorder . . . 299

MPC.09p *V. A. Kosobukin*
Propagation of circularly polarized light waves in magneto-photonic crystals . . . 301

MPC.10p *T. V. Murzina*, O. A. Aktsipetrov, R. V. Kapra, I. E. Razdolskii and M. Inoue
Giant magnetic nonlinear-optical effects in magnetophotonic microcavities . . . 303

MPC.11p *A. N. Poddubny* and E. L. Ivchenko
Exciton polaritons in three- and two-dimensional photonic crystals . . . 305

MPC.12p *S. G. Romanov*, C. M. Sotomayor Torres, J. Ye and R. Zentel
Light scattering in hetero-opals . . . 307

MPC.13p *S. G. Romanov*, M. Bardosova, C. M. Sotomayor Torres, M. Pemble, N. Gaponik and A. Eychmüller
CdTe nanocrystal emission in the vicinity to 2D Langmuir–Blodgett colloidal photonic crystal . . . 309

MPC.14p *I. A. Shelykh*, Yu. G. Rubo, G. Malpuech, D. Solnyshkov and A. V. Kavokin
Superfluid transition and propagation of spinor polariton condensates . . . 311

MPC.15p *O. A. Usov*, A. V. Nashchekin, S. A. Blokhin, E. M. Arakcheeva and E. M. Tanklevskaya
Design, dispersion analysis and fabrication of a photonic microcavity resonant structures . . . 313

MPC.16p *M. M. Voronov*, E. L. Ivchenko, A. N. Poddubny and V. V. Chaldyshev
Special frequencies in optical spectra of resonant Bragg structures . . . 315

Metal Nanostructures

MN.01o S. L. Rumyantsev, *M. E. Levinshtein*, S. A. Gurevich, V. M. Kozhevin, D. A. Yavsin, M. S. Shur, N. Pala and A. Khanna
Low frequency noise in monodispersed platinum nanostructures close to the percolation threshold . . . 317

MN.02o D. Kaczorowski, *M. S. Kononchuk*, R. V. Parfeniev, S. G. Romanov and D. V. Shamshur
Low-temperature magnetic properties of In-opal nanocomposites . . . 319

MN.03o *O. A. Aktsipetrov*, E. M. Kim, T. V. Murzina and A. F. Kravets
Nanomagnetism and nonlinear magneto-optics:
magnetization-induced third-harmonic generation in Co nanostructures . . . 321

MN.04p *O. A. Aktsipetrov*, E. M. Kim, S. S. Elovikov and T. V. Murzina
Giant optical third-harmonic generation in Ag nanoparticles:
nonlinear-optical spectroscopy of local fields in nanostructures . . . 323

MN.05p *A. P. Boltaev* and F. A. Pudonin
Effect of increase of conductivity in nanometer island metallic films under the influence of weak electric field . . . 325

MN.06p *V. A. Kulbachinskii*, P. S. Gurin, R. A. Lunin, Yu. A. Danilov, E. I. Malysheva, Y. Horikoshi and K. Onomitsu
Ferromagnetic clusters and transport in Mn and Mg co-implanted GaAs . . . 327

MN.07p E. M. Epshtein, Yu. V. Gulyaev and *P. E. Zilberman*
Current driven magnetization switching and resistance hysteresis in ferromagnetic nanojunctions . . . 329

Infrared and Microwave Phenomena in Nanostructures

IRMW.01i *D. B. Veksler*, A. El Fatimy, N. Dyakonova, F. Teppe, W. Knap, N. Pala, S. Rumyantsev, M. S. Shur, D. Seliuta, G. Valusis, S. Bollaert, A. Shchepetov, Y. Roelens, C. Gaquiere, D. Theron and A. Cappy
Detection and emission of terahertz radiation by nanometer-size InGaAs and GaN field-effect-transistors 331

IRMW.02o *S. A. Vitkalov*, Jing-qiao Zhang, Z. D. Kvon, J. C. Portal and A. Wieck
Rectification of microwave radiation by asymmetric ballistic dot 334

IRMW.03o *Y. M. Meziani*, T. Otsuji, M. Hanabe, T. Ishibashi, T. Uno and E. Sano
Emission of terahertz radiation from new grating-bicoupled HEMT device 336

IRMW.04o M. Debbichi, A. Ben Fredj, A. Bhouri, M. Saïd, J.-L. Lazzari, P. Christol, Y. Cuminal, *A. Joullié* and V. K. Kononenko
Nitride-based quantum-well lasers on InAs substrate for midwave-infrared emission 338

IRMW.05p *A. A. Dubinov*, A. A. Afonenko and V. Ya. Aleshkin
The generation of terahertz radiation in GaP-based semiconductor waveguide 340

IRMW.06p *D. A. Firsov*, L. E. Vorobjev, V. A. Shalygin, V. Yu. Panevin, A. N. Sofronov, D. V. Tsoy, A. Yu. Egorov, A. G. Gladyshev and O. V. Bondarenko
Spontaneous terahertz emission from stressed GaAsN/GaAs heterostructures 342

IRMW.07p *S. V. Morozov*, K. V. Maremyanin, E. V. Demidov, V. I. Gavrilenko, W. Knap, J. Lusakowski, M. A. Poisson, E. Moran, C. Dua, C. Caquiere and D. Ducatteau
Electron transport and detection of terahertz radiations by GaN/AlGaN submicronic field effect transistor 344

IRMW.08p *V. V. Popov*, G. M. Tsymbalov, D. V. Fateev and M. S. Shur
Slit-grating gate field-effect transistor: a plasmonic device for high terahertz frequencies 346

2D Electron Gas

2DEG.01p *A. A. Bykov*, Jing-qiao Zhang, S. Vitkalov, A. K. Kalagin, D. R. Islamov and A. K. Bakarov
Effect of dc and ac excitations on the longitudinal resistance of a 2D electron gas in highly doped GaAs quantum wells 348

2DEG.02p *A. V. Germanenko*, G. M. Minkov, O. E. Rut, A. A. Sherstobitov, V. A. Larionova, A. K. Bakarov and B. N. Zvonkov
Interaction correction to the conductivity of 2D electron gas in the diffusion regime 350

2DEG.03p *I. N. Kotel'nikov*, E. M. Dizhur, A. N. Voronovskii and S. E. Dizhur
Tunnel density of states at the Fermi level in the two-dimensional electron system of the delta-doped layer in GaAs . . 352

2DEG.04p *G. M. Minkov*, A. V. Germanenko, O. E. Rut, A. A. Sherstobitov, L. E. Golub and B. N. Zvonkov
The transparent case of the metallic-like temperature dependence of the conductivity in 2D system 354

2DEG.05p *A. B. Vorob'ev*, K.-J. Friedland, H. Kostial, R. Hey, Ju. S. Yukecheva, U. Jahn, E. Wiebicke and V. Ya. Prinz
Magnetotransport properties of high-mobility two-dimensional electron gas on cylindrical surface 355

2DEG.06p A. V. Chaplik and *L. I. Magarill*
Bound states in a 2D short range potential induced by spin-orbit interaction 357

Si-Ge Based Nanostructures

SGBN.01p M. V. Shaleev, *A. V. Novikov*, A. N. Yablonskiy, O. A. Kuznetsov, Yu. N. Drozdov, D. N. Lobanov and Z. F. Krasilnik
Effect of tensile-strained Si layer on photoluminescence of Ge(Si) self-assembled islands grown on relaxed SiGe/Si(001) buffer layer 359

SGBN.02p *V. A. Zinovyev*, G. Vastola, F. Montalenti and Leo Miglio
Strain mapping at the surface of nanometric Ge/Si(100) 3D islands 361

SGBN.03p *A. F. Zinovieva*, A. V. Nenashev and A. V. Dvurechenskii
Fluctuation-stimulated spin relaxation in array of Ge quantum dots 363

Tunnelling Phenomena

TP.01p A. A. Gorbatsevich, *V. V. Kapaev* and M. N. Zhuravlev
Inverted resonant tunneling heterostructures 365

TP.02p *V. G. Popov*, Yu. V. Dubrovskii, L. Eaves and M. Henini
Elastic 2D-2D tunnelling and the zero-bias anomaly in an in-plane magnetic field 367

TP.03p *V. A. Sablikov*
The inter-subband interaction effect on the electron transport in quantum contacts 369

Closing Session

CPS.02i J. Kasprzak, M. Richard, S. Kundermann, A. Baas, P. Jeambrun, J. Keeling, F. M. Marchetti, M. H. Szymanska, R. André, J. L. Staehli, P. B. Littlewood, B. Deveaud and *Le Si Dang*
Bose–Einstein condensation of microcavity polaritons — myth or reality? 371

Author Index 372

Unprinted Papers

The papers listed below are included in the Symposium Programme, but not printed in the Proceedings, as the authors had not submitted electronic files in due time.

OPS.01pl *L. V. Keldysh*
The title will be announced later

LOED.01i *E. L. Portnoi*
Picosecond quantum dot heterostructure laser

NT.05i *O. G. Schmidt*
Connecting bottom-up and top-down: seeded quantum dot crystals, flexible ring resonators, radial superlattices and nanochannel network

NT.17p *A. A. Lebedev*, A. M. Strel'chuk, A. N. Kuznetsov, L. M. Sorokin, A. S. Tregubova, G. N. Mosina, P. L. Abramov, A. E. Cherenkov and A. V. Sadokhin
SiC Nanostructures grown by sublimation epitaxy

NC.01i *M. Wu*
Optoelectronic tweezers — a new tool for optical manipulation of micro and nano objects

NC.06p *S. Yu. Davydov*, A. A. Lebedev and O. V. Posrednik
On the estimations of the transition energies in eterostructures based on the silicon carbide polytypes

IN.01o V. P. Chaly, Ju. V. Pogorelsky, *A. N. Alexeev*, A. H. Filaretov
Russian MBE systems as a tool for nanoelectronics

IN.02o *V. A. Bykov*, V. P. Chaly, V. Polyakov
NANOFABs as instruments for nanoelectronics — concept of the development

TN.01i *H. Kalt*
Quasi-ballistic transport of excitons in quantum ells

TN.07p *V. A. Gergel* and M. N. Yakupov
Quasi-hydrodynamic simulation of electroconductivity of nano-dimensional multilayered uniform doped heterostructures

ND.10p O. P. Pchelyakov, V. V. Preobrazhenskii, M. A. Putyato, *A. A. Kovalyov* and N. N. Rubtsova
New technique of phase control for laser mirrors based on semiconductor heterostructures

CPS.01i *F. Beltram*
Surface acoustic waves for single-electron manipulation and single-photon generation

CPS.03i *Ren Xiaomin*
High speed, high quantum efficiency, narrow linewidth and tunable selective photodetection based on novel device structures

AIXTRON Young Scientist Award

In 1999, the Symposium Programme Committee and the Board of AIXTRON AG (Germany) established a special award to honour a young scientist who will present at the Symposium the best paper in the field of solid state nanostructures. The award comprises a diploma and since 2004 a $1000 reward sponsored by AIXTRON.

The AIXTRON Young Scientist Award recipients are:

1999 **Alexey R. Kovsh**, Ioffe Institute, St Petersburg, Russia
2000 **Thomas Gruber**, Physikalisches Institut, Universität Würzburg, Würzburg, Germany
2001 **Ivan Shorubalko**, Department of Solid State Physics, Lund University, Lund, Sweden
2002 **Scott Kennedy**, Department of Electrical and Computer Engineering, University of Alberta, Edmonton, Canada
2003 **Sergey A. Tarasenko**, Ioffe Institute, St Petersburg, Russia
2004 **Ivan A. Dmitriev**, Ioffe Institute, St Petersburg, Russia
2005 **M. Kuntz**, Institut für Festkörperphysik, Technische Universität Berlin, Germany

Dr. M. Kuntz
became the recipient of AIXTRON Award for the presentation of the paper:

10 Gb/s data modulation and 50 GHz mode locking using 1.3 µm InGaAs quantum dot lasers

Co-author: *G. Fiol, M. Lämmlin, D. Bimberg, A. R. Kovsh, S. S. Mikhrin, A. V. Kozhukhov, N. N. Ledentsov, C. Schubert, V. M. Ustinov, A. E. Zhukov, Yu. M. Shernyakov, A. Jacob and A. Umbach.*

PROCEEDINGS

14th Int. Symp. "Nanostructures: Physics and Technology"
St Petersburg, Russia, June 26–30, 2006

Growth-related aspects of nanowire fabrication

W. Seifert
Solid State Physics, Lund University, Box 118, S-221 00 Lund, Sweden

Abstract. The progress in realization of nanoscale devices and systems is dependent on the ability to produce nanostructures and nanostructured materials with controlled morphology and composition. Such structures in form of, e.g. nanowires, grow in a highly anisotropic growth mode typically assisted by catalysts like Au, oxygen, or simply defined by growth on templates. We focus in the presentation on (i) the present understanding of the role of Au in vapor-liquid-solid growth processes, (ii) the ways to affect the crystallographic perfection of nanowires by chosing different growth directions and (iii) ways to avoid Au as a catalyst.

Introduction

Semiconductor nanowires (NWs) as one-dimensional structures and building blocks for nano-devices have received increased attention in recent years. Controlling the one-dimensional growth on a nanometer scale offers unique opportunities for combining materials, manipulating properties, and designing novel devices. For most cases nanowire growth has been performed by using "catalysts" in the so-called vapor-liquid-solid (VLS) [1] or vapor-solid-solid (VSS) mechanisms [2, 3]. A very common catalyst metal is Au, which is, however, known to produce unwanted deep levels, especially in silicon [4]. Alternatively, nanowires can be grown by self-catalytic processes. Here one constituent of the wire material forms the catalytic droplet, enabling VLS-growth on top of the wire, for example in In(liquid)/InP wire growth [5]. Also examples of catalyst-free growth have been reported, the detailed mechanisms for these cases are still under debate [6, 7]. In some cases, traces of other materials, as for instance oxygen, have been found to be involved in growth (oxygen-assisted growth [8]). In this presentation we will analyze some aspects of growth when Au is used as a catalyst.

1. Functional elements to be realized in NWs

Nanowire growth processes are characterized by highly anisotropic growth in axial direction, whereas growth in radial direction is kinetically suppressed. One can use such one-dimensional structures simply as nanowires. By building in segments of another material, see Figure 1a, one can get barriers or quantum dots within these wires, which can be used for a variety of applications as for instance single electron transistor structures [9], resonant tunneling devices [10] or, in multiple heterostructures, for e.g. quantum cascade effects. By a proper change of growth conditions (temperature, composition, ...) the kinetic hindrance for growth on the side-facets can be overcome and core-shell structures can be fabricated, see Figure 1b. Such core-shell structures have a high potential for several applications: (i) the bandstructure of the core can be tuned by stress in the core/shell materials combination, (ii) the shell can be modulation doped and one-dimensional electron gas or one-dimensional hole gas structures can be expected, (iii) with multiple shells complete LED-structures can be produced [13] and, (iv) as a last example, by selectively etching out the core-material, nanotubes can be fabricated [12]. Besides the structures demonstrated in Figure 1 more complex hierarchical structures can be realized, as for instance nanotrees by sequential seeding of the Au-catalyst [15].

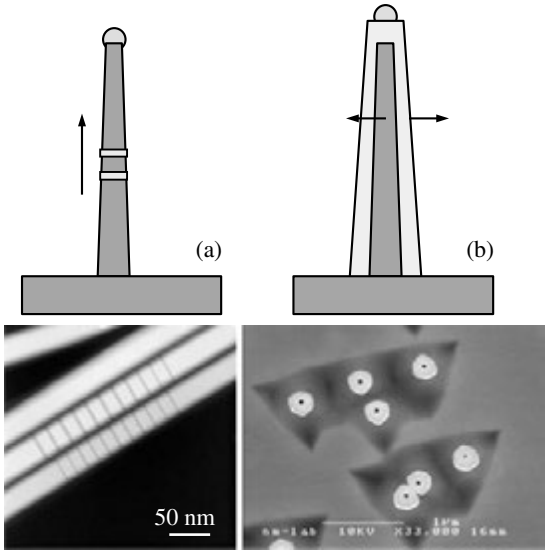

Fig. 1. Schematics of realisation of functional elements in nanowires for Au-assisted growth in (a) axial direction, and (b) radial direction. The arrows indicate the growth direction. The TEM-image on the left shows NWs of InAs with segments of InP, grown by CBE (Linus Fröberg *et al* [11]). The SEM-image on the right is a top-view on GaAs/AlInP core-shell structures grown by MOVPE after selectively etching out the GaAs-core, result: AlInP nanotubes (Niklas Sköld *et al* [12]).

2. Peculiarities when using Au as growth-catalyst

Au was for long time thought to be an ideal catalyst for nanowire growth. It is considered to be inert to large degree and is over long growth-times remaining as a droplet on top of the wires. The solubility in the growing materials is low. Unwanted electronic levels are known only for silicon. However, more detailed investigations have shown that this view needs to be specified:

(i) the Au-particle must not necessarily be a liquid droplet [2, 3]. For growth at lower temperatures Au can be active also in a solid state (vapor-solid-solid growth). For growth of InAs-wires in MOVPE we could show that wires grow only when Au is solid, whereas above the melting point at $\approx$ 490 °C Au does not support wire growth [16]. This has nothing to do with the thermal instabilty of InAs at higher temperatures, since by changing the growth mechanism InAs wires grow also at much higher temperatures (e.g. oxygen-assisted).

(ii) TEM investigations performed in-situ during Au-assisted growth of Si nanowires have shown that Au wets the sur-

faces [17]. Surface diffusion of Au can lead to depletion of Au in the particles with the consequence that wire growth eventually terminates. Simultaneously, these diffusion processes can mediate some interactions between the different wires in a growing ensemble with results in analogy to Ostwald ripening, i.e., the larger Au particles increase on cost of the smaller particles.

(iii) It is worth to be mentioned that Au in many cases does not act as a real catalyst, but more as a very efficient collector of precursor components from the growth environment [18]. This becomes obvious if one compares the Arrhenius activation energies, E_A, which one can extract from the plot $\ln(R_L) = f(1/T)$ (with R_L the length growth rate). For GaAs wire growth in MOVPE, E_A is in the order of 67–75 kJ/mol [19], the same value as has been found for GaAs planar growth without Au [20]. For Au-assisted growth of Si-wires the same effect: $E_A \approx 170$ kJ/mol in Wagners wire growth experiments as well as in planar Si growth [1]. However, under certain circumstances this activation barrier can be lower, i.e., a real catalytic effect has to be considered, as has been observed in the TEM-investigations with rather low Si_2H_6 precursor pressures and low growth rates [21].

(iv) By considering the Au particle as the sink in supersaturation, embedded in a supersaturated vapor phase, one can model the growth process in a simple way [18], assuming that precursor components diffuse within a distance λ towards the Au particle, where they will be incorporated at the Au/nanorod interface. The length growth rate R_L for wires with a diameter of $2r$ is then:

$$R_L \propto (P - P_\infty \exp[(2\sigma_{vl}\Omega)/rkT])/(2\pi mkT)^{1/2} \times (1+\lambda/r) .$$

P stands for the reactant pressure surrounding the wire, P_∞ is the reactant pressure within the droplet of infinite size, σ_{vl} is the surface energy density at the vapor-liquid interface, Ω is the molar volume of the reactant species and m their mass. This proportionality can be discussed as follows: For wire growth with small particles, working close to equilibrium, the r-dependence in the left part of the formula can be dominating. The consequence is that thicker wires grow faster than thinner ones and, in the extreme case, that wires don't grow below a certain minimum radius. This is what Givargizov found for growth of Si wires in the $SiCl_4/H_2$ system [22]. For wire growth with larger particles and under high supersaturations, the Gibbs/Thomson effect can be neglected, the length growth rate increases with the reactant pressure P and, due to the term λ/r, thinner wires grow faster than thicker wires. This is the common case observed in MOVPE [23] as well as MBE [24, 25] experiments.

3. Au-free growth techniques

III–V nanowires, especially nanowires of InAs, have a high potential to be used complementary in combination with Si for high-mobility applications. For this purpose, however, nanowires grown Au-assisted impose severe restrictions due to the introduction of deep-level defects into Si. We reported recently that InAs nanowires can be obtained epitaxially on various substrates without any metal catalyst when one covers the substrates by a thin layer of SiO_x ($x \approx 1$) prior to InAs growth [26]. The mechanism is to classify as an oxide-assisted growth mechanism. X-ray diffraction measurements indicate

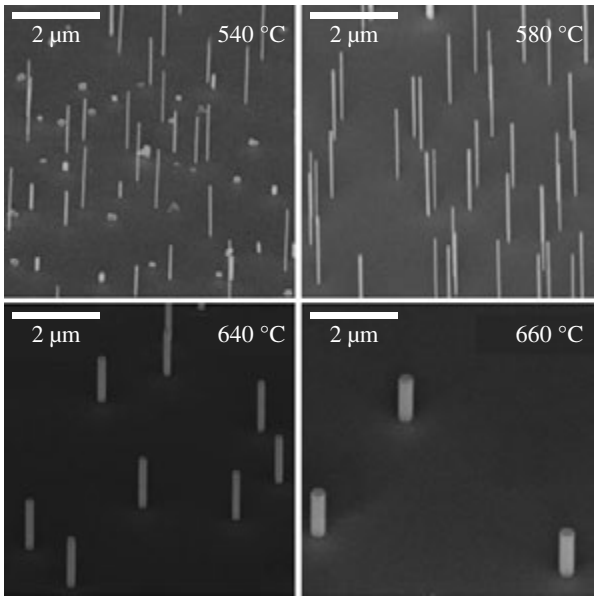

Fig. 2. SEM images (45 ° tilt) of InAs wires grown Au-free (SiO_x-assisted) in MOVPE on InP(111)B at different temperatures, growth time was 60 s. Note that for growth at lower temperatures InAs clusters compete with nanowires.

that the wires form in part in the wurtzite modification and grow spontaneously in c-direction [000.$\bar{1}$], equivalent to the cubic [$\bar{1}\bar{1}\bar{1}$] direction. One characteristics of these wires is that they grow with no detectable tapering, i.e., their thickness is equal over the whole length of the wire. There are some similarities to the wires grown template-assisted out of holes in SiO_2 masked areas [7].

4. Growth directions and crystallographic perfection

In most cases (particle assisted as well as oxide-assisted) nanowires grow spontaneously in c-direction, i.e. ⟨111⟩B or ⟨000.1⟩B. This direction is characterized by an easy formation of twins and stacking faults, which can be avoided by growth in other directions, as for instance ⟨001⟩, ⟨211⟩, ⟨11$\bar{2}$.0⟩, or ⟨10$\bar{1}$.0⟩. These alternative growth directions are sometimes observed to occur sporadically. A deliberate definition, however, has been demonstrated to be possible by careful selection of substrate orientations [13, 27, 28]. In case of Au-assisted growth of InP it has been shown that InP wires with high crystallographic perfection can be grown in ⟨001⟩ direction on (001) substrates simply by suppressing pre-reactions of the Au-particle with the (001) substrate before wire growth [28].

5. State of the art and outlook

A few examples of wire-based working devices will be discussed: (i) LEDs made from p- and n-doped GaAs [29], and, more recently, blue emitting LEDs made from GaN/GaInN nanowires grown in axial direction [30] as well as GaN/GaInN core-shell structures, grown radially [13]; (ii) single-electron transistors based on InAs/InP heterostructures [9] and (iii) resonant tunneling devices made in the same material combination but with different spacings between the tunneling barriers [10].

Acknowledgements

This work was carried out within the Nanometer Structure Consortium in Lund and was supported by grants from the Swedish

Research Council (VR), the Swedish Foundation for Strategic Research (SSF), and the EC NoE "SANDiE", NMP4 CT-2004-500101. The author would like to express his thanks for the contributions from L. Samuelson, J. Johansson, T. Mårtensson, K. Dick, B. Wacaser, N. Sköld, L. Fröberg, B. Mandl, J. Stangl and G. Bauer.

References

[1] R. S. Wagner and W. C. Ellis, *Appl. Phys. Lett.* **4**, 89 (1964).
[2] T. I. Kamins *et al*, *J. Appl. Phys.* **89**, 1008 (2001).
[3] A. I. Persson *et al*, *Nature Materials* **3**, 677 (2004).
[4] S. T. Pantelides ed. *Deep centers in semiconductors*, Gordon and Beach: New York (1986).
[5] C. J. Novotny and P. K. L. Yu, *Appl. Phys. Lett.* **87**, 203111 (2005).
[6] P. J. Poole, J. Lefebvre and J. Fraser, *Appl. Phys. Lett.* **83**, 2055 (2003).
[7] J. Motohisa *et al*, *J. Cryst. Growth* **272**, 180 (2004).
[8] S. T. Lee, N. Wang and C. S. Lee, *Materials Sci. Engn.* **A286**, 16 (2000).
[9] C. Thelander *et al*, *Appl. Phys. Lett.* **83**, 2052 (2003).
[10] M. T. Bjork *et al*, *Appl. Phys. Lett.* **81**, 4458 (2002).
[11] L. Froberg *et al*, unpublished.
[12] N. Skold *et al*, unpublished.
[13] F. Qian *et al*, *Nano Letters* **4**, 1975 (2004).
[14] P. Mohan *et al*, *Appl. Phys. Lett.* **88**, 013110 (2006).
[15] K. Dick *et al*, *Nature Materials*, **3**, 380 (2004).
[16] K. Dick *et al*, *Nano Letters* **5**, 761 (2005).
[17] J. B. Hannon *et al*, *Nature* **440**, 69 (2006).
[18] W. Seifert *et al*, *J. Crystal Growth* **272**, 211 (2004).
[19] M. Borgstrom *et al*, *J. Cryst. Growth* **260**, 18 (2004).
[20] D. H. Reep and S. K. Gandhi, *J. Electrochem. Soc.* **131**, 2697 (1984).
[21] S. Kodambaka *et al*, *Phys. Rev. Lett.* **96**, 096105 (2006).
[22] E. I. Givargizov, *J. Cryst. Growth* **31**, 20 (1975).
[23] J. Johansson *et al*, *J. Phys. Chem.* **B 109**, 13567 (2005).
[24] L. Schubert *et al*, *Appl. Phys. Lett.* **84**, 4968 (2004).
[25] V. G. Dubrovski *et al*, *Phys. Rev.* **B 71**, 205325 (2005).
[26] B. Mandl *et al*, *Nano Letters*, submitted.
[27] T. Kuykendall *et al*, *Nano Letters* **3**, 1063 (2003).
[28] U. Krishnamachari *et al*, *Appl. Phys. Lett.* **85**, 2077 (2004).
[29] K. Haraguchi *et al*, *Appl. Phys. Lett.* **60**, 745 (1992).
[30] H. M. Kim *et al*, *Nano Letters* **4**, 1059 (2004).

14th Int. Symp. "Nanostructures: Physics and Technology"
St Petersburg, Russia, June 26–30, 2006

Tunnel injection quantum dot lasers on GaAs, InP, and silicon

P. Bhattacharya[1], Z. Mi[1], J. Yang[1] and S. Fathpour[2]

[1] Solid-State Electronics Laboratory, Department of Electrical Engineering and Computer Science, University of Michigan, Ann Arbor, MI 48109-2122, USA
[2] Electrical Engineering Department, University of California, Los Angeles, CA 90095-1594, USA

Abstract. We have investigated the molecular beam epitaxial growth and characteristics of In(Ga)As tunnel injection quantum dot lasers on GaAs, InP, and Si substrates. These devices exhibit nearly ideal characteristics, such as ultralow threshold current ($\sim$ 70 A/cm^2), temperature invariant operation ($T_0 \approx \infty$), large modulation bandwidth ($f_{-3\mathrm{dB}} = 24.5$ GHz), and near-zero α-parameter and very low chirp ($\sim$ 0.1 Å).

Introduction

Conventional quantum dot (QD) lasers suffer from hot carrier problems due to the presence of a two-dimensional wetting layer [1]. The wetting layer and the localized QD states form an electronically coupled system. At room temperature, the injected electrons predominantly reside in the wetting layer due to its much higher number of available states, and the system can not be described by equilibrium quasi-Fermi statistics. The hot carrier problem leads to severe gain saturation at the QD ground-state lasing energy and limits the modulation bandwidth of QD lasers at room temperature.

Tunnel injection has been used very effectively in suppressing hot-carrier related problems and achieving high speed modulation in quantum well (QW) lasers [2]. In this technique, cold carriers (electrons) are injected by tunneling in the QD lasing states and so they do not heat other carriers or phonons as much, resulting in reduced carrier leakage from the active region and recombination in the cladding layers. As a result, the characteristic temperature T_0 is enhanced and the differential gain $\mathrm{d}g/\mathrm{d}n$ increases substantially, leading to enhanced modulation bandwidth (24.5 GHz in 1.1 μm QD lasers) and reduced threshold current. Fig. 1(a) illustrates the scheme of tunnel injection from an InGaAs QW to an InGaAs QD through an AlGaAs tunneling barrier.

We present a thorough study of the growth and characteristics of tunnel injection quantum dot lasers with operation wavelength λ ranging from 1.0 to 1.7 μm on GaAs and InP. The lasers exhibit nearly ideal characteristics, such as ultralow threshold current ($\sim$ 70 A/cm^2), temperature invariant operation ($T_0 \approx \infty$), large modulation bandwidth ($f_{-3\mathrm{dB}} = 24.5$ GHz), and near-zero α-parameter and very low chirp ($\sim$ 0.1 Å). In addition, we have also investigated the growth and characteristics of QD lasers directly on Si substrates.

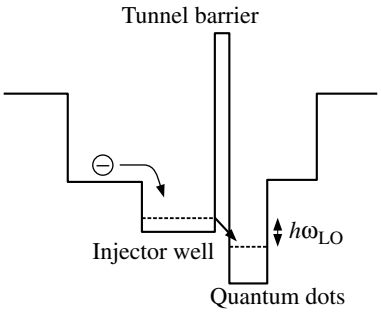

Fig. 1. Illustration of electron injection into a quantum dot gain region by tunnel injection directly into the lasing state of the dot.

1. In(Ga)As quantum dot tunnel injection lasers on GaAs

The active region of the 1.1 μm $In_{0.5}Ga_{0.5}As$ tunnel injection QD lasers consists of a 95 Å $In_{0.27}Ga_{0.73}As$ injector well, a 20 Å $Al_{0.55}Ga_{0.45}As$ tunnel barrier, and three coupled $In_{0.50}Ga_{0.50}As$ quantum dot layers, as illustrated in Fig. 2(a). The growth conditions and parameters of both the injector well and QD layers are carefully controlled so that the ground state of the injector well is approximately one phonon energy ($\sim$ 36 meV) above the lasing ground state of the QDs, allowing efficient LO phonon- assisted tunneling to take place from the injector layer to the dots. The active region of the 1.3 μm InAs tunnel injection QD laser consists of 5 periods of injector well and active QD layer, separated by 400 Å of GaAs barriers. The room-temperature PL emission is shown in Fig. 2(b), where the emission peaks from the QW and QDs are identified. In this design, electrons are tunneled from the ground state of the QW to the first excited states of the QDs. The relaxation time from the dot excited states to the ground state is very small, $\sim 1-2$ ps, due to very efficient electron-hole and electron-electron scattering in the dots under large injection (lasing) conditions. In

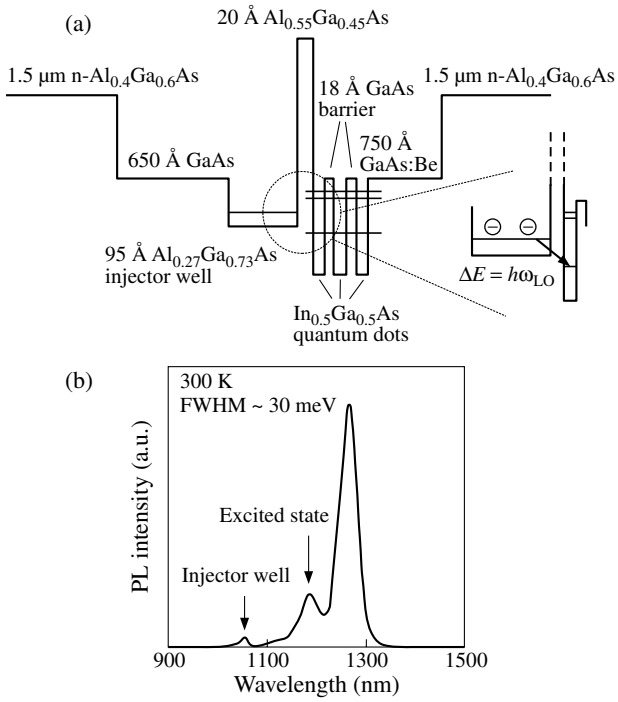

Fig. 2. (a) Conduction band diagram of 1.1 μm p-doped QD tunnel injection laser, and (b) room-temperature PL spectrum of the 1.3 μm p-doped tunnel injection laser heterostructure.

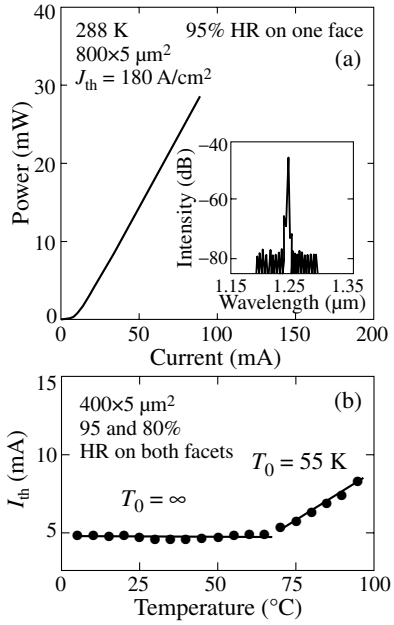

Fig. 3. Characteristic of 1.3 μm tunnel injection quantum dot lasers: (a) light current and output spectrum (inset) and (b) variation of threshold current with temperature.

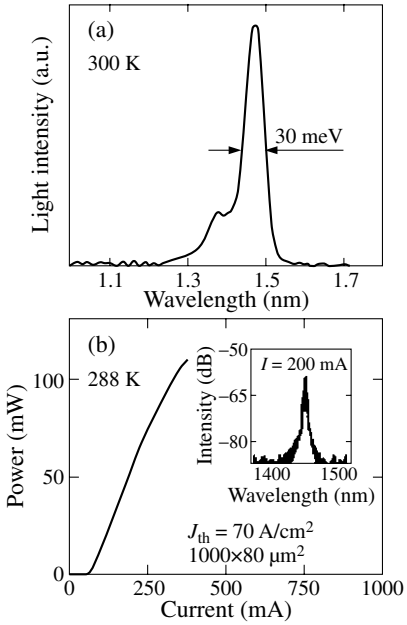

Fig. 5. (a) Photoluminescence emission spectra of InAs metamorphic QDs grown on GaAs, and (b) light-current characterstics of InAs metamorphic QD lasers.

both lasers, the QDs are p-type modulation doped with beryllium.

These devices exhibit low threshold current and large T_0 (upto ∞). The light-current characteristics and variation of of threshold current with temperature of the 1.3 μm lasers are shown in Fig. 3(a) and (b), respectively. We measure a maximum 3-dB bandwidth of $\sim$ 25GHz (Fig. 4(a)) and 11 GHz in the 1.1 and 1.3 μm tunnel injection lasers, respectively. Near-zero α-parameter and negligible chirp ($\sim$ 0.1 Å) are also measured in both 1.1 and 1.3 μm tunnel injection QD lasers, as shown in Fig. 4(b) and (c). The derived dg/dn are 2.7×10^{-14} and 9.8×10^{-15} cm^2 for the 1.1 and 1.3 μm lasers, respectively.

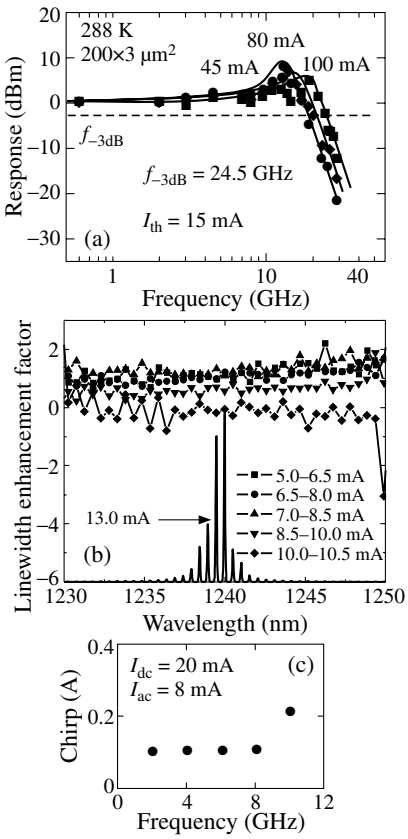

Fig. 4. ((a) Measured small-signal modulation response of 1.1 μm tunnel injection QD laser, and measured α-factor (b) and chirp (c) of 1.3 μm tunnel injection QD laser.

To extend the emission wavelength to 1.55 μm, metamorphic QD heterosructures have to be used due to the large strain. By detailed investigation of the growth kinetics, we have achieved high quality 1.5 μm InAs QDs on GaAs and demonstrated high performance metamorphic QD lasers that exhibit, for the first time, ultra low J_{th} (70 A/cm^2), $T_0\infty$, f_{-3dB} = 5 GHz, chirp $\leq$ 0.3 Å, $\alpha \sim$ 1.0, as shown in Fig. 5(a) and (b). We are currently investigating 1.5 μm InAs tunnel injection QD lasers to achieve large modulaton bandwidth and near-zero α-factor.

2. InAs tunnel injection quantum dash lasers on InP

Self-orgnaized InAs nanostructures grown on InP typically exhibit quantum confined dash-like properties, due to the longer In diffusion length along the [1$\bar{1}$0] direction. Under optimized growth conditions, we have achieved high quality InAs quantum dash layers with significantly reduced inhomogeneous broadening (linewidth $\sim$ 50 meV) at room-temperature. $In_{0.52}Al_{0.24}Ga_{0.24}As/In_{0.52}Al_{0.48}As$ separate confinement heterostructure (SCH) InAs tunnel injection quantum dash lasers were grown on n$^+$ (001) InP substrates. The active region consists of six stacks of coupled well and dash tunnel heterostructures, separated by 400 Å InAlGaAs barriers. In each period, an 80 Å $In_{0.45}Ga_{0.55}As$ quantum well, with PL emission at $\sim$ 1.49 μm, was grown as the injector well. The injector well and quantum dash layer are separated by 25 Å $In_{0.52}Al_{0.48}As$ tunnel barrier. Each quantum dash layer is modulation doped p-type using Be, averaging $\sim$ 50 holes per dash. The devices exhibit relatively low threshold current (J_{th} = 1480 A/cm^2) (Fig. 6(a)), very large T_0 (204 K) (Fig. 6(b)), large modulation bandwidth (f_{-3dB} = 12 GHz), and near-zero α-parameter and

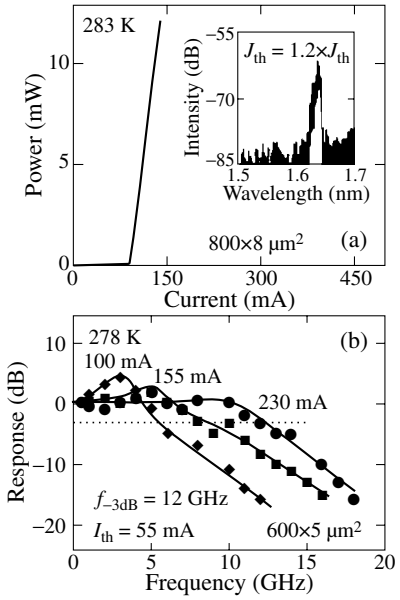

Fig. 6. Characteristics of 1.65 μm InAs tunnel injection quantum dash lasers grown on InP (001): (a) light-current and output spectrum (inset) and (b) small-signal modulation response at various injection currents.

low chirp ($\sim$ 0.3 Å).

3. InGaAs quantum dot lasers monolithically grown on silicon

We have also investigated the growth and characteristicoom-temper misoriented 4° towards [111] are used. A thin ($\leq$ 2 μm) GaAs buffer layer is first grown by metal organic vapor phase epitaxy. To further reduce defect densities in device active regions, ten stacks of InAs QD layers (separated by 500 Å GaAs barriers) were grown near the GaAs/Si interface to serve as three-dimensional dislocation filters. The active region of the GaAs/AlGaAs SCH QD laser heterostructures consists of three sets of coupled $In_{0.5}Ga_{0.5}As$ QDs.

Figure 7(a) shows a cross-sectional transmission electron microscopy (XTEM) image of the InAs QD buffer region, where bending of dislocations induced by InAs QD layers is evident. The XTEM image of the device active region is shown in Fig. 7(b), which is free of any dislocations. The best lasers are characterized by relatively low threshold current ($J_{th} \sim 900$ A/cm^2), high output power ($>$ 150 mW), large characteristic temperature ($T_0 = 244$ K) and constant output

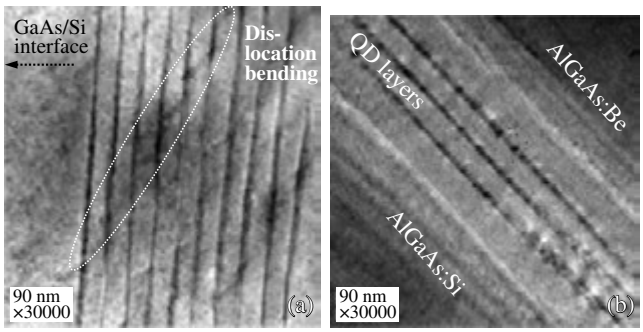

Fig. 7. Cross-sectional transmission electron microscopy of (a) the InAs quantum dot dislocation blocking layer and (b) quantum dot active region from an InGaAs quantum dot laser grown on Si with the incorporation of InAs quantum dots as dislocation filters.

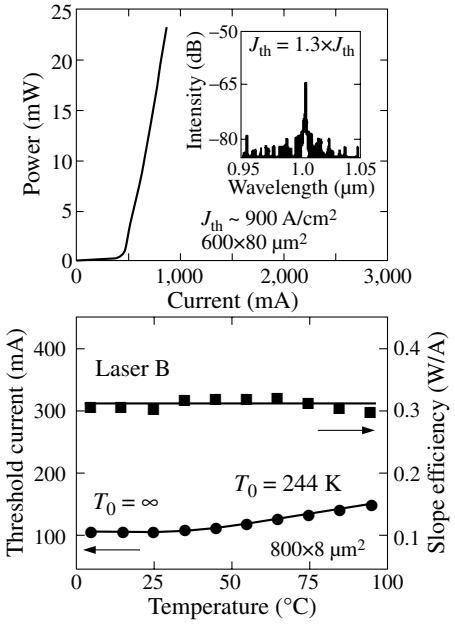

Fig. 8. Output characteristics under pulsed mode (1% duty cycle): (a) light-current and output spectrum (inset) of an undoped layer on Si; and (b) variation of threshold current and slope efficiency with temperature of a p-doped QD laser on Si.

slope efficiency ($\geq$ 0.3 W/A) in the temperature range of 5 to 95 °C, as shown in Fig. 8(a) and (b). We are currently investigating the growth and characteristics of 1.3 μm tunnel injection QD lasers on Si (001) and their integration with Si waveguide.

4. Conclusions

In conclusion, we have demonstrated high performance QD lasers on GaAs, InP, and Si substrates. Utilizing the technique of tunnel injection, nearly ideal characteristics have been achieved, for the first time, in QD lasers. These devices present a practical approach for applications in optical communications and integration with CMOS chips.

Acknowledgements

We wish to thank S. Huang and D. L. Huffaker at the University of New Mexico for the TEM studies on our samples, P. Kondratko and S. L. Chuang at the University of Illinois at Urbana-Champaign for the measurement of α-parameters on 1.3 μm QD lasers. The work is being supported by the Army Research Office and DARPA.

References

[1] D. R. Matthews *et al*, Appl. Phys. Lett. 81, 4904 (2002).
[2] P. Bhattacharya *et al*, IEEE J. Quantum Electronics 32, 1620 (1996).

14th Int. Symp. "Nanostructures: Physics and Technology"
St Petersburg, Russia, June 26–30, 2006

Optical power of a quantum dot laser

Levon V. Asryan
Virginia Polytechnic Institute and State University, Blacksburg, Virginia 24061, USA

Abstract. Light-current characteristic (LCC) of a semiconductor quantum dot laser is thoroughly analyzed in the presence of carrier-density-dependent internal loss in the optical confinement layer. Transformation from the conventional roll-over-shape LCC into the roll-over-shape LCC with two-branches is shown to occur with increasing nonuniformity of quantum dots.

Introduction

Self-organized quantum dots (QDs) have attracted considerable recent attention as a new class of materials for a wide spectrum of applications, among which are notably diode lasers [1, 2]. The advantages of QD lasers stem from a delta-function density of states in individual dots [3, 4]. If all QDs were identical, the gain spectrum would also be very narrow. However, the QDs in actual structures vary, primarily in size and shape, but also in the local strain. The QD-parameter dispersion causes fluctuations in the quantized energy levels and leads to an inhomogeneous broadening in the optical transition energy. Nonuniformity of QDs is the key factor adversely affecting the laser characteristics. Due to the QD-parameter dispersion the maximum gain of the laser decreases [5], threshold current increases [5] and becomes more sensitive to temperature (the characteristic temperature decreases) [6], multimode generation threshold decreases [7], internal differential efficiency and output power both decrease [8]. The QD laser advantages can only be realized if the QDs are sufficiently uniform.

A general trend of the output power degradation with increasing nonuniformity of QDs has been discussed in [8]. In this work, the effect of nonuniformity of QDs on the shape of the light-current characteristic (LCC) is discussed in the presence of carrier-density-dependent internal loss. Such loss is typical in semiconductor lasers with a quantum-confined active region [9]–[12]. Here, a fascinating behavior of the LCC of a QD laser is revealed in the presence of carrier-density-dependent internal loss in the optical confinement layer (OCL).

1. Theoretical model

To calculate the number of photons N in the lasing mode and then the output optical power P, the following rate equations are used.

For carriers confined in a QD (assuming $f_n = f_p$)

$$\frac{\partial f_n}{\partial t} = \sigma_n v_n n\,(1 - f_n) - \sigma_n v_n n_1 f_n - \frac{f_n^2}{\tau_{QD}} - \frac{c}{\sqrt{\epsilon_g}}\frac{g^{max}}{N_S\,S}\,(2f_n - 1)\,N\,. \quad (1)$$

For free carriers in the OCL (assuming $n = p$)

$$\frac{\partial n}{\partial t} = \sigma_n v_n n_1 \frac{N_S}{b} f_n - \sigma_n v_n n \frac{N_S}{b}\,(1 - f_n) - Bn^2 + \frac{j}{eb}\,. \quad (2)$$

For photons

$$\frac{\partial N}{\partial t} = \frac{c}{\sqrt{\epsilon_g}}\,g^{max}\,(2f_n - 1)\,N - \frac{c}{\sqrt{\epsilon_g}}\,(\beta + \alpha_{int})\,N\,. \quad (3)$$

Here σ_n is the cross-section of carrier capture from the OCL into a QD, v_n and n are the free-carrier thermal velocity and density in the OCL, respectively, f_n is the confined-carrier level occupancy in a QD, $n_1 = N_c \exp(-E_n/T)$, N_c is the effective density of states in the OCL, E_n is the carrier excitation energy from a QD to the OCL, the temperature T is measured in units of energy, τ_{QD} is the spontaneous radiative lifetime in a QD, c is the light velocity in vacuum, $\sqrt{\epsilon_g}$ is the group index of the dispersive OCL material, N_S is the surface density of QDs, $S = WL$ is the cross-section of the junction (the QD layer area), W is the lateral size of the device (the QD layer width), L is the cavity length (the QD layer length), g^{max} is the maximum (saturation) value of the modal gain, b is the OCL thickness, B is the radiative constant for the OCL, j is the injection current density, and β is the mirror loss.

In Eq. (3), the internal loss coefficient in the OCL is presented as [11]

$$\alpha_{int} = \alpha_0 + \sigma_{int} n\,, \quad (4)$$

where α_0 is the constant component, which can be caused by scattering at rough surfaces or absorption in the cladding layers; σ_{int} is the effective cross section for internal absorption loss processes. The component $\sigma_{int} n$, which increases linearly with n, can be caused by free-carrier and intervalence band absorption in the OCL.

Eqs. (1)–(4) are analyzed in a steady state ($\partial/\partial t = 0$) and the output optical power is calculated as follows:

$$P = \hbar\omega \frac{c}{\sqrt{\epsilon_g}} \beta N\,, \quad (5)$$

where $\hbar\omega$ is the photon energy.

2. Results and discussion

At small fluctuations in QD sizes or/and low internal loss, the output power increases with the pump current over the entire range of interest [Fig. 1(a)]. Since the maximum gain g^{max} of the laser is controlled by the QD-size dispersion (g^{max} is inversely proportional to the root mean square (RMS) δ of relative QD-size fluctuations [5]), this corresponds to the case of relatively high modal gain.

At larger fluctuations in QD sizes, the slope efficiency changes from positive to negative with increasing pump current [Fig. 1(b)]; the output power goes continuously to zero, which marks the stop of lasing. In what follows, such a shape of the LCC is referred to as a "conventional" roll-over to distinguish from the case of strongly nonuniform QDs.

With increasing RMS of relative QD-size fluctuations up to a certain value, the LCC retains a conventional roll-over shape. Above that value of the RMS, the LCC transforms qualitatively

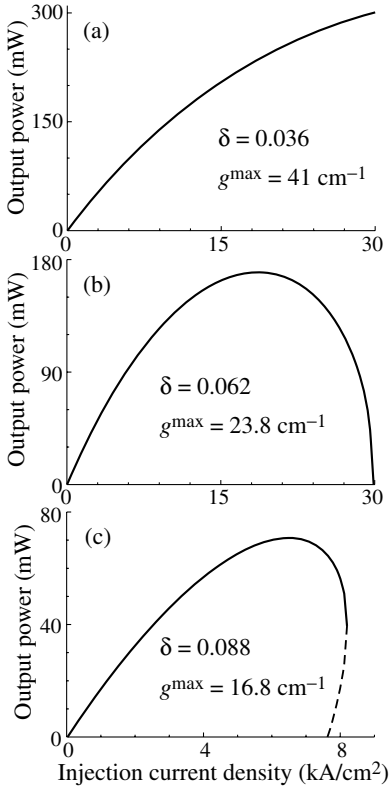

Fig. 1. Light-current characteristics for different values of the RMS δ of relative QD-size fluctuations. Corresponding values of g^{max} of a laser with a single-layer of QDs are also presented. InGaAsP-based structure emitting near 1.55 μm is considered. The internal absorption loss cross-section $\sigma_{int} = 2\times10^{-18}$ cm^2, and the constant component of the internal loss $\alpha_0 = 2$ cm^{-1}.

[Fig. 1(c)]. The stop of lasing with increasing injection current occurs now at a nonvanishing output power: at the maximum operating current, the conventional branch of the LCC (solid portion of the curve) is detached from the X-axis. This upper branch of the LCC is now continued by the second, lower, branch (dashed portion of the curve); in general, with reducing the pump current the output power can follow either the upper (conventional) or lower branch. (The existence of the second branch of the light-current characteristic in semiconductor lasers with a quantum-confined active region in the presence of carrier-density-dependent internal loss was revealed in [11] when discussing the threshold characteristics of the laser.) The quenching of lasing at a nonvanishing output power, often observed experimentally in diode lasers, can suggest the presence of high carrier-density-dependent internal loss and, in the case of QD lasers, large QD-parameter dispersion, thus supporting the model developed here. In this work, the LCC is comprehensively analyzed and the conditions for the conventional roll-over-shape LCC and the LCC with two-branches are formulated.

3. Conclusion

Two considerably different shapes of light-current curves are shown to exist in quantum dot lasers in the presence of carrier-density-dependent internal loss — "conventional" roll-over with single-branch (relatively uniform dots), and roll-over with two-branches (nonuniform dots).

Acknowledgements

This work was supported by the U.S. Army Research Office Grant No. W911-NF-05-1-0308.

References

[1] D. Bimberg, *J. Phys. D.* **38**, 2055 (2005).
[2] A. E. Zhukov, A. R. Kovsh, V. M. Ustinov, N. N. Ledentsov, Zh. I. Alferov, *Microelectronic Engineering* **81**, 229 (2005).
[3] R. Dingle and C. H. Henry, *U.S. Patent 3982207* (1976).
[4] Y. Arakawa and H. Sakaki, *Appl. Phys. Lett.* **40**, 939 (1982).
[5] L. V. Asryan and R. A. Suris, *Semicond. Sci. Technol.* **11**, 554 (1996).
[6] L. V. Asryan and R. A. Suris, *IEEE J. Quantum Electron.* **34**, 841 (1998).
[7] L. V. Asryan and R. A. Suris, *IEEE J. Quantum Electron.* **36**, 1151 (2000).
[8] L. V. Asryan, S. Luryi and R. A. Suris, *IEEE J. Quantum Electron.* **39**, 404 (2003).
[9] L. A. Coldren and S. W. Corzine, *Diode Lasers and Photonic Integrated Circuits*, (New York: Wiley) 594, 1995.
[10] P. S. Zory, Jr., Ed., *Quantum Well Lasers*, (Boston: Academic) 504, 1993.
[11] L. V. Asryan and S. Luryi, *IEEE J. Quantum Electron.* **40**, 833 (2004).
[12] L. V. Asryan, *Appl. Phys. Lett.* **88**, 073107–1 (2006).

14th Int. Symp. "Nanostructures: Physics and Technology"
St Petersburg, Russia, June 26–30, 2006

High-performance vertical-cavity surface-emitting lasers based on sub-monolayer InGaAs quantum dots

S. A. Blokhin[1], N. A. Maleev[1], A. G. Kuzmenkov[1], A. V. Sakharov[1], M. M. Kulagina[1], Yu. M. Shernyakov[1], I. I. Novikov[1], M. V. Maximov[1], V. M. Ustinov[1], A. R. Kovsh[2], S. S. Mikhrin[2], N. N. Ledentsov[2], G. Lin[3] and J. Y. Chi[3]

[1] Ioffe Physico-Technical Institute, St Petersburg, Russia
[2] NL-Nanosemiconductor GmbH, 44227 Dortmund, Deutschland
[3] Industrial Technology Research Institute, Chutung, Hsinchu, 310, Taiwan, Republic of China

Abstract. MBE-grown 0.98 μm vertical-cavity surface-emitting lasers (VCSELs) with sub-monolayer (SML) InGaAs quantum dot (QD) active region and doped AlGaAs/GaAs distributed Bragg reflectors are studied. The devices show very low internal optical losses, less than 0.1% per one pass. SML QD VCSELs with 3 μm tapered aperture show high single-mode output power of 4 mW and external quantum efficiency of 68% at 20°C.

1. Introduction

Vertical cavity surface emitting lasers (VCSELs) are attractive low-cost, high-performance light sources for fiber-optic communication systems, spectroscopy, laser printing and sensors [1]. Current apertures obtained by isolating implantation or selective oxidation technique provide sufficient improvements in VCSELs performance by reducing optical losses and current spreading. However, in case of small-size VCSELs with quantum well active region, the carrier leakage due to lateral diffusion increase the threshold current and decrease the differential efficiency. It is limited VCSEL operation in the fundamental transverse mode, which requires ultra-small current aperture diameter (usually below 4 μm). Using of self-assembled quantum dots (QDs) as the active material of semiconductor lasers can overcome this problem [2]. Besides, it allows achieving the operation in broad spectral range (0.92−1.3 μm for devices monolithically grown on GaAs) and fabricating the sub-micron aperture devices without increase of threshold current.

In the present work, we demonstrate the possibility of using InGaAs QDs formed by sub-monolayer (SML) deposition as an active region for high-performance VCSELs with doped AlGaAs/GaAs distributed Bragg reflectors (DBRs).

2. Experiment

The VCSEL structures were grown on an n^+-type GaAs (001) substrates by molecular-beam epitaxy (MBE) using a Riber 49 system. The epitaxial structure consists of a 33-pair *n*-doped GaAs/$Al_{0.9}Ga_{0.1}As$ quarter-wave bottom DBR, an undoped $Al_{0.15}Ga_{0.85}As$ λ-cavity, and 20-pair *p*-type GaAs/$Al_{0.9}Ga_{0.1}As$ quarter-wave top DBR. Three InGaAs QD layers were formed by sub-monolayer deposition and placed at an antinode of the optic-field intensity. The thickness and composition were chosen in order to obtain 0.98 μm resonance wavelength. The oxide tapered apertures with diameter in 3−12 μm range were formed by selective oxidation of *p*-($AlAs/Al_{0.9}Ga_{0.1}$) layer. This layer was placed at the minimum of optical-field in order to reduce the lateral optical loss. The details of VCSEL structure and processing are described elsewhere [3]. The VCSEL crystals were mounted *n*-side down on cooper heat sinks. The fabricated devices were characterized in pulsed (200 ns pulse width, 1 kHz period) and continuous-wave (CW) regimes in 280−360 K temperature range. The studies of near- and far-filed patterns were carried out by CCD camera in CW regime at room temperature (RT).

3. Results and discussion

3.1. Optical losses

One of the most important characteristic of VCSEL is internal optical losses, which determine the possibility of achievement of the low threshold current, the high external quantum efficiency and output power. Generally, the internal loss includes the absorption losses inside cavity, distributed losses in the DBR mirrors and optical losses due to diffraction at the oxide current aperture. Note that the devices with large aperture size (> 10 μm) have negligible optical scattering losses and modal radiation behavior is relatively weakly depended on injection current.

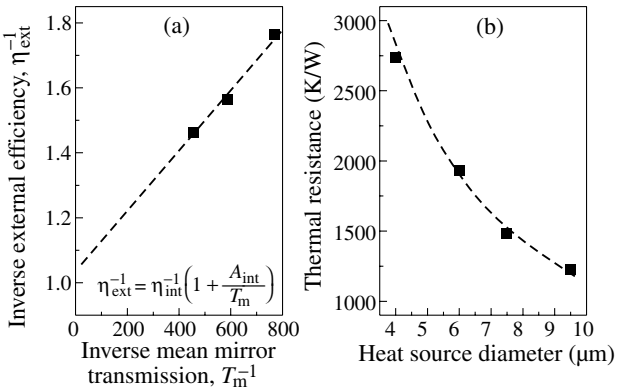

Fig. 1. (a) Inverse external quantum efficiency as a function of inverse mean mirror transmission for 12 μm tapered aperture SML QD VCSELs with 20-top DBR pairs; (b) The measured (fill square) and calculated (dashed line) thermal resistances of SML QD VCSEL as function of heat source size.

The internal losses were derived from the dependence of external quantum efficiency on mirror reflectivity by consequent removing the parts of top DBR (see Fig. 1.a) [4]. As the number of pairs in the top DBR is reduced, the mirror reflectivity is dropped, resulting in the increase of the output optical power and the external quantum efficiency (from 50% up to 64%). The 12 μm tapered aperture SML QD VCSELs demonstrate very low internal one-pass optical losses ($A_{int} = 0.09\%$). The

obtained internal losses are smaller than the best published result for optimized quantum well VCSELs with doped mirrors [5] and only slightly higher than record value for intra-cavity-contacted VCSEL with undoped DBR [4].

3.2. Thermal resistance

Thermal resistance is another important characteristic for any type of VCSELs. It determines the temperature rise in the device with total dissipated power. The internal laser temperature directly influences emission wavelength and threshold current. So, the thermal resistance of the lasers can be estimated by dividing the wavelength shift versus dissipated power to the temperature wavelength shift.

Figure 1b shows the dependence of thermal resistance on the heat source diameter. Note that sizes of heat source and current aperture are unequal due to complex tapered aperture form and current spreading effects. This experimental result agrees well with the thermal resistance calculated in the anisotropic cylinder model of VCSEL [6]. Note that in spite of poor thermal conductivity of AlGaAs alloys in comparison with GaAs and AlAs, the presence of graded interfaces in DBR's are not so critical.

3.3. Single-mode operation

The light-current characteristic of SML QD VCSEL with 3 μm tapered aperture and 18-pair top DBR are shown in Fig. 2. Devices show the room temperature lasing in CW regime with threshold current of 0.6 mA, external quantum efficiency as high as 68% and 4.8 mW maximum output power. The insets in Fig. 2 show spectra of investigated VCSEL at different operation currents in CW regime.

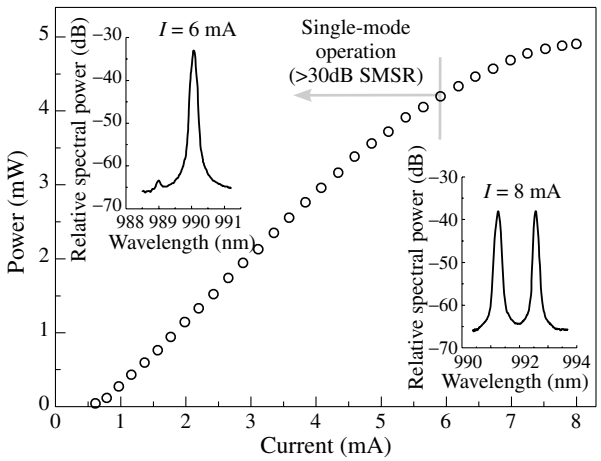

Fig. 2. CW L-I characteristic and lasing spectra (on insets) of 3 μm tapered aperture SML QD VCSEL with 18-pair top DBR at 20°C.

Far-field pattern of investigated VCSEL has Gaussian intensity profile with full-width at half maximum of 6.5° up to 6 mA (see Fig. 3). Further increase of the injection current results in far-field pattern changing and broadening up to 14.5°. Near-filed patterns corresponding to single-mode and multimode CW RT operation are shown in insets to Fig. 3. Above threshold VCSEL emits at fundamental LP_{01} mode, but at higher currents (more than 6 mA), lasing switches to the transverse LP_{11} mode. Maximum CW output power of 4 mW in single-mode regime was achieved at 6 mA with side-mode suppression ratio (SMSR) higher than 30 dB. To the best of our knowledge, this is the highest single-mode output power reported for QD VCSELs.

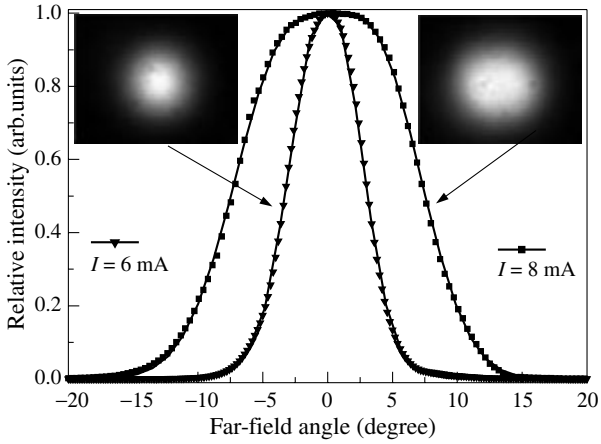

Fig. 3. Far-filed and near-filed (on insets) patterns at operation current corresponding single-mode (6 mA) and multimode (8 mA) CW regime measured at 20°C.

The 3 μm tapered-aperture SML QD VCSELs show the thermal impedance about 2700 K/W. High thermal resistance of these VCSELs results in significant increasing of the active region temperature with injection current (up to 55°C at 6 mA). Nevertheless the device operates in CW regime up to 90°C with maximum single-mode output power of 2.0 mW and threshold current of 2.1 mA.

4. Conclusion

Vertical-cavity surface-emitting lasers with sub-monolayer deposited InGaAs quantum dots in the active region and doped AlGaAs/GaAs mirrors were grown by MBE. Ultimately low internal optical losses (less than 0.1% per one pass) were measured for 10−12 μm aperture multi-mode SML QD VCSELs. The experimental thermal resistances of lasers decrease with increasing aperture and agree well with the thermal resistance calculated in the anisotropic cylinder model of VCSEL. The 3 μm tapered-aperture SML QD VCSELs show lasing at 0.98 μm with threshold current of 0.6 mA, maximum single-mode output power of 4 mW and external differential efficiency of 68%.

Acknowledgements

This work was supported by the Russian Foundation for Basic Research, SANDiE (NMP4-CT-2004-500101) and the Nanophotonics Project (MOEA, Taiwan).

References

[1] C. W. Wilmsen, H. Temkin, L. A. Coldren, *Vertical-Cavity Surface-Emitting Lasers*, Cambridge University Press, 1999.

[2] V. M. Ustinov, A. E. Zhukov, A. Y. Egorov, N. A. Maleev, *Quantum dot lasers*, Oxford University Press, 2003.

[3] S. A. Blokhin, *et al*, *Semicond.* **40**, 663 (2006).

[4] G. M. Yang, M. H. MacDugal, V. Pudikov, P. D. Dapkus, *IEEE Photon. Technol. Lett.* **7**, 1228 (1995).

[5] M. Jungo, F. M. di Sopra, D. Erni, W. Baechtold, *J.Appl. Phys.* **91**, 5550 (2002).

[6] W. Nakwaski, M. Osinski, *Int. J. of High Speed Electronics and System* **5**, 139 (1994).

14th Int. Symp. "Nanostructures: Physics and Technology"
St Petersburg, Russia, June 26–30, 2006

Nonlinear quantum cascade lasers: physics and applications

F. Xie, D. Smith and *A. Belyanin*
Department of Physics, Texas A&M University, College Station, TX77843, USA

Abstract. We describe physics and performance of nonlinear quantum-cascade lasers which support both laser action on the intersubband transition and, at the same time, nonlinear self-conversion of laser light into coherent radiation at different frequencies. Such devices fully utilize huge resonant nonlinearities of the intersubband transitions ($\chi^{(2)} \sim 10^6$ pm/V) and demonstrate high nonlinear efficiency combined with compactness of injection lasers. We show that the proposed approach can greatly enhance the performance of quantum cascade lasers and provide new functionalities. We discuss in detail two examples: extreme frequency up-conversion and broad electric tuning.

Introduction

We have recently shown [1–6] that the standard active region of a quantum cascade (QC) laser can be integrated with a cascade of intersubband transitions designed for the nonlinear conversion of laser light into coherent radiation at a different frequency. In other words, the laser field serves as an intracavity optical pump or drive for the desired nonlinear optical interaction. Any losses of the intracavity optical pump due to resonant absorption or nonlinear optical process can be compensated by laser gain in the active nonlinear medium. This approach allows one to utilize giant resonant optical nonlinearities associated with intersubband transitions in coupled quantum wells (QWs). Generation of the second and third harmonics [4] and sum frequency have been demonstrated. Milliwatt power level for second harmonic generation has been achieved [5]. Recently the first successful experiment on Raman injection laser has been reported [6].

The experiments reported in Refs. [1–6] were mainly a proof of principle. The natural question to ask is whether this kind of devices may have any potential practical benefits as compared to standard QC lasers. One can envision at least several benefits that are usually associated with nonlinear optical sources:

1. Generation at wavelengths that are not easily accessible for QC lasers in general, or within a given material system: for example, in the THz range or at short wavelengths below 3–4 μm;

2. Simultaneous generation at widely separated wavelengths, for example in the mid- and far-infrared;

3. Significantly better tunability and wavelength agility as compared to standard QC lasers;

4. Higher operating temperature, which is essentially defined in our devices by the operating conditions for the drive laser. The drive wavelength can be chosen to fit within the "sweet spot" of the QC lasers (7–9 μm for InGaAs/AlInAs structures) where they are most powerful, efficient, and capable of the continuous-wave room-temperature operation;

5. Other benefits, such as small beam divergence or generation of light with interesting statistical properties, e.g., squeezed or entangled light. Here we consider some examples from the above list and argue that integrated nonlinear QC sources can indeed provide new or enhanced functionalities.

1. Short-wavelength QC lasers

There is currently a lot of interest in trying to push the wavelength of QC lasers to the short-wavelength mid-IR region below 4 μm. In the most mature and well-developed InGaAs/AlInAs material system the shortest attainable wavelength is limited by the band offset $\Delta E_c = 520$ meV. Moreover, the requirements of resonant tunneling and depopulation of the lower laser level limit the energy of the laser transition to about ½ of ΔE_c, i.e. about 5 μm. In strained InGaAs/AlInAs structures the wavelengths of ~ 3.6 μm have been achieved, at the expense of the material quality and deteriorated perfromance. In heterostructures with a very large band offset, for example in InAs/AlSb material system one can have ΔE_c close to 2 eV at the Γ-point. This development created hopes of solving this problem. However, only the small part of this band offset is actually available for lasing in QC devices pumped by resonant tunneling, because lateral L- and X-valleys are located only several hundred meV above the bottom of the conduction band of QWs in these materials. When the upper laser state is higher than the position of lateral valleys, the injection efficiency drops dramatically, essentially killing the laser. No lasing below 4 μm has been reported.

We propose to generate short-wavelength radiation below 4 μm in our integrated nonlinear QC devices by frequency up-conversion of the intracavity optical laser pump via second harmonic generation. We have already demonstrated the second-harmonic generation at 5 μm wavelength with milliwatt power level in InGaAs/AlInAs QC lasers operating at 10 μm [5] (Fig. 1). It is straightforward to redesign the coupled-QW active region in such devices for lasing at ~ 6 μm wavelength and

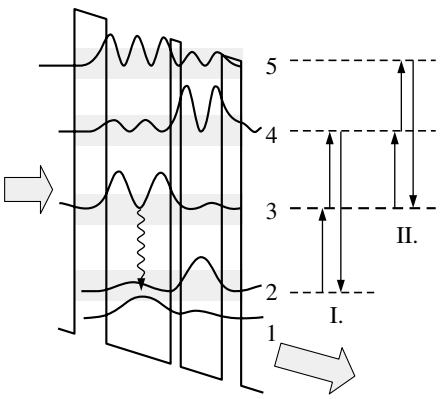

Fig. 1. Conduction band diagram and moduli squared of the essential wavefunctions for the two-quantum-well active region, in which simultaneous generation of the fundamental laser frequency and its second harmonic occur in the vertical cascade of intersubband transitions, as shown by arrows (from [2]). Note the presence of two cascades in this particular structure.

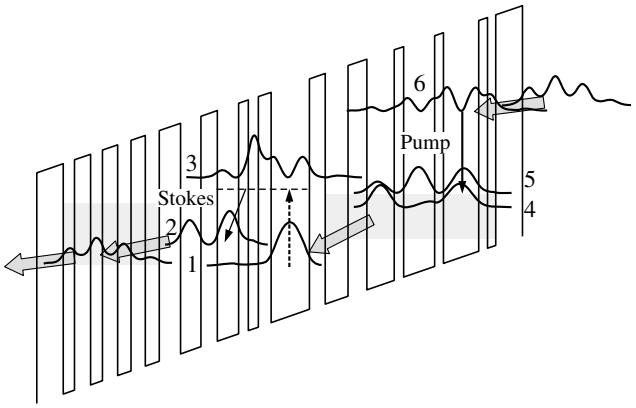

Fig. 2. Active region of Raman injection laser that integrates the fundamental laser cascade 6-5-4 and the resonant cascade of transitions 1-3-2-1 for Raman Stokes lasing [6]. Laser radiation at wavelength 6 μm generated in the fundamental laser cascade (solid blue arrow) serves simultaneously as an internal optical pump in the Raman cascade (dotted blue arrow) for the Stokes laser at 9 μm wavelength (red arrow).

resonant second-harmonic generation at ~ 3 μm. However, it turns out to be important to group the SHG nonlinear section of the device in a separate stack from the pump laser active region, similarly to what is shown in Fig. 3. The calculated frequency up-conversion efficiency is 200 mW/W^2, which corresponds to about 10 mW of the nonlinear power.

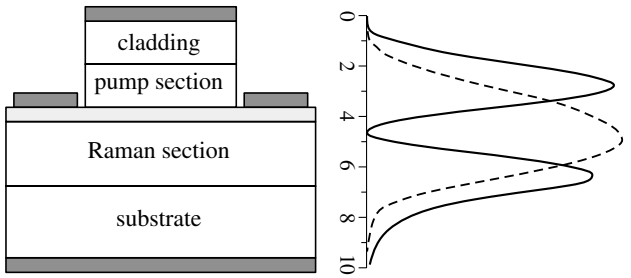

Fig. 3. Design of a broadly tunable Raman laser with independent biasing of the drive and Raman sections. Also shown are the magnetic field squared of the TM_1 mode (solid line) and TM_0 mode (dashed line) at the drive laser wavelength of 6 μm.

2. Electric tuning by Stark effect in Raman lasers

Conventional QC lasers are based on resonant tunneling through a stack of coupled QWs and superlattices. They "resist" any tuning by Stark effect above laser threshold, after the alignment between the injector and the upper laser state is reached and the population inversion gets pinned down to a threshold value. As a result, QC lasers can only be tuned over a limited range of few cm^{-1} by changing the temperature of the heat sink or the injection current. In practice, wide tuning range in QC laser-based sensors is achieved by using an external cavity system. Such systems require external optical elements and moving mechanical parts. Integration of QC lasers with resonant optical nonlinearities provides a new opportunity for fast and broad tuning by changing the bias voltage applied across the nonlinear optical element. Let us consider this tuning mechanism in integrated Raman lasers of the kind realized in Ref. [6] (Fig. 2).

Tunability in conventional Raman lasers or amplifiers is associated with changing the wavelength of the external optical laser pump, while the amount of frequency shift remains fixed and is determined by the phonon frequency. In the integrated devices we have an opposite situation: the drive laser serving as an optical drive for Raman laser is internally generated and its tunability is limited for the same reason as in standard QC lasers. At the same time, the Raman shift is not fixed anymore. It is determined by the energy separation between subbands denoted by 1 and 2 in Fig. 2 below. Since the transition 1-2 is diagonal in space, its energy can be efficiently tuned by the electric field (the linear Stark effect). Calculations show that the change in the electric field by 15 kV/cm leads to a large shift in the Stokes frequency by 120 cm^{-1}. At the same time, the detunings of both pump and Stokes fields from their respective transitions 1-3 and 2-3 remain practically unchanged: their shift is only 1 meV. The dipole moments of these transitions are also changed very little — by less than 0.2 nm. The resulting change in the Raman gain calculated using density-matrix approach is only 3 per cent. Therefore, the wide-range electric tuning of the Stokes radiation is not accompanied by a significant modulation of the output intensity. This is an important advantage of the device.

To increase the electric tuning range and flexibility, the Raman active region should be grouped in a separate stack from the drive laser, so that it can be independently contacted and biased. This design is shown in Fig. 3. Note that the device is expected to generate the TM_1 modes that have zero field at the position of a strongly doped side contact layer, thus minimizing the losses. Also, the TM_1 mode provides better confinement factor and the overlap of the drive field with the nonlinear Raman region.

Acknowledgement

This work has been supported by the National Science Foundation and the Air Force Office for Scientific Research. We thank F. Capasso, C. Gmachl, J. Faist, and C. Sirtori for many useful discussions.

References

[1] N. Owschimikow *et al*, *Phys. Rev. Lett.* **90**, 043902 (2003).
[2] C. Gmachl *et al*, *IEEE J. Quant. Electron.* **39**, 1345 (2003).
[3] O. Malis *et al*, *Appl. Phys. Lett.* **84**, 2721 (2004).
[4] O. Malis *et al*, *Optics Express* **12**, 2972 (2004).
[5] O. Malis *et al*, *Electron. Lett.* **40**, 1586 (2004).
[6] M. Troccoli *et al*, *Nature* **433**, 845 (2005).

14th Int. Symp. "Nanostructures: Physics and Technology"
St Petersburg, Russia, June 26–30, 2006

Thermal effects in quantum cascade lasers

C. A. Evans, V. D. Jovanović, D. Indjin, Z. Ikonić and *P. Harrison*
School of Electronic and Electrical Engineering, University of Leeds, Leeds, LS2 9JT, UK

Abstract. A thermal model of a quantum cascade laser (QCL) is presented. The modelling focuses on an InGaAs/AlAsSb QCL presented in the literature. Using the thermal model in conjunction with a scattering rate calculation allows maximum heat sink temperatures to be calculated for different device geometries and driving conditions. Including thermal effects in the simulations also seem to explain why QCL threshold current densities are often underestimated at higher temperatures.

Introduction

In general QCLs suffer from large threshold current densities which causes significant heating in the active region of the devices and is detrimental to performance. As the temperature increases, more and more carriers are thermally activated into the continuum-like states and the population inversion decreases. This factor makes room-temperature, continuous-wave (cw) operation difficult to achieve. It has been possible, however, using a buried structure in the InP-based material system to develop a mid-infrared ($\lambda \sim 9.1$ μm) QCL operating at room-temperature in cw mode with several milliwatts of output power [1]. This result is encouraging for the many potential applications, in particular gas sensing, which would benefit from high-power, cw, robust, infra-red devices operating at high temperature. In order to improve the temperature performance of QCLs, the effects of thermal heating in the active region must be known and methods developed to improve the heat dissipation from the active region.

The aim of this work is to investigate the effects of device structure and driving conditions on the thermal dynamics inside a QCL device and how these relate to device performance. The QCL modelling extends a previously reported simulation [2] of an experimentally measured $\lambda \sim 3.1$ μm InGaAs/AlAsSb QCL [3].

1. Theory

The QCL output characteristics are calculated using a self-consistent rate equation model [4]. The electron energies and wavefunctions are used to evaluate all the principal electron-electron and electron-longitudinal optical (LO) phonon intra- and interperiod scattering rates. The self-consistent procedure yields the nonequilibrium electron density in each of the subbands, from which the output characteristics (current density J and local gain g) can be calculated. By calculating the waveguide parameters, i.e. the confinement factor (Γ) and waveguide and mirror losses (α_W and α_M), the threshold current can then be determined. To further extend the effects of temperature on the QCL output characteristics, α_W is calculated as a function of temperature.

In order to investigate the thermal dynamics inside a QCL device structure, a thermal modelling scheme was developed based upon the heat equation in two-dimensions

$$\rho c_p \frac{\partial T}{\partial t} = \nabla \cdot [k \nabla T] + g \,, \qquad (1)$$

where ρ is the density of the material, c_p is the specific heat capacity, T is the temperature, k is the thermal conductivity and g is the source power density. Since ρ, c_p and k are temperature dependant, equation (1) is non-linear and is solved explicitly using a finite-difference method to give the nodal temperatures at each time step. Both cw and pulsed mode operating conditions can be simulated by varying the source power density accordingly. Typically, QCL experimental measurements are made *in vacuo* meaning adiabatic boundary conditions are applied to the surfaces in the vacuum, with a constant temperature boundary condition applied to the surface bonded to the heat sink.

The active region of the QCL is made up from a multitude of thin semiconductor layers and due to increased phonon scattering at the interfaces between these layers, the thermal conductivity perpendicular to the layers ($k_{\perp \mathrm{AR}}$) is found to be approximately an order of magnitude smaller than the thermal conductivity in the plane of the layers ($k_{\parallel \mathrm{AR}}$) [5]. In order to accurately model the thermal dynamics inside the QCL, both the non-linear material parameters and the anisotropic active region thermal conductivity must be taken into account. In this work, the temperature dependant $k_{\parallel \mathrm{AR}}$ is taken to be that of bulk InGaAs, and $k_{\perp \mathrm{AR}}$ a tenth of the bulk value. The device structure is taken to be a typical ridge structure of width 10 μm, on an InP substrate with a waveguide configuration as described in [2].

2. Results

The QCL electron dynamics simulation was run at a range of temperatures and an electric field–current density curve calculated at each. By extracting the current densities at the operating bias point (135 kV/cm) for each temperature, the source power density was calculated as function of temperature ($= 1000 \exp(T/1023)$ GW/m^3). This 'quantum source term' was then inserted into the thermal simulations to succinctly describe the heating effects inside the QCL active region due to quantum mechanical processes. The modal gain was calculated at each temperature and by estimating the waveguide and mirror losses at each temperature, a relationship between threshold current and active region temperature was found ($= 2.01 + 1.15 \exp(T/T_0)$ kA/cm^2, where $T_0 = 191$ K, see Fig. 1). However, it is a common problem in QCL calculations to underestimate the threshold current density at higher temperatures [6]. The maximum active region lattice temperature at which laser action at $\lambda \sim 2.85$ μm is predicted was found to be 300 K.

For a pulsewidth of 100 ns with a 10 kHz repetition rate (0.1% duty cycle), thermal simulations were run to find the corresponding heat sink temperature for each of the active region temperatures and calculate the new threshold current–temperature relationship. This value of repetition rate was cho-

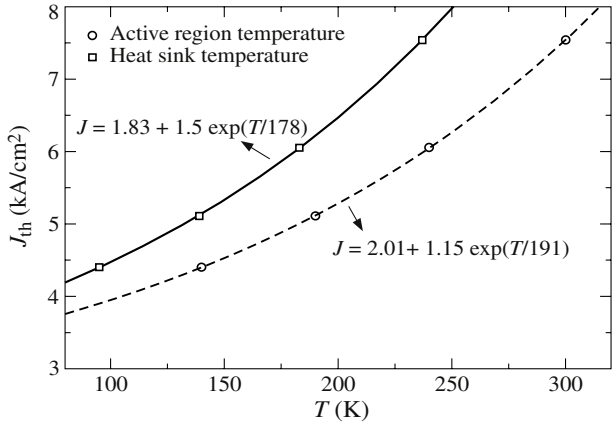

Fig. 1. Calculated threshold current–temperature plots for both heat sink and active region temperatures, for 100 ns pulse widths at a frequency of 10 kHz. The characteristics temperatures are shown, and are calculated using exponential fits of the form $J_{\mathrm{th}} = J_0 + J_1 \exp(T/T_0)$.

sen as it was discovered that the period length was sufficiently long for the active region temperature to recover the heat sink temperature at the end of the voltage pulse, and hence heat accumulation effects could be neglected (see Fig. 2b). It was found that under these driving conditions, a heat sink temperature of 236 K corresponds to a maximum active region temperature of 300 K. The calculated threshold current–temperature plot is shown in Fig. 1. It can be seen from the figure that at the higher heat sink temperatures, the threshold current density is much higher than at the equivalent active region temperature ($T_0 = 178$ K). The reason for this is two fold. Firstly, the thermal conductivities of the materials in the device decrease with increasing temperature. Therefore, at the higher heat sink temperatures the device becomes less able to dissipate heat away from the active region. Secondly, the quantum source term increases with temperature. At higher temperatures, more current flows through the device and hence the active region heating increases.

Using the thermal model, it is also possible to deduce the heat sink temperature which corresponds to the maximum active region temperature (300 K) for various device geometries and driving conditions. Investigations were made into higher repetition rate operation. It was discovered that with a 100 ns pulse width and 100 kHz repetition rate (1% duty cycle), a heat sink temperature of 220 K is possible without the active region

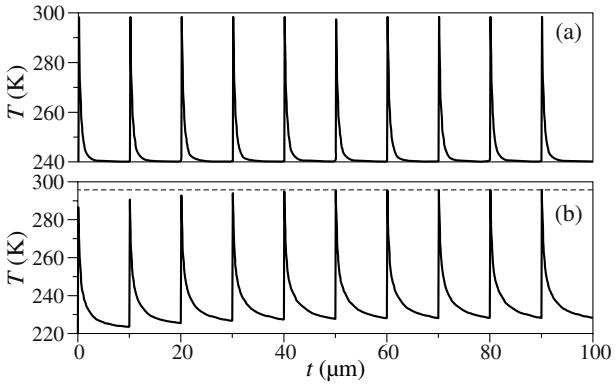

Fig. 2. Temperature time profiles with 100 ns pulses and 100 kHz repetition rate for (a) Epilayer-down mounted device at 240 K, and (b) Epilayer-up mounted device at 220 K.

temperature rising above 300 K (see Fig. 2b). It can be seen that during the first few periods, a slight heat accumulation effect takes place before the device temperature profile settles down to its final steady state behaviour with a maximum temperature of 296 K and a minimum of 228 K. The device structure was modified to investigate the effect of epilayer-down mounting. The laser ridge was defined by including 5 μm wide channels on both sides and the device considered to be mounted epilayer-down on a copper heat sink. For the same driving conditions as before (100 ns, 100 kHz), it is possible to raise the maximum heat sink temperature to 240 K without the active region temperature rising above 300 K (Fig. 2a). There are also no heat accumulation effects, indicating heat dissipation is more efficient in epilayer-down mounted devices.

3. Conclusions

It has been shown that the thermal model, in conjunction with the scattering rate calculation is a useful tool in investigating the thermal behaviour of QCLs. Driving conditions appropriate for a particular device and geometries designed to maximise device performance can be suggested. Modelling the effects of active region heating has been shown to go some way to explaining the underestimation of threshold current densities at higher heat sink temperatures. The results of the simulations show that mounting the device epilayer-side down allows heat to dissipate from the active region much quicker than in the equivalent substrate-side mounted devices, allowing higher heat sink temperatures and the possibility of higher pulse frequencies. For the device geometry investigated, cw operation would not be able to be attained due to the high active region heating under such operating conditions. In order to reduce the active region heating, heat dissipation channels in the plane of the active region layers, where the thermal conductivity is much higher than in the direction perpendicular to the layers, should be promoted. This could be in the form of using either a buried heterostructure as in [1], where insulating InP is deposited at the sides of the laser allowing heat to be removed in all directions, or by coating the laser ridge sidewalls in thick layers of gold to help extract the heat in the plane of the active region layers [7].

References

[1] M. Beck *et al*, *Science* **295**, 301 (2002).
[2] C. A. Evans *et al*, *Appl. Phys. Lett.* **87**, 141109 (2005).
[3] D. G. Revin *et al*, *Electron. Lett.* **40**, 874 (2004).
[4] D. Indjin *et al*, *Appl. Phys. Lett.* **82**, 1347 (2003).
[5] C. Pfügl *et al*, *Appl. Phys. Lett.* **82**, 1664 (2003).
[6] J. Faist *et al*, *Appl. Phys. Lett.* **78**, 147 (2001).
[7] Q. Yang *et al*, *IEEE Photon. Technol. Lett.* **17**, 2283 (2005).

14th Int. Symp. "Nanostructures: Physics and Technology"
St Petersburg, Russia, June 26–30, 2006

Lasing characteristics of microdisks with In(Ga)As quantum dots in temperature diapason from 5 to 300 K

N. V. Kryzhanovskaya[1], A. G. Gladyshev[1], N. A. Maleev[1], A. G. Kuzmenkov[1], A. E. Zhukov[1], S. A. Blokhin[2], A. M. Nadtochy[2], E. M. Arakcheeva[2], E. M. Tanklevskaya[2], A. P. Vasil'ev[2], E. S. Semenova[1], M. V. Maximov[1], V. M. Ustinov[1,2], E. Stock[3], D. Bimberg[3] and N. N. Ledentsov[2,4]

[1] St Petersburg Physico-Technical Centre of RAS for Research and Education, 194021, St Petersburg, Russia
[2] Ioffe Physico-Technical Institute, St Petersburg, Russia
[3] Institut für Festkorperphysik, Technische Universität, D-10623, Berlin, Hardenbergst. 36, Berlin, Germany
[4] NL Nanosemiconductor GmbH, Konrad-Adenauer-Allee 11, 44263 Dortmund, Germany

Abstract. Lasing characteristics under optical pumping of GaAs/$(AlGa)_xO_y$ microdisks with 1 μm emitting InGaAs quantum dots and with 1.3 μm emitting InAs/InGaAs quantum dots are compared in the temperature diapason from 5 K to 300 K. Room temperature lasing at 1.3 μm is demonstrated from 6 μm diameter microdisk with InAs/InGaAs quantum dots. The microdisk quality factor is found to be $\sim 10^4$.

Introduction

Microdisk lasers based on whispering gallery optical resonances propagating along the periphery of the disk have recently attracted considerable attention. The interest in microdisks is driven by their potential for low threshold power, due to high quality factor and low modal volume of whispering gallery modes (WGM) confined by total internal reflection [1]. The microdisk lasers based on quantum dots (QDs) can extend the above advantages to high-speed and temperature-insensitive operation because of the high spatial localization of carriers within the QDs. Conventional microdisk lasers are the 2–7 μm diameter disks, placed on top of the pedestal with smaller diameter formed by selective etching. In such microdisks high quality factor $Q \sim 17000$ [2] and record 12-times increase of recombination rate [3] have been achieved. However, conventional microdisks suffer from poor heat-sinking and poor mechanical stability as a result of their geometry. In this work the laser characteristics of microdisks with improved design free of these drawbacks were studied in the temperature diapason from 5 K to 280 K. The microdisk were placed on top of the broad $(AlGa)_xO_y$ pedestal formed by selective oxidation of high Al-content AlGaAs layer [4]. The InAs/$In_{0.15}Ga_{0.85}As$ QDs emitting at 1.3 μm at RT or formed by the submonolayer deposition InGaAs QDs emitting at 1 μm at RT were used as the active area. CW lasing under optical excitation at 1.3 μm at RT from microdisk is achieved.

1. Experiment

The structures were grown by molecular-beam epitaxy on (100) semi-insulating GaAs substrates and initially consist of a GaAs buffer layer, 500 nm $Al_{0.97}Ga_{0.03}As$ and GaAs waveguide with single layer of QDs clad with 20 nm $Al_{0.3}Ga_{0.7}As$ bottom and top barriers preventing carrier escape to the surface and to the substrate. The thickness of GaAs waveguide was 190 nm in case of self-organized InAs/$In_{0.15}Ga_{0.85}As$ QDs emitting at 1.3 μm at RT and 100 nm in case of InGaAs QDs emitting at 1 μm at RT. The QDs were placed in the middle of GaAs waveguide. Microdisks with 5–6 μm diameters were formed by optical lithography. Following dry etch using Ar^+ ions transferred the microdisk patterns through the waveguide part and the $Al_{0.97}Ga_{0.03}As$ layers. The total etch depth was 0.7 μm. After that wet thermal oxidation was performed to convert the $Al_{0.97}Ga_{0.03}As$ layer into $(AlGa)_xO_y$, which functions as low refractive index cladding for waveguiding of the resonant modes and as heat conducting layer. The microdisks were optically pumped at normal incidence by an YAG:Nd laser ($\lambda = 532$ nm, $P = 3.3{-}470$ μW) operating in CW mode. The pump beam was focused onto the microdisk by an objective Olympus Plan View IR 100 NA 0.85. The emission from the microdisks was collected through the same objective. The signal was detected either by cooled Si-CCD camera (100×1340 pixels) with spectral resolution 1 Å or by cooled InGaAs detector Roper Scientific (1024 pixels), with spectral resolution 0.3 Å. For measurements in the temperature range from 5 to 300 K the samples were mounted in a liquid-helium-flow optical cryostat Oxford Microstat.

2. Results and discussion

Figure 1 shows the low temperature emission spectra obtained at different excitation densities from 5 μm diameter microdisk with InGaAs QDs (a) and from 6 μm diameter microdisk with InAs/InGaAs QDs (b). Several sharp peak superimposed on a background signal are observed. The background corresponds to free QD emission, whereas the sharp peaks correspond to emission from QDs which couple to microdisk modes. Our theoretical estimate of WGMs with radial mode order $n = 1$ and 2 are given at Fig. 1a for 5 μm diameter microdisk with InGaAs QDs. The increase of the higher radial number modes in case of 6 μm diameter microdisk with InAs/InGaAs QDs leads to complication of the WGMs identification. The resonant line is denoted as line A (Fig. 1b). Increasing of the excitation power density leads to superlinear intensity increase and spectral narrowing that are evidences of the lasing. The threshold power densities P_{th} for line $TE_{43,1}$ and for line A were found to be 35 μW and 40 μW respectively. The quality factor values ($Q = \lambda/\Delta\lambda$) were determined near transparency threshold. The Q factor for line $TE_{43,1}$ was found to be more than 10000 and limited by the resolution of the optical system. The Q factor for line A was found to be 9900. As the absorption in QDs is low the reason limiting Q factor of our microdisks is scattering on the surface roughness.

The lasing characteristics were investigated in the temper-

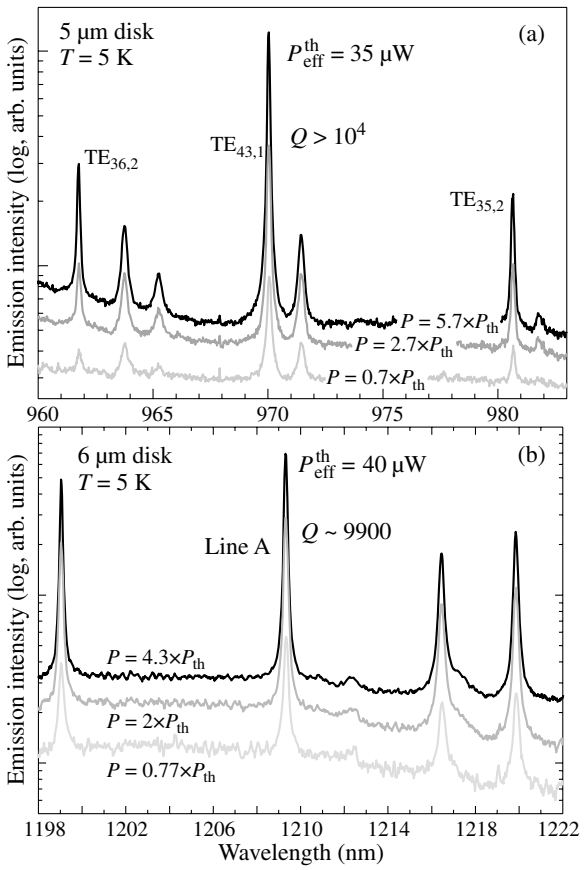

Fig. 1. Spectra obtained at 5 K below and above the threshold power from the microdisks with submonolayer InGaAs QDs (a) and from the microdisks with InAs/InGaAs QDs (b).

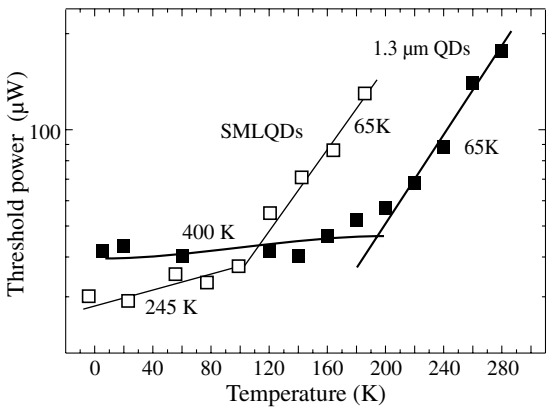

Fig. 2. Temperature dependence of the threshold.

ature diapason from 5 K to 300 K. The temperature dependences of the threshold power for both microdisks are shown at Fig. 2. At low temperatures the threshold determined by the Q is low, but increase of the temperature leads to increasing of the threshold power. This behavior can be explained by two reasons. First reason is the difference between the temperature shift of the microdisk resonant lines governed by the temperature change of the effective refractive index ($\sim$ 0.05 nm/K) and the temperature shift of the QDs emission line corresponding to the temperature bandgap shrinkage ($\sim$ 0.3 nm/K). Thus, increase of the temperature leads to the detuning between the spectral position of QDs ground state gain maximum and microdisk resonant line. Therefore at high temperatures lasing at

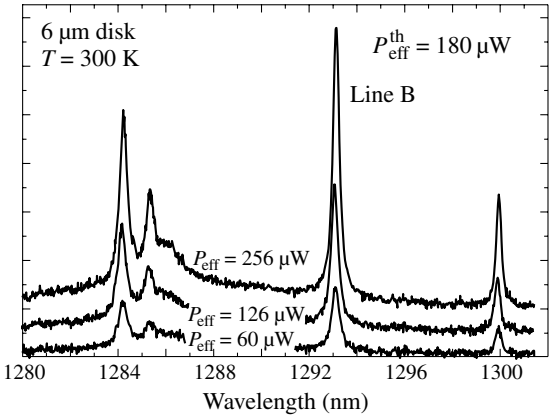

Fig. 3. Spectra obtained below and above the threshold power from the microdisks with InAs/InGaAs QDs.

resonant lines $TE_{43,1}$ and A occurs via excited QDs states. The second reason is the temperature carrier escape from the QDs and their following nonradiative recombination on the defects. Since the localization energy of the InGaAs QDs is lower than that of InAs/InGaAs QDs the temperature at which the threshold power starts to grow up with $T_0 = 65$ K is also lower. Room temperature lasing was observed in the microdisk with InAs/InGaAs QDs at the resonant line B at 1293 nm (Fig. 3), which spectral position coincides with the maximum of QDs gain spectra at this temperature. The threshold power density P_{th} is 180 μW.

In conclusions, we fabricated microdisks by photolithography, dry etching in Ar^+ beam and selective oxidation of AlGaAs layer on top of which the microdisks were placed. Temperature dependencies of lasing parameters have been studied in temperature diapason from 5 K to 300 K. The threshold power density P_{th} increase with temperature is explained by the growing detuning between the spectral position of QDs ground state gain maximum and microdisks resonant line and by the temperature escape of the carriers from the QDs and their nonradiative recombination. Room temperature CW lasing at 1.3 μm under optical excitation is realized.

Acknowledgements

The work is supported by SANDiE NMP4-CT-2004-500101, CRDF, SFB 296, RFBF No. 05-02-19967. A.E.Z. acknowledges support from the Grant (MD-4277.2004.2) of the President of the Russian Federation and the Russian Science Support Foundation.

References

[1] R. E. Slusher, A. F. J. Levi, U. Mohideen, S. L. McCall, S. J. Pearton and R. A. Logan, *Appl. Phys. Lett.* **63**, 1310 (1993).

[2] P. Micher, A. Kiraz, L. Zhang, C. Becher, E. Hu and A. Imamoglu, *App. Phys. Lett.* **77**, 184 (2000).

[3] B. Gayral, J.-M. Gerard, B. Sermage, A. Lemaitre and C. Duppuis, *Appl. Phys. Lett.* **78**, 2828 (2001).

[4] S. A. Blokhin, N. V. Kryzhanovskaya, A. G. Gladyshev, N. A. Maleev, A. G. Kuzmenkov, E. M. Arakcheeva, E. M. Tanklevskaya, A. E. Zhukov, A. P. Vasil'ev, E. S. Semenova, M. V. Maximov, N. N. Ledentsov, V. M. Ustinov, E. Stock and D. Bimberg, *Fizika I Technika Poluprovodnikov* **40**, 482 (2006).

14th Int. Symp. "Nanostructures: Physics and Technology"
St Petersburg, Russia, June 26–30, 2006

Interband cascade lasers with tunnel junction demonstrate dual-wavelength generation

K. V. Marem'yanin[2], A. A. Biryukov[1], S. M. Nekorkin[1], B. N. Zvonkov[1], V. Ya. Aleshkin[2], A. A. Dubinov[2], V. I. Gavrilenko[2], S. V. Morozov[2], A. A. Belyanin[3,4], V. V. Kocharovsky[3,4] and Vl. V. Kocharovsky[4]

[1] Research Physical-Technical Institute of the Nizhny Novgorod State University, Nizhny Novgorod, Russia
[2] Institute for Physics of Microstructures RAS, 603950 Nizhniy Novgorod, Russia
[3] Institute for Quantum Studies and Department of Physics, Texas A and M University, College Station, USA
[4] Institute of Applied Physics RAS, Nizhny Novgorod, Russia

Abstract. We design, fabricate and study new type of injection heterolasers — interband cascade lasers, based on the InGaAs structures containing two active quantum-well regions in one waveguide with a tunnel junction in between. We investigate their volt-ampere characteristics as well as spectral and directional radiation patterns. For the first time, we obtain dual-wavelength generation in such tunnel-junction lasers, which makes it possible to achieve the intracavity nonlinear mode mixing and, hence, to produce coherent far-infrared and terahertz emission at room temperature.

Introduction

Following our recent suggestions [1–9], we develop and investigate experimentally a novel class of injection heterolasers — interband cascade lasers, based on GaAs/InGaAs/InGaP structures containing two active regions of different quantum wells (QWs) with a tunnel junction in between, which provide simultaneous generation of two optical or near-IR modes in an interband quantum-well (QW) laser configuration and makes it possible their *intracavity nonlinear mixing* in one and the same laser waveguide resulting in the mid/far-IR radiation. Due to inversionless nature of the difference-frequency generation (DFG) and moderate threshold current associated with lasing on the interband transitions, the proposed mid/far-IR DFG-lasers are capable of long-pulsed and continuous-wave (CW) room-temperature operation.

1. The tunnel-junction laser design

To facilitate two-wavelength lasing, we use a stacked tunnel-junction laser design (a nonlinear-mixing interband cascade laser). In this design, an intermediate, very thin (20–50 nm) n^{++}/p^{++} tunnel junction is grown in between two or several multiple quantum-well (MQW) active regions. It works as a back diode and enables the total current to flow through each active region in series, thus avoiding current splitting between active regions and strong mode competition for the injected carriers. This is shown in Fig. 1 (see [5, 6] and references therein), where two different p-i-n MQW active regions support lasing at two distinct wavelengths in one optical waveguide. A schematic of the device cross-section is shown in Fig. 2.

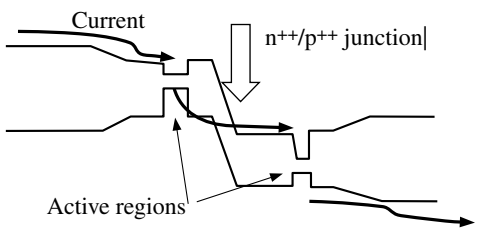

Fig. 1. Current path in the interband cascade laser with a tunnel junction between 2 QWs (after Kim *et al* 1999; see refs. in [5]).

2. Dual-wavelength generation

The structure was grown by the MOCVD method on a doped GaAs substrate with donor density 10^{18} cm^{-3}. According to the upper part of Fig. 2, the structure consists of two almost symmetric n/p transitions (of 1600 nm and 1700 nm width, respectively) separated by a highly-doped (up to 10^{19} cm^{-3}) tunnel p/n transition (of 40+50 nm width). The laser waveguide is formed by 600-nm-wide n-InGaP layer of the lower p/n transition and 600-nm-wide p-InGaP layer of the upper p/n transition. Two short-wavelength QWs (separated by 50-nm-wide i-GaAs layer) in the lower p/n transition and one long-wavelength QW have one and the same width, 7 nm, but different In-percentage, 19% and 24%, respectively. The overall thickness of the active area, including the tunnel junction, is 2.2 microns. In the present experiments, there is no a DFG-waveguide for the far-IR mode shown in Fig. 2. We have investigated volt-ampere characteristics as well as spectral and directional radiation patterns of all-sides-cleaved laser chips with different sizes, typically $1\times1/4$ mm^2, under 350-ns-pulsed injection pumping at the level from several to several tens amperes at room temperature.

Above a threshold about 15–20 A (depending on a sample), the desired dual-wavelength lasing is observed at multi-mW power (Fig. 3). The transverse-to-QW-plane directional radiation pattern corresponds mainly to the TE 1 mode in the long-wavelength emission and contains also higher transverse modes in the short-wavelength emission. Typical in-QW-plane

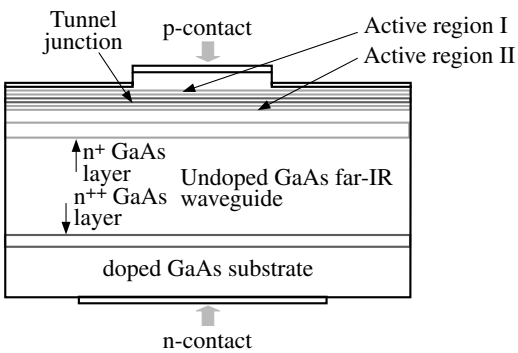

Fig. 2. Sketch of the cross-section of the nonlinear-mixing dual-wavelength interband cascade laser with a tunnel junction.

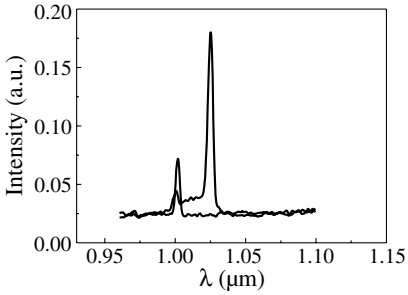

Fig. 3. Typical spectrum of the dual-wavelength generation of the GaAs/InGaAs/InGaP all-sides-cleaved $1\times1/4$ mm laser with a tunnel junction under 350-ns-pulsed injection pumping of 20 A at room temperature along long (1) and short (2) axes.

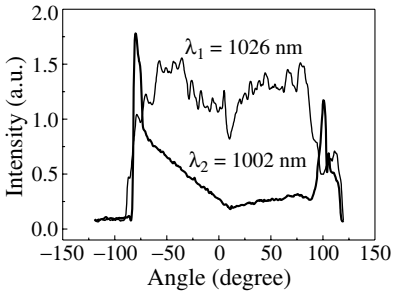

Fig. 4. Typical in-QW-plane directional patterns of the same dual-wavelength laser chip as in Fig. 3 under injection current 20 A (zero direction corresponds to the long axis of the chip).

directional patterns shown in Fig. 4 tell in favor of coexistence of whispering-gallery modes. Fabrication of laser chips with long injection stripes which coved provide lasing of standard (Fabri–Perot) modes instead of whispering-gallery modes is underway.

In Fig. 5 typical current-voltage characteristics at CW injection are shown. There is current switching at the voltage corresponding to the double energy gap of GaAs. We suppose that current switching is related to a minor carrier injection in the region of the tunnel p/n junction, by analogy to the thyristor effect. This current switching is parasitic effect which weakens the light emission. The voltage threshold of the current switching decreases with a temperature rise. At present we are working on the optimization of the tunnel-junction laser design in order to have lower dual-wavelength lasing threshold, higher current switching threshold, and better mode selection.

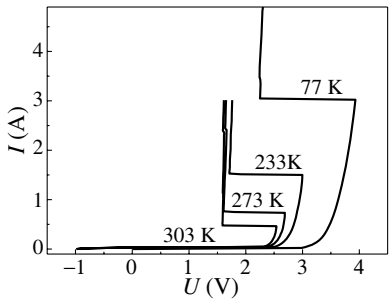

Fig. 5. Typical current-voltage characteristics of the cascade laser diode with tunnel-junction at different temperatures.

3. Conclusions

In conclusion, for the first time to our knowledge, we obtain dual-wavelength generation in the newly designed interband cascade lasers with a tunnel-junction, which allows for the intracavity nonlinear mode mixing and, hence, emission of coherent far-infrared and terahertz radiation at room temperature.

Acknowledgements

The work was supported by US Civilian Research and Development Foundation (CRDF, grant # Rue1-2657-NN-05), NSF, AFOSR, the Research Corporation, Russian Ministry of Education (BRHE, REC-NN-001 grant # Y1-P-01-06), RFBR (No. 04-02-17432), ISTC (No. 2293), NATO (SfP-973799 Semiconductors), RAS and Ministry of Education and Science of Russian Federation, the Physics Science Branch of RAS (program "Coherent optical emission of semiconductor materials and structures"), and the Council for Support of the Leading Scientific Schools of the Russian Federation (grant 1744.2003.2).

References

[1] A. A. Belyanin *et al*, *Phys. Rev. A* **63**, 053803 (2001).
[2] A. A. Belyanin *et al*, *Nanotechnology*, **12**, 450 (2001).
[3] V. Ya. Aleshkin *et al*, *Semiconductors* **35**, 1203 (2001).
[4] A. A. Belyanin *et al*, *Phys. Rev. A* **65**, 053824 (2002).
[5] A. A. Belyanin *et al*, *Physics-Uspekhi* **46**, 986 (2003).
[6] S. A. Akhlestina *et al*, *Proc. of the Conf. "Nanostrtuctures: Phys. and Technol."* Ioffe Institute, St Petersburg, 81 (2004).
[7] V. Ya. Aleshkin *et al*, *Proc. of the Conf. "Nanostrtuctures: Phys. and Technol."* Ioffe Institute, St Petersburg, 238 (2005).
[8] A. A. Biryukov *et al*, *J. Mod. Opt.* **52**, 2323 (2005).
[9] V. Ya. Aleshkin *et al*, *Semiconductors* **39**, 171 (2005).

14th Int. Symp. "Nanostructures: Physics and Technology"
St Petersburg, Russia, June 26–30, 2006

Two-color vertical external-cavity surface-emitting laser

Yu. A. Morozov[1], M. Pessa[2], T. Leinonen[2], A. Härkönen[2] and M. Yu. Morozov[3]

[1] Institute of RadioEngineering and Electronics of Russian Academy of Sciences,
38 Zelyonaya Str., Saratov, 410019, Russia
[2] Optoelectronics Research Center, Tampere University of Technology, P.O. Box 692, 33101 Tampere, Finland
[3] Saratov State University, 83, Astrakhanskaya Str., Saratov, 410026, Russia

Abstract. The analysis of novel vertical external-cavity surface-emitting laser (VECSEL) designed for simultaneous dual-wavelength emission is presented. Inhomogeneous optical pumping of nonidentical quantum wells located in different Sections of the active region has been studied. Physical nature of steady-state stability violation is cleared up and the dynamics of dual-wavelength lasing is calculated.

Introduction

VECSELs are currently subject of growing interest due to combination of many attractive features. Among those one could point out a capability to emit circular near-diffraction limited beam, possibility for power scaling and for intracavity nonlinear frequency conversion [1]. Moreover, an application range of VECSELs should likely be expanded if dual-wavelength emission is obtained. Indeed, a great demand exists for laser sources which emit coaxial beams at two different wavelengths. These lasers could be applied for dual-wavelength interferometry [2] and, what is even more important, for convenient frequency down-conversion to middle- and far-infrared ranges [3].

Dual-wavelength lasing have been demonstrated making use of several different approaches [2–6]. Most interest ones of them are concerned with usage of vertical coupled-cavity geometry [4–6]. However, because of undamped optical mode competition, stable two-frequency emission with essential wavelength separation is hardly possible with this technique. As far as we aware, the said parameter of coupled-cavity laser doesn't exceed approximately 30 nm [6].

Dual-wavelength simultaneous emission has been recently observed from optically pumped VECSEL for the first time [7]. We have obtained single transverse mode continuous-wave (CW) operation at the wavelength of 984 and 1042 nm with the efficiency about 10 percents. However, some of experimental observations have not been well understood then. For example, physical nature of intricate laser dynamics containing multiple frequency self-pulsation at high level of optical pumping has been undiscovered.

This paper is devoted to the analysis of novel dual-wavelength VECSEL [7] in more detail.

1. Design of laser structure

Fig. 1 shows the band diagram for the laser structure which is specially designed for dual-wavelength operation.

The active region is separated in three Sections by thin blocking layers. Section I and III contain two by two quantum wells made of $In_{0.17}Ga_{0.83}As$ (QW_S) emitting at the wavelength of λ_S. Four quantum wells of $In_{0.23}Ga_{0.77}As$ (QW_L) with maximal gain at $\lambda_L > \lambda_S$ are located in Section II. As usual, to enhance the achievable gain coefficient the positions of all quantum wells coincide with the antinodes of "own" standing waves, i.e., $QW_{L,S}$ location corresponds to standing wave at $\lambda_{L,S}$. On the other hand, QW_L's are placed near the nodes of the "foreigner" λ_S cavity mode to minimize optical absorption of short-wavelength emission in the deeper quantum wells. The said blocking layers, made of wide bandgap AlAs, being transparent to the pump light and laser emission, are impenetrable for carrier transport between Sections. Therefore, nearly equal pumping of nonidentical quantum wells is ensured.

2. Optical pumping of sections

To calculate the field distribution and the geometry of the device, we have solved the boundary eigenvalue problem for the Helmholtz equation within the well-known one-dimensional transfer matrix approach. It is of common use in VECSEL geometry that incident pump power comes to absorber region through the output window for laser emission (Fig. 1). Quantum-well barrier region made of GaAs plays the role of pump absorber region.

To describe carrier distribution in the latter region, we have solved the diffusion equation with no drift contribution [8]. This equation should be supplemented with one defining carrier balance among quantum well and continuous state above it and the rate equation in QW with capture, escape and recombination phenomena taken into account. Finally, by assuming the continuity of the carrier density across QW layer separating two barriers one could determine the total carrier distribution in the active region of the laser (Fig. 2). One can see that independent pumping of each Section manifests itself in step-wise profile of carrier density in the absorber layers with the jumps appearing at the positions of blocking layers. The carrier gath-

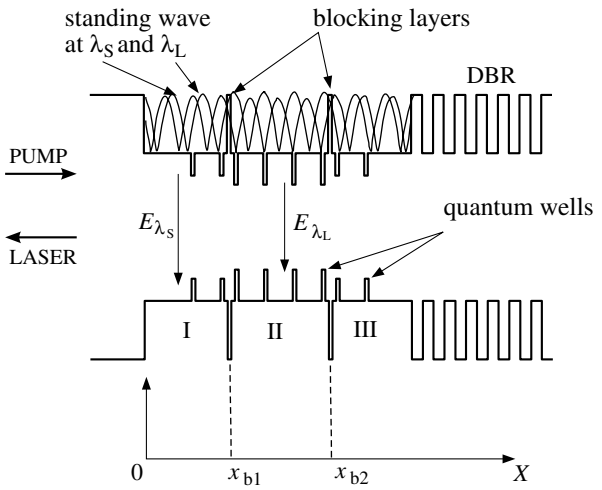

Fig. 1. Band diagram of dual-wavelength VECSEL.

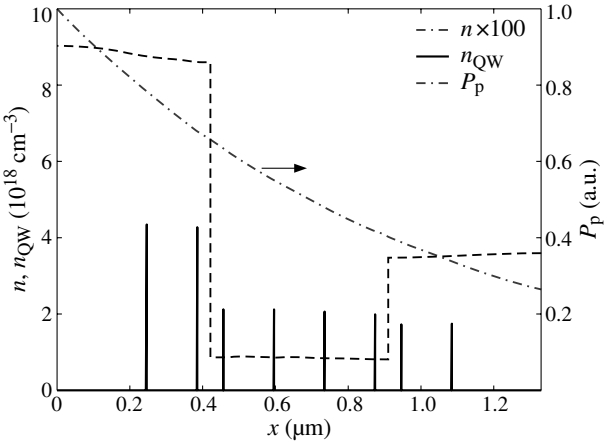

Fig. 2. Carrier density distribution in absorber (n), QW layers (n_{QW}) and pump power P_p decay along the active region.

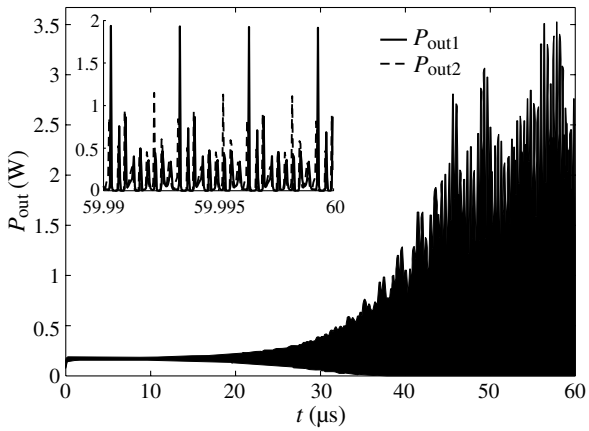

Fig. 3. Dynamics of dual-wavelength emission at the parameter's values corresponding to steady-state stability violation.

ering of QW_L is evidently more effective than that of QW_S. This is because of both longer carrier escape time and shorter capture time in QW_L [9]. Therefore, if one consider an active region containing the nonidentical quantum wells with no blocking layers inserted, almost all carriers would be collected by deeper QW_L and the attainment of threshold population in the QW_S would be hardly possible.

3. Simulation of laser dynamics

Laser under examination can be modelled as a device with high feedback external cavity. The theory of ordinary semiconductor laser with high feedback reflectivity has been derived, for example, in [10]. To restrict the number of rate equations, we assume the gain coefficient of each Section to be lumped to the single equivalent QW per Section.

The one-mode rate equation from [10] can be modified to attain those for dual-wavelength emission in VECSEL

$$\begin{aligned}
\dot{S}_1 &= v_g\Big[\sum_{j=1}^{3}\Gamma_{1j}g_{1j} - \alpha_{s1} + \tfrac{1}{2L_{in}}\ln\Big(\tfrac{S_1(t-\tau_{ext})}{S_1(t)}\Big)\Big]S_1\\
\dot{S}_2 &= v_g\Big[\sum_{j=1}^{3}\Gamma_{2j}g_{2j} - \alpha_{s2} + \tfrac{1}{2L_{in}}\ln\Big(\tfrac{S_2(t-\tau_{ext})}{S_2(t)}\Big)\Big]S_2\\
\dot{N}_1 &= \tfrac{1}{t_{QW}}(J_-^{(1)} - J_+^{(1)}) - \tfrac{N_1}{\tau_r} - v_g(g_{11}S_1 + \tfrac{\Gamma_{21}}{\Gamma_{11}}g_{21}S_2)\\
\dot{N}_2 &= \tfrac{1}{t_{QW}}(J_-^{(2)} - J_+^{(2)}) - \tfrac{N_2}{\tau_r} - v_g(g_{22}S_2 + \tfrac{\Gamma_{12}}{\Gamma_{22}}g_{12}S_1)\\
\dot{N}_3 &= \tfrac{1}{t_{QW}}(J_-^{(3)} - J_+^{(3)}) - \tfrac{N_3}{\tau_r} - v_g(g_{13}S_1 + \tfrac{\Gamma_{23}}{\Gamma_{13}}g_{23}S_2).
\end{aligned} \tag{1}$$

where $S_{1,2}$ are the photon densities at wavelength $\lambda_{S,L}$, respectively, $\Gamma_{i,j}$ and $g_{i,j}$ are the confinement factor and the gain coefficient of i-th optical field regarding to j-th equivalent QW, v_g is the group velocity of optical fields, L_{in} is the subcavity length, τ_{ext} is the round-trip time in the external cavity, $N_{1,2,3}$ is the carrier density in the QWs, $J_-^{(j)} - J_+^{(j)}$ is the carrier flux density into j-th QW, τ_r is the carrier lifetime, t_{QW} is the thickness of QWs. The total loss coefficient is given by

$$\alpha_{s1,s2} = \alpha_{in} - \frac{1}{L_{in}}\ln\Big[r_{ext}(1-r_f^2)r_{DBR}(\lambda_{S,L})\Big],$$

here α_{in} is the loss factor inside the subcavity, r_f, r_{ext} and r_{DBR} are the subcavity facet, external mirror and DBR mirror reflectivity, respectively.

By analyzing the steady-state stability of the equations (1), one can determine the room of parameters' values ensuring CW or self-modulated regime of operation. In particular, the steady-state stability violation occurs if Γ_{12}, which is the measure of influence of short-wavelength absorption in the deeper QW_L's on laser characteristics, reaches the value about 0.001. Note, that if the QW_L's position exactly coincide with the nodes of the cavity mode at λ_S, the above confinement factor is calculated to be about 0.00015 and only CW emission could be observed.

Fig. 3 shows dual-wavelength emission calculated at the confinement factor values given by the matrix

$$\hat{\Gamma} = \begin{pmatrix} 0.01 & 0.002 & 0.01 \\ 0.003 & 0.02 & 0.003 \end{pmatrix}.$$

Incident pump power P_{in}, the loss coefficients $\alpha_{s1,s2}$ and the external round trip-time τ_{ext} taken to be 1 W, 20 cm^{-1} and 3 ns, respectively.

Initially small fluctuations of output then transform to nearly random, strong pulsed regime of oscillations. One can see that rise time of instability is in the order of tens of microseconds. The final bit of the pulse sequence is shown in the inset of Fig. 3. Short-wavelength P_{out1} and long-wavelength P_{out2} emission being nearly coinciding in time, build up the pulse train of short spikes. An additional analysis shows that considered pulses originate from the relaxation oscillations. Characteristic period of pulse train equals to τ_{ext}. Therefore, as it follows from the graphs, laser's dynamics can be characterized in different time scales. In our opinion, the main cause of the stability violation is the passive Q-switching which is due to saturable absorption of the short-wavelength optical field in the QW_L.

References

[1] A. C. Tropper *et al*, *Journ. of Phys. D: Applied Phys.* **37**, R75 (2004).
[2] C. L. Wang *et al*, *Opt. Lett.* **20**, 1071 (1995).
[3] C. L. Wang *et al*, *Opt. Lett.* **20**, 1767 (1995).
[4] P. Pellandini *et al*, *Appl. Phys. Lett.* **71**, 864 (1997).
[5] M. Brunner *et al*, *IEEE Phot. Techn. Lett.* **12**, 1316 2000.
[6] V. Badilita *et al*, *IEEE JQE* **40**, 1646 (2004).
[7] T. Leinonen *et al*, *IEEE Phot. Techn. Lett.* **17**, 2508 (2005).
[8] J. Geske *et al*, *IEEE JQE* **40**, 1155 (2004).
[9] C.-Y. Tsai *et al*, *IEEE Journ. of Sel. Top. in QE* **1**, 316 (1995).
[10] J.-D. Park *et al*, *IEEE JQE* **26**, 1353 (1990).

14th Int. Symp. "Nanostructures: Physics and Technology"
St Petersburg, Russia, June 26–30, 2006

Influence of Stark and Stokes effects on operation of bistable QD lasers

V. V. Nikolaev[1], N. S. Averkiev[1], A. E. Gubenko[1,2], A. R. Kovsh[2] and E. L. Portnoi[1]

[1] Ioffe Physico-Technical Institute, St Petersburg, Russia
[2] NL-Nanosemiconductor-GmbH, 44227, Dortmund, Germany

Abstract. Two-sectional bistable laser structures based on InAs/InGaAs quantum dots (QDs) are investigated experimentally and theoretically. Parameters of QD ground-state optical transition, i.e. inhomogeneous broadening, peak absorption coefficient, transition-energy dependence on the applied field (Stark effect), are extracted from experiment. Anomalously large redshift of the luminescence peak (Stokes shift), which increases with pumping current, is observed and explained theoretically as a consequence of indirect capture of electrons from wetting layer (WL) through the QD excited level to the ground level. The broadening of the hysteresis loop in power-vs-current dependence with the increase of the absorber reverse bias is explained in terms of combination of quantum-confined Stark effect and the redshift of gain maximum, caused by indirect electron capture.

Introduction

The bistability of laser generation in QD structures with two electrically-separated sections, where one of the sections is pumped by the current (gain section) and another is biased in the opposite direction (integrated saturable-absorber section), has been observed by several groups in the past few years [1,2]. The laser bistability, which manifests itself by the appearance of the hysteresis loop in the power-vs-current curve, has its origin in the highly nonlinear behavior (with respect to the photon number in the lasing mode) of the saturable absorber based on QDs [3]. Substantial broadening of the hysteresis loop and its shift to higher currents with the increase of absorber reverse bias is a trade-mark of the QD laser structures, since in case of quantum-well bistable lasers [4] hysteresis usually shrinks and vanishes with the increase of the reverse bias. In this work we present results of extensive experimental and theoretical study of two-sectional QD structures and offer an explanation of this anomalous behavior.

1. Samples and experiment

The samples with several layers of InAs/InGaAs QDs were grown by molecular beam epitaxy. Light confinement is provided by forming shallow mesa stripe. The length of the gain and absorber sections were varied by cleaving and changing the isolation gap position. For the structures with the reduced length of the absorber exceeding 0.1 laser power-vs-current curve exhibits a broad hysteresis which persists for the absorber bias as high as 7 V. In order to investigate the parameters of the QDs, room-temperature EL spectra at different absorber biases and gain-section currents below generation threshold were measured (Fig. 1). The luminescence was collected from the absorber-facet side, to ensure that the light has passed trough the absorber.

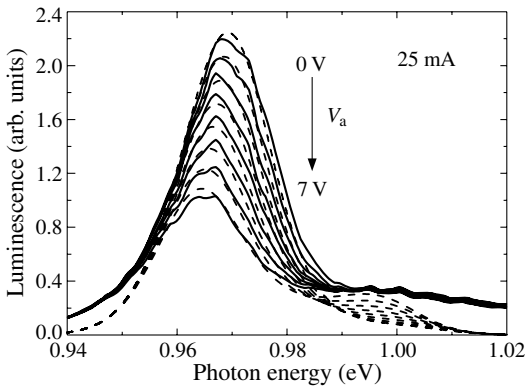

Fig. 1. Experimental (solid curves) and theoretical (dashed curves) luminescence spectra measured from the absorber facet for different reverse bias of the absorber ($V_a = 0$ V, 1 V, 2 V, ..., 7 V).

2. Results and discussion

The luminescence spectra for the emission passed through the absorber for a given absorber bias V_a can be described by the following formula

$$P(V_a, E) = P_g(E) \exp\left(-L_a \alpha_{max} \sqrt{2\pi}\, \Delta\epsilon^0_{inh}\, w_a(V_a, E)\right), \quad (1)$$

where $P_g(E)$ is the emission of the gain section, L_a is length of the absorber section and the α_{max} is the peak absorption of the ground QD transition. We assume that the energy distribution of QD transitions can be approximated by the Gaussian function [5]:

$$w_a(V_a, E) = \frac{1}{\sqrt{2\pi}\,\Delta\epsilon^0_{inh}} \exp\left(\frac{1}{2}\left(\frac{E - E_{0a}(V_a)}{\Delta\epsilon^0_{inh}}\right)^2\right), \quad (2)$$

where ϵ^0_{inh} is the inhomogeneous broadening factor of the ground transition and $E_{0a}(V_a)$ is the average QD transition energy, dependent on the absorber bias.

The change of the absorption with the applied bias is extracted from electroluminescence spectra, Fig. 1, and modeled using Eq. (1). One can see, that a remarkable agreement between theory and experiment for the red part of the spectrum ($\hbar\omega < 0.98$ eV)has been achieved. The discrepancy in the blue part of the spectrum is natural, since the higher QD transitions are not taken into account in Eqs. (1, 2).

The analysis of experimental spectra (Figs. 1, 2) yields the value of homogeneous broadening of ground QD radiation transition $\Delta\epsilon^0_{inh}$ of 11.3 meV and the peak absorption coefficient of the ground state transition of 25 cm^{-1}. Linear dependence (see inset in Fig. 2) of the average QD ground

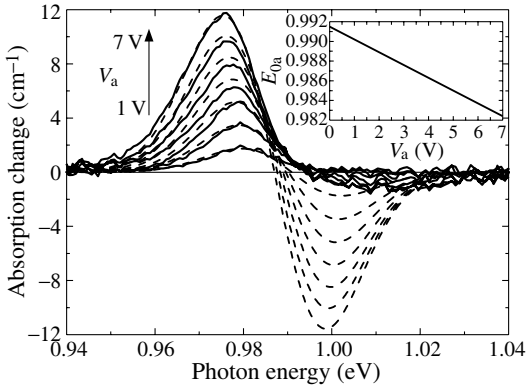

Fig. 2. Experimental (solid curves) and theoretical (dashed curves) spectra of the absorption change with the variation of the absorber bias. *The inset*: Dependence of the absorption peak position on the reverse bias, extracted from experimental data.

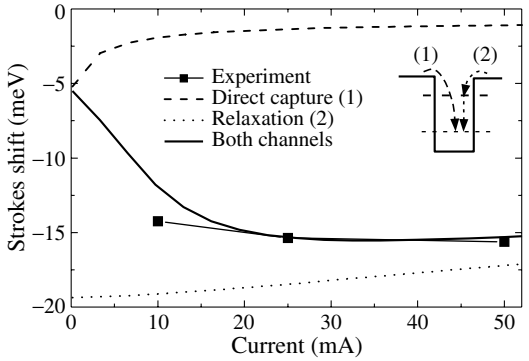

Fig. 3. Stokes shift dependence on gain-section current. Solid squares — experiment, dashed curve — calculation with direct capture of electron from WL on QD ground level (arrow (1) in the inset), dotted — calculation with electron scattering from excited QD level (2), solid curve — calculation with both channels.

transition energy on the applied field (Stark effect) signifies inverted electron-hole wavefunction alignment [6] in the QD, with the electron-hole separation of $d = 0.55 \pm 0.08$ nm.

After finding the parameters of the absorber, we extract the luminescence spectra of the gain section $P_g(E)$, Eq. (1). Experimentally obtained dependence of the difference between the luminescence peak energy and average QD ground transition energy in the gain section (Stokes shift) is presented in Fig. 3.

If the process of carrier excitation from QD levels to WL and subsequent recapture is effective, QD levels will be in the state of quasiequilibrium (QE). In QE, the maximum Stokes shift is given by the formula $S_{QE} = -(\Delta\epsilon^0_{inh})^2/T$, where T is temperature in energy units, which gives approximately -5 meV in our case. The QE approximation predicts the decrease of the absolute value of Stokes shift with the increase of pumping current due to QD level filling [5]. As can be seen from Fig. 3, the experimentally measured Stokes shift is three times larger then that predicted by QE approximation, and luminescence peak red-shifts with the increase of the current. This suggests that at room temperature the ground level population is far from QE.

It has been pointed out that effective electron capture on QD ground level can be hampered by so-called phonon bottleneck effect. Resent research shows [7] that Coulomb scattering of electrons from the excited level to the ground level plays important role. We show that in the situation when the electron capture on ground level goes through the excited level and QD excited levels are in the state of QE, the maximum Stokes shift is approximately equal to

$$S = \left(1 + \frac{\Delta\epsilon^{ex}_{inh}}{\Delta\epsilon^{0}_{inh}}\right) S_{QE}\,, \qquad (3)$$

where $\Delta\epsilon^{ex}_{inh}$ is the inhomogeneous broadening of the excited QD transition. Since the broadening of the excited states in QD is usually much larger then that of the ground state, substantial enhancement of the Stokes shift is predicted. This result can be treated qualitatively as a reduction of effective electron temperature on the ground QD level.

The capture rate on the ground QD electron level can be written as a sum of direct-capture term and Coulomb-scattering term

$$R^0_{cap} = k_0 n_{WL}\,(1 - f_0) + \frac{f_1 f_h}{\tau_{rel}}\,(1 - f_0)\,, \qquad (4)$$

where k_0 is a constant describing direct capture from WL, n_{WL} is the electron density in WL; f_0, f_1 and f_h are the electron ground-level, electron excited-level and hole ground-level occupation numbers, respectively. Time constant τ_{rel} describes the Coulomb scatering of electron from excited to the ground level with the hole being ejected in WL. Calculations in Fig. 3 are done for the case when one of the two or both terms in Eq. (4) are present. Apart from strong enhancement of the Stokes shift, calculations show that, in the presence of indirect electron capture, non-monotonic dependence of luminescence maximum on the pumping current occurs, which is a qualitatively new result.

The effect of indirect Coulomb-assisted capture strongly shifts the gain maximum in the laser gain section to the region of smaller QD transition energies. Because of this the laser with zero absorber bias starts to generate on the wavelength where absorption is relatively small. Increasing the bias causes the redshifth of the average QD transition energy in the absorber (Stark effect), which increases the absorption at lasing wavelength and enhances laser bistability. We calculate the gain-power current using the full rate-equation model which includes indirect electron capture assisted by Coulomb scattering. The broadening of the hysteresis loop with the absorber bias is obtained with a good agreement with experimental results.

References

[1] X. Huang *et al*, *IEEE J. Quantum Electron.* **37**, 414 (2001); X. Huang *et al*, *Appl. Phys. Lett.* **78**, 2825 (2001).
[2] A. E. Gubenko *et al*, *Proc. of 12th Int. Symp. "Nanostructures: Physics and Technology"*, 69, 2004.
[3] N. S. Averkiev *et al*, *Proc. of 13th Int. Symp. "Nanostructures: Physics and Technology"*, 2005.
[4] K. Y. Lau *et al*, *J. Lightwave Trchnol.* **7**, 400 (1989).
[5] L. V. Asryan and R. A. Suris, *Semicond. Sci. Technol.* **11**, 554 (1996).
[6] P. W. Fry *et al*, *Phys. Rev. Lett.* **84**, 733 (2000).
[7] T. B. Norris *et al*, *J. Phys. D: Appl. Phys.* **38**, 2077 (2005).

14th Int. Symp. "Nanostructures: Physics and Technology"
St Petersburg, Russia, June 26–30, 2006

Interband photoluminescence in stepped and tunnel-coupled quantum wells

V. Yu. Panevin[1], B. Eichenberg[3], V. A. Shalygin[1], L. E. Vorobjev[1], D. A. Firsov[1], E. M. Araktcheeva[2], N. V. Kryzhanovskaya[2], A. G. Gladyshev[2], A. E. Zhukov[2], V. M. Ustinov[2], S. Hanna[3] and A. Seilmeier[3]

[1] St Petersburg State Polytechnic University, 195251 St Petersburg, Russia
[2] Ioffe Physico-Technical Institute, St Petersburg, Russia
[3] Universität Bayreuth, 95447 Bayreuth, Germany

Abstract. Investigations of interband stimulated and spontaneous emission from structures with stepped quantum wells (QWs) and tunnel coupled QWs under optical excitation are presented. The interband photoluminescence in a InGaAs/AlGaAs structure with stepped QWs embedded in a waveguide is studied at different excitation levels. Pinning of the electron concentration at the ground state of the QWs is observed at excitation levels exceeding the interband lasing threshold. This finding is important for maintaining a potential intersubband population inversion in interband pumped structures [1]. Interband stimulated emission in semiconductor nanostructures with tunnel-coupled QWs is investigated by travelling wave excitation for the first time. The advantages of travelling wave excitation compared to standard excitation are a lower threshold and an improved emission efficiency from excited subbands. The conditions for simultaneous two-state stimulated emission from QW laser structures are discussed. The results are important for the realization of mid IR sources based on difference frequency generation.

Introduction

Nanostructures containing quantum wells (QWs) with complex potential profiles are of interest for the realization of mid IR lasers based on intersubband transitions [1], as well as of coherent light sources based on difference frequency generation [2]. In the present work the interband stimulated emission is studied in structures with stepped and tunnel-coupled QWs. Both structures are designed with the objective of obtaining an intersubband population inversion between the second and the first excited subbands of the QWs via interband optical pumping [1]. Pinning of the electron concentration at the QW's ground state after the set in of interband lasing is studied in stepped QWs. This phenomenon is one of the necessary requirements for an intersubband population inversion between excited subbands of the QW (levels e3 and e2 in the insert of Fig. 1) at high excitation levels [1]. The investigations on tunnel-coupled QW structures are related to the elaboration of mid IR devices based on difference frequency generation. One of the main problems of this application is the creation of an efficient active region for the generation of the two basic frequencies with enough power. In this report, we present investigations of interband stimulated emission in semiconductor nanostructures with tunnel-coupled QWs performed under travelling wave excitation for the first time. The possibility of efficient and simultaneous two state interband emission from the ground subband and the first excited subband in a structure with tunnel coupled QWs is demonstrated with that excitation technique.

1. Stepped QWs

Investigations were performed on a structure with 3 undoped stepped quantum wells consisting of InGaAs/AlGaAs layers. The potential profile of QWs for electrons (see insert for Fig. 1) was designed with respect to a long electron lifetime in the excited subband e3 allowing an intersubband population inversion [1]. The structure contains a waveguide formed by $Al_xGa_{1-x}As$ layers with graded composition x which provides optical confinement for radiation connected to interband carrier transitions. Details of the sample are published in Ref. [3]. To demonstrate the electron concentration pinning in the QW ground state, the sample was prepared as a Fabry–Perot resonator (both facets were cleaved). Optical interband excitation was performed by frequency doubled single pulses from a Nd:YLF laser (wavelength 526.5 nm, pulse duration 100 ns, repetition rate 10 kHz, and pulse intensity up to 6 kW/cm^2). The sample area between the two facet mirrors was excited homogeneously with the help of a cylindrical lens.

The photoluminescence (PL) spectra from the surface of the sample as well as from the edge were taken at different excitation intensities in the spectral region corresponding to interband transitions between the ground subbands of the stepped QWs. The PL intensity versus pump intensity taken at the maximum of the PL peak is presented in Fig. 1. At weak excitation intensities only a linear dependence of the spontaneous emission on the pump intensity was observed both from the edge and from the surface of the sample. This emission is con-

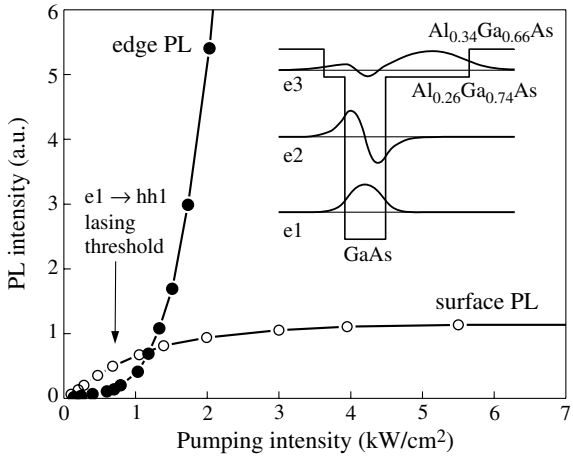

Fig. 1. Surface (circles) and edge (dots) PL intensity versus pump intensity for the structure with 3 stepped QWs. Insert: potential profile of the QW for electrons.

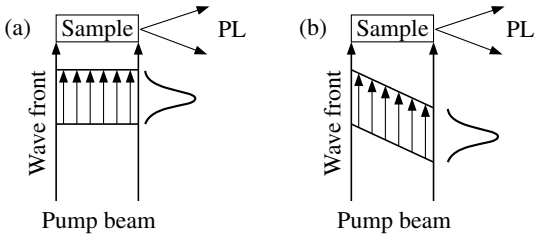

Fig. 2. (a) PL-excitation in standard geometry; (b) PL-excitation in travelling wave geometry.

nected with spontaneous radiative recombination of electrons and holes. With increasing excitation intensity, the interband lasing threshold is reached and stimulated emission with high intensity from the edge of the sample is found. At the same time the intensity of spontaneous emission from the surface saturates. This fact gives evidence for electron concentration pinning in the ground subband of the QW due to interband lasing.

2. Tunnel-coupled QWs

Edge photoluminescence was studied in a tunnel-coupled GaAs/AlGaAs QW structure with standard excitation and under travelling wave excitation using a picosecond pulses. The sample contains a single pair of tunnel-coupled 70 and 47 Å GaAs QWs separated by a 15 Å $Al_{0.31}Ga_{0.69}As$ barrier. This tunnel-coupled QW is embedded in a waveguide structure for guiding interband photoluminescence emission.

Travelling wave condition means, that - in contrast to standard edge photoluminescence, where the wave front of the excitation pulse is parallel to the surface of the sample (Fig. 2a) — the wave front of the picosecond pulse is tilted under a well-defined angle (Fig. 2b). A continuous delay over the pumping-wave front is introduced by reflection on a grating in 1st order. This delay is defined by the following condition: the excited volume near the surface and the PL radiation in the sample are travelling along the sample with the same velocity. In that way, a high, rapidly relaxing population in the sample is excited by the ultrashort pulse exactly at the time position, when the luminescence signal is arriving in the corresponding volume. That condition is wavelength dependent due to $n(\lambda)$. Consequently, the amplification at higher interband photoluminescence bands can be optimized by simply changing the angle of the grating.

For optical excitation of the sample frequency doubled single pulses from a Nd:YLF laser are used. The pulses have a wavelength of 523.5 nm, a duration of 4 ps, a repetition rate of 10 Hz and a few mJ/cm^2 average energy density. The necessary tilt angle of the wave front in the travelling wave geometry is created by use of a reflection grating with 600 lines per mm [4]. After reflection at the grating the laser beam is focused on the sample with a cylindrical lens.

Figure 3 shows two edge photoluminescence spectra taken by standard excitation (dashed line) and by travelling wave excitation (solid line) with 0.1 GW/cm^2 pump intensity. Both of them show three maxima. The peak at $\sim$ 1.51 eV represents the recombination of electrons and holes due to e1-hh1 and e1-lh1 transitions. The peak at 1.6 eV is due to e2-hh2 and e2-lh2 recombination. The peak at 1.8 eV corresponds to the radiative recombination in the $Al_{0.31}Ga_{0.69}As$ barrier of the QW. From Fig. 3, it is obvious that for equivalent pump power the edge photoluminescence spectra from standard excitation and from

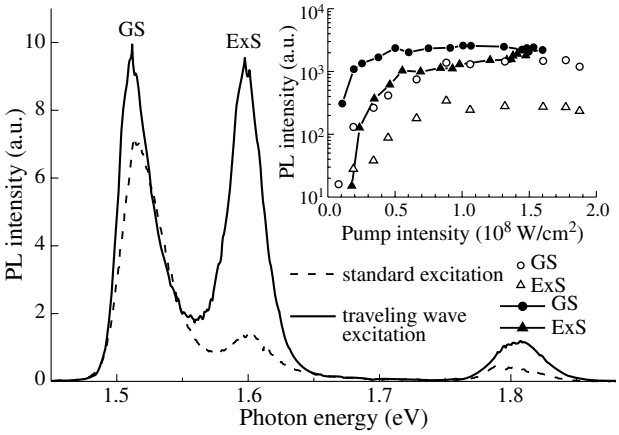

Fig. 3. PL spectra with standard excitation and with travelling wave excitation at 0.1 GW/cm^2 pump intensity; insert: edge photoluminescence signals versus pump intensity with travelling wave excitation and with normal excitation.

travelling wave excitation are different. Using travelling wave excitation the second peak in Fig. 3 is enhanced in comparison to the experiment with standard excitation.

The dependence of PL signals at these two peaks versus pump intensity in a wide range of excitation is shown in the inset of Fig. 3. Here one can see that in case of travelling wave excitation the PL signal related to excited levels of the QW can be increased by optimizing the travelling wave conditions for specific recombination energies.

Using travelling wave excitation specific interband recombination bands can be enhanced. The technique opens the possibility to create two different emission wavelengths in near infrared region with comparable power, which are very close together. A standard difference frequency generation between these two wavelengths would give easy access to a coherent mid infrared light source.

Acknowledgement

This work was supported by grants of INTAS YSF 03-55-2111, RFBR and Russian Ministry of Education and Science.

References

[1] A. Kastalsky, L. E. Vorobjev, D. A. Firsov, V. L. Zerova, E. Towe, *IEEE Journal of Quantum Electronics* **37**, 1356 (2001).

[2] K. L. Vodopyanov, K. O'Neill, G. B. Serapiglia, C. C. Phillips, M. Hopkinson, I. Vurgaftman and J. R. Meyer, *Appl. Phys. Lett*, **72**(21), 2654 (1998).

[3] V. A. Shalygin, L. E. Vorobjev, V. Yu. Panevin, D. A. Firsov, S. Hanna, H. Knieling, A. Seilmeier, E. M. Araktcheeva, N. V. Kryzhanovskaya, A. G. Gladyshev, A. E. Zhukov, V. M. Ustinov, *International Journal of Nanoscience* **2**(6), 427 (2004).

[4] H. Lobentanzer, T. Elsaesser, *Appl. Phys. B* **41**, 139 (1986).

14th Int. Symp. "Nanostructures: Physics and Technology"
St Petersburg, Russia, June 26–30, 2006

Anomalous dynamics of the two-state lasing quantum dot laser diodes

G. S. Sokolovskii[1], I. I. Novikov[1], M. V. Maximov[1], A. E. Zhukov[1], A. G. Deryagin[1], V. I. Kuchinskii[1], V. M. Ustinov[1], W. Sibbett[2], M. A. Cataluna[2] and E. U. Rafailov[3]

[1] Ioffe Physico-Technical Institute, St Petersburg, Russia
[2] School of Physics and Astronomy, University of St Andrews, North Haugh, St Andrews, Fife KY16 9SS, UK
[3] Division of Electronic Engineering and Physics, University of Dundee, Dundee DD1 4HN, UK

Abstract. We report experimental study of spectrally-resolved dynamics of the two-state lasing quantum dot laser diodes. Under 30 ns pulse electrical pumping conditions, we have observed total turn-off of the laser radiation for a time up to > 10 ns depending on pumping amplitude. After re-turn-on short optical pulses of 200–300 ps duration were also observed in the laser radiation from the excited state preceded by the dark pulses of the same duration from ground state. Energy transfer between two lasing states is proposed as an explanation for both observed phenomena.

Introduction

Quantum-dot (QD) laser diodes have been intensively studied in recent years due to the numerous highly desirable and promising properties that result from the specific physical properties of the dots, e.g. their discrete energy levels. Recently, experimental observations of simultaneous lasing from ground state (GS) and excited state (ES) in quantum dot lasers has been reported [1] and analyzed experimentally [2, 3] and theoretically [4]. In this paper we report the anomalous dynamical properties of the two-state lasing QD laser diodes, which are very distinct from the results reported in last few years.

1. Experimental results

The structure was grown by MBE with five layers of InAs QDs capped by 5.3 nm-thick $In_{0.14}Ga_{0.86}As$ layer as active medium and GaAs as spacer layer. The ridge waveguide laser structure was processed into 4 μm width and was cleaved at both facets to form a laser cavity of a length from 1.5 to 2.5 mm for different samples. The facets were HR and AR coated in order to enhance the output.

A scheme of the experimental setup is shown in Fig. 1. Radiation of QD laser diode (LD) electrically pumped by the pulse generator (PG) was coupled to a single-mode optical fibre. The experimental setup was assembled to allow incorporation of a Bragg optical filter to cut-off the longer-wavelength part of the laser diode emission. The optical fibre had a single-fused 1×3 coupler, terminating in three outputs that were switched to the power-meter (PM), optical spectrum analyser (OSA) and fast photodiode (PD) connected to the 50 GHz oscilloscope. All these devices were controlled by the computer, allowing simultaneous dynamical, spectral and power measurements.

Anomalous dynamical properties were observed for the two-state lasing QD laser diodes under 30 ns pulsed electrical pumping with 100 kHz repetition frequency. These pulse duration and repetition frequency were chosen to prevent overheating of the device. It must be noted that no anomalous dynamics was observed under low pumping amplitudes when only the ground-state (GS) lasing takes place. Increasing pumping pulse amplitude above the certain value defined by the length of the device led to the gain saturation resulting in drop of the GS lasing. We believe that this gain saturation takes place due to saturation of the GS occupancy at QDs and leads to significant increase of carrier concentration at the ES, as can be clearly seen from the corresponding optical spectra taken by the OSA (Fig. 2).

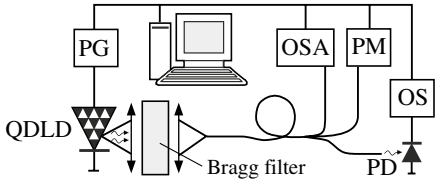

Fig. 1. Scheme of the experimental setup.

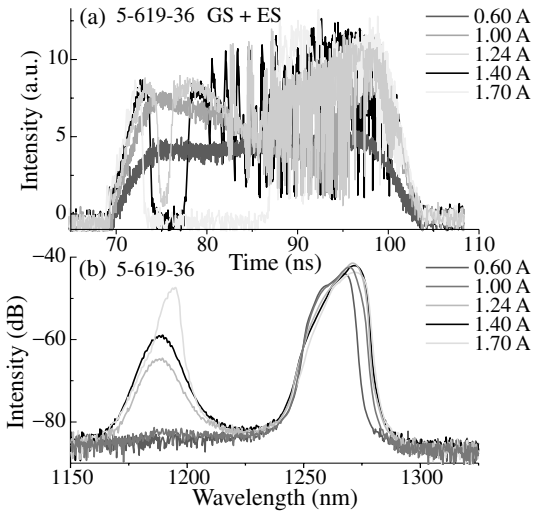

Fig. 2. Evolution of the temporal (a) and spectral (b) QD laser diode response on the rectangular 30 ns pulse of injection current with increase of the pulse amplitude.

Increased carrier filling rate at ES cause corresponding decrease of GS filling rate and total shut down of laser generation. Described situation is very unusual: lower state already can not lase due to decreased filling rate, while the upper state still doesn't have enough concentration to start lasing. Electrical pumping serves to filling of both QD states, but the time necessary for restart of lasing was found to increase significantly with increased pumping pulse amplitude. Depending on the sample length at maximum current that could be applied (2A) the restarting delay could be as big as 10 ns and more. The nature of this dependence will be discussed later.

After restart of lasing a sequence of dark pulses [5, 6] oc-

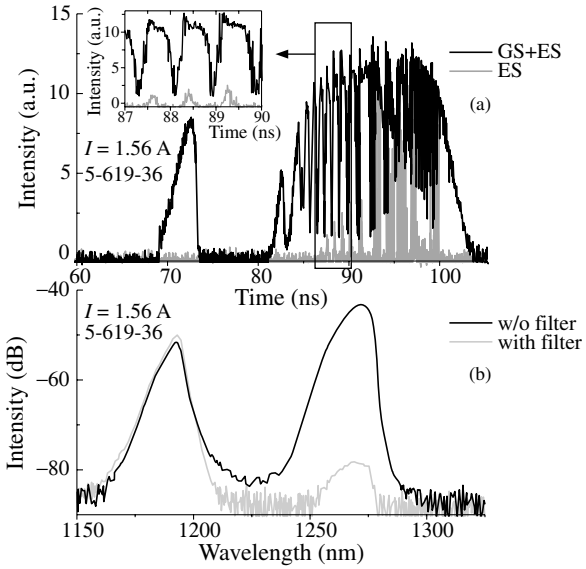

Fig. 3. (a) Temporal response of QD laser diode for the rectangular 30 ns pulse of injection current with amplitude $I = 1.56$ A for ground state and excited state lasing. (b) Laser spectra for both GS and ES (without filter) and for ES only (GS filtered).

cur in the laser radiation. Using Bragg filter to cut the GS emission one can notice that only GS exhibit 200–300 ps dark pulses while the ES emit short pulses of radiation of nearly the same duration shifted approximately half pulse width from the dark pulse. We believe that this phenomenon originates from energy transfer between two QD states. In other words, one QD state acts like a saturable absorber for another. The difference from the well-known saturable absorption (widely used for Q-switching and mode-locking of semiconductor lasers [7]) is that not the light absorption is saturated, but the filling rate of the QD state.

Although absorption at mesa-edges is well-known to cause similar Q-switching of bulk and QW laser diodes [7], but here this explanation is not satisfactory as we have observed the same phenomenon at the broad-stripe two-state QD laser, where absorption at mesa edges is negligible.

The idea of energy transfer between the QD states as the origin of the observed self-pulse formation was proved when we considered dynamics of a three-state lasing laser diode. We have observed no time delay between dark pulses of GS and the first excited state (ES1) radiation (compare to the two-state lasing dynamics in Fig. 3). We believe that the absence of time shift in this case is due to energy transfer not between GS and ES as in former case, but between GS+ES1 and the second excited state (ES2). Unfortunately, the power of ES2 radiation is several orders of magnitude smaller comparing to GS+ES1. This made impossible to separate of ES1 and ES2 emission in our first experiments and needs further investigation.

2. Discussion of the results

Discussion of the observed anomalous dynamics of the QD laser diodes should be started from the fact that the turn-off was found to occur only at certain level of the laser output power (Fig. 2). This makes us to believe that the said turn-off originates from the gain saturation due to the limited number of GS states making impossible to preserve high gain at high photon concentrations. Saturation of GS occupancy causes increase of ES carrier concentration. Nevertheless, this increased ES occupancy is far from transparency and cause only losses, but no lasing (Fig. 3). This fact can be described as a drop of pumping efficiency $\hat{\eta}$:

$$\hat{\eta} = \frac{N_{\mathrm{GS}}}{N_{\mathrm{GS}} + N_{\mathrm{ES}}}\,, \tag{1}$$

resulting in the increase of the effective threshold I_{th}:

$$I_{\mathrm{th}} = I_{\mathrm{th}_0}/\hat{\eta} = I_{\mathrm{th}_0}\,(1 + \beta I)\,, \tag{2}$$

where N_{GS} and N_{ES} are the carrier densities on GS and ES respectively, $I_{\mathrm{th}0}$ is the threshold current unaffected by the discussed nonlinear effects, I is the amplitude of pumping pulse and β is the coefficient describing increase of ES carrier concentration with current.

In other words, presence of the ES makes gain saturation at GS extremely important for laser dynamics due to increase of the effective laser threshold because of internal absorption of ES radiation, which leads to turn-off of all emission. After turn-off the Ohmic heating of the active region becomes very important leading to the additional increase of the effective threshold due to increase of internal losses with temperature:

$$I_{\mathrm{th}} = I_{\mathrm{th}_0}(1 + \alpha I)/\hat{\eta} = I_{\mathrm{th}_0}(1 + (\alpha + \beta)I + \alpha\beta I^2)\,, \tag{3}$$

where α is the coefficient of increase of the internal losses. Increase of the active region temperature with current during turn-off can be seen from the red shift of the spectra in Fig. 2 (It is well-known that only strong non-linear effects can cause LD heating at the pulsed pumping with pulse duration less than 50 ns).

Quadratic reciprocity (3) of the effective value of the threshold on pump current found by simple phenomenological derivations after substitution in the well-known formula for turn-on delay Δ

$$\Delta = \tau_{\mathrm{s}} \ln \frac{I}{I - I_{\mathrm{th}}}\,, \tag{4}$$

where τ_{s} is the spontaneous recombination lifetime, gives us a good idea for explanation of the observed anomalous increase of the QDLD turn-off duration with pump current.

3. Summary

In this paper we report experimental study of spectrally-resolved dynamics of the two-state lasing QD laser diodes. Energy transfer between two lasing states is proposed as explanation for observed anomalous dynamical phenomena in laser radiation. The new properties of the QD lasers will be studied in more details both experimentally and theoretically and could be extremely useful for laser modulation for telecommunication applications.

References

[1] M. V. Maximov *et al*, *IEEE J. Quant. El.* **37**, 676 (2001).
[2] M.-H. Mao *et al*, *LEOS 2005*, Sydney, Australia, MB4.
[3] M. A. Cataluna, *et al*, *CLEO 2006*, Long Beach, USA, CThH3.
[4] A. Markus *et al*, *Appl. Phys. Lett.* **82**, 1818 (2003).
[5] P. E. Selbmann *et al*, *Appl. Phys. Lett.* **75**, 3760 (1999).
[6] A. V. Platonov *et al*, *Appl. Phys. Lett.* **81**, 1177 (2002).
[7] E. A. Avrutin *et al*, *IEE. Proc. Optoel.* **147**, 251 (2000).

14th Int. Symp. "Nanostructures: Physics and Technology"
St Petersburg, Russia, June 26–30, 2006

Distribution of the non-equilibrium carriers in ZnSe-based electron beam pumped heterostructures

M. M. Zverev[1], D. V. Peregoudov[1], E. V. Zdanova[1], N. A. Gamov[1], V. B. Studionov[1], S. V. Ivanov[2], S. V. Sorokin[2], I. V. Sedova[2], P. S. Kop'ev[2] and Le Si Dang[3]

[1] Moscow State Institute of Radio Engineering, Electronics and Automations, Moscow, Russia
[2] Ioffe Physico-Technical Institute, St Petersburg, Russia
[3] Université Joseph Fourier, Grenoble, France

Abstract. Spatial distribution of non-equilibrium carriers in CdSe/ZnSe/ZnMgSSe laser structures pumped by electron beam has been calculated. The results were used for simulation of the cathodoluminescence intensity for different values of the electron beam energies. It is shown experimentally that minimum of threshold current density and maximum of cathodoluminescence of CdSe quantum dots correspond to the same value of the electron beam energy.

Electron-beam-pumped (EBP) green semiconductor lasers based on ZnSe can be successfully used for numerous applications, such as projection television, optical communications via plastic fibers, medicine etc. The lasing with microgun excitation both in infrared at room temperature (RT) and in blue-green spectral region at cryogenic temperatures have been demonstrated [1, 2]. Fabrication of low-threshold EBP green RT lasers pumped by electron beam with energy of 8–25 keV based on alternately-strained superlattice waveguide with efficiency of 4% per facet has been reported [3, 4].

To improve the laser efficiency one has to optimize the collection of non-equilibrium carriers in the active zone. In order to choose the optimum design of laser structure we calculated the spatial distribution of carriers in semiconductor structures at different values of electron beam. Supposing that the cathodoluminescence intensity is proportional to the total number of carriers in the active zone we are able to compare our simulations with the experimental results.

The CdSe/ZnSe/ZnMgSSe laser structures were grown by molecular beam epitaxy on GaAs (001) substrates. The structures consisted of a 0.7 μm-$Zn_{0.92}Mg_{0.08}S_{0.15}Se_{0.85}$ bottom cladding layer followed by a 0.2 μm-$ZnS_{0.14}Se_{0.86}$/ZnSe superlattice waveguide. The structure was capped with either $H = 0.1$ μm or 0.2 μm-$Zn_{0.92}Mg_{0.08}S_{0.15}Se_{0.85}$ cladding layer followed by a 5 nm-thick ZnSe layer. A ZnSe QW was placed in the center of the waveguide, embedding a CdSe sheet of nominal thickness $\sim$ 2.8 monolayers. Earlier it has been shown that such an inserted CdSe sheet transforms into a dense array of self-assembled CdSe quantum dots. Lasers based on such structures demonstrated the lowest ever reported RT threshold power density under electron beam pumping [4].

The electron beam with energy up to 30 keV was used for excitation of cathodoluminescence and pumping of lasers. All experiments were performed at RT.

Experimental results are shown on Figs. 1,2. Curves 1, 2, 3 on Fig. 1 and data of Fig. 2 correspond to the structure with $H = 100$ nm, curve 4 on Fig. 1 corresponds to structure with $H = 200$ nm. One can see that minima of threshold current density for the structure with $H = 100$ nm and maximum of cathodoluminescence of CdSe quantum dots correspond to the same value of the electron beam energy ($\sim$ 16 keV). We may reasonably assume that maximum of cathodoluminescence for $H = 200$ nm structure should occur at approximately 20 keV.

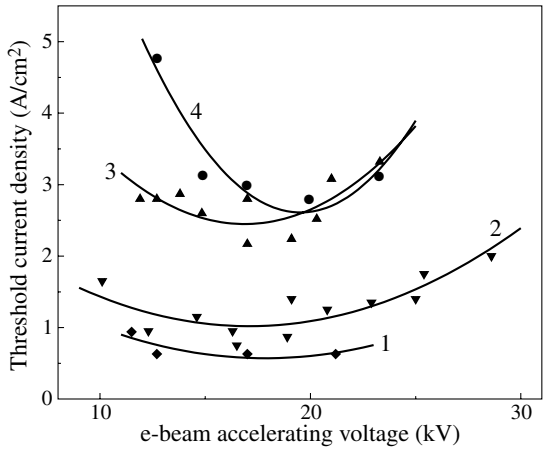

Fig. 1. Dependences of threshold current density on electron beam energy. 1, 2, 3 — $H = 100$ nm, 4 — $H = 200$ nm. Cavity length: 1 — 1.35 mm, 2 — 0.95 mm, 3 — 0.5 mm, 4 — 0.62 mm.

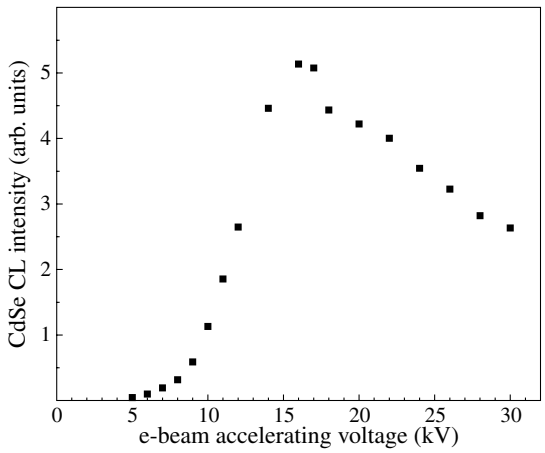

Fig. 2. Dependence of cathodoluminescence intensity on electron beam energy.

The results of simulation of cathodoluminescence intensity in such structure are presented below. Our model takes into account diffusion, non-radiative recombination and difference of band gap in different layers. We solve the Fokker–Planck equation

$$0 = \frac{\partial}{\partial x} D(x) \frac{\partial n}{\partial x} + \frac{\partial}{\partial x} n \frac{\partial U(x)}{\partial x} - n/\tau(x) + W(x) .$$

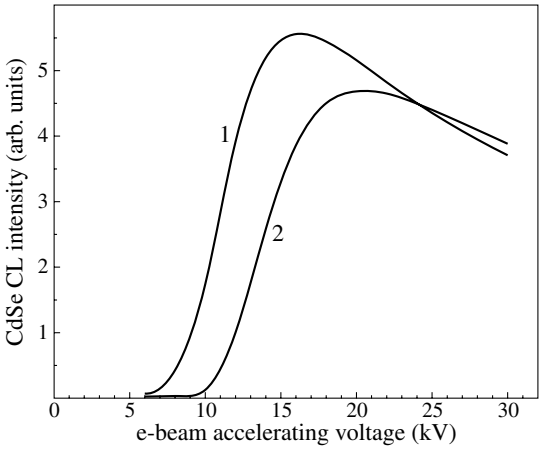

Fig. 3. Calculated dependence of cathodoluminescence intensity on electron beam energy. 1 — $H = 100$ nm, 2 — $H = 200$ nm.

Here n — concentration of carriers, $D(x)$ — diffusion coefficient, $D = L^2/\tau$, L — diffusion length, $\tau(x)$ — lifetime of carriers, $W(x)$ — pumping, $U(x)$ — effective potential arising from difference of band gaps in different layers. On the free surface we use the boundary condition $D(0)(\partial n/\partial x)(0) = sn(0)$, where s stands for the surface recombination rate.

Calculations were made with the following values of parameters: $L = 0.2\ \mu$m, $\tau = 0.4$ ns in superlattice and 0.004 ns in claddings, $s = 1000$ m/s. We used the depth distribution of electron energy losses of Ref. [5], which was calculated for bulk ZnSe for electron energies of 5, 7.5, 10, 15, 20, 25, 30 keV. We found out that the curves of Ref. [5] can be excellently approximated with a shifted Gaussian function. Thus we were able to calculate the distribution for any intermediate value of the electron beam energy. We found that the maximum of calculated cathodoluminescence intensity of CdSe quantum dots corresponds to smaller values of the electron beam energy (around 12 keV) than the experimental ones (around 16–20 keV). We have to notice that playing only with the parameters L, τ and s we cannot reproduce the experimental observation. However if we scale the energy losses distribution by the factor of 0.4 we find good agreement with the experiment (see Fig. 3). Curve 1 on Fig. 3 corresponds to 100 nm upper cladding layer and curve 2 corresponds to 200 nm. Both maxima are in good agreement with data of Figs. 1 and 2. Probably the spatial distribution of electron beam losses in multilayered structures is not the same as in bulk materials. However, the agreement between experimental and calculated results seems to be achieved without scaling the energy losses distribution by modernization of our theoretical model if we take into account non-radiative recombination on the inner boundaries between the layers.

Thus, the dependence of the cathodoluminecsence intensity of the semiconductor structures on the electron beam energy gives us the opportunity to optimize the pumping parameters of the electron beam excited lasers.

Acknowledgements

This work has been supported in part by INTAS project 03-51-5019 and R.F. Ministry of Education and Science Award RNP.2.1.2.1087.

References

[1] E. Molva, R. Accomo, G. Labrunie, J. Cibert, C. Bodin, L. S. Dang and G. Fenillet, *Appl. Phys. Lett.* **62**, 796 (1993).

[2] D. Herve, R. Accomo, E. Molva, L. Vanzetti, J. J. Paggel, L. Sorba and A. Francioci, *Appl. Phys. Lett.* **67**, 2144 (1995).

[3] M. M. Zverev, S. V. Sorokin, I. V. Sedova, D. V. Peregoudov, S. V. Ivanov and P. S. Kop'ev, *Phys. Stat. Sol. (c)* **2**, 923 (2005).

[4] M. M. Zverev, S. V. Sorokin, I. V. Sedova, D. V. Peregoudov, S. V. Ivanov and P. S. Kop'ev, *Quantum Electronics* **34**, 909 (2004).

[5] C. Trager-Cowan, F. Yang and K. P. O'Donnell, *Adv. Mater. Opt. Electron.* **3**, 295 (1994).

14th Int. Symp. "Nanostructures: Physics and Technology"
St Petersburg, Russia, June 26–30, 2006

Circular photon drag effect

V. A. Shalygin[1], Ch. Hoffmann[2], *S. N. Danilov*[1,2], S. A. Tarasenko[3], E. L. Ivchenko[3], V. V. Bel'kov[3], D. Schuh[2], W. Wegscheider[2] and S. D. Ganichev[2]

[1] St Petersburg State Polytechnic University, 195251 St Petersburg, Russia
[2] Fakultät Physik, University of Regensburg, 93040 Regensburg, Germany
[3] Ioffe Physico-Technical Institute, St Petersburg, Russia

Abstract. We report on the first observation of the circular photon drag effect. The longitudinal photocurrent reverses its direction as the circular polarization of radiation changes from right handed to left handed and is related to transfer of a linear and angular photon momentum to the electron system. The circular photon drag effect has been observed for direct inter-subband transition in (110)-grown n-type GaAs/AlGaAs quantum well structures. The experimental data can be described by an analytical expressions derived from a phenomenological theory. A microscopic model is also presented which describes the circular photon drag effect demonstrating that the generated current has spin-dependent origin.

Introduction

Photon drag effect is well-known phenomenon. Microscopically photon drag effect is due to the transfer of linear momentum from photons to free carriers and is present in both noncentrosymmetric and in centrosymmetric semiconductor systems. It was intensively studied in bulk semiconductors and in quantum wells (QWs) and became of great technical importance for fast infrared and terahertz radiation detection of short laser pulses [1-3]. While helicity independent photon drag effect is studied in a great detailed the photon drag current which reverses its sign by switching the circular polarization from right- to left-handed, i.e. the circular photon drag effect was theoretically considered in [4,5], but was not detected so far. Here we report on the observation of the circular photon drag effect. The circular photon drag effect has been observed at room temperature by studying transitions between two lowest size quantized subbands in (110)-grown n-type GaAs/AlGaAs quantum well structures. We show that the effect requires the transfer of the photon linear and angular momentum to free carriers and is a consequence of the spin-orbit coupling, which lifts the spin-degeneracy in k-space of charge carriers, together with spin dependent relaxation.

Experiments and discussion

The measurements were carried out on (110)-oriented n-type GaAs/AlGaAs QW MBE-grown structures containing 100 QWs of 8.2 nm width separated by 40 nm barriers. The energy of intersubband transitions in the QW structures corresponds to the spectral range of CO_2 laser. The electron concentration in every QW is 7×10^{11} cm^{-3}. In order to excite resonantly and to obtain a measurable photocurrent QW structures were irradiated with circularly polarized infrared light of a Q-switch CO_2-laser at oblique incidence. Right handed (σ^+) and left handed (σ^-) circularly polarized radiation is achieved by means of a Fresnel rhomb. The sample edges were oriented along $[1\bar{1}0]$ in the QW plane (x-axis) and perpendicular to this direction (y-axis). Ohmic contacts were centered along sample edges of 5 mm width. The experimental geometry is sketched in Fig. 1. The photocurrent is measured in unbiased structures via the voltage drop across a 50 Ω load resistor. The signal is detected in x-direction along radiation propagation and follows the temporal shape of the laser pulse. The oblique incidence in xz plane (z denotes the growth direction) provides the light

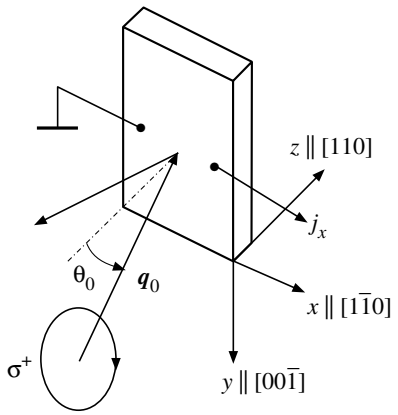

Fig. 1. The experimental geometry.

wavevector component q_x. The current is detected for right and left handed circularly polarized radiation. The helicity dependent current $j_x^{\rm circ}$, studied here, is extracted after eliminating current contributions which are helicity independent: $j_x^{\rm circ} = \left(j_{\sigma_+} - j_{\sigma_-}\right)/2$.

For structures of C_s-symmetry relevant to the experiment, the current proportional to the radiation helicity, $P_{\rm circ}$, and the photon momentum $\boldsymbol{q}$ phenomenologically is given by

$$j_x^{\rm circ} = \left\{\left[\left(\gamma_{xz} + q_z\tilde{T}_{xzz}\right)\frac{q_z}{q}\right] + q\tilde{T}_{xxx}\frac{q_x^2}{q^2}\right\} P_{\rm circ} I\,, \quad (1)$$

where I is the light intensity, $q = |\boldsymbol{q}|$, γ is the second rank pseudo-tensor describing the sum of the circular photogalvanic effect [2,3,6] and the spin-galvanic effect [2,3,7] and $\tilde{\boldsymbol{T}}$ is the third rank tensor describing the circular photon drag effect. Besides current contributions given by Eq. (1) irradiation at oblique incidence can additionally results in two helicity independent effects: linear photogalvanic effect and conventional photon drag effect. These contributions, in contrast to the current given by Eq. (1), do not change there magnitude and sign by reversing helicity. Thus subtracting the current response to left-handed circularly polarized radiation from that of right-handed circularly polarized radiation yields only the fraction of photocurrent $j_x^{\rm circ}$ proportional to helicity. More difficult task is to distinguish the circular photon drag effect from the circular photogalvanic effect and the spin-galvanic effects. As we demonstrate below this becomes possible by investigation of the photocurrent as a function of the angle of incidence θ_0.

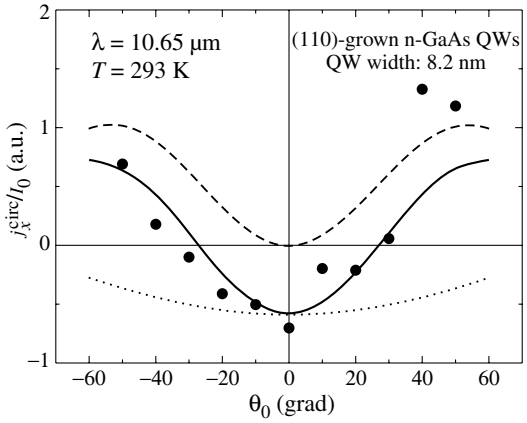

Fig. 2. The dependence of the helicity dependent photocurrent normalized to the intensity of incident light on the angle of incidence. The doted, dashed and full lines are fit after Eq. (2) and represent the term in square brackets (doted line) the last term on the right hand side of the Eq. (2) (dashed curve) and the sum of both terms (solid line), respectively.

While with increase of the angle of incidence both the circular photogalvanic and the spin-galvanic effects decrease the circular photon drag effect given by the last term in the right hand side of Eq. (1) increases and, at a certain angle of incidence, can give a dominate contribution.

Figure 2 shows the dependence of the helicity dependent photocurrent $j_x^{\rm circ}$ normalized to the incident light intensity I_0 on the angle of incidence θ_0. The current detected at normal incidence, $\theta_0 = 0$, is attributed to the sum of the circular photogalvanic effect and the spin-galvanic effect and may also have a contribution of the circular photon drag effect described by the tensor component $\tilde{T}_{xzz}$. After Eq. (1) the magnitude of all these contributions are determined by the projection of the unit vector of the light propagation on z direction, q_z/q. Thus a variation of the angle of incidence can only reduce the magnitude of the current but can not change its sign. Figure 2, however, shows that for angle of incidence $|\theta_0| > 30^\circ$ the current $j_x^{\rm circ}$ reverses its sign.

The observed sign inversion of the photocurrent can be described by the Eq. (1) if the circular photon drag effect has opposite sign to helicity dependent contribution given by the square brackets in the right hand side of the Eq. (1). For the excitation in the plane of incidence parallel to (xz) the Eq. (1) describes the angle dependence of the photocurrent as

$$\frac{j_x^{\rm circ}}{I_0} = t_p t_s \left\{ \left[\left(\gamma_{xz} + q\tilde{T}_{xzz} \cos\theta \right) \cos\theta \right] + q\tilde{T}_{xxx} \sin^2\theta \right\}, \quad (2)$$

where $\sin\theta = \sin\theta_0/n_\omega$, n_ω is the refractive index, and t_p and t_s – the transmission coefficients for p and s components of incident light polarization. The fit of the Eq. (2) to the experimental data with an ordinate scaling parameter is shown in Fig. 2. The doted, dashed and full lines in Fig. 2 represent the term in square brackets (doted line) the last term on the right hand side of the Eq. (2) (dashed curve) and the sum of both terms (solid line), respectively. It is seen that phenomenological equations describe well the experimental dependence. At a variation of the angle of incidence θ_0 the circular photon drag effect shown by the dashed curve vanishes at normal incidence and reaches its maximum at $\theta_0 \approx 50^\circ$.

Microscopic analysis taking into account the transfer of the linear and angular photon momentum to free carriers is carried out. The microscopic analysis of the observed effect demonstrates that the circular photon drag effect is a consequence of the spin-orbit coupling, which lifts the spin-degeneracy of charge carriers in k-space, together with spin dependent relaxation resulting in a spin dependent current.

Acknowledgements

We thank L.E. Golub for helpful discussion. This work was supported by the Deutsche Forschungsgemeinschaft through SFB 689, the RFBR and programs of the RAS and Russian Ministry of Education and Science.

References

[1] I.D. Yaroshetskii and S.M. Ryvkin, *The Photon Drag of Electrons in Semiconductors* (in Russian), in *Problems of Modern Physics*, ed. V.M. Tuchkevich and V.Ya. Frenkel (Leningrad: Nauka) pp. 173-185, 1980 [English translation: *Semiconductor Physics*, ed. V.M. Tuchkevich and V.Ya. Frenkel (New York: Cons. Bureau) pp. 249-263, 1986].

[2] E.L. Ivchenko, *Optical Spectroscopy of Semiconductor Nanostructures*, Harrow, UK: Alpha Science Int., 2005.

[3] S. D. Ganichev and W. Prettl, *Intense Terahertz Excitation of Semiconductors*, Oxford: Oxford University Press, 2006.

[4] E. L. Ivchenko and G. E. Pikus, *Photogalvanic Effects in Noncentrosymmetric Crystalls* (in Russian), in: *Problems of Modern Physics*, ed. V.M. Tuchkevich and V.Ya. Frenkel (Leningrad: Nauka) pp. 275-293, 1980 [English translation: *Semiconductor Physics*, ed. V.M. Tuchkevich and V.Ya. Frenkel (New York: Cons. Bureau) pp. 427-447, 1986].

[5] V. I. Belinicher, *Sov. Phys. Solid State* **23**, 2012 (1981).

[6] S.D. Ganichev, E.L. Ivchenko, S.N. Danilov, J. Eroms, W. Wegscheider, D. Weiss and W. Prettl, *Phys. Rev. Lett.* **86**, 4358 (2001).

[7] S.D. Ganichev, E.L. Ivchenko, V.V. Bel'kov, S.A. Tarasenko, M. Sollinger, D. Weiss, W. Wegscheider and W. Prettl, *Nature (London)* **417**, 153 (2002).

14th Int. Symp. "Nanostructures: Physics and Technology"
St Petersburg, Russia, June 26–30, 2006

Long-lived spin coherence of electrons in GaAs quantum wells

R. V. Cherbunin[1,2], I. A. Yugova[1,2], I. V. Ignatiev[1,2], I. Ya. Gerlovin[3], A. Greilich[1], M. Syperek[1,5], L. Fokina[1], D. R. Yakovlev[1,4], Yu. P. Efimov[2], S. A. Eliseev[3] and M. Bayer[1]

[1] Experimentelle Physik II, Universität Dortmund, 44221 Dortmund, Germany
[2] St Petersburg State University, 199036 St Petersburg, Russia
[3] Vavilov State Optical Institute, 199034 St Petersburg, Russia
[4] Ioffe Physico-Technical Institute, St Petersburg, Russia
[5] Institute of Physics, Wroclaw Univ. of Technol., 50370 Wroclaw, Poland

Abstract. We measured spin dephasing time of 2D-electrons in GaAs/(Al,Ga)As single quantum well using pump-probe Kerr rotation technic. It was found that this time may exceed 20 ns in depending on electron density.

Introduction

Optical manipulation with electron spins in semiconductors is now considered as a promising way for realizing quantum computations, and for recording and storage of information. To achieve a high efficiency of the information recording, the material should exhibit a high optical susceptibility, while the information storage requires a long-lived spin memory. Among studied semiconductor structures the slowest relaxation is displayed by quantum dots where the electron spin relaxation time may reach milliseconds [1, 2]. The main drawback of these structures is related to a large inhomogeneous broadening of the resonance transition, which significantly reduces the optical susceptibility. Much higher resonance susceptibility have structures with quantum wells (QWs). The spin relaxation times for electrons reported so far for GaAs/(Al,Ga)As and CdTe/(Cd,Mg)Te QWs do not exceed 10 and 30 ns, respectively [3, 4].

Hire we report on the the electron spin dynamics in high-quality GaAs/(Al,Ga)As QWs with a two-dimensional electron gas (2DEG) of low density. It was found that the electron spin dephasing time T_2^* can be as long as 20 ns.

1. Experimental technique

We studied GaAs/$Al_{0.3}Ga_{0.7}As$ structures grown by MBE on (100) GaAs substrates. Two structures were grown on the semi-isolated GaAs substrate. The first one (p340) contains four QWs (5.6, 9.3, 14 and 19 nm) separated by 50 nm barriers. The second one (p396) contains three QWs (8.5, 14 and 20 nm) and 40 nm barriers, and affords a better crystal quality. Another sample (p343) (with 5.7, 9.3, 14.1 and 20 nm QWs and 40 nm barriers) was grown on the n-doped substrate to allow the electrical control of 2DEG density in the QWs. The top surface of this structure was coated by semitransparent gold electrode. By our estimate, applying the electric bias between the n-doped substrate and the electrode, we could vary 2DEG density from about 10^9 ($U_{\rm bias} < 0$ V) up to 10^{10} cm^{-2} ($U_{\rm bias} = +1$ V). The samples were mounted in a liquid-helium cryostat with a split-coil superconducting magnet, which allowed us to performe the measurements in transverse magnetic field (Voigt geometry) up to 7 T. We have used the pump-probe Kerr rotation technique for the detection of the average electron spin dynamics [5]. The the signal amplitude was measured as a function of a time delay between the pump and probe pulses. Repetition rate of laser pulses was 75.6 MHz and the pulse duration was 1.5 ps. Pump and probe densities were 5 mW and 0.5 mW respectively and laser was focused into 100 μm-diameter spot. So small pump density should not cause additional mechanisms of the spin relaxation, like Dyakonov–Perel relaxation. All the experiments were performed at a temperature $T = 2$ K.

2. Experimental results

All studied samples show a pronounced signal of Kerr rotation in the region of the excitonic resonance of the QW. In the transverse magnetic field, the signal has the form of periodic oscillations, whose frequency corresponds to the electron spin precession about the field direction. The decay time of the oscillations, T_2, determined by the electron spin dephasing is found to exceed, by more than an order of magnitude, the radiative decay time of the excitons in the QW ($\tau_{\rm r} = 110$ ps) measured by means of streak-camera. These data indicate that the signal is caused by the light-induced spin orientation of resident electrons. The source of the resident electrons in the samples p340 and p396 is, most likely, to be related to the background doping. Electron density in this case is less than 10^9 cm^{-2}. We found, that an additional illumination of our samples in the range of the barrier layer absorption increases this density several times.

The effect of the resident electron density on spin dynamics was extensively studied for sample p343, where a gate voltage was used to tune the electron density. The results of the measurements are shown in Fig. 1. The 2DEG density was varied by an external electric bias. The gold electrode forms the Schottky barrier on the top surface of the sample. As a

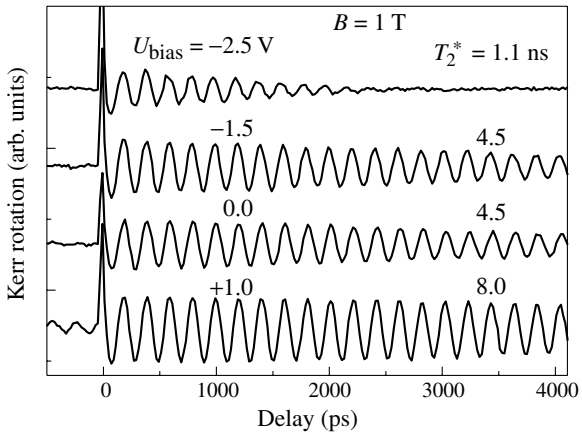

Fig. 1. Time-resolved Kerr rotation signal for different bias for 14 nm GaAs/$Al_{0.3}Ga_{0.7}As$ single QW (sample p343).

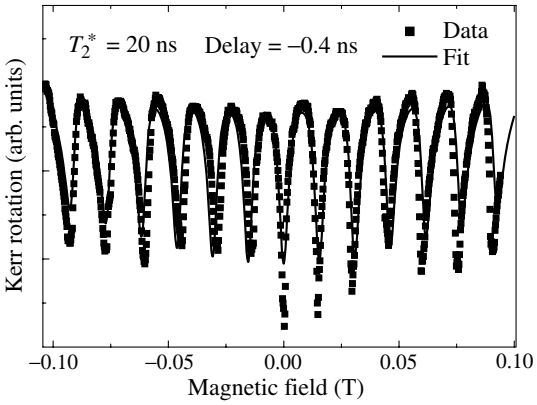

Fig. 2. RSA signal for 19 nm QW (sample p340). Squares are the experimental data, solid line is the fit using the model from Ref. [6] with the spin dephasing time $T_2^* = 20$ ns.

result, the energy structure of the conduction band is strongly tilted. Due to this fact, in the absence of the external bias, the bottom of the conduction band in the QW lies higher than the Fermi level of the doped substrate, and electrons cannot penetrate to the QW from the substrate. Indeed, the dynamics of the Kerr signal for sample p343, under these conditions, is very similar to that we observed for undoped samples in absence of additional illumination. The decay time of the oscillations, in this case, is 4.5 ns and does not change under applying the small negative bias ($U_{\rm bias} > -1.5$ V). Absence of the bias dependence evidences in favor of the background doping as the main source of the resident electrons. At high negative bias ($U_{\rm bias} < -2.0$ V), the decay time of the Kerr signal decreases, ($T_2^* = 1.1$ ns at $U_{\rm bias} = -2.5$ V, see Fig. 1), which can be explained by depletion of the QW due to the tunnelling of the electrons into the substrate. As we found experimentally the dephasing time does not shorten with increasing magnetic field up to 4 T. This means that the spread of the electron g-factor is very small (small fractions of percent) and does not affect the decay time of the oscillations.

At positive bias exceeding +0.8 V, which compensates for the Schottky barrier, the electron density in the QW starts to increase due to the electron diffusion from the doped substrate. As seen from Fig. 1, the increase in the concentration ($U_{\rm bias} = +1.0$ V) leads to a noticeably increase of the decay time of the oscillations up to 8.0 ns. In this case, the oscillating signal is observed even in the negative time delays, i.e., it does not completely decay during the pulse repetition period (13.2 ns).

Similar effect of decay time dependence on the electron density was observed for undoped samples. Namely, after additional illumination with 532-nm light, the decay time becomes longer than the repetition period. To measure so long decay time, we used the method of resonance spin amplification (RSA) [6]. The idea of the method is in detection of the Kerr rotation signal amplitude, measured at a constant time delay, as a function of the magnetic field strength. At long spin relaxation time, one detects the spin orientation created not only by the last, but also by several preceding laser pulses. In this case, the peaks of the signal are detected in the magnetic fields in which the electron spin precession frequency is equal or is an integer multiple of the laser pulse repetition frequency. The longer the spin dephasing time, the larger number of pulses contributes to the signal and the narrower peaks should be observed in the RSA signal. Figure 2 shows the experimental shape of the RSA signal of the sample p340 together with fitting by an equation given in Ref. [6]. According to the results of the fitting, the spin dephasing time $T_2^* = 20$ ns.

3. Conclusion

The main result of the present work is an observation of the long-lived spin coherence of 2DEG in GaAs/(Al,Ga)As QWs. We have found that the spin dephasing time of the electron ensemble grows with increasing electron density and is limited by spin relaxation of individual electron spin even in strong transverse magnetic field.

Acknowledgements

The work is partly supported by ISTC, grant 2679. BMBF program 'nanoqubit'. Research stay in Dortmund have been supported by the Deutsche Forschungsgemeinshaft for RVC via GK 726, for IVI via grant 436 RUS 17/144/05 and for IVY via grant 436 RUS 17/98/05.

References

[1] Miro Kroutvar, Yann Ducommun, Dominik Heiss, Max Bichler, Dieter Schuh, Gerhard Abstreiter and Jonathan J. Finley, *Nature* **432**, 81 (2004).

[2] M. Ikezawa, B. Pal, Y. Masumoto, S. Yu. Verbin and I. Ya. Ger lovin, *Phys. Rev. B* **72**, 153302 (2005).

[3] R. I. Dzhioev, V. L. Korenev, B. P. Zakharchenya, D. Gammon, A. S. Bracker, J. G. Tischler and D. S. Katzer, *Phys. Rev. B* **66**, 153409 (2002).

[4] E. A. Zhukov, D. R. Yakovlev, M. Bayer, G. Karczewski, T. Wojtowicz and J. Kossut, *Phys. Stat. Sol.(b)* in press (2006).

[5] S. A. Crooker, D. D. Awschalom, J. J. Baumberg, F. Flack, N. Samarth, *Phys. Rev. B* **15**,7574 (1997).

[6] J. M. Kikkawa and D. D. Awschalom, *Phys. Rev. Lett.* **80**, 4313 (1998).

14th Int. Symp. "Nanostructures: Physics and Technology"
St Petersburg, Russia, June 26–30, 2006

Spin physics in charge-controlled InAs-GaAs single quantum dots: optical pumping and hyperfine interaction

B. Eble[1], *O. Krebs*[1], A. Lemaître[1], K. Kowalik[1,2], A. Kudelski[1], B. Urbaszek[3], X. Marie[3], T. Amand[3] and P. Voisin[1]

[1] CNRS-Laboratoire de Photonique et Nanostructures, Route de Nozay, 91460 Marcoussis, France
[2] Institute of Experimental Physics, Warsaw University, Hoża 69, 00-681 Warsaw, Poland
[3] Laboratoire de Nanophysique Magnétisme et Optoélectronique, INSA, 31077 Toulouse Cedex 4, France

Abstract. We report on electron spin physics in a single charge-tunable self-assembled InAs/GaAs quantum dot. The hyperfine interaction between the optically oriented electron and nuclear spins leads to the polarization of the quantum dot nuclei. The sign of the resulting Overhauser-shift depends on the trion state X^+ or X^-, and remarkably its amplitude does not vanish in zero magnetic field. This explains the quenching of X^+ spin relaxation under steady-state excitation polarization.

Introduction

The spin degree of freedom of electrons confined in quantum dot (QD) attracts a lot of attention because of its expected long relaxation time. Indeed, once the electron is confined in a quantum dot, its low temperature spin dynamics is almost no longer subject to the random perturbations which lead to relaxation and decoherence in bulk or quantum wells [1]. Yet, the quantum confinement itself leads to new sources of relaxation. The most important is likely the confinement-enhanced exchange interaction between carriers which has been largely investigated in the recent years [2–5]. Its anisotropic part produces the well-known splitting of electron-hole pair states (named further excitons and labeled X^0) into linearly polarized states [6]. This effect which is quite dramatic for both spin orientation and detection by optical methods, can yet be suppressed by charging the quantum dot with a single additional carrier, electron or hole. The resulting singly-charged exciton (named further trion and labeled X^+ or X^-) becomes thus a good spin probe of the unpaired electron (in X^+) or hole (in X^-), which simultaneously opens the way towards optical pumping of the resident carrier spin. However, a second spin dependent interaction, which is also enhanced by the confinement perturbs the trion spins: the hyperfine interaction of a conduction band electron with the QD nuclei acts indeed as a random effective field of about 30 mT. For example, it must determine the spin dynamics of positive trions during their radiative lifetime producing on average a partial spin relaxation [2, 3]. Here we experimentally address this issue in a single self-assembled charge-tunable InAs/GaAs QD. Our observations show that the electron spin relaxation is indeed governed by the hyperfine interaction, but gets intrinsically quenched due to the optical pumping of nuclear spins under steady-state optical excitation.

1. Optical pumping of nuclear spins with trions

To study the influence of hyperfine interaction on spin dynamics, optical orientation experiments have been first performed in a small longitudinal magnetic field $B_z \approx 0.2$ T provided by a permanent magnet and parallel to the QD growth axis z. We used a standard micro-photoluminescence (PL) setup based on a $\times 50$ microscope objective, a double spectrometer of 0.6 m-focal length and a Nitrogen-cooled CCD array detector, providing a spectral resolution of 30 μeV and a precision on line position of about 1 μeV after deconvolution by a Lorentzian fit. The optical excitation and detection were both performed along the z axis. Thus the degree of PL circular polarization defined by $\rho_c = (I_{\sigma^+} - I_{\sigma^-})/(I_{\sigma^+} + I_{\sigma^-})$, where $I_{\sigma^{+(-)}}$ denotes the PL intensity measured in $\sigma^{+(-)}$ polarization, traces the average spin $\langle S_z^e \rangle = -\rho_c/2$ of the electron participating in the PL signal. This results from the usual assumption of pure heavy-hole ground state with angular momentum projection $m_z = \pm\frac{3}{2}$ in InAs QDs leading to optically active electron-hole pairs $|\pm 1\rangle = |\mp\frac{1}{2}, \pm\frac{3}{2}\rangle$. As a result, the PL polarization reads out the spin of the unpaired electron (hole) for X^+ (X^-) which besides determines the hole (electron) spin left in the QD after optical recombination.

The sample was grown by molecular beam epitaxy on a [001]-oriented semi-insulating GaAs substrate. The InAs QDs are grown in the Stranski–Krastanov mode 25 nm above a 200 nm-thick n^+-GaAs layer and capped by an intrinsic GaAs (25 nm)/$Al_{0.3}Ga_{0.7}As$ (120 nm)/GaAs (5 nm) multilayer. The QD charge is controlled by an electrical bias applied between a top Schottky contact and a back ohmic contact. We used a metallic mask evaporated on the Schottky gate with 1 μm-diameter optical apertures to spatially select single QDs.

Figure 1(a) shows the single QD PL intensity plotted on a gray-level scale against bias and detection energy. The identification of the different spectral lines and of the associated QD charge relies on several features. Between 0 V and $\sim$ 0.15 V the neutral exciton X^0 is identified by its fine structure [6], which is besides mirrored by the biexciton appearing under stronger excitation at lower energy (hardly perceptible in Fig. 1). Above 0.15 V the X^- trion red-shifted by $\sim$ 6 meV shows up indicating the charging of the QD with an electron [5, 7]. It first competes with the neutral exciton line which finally disappears above 0.35 V when the QD charges with 2 electrons. For stronger electric field (negative bias) the neutral exciton line disappears as a result of the electron tunnelling out of the QD. It is replaced by a 3 meV blue-shifted line assigned to the X^+ trion [8]. Although the applied bias only controls the conduction band chemical potential and thus cannot itself generates the QD charging with holes, this effect is achieved under strong intra-dot excitation. It directly creates a hole within the QD, which does not escape as the electron thanks to its larger effective mass.

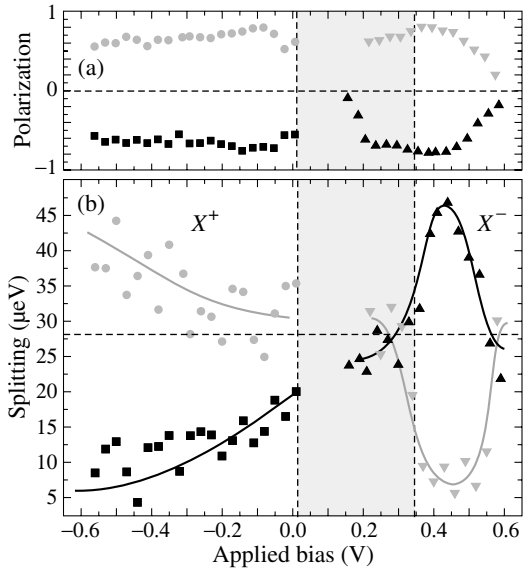

Fig. 1. (a) Gray-scale plot of the PL intensity from a single InAs QD versus detection energy and voltage under intra-dot excitation at 1.31 eV. (b) Zoom of polarization-resolved PL spectra (gray for σ^-, dark for σ^+) in 0.2 T magnetic field for the fixed voltage marked by arrows in (a) panel. Excitation polarization is indicated on the left-hand side.

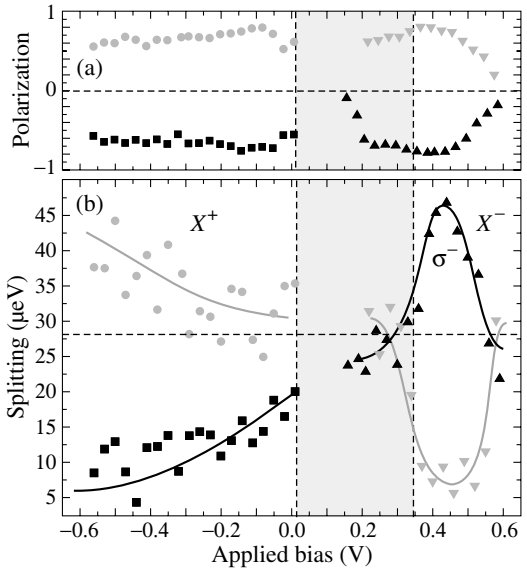

Fig. 2. (a) Circular polarization and (b) spin splitting of X^+ and X^- PL lines against applied bias at $B_z = 0.2$ T, under σ^+ (gray) and σ^- (dark) polarized excitation at 1.31 eV. The gray-shaded area represents the region of X^0 stability and the solid lines are a guide for the eye.

Figure 1(b) shows blowing up of PL spectra resolved in circular polarization for different charge states and different excitation polarizations. Under linearly polarized excitation (lin.), the Zeeman interaction simply separates the $\sigma^{\pm}$-polarized components of the trion lines by $\delta_Z = |g_X|\mu_B B_{ext}$ where g_X is the exciton g-factor and $\mu_B = 58\ \mu$eV/T is the Bohr magneton. It also increases the bright X^0 splitting to $\sqrt{\delta_1^2 + \delta_Z^2}$. We find for the three lines an average Zeeman splitting $\delta_Z \approx 28\ \mu$eV in agreement with an exciton g-factor of ≈ 3 [6]. Under circularly polarized excitation a significant deviation from the sole Zeeman interaction is now observed: the X^+ splitting gets larger in σ^+ excitation by +10 μeV and smaller in σ^- by -15 μeV. This indicates the polarization of the QD nuclear spins due to the hyperfine interaction with the optically oriented electrons, which produces the so-called Overhauser shift (OHS) denoted further δ_n. Remarkably a symmetrical but reversed effect occurs for X^- with a shift $\delta_n = +15\ \mu$eV in σ^- and $\delta_n = -25\ \mu$eV in σ^+, whereas the PL from X^- and X^+ shows the same helicity. This reversal demonstrates that in the case of X^- for which the total electron spin is zero, the mechanism leading to nuclear polarization doesn't operate during its lifetime but takes place after optical recombination through the interaction with the spin polarized electron left in the QD. An other remarkable feature is the OHS asymmetry observed when changing the excitation from σ^+ to σ^-. This clearly appears in Fig. 2 which reports the voltage dependence of circular polarization and trion spin splitting. This asymmetry reveals that polarizing the nuclear spins in the direction which produces a larger effective field for the electron is more difficult than in the opposite direction. The total electron spin splitting represents indeed an energy cost for every electron-nuclei *flip-flop* process and plays thus a crucial role in the mechanism of nuclear polarization as discussed below.

2. Model of nuclear polarization

The Hamiltonian of the hyperfine interaction of a single electron spin $\hat{S}^e = \frac{1}{2}\hat{\sigma}^e$ with N nuclear spins is given by [9,10]:

$$\hat{H}_{hf} = \frac{\nu_0}{2} \sum_j A^j \left|\psi(\mathbf{r}_j)\right|^2 \left(\hat{I}_z^j \hat{\sigma}_z^e + \frac{\hat{I}_+^j \hat{\sigma}_-^e + \hat{I}_-^j \hat{\sigma}_+^e}{2} \right), \quad (1)$$

where ν_0 is the two-atom unit cell volume, $\mathbf{r}_j$ is the position of the nuclei j with spin $\hat{I}^j$, A^j is the constant of hyperfine interaction with the electron and $\psi(\mathbf{r})$ is the electron envelope function. The sum goes over the nuclei interacting significantly with the electron (i.e. essentially in the effective QD volume defined by $V = (\int |\psi(\mathbf{r})|^4 d\mathbf{r})^{-1} = \nu_0 N/2$). This interaction acts as an effective magnetic field $\mathbf{B}_n \approx \sum_j A^j \mathbf{I}^j / (N g_e \mu_B)$ on the electron spin of g-factor g_e. In absence of nuclear polarization, this random nuclear field averages to zero but shows fluctuations $\propto A/\sqrt{N}$ of the order of 30 mT [2, 3]. In a classical description the electron spin precess around the total magnetic field $\mathbf{B} = \mathbf{B}_z + \mathbf{B}_n$. This precession actually corresponds to a flip-flop mechanism which conserves the total spin (second term of Eq. (1)) between the electron and nuclear spins. Since it stops randomly within a correlation time τ_c (due to optical excitation/recombination or QD charging), it leads to the transfer of spin polarization towards the nuclei. The latter accumulates then in the QD giving rise to the OHS through the first term of Eq. (1). The equilibrium polarization reached by this process is determined by the average electron spin as well as by possible nuclear depolarization mechanisms. In principle, it requires at least the quenching of the nuclear spin diffusion due to dipole-dipole interaction by applying a small magnetic field above 1 mT. It is also crucial to note that the hyperfine interaction couples non-degenerated states, since the total electron spin splitting is much larger than the nuclear spin splitting. Along these considerations, we find the following implicit equation

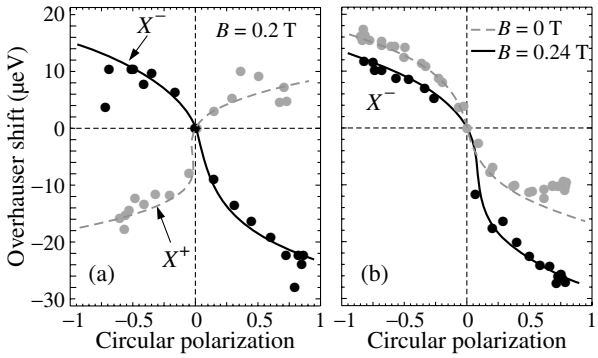

Fig. 3. Overhauser shift versus circular polarization measured for different excitation polarizations (from σ^+ to σ^-) (a) for X^- and X^+, and (b) for the X^- of an other QD under the resonant excitation of a P-shell transition providing a better signal to noise ratio. Solid lines are theoretical fits made with Eq. (2).

for the equilibrium nuclear polarization [11]:

$$\delta_n = \frac{-\Delta^* \langle S_z^{\rm e} \rangle}{1 + \kappa \left[(\hbar/\tau_{\rm c})^2 + (\frac{g_{\rm e}}{g_{\rm X}} \delta_{\rm Z} + \delta_n)^2 \right]}, \qquad (2)$$

where $\Delta^* \approx 1.3$ meV in a realistic In(Ga)As QD, $\langle S_z^{\rm e} \rangle = \mp \rho_{\rm c}$ for $X^{\pm}$ state and the coefficient $\kappa \propto \tau_{\rm c}/T_{\rm d}$ includes the dependence on the depolarization time $T_{\rm d}$ of the nuclei. Equation (2) shows that the electron spin splitting $(\frac{g_{\rm e}}{g_{\rm X}} \delta_{\rm Z} + \delta_n)$ produces a feedback on the equilibrium polarization δ_n with a "gain factor" κ. The correlation time $\tau_{\rm c}$ of the hyperfine interaction plays thus a crucial role. In QD, it can be reasonably ascribed to the lifetime of the spin polarized electron. For X^+, it likely governs the nuclear polarization change reported in Fig. 2(b): the electron spin polarization remains essentially constant around 70% whereas the OHS increases with the electric field due to the reduction of trion lifetime activated by the field-induced electron escape.

For X^-, the nuclear polarization dynamics is driven by the single electron left in the QD after optical recombination. If its lifetime is too long, the electron spin coherently precess in the nuclear field and no nuclear polarization occurs. This explains why the latter builds up only above 0.35 V when this lifetime gets strongly limited by the fast capture of a second electron from the n-GaAs layer. Yet, to definitely check the validity of this model it is more direct to vary at fixed bias the average spin $\langle S_z^{\rm e} \rangle$ by rotating the quarter-wave plate which defines the excitation polarization. The measurements of $\rho_{\rm c}$ and δ_n are reported in Fig. 3 together with a theoretical fit which gives a fair agreement, in particular regarding the asymmetrical and non-linear dependence.

3. Hyperfine interaction-induced spin relaxation

Figure 3(b) presents results from an other QD for two different magnetic fields. Surprisingly in zero magnetic field there is still a pronounced nuclear polarization induced by the polarized excitation. A similar effect has been recently reported by C. W. Lai *et al* who interpret it as the screening of nuclear spin interactions by the electronic Knight field itself [12]. Within the framework of our model, it just reveals that the zero magnetic field depolarization time is not much shorter than at 0.2 T. This nuclear polarization which appears spontaneously under steady-state excitation likely explains the strong

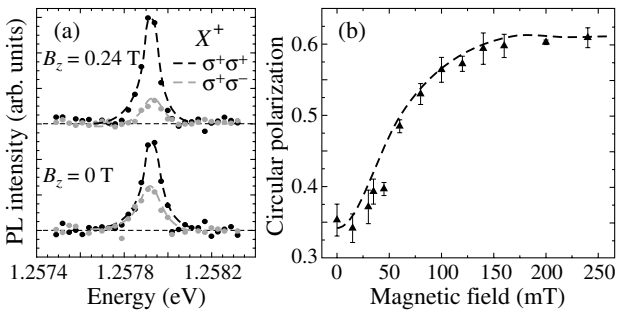

Fig. 4. (a) Polarization resolved spectra of X^+ for two different magnetic field and (b) circular polarization versus applied magnetic field, under σ^+/σ^- 50 kHz-modulated excitation polarization. Dashed line is a theoretical fit made with a model based on Ref. [3].

circular polarization ($\approx$ 70%) of X^+ that we still observe in zero magnetic field. Indeed the nuclear field fluctuations (≈ 2 μeV) get largely screened by the average nuclear field itself ($\delta_n \approx 10$ μeV).

To check this assumption, we have measured the X^+ circular polarization by using a gated single-channel detection synchronized to the σ^+/σ^- 50kHz-alternated excitation polarization provided by a photo-elastic modulator. This prevents the building up of any nuclear polarization since the electron spin polarization averaged over the time required for such building is basically zero. As shown in Fig. 4 the X^+ circular polarization is dramatically reduced to about 30%, which is not the case for X^- (not shown). An external magnetic field can now screen the hyperfine-induced spin relaxation as illustrated in Fig. 4(b). This effect was predicted by I. A. Merkulov *et al* for an ensemble of spin polarized resident electrons [3]. We have applied their model to the case of a positive trion by taking into account its finite radiative lifetime of $\approx$ 700 ps. With a typical amplitude of nuclear field fluctuations $\Delta_{\rm B} = 33$ mT we obtain a very good agreement with the experimental results.

Acknowledgements

This work has been supported by contract BoitQuant of *Fonds National pour la Science* and the European network of excellence SANDIE.

References

[1] M. Kroutvar *et al*, *Nature* **432**, p81 (2004).
[2] P.-F. Braun *et al*, *Phys. Rev. Lett.* **94**, 116601 (2005).
[3] I. Merkulov *et al*, *Phys. Rev. B* **65**, 205309 (2002).
[4] J. M. Smith *et al*, *Phys. Rev. Lett.* **94**, 197402 (2005).
[5] S. Laurent *et al*, *Phys. Rev. Lett.* **94**, 147401 (2005).
[6] M. Bayer *et al*, *Phys. Rev. B* **65**, 195315 (2002).
[7] B. Urbaszek *et al*, *Phys. Rev. Lett.* **90**, 247403 (2003).
[8] M. Ediger *et al*, *Appl. Phys. Lett.* **86**, 211909 (2005).
[9] F. Meier and B. Zakharchenya, *Optical Orientation*, vol. 8 of *Modern Problem in Condensed Matter Sciences* (1984).
[10] D. Gammon *et al*, *Phys. Rev. Lett.* **86**, 5176 (2001).
[11] B. Eble *et al*, *arXiv:cond-mat/0508281* (2005).
[12] C. W. Lai *et al*, *arXiv:cond-mat/0512269* (2005).

14th Int. Symp. "Nanostructures: Physics and Technology"
St Petersburg, Russia, June 26–30, 2006

Spin properties of charge tunable single Mn-doped quantum dot

L. Besombes, Y. Léger, L. Maingault, D. Ferrand and H. Mariette

CEA-CNRS group "Nanophysique et Semiconducteurs", Laboratoire de Spectrométrie Physique,
CNRS & Université Joseph Fourier-Grenoble I, BP 87, 38402 St Martin d'Hères, France

Abstract. We report on electron spin physics in a single charge-tunable self-assembled InAs/GaAs quantum dot. The hyperfine interaction between the optically oriented electron and nuclear spins leads to the polarization of the quantum dot nuclei. The sign of the resulting Overhauser-shift depends on the trion state X^+ or X^-, and remarkably its amplitude does not vanish in zero magnetic field. This explains the quenching of X^+ spin relaxation under steady-state excitation polarization.

Precise control of electronic spins in semiconductors should lead to the development of novel electronic systems based on the carriers' spin degree of freedom. Magnetic semiconductor quantum dots (QDs), where carriers can strongly interact with the magnetic atoms, hold particular promise as building blocks for such spin-based systems. They have been proposed as single-spin filter or single spin aligner in quantum information processing devices. Developing such devices requires, however, the ability to detect and manipulate individual spins.

QDs based on II–VI semiconductor compounds offer the unique possibility of incorporating magnetic ions (Mn^{2+}) isoelectronically into the crystal matrix. This provides a way to study the interaction between a controlled number of injected carriers and the localized magnetic ions. We will show in this presentation how we can optically probe the magnetic state of a single Mn atom embedded in an individual QD and control of the interaction between individual injected carriers and the localized Mn atom.

Magneto-optics micro-spectroscopy is used to study the optical properties of individual Mndoped QDs. The fine structure of a confined exciton in the exchange field of a single Mn^{2+} ion (S=5/2) is analyzed in detail [1]. The exciton-Mn exchange interaction shifts the energy of the exciton depending on the Mn spin component and six emission lines are observed at zero magnetic field. It is then possible to probe the statistic spin state of the Mn atom through the emission intensities of the different discrete exciton levels.

The influence of the system geometry, namely the QD in-plane asymmetry and the position of the Mn atom, will be demonstrated [2]: the fine structure of the X-Mn system can be explained by the interplay between the exciton-Mn exchange interaction (depending on the Mn position) and the anisotropic part of the electron-hole exchange interaction (related to the QD asymmetry).

Bias controlled single carrier charging combined with photodepletion mechanism permits to inject excess carriers in the dots. Investigating the biexciton, the exciton and the charged excitons fine structure in the same Mn-doped QD we analyze the influence of the number of confined carriers on the spin splitting of the Mn atom. The injection of a second electron-hole pair cancels the exchange interaction with the magnetic atom and the Mn spin splitting is significantly reduced [3]. The fine structure of charged excitons coupled with a single Mn spin differs strongly from the exciton-Mn one [4]. This can be attributed to the absence of electron-hole exchange interaction in the case of charged excitons and to the influence of slight valence band mixing [5].

For X^+-Mn, the exchange interaction lift the spin degeneracy of the hole-Mn ground state. An enhancement of the spins relaxation times is then expected. It follows that a positively charged quantum dot containing a single Mn atom could be an efficient systems to control a localized spin on a long time scale. More generally, this study shows that the spin state of a single magnetic atom can be manipulate by the injection of a discrete number of carriers in a single quantum dot.

References

[1] L. Besombes *et al*, *Phys. Rev. Lett.* **93**, 207403 (2004).
[2] Y. Léger *et al*, *Phys. Rev. Lett.* **95**, 047403 (2005).
[3] L. Besombes *et al*, *Phys. Rev. B* **71**, 161307(R) (2005).
[4] Y. Léger *et al*, submitted to *Phys. Rev. Lett.*
[5] Y. Léger *et al*, *Phys. Rev. B* **72**, 241309 (2005).

14th Int. Symp. "Nanostructures: Physics and Technology"
St Petersburg, Russia, June 26–30, 2006

Optical generation of electron spin coherence in singly charged (In,Ga)As/GaAs quantum dots

D. R. Yakovlev[1,2], A. Greilich[1], R. Oulton[1], E. A. Zhukov[1,5], I. A. Yugova[1,6], M. Bayer[1], A. Shabaev[3,7], Al. L. Efros[3], I. A. Merkulov[2], V. Stavarache[4], D. Reuter[4] and A. Wieck[4]

[1] Experimentelle Physik II, Universität Dortmund, 44221 Dortmund, Germany
[2] Ioffe Physico-Technical Institute, St Petersburg, Russia
[3] Naval Research Laboratory, Washington, DC 20375, USA
[4] Angewandte Festkörperphysik, Ruhr-Universität Bochum, 44780 Bochum, Germany
[5] Faculty of Physics, M. V. Lomonosov Moscow State University, 119992 Moscow, Russia
[6] Institute of Physics, St Petersburg State University, 198504, St Petersburg, Russia
[7] School of Computational Sciences, George Mason University, Fairfax VA 22030, USA

Abstract. Electron spin coherence has been generated optically in n-type modulation doped (In,Ga)As/GaAs quantum dots (QDs) which contain on average a single electron per dot. The coherence arises from resonant excitation of the QDs by circularly-polarized laser pulses, creating a coherent superposition of an electron and a trion state. Time dependent Faraday rotation is used to probe the spin precession of the optically oriented electrons about a transverse magnetic field. Spin coherence generation can be controlled by pulse intensity, being most efficient for $(2n+1)\pi$-pulses.

Introduction

An electron spin in a single QD represents a qubit candidate that is very attractive for solid state quantum information processing, as has been suggested by long electron spin coherence times, T_2, measured in bulk semiconductors [1]. These long times are required for performing a sufficient number of quantum manipulations during which coherence needs to be retained. Recent QD studies have demonstrated long electron spin relaxation lifetimes, T_1, in the millisecond-range at cryogenic temperatures [2]. This has raised hopes that T_2, which may last as long as $2T_1$ [3], could be similarly long, with encouraging indications to that effect found lately [4]. Generation of the electron spin coherence was recently reported for charged GaAs/AlGaAs interface QDs [5]. However, only rather low excitation powers were used in those experiments, so that coherent control of electron spin polarization in form of Rabi oscillations did not occur.

In this Report we demonstrate by pump-probe Faraday rotation (FR) that electron spin coherence can be generated by circularly polarized optical excitation of singly charged QDs. Resonant excitation creates an intermediate superposition of a singlet trion and an electron, which after trion radiative decay is converted into a long lived electron spin coherence. The coherence is controlled by the pump pulse area, $\propto \int E(t)dt$, where $E(t)$ is the electric field amplitude. It reaches maximum for $(2n+1)\pi$-pulses [6], in good accord with our theoretical model.

1. Results and discussion

The experiments were performed on (In,Ga)As/GaAs self-assembled QDs. To obtain strong enough light-matter interaction, the sample contained 20 layers of QDs separated by 60 nm wide barriers. It was fabricated by molecular beam epitaxy on a (001)-oriented GaAs substrate. The layer dot density is about 10^{10} cm^{-2}. For an average occupation by a single electron per dot, the structures were n-modulation doped 20 nm below each layer with a Si-dopant density roughly equal to the dot density. The sample was thermally annealed so that its emission occurs around 1.396 eV, as seen from the luminescence spectrum in Fig. 1(a). The full width at half maximum of the emission line is 10 meV, demonstrating good ensemble homogeneity. Further optical properties of these dots and undoped reference sample can be found in Ref. [7].

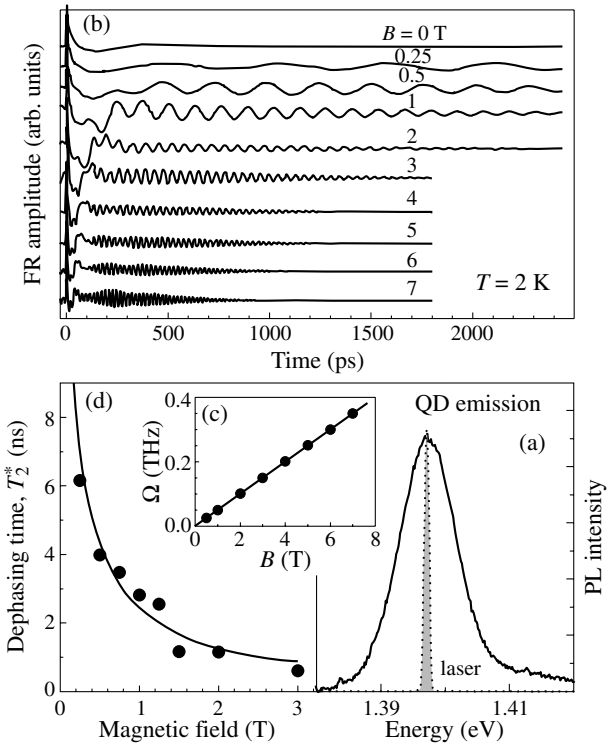

Fig. 1. (a) Photoluminescence spectrum of n-doped (In,Ga)As/GaAs QDs compared to laser spectrum in FR studies. (b) FR traces of these QDs vs delay between pump and probe at different B. Pump power was $\sim$ 10 mW. (c) Magnetic field dependence of electron precession frequency. (d) Spin dephasing time $T_2^\star$ vs B (symbols). Line is a $1/B$-fit to data.

The sample was immersed in liquid helium at temperature $T = 2$ K. The magnetic field $B \leq 7$ T was aligned perpendicular to the structure growth direction z. In the FR pump-

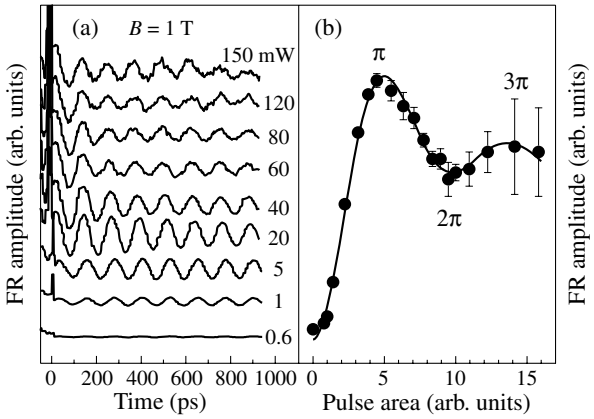

Fig. 2. (a) Closeup of FR rotation signal at $B = 1$ T for different pump powers. (b) FR amplitude vs laser pulse area. Line is guide to the eye. $T = 2$ K.

probe studies [1] a Ti-sapphire laser emitting pulses with a duration of ~ 1 ps (full width at half maximum of ~ 2 meV) at 75.6 MHz repetition rate was used, hitting the sample along z. The laser was tuned to the QD ground state transition energy (see Fig. 1(a)). The circular polarization of the pump beam was modulated at a frequency of 50 kHz. For detecting the rotation angle of the linearly polarized probe pulses, a homodyne technique based on phase-sensitive balanced detection was used.

Figure 1(b) shows the FR signal of the QDs vs delay between pump and probe for different magnetic fields. Pronounced electron spin quantum beats are observed with some additional modulation at high B. With increasing delay time the beats become damped. The oscillations at low B last much longer (for example, about 4 ns at 0.5 T) than the radiative trion lifetime of $\tau_r = 400$ ps, as measured by time-resolved photoluminescence and therefore are due to long-lived residual electrons. Two features are to be noted:

1) The oscillation frequency increases with magnetic field as expected from the spin-splitting of electron states: $\hbar\Omega_e = g_e\mu_B B$, where g_e is the electron g-factor and μ_B is the Bohr magneton. We have analyzed the FR dynamics in Fig. 1(b) by an oscillatory function with exponentially damped amplitude, $\propto \exp\left(-t/T_2^\star\right)\cos\left(\Omega_e t\right)$. The resulting B-field dependence of the electron precession frequency is shown in Fig. 1(c). From a B-linear fit we obtain $\mid g_e \mid = 0.57$.

2) The spin beats become increasingly damped with increasing magnetic field, corresponding to a reduction of the ensemble spin dephasing time $T_2^\star$, plotted in Fig. 1(d). The damping of the spin precession arises from variations of the electron g-factor within the QD ensemble, causing an enhanced spread of Ω_e with increasing B, whose impact on the dephasing time can be described by $\left[T_2^\star(B)\right]^{-1} = \left[T_2^\star(0)\right]^{-1} + \Delta g_e \mu_B B/\sqrt{2}\hbar$. The solid line in Fig. 1(d) shows a $1/B$ fit to the experimental data for $T_2^\star$, from which a g-factor variation of $\Delta g_e = 0.005$ can be extracted. From the data one can also conclude that $T_2^\star(0)$ is longer than 6 ns. The zero-field dephasing is mainly caused by electron spin precession about the frozen magnetic field of the dot nuclei in a QD [8]. The net orientation of nuclei varies from dot to dot, and it is these variations that lead to ensemble spin dephasing.

Figure 2(a) shows FR signals at $B = 1$ T for different pump powers. The corresponding FR amplitude is plotted in Fig. 2(b) as function of the pulse area, which is defined as $\Theta = 2\int[\mathbf{dE}(t)]\,dt/\hbar$ in dimensionless units, where $\mathbf{d}$ is the dipole transition matrix element. For pulses of constant duration, but varying power, as used here, the pulse area is proportional to the square root of excitation power, and it is given in arbitrary units in Fig. 2(b). The amplitude shows a non-monotonic behavior with increasing pulse area. It rises first to reach a maximum, then drops to about 60%. Thereafter it shows another strongly damped oscillation. This behavior is very similar to the one known from Rabi-oscillations of the Bloch vector for varying excitation power [9]. The FR amplitude becomes maximum when applying a π-pulse as pump, for which the z-component of the Bloch vector is fully inverted. It becomes minimum for a 2π-pulse, for which the Bloch vector is turned by 360 °, and so on. These observations are important input for identifying the origin of spin coherence.

Theoretical description of the process of electron spin coherence generation in singly charged QDs is based on the approach suggested in Ref. [10]. A short pulse of circularly polarized light is a remarkable tool for controlling coherently an electron spin in a transverse magnetic field. It generates a coherent superposition of electron and trion state and this coherent superposition is uniquely determined by the pulse area.

In conclusion, we have shown experimentally and theoretically that pulses of circularly polarized light allow for a coherent phase control of an electron spin in a QD. The coherent control results in FR amplitude oscillations with varying laser pulse area.

Acknowledgements

This work was supported by the BMBF program 'nanoquit', ONR, and CRDF. RO thanks the Alexander von Humboldt foundation. Research visits to Dortmund have been financed by DFG: for EAZh via grant 436 RUS 17/93/05 and for IAY via grant 436 RUS 17/98/05.

References

[1] J. M. Kikkawa and D. D. Awschalom, *Science* **287**, 473 (2000).
[2] J. M. Elzerman *et al*, *Nature* **430**, 431 (2004]; M. Kroutvar *et al*, *Nature* **432**, 81 (2004).
[3] W. A. Coish and D. Loss, *Phys. Rev. B* **70**, 195340 (2004).
[4] J. R. Petta *et al*, *Science* **309**, 2180 (2005).
[5] M. V. Gurudev Dutt *et al*, *Phys. Rev. Lett.* **94**, 227403 (2005).
[6] M. O. Scully and M. S. Zubairy, *Quantum Optics.*, Cambridge University Press (1997).
[7] A. Greilich *et al*, cond-mat/0505446 and /0601107.
[8] I. A. Merkulov, Al. L. Efros and M. Rosen, *Phys. Rev. B* **65**, 205309 (2002).
[9] see, for example, T. H. Stievater *et al*, *Phys. Rev. Lett.* **87**, 133603 (2001); A. Zrenner *et al*, *Nature* **418**, 612 (2002) and references therein.
[10] A. Shabaev *et al*, *Phys. Rev. B* **68**, 201305(R) (2003).

14th Int. Symp. "Nanostructures: Physics and Technology"
St Petersburg, Russia, June 26–30, 2006

Imaging electrical spin injection and spin flow in ferromagnet-semiconductor devices

S. A. Crooker[1], M. Furis[1], X. Lou[2], C. Adelmann[3], D. L. Smith[4], C. J. Palmstrøm[3] and P. A. Crowell[2]

[1] National High Magnetic Field Laboratory, Los Alamos National Laboratory, Los Alamos, NM 87545, USA
[2] School of Physics and Astronomy, University of Minnesota, 116 Church Street SE, Minneapolis, MN 55455, USA
[3] Department of Chemical Engineering and Materials Science, University of Minnesota, 421 Washington Avenue SE, Minneapolis, MN 55455, USA
[4] Theoretical Division, Los Alamos National Laboratory, Los Alamos, NM 87545, USA

Abstract. Using techniques for scanning magneto-optical Kerr microscopy, we directly image the electrical injection and accumulation of spin-polarized electrons in the GaAs channel of lateral ferromagnetic/semiconductor spin transport devices. These lateral devices have epitaxial Fe source and drain Schottky tunnel-barrier contacts at either end of a lightly-doped GaAs channel. The injection and transport of spins from the source is directly observed, and also a region of spin accumulation is imaged near the ferromagnetic drain contact. Both injected and accumulated spins have the same orientation (antiparallel to the Fe magnetization). By controlling the strain in the sample, we show that the accumulated spin polarization is actually flowing away from the drain (against the net electron current), suggesting spin polarized reflection of electrons from the drain contact. Further, the electrical conductance of the device can be modulated by controlling the spin orientation of optically-injected electrons flowing through the drain.

Introduction

The ability to control and measure the spin of an electron in semiconductors has recently been proposed as the operating principle for a new generation of spin-electronic, or "spintronic" devices [1]. By taking advantage of the electron's spin degree of freedom, today's charged-based microelectronics may realize significant improvements in operating speed and power consumption. Many designs for functional spintronic devices have been recently proposed; for example, the "spin transistor" — a device whose 'on' and 'off' states depend on whether the current-carrying electrons are polarized spin-up or spin-down. Proposed schemes for spintronic devices generally require three essential elements: (i) a mechanism for *electrically injecting* spin-polarized electrons into semiconductors, (ii) a practical means for *spin manipulation and transport*, and (iii) an electronic scheme for *detecting* the resulting spin polarization.

Here we describe the direct observation of spin injection, transport, accumulation, and detection in devices with metallic ferromagnetic source and drain contacts at opposite ends of a n-GaAs channel. These results were recently reported in Ref. [2]. Each contact, which can be used as either an injector or detector, is a Schottky tunnel barrier formed by an epitaxial iron (Fe) film grown on a highly-doped n^+-GaAs layer. Scanning Kerr microscopy is used to image the spin transport in the channel region.

1. Experimental

Figure 1(a) shows a photomicrograph of a typical device. These Fe/GaAs devices are grown by molecular-beam epitaxy on semi-insulating (100) GaAs. A 300 nm buffer layer of undoped GaAs is first deposited, followed by 2 μm of lightly Si-doped n-GaAs ($n = 2\times10^{16}$ cm^{-3}, to give long spin lifetimes [3]). The doping is then increased to $n^+ = 5\times10^{18}$ cm^{-3} over the next 15 nm, followed by a 15 nm $n^+ = 5\times10^{18}$ cm^{-3} layer. 5 nm of Fe is then deposited at 273 K, followed by 2 nm of aluminum. The Fe contacts have a significant magneto-crystalline anisotropy, with the easy axis along the [011] (or $\hat{x}$) direction, a typical coercivity of 150 G, and nearly perfect remanence. The source and drain contacts are magnetized in the same direction. Magnetic force microscopy of the contacts shows a uniformly magnetized Fe film. The narrow depletion region at the Fe/GaAs interface forms a triangular Schottky tunnel barrier [4]. A 100×380 μm mesa is defined by wet-etching through all of the epitaxial layers. An additional etch defines the 40×100 μm Fe contacts, and we also remove the n^+-GaAs layer from the 100×300 μm channel between the contacts. Gold vias to the Fe contacts are deposited on SiN isolation layers, and each contact can be used either as a spin injector or detector.

We measure the $\hat{z}$-component of electron spin polarization (S_z) of in the n-GaAs channel via the polar Kerr rotation angle θ_K imparted on a linearly-polarized probe laser that is reflected from the surface at normal incidence. Positive θ_K indicates positive S_z. The probe laser beam (50–100 μW), derived from a cw Ti:Sapphire laser, is tuned just below the 1.515 eV GaAs band edge and focused to a 4 μm spot. 2-D images are obtained by scanning the probe laser in the $x-y$ sample plane. Lock-in detection of electrically injected and accumulated spins is enabled by modulating the device bias from 0 to V_{bias} with a 3.1 kHz square wave. Helmholtz coils generate small in-plane magnetic fields (B_y). Nuclear spin effects are not observed in these experiments. Background images, measured in large B_y ($>$ 60 G, where spins are completely dephased), are subtracted from the raw image data, eliminat-

ing any spurious birefringent or dichroic effects that are not explicitly due to spin precession. The devices were mounted, strain-free, on the 4 K vacuum cold finger of a small magneto-optical cryostat. Uniform uniaxial stress along the [011] GaAs crystal axis could be applied *in situ* using a cryogenic vise built into the cold finger [5].

2. Data and discussion

Figure 1(b) shows 2-D images of the measured Kerr rotation (electron spin polarization) in the GaAs channel adjacent to the Fe source and drain contacts. Electrical injection (and transport) of spins from the source contact (the left contact) is clearly observed. A small in-plane field B_y is used to tip the injected spins out-of-plane (from $\pm\hat{x}$ to $\pm\hat{z}$) so that they can be measured via the polar Kerr effect. We independently verify that these injected spins have initial spin orientation **S** that is *anti*parallel to **M** (per expectation — the majority electron spin polarization in Fe is antiparallel to **M**).

The GaAs channel is 300 μm long, much longer than the typical spatial decay length (50 μm) of the injected spin polarization. Therefore, the injected electrons lose their polarization well before they reach the drain contact. Nonetheless, Fig. 1(b) reveals an accumulation of electron spin polarization in the channel within $\sim$ 10 μm of the drain contact (right contact). The Kerr signal has the same sign, demonstrating that the accumulated spin polarization near the drain is also oriented antiparallel to **M**. When the electrical bias is reversed, as shown in Figure 1(c), the roles of the source and drain are also reversed. Fig. 1(c) now shows spin injection from the right contact (now the source), and spin accumulation near the left contact (now the drain). We also verify that the sign of the Kerr signal switches when we switch the magnetization **M** of the Fe contacts. The 2-D images are modeled very well by numerically solving a set of coupled spin-drift-diffusion equations [5,6].

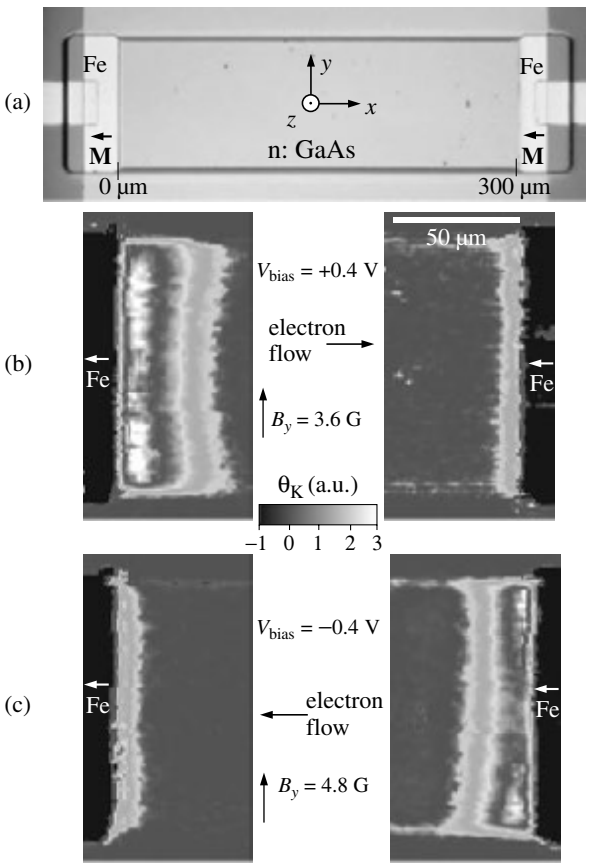

Fig. 1. (a) Photo of a lateral Fe/GaAs spin transport device. The Fe/GaAs tunnel-barrier source and drain contacts are magnetized along $-\hat{x}$ as shown. The GaAs channel is 300 μm long. (b) 2-D images of electron spin polarization (Kerr rotation angle $\theta_K \propto S_z$) near the source and drain contacts. $V_{bias} = +0.4$ V. Efficient electrical spin injection from the source (left) contact is clearly observed. The spin polarized electrons that accumulate near the drain (right) contact are actually flowing "upstream" (against the net electron current). (c) Images taken with the electrical bias reversed ($V_{bias} = -0.4$ V). Note the roles of the source and drain contacts are reversed. Images adapted from Ref. [2].

By applying a controlled uniaxial stress to the device substrate, it is possible to determine in which direction the spin-polarized electrons are moving. Stress along the [011] GaAs axis results in off-diagonal elements of the strain tensor $\epsilon_{\alpha\beta}$, which leads to effective magnetic fields felt by moving electrons due to spin-orbit coupling [5,7]. For electrons moving laterally in the $x-y$ sample plane, the spin-orbit Hamiltonian is $H_S \propto \epsilon_{\alpha\beta}(\sigma_y k_x - \sigma_x k_y)$, which describes an effective magnetic field $\mathbf{B}_\epsilon$ that is always in-plane and orthogonal to the electron momentum **k** (note this has a similar form to the Rashba Hamiltonian for 2D electrons moving in an asymmetric potential [8]). For electrons moving along $\pm\hat{x}$, as in our devices, $\mathbf{B}_\epsilon$ either augments or opposes the applied field B_y, thereby shifting the measured 'Hanle curves' ($\theta_K(B_y)$) to the right or left depending on the spin flow direction. As detailed in Ref. [2], the Hanle curves measured near the source and drain contacts shift in *opposite* directions with increasing uniaxial strain, indicating

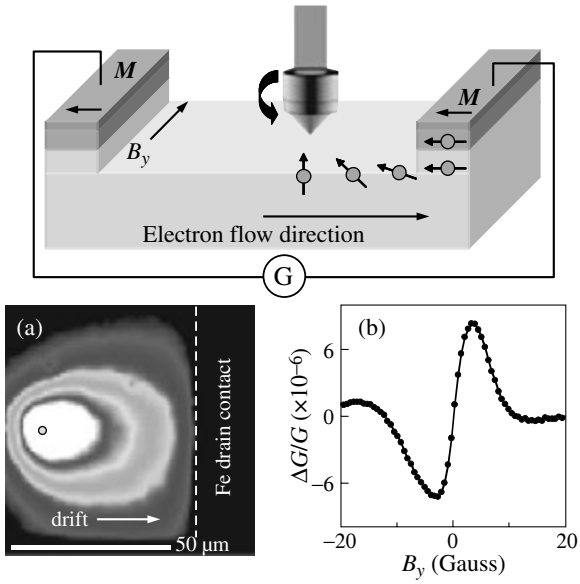

Fig. 2. Electrical spin detection: spin-polarized electrons are optically injected and then transported through the Fe drain contact. An in-plane magnetic field B_y forces these spins to precess parallel or antiparallel to the drain magnetization **M**. a) A 2-D image of optically injected electrons, spin polarized along $\hat{z}$, flowing to the drain contact ($V_{bias} = +0.36$ V). Data adapted from Ref. [2]. b) The device conductivity $\Delta G/G$ vs. B_y. G is larger (smaller) when the electron current at the drain is spin-polarized parallel (antiparallel) to the drain magnetization **M**.

that the spin polarized electrons that accumulate near the drain contact are flowing 'upstream', against the net electron current. This is consistent with the accumulated spin polarization being due to spin-sensitive reflection of electrons from the Fe/GaAs Schottky tunnel barrier [9, 10].

Finally, we demonstrate that the Fe/GaAs Schottky tunnel barriers can also function as electrical spin detectors (in addition to their role as spin injectors). Here we measure the conductivity G of the device while optically injecting spin polarized electrons, as shown schematically in Figure 2. These optically injected electrons, spin polarized along $\pm\hat{z}$, are made to flow through the drain contact by an electrical bias (see experimental image of this spin flow in Figure 2a). A small in-plane magnetic field $\pm B_y$ forces precession of these spins such that they arrive at the drain contact with spin orientation parallel or antiparallel to the drain magnetization **M**. We measure the corresponding modulation of the device's conductance ΔG. Figure 2(b) shows that the device conductance is indeed modulated by the spin polarization of the electrons flowing through the drain contact, such that the high conductance state occurs when the electron spins are polarized parallel to **M**. In a simple picture of a semiconductor/ferromagnet tunnel barrier with spin-sensitive transmission and reflection coefficients, this is consistent with the previous observation (Fig. 1b) of accumulated electrons that are spin polarized antiparallel to **M**. These $\Delta G(B_y)$ curves invert when **M** is reversed, as expected. These data provide conclusive evidence that the Fe/GaAs Schottky tunnel barriers can function both as spin detectors and injectors.

These studies provide a detailed picture of spin transport in simple ferromagnet/semiconductor lateral structures. All aspects of a functional spin transport device — electrical spin injection, spin transport and manipulation, and electrical spin detection — can be separately investigated in a single device. These magneto-optical studies provide insight into the signals and backgrounds one can expect in purely electrical measurements of similar devices [11].

Acknowledgements

This work has been supported by the DARPA SpinS and Los Alamos LDRD programs, NSF DMR 02-12032, the Office of Naval Research, and the Minnesota Nanofabrication Center.

References

[1] S. A. Wolf *et al*, *Science* **294**, 1488 (2001).
[2] S. A. Crooker, M. Furis, X. Lou, C. Adelmann, D. L. Smith, C. J. Palmstrøm and P. A. Crowell, *Science* **309**, 2191 (2005).
[3] R. I. Dzhioev, K. V. Kavokin, V. L. Korenev, M. V. Lazarev, B. Ya. Meltser, M. N. Stepanova, B. P. Zakharchenya, D. Gammon, D. S. Katzer, *Phys. Rev. B* **66**, 245204 (2002).
[4] A. T. Hanbicki *et al*, *Appl. Phys. Lett.* **82**, 4092 (2003).
[5] S. A. Crooker and D. L. Smith, *Phys. Rev. Lett.* **94**, 236601 (2005).
[6] M. Hruska, S. Kos, S. A. Crooker, A. Saxena, D. L. Smith, *Phys. Rev. B* **73**, 075306 (2006).
[7] G. E. Pikus, A. N. Titkov, in *Optical Orientation*, F. Meier, B. P. Zakharchenya, Eds. (North-Holland, Amsterdam, 1984), pp. 73–131.
[8] Y. A. Bychkov and E. I. Rashba, *J. Phys. C* **17**, 6039 (1984).
[9] C. Ciuti, J. P. McGuire and L. J. Sham, *Phys. Rev. Lett.* **89**, 156601 (2002).
[10] J. Stephens *et al*, *Phys. Rev. Lett.* **93**, 097602 (2004).
[11] X. Lou, C. Adelmann, M. Furis, S. A. Crooker, C. J. Palmstrøm and P. A. Crowell, *Phys. Rev. Lett. in press* (2006), cond-mat/0602096.

14th Int. Symp. "Nanostructures: Physics and Technology"
St Petersburg, Russia, June 26–30, 2006

Manifestation of pure spin currents induced by spin dependent scattering processes

S. D. Ganichev[1], V. V. Bel'kov[1,2], S. A. Tarasenko[2], S. N. Danilov[1], *S. Giglberger*[1], Ch. Hoffmann[1], E. L. Ivchenko[2], D. Weiss[1], C. Gerl[1], D. Schuh[1], W. Wegscheider[1] and W. Prettl[1]

[1] Fakultät Physik, University of Regensburg, 93040, Regensburg, Germany
[2] Ioffe Physico-Technical Institute, St Petersburg, Russia

Abstract. We show that in gyrotropic semiconductor structures spin-dependent asymmetry of electron scattering induce a pure spin current which, in contrast to the spin Hall effect, does not require an electric current to flow. The effect is observed in GaAs/AlGaAs single heterojunction at free-carrier absorption of terahertz radiation in a wide range of temperatures from liquid helium temperature up to room temperature. The results agree with the phenomenological description based on the symmetry. Experimental and theoretical analysis evidences unumbiguously that the observed photocurrents are spin-dependent and related to the gyrotropy of the low-dimensional structures. Microscopic theory of this effect based on asymmetry of photoexcitation and relaxation processes are developed being in a good agreement with experimental data.

The spin-orbit coupling provides a versatile tool to generate and to manipulate the spin degree of freedom in low-dimensional semiconductor structures. The spin Hall effect, where an electrical current drives a transverse spin current and causes a nonequilibrium spin accumulation near the sample boundary, the spin-galvanic effect, where a nonequilibrium spin polarization drives an electric current or the reverse process, in which an electrical current generates a nonequilibrium spin polarization, are all consequences of spin-orbit coupling. In order to observe a spin Hall effect a bias driven current is an essential prerequisite. Then spin separation is caused via spin-orbit coupling either by Mott scattering (extrinsic spin Hall effect) or by spin splitting of the band structure (intrinsic spin Hall effect).

Here we provide evidence for an elementary effect causing spin separation which is fundamentally different from that of the spin Hall effect. In contrast to the spin Hall effect it does not require an electric current to flow: it is spin separation achieved by spin-dependent scattering of electrons in media with suitable symmetry. We show that by free carrier (Drude) absorption of terahertz radiation spin separation is achieved in a wide range of temperatures from liquid helium temperature up to room temperature. Moreover the experimental results demonstrate that simple electron gas heating by any means is already sufficient to yield spin separation due to spin-dependent energy relaxation processes of nonequilibrium carriers.

In order to demonstrate the existence of the pure spin current due to asymmetric scattering we converted the pure spin current into an electric current. It is achieved by application of a magnetic field which polarizes spins. This is analogues to spin-dependent scattering in transport experiments: spin-dependent scattering in an unpolarized electron gas causes the extrinsic spin Hall effect, whereas in a spin polarized electron gas a charge current, the anomalous Hall effect, can be observed.

The experiments are carried out on grown by MBE (001)-oriented n-type GaAs/AlGaAs single heterojunctions. A molecular terahertz laser has been used as radiation source delivering 100 ns pulses with a radiation power up to 1 kW. Several lines in the wavelength range between 77 and 496 μm have been selected. The terahertz radiation causes indirect optical transitions within the lowest size-quantized subband. The samples are irradiated under normal incidence along the growth direction. The magnetic field with a maximum field strength of 0.3 T is applied parallel to the heterostructure interface. In experiments the angle α between the polarization vector of the linearly polarized light and the magnetic field is varied. The photocurrent is measured both in the direction normal and parallel to the magnetic field.

Irradiation of the samples at zero magnetic field does not lead to any photocurrent. A current response was obtained only when a magnetic field was applied. The current detected in two directions, normal and parallel to the in-plane magnetic field, increases linearly with magnetic field strength and changes sign upon reversal of the magnetic field direction. The photocurrent is measured as a function of magnetic field, temperature, mobility, carrier concentration and polarization of radiation. The polarization dependence of the current in the transverse geometry is described by $\cos 2\alpha$, while it follows a $\sin 2\alpha$ dependence for the longitudinal geometry. The observed polarization dependences of the photocurrent correspond to that given by phenomenological consideration. With increasing of the radiation wavelength the current raises as a wavelength square.

Microscopic analysis taking into account the scattering asymmetry induced contribution to the photocurrent is carried out being in a good agreement with experiment. All central experimental features of the terahertz photocurrent, namely magnetic field, temperature, mobility, and concentration dependences provide evidence that the observed photocurrent is solely determined by the spin degree of freedom. It can only be understood if the photocurrent is proportional to the equilibrium spin polarization. The results of this work demonstrate that spin-dependent scattering provides a new tool for spin manipulation.

Acknowledgements

This work was supported by the Deutsche Forschungsgemeinschaft through SFB 689, the RFBR and programs of the RAS and HBS.

References

[1] S. A. Tarasenko and E. L. Ivchenko, *Pis'ma Zh. Eksp. Teor. Fiz.* **81**, 292 (2005) [*JETP Lett.* **81**, 231 (2005)].

[2] V. V. Bel'kov, S. D. Ganichev, E. L. Ivchenko *et al*, *J. Phys.: Condens. Matter* **17**, 3405 (2005).

14th Int. Symp. "Nanostructures: Physics and Technology"
St Petersburg, Russia, June 26–30, 2006

Interplay of Rashba and Dresselhaus spin splittings in 2D weak localization

M. M. Glazov and L. E. Golub
Ioffe Physico-Technical Institute, St Petersburg, Russia

Abstract. The effects of structural (Rashba) and bulk (Dresselhaus) spin-orbit interaction terms on the low-field magnetoresistance are investigated in high-quality two dimensional systems. The weak localization theory accounting for both of these terms valid in the whole range of magnetic fields is proposed. The suppresion of antilocalization correction as Rashba and Dresselhaus terms strengths approach each other is demonstrated. The effect of cubic in the wavevector spin-splitting term is analyzed.

Introduction

Spin properties of carriers in semiconductor heterostructures attract now great attention due to spintronics proposals. From the point of view of fundamental physics as well as of possible applications the control of spin-orbit splitting of electronic energy spectrum in two-dimensional systems is one of the most important aspects. There are two contributions to the spin-orbit splitting in two-dimensional semiconductor structures: the Rashba and the Dresselhaus terms caused by structure and bulk inversion asymmetry respectively. Their magnitudes can be measured in various optical and transport experiments. In this work we investigate the effect of these spin splittings on low-field magnetoresistance caused by weak localization.

As the nature of Dresselhaus and Rashba terms is different they possess different symmetry and they are not additive in various kinetic phenomena. The weak antilocalization theory developed in Ref. [1] was limited to extremely weak magnetic fields where the electron motion can be considered as diffusive and to small values of spin-splittings. The theory valid in the whole range of the magnetic fields was developed in the Ref. [2] for the case of only one term being relevant. However, the experiment evidences the comparable magnitudes of both contributions, see e.g. Ref. [3]. An attempt to account simultaneously both Dresselhaus and Rashba terms was carried out in [3] but their theory was limited by rather high magnetic fields.

Here we present a general theory which allows to compute quantum conductivity corrections in the whole range of classically weak magnetic fields and for arbitrary values of Dresselhaus and Rashba spin-orbit splittings. We demonstrate that, for equal magnitudes of these contributions, the weak-localization conductivity correction exactly equals to that in the absence of spin-orbit interaction. In such a case even small cubic in wavevector spin-splitting modifies strongly of magnetoresistance leading to antilocalization minimum.

1. Theory

In what follows we concentrate on zince-blende lattice-based quantum wells grown along [001] direction. The spin-orbit interaction is described by the following Hamiltonian

$$H_{\rm SO}(\boldsymbol{k}) = \hbar\boldsymbol{\sigma}\cdot[\boldsymbol{\Omega}_{\rm R}(\boldsymbol{k}) + \boldsymbol{\Omega}_{\rm D}(\boldsymbol{k})]\,, \qquad (1)$$

where $\boldsymbol{k}$ is the electron wave vector, $\boldsymbol{\sigma}$ is the vector of Pauli matrices. $\boldsymbol{\Omega}_{\rm R(D)}$ characterizes the spin precession frequency due to Rashba (Dresselhaus) term which explicitly read: $\boldsymbol{\Omega}_{\rm D}(\boldsymbol{k}) = \Omega_{\rm D}(\cos\chi, -\sin\chi)$ and $\boldsymbol{\Omega}_{\rm R}(\boldsymbol{k}) = \Omega_{\rm R}(\sin\chi, -\cos\chi)$. Here χ is the angle between $\boldsymbol{k}$ and [100] axis and $\Omega_{\rm D}$, $\Omega_{\rm R}$ are the coupling strengths.

In accordance with Eq. (1) the electron motion is accompanied with spin rotation yielding the appearance of spin-dependent phase in the Green's function [2]

$$G^{\rm R,A}(\boldsymbol{r},\boldsymbol{r}') = G_0^{\rm R,A}(R)\exp\left[{\rm i}\varphi(\boldsymbol{r},\boldsymbol{r}') - {\rm i}\boldsymbol{\sigma}\cdot\boldsymbol{\omega}(\boldsymbol{R})\right]\,, \qquad (2)$$

where $\boldsymbol{R} = \boldsymbol{r} - \boldsymbol{r}'$, $G_0^{\rm R,A}$ are retarded (R) and advanced (A) Green's function for electron's propagation in the short-range random potential without magnetic field $B = 0$ and spin splitting $\boldsymbol{\Omega} = 0$, $\varphi(\boldsymbol{r},\boldsymbol{r}') = (x+x')(y'-y)/2l_B^2$ with $l_B = \sqrt{\hbar/eB}$ being the magnetic length and vector $\boldsymbol{\omega}(\boldsymbol{R}) = \boldsymbol{\Omega}_{\rm R}(k_{\rm F}l^{-1}\boldsymbol{R}) + \boldsymbol{\Omega}_{\rm D}(k_{\rm F}l^{-1}\boldsymbol{R})$, $k_{\rm F}$ is the Fermi wavevector, l is the mean free path.

Following the general theory of quantum-conductivity corrections [4] we solve the equation for the interference magnitude Cooperon $\mathcal{C}(\boldsymbol{r},\boldsymbol{r}')$

$$\mathcal{C}(\boldsymbol{r},\boldsymbol{r}') = \frac{\hbar^3}{m\tau}\mathcal{P}(\boldsymbol{r},\boldsymbol{r}') + \int d\boldsymbol{r}_1\mathcal{P}(\boldsymbol{r},\boldsymbol{r}_1)\mathcal{C}(\boldsymbol{r}_1,\boldsymbol{r}')\,, \qquad (3)$$

where m is electron effective mass, τ is the scattering time, $\mathcal{P}_{\alpha\gamma,\beta\delta}(\boldsymbol{r},\boldsymbol{r}') = \hbar^3/m\tau G^{\rm R}_{\alpha\beta}(\boldsymbol{r},\boldsymbol{r}')G^{\rm A}_{\gamma\delta}(\boldsymbol{r},\boldsymbol{r}')$, expanding the quantities entering Eq. (3) in the series over the wavefunctions of spinless particle with charge $2e$. In the general case where both Rashba and Dresselhaus terms are present in the spin-orbit Hamiltonian, the isotropy of the energy spectum in the system is removed and all the 'Landau levels' of $2e$ particle become intermixed as opposed to the case of one term being relevant. In the latter situation the total angular momentum is conserved allowing to separate full Cooperon matrix into finite blocks [2]. Finally, as Cooperon is known the computation of conductivity reduces to the simple linear-algebra problem [5].

2. Results and Discussion

Figure 1 presents the quantum conductivity correction plotted vs. $B/B_{\rm tr}$ ($B_{\rm tr} = \hbar/2el^2$) for different relation of Rashba and Dresselhaus constants. The value of Dresselhaus term is fixed to be $\Omega_{\rm D}\tau = 1$ for all curves in the figure while Rashba term took different values $\Omega_{\rm R}\tau$.

The curve corresponding to $\Omega_{\rm R} = \Omega_{\rm D}$ exactly coincides with the result for spinless particles [4]. The magnitude of the quantum correction decreases with the magnetic field as long trajectories (longer than l_B) are suppressed in the magnetic

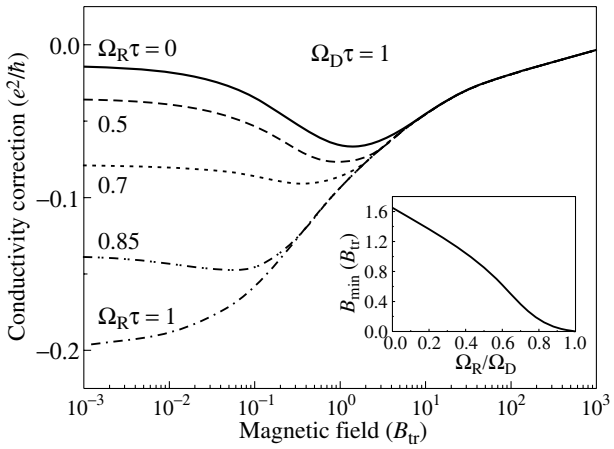

Fig. 1. Magnetoconductivity computed for the constant Dresselhaus term $\Omega_D\tau = 1$ and different values of Rashba term $\Omega_R\tau$. The phase-breaking time τ_ϕ equals to $\tau_\phi = 100\tau$. The inset shows the minimum position vs. Ω_R/Ω_D.

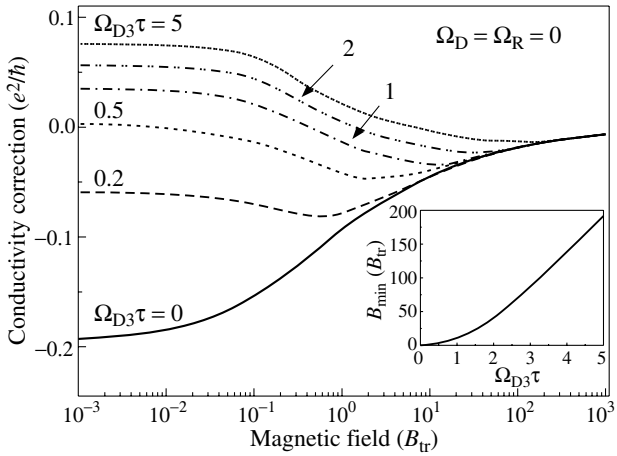

Fig. 2. Conductivity correction computed for case of zero linear-$\boldsymbol{k}$ contribution $\Omega_R = \Omega_D = 0$ and different values of $\boldsymbol{k}$-cubic term $\Omega_{D3}\tau$ and $\Omega_D = \Omega_R = 0$. The inset demonstrates the antilocalization minimum position vs. $\Omega_{D3}\tau$.

field. In this case the spin precession axis is directed along either $[1\bar{1}0]$ or $[110]$ for any wavevector $\boldsymbol{k}$ and the spin rotation angle for closed trajectories is zero.

With the decrease of the Rashba term, the spin rotation angle for closed loops is no longer equals to zero and the magnetoconductivity becomes non-monotonous. As for the given trajectory the spin rotation angle will be the greater the greater $|\Omega_R^2 - \Omega_D^2|\tau^2$, the decrease of the Rashba term (at fixed Dresselhaus one) will manifest itself as an increase of spin-orbit interaction [1]. The minimum of the magnetoconductivity shifts to the smaller fields (see inset to Fig. 1) and its depth decreases.

3. Effect of k-cubic term

Besides the linear-$\boldsymbol{k}$ terms studied above the spin-orbit interaction Eq. (1) contains also cubic in the wavevector contribution originated from the bulk Dresselhaus term

$$\Omega_3^D(\boldsymbol{k}) = \Omega_{D3}(\cos 3\chi, \sin 3\chi)\,. \qquad (4)$$

The constant Ω_{D3} can be of the same order of magnitude as Ω_D and Ω_R [1,3] thus its effect on quantum conductivity corrections may be important. Also, the calculation of the zero-field correction shows that for $\Omega_R/\Omega_D = 1$ where linear in $\boldsymbol{k}$ terms compensate each other the conductivity correction is determined to within the 10% by cubic contribution Eq. (4). Thus, we focus on the case where only $\boldsymbol{k}$-cubic term is present in the effective Hamiltonian and compute magnetoconductivity for the different values of the $\Omega_{D3}\tau$ and $\Omega_D = \Omega_R = 0$, see Figure 2.

Qualitatively the behavior of the curves in Figure 2 concides with that found for case of linear in the wavevector spin splitting [2]. In the high field case $B \gg \max\left[(\Omega_{D3}\tau)^2, 1\right] B_{tr}$ all curves have the same asymptotics. As it can be seen from the figure inset the magnetoconductivity minimum shifts to the higher field range with an increase of $\Omega_{D3}\tau$. The minimum depth is a non-monotonous function of the spin splitting: for the small spin splitting values the increase of the splitting leads to an increase of mininum depth while for higher splittings the behavior is opposite.

Conclusion

We put forward a general theory of quantum conductivity corrections valid in the whole range of classically weak magnetic fields and taking into account the conduction band spin-splitting. Both Rashba and Dresselhaus terms were considered. We have shown that if Rashba and Dresselhaus terms are exactly equal the weak-localization correction is the same as in the spin-less case. The crossover between weak localization and weak antilocalization is demonstrated as Rashba term value approaches to that of Dresselhaus term. The effect of cubic in the wavevector part of Dresselhaus term is comprehensively studied. The proposed theory can be used in the analysis of the low-field magnetoresistance to precisely extract the spin-splitting magnitudes from the transport measurements.

Acknowledgements

This work is financially supported by RFBR, Russian President grant for young scientists and by "Dynasty" Foundation–ICFPM.

References

[1] F. G. Pikus and G. E. Pikus, *Phys. Rev. B* **51**, 16 928 (1995).
[2] L. E. Golub, *Phys. Rev. B* **71**, 235310 (2005).
[3] J. B. Miller, D. M. Zumbühl, C. M. Marcus, Y. B. Lyanda-Geller, D. Goldhaber-Gordon, K. Campman and A. C. Gossard, *Phys. Rev. Lett.* **90**, 076807 (2003).
[4] V. M. Gasparyan and A. Yu. Zyuzin, *Fiz. Tverd. Tela* **27**, 1662 (1985) [*Sov. Phys. Solid State* **27**, 999 (1985)].
[5] M. M. Glazov and L. E. Golub, *Semiconductors*, in press.

14th Int. Symp. "Nanostructures: Physics and Technology"
St Petersburg, Russia, June 26–30, 2006

Evanescent states in cubic semiconductors with inversion asymmetry and spin-orbit interaction

T. Nguyen-Quang, *J.-M. Jancu* and P. Voisin
Laboratoire de Photonique et de Nanostructures, CNRS, route de Nozay, F-91460, Marcoussis, France

Abstract. We examine the complex band structure in zinc-blende semiconductors with inversion asymmetry and spin-orbit interaction. Due to odd powers of k in the spin-split dispersion relation, purely imaginary wavevectors are no longer eigenvectors for the evanescent states. Solving the complex band structure requires a non-trivial exploration of the complex plane. This issue is addressed using a 14×14 $\mathbf{k} \cdot \mathbf{p}$ Hamiltonian and a 40-band tight-binding model. We find that evanescent states exist for any direction in the Brillouin zone. The relevance of the present results to the spin dependent tunneling probabilities is discussed.

There is presently a strong revival of the interest in spin effects in semiconductors, stimulated by the goal of developing a new generation of electronic devices based on the control of the carrier spin besides of their electric charge [1,2]. Among the possible devices, spin-dependent tunnel diodes have shown some promises [3]. However, to the best of our knowledge, spin-related phenomena in the complex band structure have not yet been thoroughly considered from a theoretical point of view. Bulk inversion asymmetry (BIA) in III–V semiconductors results in a lifting of spin degeneracy in the conduction band, proportionnal to the third power of the real wave-vector near the center of the Brillouin zone [5]. This rises an interesting problem relative to evanescent states for an electron impinging on a potential barrier: clearly, considering an imaginary wave-vector together with a k^3 term in the dispersion relation introduces a non-physical imaginary component of the eigenenergy.

In a recent paper, Rougemaille *et al* [4] have examined this problem in the framework of the 14-bands $\mathbf{k} \cdot \mathbf{p}$ theory. Very stimulating and drastic conclusions are reached in [4] concerning the spin properties of evanescent states. A most salient prediction is the strict disappearance of evanescent states for an electron impinging on a potential barrier in the [110] direction. These conclusions are reached from solutions (or lack of solutions) of the 14-bands $\mathbf{k} \cdot \mathbf{p}$ Hamiltonian for an imaginary value of the wave vector. Many paradoxical conclusions can be extrapolated from the results of [4]. For instance, a GaAs/AlGaAs superlattice grown along the [110] direction should be dispersion-less whatever the superlattice period is. Furthermore, when turning on the inversion asymmetry parameters, the evanescent states in this direction would disappear abruptly for an infinitesimal asymmetry. It is clear that such conclusions are unlikely and question the validity of the corresponding calculation. Here, we re-examine the spin-orbit coupling effect on the complex band structure of zinc-blende semiconductors.

During the tunneling process through a potential barrier, the momentum of an incoming electron can be split into an in-plane component $k_\parallel$ parallel to the interface which is purely real, and a complex component k_z, leading an electron state decaying exponentially into the barrier. We insist that in general, the complex number k_z may have a real part. In the case of semiconductor superlattices, the exponential tail of a wavefunction gives rise to tunnel coupling of adjacent wells and finite dispersion of the superlattice states. In Fig. 1 we illustrate

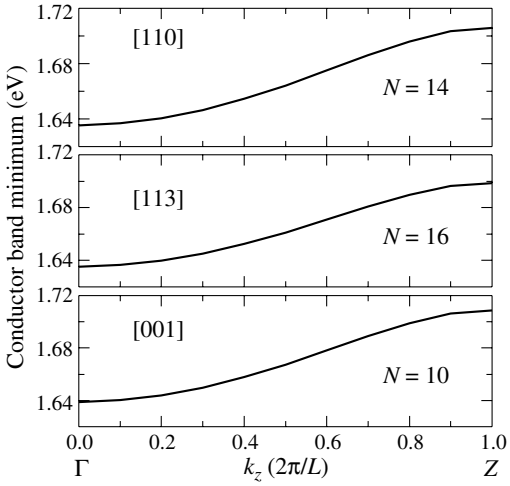

Fig. 1. Miniband dispersion of the two spin states in (klm)-oriented $(GaAs)_N$–$(Al_{0.3}Ga_{0.7}As)_N$ superlattices, with a layer thickness of 30 Å both for the well and the barrier, calculated with a nearest-neighbor $sp^3d^5s^*$ tight-binding model. The Z point represents the boundary of the superlattice Brillouin zone. Energy is referred to the valence-band maximum of GaAs. The spin degeneracy is broken for the [110] and [113] directions except at Γ and Z.

this and show that the conduction bandwidth of (klm)-oriented $(GaAs)_N/(AlGaAs)_N$ superlattices is nearly insensitive to the growth direction, which is in sharp contrast with a prediction straightforwardly extrapolated from Ref. [4]. Electronic band structure calculations of Fig. 1 were performed within the tight-binding approximation using an $sp^3d^5s^*$ nearest neighbor model [6] that ncludes spin-orbit coupling and inversion asymmetry in a similar way of the 14-bands $\mathbf{k} \cdot \mathbf{p}$ model. This model actually provides a perfect fit of both the $\mathbf{k} \cdot \mathbf{p}$ theory and known experimental data, albeit with revised parameters differing significantly from those used in Ref. [4]. In a recent paper, Jancu *et al* [7] have indeed reexamined the parameterization issue and shown that the off-diagonal spin-orbit interaction $\bar{\Delta}$ coupling the valence and conduction p-states governs the BIA spin splitting in the conduction band, while the inversion asymmetry-induced parameter P' (momentum matrix element between s and p conduction states) was overestimated in previous works.

To check the role of $\mathbf{k} \cdot \mathbf{p}$ parameters, we first reproduced the calculations of Ref. [4] using the parameterization of Ref. [7], and found only minor quantitative differences. In particular

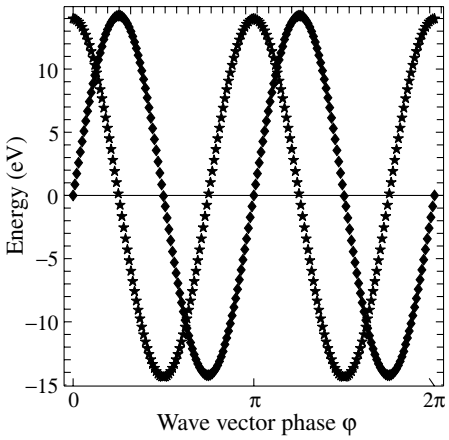

Fig. 2. Real (red curve) and imaginary (blue curve) parts of the conduction-band energy as function of the wave-vector phase φ for $|k| = 0.01\ (2\pi/a)$. The reference energy is the lowest Γ_{6c} conduction-band state.

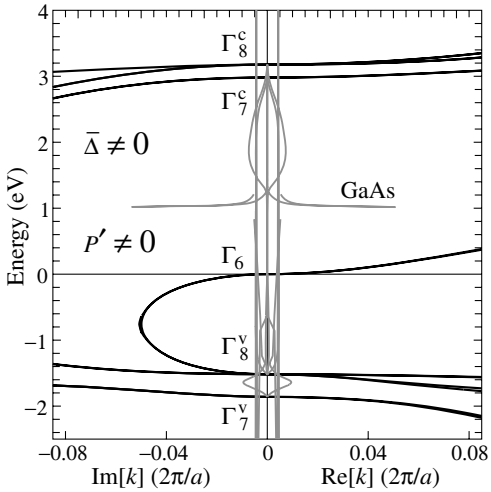

Fig. 3. Complex band structure of GaAs along the [110] direction calculated using the 14×14 $\mathbf{k} \cdot \mathbf{p}$ model.

the disappearance of any solution for a purely imaginary wave vector in the [110] direction is a robust conclusion, whatever finite inversion asymmetry parameters are used: the mistake does not lie in the parameterization issue, but in a more subtle difficulty. Again, an evanescent state is not necessarily characterized by a purely imaginary wave vector and looking for evanescent waves at some energy within the band gap requires a non-trivial exploration of the complex plane [8].

What happens in [4] is that the authors have numerically missed the solutions corresponding to the complex bands. They are easily restored using the following trick: setting $\mathbf{k} = |k|e^{i\varphi}$, one gets a non-hermitian $\mathbf{k} \cdot \mathbf{p}$ Hamiltonian that admits, in general, complex eigenvalues $\mathrm{Re}[E] + i^*\mathrm{Im}[E]$. For a given eigenenergy, the wavevector solutions are fourfold degenerate: $k, k^*, -k$, and $-k^*$, owing to the reflection symmetry along the crystal axis. By rotating the wave vector phase φ, one changes both the real and imaginary parts of an eigensolution E, as shown in Fig. 2. At $\varphi = 0$ and $\varphi = \pi$, corresponding to the real wave vectors, one finds the usual real bands propagating along the positive and negative axis respectively. Similarly for k purely imaginary, i.e. evanescent states, there are also only 2 distinct solutions that can also be classified into forward $\varphi = \pi/2$ and backward $\varphi = 3\pi/2$, decaying along the positive and negative axis respectively. However, the corresponding eigenergies have a complex component and do not correspond to physical solutions. For $\mathbf{k}$ complex, which also corresponds to an evanescent wave, the quartet of possible solutions are all distinct but the non-physical imaginary part of the eigenenergy can vanish for some values of φ, differing in general from $\pi/2$ or $3\pi/2$. These non-trivial values of φ correspond to the evanescent states. Note that for small k, an analytical solution is easily found.

The dispersion of evanescent states in the [110] direction, using the $\mathbf{k} \cdot \mathbf{p}$ parameters of [7], is illustrated in Fig. 3. As seen in Fig. 3, the complex bands emerge from the extrema of the band structure in real k space and form complete loops connecting the conduction and valence bands, just as in the classical case of the quasi-Ge hamiltonian. The main difference is the finite real component of the mostly imaginary wavevectors. Due to bulk inversion asymmetry, the evanescent states are spin-split, and their spin splitting can become large in the midgap region where the looped dispersion is nearly vertical. Note that the real parts of the two spin-split eigenvectors at a given energy within the gap have opposite signs. This spin splitting suggests that with appropriate band structure engineering, one could design spin-dependent tunnel diodes acting as spin filters. However, to address this issue, $\mathbf{k} \cdot \mathbf{p}$ calculations have to face another difficulty arising from interface symmetry reduction to C_{2v} and related complication of boundary conditions [9,10]. In the tight-binding calculation, that is free from this difficulty, spin dependent tunneling manifests itself as a spin-splitting of the superlattice dispersion away from mini-band extrema. For the example shown in Fig. 1, at the mid-band energy, we obtain a spin-splitting of 0.05 meV only. We finally note that such spin splitting does not break Kramers degeneracy: the design of an effective spin filter has to involve a more subtle process (decoherence) breaking the emittor/collector symmetry.

References

[1] I. Žutić, J. Fabian and S. Das Sarma, *Rev. Mod. Phys.* **76**, 323 (2004).
[2] R. Winkler, *Spin-orbit coupling effects in two-dimensional electron and hole systems*, (Springer, Berlin 2003), p. 74.
[3] A. T. Hanbicki, O. M. J. van't Erve, R. Magno, G. Kioseoglou, C. H. Li, B. T. Jonker, G. Itskos, R. Mallory, M. Yasar and A. Petrou, *Appl. Phys. Lett* **82**, 4092 (2003).
[4] N. Rougemaille, H-J. Drouhin, S. Richard, G. Fishman and A. K. Schmid, *Phys. Rev. Lett.* **95**, 186406 (2005).
[5] G. Dresselhaus, *Phys. Rev.* **100**, 580 (1955).
[6] J-M. Jancu, R. Scholz, F. Beltram and F. Bassani, *Phys. Rev. B* **57**, 6493 (1998).
[7] J-M. Jancu, E. A. de Andrada e Silva, R. Scholz and G. C. La Roca, *Phys. Rev. B* **72**, 193201 (2005).
[8] D. L. Smith and C. Maillot, *Rev. Mod. Phys.* **62**, 173 (1990).
[9] E. L. Ivchenko, A. Kaminski and U. Rössler, *Phys. Rev. B* **54**, 5852 (1996).
[10] B. A. Foreman, *Phys. Rev. Lett.* **81**, 425 (1998).

14th Int. Symp. "Nanostructures: Physics and Technology"
St Petersburg, Russia, June 26–30, 2006

Theory of spin detector and injector based on spin-dependent resonant tunneling

P. S. Alekseev, V. M. Chistyakov and I. N. Yassievich
Ioffe Physico-Technical Institute, St Petersburg, Russia

Abstract. A theory of resonant spin-dependent tunneling controlled by applying external electric field has been developed. The spin-orbit interaction is taken into account by means of the Dresselhaus term in the effective Hamiltonian. It has been shown that the GaAlSb double-barrier structure can be used as detector and injector of spin-polarized electrons.

Investigations of spin-polarized electrons in nonmagnetic semiconductor materials in aims of creating spin filters and detectors have attracted a great deal of attention recently. It has been pointed out on the possibility of creating spin filter using spin-dependent tunneling via an asymmetrical non-magnetic semiconductor barrier [1], where spin dependance is originated by the so-called Rashba phenomenological term in the effective Hamiltonian. Their method includes spin-dependent boundary conditions and a non-parabolic dispersion of the effective mass. A theoretical model of the spin injector based on a symmetrical semiconductor barrier has been built [2], where the spin-orbit interaction has been taken into account by means of the effective Dresselhaus Hamiltonian [3]. It has been shown that the resonant spin-dependent tunneling through a double barrier structure is a far more effective method to get spin-polarized electrons [4].

In this paper we consider the spin-dependent resonant tunneling through double-barrier structure in the presence of external electric field applied normally to interface and demonstrate the possibility to create spin detector on the basis of GaAlSb heterostructure (see Fig. 1). The electric field provides a way to control spin-dependent resonant tunneling effectively.

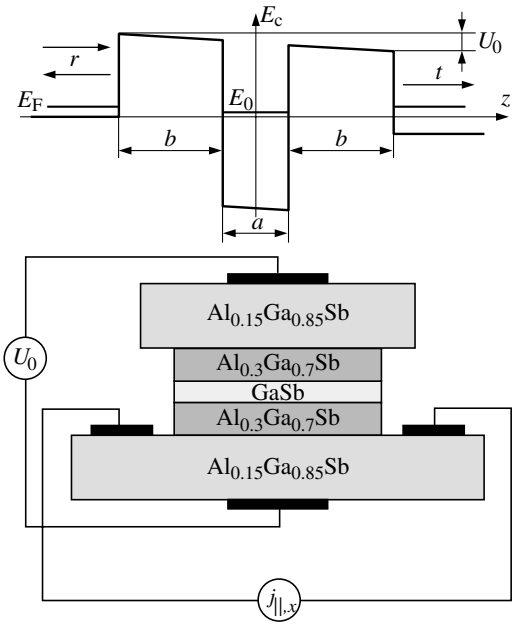

Fig. 1. The the scheme of the heterostucture: the composition of barrier layers and the well are $Al_{0.3}Ga_{0.7}Sb$ and GaSb and their widths are $b = 6.0$ nm and $a = 2.6$ nm, respectively; the composition of substrate and cap layers is $Al_{0.15}Ga_{0.85}Sb$; U_0 is the voltage applied.

Calculations have been produced for GaAlSb symmetrical double-barrier heterostructure grown along $z \parallel [001]$ direction (see Fig. 1). The parameters, shown in Fig. 1 are chosen to put the resonant level in the well close to the conduction band edge in cap and substrate layers. As shown in [3], Dresselhaus term, which is a dominating term in spin-orbit interaction here, can be presented in a form:

$$H_D = \gamma \left(\hat{\sigma}_x k_x - \hat{\sigma}_y k_y\right) \frac{\partial^2}{\partial z^2}\,, \tag{1}$$

where γ is the Dresselhaus constant, $\hat{\sigma}_{x,y}$ are the Pauli matrices, the coordinate axes x, y, and z are assumed to be parallel to the crystallographic axes [100], [010], and [001], respectively.

This Hamiltonian is diagonalized by spinors:

$$\chi_\pm = \frac{1}{\sqrt{2}} \begin{pmatrix} 1 \\ \mp e^{-i\varphi} \end{pmatrix}, \tag{2}$$

which describe the electron states "+" and "−" of opposite spin direction. Here φ is an polar angle of $k_\parallel$ in the plane xy.

The heterostructure becomes asymmetrical when an external electric field $\mathcal{E}$ is applied along z-axis: $U_0 = e\mathcal{E}(2b + a)$ (see Fig. 1). As shown in [4], spin-orbit interaction (1) leads to the change of the electron effective mass. The effective Hamiltonian of motion along z-direction takes a simple form:

$$H_\pm = -\frac{\hbar^2}{2m_\pm}\frac{\partial^2}{\partial z^2} + \frac{\hbar^2 k_\parallel^2}{2m^*} + V(z) + e\mathcal{E}z\,, \tag{3}$$

$$m_\pm = m^* \left(1 \pm \frac{2\gamma k_\parallel}{\hbar^2}\right)^{-1}, \tag{4}$$

where $V(z)$ is a heterostructure potential and m^* is the effective mass of electron.

Following to [4], we have found transparency of the structure under investigation (see Fig. 1) by using the exact solution of the Schrodinger equation with the Hamiltonian (3) using the continuity of wave functions and electron fluxes at the interfaces as boundary conditions. The wave functions are expressed by the Airy functions with the frequency growing proportionally to $1/\mathcal{E}$. It has been proved that the transparency coefficient for the spin states "+" and "−" can be calculated approximating real potential profile with step functions. The numerical calculations have proven that the step-like profile gives virtually the same values for transparency coefficient as calculations with Airy functions. This step approximation allows to get the analytical formulae for the transparency coefficients. In Fig. 2, the obtained transmission coefficients of

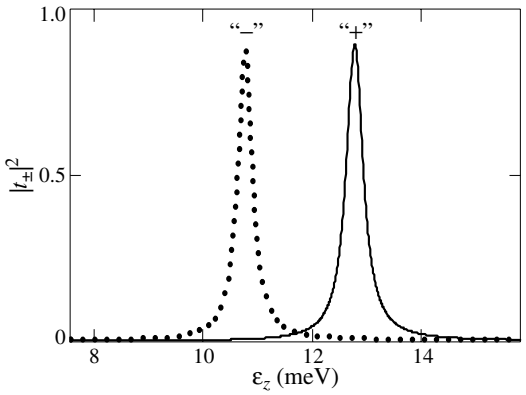

Fig. 2. The transparency coefficient of electrons in "+" and "−" states as a function of their kinetic energy ε_z along z-axis. The electric field $\mathcal{E} = 16$ kV/cm in the structure corresponds to applied voltage $U_0 = 24$ mV.

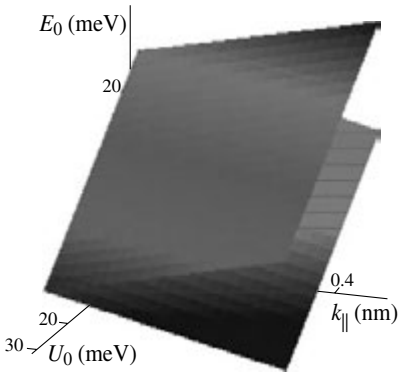

Fig. 3. Splitting of the resonant level in the well in depends on the of voltage, applied to heterostructure, and the wave vector of motion electron in the interfaces.

"+" and "−" states for $U_0 = 24$ mV are presented. They have a resonant character, which can be characterized by the resonant levels $E_0^{\pm}(k_\parallel, \mathcal{E})$ and their widths. In Fig. 3 we show the splitting of the resonant levels for "+" and "−" states as a function of potential applied to the structure and the wave vector of electron in the cap layer.

The density of current j_z as well as interfaced current $j_\parallel$ of spin-polarized electron transmitted through tunneling structure have been calculated by using the spin-density matrix technique [4]. The results of calculations for electrons with concentration $n = 1.3\times10^{18}$ cm^{-3} and degree of polarization $p_s = 0.1$ in the plane xy at the temperature 7 K are displayed in Fig. 4. The resonant tunneling current j_z (see Fig. 4a) does not depend on polarization of carriers in linear regime. The interface current $\mathbf{j}_\parallel$ changes the direction according to the polarization direction. For its x-projection, which is measured at the device (see Fig. 1), one has $j_{\parallel,x} = -j_\parallel \cos(\alpha)$, where α is the angle between the spin orientation of electrons and x-axis, and $j_{||}$ is presented in Fig. 4b as function of the voltage applied.

The peculiarities of the interface current $j_{\parallel,x}$ field dependence (see Fig. 4) correspond to the change of resonant level energy for the given spin state.

It has been shown that applying voltage along interface in substrate layer caused the polarization of electron in cap layer for opposite direction of tunneling. The calculation of the polarization degree as function of applied electric field has been produced. This effect may be employed for spin injection.

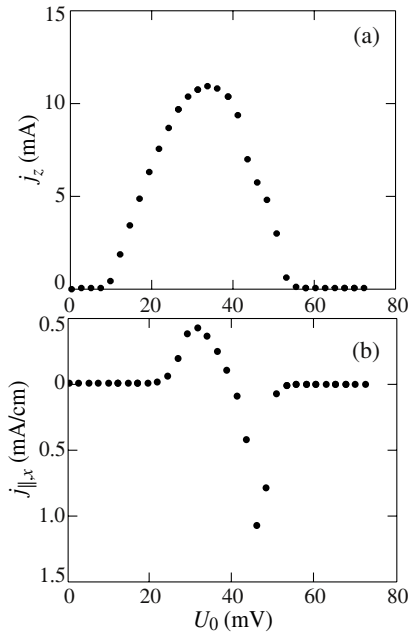

Fig. 4. The calculated current along the normal to (a) and in the plane of (b) interfaces as a function of the voltage between contacts are presented. The temperature is 9 K, the electron density is 1.3×10^{18} cm^{-3} (Fermi energy equals to 10 meV), the degree of polarization is assumed to be $p_s = 0.1$.

In conclusion, we have demonstrated the possibility to use the double barrier GaAlSb structure as detector and injector of spin-polarized electrons. The calculated parameters of optimized structure have been presented.

Acknowledgements

The authors thank S. A. Tarasenko for useful discussion. This work is supported by RFBR, programs of the RAS, and "Dynasty" foundation (ICFPM).

References

[1] A. Voskoboinikov, S. S. Liu and C. P. Lee, *Phys. Rev. B* **58**, 15397 (1998).

[2] V. I. Perel', S. A. Tarasenko, I. N. Yassievich, S. D. Ganichev, V. V. Bel'kov and W. Prettl, *Phys. Rev. B* **67**, 201304 (2003).

[3] G. Dresselhaus, *Phys. Rev.* **100**, 580 (1955).

[4] M. M. Glazov, P. S. Alekseev, M. A. Odnobludov, V. M. Chistyakov, S. A. Tarasenko and I. N. Yassievich, *Phys. Rev. B* **71**, 155313 (2005).

14th Int. Symp. "Nanostructures: Physics and Technology"
St Petersburg, Russia, June 26–30, 2006

Energy bands and spin polarization in 2DEG with spin-orbit coupling subject to periodic potential

V. Ya. Demikhovskii and D. V. Khomitsky
University of Nizhny Novgorod, Gagarin Avenue 23, 603950 Nizhny Novgorod, Russia

Abstract. The Bloch spinors, energy spectrum and spin polarization in energy bands are studied for the 2D electron gas with Rashba spin-orbit (SO) interaction subject to 1D periodic electrostatic potential. The anticrossing of energy dispersion curves due to the interplay between the SO and periodic terms is found, and the new topological properties of spin polarization are studied. New transport effects in periodic structures with SO interaction are discussed.

Introduction

In the past years, an increasing attention has been drawn to the spin related phenomena in semiconductor structures. This research area has developed in the new branch of condensed matter physics and spin electronics. The problem of spin-dependent quantum states and transport phenomena in these systems are currently attracting a lot of interest also due to their potential for future electronic device applications.

In two-dimensional semiconductor heterostructures the spin-orbit interaction is usually dominated by the Rashba coupling [1] stemming from the structure inversion asymmetry of confining potential. The strength of other terms, such as Dresselhaus term, can be investigated, for example, by optical methods [2].

The low-dimensional semiconductor structures with SO interaction were studied experimentally and theoretically in numerous papers [3]. As it was demonstrated by the experiments, in the SO structures interesting effects may be observed, such as the spin Hall effect [4] and the spin-galvanic effect [5]. The 1D periodic systems with SO coupling have also been studied [6].

In the present paper we study quantum states and the electron spin distribution in a system combining the spin-splitting phenomena caused by the SO interaction and the external gate-controlled periodic electric potential. We thus want to investigate the spin orientation and spin polarization that can be achieved in currently manufactured gated semiconductor structures with lateral superlattice. For example, the 1D superlattice can be fabricated by the metal gate evaporation with typical period of 50–200 nm. We use the value of lateral period in the x-direction to be $a = 60$ nm which gives us the energy scale $\pi^2\hbar^2/2ma^2$ of the order of 2 meV for the effective mass $m = 0.067m_0$ in GaAs. Such energy scale means that the vawevector is measured in units of π/a, leading to typical energies of 2D electron gas to be of the order of 10 meV. The values of Rashba coupling constant for the most important semiconductors is in the range of $1-5\cdot10^{-11}$ eVm. We use the values $\alpha = 5\cdot10^{-11}$ eVm in our calculations which gives the typical shift of the energy dispersion curves k_{SO} to be of the order of π/a. So, in the structures studied in the paper the electron kinetic energy $\pi^2\hbar^2k^2/2m$ will be comparable to the Rashba energy αk which will help to distinguish the effects of SO interaction and periodic potential. It should be mentioned also that the energy scale of 10 meV means that the effects discussed in the paper can be clearly observed experimentally at helium temperatures.

1. Quantum states

The Hamiltonian of our problem is the sum of the Rashba Hamiltonian $\hat{H}_0$ with the strength α,

$$\hat{H}_0 = \frac{\hat{p}^2}{2m} + \alpha(\hat{\sigma}_x\hat{p}_y - \hat{\sigma}_y\hat{p}_x), \tag{1}$$

and the one-dimensional periodic potential $V(x)$ of a 1D superlattice with the period a. We choose the simplest form of the periodic potential

$$V(x) = V_0\cos\frac{2\pi x}{a}. \tag{2}$$

We construct the wavefunction as a superposition of two-component spinors which are the eigenstates of the Rashba Hamiltonian (1). In the presence of the periodic potential the wavevectors of the basis states are shifted by the reciprocal lattice vector $\mathbf{b}$ of the supelattice:

$$\mathbf{k}_n = \mathbf{k} + n\mathbf{b} = \left(k_x + \frac{2\pi}{a}n, \quad k_y\right), \tag{3}$$

$n = 0, \pm1, \pm2, \ldots$. The eigenstate thus has the form

$$\psi_{s\mathbf{k}} = \sum_{\lambda n} a^s_{\lambda n}(\mathbf{k})\frac{e^{i\mathbf{k}_n\mathbf{r}}}{\sqrt{2}}\begin{pmatrix}1\\ \lambda e^{i\theta_n}\end{pmatrix}, \quad \lambda = \pm1 \tag{4}$$

where $\mathbf{k}$ is the quasimomentum in the 1D Brillouin zone and s is the band number, and $\theta_n = \arg[k_y - ik_{nx}]$. After substituting the wavefunction (4) into the Schrödinger equation the coefficients $a_{\lambda n}$ are determined by the standard eigenvalue problem

$$\sum_{\lambda' n'}\left[\left(E^R_{\lambda' n'} - E\right)\delta_{\lambda n\lambda' n'} + V_{\lambda n\lambda' n'}\right]a^s_{\lambda' n'} = 0, \tag{5}$$

where $E^R_{\lambda n}$ is the energy of a free Rashba quantum state $E^R_\lambda = \hbar^2k^2/2m + \lambda\alpha k$ taken at the point in $\mathbf{k}$-space defined by (3), i.e. $E^R_{\lambda n} = E^{RD}_\lambda(k_x + 2\pi n/a)$. The matrix elements in the system (5) have the form:

$$\begin{gathered}V_{\lambda n\lambda' n'} = V_0A_{nn'}(1 + \lambda\lambda' e^{i(\theta_n - \theta_{n'})}),\\ A_{nn'} = \tfrac{1}{2}\delta_{n,n'\pm1}, \quad n = n' \pm 1.\end{gathered} \tag{6}$$

In Fig. 1a we give an example of energy spectrum $E(k_x)$ at fixed $k_y = 0$. In accordance with the Kramers theorem the symmetry $E_{s\uparrow}(\mathbf{k}) = \mathbf{E}_{s\downarrow}(-\mathbf{k})$ takes place, and we thus show

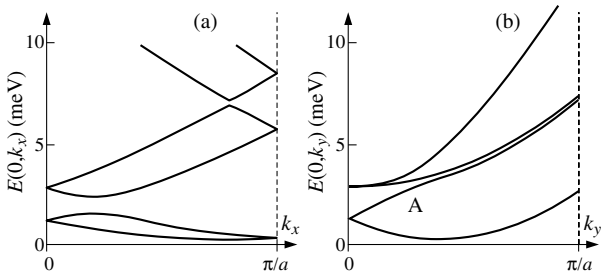

Fig. 1. Energy spectrum at $\alpha = 5{\cdot}10^{-11}$ eVm, $V_0 = 1.7$ meV shown (a) as a function of k_x at $k_y = 0$ and (b) as a function of k_y at $k_x = 0$. In the latter case the anticrossing takes place at the point A.

the spectrum only at positive k_x and k_y. One can see that the spin degeneracy at $k_y = 0$ is not lifted at the center and at the borders of the BZ $k_x = \pm\pi/a$. The nature of this effect is due to the specific k_x and k_y dependence of matrix elements (6). The elements $V_{nn\pm1}^{\lambda=\lambda'}$ which are responsible for the degeneracy lifting at $k_x = \pm\pi/a$ and $k_y = 0$ vanish at $k_y = 0$. The other set of elements $V_{nn\pm1}^{\lambda=-\lambda'}$ is non-zero at $k_y = 0$, and it opens the gaps inside the BZ. The k_y-dependence of the energy bands at $k_x = 0$ is shown in Fig. 1b. The degeneracy at $k_y = 0$ is lifted at finite k_y by mutual influence of linear k_y terms in (1) and by the matrix elements (6). At certain conditions the anticrossing of the dispersion curves from different bands [3] may take place. An example of the anticrossing effect can be see in Fig. 1b near the point A. Below we shall see that the anticrossing leads to the spin flip in the (k_x, k_y) plane.

2. Spin polarization

The control on the spin polarization is crucial for practical implementation of spintronics. It is of both interest to calculate the polarization of spin both in real and reciprocal spaces. The latter determines the spin orientation of electrons with different momentum and thus describes the spin polarization of electrons travelling in different directions. We have calculated the space distribution of spin density $S_{i\mathbf{k}}(x, y) = (\psi_{\mathbf{k}})^{\dagger}\hat{\sigma}_i\psi_{\mathbf{k}}$ for a quantum state $(s, \mathbf{k})$ and after the space integration obtained the vector field of spin expectation values in the Brillouin zone:

$$\sigma_i(\mathbf{k}) = \langle\psi_{\mathbf{k}} \mid \hat{\sigma}_i \mid \psi_{\mathbf{k}}\rangle. \qquad (7)$$

In Fig. 2 we show the calculated distribution of $(\sigma_x, \sigma_y)_{s\mathbf{k}}$ where one can see that the spin polarization is qualitatively modified by periodic potential. First of all, in the lowest energy subband shown in Fig. 2a the uniform curl distribution of spins in (σ_x, σ_y) plane is conserved near the BZ center, and it is destroyed at the borders $k_x = \pm\pi/a$. The principal difference is that at $k_x = \pm\pi/a$ the spins are polarized along x and $\sigma_y = 0$, and a new type of singularity appears at $k_x = \pm\pi/a$, $k_y = 0$. More complicated picture shown in Fig. 2b takes place for the spin polarization in the next energy band, see Fig. 1. We see that at the BZ center the topology of spin polarization is unchanged. The greatest changes from the uniform curl distribution with reversed angular velocity in accordance with $\lambda = 1$ on the upper Rashba band come from the borders $k_x = \pm\pi/a$ of the BZ where a new curl has emerged. Another important feature of this spin distribution is the spin flip at the point A shown on the axis $k_x = 0$ in the BZ. One can easily establish this point as the anticrossing point for the energy spectrum $\varepsilon = \varepsilon(k_x = 0, k_y)$ shown in Fig. 1b.

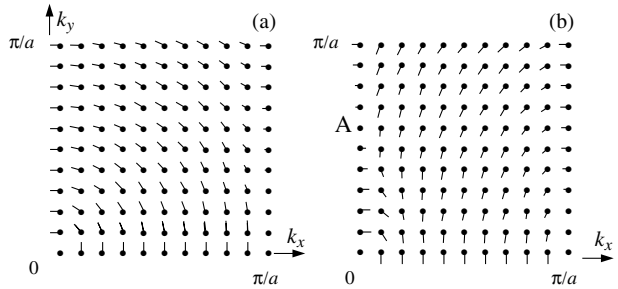

Fig. 2. Spin polarization shown in one quarter of the BZ for of the lowest (a) and the next (b) energy subbands. In the latter case the anticrossing takes place at point A, leading to the spin flip in the (k_x, k_y) plane. The parameters are the same as in Fig. 1.

In addition, the effects of charge and spin transport, and optical effects in SO superlattices will be discussed in the report.

Acknowledgements

This work was supported by the Program "Development of the Higher school research potential", by the Russian Foundation for Basic Research, by the CRDF Award RUX0-001-NN-06, and by the Dynasty Foundation.

References

[1] E. I. Rashba, *Fiz. Tverd. Tela* (Leningrad) **2**, 1224 (1960) [Sov. Phys. Solid State **2**, 1109 (1960)]; Y. A. Bychkov and E. I. Rashba, *J. Phys. C* **17**, 6039 (1984).

[2] S. D. Ganichev, V. V. Bel'kov, L. E. Golub, E. L. Ivchenko, P. Schneider, S. Giglberger, J. Eroms, J. De Boeck, G. Borghs, W. Wegscheider, D. Weiss and W. Prettl, *Phys. Rev. Lett* **92**, 256601 (2004).

[3] A. V. Moroz and C. H. W. Barnes, *Phys. Rev. B* **60**, 14272 (1999); F. Mireles and G. Kirczenow, *Phys. Rev. B* **64**, 024426 (2001); M. Governale and U. Zülicke, *Phys. Rev. B* **66**, 073311 (2002); X. F. Wang and P. Vasilopoulos, *Phys. Rev. B* **67**, 085313 (2003).

[4] S. Murakami, N. Nagaosa and S. C. Zhang, *Science* **301**, 1348 (2003); J. Wunderlich, B. Kaestner, J. Sinova and T. Jungwirth, *Phys. Rev. Lett.* **94**, 047204 (2005).

[5] S. D. Ganichev, V. V. Bel'kov, P. Schneider, E. L. Ivchenko, S. A. Tarasenko, W. Wegscheider, D. Weiss, D. Schuh, E. V. Beregulin and W. Prettl, *Phys. Rev. B* **68**, 035319 (2003).

[6] X. F. Wang, *Phys. Rev. B* **69**, 035302 (2004); I. Vurgaftman and J. R. Meyer, *Phys. Rev. B* **70**, 205319 (2004); P. Kleinert, V. V. Bryksin, O. Bleibaum, *Phys. Rev. B* **72**, 195311 (2005).

14th Int. Symp. "Nanostructures: Physics and Technology"
St Petersburg, Russia, June 26–30, 2006

Circularly-polarized electroluminescence from InGaAs/GaAs quantum well heterostructures with ferromagnetic Schottky contact

M. V. Dorokhin[1], V. D. Kulakovskii[2], S. V. Zaitsev[2], V. Ya. Aleshkin[3], N. V. Baidus'[1], Yu. A. Danilov[1], P. B. Demina[1], E. A. Uskova[1] and B. N. Zvonkov[1]

[1] Physico-Technical Research Institute, University of Nizniy Novgorod, 603950 Nizhny Novgorod, Russia
[2] Institute of Solid State Physics RAS, 142432 Chernogolovka, Moscow district, Russia
[3] Institute for Physics of Microstructures RAS, 603950 Nizhny Novgorod, Russia

Abstract. Electroluminescence of InGaAs/GaAs quantum well heterostructures with ferromagnetic Schottky contacts has been studied at 1.5 K and magnetic fields up to $B = 10$ T. Peak of electroluminescence splits into Landau level peaks and displays a circular polarization significantly exceeding that in similar structures but with nonmagnetic (Au) contact. The circular polarization degree is connected with polarization of injected holes. The circular polarization of electroluminescence was found to be the non-monotonous function of the magnetic field correlating with Landau level filling. The maximum circular polarization degree is about 42% fields assumingly indicates an effective spin injection from magnetic contact.

Introduction

The latest achievements in the area of spintronics caused a strong interest in investigating various magneto-optical effects. The main objective of these studies is to understand the basic mechanisms of controlling carrier spin injection. One of them is the spin injection from ferromagnetic Schottky contact into a semiconductor. It is typically studied via electroluminescence (EL) of a quantum well (QW) heterostructures [1, 2]. Despite the low quantum efficiency of the EL from Schottky diodes, conductivity mismatch problem [3] and problems related with uneven ferromagnetic metal (FM)-GaAs interface [4], the EL is one of advanced methods for a spin injection detection, as reported in [1–3].

In this work we investigated the EL of InGaAs/GaAs QW heterostructures with the Ni or Co Schottky contacts in magnetic fields up to 10 T.

1. Experimental

The structures were grown on the n-GaAs substrates by Metal-Organic Vapor Phase Epitaxy at atmospheric pressure. The $In_xGa_{1-x}As$/GaAs QW with the thickness of 6 nm and average In content $x = 0.16$ was placed at the distance of 20, 30, and 100 nm from the surface. A FM Schottky contact with the diameter of 0.5 mm was performed by the deposition of nickel or cobalt. Moreover, a three layer contact with an intermediate gold layer between a FM metal and a semiconductor, and a covering gold layer on a ferromagnetic film (Au/Ni/Au or Au/Co/Au) was performed. The reference sample was similar structure with nonmagnetic Au-contact.

The forward bias EL measurements were performed at 1.5 K in a liquid helium cryostat with the superconducting magnet. The operating current range was 1–10 mA. The experiments were carried out in Faraday geometry, i.e. the magnetic field direction was normal to sample surface. In such geometry the saturation magnetization of FM film occurs at strong magnetic fields (up to 5 T). The degree of circular polarization is determined as $P = (I^+ - I^-)/(I^+ + I^-)$, where $I^+(I^-)$ are the EL intensity of the right (left) circularly polarized component determined by integrating the area under the corresponding part of a spectrum.

2. Results and discussion

The peculiarity of forward biased EL from Schottky diodes with n-type GaAs is the injection of holes from metal into a semiconductor. The EL properties of the structures with Schottky contact without magnetic field were described in detail in [4]. Fig. 1–3 display the results obtained for a three layer Schottky contact. A magnetic field (B) leads to the increase of the EL intensity and the blue shift of the EL line (Fig. 1). The line is related to electron-hole radiative recombination in InGaAs QW. A magnetic field splits the broad line into number of peaks corresponding to electron-hole transitions between the different Landau levels (LLs).

With the increased magnetic field the high energy peaks disappear one by one due to emptying of the upper Landau levels in the conduction band. At 10 T only one Landau level is observed.

Fig. 2 shows that the detected EL radiation is circularly

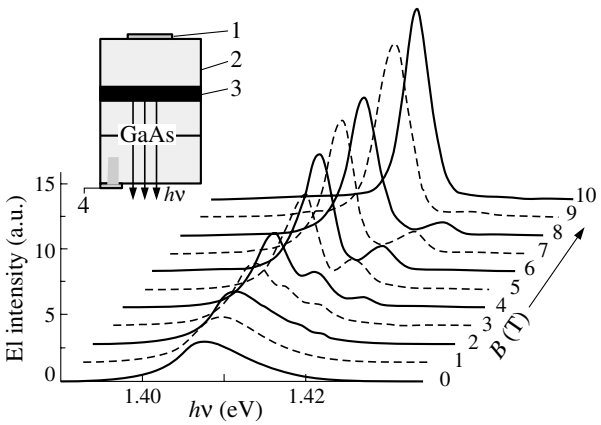

Fig. 1. The EL spectra at various magnetic fields for σ^+ polarization. Au/Co/Au Schottky contact. The inset shows the device scheme. 1 — Schottky contact, 2 — GaAs cap layer, 3 — InGaAs QW, 4 — back ohmic contact.

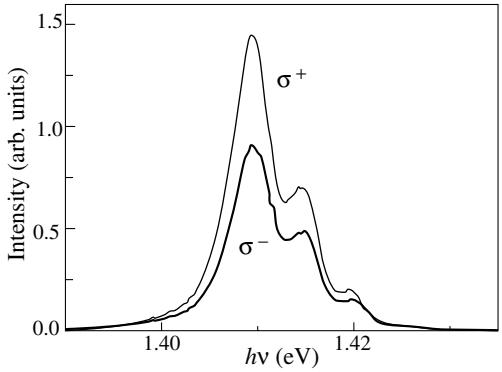

Fig. 2. The σ^+ and σ^- polarized EL spectra for Au/Co/Au Schottky contact. $B = 4$ T.

polarized. The polarization degree (P) is largest for the peak, corresponding to the lowest Landau level. It shows a non-monotonous dependence on the magnetic field (Fig. 3) with a local minimum at 5–6 T and maximum at 7.5–9 T for different samples. The position of minimum and maximum weakly depend on the operating current. This type of dependence $P(B)$ is present for all investigated Schottky diodes in the whole investigated current range.

For that reason they are thought to originate from QW electron gas properties in the magnetic field namely, from the variation of a spin scattering LL.

In contrast the magnitude of polarization degree strongly depends on the type of metal/semiconductor interface and structure parameters. The maximal polarization degree was observed for the samples with a thin cap layer of 20 nm and three layer Au/Co/Au and Au/Ni/Au Schottky contacts. That was equal to 40 and 42%, respectively. The similar structures with pure Ni or Co contact showed a markedly smaller polarization degree of 30 and 20%, respectively. The P value in a reference sample with nonmagnetic gold contact was approximately 10%.

There are several reasons for EL polarization in a magnetic field. First, the Zeeman splitting of QW energy levels leads to a difference between the population of spin-up and spin-down levels and, hence, the different intensity of σ^+ and σ^--components of EL. However, it is natural to expect that the polarization degree due to this reason is nearly independent of the contact located rather far from the QW. The most believable reason for a highly enhanced EL polarization in the case of samples with FM contact is the spin injection from a FM metal into semiconductor.

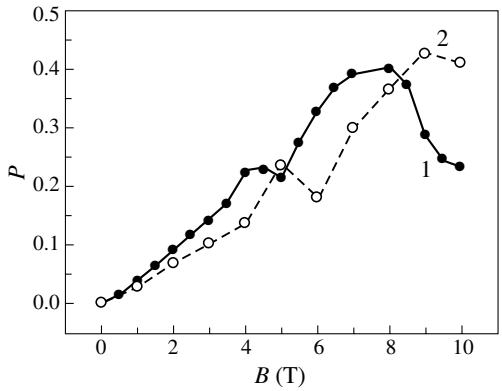

Fig. 3. The dependence of circular polarization degree on magnetic field for diodes with Au/Co/Au (1) and Au/Ni/Au (2) Schottky contacts. Cap layer thickness is 20 nm. $I = 10$ mA.

Thus we have demonstrated the high circular polarization of the EL from QW heterostructures with FM Schottky contact assumingly indicating an effective spin injection. The polarization degree is the non-monotone function of the magnetic field because of the dependence of spin relaxation time on the electron LL filling.

Acknowledgements

This work was supported by RFBR grant 05-02-16624, Russian Ministry of education (project DSP.2.1.1.2741) and CRDF (RUX0-001-NN-06/BP1M01).

References

[1] I. Zutic, J. Fabian and S. Das Sarma, *Rev. Mod. Phys.* **76**, 323 (2004).

[2] V. F. Motsnyi, P. Van Dorpe, W. Van Roy, E. Goovaerts, V. I. Safarov, G. Borghs and J. De Boeck, *Phys. Rev. B.* **68**, 245319 (2003).

[3] E. I. Rashba, *Phys. Rev. B* **62**, R16267 (2000).

[4] N. V. Baidus', P. B. Demina, M. V. Dorokhin, B. N. Zvonkov, E. I. Malysheva and E. A. Uskova, *Semiconductors* **39**, 17 (2005). *Appl. Phys. Lett.* **79**, 3125 (2001).

14th Int. Symp. "Nanostructures: Physics and Technology"
St Petersburg, Russia, June 26–30, 2006

Spin-dependent phenomena in new nanoobject — 2d layer on the internal interface Te-SiO_2

N. S. Averkiev, V. N. Bogomolov, V. A. Berezovets, K. S. Romanov and *I. I. Farbstein*
Ioffe Physico-Technical Institute, St Petersburg, Russia

Abstract. We present the experimental and theoretical study of the magnetoconductivity of the nanocluster Te in synthetic opal structures. The experimental data show the anomalous magnetoconductivity taking place in extremely large magnetic fields. The proposed theoretical model gives the good qualitative explanation of this phenomena taking into account peculiarities of spin-orbit interaction in Te.

Introduction

The progress in growth technologies allowed to create and study new complex structures. One of the most interesting and unusual among them is the structure SiO_2:nanocluster Te with Te in opal structure void. The synthetic opal (SiO_2) itself is a system of silicate spheres of amorphous SiO_2. These spheres are tightly packed producing fcc cubic lattice. It is possible to inject Te into free spaces between SiO_2 spheres. Using electron microscopy it was shown that the introduced Te crystallizes in the voids and forms a single-crystal structure (see Figure 1).

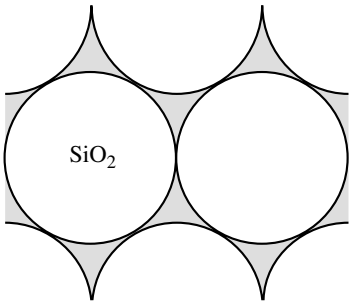

Fig. 1. The SiO_2/Te system. Te (dashed) is in the voids between SiO_2 spheres (white).

Magnetotransport experiments showed that such SiO_2/undoped Te system reveals two-dimensional conductivity character [1]. It was explained by the presence of 2D conductive p-type layer on the interface between opal and Te — the so-called interface bubble lattice (IBL). However magnetoresistance have anomalous dependence on the magnetic field in a very broad range of magnetic fields — up to 12 T [2]. In contrast for the 2D flat layers of monocrystallic Te the classical behavour of magnetoresistance takes place at fields higher than 0.5 T.

We review results of experimental investigations of nanocluster Te magnetoresistance and present the developed theoretical model. This model takes into account peculiarities of SiO_2/Te internal structure and qualitatively explains the behavour of magnetoresistance.

1. Details of the experiment

Nanocluster crystals were prepared by injecting pure melted Te under pressure into a synthetic opal matrix. The magnetoresistance measurements were performed at temperatures 1.6–4.2 K with an 11 Hz ac current. The current did not exceed 10 mA. The magnetic field up to 12 T was created by superconductive magnet.

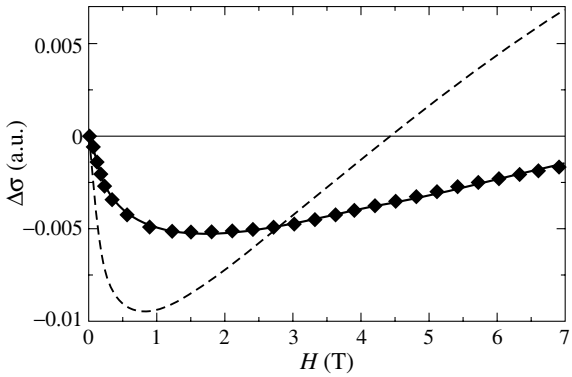

Fig. 2. The experimental (dots) and two theoretical dependencies of magnetoconductivity on the magnetic field at 1.6 K. The solid line corresponds to the data obtained using averaging of the magnetic field. The dash line presents the reconstruction $\Delta\sigma_{WL}$ for the flat 2d layers in the perpendicular magnetic field with the above parameters.

The Figure 2 shows the dependence of low temperature magnetoconductivity on the magnetic field for the sample with initial hole concentration at $T = 77$ K $p_{77} = 1.0\times10^{14}$ cm^{-3}. The magnetoconductivity reveals anomalous character. At magnetic fields below 8 T the magnetoconductivity (MC) is negative (magnetoresistance is positive). At magnetic fields upper 8 T the magnetoconductivity is positive (magnetoresistance is negative).

2. Model

Dependencies of the anomalous MR on the magnetic field and the temperature are qualitatively similar to those of 2D accumulating layers created on the flat area elements of monocrystallic Te [3,4]. In the latter case the magnetoresistane is described well by the weak localization (WL) theory with the account of the peculiarities of Te electron spectrum and without account of electron-electron interactions. Anomalous positive magnetoresistance at low magnetic fields points out the existence of relaxation phase due to spin scattering. It is non-trivial for Te where strong spin-orbit interaction results in full lifted of spin degeneracy in the valence band. Unfortunately this theory is not directly applicable to the SiO_2/Te system because it results in too large character magnetic fields (or too small relaxation times). To explain this contradiction we proposed to take into account a role of geometry factor in WL for the new nanoobject SiO_2/Te.

Let us neglect the differences in hole concentration and mo-

bility between IBL and flat conductive layer. Then the discrepancy between magnetoconductivities of 2D flat hole layer and IBL can be explained by different shapes of these conductive surfaces.

Let us divide the complex conductive surface of the SiO_2/Te system to elementary flat areas. To describe the anomalous MC of the elementary area one can use the formula for flat 2D Te surface [5,6]:

$$\Delta\sigma_{\rm wl}(H)=\sigma_0\left\{f_2\left(\frac{H}{H_\phi+H_v+H_\gamma}\right)+\right.$$
$$\left.+\frac{1}{2}f_2\left(\frac{H}{H_\phi+2H_v}\right)-\frac{1}{2}f_2\left(\frac{H}{H_\phi}\right)\right\}, \quad (1)$$

where H is the magnetic field component normal to the conductive surface, f_2 is the digamma function, H_ϕ is the magnetic field describing phase relaxation of an electron wave function due to the scattering on phonons, H_v and H_γ describe elastic scattering and σ_0 is the normalization constant.

One should take into account that 2D WL correction depends on the normal to the conductive surface component of magnetic field only and does not depend on other components. Therefore the anomalous MC of elementary area is given by $\sigma_{2d}(H\cos\theta)$, where H is the magnetic field, θ is the angle between the normal to the surface and the direction of the magnetic field. The consequence of this effect is that the resulting magnetic field that destroys quantum interference is much lower than the one applied to the sample.

To obtain the total anomalous MR correction one should solve complicated electrotechnical problem. Let us approximate the conductive surface by the lattice of spheres. Each of these spheres contacts neighboring ones in 6 areas. The large number of contacts leads to uniform distributions of the angle between the current and the magnetic field and the angle between the magnetic field and the normal to the surface. Thus the role of the IBL geometrical structure reduces to the averaging of the conductivity correction over all the angles between the magnetic field and the normal to the IBL surface. To take into account this averaging one should replace function f_2 by

$$g_2(|H|)=\frac{1}{2}\int_0^\pi f_2\left(|H|\cos\theta\right)\sin\theta d\theta\,. \quad (2)$$

3. Results

The parameters of the model have been determined. Parameters best describing the anomalous magnetoconductivity at $T=1.6$ K are: $H_\phi=0.032$ T, $H_v=0.0094$ T, $H_\gamma=2$ T and $\sigma_0=0.046$. This magnetic field values are quite reasonable for SiO_2/Te interface.

However these magnetic fields exceeds the same parameters for 2D Te surface (0001) and are close to the ones of $(10\bar{1}0)$ [3, 4]. This is natural because the statistical weight of the surface orientation parallel to the main axis of the C3 crystal is three times greater than weights of the surfaces perpendicular to the main axis.

Discrepancies between parameters obtained for different boundaries Te/TeO_2 and SiO_2/Te can be explained by different heights of barriers and therefore different concentrations and mobilities of 2d holes. Moreover the quality of the interface SiO_2/Te is worse than in [3,4].

Therefore the account of the complex geometry of IBL allows to describe observable anomalies in the MRC and gives typical parameters comparable to ones for 2D layer on $(10\bar{1}0)$ Te surface.

4. Conclusions

The anomalous magnetoresistance of the internal interface in SiO_2/Te have been qualitatively analyzed for the first time. It was shown that the typical magnetic fields, large in comparison to the flat 2D Te surface, are determined mostly by geometrical structure of SiO_2/Te.

Acknowledgements

This work was supported in part by grants from the Russian Foundation for Basic Research, INTAS, the Grant for the Support of Russian Science Schools SSCH-5596.2206.2 and scientific programs of Russian Academy of Science.

References

[1] V. A. Berezovets, V. N. Bogomolov, I. I. Farbstein and V. I. Nizhankovskii, *Physics of the Solid State*, **44**, 1774 (2002).
[2] V. A. Berezovets, V. N. Bogomolov, I. I. Farbstein and V. I. Nizhankovskii, *Proc. of 11th Int. Symp. Nanostructures: Physics and Technology*, St Petersburg, Russia, June 23–28, p. 396 (2003).
[3] V. A. Berezovets, I. I. Farbstein and A. L. Shelankov, *JETP Lett.* **39**, 74 (1984).
[4] N. S. Averkiev, V. A. Berezovets, N. I. Sablina and I. I. Farbshtein, *Physics of the Solid State*, **41**, 796 (1999).
[5] A. L. Shelankov, *Sol. St. Communs.* **53**, 465 (1985).
[6] N. S. Averkiev and G. E. Pikus, *Physics of the Solid State* **39**, 1481 (1997).

14th Int. Symp. "Nanostructures: Physics and Technology"
St Petersburg, Russia, June 26–30, 2006

Spin relaxation in a ferromagnet/semiconductor hybrid structure

V. N. Gridnev
Ioffe Physico-Technical Institute, St Petersburg, Russia

Abstract. We study theoretically dynamics of spin proximity polarization (SPP) arising after photoexcitation in a semiconductor film embedded between two metal ferromagnetic films. We analyze the influence of an external bias voltage applied across the structure on the leakage of SPP through the interfaces. A relation between the time decay of SPP and the charge current flowing through the structure is derived.

Introduction

Since the device proposal of Datta and Das [1] a hybrid ferromagnet/semiconductor (F/S) structure is considered as a key element of spintronics. All methods of spin generation in semiconductors by using such structures can be divided into two essentially different groups. In most experiments the spin polarization is produced by spin injection, i.e., by a spin-polarized current flowing through a F/S interface. The second group consists of experiments [2,3,4] where the spin polarization appears due to the dynamic ferromagnetic proximity effect. The physical essence of the effect was demonstrated most brightly by time-resolved Faraday rotation experiments [3] where unpolarized nonequilibrium electrons in the semiconductor (n-doped GaAs) spontaneously acquired a net spin polarization due to the proximity of a ferromagnet (Fe or MnAs). This spin proximity polarization (SPP) is driven by a deviation from equilibrium caused by optical excitation.

As was explained in [7] temporal evolution of SPP is characterized by two different time scales. SPP arises on short time scale ~ 10 ps after the photoexcitation due to a spin-polarized photocurrent flowing from the semiconductor to the ferromagnet. The second, slow stage consists in the relaxation of the net spin in the semiconductor due to both the spin leakage through the interface and an intrinsic spin relaxation in the semiconductor.

The experiments [3] have been treated theoretically in several publications [5,6,7], but all these theories neglect a spatial variation of SPP across the semiconductor film. This is justified in a ballistic regime when the thickness of the semiconductor film is larger than the electron mean-free path. In the opposite, diffusive case, the nonuniform spatial distribution of the spin density essentially influence spin transport through the F/S interface and the temporal decay of the spin density in the semiconductor. While the intrinsic spin relaxation depends only weakly on spin interactions at the F/S interface, the spin flow through the interface depends strongly on the Schottky barrier transparency and varies significantly with an applied bias voltage.

Here we consider the influence of the applied bias voltage on the relaxation of the dynamic proximity spin polarization in the hybrid F/S structure.

1. Spin drift and diffusion in a biased F/S/F structure

To make physics more transparent we will consider a hybrid structure with two ferromagnetic films, i.e. F/S/F structure, as is shown in Fig. 1. An external magnetic field $\mathbf{B} \parallel \mathbf{z}$ and the ferromagnet's magnetizations $\mathbf{m}^{(1)}$ and $\mathbf{m}^{(2)}$ lie in the interface (yz) plane. We study temporal evolution of the SPP in the

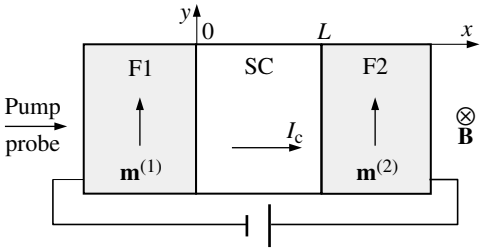

Fig. 1. Schematic of F/S/F hybrid structure excited by the normally incident light. I_c is a charge current induced by an externally applied bias voltage.

semiconductor arising after a photoexcitation by the normally incident linearly polarized light. At $t = 0$ SPP has some initial spin density distribution $\mathbf{S}(0, x)$ depending on the orientation of $\mathbf{m}^{(1)}$ and $\mathbf{m}^{(2)}$.

We derive the time dependence of the spin density $\mathbf{S}(x, t)$ in the semiconductor film by solving the spin diffusion equation. The diffusion equation for $\mathbf{S}(x, t)$ reads [8]

$$\frac{\partial \mathbf{S}(x,t)}{\partial t} + \frac{\partial \mathbf{J}_s}{\partial x} - \mathbf{\Omega}_L \times \mathbf{S}(x,t) + \hat{R}\mathbf{S}(x,t) = 0\,, \qquad (1)$$

$$\mathbf{J}_s = -D\frac{\partial \mathbf{S}}{\partial x} - \nu E\mathbf{S}\,, \qquad (2)$$

where $\mathbf{J}_s$ is the spin-current density, $\mathbf{\Omega}_L = g\mu_B\mathbf{B}/\hbar$ is the Larmor frequency in the magnetic field $\mathbf{B}$, D is the diffusion coefficient, ν is the mobility, $\hat{R}$ is the spin relaxation tensor: $R_{ij} = \delta_{ij}T_i^{-1}$, where $T_1 = T_z$ and $T_2 = T_x = T_y$ are longitudinal and transverse relaxation times, respectively. The electric field E is directed along the interface normal.

The boundary conditions are given by

$$D\frac{\partial \mathbf{S}}{\partial x} + \nu E\mathbf{S} = \mathbf{I}_s^{(1)}(t)\,, \qquad (3)$$

$$D\frac{\partial \mathbf{S}}{\partial x} + \nu E\mathbf{S} = \mathbf{I}_s^{(1)}(t)\,, \qquad (4)$$

where $\mathbf{I}_s^{(1)}(t)$ and $\mathbf{I}_s^{(2)}(t)$ are the spin currents through the F1/S and F2/S interfaces, respectively.

$$\mathbf{I}_s^{(1)} = 2\mathrm{Re}G_{\uparrow\downarrow}^{(1)}\boldsymbol{\mu}_s - 2\mathrm{Im}G_{\uparrow\downarrow}^{(1)}\left(\mathbf{m}^{(1)} \times \boldsymbol{\mu}_s\right) + 2\left(R^{(1)} - \mathrm{Re}G_{\uparrow\downarrow}^{(1)}\right)\left(\mathbf{m}^{(1)} \cdot \boldsymbol{\mu}_s\right)\mathbf{m}^{(1)}\,, \qquad (5)$$

where $\mathbf{m}^{(1)}$ is a unit vector in the direction of the magnetization in the ferromagnet F1, $\boldsymbol{\mu}_s$ is the spin chemical potential in the semiconductor close to the ferromagnetic interface, $G_{\uparrow}^{(1)}$, $G_{\downarrow}^{(1)}$, and $G_{\uparrow\downarrow}^{(1)}$ are the spin-dependent interface conductances [7],

$$R^{(1)} = 2G_{\uparrow}^{(1)}G_{\downarrow}^{(1)}/g^{(1)}\,, \quad g^{(1)} = G_{\uparrow}^{(1)} + G_{\downarrow}^{(1)}\,.$$

A relation between the spin chemical potential and the spin density depends on electron statistics. We assume the degenerate statistics when $\mathbf{S} = N_0\boldsymbol{\mu}_s$, where N_0 is the density of states. In writing Eq. (5) we have assumed that a deviation from equilibrium in the ferromagnet's films is negligibly small.

The spin current at S/F2 interface is given by Eq. (5) with relevant interface conductances $G_{\uparrow}^{(2)}$, $G_{\downarrow}^{(2)}$, $G_{\uparrow\downarrow}^{(2)}$ and magnetization direction $\mathbf{m}^{(2)}$.

Note, that in general the interface conductances strongly depend on the applied bias voltage due to existence of the Schottky barriers near the interfaces.

2. Time decay of SPP in the semiconductor film

We assume that the thickness of the semiconductor film L is much smaller than the spin diffusion length $l_s = \sqrt{DT_2}$. Then the time decay of the spin density $\mathbf{S}(x,t)$ is independent of an initial distribution $\mathbf{S}(x,0)$ (at not too small times). In this case the solution of Eq. (1) is determined mainly by slowest modes of the diffusion equation and can be represented in the form

$$\mathbf{S}(x,t) = \sum_{\sigma=-1,0,1} \mathbf{e}_\sigma \left(C_{+,\sigma} e^{q_{+,\sigma}x} + C_{-,\sigma} e^{q_{-,\sigma}x}\right) e^{-\lambda_\sigma t}\,, \tag{6}$$

where λ_σ is the eigenvalue of the diffusion equation, $C_{+,\sigma}$ and $C_{-,\sigma}$ are coefficients which should be determined from the diffusion equation and initial conditions, and the sum over σ includes two transverse modes with the polarizations $\mathbf{e}_{\pm1} = \frac{1}{\sqrt{2}}(\mathbf{e}_x \pm i\mathbf{e}_y)$ and the longitudinal one polarized along the external magnetic field: $\mathbf{e}_0 = \mathbf{e}_z$.

Parameters $q_{+,\sigma}$ and $q_{-,\sigma}$ are given by

$$q_{\pm,\sigma} = -\frac{\mu E}{2D} \pm \sqrt{\left(\frac{\mu E}{2D}\right)^2 + \frac{1}{D}\left(\lambda_\sigma^{(0)} - \lambda_\sigma\right)}\,, \tag{7}$$

where

$$\lambda_\pm^{(0)} = \pm i\Omega_L + \frac{1}{T_2}\,, \tag{8}$$

$$\lambda_0^{(0)} = \frac{1}{T_1}\,, \tag{9}$$

are the eigenvalues describing spin dynamics in the semiconductor film with non-transparent F/S interfaces. In this case $\mathbf{I}_s^{(1)} = 0$ and $\mathbf{I}_s^{(2)} = 0$, i.e., there is no spin flow through the interfaces (the charge current I_c and the electric field also vanish).

When $\mathbf{I}_s^{(1)}$ and/or $\mathbf{I}_s^{(2)}$ become non-zero the relaxation rate of the net semiconductor spin increases. We assume that the spin relaxation time still remains much longer than the diffusion time across the semiconductor film. Then, in the small electric field, $v|E|T_2 < l_s$, we obtain from the boundary conditions

$$\lambda_\sigma = \lambda_\sigma^{(0)} + \frac{vE}{2D}\left(\alpha_\sigma^{(1)} - \alpha_\sigma^{(2)}\right) + \frac{\alpha_\sigma^{(1)} + \alpha_\sigma^{(2)}}{L}\,, \tag{10}$$

where $\alpha_\sigma^{(i)} = \mathbf{e}_\sigma^* \cdot \mathbf{I}_s^{(i)}(\mathbf{e}_\sigma)$. In case of non-transparent F2/S interface ($\alpha_\sigma^{(2)} = 0$ and hence $E = 0$) we obtain for $\lambda_{\pm1}$ measured in the time-resolved Faraday rotation experiments [3, 4]:

$$\lambda_{\pm1} = \lambda_{\pm1}^{(0)} + \frac{2}{w}\left(R^{(1)} + \mathrm{Re}G_{\uparrow\downarrow}^{(1)}\right)\,. \tag{11}$$

This result coincide with that obtained in [7] but only in the case when $\mathrm{Im}G_{\uparrow\downarrow}^{(1)} = 0$. Due to the different approximations made in this work and in [7] the influence of $\mathrm{Im}G_{\uparrow\downarrow}^{(1)}$ on spin dynamics differs in both approaches. In our work the imaginary part of the mixing conductance does not influence the dynamical behavior of SPP at all, but in [7] $\mathrm{Im}G_{\uparrow\downarrow}^{(1)}$ acts as an effective magnetic field directed along the ferromagnet magnetization.

In case of high electric field, $vET_2 \gg l_s$, λ_σ is given by

$$\lambda_\sigma = \lambda_\sigma^{(0)} + \frac{\mu E}{2D}\left(\alpha_\sigma^{(1)} - \alpha_\sigma^{(2)}\right) + \frac{\mu|E|}{2D}\left(\alpha_\sigma^{(1)} + \alpha_\sigma^{(2)}\right)\,. \tag{12}$$

This equation shows that in the high-field regime the spin leakage occurs only through one of two interfaces, F1/S or F2/S, depending on the sign of the electric field. The high electric field creates a large difference between the spin densities near F1/S and F2/S interfaces, thus leading to the large difference in spin flows through the interfaces.

In conclusion, the relaxation rate of the net spin in the semiconductor film in F/S/F hybrid structure strongly depends on the applied bias voltage due to non-linear I–V characteristics of the Schottky barriers near the interfaces between the semiconductor and ferromagnets. Such strong dependence of the spin relaxation rate was observed in the experiments [4]. The theoretical dependence, Eq. (12), can be used to extract the spin-dependent interface resistance from experiments on spin relaxation in hybrid F/S structures.

Acknowledgements

This work was supported by RFBR and the Russian program "Nanostructures".

References

[1] S. Datta and B. Das, *Appl. Phys. Lett.* **56**, 665 (1990).
[2] R. K. Kawakami, *et al*, *Science* **294**, 131 (2001).
[3] R. J. Epstein, *et al*, *Phys. Rev. B* **65**, 121202(R) (2002).
[4] R. J. Epstein, *et al*, *Phys. Rev. B* **68**, 041305(R) (2003).
[5] C. Ciuti, J. P. McGuire and L. J. Sham, *Phys. Rev. Lett.* **89**, 156601 (2002).
[6] V. N. Gridnev, *JETP Lett.* **77**, 187 (2003) [*Pis'ma Zh. Eksp. Teor. Phys.* **77**, 217 (2003)].
[7] G. E. W. Bauer, *et al*, *Phys. Rev. Lett.* **92**, 126601 (2004).
[8] A. G. Aronov and G. E. Pikus, *Phys. Tech. Poluprovodn.* **10**, 1177 (1976) [*Sov. Phys. Semicond.* **10**, 698 (1976)].

14th Int. Symp. "Nanostructures: Physics and Technology"
St Petersburg, Russia, June 26–30, 2006

Spin dynamics in the regime of hopping conductivity

I. S. Lyubinskiy, A. P. Dmitriev and *V. Yu. Kachorovskii*
Ioffe Physico-Technical Institute, St Petersburg, Russia

Abstract. We consider spin dynamics in the impurity band of a semiconductor with spin-split spectrum. Due to the spin-orbit coupling, phonon-assisted hops from one impurity to another are accompanied by rotation of the electron spin, which leads to the spin relaxation. We demonstrate that depending on the strength of the spin-orbit coupling several regimes can be realized. At very small coupling, the spin decays exponentially. In this case, there are two contributions to spin relaxation rate. One contribution comes from electron diffusion on the large distances (this mechanism is analogous to Dyakonov–Perel relaxation in the metallic regime). Another contribution is due to relaxation in small nontypical closed orbits where relaxation is very fast. At larger values of coupling it is convenient to divide the system into two parts: the infinite cluster, where relaxation is very fast and a number of finite clusters where relaxation is relatively slow. The spin relaxation in this regime is due to slow escape of electrons from finite clusters to infinite one. Finally, at very large spin-orbit coupling, the spin dynamics is determined by "spin traps", i.e. impurities and pairs of impurities having very weak connection with the rest of the system. Both in the case of intermediate coupling and in the case of strong coupling the spin relaxation is non-exponential.

Spin dynamics in semiconductors has attracted much attention in the last decades (for review, see Ref. [1]). A great number of publications were devoted to the study of the spin relaxation in the metallic regime, where the spin relaxation is usually due to Dyakonov–Perel mechanism. In this mechanism, the spin relaxation rate is proportional to the diffusion coefficient [2]. Recently, the idea was put forward [3] that this proportionality goes beyond the metallic regime and stays valid in the range of exponentially small hopping conductivity. In this talk we discuss spin dynamics in the hopping regime and show that a number of different spin relaxation regimes can be realized in addition to the mechanism discussed in Ref. [3]. For simplicity, we focus on the simplest limiting case when the temperature is much higher than the width of the impurity band and assume that distance between impurities L_h is much larger than the Bohr radius a. We also neglect electron-electron interaction.

Due to the spin-orbit coupling, phonon-assisted hop from a certain impurity i to impurity j is accompanied by rotation of the electron spin by the angle $\varphi \sim \Omega t$, where $\Omega = \Omega(\mathbf{p})$ is proportional to spin-orbit spectrum splitting ($\Omega \sim p^3$ in the 3D case and $\Omega \sim p$ in the 2D case), $\mathbf{p} \approx i(\hbar/a)\mathbf{n}$ is the tunneling momentum, $t = mr_{ij}/p$, a is the Bohr radius, m is the electron mass, $\mathbf{n} = \mathbf{r}_{ij}/r_{ij}$ and $\mathbf{r}_{ij}$ is the vector directed from impurity i to impurity j. Random hops between different impurities lead to spin relaxation.

Let us assume that at $t = 0$ the homogeneous distribution of the spin density $\mathbf{S}_0$ is created in the sample (for example, by means of optical orientation) and study the dynamics of averaged spin $\mathbf{S}(t)$ in the system. The system under discussion is strongly inhomogeneous due to exponential variation of hopping times. At sufficiently weak spin-orbit coupling, the distance covered by the electron trajectory during the spin relaxation time exceeds the scale of the inhomogeneity, so one can introduce averaged value of spin relaxation rate $1/\tau_S$. The spin polarization in this regime obeys exponential law: $\mathbf{S}(t) = \mathbf{S}_0 \exp(-t/\tau_S)$. There are two contributions to $1/\tau_S$. The first contribution is due to electron diffusion on the scales larger than the characteristic scale of inhomogeneity. This contribution is analogous to the usual Dyakonov–Perel relaxation (see Ref. [3]). However, there is another contribution neglected in Ref. [3] which comes from the electron relaxation on small closed hopping orbits. Such orbits are mostly small nontypical pairs and triangles of impurities with the distances between impurities of the order of a. Since electron hops between such impurities are exponentially fast compared to the typical hops, they might give the leading contribution to the spin relaxation, even though such configurations of impurities are very rare.

With increasing the spin-orbit coupling, τ_S decreases. As a result, some finite isolated clusters becomes effectively separated from the rest of the system on the time scale of τ_S. Therefore, one can no longer describe the spin dynamics by a single time τ_S, so the spin relaxation becomes non-exponential. It turns out that for such finite isolated clusters both mechanism described above become ineffective. Indeed, the diffusion coefficient for the finite area is strictly equal to zero, which suppresses mechanism proposed in Ref. [3]. The very rare impurity configurations favorable for spin relaxation also do not work for finite clusters, since the probability to find such impurity configurations in a finite cluster is rather small. This means that the spin of electrons captured on such isolated clusters does not relax until they escape to the infinite cluster. The spin dynamics in this regime is described by a simple equation $\mathbf{S}(t) = \mathbf{S}_0 \nu(t)$, where $\nu(t)$ is the relative fraction of electrons captured in the isolated clusters on the time scale of t. The function $\nu(t)$ decreases with time due to escape to the infinite cluster. This function is given by $\nu(t) = 1 - P(t)$, where $P(t)$ is a fraction of electrons on the infinite cluster. To find the function $P(t)$ we will use the standard approach of the theory of hopping transport [4]. The time τ_{ij} needed for electron transition from impurity i to impurity j exponentially depends on the distance L_{ij} between impurities: $\tau_{ij} = \tau_0 \exp(2L_{ij}/a)$, where τ_0 is the hopping time for the impurities separated by the distance of the order of a. Following Ref. [4], we assume that the impurities are effectively connected if $\tau_{ij} < t$ ($L_{ij} < L(t) = a/2\ln(t/\tau_0)$) and disconnected if $\tau_{ij} > t$ ($L_{ij} > L(t)$). For $L(t)$ larger than a certain critical length which is of the order of L_h, the connected impurities form infinite cluster. The fraction of impurities in the infinite cluster $P(L)$ is shown in Fig. 1 (see Ref. [4]). Therefore, the spin dynamics is given by

$$\mathbf{S}(t) = \mathbf{S}_0 \left[1 - P(t)\right], \qquad (1)$$

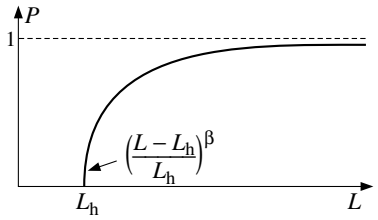

Fig. 1. Fraction of impurities belonging to the infinite cluster as a function of the maximal distance L between connected impurities. In the vicinity of the critical length L_h, function $P(L)$ increases as $([L - L_h]/L_h)^\beta$, where β is a critical index.

where $P(t) = P(L(t))$. Since $P(L)$ depends actually on L/L_h [4], the spin polarization is a function of a single dimensionless parameter $(a/L_h)\ln(t/\tau_0)$. It worth noting that the dynamics of the spin relaxation in this regime does not depend on the strength of spin-orbit coupling.

With the further increase of the spin-orbit coupling, the spin relaxation on the finite clusters comes into play. Finally, at extremely high coupling the spin rotates by a large angle after one typical hop. In this case, the spin relaxes on any finite clusters except isolated impurities or pairs of impurities (small clusters containing one or two impurities) separated from the rest of the system by distances larger than typical distance L_h. The spin at a moment t is proportional to the number of electrons captured on such "traps":

$$\mathbf{S}(t) = \mathbf{S}_0 \exp\left[-\left(\frac{a}{L_h}\ln\frac{t}{\tau_0}\right)^d\right], \qquad (2)$$

where $d = 2,\ 3$ is dimensionality of the system. It is seen from this equation that just as in the case of intermediate coupling the spin dynamics does not depend on the spin-orbit strength and determined by the only parameter $(a/L)\ln(t/\tau_0)$. We are grateful to M. I. Dyakonov, V. I. Perel and B. I. Shklovskii for useful discussions.

Acknowledgements

This work has been supported by RFBR, a grant of the RAS, a grant of the Russian Scientific School 2192.2003.2, and a grant of the foundation "Dynasty" — ICFPM.

References

[1] Semiconductor Spintronics and Quantum Computation, eds. D. D. Awschalom, D. Loss and N. Samarth, (Springer–Verlag, Berlin, 2002).
[2] M. I. Dyakonov and V. I. Perel', *Sov. Phys. Solid State* **13**, 3023 (1972).
[3] B.I. Shklovskii, cond-mat/0602221.
[4] B. I. Shklovskii and A. L. Efros, *Electronic Properties of Doped Semoconductors* (Springer–Verlag, Berlin, 1984).

14th Int. Symp. "Nanostructures: Physics and Technology"
St Petersburg, Russia, June 26–30, 2006

Optical pumping and spin-dependent recombination in GaAsN alloys

V. K. Kalevich[1], E. L. Ivchenko[1], M. M. Afanasiev[1], A. Yu. Egorov[1], A. Yu. Shiryaev[1], V. M. Ustinov[1], B. Pal[2] and Y. Masumoto[2]

[1] Ioffe Physico-Technical Institute, St Petersburg, Russia
[2] Institute of Physics, University of Tsukuba, Tsukuba 305-8571, Japan

Abstract. Spin-Dependent Recombination (SDR) has been observed in GaAsN alloys at room temperature. It reveals itself in a strong decrease of the edge photoluminescence (PL) when either the polarization of exciting light is changed from circular to linear or a transverse magnetic field is switched on. The interband absorption of circularly polarized light results in a spin polarization of conduction electrons which reaches 35% with increasing the pump intensity. The effects observed are explained by dynamical polarization of deep paramagnetic centers and spin-dependent capture of conduction electrons by these centers. The PL depolarization in a transverse magnetic field (Hanle effect) allows us to estimate the electron spin relaxation time in the range of 1 ns. Theoretically, it has been concluded that, due to the SDR, this long time is controlled by slow spin relaxation of bound electrons.

In recent years Ga(In)AsN alloys grown on GaAs substrates have attracted an increasing attention due to their unusual physical properties and application in near-infrared optoelectronics [1]. Evidently, the understanding of the free-carrier kinetics and recombination mechanisms in these materials are important from the point of view of both fundamental physics and practical applications. In this work we investigated the SDR in GaAsN alloys. At room temperature it manifests itself in a decrease of the edge PL intensity by more than a factor of 3 when either the polarization of the exciting light is changed from circular to linear or the transverse magnetic field of $\sim$ 300 gauss (G) is applied. A high spin polarization ($\sim$ 35%) and long-term spin memory ($\sim$ 1 ns) of conduction electrons, both related to the SDR, were observed also at room temperature.

We studied the 0.1 μm thick undoped $GaAs_{1-x}N_x$ films ($x = 2.1, 2.7, 3.4\%$) grown by the MBE on a semi-insulating GaAs (001) substrate [2]. The spin polarization of conduction electrons was created under interband absorption of the circularly polarized light [3]. Its magnitude was determined by measuring the degree of PL circular polarization $\rho = (I^+ - I^-)/(I^+ + I^-)$, where I^+ and I^- are the intensities of the right (σ^+) and left (σ^-) circularly polarized PL components. The measurements were carried out at 300 K. Since the main experimental results are qualitatively the same for all the samples under study we present below the data for $GaAs_{1-x}N_x$ alloy with $x = 2.1\%$.

Fig. 1 shows the PL spectra and circular polarization measured in the $GaAs_{0.979}N_{0.021}$ alloy under excitation by the σ^+-polarized light of high intensity. Each PL spectrum consists of two strongly overlapping bands. Relative to the polarization of the pump beam, the low- and high-energy bands of the PL spectrum are polarized negatively and positively, respectively. The presence of two PL bands and the opposite signs of their polarization were interpreted in our previous work [2] as originating from the strain-induced splitting of the light- and heavy-hole valence subbands.

Spectrum 2 in Fig. 1 is obtained under excitation by linearly (π) polarized light. It is seen from curves 1 and 2 that the change of pump polarization from circular to linear leads to a decrease of PL intensity I near the PL maximum by a factor of 3. The same decrease in I occurs when the transverse magnetic field of 400 G is switched on.

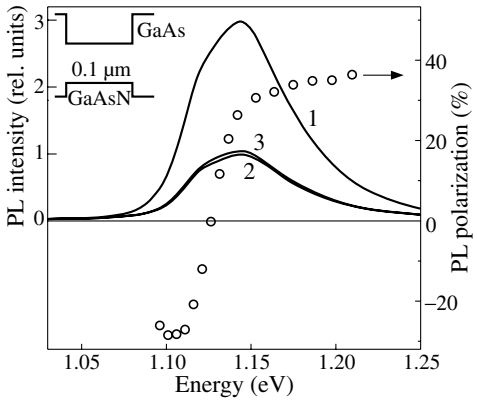

Fig. 1. PL spectra under excitation by circularly (curves 1, 3) and linearly (curve 2) polarized light and the PL circular polarization spectrum (circles) of the $GaAs_{0.979}N_{0.021}$ film. Spectrum 3 is obtained in the transverse magnetic field $B = 400$ G. Excitation intensity $J = 150$ mW; $\hbar\omega_{\rm exc} = 1.305$ eV; $T = 300$ K.

Fig. 2a represents the dependencies $\rho(B)$ measured in the alloy $GaAs_{0.979}N_{0.021}$ in a transverse magnetic field **B** for different intensities of the σ^+ excitation near the maximum of heavy-hole-related PL band. The dependencies are well approximated by Lorentz curves (solid lines in Fig. 2a)

$$\rho(B) = \rho^* + \rho_0 \left[1 + \left(B/B_{1/2}\right)^2\right]^{-1}, \qquad (1)$$

where ρ^* is a constant component ($\approx 5\%$), $B_{1/2}$ is the half-width of the curve at half-height, ρ_0 is the maximum change of ρ in the magnetic field. Values of $B_{1/2}$ and ρ_0 are strongly dependent on the pump intensity.

Fig. 2b shows the magnetic-field dependence $I(B)$ which can be fitted by a Lorentz curve (solid curves) with the width coinciding with that of the Hanle curve $\rho(B)$ taken at the same excitation intensity.

Experimental results presented in Figs. 1 and 2 can be explained in the SDR model [4]. We use this model and assume that each deep center can contain either one electron with uncompensated spin $\pm 1/2$ or two electrons in the singlet state with the zero total spin. Let us introduce the notations $n_\pm$ and $N_\pm$, respectively, for the concentration of the free electrons and paramagnetic centers with the electron spin component $\pm 1/2$, and $N_{\uparrow\downarrow}$ for the concentration of centers

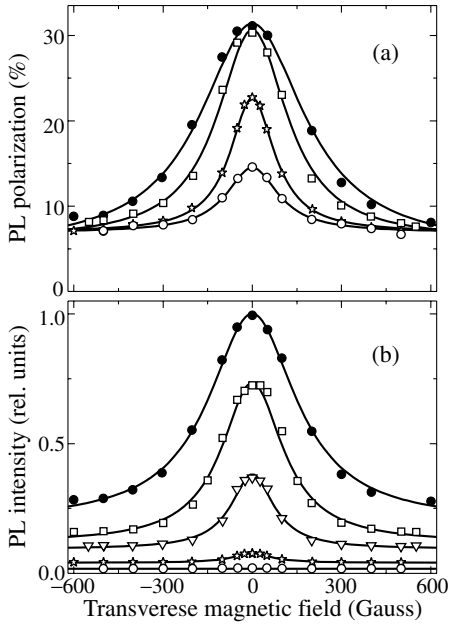

Fig. 2. Degree of PL circular polarization at detection energy $\hbar\omega_{\rm det} = 1.159$ eV (a) and the peak PL intensity (b) in $GaAs_{0.979}N_{0.021}$ vs. transverse magnetic field at different intensities J of the circularly polarized excitation. Excitation energy $\hbar\omega_{\rm exc} = 1.311$ eV; $T = 300$ K; J(mW) = 240 (•), 150 (□), 100 (▽), 50 (⋆), 25 (○).

with two electrons. In this SDR model the contribution of the band-to-band recombination is neglected in the balance equations and the rate of free-carrier capture by deep levels is described by $\left(dn_\pm/dt\right)_{\rm rec} = -\gamma_e n_\pm N_\mp$ for electrons and $\left(dp/dt\right)_{\rm rec} = -\gamma_h p N_{\uparrow\downarrow}$ for holes, where p is the density of holes assumed to be unpolarized irrespective of the incident-light polarization. In addition to the recombination constants γ_e and γ_h, the system is characterized by two times, namely, the spin relaxation times of free and bound electrons, respectively, τ_s and τ_{sc}. Apparently, at room temperature $\tau_s \ll \tau_{sc}$.

For a qualitative interpretation of the behavior of the PL intensity and circular polarization as functions of the incident-light polarization and the magnetic field strength, it suffices to analyze the limiting case of weak photoexcitation where P_c is small and one has [4]:

$$I \propto 1 + a P_c P, \quad \rho = b\,(P_i + P_c)\ . \tag{2}$$

Here $P = (n_+ - n_-)/(n_+ + n_-)$ and $P_c = (N_+ - N_-)/(N_+ + N_-)$ are the degrees of spin polarization of free and bound electrons, P_i is the spin-polarization degree of photoelectrons at the moment of generation, and a, b are positive coefficients. Since the linearly polarized excitation gives rise to no optical orientation of electron spins, the ratio I(circ)/I(lin) of PL intensities under circularly and linearly polarized pumping is given by $(1 + aP_cP)$. The product P_cP is positive and independent of the sign of the incident circular polarization. Therefore, I(circ) $>$ I(lin). In a transverse magnetic field, $\mathbf{B} \perp z$, so that $|g_e|\mu_{\rm B}B\tau_s/\hbar \ll 1$ but values of $|g_c|\mu_{\rm B}B\tau_{sc}/\hbar$ are arbitrary (g_e, g_c are the free- and bound-electron g-factors, $\mu_{\rm B}$ is the Bohr magneton), one can neglect the rotation of free-electron spin due to the Larmor precession. In this case Eq. (2) is valid for non-zero B as well if P_c is understood as the bound-electron spin polarization along the z axis, $P_c(B) = P_c(0)[1+(\Omega_c T_{sc})^2]^{-1}$. Here $\Omega_c = g_c\mu_{\rm B}B/\hbar$ is the bound-electron Larmor frequency, $T_{sc}^{-1} = \tau_{sc}^{-1} + \tau_c^{-1}$, $\tau_c^{-1} = \gamma_h N_{\uparrow\downarrow}(p/N)$ is the capture rate of holes by the centers with two electrons. The increasing magnetic field results in a depolarization of the bound-electron spins reducing the intensity from I(circ) to I(lin) and the polarization ρ from $b(P_i + P_c)$ to $bP_i \equiv \rho^*$.

We show that in spite of the short spin-relaxation time $\tau_{\rm s}$, there also exists a long time of evolution of free-electron spins. For this purpose we reduced the rate equations for $n_\pm$ and $N_\pm$ to the following equations for polarizations:

$$\frac{{\rm d}P}{{\rm d}t} = -\frac{P}{\tau_{\rm s}} + \frac{P_c}{\tau_0}\left(1 - P^2\right) + \frac{G}{n}\left(P_i - P\right)\ , \tag{3}$$

$$\frac{{\rm d}P_c}{{\rm d}t} = -\frac{P_c}{T_{sc}} + \frac{n}{N}\frac{1}{\tau_0}P\left(1 - P_c^2\right)\ , \tag{4}$$

where G is the total photogeneration rate, and $\tau_0 = (2/\gamma_e N)$ is the capture time of conduction-band electrons in the absence of SDR. The second term in the right-hand side of Eq. (3) is related to the SDR and plays the role of spin-generation rate. By using Eq. (3) one can readily show that, under abrupt cutting off the steady-state optical excitation, the polarization time-resolved decay $P(t)$ comprises both fast and slow components: the first one decays within the time $\sim\tau_{\rm s}$, whereas the second contribution can be approximated by $P(t) \approx (\tau_{\rm s}/\tau_0)P_c(t)$.

The proximity of the maximum value of PL polarization ($\sim$35%) in Fig. 2a to its limiting value of 50% indicates a long-term spin memory of conduction electrons. As shown above, the spin memory of the nonlinearly coupled spin subsystems of free and bound electrons is controlled by the long spin lifetime T_{sc} of bound electrons. The latter can be easily determined from the Hanle effect as $T_{sc} = \hbar/(g_c\mu_{\rm B}B_{1/2})$. The smallest half-width found from Fig. 2a is $B_{1/2}^{\rm min} = (91 \pm 5)$ G. Taking into account that $\tau_{sc}^{-1} < T_{sc}^{-1}$ and $g_c \approx 2$, we obtain that τ_{sc} exceeds 0.6 ns.

In conclusion, the strong SDR has been observed in alloys GaAsN at room temperature. Giant electron spin lifetime and high polarization have been found under optical pumping conditions. Therefore, the nitrogen-containing alloys GaAsN can be considered as a promising material for the development of spintronics devices. A model of SDR has been applied to explain the observed dependencies of the electron lifetime, spin relaxation time and spin polarization degree on the pump intensity. It has been shown that, in spite of the very short spin relaxation time of free electrons, the behavior of the coupled system of spin-polarized free and bound electrons is controlled by the long spin relaxation time of bound electrons that amounts 1 ns.

Acknowledgements

The work was partially supported by RFBR, JSPS and the Russian Academy of Sciences Program "Quantum nanostructures".

References

[1] W. Walukiewicz *et al*, *Physica E* **20**, 300 (2004).
[2] A. Yu. Egorov *et al*, *J. Appl. Phys.* **98**, 13539 (2005).
[3] *Optical orientation*, eds. F. Meier and B. Zakharchenya (North-Holland, Amsterdam, 1984).
[4] C. Weisbuch and G. Lampel, *Solid State Commun.* **14**, 141 (1974).

14th Int. Symp. "Nanostructures: Physics and Technology"
St Petersburg, Russia, June 26–30, 2006

Control of spin relaxation in GaAs/AlGaAs coupled quantum wells by means of electric field

A. V. Larionov[1,2], V. E. Bisti[1], M. Bayer[2], J. Hvam[3] and K. Soerensen[3]

[1] Institute of Solid State Physics RAS, 142432 Chernogolovka, Russia
[2] Experimentelle Physik II, Dortmund University, D-44221 Germany
[3] Microelectronic Centre, DK 2800 Lyngby, Denmark

Abstract. The electrons spin dynamics has been investigated in GaAs/AlGaAs coupled quantum wells (n-i-n heterostructures). The electrons spin dephasing times as function of electrical bias have been measured by the spin-beats spectroscopy based on a time-resolved Kerr rotation technique. A strong nonmonotomic dependence of electrons spin-flip time and g-factor value in quantum well plane versus applied bias has been found.

Introduction

The electron spin is a fundamental quantum object, which is very important for many physical phenomena. Electron spin manipulation for the construction of fundamentally new devices is an established idea which undergoes currently a rebirth due to a modern nanotechnology development. The fundamental aim in this context is to discover regimes in which carefully prepared quantum states based upon spin can evolve coherently over times long enough to allow storage, manipulation and readout of quantum information in devices.

Among the quasi-two-dimensional objects based on semiconductor heterostructures, coupled quantum wells (CQWs) are of special interest because they provide spatial separation of photoexcited electrons and holes in neighboring quantum wells [1]. In n-i-n types GaAs/AlGaAs CQWs with tilted bands due to bias application, there is a possibility to tune the electron-hole overlap integral through the tunneling barrier height and in a such way to control the electrons escape from quantum well due to radiative annihilation with holes.

This works' goal was to investigate the possibilities for manipulation of the electron spin relaxation rate by means of an external electric field.

1. Experimental

The CQWs system studied here consists of two GaAs quantum wells (width $\approx$ 120 Å) separated by a narrow (4 monolayers) AlAs barrier. The QWs were separated from the Si-doped (10^{18} cm^{-3}) GaAs layers by 0.15 μ thick AlGaAs ($x = 0.33$) barriers. The upper part of the structure was covered with a 100 Å GaAs layer. Mesa structures were fabricated on the as-grown structure by a lithographic technique. Metal contacts of Au + Ge + Pt alloy were deposited as a frame on the upper part of the mesa and also the doped buffer layer.

The electrons spin dynamics has been examined by means of a time-resolved Kerr rotation technique. This setup consists of a high precision mechanical delay line, an elasto-optical modulator, a holographic grating with optical slits for pulse shaping. The detection of the nonlinear signal is provided by a Si p-i-n photodiodes balanced detector with a lock-in detector. As source of pulsed photoexcitation we have used a pulsed Ti-Sapphire laser with pulse duration of about 1 ps.

An example of time-resolved spin beats in CQWs detected in a magnetic field of 2 T (Voigt configuration) is given in Fig. 1 for different bias. The energy of pump and probe picosecond

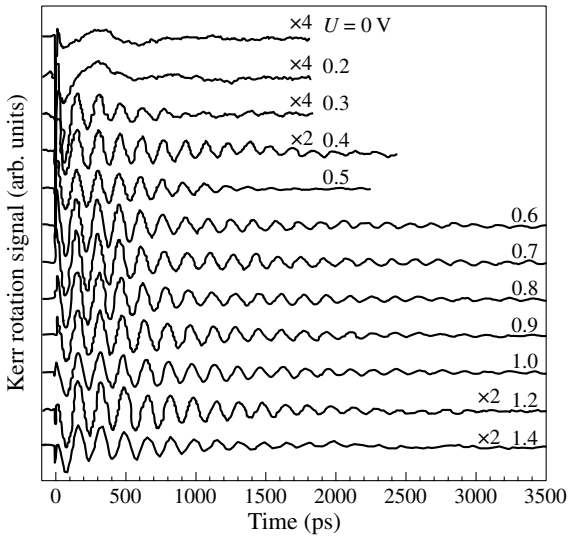

Fig. 1. Kerr rotation signal for varying applied bias. Experimental curves have been recorded at $T = 1.8$ K and photoexcitation power density $P \approx 2\times10^3$ W/cm^2.

laser beams has been tuned to the maximum of the photoluminescence line corresponding to radiative annihilation of the 1sHH exciton. At the beginning every curve shows a fast coherent part, which corresponds to the zero time delay. Here we are not going to discuss the physics related to the coherent part and will instead concentrate on the electron spin beats whose decay lasts typically 300–2000 ps. The periodic oscillations at longer delays are due to the precession of coherently excited electron spins around the external magnetic field. The period of the oscillations is proportional to the electron spin splitting ΔE in the conduction band. This experimental technique is not sensitive to the sign of the g-factor, but allows to measure the g-factor value in the quantum well plane (g_e^{xy}) with high precision, as the precession frequency ω ($\omega = 2\pi/T$ with the oscillation period T is given by: $\hbar\omega = \Delta E = \mu_B g_e^{xy} B$.

The set of experimental data can be fitted by an exponentially damped oscillation containing the beat frequency ω and a single decay time:

$$I = I_0 \exp(-t/\tau) \cdot \cos(\omega t)\,, \qquad (1)$$

As result of such fitting the dependence of electrons spin-flip time versus applied bias has been received in addition to g_e^{xy} and it is shown on Fig. 2.

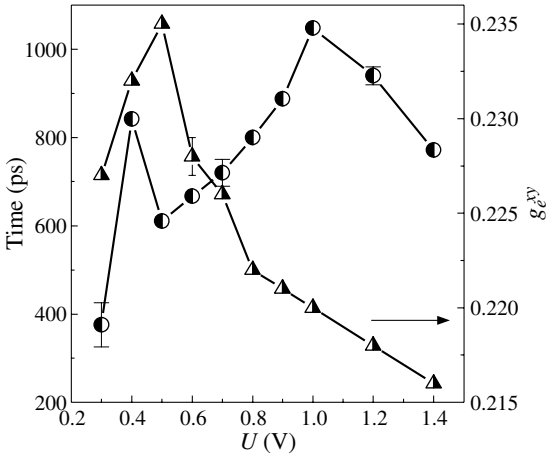

Fig. 2. Dependence of electrons spin-flip time (circular symbols) and g_e^{xy} (triangular symbols) on applied bias at $T = 1.8$ K and $P \approx 2\times10^3$ W/cm^2.

As can be seen also from Fig. 1 that there is a sharp change of Kerr signal oscillations with increasing bias at about 0.2 V. From the results of the fits to the data with expression (1) we conclude that curves at bias more than 0.2 V reflect the electrons spin-flip decay because they show long-lived oscillations according to the electronic g-factor value $g_e^{xy} \approx 0.2$. In contrast, at smaller bias close to a flat band situation we have most likely observe exciton spin-flip oscillations. This boundary is rather sharp in terms of applied voltage $0.17 \pm 0.05V$. We do not see smooth dependence like in work [1].

With further increase of external voltage the electrons spin-flip time and electronic g-factor g_e^{xy} show a strong non-monotonic behavior (see Fig. 2).

2. Discussion and summary

We suggest that the observed strong non-monotonic behavior of electrons spin-flip time (diregarding the data point at 0.4 V) arise from the competition of two possible electron spin-flip mechanisms. One of them is the exchange interaction splitting between "bright" $|\pm 1\rangle$ and "dark" $|\pm 2\rangle$ excitons [2]. The second mechanism is related to a dependence of spin-flip time on the quantum well width [3]. A non-monotonic spin-flip time dependence for the selected field direction along the (110) axis (for an ordinary (001) quantum well) has been reported in [3] as consequence of an interference of two types of spin-orbit interaction (bulk inversion asymmetry, independent on electric field, and structure inversion asymmetry, strongly dependent on applied electric field). This mechanism can be efficient in our case, too.

As far as the electronic g-factor value g_e^{xy} is concerned, at the moment we do not understand the non-monotonic behavior on bias. Based on the penetration of the electron wave function into the barrier or (and) an effective weak decrease of well width, it should monotonically decreases with increasing electrical bias [4].

In conclusion, for the first time a strong non-monotonic dependence of electrons spin-flip time and electronic g-factor value in quantum well plane versus applied bias has been observed.

Acknowledgements

This research was supported by DFG (Grant No. 436 RUS 17/29/05), RFBR, the Russian Science Support Foundation and by Russian President grant for young scientists.

References

[1] I. Ya. Gerlovin *et al*, *Phys. Rev. B* **69**, 035329 (2004).
[2] M. Dyakonov *et al*, *Phys. Rev. B* **56**, 10412 (1997).
[3] N. S. Averkiev, L. E. Golub and M. Willander, *Journal of physics: condensed matter* **14**, R271–283 (2002).
[4] L. A. Yugova, A. Greilich, D. R. Yakovlev, A. Kiselev, M. Bayer *et al*, *will be published in Phys. Rev. B*.

14th Int. Symp. "Nanostructures: Physics and Technology"
St Petersburg, Russia, June 26–30, 2006

Spin splitting in SiGe/Si heterostructures

M. O. Nestoklon, L. E. Golub and E. L. Ivchenko
Ioffe Physico-Technical Institute, St Petersburg, Russia

Abstract. Spin and valley-orbit splittings are calculated in symmetric SiGe/Si/SiGe quantum wells (QWs) by using the tight-binding approach. In accordance with the symmetry considerations an existence of spin splitting of electronic states in perfect QWs with an odd number of Si atomic planes is demonstrated. The spin splitting oscillates with QW width and these oscillations are related to the inter-valley reflection of an electron wave from the interfaces. It is shown that the splittings under study can efficiently be described by an extended envelope-function approach taking into account the spin- and valley-dependent interface mixing. The obtained results provide a theoretical base to the experimentally observed electron spin relaxation times in SiGe/Si/SiGe QWs.

Introduction

At present various semiconductor materials are being involved in the spintronics activities. SiGe/Si QW structures are among them. Silicon-based systems can be particularly promising due to a comparatively weak spin-orbit interaction and long electron spin-relaxation times. Although bulk Si and Ge have an inversion center, QW structures grown from these materials can lack such a center and allow the spin splitting of the electronic subbands, even in the absence of structure inversion asymmetry [1]. An ideal SiGe/Si/SiGe QW structure with an odd number of Si atomic planes is characterized by the D_{2d} point-group symmetry and, therefore, allows spin-dependent linear-$\mathbf{k}$ terms in the electron effective Hamiltonian

$$\mathcal{H}^{(1)}(\mathbf{k}) = \alpha \left(\sigma_x k_x - \sigma_y k_y\right) , \qquad (1)$$

where σ_x, σ_y are the spin Pauli matrices, $\mathbf{k}$ is the two-dimensional wave vector with the in-plane components k_x, k_y, and $x \parallel [100]$, $y \parallel [010]$.

In the present work we use both the microscopic tight-binding model and the envelope-function approach to calculate the spin splitting of the conduction subbands in diamond-lattice QWs. The obtained results are of particular interest in connection with the experimental studies of electron spin relaxation in Si/SiGe heterostructures [2]. The consideration of a Si/SiGe structure with perfect interfaces and without built-in electric fields allows one to put the upper limit to the electron spin relaxation time.

1. Extended envelope function method

Let us consider a QW layer A sandwiched between barriers of material B. The two bulk materials $j = $ A, B have the diamond-like lattice, the structure is grown along the principal crystallographic axis $z \parallel [001]$, and the lowest conduction subband $e1$ is formed by electronic states in the two Δ valleys with the extremum points $\pm\mathbf{k}_{0j} = (0, 0, \pm k_{0j})$. Note that, in the $Si_{1-x}Ge_x$ solid solution, the extremum-point position is a function of the content x and values of k_{0j} are layer dependent. Because of the lattice constant mismatch some of the structure layers are strained. The barrier layers are assumed to be thick enough for the tunneling tails of the quantum-confined $e1$ states to decay within these layers so that they can be considered as semi-infinite.

In the generalized envelope-function approximation the electron wave function $\Psi(\mathbf{r})$ inside the layer j is written as

$$\Psi(\mathbf{r}) = \mathrm{e}^{\mathrm{i}\mathbf{k}\cdot\rho}\left[\varphi_1(z;\, j)\psi_{\mathbf{k}_{0j}}(\mathbf{r}) + \varphi_2(z;\, j)\psi_{-\mathbf{k}_{0j}}(\mathbf{r})\right] . \qquad (2)$$

Here $\psi_{\pm\mathbf{k}_{0j}}(\mathbf{r}) = \mathrm{e}^{\pm\mathrm{i}k_{0j}z}u_{\pm\mathbf{k}_{0j}}(\mathbf{r})$ are the scalar Bloch functions at the Δ extremum points, $u_{\pm\mathbf{k}_{0j}}(\mathbf{r})$ are the Bloch periodic amplitudes, $\varphi_1(z;\, j)$ and $\varphi_2(z;\, j)$ are the smooth spinor envelopes defined within the layer j, ρ is the in-plane component of the three-dimensional radius-vector $\mathbf{r}$.

The two-valley effective Hamiltonian $\mathcal{H}$ is presented as a sum of the zero-order valley- and spin-independent term $\mathcal{H}_0$ and the interface-induced δ-functional perturbation

$$\mathcal{H}' = V_{\mathrm{L}}\delta(z - z_{\mathrm{L}}) + V_{\mathrm{R}}\delta(z - z_{\mathrm{R}}) . \qquad (3)$$

Here z_{L} and z_{R} are the coordinates of the left- and right-hand side interfaces, V_{L} and V_{R} are both valley- and spin-dependent operators. The form of V_{L}, V_{R} can be specified by applying the symmetry considerations.

The numerical calculations presented below confirm the hierarchy

$$E_X - E(\mathbf{k}_0) \gg E_{e1} \gg \Delta_{\mathrm{v-o}} \gg \Delta_{\mathrm{spin}} \equiv \alpha_{\pm}k . \qquad (4)$$

Here $E(\mathbf{k}_0)$ and E_X are the conduction-band energies at the extremum point $\mathbf{k}_0$ and the X point in the bulk material A, E_{e1} is the quantum-confinement energy for the lowest conduction subband, $\Delta_{\mathrm{v-o}}$ and Δ_{spin} are the valley-orbit and spin splittings of the $e1$-subband.

The symmetry analysis of Eq. (3) allows one to derive the following equation for the valley-orbit splitting at $k_x = k_y = 0$

$$\Delta_{\mathrm{v-o}} = 4\,|\chi\,(z_{\mathrm{if}})|^2\,\lambda|\cos(k_0L - \phi_\lambda)| , \qquad (5)$$

where $\chi\,(z_{\mathrm{if}})$ is envelope function at the interface and λ, ϕ_λ are real parameters, their values can be found from comparison with the results of a microscopical calculation. For small values of $\mathbf{k}$ the coefficients $\alpha_\pm$ in (4) are $\mathbf{k}$-independent and given by

$$\alpha_\pm = 2\,|\chi\,(z_{\mathrm{if}})|^2\left[S \pm p\eta\cos(k_0L - \phi_p)\right] . \qquad (6)$$

In equations above $\eta = \mathrm{sign}\{\cos(k_0L - \phi_\lambda)\}$ is the parity of the lower valley-orbit-split state with respect to $\mathcal{S}_4$ operation, and S, p, ϕ_p are free parameters of the theory. While deriving Eq. (6) we took into account both the intra- and inter-valley contributions to V_m.

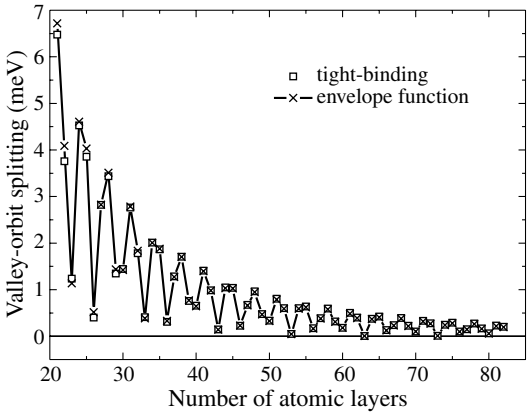

Fig. 1. Valley-orbit splitting $\Delta_{\mathrm{v-o}}$ in a $Si_{1-x}Ge_x/Si/Si_{1-x}Ge_x$ ($x = 0.25$) QW versus the number of Si mono atomic layers. Analytical results shown by crosses are calculated using Eq. (5) with $\lambda = 385$ meV Å, $\phi_\lambda = 0.3\pi$.

2. Microscopical calculation

In order to estimate values of spin and valley-orbit splittings we have performed calculations of the electron dispersion in the $e1$ conduction subband by using the nearest-neighbor sp^3s^* tight-binding model optimized for the conduction band [3]. This model is a reasonable compromise between the numerical load and the accuracy of representation of the band structure. The applicability of the sp^3s^* model is confirmed by the fact that values of the valley-orbit splitting $\Delta_{\mathrm{v-o}}$ calculated in this work and by using the $sp^3d^5s^*$ model [4,5] are of the same order of magnitude.

In the tight-binding method the electron Hamiltonian is presented by a set of matrix elements taken between atomic orbitals. For diamond crystals the basis functions are constructed of functions centered on each atom in the crystal. It is assumed that the only nonzero Hamiltonian matrix elements are those between orbitals on the same or neighboring atoms. Then the electron Hamiltonian in a hereterostructure grown along [001] direction for a given lateral wave vector **k** can be written as a banded matrix. Its eigenvalues give electron energies in this approach.

Squares in Fig. 1 show results of tight-binding calculations of the valley-orbit splitting $\Delta_{\mathrm{v-o}}$ in symmetrical $Si_{0.75}Ge_{0.25}/Si/Si_{0.75}Ge_{0.25}$ QWs as a function of the number N of Si atomic planes sandwiched between the thick barriers $Si_{0.75}Ge_{0.25}$. The valley-orbit splitting exhibits oscillations with the increasing QW width, in agreement with Ref. [4]. Crosses in Fig. 1 represent the calculation of $\Delta_{\mathrm{v-o}}$ in the envelope-function approximation, Eq. (5), with $k_0 = 0.62\times 2\pi/a_0$. While calculating the electron envelope function at the interface, $\chi(z_{\mathrm{if}})$, we used values of $V = 150$ meV for the conduction-band offset and of $0.907m_0$ for the effective mass. The parameter λ and the phase ϕ_λ in Eq. (5) were considered as adjustable parameters. Their best fit values turned out to be $|\lambda| = 385$ meV Å, $\phi_\lambda = 0.3\pi$. It is seen from Fig. 1 that the simple analytical theory is in complete agreement with the results of sophisticated tight-binding calculations.

In Fig. 2 the spin-orbit splitting for the two valley-orbit subbands $E_{e1,-}$ and $E_{e1,+}$ is presented. We define the splitting Δ_{spin} in Fig. 2 as the energy difference between the states with the spin parallel and antiparallel to the x axis (for $k_x \neq 0$, $k_y = 0$). As one can see the valley-orbit and spin splittings

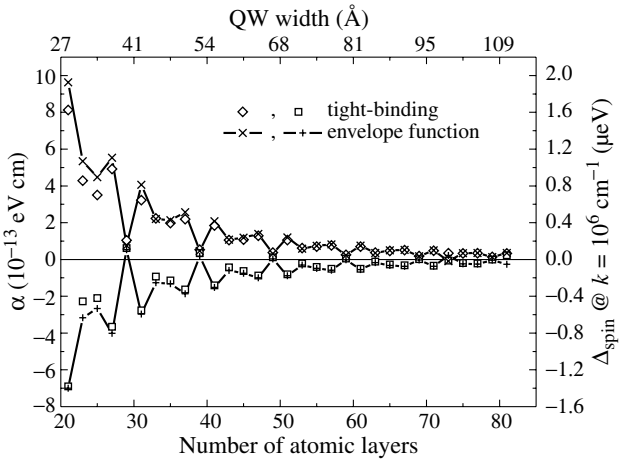

Fig. 2. Spin-splitting constant α versus the QW width (odd N are taken in consideration only). The spin splitting of the lower subband E_{e1-} is shown by diamonds (tight-binding calculation) and x-shaped crosses (envelope function approximation), those for the upper subband E_{e1+} are shown by squares and conventional crosses.

are conveniently presented in the meV and μeV scales confirming the assumption (4). Squares and diamonds in Fig. 2 show results of tight-binding calculation. The spin splitting is plotted only for odd number of Si monoatomic planes because, for even N, Δ_{spin} in the symmetric structures vanishes. Conventional and x-shaped crosses are obtained as the best fit using Eq. (6) and choosing the same values for k_0 and ϕ_λ as in Fig. 1 and the additional adjustable parameters $p = 0.53\times 10^{-5}$ eV cm^2, $\phi_p = 0.55$, $S = 0.15p$. Figure 2 shows that the spin splitting Δ_{spin} is an oscillating function of the QW width. This demonstrates that the inter-valley spin-dependent mixing at the interfaces prevails over the intra-valley contribution to $\alpha_\pm$.

Comparison between theory and experiment shows that the tight-binding value of α_- is smaller by a factor ~ 6 than that estimated by Wilamowski *et al* [2] from experiment of electron spin resonance. This means that the experimental value of the spin splitting is not so far from the limit for a perfect QW structure considered in this work.

Acknowledgements

This work was financially supported by the RFBR, programmes of RAS, "Dynasty" Foundation — ICFPM, RSSF, and Russian President grant for young scientists.

References

[1] L. E Golub and E. L. Ivchenko, *Phys. Rev. B* **69**, 115333 (2004).
[2] Z. Wilamowski *et al*, *Phys. Rev. B* **66**, 195315 (2002).
[3] G. Klimeck *et al*, *Superlatt. Microstruct.* **27**, 77 (2000).
[4] T. B. Boykin *et al*, *Phys. Rev. B* **70**, 165325 (2004).
[5] J.-M. Jancu *et al*, *Phys. Rev. B* **70**, 121306 (2004).

14th Int. Symp. "Nanostructures: Physics and Technology"
St Petersburg, Russia, June 26–30, 2006

Fine structure and spin dynamics in InGaAs quantum wells

I. A. Yugova[1,2], A. Greilich[1], I. V. Ignatiev[1,2], *V. A. Nicoluk*[2], D. R. Yakovlev[1,3], M. Bayer[1], V. Stavarache[4], D. Reuter[4] and A. Wieck[4]

[1] Experimentelle Physik 2, Universitat Dortmund, 44221 Dortmund, Germany
[2] Institute of Physics, St Petersburg State University, 198504, St Petersburg, Russia
[3] Ioffe Physico-Technical Institute, St Petersburg, Russia
[4] Angewandte Festkörperphysik, Ruhr-Universität Bochum, D-44780 Bochum, Germany

Abstract. Spin dynamics of the excitons and carriers in InGaAs/GaAs quantum well was studied by polarized pump-probe methods. The main mechanisms of spin relaxation are discussed and the electron and exciton g-factors are determined.

Spin dynamics in nanostructures is extensively studied last several years due to promising prospects for spin memory. InGaAs/GaAs quantum wells (QWs) are less studied nanostructures [1, 2] in this respect relative to other type of A_3B_5 heterostructures like GaAs/AlGaAs QWs and InGaAs/GaAs quantum dots (QDs). Advantage of structures with the InGaAs/GaAs QWs is transparency of GaAs substrate at the QW exciton transition that allows one to perform experiments in transmission geometry. Investigation of the spin dynamics in InGaAs/GaAs QWs is of large interest not only from fundamental point of view but also for understanding of spin-related processes in chemically similar InGaAs/GaAs nanostructures with QDs which study is complicated by large inhomogeneous broadening of the QD ensemble.

In this work, we studied a heterostructure with two coupled $In_{0.09}Ga_{0.91}As$/GaAs QWs separated by thin (1.7 nm) GaAs barrier. The structure was intentionally undoped, but contains residual electrons in QW due to barrier donors. Two-dimensional electron gas density in QW does not exceed 10^{10} cm^{-2}.

The QW exciton photoluminescence (PL) peak with full width at half maximum (FWHM) 0.8 nm is centered at 861.8 nm, lifetime of the PL, $\tau_{PL} \approx 300$ ps.

For study of the spin dynamics we have used two polarized pump-probe methods similar to those described in Refs. [3,4]. The first one exploits the intense circularly polarized pump pulses for optical inducing the circular dichroism (CD) caused by orientation of spins in QWs. The second one, optically induced linear dichroism (LD), exploits linearly polarized pump beam which creates optical alignment of excitons in the QWs. Optical anisotropy induced by pump pulses was detected as the polarization rotation angle of the weak linearly polarized probe pulses. Sample was mounted in a cryostat with split-coil superconductive magnet that allowed us to perform experiments in Faraday and Voigt configurations. We measured the CD and LD signals in transmittion geometry varying angle θ between magnetic field direction and growth axis of the sample. All the experiments were done at temperature 1.6 K.

Fig. 1 shows typical time dependences of the CD and LD signals in zero magnetic field. Rise time of a few picoseconds of the signals are limited by the pump and probe pulse duration. The second peak is caused by replica of the pump pulse which is reflected from the back surface of our sample and excites the QW again. Inset in Fig. 1 shows spectral dependence of amplitude of the time-resolved signals measured at the second maximum. These spectral dependences should be mainly determined by the resonant absorption at the QW

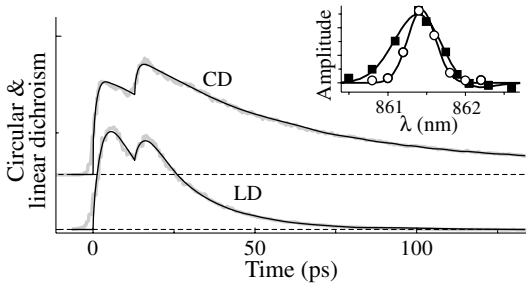

Fig. 1. Typical time dependences of the optically induced circular (CD) and linear (LD) dichroism (thick gray curves). Thin black curves are the fits by equation (1) with parameters: $\tau_1 = 20$ ps for LD, $\tau_1 = 50$ ps and $\tau_2 = 10000$ ps for CD; $\tau_r = 2$ ps. Inset: spectral dependence of amplitude of the time-resolved signals. Black filled squares are the CD data, open circles are the LD data.

exciton transition. FWHM of the dependences is close to that observed for the PL spectrum.

The CD and LD kinetics can be well fitted by equations:

$$I(t) = f(t) + \alpha f(t - \Delta t)\,,$$
$$f(t) = \left[A_1 e^{-t/\tau_1} + A_2 e^{-t/\tau_2} - B e^{-t/\tau_r}\right]\Theta(t)\,. \quad (1)$$

Here $\Theta(t)$ is Heviside function, $\alpha f(t - \Delta t)$ describes the second peak in the signal. Function $f(t)$ describes the spin evolution. The first two terms in $f(t)$ model the decay of spin polarization and the last one models initial rise of the polarization. As we have found, spin relaxation is one-exponential for LD with $\tau_1 \sim 20$ ps and two-exponential for CD with $\tau_1 \sim 50$ ps and $\tau_2 > 1000$ ps.

Circular dichroism can be created by orientation of both the electron and hole spins therefore it may exist while *the slowest relaxation process* destroys it. In the case of the linearly polarized pumping, coherent superposition of $|+1\rangle$ and $|-1\rangle$ states is created. Lifetime of this superposition is limited by *the fastest spin relaxation process*. This principle difference of the LD and CD behavior explains, in general, difference in the polarization relaxation presented in Fig. 1. However, decay time of LD signal as seen is shorter than even the fastest component of decay of the CD signal. We should note here that the CD can be destroyed only by interaction with the phonons which can change angular momentum. At the same time, there is no such kind of selection rules for phonons destroying the LD that results in so fast LD relaxation.

In Fig. 2 typical quantum beats observed in the Faraday rotation signal are shown for magnetic field $B = 5$ T (Voigt configuration, $\theta = 90°$). It is clearly seen that the signal con-

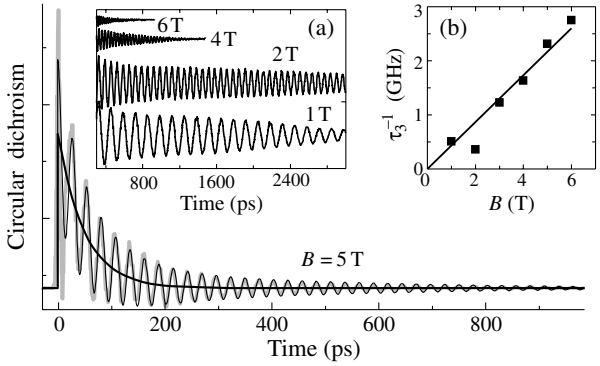

Fig. 2. The CD signal at $B = 5$ T (Voigt configuration). Thick gray curve is the experimental data. Thin black oscillating function is a fit by sum of function (2) and non-oscillating component $A_1 \exp(-t/\tau_1)$ shown by the thick black curve. Inset (a): dependence of the long-lived spin beats on magnetic field. Inset (b): relaxation rate $1/\tau_3$ as a function of magnetic field. Black squares are experimental data. Line is a fit by dependence: $1/\tau_3 = \Delta g_{e\perp} \mu_B B/\hbar$, $\Delta g_{e\perp} = 0.005$.

sists of two components. First, there is non-oscillating component exponentially decaying with time of about 50 ps. It can be ascribed to the relaxation of the hole spin [5]. Absence of oscillations in transverse magnetic field is related to almost zero in-plane component of the heavy hole g-factor.

Oscillating part of the signal is well approximated by function consisting of two components:

$$y = A_2 e^{-t/\tau_2} \cos(\omega_2 t) + A_3 e^{-0.5(t/\tau_3)^2} \cos(\omega_3 t)\,. \quad (2)$$

The oscillations in both the components are related to the electron spin precession about the magnetic field direction. The first component with exponential decay is characterized by the relatively short decay time $\tau_2 \sim 200$ ps which as we found does not depend on magnetic field in the range 0–6 T. We ascribe this process to relaxation of the electron spin in exciton which is related mainly to the electron-hole recombination. The second component of oscillations is characterized by very long decay and can be ascribed to spin precession of resident electrons in the QW. The decay time of the component depends on the magnetic field strength (see inset (a) in Fig. 2). At higher magnetic fields decay of the oscillations can be approximated by the Gaussian-like, rather than exponential, envelope function. Experimentally obtained behavior of the long-lived oscillations is the evidence that their decay is mainly caused by a spread of the transverse component of the electron g-factor. The spread gives rise to destructive interference of the oscillating signals with different frequencies. Almost linear magnetic field dependence of inverse characteristic time of the relaxation, $1/\tau_3$, (see inset (b) in Fig. 2) allows us to determine this spread: $\Delta g_{e\perp} = 0.005$.

Spin precession frequencies for electrons coupled with holes and for resident electrons, ω_2 and ω_3, measured in the Voigt configuration are found to be very close to each other. This means that the exchange interaction in exciton is relatively small in our structure ($\delta < 0.02$ meV). This conclusion is also supported by the linear field dependence of Zeeman splitting $\Delta E = \hbar\omega_2$ passing through origin of energy as shown in Fig. 3(a).

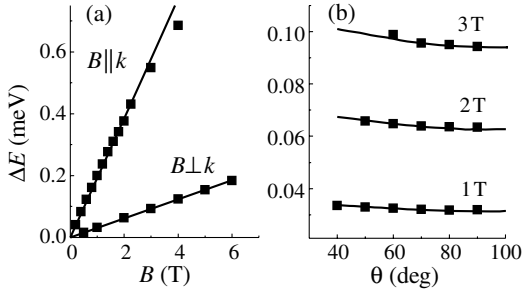

Fig. 3. (a) dependences of the oscillations frequencies in energy units on transverse ($B \perp k$) and longitudinal ($B \| k$) magnetic field strength. (b) Angular dependence of the oscillations frequency for three different magnetic field. Black squares are experimental data. Lines are fits as noted in the text.

Figure 3(a) also shows dependence of the oscillations frequency on the longitudinal magnetic field. The oscillations are caused by quantum beats of Zeeman states $|+1\rangle$ and $|-1\rangle$ coherently excited by the linearly polarized pump. As seen this dependence is well fitted by relation $\Delta E = \hbar\omega = g_{ex}\mu_B B$ that allows us to determine the exciton g-factor $|g_{exc}| = |g_{e\|} + g_{h\|}| = 3.2 \pm 0.01$. Experiments show that these quantum beats rapidly decay with characteristic time of about 20 ps which is independent of magnetic field strength.

We also have studied quantum beats in tilted magnetic field excited by the circularly polarized pump beam. Quantum beats only with single frequency observed in this geometry of experiment which is due to small exchange interaction in our QWs. Angular dependence of the beat frequency for different magnetic field is shown in Fig. 3b. It is well described by equation

$$\Delta E = \hbar\omega = \mu_B B \sqrt{\left(g_{e\|} \cos\theta\right)^2 + \left(g_{e\perp} \sin\theta\right)^2}\,, \quad (3)$$

that allows us to determine longitudinal and transverse components of electron g-factor, $|g_{e\perp}| = 0.54$, $|g_{e\|}| = 0.6$. The obtained electron and excition g-factor values can be used for determination of the hole g-factor, $|g_{h\|}| = 2.6$, which well agrees with data obtained in Ref. [6].

Acknowledgements

The authors thank Dr. Gerlovin for fruitful discussion. The work is partly supported by ISTC, grant 2679, by BMBF program 'nanoqubit', by the DFG through 436 RUS 17/39/04, 436 RUS 17/102/04.

References

[1] A. Malinowski *et al*, *Phys. Rev. B* **60**, 7728 (1999).
[2] A. Malinowski *et al*, *Solid State Commun.* 116, 333 (2000).
[3] S. A. Crooker*et al*, *Phys. Rev. B* **56**, 7574 (1997).
[4] R. E. Worsley *et al*, *Phys. Rev. Lett.* **76**, 3224 (1996).
[5] N. Linder, L. J. Sham, *Physica E* **2**, 412–416 (1998).
[6] N. J. Traynor *et al*, *Phys. Rev. B* **51**, 7361 (1995).

14th Int. Symp. "Nanostructures: Physics and Technology"
St Petersburg, Russia, June 26–30, 2006

Spin and orbital quantization of electronic states as origins of second harmonic generation in semiconductors

I. Sänger[1], B. Kaminski[1], D. R. Yakovlev[1,2], R. V. Pisarev[2], *V. V. Pavlov*[2], M. Bayer[1], G. Karczewski[3], T. Wojtowicz[3] and J. Kossut[3]

[1] Experimental Physics II, Dortmund University, 44227 Dortmund, Germany
[2] Ioffe Physico-Technical Institute, St Petersburg, Russia
[3] Institute of Physics, Polish Academy of Sciences, PL-02668 Warsaw, Poland

Abstract. Application of a magnetic field induces the optical second harmonic generation (SHG) in noncentrosymmetric semiconductors. Different mechanisms of SHG, induced by the external magnetic field, have been experimentally studied in semiconductors GaAs, CdTe and (Cd, Mn)Te. For diamagnetic GaAs and CdTe the SHG response is governed by orbital quantization of electronic states, in contrast to paramagnetic (Cd, Mn)Te with its dominating spin quantization. The mechanisms can be identified by the distinct magnetic field dependence of the SHG intensity.

Introduction

Among the nonlinear optical phenomena, second harmonic generation (SHG) plays a particularly important role as the simplest such process. An incident laser light beam $\mathbf{E}^{\omega}$ with frequency ω creates a nonlinear polarization $\mathbf{P}^{2\omega}$ in a medium at twice the frequency

$$\mathbf{P}^{2\omega} \propto \chi^{eee} : \mathbf{E}^{\omega}\mathbf{E}^{\omega} , \qquad (1)$$

where χ^{eee} is a polar third rank tensor [1], which is determined by the electron distribution in the crystal unit cell. Recently, SHG has been proven to be a very powerful tool for probing magnetic and electronic structures of metals and insulators [2,3,4]. Also semiconductors have been probed by SHG, however, generally under very restricted experimental conditions. Only lately, reports have been made on SHG over wide spectral ranges, whose generation application of a magnetic field was a central point [6,7,5].

Presence of an external magnetic field or spontaneous magnetization results in the occurrence of new nonlinear magneto-optical contributions to optical second harmonic generation [8,3]. The magnetic-field-induced contributions to the nonlinear polarization can be written as [6]

$$\mathbf{P}^{2\omega} \propto \chi^{eeem} : \mathbf{E}^{\omega}\mathbf{E}^{\omega}\mathbf{H}^{0} + \chi^{eeekm} : \mathbf{E}^{\omega}\mathbf{E}^{\omega}\mathbf{k}^{\omega}\mathbf{H}^{0} , \qquad (2)$$

where the first term describes the leading order electric-dipole SHG contributions in magnetic field $\mathbf{H}^0$ and the second term takes into account explicitly the nonlinear magneto-optical spatial dispersion.

In this paper we present an experimental study of the magnetic-field-induced SHG in model semiconductors GaAs, CdTe, and (Cd, Mn)Te. For diamagnetic CdTe and GaAs the SHG response is governed by orbital quantization of electronic states, in contrast to paramagnetic (Cd, Mn)Te with its dominating spin quantization. The mechanisms can be identified by the distinct magnetic field dependence of the SHG intensity, which scales as H^2-dependence observed for the diamagnetic case, and it scales with the spin splitting for the paramagnetic case.

1. SHG in diamagnetic GaAs and CdTe

In the diamagnetic semiconductors GaAs and CdTe a strong magneto-optical contribution to SHG was found by applying external magnetic field. SHG spectra were recorded in transmission geometry using 8 ns light pulses with a 10 Hz repetition rate, generated by an optical parametric oscillator pumped by the third harmonic of a solid-state Nd:YAG laser. The SHG signals were detected by a liquid nitrogen-cooled charged-coupled-device camera. A double pass monochromator and optical filters were used to suppress undesired luminescence. External magnetic fields up to 11 T were applied in the Voigt geometry perpendicular to the light wave vector: $\mathbf{H}^0 \| \mathbf{x}$ and $\mathbf{k}^{\omega} \| \mathbf{z}$. The sample temperature was varied from 4.5 up to 300 K.

In electric-dipole approximation no χ_{yyyx} SHG signal is expected for $\mathbf{E}^{2\omega} \| \mathbf{E}^{\omega} \| \mathbf{y}$. It becomes allowed taking into account nonlinear magneto-optical spatial dispersion described by Eq. (2). Surprisingly, for this geometry strong SHG signal appears with an intensity that is 50 times larger than that for the dipole-allowed χ_{xyyx} contribution (see results for GaAs in Fig. 1). Temperature and field variations of this contribution were studied. Fine structure of the SHG spectrum is caused by the Landau-level (LL) orbital quantization [9] of valence and conducting bands:

$$E_{\mathrm{LL}} = \frac{e\hbar}{c}\left[\frac{1/2 + N_{\mathrm{e}}}{m_{\mathrm{e}}} + \frac{1/2 + N_{\mathrm{h}}}{m_{\mathrm{h}}}\right] H , \qquad (3)$$

where m_{e} and m_{h} are the electron and heavy-hole effective masses, $N_{\mathrm{e}} = N_{\mathrm{h}} = 0, 1, 2, \ldots$ are the Landau-level numbers. We do not account here for the exciton Zeeman splitting which does not exceed 1 meV below 7 T for GaAs.

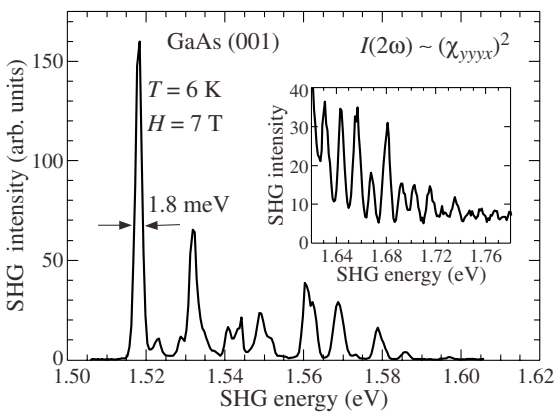

Fig. 1. SHG spectra of GaAs measured for $\mathbf{k}^{\omega} \| \mathbf{z}$, $\mathbf{H}^0 \| \mathbf{x}$ in geometry $\mathbf{E}^{2\omega} \| \mathbf{E}^{\omega} \| \mathbf{y}$. Inset shows the extended photon energy SHG spectrum.

Thus, it is shown, that the magneto-optical contributions to SHG are related with both electric-dipole and nonlinear magneto-optical spatial-dispersion mechanisms. The phen-m-nological analysis and model calculations of observed phenomena confirm this conclusion.

2. SHG in paramagnetic (Cd, Mn)Te

Fig. 2 shows SHG spectra of $Cd_{0.84}Mn_{0.16}Te$ measured in external magnetic field for $\mathbf{k}^{\omega}\|\mathbf{z}$ and $\mathbf{H}^{0}\|\mathbf{x}$ and for two polarization combinations. The integrated SHG intensity as a function of external magnetic field is given in the inset. The Brillouin function (it is shown by the solid line) describes the giant Zeeman effect observed in diluted magnetic semiconductors [10]. The rotational anisotropies of SHG intensity were measured in two different geometries $\mathbf{E}^{2\omega}\|\mathbf{E}^{\omega}$ and $\mathbf{E}^{2\omega}\perp\mathbf{E}^{\omega}$.

The process of SHG in the vicinity of the semiconductor band gap involves electronic states from the bottom of the conduction band and the top of the valence band. Application of a magnetic field gives rise to Landau orbital quantization and to spin splitting due to the Zeeman effect. For the sake of simplicity, we do not include the Coulomb attraction between electrons and holes in our consideration. For modelling the optical spectrum, we consider here only transitions between LLs with equal quantum numbers $N = 0,\ 1,\ \ldots$ for electron and hole, as they have the largest oscillator strength and therefore dominate in the spectra. With these approximations, the energy spectrum near the band gap can be described by:

$$E = E_{\mathrm{g}} + E_{\mathrm{LL}}(N) + E_{\mathrm{Z}}(S,\,J) + E_{\mathrm{GZ}}(S,\,J)\,. \qquad (4)$$

Here E_{g} is the band gap and E_{LL} describes the LL quantization. The third term in Eq. (4) accounts for the spin splitting due to the Zeeman effect:

$$E_{\mathrm{Z}}(S,\,J) = (Sg_{\mathrm{e}} + Jg_{\mathrm{h}})\mu_{\mathrm{B}}H\,, \qquad (5)$$

with projections on the field direction of the electron spin $S = \pm 1/2$ and the hole total angular momentum $J = \pm 3/2,\ \pm 1/2$. $g_{\mathrm{e(h)}}$ are the g-factors of electrons (holes). μ_{B} is the Bohr magneton. The last term in Eq. (4) is the giant Zeeman splitting in diluted magnetic semiconductors [10]:

$$E_{\mathrm{GZ}}(S,\,J) = xS_0N_0\left(\frac{\beta}{3}J - \alpha S\right)B_{5/2}\left[\frac{5\mu_{\mathrm{B}}g_{\mathrm{Mn}}H}{2k_{\mathrm{B}}\,(T_{\mathrm{Mn}} + T_0)}\right], \qquad (6)$$

where $g_{\mathrm{Mn}} = 2$, k_{B} is the Boltzmann constant, and T_{Mn} is the temperature of the Mn-spin system (in our experiment $T_{\mathrm{Mn}} = T$). S_0 and T_0 are the Mn-Mn antiferromagnetic interaction constants. $B_{5/2}$ is the modified Brillouin function. $N_0\alpha = 220$ meV and $N_0\beta = -880$ meV are the exchange integrals for the conduction and valence band states, interacting with the localized magnetic moments of the Mn^{2+} ions [10].

Spin and orbital quantization have different functional dependencies on magnetic field. E_{GZ} saturates with increasing field, whereas E_{LL} and E_{Z} increase linearly. In wide band gap semiconductors E_{Z} is two orders of magnitude smaller than E_{LL}. For example, in CdTe at $H = 10$ T the exciton Zeeman splitting does not exceed 0.1 meV, while the cyclotron energy amounts to 10 meV. By contrast, in diluted magnetic semiconductors E_{GZ} varies up to 100 meV, and can become comparable or even considerably larger than E_{LL}. Therefore in (Cd, Mn)Te one can realize situations in which either orbital or spin quantization dominates.

In conclusion, magnetic-field-induced SHG has been studied in GaAs, CdTe and (Cd, Mn)Te over a wide temperature range from 4.5 K up to room temperature. Two basically different mechanisms responsible for observed SHG were disclosed and distinguished: (i) orbital quantization plays a leading role in the diamagnetic semiconductors GaAs and CdTe; (ii) spin quantization prevails in the diluted magnetic semiconductor (Cd, Mn)Te due to the giant enhancement of the Zeeman effect. The different dependencies of the SHG intensity on magnetic field allow for clear identification and distinction.

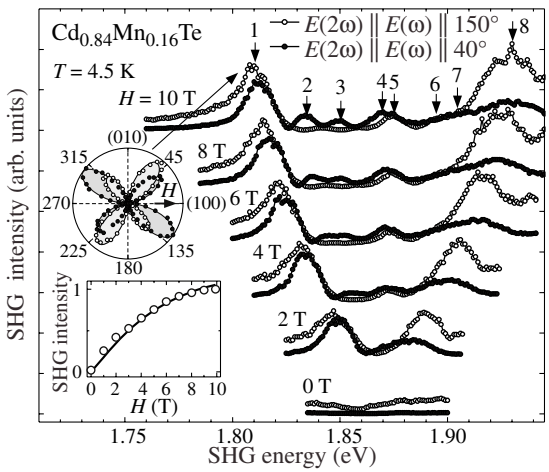

Fig. 2. SHG spectra of $Cd_{0.84}Mn_{0.16}Te$ measured for $\mathbf{k}^{\omega}\|\mathbf{z}$ and $\mathbf{H}^{0}\|\mathbf{x}$ and for two polarization combinations. Inset shows the integrated SHG intensity *vs.* magnetic field, the solid line is a fit to the data with the Brillouin function of Eq. (6). Polar plot shows SHG rotational anisotropies measured in geometries $\mathbf{E}^{2\omega}\|\mathbf{E}^{\omega}$ (light shaded area and open circles) and $\mathbf{E}^{2\omega}\perp\mathbf{E}^{\omega}$ (dark shaded area and closed circles).

Acknowledgements

This work has been supported in part by RFBR, the Program "Nanostructures" and DFG grant 436 RUS 17/56/06.

References

[1] Y. R. Shen, *The Principles of Nonlinear Optics* (New York: Wiley) 1984.
[2] *Nonlinear Optics in Metals*, Ed. by K. H. Bennemann (Oxford: Oxford University Press) 1998.
[3] M. Fiebig, V. V. Pavlov and R. V. Pisarev, *J. Opt. Soc. Am. B* **22**, 96 (2005).
[4] A. Kirilyuk and Th. Rasing, *J. Opt. Soc. Am. B* **22**, 148 (2005).
[5] Y. Ogawa, H. Akinaga, F. Takano, T. Arima and Y. Tokura, *J. Phys. Soc. Jpn.* **73**, 2389 (2004).
[6] V. V. Pavlov, A. M. Kalashnikova, R. V. Pisarev, I. Sänger, D. R. Yakovlev and M. Bayer, *Phys. Rev. Lett.* **94**, 157404 (2005).
[7] I. Sänger, D. R. Yakovlev, R. V. Pisarev, V. V. Pavlov, M. Bayer, G. Karczewski, T. Wojtowicz and J. Kossut *Phys. Rev. Lett.* **96**, 117211 (2006).
[8] P. A. Franken and J. F. Ward, *Rev. Mod. Phys.* **35**, 23 (1963).
[9] L. D. Landau and E. M. Lifshitz, *Quantum Mechanics* (Oxford: Pergamon Press) 1977.
[10] J. K. Furdyna, *J. Appl. Phys.* **64**, R29 (1988).

14th Int. Symp. "Nanostructures: Physics and Technology"
St Petersburg, Russia, June 26–30, 2006

Multiple spin transfer from a polarized hole to Mn ions in (Zn,Mn)Se/(Zn,Be)Se quantum wells

A. V. Scherbakov[1], A. V. Akimov[1,2], D. R. Yakovlev[1,2], I. A. Merkulov[1,3], M. Bayer[2], A. Waag[4] and L. W. Molenkamp[5]

[1] Ioffe Physico-Technical Institute, St Petersburg, Russia
[2] Experimentelle Physik II, Universität Dortmund, D-44227 Dortmund, Germany
[3] Oak Ridge National Laboratory, Oak Ridge, TN 37831-6016, USA
[4] Institute of Semiconductor Technology, Braunschweig Technical University, D-38106 Braunschweig, Germany
[5] Physikalisches Institut der Universität Würzburg, D-97074 Würzburg, Germany

Abstract. The magnetization kinetics in (Zn,Mn)Se/(Zn,Be)Se quantum wells is studied on a ps-time scale after pulsed laser excitation. The magnetization induced by an external magnetic field is reduced by up to 30% within about 100 ps due to spin and energy transfer from photocarriers to magnetic Mn ions. A model based on spin-momentum coupling in the valence band is suggested for explaining this transfer.

Introduction

Manipulation of spins appears to be more challenging than manipulation of charges. Therefore it is crucial to develop a detailed understanding of interaction mechanisms between spin and other excitations in the solid, from which such a manipulation might be achieved. Spin and energy transfer from photoexcited carriers to magnetic ions in diluted magnetic semiconductors (DMS) is one of the key principles for ultrafast control of the magnetization in spintronic devices.

In this work we report on the picosecond kinetics of the magnetic-field-induced magnetization in DMS (Zn,Mn)Se/(Zn,Be)Se quantum wells (QWs) after femtosecond optical excitation. We find a very efficient spin and energy transfer from the photoexcited holes to the magnetic ions even for fully spin polarized holes. We explain this observation by mixing of the heavy-hole and light-hole states at finite wave vectors, which allows a multiple angular momentum transfer from each hole to the Mn ion system without change of the hole spin orientation.

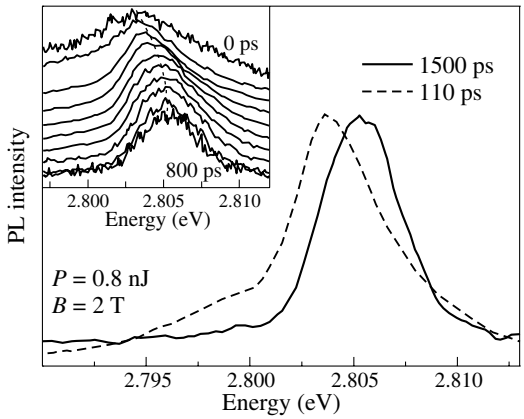

Fig. 1. Normalized PL spectra of $Zn_{1-x}Mn_xSe/Zn_{0.94}Be_{0.06}Se$ QWs measured at delay times $t = 110$ ps (dashed line) and $t = 1500$ ps (solid line) in time windows 10 ps and 220 ps correspondingly for $x = 0.013$, $P = 0.8$ nJ, $B = 2$ T, $T = 1.8$ K. The inset shows ten normalized photo-luminescence spectra measured at different delays in a time window of 80 ps.

1. Experimental

The samples under study were three nominally undoped structures, which contain five 10 nm wide $Zn_{1-x}Mn_xSe$ QWs ($x = 0.013$, 0.03 and 0.1) separated by 20 nm $Zn_{0.94}Be_{0.06}Se$ barriers [1]. Experiments were carried out at a temperature $T = 1.8$ K in magnetic fields up to 6 T applied along the structure growth axis. Light pulses (energy per laser pulse $P = 1$ nJ, focused on a spot of 100 μm diameter) from a frequency doubled 160 fs Ti-sapphire laser (photon energy 3.1 eV) with a repetition rate reduced to 4 kHz generated carriers in the barriers. The impact of laser pulses is twofold: they disturb the equilibrium magnetization of the Mn system and they also permit photoluminescence (PL) detection of the magnetization dynamics.The PL was detected using a single 0.5-m monochromator with a streak camera. The giant Zeeman splitting effect in DMS materials was used to monitor the dynamical changes of the magnetization like in our earlier work [2, 3].

Fig. 1 shows two normalized spectral lines measured at delays of $t = 110$ ps and $t = 1500$ ps after pulsed excitation in a sample with $x = 0.013$ at $B = 2$ T. The spectrum at later times is shifted to higher energies by $\delta E_{\max} = 2$ meV. This PL line shift arises from a decrease of magnetization in time. The inset in Fig. 1 shows several PL spectra for different delays measured under the same conditions. No spectral shift has been found at $B = 0$ T.

2. Analysis

To determine the PL peak energies, the spectra were analyzed by Gaussian line-shape fits and the time evolution $\Delta M(t)/M$ was obtained. $\Delta M(t)/M$ is plotted in Fig. 2 for two samples. The $\Delta M = 0$ peak energy value was taken from the PL line energy measured at low excitation ($P = 0.06$ nJ) where no dynamical shift was detected. At small $t < 20$ ps we detect a sharp rising edge, which cannot be resolved with our experimental setup. Further $\Delta M(t)/M$ increases and then saturates for $t > 600$ ps at values $\Delta M_{\max}/M$. The rise time of $\Delta M(t)/M$, τ_M, is comparable with the PL decay time $\tau_{\rm PL} = 160$ ps (see dotted line in Fig. 2). Within the experimental error, $\Delta M(t)/M$ can be well described by the same time constant, as demonstrated by the solid lines in Fig. 2, which are single exponential fits using $\tau_M = \tau_{\rm PL}$.

Both $\tau_M \simeq \tau_{\rm PL}$ are independent of magnetic field and decrease on 30 for decreasing excitation power form $P = 1$

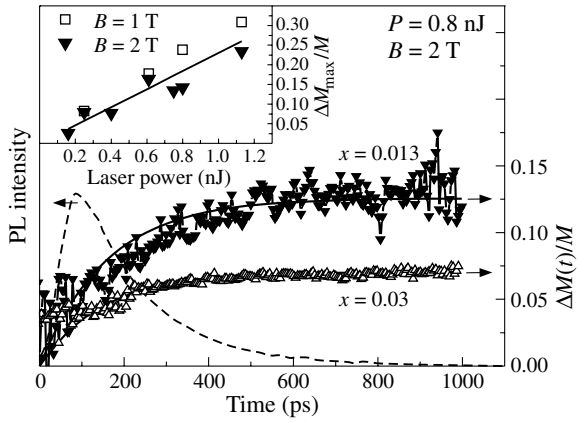

Fig. 2. Time evolution of the relative decrease of magnetization in the samples with two different x. Solid lines are single exponential fits of the experimental data with $\tau_M = \tau_{\rm PL} = 160$ ps ($x = 0.013$) and 150 ($x = 0.03$). Horizontal arrows show the values for $\Delta M_{\rm max}/M$. Dotted line is the time evolution of PL intensity $I(t)$ integrated over a spectral range of 15 meV in a sample with $x = 0.013$. The inset show the measured values $\Delta M_{\rm max}/M$ as a function of excitation energy for two values of B in a sample with $x = 0.013$. Straight line shows the linear dependence on P.

to 0.06 nJ.

The dependence of $\Delta M_{\rm max}/M$ on excitation energy P for $x = 0.013$ is shown in the inset of Fig. 2 for $B = 1$ and 2 T. The dependencies follow to a good approximation a linear dependence. The laser-induced changes of the magnetization are remarkably large (up to 30%). No shift could be detected in the sample with $x = 0.1$. The decrease of magnetization $\Delta M(t)$ has to be associated with the dynamics of spin and energy transfer processes from photoexcited carriers to the Mn-ion spin system. We can exclude the influence of nonequilibrium phonons generated during energy relaxation and nonradiative recombination of carriers from consideration. These phonons are known to be important on a longer time scale and at higher excitation density [4, 5]. Therefore, the fast photoinduced changes of the magnetization are dominated by direct spin and energy transfer from hot photocarriers to the Mn ions. Due to slow spin-lattice relaxation in Mn^{2+} ions [3] they accumulate the transferred energy and spin and $\Delta M(t)$ increases continuously with time, as long as photoexcited carriers are present, saturating at a level $\Delta M_{\rm max}$ for times $t > \tau_M \sim \tau_{\rm PL}$.

In order to understand the mechanism of spin and energy transfer that can provide the measured τ_M and the huge reduction of magnetization $\Delta M_{\rm max}$, we analyze the results basing on the theoretical approach developed in Ref. [6]. A single spin flip-flop scattering between carrier and ion takes not more than a few picoseconds, but the energy shuffled to the Mn ion is rather small, e.g. $\mu_{\rm B} g_{\rm Mn} B = 0.23$ meV at $B = 2$ T. The transfer of significantly larger amount of energy requires multiple scattering, which in principle is possible within the typical carrier lifetime of 100 ps. However, after the first flip-flop the carrier has an unfavorable spin orientation and can no longer transfer energy to an ion until its spin relaxes back by any mechanism except exchange scattering with Mn. The latter would reverse the effect of the original flip-flop process and therefore cannot be considered as contribution to multiple spin transfer, as it would transfer spin and energy back from a Mn^{2+} ion to a carrier. The electrons only can not explain the large change in magnetization, because the reverse spin-flip transition is relatively slow ($\sim$ 1 ns) [7]. Contrary to electrons the spin-relaxation time of holes is very fast ($\sim 0.1-1$ ps) even in nonmagnetic semiconductors. Due to the strong spin-orbit coupling any momentum scattering of a hole likely changes its spin state [8]. Therefore, the holes may undergo multiple spin-flip transitions. However this is valid for the holes whose kinetic energy exceeds the Zeeman splitting. For our experimental conditions this is the case only for the first 50 ps after laser excitation, when carriers relax energetically from the barriers into the QWs. Analyzing the high-energy slope of PL spectra measured at $B = 0$ for different delays hole temperature at $t = 80$ ps can be estimated by $T_{\rm h} = 32$ K only. This corresponds to a very low population of the high energy states which can not provide enough flip-flops, even for multiple hole scattering. Therefore another mechanism has to be considered, which can provide spin and energy transfer from spin-polarized holes to the Mn^{2+} ions, while the initial and the final states of the holes belong to the same spin subband $|+3/2\rangle$. Such from first sight very surprising scattering of a hole at the contact potential of Mn^{2+} is possible due to the $(\mathbf{kJ})^2$ term with the 3D hole spin operator $\mathbf{J}$ ($j = 3/2$) in the Luttinger Hamiltonian [9]. Due to this coupling, at finite k the heavy hole state $|+3/2\rangle$ becomes mixed with the light hole state $|+1/2\rangle$, resulting in non-zero matrix elements between even and odd subbands.

3. Conclusion

To conclude, in DMS quantum wells hot carriers generated by femtosecond laser pulses can efficiently transfer their excess kinetic energy to the magnetic ions on a time scale of 100 ps and thereby induce changes of the magnetization by up to 30%. The analysis shows that a flip-flop mechanism is insufficient to describe the data, which have been obtained in the regime of strong spin polarization. A mechanism that can provide a large effect on the magnetization through scattering of heavy-holes within one Zeeman subband at Mn ions is suggested.

Acknowledgements

We acknowledge financial support by the BMBF (nanoquit), the RFBR (05-02-16389) and the Russian Academy of Sciences. Research stays of AVS (No. 436RUS17/145/05) and AVA (Mercator guest professorship program) were granted by the Deutsche Forschungsgemeinschaft.

References

[1] D. Keller *et al*, *Phys. Rev. B* **65**, 035313 (2002).
[2] D. R. Yakovlev *et al*, *Phys. Stat. Sol. (c)* **1**, 989 (2004).
[3] A. V. Scherbakov *et al*, *Phys. Rev. B* **62**, R10641 (2000).
[4] J. Shah *et al*, *Phys. Rev. B* **10**, 659 (1974).
[5] A. V. Scherbakov *et al*, *Phys. Rev. B* **60**, 5609 (1999).
[6] B. König *et al*, *Phys. Rev. B* **61**, 16870 (2000).
[7] J. M. Kikkawa *et al*, *Science* **257**, 1284 (1997).
[8] F. Meier, B. P. Zakharchenya (eds.), *Optical Orientation*, Amsterdam: Elsevier Science Ltd., 1984.
[9] R. Ferreira and G. Bastard, *Phys. Rev. B* **43**, 9687 (1991).

14th Int. Symp. "Nanostructures: Physics and Technology"
St Petersburg, Russia, June 26–30, 2006

Optical orientation of electron spins by linearly polarized light in quantum well structures

S. A. Tarasenko
Ioffe Physico-Technical Institute, St Petersburg, Russia

Abstract. It is shown that absorption of linearly polarized light in low-dimensional semiconductor structures leads to spin orientation of the photoexcited carriers. Theory of such optical orientation by linearly polarized light is presented for (i) direct interband, (ii) direct intersubband, and (iii) indirect intrasubband (Drude-like) optical transitions in n-type quantum well structures.

Introduction

Spin dynamics of charge carriers and, particularly, possibilities of manipulating electron spins in semiconductor structures is attracting a great deal of attention. Experimentally, one of the most widespread and powerful methods for creating spin polarization and investigating kinetics of spin-polarized carriers is optical excitation with circularly polarized radiation [1]. The absorption of circularly polarized light results in spin orientation of charge carriers due to a transfer of photon angular momenta to the carriers. A characteristic feature of this spin orientation is that it reverses the direction upon changing the radiation helicity from left handed to right handed and vice versa.

It is shown here that in low-dimensional semiconductor structures spin orientation of carriers can be achieved by excitation with linearly or even unpolarized light. Such "optical orientation by linearly polarized light" is related to reduced symmetry of nanostructures as compared to bulk crystals and is forbidden in bulk cubic semiconductors. Microscopically, it is caused by asymmetrical spin-dependent photoexcitation of carriers followed by spin precession in an effective magnetic field induced by the Rashba or Dresselhaus spin-orbit coupling.

1. Symmetry analysis

Possibility to achieve optical orientation by linearly polarized light in nanostructures follows from symmetry analysis. Phenomenologically, spin generation by light is described by

$$\dot{S}_\alpha = I \sum_{\beta\gamma} \chi_{\alpha\beta\gamma} \frac{e_\beta e_\gamma^* + e_\gamma e_\beta^*}{2} + I \sum_{\delta} \phi_{\alpha\delta}\, \mathrm{i}\left[\mathbf{e}\times\mathbf{e}^*\right]_\delta . \quad (1)$$

where $\dot{S}_\alpha$ is the generation rate of the spin component, I is the light intensity, $\mathbf{e}$ is the unit vector of the light polarization and $\mathbf{e}^*$ is the complex conjugate vector. The pseudotensor $\phi_{\alpha\beta}$ describes "conventional" optical orientation by circularly polarized light since the vector product $\mathrm{i}[\mathbf{e}\times\mathbf{e}^*]$ is proportional to the light helicity and vanishes for linearly polarized light. In contrast, the symmetrized product $(e_\beta e_\gamma^* + e_\gamma e_\beta^*)/2$ is insensitive to the light helicity for elliptically polarized radiation and reaches maximum for linear polarization. Thus, the third-rank tensor $\chi_{\alpha\beta\gamma}$ describes spin orientation by linearly polarized light.

Symmetry analysis shows that in bulk zinc-blende- or diamond-type crystals, T_d and O_h point groups, respectively, all components of $\chi_{\alpha\beta\gamma}$ vanish, and optical orientation of electron and hole spins can be achieved by circularly polarized light only. In contrast, in low-dimensional structures nonzero components of $\chi_{\alpha\beta\gamma}$ do exist, allowing for spin orientation by light of zero helicity. In particular, in (001)-grown quantum wells (QWs) based on zinc-blende-lattice compounds, C_{2v} symmetry, optical orientation by linearly polarized light is describes by three independent constants

$$\dot{S}_x = I\chi_{xyz} e_y e_z, \quad \dot{S}_y = I\chi_{yxz} e_x e_z, \quad \dot{S}_z = I\chi_{zxy} e_x e_y, \quad (2)$$

where $x \parallel [1\bar{1}0]$ and $y \parallel [110]$ are the in-plane coordinates, $z \parallel [001]$ is the QW normal, and the polarization vector $\mathbf{e}$ is assumed to be real. It follows that the excitation with linearly polarized light under normal incidence results in orientation of electron spins along the QW normal, with the sign and magnitude depending on the light polarization plane. Indeed, the spin generation $\dot{S}_z$ is of opposite sign for the exciting light polarized along the [100] and [010] crystallographic axes and vanishes for the light polarized along the $[1\bar{1}0]$ or [110] axes. Generally, the dependence of the spin orientation on the light polarization is given by $\dot{S}_z \propto 2e_x e_y = \sin 2\varphi$, where φ is the angle between the light polarization plane and the $[1\bar{1}0]$ axis. In low-symmetrical QWs of C_s class, i.e. (113)- or (110)-grown structures, the tensor $\chi_{\alpha\beta\gamma}$ contains eight independent constants, and the in-plane spin orientation can be achieved even under excitation with unpolarized light.

2. Microscopic model: Interband transitions

Microscopically, the optical orientation by linearly polarized light is a two-stage process involving (i) asymmetrical spin-dependent photoexcitation of carriers and (ii) spin precession in an effective magnetic field induced by spin-orbit coupling [2]. The effect is most easily conceivable for direct transitions between the heavy-hole valence subband $hh1$ and the conduction subband e1 in QWs of the C_s point symmetry. In such structures the spin component along the QW normal z is coupled with the in-plane electron wave vector. This leads to $\mathbf{k}$-linear spin-orbit splitting of the energy spectrum as sketched in Fig. 1, where the heavy-hole subband $hh1$ is split into two spin branches $\pm 3/2$ shifted relative to each other in $\mathbf{k}$-space. Due to the selection rules the allowed optical transitions from the valence subband $hh1$ to the conduction subband e1 are $|+3/2\rangle \to |+1/2\rangle$ and $|-3/2\rangle \to |-1/2\rangle$, as illustrated in Fig. 1 by dashed vertical lines. Under excitation with linearly polarized or unpolarized light the rates of both transitions coincide. In the presence of the spin splitting, the optical transitions induced by photons of the fixed energy $\hbar\omega$ occur in the opposite points of $\mathbf{k}$-space for the electron spin states $\pm 1/2$. Such

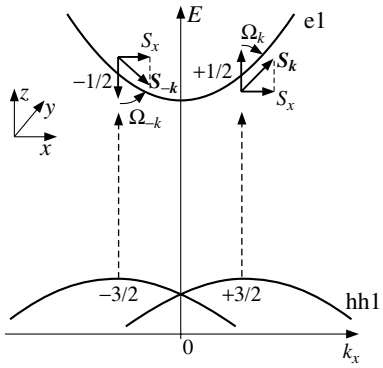

Fig. 1. Microscopic origin of the optical orientation of electrons spins by linearly polarized light. Asymmetry of photoexcitation followed by spin precession leads to appearance of average electron spin.

an asymmetry of photoexcitation results in non-equilibrium distribution where electrons with spin $+1/2$ propagate mainly in one direction, $k_x > 0$, and the electrons with spin $-1/2$ propagate in the opposite direction, $k_x < 0$. Note, that such an electron distribution represents a pure spin current, i.e. a state where particles with opposite spins flow in opposite directions, while the average electron spin is still zero. A net spin orientation of the electron gas appears as a result of the the subsequent spin dynamics of the carriers. The spin dynamics of the conduction electrons is known to be governed by spin-orbit coupling that may be considered as an effective magnetic field which acts on the electron spins. Of special note is that the direction and strength of the effective field and, correspondingly, the direction and strength of the Larmor frequency of the field, $\mathbf{\Omega_k}$, depend on the electron wave vector $\mathbf{k}$. Electron spins originally directed, according to the selection rules, along or opposite to the QW normal precess in the effective magnetic field, which has non-zero in-plane component, as shown in Fig. 1. Electrons with the initial spin $+1/2$ and wave vector $k_x > 0$ are affected by effective field with the Larmor frequency $\mathbf{\Omega_k}$, while carriers with the opposite spin, $-1/2$, and opposite wave vector are affected by field with the frequency $\mathbf{\Omega_{-k}}$. Since the effective magnetic field induced by spin-orbit coupling is an odd function of the wave vector, $\mathbf{\Omega_{-k}} = -\mathbf{\Omega_k}$, the rotation axes for carriers with the initial spins $\pm 1/2$ are opposite. As a result, the precession leads to an appearance of spin component $S_x > 0$ for carriers with both positive and negative k_x as shown in Fig. 1, yielding a net spin polarization of the electron gas. Under steady-state excitation, the spin generation rate is determined by the average angle of the spin rotation in the effective magnetic field, similarly to the appearance of a perpendicular spin component in the Hanle effect.

Direction of the optically oriented spins is determined by light polarization and explicit form of spin-orbit interaction in both the conduction and valence bands. The latter is governed by the QW symmetry and can be varied. As mentioned above, in (113)-grown QWs, absorption of unpolarized light leads to orientation of electron spins in the QW plane, along $x \| [1\bar{1}0]$. In (001)-grown QWs spin orientation can not be achieved by unpolarized light, but is allowed under excitation with linearly polarized light. In the geometry of normal incidence, the absorption of linearly polarized light leads to spin orientation along the QW normal. The corresponding spin generation rate in the electron subband e1 for interband optical transitions from the light-hole subband lh1 has the form

$$\dot{S}_z = 2e_x e_y \left(\gamma_{yx}^{(\mathrm{e1})} \gamma_{yx}^{(\mathrm{lh1})} - \gamma_{xy}^{(\mathrm{e1})} \gamma_{xy}^{(\mathrm{lh1})} \right) \frac{\mu \tau_\mathrm{e}}{\hbar^3} \dot{N} \,, \qquad (3)$$

where $\gamma_{\alpha\beta}^{(\nu)}$ ($\nu = \mathrm{e1},\ \mathrm{lh1}$) are the constants describing linear in the wave vector coupling between α-component of the electron angular momentum and β-component of the wave vector in the subbands e1 and lh1, respectively, $\mu = m_\mathrm{e} m_\mathrm{lh}^\parallel / (m_\mathrm{e} + m_\mathrm{lh}^\parallel)$ is the reduced mass, m_e and $m_\mathrm{lh}^\parallel$ are the electron and light hole effective masses in the QW plane, respectively, τ_e is the momentum relaxation time, and $\dot{N}$ is generation rate of electrons in the subband e1.

3. Microscopic model: Free-carrier absorption

Light absorption by free carriers, or the Drude-like absorption, occurs in doped semiconductor structures when the photon energy $\hbar\omega$ is smaller than the band gap as well as the intersubband spacing, and also leads to spin orientation of carriers. This effect is mostly related to spin-dependent scattering [3]. Because of the need for energy and momentum conservation, the free-carrier absorption must be accompanied by electron scattering from acoustic or optical phonons, static defects, etc. In systems with a spin-orbit interaction, processes involving change of the particle wave vector are spin-dependent. In particular, the matrix element of electron scattering by static defects or phonons in QW structures contains, in addition to the main contribution, an asymmetric spin-dependent term which is linear in the wave vector. Due to this spin-dependent asymmetry of scattering, electrons photoexcited from the subband bottom are scattered in preferred directions depending on their spin states. Such asymmetry results in an electron distribution where particles with opposite spins flow in opposite directions. Similarly to the case of interband excitation, a net spin orientation of the electron gas appears as a result of the subsequent spin precession in the effective magnetic field caused by spin-orbit coupling.

In conclusion, we note that optical orientation of electron spins by linearly polarized light, considered here, can be observed and studied with conventional methods for detection of spin orientation, e.g. by analyzing circular polarization of luminescence under electron-hole radiative recombination or by means of the magneto-optical Faraday and Kerr rotation.

Acknowledgements

This work was supported by the RFBR, President Grant for Young Scientists, Russian Science Support Foundation, and Foundation "Dynasty" — ICFPM.

References

[1] *Optical Orientation*, edited by F. Meier and B. P. Zakharchenya, (Amsterdam: Elsevier Science), 1984.
[2] S. A. Tarasenko, *Phys. Rev. B* **72**, 113302 (2005).
[3] S. A. Tarasenko, *Phys. Rev. B* **73**, 115317 (2006).

14th Int. Symp. "Nanostructures: Physics and Technology"
St Petersburg, Russia, June 26–30, 2006

Nuclear spin fluctuations in InP QDs

S. Yu. Verbin[1,3], Bipul Pal[2], M. Ikezawa[2], I. V. Ignatiev[1] and Y. Masumoto[2]

[1] V. A. Fock Institute of Physics, St Petersburg State University, 198504 St Petersburg, Russia
[2] Institute of Physics, University of Tsukuba, Tsukuba, Japan
[3] Venture Business Laboratory, University of Tsukuba, Tsukuba, Japan

Abstract. Effect of nuclear spin fluctuations on the electron spin polarization has been studied in the negatively charged InP QDs. We found that, after rapid three-fold decrease, rest of the electron spin polarization relaxes with the nuclear spin fluctuations lifetime of about 1 μs.

Introduction

Hyperfine interaction in A_3B_5 semiconductors are extensively studied for a long time [1]. This interaction is considerably enhanced in quantum dots (QDs) due to increased density of strongly localized electrons at nuclei. Due to this localization, even random correlation of nuclear spins may create a fluctuating effective magnetic field which is capable to remarkably affect the electron spin. In particular, this effect may destroy spin orientation that hampers the realization of spin memory devices based on QD structures. As it was discussed theoretically [2, 3], the nuclear spin fluctuations (NSF) can cause the three-fold decrease of the electron spin orientation in nanosecond time scale. Rapid decrease of spin polarization is really observed in kinetics experiments for InAs QDs [4]. A strong variation of spin polarization in small longitudinal magnetic field (Faraday configuration) was also treated as to be caused by the NSF [5, 6]. However, to contrast to the theoretical predictions [2, 3], the *total*, rather than three-fold, electron spin depolarization has been observed under certain experimental conditions.

Here we report on further study of effect of NSF on the electron spin polarization in the negatively charged InP QDs. We found that, after rapid three-fold decrease, rest of the electron spin polarization relaxes with the NSF lifetime. We have performed real-time experiments which allowed us to estimate the NSF lifetime.

1. Experiment and discussion

A heterostructure under study contains one layer of the InP QDs between the InGaP barrier layers. The average base diameter of the QDs is of about 40 nm and the height 5 nm, the areal QD density is 10^{10} cm^{-2}. Charged state of the QDs was controlled by an external bias applied to top of the sample. It was found that the QDs contain one resident electron per dot on average at $U_{\rm bias} = -0.1$ V [7].

For study of spin dynamics, we have used a photoluminescence (PL) pump-probe method [8]. In this method, a strong circularly polarized (σ^+ or σ^-) pump pulse creates spin polarization of the resident electrons (see inset in Fig. 1). The polarization is then tested as the polarization variations of the PL excited by the σ^+-polarized probe pulses delayed in time relative to the pump pulse. Exploiting this method, we managed to study the spin dynamics in a wide time range from picoseconds to milliseconds. Spin polarization of resident electrons was detected by means on the negative circular polarization (NCP) observed in the PL kinetics as well as in the time-integrated PL [8].

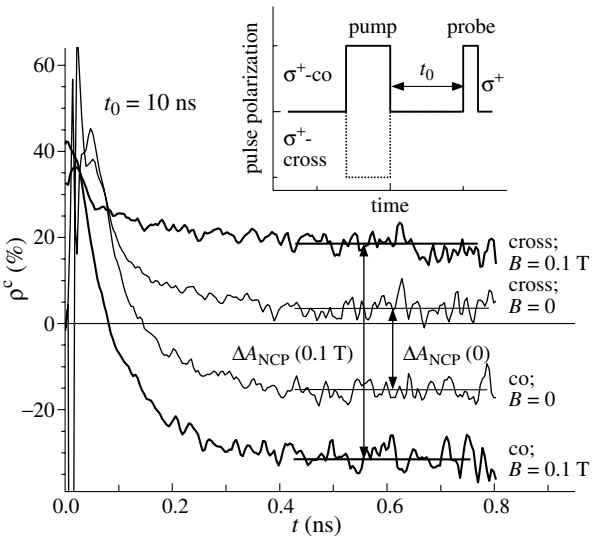

Fig. 1. Kinetics of the PL polarization degree at the two-pulse excitation. Inset: time diagram of the polarized pump-probe experiment.

Fig. 1 shows kinetics of circular polarization of the PL measured for the co- and cross-polarized pumping with the pump beam being 20 times stronger than the probe beam. As seen, the kinetics reaches some constant value which is strongly negative for the co-polarized ($\sigma^+\sigma^+$) and positive for the cross-polarized ($\sigma^-\sigma^+$) pump-probe excitation. This difference, $\Delta_{\rm NCP}$, reflects different spin orientation of the resident electrons created by the σ^+- and σ^--polarized pump pulses. Besides, it reflects high stability of the electron spin polarization which does not destroyed during the 10-ns delay of the probe pulses.

The spin polarization is very sensitive to the value of external magnetic field, B, applied along the optical axis and, correspondingly, the photocreated electron spin orientation. In particular, there is approximately three-fold difference in $\Delta_{\rm NCP}$ for $B = 0$ and 0.1 T (see Fig. 1). This difference has been treated in Refs. [5, 6] as the effect of NSF. The effect is suppressed when B is larger than the effective magnetic field of NSF, $\delta B_{\rm N}$.

Difference, $\Delta\rho$, of the PL polarizations under co- and cross-polarized excitations has also been measured in dependence on the time delay t_0 in the much larger time scale. Fig. 2 shows the time dependence of $\Delta\rho$ integrated over the PL pulse at different magnetic field values.

As seen, $\Delta\rho$ and, correspondingly, spin polarization persists for tens of microseconds for $B > 0.03$ T and decays faster at smaller magnetic field. Simultaneously, amplitude of

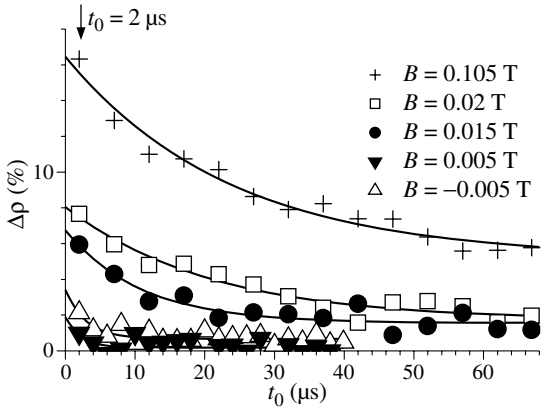

Fig. 2. Time dependence of difference in the PL polarization degree measured at co- and cross-polarized pump probe excitation for different magnetic field. Symbols show the experimental data, solid curves are the fits by $\Delta\rho = a\exp(-t/\tau_{\rm dec}) + b$.

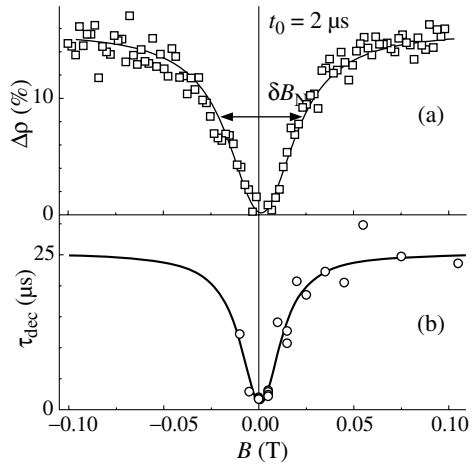

Fig. 3. Magnetic field dependence of (a) $\Delta\rho$ at time delay $t_0 = 2\ \mu$s (marked by arrow on Fig. 2) and of spin relaxation time, $\tau_{\rm dec}$ (b). Symbols show the experimental data, solid lines are guide to the eye.

the polarization measured at delay $t_0 = 2\ \mu$s decreases with decreasing B. Both the tendency were measured systematically and presented in Fig. 3.

We consider these results as clear evidence for small lifetime of NSF relative to the electron spin lifetime measured in presence of the external magnetic field suppressing the NSF effect. For zero magnetic field, the spin relaxation time is ruled by the variation of orientation and amplitude of NSF, in fact by the NSF lifetime. Though our results are noisy, analyzing all set of the experimental data obtained we can estimate this lifetime, as to be of about 1 μs.

Acknowledgements

Authors are thankful to Prof. V. K. Kalevich and Dr. I. Ya. Gerlovin for fruitful discussions. The work is partially supported by Grant-in-Aid for Scientific Research on the Priority Area "Nanospintronics" (No. 16031203) from MEXT of Japan, by ISTC, grant 2679, by Russian Ministry of Sci. & Edu., grant RNP.2.1.1.362 and by RFBR, grant 06-02-17137-a.

References

[1] *Optical Orientation. Modern Problems in Condensed Matter*, edited by F. Meier and B. P. Zakharchenya (North-Holland, Amsterdam, 1984).

[2] I. A. Merkulov *et al*, *Phys. Rev. B* **65**, 205309 (2002).

[3] A. V. Khaetskii *et al*, *Phys. Rev. Lett.* **88**, 186802 (2002).

[4] P.-F. Braun *et al*, *Phys. Rev. Lett.* **94**, 116601 (2005).

[5] I. V. Ignatiev *et al*, *Proc. 13th Int. Symp. "Nanostructures: Physics and Technology", St Petersburg, Russia (Ioffe Inst.)*, 47 (2005) also available on-line at http://arXiv.org: cond-mat/0508698.

[6] R. Oulton *et al*, *Proc. 14th Int. Symp. "Nanostructures: Physics and Technology", St Petersburg, Russia (Ioffe Inst.)*, submitted (2006).

[7] I. E. Kozin *et al*, *Phys. Rev. B* **65**, 241312(R) (2002).

[8] M. Ikezawa *et al*, *Phys. Rev. B* **72**, 153302 (2005).

14th Int. Symp. "Nanostructures: Physics and Technology"
St Petersburg, Russia, June 26–30, 2006

Demonstration of Rashba spin splitting in GaN-based heterostructures

W. Weber[1], S. D. Ganichev[1], Z. D. Kvon[2], V. V. Bel'kov[3], L. E. Golub[3], S. N. Danilov[1], S. Seidl[1], D. Weiss[1], W. Prettl[1], Hyun-Ick Cho[4] and Jung-Hee Lee[4]

[1] Fakultät Physik, University of Regensburg, 93040, Regensburg, Germany
[2] Institute of Semiconductor Physics, 630090, Novosibirsk, Russia
[3] Ioffe Physico-Technical Institute, St Petersburg, Russia
[4] Kyungpook National University, 1370. Sankyuk-Dong, Daegu 702–701, Korea

Abstract. The circular photogalvanic effect induced by infrared and terahertz radiation, has been observed in (0001)-oriented GaN low-dimensional structures. The photocurrent changes sign upon reversing the radiation helicity demonstrating the existence of spin-splitting of the conduction band in **k**-space in this type of materials. The observation suggests the presence of a sizeable Rashba type of spin-splitting, caused by the built-in asymmetry at the AlGaN/GaN interface.

Introduction

Gallium nitride is a potentially interesting material system for spintronics since it is expected to become ferromagnetic with a Curie-temperature above room temperature if doped with manganese [1]. Long spin relaxation times observed in this material are another promising property for possible applications [2]. Little is known so far about spin orbit interaction in GaN based heterojunctions like existence of spin-splitting in the band structure which would provide a potential handle for spin manipulation.Strong spin-orbit effects are expected to be in narrow-gap materials only [3]. However, a large piezoelectric effect which causes a strong electric field at the AlGaN/GaN interface and the strong polarization induced doping effect, on the other hand, may result in a sizeable Rashba contribution ($\sim$ 1 meV) to spin-splitting of the band due to spin-orbit interaction [4].

Here we report on the observation of the circular photogalvanic effect (CPGE) with strength comparable to that observed in GaAs and InAs quantum well structures [5] which unambiguously demonstrates a substantial Rashba splitting of spin subbands in GaN based heterojunctions.

Experimental results and discussion

Both AlGaN/GaN low-dimensional structures and bulk GaN belong to the family of wurtzite-type semiconductors which are gyrotropic. In these media the spin-orbit part of the Hamiltonian has the form

$$\hat{H}_{\mathrm{SO}} = \alpha[\boldsymbol{\sigma} \times \mathbf{k}]_z \,. \qquad (1)$$

Here $\boldsymbol{\sigma}$ is the vector of Pauli matrices, **k** wavevector and the z-axis is directed along the hexagonal c-axis [6]. In bulk wurtzite materials the constant α in the Hamiltonian (1) is solely due to bulk inversion asymmetry (BIA). In heterostructures, an additional source of **k**-linear spin splitting, induced by structure inversion asymmetry (SIA), exists.

By optical excitation with circularly polarized light spin-up and spin-down subbands get non-uniformly populated in **k**-space. This is a consequence of optical selection rules and energy and momentum conservation, leading to a current which is probed in experiment. The fingerprint of the CPGE photocurrent is its dependence on the helicity of the radiation field. The current reverses its direction by switching the light's polarization from right-handed circular to left-handed circular and vice versa. The experiments were carried out on $Al_{0.3}Ga_{0.7}N$/GaN heterojunctions grown by MOCVD on a C(0001)-plane sapphire substrates. The electron mobility in the 2DEG was typically about 1200 cm^2/V s at electron density $(1-1.4)\times10^{13}$ cm^{-2} at room temperature. The experiments were carried out in MIR and FIR spectral ranges. The current j generated by the circularly polarized light in the unbiased samples was measured at room and liquid nitrogen temperatures via the voltage drop across a 50 Ω load resistor in a closed circuit configuration.

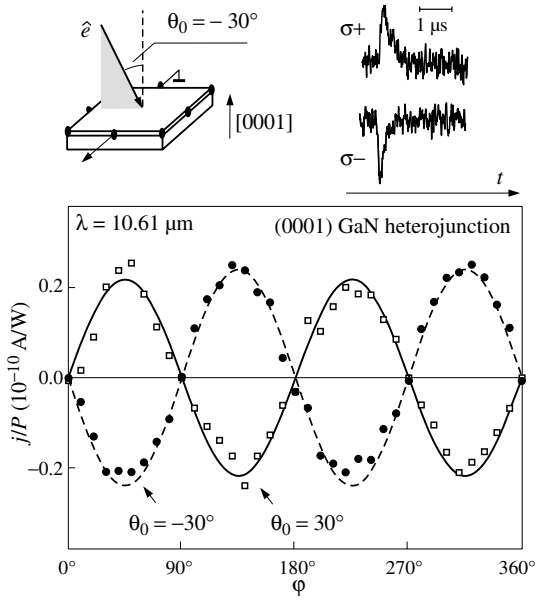

Fig. 1. Photocurrent in AlGaN/GaN heterojunction normalized by the radiation power P as a function of the phase angle φ defining helicity (angle of incidence $\Theta_0 = \pm 30°$). The dashed and solid lines represent calculated curves after Eq. (2).

Irradiating the AlGaN/GaN heterojunction by circularly polarized light at oblique incidence, as sketched in the inset of Fig. 1, causes a photocurrent signal. The current reverses its direction by switching the sign of the radiation helicity. The fact that the current is proportional to the radiation helicity proves the circular photogalvanic effect as origin of the photocurrent. The observed dependence of the photocurrent on helicity and angle of incidence can be described by phenomenological the-

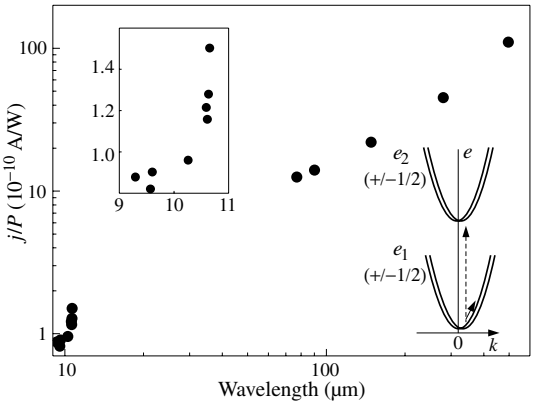

Fig. 2. Spectral dependence of the CPGE current in gallium nitride heterojunction at room temperature. Sketch demonstrates possible optical transitions.

ory adapted to wurtzite-type low-dimensional systems. Equation (1) leads to a CPGE current in the plane of the AlGaN/GaN heterojunction:

$$\mathbf{j} = P_{\mathrm{circ}} \gamma \, \hat{\mathbf{e}}_{\parallel} = \sin 2\varphi \gamma \, \hat{\mathbf{e}}_{\parallel} \,, \qquad (2)$$

where P_{circ} and $\hat{\mathbf{e}}_{\parallel}$ are the degree of circular polarization and the projection onto the heterostructure plane of the unit vector $\hat{\mathbf{e}}$ pointing in the direction of the light propagation, respectively. The second-rank pseudotensor γ is proportional to the spin-orbit constant α. It has two nonzero components and is discribed by one linearly independent constant

$$\gamma_{xy} = -\gamma_{yx} \,, \quad \gamma_{ii} = 0 \,.$$

It means that the photocurrent always flows perpendicularly to the plane of the radiation incidence. As shown in Fig. 1 the experimental results correspond to Eq. (2).

The effect is observed for all wavelengths used between 9 μm and 496 μm. While the overall signature is the same the strength of the photocurrent depends on the wavelength (see Fig. 2). The spectral dependence of the CPGE in the THz range ($\lambda \geq 77$ μm) agrees with the expected behaviour of the CPGE for indirect (Drude-like) optical transitions. However the rapid resonance-like increase of the signal at short wavelengths (see inset of Fig. 2) obtained with the Q-switch CO_2 laser (9.2−10.8 μm) cannot be explained by this mechanism.

We ascribe this spectral dependence to resonant direct intersubband optical transitions between the ground and the first excited size-quantized subbands. In GaN low-dimensional structures, which are not yet sufficiently investigated, spectroscopic data are still not available. However, we estimate that the energy separation between the two lowest subbands should be about 150 meV in the approximation of the triangular quantum well. This value slightly exceeds the photon energies used in our experiments. It is not surprising because the real shape of the quantum well is nonlinear and strength of the electrical field significantly falls as the distance from a surface increases. More accurate comparison needs self-consistent solution of Schrödinger and Poisson's equations. In addition to the CPGE current detected in the direction normal to the in-plane wave vector of radiation a signal is also observed along the in-plane propagation direction. This signal has equal magnitude and the same sign for right- and left-handed circularly polarized radiation and is ascribed to the linear photogalvanic effect and the photon drag effect [5].

The observation of the CPGE with strength comparable to that observed in GaAs and InAs quantum wells unambiguously demonstrates a substantial Rashba splitting of spin subbands in AlGaN/GaN heterojunctions. In contrast to zinc-blende based III–V QWs, where interference of BIA and SIA results in varying angles between electron spin and its momentum, $\mathbf{k}$, for different crystallographic directions, the electron spin in GaN heterojunctions is always perpendicular to $\mathbf{k}$. This is demonstrated by our experiments where the CPGE current always flows perpendicular to $\hat{\mathbf{e}}_{\parallel}$ and does not change its amplitude if the in-plane direction is varied. The reason of this axial isotropy is that both, BIA and SIA, lead to the same form of spin-orbit interaction given by Eq. (1).

Acknowledgements

This work is supported by the DFG, RFBR, "Dynasty" Foundation — ICFPM and by the grant No. R01-2003-000-10769 (2004), BK 21 of Korea Science and Engineering Foundation.

References

[1] T. Dietl *et al*, *Science* **287**, 1019 (2000).
[2] B. Beschoten *et al*, *Phys. Rev. B* **63**, 121202 (2001).
[3] R. Winkler, *Spin-orbit coupling effects in two-dimensional electron and hole systems*, in Springer Tracts in Modern Physics, Vol. 191 (Springer-Verlag, Berlin, 2003).
[4] V. I. Litvinov, *Phys. Rev. B* **68**, 155314 (2003).
[5] S. D. Ganichev and W. Prettl, *J. Phys.: Condens. Matter* **15**, R935 (2003).
[6] E. I. Rashba, *Fiz. Tverd. Tela* **2**, 1224 (1960) [*Sov. Phys. Solid State* **2**, 1109 (1960)].

14th Int. Symp. "Nanostructures: Physics and Technology"
St Petersburg, Russia, June 26–30, 2006

Spin effects in stereoscopic pictures of the *n*-$In_xGa_{1-x}As$/GaAs double quantum well magnetoresistance dependencies on the perpendicular and parallel field components

M. V. Yakunin[1], Yu. G. Arapov[1], V. N. Neverov[1], S. M. Podgornyh[1], N. G. Shelushinina[1], G. I. Harus[1], B. N. Zvonkov[2] and E. A. Uskova[2]

[1] Institute of Metal Physics, Ekaterinburg, Russia
[2] Physical-Technical Institute at Nizhnii-Novgorod State University, Russia

Abstract. Precise scanning of the ($B_\perp$, $B_{||}$) plane while measuring magnetoresistance of the *n*-InGaAs/GaAs double quantum well (DQW) reveals a number of peculiarities connected with the intricate DQW energy spectrum, which are analyzed on the basis of quasiclassical calculations. Magnetic breakdown effects are also considered. Spin effects observed are enhanced in this heterosystem compared with the traditional *n*-GaAs/AlGaAs DQWs.

Introduction

Interplay of spin- and isospin effects in a double quantum well (DQW) brings a new physics into quantum magnetotranspoprt phenomena [1], and InAs-based heterostructures are of interest in this aspect [2] since in the GaAs/AlGaAs DQWs (in which system almost all the DQW investigations have been performed so far) the GaAs layers are characterizedby a very small Lande factor $|g| = 0.4$.

1. Experimental

We present data on magnetoresistivity $\rho_{xx}(\vec{B}, \varphi)$ measured in tilted magnetic fields $\vec{B}(B_\perp, B_{||})$ (φ — angle between $\vec{B}$ and the normal $B_\perp$) of *n*-$In_xGa_{1-x}As$/GaAs ($x \approx 0.2$) DQW with thorough scanning of the ($B_\perp$, $B_{||}$) plane. InGaAs QWs are 5 nm wide, GaAs barrier — 10 nm, initial 2D electron gas total density $n_s = 2.3\times10^{15}$ m^{-2}. After exposure to IR illumination n_s increases about a factor of 1.5, and this value remains constant within about 0.5% during the whole experiment cycle. Measurements were held at 1.8 K in a precision rotator with 0.1° rotation step guaranteed.

2. Results and discussion

The data are shown before (Figs. 1a, 2a, 3) and after IR illumination (Fig. 1b, 2b, 4) as the sets of $\rho_{xx}(B_\perp)$ traces at different $B_{||}$ fixed (Fig. 1) or as $\rho_{xx}(B_\perp, B_{||})$ surfaces (Fig. 2) and the gray scale maps (Figs. 3, 4) with the superimposed calculated trajectories describing the ($B_\perp$, $B_{||}$) combinations at which the Fermi energy is crossed by the $N = 0, 1, 2\ldots$ Landau levels, with two spin orientations considered.

The DQW energy dispersion $E(k_x, k_y)$ at nonzero $B_{||}$ is a complex formation consisting of an inner surface with the fixed energy cross-sections in the shape of Lens and an outer one with the Peanut cross-sections. The above mentioned ($B_\perp$, $B_{||}$) trajectories are a set of descending lines for the inner surface and of ascending lines for the outer one (Figures 3, 4). Additionally, the electron motion in circle orbits is possible with jumps between the Lens and Peanut orbits corresponding to the magnetic breakdown effect (MB) [3, 4].

The main peculiarities observed in $\rho_{xx}(B_\perp, B_{||})$ are: the peak at filling factor $\nu = 1.5$ (left figures) moves to lower B with increasing $B_{||}$ while the peak $\nu = 3$ moves to higher $B_\perp$ and, contrary to the $\nu = 1.5$ peak, changes its shape that is especially pronounced in the after-illumination state (right figures). In the latter case it also splits at high $B_{||}$. Figures 4a, b indicate that the splitting is due to the spin-split MB, which is the main process at high magnetic fields, with effective *g*-factor $|g^*| = 3$ for the $N = 1$ Landau level. The sharp transformations of the $\nu = 3$ peak at low $B_{||}$ is due to that Lens ($N = 0$) and Peanut ($N = 1$) trajectories move in opposite directions. This Lens trajectory manifests experimentally in Figures 2b, 4 as bulbs on the $\rho_{xx}(B_{||})$ ridges for $\nu = 5, 7, 9, \ldots$. Spin split-off $\nu = 1.5$ peak position in Fig. 3 indicates the higher spin splitting than is obtained from calculations, signifying the enhancement of the effective *g*-factor due to many body effects.

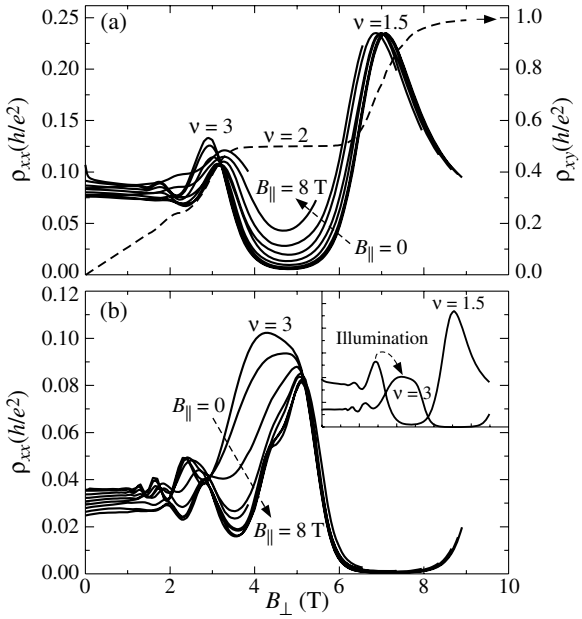

Fig. 1. Evolution of $\rho_{xx}(B_\perp)$ with increasing field component $B_{||} =$ 0(1)8 T parallel to the layers. (a) In the initial state. The Quantum Hall resistivity added. (b) After illumination. Insert: the initial and illuminated states at $B_{||} = 0$ compared.

Acknowledgements

Supported by RFBR, projects 05-02-16206 and 04-02-16614.

References

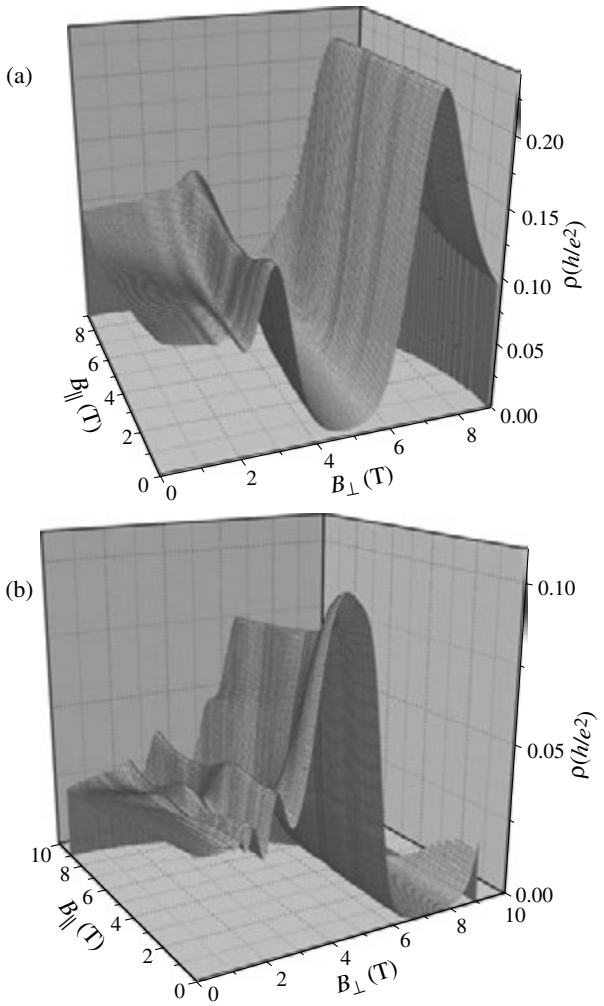

Fig. 2. The same data as in Fig. 1 in stereoscopic view (data in Fig. 1 are the cross-sections of these surfaces at different $B_{||}$ values). (a) Note a complicated behavior of $\nu = 3$ maximum as compared with the $\nu = 1.5$ maximum. (b) Unusual behavior of the $\nu = 3$ peak: fast damping and narrowing of initially dome-shaped peak at small $B_{||}$ and its splitting at higher $B_{||}$. Also note bulbs on the $\rho_{xx}(B_{||})$ ridges for $\nu = 5,\ 7,\ 9,\ \ldots$.

[1] S. Girvin and A. H. MacDonald in *Perspectives in Quantum Hall Effect*, Ed. S. Das Sarma and A. Pinczuk, Wiley, N.Y., 161–224 (1997).

[2] M. V. Yakunin *et al*, *Proc. 27th ICPS*, USA, (2004), 1003; *Semiconductors* **39**, 107 (2005); O. E. Raichev and F. T. Vasko, *Phys. Rev. B* **70**, 075311 (2004).

[3] N. E. Harff *et al*, *Phys. Rev. B* **55**, 13405 (1997); I. S. Millard *et al*, *ibid* **55**, 13401 (1997).

[4] J. Hu, A. H. MacDonald, *Phys. Rev. B* **46**, 12554 (1997).

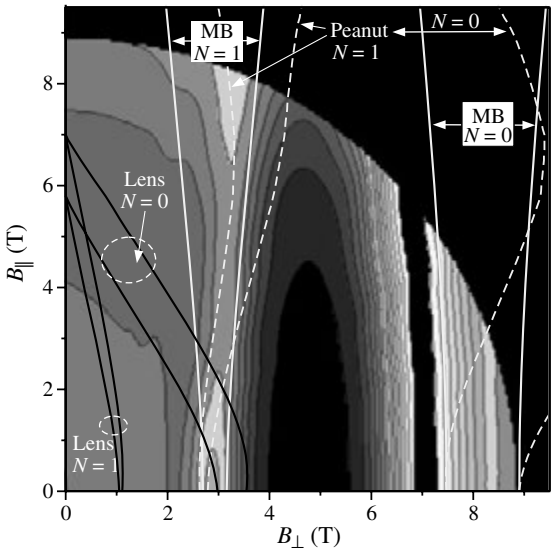

Fig. 3. The view from the top on Fig. 2a in gray scale performance, with darker/brighter regions meaning the smaller/higher values, compared with calculations. Gray dashed lines are for Peanut trajectories, black solid lines for the Lens ones, gray solid lines for the magnetic breakdown (MB). The lines are grouped in couples due to spin splittings.

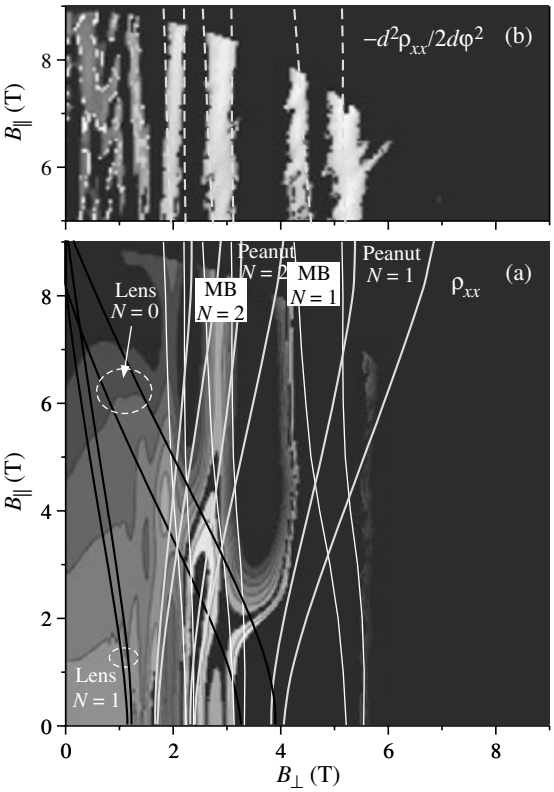

Fig. 4. (a) The same as Fig. 3, but after illumination (see Figures 1b, 2b). (b) The second derivative of the (a) data, $-\partial^2\rho_{xx}/\partial\varphi^2$, to show the spin splitting of the MB($N = 1$) peak.

14th Int. Symp. "Nanostructures: Physics and Technology"
St Petersburg, Russia, June 26–30, 2006

Strain relaxation for controlled nanostructure geometry: from growth-organizing dislocation networks to nanowhiskers

Frank Glas and Gilles Patriarche
CNRS – Laboratoire de Photonique et de Nanostructures, route de Nozay, 91460 Marcoussis, France

Abstract. We first show how the study of the interface between two identical but disoriented semiconductor crystals lead us to design dislocation networks which at the same time are efficient for organizing the growth of strained nanostructures and have an easily tunable geometry. The key factor in obtaining such networks is the interaction between the dislocations accommodating the disorientations. We then calculate the effect of strain relaxation at the free surfaces on the elastic energy of a misfitting layer grown at the top of a nanowhisker.

Introduction

The study of strain relaxation in hetero- and nanostructures has a long history. Whereas much of the earlier efforts were directed at avoiding plastic relaxation in order to benefit from the unique physical properties of the strained structures, strain was later also used as a tool for the fabrication of novel nanostructures, such as self-assembled quantum dots [1]. A natural development of this approach is to go from self-assembled to artificially-organized nanostructures. This contribution is devoted to two methods for obtaining highly strained nanostructures while retaining a well-defined geometry of the strained material, which is usually not the case with self-assembly.

In section 1, we show how a detailed study of the interface between two disoriented GaAs crystals lead us to design dislocation networks with tunable periodicity, which have already demonstrated a potential for the regular organization of strained nanostructures. In the second part, we consider another type of artificial nanostructures, nanowhiskers. These are candidates for the fabrication of highly strained heterostructures of well-defined geometry with thicknesses well beyond the critical thickness for standard planar layers. As a first step towards the calculation of the critical parameters for such systems, we quantify the huge reduction in elastic energy afforded by their lateral free surface.

1. Designing dislocation networks for the ordered growth of semiconductor nanostructures

1.1. Introduction

Quantum dots (QDs) may form spontaneously when a semiconductor is deposited epitaxially on a mismatched substrate [1], but the sizes, shapes, compositions and spatial distribution of the QDs usually remain fairly uncontrolled. A promising way to order and regularize QDs is to use the strain field induced at the growth front by a shallowly buried 2D dislocation network (DN) [2]. The strain field has the same periods as the DN and should affect the surface fluxes of the deposited species and the nucleation sites of the QDs. By choosing appropriate DNs, it should be possible to order laterally QDs having identical shapes and sizes.

The DNs should be efficient and have an easily tunable period. However, these two requirements seem incompatible. In practice, tunability requires the use of the wafer bonding technique; a subsequent nearly complete removal of one of the two crystals leaves only a thin layer bonded on a thick substrate [3, 4]. The lattice parameter mismatch and disorientations between the bonded crystals determine the characteristics of the interfacial DNs which accommodate them. Lattice mismatch is accommodated by dislocations with in-plane edge components, which are deemed efficient because they produce dilatational strain; however, their period is fixed by the mismatch and therefore not tunable. Conversely, twist is accommodated by screw dislocations. Their period depends directly on the twist and is easily tunable, but they produce only surface shear strains which have little effect on QD formation. In the following, we show that this is an oversimplification and that, because of dislocation interaction, wafer bonding may produce DNs which are both efficient and tunable. The discussion is based on our study of bonded GaAs bicrystals by transmission electron microscopy (TEM) [5], but should apply in many cases.

1.2. Summary of the experimental observations

We bond two halves of a single GaAs crystal having a vicinal [001] surface with steps close to a ⟨100] orientation, after rotating them by an angle $\pi/2 + \theta_{\text{twist}}$ around their common normal. The resulting disorientations are (i) a tilt θ_{tilt} around the bisector $\mathbf{u}_\text{b}$ of the two step directions, here close to a ⟨110] direction hereafter called [110] (we do not distinguish the orthogonal ⟨110] directions), and (ii) a twist θ_{twist}. Recall that in such crystals, all dislocations have Burgers vectors (BVs) of type $\mathbf{b} = (a/2)\langle 110\rangle$, with a the lattice parameter. As a first approximation (Fig. 1(a)), we expect the twist to be accommodated by a square network of screw dislocations of period $D_{\text{twist}} = b/\left[2\sin(\theta_{\text{twist}}/2)\right]$, aligned respectively on [110] (label '1') and $\left[\bar{1}10\right]$ (label '2'). On the other hand, as in the case of Si/Si [3] and GaAs/InP [4] bonding, the tilt should be accommodated by a 1D network of mixed dislocations (label 'm') aligned on $\mathbf{u}_\text{b}$. Whereas the screw dislocations have in-plane BVs, the BVs of the mixed dislocations have an in-plane component but also an edge component along [001]. Only the latter, of modulus $a/2$, accommodates tilt; hence, the period of the mixed network should be $D_{\text{tilt}} = a/\left[4\sin(\theta_{\text{tilt}}/2)\right]$. The mixed dislocations have eight possible BVs, but only four of these remain if, in order to minimize the total number of dislocations and thereby their energy, we assume that all the normal (tilt-accommodating) components are identical; we take it as positive along [001].

We first briefly summarize the deviations from this simple picture that we observe experimentally in a typical specimen with θ_{twist} and θ_{tilt} less than a few degrees (Fig. 1(b)). First, the

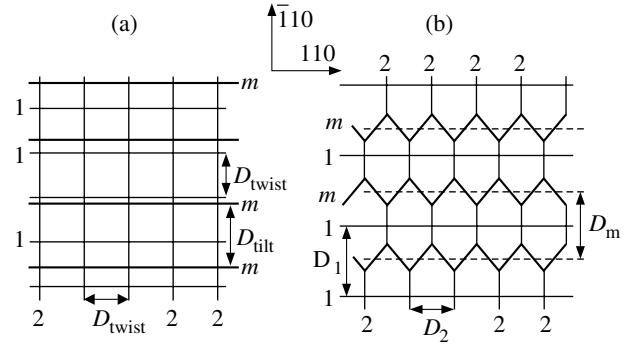

Fig. 1. Schematics of the expected (a) and observed (b) interfacial dislocation networks. Fine and thick lines show respectively (quasi)-screw (1,2) and mixed (m) dislocations. The small rotations with respect to the crystallographic axes are not shown.

dislocations of subnetwork 1 (BV $\mathbf{b} = (a/2)\,[110]$) have lines rotated with respect to [110] by a small angle ω_1; moreover, their period D_1 is well above D_{twist}. Second, screw subnetwork 2 interacts with the mixed dislocations, so that it is composed of segments close to $\left[\bar{1}10\right]$ (rotated by a small angle ω_2) with BV $\mathbf{b} = (a/2)\left(1\bar{1}0\right)$; its period is $D_2 \simeq D_{\text{twist}}$. Finally, dislocation interaction also transforms each ideal mixed line in a zigzag sequence of segments, as already observed in other cases [3, 4, 6].

1.3. Interpretation

It is striking that screw subnetwork 1 has a period larger than expected. This can be understood by considering the 2D network formed by the interaction of subnetworks 2 and m, a unit cell of which is drawn in Fig. 2. Nodal conservation rules [7] imply that each segment of mixed dislocation has its own BV and that only two 'a' and 'b' sequences of BVs are possible along a given mixed line; along each sequence, two of the four possible BVs mentioned earlier alternate. Any sequence is fully determined once one segment is known, but sequences corresponding to two mixed dislocations (*e. g.* $m1$ and $m2$ in Fig. 2) are *a priori* independent. If, in a sequence, the two types of segments are of equal lengths, their edge components cancel. On the other hand, the two sequences have different total screw components (Fig. 2). A 'b' sequence produces large screw BV components; the sum of two consecutive components is along $\left[\bar{1}\bar{1}0\right]$ and induces a twist in the same rotational direction as screw subnetwork 1. Conversely, 'a' sequences produce a smaller twist in the opposite direction. Hence, if 'b' sequences dominate, part of the twist can be accommodated by the mixed dislocations instead of the screw dislocations of subnetwork 1. Less of the latter are then needed, which explains why $D_1 > D_{\text{twist}}$. This 'replacement' is possible because the average mixed lines and subnetwork 1 are nearly parallel; nothing similar occurs for subnetwork 2, hence $D_2 \simeq D_{\text{twist}}$. The total dislocation length is thereby reduced, which makes the mechanism energetically favorable.

We confirm this mechanism in two ways. First, by using Frank's formula [7] and measured values of the periods D_1, D_2, D_m and angles ω_1, ω_2, we can calculate the ratio of the numbers of 'a' and 'b' sequences and check that 'b' sequences indeed dominate [8]. Second, TEM dislocation contrast analysis identifies the BV of each segment, and therefore the type of each sequence: in Fig. 2, full (resp. dashed) ellipses indicate segments strongly contrasted in TEM images formed with

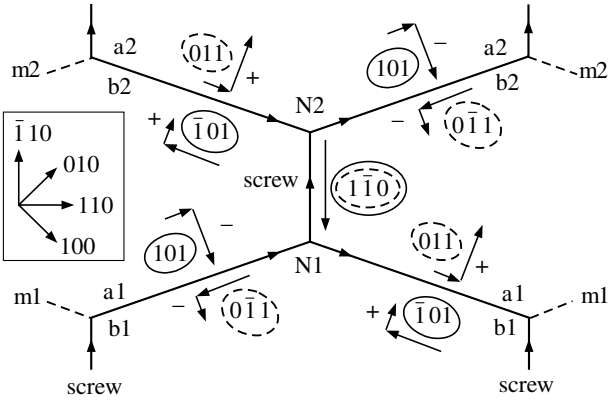

Fig. 2. Unit cell of the growth-organizing DNs. $m1$, $m2$: mixed dislocations. On-line arrows: conventional line orientation. Near each segment are given the possible BVs (in ellipses, with factor $a/2$ omitted) and the screw and edge components of their in-plane projection (fine arrows); 'a' and 'b' sequences are shown above and below the mixed segments.

diffraction vectors along [200] (resp. [020]) [4]. These images confirm the prevalence of 'b' sequences.

1.4. Growth-ordering dislocation networks

These results allow us to design DNs likely to order and regularize the growth of stressed nanostructures. Pushing the 'replacement' mechanism to its extreme, we see that screw subnetwork 1 can be fully eliminated provided that there are enough mixed dislocations to accommodate that part of the tilt which subnetwork 1 usually accommodates. It does not even matter if there are too many mixed dislocations since the proportion of 'b' and 'a' sequences can adjust to yield the exact amount of tilt needed. Such DNs were fabricated by setting the twist close to zero, keeping enough tilt to have $D_2 > D_m$. TEM confirms the absence of subnetwork 1.

We are now left with a simple hexagonal network (Fig. 2). Let us see why generating such patterns is essential for the subsequent growth of nanostructures. The in-plane edge components of two consecutive segments of each mixed dislocation have opposite directions (Fig. 2). Hence, the strains induced on a given side of the interface by each sequence alternate between in-plane dilatation and contraction, as indicated by '+' and '−' in Fig. 2. These signs remain arbitrary as long as we do not specify relatively to which crystal the figure is drawn. Let us assume that '+' corresponds to an expansion in the crystal on which growth will proceed. Fig. 3 shows several hexagons of the DN and the dilatational surface strain induced by each mixed segment. Screw segments remain neutral, since they

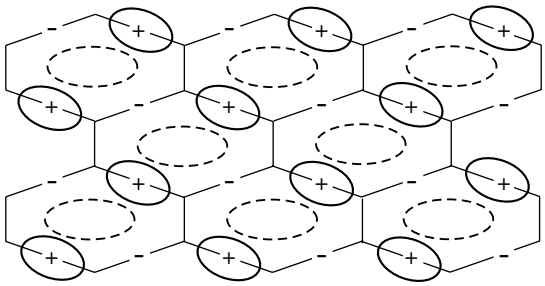

Fig. 3. Schematics of DN and strain pattern. + and − denote dilatation and contraction above the interface. Full (resp. dashed) ellipses: preferred region of growth for InAs (resp. GaAs).

only induce shear. Thus, dislocation interaction and elimination of screw subnetwork 1 generates a periodic 2D pattern of alternating compressed and dilated areas at the surface. The latter should favor the localized growth of materials having larger lattice parameters than GaAs, for instance InGaAs alloys.

Our first experiments confirm that this is the case, although we have not yet obtained proper QDs. Indeed, we observe that during a standard growth sequence, the thicknesses of both the GaAs buffer layer and the InAs layer vary. Moreover, the periods, orientations and positions of these corrugations are correlated with those of the underlying DN. More details are given elsewhere [9].

To conclude, we have designed DNs which at the same time are efficient for growing ordered nanostructures and have an easily tunable geometry. Efficiency results from dislocation interaction, which produces sequences of segments creating zones alternatively under tension and compression. Tunability is achieved by selecting the crystal miscut to vary the period of the mixed network and, even more easily, by imposing a given twist between the bonded crystals, which directly determines the period of the remaining screw DN.

2. Strain relaxation in nanowhiskers

Semiconductor whiskers with micrometric diameters were first fabricated more than 40 years ago [10]. Using modern epitaxy techniques, whiskers with much smaller diameters have recently been grown, in particular in several semiconductor systems. The interest in these nanowhiskers partly stems from their potential applications in nanoelectronics and nanooptics. The whiskers usually grow perpendicularly to the substrate with lengths up to several tens of micrometers and diameters in the nanometer-micrometer range.

For applications, it is essential to master the fabrication of whiskers containing strained heterostructures. Whiskers are particularly promising in this respect because they have free surfaces not only at the top but also at the side, which should allow efficient lateral stress relaxation (much more than for a quantum dot on a thick substrate). A given material is therefore expected to have a larger critical thickness for plastic relaxation when grown on a misfitting whisker 'substrate' than on a bulk substrate. Following the first experimental demonstrations [11], thick layers of highly misfitting materials might soon become widely available.

However, the increase in critical thickness has not been calculated yet. Ertekin *et al* considered a strained heterostructure made of two semi-infinite misfitting cylinders [12]. Obviously, this geometry is not suited to the determination of a critical thickness and, not surprisingly, these authors only estimated a critical diameter.

As a first step towards the calculation of critical parameters pertaining to nanowhiskers, we summarize our calculations of strain relaxation for whiskers with heterostructures. Consider a semi-infinite cylindrical whisker of radius r_0 with a free top surface. The upper part of the cylinder, of height h, is made of a material having a misfit ϵ_0 with respect to the lower part (Fig. 4). Calculations are carried out in the framework of linear isotropic elasticity, taking identical Young moduli E and Poisson ratios ν for the two materials.

Although such calculations can be performed numerically, we prefer finding approximate analytical solutions that will subsequently allow us to treat the plastic relaxation of the structure more easily. We start from the analytical solution for a misfitting region of finite height in an infinite cylinder [13], which satisfies the boundary conditions for stresses on the lateral free surface ($\sigma_{rr} = 0$, $\sigma_{rz} = 0$) but not on the upper free surface ($\sigma_{zz} = 0$, $\sigma_{rz} = 0$). We then add an extra stress field which nearly cancels these stresses without generating new stresses on the lateral surface.

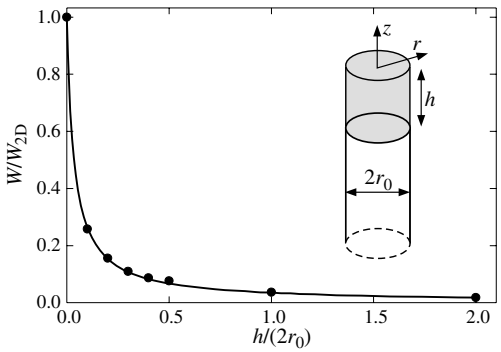

Fig. 4. Nanowhisker with a misfitting top layer. Variation of the elastic energy of the system as a function of the layer aspect ratio, normalized to the energy of the same volume of a 2D layer grown on a semi-infinite substrate with the same misfit ($\nu = 1/3$).

Fig. 4 shows the variation, as a function of the layer aspect ratio, of the elastic energy W stored in the whole system, normalized to the energy $W_{2D} = E\pi h r_0^2 \epsilon_0^2 / (1 - \nu)$ stored in the same volume cut in a 2D strained layer coherently grown on a semi-infinite substrate with misfit ϵ_0.

The effect of strain relaxation at the lateral surface is huge. Even for low aspect ratios, the elastic energy is considerably reduced, for instance to a quarter of its 2D value for $h/(2r_0) \simeq 0.1$. This opens wide prospects for the growth of highly misffitting heterostructures of uniform thickness and diameter, which are indeed QDs of well-defined geometry.

References

[1] L. Goldstein, F. Glas, J. Y. Marzin, M. N. Charasse and G. Le Roux, *Appl. Phys. Lett.* **47**, 1099 (1985).
[2] A. Bourret, *Surf. Sci.* **432**, 37 (1999).
[3] M. Benamara, A. Rocher, A. Laporte, G. Sarrabayrousse, L. Lescouzères, A. Peyre Lavigne, M. Fnaeich and A. Claverie, *Proc. Mater. Res. Soc. Symp. 378 (San Francisco, 1995)*, Materials Research Society, 863, 1995.
[4] G. Patriarche, F. Jeannès, J. L. Oudar and F. Glas, *J. Appl. Phys.* **82**, 4892 (1997).
[5] J. Coelho, G. Patriarche, F. Glas, G. Saint-Girons, I. Sagnes and L. Largeau, *Phys. Rev. B* **70**, 155329 (2004).
[6] J. G. Zhu and C. B. Carter, *Philos. Mag. A* **62**, 319 (1990).
[7] J. P. Hirth and J. Lothe, *Theory of dislocations*, (New York: Wiley) 26, 703–8, 723, 1982.
[8] F. Glas, J. Coelho, G. Patriarche and G. Saint-Girons, *J. Cryst. Growth* **275**, e1647 (2005).
[9] J. Coelho, G. Patriarche, F. Glas, G. Saint-Girons and I. Sagnes, *J. Cryst. Growth* **275**, e2245 (2005).
[10] R. S. Wagner and W. C. Ellis, *Appl. Phys. Lett.* **4**, 89 (1964).
[11] K. Hiruma, H. Murakoshi, M. Yazawa and T. Katsuyama, *J. Cryst. Growth* **163**, 226 (1996).
[12] E. Ertekin, P. A. Greaney and D. C. Chrzan, *J. Appl. Phys.* **97**, 114325 (2005).
[13] M. V. Barton, *J. Appl. Mech.* **8**, A-97 (1941).

14th Int. Symp. "Nanostructures: Physics and Technology"
St Petersburg, Russia, June 26–30, 2006

Tall silicon nanopillars characterization by SEM, IV and SE techniques

Yu. V. Nastaushev[1], S. N. Svitasheva[1], L. V. Sokolov[1,2], P. Werner[2], N. D. Zakharov[2], T. A. Gavrilova[1], O. V. Naumova[1] and A. L. Aseev[1]

[1] Institute of Semiconductor Physics, SB RAS, 630090 Novosibirsk, Russia
[2] Max-Planck Institut für Mikrostructurphysik, 06120 Halle (Saale), Germany

Abstract. Tall silicon nanopillars was grown on silicon ⟨111⟩ wafers by molecular beam epitaxy (MBE) technique. Volume density of nanopillars (NP) was found by scanning electron microscopy (SEM) and it was revealed that NP grown are single silicon nanocrystals with hexagonal symmetry and with glassy lateral facets. Spectroscopic ellipsometry (SE) in range 1.5–4.77 eV displayed homogeneity of nanopillars in plane. Electrical current-voltage (IV) dependences revealed Shottky' barrier effect.

Introduction

Small whiskers (or nanowires) are of the increasing interest due to their physical properties as well as their potential for new Nanodevices such as nanophotonics [1–3] and ULSI silicon microelectronics [4]. Comprehensive studies on the vapor-liquid-solid (VLS) grows of whiskers of silicon and other materials with sizes down to the 100 nm range already started in the sixties and seventies [5, 6]. At first semiconductor nanopillars were used as quantum dots and single-electron nanodevices [7–9]. During recent years remarkable progress has been achieved in the way of molecular beam epitaxy of silicon whiskers [10]. However, the studying of their electrical and optical properties till now has not been executed properly. The aim of this work was to investigate structural, optical and electrical properties of tall silicon nanopillars grown by means of MBE technique.

1. Experimental

After cleaning by the conventional RCA procedure, ⟨111⟩ oriented 5″ Si wafers were used as substrates. The small droplets of gold, formed from a thin film of Au, were used as seeds for whiskers growth. The both Si molecular flux and Au molecular flux had been generated by e-beam evaporators. During the following nanopillars growth the permanent Si flux amounted 0.05 nm/sec. The samples were investigated by scanning electron microscopy (SEM), Spectroscopic ellipsometry and IV characterization.

The Au-caps on the top of nanopillars can be seen in both Fig. 1 and Fig. 2. $H_{\min} = 585$ nm and $H_{\max} = 888$ nm are heights of thick NP and thin NP, respectively. Evaluation of volume parts of both thin and thick nanopillars and also average distance between nanopillars in several points where spectroscopic ellipsometric spectra were made are given in the Table.

The I–V curves nonlinear diode-like type with large difference of direct and reverse current were obtained on silicon nanopillars with top Al contact.

2. Conclusion

It was found by scanning electron microscopy (SEM) that nanopillars are silicon nanocrystals with hexagonal glassy lateral facets which have the Au-caps on the top of them as shown earlier [10]. Volume density of nanopillars, their heights and average distance between them were obtained by SEM. Spectroscopic ellipsometry (SE) in range 1.5–4.77 eV displayed disagreement in spectra of dielectric function of single Si and pseudodielectric function of nanopillars. Shottky' barrier effect was exhibited in IV diode-like dependences. Electrical properties of the nanopillars correspond to ones of c-Si heavily doped by Au impurity as theory predicts [11]. It was found the

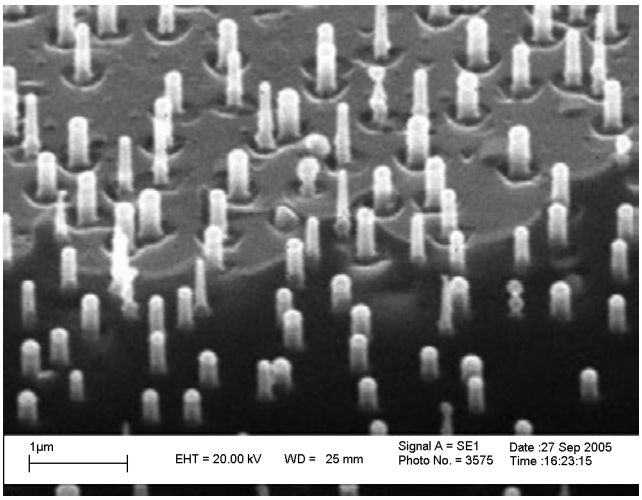

Fig. 1. SEM-image of tall NP on Si substrate.

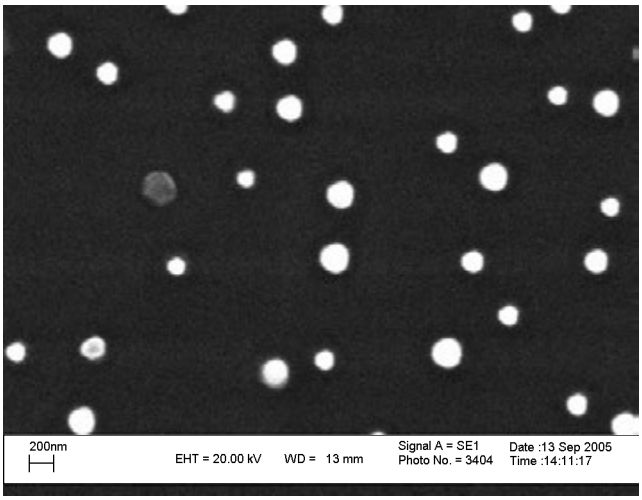

Fig. 2. SEM top view on Si NP with hexagonal facets.

Table 1.

Measurement point in Fig. 3	Average NP distance (nm)	NP volume density (%)	Thin NP volume density (%)	Thick NP volume density (%)
4	739	7.8	2.2	5.6
5	854	6	1.4	4.6
6	725	7.8	3.3	4.5

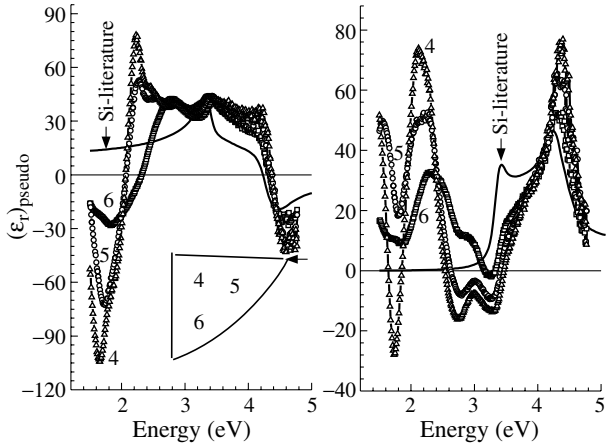

Fig. 3. Spectroscopic ellipsometric spectra of both real and imaginary pseudodielectric function were made in several points as shown in the insert. They displayed homogeneity of NP layer which optical properties differ from single Si (see critical points at 3.43 and 4.25 eV). Native oxide effect did not take into account.

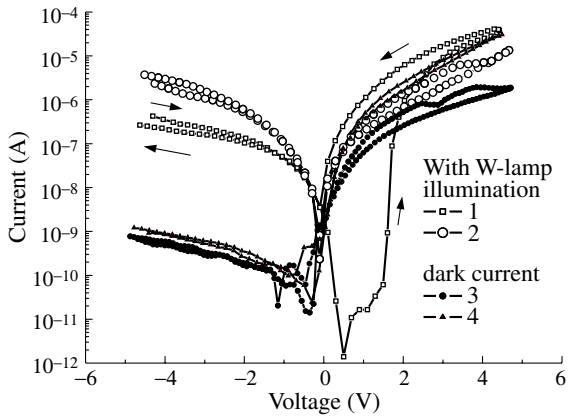

Fig. 4. The current dependencies on the voltage applied to Si nanopillars in the darkness (3, 4) and with illumination by tungsten lamp of the back side of the Si substrate (1, 2). Estimation of conductivity and carriers lifetime are about 50 Ω cm and 76 ps (< 0.1 ns) respectively.

increasing of photocurrent caused by the illumination of near infrared light.

Acknowledgement

This work was partly supported by the Russian Found of Basic Researches (04-02-16541).

References

[1] V. V. Poborchii *et al*, *Physica E* **7**, 545 (2000).
[2] G. V. Prakash *et al*, *J. Appl. Phys.* **91**, 4607 (2002).
[3] L. Dal Negro *et al*, *Physica E* **16**, 297 (2003).
[4] B. Rajendran *et al*, *Fabricating Silicon Nanocrystals — Options and Challenges*, http://www.stanford.edu/∼bipin/research/ (2002).
[5] R. S. Wagner *et al*, *J. Appl. Phys.* **35**, 2993 (1964).
[6] E. I. Givargizov *et al*, *J. Cryst. Growth* **31**, 20 (1975).
[7] J. N. Randall *et al*, *J. Vac. Sci. Technol. B* **6**, 302 (1988).
[8] D. M. Pooley *et al*, *Appl. Phys. Lett.* **74**, 2191 (1999).
[9] T. A. Kramer *et al*, *Electrical Characterization and Applications of Silicon Nanopillars*, http://www-snf.stanford.edu/Projects/Pease-Kramer/electric.html (1997).
[10] L. Shubert *et al*, *Appl. Phys. Lett.* **84**, 4968 (2004).
[11] S. M. Sze, *Physics of Semiconductor Devices*, John Wiley & Sons, (1981).

14th Int. Symp. "Nanostructures: Physics and Technology"
St Petersburg, Russia, June 26–30, 2006

Theoretical analysis of nanowire growth by MBE and CVD techniques

N. V. Sibirev[1], V. G. Dubrovskii[2,3], R. A. Suris[2], G. E. Cirlin[1,2,3], I. P. Soshnikov[2,3], V. Gorbenko[3], M. Tchernycheva[4], J. C. Harmand[4] and V. M. Ustinov[2,3]

[1] Institute for Analytical Instrumentation of the Russian Academy of Sciences
Rizhsky 26, 190103, St Petersburg, Russia
[2] Ioffe Physico-Technical Institute, St Petersburg, Russia
[3] St Petersburg Physical Technical Centre of the Russian Academy of Sciences for Research and Education,
Khlopina 8/3, 195220, St Petersburg
[4] CNRS-LPN, Route de Nozay, 91460 Marcoussis, France

Abstract. Mechanisms of nanowire formation during MBE are studied theoretically within the frame of a kinetic model that accounts for the ad-atom diffusion on the substrate surface and on the nanowire sidewalls. It is shown that the ad-atom diffusion considerably increases the vertical growth rate of nanowires and also to modify the observed length-diameter dependences. The results of experimental investigations of GaAs nanowires grown by MBE on the GaAs(111)B surface activated by Au at different conditions are presented and analyzed. Theoretical and experimental data are compared to each other and a good correlation between them is demonstrated.

Renewed interest in the fabrication of semiconductor nanowires, also known as nanowhiskers (NWs), is stimulated by recent advances in their use as building blocks for various electronic, optical and biological applications. Techniques of growth of Si and III–V NWs with a length up to ten microns and a diameter of only tens of nanometers have been developed and high quality freestanding NW arrays have been obtained. Generally accepted mechanism of NW formation is usually referred to as the vapor-liquid-solid (VLS) growth. In the traditional adsorption-induced VLS model the following growth behavior is assumed [1]. When surface is activated by a metal growth catalyst and heated above the eutectic melting point, small drops of metal form a liquid alloy with semiconductor material and act as a seed for the NW growth. The direct impingement of deposit material from vapors around the drop makes this alloy supersaturated. The interface acts as a sink for deposit particles dissolved in the drop causing their incorporation into the available adsorption sites of the lattice. This leads to the vertical growth of wire with the drop of liquid alloy riding on its top. In the diffusion-induced VLS model it is assumed that, in addition to the direct impingement, atoms may also arrive to the drop from the wafer surface due to the diffusion along the wire sidewalls. These atoms first dissolve in the drop, then diffuse to the interface and finally also incorporate into the lattice.

The aim of this work is the theoretical investigation of NW growth during MBE on the surfaces activated by the drops of a growth catalyst. We will present a generalized dynamical model of NW formation during MBE that takes into account (i) adsorption: $J = V/\Omega$ (V — deposition rate, Ω — the volume per atom in the crystal); (ii) desorption on the drop surface: $-2\pi R^2 r_l C/\tau_l$ (C is the volume concentration of deposit atoms in the droplet, R — the drop radius, r_l — the inter-atomic distance in the liquid and τ_l — the mean lifetime of deposit atoms in the drop); (iii) diffusion of atoms from the substrate surface and from the NW sidewalls to the drop $j_{\rm diff}(L)$; (iv) crystal growth on the liquid-solid interface mediated by two-dimensional nucleation from supersaturated liquid alloy, (v) growth of the surface at a rate $V_{\rm s}$. We will present theoretical dependences of NW length on the growth temperature and deposition rate. The end result will be the theoretical representation of NW morphology as function of technologically controlled conditions of NW fabrication procedure. We will discuss different growth scenarios during molecular beam epitaxy (MBE) and chemical vapor deposition (CVD) of semiconductor NWs. Some data on the kinetic Monte-Carlo simulation of NW growth in different techniques will be presented. Simulation results will be compared to recently obtained experimental data on the GaAs NWs grown by MBE on the GaAs(111)B surface activated by Au.

The generalized kinetic equation of the nanowire growth in our model is written in the following form:

$$\frac{\pi R^2}{\Omega}\frac{dL}{dt} = \left(\frac{V - V_{\rm s}}{\Omega} - \frac{2Cr_l}{\tau_l}\right)\pi R^2 + j_{\rm diff}(L)\,. \qquad (1)$$

The first term in the right hand side stands for the adsorption-desorption contribution at the drop surface and the second term describes the diffusion-induced growth. Equation (1) together with a set of 2 differential equations for finding $j_{\rm diff}(L)$ and a model for the nucleation-mediated growth on the liquid-solid interface under the drop [3] provides theoretical length-radius dependences and the dependences of nanowire length L on the technologically controlled growth conditions, such as the surface temperature T, the deposition rate V and the deposition thickness H. The general form of the $L(R)$ dependence is shown in Fig. 1. The first increasing section of the curve describes the Givargizov–Chernov VLS growth during

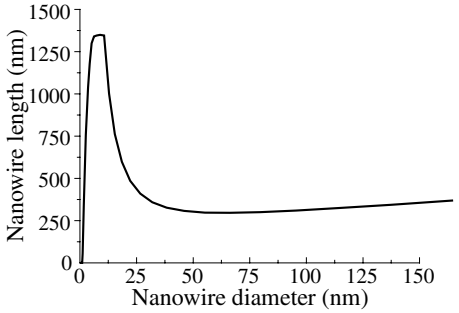

Fig. 1. General form of length-diameter curve.

CVD [1], the decreasing part relates to the diffusion-induced growth observed in MBE [2], and the last increasing section at the moment remains merely a theoretical prediction [3].

Theoretical asymptotics of the $L(R)$ dependences in different growth modes are discussed. In particular, we demonstrate how the general theory describes the known adsorption-induced growth of NWs, the diffusion-induced growth and the crossover between these growth modes. In the diffusion-induced growth of NWs is well described by the expression

$$L \cong \left[\varepsilon - \gamma + \frac{2\lambda_s K_1 (R/\lambda_s)}{K_0 (R/\lambda_s)} \right] H . \qquad (2)$$

Here, the parameter $\varepsilon = (V - V_s)/V$ accounts for the growth of non-activated surface, γ is the desorption contribution, λ_s is the adatom diffusion length on the substrate surface, K_m denote the decreasing modified Bessel functions of order m.

In the experimental part of the work, the NW formation procedure during MBE consisted of three stages. First, GaAs(111)B substrates were placed in the growth chamber of the EP1203 MBE setup, where the oxide was removed from the substrates and the GaAs buffer layer was deposited. The GaAs buffer layer thickness was kept about 300 nm in all growth runs. Second, the samples were transferred from the MBE setup into the vacuum chamber. In the vacuum chamber, a thin Au film was deposited onto the sample surface. Third, the samples were transferred back to the MBE growth chamber and heated up to the temperature of 630 °C. After the annealing, the GaAs layers with H from 500 to 1500 nm were deposited. The deposition rate of GaAs $V = 1.0$ ML/s and the substrate temperature $T = 585$ °C. The visualization of surface morphology was performed by applying the CamScan S4-90FE scanning electron microscope (SEM) with a field emission gun, operating in the regime of secondary electron emission.

From the analysis of SEM images we obtained the experimental length/diameter dependencies of NWs. For the most samples the experimental $L(R)$ curves are the decreasing functions. One of the experimental $L(R)$ curves is presented in Fig. 2. It is seen that the L/R ratio changes from 50 for the thinnest NWs down to 1 for the thickest ones. The maximum length of NWs is more than 3 times higher than the thickness of deposited GaAs. Therefore, the NWs in our experiments are formed by the diffusion-induced mechanism rather than by the classical VLS mechanism. Also, the experimental $L(R)$ curve presented in Fig. 2 is well described by the expression

$$L \cong \left[\varepsilon - \gamma + \frac{4}{\pi N_W R^2} \frac{\ln\left(\sqrt{\pi N_W}\langle R\rangle\right)}{\ln\left(\sqrt{\pi N_W} R\right)} \right] H . \qquad (3)$$

Here, N_W is the NW surface density and $\langle R\rangle$ is their average radius. Eq. (3) is the special case of Eq. (2) when the effective diffusion length of adatoms on the substrate surface is much smaller than the average distance between the NWs. Eqs. (2) and (3) allows the complete description of NW structural properties depending on the technologically controlled growth conditions. The comparison of theoretical and experimental data allows us to obtain useful information concerning the physical values of rather complex material system. In particular, the measured $L(R)$ and $L(H)$ curves provides the numeric estimates for the ad-atom diffusion flux, the growth rate of substrate surface and the desorption rate from the drop surface.

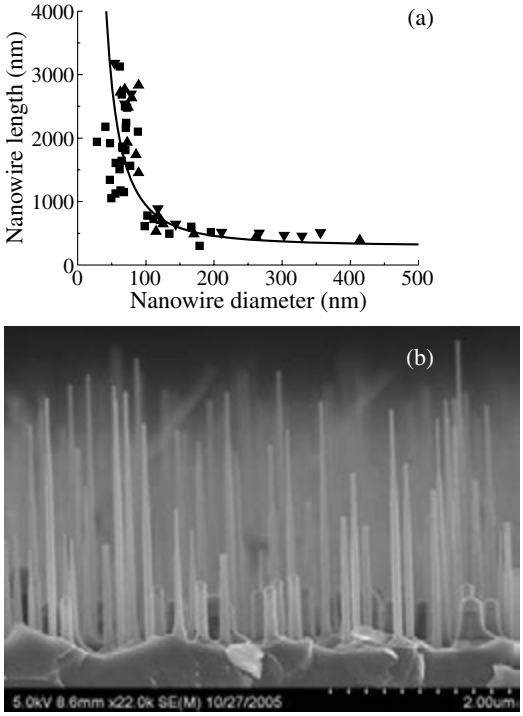

Fig. 2. (a) Theoretical (solid line) and experimental (triangles and squares) $L(D)$ dependences of GaAs NWs. (b) SEM image of the sample. The MBE growth was performed at $H = 1000$ nm, $T = 585$ °C and $V = 1$ ML/s.

In overall view, the developed kinetic approach might help in better understanding of the controlled production of NWs with the desired morphological properties for different applications.

Acknowledgements

The authors are grateful to the financial support received from SANDiE program, RFBR grants Nos. 05-02-16495, 05-02-16658 and No. 05-02-08090-OFI, scientific grant of St Petersburg Scientific Center and different scientific programs of RAS. N.S. are grateful to the financial support of the The Dynasty Foundation.

References

[1] V. G. Dubrovskii and N. V. Sibirev, *Phys. Rev. E* **70** (3), 031604 (2004).

[2] V. G. Dubrovskii, G. E. Cirlin, I. P. Soshnikov, A. A. Tonkikh, N. V. Sibirev, Yu. B. Samsonenko, V. M. Ustinov, *Phys. Rev. B* **71** (20), 205325 (2005).

[3] V. G. Dubrovskii, N. V. Sibirev, G. E. Cirlin, J. C. Harmand and V. M. Ustinov, *Phys. Rev. E* **73** (2) 021603 (2006).

14th Int. Symp. "Nanostructures: Physics and Technology"
St Petersburg, Russia, June 26–30, 2006

Molecularly thin semiconductor and metal shells: from nanotubes to nanocorrugated quantum systems

V. Ya. Prinz

Institute of Semiconductor Physics, 13, Academician Lavrentyev Avenue, Novosibirsk 630090, Russia

Abstract. Scientific efforts aimed at extending of planar technology achievements over fabrication of three-dimensional objects are briefly overviewed. Previously, we showed that ultra-thin epitaxial heterofilms (down to two monolayers for InGaAs/GaAs) can be controllably detached from substrates, and rolled or buckled, under the action of the internal strain, allowing one to form micro- and nanoshells, including tubes and corrugations. The diameter of obtained tubes was down to 2 nm, and the period of nanocorrugated systems was down to 10 nm. New experimental and theoretical results on quantum confinement and quantum transport in semiconductor and hybrid nanoshells are presented. Possible extension of this approach to the case of carbon shells is considered.

Introduction

The present brief overview focuses on the fabrication methods and properties of semiconductor and metal nanoshells based on self-rolling or buckling of ultrathin strained films. Recently, we have proposed a new method permitting precise fabrication of three-dimensional (3D) micro- and nano-shells (tubes, corrugations, scrolls, fibers, rings, helices, etc.) by self-rolling, bending or buckling of ultrathin strained films detached from substrates [1–18]. These artificial, or man-made, nanoshells can be formed from semiconductors, dielectrics, or metals, and can be used as building blocks for nanoelectronic and nanomechanical devices. This technology is fully compatible with the standard IC technology, can be applied to many materials, and allows precise control of the size, shape and location of shells on the substrate.

1. Results and discussion

The method for fabricating nanotubes from GaAs/InAs strained heterostructures using stress-driven processes [2–4] is schematically illustrated by Fig. 1. The diameter D of self-formed tubes depends on the thickness d of the initial heterofilm and on the value of the elastic stress in it; this diameter therefore can be precisely pre-defined in the MBE process. For a heterofilm made up by two layers with identical thickness d, we have $D \approx d/(\Delta a/a)$, where $\Delta a/a$ is the lattice mismatch between the two layers. The high quality of MBE-grown heterostructures makes it possible to obtain several-centimeter-long rolled tubes with diameters as small as 2 nm and with atomically

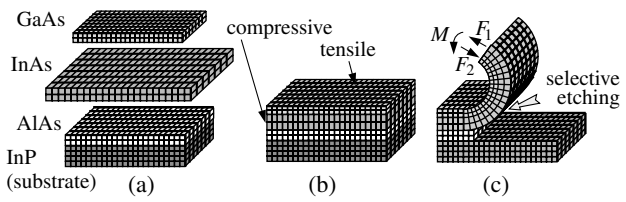

Fig. 1. The initial stages of formation of free-standing several-ML thick nanotubes (schematically). (a) free 2ML-thick InAs and GaAs layers with naturally mismatched lattice constants ($\Delta a/a$ of 7.2%); (b) matching of the layers at the interface between them in an InAs/GaAs bifilm MBE-grown on an InP substrate; (c) bending of the GaAs/InAs bifilm after its partial detachment from the substrate during selective etching of the underlying AlAs sacrificial layer.

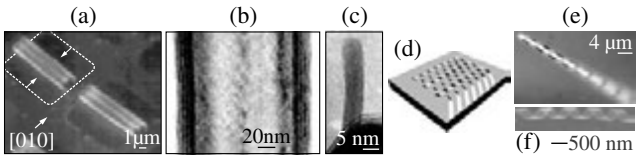

Fig. 2. SEM and HRTEM images of InGaAs/GaAs nanotubes rolled-up from bi-layered films (a) two single-wall scrolls after their collision at the end of their formation process, (b) multiwall (6 turns) nanotube. Initial-bifilm thickness — 4 ML GaAs + 4 ML $In_xGa_{1-x}As$ ($x = 0.6$); (c) single-wall nanotube prepared from a 2 ML GaAs + 1 ML InAs film. The inner diameters of the tubes shown in Figs. 2(a)–(c) are 1 μm, 120 nm and 3 nm, respectively. Schematic illustration of helical coils formation (d), and optical and SEM images of helices (e and f, respectively). In our experiments we obtained a helix with a minimum diameter of 7 nm and period of 10 nm.

smooth, uniform tube walls. From such structures, not only tubes, spirals and rings [2–4], but also other various shells, formed by locally released films, can be prepared [8, 9]. The possibility of fabricating nanoobjects has been demonstrated by us using a series of epitaxial structures (InGaAs/GaAs, InSbAs/InAs, InP/InAs, Si/GeSi, Si/GeSi/Si_3N_4/Cr, InAs, Au/Ti, Ta_2O_5/GaAs and others) grown on GaAs, InP, InAs, and Si substrates (see Fig. 2–6) [1–18]. Fabrication of a rich variety of complex shells and assembling them in configurations appropriate for various device applications [6, 12, 13, 17] have become possible with the advent of methods using directional rolling of films [8, 9, 12]. In [1, 2, 9] we proved it possible to form micro- and nanohelices. Figure 2 d, e, f shows a schematic illustrating the formation of helical coils (fibers). The rolling of strips is clearly influenced by the anisotropy of Young's modulus in A^3B^5 and Si/GeSi crystals [2]. Multilayered strained heterostructures with several sacrificial layers (e.g., several InAs/GaAs heterofilms grown on an InP substrate) allow "multi-level" constructions to be formed from tubes. It is worth noting that precise nanostructuring required development of technology and elimination of detrimental factors affecting the results of the fabrication technology. The cornerstone stages in the development of this fabrication technology enabling precise formation of variously shaped shells from semiconductor and metal nanoobjects include: (1) using highly selective etchants for the removal of sacrificial layers [1, 2, 16, 19], (2) directional film rolling yielding 3D

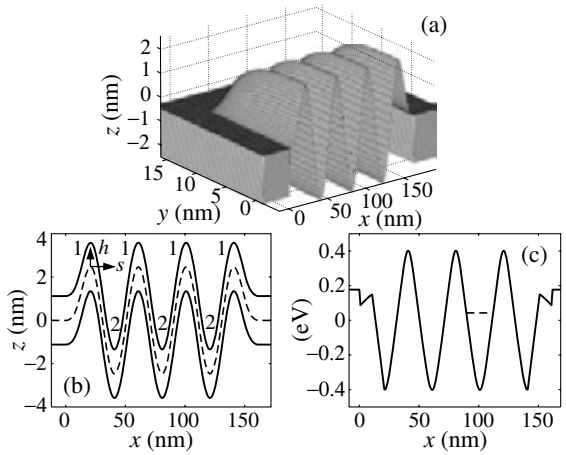

Fig. 3. (a) Schematic view of a nanocorrugated structure. (b) Cross section of the bilayer structure shown in (a): regions 1 of the top layer are under tensile strain, while regions 2 are under compressive strain. (c) Confinement potential for electrons near the upper surface of the film (solid line) and lower electron level (dotted line).

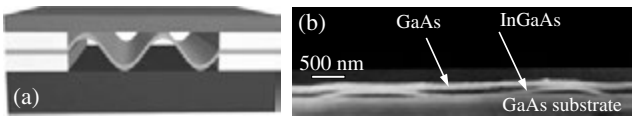

Fig. 4. Schematic view (a) and SEM image of corrugated InGaAs film sandwiched between the native GaAs substrate and GaAs cap layer (initial structure — GaAs/AlAs/InGaAs/AlAs/GaAs).

micro- and nanoshells of various shapes [8, 9, 12], (3) assembly of micro- and nanoshells in more complex architectures [3, 4], (4) supercritical drying of nanoshells [11, 14], (5) formation of nano-shells precisely controlled in all the three dimensions [10], (6) elimination of surface oxidation in ultrathin layers, and (7) overgrowing or filling of shells [2]. It was demonstrated, that being detached from the substrate the film abruptly changes its properties including the band-gap structure [18]. The processes forming the fabrication technology of cylindrical shells and the elastic and electronic properties of these shells were reviewed in [3, 4, 6]. Recent experiments showed static skin effect and ballistic transport in two-dimensional electron gas on cylindrical surface [20]. Simplicity of realization and broad spectrum of possible application of this approach attracted attention of many theorists and experimenters. In addition to the Novosibirsk group more than 20 other research teams all over the world are deeply involved in the development of the new technology and studies of fabricated novel objects. Recent references to several typical works in this field published by experimental groups headed by O. G. Schmidt, D. Grützmacher, P. O. Vaccaro, H. Yamaguchi, S. Mendach, K. H. Ploog, Max G. Lagally, W. Hansen, V. Luchnikov, R. H. Blick and theoretical groups headed by A. V. Chaplik, G. P. Nikishkov, O. V. Kibis, N. F. Morozov, A. L. Ivanovskii, A. Kleiner, and V. A. Margulis can be found in [21–41]. Below, we dwell in more detail on less known nanocurrugated structures and open shells fabricated in our laboratory.

2. Formation of precise corrugated films: quantum-dot chains and molecules

By now we have substantially extended the class of thin-film nanostructures which can be fabricated by the new technol-

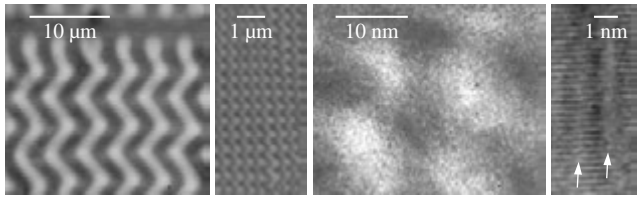

Fig. 5. Demonstration of the buckling process scalability. The periodically corrugated InGaAs structures were obtained by a buckling-based process.

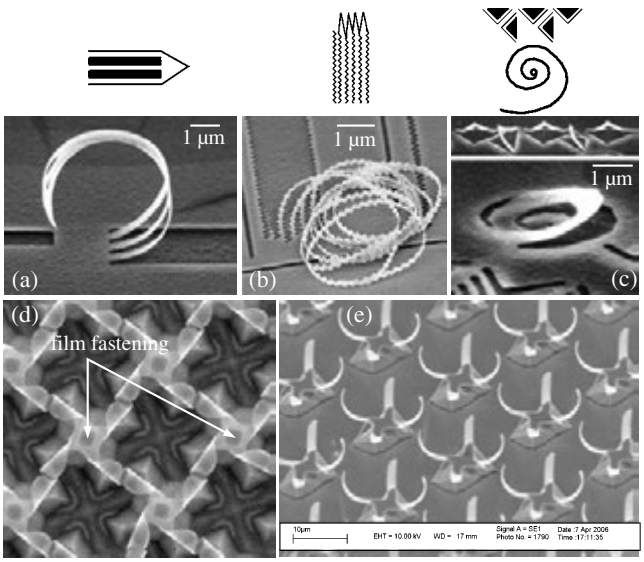

Fig. 6. Lithographic patterns and SEM images of obtained structures the shells made of SiGe/Si films: (a) bent cantilever, (b) nanosaw, (c) arrays of needles and Archimedean spiral-like strip. (d) (c) arrays of periodically ordered 3D shells made of SiGe/Si (d), and InGaAs/GaAs (e) bifilms.

ogy [4, 6, 18]. For the first time, we have fabricated nanocorrugated semiconductor systems [6]. Figure 3 illustrates a result of transformation of compressed flat film into the nanocorrugated film under its local detachment from the substrate. Such corrugations can be formed because compressed planar films locally detached from substrates are instable in their free state and undergo buckling. Numerical simulations show that nanocorrugated semiconductor films have unique quantum properties differing substantially from those displayed by other known low-dimensional objects [18]. For strained InAs corrugated bifilms with a corrugation period of 40 nm it was shown that, if the bifilm thickness is less than 3 nm, then the electronic spectrum in the bifilms is determined by quantum levels due to X-minimum electrons. It has been demonstrated that bending deformations of films significantly shift and split the X-minima. The difference in the shifts of the X_z and $X_{x,y}$ valleys in tensile (1) and compressed (2) regions of the film (Fig. 3b) gives rise to a periodic potential (Fig. 3c) providing for localization of the electron wave function and generation of quantum dots. A unique feature here is a gigantic depth of the potential well, caused by the gigantic stress in the film due to its bending. Figure 3a illustrates a simplest structure made up by a buckled strained film obtained by local removal of the underlying sacrificial layer. Molecular-beam epitaxy permits production of even more complicated precise structures in which layers are precisely spaced. In such structures (see Fig. 4), buckling emerges in a self-formed manner, resulting in a corrugated

structure with precise amplitude and corrugation period. Corrugations with periods ranging from nm to μm can be formed on one substrate. It should be emphasized that the properties of surfaces and interfaces in such ultra-thin structures, and the electric conduction in them, need to be further investigated. Yet, it is already quite clear that, from the viewpoint of electric conductivity, the shells fabricated from narrow-gap and gapless semiconductors are the most promising objects [3, 4]. With further progress of electron lithography (with resolution up to 3-nm), open micro- and nanoshells formed from lithographically structured flat films acquire ever increasing significance (see Fig. 6 a–c) [8]. Here, it is important that a huge variety of shell shapes can be realized because an array of flat structures can be transformed into a shell array of greater array power.

3. Applications

The application area of semiconductor, metal and hybrid nanotubes formed by the new technology largely coincides with that of the well-established carbon nanotubes. By now, many pilot materials and devices using microtubes and spirals have become known [3, 4, 6, 12, 13, 16, 17]. These are new instruments for biology and medicine, micro- and nano-needles, probes and syringes, dispensable single-crystal micro- and nano-needles, electrodes, AFM probes, syringes, nanojet arrays, nanofiber-based composites, elastic chemically active fast sensors, supersensitive quantum sensors, optical actuators, etc. Nanocorrugated systems find use in nanoelectronics, nanomechanics, cellular automata and dynamic quantum devices. The advantages offered by the novel structures are as follows: the bending diameters in such structures cover a wide range of values in the micro- and nano-scale region, the structures can be made thin-walled, and technology of their fabrication allows precise dimensional control and batch production. It should be noted that obtained 3D structures can not be made by any other known technology and results of our works showed record miniaturization (nanometre's bending radii and atomically sharp edges of shells, period of corrugations down to 10 nm etc.). Results of formation of individual shells and two-dimensional arrays on their basis are presented above.

Changeover to multilayer structures allowed creation of three-dimensional arrays very promising for practical applications (for instance, the structure presented in Fig. 4 can be easily repeated in vertical direction). Apparently, this technology can be also applied to carbon and hybrid carbon-semiconductor structures. Electronic properties of graphene [42] sheets are expected to be similar to ones of nanotubes. But its 2D structure is easier in handling than tube, it allows the material to be engineered to suit different device applications. This technology being extended to the case of carbon structures would enable a carbon nanoelectronics perfectly compatible with the IC technology.

Acknowledgement

The present work was supported by the Russian Foundation for Basic Research.

References

[1] V. Ya. Prinz, V. A. Seleznev, A. K. Gutakovsky, *The Physics of Semiconductors* (1999). World Scientific, Singapore, ISBN: 981-02-4030-9 (CD).

[2] V. Ya. Prinz, V. A. Seleznev, A. K. Gutakovsky, A. V. Chehovsky, V. V. Preobrazhensky, M. A. Putyato and T. A. Gavrilova, *Physica E* **6**, 828 (2000).

[3] V. Ya. Prinz, *Physica E* **23**, 260 (2004).

[4] V. Ya. Prinz, *Physica E* **24**, 54 (2004).

[5] V. M. Osadchii and V. Ya. Prinz, *Phys. Rev. B* **72**, 033313 (2005).

[6] V. Ya. Prinz, *Microelectronic Engineering* **69** (2–4), 466 (2003).

[7] V. M. Osadchii, V. Ya. Prinz, *JETP Lett.* **72**, 312 (2000).

[8] V. Ya. Prinz *et al*, *Nanotechnology* **12**, 399 (2001).

[9] A. B. Vorob'ev and V. Ya. Prinz, *Semiconduct. Sci. Technol.* **17** (6), 614 (2002).

[10] V. Ya. Prinz *et al*, *Nanotechnology* **13**, 231 (2002).

[11] V. A. Seleznev *et al*, *J. of Appl. Phys.* **42**, Part 2 (7A), L791 (2003).

[12] A. V. Prinz, V. Ya. Prinz and V. A. Seleznev, *Microelec. Eng.* **67–68**, 782 (2003).

[13] A. A. Maslov *et al*, *Novosibirsk, publ. house Nonparel*, 235 (2004).

[14] A. V. Chehovskiy and V. Ya. Prinz, *Intern. J. Nanoscience* **3**, 1&2 1 (2004).

[15] Yu. V. Nastaushev *et al*, *Nanotechnology* **16**, 908 (2005).

[16] S. V. Golod *et al*, *Appl. Phys. Lett.*, **84** (17), 3391 (2004).

[17] S. V. Golod, V. Ya. Prinz, V. I. Mashanov, *Thin Sol. Films*, 489/1–2 169 (2005).

[18] V. M. Osadchii and V. Ya. Prinz, *Phys. Rev. B* **72**, 033313 (2005).

[19] R. A. Soots and V. Ya. Prinz, *Patent of Russia* (2006).

[20] A. B. Vorob'ev *et al*, *J. Appl. Phys.* (2006).

[21] N. Y. Jin-Phillipp *et al*, *Appl. Phys. Lett.* **88**, 021913 (2006).

[22] C. Deneke, N. Y. Jin-Phillipp, I. Loa, O. G. Schmidt, *Appl. Phys. Lett.* **84** (22) 4475 (2004).

[23] N. Ohtani *et al*, *Physica E* **17** (1–4) 391 (2003).

[24] S. Mendach *et al*, *Physica E* **23** (3–4) 274 (2004).

[25] L. Zhang *et al*, *Nanotechnology* **16** (6) 655 (2005).

[26] Dominik J. Bell, *Nano Lett.*, **6** (4), 725 (2006).

[27] M. Huang *et al*, *Advanced Materials* **17** 23, 2860 (2005).

[28] M. V. Entin, L. I. Magarill, *Phys. Rev. B* **66** (20), 205308 (2002).

[29] A. V. Chaplik, R. H. Blick, *New J. of Phys.* **6** 33 (2004).

[30] A. I. Vedernikov, A. V. Chaplik, *Semiconductor* **38** (11), 1316–1322 (2004).

[31] O. V. Kibis, D. G. W. Parfitt, M. E. Portnoi, *Phys. Rev. B* **71** (3), 035411 (2005).

[32] G. P. Nikishkov, I. Khmyrova, V. Ryzhii, *Nanotechnology* **14** (7), 820 (2003).

[33] I. R. Shein *et al*, *JETP Letters*, **76** (3), 189 (2002).

[34] V. Luchnikov, O. Sydorenko, M. Stamm, *Adv. Mater.* **17** (9), 1177 (2005).

[35] E. A. Ivanova, N. F. Morozov, *Doklady Physics*, **50** (2), 83 (2005).

[36] D. V. Bulaev, V. A. Geyler, V. A. Margulis, *Phys. Rev. B*, **69** (19), 1953 (2004).

[37] H. C. Chen, K. F. Liao, S. W. Lee, L. J. Chen, *Thin Sol. Films*, 469 483 (2004).

[38] Y. Takagaki, Y. J. Sun, O. Brandt, K. H. Ploog, *Appl. Phys. Lett.* **84** (23), 4756 (2004).

[39] A. Kleiner, *Phys. Rev. B* **67** (15), 155311 (2003).

[40] D. V. Zav'yalov, S. V. Kryuchkov, *Phys. Sol. Stat.* **47** (6), 1169 (2005).

[41] M. M. A. J. Voncken *et al*, *J. Phys. Cond. Matter.* **16** (21), 3585 (2004).

[42] K. S. Novoselov *et al*, *Science* **306**, 666–669 (2004).

14th Int. Symp. "Nanostructures: Physics and Technology"
St Petersburg, Russia, June 26–30, 2006

Nanoimprint and reactive ion etching for fabrication of Si/SiO_2 NEMS structures

G. Luo[2], *I. Maximov*[1], S. Ghatnekar-Nilsson[1], D. Adolph[1], M. Graczyk[1], P. Carlberg[1], D. Hessman[1], T. Zhu[2], Z. F. Liu[2], H. Q. Xu[1] and L. Montelius[1]

[1] Division of Solid State Physics and The Nanometer Structure Consortium, Lund University, Box 118, S-221 00 Lund, Sweden
[2] Key Laboratory for the Physics and Chemistry of Nanodevices, Center for Nanoscale Science andTechnology (CNST), College of Chemistry & Molecular Engineering, Peking University, 100871, China

Abstract. Scientific efforts aimed at extending of planar technology achievements over fabrication of three-dimensional objects are briefly overviewed. Previously, we showed that ultra-thin epitaxial heterofilms (down to two monolayers for InGaAs/GaAs) can be controllably detached from substrates, and rolled or buckled, under the action of the internal strain, allowing one to form micro- and nanoshells, including tubes and corrugations. The diameter of obtained tubes was down to 2 nm, and the period of nanocorrugated systems was down to 10 nm. New experimental and theoretical results on quantum confinement and quantum transport in semiconductor and hybrid nanoshells are presented. Possible extension of this approach to the case of carbon shells is considered.

Previously we have demonstrated nanoimprint-based fabrication technology of tunable interdigitated cantilever arrays [1, 2]. They are based on interdigitated SiO_2/metal double-finger cantilevers, which are produced using nanoimprint lithography (NIL) and reactive ion etching (RIE). The dimensions are chosen so that the interdigitated cantilevers will, when electrostatically actuated, preferentially bend and move in the lateral mode whereby the shape of the interdigitated structure will change in a tunable fashion.

The structure, resembling a tunable grating structure, can be used in a variety of applications, e.g. as optical gratings for polarization filters, antireflection surfaces [3], as well as in nano electromechanical system (NEMS) devices for detection of bio-molecules [4].

For the processing of the NEMS devices we used the technology of NIL, UV-lithography and RIE. The nanoimprint lithography was performed using a 1″ stamp and a double-layer resist (PMMA/LOR) technique. The details of stamp fabrication are described elsewhere [5]. After the NIL at $T = 200\,^{\circ}\mathrm{C}$ and $P = 50$ bar, a 30 nm thick Cr layer was defined by a lift-off procedure. Then anisotropic CHF_3-based etching of the SiO_2 in combination with an isotropic SF_6/O_2-based RIE of Si released the 200 nm wide SiO_2 interdigitated cantilevers having a 600 nm periodicity. Cantilevers of different widths and periodicity were produced. Finally, a 50 nm thick Cr/Au layer was thermally evaporated to be able to apply a bias voltage to

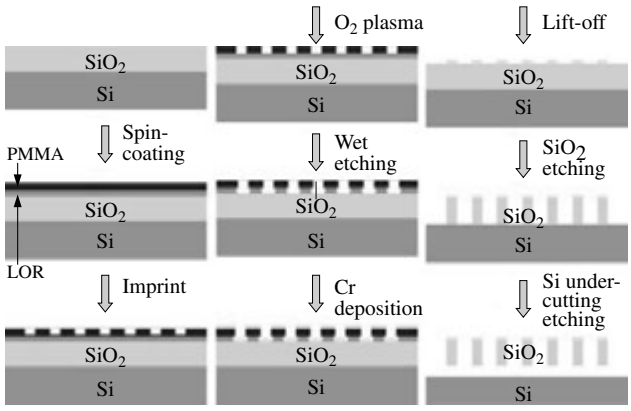

Fig. 1. The schematic of the NEMS fabricating process. The processing is based on pattern transfer using NIL in a double-layer resist system (PMMA/LOR), Cr lift-off for making etch mask, anisotropic SiO_2 etching to form grating structures and isotropic Si etching to release the cantilevers. A 50 nm thick Au layer is deposited afterwards to contact the cantilevers with the larger contact pads made using UV-lithography.

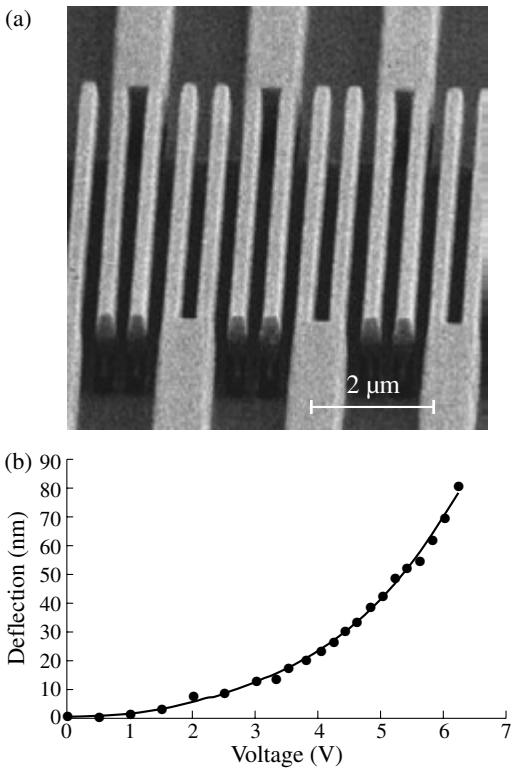

Fig. 2. (a) Example of the NEMS cantilevers after the final processing step. The width of the cantilevers is 200 nm, separation between them is 550 nm. Up to 6 NEMS devices 15 by 50 μm^2 in size are imprinted using 1" NIL stamp. (b) Optical measurements of the average deflection of the ends of the cantilevers on the NEMS device as a function of the applied voltage. Voltages larger than 6.5 V result in a "snap-in" effect, when the cantilevers stick to each other.

the grating. Figure 1 shows the fabrication steps of the NEMS structures.

In this presentation we will report about the fabrication details of the NEMS devices (Figure 2a) as well as measurements of the lateral deflection of the cantilevers (Figure 2b) as a function of applied bias. In addition, the static optical reflection of a polarized light and the possibility to use these structures to tune their optical properties will be discussed.

Acknowledgements

The support from the Swedish Foundation for Strategic Research (SSF), the Swedish Research Council (VR) and European Commission through the project NaPa (NMP4-CT-2003-500120) is gratefully acknowledged. All views expressed or implied in this paper are exclusively those of the authors and the European Community is not liable for any use that may be made of the information contained therein.

References

[1] G. Luo, I. Maximov, M. Graczyk, D. Adolph, P. Carlberg, T. Zhu, Z. F. Liu, H. Q. Xu and L. Montelius, *Proc. Micro- and Nano-Engineering (MNE) Conference*, Vienna, Austria 2005, book of abstracts.

[2] G. Luo, I. Maximov, D. Adolph, M. Graczyk, P. Carlberg, S. Ghatnekar-Nilsson, D. Hessman, T. Zhu, Z. F. Liu, H. Q. Xu and L. Montelius, *Nanotechnology*, accepted for publication (2006).

[3] Chee Wei Wong, Yongbae Jeon, George Barbastathis, Sang-Gook Kim, *J. of Microelectromechanical Systems* **13**, 998 (2004).

[4] H. C. Craighed, *Science* **290**, 1532 (2000).

[5] I. Maximov, P. Carlberg, D. Wallin, I. Shorubalko, W. Seifert, H. Q. Xu, L. Montelius and L. Samuelson, *Nanotechnology* **13**, 666 (2002).

14th Int. Symp. "Nanostructures: Physics and Technology"
St Petersburg, Russia, June 26–30, 2006

High ferromagnetic phase transition temperatures of thin GaMnAs layers annealed under arsenic capping

J. Sadowski[1,2], J. Z. Domagałai[1], V. Osinniyi[1], J. Kanski[3], M. Adell[3], L. Ilver[3], C. Hernandez[4], F. Terki[4], S. Charar[4] and D. Maude[5]

[1] Institute of Physics, Polish Academy of Sciences, al Lotników 32/46, 02-668 Warszawa, Poland
[2] MAX-lab, Lund University, SE-221 00, Lund, Sweden
[3] Department of Experimental Physics, Chalmers University of Technology, SE-41296 Göteborg, Sweden
[4] Groupe dEtude des Semiconducteurs CC074, Université Montpellier II, Montpellier, France
[5] High Magnetic Field Laboratory, CNRS-MPI, 25 Avenue des Martyrs, 38042 Grenoble, France

Abstract. Thin GaMnAs layers were grown by molecular beam epitaxy and were subjected to low temperature post growth annealing under an arsenic capping layer. Modifications of the magnetic, transport and structural properties due to the post-growth annealing are presented. It is shown that the presence of arsenic capping significantly shortens the annealing time for complete removal of Mn interstitials from the GaMnAs volume. As a result the concentration of free carriers is increased, and the ferromagnetic phase transition temperature is significantly enhanced. The GaMnAs layers annealed in this way can be further overgrown by epitaxial films.

1. Introduction

GaMnAs is a model semiconductor with carrier induced ferromagnetism. In spite of interesting features associated with the magnetic properties of GaMnAs, it is still desirable to improve its quality and obtain a material with higher ferromagnetic phase transition temperature (T_c), limited nowadays to 173 K. The mean field, Zener model of carrier mediated ferromagnetism in transition metal doped semiconductors developed by Dietl *et al* [1] predicts T_c to reach the room-temperature for GaMnAs containing 10% Mn [2], and sufficiently high concentrations of carriers (valence band holes). The T_c increase in the uniform GaMnAs films was recently achieved as a consequence of developing efficient methods leading to removal of the prevailing compensating defects — Mn in the interstitial positions (Mn_I), which, as shown both theoretically [3] and experimentally [4] are always present in the as-grown GaMnAs, with concentrations of up to about 20% of the total Mn content. As it was first demonstrated by Edmonds *et al* [4], the MnI defects can be removed by a low temperature post-growth annealing of the samples exposed to the air after the MBE growth. The annealing temperatures used in the annealing processes can be lower than the GaMnAs growth temperatures (200–250 °C), and then extremely long annealing times (up to 100 hrs) are used [4]. The low annealing temperatures are the implication of a metastable character of GaMnAs. At temperatures above 300 °C it starts to decompose to MnAs inclusions inside the GaAs matrix.

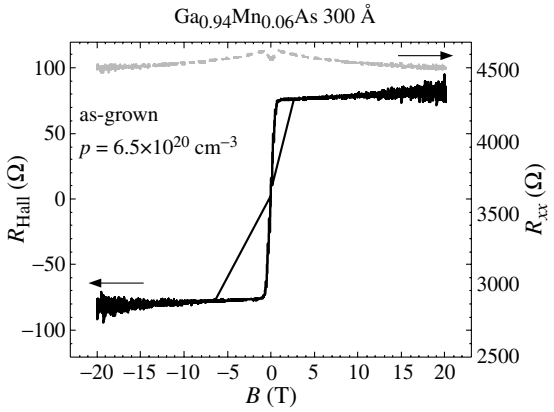

Fig. 1. Results of Hall effect measurements of as-grown 300 Å thick $Ga_{0.94}Mn_{0.06}As$. Solid curve — hall resistance R_{Hall}, dashed curve — longitudinal resistance R_{xx}. The concentration of holes in the sample is equal to 6.5×10^{20} cm^{-3}, which means 50% compensation of MnGa acceptors.

2. Sample preparation

Here we present a modification of the low temperature post-growth annealing method, which uses amorphous As layers deposited on GaMnAs surface directly after the MBE growth as a passivating medium for out-diffused Mn interstitials. This annealing treatment leaves GaMnAs surface suitable for further epitaxy, either in the same MBE system, which was used for the GaMnAs layer growth, or in another MBE system, since As capping forms a protective layer inhibiting the surface oxidation and preserving clean, atomically flat, as-grown surface.

3. Transport, magnetic and structural properties

Figs. 1 and 2 show results of high field Hall effect measurements of 300 Å thick $Ga_{0.94}Mn_{0.06}As$ layer before and after

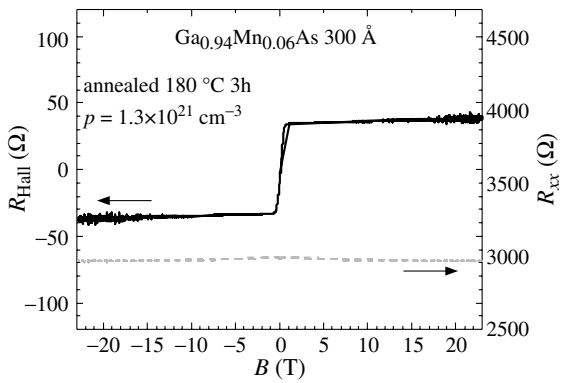

Fig. 2. Results of Hall effect measurements of the same sample as shown in Fig. 1 after the post growth annealing at 180 °C for 3 h. The concentration of holes is equal to 1.3×10^{21} cm^{-3}, which corresponds almost exactly to the content of MnGa.

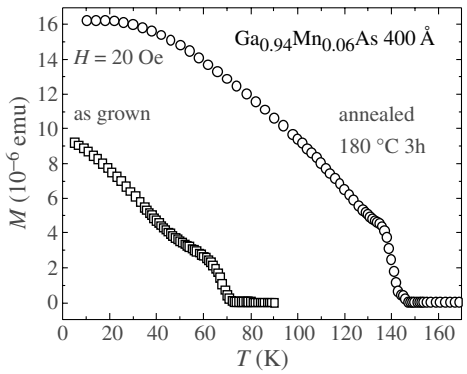

Fig. 3. Temperature dependence of magnetization for 400 Å thick $Ga_{0.94}Mn_{0.06}As$ with amorphous As capping before and after post-growth annealing at 180 °C for 3 h.

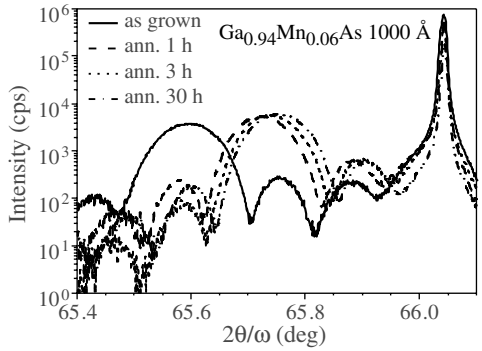

Fig. 4. (004) X-ray Bragg reflections for non annealed and annealed pieces of As capped 1000 Å thick $_{0.94}Mn_{0.06}As$ layers. The shifts of GaMnAs diffraction peaks to higher angles are due to the annealing induced reduction of GaMnAs lattice parameter.

post-growth annealing treatment.

The increase of hole concentrations in annealed GaMnAs leads to increase of T_c, as shown in temperature dependence of magnetization presented in Fig. 3. After post-growth annealing, T_c of 400 Å thick $Ga_{0.94}Mn_{0.06}As$ layer increased from 75 K to 145 K. The T_c increase is correlated with the increase of a saturation magnetisation at low temperatures. This is due to annealing induced removal of antiferromagnetically coupled pairs of Mn_{Ga}-Mn_I, which are excluded from participating in FM phase in the non-annealed sample.

The annealing efficiency is also confirmed by XRD measurements. Mn interstitials cause the GaMnAs lattice expansion, so the lattice constant decrease is expected in the samples, in which Mn_I were removed by the post-growth annealing. This effect is shown in Fig. 4. The figure shows significant shifts of (004) Bragg reflections from a $Ga_{0.94}Mn_{0.06}As$ 1000 Å thick layer after consecutive annealings.

References

[1] T. Dietl *et al*, *Phys. Rev. B* **63**, 195205 (2001).
[2] T. Dietl *et al*, *Semicond. Sci. Technol.* **17**, 377 (2002).
[3] J. Masek *et al*, *Acta Phys. Pol. A* **100**, 319 (2001).
[4] K. Edmonds *et al*, *Phys. Rev. Lett.* **92**, 037201 (2004).

14th Int. Symp. "Nanostructures: Physics and Technology"
St Petersburg, Russia, June 26–30, 2006

Self-organizating chain-like nanostructures created by Cs and Ba adatoms on GaN(0001) n-type surface

G. V. Benemanskaya, G. E. Frank-Kamenetskaya, V. S. Vikhnin and S. N. Timoshnev
Ioffe Physico-Technical Institute, St Petersburg, Russia

Abstract. We report on new effect of self-organization of regular nanostructure that is created in situ due to both multiple Cs and Ba adsorption on GaN(0001) n-type surface and ulterior temperature annealing. The nanostructure is characterized by high regularity in macroscale and by parameters of cell of the chain in nanoscale. Namely, high of cell is about of 6 nm and diameter of cell corresponds to about of 50 nm. The nanostructure has been investigated by AFM, electron microscopy and threshold photoyield spectroscopy. It is found that chain-like nanostructure is formed by solid solution with metallic-like conductivity. Photoemission from chain-like nanostructure has been found by excitation of visible light in the transparency region of GaN. Under coadsorption Cs and Ba, sharp decrease in photoemission thresholds up to 1.40 eV is revealed and shown to be due to formation of an electron accumulation layer in the near-interface region.

Introduction

We have experimentally achieved the creation of new regular superstructure that is formed in situ by Cs and Ba adatoms on GaN(0001) n-type surface. The possibility of growing of similar structures has not yet been examined. Electronic and atomic properties of III-nitride surfaces are still poorly understood and then they give rise controversy despite effective technology progress in growing of high-quality materials and their application to high power electronic, photodetectors and light emitting devices. The GaN(0001) surface and metal/GaN interfaces were studied by conventional Auger electron, core-level, X-ray and ultraviolet photoemission spectroscopies. However, atomic structure and electronic properties concerning origin of bonding and discrepancy in adsorption effect have not yet been settled. The ultrathin Cs/n-GaN and Ba/n-GaN interfaces are now studied [1, 2]. Anomalous behavior of band-bending near the surface and new phenomenon of formation of surface electron accumulation layers have been revealed. It is noteworthy to point out that accumulation layers were obtained previous to our studies exclusively on clean surfaces (InAs and InN).

1. Experimental results and discussion

The nanostructure has been created in situ in a vacuum of $P \sim 5\times10^{-11}$ Torr. The GaN(0001) n-type sample was Si-doped (3.5×10^{17} cm^{-3}) GaN epilayer of thickness $d \sim 3.6\,\mu$m grown on (0001) sapphire substrate by MOCVD. Prior to studies, sample was annealed in situ at $\sim 700\,^{\circ}$C.

To study the electronic properties of ultrathin Cs+Ba/GaN interfaces using submonolayer adatom coverages and onwards the created nanostructure, the technique of photoemission yield spectroscopy (PYS) with excitation by the s- and p- polarized light is used. Details of PYS can be found elsewhere [1–3].

To ascertain Cs and Ba coverages, sources are accurate calibrated to dosage using original technique [3]. The Cs and Ba overlayers are presented in monolayer (ML) units. Note that the 1 ML is defined as one metal adatom per GaN(0001) 1×1 surface atom and equal to 9.89×10^{14} atoms$\times$cm^{-2}. AFM image of the clean starting surface is presented in Fig. 1. As can been seen, the sample is characterized by atomically smooth surface.

Farther, in situ both the Cs and Ba submonolayer coverages are in series adsorbed on the sample.We study the photoemission and electronic properties of Cs+Ba/GaN interfaces in submonolayer coverage region. For example, the 0.2 ML of Ba and in series from 0.1 ML to 0.8 ML of Cs are adsorbed. Fig. 2 represents drastic decrease in photoemission threshold $h\nu_S$ corresponding to the work function φ ($h\nu_S = \varphi$) as a function of Cs coverage on n-GaN surface covered by 0.2 ML of Ba. The work function minimum is found to reduce up to 1.4 eV.

Photoemission from accumulation layer is revealed by excitation of visible light in the transparency region of GaN. Beyond each evaporation the photoemission studies are carried

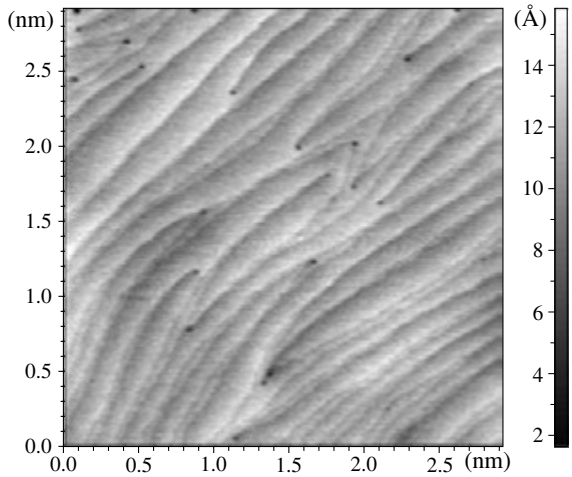

Fig. 1. AFM image of the clean n-GaN(0001) surface: topography $3\times3\,\mu$m.

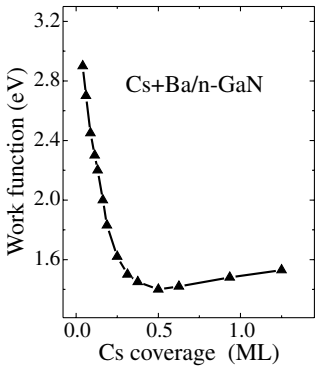

Fig. 2. Change in the work function as a function of Cs coverage on n-GaN(0001) surface with Ba coating 0.2 ML.

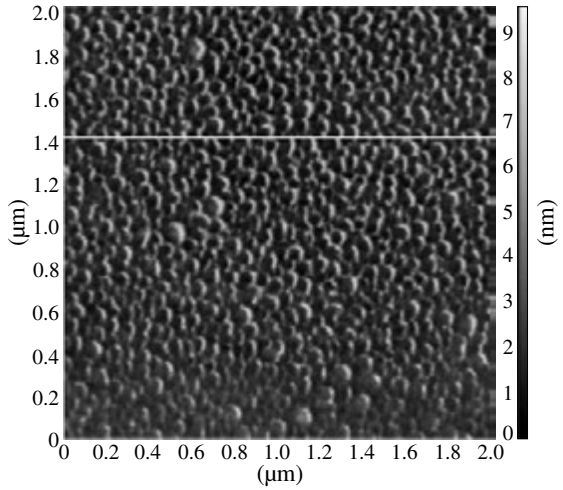

Fig. 3. AFM image of regular chain-like nanostructure on n-GaN(0001) surface: topography 2×2 *mu*m.

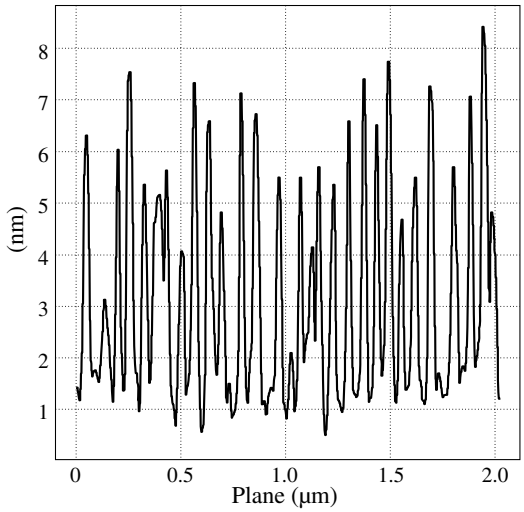

Fig. 4. AFM image of regular chain-like nanostructure on n-GaN(0001) surface: cross-section of topography 2×2 *mu*m with period of nanostructure of ∼ 60 nm.

out and then the sample is annealed at ∼ 700 °C. After, the 0.5 ML of Ba and 0.5 ML of Cs are adsorbed and so on. Each combination of coadsorbed layers is found to sharp decrease the work function and to cause the significant increase in quantum efficiently of photoyield. Then, new effect of formation of the electron accumulation layer in band-bending region of GaN in the close vicinity of the surface is found. Therefore, metallic-like accumulation layer is due to coadsorption of Cs and Ba.

We present new experimental results on self-organization of novel regular nanostructure that is revealed after multiple coadsorption Cs and Ba on n-GaN(0001) surface and temperature annealing. Figures 3 and 4 demonstrate the crated chain-like nanostructure.

As can been seen, the nanostructure is characterized by highness of regularity that is observed at anyone area of surface. Size of chain-like nanostructure is ∼ 50 nm and high of cell is ∼ 6 nm. Fig. 5 represents in detail the set of nanocells on the 3D image.

The nanostructure is stable in air condition for weeks. Data of electron microscopy show that chain-like nanostructure is formed by solid solution BaGaN. So, new effect of self-organization of regular nanostructures is discovered. This effect can

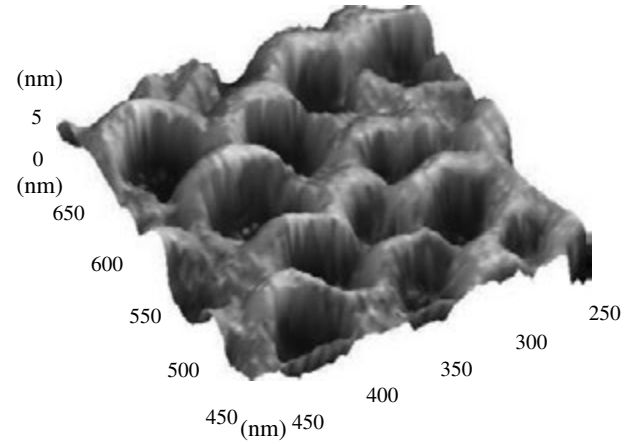

Fig. 5. 3D AFM image of chain-like nanostructure on n-GaN(0001) surface: 200 nm × 200 nm.

also lead to new properties and applications.

Acknowledgements

The authors thank N. Shmidt and M. Dunaevskii for assistance and discussions. This work was supported by grant # 04-02-17621 of RFBR and by the program P-03, grant #2 of Presidium of RAS.

References

[1] G. V. Benemanskaya, V. S. Vikhnin, N. M. Shmidt, G. E. Frank-Kamenetskaya and I. V. Afanasiev, *Appl. Phys. Lett* **85**, 1365 (2004).

[2] G. V. Benemanskaya, V. S. Vikhnin, G. E. Frank-Kamenetskaya, N. M. Shmidt, *JETP Lett* **77**, 226 (2003).

[3] G. V. Benemanskaya, G. E. Frank-Kamenetskaya, *Surf. Sci.* **523**, 211 (2003).

14th Int. Symp. "Nanostructures: Physics and Technology"
St Petersburg, Russia, June 26–30, 2006

The role of one-dimensional diffusion in a growth model of the surface of a Kossel's crystal

A. M. Boiko and R. A. Suris
Ioffe Physico-Technical Institute, St Petersburg, Russia

Abstract. 100 The kinetic mechanism of defect formation on a vicinal surface misoriented in two directions, in the case of molecular-beam epitaxy, is studied. These defects are two adatoms stuck together in a potential trench near the step edge. The effects of the surface parameters, as well as growth rate on the probability of defect formation are studied. It is shown that an increase in the misorientation angle of the surface is conducive to a drastic decrease in the number of defects during growth.

Introduction

Tokura *et al* [1] studied the system stability of straight parallel equidistant atomic steps on the growth surface with respect to fluctuations of the distances between these steps (nonflexural fluctuations) was shown that this system is stable to fluctuations of distances between atomic steps, if the rate of incorporation of an atom that came to the step from the lower terrace side is higher than the incorporation rate for an atom that arrived from the upper terrace (i.e., if there is asymmetry in the incorporation).

In 1990, Bales and Zangwill [2] published the results of a study concerning the problem of vicinal surface growth stability (composed of parallel equidistant steps), with respect to flexural fluctuations. It was shown [2] that such a system is generally unstable in respect to fluctuations in the step-edge bending form.

In 1992, Aleiner and Suris [3] suggested a new mechanism (the so-called kink-flow mechanism, in analogy with the step-flow mechanism from [1]). this mechanism made it possible to suppress the instability under consideration. In order to attain stabilization in the kink-flow mechanism, an atom must be incorporated into a kink by being captured in a potential trench, near the step, with subsequent one-dimensional (1D) diffusion to the kink, in this trench, rather than directly from the terrace. The stability is ensured by the asymmetry of the adatom capture by the step edge in the step-flow case, whereas capture asymmetry is related not only to the capture by the step edge, but also to the adatom capture by the step-edge kink, in the case of the kink-flow mechanism. The potential trench is a 1D trap for adatoms and is bounded by a reflecting edge on one side and by an adsorbing edge on the other side.

The surface formed from identical kinks and that was appropriate for accomplishing kink-flow growth was considered in [3]. On such a surface, we have existing kinks, due to surface misorientation, so crystal growth occurs owing to the motion of kink lattice, with-out the formation of new kinks, in contrast to the step-flow mechanism.

The concept of the existence of both a potential trench at a step edge and a diffusive transport mechanism was actively used in [4-6].

The potential trench at the step edge exhibits an important specific feature: if at least two atoms are found in this trench, they can stick together and form a 1D nucleus of a new atomic row (see [7]). In what follows, we use the term "1D two-atom nucleus".

In publications [8-11], origination of 1D two-atom nuclei is considered as an obstacle to diffusion along the step edge; as a result, diffusion disappears with time. That 1D nuclei can be formed was mentioned by Aleiner and Suris, who planned to study this process in detail later.

In this study, we consider the formation process of 1D two-atom nuclei in the potential trench, at the step edge, in detail. We will show that a 1D two-atom nucleus not only becomes an obstacle to free diffusion of adatoms in this potential trench, but also causes the inevitably of step edge bending (Fig. 3b); as a result, defects are produced in the kink-flow mode of growth. We will show that the formation probability of a 1D two-atom nucleus depends on atomic flux.

References

[1] Y. Tokura, H. Saito, and T. Fukui, *J. Cryst. Growth* **94**, 46 (1989).
[2] G. S. Bales and A. Zangwill, *Phys. Rev*. B **41**, 5500 (1990).
[3] I. L. Aleiner and R. A. Suris, *Fiz. Tverd. Tela (St Petersburg)* **34**, 1522 (1992)
[4] O. Pierre-Louis, M. R. D'Orsogna, and T. L. Einstein, *Phys. Rev. B* **82**, 3661 (1999).
[5] N. C. Bartelt, T. L. Einstein, and E. D. Williams, *Surf. Sci. Lett.* **240**, L591 (1990).
[6] H. Emmerich, *Phys. Rev.B* **65**, 233406 (2002).
[7] V. V. Voronkov, *Kristallografiya 15,* **13** (1970) [Sov. Phys. Crystallogr. 15, 8 (1970)].
[8] V. P. Evtikhiev, V. E. Tokranov, A. K. Kryzhanovski, *et al*, *Fiz. Tekh. Poluprovodn. (St Petersburg)* **32**, 860 (1998) [Semiconductors 32, 765 (1998)].
[9] V. P. Evtikhiev, V. E. Tokranov, A. K. Kryzhanovskii, *et al*, *J. Cryst. Growth* **201–202**, 1154 (1999).
[10] V. P. Evtikhiev, A. M. Boiko, I. V. Kudryashov, *et al*,*Solid State Technol*. **17**, 545 (2002).
[11] W. Burton, N. Cabrera, and F. Frank, *Philos. Trans. R. Soc. London, Ser.* **A** 243, 299 (1951).

14th Int. Symp. "Nanostructures: Physics and Technology"
St Petersburg, Russia, June 26–30, 2006

MnP and Ge self-assembled nanowhiskers on InP(001)

A. D. Bouravleuv[1,2], K. Minami[1], T. Ishibashi[1] and K. Sato[1]

[1] Graduate School of Engineering, Tokyo University of Agriculture and Technology, 184-8588 Tokyo, Japan
[2] Ioffe Physico-Technical Institute, St Petersburg, Russia

Abstract. Self-assembled Ge and MnP nanowhiskers as thin as 20 nm and as long as 2 μm were synthesized by molecular-beam epitaxy (MBE) technique on InP(001) surface concurrently. The growth of Ge nanowhiskers is found to be assisted by Mn-based nanocluster-mediated VLS mechanism of growth, whereas the growth of MnP nanowhiskers seems to be caused by catalyst-free mechanism. Magnetic property measurements revealed that samples with prevailing Ge nanowhiskers exhibit ferromagnetic behaviour up to room temperature.

Introduction

One-dimensional nanostructures such as nanorods, nanotubes, nanowhiskers have attracted much attention due to their importance for nanoscale device applications [1-3]. Among them magnetic self-assembled nanowhiskers deserve special attention because their fabrication makes possible to tune the Curie temperature, remanent magnetization and coercive saturation field by means of the control over their sizes, shapes and distributions that in turn allows us to utilize such materials not only for data storage and nanoscale spintronics applications, but also for the investigation of the fundamental magnetic properties of low-dimensional structures. Recently Mn-doped nanowhiskers have been successfully synthesized using different methods [4-8]. Mn-doped ZnO and GaN nanowhiskers exhibiting ferromagnetic behaviour were prepared by vapor-phase evaporation [4] and chemical vapor deposition (CVD) [5], respectively. The similar magnetic properties have been shown by Mn^+ ion implanted ZnO nanowhiskers [6]. Mn-doped CdS and ZnS nanowhiskers have been fabricated using a core/shell methodology [7]. Furtermore, MnP nanorods were synthesized via thermal decomposition of continuously delivered metal-phoshine complexes [8].

In this work, we report on a molecular beam epitaxial fabrication and characterization of Ge and MnP nanowhiskers on the InP(001) surface.

1. Methods

Contrary to usual metal catalyst vapour-liquid-solid (VLS) growth [1, 2], under that the formation of the nanowhiskers occurs due to the adsorption of the gas-phase reactants by liquid droplets formed from nanosized metal clusters, in our experiments we did not use any preliminary tailor-made metal catalyst layer. Self-assembled (SA) nanowhiskers have been grown by conventional molecular beam epitaxy (MBE) on InP(001) substrate using Knudsen cells for the Mn and Ge evaporation as well as cracking cell for the decomposing of tertiarybutylphosphine (TBP) into P_2 flux. The epi-ready InP(100) wafers were annealed at 480 °C in vacuum inside a treatment chamber in a P_2 flow for 20 minutes. The duration of growth ranged from 30 minutes up to 2 hours at the temperatures between 430−545 °C. The beam flux of Mn was adjusted in the range between $0.5-0.9\times10^{-8}$ Torr and that of Ge in the range between $0.9-1.5\times10^{-8}$ Torr using an ion gauge. The flow rate of TBP gas was set at 2.0 sccm by using a mass flow controller, whereas the temperature of the cracking cell was kept in the range of 810−835 °C to assure efficient decomposition of TBP into P_2 during the MBE growth. The growth process was monitored using in-situ reflection high energy electron diffraction (RHEED) measurements.

The morphology and microstructure of nanowhiskers were examined by scanning electron microscope (SEM,Hitachi S-4500) and scanning transmission electron microscope (STEM, FEI TECNAI-F20). Chemical compositions were measured using an energy-dispersive X-ray analysis (EDX) attached to the SEM and STEM apparatus. The crystals were analyzed by X-ray diffraction technique using an X-ray diffractometer (XRD, Philips X'Pert type). Temperature and magnetic-field dependences of magnetization were measured by a superconducting quantum interference device (SQUID) and vibration sample (VSM, TOEI VSM-5-19) magnetometers.

2. Results and discussion

SA nanowhiskers grown at different temperatures are shown on Fig. 1. At low temperatures around 430 °C the nanowhiskers with typical diameters close to 20 nm and length up to 2 μm which are spaced at different intervals can be obtained (Fig. 1a and 1b). These individual SA nanowhiskers have preferential direction for growth which corresponds to the ⟨111⟩ crystallographic orientation and seems to be dependent on the crystallographic form and orientation of the host substrate. On further increasing the growth temperature, intervals between

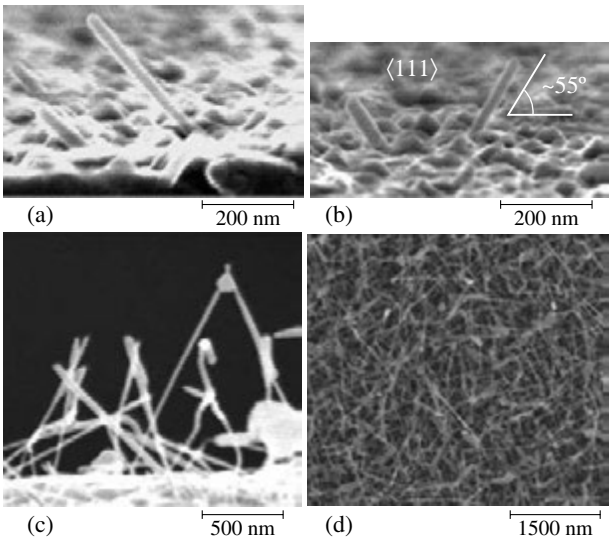

Fig. 1. SEM images of individual (a), (b); arrays (c), (d) SA nanowiskers grown on InP(001) surface. The temperature of the growth: (a), (b) — 435 °C; (c) — 500 °C; (d) — 520 °C.

individual nanowhiskers become smaller and an even distribution of self-assembled nanowhiskers can be fabricated as well (Fig. 1d).

The X-ray diffraction θ-2θ scan data of the samples showed few dominant peaks inherent to all samples. The first of them is a diffraction peak observed at $2\theta \sim 66,4^\circ$, that can be assigned to the $MnGeP_2$ 008 diffraction [9]. Other peaks, which may be related to the MnP 111, 202 and 121, were also detected, therewith at elevated temperatures the signal most likely corresponding to MnP 111 became extinct. However, it should be noted, that the growth of nanowhiskers can be accompanied by the growth of thin film. In this connection some of these peaks may be assigned not only to nanowhiskers but also to the different phases of thin film.

Therefore, we have performed TEM and EDX study of the samples. For these investigations nanowhiskers were transferred onto Cu TEM grid. Energy dispersive X-ray analysis showed that two different types of nanowhiskers can be obtained concurrently: Ge nanowhiskers and MnP nanowhiskers with atomic ratio Mn:P∼65:20. The growth of MnP nanowhiskers is apt to be caused by non-catalytic growth mechanism which has not been thoroughly investigated [10]. The formation of MnP nanowhiskers seems to be dominated at low temperatures (Fig. 1a and 1b) that is in line with XRD results, whereas that of Ge nanowhiskers prevails at high temperatures (Fig. 1c and 1d). In turn, despite the fact that we did not use an tailor-made catalyst compound, the growth of Ge nanowhiskers is found to be amenable to VLS mechanism of growth [1,2] (see Fig. 2). The role of the catalyst for the growth in this case plays Mn-based nanoclusters which seem to be self-assembled at an initial stage of the growth with atomic composition of elements close to Mn:P:Ge 78:5:6%. TEM images (Fig. 2) demonstrate that growth direction of Ge nanowhiskers is along ⟨110⟩. Besides the diameters of Ge nanowhiskers are uniform along their length.

The temperature and magnetic field dependences of magnetization have been measured for the nanowhiskers grown at high temperatures (Fig. 1c and 1d). The measurements have

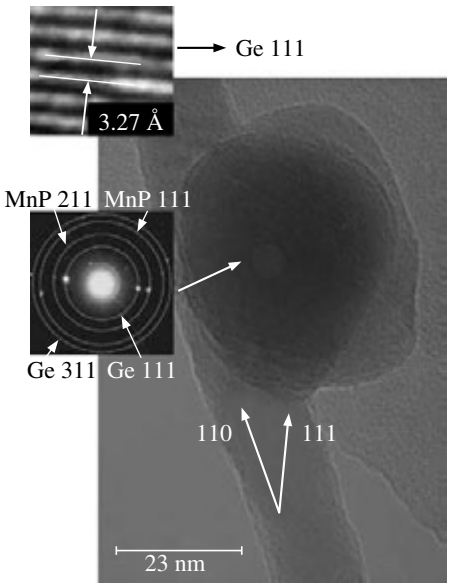

Fig. 2. TEM characterization of Ge nanowhisker with Mn-based nanocluster. Insets: HRTEM image of Ge nanowhiskers and the diffracrion pattern of Mn-based nanocluster.

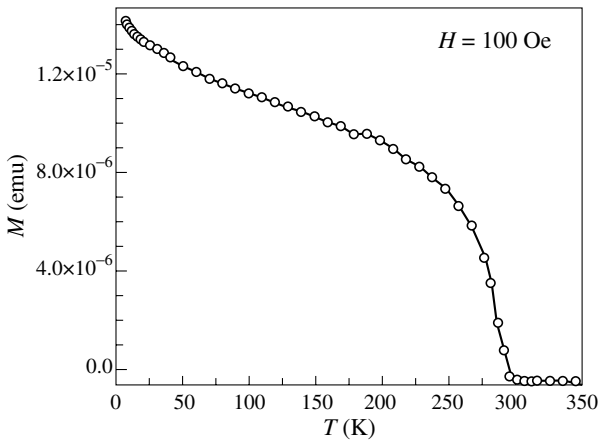

Fig. 3. The temperature dependence of magnetization for pilled off SA nanowhiskers which were grown at 520 °C (see Fig. 1d)

been carried out for both SA nanowhiskers on InP substrates and nanowhiskers which have been pilled off from wafers (see Fig. 3). The magnetization is observed to exhibit ferromagnetic behaviour up to room temperature therewith it is distinct from that of $MnGeP_2$ thin film [9]. This behaviour may be caused by most likely the presence of Mn_3Ge_5 phase [11], and yet we have to take into account that MnP can also be responsible for it [8]. Although the nature of this ferromagnetism is still an open question that requires an additional clarification such structures would be expected to exhibit the size-depended magnetic properties which are of particular interest for nanometer scale spintronics applications.

Acknowledgements

This work has been supported by 21st Century COE Program Future Nano-Materials of TUAT and Japanese Society for Promotion of Science (P 06112). We sincerely thank S. Mitani from Tohoku University, H. Sosiati and N. Kuwano from Kyushu University for their help in measurements.

References

[1] F. Patolsky, C. M. Lieber, *Materials Today* **8/4**, 20 (2005).
[2] L. Samuelson *et al*, *Physica E* **21**, 560 (2004).
[3] G.-C. Yi *et al*, *Semicond. Sci. Technol.* **20/4**, S22 (2005).
[4] Y. Q. Chang *et al*, *Appl. Phys. Lett.* **83/19**, 4020 (2003).
[5] L. Sun *et al*, *Appl. Phys. Lett.* **86**, 032506 (2005).
[6] K. Ip *et al*, *J. Vac. Sci. Technnol. B* **21/4**, 1476 (2003).
[7] P. V. Radovanovic *et al*, *Nano Lett.* **5/7**, 1407 (2005).
[8] J. Park *et al*, *J. Am. Chem. Soc.* **127**, 8433 (2005).
[9] K. Sato *et al*, *J. Chem. Solids* **66/11**, 2030 (2005).
[10] W. I. Park *et al*, *Adv. Mater.* **14**, 1841 (2002).
[11] R. P. Panguluri *et al*, *Phys. Stat. Sol. (b)* **242/8**, R67 (2005).

14th Int. Symp. "Nanostructures: Physics and Technology"
St Petersburg, Russia, June 26–30, 2006

STM and AFM imaging and manipulation of individual CdSe nanorods

G. Comtet[1], R. Bernard[1], E. Boer-Duchemin[1], G. Dujardin[1], A. J. Mayne[1] and V. Huc[2]

[1] Laboratoire de Photophysique Molèculaire, bât. 210,Universitè Paris-Sud, 91405 Orsay France
[2] Laboratoire de Chimie Inorganique, bât. 420, Universitè Paris-Sud,
91405 Orsay France

Abstract. Self-assembled Ge and MnP nanowhiskers as thin as 20 nm and as long as 2 μm were synthesized by molecular-beam epitaxy (MBE) technique on InP(001) surface concurrently. The growth of Ge nanowhiskers is found to be assisted by Mn-based nanocluster-mediated VLS mechanism of growth, whereas the growth of MnP nanowhiskers seems to be caused by catalyst-free mechanism. Magnetic property measurements revealed that samples with prevailing Ge nanowhiskers exhibit ferromagnetic behaviour up to room temperature.

We have studied the adsorption and the manipulation of CdSe individual nanorods on the hydrogenated silicon Si (100), hydrogenated diamond C (100) and HOPG graphite surfaces. Objectives are to control the relative positions of the CdSe nanorods and to explore their electromagnetic and/or electronic couplings.

A new deposition method of nano-hybrids on perfectly cleaned and atomically reconstructed surfaces has been finalized, using a pulse valve under ultra high vacuum. The self-organization of the nanorods has been observed on the hydrogenated Si (100) surface with a scanning tunneling microscope (STM), on the HOPG graphite surface with the scanning electron microscope (SEM) and on the hydrogenated diamond surface with the atomic force microscope (AFM). A self-ordering of the nanorods following particular cristallographic orientations has been observed, in the case of silicon and graphite surfaces. This self-ordering is explained by the role of the phosphonate ligands surrounding the nanorods. The van der Waals interactions determine specific orientations of the ligands on these surfaces, which drive the nanorods along directions perpendicular to the ligand orientations. The cooperative effect of hundred of ligands to orientate a CdSe nanorod illustrates a "Lilliputien" effect at the nanoscale.

Preliminary experiments have shown that it is possible to move the individual nanorods on the graphite and hydrogenated diamond surface, using the AFM in "contact" and "tapping" modes.

14th Int. Symp. "Nanostructures: Physics and Technology"
St Petersburg, Russia, June 26–30, 2006

Kinetic origin of III–V and II–VI quantum dot formation

V. G. Dubrovskii[1,2], G. E. Cirlin[1–3], Yu. G. Musikhin[1], A. A. Tonkikh[1–3], Yu. B. Samsonenko[1–3], N. K. Polyakov[1–3], S. V. Sorokin[1], I. V. Sedova[1], A. A. Sitnikova[1], S. V. Ivanov[1] and V. M. Ustinov[1,2]

[1] Ioffe Physico-Technical Institute, St Petersburg, Russia
[2] St Petersburg Institution for Research and Education RAS, St Petersburg, Russia
[3] Institute for Analytical Instrumentation RAS, St Petersburg, Russia

Abstract. We report on the kinetic origin of quantum dot formation in the InAs/GaAs and CdSe/ZnSe heteroepitaxial systems. We present a kinetic model of stress-driven quantum dot formation and the experimental data on the dependence of surface morphology on the MBE growth conditions such as the surface temperature and deposition rate. The results obtained demonstrate that the mean size of islands increases and their density decreases at higher surface temperature and lower deposition flux for the both material systems studied.

1. Introduction

Self-organized growth of dense and uniform ensembles of different III–V and II–VI quantum dots (QDs) by molecular beam epitaxy (MBE) in highly mismatched material systems [1] is now widely used for the fabrication of advanced nanostructures for electronic, optical and biological applications. One of the key issues in the QD growth technology is the development of reliable techniques for the production of controllably structured QDs with the desirable properties. Recently, some of the authors of this work developed kinetic approach to QD formation during MBE [2] that enables one to tune structural properties of QD ensembles by changing technologically controlled growth conditions. The potential of this approach has been demonstrated in the case of InAs/GaAs(100) and Si/Ge(100) material systems [3].

In this work, we continue the studies of InAs/GaAs QDs and also try to expand the existing kinetic approach to GdSe/ZnSe QDs. It will be demonstrated that, while the physics of self-organized growth and qualitative characteristics of QDs in these two systems are very different, qualitative temperature and flux dependences of QD size and density remain the same and therefore can be tuned by relatively simple modifications of growth schemes. The presented results also support our previous conclusions on the essentially kinetic origin of QD formation within a wide range of parameters and material systems.

2. Theory

Kinetic models [2–4] treat the process of island formation in highly mismatched heteroepitaxial systems as a first-order phase transition, with a sea of adatoms or a wetting layer playing the role of a metastable phase and 3D coherent strained islands being the nuclei of a new phase. Nucleation and growth of islands is essentially stress-driven: islands are formed because the elastic energy in a 3D island is smaller than in a 2D layer.

In Ref. [2] it has been shown that, under certain assumptions, the theory allows a complete dynamical description of different stages of QF formation and the calculation of island distribution function depending on the growth time t. In the case of Stranski–Krastanow growth from a metastable wetting layer, the following equations for the surface density N, the mean lateral size $L_*(t)$, and the lateral size distribution $g(L,t)$ of QDs have been obtained [2, 3]

$$N = \frac{4}{l_0^2}\frac{h_{\rm eq}}{d_0}\frac{T}{T_{\rm e}}\left(\frac{u(Q)}{Q}\right)^{3/2}, \tag{1}$$

$$\begin{cases} 3l\frac{dl}{dt} + l^3 = \varphi^3(t)\,, \\ l(t=0) = 0\,, \end{cases} \tag{2}$$

$$g(L,t) = cN\exp\left(cx(L,t) - e^{cx(L,t)}\right) \tag{3}$$

Here, $Q \propto \frac{1}{VT}\exp\left(-\frac{T_{\rm D}}{T}\right)$ is the kinetic parameter, T is the surface temperature, V is the deposition rate, $T_{\rm D}$ is the characteristic temperature of stress-driven diffusion to the islands, c is the constant related to the distribution width, $x(L,t) = \frac{L_*^2(t)-L^2}{(\alpha l_0)^2}$, $h_{\rm eq}$ is the equilibrium wetting layer thickness, l_0 is the lattice spacing, d_0 is the height of a monolayer (ML), $T_{\rm e}$ is the quasi-equilibrium temperature containing all energetic parameters of heteroepitaxial system [3] and $u(Q)$ is the function determined by recurrent formula $u^{(n+1)}(Q) = \ln Q - \ln\left[(5/2)u^{(n)}(Q)\right], n = 0,\ 1,\ 2\ldots$ ($u^{(0)} \equiv 2/5$). Mean lateral size $L_*(t)$ is found from numerical solution of Eq. (2), where $l(t) = L_*(t)/L_{\rm R}$ and the mean size at the end of size-relaxation stage is given by

$$L_{\rm R} = \left[\frac{6d_0(H_0 - h_{\rm eq})\operatorname{cotan}\varphi}{N}\right]^{1/3} \tag{4}$$

with ϕ being the contact angle of pyramidal island with square base $L \times L$. Input of energetic parameters of heteroepitaxial system provides the numerical value of $T_{\rm e}$, while the growth conditions during MBE determine the parameters $T_{\rm D}$ and c. After that, we simulate the time-dependent island size distribution and, in particular, calculate the mean QD size and their density at given amount of deposited material as function of growth temperature T and deposition rate V.

3. Experiment: III–V QDs

In the case of InAs/GaAs(100) QDs the comparison between theory and experiment is presented in Figs. 1 and 2. Experimental details can be found, for example, in Ref. [3]. Samples were grown by MBE at different T and V and at fixed $H = 2$ ML and then studied by applying transmission electron microscopy (TEM) method. TEM images in Fig. 1 and

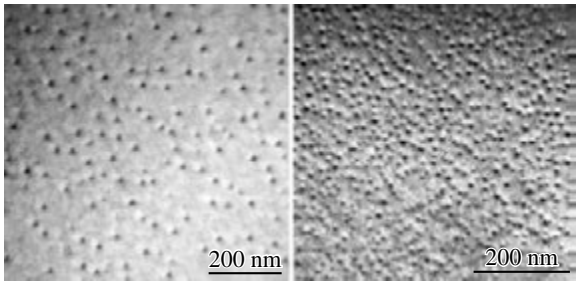

Fig. 1. TEM image of 2 ML InAs QD on GaAs(100), (a) $T = 485\,^{\circ}$C and $V = 0.03$ ML/s; (b) $T = 440\,^{\circ}$C and $V = 0.05$ ML/s.

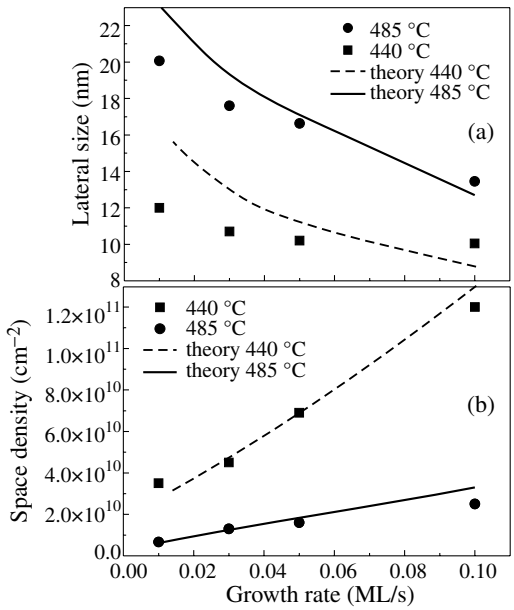

Fig. 2. Theoretical (lines) and experimental (dots) dependences of lateral size of InAs QDs on the deposition rate at two different surface temperatures (a) and for QD surface density (b).

theoretical and experimental dependences $L_*(V)$, $N(V)$ at the two different growth temperatures quantitatively demonstrate the effect of the increase in the density with the simultaneous decrease in the size at higher growth rate and lower growth temperature.

4. Experiment: II–VI QDs

CdSe/ZnSe heterostructures were grown on GaAs (001) substrate in two-chamber MBE system EP-1203. CdSe insertions were formed in a ZnSe matrix by a standard MBE technique. All structures have the similar design comprising ZnSSe buffer layer of 100 nm thick, 10 nm bottom ZnSe layer, single CdSe QD region and cap ZnSe layer of 20 nm thick. The growth temperature during CdSe deposition was varied from $T = 280\,^{\circ}$C (samples 1 and 2) to $T = 340\,^{\circ}$C (sample 3). The CdSe sheets in samples 2 and 3 were deposited at average CdSe growth rate V of 0.2 ML/s, while during the deposition of CdSe layer in sample 1 Cd flux was ten times lower ($V = 0.02$ ML/s). The MBE growth of all structures was monitored by reflection high energy electron diffraction. The grown samples were then studied by TEM, typical TEM images of CdSe QDs in the ZnSe matrix is shown in the insert to Fig. 3. The results of analysis of TEM images for samples 1, 2 and 3 are presented in Fig. 4. The values of mean lateral size and surface density of islands are summarized in Table 1. It

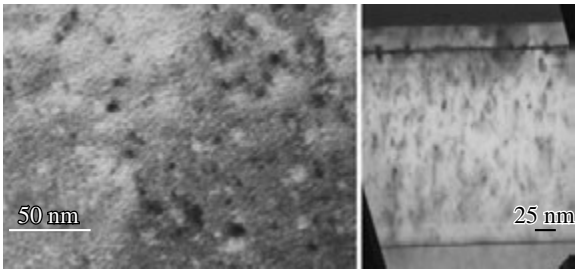

Fig. 3. (a) TEM image of CdSe QDs in the ZnSe matrix, sample 3, plan view. (b) Cross sectional TEM image of sample 3 with CdSe/ZnSe QDs.

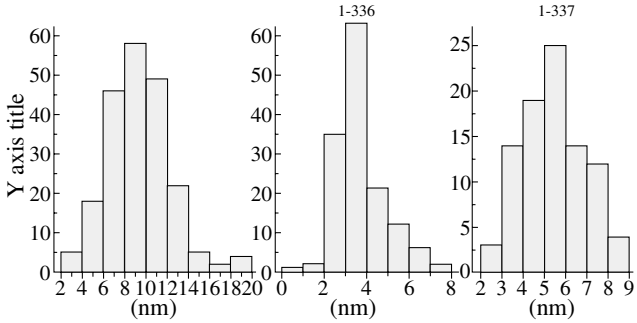

Fig. 4. Size distribution of CdSe QDs for samples 1 (a), 2 (b), 3 (c).

is seen that the qualitative dependence of the island size and density in the CdSe/ZnSe material system is the same as in the InAs/GaAs one, i.e. the island size increases and the density decreases with increasing the surface temperature and decreasing the deposition rate. Comparing samples 1 and 2 grown at fixed T but different V, we note that the island size in sample 1 is 2.6 times larger than in sample 2, which demonstrates the kinetic origin of QD formation (equilibrium structure of the surface must be flux independent).

Table 1. Growth conditions and structural parameters of CdSe QDs.

Sample No.	Growth T (°C)	Flux V (ML/s)	Mean size L_* (nm)	Density N (10^{10} cm^{-2})
1	280	0.02	9	2.5
2	280	0.2	3.5	8.5
3	340	0.2	5.5	5.5

Acknowledgements

The authors are grateful to the financial support received from SANDiE program and RFBR grant No. 05-02-16658-a.

References

[1] V. M. Ustinov, A. E. Zhukov, A. Yu. Egorov, N. A. Maleev, *Quantum dot lasers*, New York: Oxford University Press, 2003.

[2] V. G. Dubrovskii, G. E. Cirlin, V. M. Ustinov, *Phys. Rev. B* **68**, 075409 (2003).

[3] V. G. Dubrovskii, G. E. Cirlin, Yu. G. Musikhin, Yu. B. Samsonenko, A. A. Tonkikh, N. K. Polyakov, V. A. Egorov, A. F. Tsatsul'nikov, N. A. Krizhanovskaya, V. M. Ustinov, P. Werner, *J. Cryst. Growth* **267**, 47 (2004).

[4] A. V. Osipov, S. A. Kukushkin, F. Schmitt, P. Hess, *Phys. Rev. B* **64**, 205421 (2001).

14th Int. Symp. "Nanostructures: Physics and Technology"
St Petersburg, Russia, June 26–30, 2006

Homogeneous arrays of Ge nanocrystals grown by pulsed ion-beam nucleation during deposition on dielectric

A. V. Dvurechenskii[1,2], N. P. Stepina[1,2], V. A. Armbrister[1,2], V. G. Kesler[1], P. L. Novikov[1,2], Zh. V. Smagina[1,2], A. K. Gutakovskii[1,2] and V. N. Brudnyi

[1] Institute of Semiconductor Physics, SB RAS, 630090 Novosibirsk
[2] Tomsk State University, Nanoelectronic Center

Abstract. The pulsed low-energy (100–200 eV) ion-beam-induced nucleation was found to stimulate Ge nanocrystals homogeneous array formation on SiO_2 films during deposition in UHV chamber in temperature range 250−400 °C. The density of small size (about 7 nm) nanocrystals increases with top value up to 10^{12} cm^{-2} as the substrate temperature goes down. The noticeable Ge desorption enhancement takes place with increasing substrate temperature during deposition.

Introduction

The use of floating gate composed of isolated dots reduces the problems of charge loss encountered in conventional Flash memories, allowing for thinner injection oxides and, hence, smaller operating voltages, better endurance, and faster write/erase speeds. Moreover, the performance and the success of such a memory structure strongly depend on (a) the process ability for making uniform and reproducible thin tunnel oxides and (b) the characteristics of islands (such as crystallinity, size, shape, spatial distribution) that influence both the potential energy of trapped electrons and the Coulomb blockade energy, which prevents the injection and storage of additional electrons. The Flash memory performance also strongly depends on the islands characteristics [1]. In our previous work pulsed low-energy (100–200 eV) ion-beam-induced nucleation was found to stimulate Ge nanocrystals array formation on relatively thick films of SiO_2 (about 100 nm) prepared by thermal oxidation of Si [2]. It was shown that the ion-beam action causes an increase in nanocrystal density and size homogeneity. The idea of using the ion-beam action is that each ion impact into the SiO_2 surface (a) produces a vacancy depression with a surface steps being nucleation sites for nanocrystals growth; (b) generates adatoms assisting in nuclei growth; c) stimulates surface reconstruction modifying adatom diffusion. Ion energy should be low enough to avoid introducing defects into SiO_2 film, but high enough as compared to that of thermal energy of deposited atoms. The regime of pulsed ion-beam irradiation allows synchronous nucleation of new phase, favorable for highly homogeneous nanocrystal size distribution. In the present work pulsed low-energy (100–200 eV) ion-beam-induced nucleation during Ge deposition on SiO_2 was used to study the formation of Ge nanoisland arrays on thin films of dielectric usually used as tunnel layer in memory devices. The goal of the present study is to reveal and discuss the nucleation and growth of Ge nanocrystals on thin layers of SiO_2 with low-energy Ge ion-beam action during Ge deposition.

1. Experimental set-up

The experiments were carried out in an ultrahigh-vacuum (UHV) chamber of molecular beam epitaxy setup equipped with effusion cell (boron nitride crucible) for Ge. The system of ionization and acceleration of Ge^+ ions provided the degree of ionization of Ge molecular beam from 0.1% to 0.5%. A pulse accelerating voltage supply unit generated ion-current pulses with duration of 0.5–1 s and ion energy of 100–200 eV. The angle of incidence of the molecular and ion beams on the substrate was 54 degree to surface normal. The analytical assembly unit of the chamber included a reflection high energy (20 keV) electron diffraction (RHEED) unit.

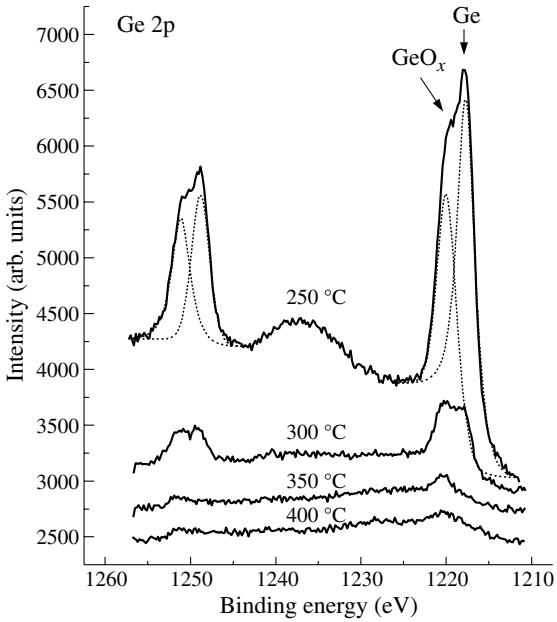

Fig. 1. Detailed spectra of the Ge 2p core level from surfaces of samples, grown at difference temperatures. The rate of Ge deposition is 0.125 ML per second. After the deposition of 3 ML pulse ion-beam actions were applied in series at the effective Ge layer thickness 3 ML, 4 ML and 5 ML.

Prior to the deposition, the SiO_2 layer of 35 Å thick was formed by thermal oxidation of Si(111). After dioxide formation the wafers were washed, dried-up and inserted into the UHV chamber. The substrate temperature of Ge deposition was varied from 250 to 400 °C. The total Ge effective thickness of deposition was 20 monolayers (ML). The rate of Ge deposition was 0.08–0.19 ML/s. Three ML of Ge were deposited without ion-beam action. Pulsed ion-beam actions were applied in series at the effective Ge layer thickness 3 ML, 4 ML and 5 ML. Ge nanocrystal density and size distribution were studied with high resolution electron microscopy (HREM) using JEM-4000EX with resolution of 0.17 nm at accelerating voltage 200 keV. To prevent Ge oxidation some Ge/SiO_2 samples were capped by Si thin layer before taking out from UHV chamber.

The chemical content of the uncapped samples were studied with Electron Spectroscopy for Chemical Analysis (ESCA) by transferring samples via ambient atmosphere to ESCA spectrometer. Al source with Ka line 1486.6 eV was used for exciting X-ray Photoelectron spectra. The source power was 300 Watt, and X-ray beam diameter was 4–5 mm. The energy resolution of analyzer was 0.7 eV and the depth of probing was 1–4 nm. As a measure of Ge concentration the intensity of Ge 2p x-ray photoelectron line was chosen due to high surface sensitivity and small probing depth (inelastic mean free path of signal electrons $\lambda = 0.89$ nm).

2. Experimental results and discussion

The detailed spectra of Ge 2p doublet from samples grown at difference temperatures are presented in Fig. 1. The Ge 2p states are clearly resolved with a spin-orbit splitting of 31.1 eV. Both Ge $2p_{1/2}$ and Ge $2p_{3/2}$ lines show pronounced superposition of two components with energy shift of 2.3 eV. Ge $2p_{3/2}$ line components located at 1217.7 eV and at 1220.0 eV binding energies are related with germanium and partially oxidized Ge. The relative intensity of Ge-Ge component is reduced with the increasing of deposition temperature. That is indication of decreasing of Ge layer thickness on SiO_2 versus deposition temperature. The estimated effective thicknesses of Ge film were 8.5 ML at deposition temperature 250 °C, 1 ML at 300 °C and 0.27 ML at 350 °C. There is clear indication of Ge desorption during deposition with increasing rate as substrate temperature increases. There was no noticeable decreasing of SiO_2 underlying film thickness after Ge deposition. The HREM image shows homogeneous nanocrystals of 7 nm average size on SiO_2 surface (Fig. 2). The density of nanocrystals increases with top value up to 10^{12} cm^{-2} as the substrate temperature goes down (Fig. 3). From comparison of ESCA and HREM data one may conclude, that the Ge island shape depends upon the temperature of deposition. Ge island height apparently increases as the temperature of deposition decreases.

Additionally, Monte Carlo simulation was carried out to clarify the influence of ion beam action, surface atomic diffusion and desorption on the kinetics of nanocrystal formation.

Acknowledgements

The work was supported by Rosnauka grant (02.435.11.2012) and RFBR (Project 05-02-16285 and 05-02-39006 GFEN).

References

[1] S. Tiwari, F. Rana, H. Hanafi, A. Hartstein, E. F. Crabbe and K. Chan, *Appl. Phys. Lett.* **68**, 1377 (1996).

[2] A. V. Dvurechenskii, P. L. Novikov, Y. Khang, Zh. V. Smagina, V. A. Armbrister, V. G. Kesler and A. K. Gutakovskii, *Proc. SPIE*, 2006 (to be published).

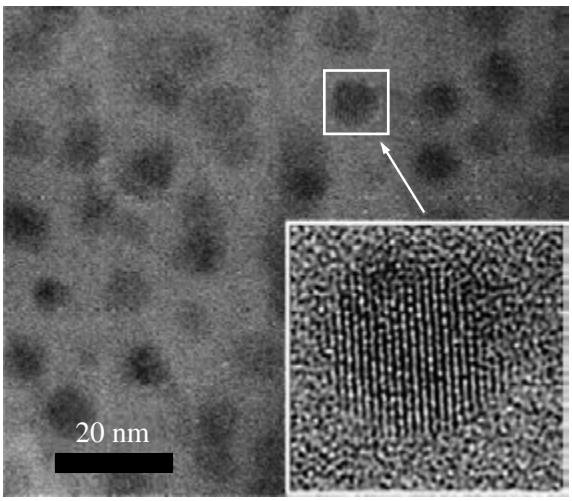

Fig. 2. HREM image (plan view) of nanocrystals on SiO_2.

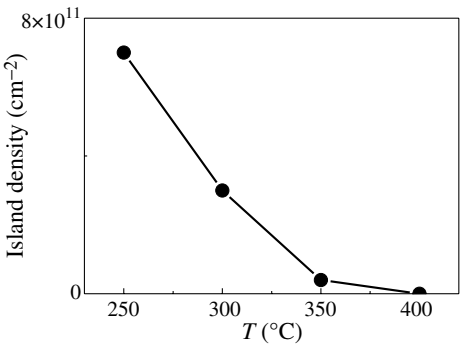

Fig. 3. Density of nanocrystals *vs* substrate temperature.

14th Int. Symp. "Nanostructures: Physics and Technology"
St Petersburg, Russia, June 26–30, 2006

Novel type of quantum dots based on bell-shaped nanoshells: modeling, fabrication, and properties

A. V. Kopylov, A. V. Prinz and V. Ya. Prinz
Institute of Semiconductor Physics, 13, Academician Lavrentyev Avenue, Novosibirsk 630090, Russia

Abstract. The pulsed low-energy (100–200 eV) ion-beam-induced nucleation was found to stimulate Ge nanocrystals homogeneous array formation on SiO_2 films during deposition in UHV chamber in temperature range 250−400 °C. The density of small size (about 7 nm) nanocrystals increases with top value up to 10^{12} cm^{-2} as the substrate temperature goes down. The noticeable Ge desorption enhancement takes place with increasing substrate temperature during deposition.

As it was shown in [1], an ultra-thin (thickness down to 2 ML) film epitaxially grown on a substrate can be subsequently detached from it using selective etching of an underlying sacrificial layer. Being locally detached from the substrate, under the action of the internal stress such a compressed film undergoes buckling [2]. Depending on particular boundary conditions, such buckling allows one to fabricate a broad spectrum of nanoshells heavily strained in their bending regions, where the mechanical stress amounts to 10 GPa. This stress gives rise to local deep (up to 1 eV) potential wells for electrons, thus allowing one to obtain quantum dots or wires. For the first time, this possibility was demonstrated in [3, 4] with the example of a nanocorrugated (buckled) bifilm.

In the present work, we introduce a new type of quantum structures, — bell-shaped nanoshells. Such nanoobjects, self-formed from ultimately thin films of a molecular thickness, are attached to the substrate around their perimeter. One of the main properties of these nanoobjects is their good precision resulting from the fact that the thickness and the internal stress in them can be precisely predefined at the MBE stage. Such nanostructures offer promising buildings blocks for quantum devices.

The possibility to fabricate bell-shaped nanoshells was experimentally demonstrated with the example of InAs/InP systems (with lattice mismatch $\Delta a/a$ of 3.2%). Three methods for preparation of such nanoshells were proposed. In the simplest method, the starting structures were strained heterostructures involving a substrate, a sacrificial layer, and a top compressed film. To locally detach the film from the substrate, in the upper layer we opened a nano-window to provide access for a selective etchant to the sacrificial layer. After the etching, the freed part of the film acquired a bell-like shape. Figure 1a shows a photograph of an 8×8 μm^2 bell-shaped microshell made of an InGaAs film. This photo demonstrates a nano-window in the film though which the selective etchant could reach the sacrificial layer (1) and interference fringes observed on the prepared bell-shaped shell (2). Figure 1b shows a surface covered with 1.5×1.5 μm^2 bell-shaped shells. Figure 2a presents a 100×100 nm^2 bell-shaped nanoshell made of an 8 nm thick $In_{02}Ga_{08}As$ film. More complicated procedures for fabricating bell-shaped shells using no windows were also invented. At the final stage, the structures were given supercritical drying in order to avoid their mechanical damaging that happens when the obtained structures are withdrawn from the solution directly into the ambient air.

We numerically analyzed particular cases of InAs/InP structures with a film detachment area of 50×50 nm^2 prepared from

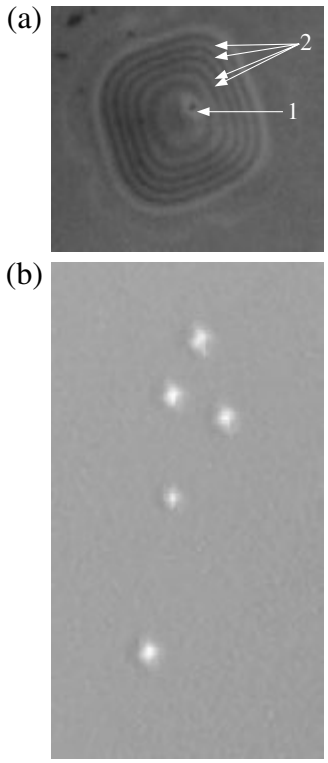

Fig. 1. Bell-shaped shells obtained by local detachment of MBE-grown films from substrates over square regions. (a) an 8×8 μm^2 InGaAs microshell (1 — window in the film opened to provide access of selective etchant to the sacrificial layer, 2 — interference fringes); (b) 1.5×1.5 μm^2 InGaAs microshells.

starting heterostructures with 1.1 nm (4 ML) and 3 nm (10 ML) thick films. Within the framework of continuous elasticity theory, we developed a numerical model for the self-formed bell-shaped shells. Based on the constructed solution of elastic-theory equations, both the shape of the self-formed nanoshells and the distribution of mechanical stresses and deformations in them were predicted (see Figures 2b, 2c). For instance, the mechanical stresses in them vary from a compression stress around the periphery to a tensile stress at the bell apex. The strain distribution thus obtained makes it possible to calculate the potential relief in bell-shaped shells. The potential relief obtained defines the position of energy levels of electrons in the shells. At room temperature the calaculated distance between quantum levels is comparable with kT even for shells with detachment area of 50×50 nm^2. The bell-shaped shells prepared in this way could be scaled down to 10×10 nm^2.

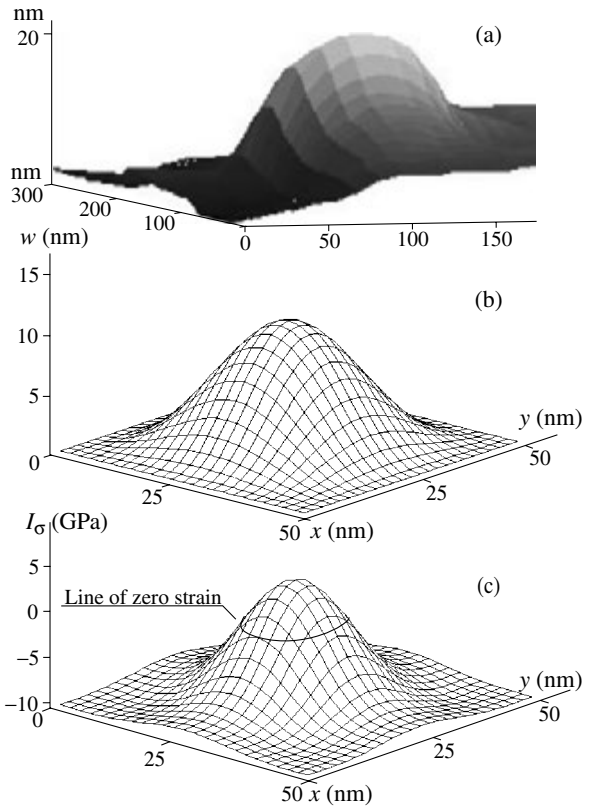

Fig. 2. Bell-shaped shells obtained by local detachment of MBE-grown films from substrates over square regions. (a) a 100×100 nm^2 InGaAs nanoshell, the measurements were made with NT-MDT atomic-force microscope; (b) shape of a 50×50 nm^2 InGaAs nanoshell predicted by the elastic theory under continual approximation; (c) First-invariant shape of elastic stresses tensor in the middle plane of the elastically compressed film.

The first obtained scanning tunnel microscopy data were found to be in a qualitative agreement with the simulation results.

We selected InAs, however, it is not the most suitable material in spite of the fact that InAs films with thickness of down to 3–6 nm remain conductive due to native electron accumulation [5] and does not need electron passivation of surface. In fact, there are many materials in which such effects are manifested even more clearly. Such materials are narrow-band or gapless semiconductors, and semimetals. In the present work, we give a brief review of such materials which a promising material for fabricating quantum-dot arrays.

Acknowledgements

This work was supported by the Russian Foundation for Basic Research under Grants Nos. 05-02-16991 and 06-02-17485.

References

[1] V. Ya. Prinz, V. A. Seleznev, A. K. Gutakovsky, A. V. Chehovsky, V. V. Preobrazhensky, M. A. Putyato and T. A. Gavrilova, *Physica E* **6**, 828 (2000).
[2] V. Ya. Prinz, *Physica E* **24**, 54–62 (2004).
[3] V. M. Osadchii and V. Ya. Prinz, *Phys. Rev. B* **72**, 033313 (2005).
[4] A. V. Prinz, V. Ya. Prinz, *Patent of Russia*, favourable decision (2005).
[5] H. Yamaguchi, J. L. Sudijono, B. A. Joyce, T. S. Jones, C. Gatzke, R. A. Stradling, *Phys. Rev. B* **58**, (8) R4219 (1998).

14th Int. Symp. "Nanostructures: Physics and Technology"
St Petersburg, Russia, June 26–30, 2006

Optimal composition of microcavity structures with selectively oxidized apertures and DBRs

A. G. Kuzmenkov[1], S. A. Blokhin[2], N. A. Maleev[2], A. P. Vasil'ev[2], A. E. Zhukov[1] and V. M. Ustinov[1]

[1] St Petersburg Physico-Technical Centre of RAS for Research and Education, 194021, St Petersburg, Russia
[2] Ioffe Physico-Technical Institute, St Petersburg, Russia

Abstract. The problems of selective wet oxidation for AlGaAs/GaAs microcavity structures with oxidized Al(Ga)O apertures and Al(Ga)O/GaAs distributed Bragg reflectors (DBRs) are discussed. The upper limit of oxidation time for Al(Ga)O/GaAs DBRs is founded. The method for choice of the optimal oxidation rates and aperture layer composition is proposed.

1. Introduction

Aluminum oxide (Al_xO_y) formed by selective wet oxidation of high aluminum (Al) content $Al_xGa_{1-x}As$ ($x > 0.85$) layers is promising material for application in vertical-cavity surface-emitting-lasers (VCSELs) and other microcavity devices [1]. Particularly Al_xO_y layers widely used as current apertures of high-performance VCSELs [2]. Selectively oxidized Al_xO_y /GaAs distributed Bragg reflectors (DBRs) provide ultra-low optical losses and broad stop-band. Therefore it is interesting to combine oxidized apertures with oxidized DBRs. This approach was applied successfully for ultra-low threshold current quantum well (QW) and quantum dot (QD) VCSELs [3, 4]. Unfortunately the fabrication process for such devices is rather complicated and consists of many technology steps. Therefore it is very attractive to make DBRs and aperture oxidation simultaneously. This is possible only at the optimal choice of the layers thickness and composition because oxidation rates are strongly depending on these parameters. Moreover device mechanical stability is also affected by structure design and oxidation conditions.

In the present work, we investigate dependence of the optical reflectivity on oxidation process time for Al(Ga)O/GaAs DBRs. The upper limit for maximum possible oxidation time was founded. The method for determination of the optimal oxidation rates and layer compositions is proposed. It is based on modelling of the oxidation process and takes into account different features of the real selective oxidation technology.

2. Permissible process time at selective oxidation of the Al_xO_y/GaAs DBRs

It is well known that selective oxidation of AlAs layers results in mechanically unstable DBR structures. Therefore practical microcavity devices usually employ Al(Ga)O layers obtained by selective wet oxidation of the $Al_xGa_{1-x}As$ ($0.98 > x > 0.95$) layers [1].

We investigate the optical reflectivity of Al(Ga)O/GaAs DBRs depending on oxidation time. The epitaxial structure were grown on an semi-insulating GaAs (001) substrates by molecular-beam epitaxy (MBE) using a Riber 32 system. It consists of (from top to the bottom) a 5-pairs GaAs/$Al_{0.97}Ga_{0.03}As$ (61 nm/155 nm) and cap GaAs layer (340 nm). To reduce mechanical strain the 15 nm layers with graded Al composition were inserted at the each interface. The layer thicknesses and compositions were selected to obtain high reflectivity for wavelengths range of 900−1200 nm. Using modified photolithography and deep Ar^+ beam dry etching [5] the square mesa structures with size of about 40×40 μm and the etching depth of 2.0 μm were fabricated. In order to avoid surface damage and contamination from the dry etching, an additional chemical etching in a NH_4OH:H_2O_2:H_2O (1:2:50) solution for 4−5 s at room temperature was carried out. The DBRs were formed by the lateral selective wet oxidation of $Al_{0.97}Ga_{0.03}As$ layers. In order to achieve the high mechanical stability the two-stage selective oxidation method was used [6]. The optical reflectivity spectra from individual mesa structures were measured using μ-reflectivity spectroscopy based on optical microscope.

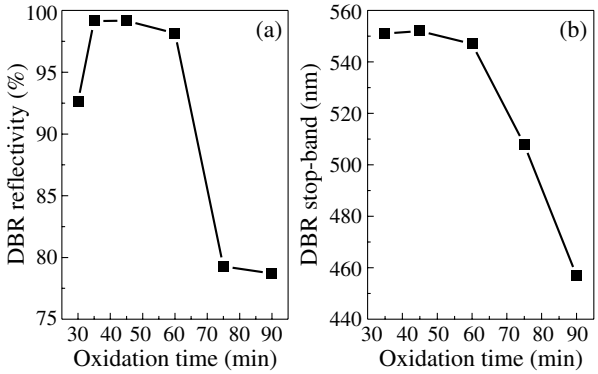

Fig. 1. (a) The maximal DBR reflectivity at $\lambda = 980$ nm as a function of the wet oxidation time; (b) Stop-band as a functions of the wet oxidation time.

The measured DBR reflectivity (R) at wavelength of 980 nm as a function of the oxidation time is shown in Fig. 1. For oxidation time less than 35 min the mesa structure is not yet completely oxidized and reflectivity is smaller than project value. The magnitude of R reaches maximum at about 35−40 min. As was founded from scanning electron microscopy (SEM) measurements this moment corresponds to complete oxidation of DBR mesa-structures. However at the further oxidation of mesa-structures the measured value of R starts to decrease as well as DBR stop band (see Fig. 1). For oxidation time > 60 min the SEM measurements demonstrate noticeable shrinkage of the oxidized layers. Simultaneously optical microscopy shows some degradation of the surface morphology. Based on similar experiments for several Al(Ga)O/GaAs DBR structures the oxidation process should not be longer than the complete oxidation time multiplied by factor (1.2−1.3).

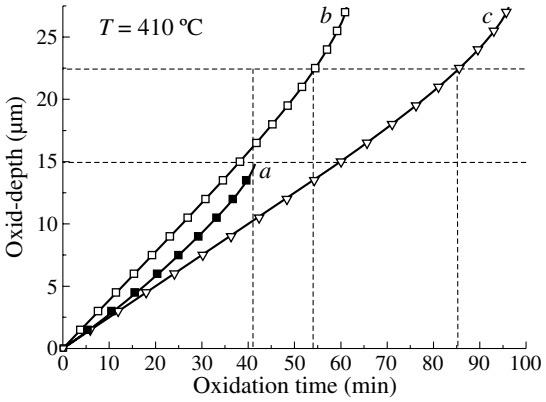

Fig. 2. Calculated dependencies of oxidation depth for cylindrical mesa-structures: (a) —160 nm $Al_{0.97}Ga_{0.03}As$ layer for top DBR; (b) —65 nm $Al_{0.97}Ga_{0.03}As$ aperture layer; (c) —65 nm $Al_{0.98}Ga_{0.02}As$ aperture layer.

3. Method for determination of the optimal oxidation rates and layer compositions

The QW and QD VCSELs with Al(Ga)O/GaAs DBRs usually utilize double intra-cavity contact approach [3, 4]. The first (top DBR) and second (cavity) mesa sizes are depend on certain device design (aperture size, contact pads, bounding technique etc.). To provide simultaneous selective wet oxidation of the top (bottom) DBR and current aperture the AlGaAs layer thicknesses and compositions should be optimized. The modelling of the selective oxidation process is powerful tool for prediction of the oxidation depth depending on layer thickness and composition [7]. In our calculations we use model proposed in [8] for selective wet oxidation of the AlAs in cylindrical mesa-structures. Using our experimental data the model parameters were adjusted for $Al_xGa_{1-x}As$ layers.

Let consider the double intra-cavity bottom-emitting InGaAs QW VCSEL structure with top Al(Ga)O/GaAs DBR, Al(Ga)O aperture at the antinode of optical field and bottom AlGaAs/GaAs DBR [9]. The fist (top DBR) mesa diameter is 30 μm and second (cavity) mesa diameter is 55 μm. 7-pairs GaAs/$Al_{0.97}Ga_{0.03}As$ (68 nm/160 nm) structure is selected for top DBR to provide reproducible oxidation process and mechanical stability. It is known that for $Al_xGa_{1-x}As$ ($0.98 > x > 0.95$) thickness more than about 55 nm the oxidation rate only slightly depend on layer thickness [1]. Therefore $Al_xGa_{1-x}As$ aperture layer thickness of 65 nm is selected. This value is enough to obtain optimal redistribution of the optical field inside of microcavity. The problem is determination of optimal Al content in $Al_xGa_{1-x}As$ layer to obtain aperture diameter is about 10 μm (for multi-mode VCSEL).

Figure 2 shows calculated dependencies of oxidation depth for used top $Al_{0.97}Ga_{0.03}As$/GaAs DBR and $Al_xGa_{1-x}As$ aperture layers with Al content $x = 0.97$ and 0.98. It is clearly seen that in case of $Al_{0.97}Ga_{0.03}As$ aperture layer the total oxidation time is about two times larger than complete oxidation time for top $Al_{0.97}Ga_{0.03}As$/GaAs DBR. Therefore this aperture composition is not suitable for VCSEL. At the same time the $Al_{0.98}Ga_{0.02}As$ aperture layer provides optimal regime for simultaneous oxidation with top $Al_{0.97}Ga_{0.03}As$/GaAs DBR.

Designed structure was used successfully for realization of VCSEL matrix [9]. Matrix emitters with 8×8 bottom-emitting InGaAs QW VCSELs were fabricated. Individual emitters with 8−10 μ oxidized apertures demonstrate room-temperature continuous-wave lasing at 960−975 nm with room-temperature threshold current of 1−2 mA, external efficiency > 0.3 mW/mA and maximum output power 2−3 mW. All fabricated devices are mechanically stable.

4. Conclusion

The dependence of the optical reflectivity on selective oxidation time was investigated for Al(Ga)O/GaAs DBRs. To keep high reflectivity the oxidation process should not be longer than (1.2−1.3)-fold complete oxidation time for $Al_xGa_{1-x}As$ layers. The method for determination of the optimal oxidation rate and aperture layer composition is proposed. It is based on modelling of the selective wet oxidation process for $Al_xGa_{1-x}As$ in cylindrical mesa-structures.

Acknowledgements

The authors would like to thank M. M. Kulagina and Yu. M. Zadiranov for performing the test structure fabrication.

This work was supported by the Russian Foundation for Basic Research and SANDiE (NMP4-CT-2004-500101).

References

[1] K. D. Choquette and H. Q. Hou, *Proc. IEEE* **85**, 1730 (1997).
[2] C. W. Wilmsen, H. Temkin, L. A. Coldren, *Vertical-Cavity Surface-Emitting Lasers*, Cambridge University Press, 1999.
[3] M. H. MacDougal, P. D. Dapkus, A. E. Bond, C. K. Lin, J. Geske, *IEEE J. Selected Topics in Quantum Electron.* **3**, 905 (1997).
[4] V. M. Ustinov, A. E. Zhukov, A. Y. Egorov, N. A. Maleev, *Quantum dot lasers*, Oxford University Press, 2003.
[5] N. A. Maleev, A. P. Kovsh, A. E. Zhukov, A. P. Vasil'ev, S. S. Mikhrin, A. G. Kuzmenkov, D. A. Bedarev, Yu. M. Zadiranov, M. M. Kulagina, Yu. M. Shernyakov, A. S. Shulenkov, V. A. Bykovski, Yu. M. Solov'ev, C. Möller, N. N. Ledentsov, V. M. Ustinov, *Semicond.*, **37**, 1265 (2003).
[6] S. A. Blokhin, A. N. Smirnov, A. V. Sakharov, A. G. Gladyshev, N. V. Kryzhanovskaya, N. A. Maleev, A. E. Zhukov, E. S. Semenova, D. A. Bedarev, E. V. Nikitina, M. M. Kulagina, M. V. Maximov, N. N. Ledentsov, V. M. Ustinov, *Semicond.* **39**, 782 (2005).
[7] P. C. Ku, C. J. Chang-Hasnain, *IEEE Journal of Quantum Eelectronics* **39**, 577 (2003).
[8] M. Osin'ski, T. Svimonishvili, G. A. Smolyakov, V. A. Smagley, P. Mac'kowiak, W. Nakwaski, *IEEE Photon. Technol. Lett.* **13**, 687 (2001).
[9] S. V. Chumak, N. A. Maleev, A. G. Kuzmenkov, A. S. Shulenkov, A. E. Zhukov, A. P. Vasil'ev, S. A. Blokhin, M. M. Kulagina, M. V. Maximov, V. M. Ustinov, *13th International Symposium Nanostructures: Physics and Technology*, 20–25 June, 2005, St Petersburg, Russia, p. 100.

14th Int. Symp. "Nanostructures: Physics and Technology"
St Petersburg, Russia, June 26–30, 2006

Novel continuous regular 3D micro- and nanoshell systems design, fabrication, study and possible applications

E. V. Naumova, V. Ya. Prinz, S. V. Golod and V. A. Seleznev
Institute of Semiconductor Physics, Novosibirsk, Russia

Abstract. Possibilities of fabrication of continuous micro- and nanoshell systems of complex configurations on the basis of SiGe/Si and InGaAs/GaAs bifilms by the strain-driven process were demonstrated. Presented configurations include systems with dyad and tetrad axes of symmetry. Prospects of practical applications of such systems are discussed.

Development of micro- and nanostructuring methods brings into life so called metamaterials, novel artificial media with unusual electromagnetic properties even the properties ne-ver found in nature [1, 2]. These novel composite media are fabricated on the basis of substantially subwavelength electromagnetic elements playing a role of atoms and molecules. Recently, bulk metamaterials for microwave range were de-monstrated, where averaged electromagnetic response of such "man-made atoms" created simultaneously negative dielectric permittivity and magnetic permeability, i.e. negative index of refraction [3]. Some other artificial electromagnetic media were suggested, which properties are significantly different from ones of materials they are made from [4, 5]. Invention of novel electromagnetic media, study of their properties, scaling of elements down to nanometers, and development of their practical applications are the main problems in this area.

Presented work is devoted to the newly developed class of artificial electromagnetic materials [6], regular systems of three-dimensional micro-and nanoshells formed from bifilms by the strain-driven process [7]. The fabrication procedure was as follows: on the substrate the strained bifilm was grown by molecular-beam epitaxy, tesselation patterns were formed by photo- and electronic lithography, and then this patterned bifilm was transformed into the system of three-dimensional shells under action of internal strains (tesselation means regular divisions of the plane by closed shapes that completely cover the plane without overlapping and gaps [8]). To achieve a high precision and multiformity of obtained shapes of micro- and nanoshells a range of methods was used: a) directional rolling of films; b) super-critical drying of micro-and nanoshells; c) assembling of micro- and nanoshells into more complex architectures [9].

Special patterns were developed that determined bifilm regions to be transformed into the free-standing shells. The bifilm represents monocrystal and symmetry of final three-dimensional shell depends on symmetry of the lithographic pattern and its orientation relative to crystallographic axes. Continuous regular systems with dyad and tetrad axes of symmetry were created on the basis of SiGe/Si and InGaAs/GaAs bifilms. Method of strain-driven formation of micro and nanoshells has got further development — it was shown that formation of continuous micro- or nanostructured systems by the strain-driven process can be realized over large area with excellent regularity of three dimensional elements in case of strict observation of directional rolling and drying conditions. Two-dimensional regular systems of three-dimensional shells with features in the range from hundreds of micrometers to hundreds of nanometers were created. The simplest fabricated regular configurations

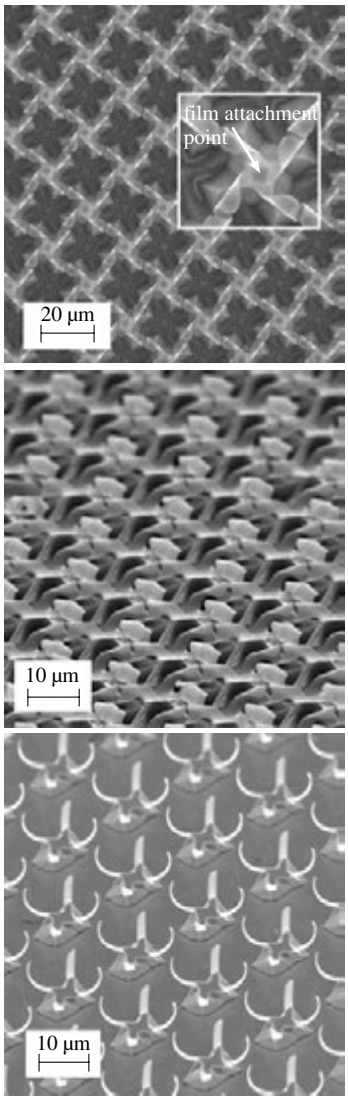

Fig. 1. Examples of created systems of three-dimensional microshells on the basis of epitaxial SiGe/Si (a, b) and InGaAs/GaAs (c) bifilms. Free microshells are placed on pedestals making up a one piece with a substrate, the strict regularity seen on these figures was observed over the whole substrate area.

are presented in Fig. 1. Due to the high stability of shape and elasticity the continuous microshell systems can be detached from the substrate without destruction. The electromagnetic properties of created systems of three-dimensional micro and nanoshells were studied in optical and GHz range. Multiformity of configurations, repeatability of shapes, scalability of sizes, variety of used materials make micro- and nanoshells

arrays very attractive as a basis for novel artificial composite media with tailored electromagnetic properties. Prospects of practical applications of such systems in optics, sensor devices, micro- and nanomechanics are discussed.

References

[1] V. G. Veselago, *Sov. Phys. Usp.* **10**, 509–514 (1968).
[2] D. R. Smith *et al*, *Science* **305**, 788–792 (2004).
[3] R. A. Shelby *et al*, *Science* **292**, 77–79 (2001).
[4] S. V. Zhukovsky *et al*, *Europhys. Lett.* **66** 3, 455–461 (2004).
[5] A. N. Lagarkov *et al*, *Dokl. Phys.* **46**, 163–165 (2001).
[6] E. V. Naumova, V. Ya. Prinz, *PCT Patent Application* (2006).
[7] V. Ya. Prinz *et al*, *Physica E* **6**, 828–831 (2000).
[8] www.mathacademy.com/pr/minitext/escher/index.asp
[9] V. Ya. Prinz *Physica E* **24**, 54–62 (2004).

14th Int. Symp. "Nanostructures: Physics and Technology"
St Petersburg, Russia, June 26–30, 2006

Initial stage of Ag adsorption on Si(110) surface

A. I. Oreshkin[1], I. V. Radchenko[1], S. I. Oreshkin[1,2], S. V. Savinov[1], N. S. Maslova[1] and V. I. Panov[1]

[1] Physical Department, Moscow State University, 119992 Moscow, Russia
[2] Sternberg Astronomical Institute, Moscow State University, 119992 Moscow, Russia

Abstract. We report the results of STM investigation of initial stage of Ag adsorption on the Si(110) surface. At 0.21 ML Ag coverage the size and orientation of unit cell corresponds to parameters of "16×2" unit cell of clean Si(110) surface. With increasing of Ag coverage up to 0.42 ML the basic type of surface reconstruction is changing to 4×1-Si(110)-Ag structure.

Introduction

A lot of structures, for example, 5×4, 1×2, 1×5, 16×2 [1, 2] have been found on clean Si(110) surface. In refs. [3, 4] it is stated that the Si(110)-("16×2") is the only structure that should be observed on clean surface and that all other structures are Ni induced (0.02 ML is enough). It is known from the previous experimental results that a "16×2" reconstructed Si(110) surface consists of equally spaced and alternatively raised (up-stripes) and lowered (down-stripes) stripes parallel to the $[\bar{1}12]$ or $[1\bar{1}2]$ directions [5, 6]. Two possible domains of "16×2" reconstruction must look as

$$\begin{pmatrix} 5 & 11 \\ -2 & 2 \end{pmatrix} \quad \text{and} \quad \begin{pmatrix} -5 & 11 \\ 2 & 2 \end{pmatrix}$$

(the basic translation vectors $a = [001]$ and $b = 1/2[1\bar{1}0]$ are used here; $|a| = 0.543$ nm, $|b| = 0.384$ nm). But until now there is no commonly adopted model for explanation of observed structure of the stripes. STM investigation [5, 7, 8] has shown that different local atomic structures can be observed. The stripes are stacks of paired elements whose shape is different in the various STM measurements. This shape was interpreted as octets [9], as pentagons [8] and as an arrangement of centered stretched hexagons [7]. So, the precise atomic arrangement has not been elucidated yet. Our experimental results [10] have confirmed the model suggested in [8] and are in good accordance with the theoretical calculations [11].

1. Experimental

The Ag/Si(110) system was studied by UHV STM under the initial stage of Ag adsorption at room temperature. Ag evaporation was performed using a Knudsen-cell type of evaporator. The base pressure during Ag deposition was 5×10^{-10} torr. Empty Knudsen cell was cleaned up by annealing during 48 hours. The evaporation rate was estimated from the experiments with Ag deposition on 7×7-Si(111) surface. Ag deposition was conducted at 820 °C with shutter opening time 10 seconds and subsequent 3 min. annealing at 520 °C. The follow constituent reconstructions of surface have been found: 3×1-Si(111)-Ag, $\sqrt{3}\times\sqrt{3}$-Si(111)-Ag and 7×7-Si(111). Relative areas occupied by these surface reconstructions are 18%, 42% and 40% correspondingly. The amount of Ag inducing above mentioned reconstructions is reported in [12, 13]. So, in our geometry the Ag evaporation rate at 820 °C is about 0.4 $\text{nm}^{-2}\cdot\text{sec}^{-1}$. Samples (12×2×0.5) mm^3 in size were cut from P-doped (110) orientated Si wafers with sheet resistance about 1–3 $\Omega\cdot$cm, the nominal doping concentration was about 3×10^{18} cm^{-3}. Sample was ultrasonically cleaned in acetone and distilled water. With the help of "Ni-free" instrument it was mounted on tantalum sample holder. Sample was degassed at 600 °C during 24 hours and processed with argon-ion-sputtering (5 kV, 50–60 A, 60 min). In the final stage of surface preparation the sample was flash heated at 1200 °C by a direct current. STM image of Si(110) surface after 0.21 ML Ag deposition is presented in Fig. 1. The size and orientation of unit cell (marked by white rectangle) corresponds to parameters of "16×2" unit cell on clean Si(110) surface. It was established that Ag atoms precipitate in region of down-stripes. The priority adsorption sites are marked by dashed line on Fig. 1. "16×2" unit cell has 64 atoms in one atomic layer. Therefore at 0.21 ML Ag surface coverage, there should be about 13 Ag atoms in the unit cell of "16×2"-Si(110)-Ag structure. So, most probably part of silicon adatoms diffuse from original "16×2"-Si(110) structure into the bulk of crystal or precipitate on domain boundaries. The dependencies of local density of electronic states on bias voltage measurements above clean Si(110) surface and the "16×2"-Si(110)-Ag are shown on Fig. 2. As can be seen from tunneling conductivity spectra (Fig. 2a) the band gap for clean silicon surface is about 1.15 eV (that is comparable with bulk value of Si (1.1 eV)). Surface states peaks SS1 and SS2 (-0.35 eV and -0.8 eV correspondingly) are clearly distinguishable inside the band gap. Fermi level is situated 0.15 eV below the conduction band bottom. After 0.21 ML Ag deposition (Fig. 2b) the width of measured band gap becomes smaller by 0.25 eV, most probably due to band bending. In this case the edge of valence band goes higher in energy then energy of surface states SS2 band, so the peak in the normalized tunneling conductivity spectrum corresponding to surface states SS2 band becomes unresolved. The

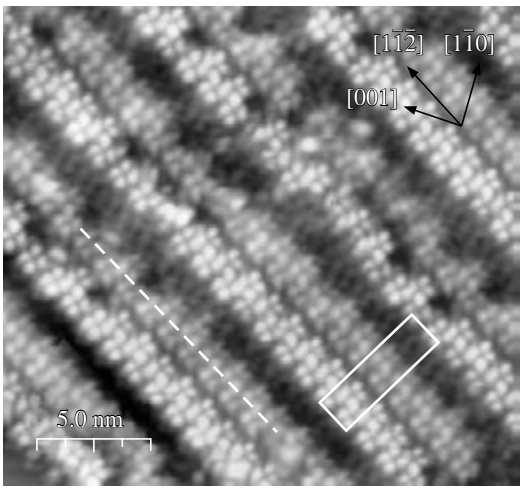

Fig. 1. "16×2"-Si(110)-Ag, $U = -0.52$ V, $I = 51$ pA.

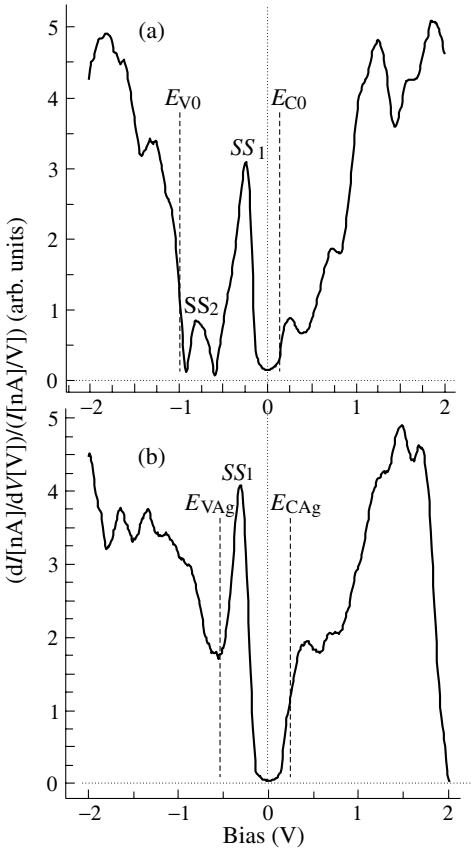

Fig. 2. Normalized tunneling conductivity spectra above a) clean Si(110) surface; b) above "16×2"-Si(110)-Ag surface.

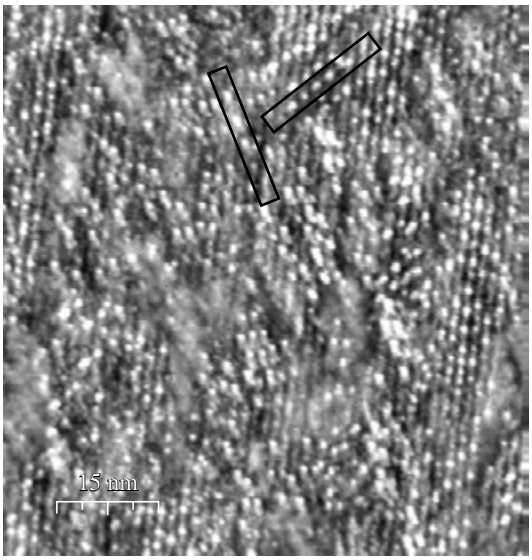

Fig. 3. 4×1-Si(110)-Ag surface.

position of surface states SS1 band peak remains unchanged. The determination of band gap value when surface states are present is not straightforward task, further investigations are needed.

With increasing of Ag coverage up to 0.42 ML we were able to observe new type of surface reconstruction (Fig. 3) with 5.4 Å periodicity along the [001] direction ($\sim$ 5.43 Å of the Si(110) unit cell). The periodicity along the $[1\bar{1}0]$ direction is 15.5 Å, i.e., 4× the length of 3.84 Å of the Si(110) unit cell. So, we can conclude from our STM measurements that the basic type of surface reconstruction for Si(110)-Ag system is changing from "16×2"-Si(110)-Ag to 4×1-Si(110)-Ag structure with increasing of Ag coverage. The unit cell of 4×1-Si(110)-Ag reconstruction consists of 8 atoms. Therefore under 0.42 ML Ag coverage the unit cell of formed structure should contain 3 atoms of Ag. The arrangements of atoms of 4×1-Si(110)-Ag structure (Fig. 3, marked by rectangles) are aligned in $[1\bar{1}2]$, $[1\bar{1}\bar{2}]$ directions, which correspond to the directions of up- and down-stripes in "16×2"-Si(110) structure. We explain this fact with possible diffusion of Si atoms during formation the 4×1-Si(110)-Ag surface reconstruction. To the best of our knowledge there is the only one work dedicated to Ag adsorption on the Si(110) surface [14]. Most probably this is caused by very complicated method of substrate preparation. It is very difficult to obtain large uniform area of "16×2"-Si(110) surface. In [14] Ag/Si(110) system has been studied by means of reflection high-energy electron diffraction-total reflection angle X-ray spectroscopy. The $\begin{pmatrix} 3 & 9 \\ 3 & -9 \end{pmatrix}$Ag induced structure was reported to be the base surface structure for Ag coverage up to 0.44 ML. We could not observe this reconstruction at initial stage of Ag adsorption. We suppose that this fact can be explained by different method of sample preparation. The other possibility is the difference in the doping concentration of samples under investigation. Anyway more detailed study of the Ag/Si(110) system with different conditions of surface preparation, different type of bulk conductivity (n-, p-type) and doping concentration is required.

Acknowledgements

The research was partially supported by RFBR grant 05-02-19806-MF_a. Support from Samsung corp. is gratefully acknowledged.

References

[1] F. Jona *et al*, *IBM J. Res. Dev.* **9**, 375 (1965).
[2] B. Z. Olshanetsky *et al*, *Surf. Sci.* **67**, 581 (1977).
[3] T. Ichinokawa *et al*, *Phys. Rev. B* **31**, 5183 (1985).
[4] Y. Yamamoto *et al*, *J. Appl. Phys.* **25**, L331 (1986).
[5] Y. Yamamoto, *Phys. Rev. B* **50**, 8534 (1994).
[6] H. Ampo *et al*, *Phys. Rev. B* **34**, 2329 (1986).
[7] William E. Packard *et al*, *Phys. Rev. B* **55**, 23, 15643 (1997).
[8] T. An *et al*, *Phys. Rev. B* **61** 4, 3006 (2000).
[9] E. J. Van Loenen *et al*, *J. Microsc.* **152**, 487 (1988).
[10] A. I. Oreshkin *et al*, *Will be published elsewhere*.
[11] A. A. Stekolnikov *et al*, *Phys. Rev. Lett.* **93** 13, 136104–1 (2004).
[12] K. J. Wan *et al*, *Phys. Rew. B* **47**, 13700 (1993).
[13] T. Fukuda *et al*, *Phys. Rew. B* **47**, 13700 (1993). *et al*, *Phys. Rew. B* **50**, 1969 (1994).
[14] Y. Yamamoto, *Jpn. J. Appl. Phys.* **31**, 2241 (1992).

14th Int. Symp. "Nanostructures: Physics and Technology"
St Petersburg, Russia, June 26–30, 2006

Passivation of an $Al_xGa_{1-x}N$/GaN heterostructure by a nano-crystalline GaN layer deposited under electron cyclotron resonance plasma conditions

S. Shapoval[1], A. Kovalchuk[1], V. Sirotkin[1], V. Zemlyakov[2], V. Krasnik[2], K. Dudinov[2], V. Lundin[3], E. Zavarin[3], A. Sakharov[3], A. Tsatsulnikov[3] and V. Ustinov[3]

[1] Institute of Microelectronics Technology RAS, 142432 Chernogolovka, Moscow region, Russia
[2] R&D Corporation "Istok", Fryazino, Moscow region, Russia
[3] Ioffe Physico-Technical Institute, St Petersburg, Russia

Abstract. In this work a passivation method of an $Al_xGa_{1-x}N$/GaN heterostructure by a nano-crystalline gallium nitride GaN(pas.) layer is proposed which helps solve the problem of current collapse in $Al_xGa_{1-x}N$/GaN HEMTs and radically increase the target capacity of a transistor by improving the efficiency of heat removal from heat zones. One of the advantages of this method is its technological and physical-chemical compatibility. 3D thermal simulation of power multi-finger HEMTs with a GaN(pas.) layer is performed. Numerical results show that the deposition of a passivation layer has a beneficial effect on the thermal behavior of the transistors.

Introduction

Passivation by a submicron silicon oxide or silicon nitride layer is known to reduce the current collapse effect in $Al_xGa_{1-x}N$/GaN heterostructures. The presence of bonded hydrogen and superfluous silicon in a passivation layer of amorphous silicon nitride is of importance for the technology of $Al_xGa_{1-x}N$/GaN heterojunction-based transistors. Variation of $(Si\text{-}H)_x$ and $(N\text{-}H)_y$ hydrogen bond concentrations (x, y) in a passivation silicon nitride $H_xSi_rN_zH_y$ layer was earlier shown to control the main parameters of $Al_xGa_{1-x}N$/GaN HEMTs [1].

In this work, a method of $Al_xGa_{1-x}N$/GaN heterostructure surface passivation by a nano-crystalline gallium nitride $H_xGa_rN_zH_y$ (GaN(pas.)) film deposited under electron cyclotron resonance (ECR) plasma conditions is proposed. From the standpoint of technological and physical-chemical compatibility, this method helps solve the problem of current collapse and substantially raise the target capacity of a transistor by increasing the efficiency of heat removal from heat zones.

1. Experimental

To determine their chemical composition and crystal structure, gallium nitride layers were deposited under microwave ECR plasma conditions onto high-ohmic Si (111) plates 400 μm thick which were pretreated in 25% HF solution for 10 min followed by 10 min treatment by hydrogen ECR plasma. Directly before deposition, the wafers were subjected to nitrogen ECR plasma for 10 min. Then a pre-determined flow of gallium trimethyl was added to nitrogen plasma. The deposition conditions were varied by changing the microwave power $W = (20-100)$ watt, the value of self-bias voltage $U_b = -(30-160)$ V upon 13.56 MHz field application, the total pressure $P = (0.1-2)$ mTorr, the ratio of nitrogen $F(N_2)$ to gallium trimethyl $F(TMG)$ flows $R = (1-24)$, and the substrate temperature $T = (20-300)$ °C [2].

Fourier transmission infrared spectrometry (FTIR) was used for an express analysis of the chemical composition of a deposited $H_xGa_rN_zH_y$ layer. The FTIR spectra were recorded on a 1720X Perkin–Elmer spectrometer. Structural analysis was performed on a JEOL 2000FX transmission electron microscope with an accelerating voltage of 150 kV.

For the passivation purposes, a nano-crystalline $H_xGa_rN_zH_y$ film was deposited in microwave ECR plasma onto the surface of $Al_xGa_{1-x}N$/GaN HEMTs (0.25×200 μm^2 T-gate) at $T = (20-250)$ °C.

2. Results and discussion

I–V characteristics of $Al_xGa_{1-x}N$/GaN HEMT (0.25×200 μm^2 T-gate) before and after passivation are shown in Fig. 1. The steepness of the characteristics after passivation rises considerably. After passivation we measured the of transistor S-parameters DB(|S(1,1)|), DB(|S(2,1)|) and DB(|S(2,2)|) in the 50-Ohm microwave transmission line. From the dependence of *S*-parameters on the frequency, the model of the transistor has been restored and the highest possible of amplification factor MS21 is calculated. Fig. 2 presents the dependence of the highest possible factor of amplification MS21 on frequency.

3D thermal simulation

Here we describe the results of 3D thermal simulation for power $Al_xGa_{1-x}N$/GaN HEMTs with a ten-finger gate, aimed at de-

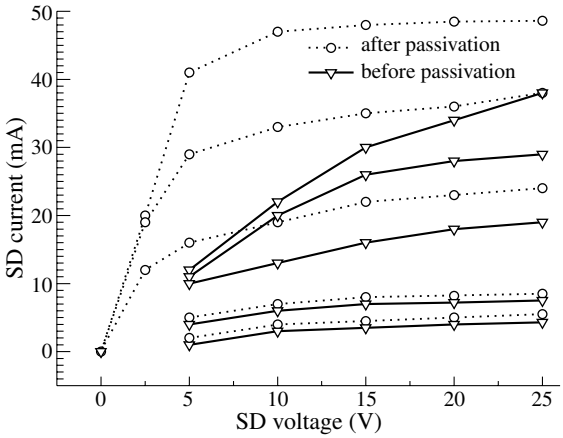

Fig. 1. I–V characteristics of $Al_xGa_{1-x}N$/GaN HEMT (0.25×200 μm^2 T-gate) before and after passivation by a $H_xGa_rN_zH_y$ 100 nm thick layer at various gate voltages V_g. Maximum $V_g = 5$ V, a step 1 V.

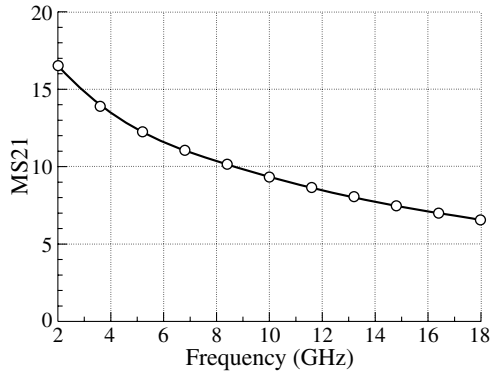

Fig. 2. The highest possible factor of amplification MS21 of $Al_xGa_{1-x}N$/GaN HEMT (0.25×200 μm^2 T-gate) vs frequency.

termining how $H_xGa_rN_zH_y$ passivation layer (GaN(pas.)) deposition influences the thermal behavior of the transistors.

The tested HEMTs have the following key dimensions: gate length is 300 nm, unit finger gate width is 100 mm (total gate width is equal to 1 μm), total channel length is 2 μm, gate-gate pitch is 52 μm and total chip area is 870×400 μm^2. We assume that the transistors are grown on a SiC substrate (300 μm thick). The epilayer structure contains an AlN nucleation layer (20 nm), of undoped GaN buffer (1 μm), and of $Al_{0.3}Ga_{0.7}N$ (20 nm). The thermal simulation is performed under steady-state conditions. The heat sources in the transistors are supposed to be positioned on the boundary between undergate and buffer layers and their joint configuration is similar to the form of the ten-finger gate. A $10\times10\times1$ mm^3 copper heat sink is used to cool semiconductor structures. The backside of the heat sink is maintained at the constant temperature 300 K. All other surfaces of the investigated structures are assumed to be thermally isolated. In the numerical model, thermal properties of the materials are assumed to depend on temperature. Figs. 3 and 4 give the calculated results. Fig. 3 depicts the influence of $H_xGa_rN_zH_y$ passivation layer thickness on maximum temperature of HEMT T_P^{max} obtained at fixed dissipated power. In addition, the figure shows the effect of layer deposition on dissipated power (P_T) at maximum temperature of HEMT does not exceed 400 K.

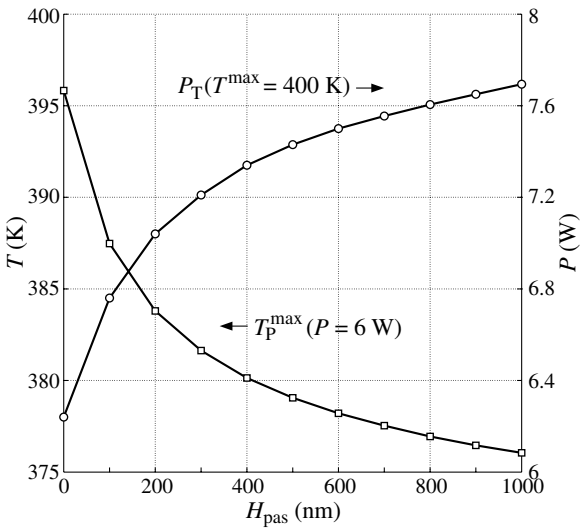

Fig. 3. Influence of $H_xGa_rN_zH_y$ passivation layer thickness H_{pas} on maximum temperature of HEMT T_P^{max} obtained at fixed dissipated power $P = 6$ W and dissipated power P_T, at maximum temperature of HEMT does not exceed 400 K.

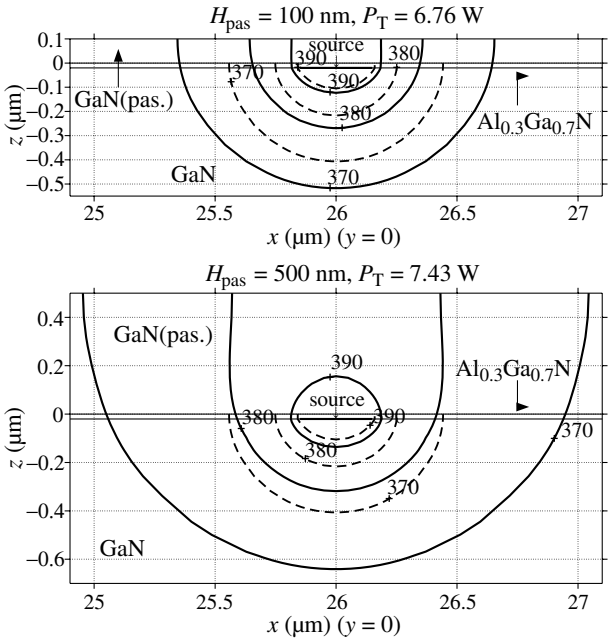

Fig. 4. Calculated distributions of isotherms (370 K, 380 K and 390 K) in the vicinity of one of the thermal sources. The dashed lines show positions of the isotherms in the HEMT structure without a passivation layer. Thermal simulation of the HEMT structures is performed at different values of H_{pas} and corresponding dissipated power P_T from Fig. 3.

Note that at passivation layer thickness 100 nm, the dissipated power P_T increases by 8.3%. For a layer thickness of 500 nm, the dissipated power P_T enhancement is equal to 19%. The reason of this increase is high thermal conductivity of the $H_xGa_rN_zH_y$ passivation layer. The greater the layer thickness, the better the source heat is dissipated (see Fig. 4).

The simulation results for HEMT with a "standard" $H_xSi_rN_zH_y$ passivation layer (we do not present them to save room) are very much like those for HEMT without a passivation layer. This finding can be explained by that the thermal conductivity of $H_xSi_rN_zH_y$ is about 10 times less than that of $H_xGa_rN_zH_y$.

References

[1] S. Shapoval, V. Sirotkin, A. Kovalchuk, V. Zemlyakov, E. Yakimov and V. Gudkov, *Proc. of WOCSDICE-2004 (Smolenice Castle, Slovakia, 2004)*, 15–16, 2004.

[2] S. Shapoval, A. Kovalchuk and V. Gorbunov, *Proc. of WOCSDICE-2005 (Cardiff, United Kingdom, 2005)*, 65–67, 2005.

14th Int. Symp. "Nanostructures: Physics and Technology"
St Petersburg, Russia, June 26–30, 2006

Examination of 3 BL step structure on Si(557) by Tersoff potential

I. G. Neizvestny, *N. L. Shwartz*, S. A. Teys, A. V. Vershinin, Z. Sh. Yanovitskaya and A. V. Zverev
Institute of Semiconductor Physics RAS SB, Novosibirsk, 630090, Russia

Abstract. Detailed investigation of 3 BL step structure on Si(557) was fulfilled by interatomic potential calculations and STM image analyses. Calculations verify the hypothesis of perpendicular dimer row formation along the boundary of 3 BL step. New peculiarities of atomic structure of 3 BL steps on Si(557) surfaces were revealed.

Introduction

Stepped vicinal Si(111) surfaces are attractive for growth of such low-dimensional structures as "quantum wires" since steps on these surfaces have low kink density [1]. Recently Si(557) surface was demonstrated to be promising for nanostructure self-organization [2, 3]. This surface represents the system of parallel three-bilayer (3 BL) steps with a period of 5.73 nm: the system of alternating facets (111) and $\langle\bar{1}\bar{1}2\rangle$ [4]. The hypothesis of perpendicular dimer row formation along three-bilayer step on the vicinal Si(111) surface deflected in direction, explaining their stability was suggested in [5]. In the present work examination of the structure of 3 BL steps on Si(557) surface were carried out using Tersoff potential [6]. Our calculations confirm previously suggested idea of dimer row formation along 3 BL step and specify details of atom arrangement in this row.

Results and discussion

Fig. 1a shows the fragment of STM image of Si(557) with 3 BL step after computer processing. In Fig. 1b are demonstrated horizontal profiles along lines 1–5. In STM image on the top terrace DAS atoms of (7×7) reconstruction are clearly seen and at the step edge in the third bilayer of the step one can notice the row of edge horizontal $D^{\parallel}{}_{(7\times7)\mathrm{ed}}$ dimers. The horizontal line 1 indicates their position. The existence of two well-defined maxima near every edge adatom along line 1 (Fig. 1b) points out the presence of $D^{\parallel}{}_{(7\times7)\mathrm{ed}}$-dimers. Line 2 indicates position of adatom row on the level of second bilayer, lines 3 and 4 are drawn along step edge at the height between the first and second bilayers, and line 5 corresponds to position of unreconstructed substrate atoms. Profile along line 2 demonstrates the periodicity ×2 and along line 5 the periodicity ×1. Similar two non-identical chains with the periodicity ×1 and ×2 were observed in Au/Si(557) STM image [7]. The elongated objects between bottom and second bilayers are clearly visible in Fig. 1a. Horizontal line 3 drawn across the elongated objects has periodicity ×2 and line 4 — periodicity ×1. In [5] such elongated objects were associated with the row of buckling dimers. However details of atom arrangement in this dimer row was unclear.

To specify atom location along 3 BL step energy calculations of the silicon cluster was carried out using Tersoff potential. A silicon cluster with sizes 4.8×4.1×1.9 nm, including 1814 atoms was used for modeling. Cyclic boundary conditions were applied in lateral directions. Only one 3 BL step was considered, so in vertical direction cluster had only 6 BLs.

In Fig. 2a three different configuration of step edge are presented. $D^{\perp}{}_{\mathrm{r}}$ and $D^{\perp}{}_{\mathrm{i}}$ dimer rows along step edge and alternate $D^{\perp}{}_{\mathrm{r}}$ and $D^{\perp}{}_{\mathrm{i}}$ dimers. In "iregular" $D^{\perp}{}_{\mathrm{i}}$ dimer, perpendicular to the step edge, one atom in dimer row is three-coordinated and has one dimerized bond, and the second two-coordinated atom has one dimerized bond and one dangling bond. In "regular" $D^{\perp}{}_{\mathrm{r}}$ dimer, both atoms are two-coordinated and have one dimerized and one dangling bond. Atom in "irregular" dimer represented with a largest circle (Fig. 2a) belongs to the bottom terrace and is three-coordinated. Results of our calculations gives following: maximal energy has step without dimers, steps with $D^{\perp}{}_{\mathrm{r}}$ or $D^{\perp}{}_{\mathrm{i}}$ dimer row are more favorable. Dimer rows with and without buckling have approximately the same energy. It was turned out that minimal energy of the system corresponds to configuration with the row of alternate $D^{\perp}{}_{\mathrm{r}}$

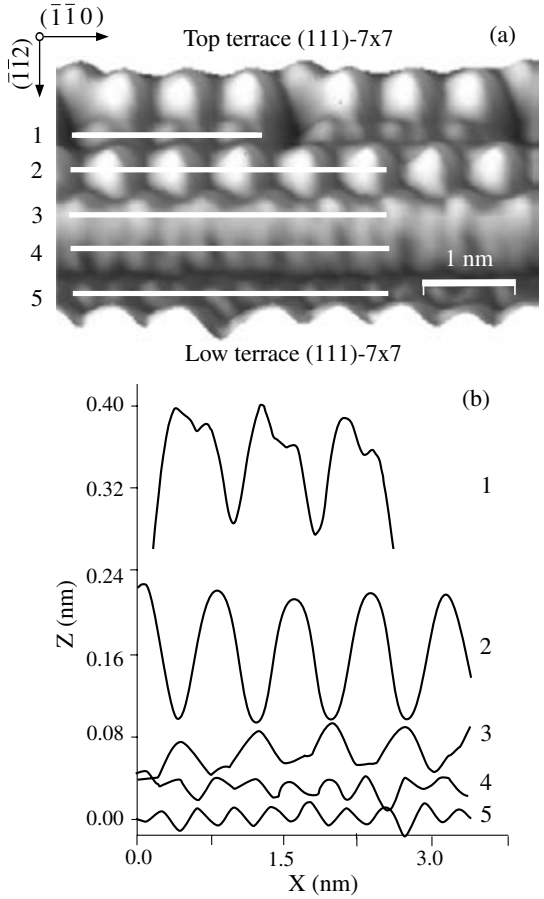

Fig. 1. (a) STM image of enlarged fragment of the edge of 3 BL step on Si(557) (after computer processing) at a positive sample bias. Horizontal line 1 indicates position of $D^{\parallel}{}_{(7\times7)\mathrm{ed}}$ dimers, line 2 — position of adatom row on the level of the second bilayer, line 3 and 4 are drawn along step edge at the height less than 2 BL, and line 5 corresponds to unreconstructed atomic row on the bottom terrace just before the step; (b) horizontal profiles along lines (1)–(5) marked in Fig. 1a.

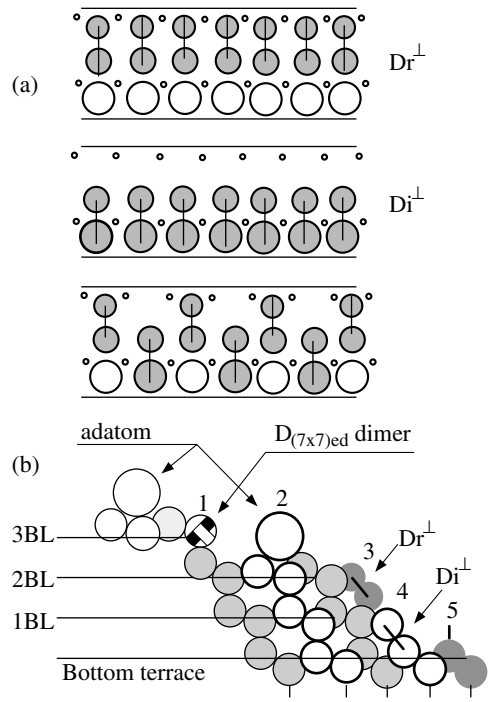

Fig. 2. (a) Schematic representations of atom arrangement at 3 BL step edge along the step (only 2 BL from the bottom terrace are considered): row of $D^{\perp}{}_{\mathrm{r}}$ dimers (atoms in the dimer are atoms of the first and second BLs), row of $D^{\perp}{}_{\mathrm{i}}$ dimers (atoms in the dimer are atoms of the bottom terrace and 1-st BL); row of alternate $D^{\perp}{}_{\mathrm{r}}$ and $D^{\perp}{}_{\mathrm{i}}$ dimmers. Atoms of the lower layer at the step are indicated with small circles; (b) schematic view of cross-section of the 3 BL step on Si(557). Numerals correspond to profile positions in Fig. 1. Circles marked in different colors lay in different planes.

and $D^{\perp}{}_{\mathrm{i}}$ dimers. In Fig. 2b a schematic view of cross-section of the 3 BL step on Si(557) is shown. Circles marked in different colors lay in different planes. Such atomic arrangement is in accordance with experimental profiles (1–5) in Fig. 1b. Profiles 4 and 5 are in antiphase, since atoms along these lines are in different planes. $D^{\perp}{}_{\mathrm{r}}$ dimers are located between adatoms 2, and $D^{\perp}{}_{\mathrm{i}}$ dimers opposite adatoms in the same plane (colored in white). Therefore maxima in curve 2 (Fig. 2b) coincide with maxima in curve 4. Suggested in this work configuration 3 BL step on Si(557) agrees with all experimental STM images presented in [5] and improve position of unreconstructed atomic row in STM image.

Summary

Atom arrangement at 3 BL step on Si(557) surface has been investigated using STM and interatomic potential calculations. Energy calculations of Si cluster including fragment of 3 BL step were carried out using Tersoff potential. Energy minimum corresponds to cluster configuration with the row of alternate $D^{\perp}{}_{\mathrm{r}}$ and $D^{\perp}{}_{\mathrm{i}}$ dimers along 3 BL step edge. Existence of dimer row along 3 BL step was confirmed in this work. Fulfilled calculations allow to give more accurate interpretation of STM images: dimer row consists not of buckling regular dimers perpendicular to step edge $D^{\perp}{}_{\mathrm{r}}$ but of alternate regular and irregular dimers.

Acknowledgement

This work was supported by the RFBR (05–02–16455, 06–02–17275).

References

[1] J. Viernow, J.-L. Lin, D. Y. Petrovykh, F. M. Leibsle, F. K. Men and F. J. Himpsel, *Appl. Phys. Lett.* **72**, 948 (1998).
[2] R. A. Zhachuk, S. A. Teys, A. E. Dolbak and B. Z. Olshanetsky, *Surf. Sci.* **565**, 37 (2004).
[3] G. Jin, Y. S. Tang, J. L. Liu, K. L. Wang *Appl. Phys. Lett.* **74**, 2471 (1999).
[4] A. Kirakosian, R. Bennewitz, J. N. Crain, Th. Fauster, J.-L. Lin, D. Y. Petrovykh and F. J. Himpsel, *Appl. Phys. Lett.* **79**, 1608 (2001).
[5] A. V. Zverev, I. G. Neizvestny, I. A. Reizvikh, K. N. Romanyuk, S. A. Teys, N. L. Shwartz and Z. Sh. Yanovitskaya, *Sov. Phys. Semicond.* **39**, 967 (2005).
[6] J. Tersoff, *Phys. Rev. B.* **37/12**, 6991 (1988).
[7] J. R. Ahn, H. W. Yeom, E. S. Cho and C. Y. Park, *Phys. Rev. B* **69**, 233311 (2004).

14th Int. Symp. "Nanostructures: Physics and Technology"
St Petersburg, Russia, June 26–30, 2006

Hybrid AlGaAsSb/InAsSb/CdSeTe heterostructures lattice-matched to GaSb for mid-IR applications

S. V. Sorokin, I. V. Sedova, A. N. Semenov, T. V. L'vova, O. G. Lyublinskaya, V. A. Solov'ev, A. A. Usikova and S. V. Ivanov

Ioffe Physico-Technical Institute, St Petersburg, Russia

Abstract. Peculiarities of molecular beam epitaxy growth of CdSeTe layers on InAsSb are discussed in detail. CdSeTe layers lattice-matched to GaSb have been used for fabrication of hybrid III–V/CdSeTe laser diode heterostructures demonstrating lasing at a wavelength of 3.86 μm ($T = 60$ K) with the threshold current density of ~ 2 kA/cm^2 under pulse injection pumping.

Introduction

Remarkable progress in mid-infrared semiconductor lasers has been achieved in recent years [1–5]. Different laser structure designs aimed at room-temperature continuous-wave laser operation have been employed. Among them are conventional type-I InGaAsSb/AlGaAsSb double heterostructure separate confinement quantum well (QW) lasers [2], quantum cascade (QCL) [3] and interband cascade (ICL) [4] lasers, as well as lasers based on the type-II InAs/GaInSb/InAs/Al(Ga)Sb multiple QW heterostructures with "W-like" band line-ups [5]. Another approach uses a hybrid pseudomorphic AlGaAsSb/InAs/CdMgSe heterostructure with a III–V/II–VI heterovalent interface at the InAs active region [6]. It provides above 1 eV asymmetric barriers for both electrons and holes in InAs, inhibiting carrier leakage from the active region. Recently, we have reported on bright photoluminescence (PL) up to room-temperature in the 3.2–4.2 μm wavelength range, measured in type II InSb/InAs quantum dot (QD) nanostructures [7]. The hybrid p-AlGaAsSb/InAs/n-CdMgSe heterostructure with 0.8 monolayer-InSb/InAs nanostructures in the active region has been grown by molecular beam epitaxy (MBE) and demonstrated stimulated emission at a wavelength of 3.075 μm ($T =$ 60 K) with the threshold current density of 3–4 kA/cm^2 under pulse injection pumping [8].

The use of InAsSb matrix instead of InAs one allows employing GaSb substrates for MBE growth, which have the wider band gap and higher structural quality than InAs. We believe that such approach allows us to improve appreciably laser diode characteristics (specifically, to reduce leakage currents and threshold current density) and to achieve coherent emission at room temperature. The using of GaSb substrates instead of InAs imposes restrictions on the choice of an appropriate II–VI alloy to adjust its lattice parameter to that of GaSb. The CdSeTe alloy has been adopted as the II–VI part of hybrid laser heterostructure.

This paper reports on the MBE growth and study of CdSeTe alloys lattice-matched to GaSb, aimed at the hybrid III–V/II–VI mid-IR laser fabrication.

1. Experimental

The CdSeTe layers were grown pseudomorphically on InAsSb buffer layers at $T_S = 295-310$ °C under group VI rich conditions. The elemental Zn, Cd, Te effusion cells and Se valve cracking cell were used as the respective molecular beam sources. The standard Bayard–Alpert ion gauge placed at the substrate position was used for flux measurements. The quality of the InAsSb/CdSeTe heterovalent interface is of crucial importance for the hybrid mid-IR laser heterostructures. We have extended a technology of InAs(001) surface preparation [9] to the $InAs_{1-x}Sb_x$ layers with relatively small Sb content ($x \sim 0.06$–0.1) lattice-matched to GaSb substrate ($a_{GaSb} = 6.096$ Å). The procedure of pre-epitaxial sulfur chemical passivation of InAs(001) includes the treatment of InAs(001) surfaces by Na_2S-water solution. It has been found that Na_2S-based chemical treatment removes the surface oxides only without any noticeable etching of InAs. Contrary to that, the existence of chemical etching mode has been observed for the case of InAsSb (001) epilayers. The etching rate and kinetics of the etching process have been studied to define both optimum concentration of Na_2S solution and treatment time.

According to the Vegard's law, CdSeTe layers with Te content of $\sim 4.7\%$ are lattice-matched to GaSb. The procedure of the II–VI growth initiation is of great importance. We have tried different procedures — short-time Te pre-exposure, migration enhanced epitaxy (MEE) of low temperature CdSe buffer and thin ZnTe layer, followed by the ternary CdSeTe deposition. The best results were obtained using ZnTe buffer layer, just in the same way as for the InAs/CdMgSe heterointerface [10]. Direct deposition of CdSeTe on InAsSb template results in 3D initial growth mode. It should be mentioned that the idea of ZnTe buffer layer was proposed and realized more than 10 years ago for MBE growth of ZnMgSeTe layers on InAs(001) substrates [11]. In quoted paper unlike current report the temperature of ZnTe buffer layer was reduced about 50–100 K lower the growth temperature of CdSeTe layer.

2. Results and discussion

The composition control of CdSeTe alloy was expected to be quite different from that of CdMgSe, as in this case we have two volatile group VI elements. Despite the formation enthalpy of CdSe is larger than the CdTe one, the much higher Te incorporation coefficient was assumed to govern the group VI atom incorporation under the group-VI-enriched growth conditions, like Se does in the ZnSSe case [12]. However, we observed the preferential Se incorporation in the CdSeTe layer, that implies dominance of thermodynamic factors if the absolute value of the incorporation coefficient of the more volatile group VI element is not negligible. This situation is similar to that observed in ZnSeTe MBE [11, 13]. At high Se fluxes ($J_{Se}/J_{Cd} > 1$) and $J_{Te} < 0.1 J_{Cd}$, there is no noticeable Te incorporation in

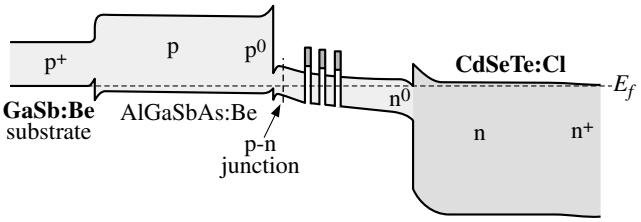

Fig. 1. Schematic band diagram of the hybrid p-AlGaAsSb/InAsSb/n-CdSeTe laser structure.

the layer, which is confirmed by both electron probe microanalysis (EPMA) and photoluminescence (PL) data. The Te incorporation starts only at the Se flux reducing to the conditions $J_{Se}/J_{Cd} \sim 1$, that confirms the similarity of ZnSeTe and CdSeTe systems. To control the composition of CdSeTe the following requirements should be met: $J_{Se}+J_{Te} > J_{Cd} > J_{Se}$. In this case all impinging Se atoms are incorporated in the layer and the rest free sites are occupied with Te atoms.

Two series of CdSeTe layers have been grown — with low ($(1.5-2)\times10^{-8}$ Torr) and high ($\sim 1\times10^{-7}$ Torr) Te flux intensity. The Se flux was varied within $(2-7)\times10^{-7}$ Torr range, while the Cd flux intensity was kept constant at $\sim 3\times10^{-7}$ Torr. All the above fluxes were measured by Bayard–Alpert ion gauge and are given in beam equivalent pressures (BEPs). One should note that in our growth geometry at substrate temperature $\sim$ 300 °C the $J_{Se}/J_{Cd} \sim 1$ flux ratio at the growth surface, controlled via the transition of (2×1)Se surface reconstruction to c(2×2)Cd one, corresponds to BEP ratio of $BEP_{Se}/BEP_{Cd} \sim 1.5$. The samples grown under the Se-rich conditions with the low tellurium flux intensity demonstrate no Te incorporation; the samples of this group also demonstrate the similar growth rate of $\sim$ 95 Å/min even at relatively high Se flux. Contrary to that, the increase of Te flux intensity up to five times results in simultaneous increase in the CdSeTe growth rate to the 140−150 Å/min range, i.e. causes the 1.5 times rising of Cd and Se sticking coefficients. It is quite surprising, that the increase of the Te flux intensity could increase the CdSeTe growth rate even for the samples demonstrating no Te

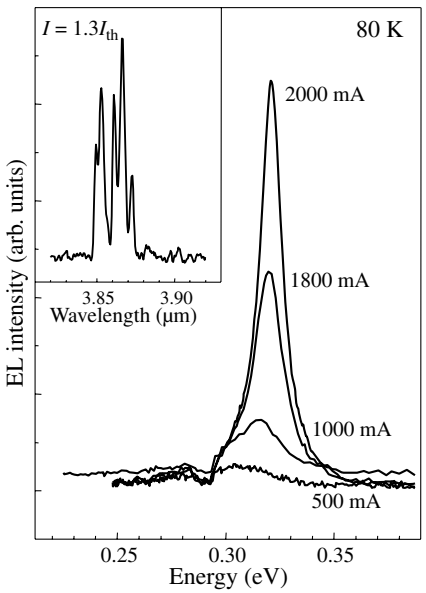

Fig. 2. Electroluminescence spectra of the hybrid laser structure measured at different injection currents. The inset shows spectrum of laser generation ($T = 60$ K).

incorporation (virtually "pure" CdSe). The nature of the phenomenon is not clear yet. The *in-situ* control of Te content in growing layer has been provided through RHEED monitoring. The Se flux has been adjusted in each growth run to provide slight (2×1)Se growth conditions. This was reproducibly resulted in 3–4% of Te content under the above Cd and Te flux intensities.

The developed technology of pseudomorphic MBE growth of CdSeTe layers lattice-matched to GaSb has been applied to fabrication of the hybrid mid-IR laser heterostructure. The design of the laser structure is the same as described in the reference [8] except for the InAs waveguide and CdMgSe n-cladding layers have been exchanged by InAsSb and CdSeTe, respectively (Fig. 1). No influence of the InAsSb/CdSeTe heterovalent interface on the I–V characteristics of the hybrid diode has been observed. The 0.6 m-thick InAsSb waveguide layer contained five 1 monolayer-thick InSb insets. The structure demonstrated stimulated emission at a wavelength of 3.86 μm ($T = 60$ K) with the threshold current density of $\sim$ 2 kA/cm^2 under pulse injection pumping (Fig. 2).

3. Conclusions

In summary, the peculiarities of MBE growth of CdSeTe on InAsSb epilayers mediated by a sulphur passivation procedure have been discussed. The main attention has been paid to composition control of the layers. CdSeTe layers lattice-matched to GaSb have been used for fabrication of the hybrid III–V/CdSeTe laser haterostructure, which demonstrates lasing at wavelength of 3.86 μm ($T = 60$ K) with the threshold current density of $\sim$ 2 kA/cm^2 under pulse injection pumping.

Acknowledgements

The work was partly supported by RFBR and Program of the Physical Sciences Department of RAS.

References

[1] J. Wagner *et al*, *Appl. Phys. A* **78**, 505 (2004).
[2] C. Lin *et al*, *Appl. Phys. Lett.* **84**, 5088 (2004).
[3] J. S. Yu *et al*, *Appl. Phys. Lett.* **87**, 041104 (2005).
[4] R. Q. Yang *et al*, *Appl. Phys. Lett.* **87**, 151109 (2005).
[5] W. Bewley *et al*, *Appl. Phys. Lett.* **85**, 5544 (2004).
[6] S. V. Ivanov *et al*, *Appl. Phys. Lett.* **82**, 3782 (2003).
[7] V. A. Solov'ev *et al*, *Appl. Phys. Lett.* **86**, 011109 (2005).
[8] V. A. Solov'ev *et al*, *Tech. Phys. Lett.* **31**, 235 (2005).
[9] S. V. Ivanov *et al*, *Appl. Phys. Lett.* **84**, 4777 (2004).
[10] S. V. Sorokin *et al*, *Proc. 11th Int. Symp. "Nanostructures: Physics and Technology", St Petersburg, Russia*, 59 (2003).
[11] M. Th. Litz *et al*, *J. Crystal Growth* **159**, 54 (1996).
[12] S. V. Ivanov *et al*, *J. Crystal Growth* **159**, 16 (1996).
[13] T. Yao, Y. Makita *et al*, *J. Crystal Growth* **45**, 309 (1978).

14th Int. Symp. "Nanostructures: Physics and Technology"
St Petersburg, Russia, June 26–30, 2006

Growth and characterization of GaAs and InAs nanowires by molecular beam epitaxy

M. Tchernycheva[1], J. C. Harmand[1], G. Patriarche[1], L. Travers[1] and G. Cirlin[2,3]

[1] CNRS-LPN, Route de Nozay, 91460 Marcoussis, France
[2] Ioffe Physico-Technical Institute, St Petersburg, Russia
[3] Institute for Analytical Instrumentation RAS, Rizhsky 26, 190103, St Petersburg, Russia

Abstract. We report on the MBE growth of GaAs and InAs nanowires using vapor-liquid-solid growth mechanism catalyzed by gold particles. The diffraction of solid catalyzer particles at low temperature and their melting were observed *in situ* using RHEED. Cylindrical shape nanowires with diameters in 20–200 nm range and lengths up to 8 μm were synthesized. Both materials crystallize in wurtzite structure showing the presence of stacking faults for GaAs nanowires and almost pure hexagonal structure for InAs ones. The temperature window where the wire formation is possible and the influence of growth conditions on the wire morphology were determined.

Introduction

The increasing attention to semiconductor nanowires (NWs) is motivated by the interest to fundamental physical phenomena in 1D systems as well as by their potential applications in electronics and photonics [1]. The vapor-liquid-solid (VLS) growth mechanism [2] for wire formation is of particular interest because it can be applied to the dislocation-free growth of highly mismatched materials and because of the possibility to fabricate p–n junctions and/or heterostructures along the wire axis.

In this presentation, we report on VLS growth of GaAs and InAs NWs on GaAs (111)B substrates using molecular beam epitaxy (MBE) and gold particles as a catalyzer. The temperature limits where the NW formation is possible were determined. The influence of the growth conditions on wire morphology and crystallographic structure was investigated using scanning electron microscopy (SEM) and transmission electron microscopy (TEM) analyses, showing that the NWs cristallize preferentially in the wurtzite structure. RHEED analyses were used to observe *in situ* the catalyzer phase transition and to monitor the NW growth.

1. Growth and characterization

NWs were synthesized in an MBE system equipped with standard effusion cells for Ga and In and a source with cracker to provide dimers of As. Growth started with a 100 nm thick GaAs buffer layer deposited on the deoxidized substrate. The sample was then transferred under ultra-high vacuum into the gold evaporation chamber where an amount of gold equivalent to 3 nm was deposited on the sample surface at room temperature. After that the sample was returned to the III–V growth chamber, the temperature was set to the desired value and GaAs or InAs NW growth was initiated. For all samples, the nominal growth rate was fixed to 0.2 nm/s and the V/III flux ratio was equal to 2 for GaAs and 3 for InAs. The growth temperature and growth duration were varied.

Growth of NWs was monitored *in situ* using Reflection High Energy Electron Diffraction (RHEED). This technique allows observing the phase change of the catalyser prior to the start of the growth. At low temperature we observed the diffraction from solid catalyzer particles, which disappeared with heating because of the catalyser melting. During the NW growth, RHEED probed the electron diffraction through the volume of nanocrystals. The obtained diffraction pattern was typical for crystal with hexagonal symmetry indicating that GaAs and InAs NWs mainly crystallize in wurtzite phase. This conclusion was confirmed by high-resolution TEM measurements of crystallographic structure.

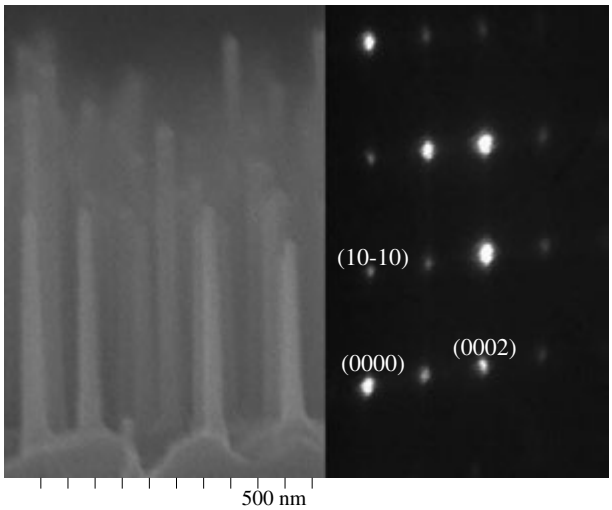

Fig. 1. Left — SEM image of GaAs NWs grown at 560 °C during 20 min, right — the corresponding RHEED pattern during growth.

For TEM characterization the NWs were separated from their substrate and picked up by touching the substrate with Cu TEM grid with a lacey carbon film. For image recording, NWs were oriented to get the viewing direction parallel to the $\langle 1{-}210 \rangle$ zone axis. The morphology of NW ensembles was investigated using field-emission SEM operated at 5 kV.

2. Influence of growth parameters on the nanowire morphology

2.1. GaAs nanowires

GaAs NWs can be synthesized in a large temperature domain from 320 to 630 °C. The low-temperature limit is imposed most probably by the solidification of the catalyzer particle. The highest growth rate and optimal morphology were obtained at 550 °C. Above this value, the NW growth rate decreases and is completely suppressed at 630 °C due probably to the melting

of GaAs substrate under the catalyzer droplets.

Low-temperature NW growth ($T < 400$ °C) is accompanied with the formation of "branches" connecting neighboring NWs together. The corresponding RHEED pattern shows arc-shaped elongated spots connected with trails. TEM analyses reveal very high density of stacking faults for low temperature synthesized NWs.

When the temperature is raised above 400 °C, the formation of branches is suppressed and the crystalline structure of NWs becomes more regular with dominating wurtzite phase, however stacking faults cannot be completely eliminated. Fig. 1 shows the SEM image illustrating the resulting NW shape and the corresponding RHEED pattern recorded for the $\langle 1-10 \rangle$ substrate orientation.

Fixing the growth temperature to its optimal value (∼550 °C), different growth durations were investigated. Up to 3 μm (40 min growth), the NWs grow at ∼ 0.8 nm/s and present almost cylindrical shape with hexagonal cross-section and typical diameter from 30 to 60 nm. Over this critical length, the NWs develop conical ends. This should be a consequence of the limited migration length of Ga adatoms on the NW surface, which can desorb or nucleate before reaching the catalyzer. In this case the side-diffusion no longer compensates the consumption of Ga, therefore the volume of the metallic particle decreases gradually, followed by the diminution of the wire diameter [3]. Nucleation on the sidewalls may also contribute to the increse of the diameter in the lower part of the NWs.

2.2. *InAs nanowires*

We have demonstrated that unlike the GaAs wires, the formation of InAs NWs on GaAs (111)B substrate is possible only in a very narrow substrate temperature window between 390 and 420 °C. In this temperature domain, which lies below the eutectic point of In-Au alloy (454 °C) [4], the catalyzer particles should be solid. This unexpected finding may indicate that the InAs NW growth relies on mechanisms other than VLS as suggested in ref [5]. However, RHEED analyses have not confirmed the presence of catalyzer solid phase. To eliminate the possible influence of the Ga containing substrate on the initial catalyzer composition, substrate has been changed to InP (111)B. As a result, the upper temperature limit was shifted to 450 °C.

Growth at 420 °C occurs with vertical growth rate of 1.4 nm/s and results in NWs of regular cylindrical shape with a hexagonal cross section and the diameter defined by the catalyzer size (in the 30–40 nm range) (Fig. 2(a)). However, when the NW length attains the critical value of ∼ 3 μm, further axial growth becomes accompanied with lateral growth leading to the increase of the diameter over almost the entire wire length except at its end (Fig. 2(b)). The NW develops cylindrical shape with tapered end; the catalyzer volume remains unchanged. The maximum growth time of 1 h 40 min resulted in NWs of 8 μm. Similar modification of the NW shape is observed if the growth temperature is decreased. The lateral growth may be a consequence of the limited diffusion length of In adatoms at these relatively low temperatures leading to the nucleation on the NW sidewalls.

TEM analyses illustrated in Fig. 2(c) show that InAs NWs crystallize in wurtzite structure almost without stacking faults (length of pure hexagonal segments can be as long as 0.5 μm). The possibility to synthesize defect-free NWs is very favorable for transport studies.

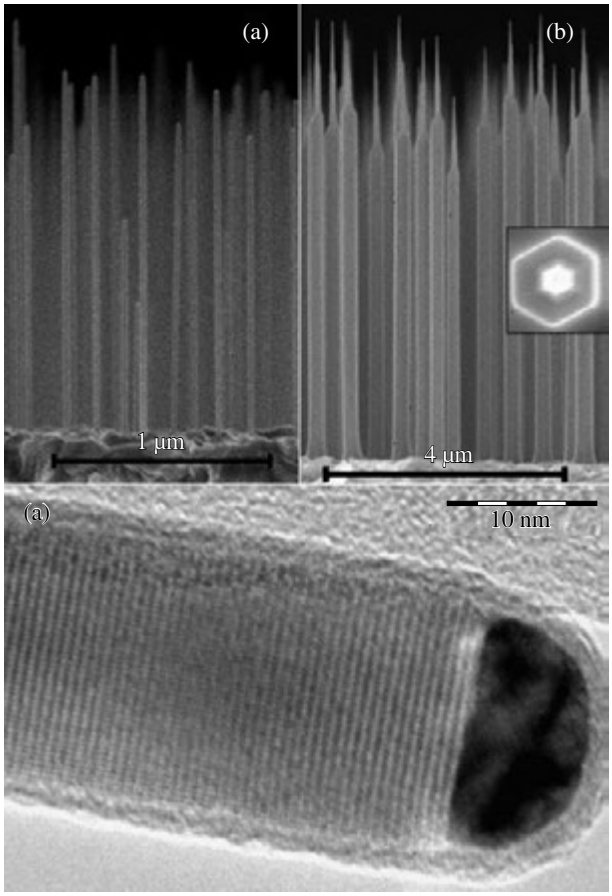

Fig. 2. SEM images of InAs nanowires grown at 420 °C for 20 min (a) and 75 min (b). NW length (diameter) is equal to 1.51 ± 0.34 μm (35±4 nm) and 6.07±0.26 μm (226±22 nm), respectively. Inset in (b) shows the top view of a single NW. (c) — high-resolution TEM image showing defect-free InAs NW crystallized in wurtzite phase.

Acknowledgements

The financial support of PNANO Filemon35 project, SANDiE European project and that of different RFBR grants is acknowledged.

References

[1] M. S. Gudiksen *et al*, *Nature* **415**, 617 (2002).
[2] R. S. Wagner, *Whisker Technology*, *Wiley*, Ney York (1970).
[3] J. C. Harmand *et al*, *Appl. Phys. Lett.* **87**, 203101, (2005).
[4] T. B. Massalski (ed.), *"Binary alloy phase diagrams"*, 2nd edn, **1**, 369, *ASM International*, Metals Park, Ohto (1990).
[5] K. A. Dick *et al*, *Nano Lett.* **5**, 761, (2005).

14th Int. Symp. "Nanostructures: Physics and Technology"
St Petersburg, Russia, June 26–30, 2006

Fabrication of InGaAs/InAsSb micro- and submicron tubes with two-dimensional electron gas on Al_2O_3(0001) and GaSb(100)substrates

Yu. S. Yukecheva, A. B. Vorob'ev, V. Ya. Prinz, V. V. Preobrazhenskii, M. A. Putyato and A. K. Gutakovsky
Institute of Semiconductor Physics, Novosibirsk, Russia

Abstract. For the first time, semiconductor tubes and helices containing two-dimensional electron gas (2DEG) with curvature radii of 300–800 nm were fabricated. Rolling of MBE-grown pseudomorphic InAsSb/InGaAs heterofilms with thickness of 18–25 nm on GaSb(100) and Al_2O_3(0001) substrates was used for their fabrication. Monocrystalline structure of these tubes and helices was confirmed by HRTEM measurements. Substrates used for heterofilm growth do not contribute to the total conductivity, thus allowing investigations of electron magnetotransport in the created objects and implementation of some device applications.

Introduction

Recently it was shown, that ultrathin epitaxial heterofilms (down to two monolayers for the case of InGaAs/GaAs) can be controllably detached from substrates and rolled, under the action of internal strains, into various cylindrical micro- and nanoshells (tubes, scrolls, rings, spirals, etc.) [1]. Investigation of electron transport in such structures is a task of particular interest.

Electrons in helices made of materials without inversion center demonstrate asymmetric dispersion law in magnetic fields: $E(k) \neq E(-k)$, what is expected to cause new effects regarding electron-phonon interaction. It was predicted theoretically, that for helical quantum wire of 1 μm radius, the relaxation time, determined by phonon scattering, should increase by some orders of magnitude as compared to straight quantum wire [2]. The effect of non-homogeneous magnetic field on a 2DEG has been studied theoretically both in the diffusive and ballistic regimes [3]. It was shown, that depending on electron wave vector, the resulting magnetic field can act as a scattering centre, but also bind electrons [4].

Electrons on the tubular surface are affected only by normal component of the magnetic field, which is spatially nonuniform. This leads to the Landau levels (LLs) bending and to the formation of current stripes, similar to edge states. Taking into account spin splitting of the LLs, these current stripes are expected to be spin-polarized [5]. If the current is directed along the cylinder axis, the total conductivity is determined by the sum of individual current stripes, that results in stair-like longitudinal magnetoresistance [6]. In case of azimuthal current direction, electric field redistribution results in current concentration along one of the sample edges, depending on the sign of magnetic field gradient [7], that leads to the strong longitudinal magnetoresistance asymmetry [8]. These effects caused by magnetic field gradient were observed in diffusive regime InGaAs tubes with diameter of 10–50 μm [6, 8]. Smaller curvature radii should produce even stronger magnetic field gradients thus giving rise to effects caused by electric field and current spatial redistribution. However, fabrication of GaAs-based submicron helices and nanotubes containing 2DEG by means of the developed technology seems to be questionable. Surface depletion layer in GaAs limits the thickness of initial heterofilm to the value of 40 nm, that corresponds to tube diameter of at least 10 μm. To overcome this problem, surface electronic passivation or materials with surface accumulation layer, are needed.

Absence of surface depletion layers in InAs and high electron mobility in this material allow fabrication of highly conductive tubes and helices with wall thickness of 10 nm and curvature radii of < 1 μm correspondingly [9]. However, for electron magnetotransport investigations non-conductive substrates are needed.

1. Experimental results and discussion

Al_2O_3(0001) with GaSb buffer layer, and GaSb(100) which is semi-insulating at helium temperatures, were used as insulating substrates for MBE growth. So as to increase the critical thickness of pseudomorphic layers, the growth temperature was lowered down to 250 °C. Heterofilms consisted of i) sacrificial AlSb layer, ii) InAsSb layer as quantum well for electrons, iii) strained Si-modulation doped InGaAs layer. An order, composition and thickness of the layers were determined from i) critical thicknesses of strained layers, ii) strains, needed for fabrication of tubes and helices of given radii, iii) possibility of highly selective removal of sacrificial layer.

InAsSb/InGaAs tubes with radius of 5 μm were obtained by etching of the sacrificial layer from metamorphic heterostructures grown on Al_2O_3(0001). This value is two times higher than the calculated one, that indicates the presence of a large number of dislocations, which should strongly limit electron mobility in such structures.

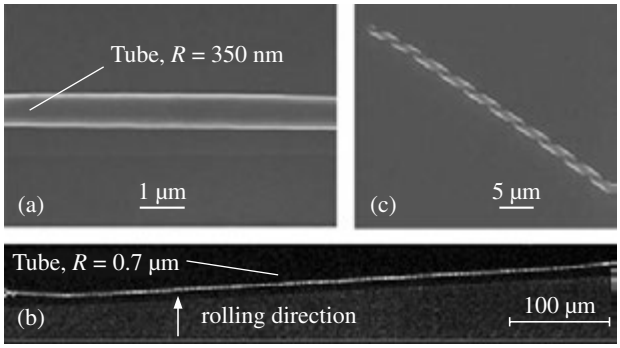

Fig. 1. InAsSb/InGaAs tubes (a, b) and helix (c) with 2DEG on GaSb(100) substrate.

The presence of 2DEG in the initial planar heterofilms grown on GaSb(100), was confirmed by observation of SdH oscillations. Electron concentration found on the basis of their period was 1.1×10^{12} cm^{-2}. Hall mobility of the 2DEG was found to be 3.7×10^{3} cm^2/V s. Such a low mobility value is attributed mainly to the reduced growth temperature. The mobility value of 10^4-10^5 cm^2/V s is expected to be achieved by optimization of growth conditions and profiles of heterostructures.

Highly conductive InAsSb/InGaAs tubes and helices of submicron curvature radii ($300 < R < 800$ nm) and of 18–25 nm wall thickness were fabricated from these heterofilms. Aspect ratio (length/radius) of these structures was about 1000 (Fig. 1). HRTEM images have revealed monocrystalline structure of these objects.

So as to create InGaAs/InAsSb tubes and helices with ohmic contacts, the directional rolling of heterofilms with the channel and contact fields formed by lithography, is realized. Results of magnetotransport measurements performed on the fabricated structures, are discussed.

Submicron tubes and helices described above can be used in device applications as well. For instance, they can be used as MEMS/NEMS components, needles of constant radii for spin-polarized tunneling spectroscopy, 3D sensors of magnetic field and magnetic field gradient.

In conclusion, exploring rolling process of MBE-grown pseudomorphic heterofilms, InAsSb/InGaAs tubes and helices containing 2DEG were fabricated. Curvature radius of these objects was found to be 300–800 nm, aspect ratio was about 1000. The substrates used for the MBE growth do not contribute to the total conductivity, thus allowing investigations of electron magnetotransport in the created structures and implementation of some device applications.

Acknowledgements

This work was partly supported by the Russian Foundation for Basic Research (grants 04-02-16910 and 06-02-16005) and the Russian Science Support Foundation.

References

[1] V. Ya. Prinz, V. A. Seleznev, A. K. Gutakovsky, A. V. Chehovskiy, V. V. Preobrazhenskiy, M. A. Putyato and T. A. Gavrilova, *Physica E* **6**, 828 (2000).
[2] O. V. Kibis, *Fiz. Tekh. Poluprovodnikov* **33**, 1332 (1999).
[3] A. Matulis, F. M. Peeters, *Phys. Rev. B* **62**, 91 (2000).
[4] J. Reijniers, F. M. Peeters, *J. Phys. C* **12**, 9771 (2000).
[5] A. Kleiner, *Phys. Rev. B* 155311 (2003).
[6] A. B. Vorob'ev, V. Ya. Prinz, Yu. S. Yukecheva, A. I. Toropov, *Physica E* **23**, 171 (2004).
[7] A. V. Chaplik, *JETP Lett.* **72**, 723 (2000).
[8] A. B. Vorob'ev, K.-J. Friedland *et al*, *to be published*.
[9] A. Vorob'ev *et al*, *Jpn. J. Appl. Phys.* **42,**, Part 2 (1A/B) L7 (2003).

14th Int. Symp. "Nanostructures: Physics and Technology"
St Petersburg, Russia, June 26–30, 2006

Systematic size-dependence of anisotropic exchange interaction in InAs/GaAs quantum dots

R. Seguin, A. Schliwa, S. Rodt, K. Pötschke, U. W. Pohl and D. Bimberg
Institut für Festkörperphysik, Technische Universität Berlin, Hardenbergstr. 36, 10623 Berlin, Germany

Abstract. A comprehensive study of the exchange interaction between charge carriers in self-organized InAs/GaAs quantum dots is presented. A systematic variation of its anisotropic part with quantum dot size is observed, leading to a change of the exciton fine-structure splitting from -80 μeV for small quantum dots to 520 μeV for large quantum dots and to a variation of the intermixing degree of the different excited trion triplet states.

Introduction

Electron-hole exchange interaction in semiconductor quantum dots has been subject of a lively debate in recent years [1]. In low symmetry systems its anisotropic part lifts the twofold degeneracy of the exciton bright states yielding the so-called excitonic fine-structure splitting (FSS). The FSS is the key parameter determining the suitability of quantum dots for producing entagled photon pairs for quantum cryptography [2] and quantum computing. It can be measured directly in luminescence experiments, since the two bright exciton (X) states yield two spectrally narrow lines which are commonly polarized in the [110] and [1$\bar{1}$0] crystal directions, respectively. Since the biexciton (XX) net spin is 0, its ground state remains degenerate under exchange interaction. The FSS can thus also be observed in the XX to X decay (Fig. 1(a)).

Anisotropic exchange also mixes the different excited positive trion (X+*) triplet states (total angular momentum $M = \pm 1/2,\ \pm 5/2$) [3]. In order to probe the energetic structure of the X+*, luminescence lines from the positively charged biexciton (XX+) to X+* decay are analyzed. Since the ground state of the initial state, namely the XX+, is completely degenerate, the lines directly yield the energetic structure of the final state, namely the X+*, analogous to the XX to X decay. The polarization degree of these lines resembles the intermixing degree of the different charged trion states and therefore the magnitude of the anisotropic exchange interaction (Fig. 1(b)) [2]. Understanding this effect is crucial for the use of the X+* states in future spin memory devices [5].

Anisotropic electron-hole exchange in quantum dots arises, when the the symmetry of the confining potential is lower than D_{2d}. Sources for such a symmetry lowering include structural anisotropies of the quantum dots, strain-induced piezoelectricity [6, 7], and interfacial symmetry lowering [8]. Recent publications have emphasized the role of piezoelectricity when calculating the electronic structure of quantum dots [9, 10].

We examine here the dependence of the anisotropic exchange on quantum dot size.

Experimental

The sample examined consists of a single layer of InAs quantum dots embedded in a GaAs matrix. Details on the growth procedure can be found elsewhere [11].

The sample was examined with a JEOL JSM 840 scanning electron microscope equipped with a cathodoluminescence setup [12]. It was mounted onto a He flow cryostat, which provided temperatures as low as 6 K. The luminescence

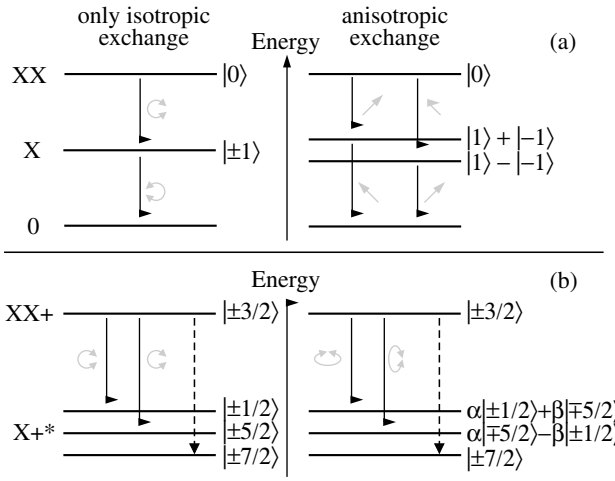

Fig. 1. Influence of the anisotropic electron-hole exchange interaction on the biexciton-exciton-0 (a) and the charged biexciton-excited trion (b) cascades. $|M\rangle$ gives the total angular momentum of the corresponding excitonic complex. Grey circles, arrows, and ellipses mark the polarization of the corresponding emission. The $|\pm 3/2\rangle$ to $|\pm 7/2\rangle$ transition is forbidden due to spin selection rules.

was dispersed by a 0.3 m spectrometer. The detection system consisted of a liquid-nitrogen cooled Si charge-coupled-device camera and a liquid-nitrogen cooled InGaAs diode array. Metallic shadow masks were applied in order to reduce the number of simultaneously probed quantum dots.

The quantum dots examined form a series of subensembles, each representing quantum dots with a fixed height, ranging from two to more than nine InAs monolayers. In the ensemble spectra, the subensembles emit rather narrow peaks (FWHM $\approx$ 30 meV). They superimpose to give the complete ensemble spectrum, consisting of eight of such peaks. This allows for a precise assignment of a given emission energy to a corresponding quantum dot height.

Two sample spectra of a large and a small single quantum dot emitting at low and high energies respectively are shown in Fig. 2. The different excitonic complexes were identified according to Ref. [13]. From the spectra it is evident, that the FSS for the high quantum dot is considerably larger than for the small quantum dot. Likewise, the polarization degree of the XX+ emission lines is larger for the high quantum dot than for the small one.

In order to examine the influence of quantum dot height on the magnitude of anisotropic exchange a number of quantum dots were probed with transmission energies ranging from 1.05 to 1.35 eV. The FSS values were determined by taking

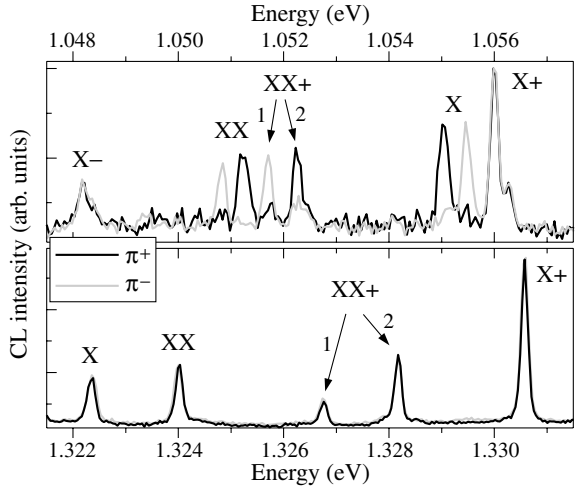

Fig. 2. Linear Polarized spectra for two different quantum dots emitting at high and low energies are shown. The different FSS magnitudes and the different XX+ degrees of polarization are clearly visible.

the average of the differences of the two polarized X and the two polarized XX lines. The FSS is defined to be positive, if the X line at lower energy is polarized along the $[1\bar{1}0]$ crystal direction. The polarization degrees p of the XX+ lines were determined by measuring their intensity for both polarization direction and applying

$$p = \frac{I_{\pi+} - I_{\pi-}}{I_{\pi+} + I_{\pi-}} \,. \tag{1}$$

The results can be seen in Fig. 3. The FSS values range from -80 μeV to more than 500 μeV exceeding all other values reported so far for this material system. Note that only absolute values of polarization degrees are shown in Fig. 3(c) for simplicity. The preferential polarization axis for the XX+ line at lower (higher) energy is always along the [110] ($[1\bar{1}0]$) crystal direction.

The measurements clearly show, that the anisotropic part of electron-hole exchange is a function of quantum dot size.

Piezoelectricity provides a possible explanation for the observed trend [9]. Its magnitude is proportional to the ocurring shear strain in the QDs. Due to the lattice mismatch between GaAs and InAs, the shear strain is larger for larger QDs [6]. Hence small (big) QDs have weak (strong) shear strain components leading to weak (strong) piezoelectric fields and consequently to a small (large) value of the fine-structure splitting.

Conclusion

While the number of participating particles varies between two (excitons) and three (trions), the underlying physical effect leading to the FSS and a finite polarization degree of the XX+ lines is the same, namely the anisotropic exchange interaction. We have shown that the magnitude of the excitonic FSS and the polarization degree of the charged XX lines are indeed correlated. They both increase with decreasing exciton recombination energy and thus increasing quantum dot size.

Acknowledgements

This work has been supported in part by the Deutsche Forschungsgemeinschaft through SFB 296 and the SANDiE Network of Excellence of the European Comission, Contract No. NMP4-CT-2004-500101.

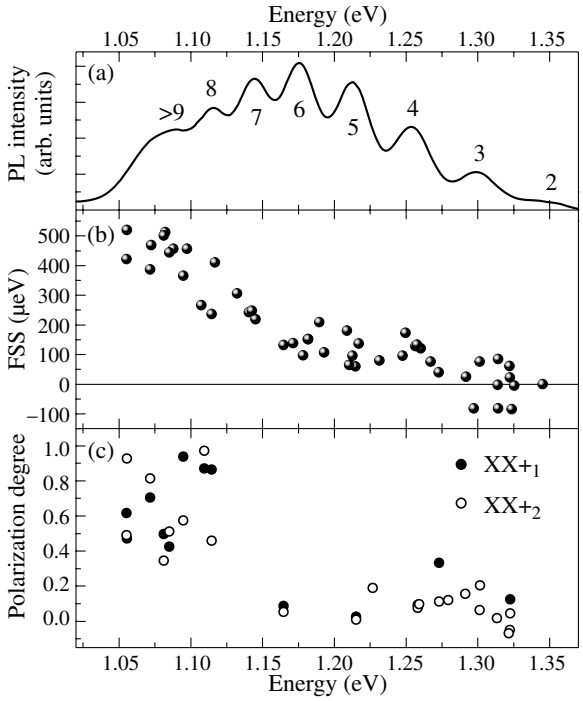

Fig. 3. (a) Ensemble photoluminescence spectrum. The numbers indicate the corresponding quantum dot height in units of InAs monolayers. (b) Measured FSS values and (c) Degree of polarization for the two XX+ emission lines over the corresponding exciton transition energy.

References

[1] e.g. M. Bayer *et al*, *Phys. Rev. B* **65**, 195315 (2002); K. Kowalik *et al*, *Appl. Phys. Lett.* **86**, 041907 (2005); R. J. Young *et al*, *Phys. Rev. B* **72**, 113305 (2005).
[2] O. Benson *et al*, *Phys. Rev. Lett.* **84**, 2513 (2000).
[3] K. V. Kavokin, *Phys. Stat. Sol. A* **195**, 592 (2003).
[4] I. A. Akimov *et al*, *Phys. Rev. B* **71**, 075326 (2005).
[5] S. Cortez *et al*, *Phys. Rev. Lett.* **89**, 207401 (2002).
[6] M. Grundmann *et al*, *Phys. Rev. B* **52**, 11969 (1995).
[7] O. Stier *et al*, *Phys. Rev. B* **59**, 5688 (1999).
[8] G. Bester *et al*, *Phys. Rev. B* **67**, 161306(R) (2003).
[9] R. Seguin *et al*, *Phys. Rev. Lett.* **95**, 257402 (2005).
[10] G. Bester *et al*, *Phys. Rev. B* **71**, 045318 (2005).
[11] U. W. Pohl *et al*, *Phys. Rev. B* **72**, 245332 (2005).
[12] J. Christen *et al*, *J. Vac. Sci. Technol. B* **9**, 2358 (1991).
[13] S. Rodt *et al*, *Phys. Rev. B* **71**, 155325 (2005).

14th Int. Symp. "Nanostructures: Physics and Technology"
St Petersburg, Russia, June 26–30, 2006

Single versus ensemble quantum dot emission in near-field spectra of InGaN QWs

A. M. Mintairov[1,2], J. L. Merz[1], D. S. Sizov[2], V. S. Sizov[2], V. V. Lundin[2], E. E. Zavarin[2], A. F. Tsatsul'nikov[2], A. S. Vlasov[2] and N. N. Ledentsov[2]

[1] Department of Electrical Engineering, University of Notre Dame, IN, 46556, USA
[2] Ioffe Physico-Technical Institute, St Petersburg, Russia

Abstract. Spectral features related to single quantum dots (QDs), In-rich islands and larger QD ensembles have been identified in spatially resolved near-field magneto-photoluminescence spectra of blue-green InGaN quantum wells (QWs). We found that individual QDs and In-rich islands appear to be located in defect regions and have activation energies below 30 meV. We found that at $T > 90$ K emission from the InGaN QW occurs from "hot spots" of size ~ 100 nm and density $\sim 5\times10^8$ cm^{-2} containing many deep QDs, having activation energy ~ 800 meV. The high emission intensity of these hot spots, occupying only 10% of the QW area, is attributed to the large oscillator strength of the optical transition in InGaN.

Introduction

Strong localization of carriers in In-rich nanoscale islands or quantum dots (QDs), suppressing carrier capture by dislocations or other non-radiative defects, is considered to be responsible for effective light emission of InGaN/GaN structures [1]. Dense arrays of InGaN QDs (10^{12} cm^{-2}) with lateral size ~ 3 nm can be formed during MOCVD growth of InGaN/GaN quantum well (QW) structures having just a few nm thick InGaN layers with In composition 10–20% [2]. The activation energy of such structures emitting in the violet-green spectral region can be as high as ~ 800 meV [3]. Recent low temperature μ-PL studies resolve sharp emission lines in InGaN/GaN QWs, which are related to individual InGaN QDs [4]. It was shown that these lines correspond to QDs having activation energies less then 30 meV. Single dot resolution of the μ-PL indicates typical values of QD density to be $\sim 10^9$ cm^{-2}, which is surprisingly close to the typical value of dislocation densities in InGaN structures.

In the present paper we used high spatial resolution ($\sim$ 100 nm) near-field magneto-photoluminescence spectroscopy [5] to study single and ensemble dot emission from MOCVD-grown InGaN/GaN and InGaN/InGaN QW structures having dense arrays of QDs.

1. Experimental

The growth of InGaN/GaN and InGaN/InGaN structures studied here was described in ref [3]. The active layers consist of 3 nm ($\sim$ 12 mono-layer) InGaN with average InN composition $\sim 12\%$.

The near field spectra were measured using collection-illumination mode. The spectra were excited using 351 nm emission from an Ar laser and measured with a 270 mm focal length spectrometer and liquid nitrogen cooled CCD detector. The spectral resolution was 0.6 meV. Near-field PL (NPL) spectra were measured at temperatures 10–90 K and magnetic field strengths 0–9 T.

2. Results and discussion

Fig. 1 presents low temperature spectra of an InGaN/GaN structure having five QWs and an InGaN/InGaN structure having a single QW taken with spatial resolution 300 nm and 2 μm. A series of sharp lines (up to twenty) are observed at high spatial resolution (300 nm), indicating that these sharp lines are

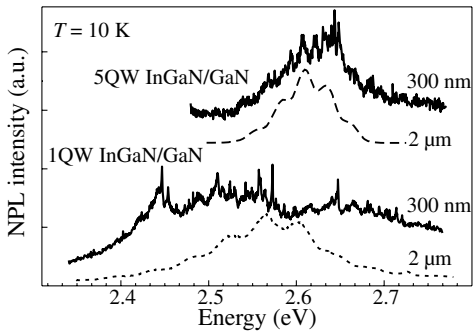

Fig. 1. NPL spectra of 5QW InGaN/GaN and 1QW InGaN/InGaN structure taken with spatial resolution 300 nm and 2 μm. $T = 10$ K, $P = 200$ W/cm^2.

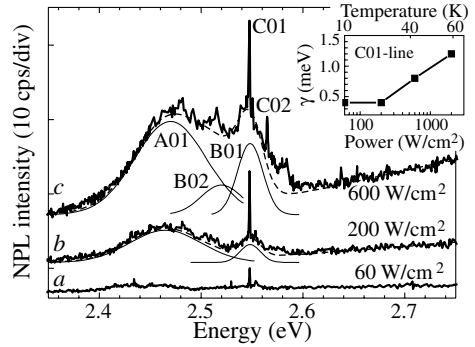

Fig. 2. NPL spectra and Gaussian modeling of InGaN/InGaN structure taken $P = 60$, 200 and 600 W/cm^2 ($T = 10$ K, aperture 100 nm). Insert shows halfwidth (γ) of the C01 line versus power density.

common features of our structures. Using higher spatial resolution ($\sim$ 100 nm, Fig. 2) allows the observation of a few sharp lines (C01 and C02); such lines will subsequently be referred to as C-lines. These sharp lines have been observed previously in μ-PL spectra [4] and were attributed to individual InGaN QDs. The analysis of the NPL spectra taken at different power density ($P = 60$, 200 and 600 W/cm^2 in Fig. 2) reveals additional broader features. One is the A-type band (A01 in Fig. 2), which is centered at ~ 2.45 eV and has halfwidth $\gamma \sim 80$ meV. It reveals a fine structure consisting of several weak peaks separated by ~ 20 meV. Two others are B-type bands (B01 and B02 in Fig. 2). They were observed at higher energies (> 2.5 eV) with halfwidths ~ 30 meV.

We found from measurements of the diamagnetic shift [5]

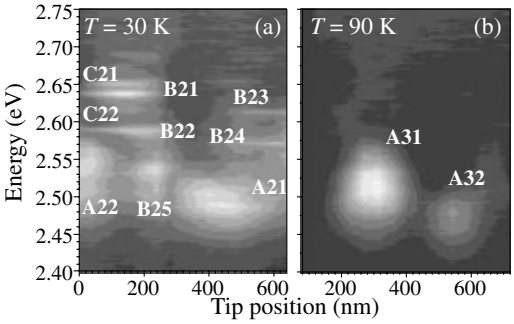

Fig. 3. Spatially and spectrally resolved NPL intensities of InGaN/InGaN structure at $T = 30$ (a) and 90 K (b) ($P = 200$ W/cm^2, aperture 100 nm). The spectra (a) and (b) taken from different places of the sample.

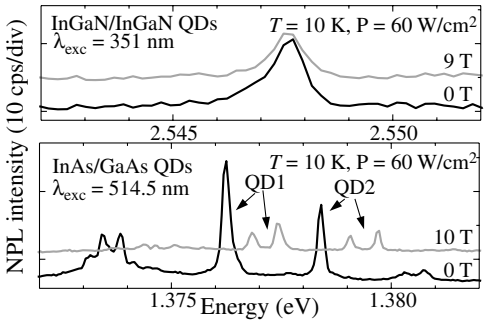

Fig. 4. NPL spectra of single InGaN/InGaN (a) and InAs/GaAs (b) QDs ($T = 10$ K, $P = 200$ W/cm^2) at magnetic field 0 and 9 T. The absence of the Zeeman splitting in InGaN QD can be explained by compensation of the spin splitting in the conduction band by holes in the valance band for an exciton confined in a QD [7].

that the sharp emission C-lines and the B-bands can be attributed to individual QDs and In-rich islands of size ~ 3 and ~ 30 nm, respectively. The density of these QDs and In-rich islands is found to be $\sim 10^9$ cm^{-2}. The A-bands, on the other hand, can be attributed to unresolvable QD ensembles, having density 10^{12} cm^{-2}. The integrated intensities of the A- and B- bands exceed the emission intensity of a single line by two orders of magnitude. The two orders-of-magnitude higher intensity of the B-bands compared with the C lines is consistent with a two-orders-of-magnitude larger volume of the island. Similarly, the integrated intensity of the A-band results from a few hundred QDs contributing to the ensemble emission.

The insert in Fig. 2 shows a broadening of the line C01 at power densities > 200 W/cm^2. This is evidence of sample heating (see top axis in the insert) and of low activation energy (< 30 meV) of these QDs [4]. This is in agreement with strong thermal quenching of C-line intensities at $T > 40$ K, observed in direct measurement of the spectra at temperatures between 10 and 90 K. The thermal quenching of the C-lines is clearly seen in Fig. 3. Here the spatially and spectrally resolved near-field PL intensities are plotted using a set of spectra taken along a ~ 600 nm linear scan at 30 and 90 K. One can see that C lines are absent in the NPL spectra at $T = 90$ K. Also the B-bands are absent in the spectra at $T = 90$ K which indicates that 30 nm In-rich islands have the same low activation energies as 3 nm QDs. We should point out that thermal quenching of the A-lines and B-bands is not accompanied by the appearance of new, higher energy emission (excited states), which indicates that carriers recombine non-radiatively after thermal activation from their ground states. This suggests that these InGaN QDs and islands are located near defects (dislocations).

In contrast to C-lines and B-bands, the A-bands have strong intensity at both 30 and 90 K (see Fig. 3a and b). This indicates that the A-band has a relatively high activation energy. From this result and from our far-field resonant excitation experiments [3] we can assign this band to an ensemble of deep InGaN/InGaN QDs having activation energies ~ 800 meV. Furthermore, from the data showing the spatial variation of the band intensities one can see that the deep and the shallow QDs are located in different regions of the QW. Indeed in Fig. 3a the A21 and A22 bands have maximum intensity at tip positions 0 and 420 nm, respectively, while the lines C21 and C22 and bands B21, B22 and B25 are at 200 nm and bands B23 and B24 are at 600 nm.

The size and the density of the areas with deep QDs (i.e. A-bands) can be estimated to be ~ 100 nm and 5×10^8 cm^{-2}, respectively. From this we estimate that the regions of multiple deep QDs occupy only about 10% of the entire QW. However, this small fraction creates "hot spots" which emit light at high temperature (see Fig. 3b).

Fig. 4a and b show the NPL spectra of single InGaN/InGaN and InAs/GaAs QD, respectively, taken at the same power density 60 W/cm^2. One can see that both spectra have similar intensities. However InAs QDs have a lateral size ~ 10 nm, i.e., an order of magnitude larger emission volume. High emission efficiency of small InGaN QDs is consistent with the order of magnitude larger oscillator strength of optical transitions in InGaN materials compared with other III–Vs [6]. Thus, the large oscillator strength of the optical transition leads to high emission efficiency in InGaN QWs, despite the fact that less than 10% of the material emits light.

3. Conclusions

We used high spatial resolution (~ 100 nm) near-field magneto-photoluminescence spectroscopy to study single dot emission in MOCVD grown InGaN/GaN and InGaN/InGaN structures having dense arrays of QDs. At low temperature (10–30 K) we observe emission from individual QDs and from In-rich islands of size ~ 3 and ~ 30 nm, respectively, which we believe are located near dislocations. We found that for $T > 60$ K emission from the InGaN QW occurs in "hot spots" of ~ 100 nm size and density $\sim 5\times10^8$ cm^{-2} containing dense arrays of small, deep QDs.

Acknowledgements

The work was supported by Collaborative NATO Grant CBP.NR. CLG 981516 and by the RFBR program.

References

[1] S. Chichibu *et al*, *Appl. Phys. Lett.* **71**, 2346 (1997); K. P. O'Donnell *et al*, *Phys. Rev. Lett.* **82**, 237 (1999).
[2] I. L. Krestnikov *et al*, *Phys. Rev. B* **66**, 155310 (2002).
[3] D. S. Sizov *et al*, "Nanostructures: Physics and Technology", St Petersburg, June, 2005.
[4] O. Moriwaki *et al*, *Appl. Phys. Lett.* **76**, 2361 (2000); J. W. Robinson *et al*, *Appl. Phys. Lett.* **83**, 2674 (2003); R. Seguin *et al*, *Appl. Phys. Lett.* **84**, 4023 (2004); H. Schömig *et al*, *Phys. Rev. Lett.* **92**, 106802 (2004).
[5] A. M. Mintairov *et al*, MRS Fall 2005 Proc. (in press).
[6] T. Tawara *et al*, *Phys. Rev. Lett.* **92**, 256402 (2004).
[7] R. Stepniewski *et al*, *Phys. Rev. B* **60**, 4438 (1999).

14th Int. Symp. "Nanostructures: Physics and Technology"
St Petersburg, Russia, June 26–30, 2006

5 ms storage time at room temperature in InGaAs quantum dots

M. Geller[1], *A. Marent*[1], A. P. Vasil'ev[2], E. S. Semenova[2], A. E. Zhukov[2], V. M. Ustinov[2] and D. Bimberg[1]

[1] Institut für Festkörperphysik, Technische Universität Berlin, Hardenbergstrasse 36, 10623 Berlin, Germany
[2] Ioffe Physico-Technical Institute, St Petersburg, Russia

Abstract. We studied carrier storage and thermal activation of holes in self-organized InGaAs/GaAs quantum dots (QDs) with an additional AlGaAs barrier. A thermal activation energy from the hole ground states over the AlGaAs barrier of 560 meV is measured using deep level transient spectroscopy (DLTS). This activation energy leads to a storage time of about 5 ms at room temperature, which could also be directly measured. The hole retention time in self-organized InGaAs QDs is, hence, comparable to the important value of the refresh time of a dynamic random access memory (DRAM). Such QDs have the potential for novel high density DRAMs.

Introduction

Self-organized semiconductor quantum dots (QDs) [1] are promising building blocks for future non-volatile single-electron memories [2] with storage densities up to 1 Tbit/inch^2. The first milestone towards the realization of such memories is the demonstration of a charge carrier storage time of milliseconds at room temperature, which is the typical refresh time of a dynamic random access memory (DRAM). At room temperature thermally activated carrier emission is the major process limiting the storage time.

We studied thermal activation and storage of holes in self-organized InGaAs/GaAs QDs with an additional AlGaAs barrier with respect to future QD-based memory devices. Previously presented investigations of the first self-organized QD memories have the difficulty of a well-defined carrier storage in the QDs [3, 4], i.e. carrier storage in defect levels cannot be excluded. Here, we employed time-resolved capacitance spectroscopy (DLTS), which allow us to unambiguously identify the carrier emission from QDs and determine their storage times. Previously, we had shown that for InGaAs/GaAs QDs the thermally activated charge carrier escape time in an applied electric field is only in the order of picoseconds at room temperature [5]. To reach longer storage times, we also studied the hole confinement in the particularly interesting GaSb/GaAs [6] system. A ground state activation energy of 450 meV has been observed and the retention time at room temperature is in the microsecond range. In this paper we report an even larger activation energy of 560 meV for holes in InGaAs/GaAs QDs by adding an additional AlGaAs barrier below the QD layer. Now, the retention time is about 5 ms at room temperature, reaching the important value of the refresh time of a DRAM memory cell.

1. Sample structure

We studied a sample with self-organized InGaAs/GaAs QDs, grown by molecular beam epitaxy (MBE). Below the QD layer a 20 nm nominally undoped $Al_{0.6}Ga_{0.4}As$ barrier was included to increase the hole storage time to milliseconds at room temperature. In detail, the sample consists of a semi-insulating GaAs substrate, followed by a 300 nm thick highly p-doped GaAs contact layer ($p = 2\times10^{18}$ cm^{-3}) and a 1000 nm thick p-doped GaAs layer ($p = 2\times10^{15}$ cm^{-3}). After the deposition of the AlGaAs barrier, a layer of In(Ga)As QDs (nominally $\sim$ 2.2 ML) was deposited with a growth rate of about 0.1 ML/sec at 485 °C. The QD layer is sandwiched between 7 nm thick undoped GaAs spacers. After deposition of 1500 nm p-doped GaAs ($p = 2\times10^{15}$ cm^{-3}), 400 nm of highly n-doped GaAs ($n = 2\times10^{18}$ cm^{-3}) was grown to from a n^+p diode structure. To form devices, processing based on standard optical lithography was applied. Circular mesas with 800 μm diameter were created by wet chemical etching and Ohmic contacts to the p^+ back and the n^+ top layer were formed by evaporation and alloying of Ni-Zn-Au and Ni-Au/Ge-Au, respectively.

2. Capacitance spectroscopy

Figure 1 displays charge-selective DLTS [6] spectra for increasing reverse bias V_r from 0.2 V up to 3.2 V. The pulse length and reference time constant were set to 1.0 s/5 ms, respectively. The pulse bias was always set to $V_p = V_r - 0.2$ V. As a consequence, on average less than one hole per QD is emitted and narrow peaks appear in the DLTS spectra. This is in contrast to a reverse/pulse bias condition in previous DLTS measurements, where the depletion of completely charged QDs is probed and, hence, a broadened DLTS peak is observed (cf. [6]). A DLTS maximum appears at $T = 300$ K for $V_r = 3.2$ V in Fig. 1 where the emission time equals approximately the applied reference time constant τ_{ref} (cf. [7]). That means, at room temperature we directly observe a storage time of about 5 ms. The observed DLTS peak corresponds to thermal activation from the QD hole ground state over the AlGaAs barrier (upper schematic inset

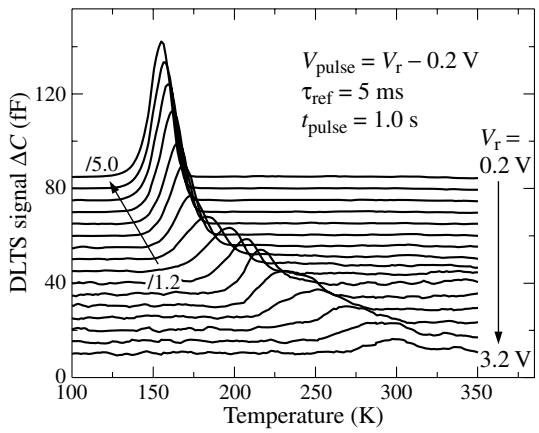

Fig. 1. Charge-selective DLTS spectra of an InGaAs/GaAs QD sample with an additional AlGaAs barrier. At a reverse bias V_r of 3.2 V a peak appears at 300 K, which is related to thermal emission from the hole ground state over the AlGaAs barrier. The spectra are vertically shifted for clarity.

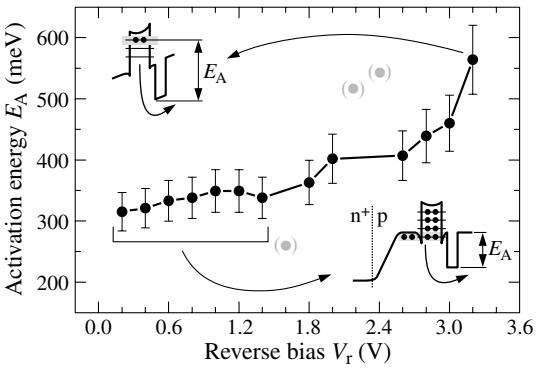

Fig. 2. Dependence of the thermal activation energy on the reverse bias V_r. The observed maximum activation energy of 560 meV at $V_r = 3.2$ V corresponds to the thermal activation of holes from the QD ground state over the AlGaAs barrier [upper schematic inset]. At reverse biases between $V_r = 0.2$ V and 1.4 V the thermal activation energy corresponds to the AlGaAs barrier height [lower schematic inset].

in Fig. 2). The DLTS maxima for reverse biases V_r between 0.2 V (at $T = 160$ K) and 1.4 V represent the thermal activation of holes from the valance band edge over the AlGaAs barrier (lower schematic inset in Fig. 2).

3. Activation energies

Using Arrhenius plots of the DLTS peak position for varying reference time constants τ_{ref}, activation energies for hole emission from differently charged QDs are obtained (Fig. 2). The hole ground state activation energy is determined to (560 ± 60) meV at a reverse bias of $V_r = 3.2$ V. With decreasing reverse bias a decrease in the activation energy down to (340 ± 40) meV is observed. The decrease in activation energy corresponds to an increase in the average occupation of the QDs. With increasing number of charge carriers in the QDs state filling lowers the thermal activation barrier. The average activation energy of about 340 meV for a reverse bias between 1.4 V and 0.2 V represents the AlGaAs barrier height [see inset in Fig. 2]. The barrier height is in good agreement with an expected value of about 330 meV [8] for an aluminum mole fraction of about 60 percent.

An InGaAs QD reference sample *without* an embedded AlGaAs barrier shows a maximum at $T = 90$ K for a reference time constant τ_{ref} of 5 ms (not shown here, see [9]) for thermal emission of holes from the QD ground states. From an Arrhenius plot an ground state activation energy of 210 meV is obtained. In this article, we showed that the AlGaAs barrier shifts the DLTS signal for the ground state emission up to $T = 300$ K (Fig. 1) and the activation energy increases accordingly from about 210 meV (without an AlGaAs barrier) up to 560 meV. Now we are able to draw a consistent picture of the energy diagram for the valence band in the InGaAs QD sample with the additional AlGaAs barrier (Fig. 3).

4. Conclusion

For InGaAs/GaAs QDs with an additional AlGaAs barrier below the QD layer we observe in charge-selective DLTS experiments a hole ground state activation energy of about 560 meV. This activation energy leads to a storage time of about 5 ms at room temperature, which we directly observe in the DLTS

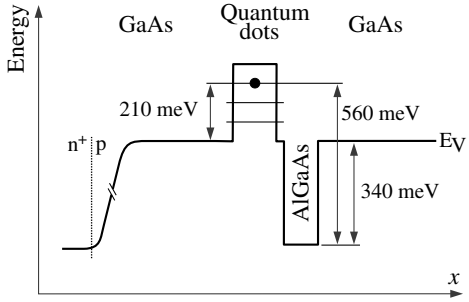

Fig. 3. Energy diagram of the valence band. The values are obtained from the DLTS experiments.

measurements. The hole retention time in InGaAs QDs is now comparable to the refresh time of a DRAM memory cell.

Acknowledgements

This work was funded by the SANDiE Network of Excellence of the European Commission, contract number NMP4-CT-2004-500101, SFB 296 of DFG, and Russian Foundation for Basic Research (RFBR).

References

[1] D. Bimberg, M. Grundmann and N. N. Ledentsov, *Quantum Dot Heterostructures* (John Wiley & Sons, Chichester, 1998).
[2] S. M. Sze, *Future Trends in Microelectronics*, edited by S. Luryi, J. Xu and A. Zaslavsky (John Wiley & Sons, Inc., 1999), p. 291.
[3] K. Koike, K. Saitoh, S. Li, S. Sasa, M. Inoue and M. Yano, *Appl. Phys. Lett.* **76**, 1464 (2000).
[4] C. Ballocco, A. M. Song and M. Missous, *Appl. Phys. Lett.* **85**, 5911 (2004).
[5] C. M. A. Kapteyn, M. Lion, R. Heitz *et al*, *Appl. Phys. Lett.* **76**, 1573 (2000).
[6] M. Geller, C. Kapteyn, L. Müller-Kirsch, R. Heitz and D. Bimberg, *Appl. Phys. Lett.* **82**, 2706 (2003).
[7] D. V. Lang, *J. Appl. Phys.* **45**, 3023 (1974).
[8] J. Batey and S. L. Wright, *J. Appl. Phys.*, **59**, 200 (1986).
[9] A. Marent, M. Geller, A. P. Vasi'ev, E. S. Semenova, A. E. Zhukov, V. M. Ustinov and D. Bimberg, *Appl. Phys. Lett.* (submitted).

14th Int. Symp. "Nanostructures: Physics and Technology"
St Petersburg, Russia, June 26–30, 2006

Computer simulation of resonant tunneling through quantum antidot in the fractional quantum Hall regime: evidence of fractional quantization of electric charge

Eugene V. Tsiper
George Mason University, Fairfax, Virginia,
Naval Research Laboratory, Washington, DC, USA

Abstract. I present the results of a computational experiment set up to model the quantum antidot electromemer used in the first observation of fractional charge in FQHE. Exact diagonalization for a cluster large enough to contain two independent edges reveals a series of ground state reconstruction events interpreted as a quasiparticle tunneling between the edges through the bulk of the fractional quantum Hall state. The periodicity of the events is consistent with the transferred charge of $e/3$ and $e/5$ in the parameter regions that correspond, respectively, to the 1/3 and 2/5 fractional states, in line with experimental observations. Traces of what might appear as charge quantization in units of $e/7$ are also discussed.

Fractional quantum Hall effect (FQHE) [1] has occupied the minds of many physicists in the past two decades. The theory of FQHE [2] has suggested the existence of quasiparticles whose electric charge is a simple fraction of the elementary charge e. Resonant tunneling through a quantum antidot (a potential hill) has been used in the first direct observation of quasiparticles of fractional charge $e/3$ and $e/5$ [3–5]. In these experiments, a periodic sequence of conduction peaks was observed as either the magnetic field H or the backgate voltage $V_{\rm BG}$ were varied. The peaks corresponds to the resonant tunneling of a quasiparticle between the outer edge of the sample and the inner edge around the antidot through the bulk of the incompressible FQH state. The periodicities ΔH and $\Delta V_{\rm BG}$ were related [3] to the quasiparticle charge e^*.

Since the bulk FQHE state is an insulator, the most interesting transport properties of the system are associated with the edges, in particular, with tunneling into or between the edges [3–7]. Computational studies of edge physics have focused on the properties of a single edge, such as non-universality of the tunneling exponent [8, 9] or reconstruction of the charge density [10–12], because they are particularly affected by the cluster size limitations imposed by the rapidly growing dimensionality of the Hilbert space. Study of edge to edge tunneling trough the bulk of an FQHE state requires clusters large enough to contain two independent edges.

In the past we have perfected the Lanczos technique [13], both Hermitian [14, 15] and non-Hermitian [16–18], and are able to solve exactly clusters with up to about 12 fermions at $f = 1/3$ or 16 fermions at half filling [14], when the Hilbert space dimensionality is $\sim 10^9$. While exact solutions for up to $N = 22$ are sometimes possible [15], the systems with $N \geq 12$ normally require approximate methods.

I have set up a *computer experiment* using a planar cluster in disk geometry to resemble the key features of the Goldman's quantum antidot electrometer [3]. Consider N electrons in the lowest Landau level, confined by a potential of a uniformly-charged disk with a hole in the center (inset in Fig. 1), positioned in the plane of two-dimensional (2D) electron gas. The positive charge density σ and the inner radius R_1 of the disk are free parameters. The outer radius R_2 is always chosen such that the whole system is neutral. The electronic density $\rho(r)$ confines itself between R_1 and R_2, falling off sharply beyond

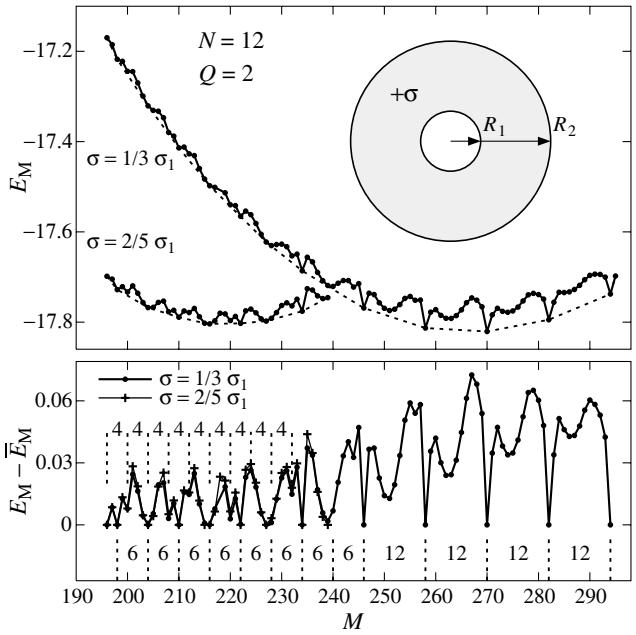

Fig. 1. Exact ground-state energy of $N = 12$ electrons in 2D confined by Coulomb attraction to a uniformly-charged annulus (inset) of charge density $\sigma = 1/3\sigma_1$ and $2/5\sigma_1$. σ_1 is the density of the completely filled Landau level. The units are $e^2/\ell_{\rm H}$.

this range. Setting σ to a fraction $\nu = 1/3$, 2/5, etc. of the density σ_1 of the completely filled Landau level controls the fractional state, with $\rho(r)$ approaching $\nu\sigma_1$ (for $N \to \infty$) far from both edges. Near the edges $\rho(r)$ is known to exhibit oscillatory behavior that is thought to decay slowly into the bulk [11].

Increasing R_1 increases the antidot strength and expells charge from inside of the antidot towards the outer edge. I prefer to use the "missing charge" $Q = \sigma\pi R_1^2/e$ as a variable, instead of R_1. Although I tune Q continuously, the ground state of the system reconstructs via a step-like process. A reconstruction event corresponds to a ground state degeneracy, where it costs no energy to move a quasiparticle from the inner to the outer edge. This is precisely the condition for the resonant tunneling through the antidot.

In the axially-symmetric geometry the single-particle states ψ_m in the lowest Landau level are characterized by the angular

momentum $m = 0, 1, \ldots$, and the total angular momentum $M = \sum m$ is conserved. The Coulomb matrix elements in the basis ψ_m are known [19,20]. I find the matrix elements of the confining potential to be $V_m = V_m(R_2) - V_m(R_1)$, where the integrals

$$V_m(R) = \int\limits_{r'<R} \int d^2r'\, d^2r \frac{e\sigma}{|\mathbf{r}-\mathbf{r}'|} |\psi_m(r)|^2 \qquad (1)$$

can be evaluated analytically.

For a given set of N, Q, and σ I find the lowest energy $E_M(Q)$ at each M. The ground state energy is then $E(Q) = \min E_M(Q)$. The ground state reconstruction events occur via level crossings of branches with different M and lead to a stepwise function $M(Q)$. The number p of the steps that occur when Q increases by one may be related to the charge e/p that is moved from the inner to the outer edge per one reconstruction event.

Figure 1 shows the exact energy $E_M(Q)$, $N = 12$, $Q = 2$. The sequence of sharp cusps on the right curve are the 1/3 fractional states. The state at $M = 270$ is the true ground state at $Q = 2$ and $\sigma = 1/3\sigma_1$, whereas the states with $M = 270 \pm 12$, $M = 270 \pm 24$, etc. are candidates for the ground state at different Q. The quasi-periodicity with $\Delta M = 12$ is due to the approximate invariance of the antidot Hamiltonian with respect to the Laughlin's quasihole creation operator $\mathcal{A}_0$ [2], also known to be the generator of infinitesimal magnetic translations [21]. Applied to an arbitrary many-electron wave function Ψ, it translates it in the angular momentum space, $m \to m+1$. The total angular momentum then transforms as $M \to M + N$:

$$\Psi_{M+N} \approx \mathcal{A}_0 \Psi_M \,. \qquad (2)$$

At $Q = 0$ the ground state occurs, approximately, at the Laughlin's angular momentum [22]

$$M^*(Q=0) = \frac{N(N-1)}{2\nu} \,. \qquad (3)$$

For a disk with the missing charge Q we can generalize this naturally to

$$M^* = \frac{(N+Q)(N+Q-1)}{2\nu} - \frac{Q(Q-1)}{2\nu} \,. \qquad (4)$$

For $N = 12$ and $Q = 2$ we get $M^*_{1/3} = 270$ and $M^*_{2/5} = 225$ (cf. Fig. 1).

The single-particle orbitals $\psi_m(r)$ are localized near $r = \ell_H\sqrt{2m}$, where ℓ_H is the magnetic length. Therefore, in a macroscopic system whose density approaches a constant $\nu\sigma_1$ in the bulk, the operator $\mathcal{A}_0$ pushes the density out of the center, creating an effective positive charge $e^* = \nu e$. This is an exact formal property of $\mathcal{A}_0$ but relates to the physical system through the above mentioned approximate invariance. Indeed, Eq. (4) can be obtained from (3) by applying $\mathcal{A}_0^{(Q/\nu)}$:

$$M^* = M^*(Q=0) + NQ/\nu \,. \qquad (5)$$

Figure 1, therefore, suggests that the ground state of the 1/3 system changes in steps of $\Delta M = N$, transferring charge $e^* = e/3$ from the inner to the outer edge at every step. Accoriding to (5) the steps should occur at $\Delta Q \approx \nu = 1/3$.

Remarkably, the range of M corresponding to the 2/5 fractional state exhibits double periodicity. This causes branch crossings twice as often, $\Delta M = N/2$, $\Delta Q \approx \nu/2 = 1/5$, resulting in the charge $e^* = \nu e/2 = e/5$ transferred per reconstruction event, as expected from the experiment [4]. I also have observed the double periodicity in $E_M(Q)$ for $\sigma = \frac{2}{5}\sigma_1$ for $N = 11$, 10, 9, and 8, though it becomes less pronounced for smaller N.

The lower panel in Fig. 1 exposes the tiny structure in $E_M(Q)$ by subtracting its greatest convex minorant $\overline{E}_M$ [dotted blue line]. I notice that this structure, which is the manifestation of the FQHE, is insensitive to the confining potential, and is practically the same for $\sigma = 1/3\sigma_1$ and $2/5\sigma_1$. It hints towards rigidity of the wave function with respect to the confining potential [$\delta\Psi_M/\delta V(r)$ being small by some measure], the principal effect of the latter being to select which M is the ground state. Inspection of the region about $M = 210$ also suggests that traces of $\Delta M = 4 = N/3$ periodicity, that by the same logic would correspond to $e^* = e/7$, may be present in the area near $M^*_{3/7} = 210$, although larger clusters are needed to separate the 2/5 and 3/7 states. Indeed, from Eq. (3), the condition $M^*_{2/5} - M^*_{3/7} \geq N$ leads, at $Q = 0$, to $N \geq 13$.

References

[1] D. S. Tsui, H. L. Stormer and A. C. Gossard, *Phys. Rev. Lett.* **48**, 1559 (1982).
[2] R. B. Laughlin, *Phys. Rev. Lett.* **50**, 1395 (1983).
[3] V. J. Goldman and B. Su, *Science* **267**, 1010 (1995).
[4] V. J. Goldman, *Surf. Science* **361**, 1 (1996).
[5] V. J. Goldman, *Physica E* **1**, 15 (1998).
[6] A. M. Chang, *Rev. Mod. Phys.* **75**, 1449 (2003).
[7] A. Boyarsky, V. V. Cheianov, O. Ruchayskiy, *Phys. Rev.* **B70**, 235309 (2004).
[8] X. Wan, F. Evers and E. H. Rezayi, *PRL* **94**, 166804 (2005).
[9] V. J. Goldman and E. V. Tsiper, *PRL* **86**, 5841 (2001).
[10] X. Wan, K. Yang and E. H. Rezayi, *PRL* **88**, 56802 (2002).
[11] E. V. Tsiper, V. J. Goldman, *Phys. Rev.* **B64**, 165311 (2001).
[12] G. S. Jeon and J. K. Jain, *Phys. Rev.* **B71**, 45337 (2005).
[13] C. Lanczos, *J. Res. Natl. Bureau of Standards* **45**, 255 (1950).
[14] E. V. Tsiper and A. L. Efros, *Phys. Rev.* **B57**, 6949 (1998).
[15] E. V. Tsiper and A. L. Efros, *J. Phys. C* **9**, L561–L567 (1997).
[16] E. V. Tsiper, *JETP Letters* **70** 11, 751 (1999).
[17] V. Chernyak *et al*, *J. Chem. Phys.* **113**, 36 (2000).
[18] E. V. Tsiper, *J. Phys. B* **34**, L401 (2001).
[19] E. V. Tsiper, *J. Math. Phys.* **43**, 1664 (2002).
[20] S. M. Girvin and T. Jach, *Phys. Rev. B* **28**, 4506 (1983).
[21] Yu. A. Bychkov and E. I. Rashba, *JETP* **63**, 200 (1986).
[22] C. Yannouleas, U. Landman, *Phys. Rev.* **B68**, 35326 (2003).

14th Int. Symp. "Nanostructures: Physics and Technology"
St Petersburg, Russia, June 26–30, 2006

Hyperfine interaction in InGaAs QDs

R. Oulton[1], R. V. Cherbunin[1,2], A. Greilich[1], *I. V. Ignatiev*[1,2], D. R. Yakovlev[1,3] and M. Bayer[1]

[1] Experimentelle Physik II, Universität Dortmund, 44221 Dortmund, Germany
[2] St Petersburg State University, 199036 St Petersburg, Russia
[3] Ioffe Physico-Technical Institute, St Petersburg, Russia

Abstract. I present the results of a computational experiment set up to model the quantum antidot electromemer used in the first observation of fractional charge in FQHE. Exact diagonalization for a cluster large enough to contain two independent edges reveals a series of ground state reconstruction events interpreted as a quasiparticle tunneling between the edges through the bulk of the fractional quantum Hall state. The periodicity of the events is consistent with the transferred charge of $e/3$ and $e/5$ in the parameter regions that correspond, respectively, to the 1/3 and 2/5 fractional states, in line with experimental observations. Traces of what might appear as charge quantization in units of $e/7$ are also discussed.

Introduction

Strong localization of electrons in quantum dots (QDs) designed from A_3B_5 semiconductors considerably strengthens the hyperfine interaction with nuclear spins, due to increase of the electron density on the nuclei [1]. As it was proposed theoretically [2], this should result in the increased efficiency of the electron spin relaxation, caused by precession of the electron spins in the random effective magnetic field of the nuclear spin fluctuations in the QD ensemble. This effect has already been observed for InP [3] and InAs [4] QDs.

Here we present results of detailed investigations of hyperfine interaction in n-doped InGaAs QDs. Exploiting several experimental methods, we have studied the effect of nuclear spin fluctuations (NSF) as well as of the dynamic nuclear polarization (DNP) created by the hyperfine interaction with optically oriented electron spins.

1. Experimental

We have studied several samples containing 20 layers of InGaAs QDs separated by thick delta *n*-doped GaAs barrier layers. The as-grown InAs QD samples underwent a post-growth rapid thermal annealing process at temperatures ranging from 800 °C to 960 °C for 30 s. This leads to a diffusion of indium from the QD, and results in a reduction in vertical confinement and lateral spreading of the wavefuntion, thus shifting the wavelength from $\sim$ 1200 nm to $\sim$ 890 nm. We show results here from a sample strongly annealed at 900 °C. Electron concentration in the QDs due to the barrier delta-doping corresponds to approximately one electron per dot, as confirmed by Faraday rotation spectroscopy [13].

1.1. PL polarization

Presence of the resident electrons in the QDs gives rise to negative circular polarization (NCP) of the PL, created by circularly polarized optical excitation into the wetting layer (Fig. 1) [14]. Amplitude of the NCP may be used as a measure of spin orientation of the resident electrons [5].

We found that the NCP amplitude and, correspondingly, the electron spin orientation strongly depends on the relatively small magnetic field, B, applied along the optical axis of the excitation (Faraday configuration) as shown in Fig. 2. At relatively weak excitation, the magnetic field dependence of the NCP amplitude, $A_{\rm NCP}(B)$, reveals a well-resolved dip at around zero magnetic field, with a full width at half maximum (FWHM), $\delta B_{\rm N}$, of the order of a few tens of mT (upper curves in Fig. 2). Behavior of the dip is independent of the helicity of circular polarization of excitation within the experimental error. Under strong excitation, dependence $A_{\rm NCP}(B)$ becomes asymmetric relative to zero magnetic field, and strongly depends on the helicity of the excitation (lower curves in Fig. 2). All the experimental dependences may be well approximated by a phenomenological function:

$$A_{\rm NCP}(B) = -S_0 + P\frac{1 + 2f(B - B_{\rm N})/\delta B_{\rm N}}{(2(B - B_{\rm N})/\delta B_{\rm N})^2}\,. \qquad (1)$$

where S_0 characterizes spin polarization at large magnetic field, P — amplitude of the dip, f — asymmetry of the dependence, $B_{\rm N}$ — the shift of the dip from zero magnetic field. For the curves shown in Fig. 2, $\delta B_{\rm N} = 50$ mT, with $f = 0$ for weak excitation and $\delta B_{\rm N} = 70$ mT, $f = -1.8$ (σ^+), $f = 1.4$ (σ^-) for strong excitation, and $B_{\rm N} = 0$ in all cases, within the experimental error.

The behavior of the spin polarization in external magnetic field discussed above can be treated as a result of the effects of NSF and DNP. Due to the limited number of nuclear spins interacting with the electron spin in a QD, typically $n \sim 10^5$, random correlation of nuclear spins may create a fluctuating nuclear polarization acting on the electron spin as an effective magnetic field $\delta B_{\rm N}$, with random magnitude and orientation [2]. As the spin orientation of the nuclear system evolves slowly (over a timescale of $\sim 1\ \mu$s), the electrons see a "snapshot" of the nuclear system. The electron precesses about the

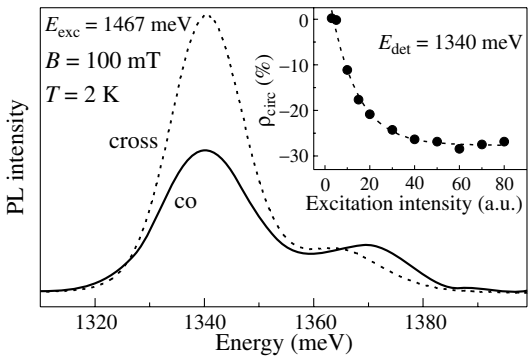

Fig. 1. (a) PL spectra in co- and cross-polarizations at σ^+-polarized excitation. (b) Spectrum of the degree of circular polarization of the PL calculated in the standard manner.

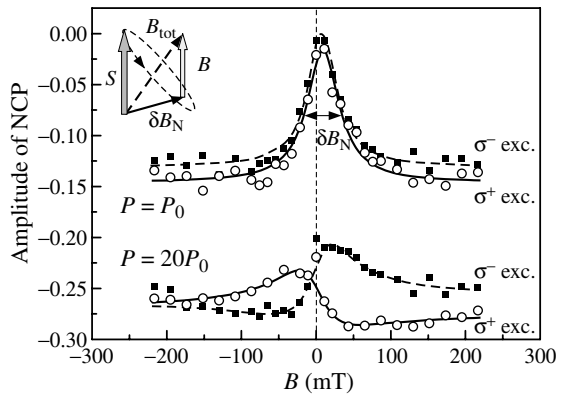

Fig. 2. Magnetic field dependence of the NCP amplitude at weak ($P = P_0 \sim 10$ W/cm^2, upper curves) and strong ($P = 20P_0$, lower curves) excitations. Symbols show experimental data and solid lines the fits by function (1). Inset: electron spin precession about $B_{\rm tot} = B + \delta B_{\rm N}$.

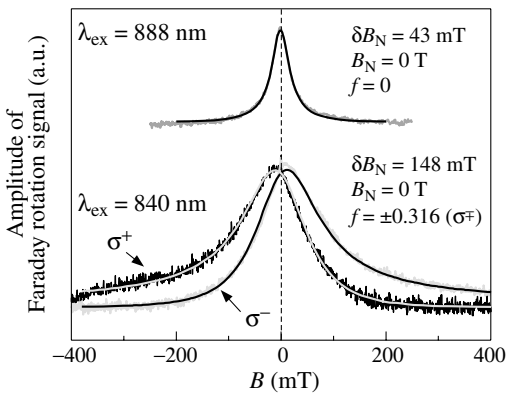

Fig. 3. Faraday rotation signal for resonant (upper curve) and non-resonant excitation. $P = P_0 \sim 10$ W/cm^2. Fits by function (1) are shown by open circles. Fit parameters: $\delta B_{\rm N} = 43$ mT, $B_{\rm N} = 0$, $f = 0$ for upper curve; $\delta B_{\rm N} = 148$ mT, $B_{\rm N} = 0$, $f = -0.316$ (σ^+), $f = 0.316$ (σ^-) for lower curves. Sign of signal for σ^--polarized excitation is inverted. Small linear slopes of the lower curves which are probably caused by the electron spin freezing at the lower Zeeman sublevel are subtracted.

random nuclear field, with the result that the projection of the electron polarization onto the optical axis is initially reduced, and then remains stable. The resulting PL polarization should be reduced to one third of the initial value, as long as the electron spin lifetime is less than ~ 1 μs. In QDs however, the electron spin may be stable over longer timescales: thus in this case, the "snapshot" of the nuclear field will change, and lead to further decrease in electron spin polarization.

An external magnetic field $B > \delta B_{\rm N}$ applied along the optically oriented electron spin direction suppresses the effect of NSF and, correspondingly, restores the electron spin polarization. Theoretical calculations [2] give rise a smooth dependence of the electron spin polarization on the external magnetic field, which we modeled in the case of weak excitation using a Lorentzian-like dependence (1) when the parameter of asymmetry $f = 0$.

Strong excitation by circularly polarized light of one helicity (σ^+ or σ^-) should create dynamic nuclear polarization via hyperfine interaction with optically oriented electron spins (see e.g. ref. [6]). The DNP affects the electron spin as an effective magnetic field, $B_{\rm N}$, which is added to or subtracted from the external magnetic field B. We would expect some shift of the experimentally observed dip in spin polarization from $B = 0$ to $B = -B_{\rm N}$. Such an effect has been observed previously as the Overhauser shift of the optical transitions in single GaAs [7] and InAlAs [8] QDs. However in our experiments, no clearly detectable shift of the dip is observed. At strong excitation, which is favorable for creation of the DNP, a decrease of the dip amplitude and the appearance of asymmetry in the B-field dependence of $A_{\rm NCP}(B)$ is observed instead of the shift. Though the quantitative description of the dependence is a problem for a future theory, we can give a few comments for this observation.

Dynamical nuclear polarization is created via hyperfine interaction with polarized electrons. However the electron spin polarization may be efficiently destroyed due to the electron spin precession about the total magnetic field (see inset in Fig. 2) in those QDs where the angle between vectors S_0 (the photocreated electron spin) and $\delta B_{\rm N}$ is large and the absolute value of $\delta B_{\rm N}$ exceeds that of the external magnetic field. Due to the random distribution of $\delta B_{\rm N}$, the dynamic nuclear polarization should be also randomly distributed over the QD ensemble. We therefore expect an enlargement of the dip width and an appearance of asymmetry with optical pumping.

1.2. Faraday rotation

In photoluminescence experiments, the fact that excitons (trions) must be present to observe PL means that several physical processes must be taken into account. In particular, the exchange interaction responsible for the NCP may be dependent on applied field. Therefore, alternative physical mechanisms for the dependence of $A_{\rm NCP}(B)$ on field may exist, and are discussed in the literature [9, 10].

To eliminate these various processes, and to verify the interpretation of the nuclear spin effects discussed above, we studied the magnetic field dependence of the electron spin polarization by another method, namely by measuring the Faraday rotation signal in polarized pump-probe experiments [11]. In this method, the circularly polarized pump pulses create a spin orientation of the resident electrons. The electron spin orientation is then detected as the rotation angle of linearly polarized probe pulses, delayed in time relative to pump pulses. We monitored the Faraday rotation intensity for a large fixed delay of about 12 ns, when all other transient processes (e.g. trion recombination) created by the pump have radiatively decayed, and the measured signal results solely from the spin orientation of the resident electrons. Due to the extremely long lifetime of the electron spin orientation in the QDs under study (orders of magnitude greater than the laser repetition rate [12, 13]), the Faraday rotation signal may be easily observed at this large delay.

In Fig. 3, the upper noisy curve shows the typical magnetic field dependence of the signal under strictly resonant excitation to the lowest optical transition of the QDs under study. Again, a dip very similar to that observed in the PL polarization (Fig. 2) is observed around zero magnetic field. This observation supports our interpretation given above of the spin depolarization at zero magnetic field as being due to the hyperfine interaction with the fluctuating effective nuclear spin field.

The dip in the Faraday rotation signal observed at resonant excitation may be successfully fitted by function (1) with factor $f = 0$. The width $\delta B_{\rm N}$ of the dip varies from 30 to 50 mT

depending on the pump power density and independent of the helicity of the excitation polarization. No asymmetry of the dip is observed at this excitation. This is probably due to small absorption coefficient at the QD transitions and, therefore, weak pumping of the nuclear spin system.

To increase the pumping efficiency, we used a two-color pump-probe method, whereby the pump beam wavelength is tuned to the wetting layer absorption maximum and the probe beam wavelength is kept resonant to the lowest optical transition in the QDs. Under these conditions, the dip becomes much wider and asymmetric (lower curves in Fig. 3). As in the PL experiment (Fig. 2), the asymmetry is dependent on the helicity of the pump beam polarization. However, no shift B_N of the dip from zero magnetic field is observed, even under these excitation conditions. This suggests that the DNP created is inhomogeneous, with many QDs experiencing no DNP, such that the peak remains at zero.

In conclusion, the experiments performed have allowed us for the first time to determine the effective magnetic field of the nuclear spin fluctuations in the quantum dots under study. Its value is characterized by a Lorentzian distribution with full width at half maximum of about 30 mT at low limit of the excitation, and a much wider and asymmetric distribution under strong pumping. These experiments also allowed us to study the dynamic nuclear polarization under strong excitation by circularly polarized light. An effective magnetic field of the nuclear polarization is found to be surprisingly low and inhomogeneous. Physical origin of such inefficient nuclear spin polarization in InGaAs/GaAs should be studied further.

Acknowledgements

The work is partly supported by ISTC, grant 2679.

References

[1] D. Gammon, Al. L. Efros, T. A. Kennedy, M. Rosen, D. S. Katzer, D. Park, S. W. Brown, V. L. Korenev and I. A. Merkulov, *Phys. Rev. Lett.* **86**, 5176 (2001).

[2] I. A. Merkulov, Al. L. Efros and M. Rosen, *Phys. Rev. B* **65**, 205309 (2002); A. V. Khaetskii, D. Loss and L. Glazman, *Phys. Rev. Lett.* **88**, 186802 (2002).

[3] I. V. Ignatiev, I. Ya. Gerlovin, S. Yu. Verbin, B. Pal and Y. Masumoto, *Proc. 13th Int. Symp. Nanostructures: Physics and Technology*, (St Petersburg, 2005), Ioffe Inst., p. 47, 2005; also available on-line at http://arXiv.org: cond-mat/0508698.

[4] P.-F. Braun, X. Marie, L. Lombez, B. Urbaszek, T. Amand, P. Renucci, V. K. Kalevich, K. V. Kavokin, O. Krebs, P. Voisin and Y. Masumoto, *Phys. Rev. Lett.* **94**, 116601 (2005).

[5] M. Ikezawa, B. Pal, Y. Masumoto, I. V. Ignatiev, S. Yu. Verbin and I. Ya. Gerlovin, *Phys. Rev. B* **72**, 153302 (2005).

[6] Edited by F. Meier and B. P. Zakharchenya, *Optical Orientation. Modern Problems in Condensed Matter*, Amsterdam: Publisher, 1984.

[7] A. S. Bracker, E. A. Stinaff, D. Gammon, M. E. Ware, J. G. Tischler, A. Shabaev, Al. L. Efros, D. Park, D. Gershoni, V. L. Korenev and I. A. Merkulov, *Phys. Rev. Lett.* **94**, 047402 (2005).

[8] T. Yokoa, S. Adachi, S. Muto, H. Sasakura, H. Z. Zong, S. Horose, T. Usuki, *Physica E* (2005).

[9] V. L. Berkovits, A. I. Ekimov, V. I. Safarov, *JETP* **65**, 346 (1973).

[10] V. K. Kalevich, I. A. Merkulov, A. Yu. Shiryaev, K. V. Kavokin, M. Ikezawa, T. Okuno, P. N. Brunkov, A. E. Zhukov, V. M. Ustinov and Y. Masumoto, *Phys. Rev. B* **72**, 045325 (2005).

[11] Edited by D. D. Awschalom, D. Loss and N. Samarth, *Semiconductor Spintronics and Quantum Computation*, Berlin: Springer, 2000.

[12] S. Yu. Verbin, A. Greilich, D. R. Yakovlev, M. Bayer, V. Stavarache, D. Reuter and A. Wieck, *Proc. 13th Int. Symp. Nanostructures: Physics and Technology, (St Petersburg, 2005)*, Ioffe Inst., p. 39, 2005.

[13] A. Greilich, R. Oulton, E. A. Zhukov, I. A. Yugova, D. R. Yakovlev, M. Bayer, A. Shabaev, Al. L. Efros, I. A. Merkulov, V. Stavarache, D. Reuter and A. Wieck, submitted to *Phys. Rev. Lett.* (submitted Nov 05).

[14] R. I. Dzhioev, B. P. Zakharchenya, V. L. Korenev and M. V. Lazarev, *Phys. Sol. State* **41**, 2014 (1999); S. Cortez, O. Krebs, S. Laurent, S. Senes, X. Marie, P. Voisin, F. Ferreira, G. Bastard, J.-M. Gerard and T. Amand, *Phys. Rev. Lett.* **89**, 207401 (2002).

14th Int. Symp. "Nanostructures: Physics and Technology"
St Petersburg, Russia, June 26–30, 2006

Electron-hole liquid in SiGe potential wells of nanostructures Si/SiGe/Si

T. M. Burbaev[1], V. A. Kurbatov[1], M. M. Rzaev[1], N. N. Sibeldin[1], V. A. Tsvetkov[1] and F. Schäffler[2]

[1] P. N. Lebedev Physical Institute, RAS, 119991 Moscow, Russia
[2] Institut für Halbleiter- und Festkörperphysik, J. Kepler Universität Linz, Austria

Abstract. Low-temperature photoluminescence spectra of $Si/Si_{1-x}Ge_x/Si$ nanostructures as a function of temperature and excitation level are investigated. Formation of electron-hole liquid in the layers of $Si_{1-x}Ge_x$ solid solution is observed. It is found that under the conditions of spatial localization of the photoexcited charge carriers in SiGe-layer, which is a potential well for holes, the threshold power of excitation is lower and the threshold temperature of formation of liquid is noticeably higher than in bulk material of the same composition.

Introduction

The phenomenon of condensation of excitons into the electron-hole liquid (EHL) was predicted by L. V. Keldysh in 1968 [1]. After that, in a large number of theoretical and experimental publications basic characteristics of the phase transition gas of excitons — EHL and properties of the liquid phase of bulk semiconductors have been investigated in detail (see reviews [2–4]). However, until recently, in the literature there were practically no papers dedicated to the experimental studies of this phenomenon in low-dimensional objects. Apparently, nanostructures on the basis of silicon and germanium are the most promising for the investigation of condensation of excitons in low-dimensional objects because bulk silicon and bulk germanium are classical materials for the studies of EHL. Recently, EHL has been detected in thin silicon layers of the high-quality Si/SiO_2 heterostructures, grown by the methods of silicon integrated technology [5, 6].

We investigated low-temperature photoluminescence (PL) spectra of high-quality $Si/Si_{1-x}Ge_x/Si$ nanostructures, grown by molecular beam epitaxy (MBE), as a function of temperature and a level of excitation. The formation of EHL in a layer of $Si_{1-x}Ge_x$ solid solution and also in the buffer and the cap layers of silicon was detected at the temperatures of liquid helium. It is shown that owing to accumulation of the photoexcited charge carriers in the spatially confined potential well of the structure (in a thin SiGe-layer), EHL in this layer forms at a lower level of excitation of the structure (at the given temperature) and at a higher temperature (at the given level of excitation), than in bulk material of the same composition.

1. Experimental results and discussion

$Si/Si_{1-x}Ge_x/Si$ structures with various thicknesses of SiGe-layers and various content of germanium x in layers have been grown by MBE in J. Kepler University, Linz (Austria). Properties of these layers depending on content x, thickness of a layer, deposition rate, temperatures of growth and annealing have been investigated by methods of atomic-force and transmission microscopy. As the result, structures with high-quality layers of SiGe ($x = 0.05$) without dislocations with the thickness of 70 and 25 nm have been grown. Investigations of the PL spectra in the temperature region 2–50 K and with the levels of excitation varying from 2 W/cm^2 to 200 W/cm^2 have been made at P. N. Lebedev Physical Institute (Russia). He-Cd and semiconductor lasers with the wavelengths of 0.44 and 0.66 μm accordingly were used to excite structures. For the comparison PL spectra of bulk $Si_{1-x}Ge_x$ alloys of the same composition were also investigated.

Transformation of PL spectra with changing the temperature is shown in Fig. 1 (the density of excitation was 20 W/cm^2). At $T \approx 10$ K, in PL spectra of SiGe layers of the structure two lines of radiation with the threshold behavior (1107 and 1049 meV) arise, that are separated from each other by the energy of the optical TO-phonon in silicon (59 meV). These lines arise on the low-energy side at the distance of 9 meV from much less intensive lines, which probably correspond to free excitons in a layer of a solid solution. Increasing of their intensity with decreasing the temperature is accompanied by the reduction of the intensity of the exciton lines. At higher temperatures, when only excitonic lines are present in the PL spectrum of SiGe layer, integrated intensity of radiation increases linearly with increasing the level of pumping. While the appearance of the long-wavelength lines of radiation observed at low tem-

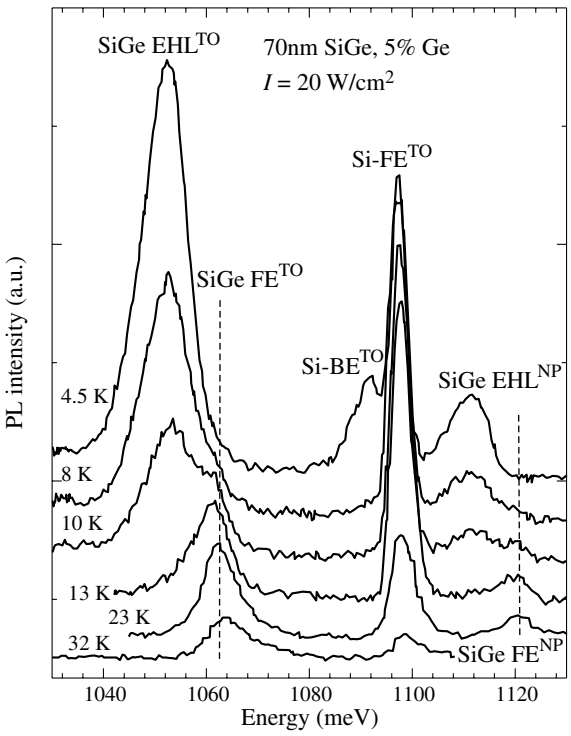

Fig. 1. Occurrence of the lines of EHL radiation with lowering temperature.

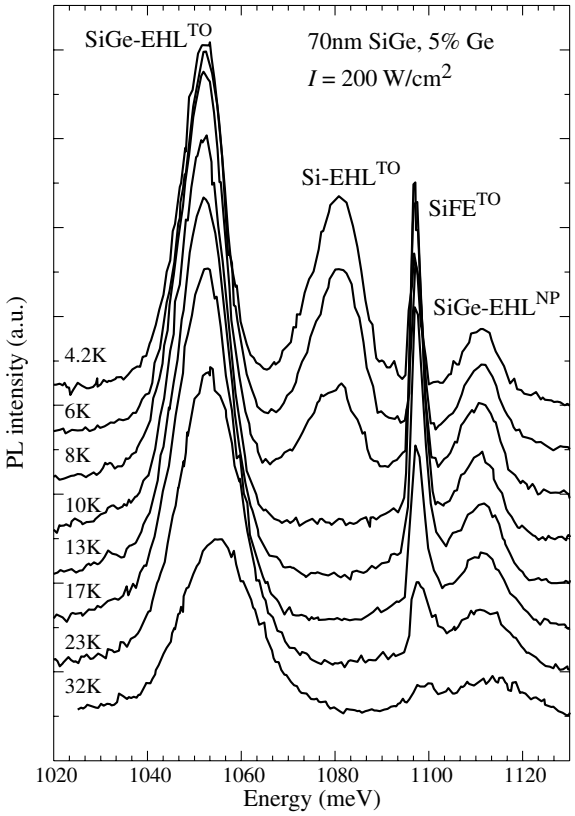

Fig. 2. PL spectra of structure at a high level of excitation.

peratures has the threshold behavior on density of excitation, the intensity of these lines near a threshold sharply increases with increasing the level of pumping. Thus, from the spectral position and the behavior of the long-wavelength components of the PL spectrum of the SiGe layer with changing the power of excitation and temperature it is possible to conclude that these lines are the zero-phonon line of radiation of EHL and its TO-phonon replica. It should be mentioned that in spectra shown on Fig. 1, TO-phonon replica lines of radiation of free and bound excitons in the buffer and the cap layers of silicon (1097 and 1092 meV) are visible whereas the line of radiation of EHL in these layers is absent. It arises at much greater intensity of excitation on a long-wavelength wing of the line of bound excitons (1082 meV for EHL). So, at the density of excitation $I = 200$ W/cm^2 the threshold temperature of formation of EHL in Si layers is close to 8 K (see Fig. 2). The investigation of the thresholds of formation of EHL on density of power of excitation and on temperature in SiGe- and Si-layers of the structure and also in bulk alloys of SiGe of the same composition and in Si has shown that in an internal layer of a solid solution of heterostructure the EHL arises at much smaller levels of pumping and at higher temperature (at the given level of excitation). It is possible that it is related to accumulation of photoexcited charge carriers in the SiGe layer, which is the potential well for holes in the heterostructure. It should be noted that owing to this circumstance one can investigate EHL at essentially smaller levels of excitation than in bulk crystals, and thereby can exclude or considerably reduce overheating of the sample by pumping radiation.

PL spectra of the structure at the high level of excitation $I = 200$ W/cm^2 are shown on Fig. 2. At the temperatures close to 30 K, the line of EHL in a SiGe-layer becomes broader and shifts to the short-wavelength side. Short-wavelength shift increases with the further increase of temperature, while intensity of the line decreases; the line of radiation of excitons in these conditions is not visible in the spectrum. It seems likely that the line of luminescence observed in this temperature range, corresponds to recombination radiation of the electron-hole plasma (EHP), and the critical temperature of the phase transition (EHL-EHP) is close to 30 K.

2. Conclusion

Thus, at low temperatures and high levels of excitation, in thin SiGe- layers of Si/Si$_{1-x}$Ge$_x$/Si ($x = 0.05$) heterostructures EHL is formed. The threshold density of excitation necessary for its formation is considerably lower and the threshold temperature is noticeably higher than in bulk material of the same composition.

Acknowledgements

We are grateful to N. V. Abrosimov for fabrication of bulk Si$_{1-x}$Ge$_x$ samples. We are indebted to E. A. Bobrik for technical assistance. This work has been supported in part by the Program of Support of Scientific Schools of Russia, by the RFBR (project 03-02-20007), by the Programs of the Presidium and the PSD of the RAS, and by the INTAS (project 03-51-5015).

References

[1] L. V. Keldysh, in *Proceedings of the 9th International Conference on Physics of Semiconductors, Moscow 1968*, Nauka, Leningrad, 1307 (1968).

[2] T. M. Rice, J. C. Hensel, T. G. Fillips and G. A. Thomas, *Solid State Physics* **32**, Academic Press, New York, (1977).

[3] *The Electron-Hole Drops in Semiconductors*, in: *Modern Problems in Condensed Matter Sciences* (Gener. eds. V. M. Agranovich and A. A. Maradudin) **6** (eds. C. D. Jeffries and L. V. Keldysh), Amsterdam: North-Holland (1983).

[4] L. V. Keldysh and N. N. Sibeldin, *Ibid* **16**, 455 (eds. W. Eisenmenger and A. A. Kaplyanskii) (1986).

[5] M. Tajima and S. Ibuka, *J. Appl. Phys.* **84**, 2224 (1998).

[6] N. Pauc, V. Calvo, J. Eymery, F. Fournel and N. Magnea, *Phys. Rev. Lett.* **92**, 236802–1 (2004).

14th Int. Symp. "Nanostructures: Physics and Technology"
St Petersburg, Russia, June 26–30, 2006

The slowing down of intraband relaxation of CdSe/ZnS quantum dots at high density of the excited carriers

I. I. Dobinde, *A. N. Santalov*, E. A. Zhukov and V. S. Dneprovskii
Physics Department, M. V. Lomonosov Moscow State University, 119992 Leninskie Gory, Moscow, Russia

Abstract. Pump and probe technique using powerful ultrashort (7 ps) laser pulse has been applied to investigate the process of intraband relaxation of the excited carriers (the relaxation through the energy levels of size quantization) in CdSe/ZnS quantum dots (QDs). The selection of QDs with appropriate radius has allowed to excite electrons resonantly at $1P_e$ state (the first excited state of electrons). The intraband LO-phonon energy relaxation of electrons is sufficiently suppressed in this case because the energy of the excited hot electron considerably exceeds the energy of LO-phonon.
The peculiarities of differential transmission spectra — the decrease of transmission at the frequency of excitation, bleaching at frequencies of the lower $1S_{3/2}(h) - 1S_e$ transition and the transitions between excited states of holes and main electron energy state $1S_e$ during the pumping pulse, the slowing down of these processes with the increasing of the intensity of exciting picosecond laser pulse — are explained by: 1. fast intraband relaxation and the absence of phonon bottleneck owing to transmission of excess energy of electrons to effectively relaxing holes in QDs, 2. relaxation through the intermediate hole energy levels of size quantization, 3. slowing down of intraband relaxation with increasing of the quantity of excited electron-hole pairs in QD.

Introduction

The investigation of intraband relaxation in QDs with discrete energy levels is conditioned by the application of QDs as an effective active media for semiconducting lasers. The discrete energy spectra of QDs lead to lower threshold of semiconducting QD-lasers generation, weak dependence of their parameters on temperature, high value of the amplification coefficient.

The main channel of intraband energy relaxation in bulk polar semiconductors leading to subpicosecond cooling dynamics is interaction with LO phonons. In QDs of small radius the energy level spacing of electrons can greatly exceed the energy of LO phonon, and phonon-dominated intraband relaxation may be significantly inhibited (the probability of energy losses via multi-phonon processes is negligibly small). This phenomenon was called phonon bottleneck and allowed to explain slow intraband carrier relaxation in some QDs [1–3]. However, some studies report rapid carrier relaxation (about 1 ps) [4–6]. The rapid intraband relaxation was explained in [7] by the effective transmission of the excess energy of hot electrons in QDs to holes (the Auger-like process) that can rapidly relax through the hole energy states having small energy spacing.

Experimental details

Colloidal CdSe/ZnS QDs were prepared using moderate-temperature organometallic reactions. QDs were precipitated on the glass substrate. The selection of QDs having appropriate radius was realized by measuring their absorption and luminescence spectra that allowed to determine the energy of the main $1S_{3/2}(h) - 1S_e$ optical transition.

The differential transmission spectra $DT(\lambda) = [T(\lambda) - T_0(\lambda)]/T_0(\lambda)$, where $T(\lambda)$ and $T_0(\lambda)$ are the transmission spectra of excited and unexcited sample, were measured for QDs with 3.4 ± 0.4 nm radius. For QDs of such radius it is possible to excite electrons at the first excited state by the photons of the second harmonic ($h\gamma = 2.353$ eV) of Nd^{3+}-phosphate mode-locked laser basically owing to resonant absorption at the frequencies of $1P_{3/2}(h) - 1P_e$ and $1P^l_{1/2}(h) - 1P_e$ transitions. At the same conditions the absorption with direct excitation of electrons at the main energy state $1S_e$ may arise in small number of QDs belonging to the shoulders of size dispersion ($1S_{1/2}(h) - 1S_e$ transition for QDs of the smaller and $2S_{1/2}(h) - 1S_e$ transition for greater radius). Wide-band picosecond pulse of white light (picosecond continuum) obtained by four-wave mixing of the part of pump radiation focused in the cell with heavy water was used as a probe pulse. The central part of the QD sample's excited area was probed. The application of the optical delay line has allowed to measure the differential transmission spectra of QDs at different moments of time during and after excitation by ultrashort pulses.

Experimental results and discussion

The differential transmission spectra of CdSe/ZnS QDs with 3.4 ± 0.4 nm radius obtained at different time (during and after excitation) and at different intensity of the exciting pulse are presented in Fig. 1 and 2. As it can be seen in Fig. 1 in the case when the delay between the pump and probe pulses is absent ($\Delta t = 0$, full overlapping of the pulses) the bleaching bands arise (the transmission increases) not only at the frequencies of resonantly excited transitions $1P_{3/2}(h) - 1P_e$ and $1P^l_{1/2}(h) - 1P_e$, but also at the frequencies of the main lower transition $1S_{3/2}(h) - 1S_e$ and at intermediate frequencies that correspond to the optical transitions between excited states of holes and main electron state $1S_e$. At the delay of the probe pulse $\Delta t = 3$ ps (pump and probe pulses overlap partly) the differential transmission spectrum considerably changes. In this case the bleaching band corresponding to the main $1S_{3/2}(h) - 1S_e$ transition dominates, the transmission at the frequency of resonant excitation decreases sharply, and the transmission at intermediate frequencies arises. Only one bleaching band corresponding to the main lower optical transition is retained at grate delays ($\Delta t > 20$ ps).

The increasing of the pump intensity arise essential changes in differential transmission spectra. At the delay $\Delta t = 3$ ps the transmission at the frequency of resonant excitation decreases weakly that differs from the case of lower excitation, the amplitudes of bleaching bands at the frequencies of main lower and intermediate transitions increase not so effectively as in Fig. 1.

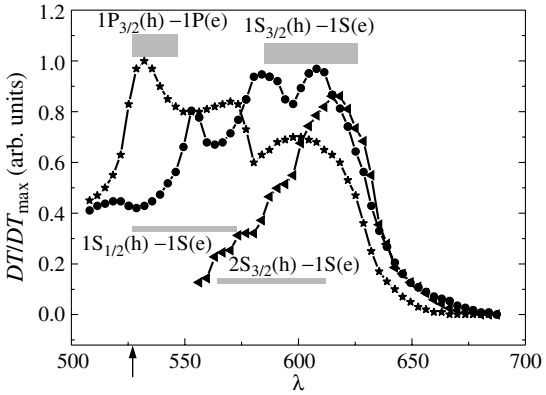

Fig. 1. The normalized differential transmission spectra of CdSe/ZnS (300 K) quantum dots with 3.4 ± 0.4 nm radius at 0 ($\star$), 3 ($\bullet$) and 20 ($\blacktriangleleft$) ps delay between the pump and probe pulses. The input pump intensity is 3×10^{16} photon/cm^2. The wavelength of the pump pulse is shown by arrow. The energies of optical transitions are pointed by stripes. Their length is determined by the size dispersion of quantum dots and the width is proportional to the oscillator strength.

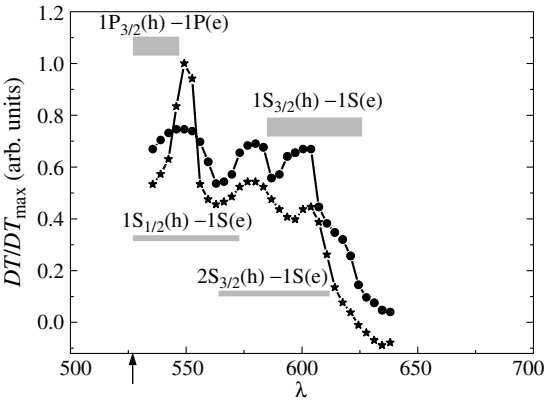

Fig. 2. The normalized differential transmission spectra of CdSe/ZnS (300 K) quantum dots with 3.4 ± 0.4 nm radius at 0 ($\star$) and 3 ($\bullet$) ps delay between the pump and probe pulses. The input pump intensity is increased to 8×10^{16} photon/cm^2.

The bleaching at the frequencies of the exciting beam, main $1S_{3/2}(h) - 1S_e$ energy transition, and at intermediate frequencies may be explained by state filling — by filling of the QD's energy levels with excited carriers. For the case presented in Fig. 1 the estimated density of the excited electrons in the $1P_e$ state per QD (≥ 10) is enough to saturate this 6-fould degenerate state. The arising of the bleaching band at the frequency of the main transition at $\Delta t = 0$ (Fig. 1) and its domination at $\Delta t = 3$ ps (fast intraband energy relaxation!) allows to exclude phonon relaxation bottleneck effect, in spite of the fact that the energy $1P_e - 1S_e$ — separation (330 meV) significantly exceeds the energy of LO-phonon (about 26 meV). As it is pointed in [7] in QDs the excess energy of the excited electrons is transmitted to efficiently relaxing holes. The bleaching of $1S_{3/2}(h) - 1S_e$ energy state at $\Delta t = 0$ besides this process may arise partly due to fast intraband relaxation of directly excited hot holes in small number of QDs belonging to the shoulders of size distribution.

The peculiarities of the differential transmission spectra obtained at higher excitation (Fig. 2) may be attributed to the slowing down of intraband relaxation in QDs in comparison to that displayed for the case shown in Fig. 1. This slowing down with increasing of the number of excited electron-hole pairs in QD arises probably because of the population of intermediate discrete hole energy states hindering the intraband relaxation of hot dots.

Conclusions

The results of the experiments allow to conclude that fast nonphonon intraband energy relaxation of electrons may be explained by transfer of the electron excess energy to a hole (intrinsic Auger-like e-h interaction) relaxing through its dense spectrum of energy states. At high density of excited e-h pairs the intraband relaxation is slowing down because of the population of the intermediate hole and lower main electron energy states.

Acknowledgement

This work was supported by Russian Foundation for Basic Research (grant 02-05-17604).

References

[1] H. Benisty, C. Sotomayor-Torres, C. Weisbuch, *Phys. Rev. B* **44**, 10945 (1991).
[2] U. Bockelmann, G. Bastard, *Phys. Rev. B* **42**, 8947 (1990).
[3] T. Kitamura, R. Ohtsubo, M. Murayama, T. Kuroda, K. Yamaguchi, A. Tackeuchi, *phys. stat. sol. (c)* **4**, 1165 (2003).
[4] U. Woggon, H. Giessen, F. Gindele, O. Wind, B. Fluegel, N. Peyghambarian, *Phys. Rev. B* **54**, 17681 (1996).
[5] K. Shum, W. B. Wang, R. Alfano, K. Jones, N. Peyghambarian, *Phys. Rev. Lett.* **68**, 3904 (1992).
[6] V. I. Klimov, *Phys. Chem. B* **104**, 6112 (2000).
[7] Al. L. Efros, V. A. Kharchenko, M. Rosen, *Solid State Commun.* **93**, 281 (1995).

14th Int. Symp. "Nanostructures: Physics and Technology"
St Petersburg, Russia, June 26–30, 2006

Fine structure of A^+ centers in GaAs/AlGaAs quantum wells

P. V. Petrov, Yu. L. Ivanov, K. S. Romanov, A. A. Tonkikh and *N. S. Averkiev*
Ioffe Physico-Technical Institute, St Petersburg, Russia

Abstract. The photoluminescence of A^+ centers in GaAs/AlGaAs quantum wells in the magnetic field was studied. The circular polarization of A^+ photoluminescence was observed for the first time. The theoretical model of A^+ fine structure was developed. Theoretical results showed good agreement with the experimental data.

Introduction

A^+ centers were first predicted by Lampert [1] as an analog of the negatively charged hydrogenium ion H^-. In semiconductors they are formed when a shallow neutral hydrogenic acceptor (A^0) binds a second hole. A^+ centers attracted attention because they play significant role in the hopping conductivity of bulk semiconductors. Nowadays, a progress in developing of doped nanostructures such as quantum wells (QW) raise again questions of the excistance, the energy structure and various other properties of A^+ centers.

It was found that these centers appear in selectively doped QW structures [1]. In [2] it was shown, that the radiative recombination of photoexcited electrons in this structures is due to the transition of electrons to the ground level of A^+ centers. Therefore spectral analysis of PL allows to measure the binding energy of A^+ centers in QW. In [3] the dependence of this energy on the width of the QW was obtained. It was also found that the characteristic size of the wavefunction of the outer hole bounded on the A^+ center greatly exceeds one of the neutral acceptor. Thus the exchange interaction between holes bounded on A^+ can be neglected. The zero-potential model calculations provided in [4] showed that the ground state of the hole in A^+ has full moment projection $\pm 3/2$. The energy gap between the first excited level and the ground level appeared to be relatively small: 1–2 meV.

In the present work the analysis of the magnetic field induced circular polarization of A^+ centers photoluminescence is performed. The fine, spin and energy structures of A^+ are discussed.

1. Experimental

The samples analyzed in this work were grown by MBE on the singular [001] surface of semiinsulating GaAs substrate. During the structure growth the selective dope with Be concentration 10^{17} cm^{-3} was realized. Each sample contained a set of 10 GaAs quantum wells divided by a 20 nm $Al_{0.35}Ga_{0.65}As$ barriers. In the center of wells a 2 nm layer was Be doped, in the center of barriers a 3 nm one was Be doped. A spectrum was detected in Faraday geometry by a grated monochromator and a nitrogen vapor cooled photomultiplier tube in a photon count mode.

Typical PL spectrum of structure with A^+ centers contains two peaks which corresponds to the radiation from A^+ centers and the recombination of excitons bounded on neutral acceptors. The best resolution between them was achieved for samples with QW widths 16 nm and 18 nm. For identification of those peaks the examination of temperature dependence of there intensity was performed [4]. It was found that the lower energy peak corresponds to the luminescence of bound exciton (BE). The higher energy one corresponds to the recombination of the weakly bounded hole of A^+.

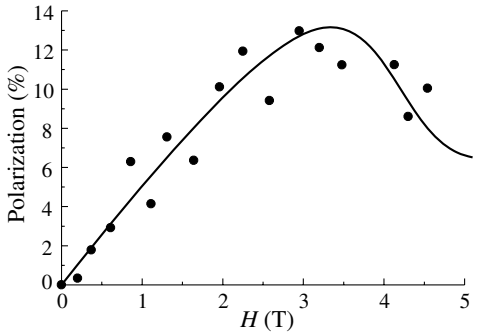

Fig. 1. Experimental (dots) and theoretical (line) dependencies of the degree of circular polarization of the A^+ photoluminescence on the magnetic field H.

The magnetic field leads to the splitting of the PL peaks with different polarization and the change of their intensity. Gaussian fitting method was used to determine energy splitting of peaks and their degree of polarization with higher accuracy. The Figure 1 shows the dependence of the degree of polarization of the A^+ recombination luminescence peak on the magnetic field.

2. Discussion

Let us consider the luminescence of A^+ center due to the recombination of a free electron with the weakly localized hole. In weak magnetic fields the circular polarization is due to the spin splitting and thermal occupancy of the bounded hole and free electron levels. In higher magnetic fields diamagnetic effects of the localized hole become more significant. This is because the radius of the A^+ ground state is relatively large and the distance between ground level and first excited level is small — 1 meV [4]. Thus in magnetic fields about 2 T the interaction between ground level and excited level appears. Dependences of both the energy of the ground state of A^+ and the energy of the excited state of A^+ on the magnetic field can be described by the Hamiltonian:

$$\hat{\mathbf{H}}_{\mathrm{h}} = \mu_0 g_{\mathrm{h}} (J_z H) + \lambda_1 (J_z^2 - 5/4) H^2 + (\Delta/2)(J_z^2 - 5/4) + \lambda_0 H^2 , \quad (1)$$

where the z-axis is the growth axis, H is the magnetic field, λ_1, λ_0 are diamagnetic splitting and diamagnetic shift parameters respectively, Δ is the energy splitting between ground and excited states in the absence of magnetic field, J_z is the operator of the hole momentum projection on the z-axis.

Let us assume that the spin splitting of electron levels can

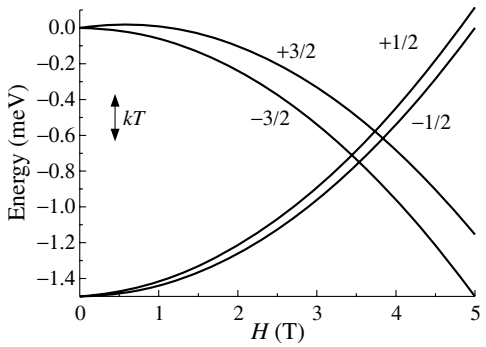

Fig. 2. The splitting of the A^+ cen ter levels in the magnetic field.

be described using the ordinary Hamiltonian:

$$\hat{\mathbf{H}}_e = \mu_o g_e (S_z H)\,, \tag{2}$$

where S_z is the operator of the electron spin projection on the z-axis.

Using (1), (2), selection rules in canonical basis and assuming that PL lines widths are greater than magnetic splittings and the population of carriers levels is equilibrium, one can get the degree of the circular polarization in the presence of magnetic field:

$$P_{\text{circ}} = \frac{3\sinh\dfrac{(3g_h+g_e)\mu_0 H}{2kT}\exp\dfrac{-\lambda H^2}{kT} + \cdots}{3\cosh\dfrac{(3g_h+g_e)\mu_0 H}{2kT}\exp\dfrac{-\lambda H^2}{kT} + \cdots} \cdots$$
$$\cdots \frac{+\sinh\dfrac{(g_h-g_e)\mu_0 H}{2kT}\exp\dfrac{\lambda H^2}{kT}\exp\dfrac{-\Delta}{kT}}{+\sinh\dfrac{(g_h-g_e)\mu_0 H}{2kT}\exp\dfrac{\lambda H^2}{kT}\exp\dfrac{-\Delta}{kT}}\,. \tag{3}$$

The parameter λ_1 is responsible for the decrease of the splitting between ground and excited states of A^+. The second parameter λ_0 defines the common shift of these two levels that is proportional to the square of magnetic field.

According to the experimental data, the degree of circular polarization decreases in magnetic fields greater than 3 T. Using selection rules one can explain this effect by onset of transitions to the hole states with spin +1/2 and -1/2 (excited states). Thus the sign of λ_1 must be chosen from the assumption that it reduces the splitting between ground and excited states. In [4] we estimated Δ as 1–2 meV. The value of electron g-factor in the QW under study is about $g_e = -0.3$ [5]. The A^+ hole g-factor is unknown, but one can use the AlGaAs valence band g-factor $g_h \approx 1$. The magnetic field should destroy A^+ weakly bounded state when the magnetic length becomes equal to the size of the bounded hole wave function. From this relation one can estimate the unknown value of λ_1.

The solid line on the Figure 1 corresponds to the calculation of the circular polarization in the magnetic field. To match the experimental data calculated values had four-fold decrease. The parameters of the model are: $g_e = -0.3$; $g_h = 0.8$; $\lambda_1 = 0.06$ meV/T^2; $\Delta = 1.5$ meV; $T = 4.2$ K. One can see that scaled results of the calculation agree well with the data of experiments. We explain the scaling of the theoretical curve by the depolarization of the radiation in the sample and experimental devices.

The Figure 2 shows results of the calculation of the A^+ energy spectrum change induced by magnetic field. The position of the vertical line denote the value of kT of samples ($T = 4.2$ K). The area of the curves cross corresponds to the lowering of the degree of polarization on Figure 1. It should be noted that the decrease of polarization is accompanied by the overall decrease of luminescence intensity. According to the theoretical model it is explained by denial of transitions to the ground state of A^+ in magnetic field higher than 3 T.

In conclusion, in this work the fine structure of A^+ centers in magnetic field is observed for the first time. It was shown that the model [4] is confirmed by experiments in the presence of the magnetic field.

Acknowledgements

This work was supported in part by RFBR, INTAS, Scientific programs of RAS and Russian Ministry of Science and Education.

References

[1] M. A. Lampert, *Phys. Rev. Lett* **1**, 450 (1958).
[2] N. V. Agrinskaya, Yu. L. Ivanov, V. M. Ustinov, D. A. Poloskin, *Semiconductors* **35**, 550 (2001).
[3] Yu. I. Ivanov, N. V. Agrinskaya, P. V. Petrov, V. M. Ustinov, G. E. Tsyrlin, *Semiconductors* **36**, 929 (2002).
[4] N. S. Averkiev, A. E. Zhukov, Yu. L. Ivanov, P. V. Petrov, K. S. Romanov, A. A. Tonkikh, V. M. Ustinov, G. E. Tsyrlin, *Semiconductors* **38**, 217 (2004).
[5] E. L. Ivchenko, G. Pikus, *Superlattices and Other Heterostructures*, Springer-Verlag, 1995.

14th Int. Symp. "Nanostructures: Physics and Technology"
St Petersburg, Russia, June 26–30, 2006

Photocurrent in nanostructures with asymmetric antidots

M. V. Entin and L. I. Magarill

Institute of Semiconductor Physics, Siberian Branch of Russian Academy of Sciences,
Novosibirsk, 630090, Russia

Abstract. The steady current induced by electromagnetic field in a 2D system with asymmetric scatterers is studied. The scatterers are assumed to be oriented cuts with one diffusive and another specular sides. This simple model simulates the lattice of half-disk which have been studied numerically recently. The model allows the exact solution in the framework of the kinetic equation.

The artificial arrays of antidot scatterers in semiconductor heterostructures are widely studied during last 10 years. (see e.g. [1, 2, 3, 4] and Refs. therein). These systems exhibit the features of chaotic dynamics due to instability of electron trajectories. Recently, the asymmetric antidot lattices attracted attention as artificial representatives of homogeneous media with no inversion symmetry able for current rectification (photogalvanic effect). The system with oriented semidisks was analyzed theoretically [5, 6, 7] by simulations of motion of a particle subjected to alternating force with zero means and collisions with hard-wall antidots. This system was realized experimentally [8] and exhibited the the steady current being subjected by high-frequency electric field.

The present report deals a simplified model similar to mentioned one but permitting analytical solution. Namely, we study the model in which the semidisks are replaced by the oriented cuts with length D (see Fig. 1). The consideration is based on the kinetic equation. It is suggested the picture of developed chaos where ergodicity of electron motion is achieved. The concentration of scatterers N is supposedly low: $ND^2 \ll 1$. In that case the regularity of the scatterers distribution is inessential.

We have solved the kinetic equation in the second order in the weak classical electric field $\mathbf{E}(t) = \mathrm{Re}(\mathbf{E}_\omega e^{-i\omega t})$. The arbitrary magnitude of asymmetric scattering on cuts is assumed, that differs the approach from one usual in the theory of photogalvanic effect. The collision integral is supplemented by the isotropic impurity scattering with the mean free path τ_i. In the second order on alternating electric field the components of steady current density are described by the phenomenological expressions

$$j_x = \alpha_{xxx}|E_x|^2 + \alpha_{xyy}|E_y|^2,$$
$$j_y = \mathrm{Re}(\alpha_{yxy})(E_x E_y^* + E_x^* E_y) + \mathrm{Im}(\alpha_{yxy})[\mathbf{E}\mathbf{E}^*]_z. \quad (1)$$

Components of photogalvanic tensor α_{xxx}, α_{xyy} and $\mathrm{Re}(\alpha_{yxy})$ determine the response to the linear-polarized light. For linear polarization along x or y axes the current flows along the x direction; the current in y direction appears for tilted linear-polarized electric field. In the case of circular polarization the y component of the current is determined by $\mathrm{Im}(\alpha_{yxy})$ (the circular photogalvanic effect) and by the sign of the rotation, while x component of the current is the sum of responses to x and y linear polarized light and does not depend on the sign of $[\mathbf{E}\mathbf{E}^*]_z$.

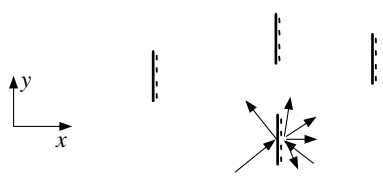

Fig. 1. Considered model system. Cuts of the length D have specular left sides and diffusive right sides. This produces anisotropy of scattering resulting in the photocurrent.

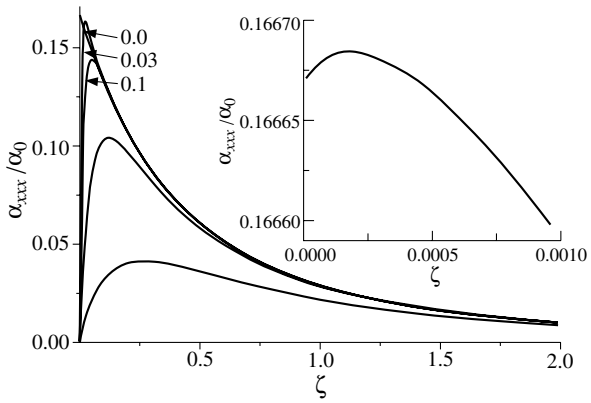

Fig. 2. The dependence of α_{xxx} on the parameter $\zeta = \tau/\tau_i$ for different frequencies $\Omega = \omega\tau = 1$, 0.3, 0.1, 0.03, 0 (marked on curves); $\alpha_0 = e^3/(4\pi^2 v_F N^2 D^2)$. Insert: the dependence of $\tilde{\alpha}_{xxx}$ for small values of the parameter ζ at $\Omega = 0$.

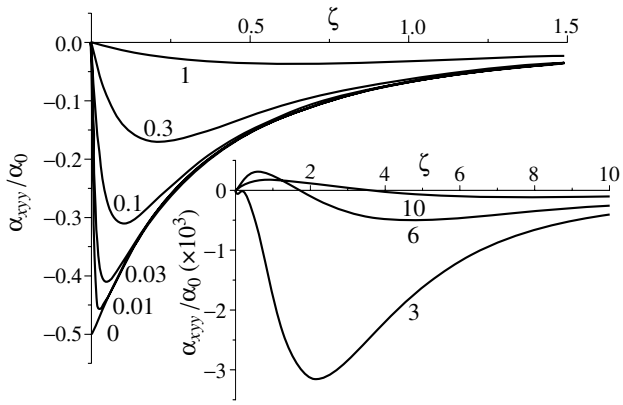

Fig. 3. The dependence of α_{xyy} on!ζ for the different parameters Ω (marked on curves).

The Figures 2–5 represent the photogalvanic tensor components at low temperatures calculated according the obtained analytical formulae as functions of the parameter $\zeta \equiv \tau/\tau_i$ ($\tau = (DNv_F)^{-1}$).

The sign of coefficient α_{xxx} is positive, while the other coefficients change sign. All components tend to zero if $\tau_i \to 0$ and exhibit non-analytical behavior if $\tau_i \to \infty$. Such behavior results from the absence of relaxation on cuts of electrons

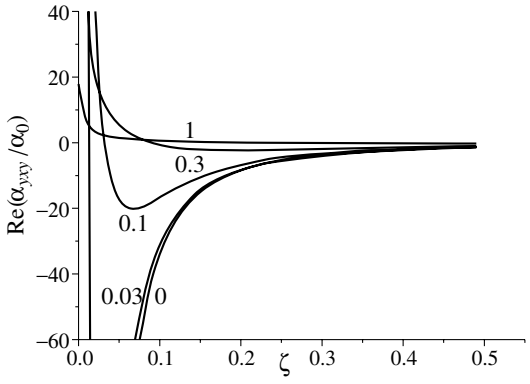

Fig. 4. The dependence of linear photogalvanic coefficient $\mathrm{Re}(\alpha_{yxy})$ on ζ for the same parameters Ω as in the Figure 2.

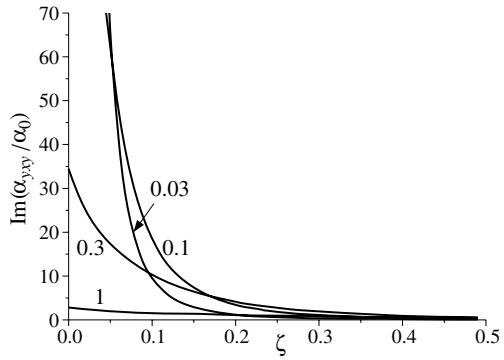

Fig. 5. The dependence of circular photogalvanic coefficient $\mathrm{Im}(\alpha_{yxy})$ for the same parameters Ω as in the Figure 2.

moving along y axis (unless the impurity scattering is taken into account). The state with $p_x = 0$ plays role of a drain for electrons. These electrons do not participate in the transport along x axis, but due to absence of relaxation they accumulate in the state $p_x = 0$; this suppresses the distribution function with finite p_x, and $j_x \to 0$. On the contrary, the transport along y axis diverges due to the same reason.

The values of coefficients α_{yxy} are essentially larger than α_{xxx} and α_{xyy}. It is a consequence of the fact that the motion along y direction is collisionless unless the impurity scattering is taken into account. Obviously, the difference is more pronounced at low ζ.

Resuming, it should be emphasized that the found features (in particular, the absence of temperature dependence and non-analyticity of photogalvanic coefficients in the system without impurities) are not specific for the considered exactly solvable model, but are valid in the semicircle antidot lattice as well.

Acknowledgements

The authors are grateful to D. L. Shepelyansky and A. D. Chepelyansky for numerous helpful discussions of the problem, and Z. D. Kvon for showing us the experimental data [8] prior to publication. The work was supported by grants of RFBR Nos. 05-02-16939 and 04-02-16398, Program for support of scientific schools of the Russian Federation No. 593.2003.2 and INTAS No. 03-51-6453.

References

[1] D. Weiss, M. L. Roukes, A. Menschig, P. Grambow, K. von Klitzing and G. Weimann, *Phys. Rev. Lett.* **66**, 2790 (1991).

[2] G. M. Gusev, Z. D. Kvon, V. M. Kudryashov, L. V. Litvin, Y. V. Nastaushev, V. T. Dolgopolov and A. A. Shashkin, *JETP Lett.* **54**, 364 (1991).

[3] Z. D. Kvon, O. Estibals, A. Y. Plotnikov, J. C. Portal and A. I. Toropov, *Physica E* **13**, 752 (2002).

[4] J. Eroms, M. Tolkiehn, D. Weiss, U. Rössler, J. De Boeck and G. Borghs, *Europhys. Lett.* **58**, 569 (2002).

[5] A. D. Chepelianskii and D. L. Shepelyansky, *Phys. Rev. B* **71**, 052508 (2005).

[6] G. Cristadoro and D. L. Shepelyansky, *Phys. Rev. E* **71**, 036111 (2005).

[7] A. D. Chepelianskii, cond-mat/0509679.

[8] Z. D. Kvon, J. Zhang, S. Vitkalov, A. E. Plotnikov, J. C. Portal, A. Wieck (private communication) (2005).

14th Int. Symp. "Nanostructures: Physics and Technology"
St Petersburg, Russia, June 26–30, 2006

The use of hexagonal symmetry for the calculation of single-particle states in III-nitride quantum dots

N. Vukmirović, Z. Ikonić, D. Indjin and *P. Harrison*
School of Electronic and Electrical Engineering, University of Leeds, Leeds LS2 9JT, United Kingdom

Abstract. A symmetry based method for the efficient calculation of single-particle states in hexagonally symmetric GaN/AlN quantum dots within the framework of a $k \cdot p$ model is presented. The symmetry group of the model is $\overline{C}_6$ and is generated by the total angular momentum operator. The envelope functions are expanded into a plane wave basis on a hexagonal lattice and the group projector method is used to adapt the basis to exploit the symmetry, resulting in block diagonalization of the corresponding Hamiltonian matrix into six matrices and classification of the states by the quantum number of total quasi-angular momentum. The method is applied to the calculation of the electron and hole energy levels in a quantum dot superlattice and the intraband optical absorption matrix elements.

Introduction

Wide band-gap III-nitride materials attracted significant research attention in the 1990s which led to the demonstration of commercially attractive emitters in the blue and ultra-violet spectral range [1]. Further improvements in GaN-based optoelectronic devices have been achieved by using GaN quantum dots in the active region, putting them at the forefront of both experimental and theoretical research. Furthermore, in the last few years, intraband transitions in the telecommunications wavelength range (1.3–1.55 μm) in GaN/AlGaN low-dimensional heterostructures at room temperature have been demonstrated [2].

Computational modelling of the electronic structure of quantum dots is a highly challenging task due to the three dimensional nature of the problem. Fortunately, the dots often exhibit a symmetrical shape, a feature that can be undoubtedly exploited in the calculation of the electronic structure, particularly within the envelope function methods. In the case of cylindrically symmetric quantum dots, the symmetry is manifested via a separation of variables both in the effective mass approach [3] and the $k \cdot p$ model within the axial approximation [4]. In the case of pyramidal quantum dots, it is much less straightforward to exploit the symmetry. However, in our recent work [5] we have shown how the symmetry can be exploited in the case of square based pyramidal quantum dots based on materials with zinc-blende crystal symmetry.

Along this line, the aim of this work is to exploit the symmetry in the calculation of energy levels of hexagonally shaped GaN/AlN quantum dots within the framework of the $k \cdot p$ method and apply the symmetry based method developed to study intraband transitions in these dots theoretically.

1. Theory

The 8-band $k \cdot p$ Hamiltonian for wurtzite crystal lattice semiconductors can be block diagonalized into two 4-band Hamiltonians for carriers with opposite values of spin assuming the spin-orbit splitting is zero. The 4-band Hamiltonian is of the form $\hat{H} = \hat{H}_k + \hat{H}_s + V_p I_4$, where $\hat{H}_k$ is the kinetic part of the Hamiltonian, $\hat{H}_s$ the strain part, V_p the potential induced due to spontaneous and piezoelectric polarizations present in III-nitride materials and I_4 the 4×4 unity matrix. The explicit expressions for $\hat{H}_k$ and $\hat{H}_s$ can be found in [6].

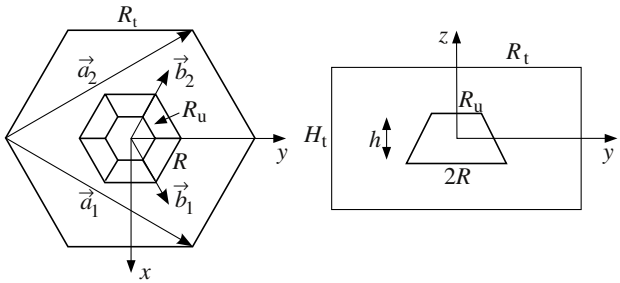

Fig. 1. Schematic view of a truncated hexagonal pyramid quantum dot with upper base radius R_u, lower base radius R and height h embedded in a hexagonal prism with radius R_t and height H_t — top view (left) and side view (right). The primitive vectors of the corresponding Bravais lattice ($\boldsymbol{a}_1$ and $\boldsymbol{a}_2$) and its reciprocal lattice ($\boldsymbol{b}_1$ and $\boldsymbol{b}_2$) are also shown in the figure.

In the plane wave expansion method the envelope functions are assumed as a linear combination of plane waves with the coefficients in the expansion to be determined. Conventionally, the dot is embedded in a rectangular box and the plane waves that form the basis are periodic on a cubic lattice. However, in this work, due to the hexagonal shape of the dots, it seems more natural to embed the dot in a hexagonal prism and take the plane waves that form the basis as periodic on a hexagonal lattice (Fig. 1).

The 4-band Hamiltonian commutes with the rotations around the z-axis by $\varphi_k = k \cdot 2\pi/6$ ($k \in \{0,\ 1,\ \ldots,\ 11\}$) which are generated by the operator of the z-component of the total angular momentum $\hat{F}_z$, which is a sum of orbital angular momentum of the envelope function $\hat{L}_z$ and total angular momentum of the Bloch function $\hat{J}_z$. The group projector method [7] was used to adapt the plane wave basis to the symmetry. In the adapted basis, the Hamiltonian matrix is block diagonal with 6 blocks of approximately equal size which significantly reduces the computational time necessary to diagonalize the Hamiltonian.

Apart from reducing the computational time within the plane wave method, the method presented introduces the quantum number m_f ($m_f \in \{-5/2,\ -3/2,\ \ldots,\ 5/2\}$) which can be interpreted as the total quasi-angular momentum. The selection rules for the interaction with electromagnetic radiation in the dipole approximation have then been derived as: $\Delta m_f = 0$ for z-polarized light and $\Delta m_f = \pm 1$ for in-plane polarized light. In the rest of the work, based on the symmetry classification discussed, we label the states in the conduction band using the

following notation: ne_{m_f} represents the n-th electron state (in ascending order of energies) among the states having quantum number m_f.

2. Results

The method presented was applied to the calculation of electron and hole energy levels in a periodic array of hexagonal truncated pyramidal GaN/AlN quantum dots. The dot radius was taken to be $R = 9.0$ nm, the height $h = 3.7$ nm, the upper base radius $R_u = 3.5$ nm and the diameter of the embedding box $2R_t = 15.0$ nm.

The first few electron and hole energy levels, when the period is varied in the interval $H_t = 4.3$ nm to $H_t = 12.3$ nm, are shown in Fig. 2. A very weak dispersion with the superlattice Bloch wave vector K_z was found and therefore only the $K_z = 0$ states are presented. The origin of such a weak electronic coupling between the dots in a superlattice is the strong internal electric field that creates a deep triangular potential well at the top of the dot for electrons (and at the bottom of the dot for holes) which prevents interaction between neighboring dots. One can see from Fig. 2 that as the superlattice period increases, the effective energy gap of the structure decreases, in contrast to the behaviour observed in InAs/GaAs. Such a behaviour is governed by the changes in the value of the internal electric field. As the distance between the dots increases, the field in the dot also becomes larger, the effective electron and hole potential wells are therefore deeper and consequently both electron and hole states are more confined. As the ground electron state has $m_f = 1/2$ and selection rules for the absorption of z-polarized radiation only allow the transitions with $\Delta m_f = 0$, it follows that the peak positions in the z-polarized radiation absorption spectrum will be determined by the positions of the energy levels having $m_f = 1/2$ symmetry. Optical absorption matrix elements $|\mathcal{M}|^2$ ($\mathcal{M} \sim \langle i|\hat{H}'|f\rangle$, where $\hat{H}'$ is the perturbation Hamiltonian) vs. energy for different intraband transitions from the ground state to excited states when the period is equal to $H_t = 8.3$ nm are therefore shown in Fig. 3. The strongest absorption occurs for the transition from the ground state to the states from the G1 group, as the matrix elements for these transitions are the largest (among them the strongest is the transition to $4e_{1/2}$). The absorption maximum occurs at 490 meV, and is followed by a weaker line

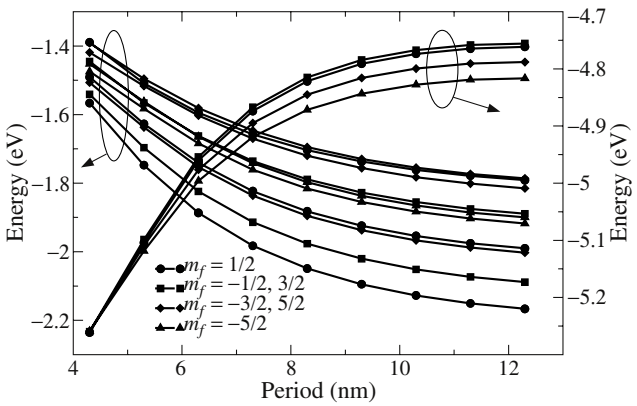

Fig. 2. The dependence of electron (left axis) and hole (right axis) energy levels on the superlattice period. For each value of m_f, the first few energy levels in the conduction band and the highest energy level in the valence band are shown.

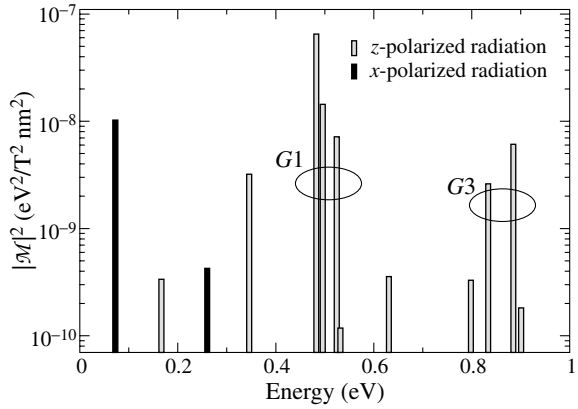

Fig. 3. Optical absorption matrix elements $|\mathcal{M}|^2$ vs. energy for different intraband transitions from the ground state to excited states when the period is equal $H_t = 8.3$ nm.

with a maximum at 860 meV originating from the transitions to the G3 group of states. These results are in reasonable agreement with the experimental results in [2], where for the same value of the period and for dots of similar size the strongest absorption occurs at 520 meV or 590 meV for the two different samples investigated, and is followed by two weaker lines at 730 meV and 980 meV or 850 meV and 970 meV. Our calculation shows that in the case of in-plane polarized light the spectrum is dominated by the transition to two degenerate first excited states.

3. Conclusion

In conclusion, a symmetry based method for the calculation of single particle states in hexagonal GaN/AlN quantum dots within the framework of the $k \cdot p$ model has been developed. The method has been applied to calculate the electron and hole states in a quantum dot superlattice and intraband absorption spectrum from the ground state in the conduction band. The absorption spectrum for in-plane polarized light is dominated by the transition to two degenerate first excited states, while for z-polarized light it is determined by the absorption to a group of excited states located $\sim$ 500 meV above the ground state having the same symmetry as the ground state. Such a result is in overall agreement with the available experimental data on intraband absorption in the conduction band in GaN/AlN quantum dots.

References

[1] S. Nakamura *et al*, *The Blue Laser Diode*, (Springer, Berlin, 1997).
[2] Kh. Moumanis *et al*, *Appl. Phys. Lett.* **82**, 868 (2003).
[3] J. Y. Marzin *et al*, *Solid State Commun.* **92**, 437 (1994).
[4] M. Tadić *et al*, *Phys. Rev. B* **65**, 165333 (2002).
[5] N. Vukmirović *et al*, *Phys. Rev. B* **72**, 075356 (2005).
[6] A. D. Andreev *et al*, *Phys. Rev. B* **62**, 15851 (2000).
[7] J. P. Elliott *et al*, *Symmetry in Physics*, (Macmillan, London, 1979).

14th Int. Symp. "Nanostructures: Physics and Technology"
St Petersburg, Russia, June 26–30, 2006

Nonlinear absorption and refraction of CdSe/ZnS quantum dots at two-photon resonant excitation

V. S. Dneprovskii, D. A. Kabanin, *V. L. Lyaskovskii*, T. Wumaier and E. A. Zhukov
Physics Department of M. V. Lomonosov Moscow State University, Leninskie Gory, 119992 Moscow, Russia

Abstract. The nonlinear transmission and refraction of colloidal CdSe/ZnS quantum dots in the case of two-photon resonant excitation by powerful picosecond laser pulses has been explained by *two-photon absorption and self-defocusing effects*. Experimental results has allowed to separate self-defocusing effects that arise 1. due to the change of bound electronic nonlinear refractive index and 2. nonlinear refraction from carriers generated by two-photon absorption.

Introduction

In recent years there has been a growth of activity in the field of nonlinear optics of semiconductors with reduced dimensionality in particular of semiconducting quantum dots (QDs). Two types of nonlinearities may arise in semiconducting QDs: fast (classical) nonlinearity due to interaction of light with bound electrons (harmonics generation, two-photon absorption, bound electronic nonlinear reflection etc.) and dynamic (resonant, strong) nonlinearity due to excited free carriers (for example nonlinear absorption and reflection as a consequence of state filling). Nonlinear effects in QDs are of great interest both for their fundamental properties and for their important possible applications in science and engineering (optical switching, optical limiting, saturable absorbers for Q-switched and mode-locked lasers etc.). The goal of our work is the investigation of nonlinear processes that arise in the case of two-photon resonant excitation of the lower main $1S^{\rm h}_{3/2} \rightarrow 1S^{\rm e}$ optical transition in colloidal CdSe/ZnS QDs.

1. Experimental details

A simple method of quantum dot's nonlinear transmission measurement using the train of variable intensity picosecond laser pulses has been utilized. The mode-locked Nd^{3+}:YAG-laser ($\hbar\omega = 1.165$ eV, single pulse duration about 30 ps) was used for resonant two-photon excitation of CdSe/ZnS quantum dots. The axial period of 12–15 pulses in the train was 7 ns. The energies of transmitted pulses through the sell with colloidal solution of CdSe/ZnS QDs in toluene and the energies of corresponding exciting pulses were measured simultaneously using optical delay line ($\Delta t = 3$ ns) and photodiode operated in the linear regime. Photodiode was coupled with fast-acting oscillograph. The time-resolution of the system was about 1 ns. The measured pulse duration of single pulses didn't vary at least in the first part of the train of pulses (inset in Fig. 1). The laser pulses were focused at the sample surface to a radius of 100 μm. Special aperture was placed behind the cell with QDs. This technique has allowed to define the sign and magnitude of nonlinear refraction (closed-aperture) as well as nonlinear absorption (open-aperture) measuring the transmission of corresponding laser pulses in the train.

2. Experimental results and discussion

Colloidal CdSe/ZnS QDs were fabricated by organometallic synthesis. QDs of appropriate radius (2.6 ± 0.4 nm) in which the energy of the main $1S^{\rm h}_{3/2} \rightarrow 1S^{\rm e}$ lower optical transition is equal to the total energy of two laser photons (2.33 eV) have been choused for two-photon resonant excitation. To define the energy of the main transition in QDs the spectra of absorption, luminescence and excitation of luminescence have been obtained and analyzed. The density of QDs in colloidal solution was about 10^{15} cm^{-3}.

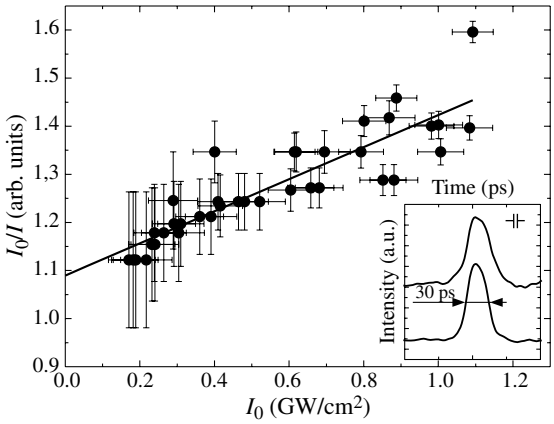

Fig. 1. Dependence of I_0/I upon I_0, where I_0 and I are the intensities of the exciting and transmitted pulses. Inset: the shape of single exiting laser pulses from the train of pulses (the interval between the pulses is 5 axial periods).

In the case of two-photon nonlinear transmission the change of the plane wave intensity

$$dI/dz = -\alpha I - \beta I^2 ,$$

where α and β are the coefficients of linear and two-photon absorption. To determine the coefficient of two-photon absorption the transmission of CdSe/ZnS QDs in the case of open aperture (the energy of the whole transmitted beam was registered by photodiode) was measured. It is convenient (Fig. 1) to present the obtained results as a linear dependence of I_0/I upon I_0, where I_0 and I are the intensities of the exciting and transmitted pulses:

$$\frac{I_0}{I} = \frac{e^{\alpha L}}{(1-R^2)} + \frac{\beta(e^{\alpha L}-1)}{\alpha(1-R)} I_0 , \qquad (1)$$

L is the length of the sell with colloidal solution of CdSe/ZnS QDs, R — the coefficient of the cell's reflection. The data in Fig. 1 are approximated using (1). The measured value of $e^{\alpha L}/(1-R^2)$ is 1.09. The slope of the line has allowed to calculate the coefficient of two-photon absorption (and [1] the imaginary part of third order nonlinear susceptibility): $\beta = 1.6 \pm 0.02$ cm/GW; $\mathrm{Im}\,\chi^{(3)} \equiv \beta c^2 n^2/(32\pi^2\omega) \cong 6{\cdot}10^{-13}$ cm^{3}erg^{-1}.

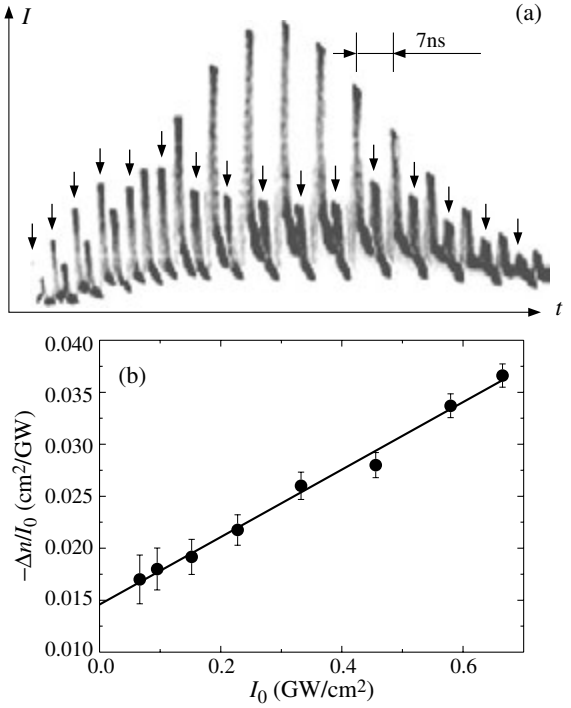

Fig. 2. (a) oscillogram of the train of transmitted (pointed by arrows) and delayed for 3 ns exiting pulses; (b) the dependence of $-\Delta n/I_0$ upon I_0 allowing to separate self-defocusing effects arising from bound and two-photon excited electrons.

The utilizing of aperture between the sample and photodiode has allowed to measure the nonlinear reflection of QDs. The oscillogram of the train of pump and transmitted picosecond pulses is presented in Fig 2a. We suppose that considerable decreasing of the energy of transmitted pulses in the case of closed aperture arises due to the nonlinear change of the coefficient of reflection Δn (due to self-defocusing of the laser beam in the colloidal solution of CdSe/ZnS QDs). The sign of the refractive nonlinearity is negative. Thermal effects were considered negligible because of low linear absorption, short pulse width and the restoration (Fig. 2a) of the transmission at the second part of the train (with the decreasing of the exciting pulse energy). The nonlinear refractive index change may be attributed to the refraction that arise due to bound electrons (electronic Kerr effect [2]) and due to refraction from carriers generated by two-photon absorption [3,4]:

$$\Delta n \equiv \Delta n^b + \Delta n^f \, .$$

The third-order refractive index $\Delta n^b = \gamma I_0$, where

$$\gamma = \frac{12\pi^2}{cn^2} \mathrm{Re}\chi^{(3)}.$$

In the latter expression n_0 is the index of linear refraction. The nonlinear refractive index that arise due to refraction from two-photon generated carriers $\Delta n^f = \xi I_0^2$ and may be expressed by the fifth-order effective (dynamic, inertial) susceptibility. The contribution of nonlinear refractive index becomes substantial at high intensity of the exciting pulse. So the summary change of refractive index:

$$\Delta n = \gamma I_0 + \xi I_0^2 \, .$$

We attribute the change of transmission at relatively low intensity of the exciting laser pulses to the effects of two-photon nonlinear absorption and self-defocusing from bound electrons. As it follows from (1) the intensity of the laser pulse transmitted through two-photon absorbing media can mount to the limiting level: $I_{\mathrm{sat}} = 1/\beta z$. So the abrupt decreasing of the transmitted pulse amplitude in Fig. 2a may be explained by dominating self-defocusing effect that arise due to both nonlinear refraction processes with comparable change of nonlinear refractive index. It is possible to separate these processes analyzing the dependence of $-\Delta n/I_0$ upon I_0 (Fig. 2b). The change of transmission of corresponding pulses of the train (Fig. 2a) allowed to calculate $\Delta n(I_0)$. The linear dependence of $\Delta n/I_0$ upon I_0 for colloidal CdSe/ZnS QDs of 10^{15} cm^{-3} density allows to get the values of $\gamma = 1.46 \cdot 10^{-18}$ cm^{2}sec erg^{-1} ($\mathrm{Re}\chi^{(3)} \simeq 10^{-9}$ cm^{3}erg^{-1}) and $\xi = 3.2 \cdot 10^{-34}$ cm^{4}erg^{-2}sec^2. The value of the latter parameter follows from the slope of the straight line.

3. Conclusions

The results of fulfilled experiments allow to conclude that nonlinear absorption of CdSe/ZnS QDs in the case of two-photon resonant excitation of the lower optical transition arise because of two-photon absorption and self-defocusing effect. The origin of the latter effect is the nonlinear change of reflection index caused by bound electrons and by two-photon excited electrons.

Acknowledgement

This work was supported by Russian Foundation for Basic Research (grant 02-05-17604).

References

[1] D. N. Klysko, *"The physical foundation of quantum electronics"*, russian edition "Nauka" (1986).
[2] I. Banyai *et al*, *Opt. Lett.* **13**, 212 (1988).
[3] A. A. Said *et al*, *J. Opt. Soc. Am.* **B 9**, 405 (1992).
[4] B. L. Justus *et al*, *Appl. Phys. Lett.* **61**, 3151 (1992).

14th Int. Symp. "Nanostructures: Physics and Technology"
St Petersburg, Russia, June 26–30, 2006

Resonant light scattering on quantum dots of any forms and sizes

S. T. Pavlov[1,2], I. G. Lang[3] and L. I. Korovin[3]

[1] P. N. Lebedev Physical Institute, Russian Academy of Sciences, 119991 Moscow, Russia
[2] Facultad de Fisica de la UAZ, Apartado Postal C-580, 98060 Zacatecas, Zac., Mexico
[3] Ioffe Physico-Technical Institute, St Petersburg, Russia

Abstract. The differential cross section of resonant elastic light scattering on any excitons in any quantum dots (QD) is calculated by means of the quantum perturbation theory. If the light wave lengths exceed QD sizes, the polarization and angular distribution of a scattered light do not depend on forms, sizes and potential configurations of QDs. The value of the total cross section in this case does not depend on QD sizes. If radiative broadening of an exciton surpasses non-radiative broadening, the total cross section is of the order of a square of a light wave length in the exact resonance.

Introduction

Measurement of elastic light scattering by size-quantized low-dimensional semiconductor objects (quantum wells, wires and dots) is a simple and convenient method of research of excitons in these objects.

It is possible to investigate light scattering theoretically in two ways. First of them we name semi-classical (see, for example, [1–5]). It is reduced to calculation of classical electric fields, whereas the description of an electron system in the semiconductor is quantum one. The second way is quantum one. The electric field is quantized, the quantum perturbation theory is used also. The semi-classical method has a lot of advantages in comparison with the quantum method, but the quantum method is much easier. Besides, the quantum method is more convenient for transition to studying of the Raman light scattering. Results of application of both methods coincide in a case of a monochromatic irradiation.

The scattering cross section

Number of quantum transitions during a second is

$$W_{\rm i} = \frac{2\pi}{\hbar}\sum_{\rm f}|M_{\rm fi}|^2\delta(E_{\rm f}-E_{\rm i})\,, \qquad (1)$$

where $E_{\rm i}$ ($E_{\rm f}$) is the energy of the initial (final) state,

$$M_{\rm fi} = \sum_m \frac{\langle f|V|m\rangle\langle m|V|i\rangle}{E_{\rm i}-E_m+i\hbar\,\delta}$$

is the compound matrix element, E_m is the energy of the intermediate state, $\delta\to+0$. The interaction of charges with an electric field is as follows

$$V = -\int d\mathbf{r}\mathbf{d}(\mathbf{r})\mathbf{E}(\mathbf{r})\,, \qquad (2)$$

where $\mathbf{d}(\mathbf{r})$ is a polarization density, which equals (see, for instance, [5])

$$\mathbf{d}(\mathbf{r}) = -\frac{ie}{m_0\omega_{\rm g}}\sum_\eta\{\mathbf{p}_{cv\eta}F^*_\eta(\mathbf{r})a^+_\eta - \mathbf{p}^*_{cv\eta}F_\eta(\mathbf{r})a_\eta\} \qquad (3)$$

in the effective mass approximation; m_0 is the free electron mass, $\hbar\omega_{\rm g}$ is the energy gap, $a^+_\eta(a_\eta)$ is the creation (annihilation) operator of an exciton with indexes η, $F_\eta(\mathbf{r})$ is the exciton envelope wave function at $\mathbf{r}_{\rm e}=\mathbf{r}_{\rm h}=\mathbf{r}$, $\mathbf{r}_{\rm e}(\mathbf{r}_{\rm h})$ is the electron (hole) radius-vector, $\mathbf{p}_{cv\eta}$ is the interband matrix element of the quasi-momentum operator.

An electric field is written in the second quantization representation (see, for instance, [6, p. 579]). In the initial state $|i\rangle$ we have 0 excitons and N_l photons with the wave vector $\mathbf{k}_l$ and polarization $\mathbf{e}_l$, at that $N_l\gg1$. In the final state $|f\rangle$ we have no any excitations, N_l-1 photons of the exciting light and 1 photon of scattered light with the wave vector $\mathbf{k}_{\rm s}$ and the polarization $\mathbf{e}_{\rm s}$. In the resonant state at $\omega_l\simeq\omega_\eta$ in the intermediate state $|m\rangle$ we have an exciton η and N_l-1 photons of the exciting light.

We obtain the transition probability

$$W_{\rm i} = \left(\frac{e^2}{\hbar c}\right)^2\left(\frac{\omega_l}{\omega_{\rm g}}\right)^4\frac{N_l}{V_0 c\nu}\sum_\mu\int dO_{\rm s}\left|\sum_\eta A_\eta\right|^2\,, \qquad (4)$$

where V_0 is the normalization volume, ν is the refraction coefficient (the same inside and outside of the QD), $\sum_\mu$ is the sum on polarizations of scattered light, $dO_{\rm s}$ is the solid angle,

$$A_\eta = (\mathbf{p}_{cv\eta}\mathbf{e}_\eta)(\mathbf{p}_{cv\eta}\mathbf{e}_\eta)^*\frac{P^*_\eta(\mathbf{k}_l)P_\eta(\mathbf{k}_{\rm s})}{(\omega_l-\omega_\eta+i\delta)}, \qquad (5)$$

$$P_\eta(\mathbf{k}) = \int d\mathbf{r}F_\eta(\mathbf{r})e^{-i\mathbf{k}\mathbf{r}}\,.$$

The expression (4) is applicable to any semiconductor objects (QWs, quantum wires, QDs) including the situation in a magnetic field.

Let us consider light scattering on a QD. The QD has any form (a sphere, cube or disk) and limited by any potential barriers (parabolic or rectangular and of any height). All these peculiarities influence only the function $P_\eta(\mathbf{k})$. The angular distribution of the scattered light depends also on a structure of vectors $\mathbf{p}_{cv\eta}$. For instance, for crystals of the cubic symmetry (of the T_d class) we have to distinguish excitons, containing heavy and light holes or holes from the valence band, splitted by the spin-orbital interaction. Any of these excitons are characterized by a set of vectors $\mathbf{p}_{cv\eta}$, since excitonic states (without of the electron-photon interaction) are degenerated [7, 8].

With the help of (4) we obtain the differential cross section of light scattering

$$d\sigma = \left(\frac{e^2}{\hbar c}\right)^2\left(\frac{\omega_l}{\omega_{\rm g}}\right)^4\frac{1}{m_0^4c^2}\sum_\mu\left|\sum_\eta A_\eta\right|^2 dO_{\rm s}\,. \qquad (6)$$

With the help of the semi-classical method it is possible to show that the exact account of the electron-electromagnetic field interaction (as well as taking into account the non-radiative broadening γ_η of excitons) results into a replacement of the factor $(\omega_l-\omega_\eta+i\delta)^{-1}$ in (5) by $(\omega_l-\tilde{\omega}_\eta+i(\gamma_{\mathrm{r}\eta}+\gamma_\eta)/2)^{-1}$, where $\gamma_{\mathrm{r}\eta}$ is the radiative broadening, $\hbar\tilde{\omega}_\eta$ is the renormalized exciton energy.

If the excitonic state is degenerated (i.e. the same energy $\tilde{\omega}_\eta=\tilde{\omega}_0$ and the function $F_\eta(\mathbf{r})=F(\mathbf{r})$ correspond to the index sets η) and only vectors $\mathbf{p}_{cv\eta}$ depend on η, the contribution of this state into the cross section equals

$$\frac{d\sigma_0}{do_{\mathrm{s}}}=\sum_\mu\frac{d\sigma_\mu}{do_{\mathrm{s}}}\,,$$
$$\frac{d\sigma_\mu}{d\sigma_{O_{\mathrm{s}}}}=\left(\frac{e^2}{\hbar c}\right)^2\left(\frac{\omega_l}{\omega_{\mathrm{g}}}\right)^4\frac{1}{m_0^4c^2}|\Xi_\mu(\mathbf{e}_l,\mathbf{e}_{\mathrm{s}})|^2 \times\frac{|P(\mathbf{k}_l)|^2|P(\mathbf{k}_{\mathrm{s}})|^2}{(\omega_l-\tilde{\omega}_0)^2+(\gamma_{\mathrm{r}}+\gamma)^2/4}\,, \tag{7}$$

where

$$\Xi_\mu(\mathbf{e}_l,\mathbf{e}_{\mathrm{s}})=\sum_\eta(\mathbf{p}_{cv\eta}\mathbf{e}_l)(\mathbf{p}_{cv\eta}\mathbf{e}_{\mathrm{s}})^*\,.$$

The total cross section equals

$$\sigma_0=\left(\frac{e^2}{\hbar c}\right)^2\left(\frac{\omega_l}{\omega_{\mathrm{g}}}\right)^4\frac{1}{m_0^4c^2}\frac{|P(\mathbf{k}_l)|^2}{(\omega_l-\tilde{\omega}_0)^2+(\gamma_{\mathrm{r}}+\gamma)^2/4} \times\int dO_{\mathrm{s}}|P(\mathbf{k}_{\mathrm{s}})|^2\sum_\mu|\Xi_\mu(\mathbf{e}_l,\mathbf{e}_{\mathrm{s}})|^2\,. \tag{8}$$

Calculating with the help of the perturbation theory the radiative broadening for any exciton in an arbitrary QD we obtain

$$\gamma_{\mathrm{r}\eta}=\frac{e^2}{2\pi\hbar c}\frac{\omega_\eta^3\nu}{\omega_{\mathrm{g}}^2m_0^2c^2}\sum_\mu\int dO_{\mathbf{k}}|(\mathbf{p}_{cv\eta}\mathbf{e}_{\mu\mathbf{k}}|^2|P_\eta(\mathbf{k})|^2\,, \tag{9}$$

where $\mathbf{k}$ is the vector with the module $k=(\omega_\eta\nu/c)$, $\mathbf{e}_{\mu\mathbf{k}}$ is one of the polarization vectors corresponding to the wave vector $\mathbf{k}$.

Let us imagine that $\gamma\ll\gamma_{\mathrm{r}}$ and use (9) for an estimation of γ_{r}. Then we have in the resonance

$$\sigma_o(\omega_l=\tilde{\omega}_0)=(c^2/\omega^2\nu^2)a=k_l^{-2}a\,, \tag{10}$$

where a is some number. If the light wave length is much more in comparison to the QD size, i.e. $kR\ll1$, we have

$$P(\mathbf{k}_l)\simeq P(\mathbf{k}_{\mathrm{s}})\simeq P(0)=\int F(\mathbf{r})\,d\mathbf{r}\,, \tag{11}$$

and in (7)–(8) for the the cross sections and in (9) for the broadening we have to use the approximation (11).

We make following conclusions. At $kR\ll1$ the polarization and the angular distribution of the scattered light are determined only by the factor $|\Xi_\mu(\mathbf{e}_l,\mathbf{e}_{\mathrm{s}})|^2$ from the RHS of (7), i.e. they do not depend on the QD form and on the envelope function of the exciton wave function. *The cross section value does not depend on QD sizes.* Naturally, the position of the level $\tilde{\omega}_0$ depends on the QD form and sizes. At $kR\ll1$ we obtain that the radiative broadening does not depend on the QD form and sizes. It follows from (10) that if the radiative broadening exceeds the non-radiative broadening (it is possible in perfect QDs), in the resonance the total cross section is of order of the square of the light wave length. This result is true at $kR\ll1$, as well as at $kR\geq1$ for any QDs. If $\gamma\gg\gamma_{\mathrm{r}}$, the cross section decreases in $(\gamma/\gamma_{\mathrm{r}})^2$ times.

Let us consider an example of an exciton produced by an electron from the twice degenerated conductivity band Γ_6 and by a hole from the twice degenerated valence band Γ_7, segregated by the spin-orbital interaction in crystals of the T_d class. Using appropriate wave functions from [8, p. 73] we obtain the four times degenerated excitonic state with corresponding vectors

$$\mathbf{p}_{cv1}=(p_{cv}/\sqrt{3})(\mathbf{e}_x-i\mathbf{e}_y),\ \mathbf{p}_{cv2}=(p_{cv}/\sqrt{3})(\mathbf{e}_x+i\mathbf{e}_y),$$
$$\mathbf{p}_{cv3}=(p_{cv}/\sqrt{3})\mathbf{e}_z\,,\ \mathbf{p}_{cv4}=-(p_{cv}/\sqrt{3})\mathbf{e}_z\,, \tag{12}$$

where $p_{cv}=i\langle S|\hat{p}_x|X\rangle$ (in designations of [8]), $\mathbf{e}_x$, $\mathbf{e}_y$ and $\mathbf{e}_z$ are unite vectors along the crystallographic axes.

Let us consider the right (left) polarization of the scattered light designated as $+(-)$. *The value of the cross section does not depend on the direction of the vector* $\mathbf{k}_l$ *relatively crystallographic axes.* Substituting (12) in (7), we obtain

$$\frac{d\sigma^{++}}{dO_{\mathrm{s}}}=\frac{d\sigma^{--}}{dO_{\mathrm{s}}}=\Sigma_0(1+\cos\Theta)^2/9\,, \tag{13}$$

$$\frac{d\sigma^{+-}}{dO_{\mathrm{s}}}=\frac{d\sigma^{-+}}{dO_{\mathrm{s}}}=\Sigma_0,\,(1-\cos\Theta)^2/9\,, \tag{14}$$

i.e. (13) and (14) describe the light scattering without changing and with changing of the polarization, respectively. Θ is the angle between $\mathbf{k}_l$ and $\mathbf{k}_{\mathrm{s}}$,

$$\Sigma_0=\left(\frac{e^2}{\hbar c}\right)^2\left(\frac{\omega_l}{\omega_{\mathrm{g}}}\right)^4\frac{p_{cv}^4}{m_0^4c^2}\frac{|P(\mathbf{k}_l)|^2|P(\mathbf{k}_{\mathrm{s}})|^2}{(\omega_l-\tilde{\omega}_0)^2+(\gamma_{\mathrm{r}}+\gamma)^2/4}\,. \tag{15}$$

At $kR\ll1$ we use in (15) the approximation (11) and obtain the result, applicable to the light scattering on any QD in the resonance with the exciton $\Gamma_6\times\Gamma_7$. It follows from (13) and (14) that in the simplest case light scattering is anisotropic and has some changed polarization.

References

[1] E. L. Ivchenko, A. V. Kavokin, *Fizika tverd. tela* **34**, 1815 (1992).

[2] D. A. Contreras-Solorio, S. T. Pavlov, L. I. Korovin, I. G. Lang, *Phys. Rev. B* **24**, 16815 (2000).

[3] L. I. Korovin, I. G. Lang, D. A. Contreras-Solorio, S. T. Pavlov, *Fizika tverd. tela* **44**, 1681 (2002) [*Phys. of Solid State* **44**, 1759 (2002)].

[4] S. V. Goupalov, *Phys. Rev. B* **68**, 125311 (2003).

[5] I. G. Lang, L. I. Korovin, S. T. Pavlov, *Fizika tverd. tela* **46**, 1706 (2004) [*Phys. of Solid State* **46**, 1761 (2004)].

[6] L. D. Landau, E. M. Liphshitz, *The electrodynamics of condenced matter*, Moscow, 1982, p. 579.

[7] J. M. Luttinger, W. Kohn, *Phys. Rev.* **97**, 869 (1955).

[8] I. M. Tsidilkovsky, *The band structure of semiconductors*, Moscow, 1978, p. 73.

14th Int. Symp. "Nanostructures: Physics and Technology"
St Petersburg, Russia, June 26–30, 2006

Anomalous in-plane magneto-optical anisotropy of self-assembled quantum dots

A. V. Platonov[2], T. Kiessling[1], G. V. Astakhov[1,2], T. Slobodskyy[1], S. Mahapatra[1], W. Ossau[1], G. Schmidt[1], K. Brunner[1] and L. W. Molenkamp[1]

[1] Physikalisches Institut (EP3) der Universität Würzburg, 97074 Würzburg, Germany
[2] Ioffe Physico-Technical Institute, St Petersburg, Russia

Abstract. We report on a nontrivial behavior of the optical anisotropy of quantum dots that is induced by a magnetic field in the plane of the sample. We find that the optical axis either rotates in the opposite direction to that of the magnetic field or remains fixed to a given crystalline direction. A theoretical analysis based on the exciton spin Hamiltonian unambiguously demonstrates that these effects are induced by isotropic and anisotropic contributions to the heavy-hole Zeeman term, respectively.

Self assembled semiconductor quantum dots (QDs) attract much fundamental and practical research interest. An important, and frequently somewhat neglected aspect of QDs is the relationship between their symmetry and their optical properties. We recently showed that extreme anisotropy of QDs can lead to efficient optical polarization conversion [1].

Because of the elongated shape and the presence of strain od actual QDs their point-group symmetry is reduced to C_{2v} or below. In this case the in-plane heavy hole g-factor is no longer isotropic [2]. Moreover, even in zero magnetic field the degeneracy of the radiative doublet is lifted due to the anisotropic exchange splitting [3]. Any of these issues will give rise to optical anisotropy, resulting in the linear polarization of emitted light.

In this paper, we discuss the optical anisotropy of QDs in the presence of a magnetic field. In the classical case, one would have the Voigt effect, i.e. the axis of the emission polarization is collinear with the direction of the magnetic field. This implies that when rotating the sample at fixed direction of the field one observes a constant polarization for the emission, which can be mathematically expressed as obeying the behavior of a zeroth order spherical harmonic. This situation changes drastically for low dimensional heterostructures because of the complicated valence band structure. Kusrayev *et al* [4] observed a second spherical harmonic component (i.e., π-periodic oscillations under sample rotation) in the polarization of emission from narrow quantum wells (QWs). This result was explained in terms of a very large in-plane anisotropy of the heavy-hole g-factor $g_{\rm hh}^{xx} = -g_{\rm hh}^{yy}$.

Here, we report the observation of a fourth harmonic in the magneto-optical anisotropy (i.e. $\pi/2$-periodic oscillations in the polarization of the emitted light under sample rotation) from CdSe/ZnSe self assembled QDs. We demonstrate that this effect is quite general for the optical polarization of QDs. An important consequence is that the polarization axis hardly follows the magnetic field direction, thus the classical Voigt effect is not observed for QD emission associated with the heavy-hole exciton. Moreover, in contrast to earlier studies of in-plane magneto-optical anisotropies, we consider the contributions of the electron-hole exchange interaction, which have been ignored for QWs [4, 5] and are exactly zero for charged QDs [2]. An anisotropic exchange splitting may lead to the existence of a compensating magnetic field $B_{\rm C}$. When the externally applied field equals $B_{\rm C}$, the amplitude of the second harmonic crosses zero, resulting in a highly symmetrical optical response of extremely anisotropic QDs.

In order to measure anisotropy we used the detection scheme suggested in [4]. The direction of the in-plane magnetic field is fixed, while the sample is rotated over an angle α. The degree of linear polarization is now defined as $\rho_\gamma(\alpha) = (I_\gamma - I_{\gamma+90^\circ})/(I_\gamma + I_{\gamma+90^\circ})$. Here the angle γ corresponds to the orientation of the detection frame with respect to the magnetic field and I_γ is the intensity of the PL polarized along the direction γ. Within an approximation of weak magnetic fields, a sample that has C_{2v} point symmetry in general may have only three spherical harmonic components [4] linking the polarization of the the emission to the sample rotation angle α. Thus, one has for $\gamma = 0^\circ$ and $\gamma = 45^\circ$

$$\begin{aligned} \rho_0(\alpha) &= a_0 + a_2 \cos 2\alpha + a_4 \cos 4\alpha \,, \\ \rho_{45}(\alpha) &= a_2 \sin 2\alpha + a_4 \sin 4\alpha \,, \end{aligned} \qquad (1)$$

with a_0, a_2 and a_4 the amplitude of the zeroth, second and fourth harmonic, respectively. $\alpha = 0^\circ$ is taken for a magnetic field parallel to the $[1\bar{1}0]$ axis.

In our experiments, we studied the magneto-optical anisotropy of CdSe QDs in a ZnSe host. The samples were fabricated on (001) GaAs substrates using molecular beam epitaxy and self-assembly after depositing one monolayer of CdSe on a 50 nm thick ZnSe layer. The QDs were then capped by 25 nm of ZnSe. For optical excitation we used a stilbene dye-laser pumped by the UV-lines of an Ar-ion laser. For detection of the linear polarization we applied a standard technique using a photo-elastic modulator and a two-channel photon counter [1]. The angle scans were performed with the samples mounted on a rotating holder controlled by a stepping motor with an accuracy better than 1°. Magnetic fields up to 4 T were applied in the sample plane (Voigt geometry), optical excitation was done using a depolarized laser beam. The degree of linear polarization of the luminescence of the QDs was measured at a temperature $T = 1.6$ K.

The example of angle scans of ρ_{45} for various magnetic field strengths and obtained values for harmonic amplitudes are shown in Fig. 1. In zero magnetic field the linear polarization is π-periodic. This demonstrates the low (C_{2v}) symmetry of the QD ensemble (the dots are elongated in the plane) resulting in a preferred crystalline polarization axis and a finite value of a_2 in Eq. (1). One can regard this measurement as

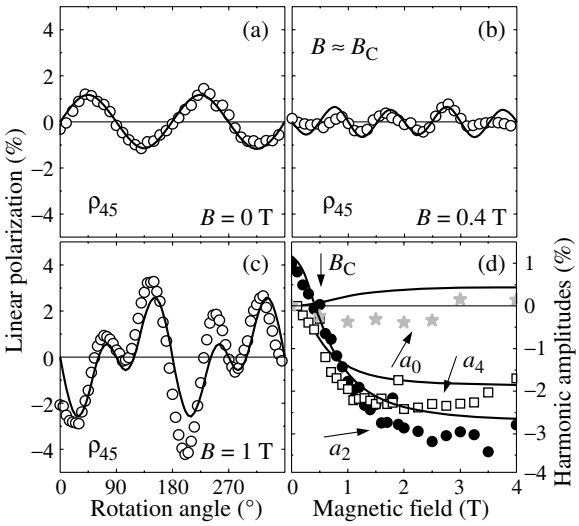

Fig. 1. Angle scans of the linear polarization. The symbols are experimental data, solid lines represent calculations based on the Hamiltonian of Eq. (2). (a) Built-in linear polarization ($B = 0$ T). (b) A highly symmetrical optical response (i.e. $\pi/2$-periodic) appears at a compensating field $B_C \approx 0.4$ T. (c) Angle scan in a magnetic field $B = 1$ T exceeding B_C. (d) Amplitudes of the zeroth (a_0), second (a_2) and fourth (a_4) spherical harmonics *vs* B. The symbols are experimental data and the solid lines result from calculations.

reflecting the 'built-in' linear polarization of the array of dots. For large magnetic fields a_2 changes sign and an additional fourth harmonic signal appears. At an intermediate magnetic field $B_C \approx 0.4$ T the second harmonic crosses zero, while the fourth harmonic remains finite (see also Fig. 1b). The resulting $\pi/2$-periodic optical response corresponds to the higher (D_{2d}) symmetry expected for circular QDs. In other words, this observation demonstrates that the in-plane optical anisotropy of QDs can be compensated by in-plane Zeeman terms. In addition, we find that the zeroth harmonic signal is weak.

Essentials of the experimental data to be analyzed are summarized in Fig. 1d. Harmonic amplitudes, i.e. coefficients a_0, a_2 and a_4, were extracted from the fits of the experimental data using Eq. (1) and plotted *vs* magnetic fields (symbols).

The exciton spin Hamiltonian $\mathcal{H}$ in the basis of the exciton functions $\Phi_{1,2} = |\pm 1\rangle$, $\Phi_{3,4} = |\pm 2\rangle$ is given by the following matrix [3]

$$\mathcal{H} = \frac{1}{2}\begin{pmatrix} \delta_0 & -i\delta_1 & \delta_e & \delta_{hh} \\ i\delta_1 & \delta_0 & \delta_{hh}^* & \delta_e^* \\ \delta_e^* & \delta_{hh} & -\delta_0 & \delta_2 \\ \delta_{hh}^* & \delta_e & \delta_2 & -\delta_0 \end{pmatrix}. \qquad (2)$$

Here, $\delta_e = \mu_B g_e^{\perp} B_+$ and $\delta_{hh} = \mu_B \left(g_{hh}^{i} B_+ + i g_{hh}^{a} B_-\right)$ are in-plane Zeeman terms, $g_e^{\perp}$ is the electron g-factor, g_{hh}^{i} and g_{hh}^{a} are the isotropic and anisotropic contributions to the heavy-hole g-factor. Effective magnetic fields are $B_{\pm} = Be^{\pm i\varphi}$. The coefficients $\delta_0, \delta_1, \delta_2$ describes an exchange splitting [3]. The quantum mechanical problem with hamiltonian (2) can be solved numerically. By using the known solution we may obtain the intensity of the luminescence component ($I_{j,(\xi)}$) being linearly polarized along the axis rotated by an angle ξ with respect to the [100] crystalline axis.

The polarization of the PL originates from the different population of exciton states. In the sample frame it can be calculated as

$$\rho'_{(\xi)} = K \frac{\sum_j P_j \left(I_{j,(\xi)} - I_{j,(\xi+90^\circ)}\right)}{\sum_j P_j \left(I_{j,(\xi)} + I_{j,(\xi+90^\circ)}\right)}, \qquad (3)$$

with the Boltzmann factor $P_j \propto e^{-E_j/k_B T}$. E_j is an energy for the state j. K is a scaling factor which has the meaning of a level of saturated polarization.

We were able to reproduce even quantitatively all experimental data using a unique set of parameters for given excitation power and excitation energy. The calculations were done taking a bath temperature $T = 1.6$ K and a coefficient $K = 0.04$. From the best fits we found exchange energies $\delta_0 = 2.9$ meV, $\delta_2 = 0.1$ meV, $\delta_1 = 0.2$ meV and g-factors $g_e^{\perp} = 1.1$, $g_{hh}^{i} = -0.5$, $g_{hh}^{a} = 0.6$. The results of the calculations are shown by solid lines in Fig. (3). They follow very closely the experimental points. We evaluated the harmonic amplitudes (a_0, a_2 and a_4) from the Fourier transform and plotted them as function of magnetic fields in Fig. 1d (solid lines). A general tendency is that the isotropic heavy-hole g-factor is responsible for the fourth harmonic and the anisotropic g-factor is essential for the second harmonic. The latter was reported previously for magnetic QWs [4] and our findings are in general agreement with other approaches [5]. Additional consideration of the exciton exchange interaction leads to a built-in linear polarization which can be compensated by a certain magnetic field (with the proper sign of heavy-hole g-factor).

In conclusion, we demonstrate experimentally and prove theoretically anomalous behavior of in-plane magnetic anisotropy in CdSe/ZnSe QDs, where the second and fourth harmonics dominate over the natural zeroth one. We show the existence of a compensating magnetic field, leading to a symmetry enhancement of QD optical response. Our findings are not limited to QDs and can be applied to other heterostructures of the same symmetry where the heavy-hole exciton is a ground state.

Acknowledgements

This work was supported by the Deutsche Forschungsgemeinschaft (SFB 410) and by the Russian Federal Agency of the Science and Innovations (2006-RI-19.0/001/529).

References

[1] G. V. Astakhov *et al*, *Phys. Rev. Lett.* **96**, 027402 (2006).
[2] A. V. Koudiniov *et al*, *Phys. Rev. B* **70**, R241305 (2004).
[3] E. L. Ivchenko, *Optical Spectroscopy of Semiconductor Nanostructures*, (Alpha Science International, Harrow, UK, 2005).
[4] Yu. G. Kusrayev *et al*, *Phys. Rev. Lett.* **82**, 3176 (1999).
[5] Y. G. Semenov and S. M. Ryabchenko, *Phys. Rev. B* **68**, 045322 (2003).

14th Int. Symp. "Nanostructures: Physics and Technology"
St Petersburg, Russia, June 26–30, 2006

Global energy minima of nanocluster structures

Ricardo Ramírez[1], José Rogan[2], Griselda García[1], Claudia Loyola[2], W. Orellana[2] and Miguel Kiwi[1]

[1] Facultad de Física, Universidad Católica de Chile, Casilla 306, Santiago 782-0436, Chile
[2] Departamento de Física, Facultad de Ciencias, Universidad de Chile, Casilla 653, Santiago 1, Chile

Abstract. By means of the implementation of the conformational space annealing (CSA) unbiased search in combination with a phenomenological potential we have been able to create a bank of local minima configurations. These minima were in turn examined by *ab-initio* methods to obtain global minima. Minimal energy clusters configurations not previously reported were found through this technique.

Nanoclusters have properties that are strongly dependent on size and the spatial distribution of the atoms in the system. Consequently, a crucial issue is to determine their minimal energy configurations. Towards this end several techniques have been implemented to single out the lowest energy configuration among a huge number of local minima.

In this work a new strategy to find global energy minima of the energy of metallic clusters is proposed. This strategy is based on a novel and powerful global optimization method, called conformational space annealing (CSA), which was put forward by Lee *et al* [1]. This method has been succesful in generating the global minima for Lennard–Jones clusters up to a size $N \leq 183$ [1] a feat no other unbiased search method has been able to accomplish.

A brief description of the CSA method is as follows: as the genetic algorithm CSA starts with a set of configurations, denominated initial population in the GA and *bank* in CSA context; in our implementation the bank contains 50 different configurations. Of them 20 are chosen at random as seeds to generate new configurations, which are incorporated into the data bank if they satisfy one of the following criteria: i) if the distance between the trial and closest configuration in the bank, as evaluated with Eq. 1, is small the largest energy one is dropped; or ii) if this distance is larger then the highest energy configuration, including the trial, is removed from the bank. The equation that specifies the distance is given by

$$D(j,k) = \sum_n n \left(2\left|H_j(1,n) - H_k(1,n)\right| + \left|H_j(2,n) - H_k(2,n)\right|\right), \quad (1)$$

where $H_j(1,n)$ $[H_j(2,n)]$ is the histogram of the number of atoms having n neighbors in the first [second] shell of the j-th configuration. To specify the shell radii we adopt the first and second neighbor distances of the respective bulk lattice, which in this particular instance is fcc. This way the bank is constantly being renewed until all members are used as seeds. The key feature that makes CSA advantageous is the fact that instead of providing just *the* global minimum, like GA does, it yields a data bank of low lying minima.

We applied this technique to 13 atoms clusters of Rh, Pd and Ag. The application of this strategy in combination with the Gupta potential yields, after just one iteration, a bank of local minima for the three elements mentioned above. This bank consists of 50 configurations.

Each configuration of this bank was next relaxed by means of the SIESTA code. The structures of minimum energy thus obtained were classified as far as total energy, geometrical structure and magnetic configuration is concerned to obtain the results displayed in Fig. 1. The configurations for the two lowest minima for each element is shown in Fig. 2.

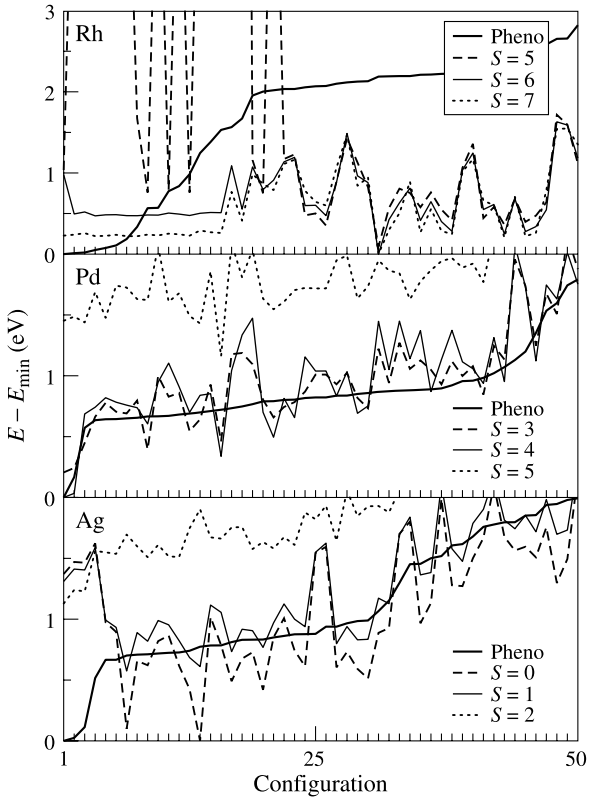

Fig. 1. Energies of the 50 configurations of the bank for Rh, Pd and Ag, obtained by a phenomenological potential and subsequently relaxed by the SIESTA code for different values of the spin.

In the SIESTA code the exchange-correlation energy was calculated within the local spin density approximation (LSDA) as parameterized by Perdew and Zunger [2]. We have used a double-ζ single-polarized (DZP) basis set [3]. Convergence tests have demonstrated that this basis yields reliable results in a variety of cases including covalent, ionic, and metallic systems [4]. Norm-conserving pseudopotentials [5], in their non-local form, were used to describe the electron-ion interaction. Pseudopotentials of Rh, Pd and Ag have been generated for the $[Kr]4d^8 5s^1$, $[Kr]4d^{10}5s^0$ and $[Kr]4d^{10}5s^1$ configurations, respectively.

Several new structures, previously overlooked in the literature, were found in this way. Not all of the global minimum configurations show high symmetry. Moreover, not all of the global minima obtained with our scheme coincide with the re-

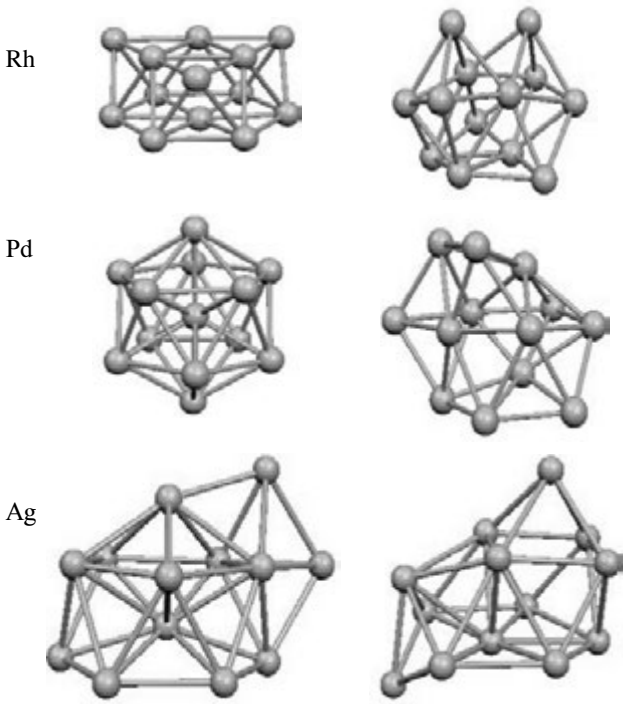

Fig. 2. The two lowest energy configurations for Rh, Pd and Ag. The structures on the left correspond to the global minima.

sults obtained using just phenomenological potentials.

It is important to emphazise that the application of method described in this work allows us to find a set of minimal energy configurations, rather than just the global minima. In this way we avoid a CSA search entirely done with an *ab-initio* calculation.

Acknowledgement

We thank Dr. Vijay Kumar for providing us with the Rh_{13} cage cluster coordinates. This work was supported by the *Fondo Nacional de Investigaciones Científicas y Tecnológicas* (FONDECYT, Chile) under grants #1030957 (MK and JR), #1040356 (RR) and #1050197 (WO), and MECESUP (GG). WO was supported by the Millennium Nucleus of Applied Quantum Mechanics and Computational Chemistry, under project P02-004-F.

References

[1] J. Lee *et al*, *J. Comput. Chem.* **18**, 1222 (1997).
[2] J. Perdew *et al*, *Phys. Rev. B* **23**, 5048 (1981).
[3] J. M. Soler *et al*, *J. Phys.: Condens. Matter* **14**, 2745 (2002).
[4] J. Junquera *et al*, *Phys. Rev. B* **64**, 235111 (2001).
[5] N. Troullier *et al*, *Phys. Rev. B* **43**, 1993 (1991).
[6] V. Kumar *et al*, *Phys. Rev. B* **66**, 144413 (2002).

14th Int. Symp. "Nanostructures: Physics and Technology"
St Petersburg, Russia, June 26–30, 2006

Biasing of stacked InAs quantum dot array: tuning of inter-dot resonance and control of electron-hole alignment

V. G. Talalaev[1,2,3], J. W. Tomm[1], N. D. Zakharov[2], P. Werner[2], U. Gösele[2], B. V. Novikov[3], A. S. Sokolov[3], A. Winzer[4], G. Gobsch[4], G. E. Cirlin[5] and A. A. Tonkikh[5]

[1] Max-Born-Institut für Nichtlineare Optik und Kurzzeitspektroskopie, 12489 Berlin, Germany
[2] Max-Planck-Institut für Mikrostrukturphysik, 06120 Halle (Saale), Germany
[3] Fock Institute of Physics, St Petersburg State University, 198504 St Petersburg, Russia
[4] Technische Universität Ilmenau, 98684 Ilmenau, Germany
[5] Ioffe Physico-Technical Institute, St Petersburg, Russia

Abstract. The optoelectronic properties of vertically stacked InAs/GaAs quantum dots (QD) are investigated. The QD arrays are grown in the intrinsic region of GaAs pin-junctions by molecular beam epitaxy. Application of external bias along the vertical (growth) direction allows to tune the energetic states of the QDs with respect to each other. By biasing the pin-junction a carrier transfer between two different QD groups along growth direction becomes possible. In this way the vertical electronic transport between QDs and eventually the optoelectronic properties of the structure become tunable and controllable. Two types of resonance are observed in photoluminescence spectra under applied electric field. Transient photoluminescence data clearly indicate the resonance associated with a maximum of carrier-pair lifetime in the QD array ($\sim$ 2 ns). This maximum is assigned to reduced wavefunction overlap between resonantly coupled electrons and localized holes. Out of resonance the phonon/polaron assisted processes are responsible for the inter-QD carrier transfer with a time constant of $\sim$ 100 ps. Tuning through resonances between the ground states of QDs is found to have substantially impact the optoelectronic properties of such structures. This paves the way for novel photonic applications.

Introduction

Most of quantum logic options are based on the tunneling phenomena in quantum media. In contrast to the quantum wells, the self-organized quantum dots (QD) have a certain size dispersion, which can not be perfectly controlled for a single QD layer. In the case of stacked layers the distribution of QD size in the columns is more predictable and controllable. Therefore stacked QDs with defined vertical alignment can be regarded as QD superlattices (QDSL). In previous investigation [1] we have found the influence of the built-in electric field of the Schottky barrier on the photoluminescence (PL) spectra of InAs/GaAs QDSLs.

The current work deals with the tuning of resonance between the states of non-identical vertically aligned InAs QDs by means of an external static electric field applied in vertical (growth) direction. We present the results of a transmission electron microscopy (TEM) and PL study of the 9 period InAs/GaAs QDSLs grown by molecular beam epitaxy. The QDSL is embedded into a pin-junction with a 140 nm intrinsic region.

1. Results and Discussion

Figure 1(a) presents a TEM cross-section image of a typical QD column. The QD cross section increases monotonically with the layer number N for the first six layers $1 \leq N \leq 6$; see squares in Fig. 1(b), CQDs. Spacing between wetting layers amounts 9 nm, between QDs — 4 nm. An anomalous behavior of the QD and spacer begins at the seventh layer. A typical QD in this particular layer has an approximately twice larger cross section and height than the previous one. In turn, the 8-th one is very small. High resolution TEM data in Fig. 1(c) demonstrates that 7-th and 8-th layers are coalescent and form associated QDs (AQD).

Strain accumulation from the bottom to the top layers is considered the driving force for both the accurate vertical QD alignment and the AQD formation. In particular the accumulation of elastic strain from layer to layer prevents a complete covering of the 7-th QD by GaAs spacer. Then the deposition of 8-th InAs layer results in coalescence of the two QDs, and finally the formation of AQD follows. Thus two groups of QDs in the column are formed, namely the CQDs with slightly different sizes and the large size AQD.

Using the TEM data we have defined the electronic structure of the QDSL within the framework of the effective mass approximation. In Fig. 1(b) the triangles present the calculated confinement energy of the electronic ground states of QDs with disc-like shapes. On the base of QD number dependence of this energy we can propose a tentative energetic structure of the conduction band within the pin-junction of our structure. This model is shown in Fig. 1(d).

Figure 2 shows PL data for the QDSL under various applied bias and excitation. The steady-state PL spectrum exhibits two bands, denoted A and C, and tentatively attributed to the two QD groups, namely AQDs and CQDs, respectively. Obviously the PL can be controlled by the external bias. Both bands exhibit different sensitivities to the applied bias as demonstrated in Figs. 2(a), (b). For an applied reverse (negative) bias, the A-band disappears from the PL spectrum earlier than the C one. The high-field limits of both the A- and C-bands depend on the excitation power, most probably due to photo-voltage compensation of the applied reverse bias. However, the nature of the disappearance of the A- and C-band is different. Step-wise effect for C-band is related to the field-induced spatial separation of electrons and holes in the QDSL. A non-symmetric bias dependence of the band intensity proves that heavy-holes in QDSL are strongly localized. The peak-wise bias dependence of A-band intensity shown in Figure 2(c) for excitation into the C-band is evidence of the other effect — the resonance between AQD and CQD states. This happens when the deeply

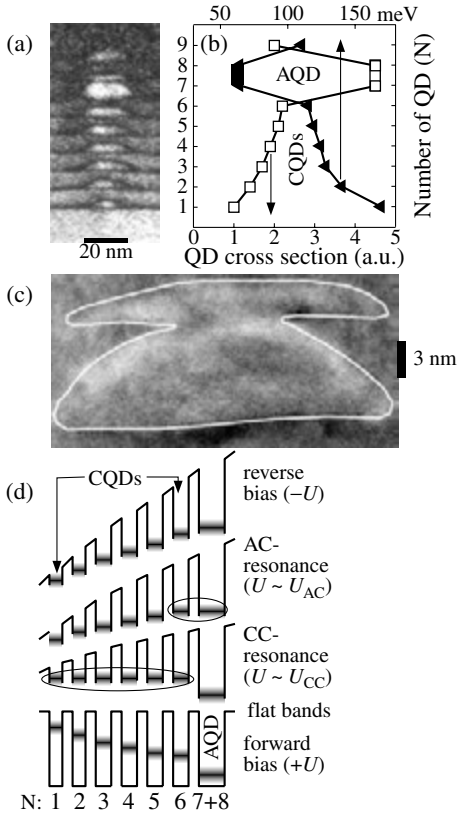

Fig. 1. (a) Cross section dark-field TEM image of a QD column in an InAs/GaAs QDSL with 9 QD layers. (b) QD cross section (squares) and calculated energies of the electronic ground state (triangles) versus number of the QD (N) within in the same column. (c) High resolved cross section TEM image of the AQD ($N = 7,\ 8$). (d) Level scheme of a InAs/GaAs QD column under external bias. The last QD ($N = 9$) is not included.

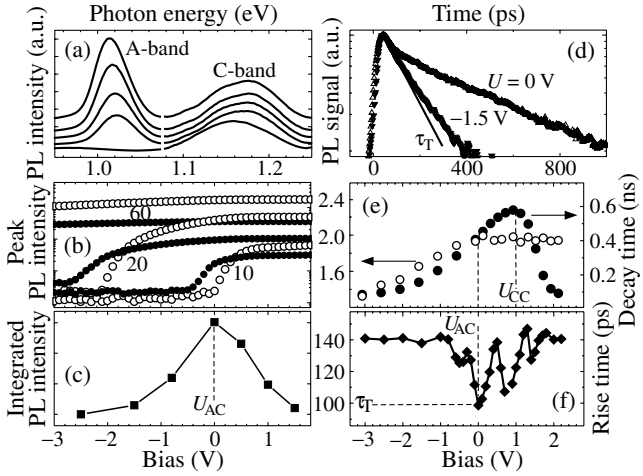

Fig. 2. (a) Steady-state PL spectra of an InAs/GaAs QDSL. The parameter is applied bias $U = +1,\ 0,\ -1,\ -2$, and -3 V (from the top to the bottom). (b) Steady-state peak PL intensity of the A- (open circles) and C-bands (full circles) versus applied bias. The parameter is the power density in Wcm^{-2}. (c) Bias dependence of AQD integrated PL intensity. (d) Transient PL profiles of C-band at the various bias. (e) Decay time constants extracted from transient PL data versus applied bias for the C-band (full circles) and A-band (open circles). (f) Bias dependence of the PL rise time for the A-band. (a) InAs wetting layer excitation. (b),(d)–(f) GaAs barrier excitation. (c) C-band excitation.

confined electron A-level is tuned through the resonance with the CQD-states; see AC-resonance in Fig. 1(d). At the AC-resonance a PL decay time of A-band reaches a maximum of 2 ns and a PL rise time reaches a minimum of 100 ps; see open circles in Fig. 2(e) and Fig. 2(f), respectively.

Basically there are two processes, which determine carrier kinetics: (i) recombination and (ii) carrier transfer between QDs. Our model in Fig. 1(d) allows to separate of these two depopulation mechanisms for the AQDs and to consider the decay time of $\sim$ 2 ns the "intrinsic" lifetime of the AQDs. Likewise the PL rise time of 100 ps can be considered as carrier transfer time from CQDs into the AQD at their resonance. In other words, this time (τ_T) is resonance tunneling time in the QDSL. Furthermore, the rise time τ_T corresponds to first (bias-independent) PL decay component τ_T of the C-band [Fig. 2(d)], which describes the relaxation of carriers out of the CQDs into the AQDs. Close to the AC-resonance the rise time constant starts to decrease periodically; see Fig. 2(f). Taking into account the sample geometry, the observed oscillation period of 0.7 V corresponds to a voltage drop between adjacent QDs of 45 mV. This value is close to the GaAs-like LO-phonon or QD-polaron state energy. The oscillation between 140 and 100 ps in Fig. 2(f) is interpreted as the switching between the "regular" trapping and phonon/polaron assisted non-resonant transfer to the AQDs.

The second time constant of C-band [Fig. 2(d)] is fiund bias-dependent and refers to the intrinsic exciton lifetime in the CQDs and its bias dependence is presented in Fig. 2(e) by full circles. The well pronounced maximum corresponds to the bias UCC, at which the ground states of the AQDs are lower than the CQD-states, and only the internal processes within the CQD-subsystem contribute to this time constant. Thus the TRPL data allow us to manifest one more resonance in the QDSL — the resonance between the states of the CQD-chain; see CC-resonance in Fig. 1(d).

At the CC-resonance the electron wavefunctions of CQDs are at most delocalized and "spread out" into the GaAs barrier. Since the heavy-hole wavefunctions are still strongly localized within the InAs QDs, the overlap integral of the electron-hole wavefunctions decreases, i.e. the oscillator strength of the transition becomes smaller and the lifetime increases; see Figs. 2(d), (e). This is almost similar to the situation, which we have previously observed for InAs QD molecules, consisting of two identical tunnel-coupled QDs [2].

2. Conclusion

In summary, by applying a bias, we are able to tune the electronic ground states of a QDSL through distinct resonances. A monitoring of electron-hole alignment in QDSL within our model becomes possible.

Acknowledgement

This work has been supported by the Russian Foundation for Basic Research (Grant No. 05–02–17780) and the EU project SANDiE.

References

[1] V. G. Talalaev *et al*, *Nanotechnology* **13**, 143 (2002).
[2] V. G. Talalaev *et al*, *Appl. Phys. Lett.* **85**, 284 (2004).

14th Int. Symp. "Nanostructures: Physics and Technology"
St Petersburg, Russia, June 26–30, 2006

Carrier capture into self-organized InGaAs quantum dots

A. Marent[1], M. Geller[1], *V. I. Zubkov*[2], I. S. Shulgunova[2], A. V. Solomonov[2] and D. Bimberg[1]

[1] Institut für Festkörperphysik, Technische Universität Berlin, Hardenbergstrasse 36, 10623 Berlin, Germany
[2] St Petersburg State Electrotechnical University "LETI", 197376 St Petersburg, Russia

Abstract. We studied the carrier capture of holes into self-organized InGaAs/GaAs quantum dots (QDs). The carrier capture is directly observed for the first time in charge-selective deep level transient spectroscopy (charge-selective DLTS) measurements. From the capacitance transients we obtain thermal activation energies and capture cross sections for emission *and* capture. The almost equal values leads us to conclude a phonon-assisted tunneling process for carrier capture into QDs.

Introduction

Self-organized semiconductor quantum dots (QDs) [1] can be used for various opto-electronic devices such as semiconductor lasers and detectors. In addition, QDs are also very interesting as an alternative approach for future single-electron memories [2]. Understanding the carrier capture as well as the carrier escape mechanisms is a crucial prerequisite for memory applications. The carrier capture defines the read access time in future QD-based memories. In addition, a detailed physical understanding of the capture process is of basic physical interest for almost every device application. This article reports the first direct observation of hole capture into InGaAs QDs, providing new information in the physics of capture mechanisms.

Capacitance spectroscopy and deep-level transient spectroscopy (DLTS) have been established as powerful tools to investigate the electronic properties and escape dynamics of various QD systems [3–5]. However, the capture time constant is in the picosecond range for QDs [6], not available for DLTS measurements. In this paper we studied the capture of holes in self-organized InGaAs/GaAs QDs by using charge-selective DLTS [4]. The QDs are now inside the depletion region of a *p*-*n* diode and the local band bending induced by an electric field provides a thermal activation barrier for the capture process. As a consequence, the capture time is increased and capture can be directly observed in capacitance transients.

1. Sample structure

We studied a sample with self-organized InGaAs/GaAs QDs, grown by metalorganic chemical vapor deposition (MOCVD). On top of a GaAs(001) substrate, a 500 nm thick highly p-doped GaAs ($\sim 1\times10^{18}$ cm^{-3}) layer followed by 700 nm slightly p-doped ($\sim 3\times10^{16}$ cm^{-3}) GaAs were deposited. Subsequently, on top of a 10 nm thick undoped GaAs layer, ~ 3 ML $In_{0.8}Ga_{0.2}As$ were deposited forming the self-organized QDs. The QDs were eventually overgrown with 7 nm undoped GaAs and a 500 nm layer of slightly p-doped ($\sim 3\times10^{16}$ cm^{-3}) GaAs. Finally, a 400 nm highly n-doped ($\sim 7\times10^{18}$ cm^{-3}) GaAs cap layer formed the n^+ contact. To form devices, processing based on standard optical lithography was applied. Mesa structures with a diameter of 800 μm with Ohmic top and back contacts were created.

2. Hole capture and emission

We used the charge-selective DLTS [4] method to measure the hole emission and capture. The QDs are always inside the depletion region. As a consequence, even for hole capture a thermal activation barrier is present [schematic inset in Fig. 3(a)] and reduces the capture rate. Transients for emission *and* capture can be observed (see Fig. 1).

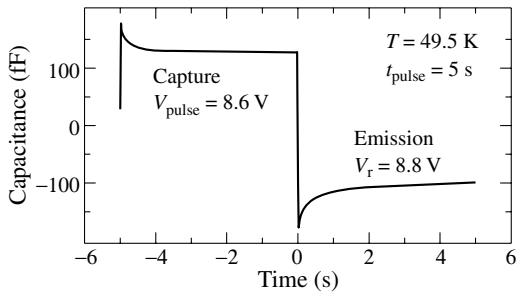

Fig. 1. Capacitance transients at temperature $T = 49.5$ K for a reverse/pulse bias 8.8 V/8.6 V, respectively. The emission and capture of holes in InGaAs QDs can be detected.

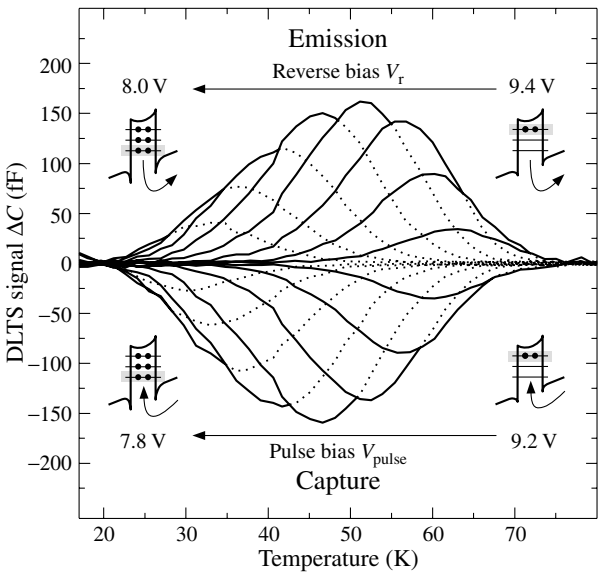

Fig. 2. Charge-selective DLTS spectra of hole emission and capture. The emission shows a positive signal while the capture has a negative signal. The pulse length and reference time constant were set to 5.0 s/53 ms, respectively. The pulse bias was always set to $V_{pulse} = V_r - 0.2$ V.

We obtained charge-selective DLTS spectra by applying the double-boxcar correlator. Figure 2 displays the capture (negative DLTS signal) and emission (positive DLTS signal) spectra for different reverse/pulse bias situations. The pulse length and reference time constant were set to 5.0 s/53 ms, respectively. The pulse bias was always set to $V_{pulse} = V_r - 0.2$ V. For these reverse/pulse bias conditions, on average less

than one hole per QD is emitted from or captured into the QDs. The maxima for the capture process appear at almost the same temperature as the maxima for the emission process.

3. Discussion

The equation for the thermal emission rate [7] allows to derive activation energies and capture cross sections from Arrhenius plots (not shown here) for differently charged QDs (black lines in Fig. 3). In an electric field the thermal activation energies $E_{\mathrm{A}}^{\mathrm{emission}}$ do not represent the binding energies of the QD states with respect to the valence band edge, as the underlying physical mechanism is a phonon-assisted escape process [3]. That means, thermal activation from a QD state into an intermediate state and subsequent tunneling through the remaining triangular barrier [see schematic inset on the left-hand side in Fig. 3(a)] occurs.

The capture rate is given by the common equation: $c_p = \sigma_\infty^p \langle v_p \rangle n$, with n as the charge carrier density at the QD position. This leads to an analogous equation for capture into QDs with an activation barrier $E_{\mathrm{A}}^{\mathrm{capture}}$:

$$c_p(T) = \gamma_p T^2 \sigma_\infty^p \exp\left(-\frac{E_{\mathrm{A}}^{\mathrm{capture}}}{kT}\right), \qquad (1)$$

with γ_p as a temperature-independent constant. The capture cross section σ_∞^p is defined for $T = \infty$ (no temperature dependence). From Arrhenius plots we obtained activation energies $E_{\mathrm{A}}^{\mathrm{capture}}$ and capture cross sections σ_∞^p from the capture transients.

Comparing emission and capture the activation energies and capture cross sections have almost the same values (Fig. 3). The activation energy of 115 meV at a reverse bias of $V_{\mathrm{r}} = 9.4$ V is attributed to hole emission from the QD ground state (see schematic inset). With decreasing reverse bias the decrease in the activation energy is observed due to the increase in the average occupation of the QDs. The capture cross section decreases from $\sigma_\infty^p \approx 1\times10^{-14}$ cm^2 at $V_{\mathrm{r}} = 9.4$ V down to $\sigma_\infty^p \approx 1\times10^{-15}$ cm^2 at $V_{\mathrm{r}} = 8.4$ V, see Fig. 3(b). This behavior can be qualitatively explained by an increase of the repulsive Coulomb potential inside the QDs for an increasing confined charge. Below the reverse bias $V_{\mathrm{r}} = 8.4$ V the capture cross section increases again, while the activation energy remains almost constant at 60 meV (gray shaded area in Fig. 3). This energy represents the Coulomb charging energy of completely charged QDs. That means, the repulsive Coulomb potential remains also constant, whereas the electric field strength in the QDs layer decreases with decreasing applied reverse bias. Therefore, the capture cross section increases as the charge carriers have to overcome a smaller electric barrier.

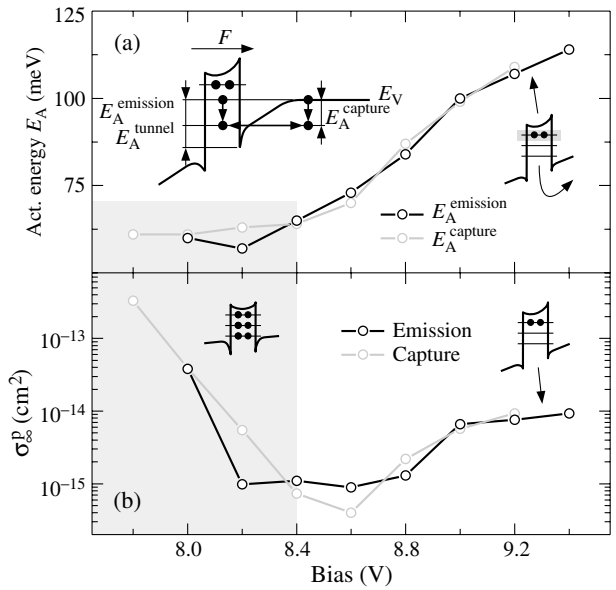

Fig. 3. Dependence of the thermal activation energy (a) and the capture cross section (b) on the bias for emission (black line) and capture (gray line). The inset in the upper left corner schematically displays the band structure.

As we obtained the same values for the capture/emission activation energy and capture cross section, we assume that the capture process into the QDs has the same underlying physical mechanism as the emission: phonon-assisted tunneling [see schematic inset on the left-hand side in Fig. 3(a)].

4. Conclusion

We studied the carrier capture of holes into InGaAs QDs using the charge-selective DLTS method. For the first time the carrier capture is observed in capacitance spectroscopy. From the capacitance transients we obtained thermal activation energies and capture cross sections for hole capture into the QDs. The almost identical values for charge carrier emission and capture lead us to conclude phonon-assisted tunneling even for carrier capture.

Acknowledgements

This work was supported in different parts by the EU project SANDiE (contract number NMP4-CT-2004-500101), SFB 296 of DFG. V. I. Z. expresses deep thanks to Dr. M. Heyen for financial support. I. S. Sh. greatly appreciates the support by DAAD.

References

[1] D. Bimberg, M. Grundmann and N. N. Ledentsov, *Quantum Dot Heterostructures*, (John Wiley & Sons, Chichester, 1998).
[2] C. Ballocco, A. M. Song and M. Missous, *Appl. Phys. Lett.* **85**, 5911 (2004).
[3] C. M. A. Kapteyn, M. Lion, R. Heitz *et al*, *Appl. Phys. Lett.* **76**, 1573 (2000).
[4] M. Geller, C. Kapteyn, L. Müller-Kirsch, R. Heitz and D. Bimberg, *Appl. Phys. Lett.* **82**, 2706 (2003).
[5] V. I. Zubkov, C. M. A. Kapteyn, A. V. Solomonov and D. Bimberg, *J. Phys.: Condens. Matter.* **17**, 2435 (2005).
[6] O. Engström, M. Kaniewska, Y. Fu, J. Piscator and M. Malmkvist, *Appl. Phys. Lett.* **85**, 2908 (2004).
[7] D. V. Lang, *J. Appl. Phys.* **45**, 3023 (1974).

14th Int. Symp. "Nanostructures: Physics and Technology"
St Petersburg, Russia, June 26–30, 2006

$1/f^{\alpha}$ tunneling current noise characteristics in the vicinity of individual impurity atoms on clean InAs(110) surface

A. I. Oreshkin[1], S. I. Oreshkin[1,2], I. V. Radchenko[1], S. V. Savinov[1], N. S. Maslova[1], D. A. Muzychenko[1], V. N. Mancevich[1] and V. I. Panov[1]

[1] Physical Department, Moscow State University, 119992 Moscow, Russia
[2] Sternberg Astronomical Institute, Moscow State University, 119992 Moscow, Russia

Abstract. We report the results of UHV STM investigations of tunneling current noise spectra in vicinity of individual impurity atoms on InAs(110) surface. It was found out that the power law exponent of $1/f^{\alpha}$ noise depends not only on the presence of impurity atom in tunneling junction area, but mostly it is driven by tunneling bias voltage. This is consistent with proposed theoretical model considering tunneling current through two state impurity complex model system. Sudden switching of interaction with the leads ON and OFF when electron transition between two levels is the microscopic origin of observed $1/f^{\alpha}$ noise behavior.

Introduction

Up to now the typical approach to $1/f$ noise problem consists of "by hand" introducing of random relaxation time τ for two-state system with probability distribution function A/τ_0^{α}. Therefore the averaged over τ_0 noise spectra of two-states system has power law singularity. But the physical nature and microscopic origin of such probability distribution function in general is unknown. We have found out that strong correlations and many-particle interaction on *microscopic scale* result in sudden switching ON and OFF of additional potential in tunneling junction area. This results in typical power law for tunneling current noise spectra.

1. Experimental

Tunneling current spectra measurements have been conducted with the use of specially designed experimental setup (including both hardware and software parts), which was incorporated into our existing UHV STM "Omicron" system. Test experiments have shown that tunneling current noise spectra are "colored" in undesirable way if STM feedback loop is turned on. At the same time in our experiments we need to go to less then 1 Hz in frequency domain, and therefore our tunneling current noise measurements are long [1,2]. Experimental run for one curve lasts for at least 100 seconds. If STM feedback loop is broken off, there is no way during all this time to maintain mean value of tip-sample separation (which obviously should stay constant) except for high mechanical stability, low level of external vibrations and the whole UHV chamber being in thermally stable state. Only if all mentioned demands are fulfilled and, besides this, the quality of STM images for selected surface is good enough, tunneling current noise measurements can be started. Our main experimental goal was to find out how different impurity atoms and defects are influencing tunneling current noise spectra. The results of tunneling current noise measurements on (110) surface of S doped semiconductor compound InAs are presented on Fig. 1.

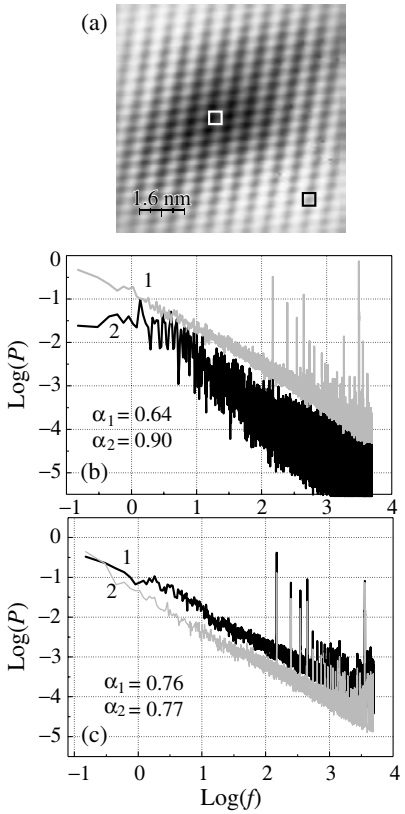

Fig. 1. (a) STM image of S doped InAs(110) surface. Scan area 85 Å. Tunneling current is $I_t = 55$ pA. Surface spots where noise measurements are performed are marked by rectangles. b), c) Tunneling current noise spectra on double logarithmic scale $\log(P)$ *vs.* $\log(f)$ above individual S impurity atom and apart from it for different parameters of tunneling junction. (b) Tunneling current setpoint is $I_t = 500$ pA, bias voltage is $U_t = -1$ V, c) Tunneling current setpoint is $I_t = 55$ pA, bias voltage is $U_t = -1.8$ V. Exponents for all cases are shown on the graphs.

In our experiments the sample preparation method is different for A_3B_5 compounds compared to elemental semiconductors. InAs clean surface was prepared using *in situ* sample cleavage. The main advantage of this method is that impurity atoms *do not* leave the surface layers during thermal annealing and, even more, atoms in few subsurface layers can be imaged by STM. We have used specially prepared InAs slabs ($2\times2\times4$ mm^3), which were cleaved *in situ* in UHV conditions. In the first set of experiments S doped InAs single crystals were investigated. The chemical doping concentration was 5×10^{17} cm^{-3}. Thus electron orbitals of S atoms, which have localization radius about 30 Å, almost overlap, re-

sulting in metallic conductivity of this samples even at liquid helium temperatures. Typical high resolution STM image of S individual impurity on InAs (110) surface is shown on Fig. 1a. At negative sample bias voltage individual S impurity atom is imaged by STM as round depression superimposed on atomic lattice of relaxed InAs surface. To clarify the role that plays individual impurity atom in formation of tunneling current noise spectrum, we have carried out noise measurements at different values of tunneling bias voltage right above the impurity atom and aside from it. The spots where experimental data points were acquired are marked by rectangles on STM images as on Fig. 1a. We have started our measurements with high negative sample bias voltage (electrons are tunneling from filled states of semiconductor). As it follows from Fig. 1c in such conditions tunneling current noise spectrum is *almost* independent on the presence of impurity atom underneath STM tip. Exponent values is this case are: $\alpha = 0.76$ above dopant atom, and $\alpha = 0.77$ aside from dopant atom. This observation can be explained by the fact, that the presence of impurity atom mostly affects sample's electronic structure *inside* band gap, while in this measurement electrons are tunneling from deep valence band energy levels. The influence of the impurity in this situation is small. But, if the energy of tunneling electron is becoming comparable with band gap width, the influence of the impurity presence on tunneling current noise spectrum is not negligible any more (Fig. 1b). In such conditions the difference in exponents is big, $\alpha = 0.64$ above dopant atom, and $\alpha = 0.90$ aside from dopant atom. Curves Fig. 1b were measured with higher value of tunneling current than curves on Fig. 1c. This factor also plays in favor of increasing of the difference between exponents, because the distance between STM tip and the surface is decreasing with increasing of the value of tunneling current setpoint.

The last set of experimental data we would like to present here concerns tunneling current noise spectra measurements in vicinity of Zn impurity atom on InAs (110) surface Fig. 2. The chemical doping concentration is around 6×10^{17} cm^{-3} and crystal has p-type bulk conductivity. Surface for STM investigations was prepared by *in situ* cleaving. A surface of p-type A_3B_5 is imaged by STM in much more complicated way than the surface of n-type samples. In contrast to donor impurities, STM images of acceptor impurities are less localized or even almost non-localized. The latter is the case for Zn doped InAs (110) surface. The STM image of Zn doped InAs(110) surface is wavy everywhere and one need to take into account some additional knowledge to identify Zn impurities. Apparently this means that local electronic density of states is highly disturbed by impurities and the tunneling current noise spectra should be very sensitive to STM tip position relative to impurity atom. Typical STM image of Zn doped InAs (110)surface can be seen on Fig. 2a. Due to bias dependent STM imaging the dark spot can be identified as Zn impurity atom. Its localization radius is about 20 Å, slightly less than that of S impurity atom 30 Å on InAs surface. The areas where experimental data was collected are marked by rectangles on the STM image. Because of complicated character of STM image we have performed the measurements in three spots: right above the impurity, as well as above "flat" area and above area with increased local density of states. The result are shown on Fig. 2b. The conclusion is really non-trivial. Above "flat" area the intensity of low frequency noise is much higher than above other spots.

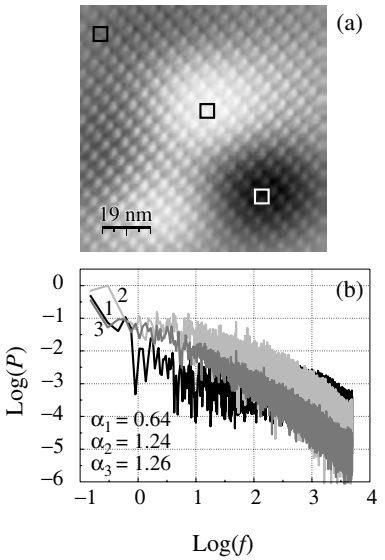

Fig. 2. (a) STM image of Zn doped InAs(110) surface. Scan area 100 Å. Tunneling current is $I_t = 400$ pA. Bias voltage is $U_t = -0.8$ V. Surface spots where noise measurements are performed are marked by rectangles. (b) Tunneling current noise spectra on double logarithmic scale $\log(P)$ *vs.* $\log(f)$ above individual S impurity atom and apart from it for the same set of tunneling junction parameters. Tunneling current setpoint is $I_t = 400$ pA, bias voltage is $U_t = -0.8$ V. Curve 1 — above "flat surface area", curve 2 — above Zn impurity atom, curve 3 — above surface area with enhanced conductivity. Exponents for all cases are shown on the graphs.

That is why exponent value above "flat" area is twice smaller $\alpha = 0.64$ above "flat" area, $\alpha = 1.24$ above dopant atom, $\alpha = 1.27$ above area with increased conductivity.

Thus, tunneling current noise spectrum is very sensitive to the presence of impurity atom in junction area in certain range of bias voltage and this behavior can be explained by sudden switching ON and OFF of many-particle interaction. Such behavior of interaction occurs when electron is trapped or leaves some localized state formed on individual dopant atom, on impurity complexes or on surface defects. Namely this is the microscopic origin of $1/f^{\alpha}$ current noise. The power law exponent of tunneling current noise spectrum can be tuned by changing of applied bias voltage and by the geometry of impurity complexes as well as by their arrangement relative to the leads.

Acknowledgements

The research was partially supported by RFBR grant 05-02-19806-MF_a. Support from Samsung corp. is gratefully acknowledged.

References

[1] R. Möller *et al*, *Appl. Phys. Lett.* **55**, 22 2360 (1989).
[2] K. Maeda *et al*, *J. Vac. Sci. Technol. B* **12**, 3 2140 (1994).

14th Int. Symp. "Nanostructures: Physics and Technology"
St Petersburg, Russia, June 26–30, 2006

Electrical, optical and structural characterizations of individual ZnO nanorods

O. V. Kononenko[1], G. N. Panin[1,2], S. V. Dubonos[1], I. I. Khodos[1], T. W. Kang[2] and A. N. Baranov[3]

[1] Institute of Microelectronics Technology, Russian Academy of Sciences, 142432 Chernogolovka, Moscow Region, Russia
[2] Quantum-functional Semiconductor Research Center, Department of Physics, Dongguk University 26, 3-ga Pildong Junggu, Seoul 100-715, Korea
[3] Moscow State University, Chemistry Department, 119992, Moscow, Russia

Abstract. ZnO nanorods were synthesized from NaCl-Li_2CO_3 salt mixture with a solution-processed Zn-containing precursor using a freeze-drying method combined with a milling technique. The nanorods were transferred onto oxidized silicon substrates. E-beam lithography was used to pattern aluminum electrodes contacting a single nanorod. I–V curves were measured using four point structures. Optical properties of nanorods were investigated by cathodoluminescence spectroscopy. Crystallographic structure was studied using transmission electron microscopy.

Introduction

Zinc oxide is one of the most important functional semiconductor oxides with a direct wide band gap (3.37 eV) and with a large excitation binding energy (60 meV) heterostructures [1, 2].

One-dimensional semiconductor nanostructures have in recent years attracted much attention due to their potential use as building blocks for future electronics and photonics, as well as for life-science applications. A large variety of ZnO one-dimensional structures have been demonstrated [1–5]. The large surface area of the nanorods and bio-safe characteristics of ZnO makes them attractive for gas and chemical sensing and biomedical applications, and the ability to control their nucleation sites makes them candidates for microlasers or memory arrays. The initial reports show a pronounced sensitivity of the nanowire conductivity to UV illumination and the presence of oxygen in the measurement ambient. Recently, a wide variety of nanodevices including UV photodetectors [6–9], sensors [10–12], field effect transistors (FET) [13–14], intramolecular $p-n$ junction diodes [15], Schottky diodes [16, 17] and light emitting device arrays [18] have been fabricated utilizing ZnO nanorods. The fact that ZnO can be grown at low temperatures on cheap substrates such as glass also makes it attractive for transparent electronics.

In this work, we report on characterization of individual ZnO nanorods using device fabricated on oxidized silicon substrate.

1. Experimental

ZnO nanorods with diameters from 40 to 150 nm were grown from NaCl-Li_2CO_3 salt mixture with a solution-processed Zn-containing precursor using a freeze-drying method combined with a milling technique, as described previously [19].

ZnO nanorods were grown from the as-prepared powder mixture with 0.5 g $Zn_2(OH)_2CO_3 \cdot x\ H_2O$/9 g NaCl/1 g Li_2CO_3 weight ratio in an alumina crucible in a muffle furnace in air at 600−700 °C for 1–6 h.

Devices for transport measurements of ZnO nanorods were fabricated using standard photo- and electron beam lithography and a lift-off technique. At first, a gold film with chrome underlayer was deposited by e-beam evaporation on oxidized silicon wafer to form contact pads and lanes. Then the wafer was cut up to obtain chips. Transfer of the nanorods from the ethanol solution to the chips is achieved by dispersing the solution onto the one, followed by evaporation of the ethanol. E-beam lithography and a lift-off process were used to pattern e-beam evaporation deposited aluminum electrodes contacting a single nanorods. Four-terminal structures were used for measurements of I–V curves (Fig. 1).

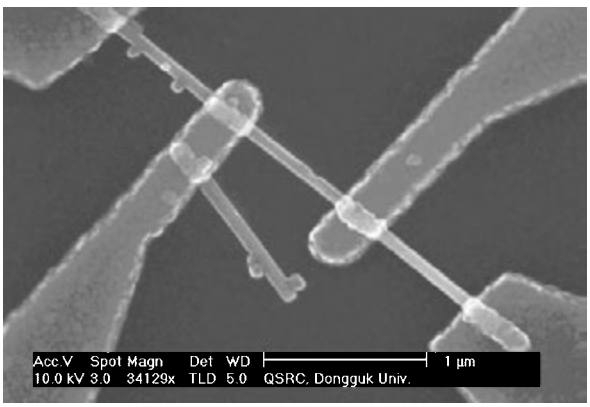

Fig. 1. SEM image of a ZnO nanorod with deposited Al contacts patterned by e-beam lithography.

To examine the samples a XL 30S field emission gun high-resolution scanning electron microscope (HRSEM) with a Mono CL system for cathodoluminescence (CL) spectroscopy was used. The light emitted from the sample can be directed into the slits of the monochromator, which is mounted on the SEM. The transmission electron microscope JEM-2000FX was used for structure analysis of nanorods.

2. Results and discussions

Fig. 2 shows TEM image of ZnO nanorods grown from NaCl-Li_2CO_3 salt mixture. The selected area diffraction patterns showed the nanorods to be single crystal with wurtzite structure.

The current-voltage (I–V) curves are given in Fig. 3 for the nanorod shown in Fig. 1. Resistivity of the nanorod obtained from the I–V characteristics is about 3 Ωcm in the dark. The I–V curves exhibit apparent rectify behavior indicating the Schottky-like barrier formation. The nanorod showed a strong, reversible response to above band gap (366 nm) ultra-

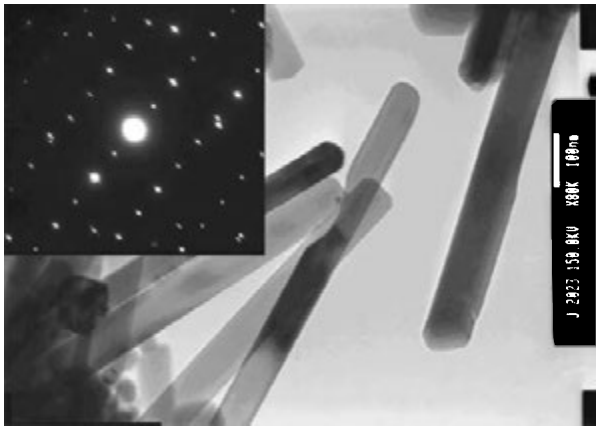

Fig. 2. TEM image and selected area diffraction pattern of single crystal ZnO nanorods.

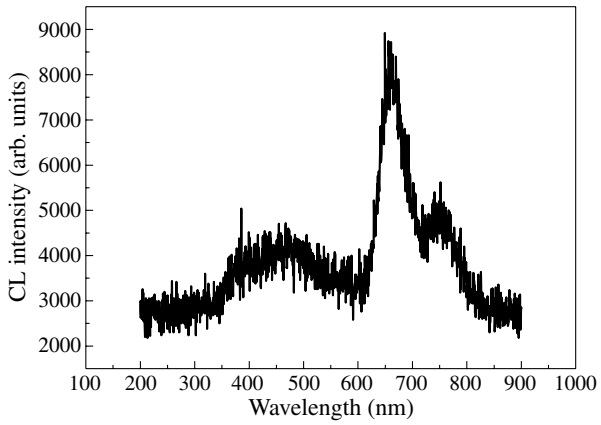

Fig. 3. Room temperature CL spectra of the ZnO nanorods.

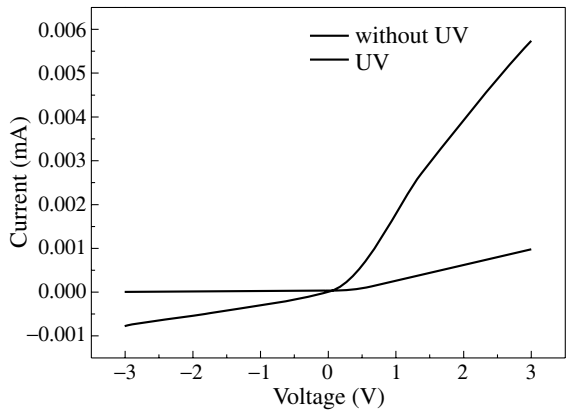

Fig. 4. I–V characteristics in the dark and under ultraviolet illumination for nanorod shown in Fig. 1.

violet light, with the UV-induced current being approximately a factor of 6 larger than the dark current at a given voltage. The same behavior of ZnO nanorods under the UV illumination was obtained in references 5 and 20.

The CL spectra for the ZnO nanorods synthesized in this work are shown in Figure 4. Four broad peaks at around 380 nm, 466 nm, 670 nm and 750 nm are observed. The luminescence at 380 nm corresponds to the near band gap transition of nanorods. The luminescence peaks at 466, 670 and 750 nm are related with point defects and residual impurities.

In conclusion, individual ZnO nanorods synthesized from the salt mixture were investigated using the e-beam pattering. The nanorods with single crystalline structure and the blue-red luminescence show around 3 Ωcm resistivity and apparent rectify behavior indicating the Schottky-like barrier formation. The strong UV response of the nanorods is observed.

Acknowledgements

This work was supported by the Ministry of Education and Science and the Federal Agency for Science and Innovation via the project “IN-12.5/002”.

References

[1] G. C. Yi *et al*, *Semicond. Sci. Technol.* **20**, S22 (2005).
[2] Z. L. Wang *et al*, *Mater. Today* **7**, 26 (2004).
[3] Y. W. Heo *et al*, *Mater. Sci. Engineering* **R47**, 1 (2004).
[4] W. I. Park *et al*, *Adv. Mater.* **15**, 526 (2003).
[5] Q. H. Li *et al*, *Appl. Phys. Lett.* **84**, 4556 (2004).
[6] K. Keem *et al*, *Appl. Phys. Lett.* **849**, 4376 (2004).
[7] O. Harnack *et al*, *Nano Lett.* **3**, 1097 (2003).
[8] H. Kind *et al*, *Adv. Mater.* **14**, 158 (2002).
[9] S. E. Ahn *et al*, *Appl. Phys. Lett.* **84**, 5022 (2004).
[10] Q. Wan *et al*, *Appl. Phys. Lett.* **84**, 3085 (2004).
[11] Q. Wan *et al*, *Appl. Phys. Lett.* **84**, 3654 (2004).
[12] Q. H. Li *et al*, *Appl. Phys. Lett.* **84**, 4556 (2004).
[13] Y. W. Heo *et al*, *Appl. Phys. Lett.* **85**, 2274 (2004).
[14] W. I. Park *et al*, *Appl. Phys. Lett.* **85**, 5052 (2004).
[15] C. H. Liu *et al*, *Appl. Phys. Lett.* **83**, 3168 (2003).
[16] W. I. Park *et al*, *Appl. Phys. Lett.* **82**, 4358 (2003).
[17] Y. W. Heo *et al*, *Appl. Phys. Lett.* **85**, 3107 (2004).
[18] W. I. Park *et al*, *Adv. Mater.* **16**, 87 (2004).
[19] A. N. Baranov *et al*, *Nanotechnology* **15**, 1613 (2004).
[20] Y. W. Heo *et al*, *Appl. Phys. Lett.* **85**, 2002 (2004).

14th Int. Symp. "Nanostructures: Physics and Technology"
St Petersburg, Russia, June 26–30, 2006

Optical study of band gap dependence on nitrogen content in GaAsN thin layers

A. Yu. Egorov[1], V. K. Kalevich[1], *M. M. Afanasiev*[1], A. Yu. Shiryaev[1], V. M. Ustinov[1], M. Ikezawa[2] and Y. Masumoto[2]

[1] Ioffe Physico-Technical Institute, St Petersburg, Russia
[2] Institute of Physics, University of Tsukuba, Tsukuba 305-8571, Japan

Abstract. The dependence of the energy gap of strained GaAsN thin layers on the nitrogen content has been measured via the study of photoluminescence (PL) spectra and polarized PL spectra. The same dependence of unstrained GaAsN has been calculated.

GaAsN and InGaAsN alloys have recently been suggested as promising materials for near-infrared optoelectronics [1] because of the strong bowing of the energy gap in the GaAs-GaN alloy system, which extends the spectral range of emission to 1.3 μm and beyond [1,2]. In addition to the bowing effect, the energy gaps of GaAsN and InGaAsN layers grown on GaAs substrate can also be changed by the strain caused by a large lattice mismatch between the layer and substrate even at low nitrogen content [2].

In this paper, we analyze the influence exerted by strain on the valence-band splitting and the energy gap in GaAsN layers grown on GaAs substrates, using circularly polarized PL. The analysis of the PL circular polarization allowed us to identify the type of recombination transitions and determine the strain-induced valence-band splitting in GaAsN alloy. Based on the results obtained, we calculated the dependence of the energy gap on the nitrogen content of unstrained GaAsN.

A series of the 0.1 μm thick GaAsN layers with the nitrogen content in the range 0.01–0.034 was grown by RF-plasma-assisted solid-source molecular-beam epitaxy at 350–450 °C on semi-insulating (001) GaAs substrates. The crystal perfection, pseudomorphic character of growth, i.e., the degree of crystal lattice relaxation, and the composition of the ternary solid solution were determined by high resolution X-ray diffraction (HRXD) technique. It evidences that the strain relaxation in the lattice of thin layer $GaAs_{1-x}N_x$ up to $x = 0.034$ does not exceed 1%, which is within the limits of the experimental accuracy. Small half-width of the peak recorded for the symmetric reflection from a nitrogen-containing layer (close to that calculated for the ideal case) confirms the good homogeneity of the layer and its high crystal perfection.

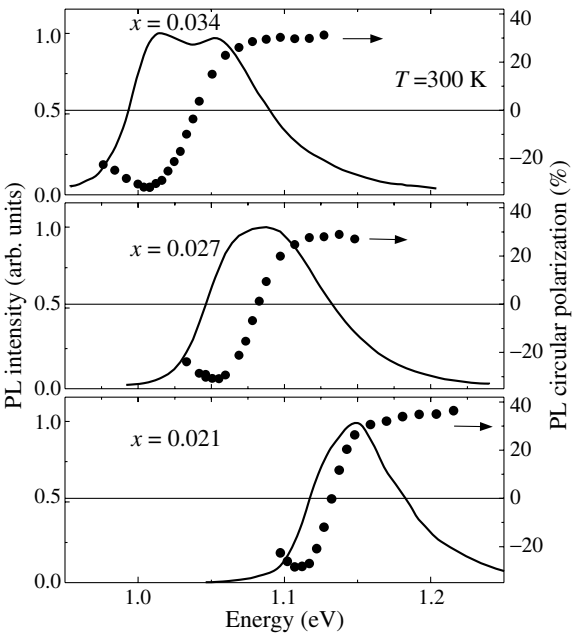

Fig. 1. PL and PL circular polarization spectra of thin $GaAs_{1-x}N_x$ layers.

Ar^+ and tunable Ti:sapphire lasers were used for the PL excitation. The PL spectra were recorded along the growth axis in the backscattering configuration, using either a Ge photodiode or an InGaAsP photomultiplier. The spin polarization of electrons was created by circularly polarized light [3]. It was monitored by measuring the degree of circular polarization of PL, which is defined as $\rho = (I^+ - I^-)/(I^+ + I^-)$, where I^+ and I^- are the right and left circularly polarized PL components, respectively. A highly sensitive polarization analyzer [4] with an InGaAsP photomultiplier, a quartz polarization modulator, and a two-channel photon counter synchronized with the polarization modulator were used to measure the circular polarization of PL up to 1.4 μm with accuracy better than 0.1%. The PL measurements were carried out at 300 K.

Figure 1 shows the spectra of PL (solid lines) and circular polarization of PL (full circles) of three thin GaAsN samples with nitrogen content of 0.021, 0.027, and 0.034. It can be seen that, for all the three samples, the PL spectra consist of two PL bands and that the low-energy PL bands are negatively polarized (relative to the polarization of the exciting beam), whereas the high-energy bands are positively polarized [5].

In the group III–V semiconductors, the interband absorption of circularly polarized light can be accompanied by electron-spin polarization [3]. At simultaneous excitation of electrons from both upper valence subbands by circularly polarized light the PL is also circularly polarized. The degeneracy at the ç point of the upper valence band in the group III–V semiconductors can be lifted by biaxial tensile strain. In this case, the top of a light-hole band lies above the heavy-hole band [6]. The signs of the circular polarization of PL were found [3,6,7] to be opposite for recombination involving light and heavy holes so that the polarization sign of light-hole recombination is opposite to that of the polarization of the exciting beam.

The PL polarization spectra in Fig. 1 were measured at simultaneous excitation of electrons from both upper valence subbands. Thus, the negative polarization of the low-energy PL line and the positive polarization of the high-energy PL line demonstrate unambiguously that the light- and heavy-hole

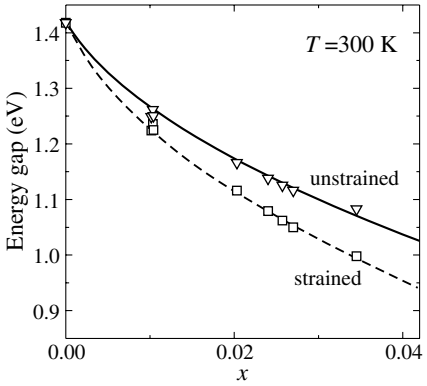

Fig. 2. Band gap for strained and unstrained $GaAs_{1-x}N_x$.

subbands in samples under study are split at the point and that the low- and high-energy PL bands are due to recombination involving light and heavy holes, respectively.

Figure 2 shows the energy positions of the peak of low-energy PL bands (squares) of the samples with different content of nitrogen. The experimental dependences in Fig. 2 is well approximated by the curve (dashed line) calculated using the dispersion relation obtained in the frame of the band anticrossing (BAC) model [8]:

$$E_-(k) = \frac{1}{2}\left[E^c(k) + E^{\mathrm{N}} - \sqrt{(E^c(k) - E^{\mathrm{N}})^2 + 4V^2x}\right],$$

where x is the nitrogen content, $E^c(0) = 1.42$ eV is the band gap of GaAs at room temperature and E^{N} is the energy of the localized states caused by the substitutional N atoms. E^{N} is known to be 0.23 eV above the GaAs conduction-band edge [9]. The adjustable hybridization parameter V describes the coupling between the localized states and the conduction-band states of the GaAs matrix. The fitting curve (dashed line) in Fig. 2 has been calculated at $V = 2.86$ eV. These value of V are close to $V = 2.7$ eV reported recently for similar samples [9]. However, the BAC model was developed for an unstrained material and therefore the strain-induced changes of the energy bands in the films under study should be taken into account for a correct application of the BAC model.

Using the elastic constants for GaAs [10], we have calculated how the energy gap between the tops of the heavy- and light-hole bands depends on the nitrogen content. The effect of incorporated nitrogen on the elastic constants and the spin-orbit splitting was disregarded. The result of the calculation is shown in Fig. 3 by solid line. The experimental energy gaps between the PL bands are shown in Fig. 3 by squares. The good agreement between the theoretical and experimental energy gaps suggests that the model of strain [10] and the elastic constants of gallium arsenide can be used to evaluate the band splitting in thin strained GaAsN layers.

The energy gap in thin strained GaAsN layers grown on GaAs substrates corresponds to the energy of an electron-hole transition involving a light hole (dashed fitting curve in Fig. 2). Calculations of the energy gap for unstrained (free-standing) GaAsN were performed for all the measured energy gap values. The calculated data are presented in Fig. 2 by triangles. The solid line in Fig. 2 is the fitting curve calculated according to BAC model with $V = 2.42$ eV. The energy gap of free-standing GaAsN steadily decreases from 1.42 to 1.08 eV as the nitrogen content grows from 0 to 3.4%.

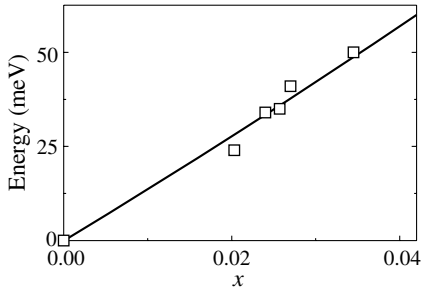

Fig. 3. The energy gap between the tops of the heavy- and light-hole bands.

In conclusion, we observed two bands in PL spectra of elastically strained ternary GaAsN alloys grown on GaAs substrates. As demonstrated by an analysis of their circular polarizations, these bands are associated with electron-hole transitions involving light and heavy holes. The energy gap between the peaks of these bands corresponds to the calculated splitting of light- and heavy-hole subbands, induced by the elastic strain of the GaAsN layer. The dependence of the fundamental energy gap on the nitrogen content for unstrained GaAsN alloys has been calculated taking into account the effect of elastic strain on the position of the energy bands.

Acknowledgements

The work was partially supported by RFBR, JSPS and the Russian Academy of Sciences Program "Quantum nanostructures".

References

[1] M. Kondow, T. Kitatani, S. Nakatsuka, M.C. Larson, K. Nakahara, Y.Yazawa, M. Okai, and K. Uomi, *IEEE. J. Sel. Top. Quantum Electron.* **3**, 719 (1997).

[2] Yong Zhang, A. Mascarenhas, H.P. Xin, and C.W. Tu, *Phys. Rev. B* **61**, 4433 (2000).

[3] *Optical orientation*, ed. F. Meier and B. Zakharchenya, Modern Problems in Condensed Matter Sciences, North-Holland, Amsterdam, vol. 8, 1984.

[4] V.D. Kulikov and V.K. Kalevich, *Instruments & Experimental Technique* **24**, 1265 (1981).

[5] A. Yu. Egorov, V. K. Kalevich, M. M. Afanasiev, A. Yu. Shiryaev, V. M. Ustinov, M. Ikezawa and Y. Masumoto, *J. Appl. Phys.* **98**, 013539 (2005).

[6] G.L. Bir and G.E. Pikus, *Symmetry and Strain-Indused Effects In Semiconductors*, Wiley, New York, 1974.

[7] M.I. Dyakonov and V.I. Perel, *Fiz. Tekhn. Poluprovodn.* **7**, 2335 (1973).

[8] W. Shan, W. Walukiewicz, J.W. Ager III, E.E. Haller, J.F. Geisz, D.J. Friedman, J.M. Olson, and S.R. Kurtz, *Phys. Rev. Lett.* **82**, 1221 (1999).

[9] W. Walukiewicz, *Physica E* **20**, 300 (2004).

[10] M.P.C.M. Krijn, *Semicond. Sci. Technol.* **6**, 27 (1991).

14th Int. Symp. "Nanostructures: Physics and Technology"
St Petersburg, Russia, June 26–30, 2006

Quantitative study of carriers leakage in operating semiconductor laser diodes by means of scanning Kelvin probe microscopy

A. V. Ankudinov[1], K. S. Ladutenko[1], A. N. Baranov[2], M. G. Rastegaeva[1], V. P. Evtikhiev[1] and A. N. Titkov[1]

[1] Ioffe Physico-Technical Institute, St Petersburg, Russia
[2] Universite Montpellier II, CEM2, UMR CNRS 5507, Montpellier, France

Abstract. An approach to study quantitatively the carriers leakage in laser diodes operating in continuos wave and pulse modes is presented. It is based on the application of the scanning Kelvin probe microscopy and utilizes the measurements of the surface voltage drop distributions across the cleaved mirrors of the tested devices. The results on the characterization of the hole leakage current in high power InGaAs/AlGaAs/GaAs laser diodes and in infra red GaInSbAs/GaAlSbAs/GaSb laser diodes are demonstrated.

Introduction

Illumination of semiconductor by interband light may lead to a surface photovoltage (SPV) [1]. The SPV arises due to subsurface band bending related with the surface states. Nonequilibrium carriers created by the light in semiconductor are separated by the electric field of the band-bending region. The process changes the surface charge and results in an additional potential difference between the surface and the bulk that may be detected as the SPV. As a rule, the sign of the SPV coincides with the sigh of minority carriers and its amplitude grows logarithmically with increasing density of minority carriers related with the photoexcitation power. In a semiconductor device structure consisting of conductive n and p regions, forward current through p-n junction may also inject nonequilibrium carriers. Injected nonequilibrium carriers may be captured by the electric field of the band-bending region, and in the following they behave similarly to the photocarriers. Owing to this analogy, one may expect on the cross-section of the device structure the variations of the potential related with the appearance of minority carriers at the surface. Recently, it was indeed observed in the scanning Kelvin probe microscopy (SKPM) study of surface voltage drop (SVD) distributions developing across the mirror of the operating semiconductor lasers [2]. The design of the modern semiconductor laser restricts intentionally the escape of injected carriers from the active region by means of potential barriers at the interfaces between quantum well-waveguide and waveguide-emitters. In spite of this, it was found that using the surface channel the holes may penetrate in the region of the grounded n^+-substrate, what resulted in high positive potentials measured at the substrate surface. The detailed analysis of obtained experimental results [2] permitted to develop a quantitative method for studying the leakage current distributions in operating semiconductor heterostructure devices containing p-n junction.

In this paper we present new results on the application of the developed method for studying high power laser diodes based on InGaAs/AlGaAs/GaAs heterostrusture with a quantum well as an active region. Also we inspect GaInSbAs/GaAlSbAs/GaSb based lasers, that are perspective as effective sources of the infrared (IR) light.

1. Experimental

We study cleaved mirrors of laser diodes operating in continuos wave (CW) and pulse modes. Details of design, growth and operation of lasers were reported earlier [3, 4]. We use commercial atomic force microscope (AFM) setups (NT MDT) operating in ambient. The AFM has an optical system to register cantilever deflections and uses for that the semiconductor light source with a wavelength about 650 nm. For cantilevers NSG11/Pt, applied in our work, the power density of light illumination at the contact of the sample with the cantilever's tip was directly measured. It could be as high as few tens of mW/cm^2, and depended on the position of the spot of the light beam focused on the cantilever [2].

The composite image presented in Fig. 1(a) consists of two layers: SVD data image superimposed over the topography data image. SVD data were collected for forward biased high power laser InGaAs/AlGaAs/GaAs diode admitting the current above the threshold of lazing. The gray scale of SVD image is adjusted to pick out the boundary where the signal is equal to 200±5 mV, and corresponds approximately to 150 A/cm^2 for the density of the hole leakage current. That equipotential line

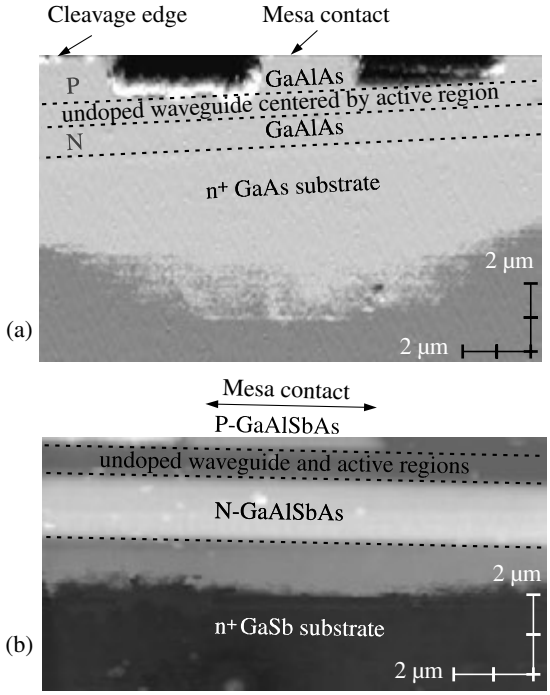

Fig. 1. Observation of the holes spreading on the cleavage of CW operating laser diodes: high power InGaAs/AlGaAs/GaAs (a) and IR GaInSbAs/GaAlSbAs/GaSb (b) lasers.

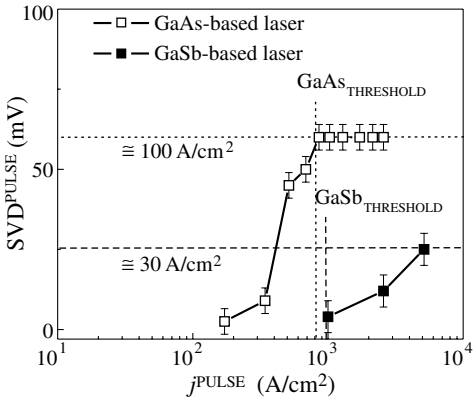

Fig. 2. SVD amplitude dependencies on the density of pulse current (pulse width 200 ns, pulse period 40 μs) across the laser measured over the n^+-substrate, under the mesa contact 10 μm away from the i-waveguide. Below horizontal lines, estimations of the maximum local density of the hole leakage current are given: high power InGaAs/AlGaAs/GaAs laser (upper dotted line) and IR GaInSbAs/GaAlSbAs/GaSb laser (bottom dashed line). Also, vertical lines for high power (dotted line) and IR (dashed line) lasers mark the corresponding values of threshold current density.

is curved and advanced most profoundly into the substrate right opposite the mesa contact. Its shape emphasizes visually the effective lateral restriction in the distribution of the injection current density. For comparison, Fig. 1(b) shows the data obtained for IR GaInSbAs/GaAlSbAs/GaSb laser. For this laser, the equipotential line 200±5 mV is almost flat, what implies a broader distribution of the injection current, than in case of the high power laser. This seems to be related to insufficient insulating property of the waveguide region in the IR laser.

Figure 2 shows the dependencies of the local amplitude of the hole leakage current on the density of the injection current in laser diodes operating in pulse mode. It is significant that, for the high power laser, the leakage grows with increasing injection current in the beginning, but than it stabilizes for currents above the threshold of generation. That stabilization is in accordance with the conception that in quantum well lasers Fermi levels clamp at threshold and above. In contrast with that, for IR laser, although being noticeably suppressed, the leakage amplitude proceeds to grow above the threshold of generation.

There is a difference in the distributions of the injection current density under mesa contacts for two studied lasers that was revealed in Fig. 1. This observation may be used to explain in Fig. 2 the dependence for IR laser. Indeed, there exists a stabilization of the carrier density in the active region directly under the mesa of lazing IR laser. However, due to weak lateral restriction of the injection current, there is also a significant peripheral current. It is this peripheral current that contributes into the hole leakage current above the threshold of generation.

Conclusion

In the paper we consider a new approach exploiting SKPM to study the carriers leakage from the active region of operating semiconductor laser diodes. The approach is demonstrated on studies of the distribution of the surface current of the hole leakage in high power InGaAs/AlGaAs/GaAs laser diodes and in IR GaInSbAs/GaAlSbAs/GaSb laser diodes. It is shown, that in high power lasers the hole leakage current grows for small injection currents, and stabilizes for currents above the threshold of generation. At the surface of IR lasers, the hole leakage current stabilization is not observed, what is supposed to be related with the weak lateral restriction of the injection current density under the mesa contact revealed for those lasers.

Acknowledgement

The work is supported by the Russian Foundation of Basic Research (Grants 06-02-17198-a and 06-02-17547-a).

References

[1] L. Kronik, Y. Shapira, *Surf. Sci. Rep.* **37**, 1 (1999).
[2] A. V. Ankudinov,*et al*, *Semiconductors* **40**, 1009 (2006).
[3] E. Yu. Kotelnikov *et al*, *Semiconductors* **34**, 1341 (2000).
[4] D.A. Yarekha *et al*, *Semicond. Sci. Technol.* **15**, 390 (2000).

14th Int. Symp. "Nanostructures: Physics and Technology"
St Petersburg, Russia, June 26–30, 2006

Nanoclusters and domains on GaAs(100) surface in the transition from As-rich to Ga-rich

G. E. Frank-Kamenetskaya, G. V. Benemanskaya and A. K. Kryzanivskii
Ioffe Physico-Technical Institute, St Petersburg, Russia

Abstract. Cs nanocluster formation and local interaction have been studied in situ for the gradually reconstructed GaAs(100) from As-rich to Ga-rich as a function of Cs dosage. The difference has been established in electronic properties of the As-rich and Ga-rich surfaces. The Cs sticking coefficient on Ga-rich surface is found to be three times more than that on As-rich surface. The intermediate reconstructed GaAs(100) surface is found to be multi-domain phases with both the As-rich and Ga-rich domains. Small nanoclusters formed by two Cs adatoms on As dimmers and on Ga dimmers are found for As-rich and Ga-rich surface, consequently.

Introduction

The GaAs(100) surface is of great interest from viewpoints of both fundamental science and its application to nanotechnologies. Atomic structure and stoichiometric composition of the surface and their dependence on several temperature treatments have attracted particular attention. It was shown that annealing at $\sim$ 400 °C leads to the (2×4) or ñ(2×8) reconstructions with As dimers in the topmost layer. At $\sim$ 570 °C, the transition to the Ga-rich $(4\times2) - c(8\times2)$ reconstruction with Ga dimers in the upper layer occurs. The atomic structure and electronic properties of the GaAs(100) surface at intermediate temperatures are discussed. Cs adsorption has been intensively studied on the GaAs(100) Ga-rich surface and much less investigated on the As-rich surface. No data have been obtained even yet on the basic problems such as the electronic structure of the Cs/GaAs(100) As-rich interface, the Cs sticking coefficient, reduction of the ionization energy depending on Cs coverage. To clarify these problems we have studied the variation of electronic properties of the Cs-adsorbed GaAs(100) surface that changes from As-rich to Ga-rich by the means of sample annealing in situ in the temperature range 450−580 °C.

1. Experiment

Photoemission studies were performed in situ in a vacuum of $\sim 5\times10^{-11}$ Torr at room temperature. Atomically clean surface of a GaAs(100) sample was obtained after removal of As cap layer. Atomically pure cesium was deposited on the sample from a standard source. The GaAs(100) surface was modified by annealing in the temperature range 450−580 °C corresponding to transition from As-rich to Ga-rich. The method employed was threshold photoemission spectroscopy (TPS). TPS is based on the separation of surface and bulk photoemission [1]. TPS consists in measuring integrated photoemission spectra $I_S(h\nu)$ and $I_P(h\nu)$ excited by the s- and p-polarized light, respectively. The measurements by means of technique of dosage-dependent-photoelectron yield under condition of the s-polarized light with constant excitation have been carried out.

2. Results and discussion

Fig. 1 shows changes in the photoemission thresholds $h\nu_S$ and $h\nu_P$ as a function of Cs dosage for GaAs (100) surface annealed in the range 450−580 °C. The ionization energy which defines the energy position of VBM relative to the Evac obtained as extrapolated threshold $h\nu_S$. The ionization-energy curves possess one minimum for both the As-rich and Ga-rich surfaces (Fig. 1b). However, the ionization-energy minimum for As-rich surface occurs at dosage $\sim 1.5\times10^{15}$ atom/cm^2 (Fig. 1b, curve 1) while for Ga-rich surface at $\sim 6.0\times10^{14}$ atom/cm^2 (Fig. 1b, curve 3). This demonstrates that the Cs sticking coefficient on the Ga-rich surface is approximately three times more that on the As-rich surface. Decrease of the ionization energy on the Ga-rich surface ($\sim$ 1.47 eV) is stronger than that on the As-rich one ($\sim$ 1.53 eV). We conclude that the value of dipole moment of Cs-Ga bond is greater on the Ga-rich surface than that of Cs-As bond onthe As-rich one. Curves 2 and 4 on the Fig. 1b which define the energy position of surface bands relative to the Evac obtained as extrapolated threshold $h\nu_P$. The difference between $h\nu_S$ and $h\nu_P$ indicates the existence of surface bands in fundamental gap under Cs adsorption. Two minima on the curve of ionization energy are revealed after annealing at 490 °C of the GaAs(100) surface (Fig. 1a). This finding indicates the simultaneous existence of the domains en-

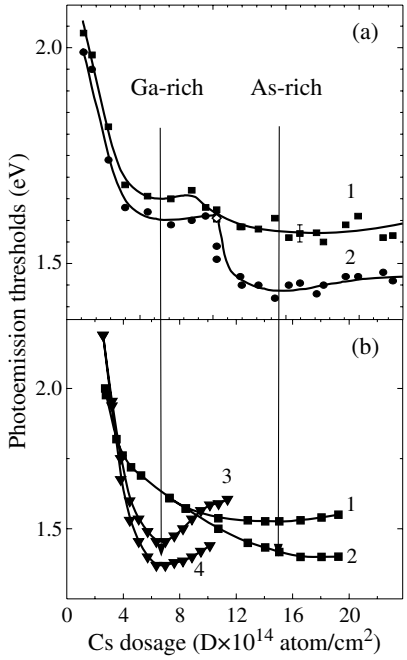

Fig. 1. Changes in photoemission thresholds $h\nu_S$ and $h\nu_P$ as a function of Cs dosage. (a) on the GaAs surface annealed at 490 °C. (b) on the GaAs surface annealed at 450 °C (curves 1, 2) on the GaAs surface annealed at 580 °C (curves 3, 4).

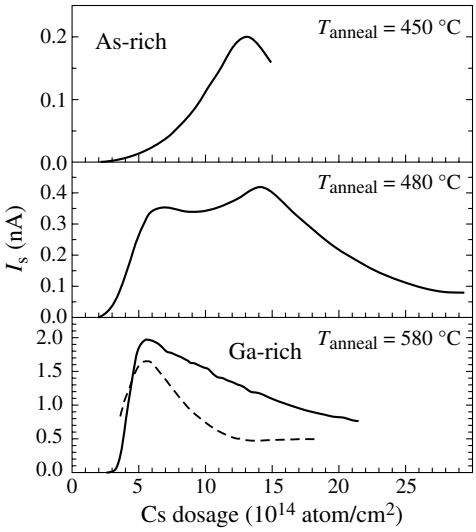

Fig. 2. Photoyield as a function of Cs dosage for the GaAs(100) surface annealed at gradually increasing temperature in the range 450−580 °C.

riched in As and in Ga on the surface. The anomalous curve is actually a superposition of one curve corresponding to interaction of Cs atoms with Ga-rich domains and the other one with As-rich domains. Curve 2 on Fig. 1a displays the existence of surface bands in fundamental gap in this case too.

Fig. 2 shows results of the independent experiments of measuring the photoelectron yield as a function of Cs dosage. For As-rich and Ga-rich surfaces, the photoyield curves have one maximum corresponding to minimum in Fig. 1. With increasing annealing temperature, modification of the photoyield curves reflects the surface reconstruction leading to an increase of the fraction of the Ga-rich domains until the entire surface becomes Ga-rich.

Fig. 3 represents the surface photoemission spectra $I_P(h\nu)/I_S(h\nu)$ at various Cs dosage for Ga-rich surface. The initial stages of Cs adsorption lead to an emergence the band A_1 at 1.86 eV and band A_2 at 1.75 eV. With the increase of dosage both peaks rapidly rise and at the ionization-energy minimum the development of the bands is completed. They merge into the single peak at 1.81 eV. These results indicate that bands A_1 and A_2 can be attributed to the process of local interaction of Cs adatoms with two specific surface sites at which the bonding is slightly different. If the Cs coverage increases, there begins a competition between the adatom-substate interaction and adatom-adatom interaction that results in decreasing the difference in energy position of peaks. The lateral interaction leads to the formation of Cs-Cs couple namely the initial cluster when Cs dosage corresponds to the ionization-energy minimum.

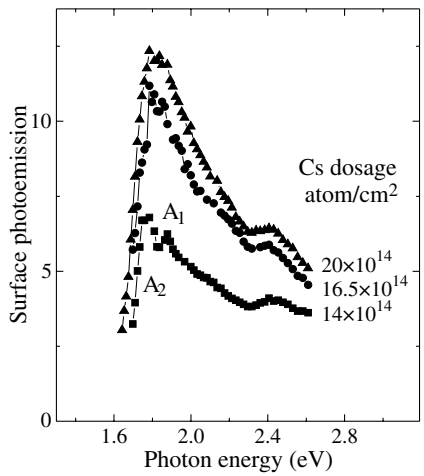

Fig. 3. Surface photoemission spectra $I_P(h\nu)/I_S(h\nu)$ as a function of Cs dosage for the GaAs (100) Ga-rich surface.

Acknowledgements

This work was supported by grant # 04-02-17621 of RFBR and by grant of Program "Industry of nanosystems and materials" LOT 4 IN-12.1/005.

References

[1] G. V. Benemanskaya, G. E. Frank-Kamenetskaya, *Surf. Sci* **523**, 211 (2003).

14th Int. Symp. "Nanostructures: Physics and Technology"
St Petersburg, Russia, June 26–30, 2006

Fano resonances in photocurrent spectra of semiconductors and quantum well heterostructures doped with shallow donors

L. V. Gavrilenko, V. Ya. Aleshkin, A. V. Antonov and V. I. Gavrilenko
Institute for Physics of Microstructures RAS, Nizhny Novgorod, Russia

Abstract. A theory describing the photocurrent peaks in the spectral region corresponding to the longitudinal optical phonon energy in semiconductors doped with shallow donors is developed. The calculated photocurrent spectra are in a good agreement with the experimental results obtained for n-GaAs.

Introduction

There are the asymmetrical peaks in impurity photocurrent spectra of semiconductors doped with shallow donors at photon energy corresponding to the longitudinal optical (LO) phonon peculiar to the material [1]. Usually these peaks are called Fano resonances [2], which appear due to electron interaction with longitudinal optical phonon.

Let us consider the absorption of light by electrons in a semiconductor doped with shallow donors in the spectral range near the LO-phonon energy. At low temperature all electrons occupy the donor ground states. There are two ways to absorb a photon. Firstly, the phonon absorption can be accompanied by the dipole electron transition from the donor ground state (1s) to the continuum (see Fig. 1). The second way is due to the second order electron transition when electron absorbs photon and emits the optical phonon. Below we discuss only the case when the final electron state for the second order transition coincides with the initial one, because only these transition are experimentally observed in n-GaAs. The complete energy of the electron-phonon system in this final state $|\phi_q\rangle$ is equivalent to the energy of continuum state electron has reached by first way, therefore this state is the resonant state. Note that the second order electron transition is realized through the set of the intermediate states.

In this paper we present general expression for photocurrent spectrum calculations describing the Fano resonance and demonstrate good agreement between calculated and measured photocurrent spectra for bulk n-GaAs doped with Si.

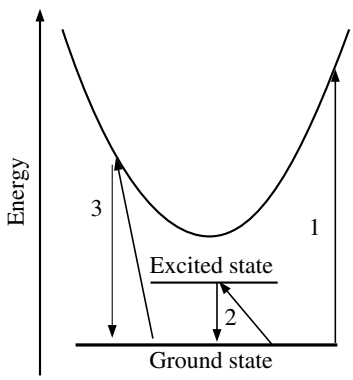

Fig. 1. Schematic diagram of the optical transitions for an electron occupying in the donor ground state and absorbing a photon with the energy $\hbar\omega_0$: 1 a transition to the continuum; 2,3 transitions to the resonant state via intermediate states in the discrete spectrum and in the continuum, respectively.

1. Light absorption probability calculation

To calculate a photocurrent spectrum we need to know the light absorption probability, the lattice absorption and reflectance spectra.

Let us consider the light induced electron transitions from initial donor ground state $|i\rangle = |\phi_{1s}, 0\rangle$ (without phonons) to the state $|\phi_q\rangle = |\phi_{1s}, 1\rangle$ (there is one LO phonon with wave vector q) (see Fig. 1). The Hamiltonian of our system is

$$H = H_0 + V_{\rm ph}\exp\left(-i\omega_{\rm ph}t\right) + V_{\rm LO}^{+}\exp\left(i\omega_0 t\right), \quad (1)$$

here H_0 is the non-perturbed system Hamiltonian, $V_{\rm ph}$, $V_{\rm LO}^{+}$ are the light absorption and LO-phonon emission operators, respectively. The matrix element of the second order transition is:

$$S_{\phi i} = \sum_m \frac{\langle\phi_q|V_{\rm LO}^{+}|m\rangle\langle m|V_{\rm ph}|i\rangle}{\hbar\omega_{\rm ph} + E_{\rm f} - E_m + i\lambda} + \frac{\langle\phi_q|V_{\rm ph}|m\rangle\langle m|V_{\rm LO}^{+}|i\rangle}{-\hbar\omega_{\rm ph} + E_{\rm f} - E_m + i\lambda}, \quad \lambda\to 0, \quad (2)$$

where $E_{\rm f}$ is the final electron state energy, index m numbers intermediate states. In our previous work [3] we considered in (2) the fist resonant term only, because it gives the main contribution to $S_{\phi i}$. In this paper we consider both the resonant and the nonresonant terms in (2).

The total light absorbtion probability is proportional to the squared modulus of the following matrix element:

$$\langle\Psi(E)|V_{\rm ph}|i\rangle = \frac{\Gamma(E)\langle\psi(E)|V_{\rm ph}|i\rangle}{2\sqrt{(E-E_{\rm f})^2 + \frac{\Gamma(E)^2}{4}}} \times\left(\alpha(E) + i + \frac{E-E_{\rm f}}{\Gamma(E)/2}\right), \quad (3)$$

here $|\Psi(E)\rangle$ is the exact wave function corresponding to the energy E which is the mixture of both discrete spectrum states $|\phi_q\rangle$ and the unperturbed continuum states $|\psi(E)\rangle$ and

$$\alpha(E) = \sum_{q,f}\frac{\langle\psi(E)|V_{\rm LO}^{+}|\phi_q\rangle}{\Gamma(E)/2\langle\psi(E)|V_{\rm ph}|i\rangle} \times 2\left(P\int_{E_{\rm f}}^{\infty} dE'\frac{\langle\phi_q|V_{\rm LO}^{+}|\psi(E')\rangle\langle\psi(E')|V_{\rm ph}|i\rangle}{E-E'} + \int_{E_{\rm f}}^{\infty} dE'\frac{\langle\phi_q|V_{\rm ph}|\psi(E')\rangle\langle\psi(E')|V_{\rm LO}^{+}|i\rangle}{-\hbar\omega_0 + E_i - E'}\right)$$

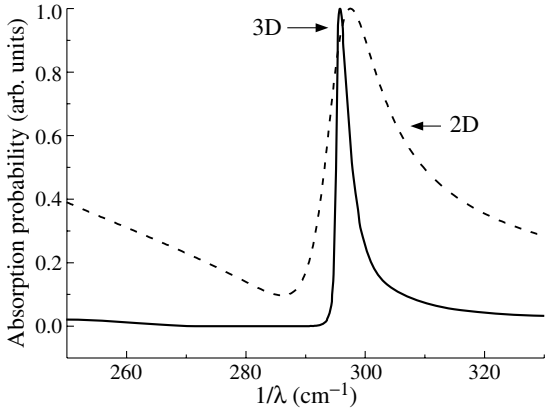

Fig. 2. Calculated absorption spectra for n-GaAs bulk material (solid line) and pure 2D case (dashed line).

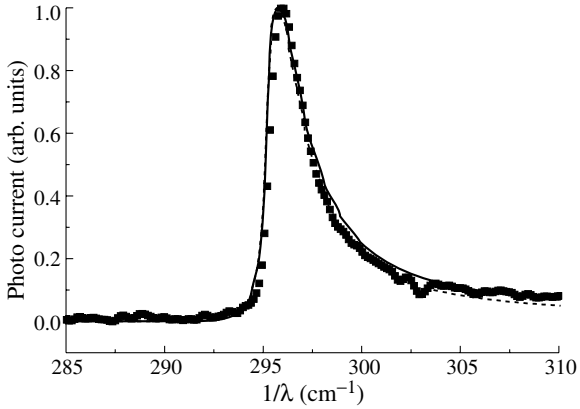

Fig. 3. Calculated (curves) and measured (squares) photocurrent spectra in n-GaAs at $T = 4.2$ K. Solid curve and dashed curve correspond to considering both terms in (2) and the first resonance term only, respectively.

and $\Gamma(E)/\hbar$ is the frequency of electron transition between the state in continuum $|\psi(E)\rangle$ and localized state $|\phi_q\rangle$ due to the spontaneous LO-phonon emission,

$$\Gamma(E) = 2\pi \sum_{q,f} \left|\langle\phi_{q,f}\right| V_{\mathrm{LO}}^{+} \left|\psi(E)\rangle\right|^2 .$$

The full light absorbtion probability is

$$W(\omega) = \frac{2\pi}{\hbar} \left|\langle\Psi\,(\hbar\omega + E_{\mathrm{f}}) \left|V_{\mathrm{ph}}\right| i\rangle\right|^2 . \qquad (4)$$

Note that we did not use explicit view of Hamiltonian H_0 to derive expression (3). Therefore Eq. (3) can be applied for describing semiconductors doped with both the donors and the acceptors.

Using Eqs. (3)–(4) and the explicit form of wave function for localized and delocalized shallow donor states we calculated Fano resonance in absorption spectrum of bulk n-GaAs, the results being present in Fig. 2.

Besides we investigated the resonant peak form in the extreme two-dimensional (2D) case that corresponds to the infinitely deep quantum well of zero width. In this case the 2D hydrogen atom-like wave functions were used to calculate the absorption spectrum. In Fig. 2 absorption probabilities for bulk material and 2D case are shown. The peak width is determined by value of Γ, i.e. by electron-phonon scattering frequency. In 2D limit Γ is approximately four times larger than in bulk n-GaAs. Though the extreme 2D case is never realized in practice, our example demonstrates the resonant peak feature in a quantum well if compared with bulk semiconductor. Note that in a real quantum well the peak width would be intermediate between bulk and extreme 2D ones.

2. The photocurrent spectrum. Comparison with experiment

Around LO phonon energy the reflectance and absorption quickly change with frequency rise due to light interaction with transversal optical phonons. Therefore, to correctly calculate photocurrent spectrum is necessary to take into consideration these dependencies. Taking into account the absorption factor $\eta(\omega)$ and reflectance $R(\omega)$ the photocurrent spectrum $J(\omega)$ spectra can be written in the form

$$J(\omega) = B\,I(\omega)\frac{W(\omega)}{|A|^2}[1 - R(\omega)] \int_0^d \exp[-\eta(\omega)x]dx\,, \quad (5)$$

where B is some constant, $I(\omega)$ is the incident light intensity, d is the thickness of the absorbing layer.

Figure 3 presents the comparison of the photocurrent spectrum calculated using the formula (5) and the measured one in bulk n-GaAs. It is seen that the calculation provides good accuracy for this material. For calculations we used follow parameters for GaAs: electron effective mass $\mu = 0.0665m_0$, m_0 is a free electron mass, low frequency permittivity $\kappa_0 = 12.46$, high frequency permittivity $\kappa_\infty = 10.58$, LO-phonon energy $\hbar\omega_0 = 36.588$ meV [4], TO-phonon energy $\hbar\omega_{TO} = \hbar\omega_0\sqrt{\kappa_\infty/\kappa_0}$.

The measurements was carried out with Fourier-transform spectrometer BOMEM at $T = 4.2$ K. n-GaAs under study was grown by liquid phase epitaxy on semiinsulator GaAs substrate. Epitaxial layer 70 micron wide was doped with Si with concentration 8.3×10^{14} cm^{-3}. The electron mobility was 5.9×10^4 cm^2/Vs at $T = 77$ K.

Acknowledgement

This work has been supported by RFBR (04-02-17178) and Russian Academy of Sciences.

References

[1] K. Jin, J. Zhang, Z. Chen *et al*, *Phys. Rev. B* **64**, 205203 (2001).
[2] U. Fano, *Phys. Rev.* **124**, 1866 (1961).
[3] V. Ya. Aleshkin, A. V. Antonov, L. V. Gavrilenko, V. I. Gavrilenko, *JETP* **101**, No. 4, 822–830 (2005).
[4] W. J. Moore, R. T. Holm, *J. Appl. Phys.* **80**, 6939 (1996).

14th Int. Symp. "Nanostructures: Physics and Technology"
St Petersburg, Russia, June 26–30, 2006

Magnetoabsorption study of InGaAs QW heterostructures in megagauss magnetic fields

V. I. Gavrilenko[1], V. Ya. Aleshkin[1], D. V. Kozlov[1], S. V. Morozov[1], N. V. Zakrevskii[1], B. N. Zvonkov[2], A. V. Filippov[3], I. M. Markevtsev[3], A. N. Moiseenko[3], V. V. Platonov[3], V. D. Selemir[3], O. M. Tatsenko[3], S. Hansel[4] and M. von Ortenberg[4]

[1] Institute for Physics of Microstructures, 603950 N. Novgorod, Russia
[2] Physico-Technical Research Institute of the Lobachevskii N. Novgorod State University, 603950 N. Novgorod, Russia
[3] Russian Federal Nuclear Center — All-Russia Research Institute of Experimental Physics, 607180, Sarov, Russia
[4] Institute of Physics of the Humboldt University at Berlin, D-101115 Berlin, Germany

Abstract. Bandgap absorption in InGaAs/GaAs QW heterostructures was studied in high magnetic fields up to 9 MG at room temperature. The results obtained are in a satisfactory agreement with the calculation data based on effective mass approximation in the magnetic fields up to 2–3 MGs (that corresponds to bandgap enhancement up to 200 meV). In the absorption spectrum measured at $\lambda = 10.6$ μm in p-type sample a sharp peak was discovered at $B \approx 80$ T, the absorption line being attributed to the *intersubband* cyclotron resonance (transition from the 1st hole subband into the 3rd one.)

Introduction

Magnetooptical investigations of semiconductors in megagauss magnetic fields allow studying the conduction and the valence band structures at the scale of tens and hundred meV [1]. In the present paper bandgap magnetoabsorption as well as the hole cyclotron resonance (CR) in InGaAs/GaAs quantum well (QW) heterostructures have been studied in ultrahigh magnetic fields for the first time.

1. Experimental

InGaAs/GaAs heterostructures under study were grown by MOCVD method on semiinsulating GaAs(100) substrates. The undoped InGaAs/GaAs structure #3899 for bandgap measurements contained 50 $In_{0.23}Ga_{0.77}As$ QWs with nominal width 60 Å separated by thick GaAs barriers. CR study was carried out in selectively doped heterostructure #4722 containing 50 $In_{0.15}Ga_{0.85}As$ QWs nominally 70 Å wide. Two carbon δ-layers were introduced from both sides of each QW 15 nm apart. The hole sheet concentration was 4.5×10^{11} cm^{-2} per QW.

Fig. 1 represents the transmission spectrum of the sample #3899 at zero magnetic field. The minimum at 1.25 eV corresponds to the excitonic absorption in the QW. At higher

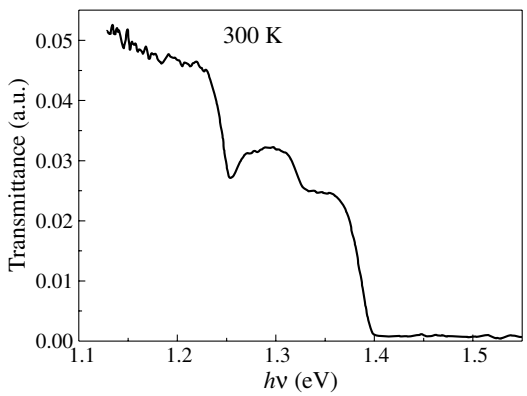

Fig. 1. Transmission spectrum in near IR range of undoped $In_{0.23}Ga_{0.77}As$/GaAs heterostructure #3899 at $T = 300$ K.

energies there are two typical flat "shelves" resulted from the constant density-of-states of 2D carriers.

Experimental investigations were carried out at room temperature with three different techniques: in pulsed magnetic fields up to 35 T, in quasi-nondestructive magnetic fields up to 2 MG using single-turn coil technique [2] and in explosive magnetic fields up to 9 MG using magnetocumulative generator MC-1 [3]. At $\lambda = 0.63$ μm, in contrast to earlier observation of the GaAs transparency at this wavelength at $B \geq 4.3$ MG [4] we did not observed a transmission signal up to 9 MG. In the following measurements were carried out at longer wavelengths 0.82 μm, 0.87 μm and 0.94 μm. CR study was carried out at wavelength 10.6 μm.

2. Results and discussion

At $\lambda = 0.94$ μm distinct oscillations of the transmission are observed (Fig. 2). In this case the photon energy is less than the bandgap in GaAs but exceeds that of $In_{0.23}Ga_{0.77}As$ QW. The dashed curve in Fig. 2 gives the results of transmission calculations carried out within simple isotropic band model taking into account the spin splitting. The electron and hole masses were assumed to be $0.06m_0$ and $0.12m_0$ respectively and the LL width was put 25 meV. The observed transmission minima at $B = 11$ T and $B = 17$ T correspond to the transitions from the 2nd hole into 2nd electron LLs and from the 1st hole into 1st electron ones.

At $\lambda = 0.87$ μm the photon energy 1.425 eV just corresponds to GaAs bandgap. However the sample becomes partly transparent at $B = 50$ T only (Fig. 3) due to the significant thickness (300 μm) of GaAs substrate and the density-of-states tails in the GaAs forbidden band owing to the lattice thermal oscillations [5]. By the same reason at $\lambda = 0.82$ μm the sample becomes transparent at $B = 150$ T (Fig. 4) though the calculation results taking into account the excitonic effects gives the value of 100 T.

14-band Kane model [6] was used to calculate the energy spectra in high magnetic fields for bulk GaAs. For the InGaAs/GaAs QWs we use 8-band Kane model for the conduction band [7] and 4×4 Luttinger Hamiltonian for the valence

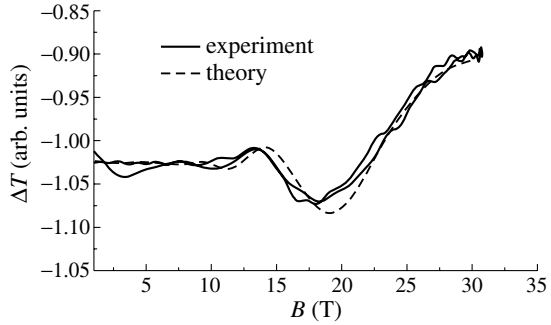

Fig. 2. Transmission modulation at $\lambda = 0.94$ μm in the sample #3899 at both the ascending and the descending magnetic fields and the calculation result.

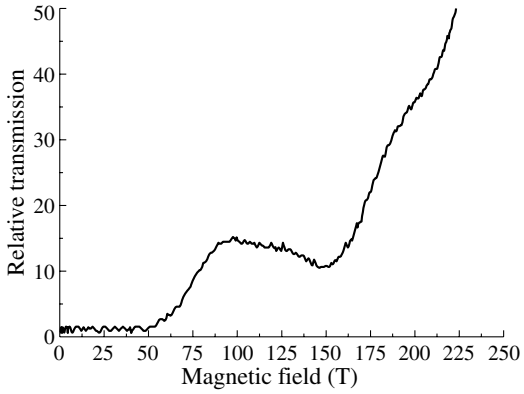

Fig. 3. Transmission of the sample #3899 at $\lambda = 0.87$ μm.

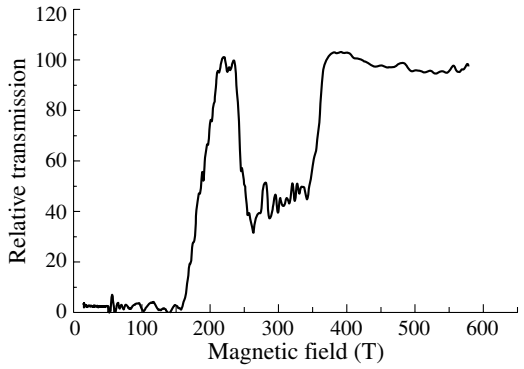

Fig. 4. #3899 sample transmission at $\lambda = 0.82$ μm.

band (in the axial approximation). At $\lambda = 0.82$ μm the absorption band in between 2.3 MG and 3.5 MG (Fig. 4) is shown to result from optical transitions from two upper hole LLs in the 1st subband into two lowest electron ones and from the same ones (shifted by $\sim$ 50 T to lower magnetic fields) between 2nd subbands, the excitonic effects being taken into account. The same transitions between the 1st hole and electron subbands at $\lambda = 0.87$ μm are responsible for a transmission peculiarity at 210 T and the minimum at $B = 150$ T (Fig. 3). The transitions between the 2nd hole and electron subbands again shifted by 50 T to lower fields seem to fall in between 100 and 150 T.

Calculations of the cyclotron mass in the 1st hole subband in low magnetic fields give $0.12m_0$ that should increase with the fields due to the valence band nonparabolicity. However we observed the absorption line at $B \approx 80$ T (Fig. 5) that corresponds to the cyclotron mass as low as $0.08m_0$. This peak seems to result from the intersubband CR (earlier observed

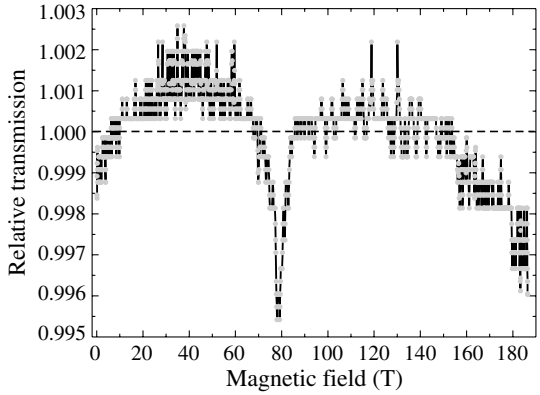

Fig. 5. Magnetic field dependence of the sample #4722 transmission at $\lambda = 10.6$ μm; $T = 300$ K.

in Ge/GeSi QWs [8]), namely, from the transition between the lowest hole LL pertained to the 1st hole subband $3a_1$ (as labeled in [8]) and $4a_3$ one pertained to the 3rd subband. Due to the anticrossing effects the wave function of $4a_3$ state has a great contribution of the 1st hole subband that makes the matrix element of $3a_1 \rightarrow 4a_3$ transition comparable with $3a_1 \rightarrow 4a_1$ one.

Acknowledgements

This work was financially supported by ISTC (project 2293) and the Russian Academy of Sciences. The authors are grateful to Yu. N. Drozdov, D. M. Gaponova and S. S. Krishtopenko for their assistance and V. Ya. Demikhovsky for fruitful discussions.

References

[1] M. Miura *et al*, *J. Phys.: Condens. Matter* **11**, 54 (1999).
[2] O. Portugal *et al*, *J. Phys. D: Appl. Phys.* **32**, 2354 (1999).
[3] A. I. Bykov *et al*, *Physica B* **294–295**, 574 (2001).
[4] A. I. Pavlovskii *et al*, *JETP Lett.* **40**, 854 (1984).
[5] D. M. Sturge, *Phys. Rev.* **127**, 768 (1962).
[6] H. Mayer and U. Rossler, *Phys. Rev. B* **44**, 9048 (1991).
[7] G. Bastard, *Wave mechanics applied to semiconductor heterostructures*, (Les Ulis, France: Halsted Press) 1988.
[8] V. Ya. Aleshkin *et al*, *Physics of the Solid State* **46**, 130 (2004).

14th Int. Symp. "Nanostructures: Physics and Technology"
St Petersburg, Russia, June 26–30, 2006

Nondestructive characterization of pHEMT epitaxial structures based on line-shape model for room temperature photoluminescence spectra

A. G. Gladyshev[1], V. G. Tikhomirov[2], N. A. Maleev[3], N. V. Kryzhanovskaya[1], V. S. Mikhrin[3], A. P. Vasil'ev[3], A. E. Zhukov[1], M. V. Maximov[3] and V. M. Ustinov[1]

[1] St Petersburg Physico-Technical Centre of Russian Academy of Science for Research and Education, 194021, St Petersburg, Russia
[2] Radioengineering and Electronics Department, St Petersburg Electrotechnical University, 197376, St Petersburg, Russia
[3] Ioffe Physico-Technical Institute, St Petersburg, Russia

Abstract. Realization of nondestructive characterization technique based on RT PL spectra fitting procedure using line-shape model for AlGaAs/InGaAs pHEMT structures are considered. For investigated non-delta-doped pHEMTs structures is obtained good agreement between results of RT PL spectra fitting and Hall measurements in sheet concentration range of $(1.5-2.2)\times10^{12}$ cm^{-2}.

Introduction

Pseudomorphic high electron mobility transistors (pHEMT) based on an AlGaAs/InGaAs quantum well system have demonstrated their high potential for low-noise, microwave power, and high-speed digital applications [1, 2]. pHEMT manufacturing requires a high quality multi layer epitaxial structure. The performance of a pHEMT depends on the two-dimensional electron gas (2DEG) which is formed by a large number of electrons confined in the InGaAs channel layer. Usually sheet carrier density ns is determined by Hall or Shubriko–de Haas measurements. However, separately fabricated samples with ohmic contacts are necessary for these measurements. Additionally above mentioned techniques is not suitable for evaluation of wafers inhomogeneity. An attractive alternative would be to determine the sheet concentration nondestructively using optical techniques which would allow deliverable wafers to be evaluated as a whole. In previous works [3–5] empirical correlation between photoluminescence (PL) linewidth at 77 K and sheet carrier density was established. But PL spectrum of pHEMT structure involves transitions from several electron subbands in the $In_yGa_{1-y}As$ quantum well and their peaks overlap. Therefore accurate determination of the PL spectra linewidth is difficult. Also it is very complicated to measure large samples (for example 3-inch wafers) at 77 K. To avoid these limitations fitting room-temperatures (RT) PL spectra using phenomenological line-shape model were suggested [6]. Later nondestructive characterization technique based on this model was demonstrated for determination of the sheet carrier density in delta-doped pHEMT structures with indium mole fraction y of 0.15–0.20 and channel thickness of 12–15 nm [7, 8]. Reasonable agreement between values of sheet carrier density ns_{PL} obtained from RT PL spectra fitting and sheet carrier density ns_{Hall} obtained from Hall measurements were achieved. At the same time there are several points which should be taken into account at practical application of above mentioned technique. Among them are optimal realization of the nonlinear fitting procedure and proper choice of the initial parameters. It will critically affects on ns_{PL} value and quality of PL spectra fitting. Another problem is possible physical limitation of using line-shape model for optical transitions in different types of pHEMT structures.

In this work we realize nondestructive characterization technique based on RT PL spectra fitting procedure using line-shape model for non-delta-doped AlGaAs/InGaAs pHEMT structures. Mathematical features of non-linear fitting procedure and experimental results are discussed.

1. PL spectra fitting procedure

The line-shape model for total PL intensity of the AlGaAs/InGaAs pHEMT structures has been accurately described by Brierley [6]. The key problems at the realization of non-linear fitting procedure are convergence, stability and selection of true solution. The several methods (reflective Newton, preconditioned conjugate gradients, trust region and Levenberg-Marquardt [9–11]) realized in MATLAB and MATCAD software were tested as applied to PL spectra fitting. Unfortunately, sometimes all above mentioned methods result in false solutions. Therefore original software based on preconditioned conjugate gradients (PCG) method was developed. Each of iteration involves the approximate solution of a large linear system using the method of PCG. The two-dimensional subspace is determined with the aid of a preconditioned conjugate gradient process described in [11]. The program assigns where is in the direction of the gradient and is either an approximate Newton direction. The philosophy behind this choice of is to force global convergence (via the steepest descent direction or negative curvature direction) and achieve fast local convergence (via the Newton step, when it exists). To avoid convergence to a false local solution the fit quality is inspected graphically. In case of false solution the fitting should be repeated with corrected initial parameter values.

2. Experiment

Investigated pHEMT structures were grown by solid-state molecular beam epitaxy on semi-insulated GaAs (100) substrates. The layers thickness/composition and doping profile were determined from preliminary calibrations. A typical structure of the samples is consists of the following layers grown sequen-

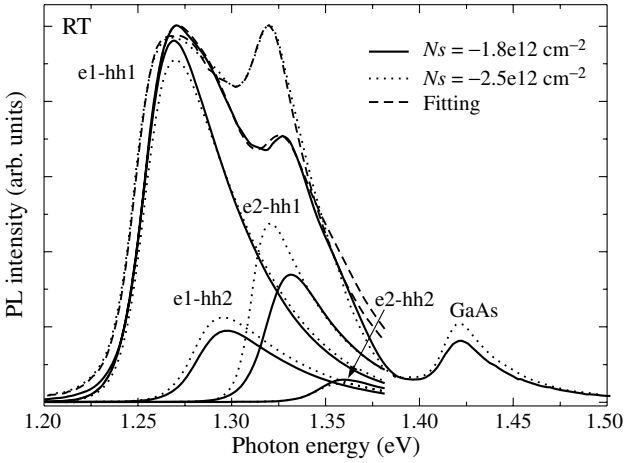

Fig. 1. PL spectra and their deconvolutions for two pHEMT structures with different sheet concentrations. Fitting results are shown by dashed lines.

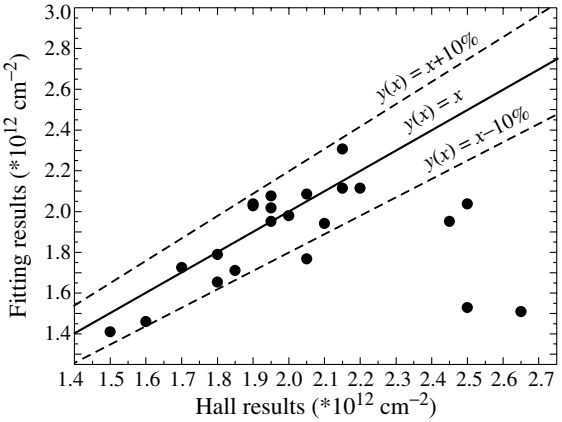

Fig. 2. Comparison between PL fitting results and Hall measurements data.

tially, from bottom to top, on a semi-insulating GaAs substrate: 200 nm GaAs first buffer layer, next ten superlattices of AlGaAs/GaAs and 400 nm GaAs second buffer layer; undoped InGaAs strained layer (channel); GaAs/AlGaAs spacer;Si-doped 13 nm n-AlGaAs source layer; Si-doped 25 nm n-AlGaAs barrier layer; Si-doped 15 nm n-GaAs barrier layer; and a Si-doped 10 nm n-GaAs high-doped cap layer. Before PL investigation sheet concentration ns_{Hall} was measured by Hall method for all samples under study. Hall measurements were performed at RT by Van der Pauw method using Bio-Rad HL5200 Hall Measurement System.

The PL spectra were excited with second harmonic of CW Nd:YAG laser (532 nm). The laser power density was 10 W/cm^2. The PL signal was recorded using a 1-m single monochromator, a cooled Ge detector and standard lock-in amplifier. After recording PL spectra were fitted using above described fitting procedure. Obtained values of ns_{PL} were compared with ns_{Hall} for set of pHEMT epi-structures. Only fitting results having less than 5% divergence with the Hall data were taken for further analysis.

3. Results

Fig. 1 shows room temperature PL spectra of two pHEMT structures with different sheet concentrations and results of PL spectra fitting (dashed lines). There is evidence in the spectrum for two peaks ($e1-hh1$ and $e2-hh1$) and two shoulders ($e1-hh2$ and $e2-hh2$) corresponding to four possible transitions between two electron and two hole states. The appearance of transverse transitions is explained by asymmetry placement of the doping leading to a high degree of asymmetry of the InGaAs quantum well. So usually forbidden by symmetry rules transitions become possible. PL spectra deconvolutions are also presented in Fig. 1. It is worth noting that peak $e2-hh1$ is more intensive in more doped structure what point to sensitivity of PL measurements to channel sheet concentration.

The results of comparison between PL fitting results and Hall data are shown in Fig. 2. The unity slope line (solid) corresponding to full coincidence of fitting and experimental data and two lines (dashed) corresponding to 10% deviation are presented in the Fig. 2 for reference. It is clearly seen that sheet densities obtained from the PL spectra correlate with Hall data for whole set of samples in sheet concentration range from 1.5 to 2.2×10^{12} cm^{-2} with approximately 10% error. In conrast with published results for delta-doped pHEMT strucutres [10, 11] divergence between fit and Hall data increase for sheet concentrations exceeding 2.3×10^{12} cm^{-2}.

In conclusions, RT PL spectra fitting procedure based on line-shape model were realized and applied for non-delta-doped AlGaAs/InGaAs pHEMT structures. For investigated pHEMTs structures the developed nondestructive characterization technique provides good agreement between ns_{PL} and ns_{Hall} values in sheet concentration range of 1.5–2.2×10^{12} cm^{-2}. At high sheet densities ($> 2.2\times10^{12}$ cm^{-2}) the PL spectra fitting systematically result in lower ns value as compare with Hall measurements. The physical explanation of this phenomenon will be subject of following investigation.

Acknowledgement

This work was supported by SANDiE.

References

[1] H. Morkoc, H. Unlu and G. Ji, *Principles and Technology of MODFETs*, (Vol.1&2 Wiley), (1991).
[2] G. E. Brehm *et al*, *Compound Semiconductor Manufacturing Technology Conference*, 28–31 (2004).
[3] A. Dodabalapur, V. P. Kesan, D. P. Neikirk and B. G. Streetman, *Appl. Phys. Lett.* **54**, 1675 (1989).
[4] H. Brugger, H. Mussig, C. Wolk, K. Kern and D. Heitmann, *Appl. Phys. Lett.* **59**, 2739 (1991).
[5] S. K. Brierley, W. E. Hoke, P. S. Lyman, H. T. Hendriks, *Appl. Phys. Lett.* **59**, 3306–3308 (1991).
[6] S. K. Brierley, *Appl. Phys. Lett.* **74**, 2760–2767 (1993).
[7] W. Lu, J.-H. Lee, K. Prasad, G.-I. Ng and P. Lindstrom, *Semicond. Sci. Technol.* **14**, 103 (1999).
[8] M. Mikhov *et al*, *GaAs MANTECH Conference* (2002).
[9] T. F. Coleman and Y. Li, *Mathematical Programming* **67**, 189 (1994).
[10] T. F. Coleman and Y. Li, *SIAM Journal on Optimization* **6**, 418 (1996).
[11] J. J. More, *The Levenberg-Marquardt Algorithm: Implementation and Theory* (Numerical Analysis, ed. G. A. Watson, Lecture Notes in Mathematics 630, Springer Verlag), 105–116 (1977).

14th Int. Symp. "Nanostructures: Physics and Technology"
St Petersburg, Russia, June 26–30, 2006

Study of optical properties of Ge nanoclusters in dielectric films using scanning ellipsometry

E. B. Gorokhov, V. A. Volodin, D. V. Marin, A. G. Cherkov, A. G. Borisov and S. V. Golod
Institute of Semiconductor Physics of SB RAS, pr. ak. Lavrentjeva 13, Novosibirsk 630090, Russia

Abstract. The complex of methods including scanning ellipsometry, high resolution transmission electron microscopy, Raman spectroscopy was applied to study heterostructures Ge clusters in GeO_2 matrix. Essential improving of accuracy of ellipsometry data interpretation allows to observe the influence of the quantum-size effect on optical properties of the heterostructure.

To study quantum-size effects for semiconductor quantum dots (QDs) in dielectric matrix one need precise methods for control of structural, electro-physical and optical properties of the heterostructures. One need to know QD concentration, it's average size, dispersion of sizes, and, for the case of multiphase structure-ratio of amorphous and crystalline parts. It is also needed to know how these structural properties impact on electrical and optical properties of the heterostructures. It is also desirable that such methods were express and non-destructive, what is possible mainly for non-direct methods. In present work we have tried to developed such methods, mainly based on ellipsometry and, for control, also Raman scattering spectroscopy and high resolution transmission electron microscopy (HRTEM) were used.

To find the optimal regimes of growth of a heterostructure with QDs it is often needed to carry out the growth in gradient of temperature and concentration of reagent gases. In this case, thickness and optical parameters of the grown film have smooth gradient. Let's choose some trajectory (l) on our structure. Scanning ellipsometry gives a set of ellipsometry angles $\Psi(l_i)$, $\Delta(l_i)$. These functions are smooth and it's derivative are also smooth. The using of theory of ellipsometry allow us to calculate from these angles the dependences of refractive index, absorption index and thickness: $n(l)$, $k(l)$, $h(l)$.

The deposition from supersaturated GeO vapor with subsequent dissociation of metastable Ge monoxide on hetero-phase system Ge:GeO_2 was applied to obtain the GeO_2 films with Ge QDs on Si substrates. In this case, the dependences of $n(l)$ and $k(l)$ are results of changes of QDs density ($\rho(l)$), sizes ($D(l)$), and phase composition ($\gamma(l)$) due to temperature and GeO concentration gradient along l. The thickness of film $h(l)$ also depends on growth condition gradient. Knowing the dependence of optical parameters from $\rho(l)$, $D(l)$, and $\gamma(l)$, one can try to solve inverse problem and to find these functions. The main interest is how the optical constant of heterofilm depends on the QDs sizes — the quantum size effect. Therefore, the $n(l)$ and $k(l)$ should be defined with maximal possible accuracy.

Usually, there is a problem to define volume ratio between QDs and matrix in heterostructures. Our heterostructure have remarkable property — due to (2GeO (solid) $\rightarrow$ Ge+GeO_2) growth procedure it has molar ratio between Ge and GeO_2 as 1:1, independently on growth condition [1]. So, the volume part of c-Ge or a-Ge clusters is $\sim 30,7\%$. Therefore, the concentration of Ge QDs and average distance between QDs depends only on the QDs average size. Some deviation in volume ratio can be due to difference in mass density of c-Ge and a-Ge. The ratio c-Ge/a-Ge can be measured from Raman spectra (see Fig. 1). The Raman spectra were registered from different part of the Ge:GeO_2 film grown in condition of temperature and GeO concentration gradient.

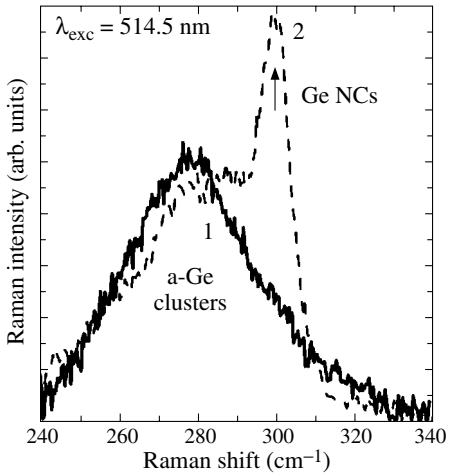

Fig. 1. Raman spectra of a Ge:GeO_2 film.

The heterofims were studied using scanning ellipsometry with step $\delta l = 0.5$ mm and the results were interpreted using above described method and specially developed algorithm. As one can see from Fig. 3, the ellipsometry angles $\Psi(l_i)$ and $\Delta(l_i)$ are depended on $n(l)$, $k(l)$ and $h(l)$ in the film. It should be mentioned, that ellipsometric data were registered at wavelength 632.8 nm (He-Ne laser).

The thickness of film smoothly reduced in direction of flow of gas because of depletion of GeO vapor. Consequently, the QDs size and ratio of c-Ge/a-Ge also reduce in that direction. As one can see from Fig. 3, the functions $n(l)$, $k(l)$ and $h(l)$ are smooth, and there is some plato in the middle of the film. The data obtained from ellipsometry are in good correspondence with Raman and HREM data. The points 1 and 2 in Fig. 3 correspond to spectra 1 and 2 in Fig. 1.

The calculations reveal the next:

— Reducing of $h(l)$ with reducing of substrate temperature and temperature of gas. It is because depletion of GeO gas in growth zone.

— The absorption of light (632.8 nm) by our heterostructures is result of presence of Ge clusters. Reducing of absorption index $k(l)$ simultaneously with reducing of $h(l)$ in direction of gas flow is the influence of quantum size effect. The smaller Ge particles is more transparent. This is in good correlation with HREM data (Fig. 2). With reducing of average Ge cluster size, the part of amorphous Ge particle grow (comparing with c-Ge clusters). It is also confirmed by Raman

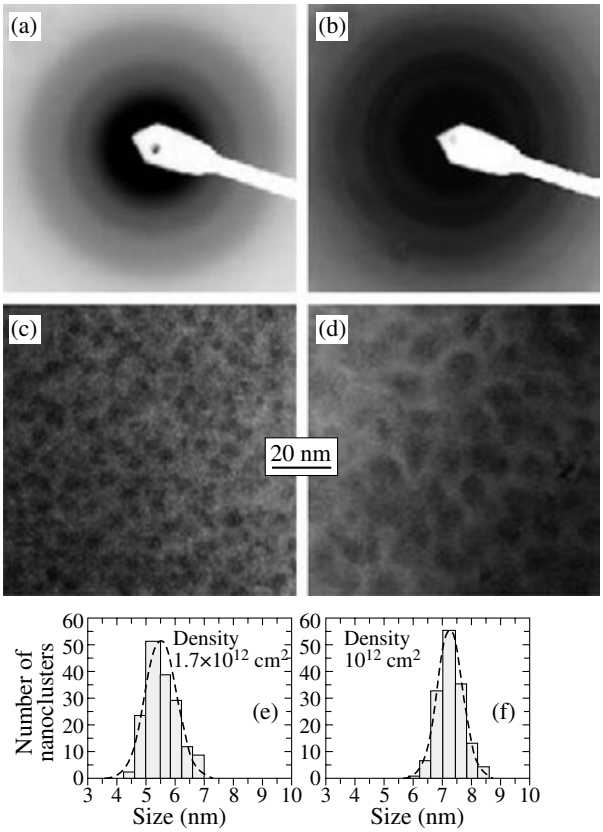

Fig. 2. HREM images from different part of Ge:GeO_2 film grown in condition of temperature and GeO concentration gradient. Microscope JEM-4000EX, 250 kV, plan-view configuration.

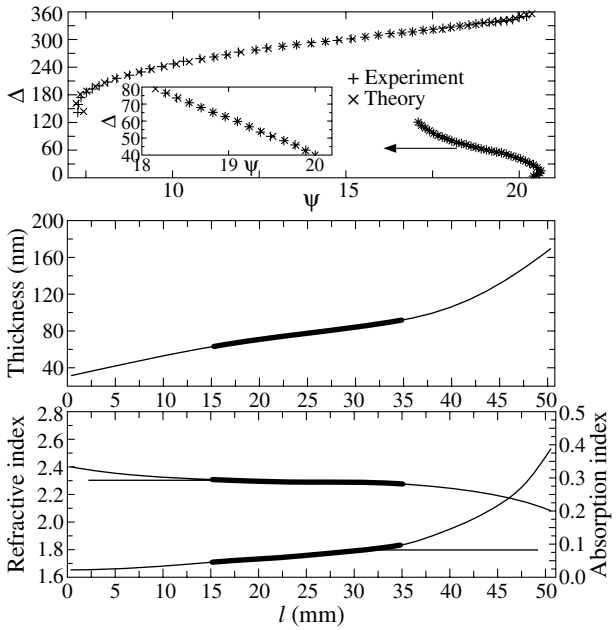

Fig. 3. Ellipsometric nomogramm and dependence of optical constant in the Ge:GeO_2 film.

data (Fig. 1) and HREM data. Comparing deposit in absorption index of quantum size effect and phase composition effect one can conclude, that for this case the first effect is more important.

— Because of for wavelength 632.8 nm amorphous Ge have bigger refractive index n than crystalline Ge, some growth of n in direction of gas flow was observed.

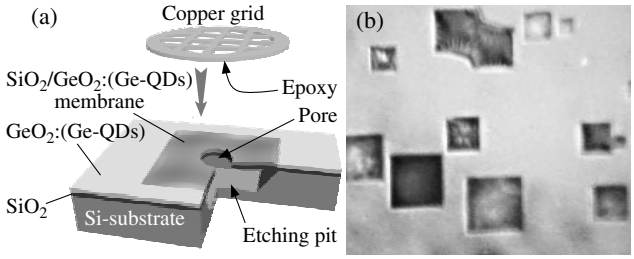

Fig. 4. (a) Scheme of process of a cop set glue on SiO_2/GeO_2:(Ge-QDs) sample with a special membrane. On a cross-section one can see etching hole and a free film — membrane. (b) The membranes from 40 nm SiO_2 on Si(100), obtained by selective etching of Si substrate through pores in oxide.

— The smooth plato in functions $n(l)$, $k(l)$ and $h(l)$ in middle of the film (despite of temperature gradient) show the importance of technological factors in controllable variation of structural properties of the films.

The dependence of QDs size from growth condition, very likely, is the most important. This parameter is very important for electrical and optical properties of the heterostructures. To obtain express HREM data the technology of special membrane was developed. In this case, the Si/SiO_2 substrate was used. The SiO_2 film contain nanopores, and selective etching was used to obtain membranes.

Therefore, development of scanning ellipsometry methods (with analytical interpretation and calculations) consequently with using of HREM and Raman data allows us to obtain experimental evidence of the quantum-size effect on optical properties of heterostructure Ge:GeO_2. The developed methods can be applied for study of others heterostructures like semiconductor QDs in dielectric matrix.

References

[1] E. B. Gorokhov *et al*, *12th International Symposium "Nanostructures: Physics and Technology"*, St Petersburg, Russia, 310–311, 2004.

14th Int. Symp. "Nanostructures: Physics and Technology"
St Petersburg, Russia, June 26–30, 2006

Cyclotron resonance study of InAs/AlSb QW heterostructures in quantizing magnetic fields

A. V. Ikonnikov[1], Yu. B. Vasilyev[2], S. S. Krishtopenko[1], V. Ya. Aleshkin[1], V. I. Gavrilenko[1], M. L. Sadowski[3], W. Knap[4], Yu. G. Sadofyev[1,5], S. R. Johnson[5] and Y.-H. Zhang[5]

[1] Institute for Physics of Microstructures of Russian Academy of Sciences, 603950 N. Novgorod, Russia
[2] Ioffe Physico-Technical Institute, St Petersburg, Russia
[3] Grenoble High Magnetic Field Laboratory, CNRS, Grenoble, France
[4] GES, University of Montpellier 2, CNRS, Place Eugene Bataillon, 21, cc074, F34095, Montpellier, France
[5] Arizona State University, Tempe, AZ 85287, USA

Abstract. Cyclotron resonance spectra in doped InAs/AlSb quantum well heterostructures in quantizing magnetic fields were studied for the first time. Large cyclotron resonance line splitting ($\Delta\omega/\omega \approx 10\%$) was found, the effect being attributed to the different Landau level spacing in the 1st and the 2nd electron subbands.

Introduction

Recently there has been considerable interest in InAs/AlSb quantum well (QW) heterostructures which are promising for novel electronic, optoelectronic and spintronic devices. These structures exhibit a number of remarkable properties such as large conduction band offset of 1.3 eV, low electron effective masses in InAs QWs down to $0.03m_0$, large electron effective g^*-factor up to -60, and high electron mobility up to 3×10^4 cm^2/V s at room temperature and up to 9×10^5 cm^2/V s at $T = 4.2$ K. Cyclotron resonance (CR) is an effective method for studying both the conduction band nonparabolicity and the spin-related phenomena [1–3]. However these studies were restricted to nominally undoped samples with sheet electron concentration up to 1.4×10^{12} that corresponds to the filling of the 1st electron subband only. In Ref. [4] we report on the CR study of selectively doped InAs/AlSb structures in moderate magnetic fields. The present paper is devoted to the CR study of the doped structures in quantizing magnetic fields.

1. Experimental

The InAs/AlSb heterostructures under study were grown by MBE on semi-insulating GaAs(100) substrates with a thick metamorphic AlSb buffer layer followed by a ten-period smoothing GaSb/AlSb superlattice [5]. The active part of the structure consists of a lower AlSb barrier 12 nm wide in the undoped sample A856 and 40 nm wide in the selectively doped ones B1445 and B1446, an InAs QW with a nominal thickness of 15 nm, an upper AlSb ($Al_{0.8}Ga_{0.2}Sb$ in the sample A856) barrier 30 to 40 nm wide and a GaSb cap layer 6 nm wide. In the samples B1445 and B1446 the upper and the lower AlSb barriers were δ-doped with Te 15 nm apart from the InAs QW. CR spectra were measured with Brucker 113V FT spectrometer. We used square samples with an area 5×5 mm^2 with two strip ohmic contacts for the Hall effect measurements. The samples were mounted in the light-pipe insert in the liquid helium cryostat in the center of a superconducting solenoid, and all measurements were carried out at $T = 4.2$ K. To suppress the interference effect the substrate was wedged with an angle of 2°. The radiation transmitted through the structure was detected with a Si bolometer. Transmission spectra were normalized to the spectrum measured in the zero magnetic field.

2. Results and discussion

The measured CR spectra in nominally undoped sample A856 with 2D electron concentration determined from the Hall effect measurements of 7.1×10^{11} cm^{-2} are given in Fig. 1. The magnetic fields corresponding to integer values of the Landau level (LL) filling factor ν are designated with arrows. It is clearly seen that a marked CR line splitting is observed at the odd values $\nu = 5$, 7. This is typical for the CR in quantizing magnetic fields in nonparabolic conduction band (see insert in Fig. 2, cf. [1, 2]). The calculated LLs in rectangular InAs/AlSb QW in two lowest electron subbands are presented in Fig. 2. 8-band Kane model [6] accounting the deformation terms and electron magnetic moment interaction with the magnetic field [7] was used. The calculations were performed using the transfer matrix technique neglecting the terms proportional to the square of the hole wave vector in the Hamiltonian. The InAs lattice constant in the plane of the structure was assumed to be equal to that of AlSb. In low magnetic fields the calculations results corresponds fairly well to semi-classical ones [6]. In the calculations we set the InAs QW width of 20.5 nm that provides the best fitting to the measured CR masses in moderate magnetic fields. Since the CR transitions occur between LLs with the same spin, the maximum CR splitting in the nonparabolic band will take place at odd filling factor value (see

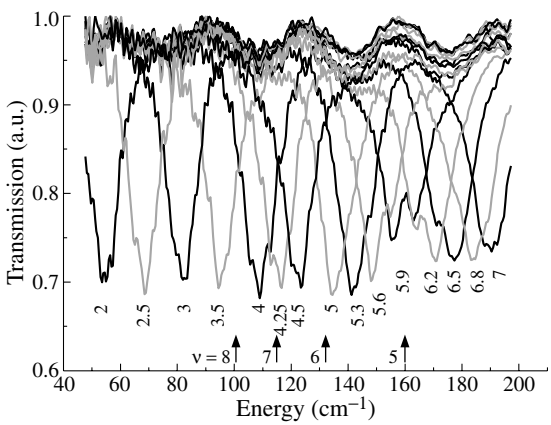

Fig. 1. CR spectra of the sample A856 ($n_s = 7.1\times10^{11}$ cm^{-2}, $\mu = 3.9\times10^5$ cm^2/V s). The values of the magnetic field (Teslas) are shown below the spectra. The magnetic fields corresponding to integer values of the LL factor ν are designated with arrows.

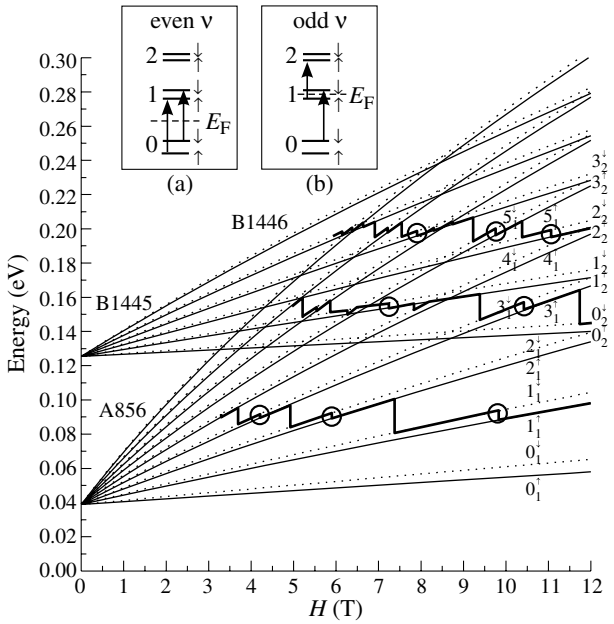

Fig. 2. The theoretical calculations of the LLs in the 2 subbands in InAs QW 205 Å width. Bold lines correspond to the Fermi level for 3 samples. In the inset: the schematic energy diagram depicting CR splitting at even (a) and odd (b) integer fill factor.

insert in Fig. 2). The Fermi level position is shown schematically by solid line in Fig. 2 for all 3 samples under investigations. Indeed, as easy to see, the magnetic fields 5.9 and 4.3 T (where the maximum CR line splitting is observed) practically correspond to the Fermi level "jump" from 5th to 6th and from 7th to 8th LLs.

Fig. 3, 4 show the CR in doped InAs/AlSb heterostructures with higher electron concentrations where both the 1st and the 2nd electron subbands are filled. In the sample B1445 the maximal CR line splitting of 20 cm^{-1} is observed at $B = 8.75$ T (Fig. 3). In contrast to the sample A856 (Fig. 1) where the two split components are of comparable amplitudes, in the sample B1445 the amplitude of the low-frequency peak is less than that of high-frequency one in all magnetic fields. That allows to attribute the low-frequency peak to the CR resonance in the 2nd electron subband where the concentration is estimated as 1/3 of that in the 1st subband [4]. As one can see from Fig. 2 the maximum CR splitting corresponds to the odd number (3) of the filled LLs in the 2nd subband. At the magnetic field decrease down to $B \approx 7$ T there is a significant CR line splitting again(see Fig. 3). However the observed splitting $\Delta\omega/\omega \approx 10\%$ (at $B = 8.75$ T) is considerably greater than both the classical CR mass difference of 4% [4] and the calculated spacing between the LLs at the Fermi energy at the 1st and the 2nd subbands that probably results from the nonrectangular shape of the InAs QW.

CR spectra in more heavily doped sample B1446 are given in Fig. 4. In this sample the population of the 2nd subband is estimated as 60% of that of the 1st one that probably explains why the two split components of the CR line at $B = 11.25$ T are of comparable intensity. Again, as easy to see from Fig. 2, this magnetic field corresponds to the odd number (5) of the filled LLs in the 2nd subband. At the magnetic field decrease the splitting at first becomes not resolved and gets the next maximum at $B = 9.5$ T that again according to Fig. 2 corresponds to the odd number (7) of the filled LL in the 2nd subband.

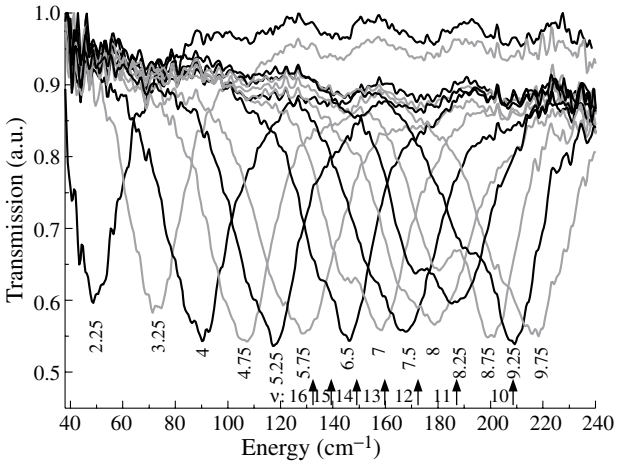

Fig. 3. CR spectra of the sample B1445 ($n_s = 2.3\times10^{12}$ cm^{-2}, $\mu = 1.0\times10^5$ $cm^2/V\,s$). The values of the magnetic field (T) are shown below the spectra. The magnetic fields corresponding to integer values of the LL filling factor ν are denoted with arrows.

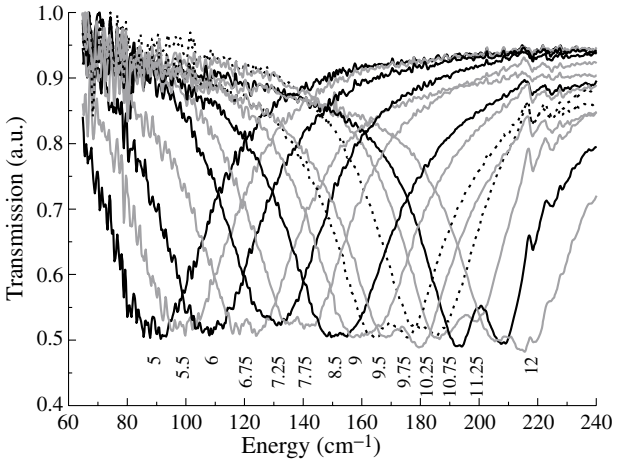

Fig. 4. CR spectra of the sample B1444 ($n_s = 4.2\times10^{12}$ cm^{-2}, $\mu = 0.53\times10^5$ $cm^2/V\,s$). The values of the magnetic field (Teslas) are shown below the spectra.

Acknowledgements

This work was financially supported by RFBR (grant 05-02-17531), INTAS (grant YS Fellowship 04-83-3169) and the Russian Academy of Sciences.

References

[1] J. Scriba *et al*, *Semicond. Sci. Technol.* **8**, S133 (1993).
[2] M. J. Yang *et al*, *Phys. Rev. B*, **47** 6807 (1993).
[3] Y. B. Vasilyev *et al*, *JETP Lett.* **79** 674 (2004).
[4] V. Ya. Aleshkin *et al*, *Semiconductors* **39**, 62 (2005).
[5] Yu. G. Sadofyev *et al*, *Appl. Phys. Lett.* **81**, 1833 (2002).
[6] E. O. Kane, *J. Phys. Chem. Solids* **1**, 249 (1957).
[7] H.-R. Trebin *et al*, *Phys. Rev.* **20**, 2 (1979).

14th Int. Symp. "Nanostructures: Physics and Technology"
St Petersburg, Russia, June 26–30, 2006

Inversion asymmetry and spin-orbit coupling in III–V semiconductors

J.-M. Jancu[1], G. C. La Rocca[2] and P. Voisin[1]

[1] Laboratoire de Photonique et de Nanostructure, CNRS, route de Nozay, F-91000, Marcoussis, France
[2] Scuola Normale Superiore and INFM, Piazza dei Cavalieri 7, I-56126 Pisa, Italy

Abstract. Multi-band $\mathbf{k}\cdot\mathbf{p}$ Hamiltonians including the spin-orbit interaction are currently used to model the spin properties of nanostructures. These $\mathbf{k}\cdot\mathbf{p}$ models depend on both momentum and spin-orbit coupling parameters between conduction and valence multiplets. We reexamine the $\mathbf{k}\cdot\mathbf{p}$ parameters of the effective 14-band bulk Hamiltonian for III–V semiconductors by comparison with a 40-band tight-binding model. New insights into the spin-orbit coupling of p-bonding and p-antibonding states are gained. These results imply significant revision of accepted values of inversion asymmetry parameters, even in the case of GaAs.

Currently, spin-related effects in semiconductor nanoscale heterostructures are investigated with a view towards developing a new generation of spintronic devices [1,2]. The spin splitting near the zone center in the conduction band of III–V semiconductor compounds, due to bulk inversion asymmetry (BIA), is equal to $\delta = \gamma_c k^3$ [3]. The value of this γ_c parameter for the different III–V compounds is essential for spintronic applications, for instance when using the interference between the Rashba and Dresselhaus terms [2,4,5]. The δ spin splitting has been investigated both experimentally [6,7] in some semiconductors and theoretically [7,8,9], but its value is not yet determined precisely for every compound. This applies in particular to InAs, often considered as a most promising material for spintronics. Clearly, there is presently a need for a systematic and reliable determination of asymmetry-related parameters in bulk III–V semiconductors and their heterostructures. Most theoretical treatments of quantum devices are based on the $\mathbf{k}\cdot\mathbf{p}$ method and its generalization in terms of the envelope-function approximation [13,14]. Hermann and Weisbuch [15] first demonstrated that a 14×14 $\mathbf{k}\cdot\mathbf{p}$ Hamiltonian is required for modelling BIA in the conduction bands. A re-examination of the 14-band model based on all the $\mathbf{k}\cdot\mathbf{p}$ interactions between the Γ_8^v and Γ_7^v valence bands and the Γ_6^c, Γ_7^c, and Γ_8^c conduction bands was discussed more recently [7,8,9,16], including the contributions of remote bands up to quadratic order in k for the states surrounding the direct gap (see Fig. 1 for their definition). The asymmetry-induced dipole matrix element P' between the Γ_6^c and $\Gamma_{7,8}^c$ states and the off-diagonal SO parameter Δ^- coupling Γ_8^c and Γ_8^v (resp. Γ_7^c and Γ_7^v) have a crucial importance for the calculation of γ_c. So far, they have been estimated from perturbative calculations [8] and fitting of a set of data [16] whose values, however, are still controversial [2].

Here, we reexamine the parameterization issue and derive $\mathbf{k}\cdot\mathbf{p}$ parameters from comparison with the $sp^3d^5s^*$ nearest neighbour tight-binding (TB) model including spin-orbit coupling [17]. This 40-band TB model adequately reproduces band parameters [18], chemical trends, and the optical response of III–V semiconductors [19], an important prerequisite for the present study. Dipole moments are calculated within the independent particle approximation using a Peierls-coupling TB scheme [20]. The 14 bands of the $\mathbf{k}\cdot\mathbf{p}$ hamiltonian mentioned above are treated explicitely as in Ref. [16], whereas the influence of the remote bands on the states surrounding the gap are included perturbatively up to second order in k, in accordance

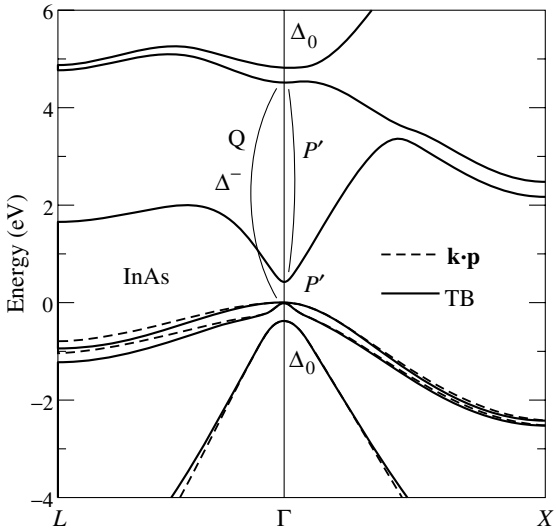

Fig. 1. Band strucure of InAs as calculated with the 40-band TB model (solid lines) and the 14×14 $\mathbf{k}\cdot\mathbf{p}$ model using parameters deduced from the TB hamiltonian.

with the definition of the Hermann–Weisbuch parameter C for the reduced mass m^* of the electrons in the Γ_6^c conduction minimum [15]. Due to the off-diagonal spin-orbit coupling Δ^-, the diagonal elements of the 14-band $\mathbf{k}\cdot\mathbf{p}$ hamiltonian do not correspond to the eigenenergies at Γ. To solve this difficulty, we expand both hamiltonians in the basis of eigenfunctions at Γ without spin-orbit interactions, and obtain $\mathbf{k}\cdot\mathbf{p}$ parameters from the fit. This fitting strategy relies only on the Γ point and its surroundings. As a result, this region of the Brillouin zone is described in the $\mathbf{k}\cdot\mathbf{p}$ approach with the same precision as in the underlying TB model. The resulting tight binding and $\mathbf{k}\cdot\mathbf{p}$ band structures for InAs are compared in Fig. 1. Agreement is essentialy perfect up to $k \approx 0.1\,\text{Å}^{-1}$ except for the upper conduction bands. For these, a better agreement could easily be obtained by including the interactions of Γ_7^c and Γ_8^c with the next higher bands in the $\mathbf{k}\cdot\mathbf{p}$ Hamiltonian, but this would go beyond the standard 14-band $\mathbf{k}\cdot\mathbf{p}$ model [21].

The parameters obtained for some semiconductors are listed in Table 1. For all the semiconductors considered, we find that the momentum matrix elements P and Q are in accordance with typical values used in previous $\mathbf{k}\cdot\mathbf{p}$ models. Conversely, large differences for Δ^- and P' are observed, as compared to former calculations [2,7,9,8,16]. The present values show,

Table 1. $\mathbf{k}\cdot\mathbf{p}$ parameters, with dipole matrix elements and spin-orbit splittings in the notation of Fig. 1.

	AlAs	GaAs	InAs	AlSb	GaSb	InSb
E_0 (eV)	3.130	1.519	0.418	2.38	0.81	0.235
E_0' (eV)	4.55	4.54	4.48	3.53	3.11	3.18
Δ_0 (eV)	0.300	0.341	0.380	0.67	0.76	0.81
Δ_0' (eV)	0.15	0.20	0.31	0.24	0.33	0.46
Δ^- (eV)	−0.19	−0.17	−0.05	−0.41	−0.40	−0.26
P (eVÅ)	8.88	9.88	9.01	8.57	9.69	9.63
P' (eVÅ)	0.34	0.41	0.66	0.51	1.34	1.2
Q (eVÅ)	8.07	8.68	7.72	7.8	8.25	7.83
C (1)	−1.07	−1.76	−0.85	−0.72	−1.7	−1.19

as should be expected, a clear correlation with ionicities and asymmetric charge distribution along the bonds. In particular, we find that Δ^- is nearly proportional to the difference of anion and cation spin-orbit constants and vanishes as it should in the case of diamond-type crystals. For bulk GaAs, for example, the previously accepted values of Δ^- ranging from −0.05 eV [9] to −0.11 eV [8], are much smaller than the present result of −0.166 eV. We note in passing that our values of the Luttinger parameters (although not relevant for the present study) are in excellent agreement with experimental values [18]. The parameter C describing the influence of remote bands on the reduced mass m^* in the conduction band has been discussed intensively [8,15,16,23]. The TB value results from the coupling between the Γ_6^c conduction minimum and the empty d bands at higher energy, and for GaAs, our calculation agrees very well with the parameter extracted from magneto-Raman experiments ($C \approx -1.7$) [24]. In addition, within an $sp^3d^5s^*$ TB model, the influence C' of these bands on the effective Landé factor g^* is approximately proportional to $C\frac{\Delta_d}{E_c-E_d}$, where Δ_d is the spin-orbit splitting of the d-symmetric conduction bands, resulting in values of the order of −0.03.

As expected from their overall agreement, the 40-band TB model and the 14×14 $\mathbf{k}\cdot\mathbf{p}$ Hamiltonian including the influence C of the remote conduction bands give similar results for the conduction band effective mass and Landé factor. Our theoretical results are in agreement with known experimental values of γ_c. For instance, in the case of GaAs, we obtain $\gamma_c = 23.3$ eVÅ^3 [2,7]. On the opposite, for InAs no reliable experimental value exists. Our result, $\gamma_c = 42$ eVÅ^3, is in sharp contrast with previous theoretical estimates [10,11,12]. In addition to the above discussion of the bulk properties, Städele [25] have demonstrated that the $sp^3d^5s^*$ TB model compares well with the measured non-parabolicity and warping of the conduction band in thin GaAs quantum wells, whereas previous $\mathbf{k}\cdot\mathbf{p}$ parametrizations showed some deviations. From the nice agreement between our new $\mathbf{k}\cdot\mathbf{p}$ parametrization and the underlying TB model, we expect an excellent transferability of the bulk $\mathbf{k}\cdot\mathbf{p}$ parameters to calculations of heterostructures in the envelope function approximation.

We have shown that a new parametrization of the 14-band $\mathbf{k}\cdot\mathbf{p}$ Hamiltonian based on comparison with the $sp^3d^5s^*$ tight-binding parametrization captures atomistic details and chemical trends in III–V semiconductors and give a better agreement with known experimental values than previous parametrizations. These inversion asymmetry parameters are of crucial importance for modelling spin plittings in both conduction and valence bands. This revised $\mathbf{k}\cdot\mathbf{p}$ model provides a valid framework for the calculation of spin-related phenomena in III–V semiconductor-based nanostructures.

References

[1] I. Žutić, J. Fabian, and S. Das Sarma, *Rev. Mod. Phys.* **76**, 323 (2004).
[2] R. Winkler, *Spin-orbit coupling effects in two-dimensional electron and hole systems*, (Springer, Berlin 2003).
[3] G. Dresselhaus, *Phys. Rev.* **100**, 580 (1955).
[4] E. A. de Andrada e Silva, *Phys. Rev. B* **46**, 1921 (1992).
[5] S. D. Ganichev *et al*, *Nature* **417**, 153 (2002).
[6] Y. F. Chen *et al*, *Phys. Rev. B* **32**, 890 (1985).
[7] G. E. Pikus, V. A. Marushchank and A. N. Titkov, *Sov. Phys. Semicond.* **22**, 115 (1988).
[8] M. Cardona, N. E. Christensen and G. Fasol, *Phys. Rev. B* **38**, 1806 (1988).
[9] H. Mayer and U. Rössler, *Phys. Rev. B* **44**, 9048 (1991).
[10] E. A. de Andrada e Silva, G. C. La Rocca and F. Bassani, *Phys. Rev. B* **50**, 8523 (1994).
[11] A. Łusakowski *et al*, *Phys. Rev. B* **68**, 081201 (2003).
[12] V. I. Perel *et al*, *Phys. Rev. B* **67**, 201304(R) (2003).
[13] G. Bastard, J.-A. Brum and R. Ferreira, in: *Solid State Physics*, ed. by H. Ehrenreich and D. Turnbull, (Academic, Boston 1991).
[14] D. L. Smith and C. Mailhiot, *Rev. Mod. Phys.* **62**, 173 (1990).
[15] C. Hermann and C. Weisbuch, *Phys. Rev. B* **15**, 823 (1977).
[16] P. Pfeffer and W. Zawadzki, *Phys. Rev. B* **53**, 12813 (1996).
[17] J.-M. Jancu *et al*, *Phys. Rev. B* **57**, 6493 (1998).
[18] I. Vurgaftman, J. R. Meyer and L. R. Ram-Mohan, *J. Appl. Phys.* **89**, 5815 (2001).
[19] J.-M. Jancu *et al*, *Phys. Rev. B* **69**, 241303 (2004).
[20] T. B. Boykin and P. Vogl, *Phys. Rev. B* **65**, 035202 (2002).
[21] S. Richard, F. Aniel and G. Fishman, *Phys. Rev. B* **70**, 235204 (2004).
[22] P. Boguslawsky and I. Gorczyca, *Semicond. Sci. Technol* **9**, 2169 (1994).
[23] T. E. Ostromek, *Phys. Rev. B* **54**, 14467 (1996).
[24] G. Ambrazevicius, M. Cardona and R. Merlin, *Phys. Rev. Lett.* **59**, 700 (1987).
[25] M. Städele *et al*, *J. Appl. Phys.* **91**, 9435 (2002).

14th Int. Symp. "Nanostructures: Physics and Technology"
St Petersburg, Russia, June 26–30, 2006

Electrical and optical properties of InAs/InSb/GaSb superlattices for mid-infrared applications

P. Christol[1], Y. Cuminal[2], J. B. Rodriguez[1], A. Joullié[1], V. K. Kononenko[3], A. A. Afonenko[4] and D. V. Ushakov[4]

[1] CEM2-UMR CNRS 5507, Université Montpellier 2, 34095 Montpellier, France
[2] LASMEA, UMR CNRS 6602, Université Clermont II, 63177 Aubière, France
[3] Stepanov Institute of Physics NASB, Fr. Scorina Pr., 70, 220072 Minsk, Belarus
[4] Belarussian State University, Fr. Scorina Pr., 4, 220050 Minsk, Belarus

Abstract. Electrical and optical investigations performed on type-II broken gap InAs/InSb/GaSb superlattices grown on GaSb substrate are reported. Inter-miniband transitions are identified by low temperature (80 K) spectra and photoresponse measurements on mesa pin diodes exhibited cut-off wavelength at around 6 μm whatever the temperature between 90 and 290 K. Hall measurements have been carried out on 300 periods SL grown on semi-insulating GaAs substrates. The variations versus temperature of carrier concentration and Hall mobility display a change in the type of conductivity of the SL at around 190 K.

Introduction

Binary InAs/GaSb superlattices (SLs) grown on GaSb substrates form an ideal material system for the fabrication of short-period SLs with broken-gap type-II band alignment. They can achieve effective energy gaps that are narrower than that of InAs itself, down to zero. Such narrow gaps are of great interest for the mid- (3–5 μm) and long-wavelength infrared region (8–12 μm) applications, as detectors [1–3], as well as emitters [4–5]. In this communication we report on some electrical and optical characterizations of InAs(N MLs)/InSb (1 ML)/GaSb(N MLs) superlattices suitable for mid-infrared applications.

1. MBE growth of InAs/InSb/GaSb superlattices

A set of SLs with $N = 8, 10, 15$ monolayers (MLs) were grown on (100) GaSb by solid source molecular beam epitaxy, using As2 an Sb2 valve cracker cells. The growth temperature of the SL was 390° C [6]. The quality of the SLs was strongly improved by inserting into each InAs on GaSb interface one ML of InSb, as it shown in the Fig. 1 where high resolution X-ray diffraction spectrum of a 300 periods SL structure with total thickness of 1.92 μm is presented. This strain compensation procedure slightly changes the band alignment at the InAs/GaSb interface, inducing a decrease of the fundamental absorption transition C1-HH1 between the heavy hole and electron minibands.

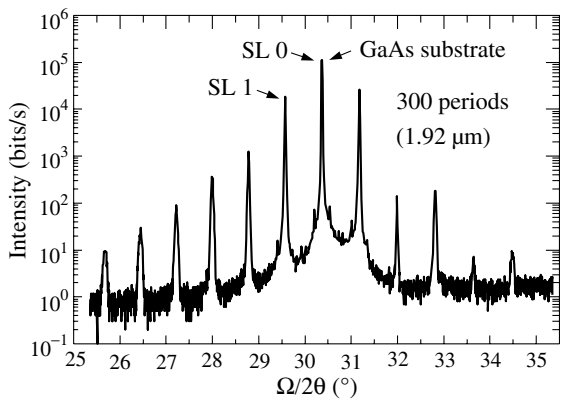

Fig. 1. HRXRD scan of a 300 periods InAs/InSb/GaSb (10/1/10) strain compensated SL.

2. Optical and electrical properties

For optical transmission measurements, SLs were epitaxied on n-type GaSb substrates, which are much more transparent than p-type ones. Absorption coefficients, deduced from transmission data performed at 80 K, are shown in Fig. 2 for three SLs having a number of $N = 8$, 10 and 15 MLs. The absorption coefficient is high (e.g. for a SL with $N = 10$ MLs, $\alpha = 3800$ cm^{-1} at a wavelength of 5 μm, 5500 cm^{-1} at 3 μm) [7]. That means that, in this indirect type II structure, the electron-hole wavefunction overlap is high near the hetero-interfaces. In addition to the C1-VH1 transition between fundamental electron and heavy-hole minibands, the other observed excitonic absorption peaks in the spectrum are due to excited inter-miniband transitions C1-VL1 and C1-VH2 which associate the lowest electron subband (C1) to the light-hole subband (VL1) and to the second heavy-hole miniband (VH2), respectively.

The photo-response (in current) was studied from mesa pin diodes grown on p-type GaSb substrates. In the case of GaSb (10 MLs)/InAs(10 MLs)/InSb(1 ML) SL structure, an impor-

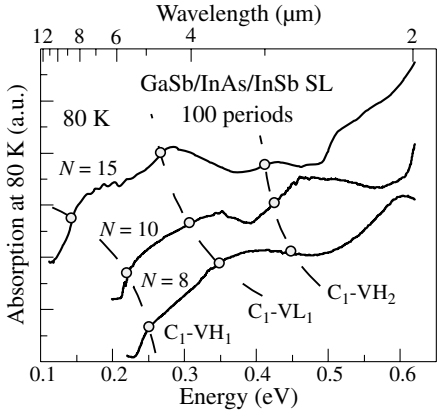

Fig. 2. Absorption spectra of 100 periods GaSb(N)/InAs(N)/InSb(1) SLs with $N = 8$, 10, 15 MLs. Circles show the calculated optical transitions while doted lines are only eye guide.

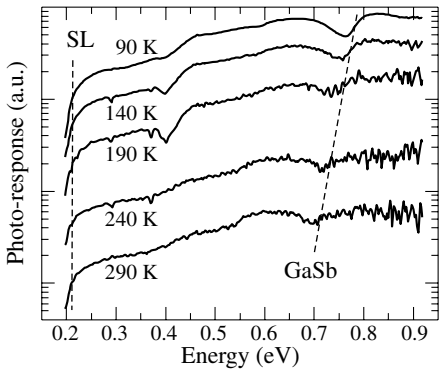

Fig. 3. Spectral responsivity at zero bias of a 250 periods GaSb(10 MLs)/InAs(10 MLs)/InSb(1 ML) SL at different temperatures.

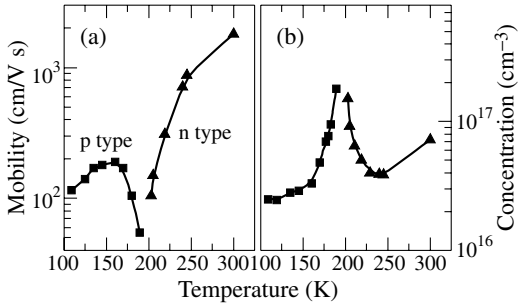

Fig. 4. Carrier mobility (a) and concentration (b) measured under a magnetic filed of 0.3 Tesla.

tant signal was obtained up to room temperature (Fig. 3). We can note that the cut-off wavelength, close to 6 μm, is slightly dependent of the temperature, in contrary to the GaSb gap evolution. This peculiarity is a signature of a broken gap type-II band alignment. Electroluminescence was observed on the same pin devices, biased in forward as well as in reverse polarisations.

Resistivity and Hall measurements were carried out on 300 periods SLs grown on (100) semi-insulating GaAs substrates. The Hall voltage linearly varies with the magnetic field up to 1 Tesla, similarly to a bulk material. Typical variations versus temperature of carrier concentration and Hall mobility are presented Fig. 4.

A change in the type of conductivity of the SL is observed at around 190 K. The superlattice is n-type at high temperature, with at 300 K a carrier concentration $n = 7\times10^{16}$ cm^{-3} and a mobility of 1800 cm^2/V s, while is p-type at low temperature, with at 100 K a carrier concentration $p = 2.5\times10^{16}$ cm^{-3} and a mobility of 100 cm^2/V s. This change in conductivity was already reported by other groups, but at lower temperatures (140 K [1] and 23 K [8]) and can be attributed to the presence of carriers arising from the surface states [9].

Acknowledgements

This work is partially supported by a cooperation project CNRS/NASB 2005-06 No. 18086. The authors would like to thank S. K. Haywood, Hull University, for low temperature absorption measurements.

References

[1] A. Rogalski *et al*, *Infrared Phys. Technol.* **48**, 39 (2006).
[2] M. Walther *et al*, *J. Crystal Growth* **278**, 156 (2005).
[3] J. B. Rodriguez *et al*, *Electron. Lett.* **41**, 362 (2005).
[4] A. N. Baranov *et al*, *Appl. Phys. Lett.* **71**, 735 (1997).
[5] D. Hoffman *et al*, *Appl. Phys. Lett.* **87**, 201103 (2005).
[6] J. B. Rodriguez *et al*, *J. Crystal Growth* **274**, 6 (2005).
[7] J. B. Rodriguez *et al*, *Physica E* **28**, 128 (2005).
[8] H. J. Haugan *et al*, *J. Crystal Growth* **278**, 198 (2005).
[9] A. Gin *et al*, *Appl. Phys. Lett.* **84**, 2037 (2004).

14th Int. Symp. "Nanostructures: Physics and Technology"
St Petersburg, Russia, June 26–30, 2006

High resolution X-ray diffraction characterization of MnF_2 epitaxial films with metastable orthorhombic phase

R. N. Kyutt[1], A. G. Banshchikov[1,2], A. K. Kaveev[1], N. S. Sokolov[1], T. Eguchi[2], Y. Ohtake[2], M. Tabuchi[2] and Y. Takeda[2]

[1] Ioffe Physico-Technical Institute, St Petersburg, Russia
[2] Venture Business Laboratory, Nagoya University, Nagoya 464-8601, Japan

Abstract. Metastable orthorhombic phase of MnF_2 grown epitaxially on a CaF_2(110)/Si(001) template was studied by High Resolution X-ray Diffractometry (HRXRD). We found strong influence of buffer uniaxial anisotropy on growth mode and crystalline characteristics of MnF_2 orthorhombic phase. Lattice parameter temperature dependence measurements enabled estimation of the Neel temperature of this metastable phase.

Introduction

It has been recently demonstrated that using CaF_2 buffer layer quite thick (up to 1.5 μm) MnF_2 epitaxial films having metastable orthorhombic phase can be grown on Si substrates [1]. These films are attractive for studies of very important in numerous applications exchange bias effect in ferromagnetic (FM) — antiferromagnetic (AFM) heterostructures [2]. It has been shown that this effect strongly depends on atomic and magnetic structure of the FM-AFM heterojunction. Though MnF_2 bulk crystals having rutile type of crystal structure are well known antiferromagnetics, magnetic ordering in its metastable orthorhombic phase still remains unexplored. Till recently there was only indirect evidence for its AFM ordering at low temperatures. No high resolution X-ray diffraction studies were reported. In this work, we present detailed structural studies of the films, including HRXRD measurements of the lattice parameter temperature dependence, which enabled evaluation of Neel temperature (T_N). This estimate agrees with very recent direct neutron diffraction measurements [3].

1. Experimental

The structures were grown on Si(001) substrates by molecular beam epitaxy (MBE). Before the growth of MnF_2 film, as thick as 1.5 μm, a CaF_2 buffer layer with 300 nm thickness was deposited at 800 °C on atomically clean silicon substrate. Morphology of the layer demonstrated strong uniaxial anisotropy with extended on several microns grooves and ridges with typical cross-section dimension 20–50 nm. The MnF_2 film was grown at 300 °C and covered by thin (2–3 nm) CaF_2 cap layer at room temperature.

The structural study of MnF_2 films was performed at Nagoya University using ATX-G (Rigaku, Co) diffractometer in double crystal setting and CuKα-radiation. The $\theta-2\theta$ curves were measured in symmetrical Bragg geometry in the (10–60°)θ range. Measurements have been carried out for two orthogonal azimuths of the samples: parallel (p) and normal (n) to the direction of the CaF_2 ridges. Diffraction peak identification provides the structural state and phase content in the films. The θ-scan curves were measured for individual reflections also.

The structural perfection of the layer studied was estimated on the basis of the peak width analysis. Comparing the FWHM-values for reflections of 2 orders from the crystallites of the same structure and orientation, we obtain the average strain inside the crystallites and their size normal to the surface from the $\theta-2\theta$-scan peaks, misorientation (tilt) of the crystallites and their lateral size from θ-scan peaks [4].

The XRD measurements of lattice expansion coefficients were carried out at the BL-4C beam-line of KEK Photon Factory (Tsukuba, Japan) using radiation with wavelength 1.54 Å. Angular positions of the reflections 400 and 040 in skew geometry were measured to obtain thermal expansion in **a**- and **b**-directions respectively.

2. Structural state of MnF_2 epitaxial layer

Two representative structures with thick metastable MnF_2 layers have been studied. In Fig. 1 $\theta-2\theta$-scan for one of these structures (#5411) is shown.

It was shown earlier that at above growth condition CaF_2 grows on Si(001) with ⟨110⟩ orientation along the surface normal. Therefore one can expect that MnF_2 grown on this buffer layer has the same growth direction. Indeed we see on diffraction pattern in addition to the Si(004) and Si(006) peaks, the strong CaF_2(220) and CaF_2(440) peaks from the fluorite buffer layer. Relatively weak peak at $\theta = 14.01$ is likely due to small inclusions of CaF_2 (111) orientations. The other reflections belong to the MnF_2 orthorhombic (α-PbO_2-type) and tetragonal (rutile type) structural modifications. The strongest among them 110, 220, 330 and 440 reflections are due to the orthorhombic phase with the (110) planes parallel to the same planes of the buffer layer and (001) plane of Si substrate. Less intense peak $\theta = 24.86$ belongs to (202) reflection of the same orthorhombic metastable phase. Considerably less intense 110, 011, 220 and 330 reflections belonging to the crystallites of stable rutile type phase can be also identified.

For the phase with orthorhombic unit cell, crystallites of three possible orientations may be grown on (110) fluorite plane: [110], [101] and [011]. It follows from the diffraction pattern that the dominating among them are the [110]-crystallites and only small

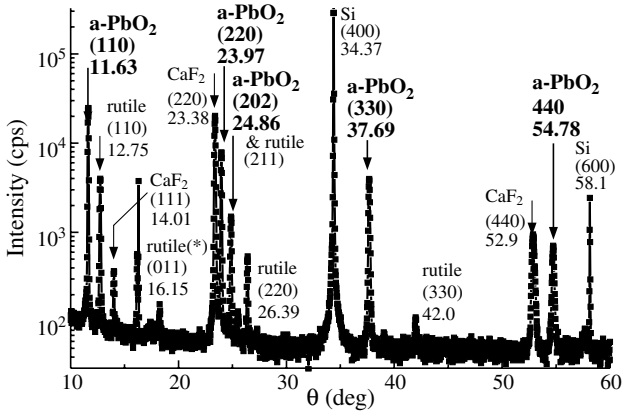

Fig. 1. Diffraction pattern ($\theta-2\theta$-scan) for epitaxial structure $CaF_2/MnF_2/CaF_2$/(001)Si measured in symmetrical Bragg geometry.

portion of [101] oriented fragments presents in the MnF_2 film studied. No [011]-crystallites are detected. This fact can be explained by the misfit values between the CaF_2-buffer and MnF_2-layers of different orientation. The $(\mathbf{a}+\mathbf{b}, \mathbf{c})$ plane unit cell of MnF_2 has the lowest misfit with $(\mathbf{a}\sqrt{2}, \mathbf{a})$ unit cell of CaF_2 in both directions in plane of interface. On other hand the [001] oriented MnF_2 has the highest misfit in one direction.

Because MnF_2 layers have been grown on strongly anisotropic ridged and grooved CaF_2 buffer layer, it was attractive to check whether this anisotropy was inherited by MnF_2 epitaxial layer. It was found that for these two azimuths, $\theta-2\theta$ scans are very similar but ω-scans showed remarkable difference (Table 1).

Table 1. Groove orientation and main reflection characteristics.

Beam & groove orientation	**n** azimuth	**p** azimuth
Reflection	Position (ω)/Width($\Delta\omega$), (deg)	
(110) α-PbO_2	11.54/**1.34**	11.56/**0.61**
(220) α-PbO_2	23.92/**0.97**	23.90/**0.61**
(202)-PbO_2 & (211)-rutile	24.86/1.60	25.25/$\sim$1.2
(220) CaF_2	23.33/0.47	23.32/0.57

Let us consider the dominant orthorhombic MnF_2 phase of (110) orientation. One can see that unlike CaF_2 buffer layer, the widths of ω-curves for 110 and 220-reflections depend on the azimuth: for the case when the diffraction plane is orthogonal to the direction of the CaF_2 ridges (**n**-azimuth) it is considerably broader than that for the parallel (**p**-azimuth). The larger FWHM value for the first order reflection indicates contribution of size effect to peak broadening. The values of the strain, tilt and dimensions in two directions obtained from the analysis of the peak broadening for this phase are presented in Tab. 2

Table 2. Crystallite parameters for orthorhombic MnF_2 layer obtained from HRXRD data.

Beam position	Strain 10^{-3}	Tilt 10^{-3}	τ_z nm	τ_x nm
Normal ridges-**n**	1.8	7.1	200	20
Parallel ridges-**p**	1.8	5.3	200	> 1000

It is seen from the Table 2 that the crystallite lateral dimension τ_x in direction normal to stripes is much smaller than in parallel direction and coincides with the average distance between the CaF_2 ridges. Moreover mean misorientation (tilt) in n-orientation is larger than that of in p-orientation. Hence we can see an influence of grooved and ridged surface morphology of CaF_2(110) buffer layer on growth mode of MnF_2-layer. Most probably the ridges promote generation of the dislocation walls (small angle boundaries) separating the growing MnF_2 layer regions.

The θ-scan peaks for other phases ([101] oriented orthorhombic and rutile) are considerably wider than those for dominate [110] orthorhombic modification indicating their much lower structural perfection. This can also be explained by larger misfit between these phases and CaF_2 buffer layer.

3. Low temperature thermal expansion of MnF_2

It is known that change of the solid-state structure causes the changes in α (coefficient of expansion). Therefore $\alpha(T)$ dependence gives us the method of determination of a phase transition temperature. In particular, at $T = T_N$ one can see the sharp maximum on $\alpha(T)$ curve and estimate T_N [5]. To estimate T_N of MnF_2 orthorhombic phase a thermal dependence of **a** and **b** lattice parameters were measured. The dependence in [00l] direction is defined by the expression $\Delta L/L = -\Delta\theta/\mathrm{tg}\theta$, where θ — Bragg angle for the corresponding

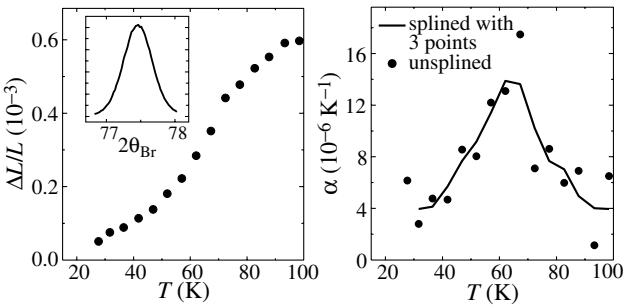

Fig. 2. The $\Delta L/L(T)$ and $\alpha(T)$ dependences for 400 reflection. The solid line at right corresponds to the spline of $\alpha(T)$. The typical 400 reflection is shown in the inset.

diffraction maximum in $\theta-2\theta$ diffraction curve, L — interplanar spacing between the equivalent crystallographic planes (00l). Thermal expansion coefficient $\alpha(T) = L^{-1}dL/dT$ in the same direction one can calculate from the $\theta(T)$ experimental dependence.

The behavior of $\Delta L/L(T)$ and $\alpha(T)$ dependences in Fig. 2 are fairly similar to the behavior known for antiferromagnetic CoF_2 and FeF_2 [5], and rutile-type MnF_2 [6]. The shoulder observed in $\Delta L/L(T)$ and maximum in $\alpha(T)$ indicate paramagnetic-antiferromagnetic phase transition at T_N. These peculiarities are clearly seen in 65–70 K temperature range for α-PbO_2 structure of MnF_2. This fact allows us to suppose closeness of T_N to the value known for the rutile-type structure of MnF_2. From data shown at left part of Fig. 2, we have estimated $\Delta L/L \sim 6\cdot10^{-4}$ along the **a** axis of α-PbO_2 structure in 20–100 K temperature range. The value $\Delta L/L \sim 2\cdot10^{-4}$ along the **b** axis, obtained from measuring of 040-reflection, is remarkably less than that of along the **a** axis.

4. Conclusions

It was shown that the crystal structure of MBE grown MnF_2 epitaxial layers is influenced by the grooved and ridged surface of CaF_2 buffer layer. HRXRD studies demonstrated that crystallite dimensions along the ridges are much larger than that for the orthogonal direction. Estimated from the temperature dependence of the lattice parameter, the Neel temperature of the metastable orthorhombic phase appeared to be close to that of bulk MnF_2 crystals with the tetragonal structure.

Acknowledgements

This work has been supported by the Russian Foundation for Basic Research (Grants Nos. 05-02-16451 and 06-02-17307) as well as RAS programs "Influence of crystal and electronic structure on solid state properties" and "Spin dependent phenomena in solids and spintronics". Support of Venture Business Laboratory of Nagoya University during visit of A. G. Banshchikov in November 2005 is greatly appreciated.

References

[1] A. K. Kaveev *et al*, *J. Appl. Phys.* **98**, 013519 (2005).
[2] J. Nogues *et al*, *J. Magn. Magn. Mater.* **192**, 203 (1999).
[3] I. V. Golosovskii *et al*, *Pis'ma ZETF* **83** (4), 185 (2006).
[4] V. V. Ratnikov *et al*, *J. Appl. Phys.* **88**, 6252 (2000).
[5] C. Ramos *et al*, *Phys. Rev. Lett.* **65** (23), 2913 (1990).
[6] P. Nordblad *et al*, *J. Magn. Magn. Mater.* **23** 333 (1981).

14th Int. Symp. "Nanostructures: Physics and Technology"
St Petersburg, Russia, June 26–30, 2006

Interface roughness scattering in type II broken-gap GaInAsSb/InAs single heterostructures

M. P. Mikhailova, K. D. Moiseev, T. I. Voronina, T. S. Lagunova, A. F. Lipaev and Yu. P. Yakovlev
Ioffe Physico-Technical Institute, St Petersburg, Russia

Abstract. We present experimental study of the influence of interface roughness (IFR) scattering on mobility in the type II broken-gap p-GaInAsSb/p-InAs heterostructures with self-consistent quantum wells and 2D-electron channel at the interface. It was shown that IFR scattering dominates carrier mobility. Low-temperature mobility decreases as $\mu \sim d^2$ by increasing acceptor (Zn) doping level of quaternary layer. Quantum well width at the interface changes from 50 to 400 Å. Parameters of IFR scattering, the height $\Delta = 12$ Å and correlation length $\Lambda = 100$ Å were evaluated from technological and photoluminescence data.

Introduction

The interface roughness (IFR) scattering is usually considered as dominating for narrow quantum wells because the mobility μ limited by this mechanism was assumed to decrease with quantum well thickness d_w according to the law $\mu \sim d^6$ [1–5]. The dependence $\mu \sim d^6$ for thin quantum wells was predicted theoretically in [1] and then considered for quantum well structures in [2–4]. It was shown in [3] that the roughness limited mobility μ_r can be expressed as: $\mu_r = \text{const} d_w^6/\Delta^2\Lambda^2 g(\Lambda, N_s, T)$, where d_w is well width, Δ is the height roughness, g is a function of correlation length Λ, N_s is sheet electron concentration and T is temperature. Key parameters to characterize IFR are Δ and Λ. The $\mu \sim d_w^6$ law was experimentally observed in Si [2], GaAs/GaAlAs [3], InAs/AlSb [5] and HgTe-CdTe [6] quantum well structures grown by MBE.

MBE grown quantum wells have a roughness about monatomic fluctuations. This results in broadening of photoluminescence spectra and substantial decrease in mobility, particularly in the case of thin quantum wells [5]. For wide-gap materials a good approximation was used [3] to evaluate $\delta E/\delta d_w$ using the simple model for a box with infinite barriers which implies $\delta E/\delta d_w - (\pi h)^2/d_w^3 m_n$ and a mobility $\mu_n \sim d^6$. However, this approach is inadequate for narrow-gap heterostructures and wider quantum well, where weaker dependence on quantum well thickness can be observed [7].

In this paper we consider for the first time interface roughness scattering mechanism for the narrow gap type II broken GaInAsSb/InAs heterostructures grown by liquid phase epitaxy (LPE) with high quality abrupt heterointerface. Electron channel with high electron mobility up to 60 000–70 000 cm^2/V s was found in isotype p-GaInAsSb/p-InAs broken-gap heterostructures [8]. It was shown that electron channel is placed on the InAs-side, so the effective mass $m^* = 0.026m_0$ was found from Shubnikov–De Haas oscillation experiment at $T = 1.5-4.2$ K at high magnetic field. Weak temperature dependence of μ_H was obtained in the range 4.2–200 K and it was shown that mobility decreases with quantum well width as $\mu_H \sim d^2$. Parameters of interface roughness for GaAsSb/InAs heterostructure under study $\Delta = 12$ Å (3 monolayer) was evaluated using our technological data and the broadening of photoluminescence spectrum at low temperature [9] and correlation length $\Lambda \approx \pi/2k_F \approx 100$ Å, where k_F is Fermi wave vector. Strong reducing of mobility at the interface with heavy acceptor (Zn) doping of quaternary GaInAsSb layer was observed. It can be ascribed to depletion of the electron channel due to its narrowing and to transition from semimetal to semiconductor conductivity.

1. Experimental results and discussion

The single $Ga_{1-x}In_xAs_ySb_{1-y}$/InAs heterostructures were obtained by LPE growth of quaternary GaInAsSb solid solutions on p-InAs(100) substrates with concentration $p = 8\times10^{16}$ cm^{-3} and with quaternary layer composition lying in the range $0.06 < x < 0.22$.

The heteroboundary quality and possible mechanism of interface formation were examined in type II heterostructure using a combine investigation including X-ray diffraction and transmission electron microscopy studies. From the TEM data we established that the InAs-GaInAsSb bottom interface is planar and has a thin transition layer 3–4 monolayers (10–12 Å, here monolayer is $a_0/2 = 3$ Å) at bottom interface. The roughness of top interface was about 500 Å. The density of the surface states at the heteroboundary N_{ss} was low due to the complete lattice matching of the epilayer to the substrate. An estimation sheet concentration from the relation $N_{ss} = 8\Delta a/a^3$ eV^{-1} yields $N_{ss} \sim 4.3\times10^{11}$ cm^{-2} at $\Delta a/a = 2\times10^{-4}$. The photoluminescence of quaternary $GaIn_{0.16}AsSb$/p-InAs solid solution with undoped quaternary layer and quantum well width at the interface $d_w \approx 100$ Å was studied in the range 7–77 K [9]. The full width at half maxima (FWHM) did not exceed 11 meV and 26 meV at 7 and 77 K respectively, which confirms high quality of the epilayers. The broadening of PL spectra is due to well size fluctuation in an atomic layer scale [10] and in our case corresponds to $\Delta\lambda \approx 22$ Å, which agrees with data of double X-ray diffraction. It was established that energy band diagram of GaInAsSb/p-InAs heterostructure is of type II with a broken gap alignment (like the InAs-GaSb system), with energy gap value between the conduction band of InAs and higher lying valence band of GaInAsSb quaternary layer $\Delta E = 60-80$ meV depending on solid solution composition and doping level of contacting materials. In the $GaIn_{0.16}As_{0.22}Sb$/p-InAs heterojunction a 2D-electron gas is formed in the quantum well at the InAs side and holes left behind near the heterointerface of the GaInAsSb epilayer side in the resulting triangular well. The intrinsic electric field formed at the interface determines the carrier population density in the semimetal channel maintained by the bulk Fermi level E_F of the GaInAsSb/InAs heterojunction at thermodynamic equilibrium. The self-consistent

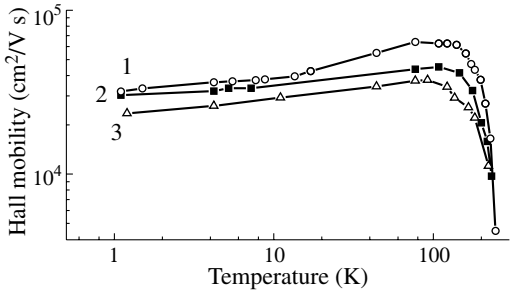

Fig. 1. Dependence of Hall mobility on temperature in the single type II broken-gap $GaIn_{0.16}As_{0.22}Sb$/p-InAs heterostructure at slight doping level of GaInAsSb: 1 — undoped, 2 — doped with Te, 3 — doped with Zn.

quantum wells for electrons and holes are near the heterointerface. A striking fact was the observation of electron-type conductivity in the p-GaInAsSb/p-InAs heterojunction under study with undoped and slightly doped quaternary layer. An electron channel with high mobility (50 000–70 000 $cm^2/V\,s$ at $T = 4.2-200$ K was found in isotype p-GaInAsSb/p-InAs heterostructures. Hall coefficient and Hall mobility were studied experimentally at weak magnetic fields. Fig. 1 represents Hall mobility versus temperature for the three samples of p-$GaIn_{0.16}As_{0.22}Sb$/p-InAs heterostructure with undoped and Zn-doped level. High Hall mobility value and its weak temperature dependence in the wide temperature range of the 1.5–200 K were obtained. The high Hall mobility value and its weak temperature dependence were similar to those reported in [11] for GaSb/InAs/GaSb single quantum well heterostructure with 2D-electron channel at the interface grown by MBE and with thick quantum wells ($d_w \approx 200$ Å for InAs). Weak temperature dependence of mobility was observed only in the temperature range 4.2–60 K.

Figure 2 demonstrates the dependence of Hall mobility on the doping level of quaternary layer by Zn in the range $5\times10^{-4}-10^{-2}$ at%. For comparison in Fig. 2 the mobility of p-GaInAsSb solid solution grown by LPE on p-GaSb substrate is shown. It reached $\mu_H = 3000\,cm^2/V\,s$ only. The parameters of the wells on the interface and concentration of 2D-carriers were established from the equation: $d_w = [(3/4)^2 a_B/\pi N_s]^{1/3}$ [10]. The decreasing of mobility at $T > 200$ K is due to polar optical phonon scattering in bulk InAs. The drastic mobility drop under heavy doping levels (Zn $> 10^{-2}$ at%) can be caused by swallowing and depletion of the electron channel upon mobile-carrier localization by random potential fluctuation at the heterointerface and increasing role of interface roughness scattering. Fig. 3 demonstrates Hall mobility μ_H in the electron

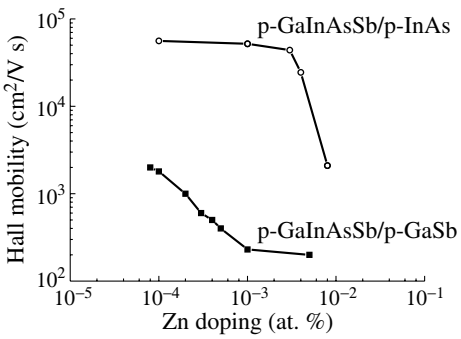

Fig. 2. Dependence of Hall mobility in a single type II heterostructure on the doping level of GaInAsSb with Zn at $T = 77$ K.

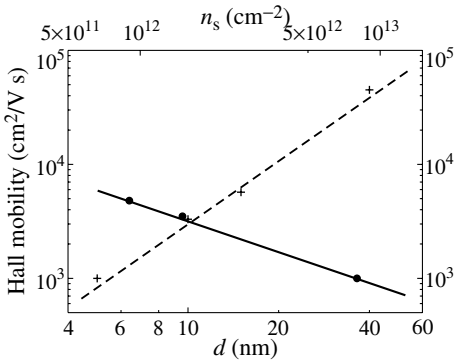

Fig. 3. Hall mobility vs width of the electron channel and 2D-electron concentration at single type II broken-gap GaInAsSb/InAs interface at acceptor doping of solid solution.

channel as a function of sheet electron concentration N_s (solid line). The dashed line plots the dependence of the mobility μ_H on the electron channel width at the interface. It corresponds to $\mu_H \sim d^2$.

2. Conclusion

We found Hall mobility changed as $\mu_H \sim d^2$ with electron channel width decreases by increasing acceptor doping content. It is similar with results for semimetal narrow-gap GaInSb/InAs superlattices, where $\mu \sim d^{2.5}$ was found [12]. It was shown theoretically in [7] that strong dependence $\mu \sim d^6$ predicted in [1, 2] is correct only for thin quantum wells. But for wider wells more weak dependence of mobility on quantum well width should be observed due to IFR scattering.

In conclusion, we demonstrated experimentally that in type II broken-gap p-GaInAsSb/p-InAs heterostructures grown by LPE with electron channel at the interface high mobility is determined by interface roughness scattering in the wide temperature range 4.2–200 K. Parameters of the interface roughness such as the height $\Delta = 12$ Å and correlation length $\Lambda = 100$ Å were established using technological and photoluminescence data.

Acknowledgements

We thank the Russian Foundation For Basic Research for the support of our work through grants 04-02-17655 and 06-02-16470.

References

[1] A. V. Chaplik, M. V. Entin, *Zhrn. Experim. Theor. Fiziki (JETP)* **55**, N 3(9), 991 (1968).
[2] A. Gold, *Phys. Rev.* **35**, 723 (1987).
[3] H. Sakaki, *et al*, *Appl. Phys. Lett.* **51**, 1934 (1982).
[4] T. Noda, M. Tanaka, H. Sakaki, *J. Chryst Growth* **111**, 348 (1991).
[5] C. R. Bolognesi, H. Kroemer, J. H. English, *Appl. Phys. Lett.* **61**, 213 (1992).
[6] J. R. Meyer, *et al*, *Phys. Rev.* **B46**, 4139 (1992).
[7] K. Schmaltz, *et al*, *Phys. Rev.* **54**, 16799 (1996).
[8] M. P. Mikhailova, K. D. Moiseev, Yu. P. Yakovlev, *Semicond. Sci. Technol.* **19**, R109–R128 (2004).
[9] K. D. Moiseev, *et al*, *J. Appl. Phys.* **90**, 2813 (2001).
[10] L. Goldstein, *et al*, *Jpn. J. Appl. Phys.* **22**, 1489 (1983).
[11] P. S. Kop'ev, *et al*, *Sov. Phys. Semicond.* **34**, 317 (1990).
[12] C. A. Hoffman, *et al*, *Solid-State Electr.* **37**, 1203 (1994).

14th Int. Symp. "Nanostructures: Physics and Technology"
St Petersburg, Russia, June 26–30, 2006

Plasmon spectrum of $C_{60}F_{18}$ and its transformation under electron irradiation

V. V. Shnitov[1], *V. M. Mikoushkin*[1], Yu. S. Gordeev[1], S. Yu. Nikonov[1], O. V. Boltalina[2] and I. V. Goldt[2]

[1] Ioffe Physico-Technical Institute, St Petersburg, Russia
[2] Chemistry Department, Moscow State University, Moscow, 119899, Russia

Abstract. Single and collective electron excitation spectrum of solid fluorinated fullerene $C_{60}F_{18}$ has been investigated by electron-energy-loss spectroscopy for the first time. The spectrum proved to be very similar to that of fullerite C_{60}. The similarity was shown to be connected with spatial molecular structure being characterized by concentration of fluorine atoms in one segment of fullerene sphere. Transformation of π-plasmon spectrum under electron irradiation was studied, and extremely high rate of $C_{60}F_{18}$ modification was revealed. The modification is caused by molecular fragmentation. The conclusion has been made that $C_{60}F_{18}$ films may be perspective as an electron-beam resist for nanolithography.

Introduction

Stability of molecules to fragmentation induced by radiation and particle impact is their important physical characteristic. A lot of studies have been devoted recently to fragmentation of fullerenes, which proved to be exceptionally stable molecules [1]. Information about stability of fullerene derivatives, such as fluorinated fullerenes $C_{60}F_x$ ($x = 18, 24, 36, 48$), is much scanty. Though fluorinated fullerenes are considered to be thermodynamically rather stable molecules both in the gas and solid states [2], there is no direct information about fragmentation and destruction of this object by particles or radiation. At the same time this information can be important for applied problem of electron lithography with lateral nanoresolution [3]. It is a known fact now that fragmentation of fullerenes and modification of fullerite (solid C_{60}) is initiated by excitation of valence electrons [1]. Therefore information about single and collective electron excitations is important not only in respect to fundamental knowledge about electronic structure of material, but also for understanding mechanisms of its modification, which are needed for enhancing the lateral resolution of electron lithography. The conducted research covers the lack of this information. Spectrum of single and collective electron excitations of $C_{60}F_{18}$ was measured both for pristine material and for the material modified by electron irradiation. Extremely high rate of destruction of these molecules was revealed which seems perspective for using this material in dry nano-lithography as an electron beam resist.

Experimental details

Fluorinated fullerite $C_{60}F_{18}$ films were grown *in situ* by thermal deposition of $C_{60}F_{18}$ powder [2] produced in Chemistry Department of Moscow State University onto silicon sub-strates in high vacuum ($P \sim 5\times10^{-9}$ Torr). Pristine material and influence of electron irradiation on atomic and electron structure of the film was studied by electron energy loss spectroscopy (EELS) and Auger electron spectroscopy (AES). The film was irradiated by the beam of electrons with the energy $E_0 = 500$ eV under the experimental conditions similar to those used in our previous studies of C_{60} films [3,4].

Single electron and π-plasmon excitations of the $C_{60}F_{18}$

EEL-spectrum of $C_{60}F_{18}$ was found to strongly depend on the irradiation doze of diagnostic electron beam. Therefore in order to get a correct spectrum, the current of the bombarding electrons was gradually decreased until identical spectra were obtained. Figure 1 (curve 1) shows EEL-spectra of pristine $C_{60}F_{18}$ and C_{60} in the energy loss region, which contains narrow molecular peaks of single-electron excitations superimposed on broad π-plasmon peak. Zero energy losses correspond to the center of the peak of elastically scatted electrons. The distance from "0" energy loss to the first raise of the EEL-spectra gives the band gap of $C_{60}F_{18}$ and C_{60}: 2.4 and 1.8 eV correspondingly. Spectra of these materials demonstrate unexpected similarity. Peak positions of the molecular single-electron excitations for $C_{60}F_{18}$ (3.6; 5.05 eV) and C_{60} (3.75; 4.85 eV) are very close to each other.

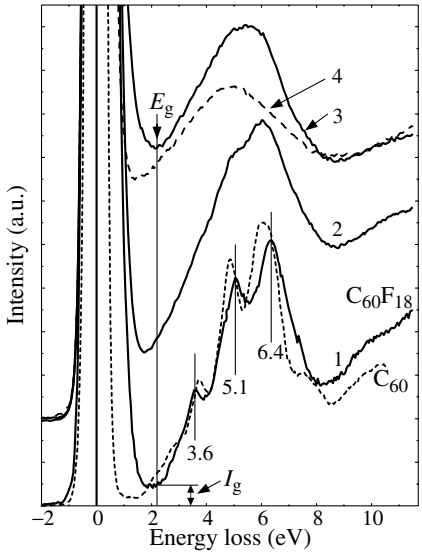

Fig. 1. EEL spectra of pristine C_{60} and $C_{60}F_{18}$ (curves 1) and of $C_{60}F_{18}$ irradiated with different doses of electrons: $Q = 0.05$ C/cm^2 (curve 2), $Q = 40$ C/cm^2 (curve 3). Curve 4 corresponds to the EEL spectrum of amorphous carbon.

The π-plasmon energy of $C_{60}F_{18}$ (6.4 eV) is also very close to that of C_{60} (6.15 eV), though the number (N) of π-electrons in $C_{60}F_{18}$ is one-third smaller than in C_{60}. One would expect the plasmon energy in $C_{60}F_{18}$ being less to 1.2 eV ($\hbar\omega \sim N^{1/2}$) as compared to that in C_{60}. This contradiction can be understood if one takes into account spatial atomic structure of $C_{60}F_{18}$ molecule (Fig. 2 [2]) and the fact that plasmon spectrum of fullerite film is rather close to that of local plasmon of separate molecule [4]. According to Figure 2, fluorine atoms are concentrated in one segment of fullerene sphere. Thus, the density of π-electrons, which defines the plasmon energy, does not change significantly on the unoccupied hemisphere of the cage. On the other hand, the expected depletion of σ-electron

Fig. 2. Atomic structure of $C_{60}F_{18}$.

density on the "nonfluorinated" part of $C_{60}F_{18}$ molecular cage should weaken an interaction between σ- and π-electron subsystems and, thereby, provide some increase (6.15 $\rightarrow$ 6.4 eV) of π-plasmon energy in the individual $C_{60}F_{18}$ molecules.

Electron induced destruction of $C_{60}F_{18}$ and π-plasmon spectrum transformation

Figure 1 (curves 2 and 3) illustrates EEL spectra of the fluorite $C_{60}F_{18}$ film in the course of electron irradiation with increasing dose Q. The figure shows radical diminishing the molecular peak intensities evidencing for destruction of the molecular structure. The shape of the spectrum (curve 3) becomes being similar to that of amorphous carbon (curve 4) after irradiation with large enough doze. To describe quantitatively modification process, parameter (P) for specifying the extent of fullerite amorphization was used [4]. This parameter is connected with the intensity (I_g) of the EEL spectrum range related to the density of states in the vicinity of the band gap. Figure 3 demonstrates the dependence of the modification parameter ($P \sim I_g$) on the irradiation dose (Q) for fullerite C_{60} (curve 1) and fluorinated fullerite $C_{60}F_{18}$ (curve 2). Both dependencies are monotonously increasing functions, but they are completely different. The dose dependence of C_{60} has a shape of exponential saturation $I_g(Q) \sim \text{const} + (1 - \exp(-Q/D_e))$. This dependence is described by one exponent. The dependence of $C_{60}F_{18}$ is more complicated. At list two different stages in the modification process described by two exponents can be distinguished in the dependence. The first stage ($Q < Q_1 \sim 0.05$ C/cm^2) is the stage of rapid modification. It is characterized by disappearance of the molecular peaks and by partial destruction of the molecular structure (Fig. 2). AES spectra show that the destruction of $C_{60}F_{18}$ is accompanied by the radical loss of fluorine atoms. Fragmentation of $C_{60}F_{18}$ and destruction of C_{60} cage due to ejection of chemically stable molecules F_2 and CF_4 were suggested to be the reason of the fluorinated fullerite destruction on the first stage of the modification. The second stage ($Q < Q_1 \sim 0.05$ C/cm^2) is the stage of slow modification.

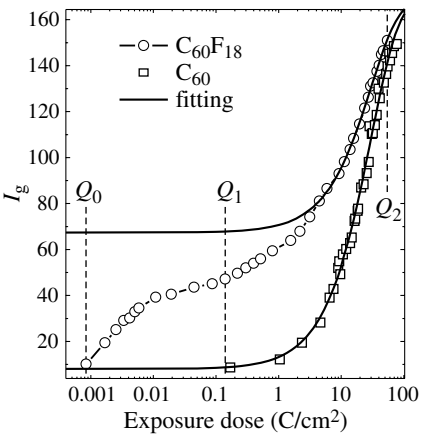

Fig. 3. Dependence of the parameter of amorphization ($P \sim I_g$) on the irradiation dose (Q) for fullerite C_{60} (curve 1) and fluorinated fullerite $C_{60}F_{18}$ (curve 2).

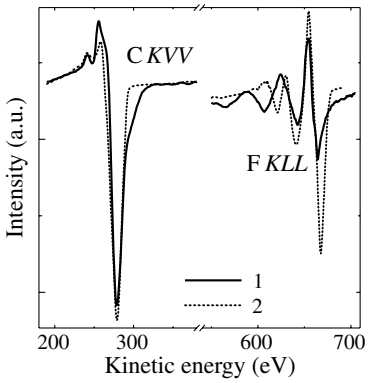

Fig. 4. Auger spectra of $C_{60}F_{18}$ before and after electron irradiation.

It is similar to the modification of ordinary fullerite C_{60}. Mechanism of destruction of the residual fullerene molecule through creation of intermolecular bonds was assumed here analogously to the case of C_{60}. The crucial question for electron lithograpy has been whether the fluorinated fullerite loses solubility or evaporability after the first stage of modification or not. Fortunately positive answer has been received. Thermal treatment experiments showed that not only heavily irradiated $C_{60}F_{18}$ but also the material after the first stage of irradiation lost evaporability while non-irradiated film retains this property. The main result of the research is that the dose required for transforming the film into hardly evaporated substance proved to be three orders of magnitude less than that to the ordinary fullerite. This fact makes the films of fluorinated fullerites perspective as an electron-beam resist for dry nanolithography.

Conclusions

Single and collective electron excitation spectrum of $C_{60}F_{18}$ film has been obtained for the first time. The revealed similarity of the spectrum to that of fullerite C_{60} was shown to be connected with spatial molecular structure being characterized by concentration of fluorine atoms on one third of fullerene sphere. Extremely high rate of $C_{60}F_{18}$ modification was revealed. It was shown that the modification is caused by molecular fragmentation with release of fluorine rich molecules. The conclusion has been made that $C_{60}F_{18}$ films are perspective as an electron-beam resist for nanolithography.

Acknowledgements

The research was supported by the Russian Academy of Sciences (program "Quantum microphysics, P-03", project 2.14), by the by the Russian Agency of Science (contract IN-13.5/002) and by Volkswagen Foundation (I77/855).

References

[1] E. E. B. Campbell, F. Rohmund, *Rep. Prog. Phys.* **63**, 1061 (2000).

[2] I. V. Goldt, O. V. Boltalina, L. N. Sidorov, *et al*, *Solid State Sciences* **4**, 1395 (2002).

[3] V. V. Shnitov, V. M. Mikoushkin, *et al*, *Microelectronic Engineering* **69**, 429 (2003).

[4] V. V. Shnitov, V. M. Mikoushkin, Yu. S. Gordeev, *Physics Solid State* **44**, 444 (2002).

[5] Yu. S. Gordeev, V. M. Mikoushkin, V. V. Shnitov, *Phys. Solid State* **42**, 381 (2000).

14th Int. Symp. "Nanostructures: Physics and Technology"
St Petersburg, Russia, June 26–30, 2006

Optical transitions probability controlled by external electric field in InGaAs/GaAs quantum wells

O. S. Komkov, A. N. Pikhtin and K. V. Bazarov
State Electrotechnical University, 197376 St Petersburg, Russia

Abstract. Using Schottky-barrier electroreflectance (ER) technique, single InGaAs/GaAs quantum wells (QWs) of different widths and depths have been investigated. To determine the probability of optical transitions from ER spectra two models have been proposed. Strong dependences of optical transitions probability induced by external electric field have been observed.

Introduction

Preliminary experimental data on the effect of electric field on the InGaAs/GaAs QWs [1] confirmed the nontrivial behavior of the intensity of spectral features in the electroreflectance spectra under changes of the internal electric field in the QW. On the assumption that the amplitude of the oscillations in the modulation spectrum varies with the field proportionally to the variations in the probability of optical transitions, we obtained good qualitative agreement between the experimental and theoretical results for the 11h and 13h transitions [2]. For quantitative comparison, however, it is necessary to separate the contributions of particular optical transitions to the modulation spectrum from each other. This problem is solved in this study by simulating the ER spectra. This enables us for the first time to determine the field dependences of optical transitions involving excited states of the QW from the experiment and to compare the dependences with the proper theoretical calculations.

1. Experimental

For the samples to be studied, we selected a series of semiconductor heterostructures with single QWs based on the $In_xGa_{1-x}As/GaAs$ system. The series involved structures with different widths of the QW and composition x of the $In_xGa_{1-x}As$ alloy. All of the samples were produced by metalorganic vapour-phase epitaxy. The QW width and composition were monitored by high-resolution two-crystal X-ray diffractometry. The parameters of different samples of the series were as follows: the QW width from 8 up to 23 nm, the alloy composition $x = 0.19$ or $x = 0.225$, and the thickness of the upper wide-gap layer 100 or 110 nm.

For measuring the ER signal, a thin semitransparent silver electrode was deposited on the upper GaAs layer of the sample to form the Schottky barrier. On the substrate side, an ohmic contact was formed by laser. A modulating sinusoidal voltage was applied to these contacts. Simultaneously with the modulating voltage, a dc bias voltage was applied to the structures.

The ER spectra were recorded by a setup assembled on the base of IKS-31 spectrometer. For the source of radiation, a 100 W halogen filament lamp was used. A light beam formed by a monochromator was incident on the sample and reflected from the area covered by the semitransparent electrode. The reflected beam was detected using a silicon photodiode with a preamplifier. Then, the signals were processed according to the principle of lock-in amplification. The resultant differential spectrum was, at every spectral point, divided by the reflectance spectra R obtained for the same sample area. The experimental setup allowed us to record the ER spectra with a resolution no worse that 0.6 meV.

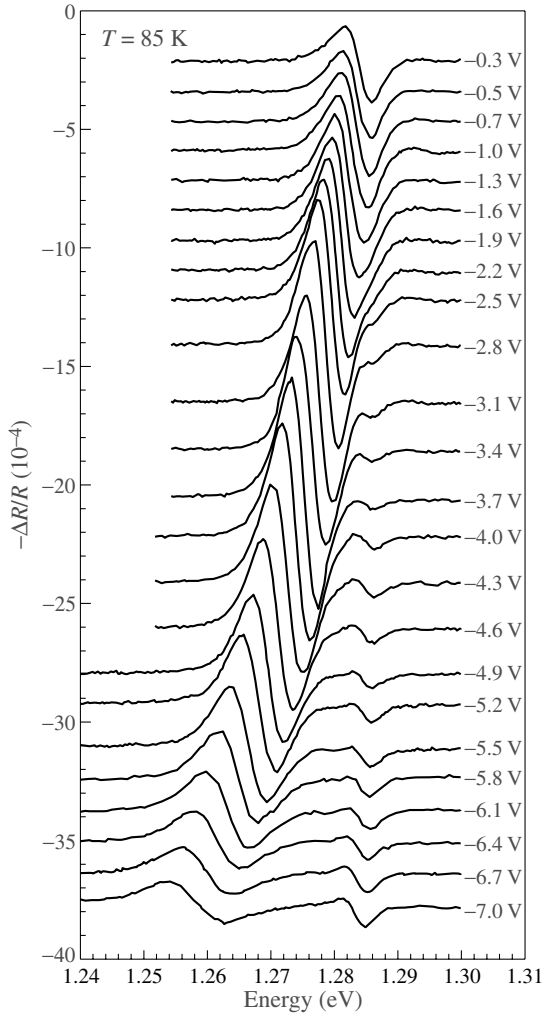

Fig. 1. Long-wavelength part of typical ER spectra, related to 11h excitonic transition in an 8 nm InGaAs/GaAs QW at different reverse bias voltages measured at $T = 85$ K.

2. Results and discussion

The long-wavelength part of the typical ER spectra, related to 11h excitonic transition in an 8 nm QW at different reverse bias voltages measured at $T = 85$ K, has been shown in Fig. 1.

The Kramers–Kronig transformation given in [3] has been applied to all measured ER spectra to obtain information about

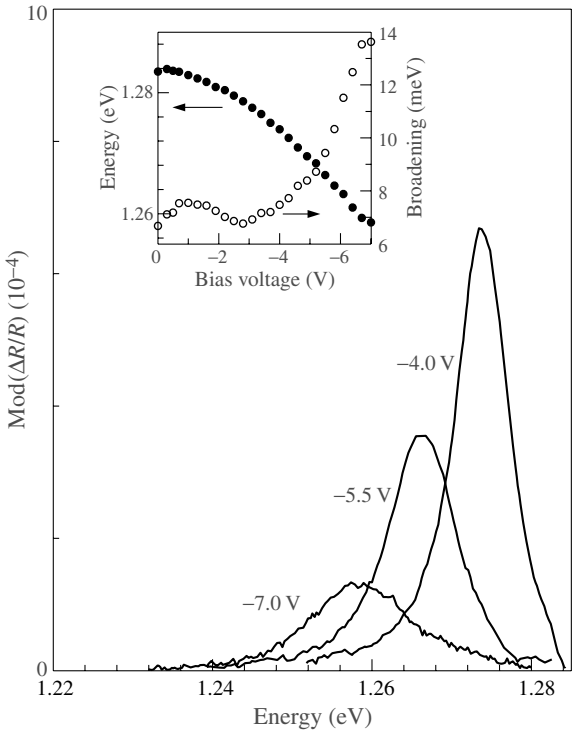

Fig. 2. Transformed ER spectra, shown in Fig. 1, for three bias voltages −7, −5.5, −4 V. The inset shows field effect on the position and broadening processes of the spectra.

transition energies and broadening processes. In Fig. 2 the transformed spectra for three bias voltages have been shown. The inset shows field effect on the position and broadening of the spectra (quantum-confined Stark effect).

Furthermore, to determine the optical transition probability in the whole voltage range a second method has been proposed. It is based on the modelling of each ER spectral feature by the difference of Lorentz functions. In the model the effect of the field on the shift, broadening and oscillator strength has been taken into consideration. It was shown that in low fields the main mechanism of modulated spectrum formation is the modulation of the optical transition probability. This has been experimentally demonstrated for the first time.

Moreover, we observed the field induced changes in the probability of optical transitions due to excited states of QW. These effects cannot be observed by the traditional photoluminescence technique. To illustrate the obtained results for excited states an 18.5 nm QW, measured at 300 K, has been used. In Fig. 3, a comparison of the experimental results to the theoretical ones, calculated as in [4], is shown. The electric field strength in the area of the QW has been determined from the period of Franz–Keldysh oscillations, observed in each ER spectrum. As shown in Fig. 3 the forbidden transition probability line shapes (12h, 13h, 21h) have nontrivial form while increasing the field in contrary to allowed transitions (for e.g. 11h). The probability of forbidden transitions arises to the maximum value and then falls.

The experimental results shown above demonstrate a possibility to control the optical transition probability in QWs by external electric field. This effect can be used to improve characteristics of existing devices with QWs: cascade lasers, devices using resonance tunnelling etc. It also creates a novel way to design new QW-based devices of nanoelectronics and optoelectronics.

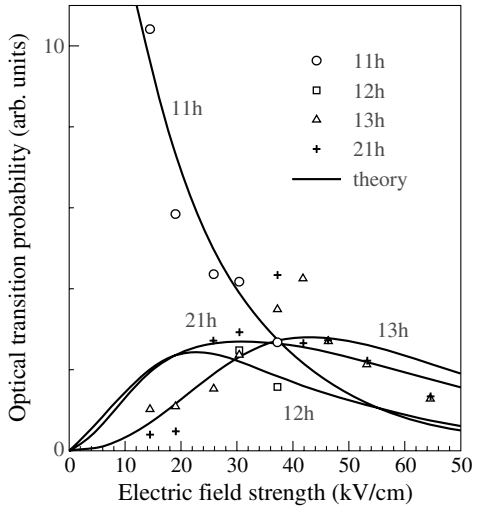

Fig. 3. Experimental (dots) and calculated (solid lines) dependences of optical transition probability in an 18 nm $In_{0.225}Ga_{0.775}As/GaAs$ QW via electric field strength.

References

[1] A. N. Pikhtin, O. S. Komkov and F. Bugge, *Proc. 12th Int. Symp. "Nanostructures: physics and technology"*, St Petersburg, Russia, 285, 2004.

[2] A. N. Pikhtin, O. S. Komkov and F. Bugge, *Phys. Stat. Sol. (a).* **202**, 1270 (2005).

[3] T. J. C. Hosea, *Phys. Stat. Sol. (b).* **189**, 531 (1995).

[4] O. L. Lazarenkova and A. N. Pikhtin, *Proc. 7th Int. Symp. "Nanostructures: physics and technology"*, St Petersburg, Russia, 416, 1999; *Phys. Stat. Sol. (a).* **175**, 51 (1999).

14th Int. Symp. "Nanostructures: Physics and Technology"
St Petersburg, Russia, June 26–30, 2006

Discovering of Wannier–Stark ladder effect in 4H-SiC natural superlattice p–n junctions

V. I. Sankin[1], P. P. Shkrebiy[1] and R. Yakimova[2]

[1] Ioffe Physico-Technical Institute, St Petersburg, Russia
[2] Department of Physics and Measurement Technology, Linkoping University, SE-581 83 Linkoping, Sweden

Abstract. The work deals with the highly important problem of qualitative character of temperature dependence of avalanche breakdown voltage in p–n junction based on 4H-SiC. Temperature coefficient of avalanche breakdown voltage (TCABV) is negative in seven SiC polytypes, including 4-SiC. It is of note that the plane of the investigated p–n junctions has coincided with the base plane 0001. This effect has been explained by the Wannier–Stark localization (WSL), which emerges in the strong electric fields in natural superlattices of SiC polytypes. However present technology prefers 4H-SiC p–n junction formation with the plane that has inclination to 0001 in 8°. This may change situation, securing weakening of the WSL and correspondingly positive TCABV. Discovering of Wannier–Stark ladder effect in 4H-SiC natural superlattice p–n junctions in this paper testifies to the WSL process and negative TCABV.

4H-SiC is a polytype with the most successful device perspective. Establishment of the basic features of impact ionization in this polytype is necessary for assessing marginal parameters for a large variety of devices. A problem of Wannier–Stark localization (WSL) [1] in natural superlattice of SiC polytypes is described in papers assembled in review [2]. Among the most significant consequences of the WSL conditions there is a breakdown voltage drop with temperature rise. It depreciates many important properties of certain SiC devices produced on axis plane. As it has been showed before, temperature coefficient of avalanche breakdown voltage (TCABV) is negative in seven SiC polytypes, including 4-SiC [2]. This effect has been explained by the WSL. It is important that WSL phenomena are realized at the field F parallel to the axis in correspondence with Wannier theory [1]. But the moderate technology of 4H-SiC epilayers fabrication prefers the plane with 8° off axis. TCABV has been investigated in some of the works, for instance [3–5]. The results have shown to be controversial: TCABV was negative in [3, 4] and positive in [5]. We think it happens because of the insufficient defining of breakdown nature. This work proposes method that permits to disregard the nature of breakdown; moreover the investigation itself is being carried out in the fields essentially lower than that of the avalanche breakdown. The principle problem, whether the 8° angle is enough to depress WSL in 4H-SiC is to be solved in the present work exactly following this way.

The p–n junction was fabricated by the following procedures: first a 5 μm thick, n-type 4H epilayer with $N_d - N_a \sim (5-7)\times10^{16}$ cm^{-3} was grown on the Si-face of a commercial 4H-SiC substrate ($N_d - N_a \sim 5\times10^{18}$ cm^{-3}) with 8° off axis angle and then a p-type epilayer with $N_a - N_d \sim 10^{18}$ cm^{-3} and 2–3 μm thick was deposited. The n^+–n^-–p^+ junction is abrupt and non-symmetric. This concentration $N_a - N_d$ is less of 2.5 order of magnitude than $N_a - N_d$ in p^+-layers of previous p–n junctions [2]. This allowed to enhance the electron diffusion lengths to $L_e \approx 1$ μm and to create conditions for increasing the electron component of the photocurrent trough the p–n junction. In order to verify the correctness of our method, such p–n junctions were also fabricated on Lely 6H-SiC on (0001) Si plane. A light with wavelength in 0.35 μm generated electrons and holes in approximately equal densities, while the 0.25 μm light generated initial electron-hole densities

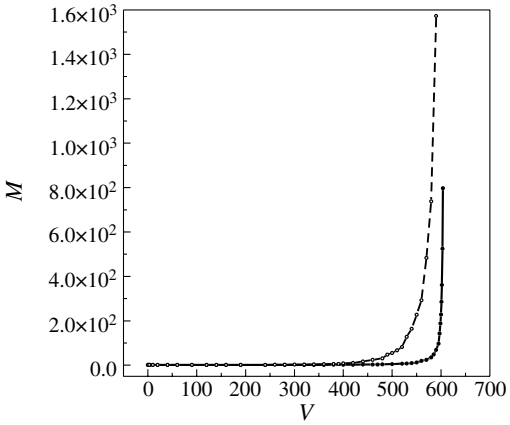

Fig. 1. Dependence of the photo multiplication on applied voltage in 6H-SiC p^+–n^-–n^+ junction. 1 — initial (I) holes photocurrent = I electron photocurrent; 2 — I electron photocurrent / I holes photocurrent = 100.

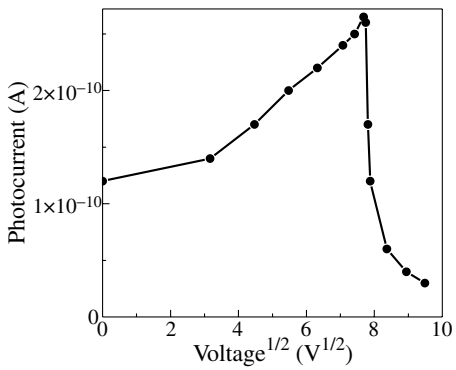

Fig. 2. Dependence of the WSL regime photocurrent on applied voltage in 6H-SiC p^+–n^-–n^+ junction.

in a ratio of 100:1. Under these conditions, in 6H-SiC strong depression of the electron component was revealed by direct measurements of the impact ionization (Fig. 1, curve 2). This effect is the evidence of the WSL process and thus of negative TCABV in 6H-SiC.

In 6H-SiC n–p junction with n-layer, doped to $N_d - N_a \sim 1.5\times10^{17}$ cm^{-3}, fabricated on p-layer, doped to $N_a - N_d \sim 1.5\times10^{18}$ cm^{-3}, it was observed negative photo conductance

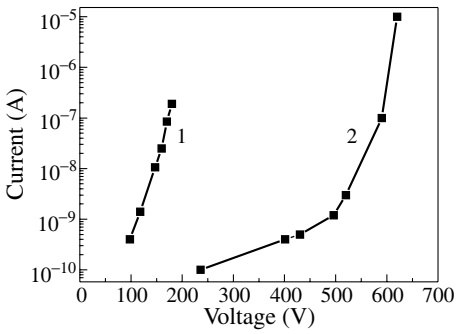

Fig. 3. Reverse I–V characteristics of p–n junctions with the same $N_d - N_a = 7\times10^{16}$ cm^{-3} in the base. 1 — 6H-SiC p^+–n^-–n^+ junction on Lely substrate; 2 — 4H-SiC p^+–n^-–n^+ junction on CREE substrate.

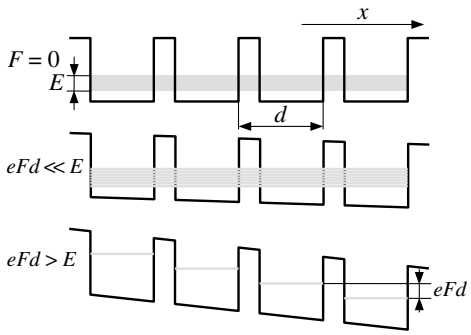

Fig. 4. The formation of W–S ladder spectrum under electrical field in one dimensional superlattice. F — electrical field; E — the minizone width; d — period of superlattice.

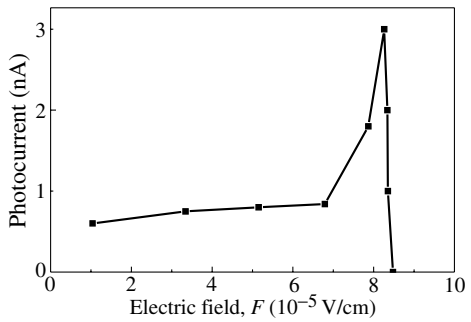

Fig. 5. Dependence of photocurrent on field in 4H-SiC p–n junction.

(Fig. 2) caused by hopping mechanism of stark-phonon interaction in Wannier–Stark ladder regime. That also is evidence of the WSL process and thus of negative TCABV in 6H-SiC but in the latter case the electric field value is more than two times less and therefore it is more readily for realization. Although a measurement system allows investigating of impact ionization in, it should be noted that 4H-SiC p–n junctions fabricated on commercial substrates have larger level of dark reverse current than those fabricated on Lely substrates with the same technology (Fig. 3). Therefore quality of the p–n junction has not allowed achieving fields, which induce the impact ionization. However the WSL evolves from relatively low fields (Bloch oscillations) to Wannier–Stark (W–S) ladder and this process ends as impact ionization with electrical breakdown at maximum fields. Therefore we can restrict our task to discovering any of the WSL phenomena at a minimal field. At relatively low quality of p–n structures one has to try to achieve the fields with the W–S ladder conditions. Electron spectrum transformation in 1d superlattice under the electric field influence is showed in Fig. 4. The emergence of these conditions must result in substantial change of the electron transport character [6–8].

Measurements of the photocurrent in a strong electric field 4H-SiC of the p–n junctions have provided a convincing attestation for it (Fig. 5). Monotonous increase of the photocurrent has given place to the more abrupt one with field being more than 700 kV/cm, which is characteristic property of these p–n junctions; with the field being more than 800 kV/cm an region with the negative differential conductivity emerges, which may testify to the appearance of the W–S ladders conditions.

$$\tau > 2\pi\hbar/eFd\,, \qquad (1)$$

where τ is the time of unperturbed electronic motion, T is the time, an electron (charge e) needs to traverse the Brilouin zone between $-\pi/d$ and $+\pi/d$ at electric field F coinciding with a crystallographic axis, d — a superlattice space parameter. In this conditions there will obviously be a virtual loss of mobility, i.e. quasi free motion capability. According to the theory, the drop mobility u depends on field F as $u \sim 1/F$ [6, 7]. It means arising of negative differential conductance. Estimations reveal that at the field more than 800 kV/cm the emergence of W–S ladders is quite possible. In accordance with [2] $\tau = 1.6\times10^{-13}$ s, while in accordance with (1) $T = 10^{-13}$ s. It should be noted that there is a possible hopping mechanism of stark-phonon interaction with resonance behavior [8]. However the wavelength of acoustic phonon is 3–4 times less than the radius of the W–S ladder states, that contradicts the basic criteria of this phenomenon.

In this work the first testimony of the presence of WSL in 4H-SiC p–n junctions, formed on the substrates with the inclination of 8° to the 0001 plane have been presented. It allows supposing that there is the negative temperature coefficient of the avalanche breakdown voltage in such p–n junctions. The proposed method has enabled to obtain important results resorting to destructive avalanche breakdown regime. At the same time for a more comprehensive study of WSL process in 4H-SiC p–n junctions similar investigations have to be done by using samples with better I–V characteristics.

Acknowledgement

The work was partially supported by Russian Foundation of Basic Researches (project No. 03-02-17617).

References

[1] G. N. Wannier, *Phys. Rev.* **11**, 432 (1960).
[2] V. I. Sankin, *Fizika i Tekhnika Poluprovodnikov* **36**, 769 (2002); [*Semiconductors* **36**, 717 (2002)].
[3] J. W. Palmour and L. A. Lipkin, *Transactors of the second International High Temperature Electron Conference*, Charlotte, NC, Vol. 1, pp. XI3–XI8, (1994).
[4] T. Kimoto, T. Urushidani, S. Kobayashi and H. Matsunami, *IEEE Electron Device Lett.* **14**, 548 (1993).
[5] P. G. Neudeck and D. J. Larkin, *Proc. of 1996 Device Research Conference* (*IEEE Electron Device Society, Santa Barbara, CA* 1996).
[6] R. Kümmel, H. Rauh and E. Bangert, *Phys. St. Sol. (b)* **87**, 99 (1978).
[7] A. Suris and B. S. Shchamkhalova, *Fiz. Tekh. Poluprovodn.* **18**, 178 (1984).
[8] D. Emin and C. F. Hart, *Phys. Rev.* **B 36**, 2530 (1987).

14th Int. Symp. "Nanostructures: Physics and Technology"
St Petersburg, Russia, June 26–30, 2006

Bias dependent shift of (2×1) reconstruction surface atomic structures on Ge(111) surface measured by LT STM

S. V. Savinov[2], P. I. Arseev[1], N. S. Maslova[2], V. I. Panov[2] and C. Van Haesendonck[3]

[1] P. I. Lebedev Physical Institution, 119991 Moscow, Russia
[2] Moscow State University, Faculty of Physics, 119992 Moscow, Russia
[3] Laboratory of Solid-State Physics and Magnetism, B3001 Leuven, Belgium

Abstract. In this work we present the results of low temperature STM investigations of clean Ge(111) surface. We report the detailed LT STM investigations of bias dependent shifts of atomic structures caused by (2×1) surface reconstruction. The comparison of experimental data with theoretical predictions for π-bonded chains model leads to the conclusion that tip-sample interaction plays significant role in STM imaging of Ge(111)-(2×1) surface.

Generally accepted point of view on cleaved Ge(111) surface is that it can be described by π-bonded chain model with buckling [1]. The localization of filled/empty surface states on up/down atoms is intrinsic feature of this theory. This means that when tunneling bias voltage is changing from filled to empty states range, there should be a shift of dimer rows on STM image in $[2\bar{1}\bar{1}]$ direction. If the buckling is large and surface states are really confined around up/down atoms this shift should be about 1 Å [2]. The value of 0.78 Å was derived from STM topographical images for Ge(111)-(2×1) surface at low temperature [3] and this value corresponds to the above stated predictions. At the same time, the analysis of the experimental data from [4] for Si(111) surface gives the shift between dimer rows in filled and empty states as big as 2.5 Å (the shift value was obtained by combining together Fig. 5–7 of [4]). The shift changes smoothly with changes of bias voltage. It should be noted that this shift was found in LDOS images, not in STM topographical images. In general there can exist the experimental situations when contrast of STM topographical images differs form the contrast of STM tunneling current images [5]. Some experimental data is also available for the bias dependent shift of individual dimers inside π-bonded chain row on Si(111)-(2×1) surface [6, 7, 8]. Importantly the phase difference between filled and empty states equals to π, i.e. maxima in filled states image are positioned at place of minima in empty states image.

The goal of our STM experiment was to determine the details of dependence on applied bias voltage of the shifts in both relevant directions of (2×1) reconstruction. The details of experimental procedure are described elsewhere [9].

Typical LT STM images of Ge(111)-(2×1) surface prepared by *in situ* sample cleavage are presented on Fig. 1 for opposite polarities of sample bias voltage. Images reveal ordered chain-like surface structure, which in case of Ge(111) surface is attributed to 2×1 reconstruction with π-bonded chains. Boundary between surface domains, formed by slightly different chain rows arrangement, are visible and has clearly resolved elementary (atomic size) structure. Domain boundaries segments are running only in three possible directions relative to the dimer stripped rows determined by surface threefold symmetry. One may also notice the changes of domain boundaries elements position from one scan to another. We suppose that this movement can be explained in terms of tip-induced (or scanning-induced) surface charge transfer. The areas of surface, used for image profiles averaging, are schematically

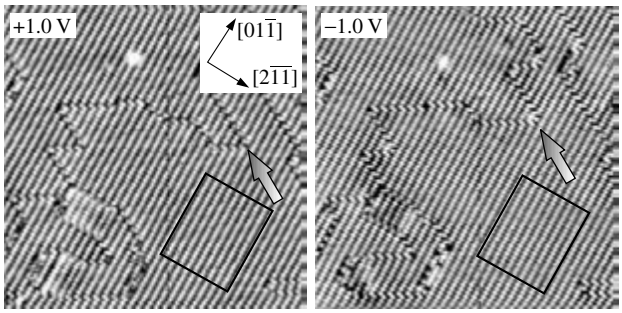

Fig. 1. STM image of Ge(111)-(2×1) surface at opposite sample bias. Tunneling current set point is 20 pA. Image size is 21 nm. Areas of surface at which image profiles have been collected are schematically depicted by black rectangles. Note the movement of domain boundary shown by arrows.

shown on Fig. 1 by rectangles.

The results of analyzes of profiles behavior along chain rows as well as in transverse direction are summarized on Fig. 2. Panes (a) and (c) illustrate the shift of π-bonded rows in $[2\bar{1}\bar{1}]$ direction with the changes of applied tunneling bias voltage. On pane a) small cuts of STM topographical images are combined together. These cuts are done at identical positions from STM images, acquired at different values of bias voltage. On pane c) cross-sections, vertically offset to give clear visual impression, are depicted. The cross-section were also collected at identical positions on STM images, acquired at different values of bias voltage.

STM images were acquired at following bias voltage values: 2, 1.5, 1.0, 0.7, 0.5, 0.3, −0.3, −0.5, −0.7, −1.0, −1.5 V. Images on panes (a) and (c) are ordered from top to bottom according to this sequence. This means that upper stripe on pane (a) of Fig. 2 is cut from STM image, obtained with 2 V bias, while the lower one is cut from STM image, obtained with −1.5 V bias. The same refer to pane (c). Panes (b) and (d) are designed in the same manner as panes (a) and (c) respectively, but they are illustrating the bias dependent shift of dimers along π-bonded row $[01\bar{1}]$ direction.

On pane (e) two graphs of bias dependent shift are shown. The set of bias voltage values is the same as for other images and is mentioned above. Dotted line corresponds to the shift of π-bonded rows in $[2\bar{1}\bar{1}]$ direction, while solid line shows the shift of dimers along π-bonded row $[01\bar{1}]$ direction, error bars are shown. The graphs were obtained by averaging of shift values obtained from different surface areas sufficiently large

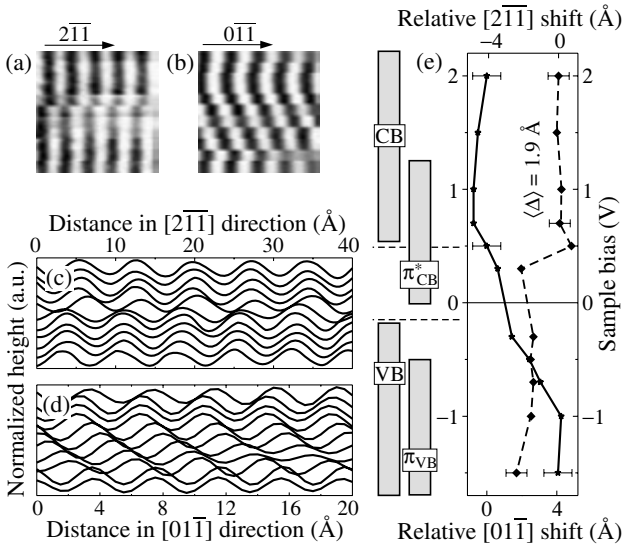

Fig. 2. Schematic representation of STM data for bias dependent shifts of surface atomic structures. (a), (c) Shift of π-bonded rows in [2$\bar{1}\bar{1}$] direction. (b), (d) Shift of dimers along π-bonded row [01$\bar{1}$] direction. (e) Dependence of relative shift in [2$\bar{1}\bar{1}$] (dotted line) and [01$\bar{1}$] (solid line) directions vs. bias voltage. Surface and bulk bands are shown as a guide for eye. On (a) and (c) images the stipes cut at the same position from different STM images are combined. On (b) and (d) cross-sections of STM images at the same position are presented. The sequence of bias voltage values used during STM image acquisition is 2, 1.5, 1.0, 0.7, 0.5, 0.3, −0.3, −0.5, −0.7, −1.0, −1.5 V. The stripes on (a), (c) and cross-sections on (b), (d) are ordered from top to bottom according to this sequence. The tunneling current was stabilized at 20 pA level.

to ensure small error. Surface band structure is depicted next to the graph, clarifying the relative position of experimental points on energy diagram.

The determination of shift in [2$\bar{1}\bar{1}$] direction is straightforward, because the contrast of STM topographical images is high for π-bonded rows of (2×1) reconstruction. Much more difficulties were experienced with the shift in [01$\bar{1}$] direction. The contrast of non-processed STM image for individual dimers along π-bonded row was not sufficient to allow accurate shift determination. Therefore we have had to apply Fourier filtering to emphasis the structure of the STM image along [01$\bar{1}$] direction. Filtering procedure was used with great care and, apparently subjectively, no artefact could be seen on filtered image. The great simplification is caused by the relative character of the measurement. Atomic structures period serve as very precise intrinsic reference point for shift determination.

Based on Fig. 2 we can make few conclusions. When changing bias voltage in the range of empty states from +2 to +0.7 V the relative shift in [2$\bar{1}\bar{1}$] direction is zero to within the accuracy. When bias passes the range of surface band gap from +0.7 to +0.3 V the shift changes its value to ~ -1.9Å, which equals also to mean value of shift in [2$\bar{1}\bar{1}$] direction (Fig. 2e). Farther decrease of tunneling bias down to −1.5 V does not lead to noticeable alteration of relative shift value. So, all the changes in relative shift of π-bonded rows are happening in bias range where surface states are the only states available for tunneling.

This is not a case for the shift of dimers inside π-bonded rows [01$\bar{1}$] direction. In contrary to previous observations on Si(111)-(2×1) surface [6,7,8], which should be similar to our case, we have determined the value which almost equals to 4 Å. This means that 2π phase shift exists between filled and empty states STM images. The dependence of relative [01$\bar{1}$] shift on bias voltage is smooth, above conduction band minimum the shift is zero, it reaches its maximum value at approximately –1 V below valence band maximum (Fig. 2e).

Minus sign of the shift direction stress the fact that relative dimer rows shift occur in the direction *opposite* to [2$\bar{1}\bar{1}$]. We should note that exact orientation of our sample in unknown, so the direction of π-bonded rows was arbitrary chosen as reference [01$\bar{1}$] direction. Therefore we are in principal not able to distinguish left and right isomers of (2×1) reconstruction.

We suppose that high values of relative shift of surface atomic structures in [2$\bar{1}\bar{1}$] direction are due to probe tip interaction with the sample. Recently it was proved [10] that relative phase of dimer rows on STM image of Si(001) is sensitive to the value of tunneling current. Next, the energy difference between left and right reconstruction isomers on Ge(111)-(2×1) surface is low [11]. Thus, STM tip-surface interaction can cause some kind of scanning induced surface dimers flip-flop motion, as on Si(001) surface [12]. This motion obviously will lead to the modification of *measured* distribution of density of states and very probably to the alteration of *measured* shift values.

Acknowledgements

This work has been supported in part by the RFBR grant 05-02-19806-MFa. Support from the Samsung Corporation is also gratefully acknowledged. C.V.H would like to thank the FSR — Flanders (Belgium) as well as the Belgian IAP and the Flemish GOA research programs.

References

[1] N. Takeuchi, A. Selloni, A. I. Shkrebtii and E. Tosatti, *Phys. Rev. B* **44**, 13611 (1991).
[2] A. A. Stekolnikov, J. Furthmüller and F. Bechstedt, *Phys. Rev. B* **85**, 5440 (2002).
[3] R. M. Feenstra, G. Meyer, F. Moresco and K. H. Rieder, *Phys. Rev. B* **63**, 081306(R) (2001).
[4] J. K. Garleff, M. Wenderoth, K. Sauthoff, R. G. Ulbrich and M. Rohlfing, *Phys. Rev. B* **70**, 245424 (2004).
[5] P. I. Arseyev, N. S. Maslova, V. I. Panov, S. V. Savinov and C. Van Haesendonck, *JETP Lett.* **77**, 202 (2003).
[6] J. I. Pascual, C. Rogero, J. Gómez-Herrero and A. M. Baró, *Phys. Rev. B* **59**, 9768 (1999).
[7] M. Schöck, C. Sürgers and H. v. Löhneysen, *Phys. Rev. B* **61**, 7622 (2000).
[8] T. Trappmann, C. Sürgers and H. v. Löhneysen, *Appl. Phys. A* **68**, 167 (1999).
[9] P. I. Arseyev, N. S. Maslova, V. I. Panov, S. V. Savinov and C. Van Haesendonck, *JETP Lett.* **82**, 312 (2005).
[10] K. Nagaoka, M. J. Comstock, A. Hammack and M. F. Crommie, *Phys. Rev. B* **71**, 121304(R) (2005).
[11] M. Rohlfing, M. Palummo, G. Onida and R. Del Sole, *Phys. Rev. Lett.* **85**, 5440 (2000).
[12] J. Nakamura and A. Natori, *Phys. Rev. B* **71**, 113303 (2005).

14th Int. Symp. "Nanostructures: Physics and Technology"
St Petersburg, Russia, June 26–30, 2006

X-ray diffraction studies of initial stages of CaF_2/Si(001) growth at high temperatures

S. M. Suturin[1], N. S. Sokolov[1], R. N. Kyutt[1], V. P. Ulin[1], O. Sakata[2], K. Sumetani[2], J. Harada[3,5], K. M. Pavlov[4], Y. Takeda[5], M. Tabuchi[5] and T. Shimura[6]

[1] Ioffe Physico-Technical Institute, St Petersburg, Russia [2] JASRI/Spring-8, Japan [3] Rigaku Co, Japan
[4] Monash University, Melbourne, Australia [5] Nagoya University, Nagoya, Japan
[6] Osaka University, Osaka, Japan

Abstract. The atomic structure of CaF_2/Si(001) interface formed by deposition of 0.8 monolayer of CaF_2 on Si(001) at 750 °C was studied by surface X-ray diffraction at SPring-8 synchrotron, Japan. Using grazing incidence 11 keV photons, 40 in-plane reflections and 2 fractional-order rods were recorded. On the basis of the collected data a preliminary model of the CaF_2/Si(001) interface is suggested.

Introduction

MBE growth of CaF_2 on Si(111) has been the object of research for already many years. This system is frequently considered as a prototype for study of the interface between a polar ionic insulator and a covalent semiconductor. Recently an intensive study of CaF_2 growth on the technologically important Si(001) surface has been undertaken [1, 2]. Combining various characterization techniques (RHEED, AFM, XPS, XAS) it has been shown that on depositing a monolayer of CaF_2 onto Si(001) surface at 650–800 °C, a reacted silicide-like layer of remarkable properties is formed. This layer grows by nucleation and coalescence of fluoride nanostripes each confined within one Si terrace and lined up parallel to Si [110] direction (Fig. 1). The nanostripes are 0.3 nm in height and their width is below the lateral resolution of the microscope ($\sim 10-15$ nm). The surface of the reacted layer exhibits a 3×1 reconstruction (see LEED pattern in Fig. 1) where the triple periodicity is observed in the direction perpendicular to the nanostripes. It is noteworthy that thicker layers of CaF_2 grow on top of the reacted layer with non-trivial epitaxial relations: CaF_2 (110) and Si (001) planes become parallel, and within these planes the CaF_2 [1$\bar{1}$0] axis, (along the nanostripes), becomes parallel to the Si [110] axis. Lattice constants of CaF_2 and Si almost coincide in this direction, while perpendicular to the nanostripes the lattice constant of CaF_2 is 1.41 times larger than that of Si. The triple periodicity in this direction, is usually associated in the previous works with the assumption that CaF_2 lattice gets stretched $\sim 6\%$ so that 2 CaF_2 (110) cells become the same size as 3 Si (001) cells. These cells together can in principle constitute a 3×1 unit cell that is observed in the experiment, however for a complete comprehension of the interface structure, data on particular positions of Si, Ca and F atoms in the unit cell is needed. An approach to solving this problem is given in the present work where the atomic structure of the CaF_2 reacted layer, was studied by surface X-ray diffraction (SXRD) at BL13XU beamline of Spring-8 synchrotron [3]. After the samples were grown in a UHV chamber mounted on a 2+2 diffractometer, 40 in-plane reflections and 2 fractional-order rods have been measured *in situ*.

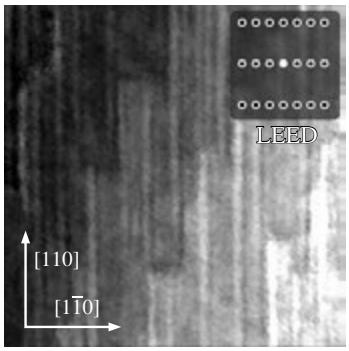

Fig. 1. AFM and LEED images of CaF_2 1 ML deposited on Si(001) at 750 °C. AFM image size 800 nm×800 nm×1.5 nm.

1. Results and discussion

Silicon substrates with small miscut angles (~ 2 arc min.) have been selected and chemically cleaned by Shiraki treatment. Silicon surface was prepared by 30 s in-vacuum thermal flash to 1100 °C, the two-domain $2\times1+1\times2$ structure confirmed by RHEED patterns. Immediately after cooling down Si substrate from 1100 °C to 750 °C, ~ 0.8 monolayer of CaF_2 has been deposited on Si from an effusion cell at the growth rate of 40–50 s per monolayer. The resulting surface showed the 3×1 RHEED pattern characteristic of the CaF_2 reacted layer.

The grazing angle SXRD measurements were carried out for photon energy of 11 keV at incidence angle of 0.6 °. Intensity of the outgoing diffracted beam was collected at the angle β of 0.5 ° for the in-plane ($L = 0.1$) measurements. Out-of-plane measurements were done in the range $L = 0.1-2.7$. Hereafter the coordinates are referenced to the bulk unit cell of Si defined by vectors $a = [0.5, 0.5, 0]$, $b = [0.5, -0.5, 0]$ and $c = [0, 0, 1]$.

Angular distribution of the in-plane diffraction intensity measured along $K = 0$ and $K = 1$ is shown in Fig. 2. Profiles almost identical to those shown, were obtained also in the perpendicular direction along $H = 0$, $H = 1$. This together with RHEED data indicates that the surface under study has two similar domains orthogonal to each other, induced by the two different types of terraces (2×1 and 1×2) present at the Si(001) surface.

A number of strong (up to 300 counts per sec) fractional and integer order reflections coming from the reacted CaF_2 layer and silicon substrate are clearly seen in Fig. 2. The strongest peak at $(H, K) = (2, 0)$ corresponds to the Si(220) bulk reflection, which is confirmed by its narrowness in both H and K directions. Relatively weak (0, 1/2) and (0, 3/2) reflections originate from the uncovered 2×1 reconstructed Si(001) surface.

Distinct fractional order reflections with H close to $N/3$ apparently come from the reacted CaF_2 layer in agreement with

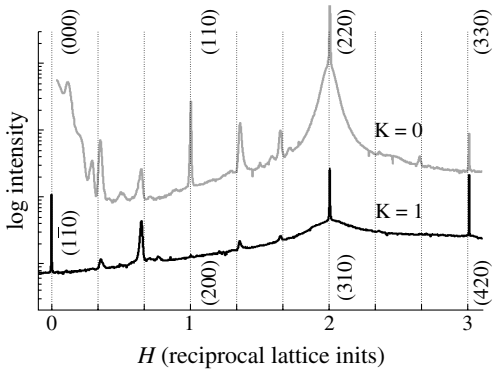

Fig. 2. SXRD profiles taken at $K = 0$ and $K = 1$.

RHEED observations. Close examination however shows that these reflections are shifted from $N \pm 1/3$ to $N \pm 6/17$ H-positions. In addition, there are other minor reflections also appearing at multiples of 1/17. These results certainly indicate that a 17×1 unit cell (measured in the lattice constants of Si) is present at the interface. This can be naturally explained by taking into account that 12 lattice constants of CaF_2 along [100] perfectly match to 17 lattice constants of Si along [110] (these directions lie in the plane of the interface and are perpendicular to the nanostripes). To account for the periodicity of 17, CaF_2 interface layer must be compressed by just 0.2% which is much easier to achieve than the 6% compression needed for the earlier proposed model with periodicity of 3. It is significant that the 3×1 observations do not contradict the present results. Moreover, since most of the SXRD reflections appear very close to $N \pm 1/3$ (with accuracy below 2% that could not be well resolved by RHEED), it can be assumed that the true atomic structure consisting of 17×1 unit cells can be at first stage approximated by simpler 3×1 unit cells. Therefore in the following analysis, the $N \pm 6/17$ reflections will be considered as $N \pm 1/3$.

All the fractional order reflections are narrow along K and broadened along H. For the $N/17$ reflections it is explained by confinement of the nanostripes in the direction of the 3 (17) periodicity. For the Si half order reflections the broadening corresponds to confinement of the uncovered Si regions by the nanostripes. Altogether it is a clear indication of that within one terrace CaF_2 nanostripes run parallel to Si dimer rows.

For further analysis, background was subtracted from the experimental profiles and the integrated intensity of each reflection was calculated taking into account the area correction factor. Although the reflections are measured only at positive H and K, the dataset can be expanded using 2 mm symmetry (known from LEED pattern analysis). The z-projected electron density is derived from the in-plane diffraction data using Patterson function and the difference Fourier map methods, assuming 2mm symmetry of the 3×1 unit cell. Only reflections broad along H are considered for the reason that they come from the nanostripes of the same domain.

The simulation shows that z-projected electron density can be constructed as the sum of 11 stand alone atom-like features with Gaussian spatial electron distribution (Fig. 3a). The corresponding diffraction intensity (Fig. 3b) shows good fit to the experimental data.

To obtain information on the positions of the atoms along the surface normal, integral intensities at (6/17, 1) and (11/17, 1) fractional rods have been measured and fitted (Fig. 3c). The fit was done by minimizing the χ^2 function using simple and

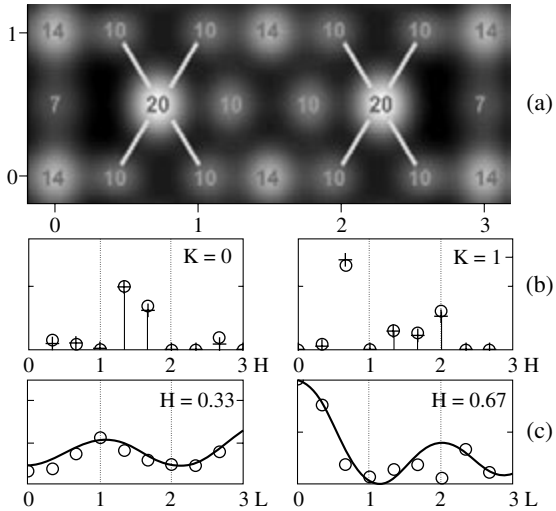

Fig. 3. Electron density map in the 3×1 unit cell (a). Calculated (solid) and experimental (circles) diffraction intensities: H-profiles at $K = 0$, $K = 1$ (b) and L-profiles at $H = 0.33$, $H = 0.67$ (c).

Table 1. Atomic configuration of the 3×1 unit cell.

atom	x	y	z	f
Si	0.000	0.0	0.000	14.8
	0.000	0.5	0.503	7.3
Si	1.500	0.0	0.209	14.5
F	±0.430	0.0	0.223	9.8
F	±1.061	0.0	0.450	9.7
Ca	±0.715	0.5	0.493	20.0
F	±1.215	0.5	0.485	10.6

gradient search methods with 7 independent parameters (for 2 mm cell symmetry). The best fit (Fig. 4) is achieved for the unit cell described in Table 1, where each atom is modeled by 3D Gaussian electron density distribution with characteristic width of $\Delta_{XY} = 0.8$ Å and $\Delta_Z = 0.3$ Å. Total charges of the atom-like features can be roughly ascribed to Si ($f \approx 14$), Ca ($f \approx 20$) and F ($f \approx 10$) atoms. Interestingly part of the electron density map (shown by cross in Fig. 3a), closely resembles the CaF_2 (110) unit cell.

2. Conlusions

Atomic structure of the CaF_2 reacted layer on Si(001) has been studied by surface X-ray diffraction. By analysing the measured in-plane and out-of-plane intensity profiles, a preliminary model of the CaF_2/Si interface is derived indicating possible positions of Ca, Si and F atoms in the unit cell. To carry out a more detailed and unambiguous analysis of the unit cell configuration, more in-plane reflections, fractional rods and crystal truncation rods need to be measured. Such an experiment is already planned by the authors.

Acknowledgements

Support of Nature COE in Nagoya University is greatly appreciated by N. S. Sokolov and S. M. Suturin.

References

[1] N. S. Sokolov, *et al*, *Appl. Surf. Sci.* **234**, 480 (2004).
[2] L. Pasquali, *et al*, *Phys. Rev. B* **72**, 045448 1–15 (2005).
[3] N. Sokolov, *et al*, report on experiment 2005A0575-ND1d-np at SPring-8.

14th Int. Symp. "Nanostructures: Physics and Technology"
St Petersburg, Russia, June 26–30, 2006

Carrier distribution in MQW InGaN/GaN LED structures

D. M. Bauman[1], N. M. Shmidt[1], P. S. Vergeles[2], *E. B. Yakimov*[2] and B. S. Yavich[1]

[1] Ioffe Physico-Technical Institute, St Petersburg, Russia
[2] Institute of Microelectronics Technology RAS, Chernogolovka, 142432 Russia

Abstract. Charge carrier depth profile in the light emitting structures based on InGaN/GaN multi-quantum well layers is studied by C–V profiling method. In addition, the EBIC measurements is used to obtain the p–n junction depth, to estimate the transparency of multi-quantum wells for the minority carrier flow and the diffusion length in the underlaying GaN layer. The results obtained demonstrate the possibilities of these methods for the characterization of InGaN/GaN multi-quantum well structures.

Introduction

Light emitting structures (LES) based on multi-quantum well (MQW) InGaN/GaN layers have received considerable attention due to their possible application as light emitting devices with spectral range from green to UV. LES efficiency is determined by the extended defect system, material nanostructural arrangement and the carrier distribution profiles, which to a great extend depend on the growth conditions. But a study of these parameters and their effect on the LES efficiency can only be accomplished by an improvement of the characterization methods. Fortunately, the dopant concentration in these structures is rather high and the diffusion length is low that provides the high spatial resolution of electrical characterization methods, such as Electron Beam Induced Current (EBIC) mode of scanning electron microscopy and capacitance-voltage (C–V) profiling. The analysis of C–V characteristics is a powerful, nondestructive method for determining the parameters of multilayer semiconductor heterostructures including the width of layers, doping profile, band discontinuities, and electron density distribution [1–3] and its application for the characterization of quantum well structures based on GaAs is well documented [1, 3]. The EBIC allows to reveal the lateral inhomogeneities of recombination rate, the diffusion length in the underlaying layers and the p–n junction depth [4]. As shown recently [5], the minority carrier recombination inside the MQW layer could be estimated from the EBIC measurements and this point needs additional investigations. However, an application of both methods for the characterization of GaN based LES up to now was very limited.

In the present paper two types of LES with different external quantum efficiency were studied by the combined application of the EBIC and C–V profiling. The electron concentration depth profile in MQW layer is studied. It is shown that individual QW are well resolved by the C–V profiling. Fitting the EBIC data allows to estimate the p–n junction depth with a precision of about 10 nm.

1. Experimental

The investigated LES were grown by the metal-organic chemical vapor deposition on (0001) sapphire substrates. The LES consist of 3 μm thick n-GaN lower layer, MQW InGaN/GaN with 5 periods of 3 nm InGaN and 10 nm GaN layers and thin p-GaN cap layer. Two LES (A and B) with the same geometry but with the p-layer grown in different conditions have been studied. The structures have different structure ordering that could be a reason [6] for the higher (5–10 times at low excitation level) quantum efficiency for the structure A than that for the structure B. For the EBIC and C–V investigations mesa structures with an area of about 0.5 mm^2 were prepared by Ar ion sputtering and p–n junctions were used for the induced current collection. The C–V measurements were done at room temperature and at 78 K using a PAR 410 capacitance meter at 1 MHz. The EBIC measurements were carried out in the scanning electron microscope JSM-840A (Jeol) using the Keithley 428 current amplifier. All EBIC measurements were done in the normal geometry with e-beam perpendicular to the p–n junction plane. To extract the quantitative information about the structures under study the dependence of current collected in the EBIC mode I_c on electron beam energy E_b was compared with simulated ones.

2. Results and discussion

The typical $I_c(E_b)$ dependences normalized on the product of I_c and E_b measured on the A structure at different bias are presented in Fig. 1 together with simulated ones. The dependences measured on the structure B are very similar. As it was shown in [5], to fit the experimental dependences measured on the LES the simulated ones should be multiplied by a correction factor of about 0.3–0.5 that is associated with the minority carrier capture and/or recombination inside the MQW layer. As seen in Fig. 1, the collection efficiency increases, when bias U is varied from 1 V (forward) to -1.2 V (reverse). Fitting these dependences shows that the observed increase of collection efficiency with the reverse bias is determined by an increase of correction factor from 0.4 to 0.55, i.e. an increase in applied reverse bias leads to an increase of MQW layer transparency

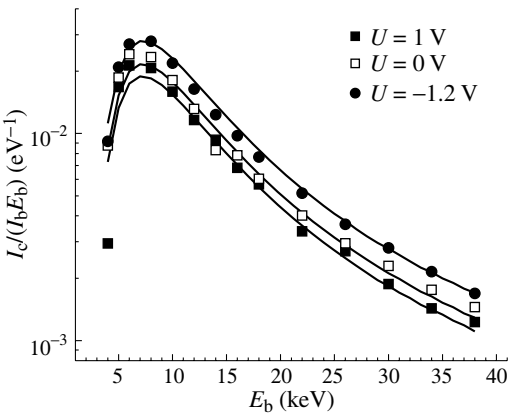

Fig. 1. Normalized $I_c(E_b)$ dependences measured on the LES A at different applied bias.

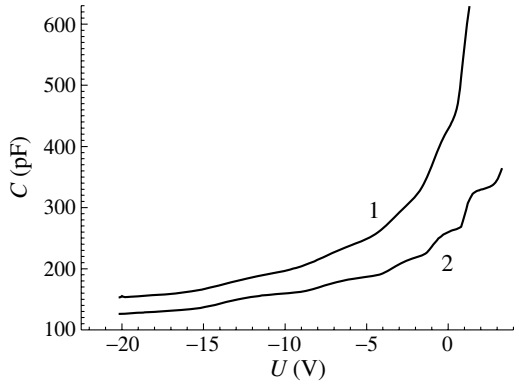

Fig. 2. C–V curves measured on the LES B at 300 (1) and 78 K (2).

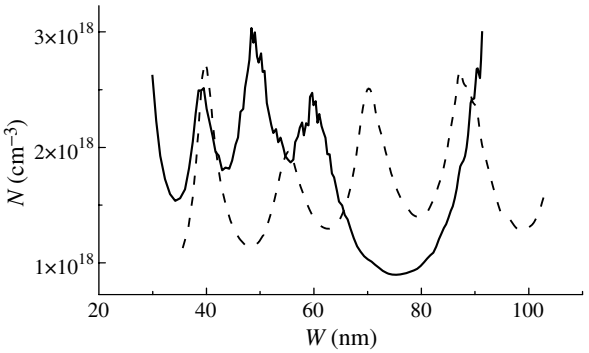

Fig. 3. The apparent carrier distributions for the LES A (solid line) and B (dashed line).

to the minority carrier flow. The comparison of experimental and simulated dependences allows also to obtain the depth of p–n junction and the diffusion length in the underlaying GaN layer. The p–n junction depth obtained by fitting the dependences shown gives a value of 100 nm that well correlates with the SIMS data. Using the dopant concentration obtained from C–V measurements allows to estimate the p–n junction depth with a precision of about 10 nm. The diffusion length in the GaN layer located under MQW layer was found to exceed 100 nm in spite of rather high dopant concentration in this layer.

To study the carrier concentration profiles and the location of MQW layer relatively the depletion region of p–n junction the C–V measurements were carried out. The C–V curves measured on the LES B at 300 and 78 K are presented in Fig. 2. Under the measurements the applied bias is varied from −20 to 1 V at 300 K and to 3–3.5 V at 78 K. The steps associated with well emptying are easily seen on the curves especially at 78 K. The apparent carrier distributions calculated from the C–V curves measured at 300 K using the expression

$$N = -\frac{4\pi C^3}{\epsilon S^2 e \frac{dC}{dU}},$$

where C is the measured capacitance and S is the mesa-structure area, for LES A and B are presented in Fig. 3 as a function of depletion region width W. First of all it should be noted that the distance between peaks for the LES A is close to 13 nm that means that the acceptor concentration in p-layer is essentially higher than the donor concentration in the MQW layer. In this case W is practically equal to the depletion region in the n-layer. At a forward bias of about 1 V three wells are outside the depletion region. For the structure B it is not the case. The acceptor concentration in it seems to be comparable with the donor one. For this reason the part of depletion region in n-layer is smaller than that in the A structure at the same bias and four wells could be revealed on the apparent carrier concentration profile. Taking into account that the Mg concentration in the p-layer, as follows from the SIMS data, is about 10^{20} cm^{-3} it could be concluded that the degree of Mg activation in the B structure is rather low. At lower temperatures larger forward voltage can be applied to the structures without an essential leakage current that allows to reveal all five wells in the structure B that means that in this structure p–n junction is located above the MQW structure. It should be noted that W at 0 V in both structures has close values that could be explained under the assumption that Mg diffuses in n-region of structure A that leads to a compensation of part of this region and as a result to an increase of W.

Thus, the results presented show that in spite of similar conditions of MQW growth their filling could depend on the p-layer growth conditions. The carrier concentration in quantum wells should be studied more carefully to search for its possible correlation with the quantum efficiency and the methods discussed are well suited for such investigations. Such studies could clarify the mechanisms of effective radiative recombination in InGaN/GaN MQW structures.

Acknowledgements

This work was partially supported by the Russian Foundation for Basic Research (Grants 04-02-16994a and 05-02-17774a).

References

[1] B. M. Tschirner *et al*, *J. Appl. Phys.* **79**, 7005 (1996).
[2] P. N. Brounkov *et al*, *J. Appl. Phys.* **80**, 864 (1996).
[3] C. R. Moon *et al*, *Appl. Phys. Lett.* **70**, 2987 (1997).
[4] H. J. Leamy, *J. Appl. Phys.* **53**, R51 (1982).
[5] N. M. Shmidt and E. B. Yakimov, *Proc. of 13 th Int. Conf. "Nanostructures: Physics and Technology" (St Petersburg, 2005)*, Ioffe Institute, 300, 2005.
[6] A. I. Besyulkin *et al*, *Phys. Stat. Sol. (c)* **2**, 837 (2005).

14th Int. Symp. "Nanostructures: Physics and Technology"
St Petersburg, Russia, June 26–30, 2006

Theory of spin states in excitonic quantum dot molecules

I. V. Ponomarev[1], M. Scheibner[1], E. A. Stinaff[1], A. Bracker[1], M. F. Doty[1], M. E. Ware[1], D. Gammon[1], T. L. Reinecke[1] and V. L. Korenev[2]

[1] Naval Research Laboratory, Washington DC, 20375, USA
[2] Ioffe Physico-Technical Institute, St Petersburg, Russia

Abstract. The photoluminescence spectrum of an asymmetric pair of coupled InAs quantum dots in applied electric field shows an abundant pattern of levels anticrossings and crossings that can be understood as a superposition of charge and spin configurations of different excitonic molecules. We present a theoretical model that provides the basis for a description of energy positions and intensities of various optical transitions in exciton, biexciton and charged exciton states of coupled quantum dots molecules. We also introduce a new nomenclature that allows us to classify different transitions in coupled quantum dots nanostructures.

Introduction

Optically addressed self-assembled InAs coupled quantum dots (CQD) are very promising candidates for gates in quantum information applications. Coherent coupling between two dots controlled by applied electric field is a critical need for manipulation of the qubits. Recent photoluminescence (PL) spectroscopy of excitonic molecules in CQDs tuned by electric field reveals a richer diversity in spectral line patterns than in their single quantum dot counterparts (Fig. 1). In this paper we present a theoretical model that classifies and explains the complexity of PL lines.

1. Experimental

We have performed PL spectroscopy on individual CQDs through aluminum shadow masks with 1 micron diameter apertures at 10 K. The QDs in this study consist of InAs grown by molecular beam epitaxy using an indium flush technique. CQDs were formed by growing two closely spaced layers (distance $d = 6$ nm) of QDs, where the second layer nucleates preferentially above the first layer of dots. In order to apply an electric field and to control the charging the QDs were embedded in a n^+-intrinsic-Schottky diode. Although both QD layers in the samples under investigation were grown with nominally the same vertical height the top QDs exhibited an energetically higher exciton ground state level. The asymmetric nature of these CQDs simplifies our interpretation of their spectra, because electron and hole resonances occur at different fields and can therefore be considered independently. For these CQDs, the bottom dot has a smaller direct transition energy than the top dot. With this ordering, a larger electric field, brings the hole levels into resonance, whereas the electron levels become detuned and the electron remains localized [1].

2. Nomenclature

A richness of CQD spectra requires an introduction of a new nomenclature that would allow us to make assignments for all new appeared lines. It can be done in the following way. ${}^{n}_{m}X^{q}$ denotes QD molecule with n electrons and m holes with total charge $q = m - n$. Obviously, ${}^{1}_{1}X^{0}$ corresponds to neutral exciton X in old abbreviation, ${}^{2}_{2}X^{0}$ to biexciton XX, ${}^{2}_{1}X^{-1}$ to the negative trion X^-, and ${}^{1}_{2}X^{+1}$ to the positive trion X^+. For CQDs a more detailed classification of configurations is given by defining how many electrons and holes occupy each QD and what are their spins configurations (if required): ${}^{(n_1,n_2)}_{(m_1,m_2)}X^{q}_{[\{S_{ei}\},\{S_{hi}\}]}$. Again, $q = (m_1 + m_2) - (n_1 + n_2)$. In order to label excitonic transitions between charge states and to indicate which charges are involved, the corresponding electron(hole) index is underlined. For example, the abbreviation ${}^{(\underline{n},0)}_{(1,\underline{m})}X^{q}$ means e-h recombination ${}^{(n,0)}_{(1,m)}X^{q} \rightarrow {}^{(n-1,0)}_{(1,m-1)}X^{q}$. Near resonance the transitions assisted by hole tunneling are also possible if number of particles in QD is appropriate. We denote such transitions by "tilde" sign, ${}^{(\underline{n},0)}_{(\underline{m_1},m_2)}\tilde{X}^{q} = {}^{(n,0)}_{(m_1,m_2)}X^{q} \rightarrow {}^{(n-1,0)}_{(m_1-2,m_2+1)}X^{q}$. Our nomenclature can be generalized on cases when more than one confined levels in each dots occupied or for multiple coupled QDs: ${}^{(n_{1s}n_{1p}\ldots,n_{2s}n_{2p},\ldots)}_{(m_{1s}m_{1p}\ldots,m_{2s}m_{2p},\ldots)}X^{q}$.

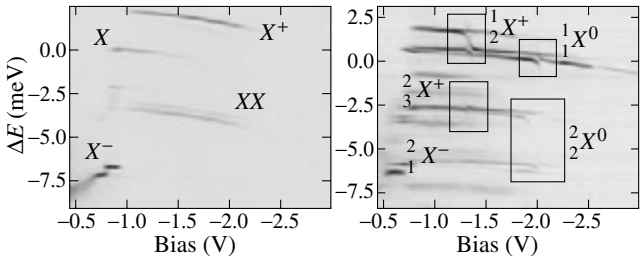

Fig. 1. Photoluminescence-Bias map of single QD (left panel) and coupled QD system (right panel). Labels indicate the excitonic charge state prior to e-h recombination. A typical sequence of differently charged excitons transforms into very reach set of PL lines in CQD. Our theoretical model identifies and explains this complex pattern.

3. Theory

We consider QDs with unequal electron and hole single-particle energies (asymmetric QDs) for which the two hole levels are close to resonance but the electron energies are different. The distance between centers of two dots is $\tilde{d}$. We take the applied electric field, $F = |e|\mathcal{E}$, to change the difference between two hole energies by $F\tilde{d}$.

In the envelope-function approximation the truncated coordinate single particle basis consists of one conduction electron state $\varphi^{\rm e}_{L}(\mathbf{r}_{\rm e})$ with electron energy $\varepsilon_{\rm e}$ in the bottom QD, and two orthonormal hole s-states $\varphi^{\rm h}_{L,R}(\mathbf{r}_{\rm h})$, which are localized primarily in the bottom or in the top QD. The single-particle hole Hamiltonian has matrix elements: $\langle L^{\rm h}|\hat{\mathbf{h}}_{\rm h}|L^{\rm h}\rangle = \varepsilon_{\rm h}$, $\langle R^{\rm h}|\hat{\mathbf{h}}_{\rm h}|R^{\rm h}\rangle = \varepsilon_{\rm h} - F\tilde{d}$, $\langle L^{\rm h}|\hat{\mathbf{h}}_{\rm h}|R^{\rm h}\rangle = -t_{\rm h}$, where $t_{\rm h}$ is the hole tunneling rate. The electron spin up and down states $|\beta^{\rm e}\rangle$, $|\alpha^{\rm e}\rangle$ correspond to $S_{\rm e} = 1/2$, $S_{{\rm e},z} = \pm 1/2$. Heavy-hole spin

states $J_{\rm h} = 3/2$, $J_{{\rm h},z} = \pm 3/2$ can be mapped on to effective fermions with isospin $S_{\rm h} = 1/2$ with the following correspondence $|3/2, \pm 3/2\rangle \to |1/2, \mp 1/2\rangle$.

The many-body basis configurations for each molecule are constructed from antisymmetrized products of single-particle states where the electron occupies only one ground state level in single QD and the hole can occupy two lowest levels of CQD system. The many-particle Hamiltonian consists of three parts. The first part is single-particle electrons and holes QD Hamiltonians, the second part describes Coulomb interactions between particles, and the third part is a short-range electron-hole exchange:

$$A \sum_{i,j=1}^{n,m} \delta(\mathbf{r}_{{\rm e}i} - \mathbf{r}_{{\rm h}j}) \hat{\sigma}^{\rm e}_{zi} \hat{\sigma}^{\rm h}_{zj} \,,$$

where A is the exchange amplitude. The Coulomb interaction between particles is treated with perturbation theory:

$$V^{\alpha,\beta}_{ijkl} = \pm \int d\mathbf{r} d\mathbf{r}' |\mathbf{r} - \mathbf{r}'|^{-1} \varphi^{\alpha *}_i(\mathbf{r}) \varphi^{\beta *}_k(\mathbf{r}') \varphi^{\alpha}_j(\mathbf{r}) \varphi^{\beta}_l(\mathbf{r}') \,.$$

The e-h exchange constants are given by

$$J^{\rm eh}_{ij} = A \int d\mathbf{r} |\varphi^{\rm e}_L|^2 \varphi^{\rm h *}_i \varphi^{\rm h}_j \,.$$

The hole tunneling $t_{\rm h}$ as well as $J^{\rm eh}_{ij}$ and $V^{\alpha,\beta}_{ijkl}$ have strong dependence on distance between QDs. The smallest matrix elements are $J^{\rm eh}_{RR}$ and $V^{\rm hh}_{LRLR}$. They responsible for exchange between particles resided in different QDs. In subsequent analysis we neglect these elements, since a fine structure induced by them is not resolved for given experimental samples (< 1 μeV). We will also neglect off-diagonal Coulomb matrix elements $V^{\alpha\beta}_{LLLR}$, $J^{\rm eh}_{LR} < 10$ μV which are responsible for small Coulomb corrections to tunneling.

The rest of Coulomb integrals will always appear in diagonal matrix elements of many-particle Hamiltonian in some combinations, which can be expressed through five independent parameters: $\gamma_{\rm eh} = V^{\rm eh}_{LLLL} - V^{\rm eh}_{LLRR}$, $\Gamma_{X^+} = V^{\rm hh}_{LLLL} - V^{\rm eh}_{LLLL}$, $\Gamma_{X^-} = V^{\rm eh}_{LLLL} - V^{\rm ee}_{LLLL}$, $\Gamma_{LR} = V^{\rm hh}_{LLRR} - V^{\rm ee}_{LLRR}$, and $J^{\rm eh} \equiv J^{\rm eh}_{LL}$. These parameters have clear physical meaning and can be calculated or extracted from the experimental data: $\Gamma_{X^\pm}$ are intra-dot energies between a positive (negative) trions and an exciton, $\gamma_{\rm eh}$ is the energy difference between direct and indirect exciton, Γ_{BT} describe the excess of energy of the positive trion compared with the direct exciton when one extra hole is added to the top QD. Finally, $J^{\rm eh}$ is the intra-dot electron-hole exchange interaction. Our quantitative estimates give the following hierarchy in energy scales $\gamma_{\rm eh} \gg \Gamma_{X^-} > \Gamma_{X^+} > t_{\rm h} \sim \Gamma_{LR} \sim J^{\rm eh}_{LL}$.

As a result the observed richness of PL spectral lines can be described with these six parameters. The theoretical predictions account well for recent experiments. As an example we consider the biexcton and exciton spectra (see Fig. 2.)

X basis has four states:

$$|1_X\rangle = |L^{\rm e} L^{\rm h}; \beta^{\rm e} \beta^{\rm h}\rangle \,, \quad |2_X\rangle = |L^{\rm e} L^{\rm h}; \beta^{\rm e} \alpha^{\rm h}\rangle \,,$$
$$|3_X\rangle = |L^{\rm e} R^{\rm h}; \beta^{\rm e} \beta^{\rm h}\rangle \,, \quad |4_X\rangle = |L^{\rm e} R^{\rm h}; \beta^{\rm e} \alpha^{\rm h}\rangle \,.$$

In this basis the exciton Hamiltonian is

$$\begin{pmatrix} J^{\rm eh} & 0 & -t_{\rm h} & 0 \\ 0 & -J^{\rm eh} & 0 & -t_{\rm h} \\ -t_{\rm h} & 0 & \gamma_{\rm eh} - F\tilde{d} & 0 \\ 0 & -t_{\rm h}+ & 0 & \gamma_{\rm eh} - F\tilde{d} \end{pmatrix} . \qquad (1)$$

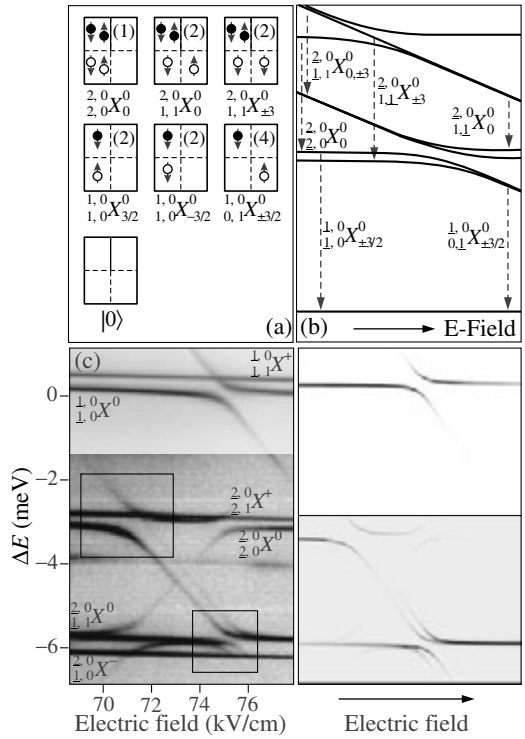

Fig. 2. (a) Energetically non-degenerate charge and spin configurations of exciton ${}^1_1X^0$ and biexciton ${}^2_2X^0$. The number of energetically degenerate states is indicated by the number in parentheses. (b) Field dependent level structure of ${}^1_1X^0$ and ${}^2_2X^0$ and optically allowed transitions. (c) left panel: PL signature of the formation of molecular states for ${}^1_1X^0$ and ${}^2_2X^0$. Right panels: theoretical simulation for the same range of fields and energies.

For the observable range of energies the XX basis consist of two singlet states:

$$|1_{XX}\rangle = |L^{\rm e}_1 L^{\rm e}_2 L^{\rm h}_1 L^{\rm h}_2; s^{\rm e}_{12}; s^{\rm h}_{12}\rangle \,,$$
$$|2_{XX}\rangle = |L^{\rm e}_1 L^{\rm e}_2, 2^{-1/2}(L^{\rm h}_1 R^{\rm h}_2 + R^{\rm h}_1 L^{\rm h}_2); s^{\rm e}_{12}; s^{\rm h}_{12}\rangle \,,$$

and three triplet states

$$|T_l\rangle = |L^{\rm e}_1 L^{\rm e}_2, 2^{-1/2}(L^{\rm h}_1 R^{\rm h}_2 - R^{\rm h}_1 L^{\rm h}_2); s^{\rm e}_{12}; \tau^{\rm h}_{12}, l\rangle \,,$$

where $l = 0, \pm 1$, $|s_{12}\rangle$ and $|\tau^{\rm h}_{12}, 0(\pm 1)\rangle$ are spin functions for the singlet and the triplet accordingly. The triplet states are degenerate and completely decoupled from $|1_{XX}\rangle$, $|2_{XX}\rangle$. They have eigenenergy $E^{XX}_3 = \varepsilon_{XX} + \gamma_{\rm eh} + \Gamma_{LR} - F\tilde{d}$, where ε_{XX} is the energy shift between XX and X, when all particles are in the same QD. The other two eigenenergies are determined from the singlet states Hamiltonian:

$$\begin{pmatrix} \varepsilon_{XX} & -\sqrt{2}t_{\rm h} \\ -\sqrt{2}t_{\rm h} & \varepsilon_{XX} + \gamma_{\rm eh} + \Gamma_{LR} - F\tilde{d} \end{pmatrix} . \qquad (2)$$

Transitions between three biexciton eigenstates and four eigenstates of the exciton Hamiltonian (1) determine the "X"-pattern and the fine structure observed in the experiment.

Acknowledgement

This work has been supported by National Research Council/ Naval Research Laboratory Research Associates.

References

[1] E. A. Stinaff *et al*, *Science* **311**, 636 (2006).

14th Int. Symp. "Nanostructures: Physics and Technology"
St Petersburg, Russia, June 26–30, 2006

Effect of multiphonon processes on the spin-relaxation of excitons localized in semiconductor quantum dots

A. Reznitsky[1], A. Klochikhin[1,2], *S. Permogorov*[1], L. Tenishev[1], E. Tsitsishvili[3], R. v. Baltz[3], H. Kalt[4] and C. Klingshirn[4]

[1] Ioffe Physico-Technical Institute, St Petersburg, Russia
[2] Nuclear Physics Institute, 188350, St Petersburg, Russia
[3] Institut für Theorie der Kondensierten Materie, Universität Karlsruhe (TH), 76128 Karlsruhe, Germany
[4] Institut für Angewandte Physik, Universität Karlsruhe (TH), 76128 Karlsruhe, Germany

Abstract. An important role of the multi-phonon processes in spin relaxation of excitons or trions in semiconductor quantum dots is demonstrated. The multi-phonon processes lead to the dephasing of single localized states and relax limitations connected with the phonon bottleneck in the energy relaxation of localized states. We have applied the developed approach to fit the experimental data on the temperature dependence of the polarization degree in the CdSe/ZnSe quantum islands.

Introduction

The spin relaxation in semiconductor quantum dots between discrete energy levels is slow and at low temperature neither the electron, nor the hole spin relax on the exciton lifetime scale [1]. The electron spin-flip processes between discrete energy levels in quantum dots were considered in Refs. [2,3,4,5,6]. Acoustic phonon-assisted flips of single spins arising due to several mechanisms originating from spin-orbit coupling were treated in Refs. [2,3,4]. It was shown that at low temperatures spin relaxation rates are governed by one-phonon emission processes while for higher temperatures two-phonon processes give the dominant contributions to spin relaxation [4]. The relaxation of exciton spin due to two optical phonons was studied in Ref. [5]. Another mechanism of exciton spin relaxation due to acoustic phonon coupling via the strain-dependent short-range exchange interaction was proposed in Ref. [6]. The hole spin-flip in the Kramers degenerate trion doublet was considered in Ref. [7] to explain the trion spin relaxation in self-assembled CdSe/ZnSe quantum islands.

The common feature of the considered processes is the necessity to use the off-diagonal matrix element of the exciton-phonon interaction. The limitations arising due to energy conservation laws create the problem of the phonon bottleneck that restricts severely the spin-relaxation rate.

The energy relaxation of localized excitations is influenced by the multi-phonon processes due to diagonal matrix elements of the exciton-phonon interaction. These processes are not able by themselves to provide the spin-flip. However, they modify the spin relaxation indirectly leading to the transformation of the discrete levels into continuum bands. The influence of this transformation (pure dephasing [8, 9]) on the relaxation probability [10] is considered in this work in the framework of the exactly solvable model.

The characteristic spectrum of phonons leading to the dephasing of localized states in the quantum well can be reconstructed from the shapes and temperature dependences of the μ-PL lines and PL spectra at resonant excitation. This allows to calculate the transition probability between two continuum electron-phonon bands taking into account the interaction with an arbitrary number of phonons [10]. Using the transition probabilities from the electron-phonon band 1 to the electron-phonon band 2 and back we can solve the master equation for the polarization degree for any of above mentioned spin-flip mechanisms.

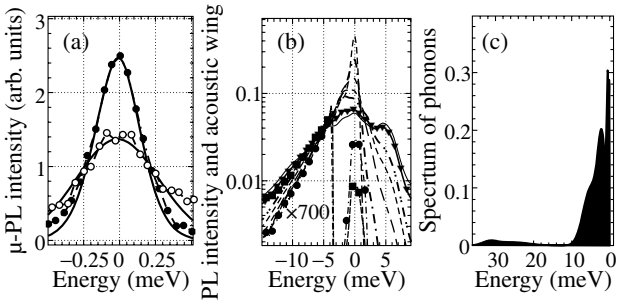

Fig. 1. (a) The shapes of the μ-PL line at two temperatures ($T = 7$ and 22 K) are presented by broken lines with symbols. Solid lines are calculated line shapes. (b) The acoustic wing of the PL band of localized states at resonant excitation at 7 and 80 K (open and closed symbols, respectively). Calculated spectra in the temperature range 10–130 K are presented by broken lines with the step of 20 K. (c) The characteristic spectrum of phonons interacting with localized states.

Variations of PL spectra with temperature

We have studied the temperature dependences of μ-PL lines and PL spectra at resonant excitation of the epitaxial samples grown by multi-cycle migration enhanced epitaxy deposition of CdSe in ZnSe matrices. Details on the growth procedure and the structure characterization by HRTEM of the samples under study can be found in Ref. [11, 12].

The temperature transformation of the μ-PL line is presented in Fig. 1a together with calculations of the line shape at different temperatures [10]. The acoustical PL wings at resonant excitation in the range of ground states [13] at two temperatures are shown in Fig. 1b. The same spectrum within the broader energy interval is shown in Fig. 3a. The characteristic single-phonon spectrum of acoustical and optical phonons which provides the best fit of calculations to the experimental spectra is demonstrated in Fig. 1c.

Probability of the transition between two continuum bands

Figure 2 shows the continuum densities Δ_1^+ and Δ_2^- of states (DOS) of two electron-phonon bands 1 and 2 resulting due to the dephasing process. In the limit of zero temperature the DOS of the first band Δ_1^+ corresponds to the emission of phonons

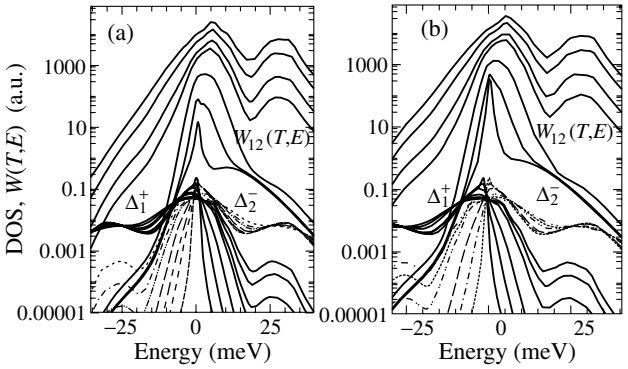

Fig. 2. The exciton-phonon DOS Δ_1^+ (solid lines) and Δ_2^- (broken lines) due to the diagonal interaction of phonons and localized excitons for degenerate (a) and split (b) bands, respectively. $W_{12}(E, T)$ is the transition probability from the energy point E in the band 1 to all energies within the band 2 in the temperature range 10–130 K. For convenience, the curves are shifted in vertical direction arbitrarily.

while the DOS of the second band Δ_2^- corresponds to the absorption of phonons. At finite temperatures both emission and absorption of phonons are responsible for the shapes of both bands [10].

Figure 2 shows also the temperature dependences of transition probabilities $W_{12}(T, E)$ from the state 1 with the energy E to all energies of the electron-phonon band of the state 2 for degenerate (Fig. 2a) and non-degenerate (Fig. 2b) states at different temperatures. In order to calculate the temperature dependence for any of the spin-flip processes accompanied by the acoustical phonon emission and/or absorption due to the off-diagonal matrix element of the exciton-phonon interaction we should calculate the transition probability $w_{12}(T) = \int_{-\infty}^{\infty} dE\, W_{12}(E, T)$.

Polarization of resonantly excited PL spectra

As it was shown in Ref. [13], the low-energy side of the PL band at interband excitation of samples under study is formed mostly by the ground states of trions, while the high-energy side corresponds to the neutral exciton states. Figure 3b demonstrates the spectrum of degree of circular polarization at resonant excitation on the low-energy side of the PL band. Figure 3c shows the temperature dependence of the circular polarization degree

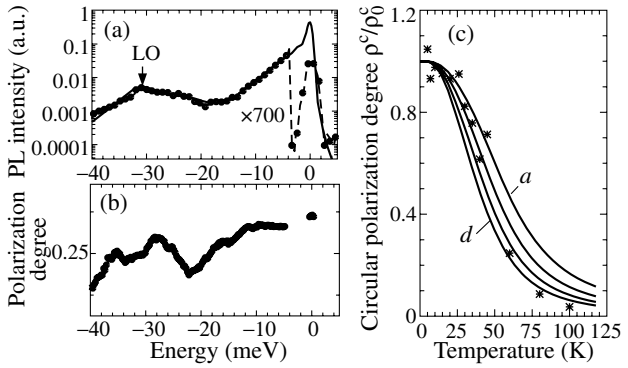

Fig. 3. (a) PL-intensity spectrum at resonant excitation at 7 K. Experimental and calculated spectra are presented by symbols and solid line, respectively, and (b) spectrum of degree of circular polarization. (c) Dependence of the circular polarization degree on temperature (symbols) and fit of this dependence using Eq. (3) with $\tau w_{12}(0) = 2 - 6 \cdot 10^{-4}$ (curves from a to d).

in the range from 6 to 12 meV below the excitation.

Solution of the master equation gives for the polarization degree

$$\rho(T) = \frac{\rho_0}{1 + 2\tau\Phi(T)}\,, \tag{1}$$

where

$$\rho_0 = \frac{1 - \tau w_{12}(0)}{1 + \tau w_{12}(0)}\,, \quad \Phi(T) = \frac{w_{12}(T) - w_{12}(0)}{1 + \tau w_{12}(0)}\,, \tag{2}$$

where τ is the exciton radiative lifetime.

The best fit of the experimental data presented in Fig. 3c corresponds to $\tau w_{12}(0) \approx 2 - 6 \cdot 10^{-4}$ and to the assumption that the states 1 and 2 are degenerate. The estimated value of $\tau w_{12}(0)$ means that at low temperatures the trion spin does not relax during the radiative lifetime. This conclusion is in appropriate agreement with the presently available experimental findings.

Summary

We presented a new sight at the temperature dependence of the spin relaxation processes between spin sublevels of localized states in semiconductor quantum dots, which is based on the exact consideration of the most important (diagonal) part of the electron-phonon interaction. This approach explains the temperature behavior of the narrow lines in μ-PL spectra, the shape of the PL spectrum at resonant excitation of the emission states in quantum islands and the temperature dependence of the degree of circular polarization of trions (degenerate spin states). The developed approach can be used also for description of the temperature dependences of the degree of linear polarization of localized excitons (split momentum states).

Acknowledgements

We thank S. Sorokin, I. V. Sedova and S. Ivanov for the samples used in the experiments. This work was partly supported by Deutsche Forschungsgemeinschaft within the Center for Functional Nanostructures (project A2), by Russian Foundation for Basic Research, and by the Programs of Russian Academy of Sciences ("Spin-dependent processes in solids and spintronics" and "Low-dimensional quantum structures").

References

[1] M. Paillard *et al*, *Phys. Rev. Lett.* **86**, 1634 (2001).
[2] Alexander V. Khaetskii and Yuli V. Nazarov, *Phys. Rev. B* **64**, 125316 (2001).
[3] D. Frenkel, *Phys. Rev. B* **43**, 14 228 (1991).
[4] L. M. Woods *et al*, *Phys. Rev. B* **66**, 161318(R) (2002).
[5] E. Tsitsishvili, R. v. Baltz and H. Kalt, *Phys. Rev. B* **66**, 161405(R) (2002).
[6] E. Tsitsishvili, R. v. Baltz and H. Kalt, *Phys. Rev. B* **67**, 205330 (2003).
[7] T. Flissikowski *et al*, *Phys. Rev. B* **68**, 161309(R) (2003).
[8] L. Besombes *et al*, *Phys. Rev. B* **63**, 155307 (2001).
[9] B. Krummheuer, V. M. Axt and T. Kuhn, *Phys. Rev. B* **65**, 195313 (2002).
[10] A. Klochikhin *et al*, *Phys. Rev. B* **69**, 085308 (2004).
[11] S. Sorokin *et al*, *J. Cryst. Growth* **201/202**, 461 (1999).
[12] N. Peranio *et al*, *Phys. Rev.* **B 61**, 16015 (2000).
[13] A. Reznitsky *et al*, *phys. stat. sol. (c)* **0**, 1544 (2003).

14th Int. Symp. "Nanostructures: Physics and Technology"
St Petersburg, Russia, June 26–30, 2006

Direct comparison of Raman intensities from carbon nanotubes under different resonant excitations: Role of exciton decay

S. V. Goupalov[1], B. C. Satishkumar[2] and S. K. Doorn[2]

[1] Ioffe Physico-Technical Institute, St Petersburg, Russia
[2] Los Alamos National Laboratory, Los Alamos, NM 87545 USA

Abstract. We present the first direct comparison of intensities of Raman scattering from the radial breathing mode of semiconducting single-walled carbon nanotubes under excitations resonant with different electronic transitions.

Introduction

Recent advances in nanotube research have allowed for the fabrication of well-separated single-walled carbon nanotubes (NTs) produced out of aggregated bulk assemblies and isolated in micelles [1]. As a result, it has become possible to assign the radial breathing mode (RBM) features observed in Raman spectroscopy to specific (n, m) semiconducting NTs. The chirality assignments deduced from Raman spectroscopy are highly reliable since both Raman excitation profile maxima positions and the RBM frequencies depend on the chiral indices (n, m). Furthermore, as has been recently shown [2]–[4], the intensity of resonant Raman signal significantly varies with the NT chirality, and quite distinctive behavior is demonstrated by semiconducting NTs with $\nu \equiv (n-m)\, mod\, 3 = -1$ as compared to NTs with $\nu = +1$. For technical reasons, all Raman measurements on semiconducting carbon NTs reported so far were performed under excitations resonant with some specific electronic transitions, usually matching the gap, E_{22}, between second singularities in electronic densities of states in the conduction and valence bands. Here we present the first direct comparison of resonance Raman intensities for semiconducting NTs under excitations resonant with E_{11} and E_{22} transitions. The intensity ratio turns out to amount one to four orders of magnitude depending on the NT chirality. We show that explanation of our data requires addressing the difference in decay rates for exciton states involved in Raman process under different excitations.

1. Experiment

In the present work Raman measurements have been carried out on HipCO SWNTs using laser excitation in the energy range of 700–1000 nm and 565–690 nm using Ti:Sapphire laser and dye lasers, respectively. The samples of solubalized NTs were prepared by shear mixing and ultrasonication of NTs and sodium dodecyl sulphate (SDS) in deuterium, followed by centrifugation at 28000 rpm for 6 hours. Examples of the observed resonance Raman excitation profiles for a (9,1) NT under E_{11} and E_{22} excitations are presented in Fig. 1a and b, respectively. Experimental data shown as circles has been fit by solid lines using the decay rates of $\Gamma_{11} = 22$ meV and $\Gamma_{22} = 78$ meV as fitting parameters. The peak structure in Fig. 1a is due to the spectral resolution of the input and output resonances [6]. Fig. 1b shows no structure which is explained by the larger value of the decay rate for the E_{22} excitation.

Both E_{11} and E_{22} transitions were accessible by the lasers for the NTs of the following semiconducting chiralities: (5,4), (6,5), (7,3) [$\nu = +1$], and (6,4), (8,3), (9,1) [$\nu = -1$] present in our samples. The chiral indices and transition energies for these NTs are listed in Table 1 along with the observed peak intensities of the Raman profiles at E_{11} and E_{22} excitations. One can see from Table 1 that for all studied chiralities the peak resonance Raman intensities under E_{11} excitations are larger than those under E_{22} excitation.

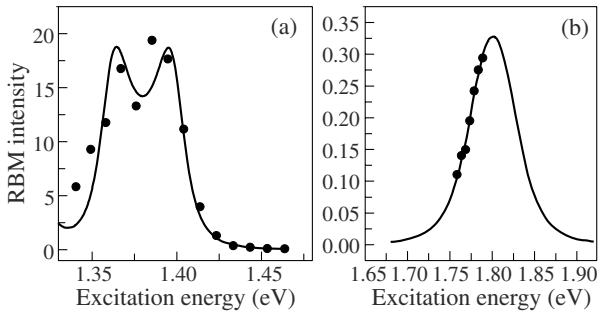

Fig. 1. Resonance Raman excitation profiles for a (9,1) NT under E_{11} (a) and E_{22} (b) excitations.

Table 1. Chiral indices, resonant transition energies and Raman intensities for carbon NTs studied in this work.

(n, m)	ν	E_{11} (eV)	E_{22} (eV)	Ratio I_{11}/I_{22}
(6,4)	−1	1.420	2.146	4.7
(8,3)	−1	1.303	1.863	12.2
(9,1)	−1	1.359	1.739	38.7
(5,4)	+1	1.485	2.566	58
(6,5)	+1	1.270	2.190	287
(7,3)	+1	1.250	2.457	11700

2. Theory

The probability of the Raman scattering event is given by

$$P = \frac{2\pi}{\hbar}\left|\sum_{n,m}\frac{\langle 0|\hat{V}_{\rm opt}|n\rangle\langle n, N\pm 1|\hat{V}_{\rm exc-ph}|m, N\rangle\langle m|\hat{V}_{\rm opt}|0\rangle}{(E_m - \hbar\Omega_{\rm i} - i\Gamma_m)(E_n - \hbar\Omega_{\rm i} \pm \hbar\omega_0 - i\Gamma_n)}\right|^2 \times\delta(\hbar\Omega_{\rm i} \mp \hbar\omega_0 - \hbar\Omega_{\rm s})\,. \quad (1)$$

Here $\Omega_{\rm s}$ ($\Omega_{\rm i}$) is the frequency of the scattered (incident) light, ω_0 is the frequency of the emitted or absorbed phonon, indices m and n denote the states of the electron-hole pair (or exciton); E_n and Γ_n are, respectively, the energy and the decay rate of the intermidiate state $|n\rangle$; N is the phonon occupation number for the given phonon mode; $\hat{V}_{\rm opt}$ and $\hat{V}_{\rm exc-ph}$ are the operators of the exciton-photon and exciton-phonon interactions, respectively.

Under resonant excitation conditions, the real part of one of the denominators in Eq. (1) vanishes, and the real part of

the other one becomes $\pm\hbar\omega_0$. Two different regimes can be distinguished. For small Γ_n the decay rate can be neglected compared to $\hbar\omega_0$: $|\pm\hbar\omega_0 - i\Gamma_n| \approx \hbar\omega_0$. The NTs studied in our work have similar radii, and the radius dependence of ω_0 in the denominator can be neglected. Thus, the Raman intensity is inversly proportional to Γ_n^2. In the opposite limiting case Γ_n is large compared to $\hbar\omega_0$ and Raman intensity is inversly proportional to Γ_n^4.

The matrix element of the operator of the exciton interaction with the RBM on the electronic states has different form for the electron-hole pairs excited by E_{11} and E_{22} transitions. For the E_{11} transition in the nearest neighbor tight binding model we have [4,5]

$$V^{11}_{\text{exc-ph}} = \frac{5}{12}\frac{a^2}{R^2}\hat{u}_r\left[\frac{\partial\gamma_0}{\partial\tau} - 3\,\delta_0\,\frac{\partial\sigma_0}{\partial\tau}\right]\left\{\frac{1}{2} - A\right\}, \qquad (2)$$

where a is the graphene lattice constant, R is the NT radius, $\hat{u}_r$ is the operator (acting on phonon variables) of radial displacement in the RBM phonon mode, $\partial\gamma_0/\partial\tau$ ($\partial\sigma_0/\partial\tau$) is the transfer (overlap) integral derivative with respect to the length of the π atomic bond, δ_0 is the on-site integral of the tight-binding model, and

$$A = -\frac{\nu 6\sqrt{3}}{5}\frac{R}{a}\cos 3\theta = -\frac{\nu 3\sqrt{3}}{10\pi}\frac{(2n+m)(n^2-2m^2+nm)}{n^2+m^2+nm}. \qquad (3)$$

Here θ is the chiral angle. For the E_{22} transition we have [4,5]

$$V^{22}_{\text{exc-ph}} = \frac{5}{12}\frac{a^2}{R^2}\hat{u}_r\left[\frac{\partial\gamma_0}{\partial\tau} - 3\delta_0\,\frac{\partial\sigma_0}{\partial\tau}\right]\{1 + A\}\,. \qquad (4)$$

One can see that Eq. (2) and Eq. (4) differ only by the terms in the curly brackets.

Further difference in the expression for the Raman intensity under different excitations comes from the chirality dependence of the optical matrix element [7]. However, this dependence is rather weak [7] and will be neglected here.

Let I_{11} and I_{22} be the experimentally measured resonant Raman peak intensities under E_{11} and E_{22} excitations. Assuming that the chirality dependence of the decay rates in Eq. (1) is negligible compared to those of the matrix elements (2)–(4), one can see that chirality dependence of $I_{ii}R^4$ will be determined by the square of the curly brackets in Eqs. (2) or (4). Thus, we have

$$I_{11}R^4 = C_{11}\{A - 0.5\}^2\,, \qquad I_{22}R^4 = C_{22}\{A + 1\}^2\,, \qquad (5)$$

where C_{11} and C_{22} are the coefficients of proportionality. If Γ_n is small compared to $\hbar\omega_0$ then from Eqs. (1)–(5) it follows that, under resonant excitation conditions, the ratio of these coefficients gives the square of the ratio of the decay rates:

$$\frac{C_{11}}{C_{22}} = \left(\frac{\Gamma_{22}}{\Gamma_{11}}\right)^2.$$

In the opposite limiting case of large Γ_n, the right hand part of this relation should be further squared.

In Fig. 2a by squares is shown experimental data corresponding to the left-hand part of the first of of Eqs. (5) as a function of the parameter A. By the solid line is shown the fit with the parabola given by the right-hand side of the first

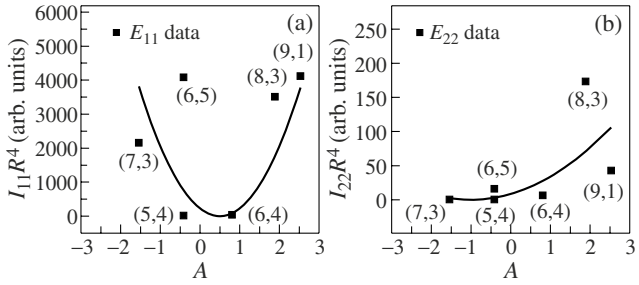

Fig. 2. A-dependencies of $I_{11}R^4$ (a) and $I_{22}R^4$ (b).

of Eqs. (5). In a similar fashion, both parts of the second of Eqs. (5) are shown in Fig. 2b. The coefficients C_{11} and C_{22} are obtained by the best parabolic fits to the experimental data. We thus obtain $C_{22} \approx 8.5$ and $C_{11} \approx 916$. Therefore, taking into account both the limits of small and large Γ_n, we obtain the following estimate for the ratio of the decay rates

$$3 \lesssim \frac{\Gamma_{22}}{\Gamma_{11}} \lesssim 10\,.$$

This result is in agreement with the ratio of decay rates that one can obtain from the fitting of excitation profiles of Fig. 1.

3. Conclusions

In summary, we have performed the first direct comparison of intensities of Raman scattering from the RBM of semiconducting single-walled carbon NTs under excitations resonant with different electronic transitions. We found that the difference in measured Raman intensities varies from one to several orders of magnitudes depending on the NT chiralities. We showed that explanation of observed results requires addressing the difference in decay rates for exciton states involved in Raman process under different excitations. We found that the exciton state excited by the E_{22} transition decays three to ten times faster than the state excited by the E_{11} transition. The ratio thus obtained is in agreement with the ratio of decay rates deduced from the fit of the resonance Raman excitation profiles. This allows us to conclude that the lineshape of the Raman excitation profiles is mainly due to homogeneous broadening originating from the decay of bright exciton states involved in the Raman process.

Acknowledgements

This work was supported by the US DOE. NT samples were provided by Prof. R. E. Smalley's group at Rice University.

References

[1] M. J. O'Connell *et al*, *Science* **297**, 593 (2002).
[2] S. K. Doorn *et al*, *Appl. Phys. A* **78**, 1147 (2004).
[3] H. Telg *et al*, *Phys. Rev. Lett.* **93**, 177401 (2004).
[4] S. V. Goupalov, B. C. Satishkumar and S. K. Doorn, *PRB* **73**, 115401 (2006).
[5] S. V. Goupalov, *Phys. Rev. B* **71**, 153404 (2005); **72**, 159901(E) (2005).
[6] J. Jiang *et al*, *Phys. Rev. B* **71**, 205420 (2005).
[7] S. V. Goupalov, *Phys. Rev. B* **72**, 195403 (2005).

14th Int. Symp. "Nanostructures: Physics and Technology"
St Petersburg, Russia, June 26–30, 2006

Optics of charged excitons in quantum wells: free versus donor-bound complexes

A. B. Dzyubenko[1,2], D. A. Cosma[1], T. D. Kelly II[1], A. R. Todd[1] and A. Yu. Sivachenko[3]

[1] Department of Physics, California State University at Bakersfield, CA 93311, USA
[2] General Physics Institute, Russian Academy of Sciences, Vavilova 38, Moscow 119991, Russia
[3] Ariadne Genomics Inc., 9700 Great Seneca Highway, Rockville, MD 20850, USA

Abstract. We theoretically study localization of quasi-two-dimensional negatively charged excitons X^- on isolated charged donors in magnetic fields. We consider donors located in a barrier at various distances L from the heteroboundary as well as donors in the quantum well. We establish how many different singlet X_s^- and triplet X_t^- bound states a donor ion D^+ can support in magnetic fields $B > 6$ T. We find several new bound states, some of which have surprisingly large oscillator strengths.

Introduction

Optical signatures of spin-singlet X_s^- and spin-triplet X_t^- charged excitons are commonly observed in semiconductor nanostructures in magnetic fields. Despite the status of X^- as one of the simplest few-body systems with Coulomb interactions and a large amount of experimental and theoretical work, some important issues remain unresolved. One of these issues is the degree of localization of charged excitons in realistic quantum wells (QW's) and how localization of X^- manifests itself in optics [1,2].

In this work, we discuss exact selection rules that govern transitions of charged excitons in magnetic fields. We also demonstrate, on a quantitative level, how these selection rules work when applied to free X^- and donor-bound (D^+, X^-) charged excitons; the latter can also be considered as excitons bound to a neutral donor (D^0, X).

1. Classification of states and selection rules

Classification of states of free charged electron-hole complexes in magnetic fields is based on magnetic translations and the axial symmetry about the magnetic field axis [2]. The corresponding orbital quantum numbers are the oscillator quantum number $k = 0, 1, 2, \ldots$ and the total angular momentum projection on the z-axis, M. The former has the meaning of the mean squared distance to the orbit guiding center; there is an infinite-fold Landau degeneracy in k. Each family of degenerate X^- states starts with its parent $k = 0$ state that has some specific value of M that follows from the solution of the Schrödinger equation. Degenerate daughter states $k = 1, 2, \ldots$ have values $M - 1, M - 2, \ldots$ for the total angular momentum projection. Selection rules for interband transitions are $\Delta M = 0$ and $\Delta k = 0$ and lead to the following results: Photoluminescence (PL) of a free X^- must leave an electron in a LL with the number n equal to the angular momentum M of the parent state, $X^- \to \hbar\omega_{X^-} + e^-_{n=M}$. Therefore, (i) families of X^- states that start with $M < 0$ are dark in PL and (ii) shake-ups to multiple Landau levels (LL's) are strictly prohibited [2].

The presence of a donor ion D^+ breaks the translational symmetry, lifts the degeneracy in k, and makes many of the previously prohibited transitions allowed. Let us discuss spectroscopic consequences of the remaining axial symmetry for a donor-bound state (D^+, X^-) with angular momentum M and wavefunction $\Psi_M(\mathbf{r}_{e1}, \mathbf{r}_{e2}; \mathbf{r}_h)$. The dipole matrix element for interband transition to a final electron state $\phi_{m_f}(\mathbf{r})$ with angular momentum projection m_f is

$$f \sim \left| p_{\rm cv} \int d\mathbf{r} \int d\mathbf{r}'\, \phi^*_{m_f}(\mathbf{r})\, \Psi_M(\mathbf{r}, \mathbf{r}'; \mathbf{r}') \right|^2 \sim \delta_{M,m_f} \,. \quad (1)$$

Conservation of angular momentum $M = m_f$ can be satisfied for a number of final states $\phi_{m_f}(\mathbf{r})$ belonging to different LL's. Therefore, shake-up processes become allowed in PL. More than that, PL of (D^+, X^-) states with $M > 0$ must proceed via shake-ups to higher LL's [3]. This is because electron states with angular momenta $m_f = M > 0$ are only available in $n = M$ or higher LL's. Note that the shake-up processes are due to the Coulomb induced admixture of LL's and are suppressed in strong fields as B^{-2}.

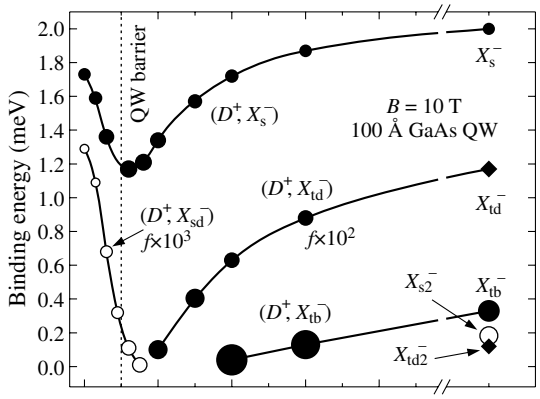

Fig. 1. Binding energies of charged excitons X^- in a 100 Å GaAs/$Al_{0.3}Ga_{0.7}As$ QW at $B = 10$ T. Sizes of the dots are proportional to the interband dipole transition matrix elements f. The solid diamonds designate dark X^- states.

2. Numerical approach

We obtain the energies and wavefunctions of the (D^+, X^-) complexes and of free X^- excitons by diagonalization of the interaction Hamiltonian using a complete basis of states compatible with both axial and electron permutational symmetries. The basis states are constructed out of the in-plane wavefunctions in LL's and size quantization levels in a QW with proper symmetrization for triplet and singlet states. We consider up to 2×10^5 basis states and, by applying an adaptive scheme, we choose out of these about 6×10^3 states to be diagonalized

in the Hamiltonian matrix. A stability for the donor-bound charged exciton is determined with respect to its dissociation to a neutral donor and a free exciton, $(D^+, X^-) \to D^0 + X$. Accordingly, a binding energy of a stable (D^+, X^-) complex is defined as the energy difference between the total Coulomb energies

$$E^{\rm b}_{(D^+,X^-)} = E^{\rm Coul}_{D^0} + E^{\rm Coul}_{X} - E^{\rm Coul}_{(D^+,X^-)} > 0\,, \qquad (2)$$

with D^0 and X being in their ground states. Binding energy (2) determines the energy difference between the positions of a neutral exciton and a donor-bound charged exciton PL emission lines, $\hbar\omega_X - \hbar\omega_{(D^+,X^-)} = E^{\rm b}_{(D^+,X^-)}$.

3. Results and discussion

The calculated binding energies of the various charged exciton states in a 100 Å GaAs QW as functions of the distance L to the donor ion D^+ are shown in Fig. 1. We estimate the accuracy in binding energies to be of the order of ± 0.1 meV.

The limiting case $L = \infty$ corresponds to free charged excitons X^-. There are three documented bound states in this limit: the bright singlet X^-_s with $M = 0$, the dark triplet X^-_{td} with $M = -1$, and the bright triplet X^-_{tb} with $M = 0$ (see [2,4,5] and references therein). We found two new bound states: the second dark triplet state with $M = -1$, labeled X^-_{td2} in Fig. 1, and the second bright singlet state with $M = 0$, labeled X^-_{s2}. These states are very weakly bound and will be discussed in more detail elsewhere.

Our results show that the parent bright singlet state X^-_s with $M = 0$ remains always bound. Its binding energy initially decreases with decreasing L, reaches its minimum when the donor D^+ is very close to the heteroboundary, and then increases again. We interpret this as an indication toward a rearrangement of the type of binding in the singlet (D^+, X^-_s) state: At very large distances L, the donor ion binds X^-_s as a whole, barely affecting its internal structure. In the opposite limit of an in-well donor, the interaction of electrons with the D^+ is stronger than that with the hole. The donor-bound complex formed in this case is better described as an exciton bound to a neutral donor (D^0, X).

Notice a systematic change in the dipole transition matrix elements f in Fig. 1: as the binding energy of a complex decreases, its spatial extent increases leading to the increase in f. This is consistent with the notion of "giant oscillator strengths" [6].

We found just one state that only exists in the presence of the D^+ and does not have its free $L = \infty$ counterpart: the dark singlet state (D^+, X^-_{sd}) with $M = 1$. It only becomes bound when the D^+ is located in a QW or very near to it. This is also the only donor-bound state that remains bound in the strictly 2D high-field limit in symmetric electron-hole systems [3]. According to (1), the PL from this state goes mostly via shake-ups to $n = 1$ electron LL. As a result, the dipole transition matrix elements f shown in Fig. 1 are very small.

In contrast to singlet states, the dark X^-_{td} and bright X^-_{tb} triplet states survive only for sufficiently large distances L to the donor ion D^+ (Fig. 1). This is because electrons in triplet states cannot simultaneously occupy the s-state in the lowest LL and, therefore, it is difficult to find a configuration with optimized electron-donor interactions. Notice the finite oscillator strengths for the PL from the donor-bound complex (D^+, X^-_{td}) originating from the dark triplet state.

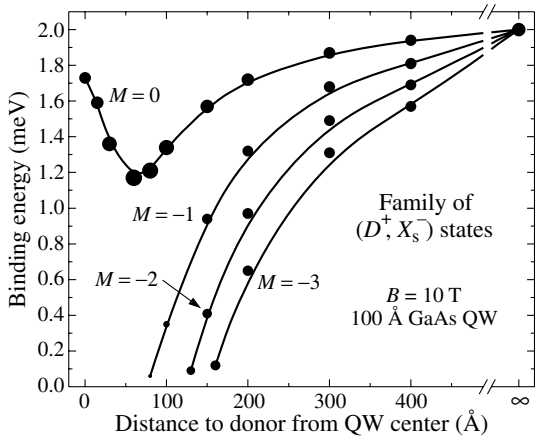

Fig. 2. Lifting of the Landau degeneracy in the family of bright singlet states X^-_s. The states are characterized by different total angular momentum projections $M = 0, -1, -2, \ldots$ and all are optically active.

We stress that each free X^- state gives rise to a family of degenerate states; only the evolution of the parent X^- states is shown in Fig. 1. The degeneracy in the in-plane position of the guiding center (quantum number k) is lifted in the presence of the donor ion D^+. Fig. 2 demonstrates this for the family of singlet bright states X^-_s. When the distance to the donor L decreases, all but one state (with $M = 0$) become one by one unbound. This leads to a number of optically active states with large oscillator strengths.

In conclusion, we have shown there is a multitude of donor-bound X^- states that may exhibit relatively weak dependencies of binding energies and oscillator strengths on positions of remote donors. Our results may be relevant for explanation of the PL from the dark triplet state X^-_{td}, of the multiple PL peaks observed in different experiments, and of the X^- shake-ups in PL.

Acknowledgements

This work is supported in part by NSF grants DMR-0203560 and DMR-0224225, and by a College Award of Cottrell Research Corporation.

References

[1] O. V. Volkov, V. E. Zhitomirskii, I. V. Kukushkin, K. von Klitzing, and K. Eberl, *JETP Lett.* **67**, 744 (1998).
[2] A. B. Dzyubenko and A. Yu. Sivachenko, *Phys. Rev. Lett.* **84**, 4429 (2000).
[3] A. B. Dzyubenko, *Phys. Lett. A* **173**, 311 (1993).
[4] A. Wójs, J. J. Quinn, and P. Hawrylak, *Phys. Rev. B* **62**, 4630 (2000).
[5] C. Riva, F. M. Peeters, and K. Varga, *Phys. Rev. B* **63**, 115302 (2001).
[6] E. I. Rashba and G. E. Gurgenishvili, *Fiz. Tverd. Tela* **4**, 1029 (1962) [*Sov. Phys. Solid State* **4**, 759 (1962)].

14th Int. Symp. "Nanostructures: Physics and Technology"
St Petersburg, Russia, June 26–30, 2006

Exciton and Mn^{2+} intracenter luminescence in ZnMnTe/ZnMgTe heterostructures under high optical excitation

V. F. Agekyan[1], I. Akai[2], N. G. Filosofov[1], T. Karasawa[2], G. Karczewski[3], A. Yu. Serov[1] and N. N. Vassiliev[1]

[1] Institute of Physics, St Petersburg State University, 198504 St Petersburg, Russia
[2] Osaka City University, 558 Osaka, Japan
[3] Institute of Physics Polish Academy of Science, 02668 Warsaw, Poland

Abstract. Exciton and manganese intracenter luminescence (IL) in the quantun well (QW) structures ZnMnTe/ZnMgTe was studied under pulsed excitation up to 10^7 W/cm^2. The strong QW exciton band broadening and Mn^{2+} IL degradation originated from the unelastic processes are observed under the high excitation. As shown by the Mn^{2+} IL kinetics in the structures with different QW widths, the $3d$-shell excitation changes only few positions during its lifetime in $Zn_{0.8}Mn_{0.2}Te$ at 5 K.

Introduction

Intracenter luminescence (IL) of the iron group elements embedded in crystalline II–VI matrices has been studied over a long period. These compounds are used in the luminescence devices, plasma displays, lasers for the micrometer range, etc. The kinetics of the Mn^{2+} IL ($^1T_4$–$^6A_1$ transition) has been measured and discussed in details for the bulk II–VI matrices [1]. The wide gap II–VI nanocrystals activated with manganese atoms are actively pursued now due to the progress in their fabrication. The special interest to these systems was initiated strongly by the discussion about the possible change of Mn^{2+} IL characteristics in nanomatrix as compared to the bulk one. It was claimed that the decay rate is several orders of magnitude higher in nanocrystals [2], but the phonon assisted relaxation within the nearest emitting electron state $^1T_4$, on contrary, strongly slows down due to the peculiar properties of the electron-phonon interaction in nanocrystals. These suggestions were disputed later by several authors (see e.g. [3]). The II–VI solid solutions with a high concentration of the cation magnetic component belong to the family of dilute magnetic semiconductors (DMS). A spectroscopic investigation of the bulk DMS and related quantum well structures (QWS), mainly, CdTe/$Cd_{1-x}Mn_xTe$ and $Cd_{1-x}Mn_xTe$/$Cd_{1-y}Mg_yTe$ has been carried out during the last decade. The problem of Mn^{2+} IL has not been usually under consideration in QWS, the QWs CdTe and $Cd_{1-x}Mn_xTe$ being nonactivated or weakly activated ($x < 0.4$). The first results on the spectral and time dependent properties of Mn^{2+} IL in QWs have been obtained in [4]. The present work deals with the exciton and Mn^{2+} luminescence in QWSs $Zn_{1-x}Mn_xTe$/$Zn_{0.6}Mg_{0.4}Te$ and is focused on the dependence of emission spectra on the structure parameters and optical excitation conditions.

1. Experimental results and discussion

There are three coupled mechanisms for the radiative recombination in these structures: barrier exciton, QW exciton and Mn^{2+} $3d$-shell. The dynamics of the electron relaxation is governed mainly by the QW width L_z, manganese concentration x and excitation level I. We shall discuss the transformation of the emission spectra for four $Zn_{1-x}Mn_xTe$/$Zn_{0.6}Mg_{0.4}T$ samples #1–4 under the excitation level which varies over a wide range from $I = 0.007\ I_0$ up to $I = I_0$ ($I_0 = 8 \times 10^6$ W/cm^2).

#1 ($x = 0.2$, L_z=26 ML). The Mn^{2+} IL saturates with the increasing I, while the QW exciton emission appears and becomes stronger. Under weak pumping conditions the QW exciton is not observed because of the large QW width and high manganese concentration. Under these conditions, the characteristic time for the energy transfer from the band states to the $3d$-shell is much less than the QW exciton radiative lifetime. The situation occurs to become quite different for $I = I_0$ due to high exciton concentration and small number of nonexcited Mn^{2+} ions. As for the emission of the barrier exciton, it is observed at any value of I, the wave functions of the barrier exciton $3d$-states of QW Mn^{2+} ions overlapping weakly.

#2 ($x = 0.2$, L_z=7 ML). The QW exciton emission is observable even at $I = 0.007I_0$. Under a higher excitation the QW exciton exhibits a broadening and becomes stronger than the barrier exciton at $I = I_0$. As concerns the Mn^{2+} IL, it does not only saturate under the increasing I, but even degrades.

#3 ($x = 0.03$, L_z=26 ML). The QW exciton band is more intensive as compared to the barrier exciton at $I = 0.007I_0$. The strong broadening of the QW exciton band and Mn^{2+} IL quenching occur with growing I at $T = 5$ K (Fig. 1, 2). It is worth to notice that at the higher temperature $T = 50$ K this broadening becomes clearly pronounced at lower value of I.

#4 ($x = 0.03$, L_z=7 ML). The intensities of QW and barrier exciton bands are nearly equal for $I = 0.007I_0$, and the QW exciton is several time stronger at $I = I_0$. A decrease of the Mn^{2+} IL is observed similar to the former case.

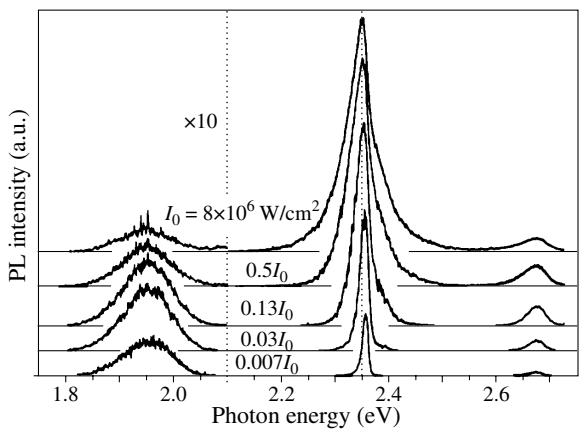

Fig. 1.

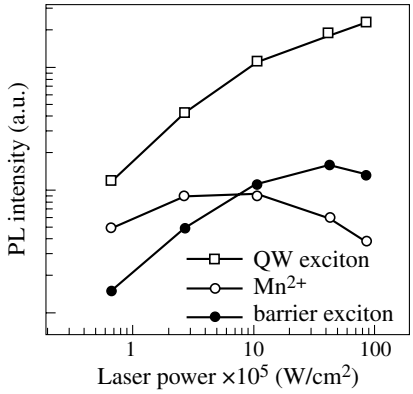

Fig. 2.

The broadening of the QW exciton emission band is the most spectacular in the sample #3 because the exciton inhomogeneous broadening is small in $Zn_{1-x}Mn_xTe$ with low manganese concentration and wide QW. At least two processes are behind the broadening. The high-energy tail originates from the transitions between the QW energy levels with the quantum number $n > 1$. An increase of the temperature favors the growth of the high-energy wing under the same excitation conditions. The similar behavior has been already observed in the QWS GaAs/GaAlAs and InGaAs/GaAs, and interpreted in terms of rapid e1hh1 exciton saturation at high temperature due to a wide distribution of the exciton quazimomentum.

We have detected the stimulated exciton emission in the similar QW structures without iron group component even at $I = 0.007I_0$. The peak intensity of this emission at $I = I_0$ is several orders of magnitude stronger compared to the spontaneous one. The stimulated emission line is shifted to the lowenergy side from the QW exciton band maximum, while exciton absorption tail becomes weaker, and the best gain conditions are realized. The background of the Mn^{2+} intracenter absorption with a threshold near 2.2 eV is the major obstacle to obtain the stimulated emission in $Zn_{1-x}Mn_xTe/Zn_{0.6}Mg_{0.4}Te$ even at $I = I_0$.

The appearance of the lowenergy tail of the QW exciton band and the simultaneous degradation of Mn^{2+} IL at $I > 3 \times 10^5$ W/cm^2 can be explained by the exciton–exciton and exciton–Mn^{2+} $3d$-shell interactions. Several mechanisms can be taken into consideration for the inelastic processes:

— transition in Mn^{2+} from $^1T_4$ to the ground state $^6A_1$ with the energy transfer to QW exciton;

— QW exciton nonradiative annihilation followed by the transition of Mn^{2+} ion from $^1T_4$ excited state to the upper $3d$-shell excited state;

— QW exciton nonradiative annihilation followed by the charge transfer from Mn^{2+} excited ion.

These Auger type processes are resulted in the exciton lowenergy tail broadening as well as by the Mn^{2+} IL degradation. The more comprehensive study has to be performed to elucidate what mechanism prevails in the case under consideration.

Let us consider now the kinetics of Mn^{2+} IL under the pulse excitation at $T = 5$ K. The emission decay is the exponential one with the same time constant 31 μs for the samples # 3 and 4. That is not surprising because the energy transfer via $3d$-shell is weak for the low manganese concentration. The kinetic curve for the sample # 1 is nearly the same as for the bulk crystal with the same manganese concentration where fast and slow components can be discriminated. However, the fast component which is due to the energy transfer between Mn^{2+} ions is much weaker for the sample # 2. Thus, the vertical migration confinement in QW is not important for $L_z = 26$ ML, but essential for $L_z = 7$ ML. This result enables us to estimate the migration length in $Zn_{0.8}Mn_{0.2}Te$: the $3d$-shell excitation changes only few positions during its lifetime.

It is known that the higher the crystal field, the lower the energy of $^1T_4 - ^6A_1$ transition. Consequently, the temperature shift of the Mn^{2+} IL band gives the information on the lattice parameter variation [5]. The band shows the lowenergy shift in $Zn_{0.80}Mn_{0.20}Te$ in the temperature range 5–65 K, the shift being larger in the narrow QW (sample #2). The shift is nearly zero in the wide QW $Zn_{0.97}Mn_{0.03}Te$ (sample #3) and has the opposite sign in the narrow QW $Zn_{0.97}Mn_{0.03}Te$. One can conclude that the temperature dependence of the crystal field in $Zn_{1-x}Mn_xTe$ QW is governed not only by the manganese concentration but also by $Zn_{0.6}Mg_{0.4}Te$ barrier. The shape of the Mn^{2+} IL contour also depends on the QW width because of the varying contribution of the interface Mn^{2+} ions.

The subpicosecond kinetic measurements show the considerable shortening of the exciton QW lifetime in $Zn_{1-x}Mn_xTe$ QW when compared to QW without the iron group elements. This establishes the fast Auger energy transfer from QW exciton to the $3d$-shell of manganese ions which is proved by the very short Mn^{2+} IL rise time about 40 ps.

Acknowledgement

This work has been supported in part by the Russian Ministry of Education through DSP.2.1.1.362.

References

[1] V. F. Agekyan *et al*, *Phys. Solid State* **45**, 1369 (2003).
[2] R. N. Bhargava *et al*, *Phys. Rev. Lett.* **72**, 416 (1994).
[3] C. de Mello Donega *et al*, *J. Lumin.* **96(2-4)**, 87 (2002).
[4] V. F. Agekyan *et al*, *Phys. Solid State* **47**, 2162 (2005).
[5] S. Biernacki *et al*, *Semicond. Sci. Technol.* **11**, 48 (1996).

14th Int. Symp. "Nanostructures: Physics and Technology"
St Petersburg, Russia, June 26–30, 2006

Exciton condensed phase structures in semiconductor quantum wells outside the laser spot

V. I. Sugakov and A. A. Chernyuk
Institute for Nuclear Research, NAS of Ukraine, Nauky Av. 47, Kiev 03680, Ukraine

Abstract. A phenomenological theory of exciton condensation in conditions of inhomogeneous excitation is proposed. In the task under consideration, the free exciton pass is smaller or of the same order as the distance between excitons and the theory of Gross–Pitaevsky is unapplicable. The investigation is applied to the study of the development of an exciton luminescence ring and the ring fragmentation at macroscopical distances from the central excitation spot in coupled quantum wells. The transition between the fragmented and the continuous ring is considered. Assuming a defect in the structure, a possibility of a localized island of the condensed phase in a fixed position is shown. Exciton density distribution is also analyzed in case of two spatially separated spots of the laser excitation.

Introduction

The paper is devoted fo explanation of interesting experiments fulfilled in [1–4]. In double quantum well (QW) structures, bases on AlGaAs and InGaAs, a spot of the laser excitation was reported to be surrounded by a concentric bright ring separated from the laser spot by an annular dark intermediate region [1–4]. The distance between the ring and the spot (hundreds μm) grew with increasing the intensity of the pumping. Sometimes an internal ring was observed nearby the laser spot. At low temperatures (about 2 K), the external ring fragmented into a structure with a strongly evaluated periodicity [1,3].

The mechanism of the ring formation was suggested in [3, 4], based on two assumptions: 1) in dark the well is populated with a certain density of electrons; 2) holes are captured by the well with a larger probability than electrons. The irradiated structure develops two differently charged spatial regions.

Ref. [5] suggested an explanation of the fragmentation of the ring by means of the nucleation of spots of a condensed phase. The possibility of exciton condensed phase formation in double quantum wells was shown in [6]. Finite lifetime of the excitons leads to the limitations on the size of the condensed phase areas, similarly to e-h droplets in bulk semiconductors. In a 2D system, these areas assume a shape of disk-like islands. The islands appear in the places of the highest exciton generation. Due to the interaction between islands via the exciton concentration fields, there is a correlation in their positions eventually resulting in a periodicity. In the present work, we go beyond the stochastic approach of [5] and solve the problem phenomenologically. We have incorporated a term containing the free energy of excitons into the equation controlling the exciton density. The resulting equation was solved taking into account the pumping and finite lifetime of excitons. This approximation allows a treatment of inhomogeneous systems and obtaining new results.

1. The exciton generation rate on the ring

The distribution of electron (n_e) and holes (n_h) concentration around the laser spot was investigated in [3–5]. The exciton generation rate is proportional to the product of n_e and n_h and has a sharp maximum at a certain distance from the center, as was calculated in [3–5]. This maximum moves farther away from the laser spot with increasing the pumping.

2. Model of the system. Exciton density equation

The free energy of the quasi-equilibrium state can be considered as a function of the exciton density, which depends on the spatial coordinates. Such description is possible at macroscopic distances, much larger than the exciton free path, on which the wave function loses coherence. Then, a phenomenological equation for the exciton density can be written down as

$$\frac{\partial n_{ex}}{\partial t} = -\mathrm{div}\mathbf{j} + G - \frac{n_{ex}}{\tau_{ex}}, \qquad (1)$$

where n_{ex} is the exciton density, τ_{ex} is the exciton lifetime, G is the number of excitons created in a time unit and in a square unit, $\mathbf{j}$ is the density of the exciton current: $\mathbf{j} = -M\nabla\mu$, M is the exciton mobility, μ is the chemical potential. We chose the free energy in the form of Landau model:

$$F[n_{ex}] = \int d\mathbf{r}\left[\frac{K}{2}(\nabla n_{ex})^2 + f(n_{ex})\right]. \qquad (2)$$

Here, the term $K(\nabla n_{ex})^2/2$ characterizes the energy of an inhomogeneity. The free energy density f is $f(n_{ex}) = \frac{a}{2}(n_{ex} - n_{ex}^c)^2 + \frac{c}{3}(n_{ex} - n_{ex}^c)^3 + \frac{b}{4}(n_{ex} - n_{ex}^c)^4$. a, b, c, n_{ex}^c are phenomenological parameters, which can be obtained from the quantum mechanical calculations, or extracted from the comparison of the theory with the experiment. Then, the exciton density equation in dimensionless units becomes

$$\frac{\partial n_{ex}}{\partial t} = -\Delta^2 n_{ex} + \left(3{n_{ex}^c}^2 - 2\beta n_{ex}^c - 1\right)\Delta n_{ex} + \\ -\left(3n_{ex}^c - \beta\right)\Delta {n_{ex}}^2 + \Delta {n_{ex}}^3 + G - \frac{n_{ex}}{\tau_{ex}}. \qquad (3)$$

3. Numerical simulation of exciton condensed phase formation on the ring

3.1. *Exciton concentration distribution*

The numerical stationary solutions of Eq. (3), with the parameters of the system as in [4], showed that the excitons condense into a ring, which can break down into separate fragments (Fig. 1). The created fragments are periodically positioned islands of the condensed phase of excitons, emergence of which is caused by the finite value of lifetime and the inter-exciton attraction. The condensed phase comprised by a periodic array of exciton islands corresponds to the fragments observed in experiments [1,3].

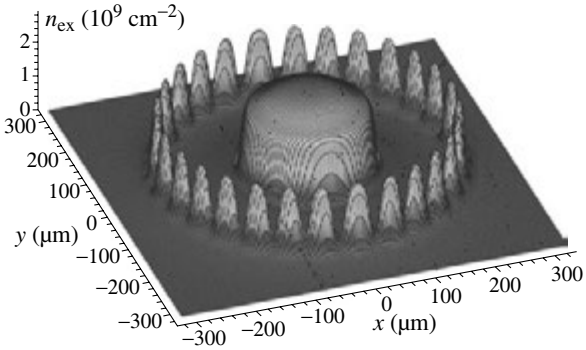

Fig. 1. The exciton density $n_{ex}(x, y)$ in the QW plane.

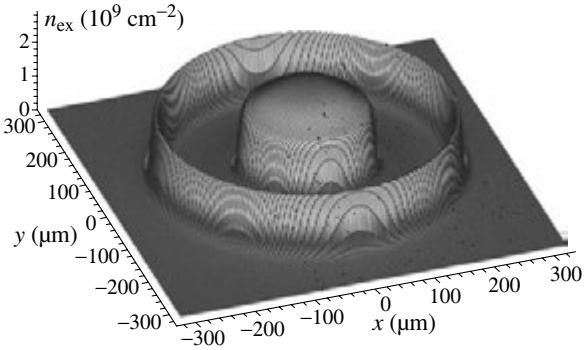

Fig. 2. The exciton density at bigger value of e-h binding parameter than in Fig. 1.

The radius of the ring of the condensed phase grows in two cases: 1) with increasing the pumping; 2) if the laser spot expands leaving the integral intensity constant. This satisfies with the experiments [1–4]. The number of the exciton islands increases with expanding the ring radius. We attribute an observation of an inner ring in the photoluminescence emission [1,3] to a specific character of the irradiation intensity profile in the vicinity of the laser spot edge.

With increasing the e-h binding rate W, the exciton generation rate becomes sharper. The results of our calculations show that with increasing W the fragmented ring of the condensed phase becomes continuous (Fig. 2).

With decreasing K, the island size of condensed excitons diminishes, so the fragmented ring passes to continuous one. The increase of K gives rise to continuous ring formation, because islands grow.

The simulation of the excitation of the system by two spatially separated irradiation sources as in the experiment [2], show the interaction of the excitation from two spots: rings become extended in the mutual direction and at a certain stage of spots rapprochement merge into a common oval-shaped ring.

3.2. *Localized spots*

Introducing a certain model for macroscopic defect structure, by the solving Eq. (3), we obtained the localized in this region condensed phase. The radiation from this region explains "localized bright spots", observed in [1,3].

3.3. *Behavior versus temperature*

To describe the temperature dependence, we assumed that the parameter a in the free enegry density can be represented according to Landau model: $a = \alpha\,(T_c - T)$, where $\alpha < 0$ and T_c is the critical temperature. The calculations show that with temperature rising, the fragmentation of the ring disappears

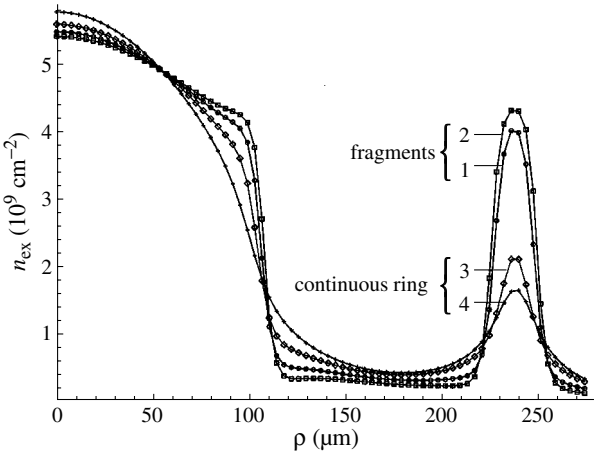

Fig. 3. The radial profile of the exciton density $n_{ex}(\rho)$ at different temperatures: 1) 2 K, 2) 1.6 K, 3) 2.7 K, 4) 4.4 K. $T_c = 3.7$ K. The curves 1 and 2 represent the fragmented ring, the curves 3 and 4 are the profiles of low continuous rings.

and its intensity falls (Fig. 3). Such transition with temperature growth is observed in [1].

4. Conclusions

To summarize, the following conclusions can be enumerated: (1) The fragmentation of the external ring of exciton density occurs at a certain threshold value of the exciton generation rate (pumping). (2) A transition from a fragmented ring to a continuous one occurs at increased value of the electron-hole recombination binding rate, with a reduction of the surface energy (the parameter K) and at higher temperature. (3) In a QW with a macroscopic defect a localized island of the condensed phase may emerge inside the external ring. (4) A possibility of the development of an internal ring depends on the character of the decrease of the irradiation intensity at the edge of the laser spot. (5) Exciton luminescence rings caused by two spatially separated laser spots attract and eventually form a common oval-shaped ring.

Acknowledgement

The work was supported by INTAS grant No.03-51-5266.

References

[1] L. V. Butov, A. C. Gossard, D. S. Chemla, *Nature* **418**, 751 (2002).
[2] D. Snoke, S. Denev, Y. Liu *et al*, *Nature* **418**, 754 (2002).
[3] L. V. Butov, V. B. Levitov, A. V. Mintsev *et al*, *Phys. Rev. Lett.* **92**, 117404 (2004).
[4] R. Rapaport, G. Chen, D. Snoke *et al*, *Phys. Rev. Lett.* **92**, 117405 (2004).
[5] V. I. Sugakov, *Solid State Comm.* **134**, 63 (2005).
[6] Yu. E. Lozovik, O. L. Berman, *JETP* **84**, 1027 (1997).

14th Int. Symp. "Nanostructures: Physics and Technology"
St Petersburg, Russia, June 26–30, 2006

Strong coupling and exciton states in artificial semimagnetic Cd(Mn,Mg)Te quantum dot molecule

S. V. Zaitsev[1], M. K. Welsch[2], A. Forchel[2], C.R. Becker[3], L.W. Molenkamp[3] and G. Bacher[4]

[1] Institute of Solid State Physics, Russian Academy of Sciences, 142432 Chernogolovka, Russia
[2] Technische Physik, Universität Würzburg, Am Hubland, D-97074 Würzburg, Germany
[3] Experimentelle Physik III, Universität Würzburg, Am Hubland, D-97074 Würzburg, Germany
[4] Lehrstuhl Werkstoffe der Elektrotechnik, Universität Duisburg-Essen,
Bismarckstrasse 81, D-47057 Duisburg, Germany

Abstract. Exciton photoluminescence in a pair of strongly tunnely coupled artificial asymmetric quantum dots (QDs) has been studied in magnetic fields up to 8 T. QD molecules have been fabricated by a selective interdiffusion technique applied to asymmetric CdTe/(Cd,Mg,Mn)Te double quantum well (QW). As grown structure with lithographically prepared nano-apertures were subjected to rapid temperature annealing to promote selective diffusion of magnetic (Mn) and nonmagnetic (Mg) atoms from asymmetric barriers into CdTe QWs. Lateral confinement potential within the QW plane induced by interdiffusion gives rice to effective zero-dimensional exciton localization. Incorporation of Mn ions in only one QD results in a pair of quantum QDs with markedly different spin splittings. In contrast to positive g-factor in nonmagnetic (Cd,Mg)Te-based QDs, ground exciton transition in nonmagnetic QD demonstrates negative g-factor, characteristic of semimagnetic QDs, indicating strong electron coupling between the QDs. At $B \geq 4$ T σ^+-polarized low-energy band with strong red shift appears indicating formation of the indirect exciton due to strong interdot Coulomb interaction.

Introduction

Semiconductor low-dimensional artificial nanostructures are among the main fields of interest during last two decades. Success of 2D systems has provided new physical phenomena as well as a number of optoelectronic applications and prompted researchers to study systems with lower dimensionality, such as quantum wires and quantum dots. QDs as zero-dimensional (0D) objects attracted special interest, because of complete spatial carrier confinement resulting in a striking manifestation of reduced dimensionality effects [1].

Great interest to the double QDs with controllable interdot coupling has arisen with the development of the idea of quantum computing using spin degree of freedom as an information bit [2]. Possibility to control energy level position and spatial localization of carriers in artificial semiconductor nanostructures has invoked a great practical interest to such nanodevices as perspective components for future electronics.

In the case of single or double self-organized QDs with typical dot densities in the range of $10^9 - 10^{11}$ cm^{-2}, various optical techniques with a high spatial resolution, such as micro-PL, near-field optical microscopy, metallic masks or etched mesas, have been developed in order to study individual dots [1]. In contrast to epitaxial techniques, the application of nanolithography for the preparation of QDs allows the definition of individual dots with adjustable size. While the straightforward access by electron beam lithography and etching creates surface states at the open sidewalls which act as non-radiative centers, a promising way for realizing buried nanostructures makes use of laterally selective intermixing between starting QW layer and barriers [3]. Selective interdiffusion causes a lateral change of the composition profile resulting in a bandgap modulation and therefore in a lateral carrier confinement. Single QDs have been realized by promoting the interdiffusion using a focused laser beam or focused ion beam implantation followed by a rapid thermal annealing [3].

In this contribution we present successful implementation of the novel approach for producing QD molecules with one nonmagnetic and another diluted magnetic semiconductor (DMS) QDs. Great advantage of DMS heterostructures is that a giant Zeeman effect in such semiconducting materials makes possible continuous tuning of band-gap and exciton energies by external magnetic field due to strong s, $p-d$ exchange interaction between free carriers and localized d-states of magnetic ions [4]. Effective g-factor of the DMS QD is strongly enhanced by incorporating of magnetic ions allowing to vary the interdot coupling after preparation, when structure parameters are fixed.

1. Experimental

Basic idea behind selective intermixing technique is depicted in Fig. 1a. CdTe/Cd(Mn,Mg)Te asymmetric double QW was grown by molecular beam epitaxy on a thick CdTe buffer at (001)-oriented CdZnTe substrate. As grown samples have two nonmagnetic (NM) 6-nm wide CdTe QWs separated by a NM $Cd_{0.8}Mg_{0.2}Te$ 3-nm thick barrier. Outer NM $Cd_{0.8}Mg_{0.2}Te$ and inner DMS $Cd_{0.8}Mn_{0.2}Te$ barriers are both 25-nm thick.

To induce lateral confinement, selective interdiffusion technique [5] was used. 80 nm thick SiO_2 mask with aperture diameters down to $D = 100$ nm were defined by electron beam lithography and lift-off. Subsequently, the structures were annealed at temperature 400 °C for 1 min, which induces selective interdiffusion between the QWs and barriers. As indicated by the arrows (Fig. 1a), diffusion is strongly enhanced below the SiO_2 mask as compared to non-covered areas [5] and results in the increase of band-gap below the masked areas, inducing a lateral confinement potential up to 0.3 eV and QD-sublevels splitting till 10 meV [5] depending on the sample and processing parameters. In addition, bigger diffusion coefficient of Mn compared to Mg [6] results in diffusion of Mn atoms into the lower CdTe quantum well layer even within the apertures. Therefore, our approach results in a pair of vertically aligned NM and DMS QDs where the incorporation of Mn in the DMS QDs drastically enhances its effective g-factor [4].

Photoluminescence (PL) was measured in superfluid He ($T \simeq 1.5$ K) in a magnetic cryostat till $B = 8$ T. Emission was excited by Ar^+ laser line 514 nm and recorded in a Faraday geometry in two circular polarizations.

2. Magneto-PL of tunnely coupled asymmetric QDs

Fig. 1b displays σ^+-polarized magneto-PL *cw* spectra of double QDs with $D = 220$ nm. At low B two different kinds of PL bands are observed: broad band at higher energy 1.706 eV, corresponding to NM lateral barrier, and two narrow lines, ascribed to the NM QD intradot excitons with orbital moments $m = 0$ and $m = 1$. In contrast to positive exciton g-factor in NM CdMgTe-based QDs and expected diamagnetic blue shift [4], the ground $m = 0$ transition demonstrates red shift with increasing B. Thus, observed negative g-factor, characteristic to DMS QWs and QDs, indicating strong coupling between the NM and DMS QDs.

Note that small linewidth of the $m = 0$ exciton transitions (1.5 meV) is reduced by a factor of 7 as compare to the 2D-lateral barrier, a consequence of 3D confinement and suppression of inhomogeneous broadening in QD. $m = 1$ exciton has large linewidth and gradually disappears with increasing B. The reason for such behavior is twofold: first, magnetic field leads to in-plane compression of exciton wave function, and, secondly, energy separation between exciton states decreases [7]. Both factors lead to increasing phonon scattering to the ground $m = 0$ state.

At $B \geq 5$ T new σ^+-polarized low-energy band appears. It demonstrates strong red shift as compare to the intradot excitons, which is characteristic to excitons in DMS QDs [4]. It is ascribed to the indirect inter-QDs exciton state, according to our calculations. Absence of anticrossing behavior points to incoherent tunneling coupling in investigated structure, caused by strong elastic scattering via alloy fluctuations due to diffusion. At the same time, intensity of the NM $m = 0$ exciton decreases, pointing to a strong energy relaxation to the new state.

We have performed calculations of the exciton states in the studied double QD molecule according to adiabatic approximation [8], which separates carrier motion in the growth and radial directions and appropriate in the case of QDs with big in-plane radius. Calculations confirm: (1) it is a strong coupling of electron levels in the DMS and NM QDs, that results

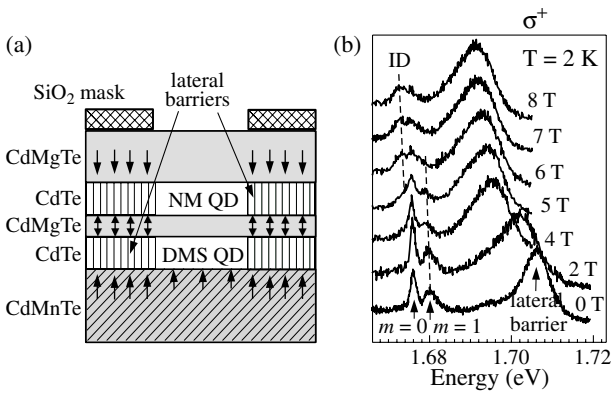

Fig. 1. (a) Schematic illustration of the selective intermixing fabrication technique for asymmetric double QDs. Arrows indicate diffusion of Mn and Mg atoms. (b) Magneto-PL σ^+-polarized spectra of double QDs with $D = 220$ nm.

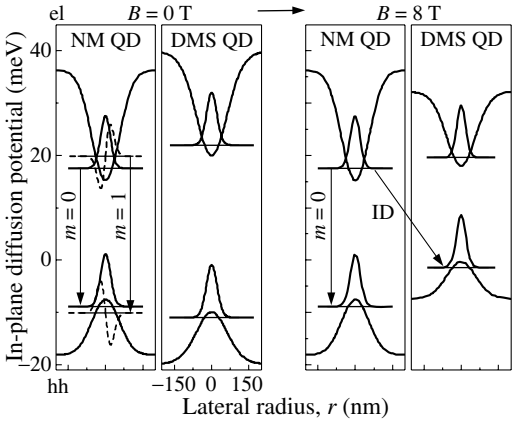

Fig. 2. Calculated electron and hole band lateral potential profiles for QDs with $D = 220$ nm at $B = 0$ T and 8 T. Electron and hole wave functions in the NM QD and DMS QD are shifted according to the level energy.

in unusual for NM QD negative exciton g-factor; and (2) energy preferable formation of indirect exciton at high B due to the giant Zeeman effect in the DMS QD and strong Coulomb interaction between the NM QD electron and DMS QD heavy hole (Fig. 2).

We have shown that the coupling between magnetic and nonmagnetic QDs at narrow barrier can be so strong that would lead to change of sign of electron g-factor in nonmagnetic QD and formation of indirect exciton at high B between electron of the nonmagnetic QD and hole of the DMS QD. Thus, strong electronic coupling and possibility to control g-factor sign is demonstrated experimentally in artificial DMS-based asymmetric QD molecule.

Acknowledgement

This work is supported by RFBR grant 04-02-17338.

References

[1] N. N. Ledentsov *et al*, *Semiconductors* **32**, 343 (1998).
[2] D. D. Awschalom *et al*, *Semiconductor spintronics and quantum computation*, (Springer–Verlag, series: NanoScience and Technology (2002).
[3] G. Bacher *et al*, *Appl. Phys. Lett.* **75**, 956 (1999).
[4] G. Bacher *et al*, *Phys. St. Sol. (b)* **229**, 415 (2002).
[5] S. Zaitsev *et al*, *Semicond. Sci. Technol.* **16**, 631 (2001).
[6] D. Tönnies *et al*, *J. Cryst. Growth* **138**, 362 (1994).
[7] U. Bockelmann, *Phys. Rev. B* **50**, 17271 (1994).
[8] M. Korkusinski and P. Hawrylak, *Phys. Rev. B* **63**, 195311 (2001).

14th Int. Symp. "Nanostructures: Physics and Technology"
St Petersburg, Russia, June 26–30, 2006

Temperature effects on exciton and trion states in CdTe quantum well structures

M. Fehr[1,2], D. Andronikov[2], V. Kochereshko[2], A. Platonov[2], S. A. Crooker[3], T. Barrick[3] and G. Karczewski[4]

[1] Technische Universität München, D-85747 Garching, Germany
[2] Ioffe Physico-Technical Institute, St Petersburg, Russia
[3] National High Magnetic Field Laboratory, Los Alamos, New Mexico 87545, USA
[4] Institute of Physics, Polish Academy of Sciences, 020668 Warsaw, Poland

Abstract. We analyze temperature dependence of photoluminescence spectra of excitons and trions in the presence of magnetic fields. We found that the observed temperature dependence cannot be explained within the Boltzman model which describes the population of exciton and trion states. Calculation of the photoluminescence kinetics of exciton-trion system has been performed. The "anomalous" temperature dependence of exciton and trion luminescence can be explained by temperature-dependent kinetics of the population of the respective states.

Introduction

Many-electron problem is one of the most fundamental problems in physics. This problem arises in a number of fields in physics: in nuclear physics, plasma physics, and condensed matter physics. Some of the most important examples of the many-electron system are bound multiple-electron complexes in semiconductor nanostructures. The simplest of them is the negatively charged exciton-electron complex consisting of one hole and two electrons (a trion). The properties of such complexes are in many respects similar to those of negatively charged hydrogen ions observed in the spectra of star atmospheres. The trions were observed experimentally for the first time in semiconductor quantum wells in 1993 [1]. Since that time trions were intensively studied in various semiconductor heterostructures. Singlet and triplet trion states have been studied in magnetic fields in quantum wells based on various semiconductor compounds with different carrier concentration. Nevertheless many properties of trions have not been thoroughly studied yet. In the present work temperature dependence of photoluminescence (PL) spectra of exciton and trion states in CdTe/CdMgTe based quantum wells with modulation doping has been analyzed in magnetic field up to 45 T.

1. Experiment

$CdTe/Cd_{0.7}Mg_{0.3}Te$ structures with a single 100 Å quantum well (QW) grown on the [100] GaAs substrate have been studied. An iodine-doped δ-layer is located 100 Å from the well. We studied a set of such heterostructures grown during one epitaxy process using wedge doping technique [2], different only in the doping level in the δ-layer (and therefore the 2DEG density). The electron concentrations in the QW varied within range from 10^{10} cm^{-2} to 10^{12} cm^{-2}. Polarized photoluminescence (PL) from these samples was measured with magnetic field applied in the Faraday configuration. A capacitor-driven 50 T pulse magnet (400 ms pulse duration) was used to yield high magnetic fields. A complete set of field-dependent PL spectra excited by a semiconductor diode pumped YAG laser with $\lambda = 532$ nm at 1.6, 4.2 and 15 K temperature was collected during each magnet pulse. Optical fibers were used for optical illumination of the sample, and the emitted light was detected in both circular polarizations σ^+ and σ^-.

2. Results

Fig. 1 shows temperature modification of PL spectra taken from the sample with electron concentration in the QW of $n_e = 3 \times 10^{10}$ cm^{-2} in σ^- circular polarization in magnetic field of 5 T. The spectra in σ^+ circular polarization are similar and show no new information. It is clearly seen that the intensity of the singlet trion PL line (T_s) grows with temperature, meanwhile the intensity of the exciton PL line falls with conservation of integral intensity. Such redistribution of the intensities from the high energy state to the low energy state looks very unusual. One could expect opposite redistribution of the intensities when high energy states get additionally populated, according to the Boltzman factor: $\exp(-\Delta E/kT)$ with temperature increasing, but not depleted.

In high magnetic fields the behavior of exciton and trion PL is also very unusual. Fig. 2 shows the PL spectra taken from the same sample in a magnetic field of 43 T at 1.6, 4.2 and 15 K. In these spectra the PL lines of optically active (T_t^b) and optically inactive (T_t^d) triplet trion states are observed along the emission lines of exciton (X) and singlet trion (T_s) [4]. The temperature-induced redistribution of the intensities of differ-

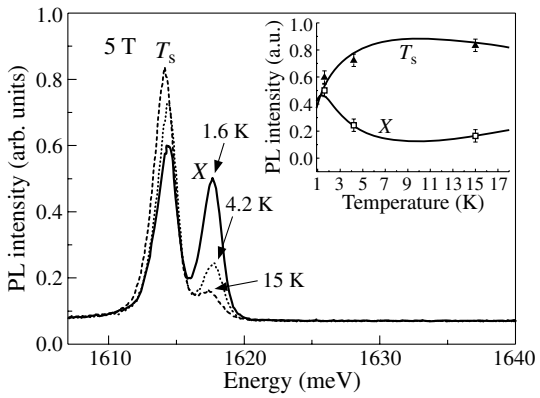

Fig. 1. Photoluminescence spectra taken in σ^- circular polarization in a magnetic field of 5 T for temperatures 1.6 (solid line), 4.2 (dotted line), and 15 K (dashed line). T_s stands for singlet trion state, X — for neutral exciton. On the inset: calculated temperature dependencies of all the lines in σ^- circular polarization in 5 T magnetic field. Triangles and open circles are scaled experimental values for respective states T_s and X at 1.6, 4.2, and 15 K.

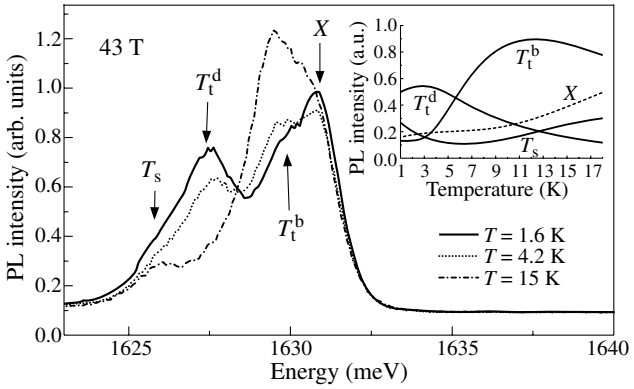

Fig. 2. Photoluminescence spectra taken in σ^- circular polarization in magnetic field of 43 T for temperatures 1.6 (solid line), 4.2 (dotted line), and 15 K (dashed line). T_s stands for singlet trion state, X — for neutral exciton, T_t^b — for bright triplet trion, and T_t^d — for dark triplet trion. On the inset: calculated temperature dependencies of all the lines in σ^- circular polarization in magnetic field of 43 T.

ent PL lines also occurs in these spectra. However, in high magnetic fields the intensities of the singlet and dark triplet trion PL lines falls, while the intensity of the bright triplet PL line increases. This also looks unusual since the binding energy of the bright triplet (1 meV) is considerably lower than that of the dark triplet trion (3 meV) [4]. Hence at 15 K temperature the bright triplet state should dissociate.

Such unusual behavior of temperature-dependent PL indicates that the observed effects have a "kinetic" nature and are related to the population process of the energy states rather than to the temperature-induced redistribution of the carriers on the sublevels. In order to verify this idea a calculation of the exciton and trion PL spectra has been performed for different magnetic field magnitudes. A system of kinetic equations for different temperatures has been solved taking into account the energy states of excitons, singlet, and triplet trion states, their formation, recombination and spin relaxation mechanisms [3, 4]. The results of this calculation are presented on the insets to Fig. 1 and Fig. 2 and show good qualitative agreement with the experiment.

To get a qualitative explanation of the PL temperature behavior, we consider the singlet trion formation mechanism (Fig. 3). In this magnetic field the background electrons are completely spin polarized, i.e., they occupy the lowest Zeeman sublevel with $S_z = +1/2$ and leave the upper Zeeman sublevel with $S_z = -1/2$ completely empty. The singlet trion can be formed by pairing the bright exciton (momentum +1), or the dark exciton (momentum -2) with these electrons, because the

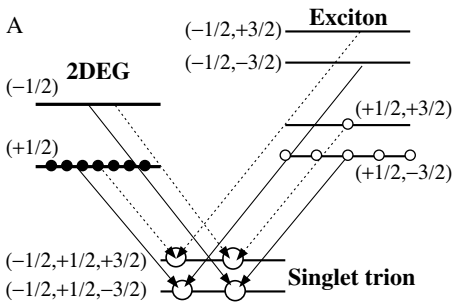

Fig. 3. Schema of singlet trion (T_s) formation in magnetic fields.

electron spins in the singlet state must be antiparallel. These exciton levels are the highest in energy and their population is small. Consequently the formation of the singlet trion is suppressed in magnetic fields at low temperature. With increasing temperature the population of the upper electron Zeeman sublevel increases and the formation of the trion becomes more effective. This reveals the increase of the T_s line intensity.

In high magnetic fields the population of the dark triplet state is at least two orders of magnitude higher than the population of other states [4]. We assumed that the relaxation between T_t^b and T_t^d triplet states, being orbital momentum relaxation (30 ps), is short in comparison to the electron spin relaxation time between triplet and singlet (150 ps). Hence, the time of the temperature "excitation" from T_t^d into T_t^b is relatively short as well. Taking into account the high population of the dark triplet level T_t^d and its long radiative recombination time (3–6 ns), it is natural to expect that temperature-induced repopulation leads to a decrease of the T_t^d line intensity, and a simultaneous increase of the T_t^b line intensity.

In conclusion: Temperature dependence of exciton and trion photoluminescence has been analyzed in the presence of magnetic fields. This dependence is contradicting the conventional assumptions concerning Boltzman distribution of carriers on Zeeman sublevels. We have explained the results in a model, which simulates the population kinetics of exciton and trion states under temperature modification.

Acknowledgements

This work was supported in part by RFBR grant and grant of the Department of Physical Sciences of Presidium RAS, MF is grateful to DAAD foundation.

References

[1] K. Kheng *et al*, *Phys. Rev. Lett.* **71**, 1752 (1993).
[2] T. Wojtowicz *et al*, *Acta Phys. Pol. A* **92**, 1063 (1997).
[3] C. R. P. L. Jeukens *et al*, *Phys. Rev. B* **66**, 235318 (2002).
[4] D. Andronikov *et al*, *Phys. Rev. B* **71**, 165339 (2005).

14th Int. Symp. "Nanostructures: Physics and Technology"
St Petersburg, Russia, June 26–30, 2006

Theory of nonlinear conductance fluctuations in quantum dots

M. L. Polianski
Département de Physique Théorique, Université de Genève, CH-1211 Genève 4, Switzerland

Abstract. The effect of magnetic flux Φ on nonlinear dc transport through a chaotic 2D cavity is investigated. The sample-to-sample fluctuations of the (anti)symmetric with respect to inversion $\Phi \to -\Phi$ component of the nonlinear conductance are found for arbitrary temperature, magnetic field, interaction strength, and number of attached contacts. For few-channel dots the effect of dephasing is investigated numerically. A comparison with recent experimental data is provided.

Introduction

Recently the non-linear dc conductance of semiconductor open mesoscopic structures and its dependence on magnetic flux Φ has found considerable experimental attention. Large applied voltages induce a rearrangement of charge and so affect the scattering properties of the sample. The charge redistribution is subject to Coulomb interactions, consequently investigation of non-linear transport reveals information on interaction. This is in marked contrast to linear transport where the dc conductance $G_{\alpha\beta} = dI_\alpha/dV_\beta$ can be accurately treated within a theory of *non-interacting* electrons. We extract interaction constants by investigating the magnetic field symmetry of nonlinear transport. Under flux Φ reversal the Onsager-Casimir relations dictate that the conductance matrix, evaluated at equilibrium, has the symmetry $G_{\alpha\beta}(\Phi) = G_{\beta\alpha}(-\Phi)$. However, away from equilibrium, the non-linear transport properties lack such a symmetry. Importantly, the deviations from Onsager symmetry are *entirely* due to interactions [1,2]. Therefore by investigating the departure from the Onsager-Casimir relations, information on the interaction properties can be obtained.

Our work [3] is motivated by very recent experiments on nonlinear transport in various open systems: carbon nanotubes, ballistic billiards, quantum rings, and, particularly, open quantum dots [4]. Due to quantum interference, the samples exhibit strong mesoscopic (sample-to-sample) fluctuations, and a theory has thus to predict statistical properties. Only recently have two theories [1,2] explored such statistics for two-terminal open samples. However, a more general theory that accounts for the effects of an arbitrary temperature and dephasing at arbitrary fields and interaction strength remains to be developed. Such a theory is the main goal of the presented work.

1. Model and Results

We consider a semiconductor chaotic 2D quantum dot, see Fig. 1, biased by several voltages $V_{1,2,\ldots}$ at the reservoirs attached to a dot via QPCs with $N_{1,2,\ldots}$ open channels. The magnetic field B through the area of the dot, as well as the capacitive coupling C to the gates with the voltage V_0 are externally controlled. The dephasing due to electron-electron elastic interaction is modeled by attaching an additional dephasing probe ϕ [5]. Our theory uses the results [6] of the Random Matrix Theory for the non-interacting electrons and the theory by Büttiker *et al* [7], which treats the Coulomb interaction on the mean-field level. Importantly, this approach is based on the gauge-invariance and charge-conservation in the mesoscopic system, and thus allows a self-consistent description of the transport through a dot for an arbitrary interaction strength.

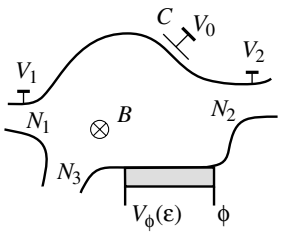

Fig. 1. Multi-terminal 2D quantum dot with perpendicular magnetic field B and dc bias voltages $V_{1,2}$ at the contacts and V_0 at the gates with capacitance C; an additional lead ϕ models dephasing. After [3].

We consider the nonlinearity in transport through the dot, expressed via $g_{\alpha\beta\gamma} = \partial^2 I_\alpha/2\partial V_\beta \partial V_\gamma$. Of particular interest for us is the statistics of the (anti)symmetrized with respect to magnetic flux inversion $\Phi \to -\Phi$ components $\mathcal{G}_{(a)s}$ of the nonlinear conductance $g_{\alpha\beta\gamma}$. These components, zero in average, strongly fluctuate from sample to sample due to quantum effects. These fluctuations are very sensitive to the flux Φ, because of the sensitivity of wave functions to the applied magnetic field.

A key result of this work, the rms of $\mathcal{G}_{a,s}$, is illustrated in Fig. 2. The fluctuations of the symmetric part $\mathcal{G}_s(\Phi)$ decrease as the magnetic flux increases from zero, while the anti-symmetric part $\mathcal{G}_a(\Phi)$ is linear [2] at low fields. As the flux grows, their values reach the same saturation value. The scale of the crossover flux Φ_c corresponds to a flux quantum $\Phi_0 = eh/c$ through a *typical trajectory* of an electron inside the dot. The correct definition of the crossover scale Φ_c is very important for the quantitative comparison of the theory with experiment. It determines the slope of $\mathcal{G}_a$ at small flux Φ. One might have expected $\Phi_c \sim \Phi_0$ but importantly we find $\Phi_c \ll \Phi_0$ in agreement with experiment [4].

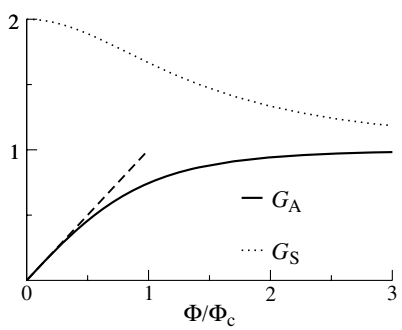

Fig. 2. Normalized fluctuation of the (anti)symmetric component $(\mathcal{G}_a)\mathcal{G}_s$ of the second order nonlinear conductance for a coherent two-terminal dot as a function of flux Φ/Φ_c, $\Phi_c \ll \Phi_0$. After [3].

For two terminal dots, we find the fluctuations of $\mathcal{G}_a$ for arbitrary flux Φ, temperature T and the Coulomb interaction strength, characterized by the capacitance C. We compare them in detail with previously considered limits [1, 2] and discuss the relevance of the results of various theoretical approaches to the experiment. We find the fluctuations of symmetrized $\mathcal{G}_s$ for the symmetric 2-terminal dots, and extend our treatment to multi-terminal dots. In the latter geometry the effect of the gate voltage V_0 is explored, which allows an experimental estimate of the electro-chemical capacitance [7,8] without an apriori unknown value of interaction strength. We numerically investigate the effect of dephasing on $\mathcal{G}_a$ at high magnetic fields, low temperatures, and strong interaction, which is relevant for experiments. The uniform (locally weak) dephasing is found to have a stronger effect then the local dephasing.

2. Comparison with experiment

Our results are applicable in a wide range of experimental regimes (arbitrary temperature, dephasing, magnetic field and interaction strength) for the multi-channel dots. They are universal, which means that the dynamics can be either diffusive (weak disorder due to impurities) or ballistic with classical chaotic dynamics (due to diffusive boundaries or irregular shape). The value of the crossover flux Φ_c is essentially defined by the two time scales: the ergodic time of the closed dot and the dwell time an electron spends inside the dot, which is characterized by the attached ballistic QPCs. The crossover flux and the crossover voltage, which we find, allow to consider the conductance linear in field and applied voltage. We present physically intuitive arguments on the semi-classical level.

A comparison with the experiment by Zumbühl *et al* [4] is also provided. Together with the value of the crossover flux Φ_c, we can qualitatively explain the dependence of the measured $d\mathcal{G}_a(\Phi)/d\Phi$ at small Φ on the number of attached open channels N. Unexpectedly, this is due to the temperature effects, which can not be neglected even though the temperature is ≈ 4 μeV. We discuss some yet unexplained experimental features and provide a relation, which allows one to estimate the interaction strength in the dots using already available data.

Acknowledgements

I acknowledge the collaboration with Markus Büttiker and useful discussions with David Sánchez, Eugene Sukhorukov and especially thank Dominik Zumbühl for discussions and experimental data. This work is supported by the Swiss NSF.

References

[1] D. Sánchez and M. Büttiker, *Phys. Rev. Lett.* **93**, 106802 (2004).
[2] B. Spivak and A. Zyuzin, *Phys. Rev. Lett.* **93**, 226801 (2004).
[3] M. L. Polianski and M. Büttiker, cond-mat/0512422.
[4] D. Zumbühl, C. M. Marcus, M. P. Hanson and A. C. Gossard, cond-mat/0508766.
[5] M. J. M. de Jong and C. W. J. Beenakker, *Physica A* **230**, 219 (1996).
[6] M. L. Polianski and P. W. Brouwer, *J. Phys. A: Math. Gen.* **36**, 3215 (2003).
[7] M. Büttiker, A. Prêtre and H. Thomas, *Phys. Rev. Lett.* **70**, 4114 (1993).
[8] P. W. Brouwer and M. Büttiker, *Europhys. Lett.* **37**, 441 (1997).

14th Int. Symp. "Nanostructures: Physics and Technology"
St Petersburg, Russia, June 26–30, 2006

Observation of quantum Hall ferromagnetic state in nanostructured quantum wire

M. V. Budantsev[1], A. G. Pogosov[1], A. E. Plotnikov[1], A. K. Bakarov[1], A. I. Toropov[1] and J. C. Portal[2,3]

[1] Institute of Semiconductor Physics, Novosibirsk 630090, Russia
[2] GHMF, CNRS/LCMI, BP-166, F-38042, Grenoble, Cedex 9, France
[3] INSA-Physique and Institut Universitaire de France, F-31077, Toulouse, Cedex 4, France

Abstract. We report on the observation of ferromagnetic state of quasi-one-dimensional quantum Hall liquid in AlGaAs/GaAs nanostructured quantum wire with periodic modulation of electrostatic potential. Magnetoresistance of the system shows pronounced hysteretic behavior at magnetic fields, corresponding to both odd and even integer filling factors. We demonstrate that the ferromagnetic state of quantum Hall liquid in the quasi-one-dimensional nanostrictured wire is sensitive to the processes in the adjacent 2DEG being in the quantum Hall zero resistance state. The role of the edge current states in the observed hysteretic behavior is discussed.

Introduction

Quantum Hall effect (QHE) attracts attention due to the variety of intriguing phenomena experimentally observed in this regime [1,2,3]. Cooperative phenomenon originating from enhanced electron–electron interaction such as fractional QHE [4], magnetic field induced metall-insulator transition [5], etc. are of particular interest. Recently, the number of works reported on the observation of ferromagnetic state of quantum Hall liquid in a macroscopic two-dimensional systems [6,7,8], created on a basis of nonmagnetic (in a common sense) semiconductor materials. The study of this phenomenon requires special experimental conditions which considerably retards the experimental investigations in this field. It was shown theoretically that the necessary condition for the observation of this effect is the availability of additional degree of freedom, so called pseudo-spin degree of freedom, which in some cases can coincide with conventional electron spin [9].

It should be noted that all of the previous observations of ferromagnetic quantum Hall liquid were performed on the macroscopic two-dimensional systems. In the present work we report on the observation of ferromagnetic state of quantum Hall (QH) liquid in nanostructured quasi-one-dimensional wire with periodic electrostatic modulation.

Experimental results and discussion

The test samples were fabricated on the basis of an AlGaAs/GaAs heterojunction containing a two-dimensional electron gas with an electron mobility $\mu = (0.8-1.1)\times10^6$ cm^2/Vs and density $N_s = (2-5)\times10^{11}$ cm^{-2}. The geometry of the quantum wire (Fig. 1a) was defined using electron lithography and subsequent anisotropic plasma-chemical etching. The characteristic width of the wire is $W = 900$ nm and the period of the electrostatic modulation is $d = 600$ nm. The nanostructured is situated in a Hall bar with dimensions $W\times L = 50\times100$ μm^2. Another Hall bar with dimensions $W\times L = 50\times250$ μm^2 situated on the same wafer was used to measure magnetoresistance of nonmodulated 2DEG. All measurements were performed in dilution refrigerator at temperature 60 mK in magnetic fields up to 15 T normal to the 2DEG plane. Magnetoresistance was measured using lock-in amplifier by passing an ac current of 10^9 A at a frequency of 7 Hz.

The experimental magnetoresistance curves $R_{2DEG}(B)$ and

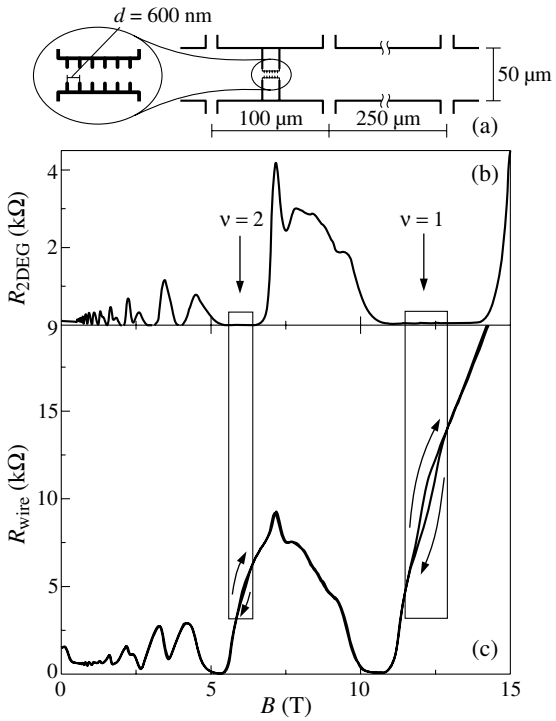

Fig. 1. (a) Schematic draw of the quantum wire geometry and Hall bar layout. (b) Magnetoresistance of 2DEG. c) Magnetoresistance of the quantum wire. Arrows show the direction of magnetic field sweep in the regions of hysteretic loops. Rectangles shows, that the ferromagnetic behavior is observed in magnetic fields, corresponding to integer filling factors in nonmodulated 2DEG. The curves a measured at $T = 60$ mK.

$R_{wire}(B)$ are shown at the Fig. 1b,c. Both dependencies demonstrate the regime of integer quantum Hall effect, manifested in a series of zero resistance plateaux. The plateaux in the quantum wire magnetoresistance are shifted towards lower magnetic fields and are much more narrower than those of the 2DEG. This allows us to conclude that the electron density in quasi-one-dimensional wire is lower than in the 2DEG. Moreover, the electron density in the wire is nonuniform due to periodic electrostatic potential.

One can see the obvious difference in $R_{wire}(B)$ measured for different magnetic field sweep directions (see Fig. 1c), manifested itself in hysteresis loops observed at integer filling fac-

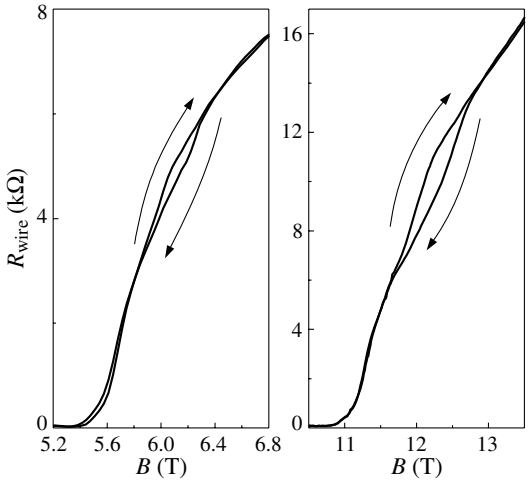

Fig. 2. Hysteresis loops corresponding to $\nu_{2DEG} = 2$ (a) and $\nu_{2DEG} = 1$ (b).

tors. The most pronounced hysteretic features are found at filling factors $\nu = 1$ and $\nu = 2$. The rectangles at Fig. 1b, c shows that they are observed at magnetic fields corresponding to the middle of the plateaux of zero resistance of the nonmodulated 2DEG.

The detailed plots of hysteretic loops at $\nu = 1$ and $\nu = 2$ are presented in Fig. 2. The form of the loops and their magnetic field positions are phenomenologically similar to the results on the magnetization [10] and on the long time relaxation phenomenon [11] in macroscopic 2DEG in QHE regime, where hysteretic behavior was observed at integer filling factors. Thus, the response of a nanostructured wire provides a unique possibility to study the processes in the adjacent 2DEG untouchable by the measurements of its resistance, when it is in the quantum Hall zero resistance state.

The obtained results allow us to conclude that we observe the ferromagnetic quantum Hall liquid state induced by quantizing magnetic field. We believe that the observed metastability is caused by insulating stripes of incompressible Hall liquid, electrically separating different areas inside the sample. The presence of insulating stripes leads to nonequilibrium electron density redistribution with the change of applied magnetic field. In this case, Landau level filling factor can be considered as a pseudo-spin degree of freedom.

Conclusion

It should be noted that the observations of similar hysteretic behavior described in the literature require special materials (materials with a low electron g factor, bilayers) or special experimental conditions (hydrostatic pressure). In contrast, the present work demonstrates that the ferromagnetic state can be achieved in a conventional AlGaAs/GaAs heterojunction by means of nanostructuring.

Acknowledgements

The work was supported by RFBR (grant 05-02-17200) and INTAS (grant 03-55-6339).

References

[1] Ed. by R. E. Prange and S. M. Girvin, *The Quantum Hall effect*, New York: Springer, 1990.

[2] Ed. by S. Das Sarma and A. Pinczuk, *Perspectives in Quantum Hall effects*, New York: Wiley, 1996.

[3] Ed. by S. L. Sondhi, S. M. Girvin and J. P. Carini, *Rev. Mod. Phys.*, **69**, 315 (1997).

[4] H. L. Stormer, D. C. Tsui and A. C. Gossard, *Rev. Mod. Phys.* **71**, S298–S305 (1999).

[5] E. L. Shangina and V. T. Dolgopolov, *Physics-Uspekhi* **46**, 777 (2003).

[6] V. Piazza, V. Pellegrini, F. Beltram, W. Wegscheider, T. Jungwirth, A. H. MacDonald, *Nature* **402**, 638 (1999).

[7] E. P. De Poortere, E. Tutuc, S. J. Papadakis and M. Shayegan, *Science* **290**, 1546 (2000).

[8] J. Eom, H. Cho, W. Kang, K. L. Campman, A. C. Gossard, T. Bichler, W. Wegscheider, *Science* **289**, 2320 (2000).

[9] T. Jungwirth, A. H. MacDonald, *Phys. Rev. Lett.* **87**, 216801 (2001).

[10] J. P. Watts, A. Usher, A. J. Matthews, M. Zhu, M. Elliott, W. G. Herrenden-Harker, P. R. Morris, M. Y. Simmons, D. A. Ritchie, *Phys. Rev. Lett.* **81**, 4220 (1998).

[11] J. Huels, J. Weis, J. Smet, K. von Klitzing, Z. R. Wasilewski, *Phys. Rev. B* **69**, 085319 (2004).

14th Int. Symp. "Nanostructures: Physics and Technology"
St Petersburg, Russia, June 26–30, 2006

Electron transport in semiconductor superlattices with narrow minigaps

A. A. Andronov[1], *D. I. Zinchenko*[1], E. P. Dodin[1], Yu. N. Nozdrin[1], A. Yu. Klimov[1], V. V. Rogov[1], A. A. Marmalyuk[2] and A. A. Padalitsa[2]

[1] Institute for Physics of Microstructures, Russian Academy of Sciences, Nizhny Novgorod GSP 105 603600, Russia
[2] SIGM plus, Vvedenskogo Str. 3, 117342, Moscow, Russia

Abstract. Transport and current oscillations in GaAs–$Ga_{0.9}Al_{0.1}As$ superlattices of 173, 175 and 195 Å periods and with weak barriers and lowest miniband laying below optical phonon energy is studied at 4–300 K. These studies is a first step to fabrication of Terahertz Bloch oscillator on such SLs, proposed earlier.

Introduction

Study of vertical transport in semiconductor superlattices (SL) with narrow minibands and narrow minigaps is of great interest as a way of realization of dynamic negative differential conductivity (NDC) caused by Bloch oscillations of electrons at Terahertz frequency and construction of Terahertz oscillator on this basis [1]. Numerical simulation shows the possibility of dynamic NDC at the Bloch frequency together with positive static differential conductivity in SL with the optical phonon energy lying below the bottom of the second miniband and under strong interminiband Zener tunneling. In this work nonlinear transport properties and Terahertz emission of such SL are investigated.

1. Experimental

We've studied GaAs/$Al_{0.1}Ga_{0.9}As$ superlattices with the parameters shown in Table 1 (we used transfer matrix method to calculate dispersion relation). Here E_0 is the bottom of the first miniband, E_1 is the top of the first miniband, E_2 is the second miniband bottom, ΔE_1 is the first miniband width, ΔE_2 is the second miniband width, E_{gap} is the minigap between first two bands, d is the superlattice period, w and b are well and barrier widths respectively, N is the number of periods.

Table 1. Sample parameters.

Sample	426	502	698
E_0 (meV)	3.2	3.7	6.5
ΔE_1 (meV)	11.2	14.8	11.8
E_1 (meV)	14.4	18.5	18.3
E_{gap} (meV)	7.1	7.9	18.0
E_2 (meV)	21.3	26.4	31.6
ΔE_2 (meV)	34.9	45.0	38.4
$d = w + b$, μm	185+10	163+10	155+20
N	100	150	500

The GaAs/$Al_{0.1}Ga_{0.9}As$ superlattices consisting of 100–500 periods were mounted in $n^+{-}n{-}n^+$ structures. The superlattice itself was undoped with background concentration $n \approx 2\times10^{15}$ cm^{-3} and the n^+ contact regions were doped with $n = 3\times10^{18}$ cm^{-3}. Studied samples are processed into mesas 500 and less micrometers in diameter. The ohmic contacts are provided by standard Au-Ni-Si deposition and thermal treatment.

2. Transport properties

Static current-voltage curve for the 698 sample is shown on Fig. 1 (inset). I–V curves for other samples (426 and 502) were presented in previous works [2]. The current plateau is shown on the main part of Fig. 1. We can see several well-defined branches with NDC between 0.3 and 3.5 V. It is known [3] that sawtooth shape of I–V could be caused by different factors: 1) changing of charge monopole position: the charge accumulation layer appears (in ideal case in single well) under conditions of resonant tunneling of electrons between ground-state subbands and adjacent wells and separates regions with high and low electric field; in real SL the number of peaks in "sawtooth" depends on the monopole size and not only on the number of periods because of various inhomogeneities in SL (deviations in period length, impurities, etc.); 2) in strong electric fields, when the Wannier–Stark splitting approaches E_{gap}, inter-Wannier–Stark level tunneling can also produce peaks in current through the SL. Depending on the relation between level broadening $h\nu$, miniband width Δ and potential drop per period eFd there are different mechanisms of conductivity: miniband conduction (eFd, $h\nu \ll \Delta$), conduction caused by sequential resonant tunneling between different minibands ($h\nu \ll \Delta$), Wannier–Stark hopping ($h\nu \ll eFd$). In this report we will discuss possible conduction mechanisms based on experimental data.

The low-voltage part of I–V (Fig. 2) shows non-Ohmic behavior, and deviation occurs at the voltage V_c that corresponds to the energy of the bottom of the first miniband for different

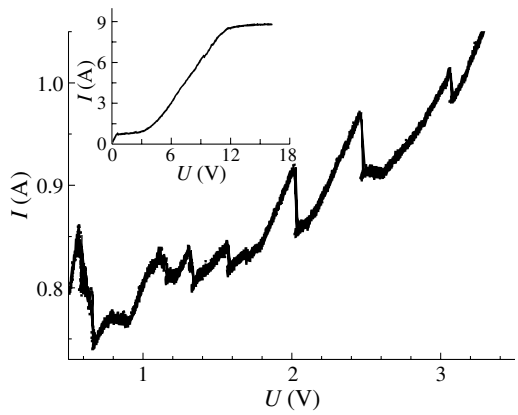

Fig. 1. Current plateau on the I–V curve for the 698 sample. Inset: full I–V curve for the 698 sample.

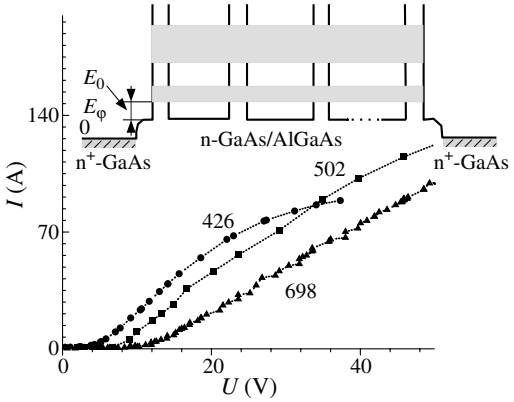

Fig. 2. Low-voltage part of the I–V curve for different samples. Inset: energy band scheme for the 698 sample.

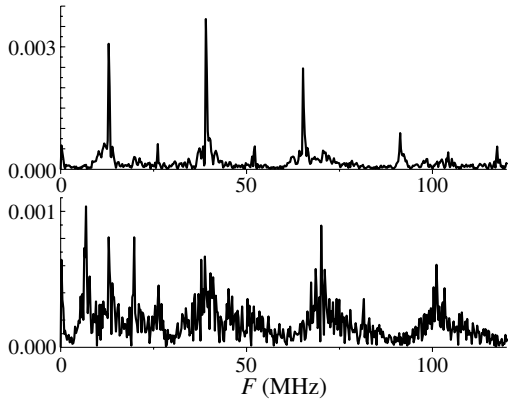

Fig. 3. Current oscillations spectrum for 2 different points of I–V curve: 0.8 and 2.5 V.

samples $eV_c = E_0 + \kappa T \ln(N_D^+/N_D) \approx E_0 + 2.5$ meV.

In all regions of NDC we've found low-frequency self-oscillations of current through SL, examples of spectra of these oscillations are shown in Fig. 3. The spectrum of these self-oscillations can change, depending on the applied voltage, from discrete (periodic oscillations) — upper part of Fig. 3 — to continuous (chaotic oscillations) — lower part of Fig. 3. Also we measured the dependence of fundamental frequency on applied voltage and observed bifurcational doubling and halving of oscillations frequency. The spectra and stability of current oscillations in a superlattice as in a complex nonlinear dynamical system with a large number of degrees of freedom is discussed on the base of the model of static and dynamic domains of high (HEFD) and low (LEFD) electric fields.

We measured spontaneous emission from our samples by

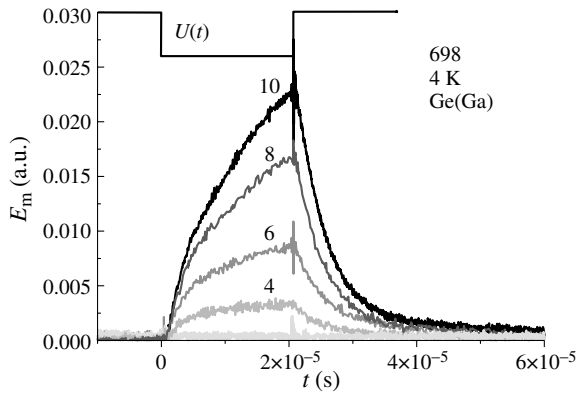

Fig. 4. Time dependence of Ge(Ga) photodetector signal.

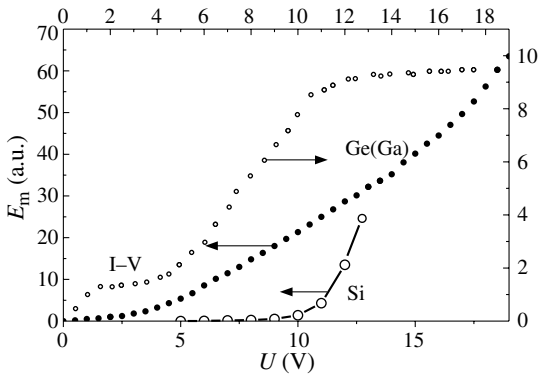

Fig. 5. Measured radiation power with 2 different photodetectors (I–V is also plotted for comparison).

placing different detectors in liquid helium nearby our structure. Fig. 4 shows the time dependence of the Ge(Ga) detector signal for different applied voltage values and Fig. 5 shows the measured detector signal amplitude at the end of voltage pulse versus voltage for Ge(Ga) and Si photodetectors.

Acknowledgements

This work is supported by RFBR grant 05-02-15468 and by RAS Program "Low dimensional structures". The authors are grateful to Yu. N. Drozdov for X-Ray characterization of the samples and to I. Yu. Shuleshova for processing the samples.

References

[1] A. A. Andronov, I. M. Nefedov, A. V. Sosnin, *Semiconductors* **37**, 378 (2003).

[2] A. A. Andronov *et al*, *Proc. of 13th Int. Symposium Nanostructures: Physics and Technology (St Petersburg, 2005)*, Ioffe Institute, 181, 2005.

[3] L. Bonilla, H. Grahn, *Rep. Prog. Phys.* **68**, 577 (2005).

14th Int. Symp. "Nanostructures: Physics and Technology"
St Petersburg, Russia, June 26–30, 2006

Quantum oscillations of the rectified voltage and the critical current of asymmetric mesoscopic superconducting loops

V. L. Gurtovoi, S. V. Dubonos, A. V. Nikulov, N. N. Osipov and *V. A. Tulin*
Institute of Microelectronics Technology, Russian Academy of Sciences,
142432 Chernogolovka, Moscow region, Russia

Abstract. The current-voltage curves and magnetic dependence of the critical current of asymmetric superconducting loops are measured. It was found that sign and value of the asymmetry of the current-voltage curves changes with value of magnetic field, periodically for single loop and system of identical loops. The obtained results allow to explain the quantum oscillation of the dc voltage, observed below superconducting transition in the previous works, as rectification of ac current or noise.

Introduction

The Bohr's quantization $\oint_l \mathrm{d}lp = n2\pi\hbar$ postulated for the explanation of the stable electron orbits in atom is the cause of various quantum phenomena [1] on the mesoscopic level. One of the most wonderful phenomena is the persistent current I_p observed in normal metal [2], semiconductor [3] and superconductor [4, 5] mesoscopic loop l. Its value and sign vary periodically with value of magnetic flux Φ inside the loop since the canonical momentum $p = mv + qA$ and therefore permitted values of velocity circulation $\oint_l \mathrm{d}lv = 2\pi\hbar(n - \Phi/\Phi_0)$, where $\Phi_0 = 2\pi\hbar/q$ is the flux quantum. For the first time the persistent current $I_\mathrm{p}(\Phi/\Phi_0) \propto n - \Phi/\Phi_0$ was predicted [4] and observed [5] in superconductor structure. Later the like periodical dependence $I(\Phi/\Phi_0)$ was predicted [6] and observed [2, 3] in non-superconducting mesoscopic structures. Recently the quantum oscillations of the dc potential difference $V_\mathrm{dc}(\Phi/\Phi_0) \propto I_\mathrm{p}(\Phi/\Phi_0)$ were observed on segments of asymmetric superconducting loops [7, 8]. It is important to investigate the cause of this phenomenon in order to clear up a question: "Could a like one be observed in normal metal or semiconductor asymmetric mesoscopic loops?".

It was found that the quantum oscillations $V_\mathrm{dc}(\Phi/\Phi_0)$ can be observed without an evident power source near superconducting transition [7], whereas at a lower temperature they can be induced by an external ac current when its amplitude exceeds a critical value [8]. It was assumed in [8] that the asymmetry of the current-voltage curves and its periodical change with magnetic field are the cause of the $V_\mathrm{dc}(\Phi/\Phi_0)$ observed in the both cases. In order to verify this assumption the current-voltage curves of asymmetric aluminum loops and its change with magnetic field are investigated in the present work.

1. Experimental

Investigated structures with thickness $d = 40-70$ nm consisted of asymmetric aluminum round loops (rings) with semiring width $w_\mathrm{n} = 200$ nm and $w_w = 400$ nm for narrow and wide parts, respectively, Fig. 1. They were fabricated by thermally evaporated on oxidized Si substrates, e-beam lithography and lift-off process. Two single loops with diameter $d = 4$ μm, width of the current stripe, see Fig. 1, $w_\mathrm{con} = 0.6$ μm and $w_\mathrm{con} = 0.7$ μm, two systems of identical 20 loops with $d = 4$ μm, $w_\mathrm{con} = 0.4$ μm and $w_\mathrm{con} = 1$ μm and two systems of double loops with different diameter $d = 4$ μm and $d = 3$ μm were investigated. For this structures, the

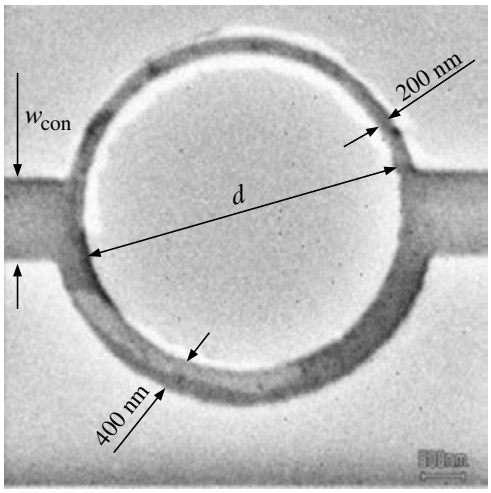

Fig. 1. An SEM photo of the asymmetric aluminum round loop (ring) used for the measurements. w_con is the width of the Al stripes used as current contacts.

sheet resistance was $0.2-0.5$ $\Omega/\diamond$ at 4.2 K, the resistance ratio R (300 K)$/R$ (4.2 K) $= 2.5-3.5$, and critical temperature was $T_\mathrm{c} = 1.24-1.27$ K.

The current-voltage curves and magnetic dependencies of the critical current $I_{\mathrm{c}+}$, $I_{\mathrm{c}-}$ measured in opposite directions on the loop, shown on Fig. 1, and systems of such loops were investigated. Magnetic field direction was perpendicular to the ring's plane. All signals were digitized by a multi-channel 16-bit analog-digital converter card.

2. Results

Three types of the current-voltage curves are observed: (1) smooth and reversible one; (2) irreversible, with smooth transition into the resistive state; (3) irreversible, with jump increase of the resistance of the whole structure at $I = I_{\mathrm{c}+}$ or $I_{\mathrm{c}-}$. The first type is observed near superconducting transition T_c, the second one in an intermediate region of temperature and the third one at low temperature. We have found that the critical current $I_{\mathrm{c}+}$, $I_{\mathrm{c}-}$ both of single loops and systems of identical loops is periodical function of magnetic field with period corresponding to the flux quantum Φ_0, Fig. 2. The magnetic dependencies of the critical current $I_{\mathrm{c}+}(\Phi/\Phi_0)$ and $I_{\mathrm{c}-}(\Phi/\Phi_0)$ measured in opposite directions are similar, Fig. 2, for all investigated structures. The anisotropy of the critical current $I_{\mathrm{c,an}} = I_{\mathrm{c}+} - I_{\mathrm{c}-}$, Fig. 2, is a consequance

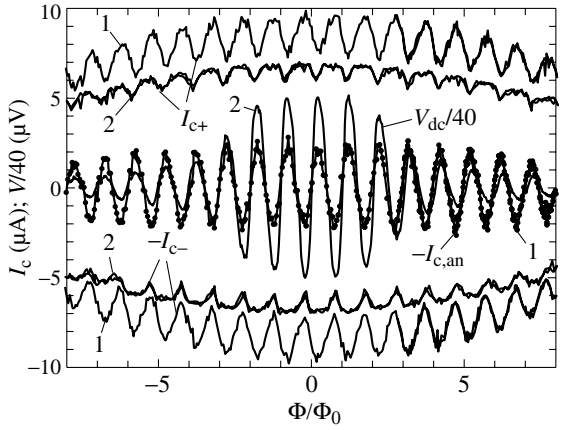

Fig. 2. The quantum oscillations of the critical current I_{c+}, I_{c-} measured in opposite directions, its anisotropy $I_{c,an} = I_{c+} - I_{c-}$ and the rectified voltage V_{dc}, induced by the ac current with frequency $f = 40$ kHz and amplitude $I_0 = 11.7$ μA at $T = 1.241$ K. The data for single loop (1) and system of identical 20 loops (2) are shown.

of a shift $\Delta\phi$ of these dependencies one relatively another, $I_{c+}(\Phi/\Phi_0) = I_{c-}(\Phi/\Phi_0 + \Delta\phi)$.

The similarity of the magnetic periodical dependencies of anisotropy of the critical current $-I_{c,an}(\Phi/\Phi_0)$ and the dc voltage $V_{dc}(\Phi/\Phi_0)$ induced by an external ac current, Fig. 2, corroborates the explanation [8] of the quantum oscillations of the dc voltage observed on segments of asymmetric superconducting loops as a consequence of rectification of the ac current [8] or noise [7]. The similarity of the magnetic dependencies $V_{dc}(B)$ and $-I_{c,an}(B)$ is observed also on double loops with different diameter, Fig. 3, although these dependencies are not periodical in this case [9].

The rectified voltage $V_{dc} = \Theta^{-1} \int_\Theta \mathrm{d}t\, V(I_{ext}(t))$ appears when the amplitude I_0 of the external current $I_{ext}(t) = I_0 \sin(2\pi f t)$ exceeds either I_{c+} or I_{c-} and its absolute value $|V_{dc}|$ decreases when I_0 exceeds both I_{c+} and I_{c-}. The amplitude V_A of the quantum oscillations $V_{dc}(\Phi/\Phi_0)$ has a maximum value [8, 9] $V_{A,max}$ at $\min(I_{c+}, I_{c-}) < I_{0,max} < \max(I_{c+}, I_{c-})$. Our measurements have shown that the relation $V_{A,max}/I_{0,max}$ is high at a low temperature $T < 0.98T_c$ where the current-voltage curves of the third type are observed: $V_{A,max}/I_{0,max} \approx 0.8$ Ω

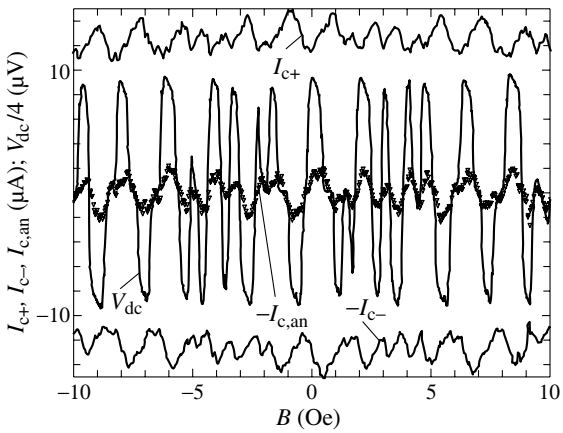

Fig. 3. The magnetic dependencies of the critical current I_{c+}, I_{c-} measured in opposite directions, its anisotropy $I_{c,an} = I_{c+} - I_{c-}$ and the rectified voltage V_{dc}, induced by the ac current with frequency $f = 0.4$ kHz and amplitude $I_0 = 17.5$ μA at $T = 1.221$ K of double superconducting Al loops.

for a single loop with the resistance in the normal state $R_n = 3.3$ Ω and $V_{A,max}/I_{0,max} \approx 20$ Ω for a systems of identical 20 loops with $R_n = 92$ Ω. The high efficiency of rectification is conditioned by the irreversibility of the current-voltage curves and it decreases near superconducting transition.

The conclusion that the potential difference $V_{dc}(\Phi/\Phi_0)$ observed at $T < T_c$ on asymmetric superconducting loop is result of rectification of an ac current or noise does not exclude a like phenomenon in normal metal or semiconductor asymmetric loops. The asymmetry of the current-voltage curves and $I_{c+}(\Phi/\Phi_0)$, $I_{c-}(\Phi/\Phi_0)$ are consequence of the persistent current $I_p(\Phi/\Phi_0)$ which is observed not only at $T < T_c$ but also at $T \approx T_c$ and even $T > T_c$ [5] where $R_l > 0$. One can expect $V(\Phi/\Phi_0) = R_{asym} I_p$ (Φ/Φ_0) at $I_p \neq 0$ and $R_l > 0$ by analogy with the case $V = R_{asym} I = (R_{ls} - R_l l_s/l) I$ of conventional circular current $I = R_l^{-1} \oint_l \mathrm{d}l\, E$ induced by the Faraday's voltage $\oint_l \mathrm{d}l\, E = -\mathrm{d}\Phi/\mathrm{d}t$ in an asymmetric loop with the segment resistance $R_{ls}/l_s \neq R_l/l$.

Acknowledgement

This work has been supported by a grant of the Program "Low-Dimensional Quantum Structures" of the Presidium of Russian Academy of Sciences, a grant "Quantum bit on base of micro- and nano-structures with metal conductivity" of the Program "Technology Basis of New Computing Methods" of ITCS department of RAS and a grant 04-02-17068 of the Russian Foundation of Basic Research.

References

[1] D. V. Nomokonov *et al*, *in Proceedings of 13th International Symposium "Nanostructures: Physics and Technology"* St Petersburg: Ioffe Institute, 2005, p. 197; B. Szafral and N. M. Peeters, *idid*, p. 203; O. A. Tkachenko *et al*, *idid*, p. 205.

[2] L. P. Levy *et al*, *Phys. Rev. Lett.* **64**, 2074 (1990); V. Chandrasekhar *et al*, *idid* **67**, 3578 (1991); E. M. Q. Jariwala *et al*, *idid* **86**, 1594 (2001).

[3] D. Mailly, C. Chapelier and A. Benoit, *Phys. Rev. Lett.* **70**, 2020 (1993); B. Reulet *et al*, *idid* **75**, 124 (1995); W. Rabaud *et al*, *idid* **86**, 3124 (2001).

[4] J. M. Blatt, *Phys. Rev. Lett.* **7**, 82 (1961).

[5] W. A. Little and R. D. Parks, *Phys. Rev. Lett.* **9**, 9 (1962).

[6] I. O. Kulik, *Pisma Zh. Eksp. Teor. Fiz.* **11**, 407 (1970) (*JETP Lett.* **11**, 275 (1970)).

[7] S. V. Dubonos, V. I. Kuznetsov and A. V. Nikulov, *in Proceedings of 10th International Symposium "Nanostructures: Physics and Technology"* St Petersburg: Ioffe Institute, 2002, p. 350.

[8] S. V. Dubonos *et al*, *Pisma Zh. Eksp. Teor. Fiz.* **77**, 439 (2003) (*JETP Lett.* **77**, 371 (2003)).

[9] V. L. Gurtovoi, R. V. Kholin, N. N. Osipov and V. A. Tulin, *in Proceedings of 13th International Symposium "Nanostructures: Physics and Technology"* St Petersburg: Ioffe Institute, 2005, p. 211.

14th Int. Symp. "Nanostructures: Physics and Technology"
St Petersburg, Russia, June 26–30, 2006

Effect of atmospheric pressure on conductance fluctuations in single-wall carbon nanotubes

S. Rumyantsev[1,2], A. Vijayaraghavan[2], S. Kar[2], A. Khanna[2], C. Soldano[2], N. Pala[2,3], R. Vajtai[2], O. Nalamasu[2], M. Shur[2] and P. Ajayan[2]

[1] Ioffe Physico-Technical Institute, St Petersburg, Russia
[2] Rensselaer Polytechnic Institute, Troy, New York 12180, USA
[3] Sensor Electronic Technology, Inc. Columbia, South Carolina 29209, USA

Abstract. Low frequency noise studies of single wall carbon nanotubes revealed that the noise in metallic and semiconducting nanotubes follows $1/f$ and I^2 dependences on frequency, f, and current, I, respectively. Semiconducting nanotubes have three orders of magnitude higher noise level than metallic nanotubes. In vacuum, noise decreased quickly (during the pumping out time of about a few tens of minutes) by over an order of magnitude for both metallic and semiconducting nanotubes. The characteristic time to restore the initial noise level after the atmosphere exposure is several tens of hours, which is an order of magnitude longer than the characteristic time to restore the initial value of the resistance.

1. Introduction

The electronic transport properties of single wall carbon nanotubes (SWNTs) have attracted tremendous attention in recent years, owing to their potential application as ballistic conductors [1], field effect transistors [2], non-volatile memories [3] and chemical and pressure sensors [4]. Temperature, surface passivation, and annealing significantly affect the charge injection into the nanotube conductance channel and, hence, the nanotube resistance. In this letter, we report on the effect of the atmospheric pressure on the noise characteristics of individual SWNTs.

2. Experimental details

SWNTs were grown randomly by thermal CVD on oxidized 100 nm Si conducting substrates. The oxide layer provided an insulating substrate, and the conducting Si acted as a back gate. Nanotubes were contacted with Ti/Au metal bi-layer electrodes with 1 μm separation, fabricated by electron-beam lithography. This yielded devices containing one or several individual SWNTs. The low frequency noise was measured in the frequency range from 1 to 3000 Hz. The voltage fluctuations S_V from the 10 kΩ resistor connected in series with the nanotubes were analyzed by a SR770 Network Analyzer.

3. Results and discussions

Two types of nanotubes — metallic (M-SWNT) and semiconducting (S-SWNT) — were studied. The metallic nanotubes (with resistance $R = 0.5-5$ MΩ) had linear and symmetrical current-voltage characteristics, which were independent of the gate voltage, V_g. Semiconducting nanotubes demonstrated non-linear, asymmetrical, and gate voltage dependent current voltage characteristics Figure 1 shows an example of the current-voltage characteristic of an S-SWNT at the atmospheric pressure and in vacuum. This current voltage characteristic is well described by an exponential function $I \approx \exp$ (eV/3.5kT). We attribute the asymmetry and non-linearity of the S-SWNT current-voltage characteristic to the Schottky metal-SWNT contacts. The inset in Fig. 1 shows the dependence of current on the substrate (gate) voltage. As seen, the current increases with an increase of the negative gate voltage. This confirms p-type conductivity of the S-SWNTs.

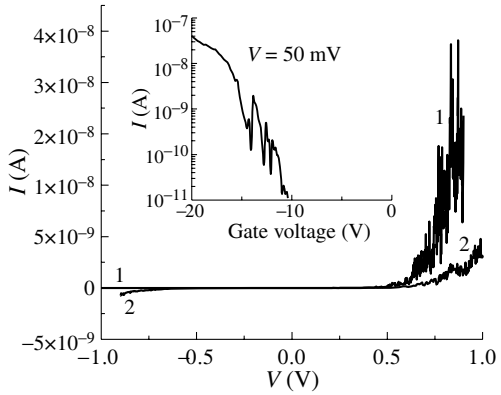

Fig. 1. Current-voltage characteristic of the S-SWNT at the atmospheric environment (line 1) and in vacuum line (line 2). The inset shows the dependence of current on the gate voltage.

Fig. 2 shows the relative spectral noise density S_I/I^2 of short circuit current fluctuations measured at different voltages (currents) for M-SWNTs and S-SWNTs. Both metallic and semiconducting SWNTs exhibited $1/f$ noise with the exponent γ close to unity ($\gamma = 1.0-1.1$). As seen from Fig. 2, the spectral noise densities S_I/I^2 measured at different currents nearly coincide indicating that the absolute value of noise, S_I, scales as $S_I \sim I^2$.

This result was reported earlier for the individual nanotubes and 2-D networks [5, 6] with linear current-voltage characteristics. The dependence $S_I \sim I^2$ is often found for the Schottky contacts to semiconductors [7]. Since resistance of S-SWNTs is dominated by the Schottky contacts, we can assume that the $1/f$ noise of S-SWNT is originated from the contacts and/or from the parts of the carbon nanotubes adjacent to the contacts. Earlier we reported on the deviation from $S_I \sim I^2$ for iron filled multi wall nanotubes with linear current-voltage characteristic [8]. Those results indicate different possible origins of the $1/f$ noise in nanotubes filled with iron. In the past, the electrical properties of SWNTs have been reported to be sensitive to their environment (for example, oxygen and moisture) [4]. We found that when the nanotubes were placed in vacuum, the resistance of the devices increased for both M-SWNTs and S-SWNTs (see Fig. 1), consistent with the previous reports [9]. However, the changes in the low frequency noise (reported in

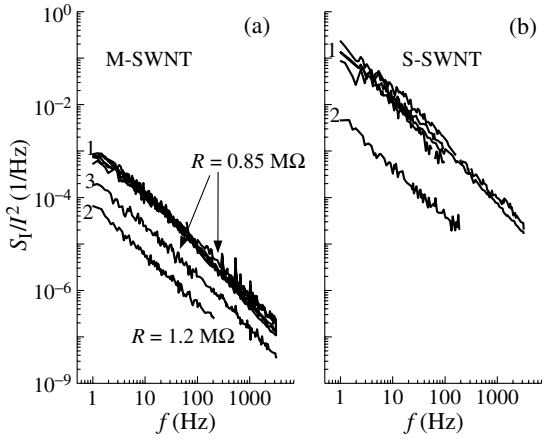

Fig. 2. Noise spectra for M-SWNT (a) and S-SWNT (b) for different voltages at the atmospheric pressure and in vacuum. 1 — in atmosphere M-SWNT: $V = 2, 5, 10, 20, 40, 80$ mV. S-SWNT: $V = 0.45, 0.51, 0.6, 0.7, 0.8$ V; 2 — in vacuum; 3 — M-SWNT after $\sim$ 24 hours exposure to the atmosphere.

this paper for the first time) were much more dramatic. The noise amplitude decreased by about an order of magnitude in vacuum for both S-SWNTs and M-SWNTs, while resistance change was $\sim$ 40% for M-SWNT and $\sim$ 250% for S-SWNT. When the devices were restored to the atmospheric pressure, the resistance and noise levels were eventually restored to the original values. However, the noise level took a much longer time to recover compared to the resistance. Even when the resistance was restored completely to its original value after several hours of exposure to the atmosphere, the noise remained much smaller than its initial value in the atmosphere. Several tens of hours were required to restore noise level to its original atmosphere value. As an example, line 3 in Fig. 2a shows S_I/I^2 for M-SWNT after $\sim$ 24 hours of the exposure to the atmosphere. As seen, for the same resistance the noise level is almost an order of magnitude smaller than the initial value. This indicates a much higher sensitivity of noise (compared to the SWNT resistance) to the environment. On possible way to characterize the $1/f$ noise level is to use the Hooge parameter $\alpha_{\rm H} = (S_I/I^2) \times f \times N$, where N is the total number of carriers in the sample [10]. This parameter $\alpha_{\rm H}$ was already used to characterize noise in carbon nanotubes and was shown to be $\alpha_{\rm H} = 4 \times 10^{-3} - 0.2$ [5]. Taking for the estimate the number of carriers to be equal to the number of atoms — clearly overestimate — (as was done in [5]) we obtained $\alpha_{\rm H} = 1 - 10$, for M-SWNTs. To conclude, the low frequency $1/f$ noise in metallic and semiconducting single wall carbon nanotubes was studied at atmospheric pressure and in vacuum. In both types of devices the spectral noise density of current fluctuations was proportional to the square of the current and the noise level decreased about one order of magnitude in vacuum. High sensitivity of noise to the environment shows a potential for chemical sensor applications based on carbon nanotube noise characteristics.

Acknowledgements

The authors acknowledge the financial support provided by the Interconnect Focus Center New York at RPI, partial support from the National Science Foundation (Project Monitor, Dr. James Mink), from the Russian Foundation for Basic Research (Grant 05-02-1772) and Civilian Research and Development Foundation (CRDF 2681).

References

[1] D. Mann *et al*, *Nano Letters* **3**, 1541 (2003).
[2] S. J. Tans *et al*, *Nature* **393**, 49 (1998).
[3] M. Radosavljevic *et al*, *Nano Letters* **2**, 755 (2002).
[4] J. Konget *et al*, *Science* **287**, 622 (2000).
[5] P. G. Collins *et al*, *App. Phys. Lett.* **76**, 894 (2000).
[6] E. S. Snow *et al*, *App. Phys. Lett.* **85**, 4172 (2004).
[7] S. Rumyantsevet *et al*, *Proc. 9th Int. Symp. Nanostr. and Techn. (St Petersburg, Russia, 2001)*, 418, 2001.
[8] M.-Y. Luo *et al*, *IEEE Trans. ED* **35**, 1351 (1988).
[9] P. G. Collins *et al*, *Sceince* **287**, 1801 (2000).
[10] F. N. Hooge *et al*, *Physics Lett. A* **29**, 139 (1969).

14th Int. Symp. "Nanostructures: Physics and Technology"
St Petersburg, Russia, June 26–30, 2006

Theory of one-dimensional double-barrier quantum pump in two-frequency signal regime

M. M. Mahmoodian and M. V. Entin
Institute of Semiconductor Physics SB RAS, 630090 Novosibirsk, Russia

Abstract. A one-dimensional system with two δ-like barriers or wells bi-chromaticaly oscillating at frequencies ω and 2ω is considered. The alternating signal leads to the direct current across the structure (even in a symmetric system). The properties of this quantum pump are studied in a wide range of the system parameters.

We study the quantum pump described by the one-dimensional time-dependent potential:

$$U(x) = (u_{11}\sin\omega t + u_{12}\sin 2\omega t)\delta(x+d) + \\ +(u_{21}\sin\omega t + u_{22}\sin 2\omega t)\delta(x-d)\,. \qquad (1)$$

The alternating voltage produces the stationary current by pumping electrons between leads $x < -d$ and $x > d$. The effect is sensitive to the phase coherence of alternating signals and can exist even in symmetric systems. The stationary current is possible also in the case of different amplitudes of alternating fields.

We have studied the system both analytically and numerically. The analytical approach is based on the perturbational (with respect to amplitudes of a.c. signal) consideration. The current contains independent contributions caused by u_{ij} and an interference term. The elastic, absorption and emission channels participate in the process. The case of strong alternating signal was studied numerically.

The Figures 1–5 show typical plots of the derivative of the stationary current with respect to the Fermi energy $\partial J/\partial E_F = \mathcal{G} \times 2e^2/h$ as a function of the Fermi momentum (Figs. 1–3), the amplitude (Fig. 4) and the frequency (Fig. 5). We use the unites $\hbar/md$ for u_{ij}, $\hbar/d$ for the momentum p, and $\hbar/2md^2$ for the frequency.

The curve in the Fig. 1 corresponds to antipodal signals with same amplitudes ($u_{12} = -u_{22}$), that demonstrates the importance of the phase coherency of the signals (in such conditions the stationary current in the same system under monochromatic voltage is vanishing [1]). The current oscillates with the Fermi momentum due to the interference of the electron waves in the structure. Besides, the current possesses singularities caused

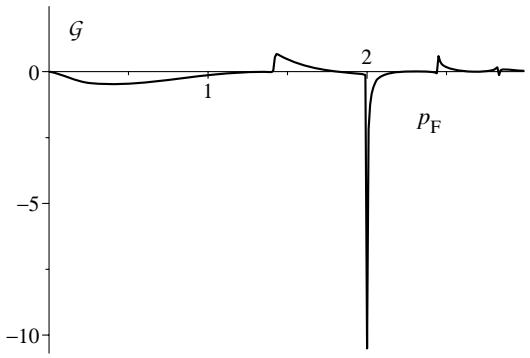

Fig. 1. The derivative of the current $\mathcal{G}$ *versus* the Fermi momentum. Here $u_{11} = u_{12} = 1$, $u_{21} = u_{22} = -1$, $\omega = 2$. The left delta-function oscillates from the barrier to zero hight, the right delta-function changes from the well to zero.

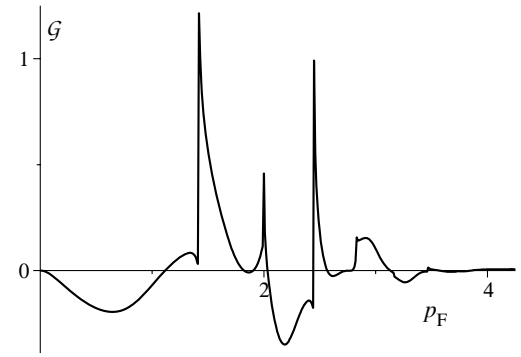

Fig. 2. The dependence of $\mathcal{G}$ on the Fermi momentum. We set $u_{11} = u_{12} = 2$, $u_{21} = u_{22} = -1$, $\omega = 2$.

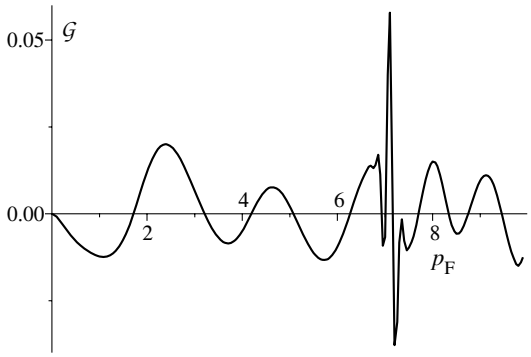

Fig. 3. $\mathcal{G}$ *versus* the Fermi momentum; $u_{11} = u_{12} = 2$, $u_{21} = u_{22} = -1$, $\omega = 50$.

by the resonances with the zero energy state and their photon repetitions.

The Figures 1–3 present the quantity $\mathcal{G}$ as a function of the Fermi momentum for $u_{21} = u_{22} = -1$, $\omega = 2$ and $u_{11} = u_{12} = 1$ (Fig. 1), 2 (Fig. 2). The peaks of the curves correspond to the multi-photon threshold resonances with zero energy state. The increasing of $u_{11} = u_{12}$ leads to the strengthening of multi-photon singularities. The Figure 3 shows the behavior of $\mathcal{G}$ for large enough frequency where the only threshold singularity exists in the concerned range of Fermi momentum values.

The Figure 4 depicts $\mathcal{G}$ *versus* u_{11} for the symmetric system ($u_{11} = u_{12} = -u_{21} = -u_{22}$).

The Figure 5 demonstrates the dependence of $\mathcal{G}$ on the frequency. The complicated structure of $\mathcal{G}$ in the low frequency region is explained by multi-photon resonances reducing for larger frequencies.

Our calculations show that the stationary current is a sophisticated function of the parameters, that reflects the interference

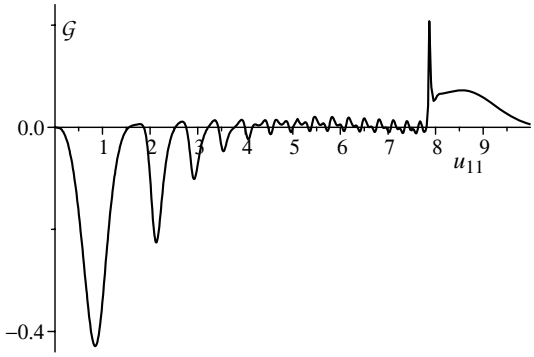

Fig. 4. The dependence of $\mathcal{G}$ on the amplitudes $u_{11} = u_{12} = -u_{21} = -u_{22}$ for $\omega = 2$, $p_{\mathrm{F}} = 0.7$.

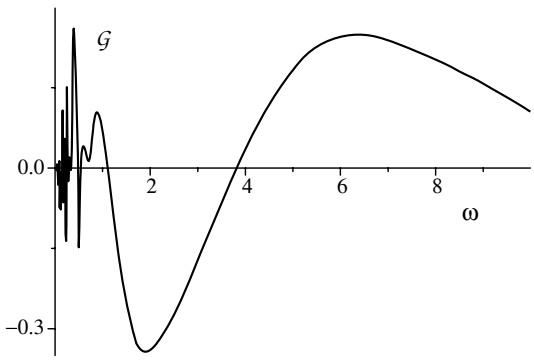

Fig. 5. The dependence of $\mathcal{G}$ on the frequency for $u_{11} = u_{12} = 1$, $u_{21} = u_{22} = -1$, $p_{\mathrm{F}} = 0.7$.

effects, presence of virtual states, and threshold singularities.

Acknowledgements

This work was supported by grants of RFBR No. 04-02-16398, the Dynasty Foundation and the grant of the President of the Russian Federation. We are grateful to L. S. Braginsky for useful discussions.

References

[1] L. S. Braginskii *et al*, *Zh. Eksp. Teor. Fiz.* **127**, 1046 (2005) [*JETP* **100**, 920 (2005)].

14th Int. Symp. "Nanostructures: Physics and Technology"
St Petersburg, Russia, June 26–30, 2006

Acoustoelectric current in 3D ballistic microconstriction

V. A. Margulis and I. A. Kokurin
Mordovian State University, 430000 Saransk, Russia

Abstract. The acoustoelectric current through a ballistic three-dimensional constriction is investigated in the presence of a longitudinal magnetic field. We obtain a convenient analytic formula for the current in the case of long wavelengths of the sound. It is found that the dependence of the current on the chemical potential (which is controlled by the gate voltage) in the terminals can exhibit both the oscillatory behaviour and the step-like one. Conditions of the step-like behaviour have been found. The effect of magnetic field and temperature on the current is studied.

Introduction

The interaction of surface acoustic waves (SAW) with electrons in mesoscopic systems has been attracting growing attention. In particular, the acoustoelectric (AE) effect (dc current induced by the SAW) was investigated experimentally in quantum channels defined in GaAs-$Al_xGa_{1-x}As$ heterostructures [1, 2]. It was shown the AE current undergoes giant quantum oscillations as a function of the applied gate voltage [1], having maxima between the plateaux of the quantized conductance. The experimental study [2] presents step-like behaviour of the AE current in a channel. It was observed clearly up to four plateaux in the AE current as a function of the gate voltage.

This problem has been considered theoretically in several papers [1, 3–6]. The AE effect in quantum channels can be described by using either of the following two approaches. In the first approach, the electron motion was described by the Boltzmann equation [1, 3], with the SAW considered as a classical force [1] or as a flux of monochromatic ultrasonic phonons [3]. The approach is valid only when the channel length is much longer than the acoustic wavelength. Second approach is of the quantum-mechanical type [4–6], i.e., is based on direct calculation of the transmission coefficients of electron through the structure. In particular, it has been realized that the AE current in the ballistic point contact does not simply represent the drag of the electrons by the SAW, but constitutes an example of a *pumping phenomenon* [5, 6]. We note that the scattering inside the channel plays a crucial role for producing the AE effect [5]. Thus, there is no pumping current in a perfectly conducting channel.

The purpose of the present work is to study the behaviour of the AE current through a 3D ballistic constriction. We consider a system which consists of two bulk electronic reservoirs connected by a constriction. We assume that the temperatures in reservoirs are equal, the same is true for electrochemical potentials. Thereby we exclude from consideration all transport effects except the acoustoelectric one.

We consider 3D constriction modelled by the following confining potential which characterizes the shape and extent of the constriction [7]

$$V(x, y, z) = V_0 + \frac{m^*}{2}\left(\omega_x^2 x^2 + \omega_y^2 y^2 - \omega_z^2 z^2\right) . \quad (1)$$

Here z is the coordinate along the constriction axis, x and y are the coordinates in the transverse directions, V_0 is the potential at the saddle point, and m^* is the effective mass of the electron; ω_x, ω_y are the characteristic frequencies of the parabolic confining potential which determine the semi-axes of elliptic cross-section of the constriction $l_j = \sqrt{\hbar/4m^*\omega_j}$ ($j = x, y$), and ω_z determines the curvature of the potential along its axis. The corresponding characteristic length l_z has the form $l_z = \sqrt{\hbar/2m^*\omega_z}$. The system is placed in the longitudinal magnetic field $\mathbf{B} = (0, 0, B)$.

1. Calculation of AE current

To calculate the AE current through microconstriction the concept of *time-dependent scattering states* [5, 6] has been used. In this case the acoustic wave of frequency $\omega_\mathbf{q}$ and wave vector $\mathbf{q}$ is represented by the moving potential profile

$$\delta U(\mathbf{r}, t) = A\cos(\mathbf{qr} - \omega_\mathbf{q} t) . \quad (2)$$

The potential created by the acoustic wave has been assumed propagating in the z direction, $\mathbf{q} = (0, 0, q)$. We suppose that the reservoirs give no contribution to the current.

Let us consider the actual case of a long wavelength of the sound ($ql_z \ll 1$), where the classical approach [1, 3] is not valid. Neglecting a weak screening of a sound potential inside microconstriction [1], we can write the AE current in zero-temperature limit as

$$\frac{J(\mu, T = 0)}{J_0} = \sum_{m,n=0}^{\infty} \frac{\exp\left[-\beta\left(\mu^* - E_{mn}\right)\right]}{\left(1 + \exp\left[-2\beta\left(\mu^* - E_{mn}\right)\right]\right)^{3/2}} , \quad (3)$$

where $J_0 = 4\pi e\omega_\mathbf{q}|A|^2/(\pi\hbar\omega_z)^2$, $\beta = \pi/\hbar\omega_z$, $\mu^* = \mu - V_0$, and μ is the chemical potential of the electron gas in the reservoirs. A discrete part of the single-electron spinless spectrum E_{mn} has the form [7]

$$E_{mn} = \hbar\omega_1(m + 1/2) + \hbar\omega_2(n + 1/2) , \quad (4)$$

and the hybrid frequencies $\omega_{1,2}$ are given by

$$\omega_{1,2} = \frac{1}{2}\left(\sqrt{\omega_c^2 + (\omega_x + \omega_y)^2} \pm \sqrt{\omega_c^2 + (\omega_x - \omega_y)^2}\right) , \quad (5)$$

where $\omega_c = |e|B/m^*c$ is the cyclotron frequency.

As follows from Eq. (3) the dependence of the AE current on the chemical potential demonstrates giant oscillations in the general case. It is interesting that each maximum of giant quantum oscillations corresponds to a threshold of the ballistic conductance [7].

For the analysis it is convenient to represent Eq. (3) as a Fourier series with help of direct and reverse Mellin transformations.

To take into account an effect of the temperature on the AE current a standard approach has been used

$$J(\mu, T) = \int_0^\infty d\varepsilon \left(-\frac{\partial f}{\partial \varepsilon}\right) J(\varepsilon, T = 0)\,, \qquad (6)$$

where $f(\varepsilon)$ is the Fermi distribution function.

Using the above-mentioned transformation and Eq. (6) it is easy to represent the AE current as the sum of the Fourier series. For the realistic case of the long constriction ($\omega_z \ll \omega_{x,y}$) we can write

$$\frac{J}{J_0} = \frac{\omega_z}{\pi\hbar\omega_1\omega_2}\Bigg[\mu^* + 2\pi^2 T\frac{\omega_2}{\omega_1}\sum_{n=1}^{\infty}\frac{(-1)^n n\sin(2\pi n\mu^*/\hbar\omega_1)}{\sinh(2\pi^2 nT/\hbar\omega_1)\sin(\pi n\omega_2/\omega_1)} + 2\pi^2 T\frac{\omega_1}{\omega_2}\sum_{n=1}^{\infty}\frac{(-1)^n n\sin(2\pi n\mu^*/\hbar\omega_2)}{\sinh(2\pi^2 nT/\hbar\omega_2)\sin(\pi n\omega_1/\omega_2)}\Bigg]. \qquad (7)$$

It should be noted that the analysis of convergence of series of the type (7) is carried out in Ref. [8]. As follows from this equation the dependence of the AE current on the chemical potential demonstrates two types of oscillations. The amplitudes of these oscillations are determined by the relations between the temperature, the parameters of the constriction, and the magnetic field. The period of each component depends only on parameters of the magnetic and size quantization ($\Delta_i\mu = \hbar\omega_i$, $i = 1,\ 2$).

2. Discussion

It is interesting to consider the sufficiently asymmetric constriction, that is $\omega_x \gg \omega_y$, or the case of a strong magnetic field which guarantees the effective asymmetry ($\omega_1 \gg \omega_2$). In the above-mentioned case the first series in Eq. (7) exhibits oscillations with a sawtooth modulation, but the second series undergoes the strictly sinusoidal oscillations as a function of the chemical potential. Finally, it leads to step-like dependence of the AE current with the fine structure which represents oscillations with the period $\Delta\mu = \hbar\omega_2$. The lengths of the plateaux are $\Delta\mu = \hbar\omega_1$. It is interesting to note the amplitude of the fine-structure oscillations varies from plateau to plateau (Fig. 1).

The temperature corresponding to the smearing of the fine-structure oscillations ($T \sim \hbar\omega_2$) is much smaller than temperature which is necessary to the smearing of thresholds of the AE current ($T \sim \hbar\omega_1$). It leads to strictly step-like behaviour (without fine structure) of the AE current in this temperature interval (Fig. 1)

$$\frac{J^{\rm step}}{J_0} = \frac{\omega_z}{\pi\hbar\omega_1\omega_2}\left[\mu^* + 2\pi T\sum_{n=1}^{\infty}(-1)^n\frac{\sin(2\pi n\mu^*/\hbar\omega_1)}{\sinh(2\pi^2 nT/\hbar\omega_1)}\right]. \qquad (8)$$

The current $J^{\rm step}$ is the sum of two parts, the monotonic part is a linear function of the chemical potential, while the series gives a sawtooth contribution to this dependence. The height of the AE current steps is given by

$$\Delta J = \frac{4e\omega_{\mathbf{q}}|A|^2}{\pi^2\hbar^2\omega_2\omega_z}\,. \qquad (9)$$

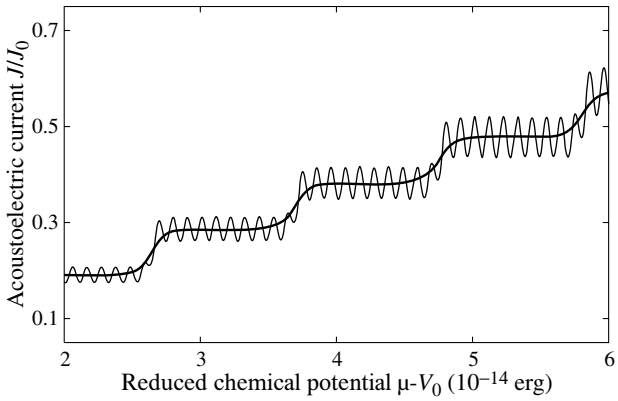

Fig. 1. The step-like dependence of the AE current vs. chemical potential. $\omega_x = 4.4 \times 10^{12}$ s^{-1}, $\omega_y = 2.3 \times 10^{12}$ s^{-1}, $\omega_z = 3 \times 10^{11}$ s^{-1}, $B = 3.4$ T, $T = 2$ K (thin line), $T = 4$ K (thick line).

We note the effect of the magnetic field on the AE current behaviour. The amplitude of the fine-structure oscillations decreases with increasing of the magnetic field while the height of the current steps increases. Moreover increasing of the magnetic field leads to the extension of the temperature interval, where the AE current is strictly step-like function of the chemical potential. In the strong magnetic field case ($\omega_{\rm c} \gg \omega_{x,y}$) the AE current undergoes Shubnikov–de Haas oscillations with the period

$$\Delta\left(\frac{1}{B}\right) = \frac{e\hbar}{m^* c(\mu - V_0)}\,. \qquad (10)$$

In the case of comparatively low temperatures $T \lesssim \hbar\omega_2$ the amplitudes of the oscillation peaks are larger than the height of the steps. That is why the AE current plateaux are destroyed by these oscillations. And finally let us describe the case $T \gtrsim \hbar\omega_2$. The temperature increasing leads to the smoothing of the thresholds of the AE current steps. This process is similar to the smoothing of the thresholds of the ballistic conductance steps. In this case there is the linear dependence of the AE current on the chemical potential. It corresponds to the first term in Eq. (7).

Acknowledgement

This work has been supported by the Russian Foundation for Basic Research (grant No. 05-02-16145).

References

[1] J. M. Shilton, D. R. Mace, V. I. Talyanskii *et al*, *J. Phys.: Condens. Matter* **8**, L337 (1996).
[2] V. I. Talyanskii, J. M. Shilton, M. Pepper *et al*, *Phys. Rev. B* **56**, 15180 (1997).
[3] V. L. Gurevich, V. B. Pevzner and G. J. Iafrate, *Phys. Rev. Lett.* **77**, 3881 (1996).
[4] F. A. Maaøand Yu. M. Galperin, *Phys. Rev. B* **56**, 4028 (1997).
[5] O. Entin-Wohlman, Y. Levinson, P. Wölfle, *Phys. Rev. Lett.* **85**, 634 (2000).
[6] O. Entin-Wohlman, Y. Levinson, P. Wölfle, *Phys. Rev. B* **64**, 195308 (2001).
[7] A. G. Scherbakov, E. N. Bogachek and Uzi Landman, *Phys. Rev. B* **53**, 4054 (1996).
[8] V. A. Geyler and V. A. Margulis, *Phys. Rev. B* **55**, 2543 (1997).

14th Int. Symp. "Nanostructures: Physics and Technology"
St Petersburg, Russia, June 26–30, 2006

Role of fluctuations in carrier transfer quantum processes in semiconductor heterostructures

I. V. Rozhansky and N. S. Averkiev
Ioffe Physico-Technical Institute, St Petersburg, Russia

Abstract. Influence of the electrical potential fluctuations on quantum transfer effects in semiconductor heterostructures is analyzed. It is shown that, contrary to the bulk 3D case, carriers capture by a quantum well (QW) or tunneling through a potential barrier is not characterized by optimal fluctuation. Spin-dependent tunneling in single-barrier nonmagnetic structures is shown to be insensitive to the fluctuations while in double-barrier structures fluctuationsf substantially reduce polarization efficiency. It is demonstrated that while for realistic AlGaAs heterostructures carriers capture by a QW keeps its resonance behavior, for presently actual InGaN-based heterostructures the capture probability becomes a smooth function of the QW parameters.

Introduction

Quantum-mechanical processes such as carriers capture by quantum wells (QW) and transfer through a multiple potential barrier systems make a basis of functioning of various semiconductor devices including rapidly developing LED, laser and spintronic applications. While these processes are constantly being under thorough theoretical investigations, fluctuations of the parameters of the realistic quantum system are usually not considered. At the same time, the significant fluctuations of the parameters such as QW depth or potential barrier width are essential for the real physical structures. Understanding the influence of the fluctuations on the derivations of the theory is crucial for correct analysis and device design. In this work we analyze different alternatives of the fluctuation influence on the quantum transfer and apply the results to a certain quantum-mechanical problems.

Generally we discriminate between three different cases:

1. Weak-dependence case. In this case fluctuations do not play any significant role and can be totally neglected.
2. Optimal fluctuation case. In this case the solution of the problem with fluctuating parameter appears to be similar to the case with no fluctuations, but the parameter value being substantially different from the average.
3. Resonance case. In this case the fluctuations dump the theoretically predicted resonance dependence on the parameters of the structure so that the solution becomes qualitatively different from that with fluctuations neglected.

Calculations

In this paper we examine several quantum-mechanical phenomena in semiconductor heterostructures that have been intensively studied recently and show how the obtained results change if the fluctuations are taken into account in each case. Effect of spin-dependent tunneling, particularly in non-magnetic semiconductors has attracted attention lately and the devices based on manipulating of spin-polarized carriers by electrical means have been suggested. We analyze fluctuations for the spin-dependent tunneling through a semiconductor single-barrier (SB) [1] and double-barrier (DB) [2] nonmagnetic structures. For the DB structure the fluctuations of the QW width with standard deviation $\sigma \approx 1$ monolayer (ML) decrease polarization efficiency and substantially change its dependence on the parameters of the QW between the barriers (Fig. 1). This is a typical example of the resonance case in the introduced classification. Contrary, the probability of spin tunneling through a SB structure has no resonance behavior: the dependence of the polarization on the barrier shape is weak (Fig. 2). Thus, despite this structure provides smaller polarization than the DB structure, the value is not affected by the fluctuations and finally the polarizations in both structures appear to be comparable ($\sim$ 1%). In the DB structure considered above the account of fluctuations cannot be reduced to any effective value of the fluctuating parameter, but rather the explicit averaging should be performed. However, in many cases the fluctuations in a quantum-mechanical problem can be described within the optimal fluctuation method (case 2 in the above classification). Tunneling through a wide potential barrier is a typical example of such a case [3, 4]. In [4] the tunnel current in back biased pn-junction has been calculated with account for fluctuations of the dopant concentration. In this problem the tunnel current depends exponentially on the barrier width while the latter is normally distributed following the fluctuations of the dopant

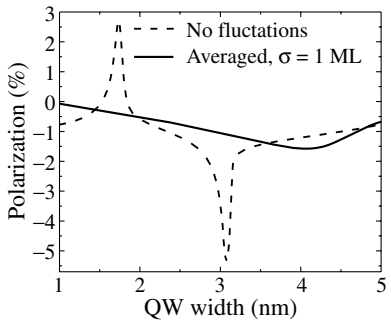

Fig. 1. Polarization in double-barrier structure.

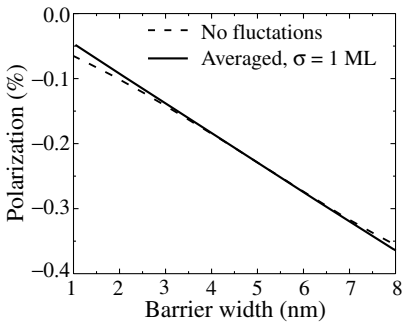

Fig. 2. Polarization in single-barrier structure.

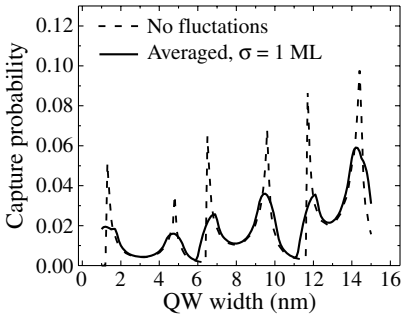

Fig. 3. Dependence of electron capture probability on QW width in $Al_{0.3}Ga_{0.7}As/GaAs$ heterostructure.

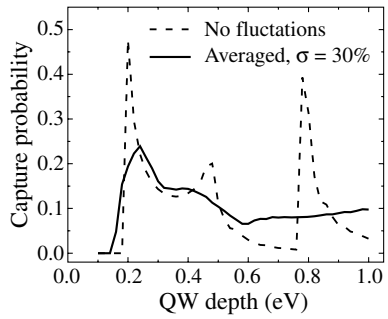

Fig. 4. Dependence of electron capture probability on QW depth in $In_xGa_{1-x}N/GaN$ heterostructure.

concentration. The relation between function strengths of both factors is such that an optimal value of the barrier thickness (substantially different from the mean value) can be found so that only the optimal barriers significantly contribute to the total current. Thus the system behaves similar to that with no fluctuation but with "effective" parameter value.

Finally we consider another quantum-mechanical process — carrier capture by a QW — the actual problem for light-emitting diodes (LED) and lasers. Correct account for the fluctuations is very important for optimization of conventional AlGaAs LEDs and lasers, and even more for the rapidly developing LED heterostructures with InGaN-based QWs. In the latter the large compositional fluctuations of QW material are imprescriptible and probably play very important role in their efficiency. In this work we give an example of calculation of carrier capture probability for $Al_xGa_{1-x}As/GaAs$ and $In_xGa_{1-x}N/GaN$ heterostructures. In the absence of fluctuations the dependence of carriers capture probability on QW parameters exhibits resonant behavior with two types of resonances [5]. However, as show the calculation, the fluctuations of the QW width and depth suppress the resonances. At that, whether the resonances remain pronounced or not depends on the amplitude of the fluctuations. For example, the fluctuations of QW width of ≈ 1 ML in high-quality $Al_{0.3}Ga_{0.7}As/GaAs$ heterostructure keep the resonant character of the dependence of capture probability on QW width (Fig. 3). Contrary, due to large In composition fluctuations ($\approx 30\%$) in realistic $In_xGa_{1-x}N$ QWs the strong dependence of the capture rate on the QW parameters is not expected (Fig. 4). We have obtained that for $In_xGa_{1-x}N/GaN$ heterostructures the capture probability constitutes 0.1–0.2 for electrons and 0.3–0.5 for the holes, the results being applicable for a wide range of QW width and height. In our opinion, the calculated values will help in quantitative description of carrier transport in the active area of InGaN-based heterostructures.

Conclusions

Several quantum transport problems have been considered to clarify possible role of the electrical potential fluctuations in quantum transfer processes. It has been shown that while in bulk samples the fluctuations can be taken into account by means of effective value or optimal fluctuation approach, in low-dimensional structures the fluctuations can substantially modify resonance character of the quantum transport. We have shown, that spin orientation appearing in the carriers tunneling through double-barrier structure is suppressed by the fluctuation of the barrier shape. Contrary, spin orientation in the tunneling through a single barrier is insensitive to these fluctuations. It has been shown that fluctuations of the QW parameters in realistic AlGaAs based heterostructures do not change the resonance character of carriers capture, but in the recently widely studied AlGaInN heterostructures with InGaN-based QWs the fluctuations suppress the resonant capture.

Acknowledgements

This work has been supported in part by INTAS, RFBR, Ministry of Science and Education of Russia and Scientific Programs of RAS.

References

[1] V. I. Perel, S. A. Tarasenko, I. N. Yassievich, *Phys. Rev. B* **67**, 201304 (2003).
[2] M. M. Glazov *et al*, *Phys. Rev. B* **71**, 155313 (2005).
[3] M. V. Krylov, R. A. Suris, *JETP* **61**, 1303 (1985).
[4] M. E. Raikh, I. M. Ruzin, *Semiconductors* **19**, 745 (1985).
[5] S. A. Solov'ev, I. N. Yassievich, V. M. Chistyakov, *Semiconductors* **29**, 654 (1995).

14th Int. Symp. “Nanostructures: Physics and Technology”
St Petersburg, Russia, June 26–30, 2006

Fixed range hopping regime for ac conduction over weakly localized states

I. P. Zvyagin
Faculty of Physics, Moscow State University, 119899 Moscow, Russia

Abstract. The relaxation ac hopping conduction over weakly localized states in dense granular disordered materials is studied in the frequency region where hopping distance becomes frequency-independent (fixed range hopping regime). It is shown that, depending on the structural characteristics of the material, the conductivity in this region can exhibit the behavior characteristic of the nearly constant loss regime or a superlinear frequency dependence.

Introduction

It is well known that the frequency dependence of the real part of the hopping conductivity of numerous disordered solids (amorphous and doped semiconductors, semiconductor glasses, polymers, ion-conducting solids, etc.) can be described by the fractional power law

$$\sigma'(\omega) = A\,\omega^s, \tag{1}$$

where A is a constant and the parameter s lies in the range $0.7 < s < 1$. Relation (1) is obeyed over wide frequency ranges covering many orders of magnitude. The conventional hopping theory of the phonon-assisted (relaxation) ac conductivity (neglecting the Coulomb correlations) predicts the dependence of the type

$$\sigma'(\omega) = A\,\omega\, r_\omega^n, \tag{2}$$

where r_ω is the frequency-dependent hopping distance logarithmically dependent on frequency and n is an integer ($n = 4$ in the 3D case) [1]. Equation (2) is well approximated by the fractional power dependence (1) with exponent s that is smaller than 1 and gradually increases with frequency and with lowering temperature.

A frequency dependence of the conductivity similar to that given by Eq. (1) was also observed in a number of inhomogeneous materials with "granular" structure: nanocrystalline conductors [2], nanocomposites [3], and doped semiconductors near the metal–insulator transition (MIT) [4, 5] (in this case, "grains" may be associated with fluctuations creating conducting inclusions similar to those in heavily doped semiconductors [6]). Recently, the ac conductivity of the arrays of self-assembled quantum dots was studied [7].

There are some specific features observed in the ac conduction of these materials such as the structural dependence of the parameters of Eq. (1) or a weak frequency dependence of the conductivity [7, 8]. These features might be related to the granular structure of the materials. Indeed, the possibility of applying the standard theory of ac hopping between point localization sites to granular structures is not obvious. In particular, this is true for dense granular arrays, where

$$\gamma^{-1}, \bar{w} \ll \bar{a}; \tag{3}$$

here, γ is the inverse decay length of the wave function in the barrier separating the grains, $\bar{w}$ is the average edge-to-edge separation between the grains and $\bar{a}$ is the average grain size. Condition (3) implies that the hybridization of the states associated with separate grains can play an important role [9, 10]. In what follows, we discuss the effect of granular structure on the relaxation ac hopping conduction.

1. General relations for the relaxation conductivity

We consider a dense array of nanograins (quantum dots) with disorder originating from random fluctuations in size and edge-to-edge separations (potential barrier widths) between the grains. We assume the conductivity mechanism to be inelastic tunnelling (hopping) between localized states associated with the grains.

In the pair approximation, the expression for the real part of the low-field ac conductivity can be written in the form [1]

$$\sigma'(\omega) = \frac{e^2\omega}{kT}\sum_{\{ij\}} \mathbf{R}_{ij}^2 F_{ij}\frac{\omega\tau_{ij}}{1+(\omega\tau_{ij})^2}. \tag{4}$$

Here, i and j are the exact (hybridized) eigenstates that may be weakly localized if the overlap of the "atomic" wave functions (those for isolated-grain problems) is important, the summation is performed over isolated pairs of localized states $\{ij\}$, $\mathbf{R}_{ij}$ is the radius vector connecting the localization sites of the pair, $F_{ij} = (1/f_i^{(j)} + 1/f_j^{(i)})^{-1}$ is the statistical factor, $f_i^{(j)}$ is the equilibrium occupancy of state i of the pair provided that the other state of the pair is empty, $\tau_{ij} = \Gamma_{ij}^{-1} F_{ij}$ is the relaxation time in the pair, $\Gamma_{ij} = W_{ij} f_i^{(j)}$ is the transition rate, and W_{ij} is the transition probability between states i and j. For the system under study, the relaxation time in a pair is expressed as [11]

$$\tau_{ij} = \tau_0 \exp(2\tilde{\gamma} l_{ij}), \tag{5}$$

where $\tilde{\gamma}$ is the renormalized inverse decay length of the wave function and the prefactor τ_0 is inversely proportional to the prefactor in Γ_{ij} that is expressed as the square of the product of the resonance integral I_{ij} by a factor determined by the electron-phonon interaction. Note that the energy levels for the transitions that determine the ac conductivity are known to lie in the layer of width kT near the Fermi level and are included into the prefactor τ_0.

2. Results and discussion

The main difference of our approach based on Eq. (5) form the conventional theory of the ac hopping conductivity [1] is that we take into account the finite size of the sites. The relaxation time (5) exponentially depends on the total tunnelling distance l_{ij} expressed in terms of the edge-to-edge separations

w_{ij} and, for $\tilde{\gamma} l_{ij} \gg 1$, is expected to be distributed over a broad range. In [11], the ac conductivity of granular structures has been considered in the low-frequency range in the extended-pair approximation (i.e., taking account of the hybridization of the states of neighboring grains). It is known that the main contribution to the right-hand side in Eq. (4) corresponds to the total tunnelling distance l_ω, for which $\omega\tau_{ij} \approx 1$, i.e., to $l_\omega = (2\tilde{\gamma})^{-1} \ln^{\nu}(1/(\omega\tau_0))$, where ν is the fractal dimensionality for the paths of minimum length on the percolation cluster. At low frequencies, where $l_\omega \gg a$, the transitions between distant hybridized states give the main contribution to the conductivity. At frequencies exceeding the frequency, at which l_ω becomes comparable to the grain size a, transitions between near neighbors (NNs) become predominant.

For NN localized states i and j, the resonance integral I_{ij} exponentially depends on the edge-to-edge separation w_{ij} between the grains,

$$I_{ij} = I_0 \exp(-\gamma w_{ij}). \tag{6}$$

It is noteworthy that the prefactor I_0 substantially depends on the grain size. For large grains $\gamma\bar{a} \gg 1$, this dependence can be approximated by the relation

$$I_0 = I_{00} (\gamma\bar{a})^{-q}. \tag{7}$$

There are two factors that determine the exponent q. First, it follows from the normalization condition that the amplitude of the wave function at the grain boundary decreases with increasing grain size. Second, the effective "contact area" between the neighboring grains depends on the grain size as well. Taking these two factors into account, we can estimate q; we obtain $q \approx 2$ for 3D systems and $q \approx 3/2$ for 2D systems.

According to Eq. (3), we have $\gamma\bar{a} \gg 1$, and the decrease (7) in I_0 due to a large grain size may be quite important. The magnitude of I_0 affects the quantum correlation between the characteristic energy levels and the crossover frequency that separates the region of NN hopping from the low-frequency region where the conductivity is controlled by the contribution of distant-neighbor transitions via virtual states [11].

Assuming the level energies to be uniformly distributed with density (per site) g_0, we can write conductivity (4) in the form

$$\sigma'(\omega) = \frac{Ce^2\bar{a}^2 g_0^2 \omega}{kT} Nz \int dw\, P(w)(kT + U(a)) \frac{\omega\tau(w)}{1+\omega^2\tau^2(w)}. \tag{8}$$

Here, C is a constant of the order of unity, N is the density of grains, $l_{ij} = w_{ij}$, $P(w)$ is the distribution function for the edge-to-edge separations, z is the average number of NNs, $U(\bar{a}) \approx e^2/(\kappa\bar{a})$ is the Coulomb correlation energy of two electrons simultaneously occupying the pair of sites considered [12], and κ is the permittivity. In deriving Eq. (8), we have neglected the quantum correlation of energy levels, related to the overlap of wave functions [13], since, due to Eq. (7), the overlap of wave functions of neighboring grains is strongly suppressed. The reduction in I_{ij} also implies that the transition from the regime of distant-neighbor transitions via virtual states [11] to the NN hopping regime is attained at substantially lower frequencies for granular structures than for systems of point localization centers.

Condition (3) implies that the charge displacement R_{ij} is much greater than the tunnelling length and we have replaced R_{ij} by $\bar{a}$. Thus the characteristic charge displacement is independent of frequency (*fixed range hopping*). Therefore, the logarithmic frequency factors (like r_ω in Eq. (2)) do not appear in Eq. (9).

The factor $\omega\tau(1+\omega^2\tau^2)^{-1}$ considered as a function of w is known to be sharply peaked at $w_\omega = (2\gamma)^{-1} \ln(1/\omega\tau_0)$(cf. [1]. Let the width of the distribution $P(w)$ be large compared to γ^{-1}, i.e., let $P(w)$ be a slowly varying function in the frequency range corresponding to the widths w near the value w_ω. Then we obtain

$$\sigma'(\omega) = \frac{C\, e^2\bar{a}^2 g_0^2}{kT} Nz\, P(w_\omega)\, \omega. \tag{9}$$

Equation (9) determines the frequency dependence of the ac hooping conductivity due to NN hopping.

3. Conclusions

We see that the distribution of edge-to-edge separations $P(w)$ is an important structural characteristic of the system. Depending on the shape of the function $P(w)$, the behavior of the conductivity can be different thus providing an opportunity to obtain information about $P(w)$ from the frequency measurements. In the frequency range where we may set $P(w) \approx$ const, the frequency dependence of the conductivity is almost linear (the nearly-constant loss behavior, which is currently observed in numerous disordered materials: amorphous semiconductors, glasses, low-loss polymers etc.). Such behavior, whose origin in different systems is still under dispute, was also observed in doped semiconductors near the MIT. Moreover, in contrast to conventional theories [1, 12], where the obtained dependence $\sigma'(\omega)$ is sublinear, dependence (9) can be superlinear if $dP(w)/dw|_{w=w_\omega} < 0$.

Acknowledgements

This study was supported by the Russian Foundation for Basic Research (grant no. 06-02-16918a).

References

[1] M. Pollak and T. H. Geballe, *Phys. Rev.* **122**, 1742 (1961).
[2] Ch. Bose *et al*, *J. Phys. Chem. Sol.* **64**, 659 (2003).
[3] H. B. Brom *et al*, *Phil. Mag. B* **81**, 941 (2001).
[4] R. B. Laibowitz and Y. Gefen, *Phys. Rev. Lett.* **53**, 904 (1984).
[5] Yi Song *et al*, *Phys. Rev. B* **33**, 380 (1986).
[6] B. I. Shklovskii, *Fiz. Tech. Poluprov.* **7**, 112 (1973).
[7] I. L. Drichko *et al*, *JETP* **101**, 979 (2005).
[8] I. L. Drichko *et al*, *cond-mat*/0311267 (2003).
[9] I. P. Zvyagin and R. Keiper, *Phil. Mag. B* **81**, 997 (2001).
[10] I. P. Zvyagin, *Proc. 7th Int. Symp. "Nanostructures: Physics and Technology", St Petersburg, 14-18 June, 1999*, St Petersburg: Ioffe Inst., 1999, p. 287.
[11] I. P. Zvyagin, *phys.stat.sol. (c)* **3**, 300 (2006).
[12] A. L. Efros, *Phil. Mag. B* **43**, 829 (1981).
[13] N. F. Mott and E. A. Davis, *Electron Processes in Non-Crystalline Materials*, 2nd ed., Clarendon Press, Oxford, 1979.

14th Int. Symp. "Nanostructures: Physics and Technology"
St Petersburg, Russia, June 26–30, 2006

Fabrication and electron transport study of three-terminal InAs nanowire junctions

D. B. Suyatin[1], D. Wallin[1], L. E. Froberg[1], L. S. Karlsson[2], I. Maximov[1], L. R. Wallenberg[2], H. Q. Xu[1] and L. Samuelson[1]

[1] Division of Solid State Physics and The Nanometer Structure Consortium, Lund University, Box 118, S-221 00 Lund, Sweden
[2] Division of Materials Chemistry and The Nanometer Structure Consortium, Lund University, Box 124, S-221 00 Lund, Sweden

Abstract. Three-terminal junction devices have been realized with branched InAs nanowires and were characterized by electrical measurements. The branched nanowires are grown with Au nanoparticles as catalysts by chemical beam epitaxy and the electrical contacts to the nanowires are made with e-beam lithography. When the voltages are applied to the trunk contacts of the nanowire junctions in push-pull and push-fix fashions, the voltage measured in the branch shows novel, interesting down-bending characteristics. These nonlinear properties of the nanowire junctions have potential applications in the nanoelectronics.

Introduction

Epitaxially grown semiconductor nanowires are of great interest due to their well-defined crystalline structure and unique electrical and optical properties with numerous applications [1]. The growth techniques for semiconductor nanowires have been quickly advanced in recent years and it is now possible to grow high-quality nanowires with controlled diameter and length. It is also possible to dope the nanowires and to grow nanowire heterostructures [2–4]. Recently, growth of branched GaP, Si, and GaN nanowire structures was reported [5, 6]. In this work we report on growth of branched InAs nanowire structures by chemical beam epitaxy (CBE) and on studies of their electrical properties.

The branched nanowires were measured in a three-terminal junction configuration. Previously, three-terminal junctions were extensively studied in the ballistic transport regime [7–9]. These three-terminal ballistic junction (TBJ) devices were formed in a 2DEG made from a high-mobility semiconductor heterostructure using conventional top-down nanofabrication techniques. The 2DEG-based TBJ devices show highly nonlinear characteristics, which can be used for realization of a variety of novel devices [10, 11]. In this paper, we report the observation of similar nonlinear characteristics in the three-terminal nanowire junctions grown by CBE. By applying a back-gate voltage and varying the voltages applied to the nanowire junction contacts, we can also tune between linear and nonlinear characteristics of the three-terminal nanowire junction devices.

1. Fabrication and experiment

The three-terminal nanowire junctions were realized with Au nanoparticle-induced growth. First, InAs nanowire trunks were grown using Au aerosol particles as catalysts by CBE. Subsequently Au aerosol particles were deposited on the surfaces of InAs nanowire trunks and InAs nanowire branches were grown by CBE on the InAs trunks, resulting in branched InAs nanowires. The diameters of the nanowire trunks and branches used in present study were controlled by the Au nanoparticle size and were in the range of 50–100 nm. Figure 1(a) demonstrates a transmission electron microscopy (TEM) image of a typical nanowire junction. These branched nanowires were transferred to Si wafers capped with a 100 nm thick silicon oxide layer. Electrical contacts to individual branched nanowires were fabricated by e-beam lithography, metal evaporation and lift-off [4]. A scanning electron micrograph of an electrically contacted three-terminal nanowire junction and a schematic circuit layout for the electrical measurements are shown in Figure 1(b).

The fabricated three-terminal nanowire junction devices were characterized by I–V measurements between all the contacts. Voltage measurements in push-pull and push-fix manners on the three-terminal junctions were performed after the characterization in the same way as previously reported for 2DEG-based structures [9, 11]. In the push-pull measurements of a three-terminal nanowire junction, voltages in an anti-symmetric configuration, $V_L = -V_R$ [cf. Fig. 1(b)], are applied to the nanowire trunk, while the central branch is used as a voltage probe. In the push-fix measurements a voltage is applied to one of the two trunk electrodes, while keeping the other one grounded, and the voltage output from the central branch is measured. Both the push-pull and push-fix measurements were done for different voltages applied to the back side of the substrate (the back-gate). The electrical current through the trunk was monitored during the measurements. The measurements were performed both at room temperature and at 4.2 K.

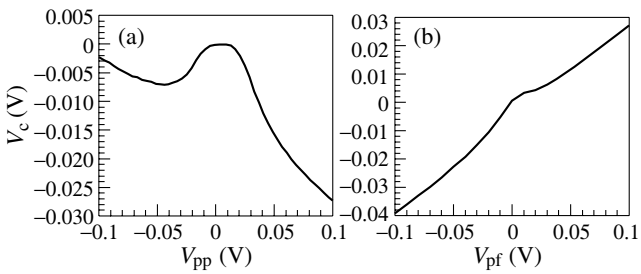

Fig. 1. (a) TEM micrograph of a typical three-terminal InAs nanowire junction with 70 nm branch diameter and 90 nm trunk diameter. Vertical lines on the micrograph correspond to stacking faults in nanowire crystalline structure. (b) SEM micrograph of a three-terminal InAs nanowire junction device with a schematic drawing of the circuit used for electrical measurements.

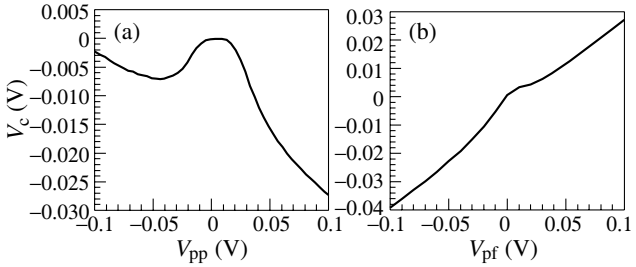

Fig. 2. Measured output voltage from the central branch, V_C, as a function of the voltage applied to the trunk of the nanowire junction in (a) the push-pull ($V_{pp} = V_L - V_R$, $V_L = -V_R$) and (b) the push-fix ($V_{pf} = V_L$, $V_R = 0$) configuration [cf. Fig. 1(b)]. The measurements were performed at 4.2 K for the back-gate voltage $V_{bg} = -3.6$ V.

2. Results and discussion

As can be seen from the TEM image [Fig. 1(a)], the CBE grown nanowire junction has a crystalline structure. The nanowire branch adopts crystalline structure from the wire trunk and the stacking faults formed during trunk growth develop into the nanowire branch. The TEM images analysis indicates that the InAs nanowires have wurtzite structure with occasions of thin cubic sections (the stacking faults). Nanowire trunks have the [000-1] growth direction, and the nanowire branches grow perpendicularly to the trunks in ⟨1120⟩ growth directions.

The I–V measurements between the two trunk contacts and between a trunk contact and the branch contact reveal similar ohmic behavior. Typical resistance between the contacts is in a range of 3–30 kΩ at room temperature. The measured back-gate dependence of the resistance implies that the charge carriers in the three-terminal nanowire junction are electrons (n-type).

The push-pull and push-fix measurements on three-terminal nanowire junctions show a complex behavior. Some of the results obtained at liquid helium temperature (4.2 K) are presented in Fig. 2. From the Fig. 2(a) one can see that at small push-pull voltages, the nanowire junction shows a down-bending parabola-like voltage output behavior. This behavior agrees well with the expected properties of a three-terminal ballistic junction with n-type carrier conduction [7]. At higher applied push-pull voltages one can see flattening of the parabola-like voltage output and a smooth transition to the region of a linear dependence of the output voltage on the applied voltage.

This linear dependence is characteristic of a junction with the electron transport in the diffusive regime. Figure 2(b) presents the measured push-fix results at the same measurement conditions. The results of the push-fix measurements also agree with the behavior expected for a three-terminal ballistic junction [8]. These results allow us to conclude that at small applied voltages between the junction contacts, the electron mean free path in the nanowires is comparable with the junction size (50–150 nm) at liquid helium temperature. This is in agreement with an independent estimation of the electron mean free path in InAs nanowires at low temperatures [12].

3. Conclusion

In this work we present fabrication and characterization of three-terminal junction devices made from branched InAs nanowire junctions. The branched nanowires were grown by CBE and the electrical measurements for the three-terminal nanowire junctions were performed in push-pull and push-fix configurations. It was shown that the three-terminal nanowire junctions show similar novel nonlinear characteristics as observed in 2DEG-based TBJ devices. These nanowire junctions can thus be used as new building blocks for novel nanoelectronic devices and circuits.

Acknowledgements

This work was supported by the Swedish Foundation for Strategic Research (SSF), the Swedish Research Council (VR), Knut and Alice Wallenberg Foundation, Office of Naval Research (ONR), and the European Commission through project NODE 015783.

References

[1] L. Samuelson, *Materials Today*, October issue, 22 (2003).
[2] M. T. Bjork *et al*, *Appl. Phys. Lett.* **80**, 1058 (2002).
[3] M. T. Bjork *et al*, *Appl. Phys. Lett.* **81**, 4458 (2002).
[4] C. Thelander *et al*, *Solid State Comm.* **131**, 5731 (2004).
[5] K. A. Dick *et al*, *Nature Materials* **3**, 380 (2004).
[6] D. Wang *et al*, *Nano Letters* **4**, 871 (2004).
[7] H. Q. Xu *et al*, *Appl. Phys. Lett.* **78**, 2064 (2001).
[8] H. Q. Xu *et al*, *Appl. Phys. Lett.* **80**, 853 (2002).
[9] I. Shorubalko *et al*, *Appl. Phys. Lett.* **79**, 1384 (2001).
[10] I. Shorubalko *et al*, *IEEE Electron Dev. Lett.* **23**, 377 (2002).
[11] H. Q. Xu *et al*, *IEEE Electron Dev. Lett.* **25**, 164 (2004).
[12] A. E. Hansen *et al*, *Phys. Rev. B* **71**, 205328 (2005).

14th Int. Symp. "Nanostructures: Physics and Technology"
St Petersburg, Russia, June 26–30, 2006

Suspended single-electron Coulomb blockade transistor

A. G. Pogosov[1], M. V. Budantsev[1], R. A. Lavrov[1], A. Ye. Plotnikov[1], A. K. Bakarov[1], A. I. Toropov[1] and J. C. Portal[2,3]

[1] Institute of Semiconductor Physics SB RAS, 630090 Novosibirsk, Russia
[2] Grenoble High Magnetic Fields Laboratory, CNRS/LCMI, BP-166, F-38042, Grenoble, Cedex 9, France
[3] INSA-Physique and Institut Universitaire de France, F-31077, Toulouse, Cedex 4, France

Abstract. Suspended single-electron Coulomb blockade transistor has been fabricated on the basis of two-dimensional electron gas in AlGaAs/GaAs membrane detached from the substrate. Dependence of the device conductance on the source-drain and gate voltages has a diamond structure specific for the Coulomb blockade. Detachment of the device from the substrate having high dielectric constant leads to essential decrease in the quantum dot capacitance C resulting in the high charging energy $E_c = e^2/C$ and critical temperature $T_c = E_c/k_B \approx 40$ K.

Introduction

Modern technology has made it possible to fabricate thin semiconductor layers detached from the substrate — *suspended membranes*. A large variety of such structures (wide membranes, narrow flat or corrugated wires, phonon cavities etc.), that can be called *phonon conductors*, opens large perspectives for studying unique kinetic phenomena. This was brilliantly demonstrated by Schwab *et al* [1] by measuring the quantum of thermal conductance theoretically predicted in [2]. Recent investigations of the conductance of a suspended quantum dot has shown that interaction between tunnelling electrons and localized phonons [3] essentially influences the Coulomb blockade effect. The mentioned paper demonstrates the suppression of Coulomb blockade peaks resulting from the so-called phonon blockade, when the process of electron tunnelling is accompanied by the emission of low-dimensional phonon that require an energy cost.

In the present work we report on the results of investigations of electronic transport through the quantum dot fabricated on the basis of a suspended membrane. Detachment of the quantum dot from the substrate, having high dielectric constant, led to essential decrease in the dot capacitance and as a result to high values of the charging energy.

1. Experimental

Experimental samples were fabricated from thin semiconductor layers — membranes detached from the substrate. The membranes were fabricated on the basis of heterostructure schematically presented in Fig. 1c. Two-dimensional electron gas (2DEG) in the GaAs quantum well is formed by electrons from Si δ-layers, inserted in the adjacent AlGaAs layers. Such heterostructure were grown on the thick AlAs sacrificial layer, which was then selectively etched. Lateral geometry of membranes was created by means of electron lithography followed by anisotropic etching of GaAs and AlAs layers. The obtained structure was then immersed into HF based etchant, selectively etching the sacrificial AlAs layer. As a result, an upper part of the structure containing the 2DEG was detached from the substrate. The width of the suspended membrane was 110 nm. Fig. 1a shows electron-phonon conductor with dimensions 5×5 μm^2 fabricated on the basis of such membrane. Electron density in the 2DEG measured at temperature 4.2 K from Shubnikov–de Haas oscillations was 5×10^{11} cm^{-2}. To study the Coulomb blockade effect, a quantum dot was fabricated in the suspended membrane. Electron micrograph of the experimental device is presented in Fig. 1b. Quantum dot was formed from a suspended wire of width 0.6 μm by two narrowings distant 0.6 μm from each other. Two suspended side gates were mounted 0.3 μm apart from the quantum dot

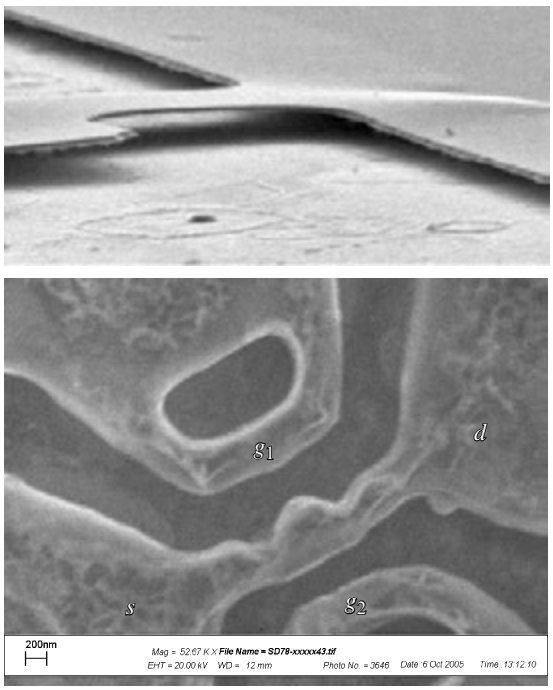

Fig. 1. (a) Electron micrograph of the suspended membrane. The picture was made at an angle of 5 DEG with electron beam normal to the surface, which enables to see the shadow under the membrane. (b) Electron micrograph of the device. One can see source s, drain d and two side-gates g_1 and g_2. (c) Schematic view of the heterostructure used.

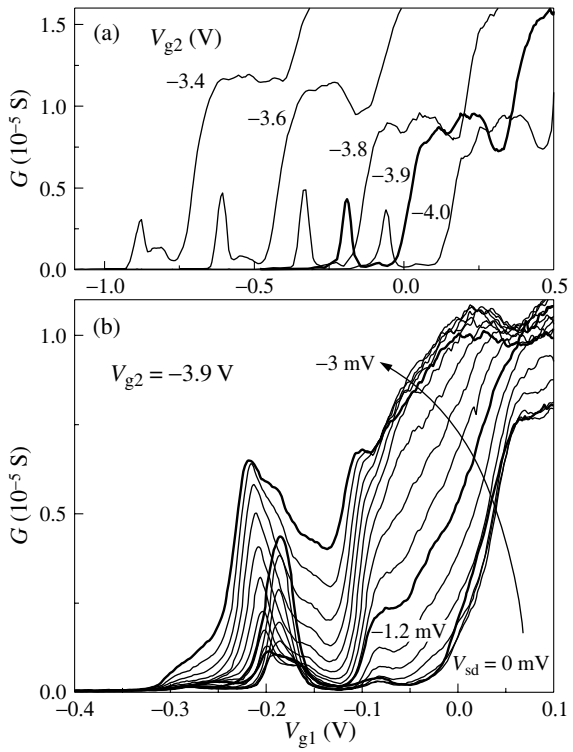

Fig. 2. (a) The set of conductance dependencies on the gate voltage V_{g1} at different voltages V_{g2}. (b) The set of conductance dependencies on the gate voltage V_{g1} measured at different source-drain voltages V_{sd} and fixed $V_{g2} = -3.9$ mV.

to operate its charge state. The measurements were performed at the temperature 60 mK.

Fig. 2a shows the set of quantum dot conductance dependencies measured by sweeping the gate voltage V_{g1} at different values of V_{g2}. One can see that at negative values of V_{g1} the conductance demonstrates an oscillating behavior, which is the most pronounced at $V_{g2} = -3.9$ V. In particular, the peak at $V_{g1} = -0.18$ V is observed against the practically zero background. In order to reveal the nature of the observed oscillations, the set of $G(V_{g1})$ dependencies were measured at different constant values of source-drain voltages V_{sd} (Fig. 2b). The figure shows that with the increase of absolute values of V_{sd} in the regions of V_{g1} corresponding to plateau (−0.12 V and −0.05 V) the conductance increases and the peak positions shift along the V_{g1}-axis. The variations of conductance as a function of V_{sd} and V_{g1} is presented in Fig. 3 as a grey-scale map. The figure shows that the dependence $G(V_{sd}, V_{g1})$ has a diamond structure specific for the Coulomb blockade [4,5]. The slope of lines defining the diamonds enables to determine the ratio of the capacitance of the left and right tunnel junctions to the capacitance between the quantum dot and the gate [4]. It gives for our case $C_l/C_{g1} \approx C_r/C_{g1} \approx 12$.

2. Discussion

An important feature of the measured conductance dependence $G(V_{sd}, V_{g1})$ is a large size of the diamonds $\Delta V_{sd} = 6$ mV, which means the large charging energy $E_c = e^2/C = \Delta V_{sd}/2$, where C is the full capacitance of the quantum dot, and as a result, high critical temperature for the Coulomb blockade effect $T_c = E_c/k_B \approx 40$ K. This result is caused mainly by the detachment of the quantum dot from the substrate having high

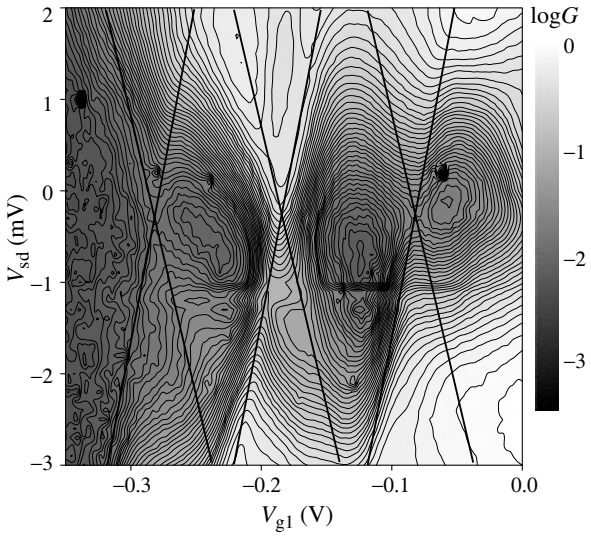

Fig. 3. The conductance dependence on the source-drain V_{sd} and the gate V_{g1} voltages at fixed $V_{g2} = -3.9$ mV.

dielectric constant. This decreases the dielectric constant of the quantum dot surrounding by more than the order of magnitude, and thus its total capacitance. This is also confirmed by the fact that the capacitance between quantum dot and gate electrodes separated by vacuum is much less than the capacitance of tunnel junctions. The total dot capacitance is thus determined by the tunnel junctions. Their capacitance, in turn, is small since the 2DEG is clamped in a narrow 10 nm well. Finally, small are the lateral dimensions of the quantum dot itself. This causes another feature of the suspended quantum dot obtained — it contains a few number of electrons (estimated as about 5). This explains a small number of Coulomb blockade peaks in the operating regions of V_{sd} and V_{g1}, as well as mesoscopic distortions of the diamond structure.

Acknowledgements

This work has been supported by RFBR (grant # 04-02-16894) and INTAS (grant # 03-55-6339).

References

[1] K. Schwab, E. A. Henriksen, J. M. Worlock and M. L. Roukes, *Nature* **404**, 974 (2000).
[2] L. G. Rego and G. Kirczenow, *Phys. Rev. Lett.* **81**, 232 (1998).
[3] E. M. Weig, R. H. Blick, T. Brandes, J. Kirschbaum, W. Wegscheider, M. Bichler and J. P. Kotthaus, *Phys. Rev. Lett.* **92**, 046804 (2004).
[4] J. Weis, R. J. Haug, K. von Klitzing and K. Ploog, Phys. Rev. B **46**, 12837 (1992).
[5] J. Weis, R. J. Haug, K. von Klitzing and K. Ploog, *Phys. Rev. B* **71**, 4019 (1993).

14th Int. Symp. "Nanostructures: Physics and Technology"
St Petersburg, Russia, June 26–30, 2006

Spin-wave based logic devices

A. Khitun, M. Bao, J.-Y. Lee, K. Galatsis and K. L. Wang

Device Research Laboratory, Electrical Engineering Department, MARCO Focus Center on Functional Engineered Nano Architectonics (FENA), University of California at Los Angeles, Los Angeles, California, 90095-1594, USA

Abstract. We present an experimental study and a theoretical analysis of logic circuits utilizing spin waves for information transmission and processing. As an alternative approach to the transistor-based architecture, logic circuits utilizing spin waves for information transmission and processing may be advantages in terms of power consumption and functional output. The most promising advantage is that information transmission is accomplished without a charge transfer. A prototype device structure with thin ferromagnetic film (spin wave bus) was used for experimental demonstration. An inductive voltage signal of the order of tens mV has been detected from a spin wave packet propagating in 100 nm thick CoFe film at room temperature. The issues related to the use of spin waves in logic circuits are discussed.

1. Introduction

There is an impetus for further development of logic devices for a new information and signal processing technology addressing "beyond CMOS" applications. Such new technology have to provide high information/signal processing rate and be scaleable beyond conventional CMOS. Recent breakthroughs in the experimental study and control of the spin dynamics in semiconductor nano structures [1–3] opens new possibilities for spin utilization in information processing.

In this work we analyze a novel type of logic circuits utilizing spin waves as a physical mechanism for information transmission. A propagating spin wave changes the local polarization of spins in ferromagnetic material. In turn, the change of the magnetic field in time results in the inductive voltage. According to the Faraday's law, the magnitude of the inductive voltage is proportional to the speed of the magnetic flux change $E_{\text{ind}} = -d\Phi/dt$. To comprehend the scale of this physical phenomenon, we would like to refer to the early experimental work accomplished by Covington *et al* [4]. An inductive voltage signal of the order of mV produced by spin waves propagating through a nanometer thin ferromagnetic film ($Ni_{81}Fe_{19}$) was clearly detected at the distances up to 50 microns at room temperature.

Our approach is to use the phase of the spin wave for information exchange and information processing. The key advantage of the proposed scheme is that information transmission is accomplished without charge transfer. Potentially, this approach may be beneficial in terms of power consumption. Besides, it may resolve the problem of interconnections and enhance architecture computing abilities. In the rest of the paper we describe the principle of operation and the material structure of the prototype logic device. Then, we present experimental data and discuss advantages and shortcoming inherent to spin-wave based devices.

2. Device structure and principle of operation

In Fig. 1 we have schematically shown the prototype logic device structure. The core of the structure consists of a ferromagnetic film (CoFe) deposited on a semiinsulating substrate (silicon). The film is entirely polarized along with the X axis (as shown in Fig. 1(a)). There are three asymmetric coplanar strip (ACPS) transmission lines on the top of the structure. The lines and the ferromagnetic layer are isolated by the silicon oxide layer. The thickness of the ferromagnetic layer is 100 nm, and the thickness of the oxide layer is 300 nm. The dimensions of the ACPS lines are adjusted to match 50 Ω of the external coaxial cable.

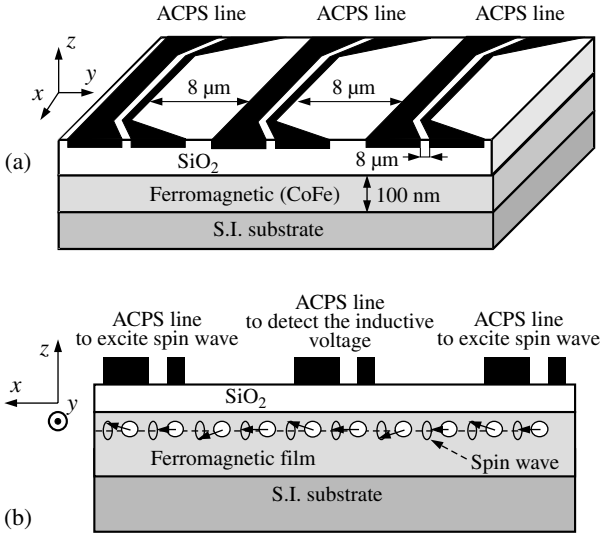

Fig. 1. (a) A prototype logic device. The ACPS lines and the ferromagnetic layer are isolated by the oxide layer. Each of the ACPS lines can be used for spin wave excitation and detection. (b) The cross-plane view of the proposed device.

Each of the ACPS lines can be used for spin wave excitation and detection. A voltage pulse applied to the ACPS line produces magnetic field perpendicular to the polarization of the ferromagnetic film, and, thus, generates a spin wave (spin wave packet). Being excited, spin wave propagates through the ferromagnetic film. As it reaches the nearest ACPS line, the amplitude and the phase of the spin wave is detected by the inductive voltage measurements. For example, the edge ACPS lines can be considered as the input ports, and the middle ACPS as the output port. The middle ACPS line detects the inductive voltage produced by the *superposition* of two waves. Depending on the relative phase of the spin waves, the amplitude of the inductive voltage may be enhanced (two waves are in phase) or decreased (two waves are out of phase) in comparison to the inductive voltage produced by a single spin wave. The relative phase is defined by the location of the ACPS lines and the time of spin wave excitation. It is convenient to code information

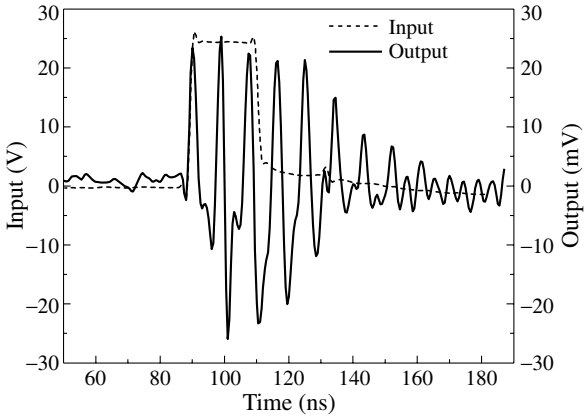

Fig. 2. Experimental data on spin wave detection from 100 nm thick CoFe film (room temperature).

into the phase of the spin wave by the selection of the time of excitation. As we will show below, it is possible to realize different logic gates AND, OR, and NOT controlling this *relative phase* of the spin waves.

In Fig. 2 we present experimental data on spin wave detection by the time-resolved inductive voltage measurement technique. The spin wave packet was excited by the edge ACPS line (pulse 24.5 V, rising time 1.2 ns, pulse length 20 ns). The output voltage signal was detected by the central ACPS line (maximum pulse 26 mV, period 9 ns).

The spin dynamics can be described using the Landau–Lifshitz–Gilbert equation as follows:

$$\frac{d\vec{m}}{dt} = -\frac{\gamma}{1+\alpha^2}\vec{m} \times \left[\vec{H}_{\text{eff}} + \alpha\vec{m} \times \vec{H}_{\text{eff}}\right], \qquad (1)$$

where $\vec{m} = \vec{M}/M_{\text{s}}$ is the unit magnetization vector, M_{s} is the saturation magnetization, γ is the gyro-magnetic ratio, and is the phenomenological Gilbert damping coefficient. We considered the combined effect of two spin wave packets superposition to demonstrate device logic functionality.

3. Conclusion

Potentially, the use of spin wave may be an efficient way for spin-based devices interconnection. The use of spin waves for information processing preserves all advantages of the phase logic. A set of logic gates can be realized in one module consisting of a number of devices united with spin wave bus. The further analysis of spin wave-based logic circuits is required.

Acknowledgement

The work was supported in part by the MARCO-FENA center (Dr. Simon Thomas).

References

[1] H. Ohno, *Science* **281** (5379), 951–6 (1998).
[2] D. Chiba *et al*, *J. Phys.-Cond. Matt.* **16** (48), S5693–6 (2004).
[3] Y. K. Kato *et al*, *Science* **306** (5703), 1910–13 (2004).
[4] M. Covington, T. M. Crawford and G. J. Parker, *Phys. Rev. Lett.* **89**(23), 237202-1–4 (2002).

14th Int. Symp. "Nanostructures: Physics and Technology"
St Petersburg, Russia, June 26–30, 2006

Unipolar optoelectronics using group III-nitride quantum wells and quantum dots

M. Tchernycheva[1,2], L. Nevou[1], L. Doyennette[1], F. H. Julien[1], A. Lupu[1], E. Warde[1], F. Guillot[3], E. Monroy[3], A.Vardi[4] and G. Bahir[4]

[1] Action OptoGaN, Institut d'Electronique Fondamentale, Universite Paris-Sud, UMR 8622 CNRS, 91405 Orsay Cedex, France
[2] CNRS-LPN, Route de Nozay, 91460 Marcoussis, France
[3] Equipe Mixte CEA-CNRS-UJF Nanophysique et Semiconducteurs, DRFMC/SP2M/PSC, CEA Grenoble, 17 rue des Martyrs, 38054 Grenoble Cedex 9, France
[4] Department of Electrical Engineering, Technion-Israel Institute of Technology, Haifa 32000 Israel

Abstract. We present the latest achievements in molecular beam epitaxial growth of ultrathin single and coupled GaN/AlN quantum wells for unipolar devices. State-of-the-art narrow Lorentzian-shaped intersubband absorptions are demonstrated. We provide the first evidence of strong electron state coupling between two GaN wells separated by an ultrathin 2 monolayer AlN barrier. The latter structures are the building blocks for modulators as well as quantum fountain and cascade lasers. Finally, we demonstrate the first GaN/AlN quantum dot photodetector based on intraband absorption and in-plane carrier transport which operates at room temperature in the wavelength range 1.3–1.5 μm.

Introduction

III-nitride heterostructures in the form of quantum wells (QWs) or quantum dots (QDs) are excellent candidates for high-speed intersubband (ISB) optical devices operating at fibre-optics telecommunication wavelengths thanks to their large conduction band offset ($\sim$ 1.7 eV for GaN/AlN). Room temperature ISB absorptions in the near-infrared wavelength range have been reported by several groups in highly doped GaN/Al(Ga)N or GaN/AlInN quantum wells grown by molecular beam epitaxy [1] or metal organic chemical vapor deposition [2] and in GaN/AlN quantum dots [3]. The ISB absorption recovery time has been measured to be as fast as 140–400 fs [4], which is significantly shorter than the corresponding time in GaAs QWs. This offers prospects for the development of ISB devices such as optical switches operating at Tbit/sec data rate. Due to rather large electron effective mass of GaN (3 times that of GaAs) and to the short target wavelengths, layers as thin as 4–6 monolayers (1 ML = 0.26 nm) are required to achieve ISB absorptions at 1.3–1.55 μm. A great effort should therefore be devoted to improve the material quality and to control the QW thickness and roughness down to 1 ML.

In this talk, we present the latest achievements in terms of growth and optical investigation of ultrathin single and coupled GaN/AlN QWs by plasma-assisted molecular beam epitaxy [6,5]. These structures form the buiding blocks of optoelectronic unipolar devices such as quantum well infrared photodetectors, electro-optical modulators, fontain and cascade lasers. We also present the first demonstration of GaN/AlN quantum dot photodetector operating at 1.3–1.5 μm wavelengths at room temperature [7,8].

1. Intersubband transitions of GaN/AlN multiple quantum wells

We first present a systematic experimental and theoretical investigation of ISB transitions of GaN/AlN multiple quantum wells with well thicknesses ranging from 4 to 10 ML [6]. The hexagonal phase quantum wells are grown on top of AlN/sapphire templates. By means of Fourier-transform infrared spectroscopy, intense ISB absorptions are observed in the wavelength range of 1.33–1.91 μm (Fig. 1 left). The full width at half maximum can be as small as 40 meV (cf. Fig. 1 right), which establishes a new state-of-the-art for nitride epitaxial growth. Depending on samples, the ISB spectrum shows either one peak or multiple peaks. One remarkable result is that each ISB absorption peak exhibits a homogeneous broadening and is perfectly fitted with a Lorentzian lineshape. We demonstrate that each peak corresponds to the ISB absorption of QW regions with a thickness equal to an integer number of ML.

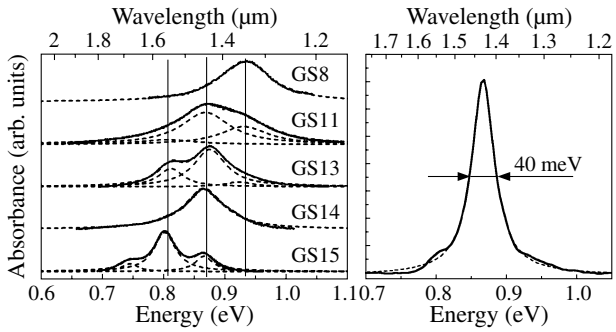

Fig. 1. Left — absorbance spectra of multiple QW samples (full lines) with corresponding multi-Lorentzian fit (dashed lines), vertical lines mark the mean energies of structures. The curves are vertically shifted for clarity. Right — absorbance spectrum showing recordly small broadening of 40 meV (full line) and the corresponding Lorentzian fit (dashed line).

The electron quantum confinement is modeled within the envelope function approximation taking into account the conduction band non-parabolicity. The doping-related effects are included via the self-consistent solution of the Schrödinger–Poisson equations with the subsequent application of the many-body corrections. The comparison of simulation and experimental results of both the ISB absorption energy and the photoluminescence energy allows to determine the polarization discontinuity at the heterointerfaces and to revise the value of the conduction band offset at the GaN/AlN interfaces, found to be 1.7 $\pm$ 0.05 eV, which is significantly smaller than the previously admitted value of 2 eV.

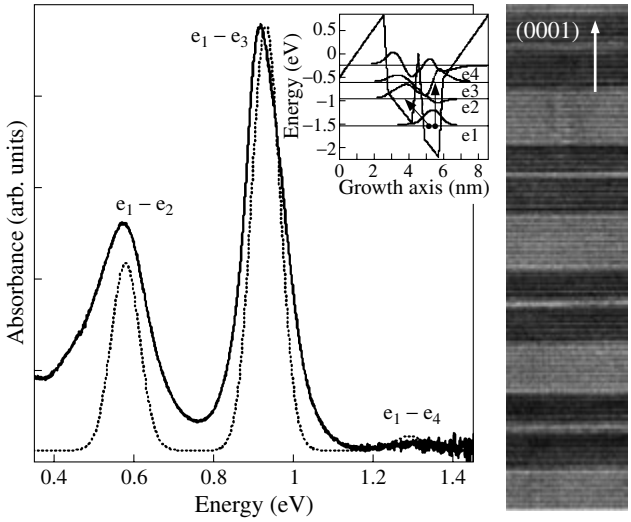

Fig. 2. Left — measured (full line) and calculated (dashed line) absorbance spectrum of coupled QW sample considering potential drop spread over 1 ML. Inset — CB profile and the corresponding electronic levels. Right — high-resolution TEM image of coupled QWs. The growth axis is directed upwards. Dark (bright) regions correspond to GaN (AlN).

2. Strong electronic coupling of GaN/AlN quantum wells

The correct description of the electronic structure of coupled QWs in presence of the internal electric field is of particular importance for the design of various unipolar devices. In the second part of the talk, we report the first observation and modeling of strong electron coupling between two GaN wells separated by 2-ML-thick AlN barrier [5].

The electron confinement in coupled QWs has been investigated by means of structural and optical measurements. The transmission electron microscopy analyses reveal sharp interfaces and the control of layer thickness down to 1 ML (Fig. 2 right). The strong coupling between the wells is evidenced by the observation of two pronounced ISB absorptions attributed respectively to the transitions between the ground states of the two coupled wells $e_1 - e_2$ and between the ground state and the excited state delocalized between the two wells $e_1 - e_3$. An excellent agreement with simulation is obtained for all investigated samples, when considering the potential drop at the GaN/AlN heterointerfaces spread over 1 ML (Fig. 2 left). This result is a direct demonstration of the effect predicted by Bernardini *et al* using *ab initio* calculations [9] that the band discontinuity between GaN and AlN builds up on the scale of 1 ML.

3. GaN/AlN quantum dot infrared photodetector

Finally, we report the first demonstration of the GaN/AlN QD photodetector based on intraband absorption and in-plane carrier transport via the wetting layer [7,8]. The device operates at low temperature and room temperature in the wavelength range 1.3–1.5 μm. The sample consists of 20 periods of Si-doped GaN QD layers separated by 3-nm thick AlN barriers [3]. Self-organized dots are formed by the deposition of 4 monolayers of GaN under nitrogen rich conditions, following the Stranski–Krastanow growth mode (dot height is 1.2 ± 0.6 nm). The sample presents p-polarized absorption peaked at 1.47 μm, which is attributed to the intraband transition between the ground

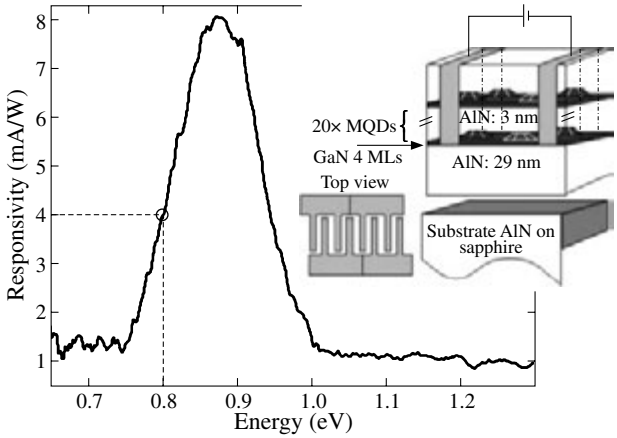

Fig. 3. Spectral detector response at room temperature with bias of 10 V. Inset — a segment of sample structure and photodetector schematic cross section.

s state and the excited p_z state of the QDs.

The device structure is schematically presented in the inset to Fig. 3: two interdigitated Ti/Al/Ti/Au contacts are fabricated using photolithography and dry etching through the active structure. The photocurrent (PC) measured at room temperature under 10 V bias is peaked at 1.41 μm, i.e. slightly blue-shifted with respect to the intraband absorption. As seen from Fig. 3 presenting the responsivity versus energy, it reaches 8 mA/W at 300 K.

We have observed an increase of the PC with temperature, which can be explained as follows. The p_z confined state in the dots has lower energy than the wetting layer ground state. The electron transfer to the wetting layer is therefore activated via phonon absorption, which becomes more efficient at higher temperature.

Acknowledgement

The authors acknowledge the support by STREP contract NITWAVE (♯ 004170) within the 6th European Framework Program.

References

[1] A. Helman *et al*, *Appl. Phys. Lett.* **83**, 5196 (2003).
[2] S. Nicolay *et al*, *Appl. Phys. Lett.* **87**, 111106 (2005).
[3] M. Tchernycheva *et al*, *Appl. Phys. Lett.* **87**, 101912 (2005).
[4] N. Iizuka *et al*, *Appl. Phys. Lett.* **81**, 1803 (2002).
[5] M. Tchernycheva *et al*, to appear in *Phys. Rev. B* (2006).
[6] M. Tchernycheva *et al*, to appear in *Appl. Phys. Lett.* (2006).
[7] L. Doyennette *et al*, *Electronics Lett.* **41**, 1077 (2005).
[8] A. Vardi *et al*, to appear in *Appl. Phys. Lett.* (2006).
[9] F. Bernardini *et al*, *Phys. Rev. B* **57**, R9427 (1998).

14th Int. Symp. "Nanostructures: Physics and Technology"
St Petersburg, Russia, June 26–30, 2006

Single-electron transistor based on highly doped silicon-on-insulator

V. A. Krupenin[1], D. E. Presnov[2], *V. S. Vlasenko*[1], N. N. Afanasiev[1] and D. N. Erkhov[1]

[1] Laboratory of Cryoelectronics, Moscow State University, 119899 Moscow, Russia
[2] Nuclear Physics Institute, Moscow State University, 119899 Moscow, Russia

Abstract. In this work we introduce the fabrication method and the characterization of SOI based SET transistor structures that demonstrate classical behavior: changes between Coulomb blockade and fully conductive states and periodical modulation of transport current driven by the gate voltage. The e-beam lithography followed with the reactive ion etching (RIE) was used to form the transistor structure. We have studied the physical properties of the SET transistors at room, liquid nitrogen (77 K) and liquid helium (4.2 K) temperatures and their perspectives as field/charge sensors in scanning probe microscopes.

Introduction

The single-electron transistor is one of the most important elements in the fast-developing nano-electronics for such devices as sensitive charge detectors, logic circuits, memory, electron pumps, etc. It consists of the small conductive island, separated from source and drain electrodes by two tunnel junctions and connected with the gate electrode through non-tunnel capacitance. The operation of this device is based on Coulomb blockade effect. Single-electron transistors have been demonstrated in numerous experiments using a wide variety of device geometries, materials, and techniques. We have developed and studied SOI based SET transistor structures that demonstrate classical behavior: changes between Coulomb blockade and fully conductive states and periodical modulation of transport current controlled by the gate electrode voltage. This type of SET transistor can be used as ultra-sensitive electrometer and has several advantages compared with other types of SET devices [1–3]: simpler fabrication technology, mechanical solidity, higher stability to overvoltage, higher operating temperatures at the same sizes of structure elements, the opportunity to manufacture suspended units. The advantages of SOI based SET transistors and methods of their fabrication enable quite convenient installation of the device on a cantilever tip of scanning probe microscope.

1. Samples fabrication

The experimental structures were fabricated from preliminary prepared highly doped silicon-on insulator film. The doping level was about 10^{20} cm^{-3}. We used SOI material with 55 nm thick silicon layer and 150 nm insulating SiO_2 layer placed on a silicon substrate. The fabrication method for the SET structures includes the following stages:

- ion implantation of SOI film with a control of a disturbance of Si lattice by X-ray reflectometry;
- recrystallization annealing of SOI film at 950 °C;
- e-beam lithography for the structure patterning;
- forming a metal mask by the evaporation of Al thin film;
- forming nanostructures by the reactive-ion etching of SOI film through the formed metal mask;
- reactive ion etching process of Si in CF_4 for downsizing the structure and final adjustment of the transistor parameters.

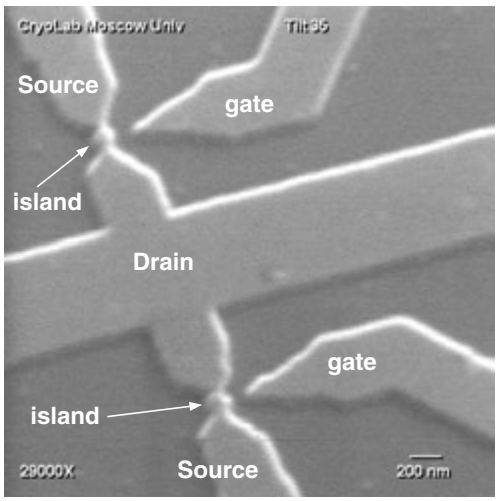

Fig. 1. Layout of typical SET transistor structures (SEM image).

We controlled the process of junction formation with the offset voltage ($V_{\rm off}$) measurements on the transistor IV-characteristics at 77 K. A typical layout of SET transistor structures on the chip is shown on Fig. 1. Scanning Electron Microscope (SEM) and an Atomic Force Microscope (AFM) were used for the structure characterization. Some structures were prepared with 4 contact electrodes in order to measure and eliminate their resistance from the structure impedance.

2. Results

Fabricated structures were characterized at 300, 77 and 4.2 K and were studied in details at 4.2 K temperature.

We have closely observed the modulation of IV-characteristics of the SET transistor structures caused by changing voltage on the gate electrode (Fig. 2). The IV-curves shape and their behavior versus gate voltage were close to those of classical Al/AlO_x SET transistors. SOI based SET transistor demonstrated blockade and completely conductive states at $V < V_{\rm off}$ and depending on the applied gate voltage. The modulation curves of the transistor demonstrate predictable current oscillations depending on the bias voltage (Fig. 3). The value of gate capacitance ($C_{\rm g}$) obtained from these data was estimated to be about 0.03 aF. The charging energy ($E_{\rm C}$) for the presented sample (Fig. 1) is more than 100 K in temperature units. It was estimated from the offset voltage ($V_{\rm off}$), which values vary from 10 to 12 mV. The noise characteristics of the investi-

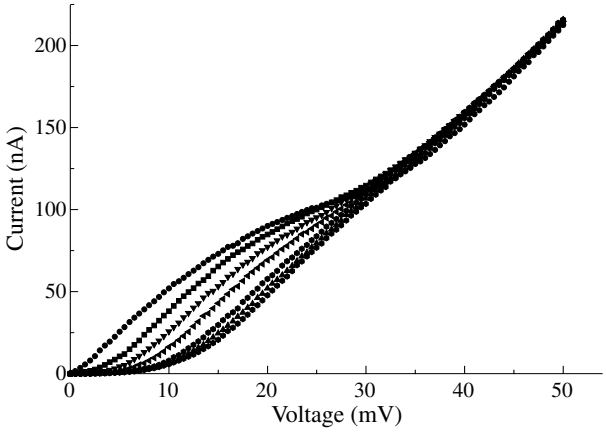

Fig. 2. IV-characteristics of SET transistor at 4.2 K.

gated structure were similar to other types of the SET transistor. Measured values of charge noise at frequency $f = 10$ Hz were in the range of $10^3 - 10^4$ e/Hz$^{1/2}$.

Noise figures were measured on the slopes of IV$_g$-characteristics (Fig. 3) that are less noisy ($V_g = 4 - 5$ V). Probably the suspended structures could solve the problem of excess charge noise for SOI based SET devices [4]. This work also involves elaboration of a transistor that can be formed on a cantilever tip of the scanning device. The main advantage of SOI based SET transistor as compared to others is the fact that the transistor can be easier fabricated close to a cantilever tip.

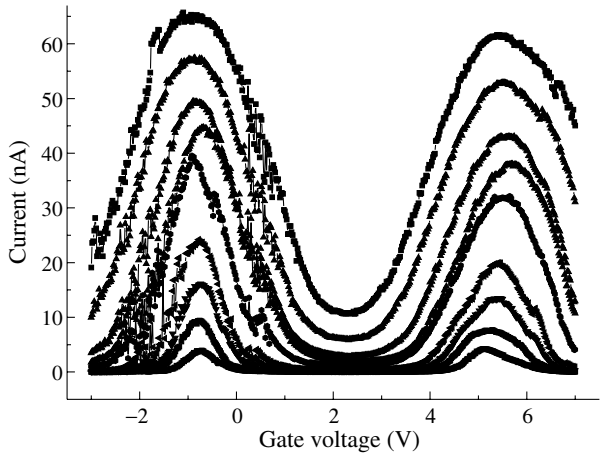

Fig. 3. Modulation curves of SET transistor at 4.2 K.

3. Results

SOI SET transistor discussed above shows the capability to alternate the classical Al/AlO$_x$ SET electrometer used as readout device in precision field/charge measurements. Simpler fabrication method compared to the Al/AlO$_x$ SET devices is also a great advantage. The linear sizes of such devices could be decreased to the dozens of nanometers so their operation temperature could be higher. And unique properties of the SOI material give us an opportunity to decrease the background charge noise of the device using the suspended structure. Further investigations are in progress to optimize the parameters of such transistors and their fabrication cycle.

Acknowledgements

The authors would like to thank M. Kupriyanov for the usefull discussions. This work was supported by the Russian Foundation for Basic Research.

References

[1] X. Jehl, M. Sanquer, G. Bertrand, G. Guegan, S. Deleonibus, D. Fraboulet, *IEEE Trans. Nano.* **2**, 308 (2003).

[2] S. H. Son, K. H. Cho, S. W. Hwang, K. M. Kim, Y. J. Park, Y. S. Yu, D. Ahn, *J. Appl. Phys.* **96**, 704 (2004).

[3] T. Kitade, K. Ohkura, A. Nakajima *et al*, *Appl. Phys. Lett.* **86**, 3118 (2005).

[4] V. A. Krupenin, D. E. Presnov, A. B. Zorin and J. Niemeyer *J. Low Temp. Phys.* **118**, 287 (2000).

14th Int. Symp. "Nanostructures: Physics and Technology"
St Petersburg, Russia, June 26–30, 2006

Dependency microscopic morphological compensation for phase-separated composite film

Chia-Fu Chang, Yi-Ci Chan and Zou-ni Wan
Kun Shan University of Technology 661, duan 1, Jhong Shan Rd, Yilan City, 260, Taiwan (R.O.C)

Abstract. The generic structure of our bimesogens is shown in and for a typical blue-phase mixture of the type we describe here we use mixtures of the ratio 33.4% ($n = 2.6$), 34.1% ($n = 6.57$), 36.6% ($n = 11.15$) with of the high twisted power (HTP) agent BD H1381 (available from Merck Chemicals and described in ref. We then studied the electric-field dependency of the selective reflection in BP I* at 20.7 °C by applying increasing and the decreasing pulsed alternating current (a.c.) electric fields (100 Hz).

1. Introduction

Solar Sailcraft, the stuff of dreams of the H. G. Wells generation, is now a rapidly maturing reality. The promise of unlimited propulsive power by harnessing stellar radiation is close to realization. Currently, efforts are underway to build, prototype and test two configurations [1]. These sails are designed to meet a 20 m sail requirement, under guidance of the In-Space Propulsion (ISP) technology program office at MSFC. While these sails will not fly, they are the first steps in improving our understanding of the processes and phenomena at work. As part of the New Millennium Program (NMP) the ST9 technology validation mission hopes to launch and fly a solar sail by 2010 or sooner. Though the Solar Sail community has been studying and validating various concepts over two decades [2], it was not until recent breakthroughs in structural and material technology, has made possible to build sails that could be launched.

2. Full-size camera-ready copy

Future NASA missions will require the collection of an increasing quantity and quality of data which, in turn, will place increasing demands on advanced sensors and advanced high bandwidth telemetry and communications-systems [3]. The capabilities of communication and telemetry systems depend, among other factors, on the stability, controllability and spectral purity of the carrier wave [4]. These, in turn, depend on the quality of the oscillator, or resonator, or the Q of the system [5]. Recent work on high Q optical resonators has indicated that the Q, or quality factor, of optical microsphere resonators can be substantially enhanced by coupling several such resonators together [1–3]. In addition to the possibility of enhanced Q and increased energy storage capacity, coupled optical resonators wide variety of interesting and potentially useful phenomena such as induced transparency and interactive mode splitting can be observed depending critically on the morphology and configuration of the microresonators Fig. 1. The purpose of this SFFP has been to examine several different coupled electromagnetic oscillator configurations in order to evaluate their potential for enhanced electromagnetic communications.Implications for flux-line lattices in high temperature superconductors are briefly discussed [6].

The irreducible decomposition technique is applied to the study of classical models of metric-affine gravity (MAG). The dynamics of the gravitational field is described by a 12-parameter Lagrangian encompassing a Hilbert–Einstein term, torsion and nonmetricity square terms, and one quadratic curvature

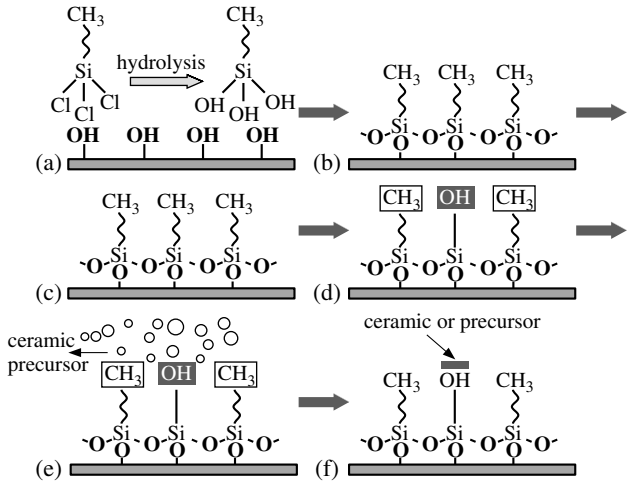

Fig. 1. Two substrates facing each other for a liquid crystal display device comprising. (a) Hydrolysis of OTS plane. (b) Self-assembly of SAMs. (c) Selective photocleavage. (d) Immersing. (e) Patterning through self assembly. (f) Pattern of ceramic oxides.

piece that is built up from Weyl's segmental curvature. Matter is represented by a hyperfluid, a continuous medium the elements of which possess classical momentum and hypermomentum e.g. [1] elp of irreducible decompositions, we are able to express torsion and traceless nonmetricity explicitly in terms of the spin and the shear current of the hyperfluid. Thereby the field equations reduce to an effective Einstein theory describing a metric coupled to the Weyl 1-form (a Procatype vector field) and to a spin fluid [7]. The service area extends over a million square kilometers. Much of that area is covered by rain forests. Thus knowledge of lightning strike characteristics over the expanse is of particular value. I have been developing a process that determines the DE over the region [8]. In turn, this provides a way to produce lightning strike density maps, corrected for DE, over the entire region of interest. This report offers a survey of that development to date and a record of present activity [9].

We propose a phenomenological equation to describe kinetic roughening of a growing surface in the presence of long range interactions. The roughness of the evolving surface depends on the long range feature, and several distinct scenarios of phase transitions are possible [10]. Experimental implications are discussed. Percolation theory deals with the formation of clusters in disordered media. At the percolation threshold for the first time an infinite cluster appears. However, research of the last years showed that at this phase transition some old ideas

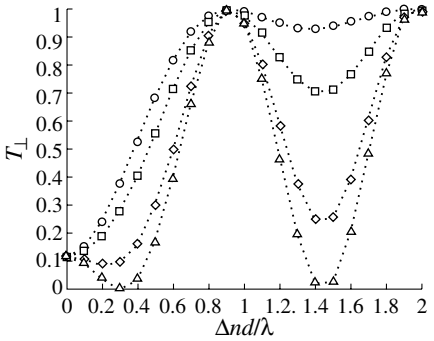

Fig. 2. The calculated values of $\Delta nd/\lambda$ and twist angle of $\phi = 70^\circ$, $\beta = 0, 15, 30, 45^\circ$.

were wrong: there can also be two or three clusters spanning from top to bottom, even in large two-dimensional lattices; and the probability of spanning is not given by simple real-space renormalization ideas.

In a Monte-Carlo study of the cluster-cluster correlations in random percolation, we find that the correlations scale with respect to the system size for any given ratio of the cluster radii at the percolation threshold ($p(c)$). With increasing cluster sizes, however, the peak of the correlation function appears to increase in height [11]. We also compare the nature of the correlations above and below $p(c)$ *Equations*.

The dynamics of the gravitational field is described by a 12-parameter Lagrangian encompassing a Hilbert–Einstein term, torsion and nonmetricity square terms, and one quadratic curvature piece that is built up from Weyl's segmental curvature. Matter is represented by a hyperfluid, a continuous medium the elements of which possess classical momentum and hypermomentum.

$$|R_\perp|^2 = |\cos\beta \sin\beta| \begin{vmatrix} \cos x - i\left(\frac{\Gamma}{2}\cdot\frac{\sin x}{x}\right) & -\phi\cdot\left(\frac{\sin x}{x}\right) \\ \phi\cdot\left(\frac{\sin x}{x}\right) & \cos x + i\left(\frac{\Gamma}{2}\cdot\frac{\sin x}{x}\right) \end{vmatrix} \times \begin{vmatrix} \cos x - i\left(\frac{\Gamma}{2}\cdot\frac{\sin x}{x}\right) & \left(\phi\cdot\frac{\sin x}{x}\right) \\ -\left(\phi\cdot\frac{\sin x}{x}\right) & \cos x + i\left(\frac{\Gamma}{2}\cdot\frac{\sin x}{x}\right) \end{vmatrix} \begin{vmatrix} -\sin\beta \\ \cos\beta \end{vmatrix}$$

A new method is introduced in order to derive displacement fields with divergence-free stress tensors [12]. Based on this method, we present an algorithm for fitting the solutions to different boundary conditions. We apply this algorithm to Volterra's edge dislocation Figure 2. We calculate the corresponding new displacement fields and the related strain and stress tensors corresponding to a crystal and a tubular cylinder. We plot the computed fringe patterns expected by the photoelasticity method. Optimum ground states are constructed in two dimensions by using so called vertex state models [13]. These models are graphical generalizations of the well-known matrix product ground states for spin chains. On the hexagonal lattice we obtain a one-parametric set of ground states for a five-dimensional manifold of $S = 3/2$ Hamiltonians.

The structure of the local density of states (DOS) in the vicinity of the impurity is significantly enhanced and therefore improves the possibility for observing the characteristic anistropic spatial modulation of the local DOS in a $d(x2-y2)$ superconductor by scanning tunneling microscopy Figure 2. Magnetic Raman scattering from a frustrated spin-1/2 Heisenberg chain is considered with a focus on the uniform phase of the spin-Peierls compound $CuGeO_3$. The Raman intensity is analyzed in terms of a Loudon–Fleury scattering process

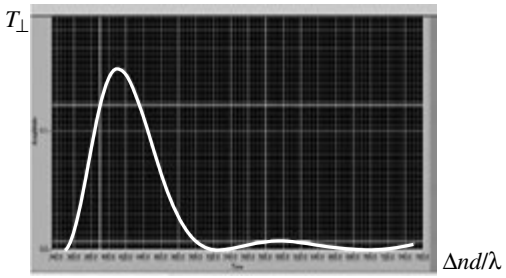

Fig. 3. The calculated values of $\Delta nd/\lambda$ and twist angle.

using a spinless-fermion mean-field theory developed for the frustrated spin chain. A comparison to experimental data is presented and the frustration and temperature dependence is studied. In good agreement with observed spectra a broad inelastic four-spinon continuum is found at low temperatures above the spin-Peierls transition.

3. Conclusion

Thereby the field equations reduce to an effective Einstein theory describing a metric coupled to the Weyl 1-form (a Proca-type vector field) and to a spin fluid. The purpose of this SFFP has been to examine several different coupled electromagnetic oscillator configurations in order to evaluate their potential for enhanced electromagnetic communications. Implications for flux-line lattices in high temperature superconductors are briefly discussed. The irreducible decomposition technique is applied to the study of classical models of metric-affine gravity (MAG). The dynamics of the gravitational field is described by a 12-parameter Lagrangian encompassing a Hilbert–Einstein term, torsion and nonmetricity square terms, and one quadratic curvature piece that is built up from Weyl's segmental curvature. Matter is represented by a hyperfluid, a continuous medium the elements of which possess classical momentum and hypermomentum. With the help of irreducible decompositions, we are able to express torsion and traceless nonmetricity explicitly in terms of the spin and the shear current of the hyperfluid.

References

[1] A. Dyadyusha, *Mol. Cryst. Liq. Cryst.* **321**, 271–281 (1998).
[2] Zongkai Wang, *Jpn. J. Appl. Phys.* **33**, L1242–L1244 (1994).
[3] Chiung-ShengWu, *Jpn. J. Appl. Phys.* **37**, L1497–L1500 (1998).
[4] Ruipeng Sun, *Jpn. J. Appl. Phys.* **33**, L1242–L1244 (1994).
[5] Hiap Liew Ong, P.O. Box 218, Yorktown Heights, New York 10598.
[6] G. V. Simonenko and V. G. Chigrinov, *Opticheskil Zhurnal* **69**, 65–70.
[7] Ecological Technology Development Center Corporate research.
[8] J. X. Guo and H. S. Kwok, Nanyang Avenue, Singapore 639798.
[9] Hiap Liew Ong, P.O. Box 218, Yorktown Heights, New York 10598.
[10] IEEE transactions on electron devices.
[11] E. Yablonovitch, T. J. Gmitter, *Phys. Rev. Lett.* **67**, 3380 (1991).
[12] A. Z. Genack, *Opt. Lett.* **23**, 1707 (1998).
[13] T. M. Swager, K. Ishikawa, H. Takezoe, *J. Appl. Phys.* **94**, 279 (2003).

14th Int. Symp. "Nanostructures: Physics and Technology"
St Petersburg, Russia, June 26–30, 2006

Multiple and single measurements of a mesoscopic quantum system with two permitted states

A. A. Burlakov, V. L. Gurtovoi, *S. V. Dubonos*, A. V. Nikulov and V. A. Tulin
Institute of Microelectronics Technology, Russian Academy of Sciences,
142432 Chernogolovka, Moscow region, Russia

Abstract. Mesoscopic loop is proposed in many works as possible solid-state quantum bit, i.e. two-state quantum system. The quantum oscillations of resistance and of rectified voltage observed on asymmetric superconducting loops give evidence of the two states at magnetic flux divisible by half of the flux quantum. But our measurements of quantum oscillations of the critical current of these loops have given results coming into irreconcilable contradictions with result of the observations of the quantum oscillations of resistance.

Introduction

One of the most intriguing problems of mesoscopic physics is possibility of quantum superposition of macroscopic states. It is especially urgent because of the aspiration for realization of the idea of the quantum computation [1]. Ambiguous experiments [2] can not be considered as an evidence of the macroscopic quantum superposition and possibility of solid-state qubit because of the obvious contradiction between quantum mechanics and macroscopic realism [3]. Quantum superposition presupposes that single measurement should give result corresponding to one of the permitted states whereas multiple measurement should give a result corresponding to an average value. We present experimental results corresponding such measurements.

1. Superconducting loop as possible quantum bit

Superconducting loop interrupted by one or several Josephson junctions is proposed in many publications [4] as possible quantum bit, i.e. a two-state quantum system which can be used as main element of quantum computer. This proposal is based on the assumption on two permitted state in such loop with half quantum $\Phi_0 = \pi\hbar/e$ of magnetic flux $\Phi = (n + 0.5)\Phi_0$. The authors [4] do not doubt that the two states exist and any observation will find a value corresponding to one of them. But nobody must be sure of anything in the quantum world till unambiguous experimental evidence. A. Einstein, B. Podolsky and N. Rosen were sure [5] that a process of measurement carried out on a one system can not affect other system in any way. But experimental results [6] have shown that it can and this phenomenon is called now Einstein–Podolsky–Rosen correlation.

The numerous observation of the Little–Parks oscillations [7] of resistance $\Delta R(\Phi/\Phi_0)$ of superconducting loop [8] prove quantization of velocity circulation $\oint_l dlv = (2\pi\hbar/m)(n - \Phi/\Phi_0)$ of superconducting pairs and that the permitted state with minimum energy has overwhelming probability even at $T \approx T_c$. The maximum $\Delta R(\Phi/\Phi_0) \propto \overline{v^2}$ [9] and zero value of the rectified voltage, corresponding to the average velocity $V_{dc}(\Phi/\Phi_0) \propto \overline{v}$ [10], observed at $\Phi = (n + 0.5)\Phi_0$ may be considered as an experimental evidence of two permitted states with the same minimum energy $\propto v^2 \propto (n - \Phi/\Phi_0)^2 = (1/2)^2$ and $(-1/2)^2$: $\overline{v^2} \propto (1/2)^2 + (-1/2)^2 = 1/2$ whereas $\overline{v} \propto (1/2) + (-1/2) = 0$. But it is needed to verify that a single measurement gives a result corresponding $v \propto 1/2$ or $v \propto -1/2$ state.

2. Multiple and single measurements of the persistent current

The measurement of the critical current of an asymmetric superconducting loop, Fig. 1, can be used for this verification. The current density equal $j_n = I_{\rm ext}/(s_n + s_w) \pm I_p/s_n$, $j_w = I_{\rm ext}/(s_n + s_w) \mp I_p/s_w$ in the loop halves because of the velocity quantization should mount the critical value, $j_n = j_c$ or $j_w = j_c$, at the external current I_{c+}, $I_{c-} = |I_{\rm ext}| = j_c(s_n + s_w) - |I_p|(s_n + s_w)/s_n$ or I_{c+}, $I_{c-} = |I_{\rm ext}| = j_c(s_n+s_w)-|I_p|(s_n+s_w)/s_w$ depending on the directions of the external current $I_{\rm ext}$ and the persistent current $I_p = 2en_s v =$

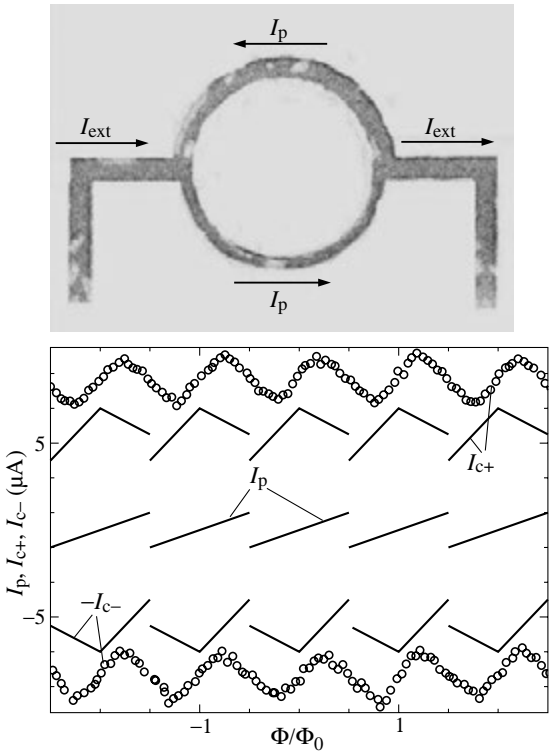

Fig. 1. Photo of the asymmetric Al round loop (ring) with semi-ring width $w_n = 200$ nm, $w_w = 400$ nm and magnetic dependencies of the critical current I_{c+}, I_{c-} expected be observed on such ring at $I_p = 2\ \mu$A $(n - \Phi/\Phi_0)$ and $j_c(s_n + s_w) = 7\ \mu$A. The experimental dependencies $I_{c+}(\Phi/\Phi_0)$, $I_{c-}(\Phi/\Phi_0)$ measured on this ring at $T = 1.225\ \text{K} = 0.99T_c$ are shown also.

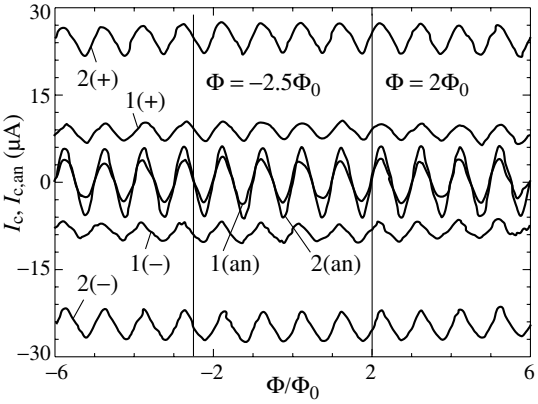

Fig. 2. The quantum oscillations of the critical current I_{c+}, I_{c-} measured in opposite directions and its anisotropy (an) $I_{c,an} = I_{c+} - I_{c-}$ observed on single loops with $w_n = 0.2$ μm, $w_w = 0.3$ μm and $T_c = 1.23$ K at (1) $T = 1.271$ K and (2) 1.243 K.

$2en_s[2s_n s_w/(s_n + s_w)](2\pi\hbar/ml)(n - \Phi/\Phi_0)$, Fig. 1. One may expect to determine not only value but also direction of the persistent current $I_p = (I_{c-} - I_{c+})(s_w/s_n - s_n/s_w)$ using the critical current I_{c+}, I_{c-} values measured in opposite directions of asymmetric loop with unequal half sections $s_n < s_w$, Fig. 1.

Our measurements of aluminum rings with radius $r = 2$ μm, thickness $d = 40-70$ nm, semi-ring width $w_n = 200$ nm, $w_w = 400$; 300; 250 nm and systems of such rings at $T < 0.99T_c$ have shown that the whole structure jumps from superconducting to normal state at $I = I_{c+}$ or I_{c-}. This means that the ring should remain in superconducting state with the same quantum number n right up to the transition into the normal state and the measurement of $I = I_{c+}$ or I_{c-} should correspond single measurement of the quantum state. One should expect gaps in the $I_{c+}(\Phi/\Phi_0)$, $I_{c-}(\Phi/\Phi_0)$ dependencies and maximum of $|I_p|(\Phi/\Phi_0) \propto |I_{c-} - I_{c+}|(\Phi/\Phi_0)$ at $\Phi = (n + 0.5)\Phi_0$, Fig. 1.

We have obtained identical $I_{c+}(\Phi/\Phi_0)$, $I_{c-}(\Phi/\Phi_0)$ dependencies at measurements of four single rings and two systems of identical 20 rings at different temperature, Fig. 2, 3, which differ from the expected one, Fig. 1, in essence. The magnetic dependencies of the anisotropy of the critical current $I_{c,an} = I_{c+} - I_{c-}$, which should be proportional to the persistent current $I_{c,an}(\Phi/\Phi_0) \propto -I_p(\Phi/\Phi_0) \propto -(n - \Phi/\Phi_0)$, cross zero at $\Phi = n\Phi_0$ and $\Phi = (n + 0.5)\Phi_0$, Fig. 2, as well as the one of the rectified voltage $V_{dc}(\Phi/\Phi_0) \propto \overline{n} - \Phi/\Phi_0$, Fig. 3, corresponding multiple, but not single, measurement of the persistent current states.

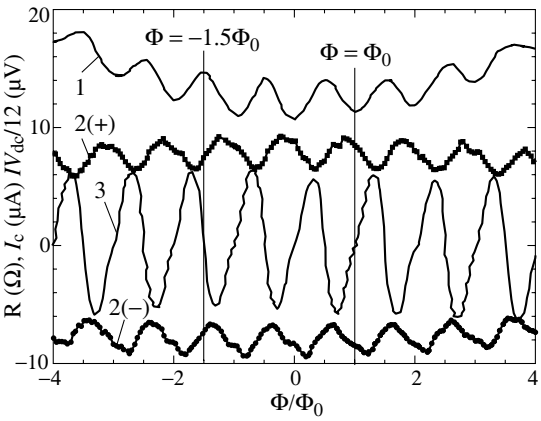

Fig. 3. Magnetic dependencies of (1) the resistance R — 23 Ω at $T = 1.228$ K of (2) the critical current I_{c+}, I_{c-} at $T = 1.208$ K, and (3) the rectified voltage $V_{dc}/12$, induced by the ac current with frequency $f = 0.5$ kHz and amplitude $I_0 = 9$ μA at $T = 1.209$ K of 20 loops with $w_n = 0.2$ μm, $w_w = 0.4$ μm and $T_c = 1.23$ K.

It is more strange that the magnetic dependencies of the critical current measured in opposite directions are similar $I_{c+}(\Phi/\Phi_0) = I_{c-}(\Phi/\Phi_0 + \Delta\phi)$ and its anisotropy results from a shift $\Delta\phi = 0.5$ of these dependencies one relatively another. It is very strange that minimum of $I_{c+}(\Phi/\Phi_0)$ and $I_{c-}(\Phi/\Phi_0)$ is observed at $\Phi = (n + 0.25)\Phi_0$ and $\Phi = (n + 0.75)\Phi_0$ but not at $\Phi = (n + 0.5)\Phi_0$ as it should be expected and as it is observed in symmetrical ring [11] since the maximum of the Little–Parks oscillations of asymmetric rings is observed at $\Phi = (n + 0.5)\Phi_0$. We hope that future investigations can clear a nature of this contradictions between results of measurements of $I_{c+}(\Phi/\Phi_0)$, $I_{c-}(\Phi/\Phi_0)$ and $\Delta R(\Phi/\Phi_0)$.

Acknowledgements

This work has been supported by a grant "Quantum bit on base of micro- and nano-structures with metal conductivity" of the Program "Technology Basis of New Computing Methods" of ITCS department of RAS, a grant of the Program "Low-Dimensional Quantum Structures" of the Presidium of Russian Academy of Sciences and a grant 04-02-17068 of the Russian Foundation of Basic Research.

References

[1] K. A. Valiev, A. A. Kokin, *Quantum computers: reliance and reality*, Moscow–Izhevsk: R and C Dynamics, 2002 (in Russian); M. A. Nielsen and I. L. Chuang, *Quantum Computation and Quantum Information* Cambridge University Press, 2000; A. M. Steane, *Rept. Prog. Phys.* **61**, 117, 1998.

[2] J. R. Friedman *et al*, *Nature* **406**, 43 (2000); C. H. van der Wal, A. C. J. ter Haar, *Science* **290**, 773 (2000).

[3] A. J. Leggett and A. Garg, *Phys. Rev. Lett.* **54**, 857 (1985).

[4] Y. Makhlin, G. Schoen and A. Shnirman, *Rev. Mod. Phys.* **73**, 357 (2001); P. Bertet *et al*, *Phys. Rev. Lett.* **95**, 257002 (2005); Z. H. Peng, M. J. Zhang and D. N. Zheng, *Phys. Rev. B* **73**, 020502(R) (2006).

[5] A. Einstein, B. Podolsky and N. Rosen, *Phys. Rev.* **47**, 777 (1935).

[6] A. Aspect, P. Grangier and G. Roger, *Phys. Rev. Lett* **47** 460 (1981); P. G. Kwiat *et al*, *idid* **75**, 4337 (1995); G. Weihs *et al*, *idid* **81**, 5039 (1998); W. Tittel *et al*, *Phys. Rev. A* **57**, 3229 (1998); J. W. Pan *et al*, *Nature* **403**, 515 (2000).

[7] W. A. Little and R. D. Parks, *Phys. Rev. Lett.* **9**, 9 (1962).

[8] H. Vloeberghs *et al*, *Phys. Rev. Lett.* **69**, 1268 1992.

[9] M. Tinkham, *Introduction to Superconductivity*, McGraw-Hill Book Company (1975).

[10] S. V. Dubonos *et al*, *Pisma Zh. Eksp. Teor. Fiz.* **77**, 439 (2003) (*JETP Lett.* **77**, 371 (2003)).

[11] D. S. Golubovic and V. V. Moshchalkov, will be published in *Appl. Phys. Lett.*, available at cond-mat/0509332.

14th Int. Symp. "Nanostructures: Physics and Technology"
St Petersburg, Russia, June 26–30, 2006

Comparative study of efficiency of InGaN/GaN MQW light-emitting diodes with different nanostructural arrangement

A. A. Greshnov, D. M. Bauman, B. Y. Ber, A. E. Chernyakov, A. P. Kovarskyi, A. M. Kovtunovich, N. M. Shmidt, B. S. Yavich and A. L. Zakgeim
Ioffe Physico-Technical Institute, St Petersburg, Russia

Abstract. The optical and transport properties of the multiple quantum well (MQW) InGaN/GaN light-emitting diodes (LED) with different nanostructural arrangement (NA) have been investigated. A comparative study of LEDs has shown a large difference in the external quantum efficiency (QE) in the region of moderate injection current (1-10mA) and only a small difference at injection current higher than 100mA. These features have been analyzed and attributed not only to the difference in NA, but also to the change in the relative position of depletion region and MQWs, caused by the magnesium diffusion tail in the active region of LEDs. This explanation is consistent with the calculated band diagram of LEDs.

Introduction

In spite of excellent success in the blue LED technology, the high values (up to 20%, without lens) of peak QE occuring at low injection current (1–10 mA) and a significant decrease of QE at injection current higher than 100 mA are not fully comprehensible. A major part of the investigations is devoted to the effects of the inhomogeneity of the In incorporation into GaN, the layer thickness in MQW InGaN/GaN structures, the polarization and the density of dislocations. At the same time the papers regarding an influence of NA are not numerous. In this paper we present a comparative study of LEDs with different NA focusing on a problem of the electroluminescence efficiency.

1. Experimental

A comparative investigation of LEDs with two types of NA has been carried out. Both LEDs based on InGaN/GaN MQW with an active region consisting of 5 periods of (3 nm InGaN and 12 nm GaN) and thin p-GaN/AlGaN cap layer were grown by MOVPE on (0001) sapphire substrates. The cap layer was highly ($N_a \approx 2 \cdot 10^{20}$ cm^{-3}) magnesium doped.

The nanostructural arrangement of LEDs determines by the extended defect system relaxation, which includes a high density of threading dislocations and a mosaic structure. The NA reflects the peculiarities of coalescence of mosaic structure domains with different angles of tilt and twist and can be classified quantitatively using a multifractal parameter, namely, the degree of order Δ [1]. LEDs of the first (I) type have $\Delta = 0.33$, typical for rather good structural arrangement with predominant coherent concordance of domains and formation of the dilatation boundaries. LEDs of the second (II) type have $\Delta = 0.345$, typical for poor structural arrangement with predominant numerous domains dislocation boundaries.

The current-voltage (I–V) characteristics measured from 10^{-12} A to 100 mA are presented in Fig. 1. The results of QE measurements carried out at injection currents from 0.1 mA to 400 mA are presented in Fig. 2.

2. Discussion

A simultaneous analysis of I–V and QE-voltage characteristics allows us to distinguish three regions of low, intermediate and high voltages. In the region of low voltages $U \lesssim 2$ V all the current flowing across the structure is due to a tunnelling

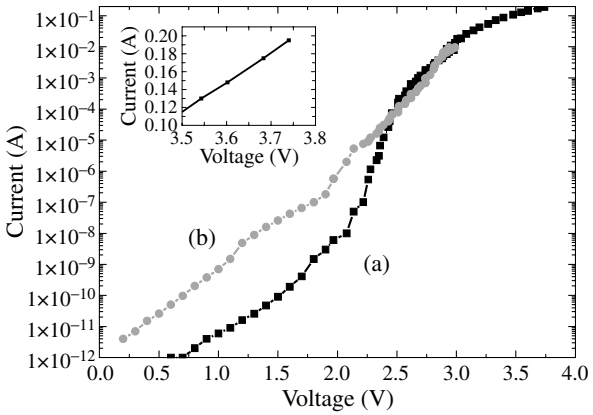

Fig. 1. Current-voltage characteristics of (a) LEDs(I) (b) LEDs(II).

recombination. A behavior of the curves (a) and (b) in Fig. 1 is very similar and can be fitted by an exponential law with the characteristic energy parameter E_t close to 160 meV and independent of the temperature, in accordance with Ref. [2]. As one can see from Fig. 1, LEDs(I) have tunnelling current almost two order of magnitude lesser than that of LEDs(II) due to the better NA.

In the intermediate region of voltages 2 V$\lesssim U \lesssim$3.2 V two types of LEDs show significantly different behavior of both I–V and QE-voltage characteristics. In LEDs of the first type a noticable QE emerges at $U_0 \approx 2.3$ V and has peak value of 12% at $U_m = 3$ V. On the contrary, in LEDs(II) $U_0 \approx 2.5$ V and only 3% peak value of QE is achieved at $U_m = 2.6$ V. Simultaneously, there is a sharp increment of the slope of curve (a) in Fig. 1 at the voltages $U \approx 2$ V whereas a behavior of the curve (b) keeps almost constant in the intermediate region of voltages. At the higher voltages $U \gtrsim 3.2$ V the difference in the characteristics between two types of LEDs becomes much smaller. In this region of voltages the ohmic current predominates and a linear I–V characteristics are observed (see inset in Fig. 1). A series resistance obtained from I–V characteristics amounts to approximately 2 Ω for both types of LEDs. A growth of electroluminescence output tends to saturate, resulting in the decreasing QE (Fig. 2).

The complicated behavior of I–V and QE-voltage curves allows us to suppose a significantly inhomogeneous distribution of the carries and electric field in the active region of LEDs and the presence of compensated layer. Indeed, secondary ion mass spectroscopy (SIMS) profiling has revealed the massive

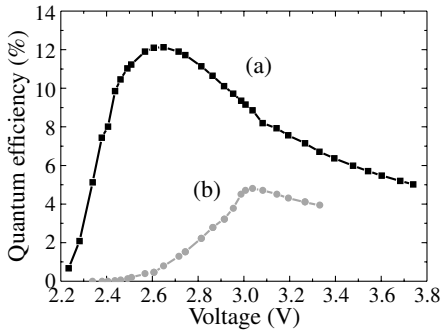

Fig. 2. External quantum efficiency-voltage characteristics of (a) LEDs(I) (b) LEDs(II).

diffusion tail of magnesium in the active region. Doping profiles of the typical LED of the type I are shown in the inset in Fig. 3.

In order to account for the effects of the inhomogeneous distributions we have calculated a band diagram of LEDs using the data of SIMS measurements. This calculation bases on the numerical solution of Poisson equation with both two-dimensional and tree-dimensional concentration of the carriers [3]. Here we assume a nearly uniform donor concentrations in the active region $N_d \approx 6 \cdot 10^{17}$ cm^{-3} for both types of LEDs. On the contrary, the magnesium diffusion tail should be taken into account more accurately. It is the higher density of dislocation domain boundaries in LEDs with worse NA that leads to the difference in the diffusion depth of magnesium between LEDs(I) and LEDs(II) [3].

The results of calculation performed for LEDs(I) and LEDs(II) are presented in Figs. 3-4. The electrostatic potential profile as well as the profile of electric field (presented in the inset in Fig. 4) are rather complicated. An important thing here is the significant difference in the occupation of QWs by carriers between two types of LEDs. There are 2 QWs occupied by holes and 3 lying in the depletion for LEDs(I) and only one QW occupied by holes for LEDs(II). Note that the band diagram calculated here significantly differs from that of presented earlier by Mamakin *et al* [4] in what concerns the occupation of QWs. The case of QWs occupied by electrons instead of holes considered in the Ref. [4] can hardly realize due to the large concentration of acceptors and appreciable value of the diffusion depth. An additional confirmation of the obtained results follows from the analysis of capacitance-voltage

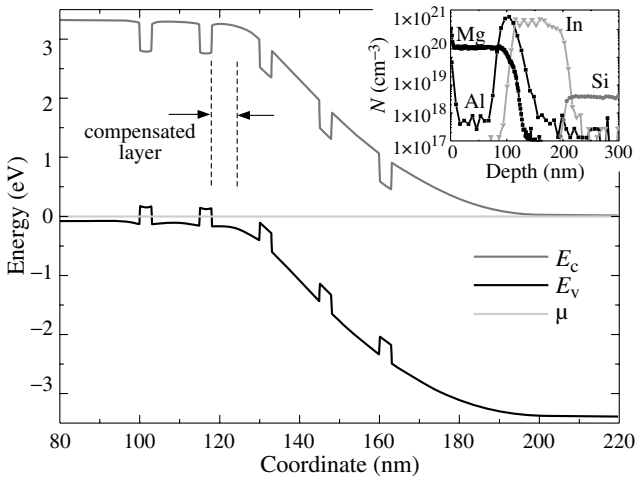

Fig. 3. Band diagram of LEDs(I).

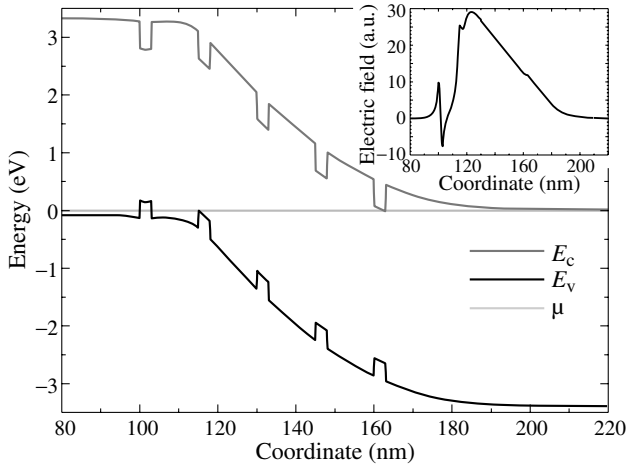

Fig. 4. Band diagram of LEDs(II).

characteristics which shows 3 QWs in the depletion region for LEDs(I) and 4 QWs for LEDs(II) [5]. These data are in full compliance with our results and serve as the direct evidence of the difference in band diagram between two types of LEDs.

Thus, there is a significant difference in the relative position of depletion region and MQWs due to the difference in the doping profiles. Obviously, such a difference keeps under the conditions of applied voltage. As a result, one can find a different number of QWs lying in the depletion region for LEDs(I) and LEDs(II) at the equal voltage. Recalling that a concurrent occupation of at least one of the QWs by electrons and holes is necessary for a noticable electroluminescence we come to the following issue. If the considered QW lies in the depletion region it is a voltage of $E_g^{\mathrm{InGaN}}/e \approx 2.6$ V which is needed to observe a significant output. However, if the QW lies outside the depletion region this value is increased by the depth of QW and amount to approximately 3.0 V. A coincidence of these values with the voltages U_m of peak QE in LEDs(I) and LEDs(II) allows us to attribute the observed features to this effect.

Acknowledgement

This work has been supported by Russian Foundation for Basic Research (05-02-16679), Federal Programme on Support of Leading Scientific Schools and Grant of Russian Academy of Science "New Materials and Structures"(1.5). One of the authors (A. A. Greshnov) appreciates the support of Dynasty Foundation.

References

[1] N. M. Shmidt *et al*, *Inst. Phys. Conf. Ser.* **169**, 303 (2001).
[2] P. Perlin *et al*, *Appl. Phys. Lett.* **69**, 1680 (1996).
[3] The details of band diagram calculation will be presented elsewhere.
[4] S. S. Mamikin *et al*, *Semiconductors* **37**, 1107 (2003).
[5] D. M. Bauman *et al*, the paper submited to 14th Int. Symp. "Nanostructures: Physics and Technology".

14th Int. Symp. "Nanostructures: Physics and Technology"
St Petersburg, Russia, June 26–30, 2006

Fabrication and characteristic investigation of resonant-cavity separate absorption and multiplication (RC-SAM) avalanche photodetector

Cheol-Koo Hahn[1], Dong Ho Kim[1,2], Cheong Hyun Roh[1], Hong Joo Song[1], Yeon-Shik Choi[1], Hoon Kim[1] and Tae Geun Kim[2]

[1]Nano-scale Quantum Devices Research Center,
KETI, Yatap-dong, Bundang-Gu, Songnam, Gyeonggi, 463-816, Korea
[2]Dept. of Electronics & Electrical Engineering, Korea University,
Anam-dong, Seongbuk-Gu, Seoul, 136-701, Korea

Abstract. InAs self-assembled quantum dot (SAQD) resonant-cavity separate absorption & multiplication (RC-SAM) avalanche photodetectors operating near ~ 1 μm were designed and fabricated. The structure of InAs SAQD RC-SAM APD was designed such that it would resonate with the light incident from the top mesa. The InAs SAQD RC-APD was grown by solid-source molecular-beam epitaxy (MBE) on a semi-insulating (SI) GaAs substrate. The area of the top mesa was 10×10 μm^2 and the absorbing region consisted of a 2.1 monolayer InAs SAQD layer sandwiched by two 75.5 nm-thick GaAs spacers. One of the InAs SAQD RC-SAM APDs exhibited a large multiplication gain factor $M \sim 200$ and a low dark current of ~ 2 nA at a breakdown voltage of ~ 19 V.

Introduction

Avalanche photodetectors (APDs) are very useful for passive optoelectronic devices such as optical fiber communication systems, data transmission systems, high resolution imaging sensors and medical diagnostic sensors operating at near-IR (NIR) region [1], since these exhibit a higher sensitivity than conventional PIN photodetectors due to a large internal gain provided by avalanche multiplication behavior. To get the modest efficiencies in NIR regime, however, Si APDs require thick absorbing regions resulting in the high breakdown voltages and low speeds. On the other hand, InGaAs APDs achieve good responsivity near NIR region but exhibit high dark currents and high multiplication noise compare to Si APDs [2]. Furthermore, sensitivities of conventional Si and InGaAs APDs near ~ 1 μm fall in a so called 'sensitivity valley' between the long wavelength limit due to absorption bandgap edge of Si APDs and the short wavelength limit due to surface absorption of InGaAs APDs. Therefore, it is necessary to develop new types of NIR photodetectors operating near ~ 1 μm with high quantum efficiency, high speed, low dark current, a high gain-bandwidth product, and low multiplication noise. Recently, resonant-cavity separate absorption and multiplication (RC-SAM) APDs have been shown to achieve all of these properties. The SAM has separated high-field multiplication and absorption regions and this result in a lower dark current [3]. Another benefit of the SAM APD structure is that only a single type of carrier is injected into the multiplication region, which is a well-known requirement for reducing the multiplication noise that arises from the stochastic nature of the multiplication process [4].

In this paper, RC-SAM APDs, using InAs self-assembled quantum dot (SAQD) as a light absorbing layer, was fabricated and its characteristics were investigated for NIR applications. The delta-function like density-of-states (DOS) profile of the RC-SAM APD light absorbing SAQDs are thought to have enhanced its internal quantum efficiency. Electrical and optical characteristics of the InAs SAQD RC-SAM APDs such as, dark currents, photocurrents, multiplication gain, are investigated. Furthermore, their output characteristics depending on various fabrication processes were characterized in detail.

1. Experiments

The epitaxial layer structure of the InAs SAQD RC-SAM APD was designed by employing the Bragg's condition which satisfied a quarter-wavelength rule.

InAs SAQDs including the whole the epitaxial layer were grown by solid-source molecular beam epitaxy (MBE). Figure 1 shows its schematic illustration of the layer structure

GaAS cap layer 10 nm
p^+-GaAs contact layer 310 nm ($N_a = 1\times10^{19}$)
p-GaAs buffer layer 77.5 nm ($N_a = 1\times10^{17}$)
GaAs spacer 77.5 nm
InAs QD absorbing layer 2.1 ML
GaAs spacer 77.5 nm
p-AlGaAs charge layer 80 nm ($N_a = 1\times10^{17}$)
Undoped AlGaAs multiplication layer 160 nm
n-GaAs buffer layer 77.5 nm ($N_d = 1\times10^{17}$)
n^+-GaAs contact layer 310 nm ($N_a = 1\times10^{19}$)
GaAs high reflective layer 77.5 nm
AlAs low reflective layer 90.3 nm
Semi-insulated (S.I.) GaAs substrate

Fig. 1. Schematic of InAs SAQD RC-SAM APD structure.

which includes, a DBR mirror-consisted of 25 pairs of 90.3 nm-thick undoped AlAs and 77.5 nm-thick undoped GaAs quarter wave stack (QWS)-, a 310 nm-thick n^+-doped (Si = 1×10^{18} cm^{-3}) GaAs contact layer, a 77.5 nm-thick layer of n-doped (Si = 1×10^{17} cm^{-3}) GaAs buffer, a 160 nm-thick undoped $Al_{0.2}Ga_{0.8}As$ multiplication layer, a uniformly p-doped (Be = 1×10^{17} cm^{-3}) $Al_{0.2}Ga_{0.8}As$ charge layer, a IR absorption layer which consists of an 2.1 ML undoped InAs SAQD layer sandwiched by two 77.5 nm-thick undoped GaAs spacer, a 77.5 nm-thick p-doped (Be = 1×10^{17} cm^{-3}) GaAs buffer and finally a 10 nm-thick p^+-GaAs (Be = 1×10^{19} cm^{-3}) top contact layer. The size and the density of the SAQD, used for the device fabrication, were 20 nm in diameter and 5×10^{10} cm^2, respectively. Polyimide (PI) thin film was deposited on the fabricated InAs SAQD RC-SAM APD for the purpose of anti-reflection coating and surface passivation. The size of the IR absorbing area was defined to 10×10 m^2 by etching with inductively coupled plasma reactive ion etching (ICP-RIE) and chemical H_3PO_4 solution. The Ohmic contacts of the device are defined by conventional lift-off technique using Ti/Au for p-contact and Ni/Au/Ge/Ni/Au for n-contact layer.

2. Summary of measured device characteristics

The photocurrents (top), dark currents (middle), and multiplication gain (bottom) of a 10×10 m^2 absorbing mesas with different etching methods (such as ICP-RIE and H_3PO_4) of InAs SAQD RC-SAM APDs were shown as a function of the reverse bias in Figure 2.

The photocurrents were measured at room temperature using Ti:Shapphire tunable laser diode of which optical power and wavelength are 1 mW/cm^2 and 970 nm. The photocurrents of InAs SAQD RC-SAM APD showed similar properties irrespective of IR absorbing mesa structure defining etching methods. The punch-through occurred at near — 3 V, and the breakdown voltage was only — 21 V (a factor of 10 to 15 lower than the operating voltage of Si APDs) [5]. The multiplication gain (M) is extracted from the photocurrent assuming that the gain at punch-through is unity-gain regime. A multiplication gain near 100 was observed at 95% of breakdown voltage. Also, the responsivity of these InAs SAQD RC-SAM APDs were calculated to 2.1 mA/W and 2.9 mA/W for the H3PO4 wet chemical and ICP-RIE dry etched one, respectively. However, the dark currents show dependency only on the IR absorbing mesa structure defining etching methods. The measured value employing ICP/RIE etching process were approximately 5 orders lower than those obtained by H3PO4 etching process (10 nA and 2 nA for the H_3PO_4 wet chemical and ICP-RIE dry etched one, respectively, at 90% of breakdown voltage (−19 V)). These are thought to be due to mesa profile difference and electric filed distributions in IR absorbing mesa structure. Table 1 summarizes the measured characteristics of the fabricated InAs SAQD RC-SAM APDs. Other characteristics, depending on the device parameter and process variation, will be presented in detail.

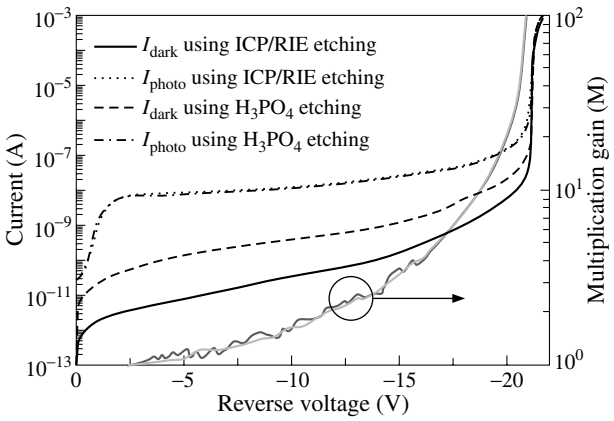

Fig. 2. The output characteristics of the InAs SAQD RC-SAM APD with IR absorbing mesa defining methods.

Table 1. Summary of output characteristics of the InAs SAQD RC-SAM APDs.

	Items	Proceess	Spec.
#1	Breakdown voltage	H_3PO_4	− 21 V
#2		ICP/RIE	− 21 V
#3	Dark current(@ −19 V)	H_3PO_4	10 nA
#4		ICP/RIE	2 nA
#5	Photo−current(@ −19 V)	H_3PO_4	76 nA
#6		ICP/RIE	93 nA
#6	Responsivity (mA/W)	H_3PO_4	2.1
#7		ICP/RIE	2.9
#8	Multiplication gain (@ Vb)	H_3PO_4	190
#9		ICP/RIE	178

Acknowledgement

This work was supported by the Driving Force Project for the Next Generation of Gyeonggi Provincial Government in Republic of Korea.

References

[1] B. L. Kasper *et al*, *J. Lightwave Technol.* **5**, 1351 (1987).
[2] H. Nie *et al*, *IEEE Photon. Technol. Lett.* **10**, 1009 (1998).
[3] K. Nishida *et al*, *Appl. Phys. Lett.* **35**, 251 (1979).
[4] R. McIntyre *et al*, *IEEE Trans. Electron Devices* **13**, 164 (1966).
[5] J. C. Campbell *et al*, *IEDM 95* (1995).

14th Int. Symp. "Nanostructures: Physics and Technology"
St Petersburg, Russia, June 26–30, 2006

Multilayer AlN/AlGaN/GaN/AlGaN heterostructures with quantum well channel for high power microwave field effect transistors

D. M. Krasovitskiy[1], A. N. Alekseev[1], S. B Aleksandrov[1], A. E. Byrnaz[1], V. P. Chaly[1], M. V. Pavlenko[1], S. I. Petrov[1], M. Yu. Pogorelsky[1], A. P. Shkurko[1], I. A. Sokolov[1], M. A. Sokolov[1], M. V. Stepanov[1], A. G. Tkachenko[1], L. E. Velikovskiy[1], I. E. Velikovskiy[1] and A. N. Pikhtin[2]

[1] JSC Svetlana–Rost, Saint Petersburg, Russia
[2] Electrotechnical University "LETI", Saint Petersburg, Russia

Abstract. Doubly electron confined AlGaN/GaN/AlGaN heterostructures were grown on sapphire substrates using 0.2 μm AlN templates also grown at 1150 °C by molecular beam epitaxy within the same process. For GaN channel thickness being low enough to form quantum well (50 Å), mobilities up to 1050 cm^2/V s (for back-doped buffer layer $Al_{0,2}Ga_{0,8}N$) and up to 1350 cm^2/V s (for undoped buffer layer $Al_{0,1}Ga_{0,9}N$)at carrier sheet electron density of 10^{13} cm^{-2} were obtained. In DHFETs, fabricated from such a structures, electron confinement is essentially improved while other DC-mode parameters were competitive to ones obtained on classic HEMT-like devices.

Introduction

In a last decade, field effect transistors based on heterostructures (HS) AlGaN/GaN demonstrated microwave performance outstanding among a number of analogous devices based on traditional semiconductors. The main peculiarity of nitride heterostructures is that the two-dimensional electron gas (2DEG) formed at AlGaN/GaN interface can reach sheet electron density more than 10^{13} cm^{-2} due to "piezo-doping" effect. 2DEG electron mobility depends essentially on crystal quality of layers in HS: values of 2000 cm^2/V s (300 K) have been published [1], while electron motilities in the range of 1000–1500 cm^2/V s are typical for most of publications. Field effect transistors (FETs) based on such a HS usually show current densities of 0.6–1.2 A/mm and transconductance in 120–200 mSm/mm range. These values together with high breakdown voltages provide in some cases an order of magnitude higher power densities as compared with GaAs. Recently, microwave power densities up to 32 W/mm for GaN-based discrete devices [2] and output power over 150 W for power amplifiers [3] have been demonstrated. The key issue for the development of high power devices is the electron confinement which is directly effects on transistors cut off and leakage [4]. Besides, hot electrons spillover under high current operation takes place and limits maximum current and thus power density. The latter essentially contributes to the so called "RF-current collapse" due to electron trapping in buffer and upper barrier layers.

Leakage in common sense can be minimized by compensation doping of GaN buffer with impurities producing deep levels, such as Fe, C, Mg etc. [5]. To reduce current collapse related to surface traps, various passivation techniques are used, for example silicon nitride-based [6]. Nevertheless, above methods cant prevent electron trapping in thick buffer GaN layer, moreover, the problem seems to be accented because an additional traps are produced during compensation doping. Alternatively, double-sided heterostructures (DHS) obviously provide better electron confinement when traditional HEMT-like structures.

GaN/InGaN/AlGaN DHS-based field effect transistors (DHFETs) were shown to have no visible RF-current collapse at all [7]. But, despite higher theoretical values of electron mobility in InN compared with GaN, mobility in really grown InGaN layers are yet often degraded due to crystal imperfection, composition fluctuations etc. Therefore, DHS AlGaN/GaN/AlGaN are still remain more reliable and technologically approved. A number of publications reporting successful realization of DHFETs based on AlGaN/GaN/AlGaN [8, 9] are available, and device parameters are competitive to ones obtained on "classic" HS GaN/AlGaN. We also previously reported on multilayer heterostructures (MHS) AlN/AlGaN/GaN/AlGaN with GaN channel thickness of 140 nm, showing DEG mobilities 1000–1350 cm^2/V s at sheet electron density (1.0−1.6) 10^{13} cm^{-2}. DHFETs based on such MHS also demonstrated current density up to 1.2 A/mm in DC-mode [10]. To improve electron confinement and so device performance, GaN thickness should be further decreased. Besides, it seems also technologically attractive due to the distance from AlGaN buffer to surface will be reduced too, thus making mesa-isolation etch and gate metallization easier and more reliable. We discuss the effect of GaN channel thickness and AlGaN buffer composition on electron density and mobility in 2DEG formed at upper barrier GaN/AlGaN interface of MHS.

1. Experimental

AlN/AlGaN/GaN/AlGaN MHS were grown on (0001) sapphire substrates by molecular beam epitaxy using specialized nitride MBE systems of EPN-series (SemiTEq). The main peculiarity of our MHS is 0.2 μm-thick AlN template, grown at 1150 °C directly before heterostructure within the same epitaxy process [10]. Properties of grown samples were studied using atomic-force microscopy (AFM), X-ray diffraction (XRD), capasitance-voltage (C-V) and temperature dependent Hall measurements.

Test transistors with 1×20 μm gate geometry were fabricated on MHS by planar processing including photolithography, e-beam metallization, rapid thermal annealing and reactive ion etching techniques.

2. Design issues of MHS with GaN QW channel

Reduction of GaN channel thickness alone, without another changes in AlN/AlGaN/GaN/AlGaN MHS design deteriorates

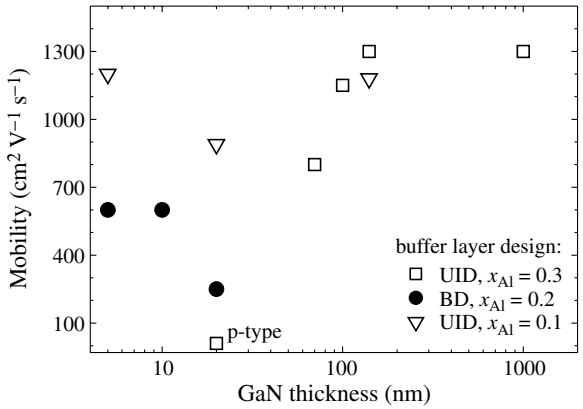

Fig. 1. Mobility versus GaN thickness in MHS with different design of AlGaN buffer layer.

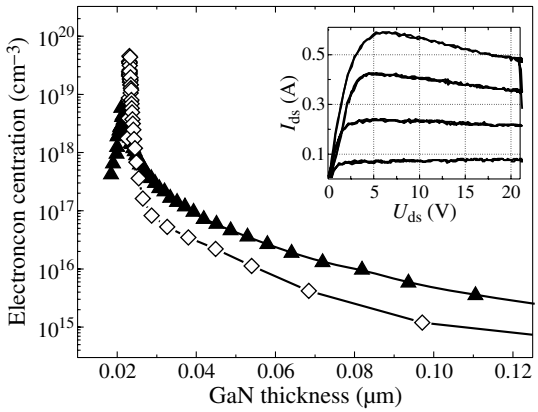

Fig. 2. C–V profiles of MHS with GaN QW (open diamonds) and 100 nm-thick GaN channel (solid triangles). DC I–V chars of DHFETs made on QW-MHS are shown on inset.

2DEG mobility due to following main reasons. First, relaxation above critical thickness may be accompanied by formation of various defects, contributing to an additional carrier scattering; so narrowing the channel to thicknesses close to this defect region result in mobility degradation. Second, polarization induced distortions of channel band diagram pronounces essentially when channel thickness is narrower, and parasitic hole conductivity appears in some cases near bottom interface AlGaN/GaN (analogous to 2DEG formation near upper GaN/AlGaN interface). Therefore, to realize quantum well for electrons in MHS it is necessary

(A) to find GaN relaxation thickness for various buffer designs (composition profiles), and

(B) to engineer bandgap close to channel region by profiling of AlGaN composition and n-doping (including so called back-doping).

Obviously, electron confinement enhances when quantum well deepens. On the other hand, critical thickness of relaxation depends on AlGaN buffer composition, too. Calculated critical Al mole fraction of $Al_xGa_{1-x}N$, depending on initial data and relaxation degree taken into account, lays in 0.11–0.15 range. So we studied two main cases of MHS buffer designs, as follows:

— $x_{Al} = 0.1$: band offset is enough for quantum confinement, no parasitic holes are formed on AlGaN/GaN interface;

— $x_{Al} = 0.2$: band offset is higher, relaxation thickness is shorter, parasitic holes are formed on AlGaN/GaN interface.

It was found that for $Al_{0,1}Ga_{0,9}N$ buffer no carrier depletion takes place, but electron mobility starts to fall when GaN channel thickness becomes less than 1000 Å due to worse crystal quality of "just-relaxed" material. Critical thickness of relaxation is estimated to be in 130–150 Å range, so at thicknesses below 100 Å electron mobility rises again (Fig. 1).

Quite different behavior was observed in the case of for MHS with $Al_{0,2}Ga_{0,8}N$ buffer design: at channel thicknesses below 1000 Å carrier density starts to decrease as well as mobility does, and at thickness of 200 Å p-conductivity was measured at room temperature (Fig. 1). Only back-doped MHS of such design demonstrated acceptable 2DEG conductivity at channel thickness below 100 Å. As a result, optimized MHS with 50 Å GaN channels were realized for both designs, mobilities up to 1050 cm^2/V s (back-doped buffer layer with $x_{Al} = 0.2$) and up to 1350 cm^2/V s (undoped buffer layer with $x_{Al} = 0.1$) at carrier sheet electron density of 10^{13} cm^{-2} were obtained. C–V profiles of QW-MHS were much more abrupt confirming better electron confinement (Fig. 2).

DHFET DC-parameters, competitive to ones obtained on classic HEMT-like devices, are also reported. Its worth to note, that I–V characteristics (inset to Fig. 2) are free from any "trapping loops" (hysteresis effects) which are often visible for unpassivated heterostructures with thicker channels. Issues of further design optimization are also discussed.

References

[1] R. Gaska *et al*, *Appl. Phys. Lett.* **78**, 1870 (2001).
[2] Y. F. Wu *et al*, *IEEE Electron Dev. Lett* **25**, 117 (2004).
[3] T. Kikkawa *et al*, *GaAs MANTECH-2004, New Orleans.* www.gaasmantech.org/Digests/2004/2004Papers/6.1.pdf.
[4] Y. K. Su *et al*, *Mat. Sci. Eng.* **B 110**, 172 (2004).
[5] H. Tang *et al*, *Solid-State Electronics* **44**, 2177 (2002).
[6] A. E. Vertiatchikh *et al*, *Elec. Lett.* **38**, 388 (2002).
[7] G. Simin *et al*, *Jpn. J. Appl. Phys.* **40**, L1142 (2001).
[8] C. Q. Chen *et al*, *Appl. Phys. Lett.* **82**, 4593 (2003).
[9] Y. Cordier *et al*, *J. Crystal Growth* **278**, 393 (2005).
[10] A. N. Alekseev *et al*, *Tech. Phys. Lett.* **31**, 846 (2005).

14th Int. Symp. "Nanostructures: Physics and Technology"
St Petersburg, Russia, June 26–30, 2006

Resonance enhancement of spin-polarized electron emission from strain-compensated AlInGaAs-GaAsP superlattices

J. S. Roberts[1], Yu. P. Yashin[2], *Yu. A. Mamaev*[2], L. G. Gerchikov[2], T. Maruyama[3], D.-A. Luh[3] and J. E. Clendenin[3]

[1] Department of Electronic Engineering, University of Sheffield, UK
[2] State Polytechnic University, 195251, St Petersburg, Russia
[3] Stanford Linear Accelerator Center, 2575 Sand Hill Road, Menlo Park, CA 94025, USA

Abstract. Resonance enhancement of the quantum efficiency of new polarized electron photocathodes based on a short-period strain-compensated AlInGaAs/GaAsP superlattice structure is reported. The superlattice is a part of an integrated Fabry–Perot optical cavity. We demonstrate that the Fabry–Perot resonator enhances the quantum efficiency by up to a factor 10 in the wavelength region of the main polarization maximum. The high structural quality implied by these results points to the very promising application of these photocathodes for spin-polarized electron sources.

Introduction

Strained short-period superlattices have been used to advantage in achieving highly spin-polarized electron photoemission [1]. In these structures, the heavy hole (hh) and light hole (lh) minibands are split due to the effects of both quantum confinement and strain-induced splitting. The enlarged valence band splitting results in a high initial electron polarization in the conduction band under excitation by circularly polarized light. Smearing of the interband absorption edge and light-heavy-hole mixture processes lead to a polarization (P) in the bandedge absorption of less than 100%. These mechanisms set a sizeable limitation for the maximum polarization of emitted electrons [2, 3]. The initial polarization can be increased by choosing strongly strained structures with a higher valence band splitting.

The thickness of the strained photocathode working layer, however, exceeds the critical thickness for strain relaxation resulting in structural defects, smaller residual strain and lower polarization. Critical thickness considerations limit the number of superlattice (SL) periods in the working layer and thus the quantum efficiency of the structures. To overcome this problem, two types of photocathodes have been proposed. The use of a strain compensated SL, whereby the composition of the SL barrier layers is chosen to have opposite (tensile) strain from that of the quantum well layers, allows the total working layer to be considerably thicker [4]. Another way to increase the quantum efficiency (QE) is to integrate the SL working layer into a Fabry–Perot optical cavity [5]. The key feature of such structures is a Distributed Brag Reflector (DBR) at the back side of the photocathode that reflects the incoming circularly polarized light back to the surface where approximately 0.3 of the intensity is reflected into cathode again and so on.

In the present work we combine these two approaches and develop a novel photocathode structure that integrates a working layer based on the strain-compensated InAlGaAs-GaAsP SL into a Fabry–Perot optical cavity. We investigate polarized electron emission from the photocathodes with and without a DBR mirror and report a tenfold enhancement of quantum efficiency due to optical enhancement from the Fabry–Perot cavity without degradation of electron polarization.

1. Experiment

The photocathode structures were grown on a p-type (100) GaAs substrate by Metal Organic Vapor Phase Epitaxy using trimethyl group III reagents and arsine. The photocathode design is shown in Table 1. It consists of a DBR mirror containing 22 pairs of alternating $\lambda/4$ plates of $Al_{0.19}Ga_{0.81}As$ and AlAs. On the top of this mirror, a 500 nm thick $Al_{0.35}Ga_{0.65}As$ buffer layer is grown that serves as the substrate for the strained SL. The superlattice contains 20 pairs of compressively-strained $(Al_{0.16}Ga_{0.84})_{82}In_{18}As$ quantum well layers and tensile-strained $GaAs_{0.83}P_{0.17}$ barrier layers. The layer compositions were designed to optimize the effect of strain magnitude and compensation on electron polarization. On top of the SL working layer, a 6-nm thick GaAs surface layer was deposited with Zn-doping concentration enlarged from 7×10^{17} cm^{-3} in the working layer to 1×10^{19} cm^{-3} to achieve negative electron affinity by the well known procedure of surface activation. Two samples have been prepared with and without a DBR layer.

Table 1. Composition of the photocathode.

As cap		
GaAs	QW	6 nm
$(Al_{0.16}Ga_{0.84})_{82}In_{18}As$	SL 20X	4 nm
$GaAs_{0.83}P_{0.17}$		6 nm
$Al_{0.35}Ga_{0.65}As$	Buffer	500 nm
GaAs		20 nm
AlAs	DBR 22X	71 nm
$Al_{0.19}Ga_{0.81}As$		58 nm
GaAs (100) – Substrate, Zn		

The structures were characterized by photoluminescence measurements, which included mapping of the structure surface. Both structures showed very good structural quality. The excitation spectra of the polarized photoemission from these structures were measured at room and at lowered (130 K) temperatures for different activation regimes. Studies of polarization growth during assisted degradation were used to identify polarization losses in the band bending region (BBR).

2. Results and discussion

The polarization and quantum efficiency data as a function of wavelength are shown in Fig. 1. The polarization spectra with and without the DBR layer are almost identical. The structures show all the typical features of SL emission including high-polarization peak at the band edge absorption and a second peak at higher energies with a well-pronounced dip between them. However these samples have different quantum yield spectra. While the sample without a DBR exhibits a typical smooth QE (λ) behavior with a cutoff below the absorption edge, the quantum yield spectrum of the sample with a DBR has additional resonance features.

To illustrate this fact, we plot in Fig. 2 the ratio of quantum efficiencies for these two samples together with the polarization curve for the DBR sample. Resonance peaks correspond to the increase of the electromagnetic field in the working layer when resonance conditions for the Fabry–Perot optical cavity are fulfilled. The largest resonance peak of quantum yield enhancement at $\lambda = 870$ nm practically coincides with the main polarization maximum of electron emission. Thus the DBR layer in the present sample increases the quantum efficiency of polarized electron emission by factor 10.

It worth to noting that the resonance enhancement of quantum yield is not accompanied by a decrease of electron polarization. This fact manifests the high structural quality of this photocathode. Since the resonance standing wave in a Fabry–Perot cavity is very sensitive to a phase shift near the resonance, even a small difference in the refraction indexes in in-plane directions as the result of a small anisotropy of the inplane lattice strain leads to a completely unpolarized wave in the working layer [6].

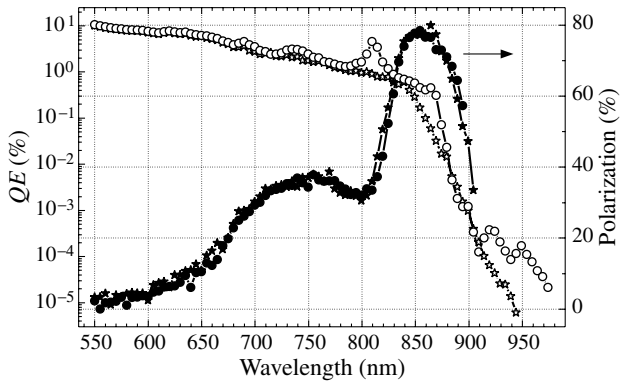

Fig. 1. Polarization (solid symbols) and quantum efficiency (open symbols) spectra of the emitted photoelectrons from photocathodes with (circles) and without (stars) DBR.

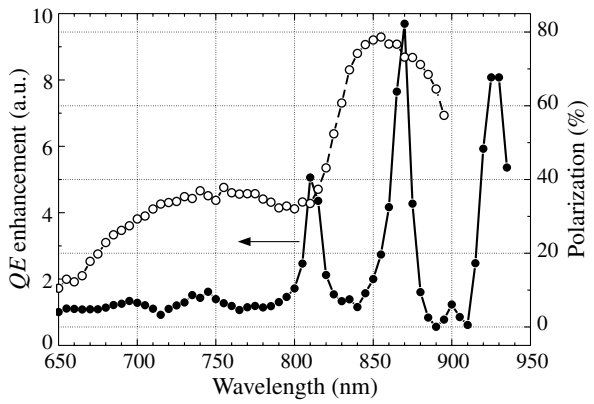

Fig. 2. Resonance enhancement of quantum efficiency (solid circles) and polarization of electron emission (open circles) from photocathode with DBR.

3. Conclusions

We have developed a novel type photocathode based on InAlGaAs-GaAsP strain compensated superlattices integrated into a Fabry–Perot optical cavity of high structural quality. We demonstrate a tenfold enhancement of quantum efficiency at the polarization maximum due to the multiple resonance reflection from DBR layer. The obtained results demonstrate the advantages of the developed photocathode as a perspective candidate for spin polarized electron sources.

Acknowledgements

We are thankful to A. V. Subashiev for fruitful discussion. This work was supported by RFBR under grant 04-02-16038, NATO under grant PST.CLG.979966 and the U.S. Department of Energy under contract DE—AC02-76SF00515.

References

[1] A. V. Subashiev, Yu. A. Mamaev, Yu. P. Yashin, J. E. Clendenin, *Phys. Low-Dimentional Structures* **1/2**, 1 (1999); A. V. Subashiev, *Physics — Uspekhi* **44**, 1310 (2001).
[2] A. V. Subashiev, J. E. Clendenin, *J. Modern Physics* **A 15**, 2519 (2000).
[3] A. V. Subashiev *et al*, *Semiconductors* **33**, 1182 (1999).
[4] A. V. Subashiev *et al*, *Appl. Phys. Lett.* **86**, 171911 (2005).
[5] T. Saka *et al*, *Jpn. J. Appl. Phys.* **32**, L1837 (1993).
[6] J. C. Groebli *et al*, *Phys. Rev. Lett.* **74**, 2106 (1995).

14th Int. Symp. "Nanostructures: Physics and Technology"
St Petersburg, Russia, June 26–30, 2006

Smallest Aharonov–Bohm interferometer, fabricated by local anodic oxidation

V. A. Tkachenko[1], *D. V. Sheglov*[1,2], Z. D. Kvon[1,2], E. B. Olshanetsky[1,3], A. V. Latyshev[1,2], A. I. Toropov[1], O. A. Tkachenko[1,2,3], J. C. Portal[3] and A. L. Aseev[1]

[1] Institute of Semiconductor Physics, 630090 Novosibirsk, Russia
[2] Novosibirsk State University, 630090 Novosibirsk, Russia
[3] Grenoble High Magnetic Fields Laboratory, MPI-FKF and CNRS, B.P.166, F-38042 Grenoble, France

Abstract. Local oxidation technology supported by modelling of 3D electrostatics of semiconductor nanodevices permits fabricating a ring interferometer with radius < 100 nm. Aharonov–Bohm oscillations (ABOs) measured in this device remained observable up to 15 K, the highest temperature for ring interferometers. Comparison of experiment and calculations shows that small amplitude of ABOs can be explained by the ring asymmetry under the condition of fully coherent transport.

Introduction

Miniaturization of ring interferometers is one of the main trends in studying of Aharonov–Bohm effect [1–5], and is a way to suppress influence of decoherence on the amplitude of ABOs. Electron lithography and subsequent reactive ion etching of AlGaAs/GaAs heterostructures allowed the fabrication of small rings with radius 130 nm [1]. Recently atomic force lithography with subsequent selective chemical etching permitted reducing ring radius twice [2], but this original method was used only by the authors. A simpler and more universal technique of local anodic oxidation uses the advantages of probe nanolithography, but does not need resist deposition and etching [3, 4, 6]. Recently an interferometer with radius 110 nm was obtained by this technique [5]. However, the rings appeared broken or close to broken even though the same lithographic template was used. It is important that AFM images of samples give neccesary information to model electrostatics of the device and to make clear the effect of technological imperfections on the geometry of electron system.

Results

New interferometer was fabricated by the technique, described in Ref. 5. Unlike that, however, and according to the results of 3D electrostatic modelling the depth of local anodic oxidation was reduced. For this purpose the voltage on the AFM tip was reduced twice. Since template of nanolithography was not changed, the depletion region around central antidot contracted, electron channels expanded, and the ring became more open than the one in Ref. 5 (Fig. 1). The ring kept its asymmetry, but the narrow place moved to another arm due to casual deviations from template in the local anodic oxidation process. Distribution of oxidation depth was obtained from AFM images of the samples. Electron density in the plane of 2DEG, charge density in the delta-doping layers and 3D electrostatic potential were calculated self-consistently from the distribution of oxidation depth and layer composition of GaAs/AlGaAs heterostructure.

Magnetotransport measurements show that effective radius of the ring is 15 nm smaller than that in Ref. 5. ABOs corresponding to radius 95 nm remain at temperatures up to 15 K (Fig. 2). This is the highest temperature of observation of Aharonov–Bohm effect in the interferometers now [4] (for ring with radius 110 nm this temperature was 9 K [7]).

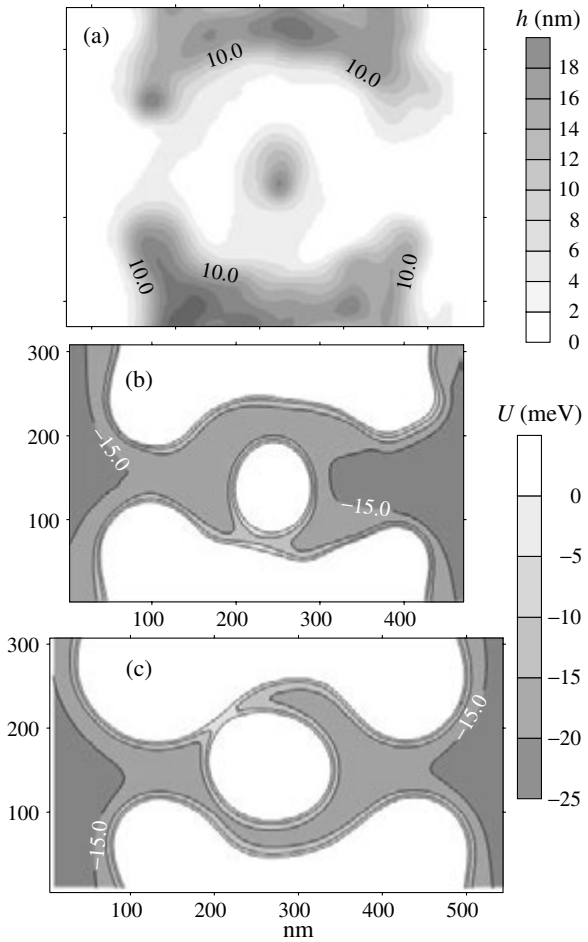

Fig. 1. (a) Map of the anodic local oxidation depth h. (b) Calculated effective potential for new ring. (c) Effective potential for ring from Ref. 5. Only area corresponding to $U_{\text{eff}} < E_{\text{F}} = 0$ is shown.

Measured amplitude of ABOs agrees well with calculations of two-dimensional magnetotransport for effective potential, obtained from solving 3D electrostatic problem for the studied device. The magnetic field dependence of the conductance was calculated by the method of recursive Green's functions [8]. Calculation shows that amplitude of ABOs does not exceed $e^2/2h$ on the assumption of fully coherent transport (Fig. 3).

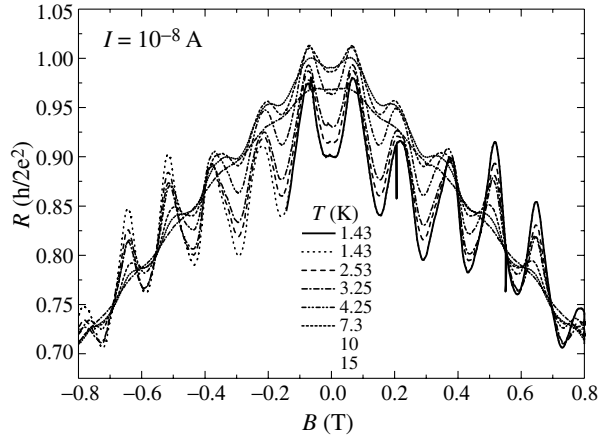

Fig. 2. Measured magnetoresistance of the ring interferometer with effective radius $r_{\rm eff} \approx 95$ nm.

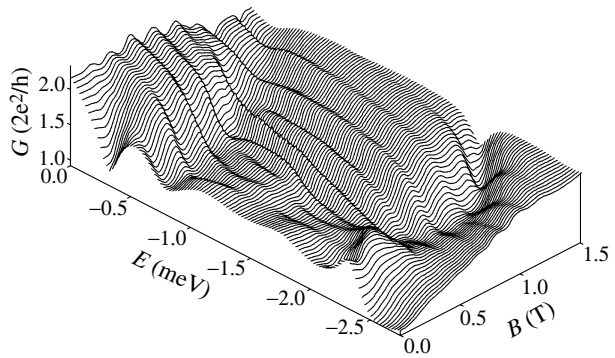

Fig. 3. Calculated conductance as a function of magnetic field and Fermi energy for the effective potential shown in Fig. 1b.

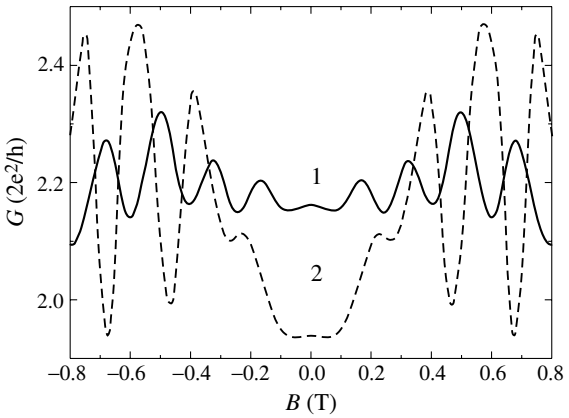

Fig. 4. Conductance as a function of magnetic field for $E_{\rm F} = 0$: (1) — for asymmetrical ring, (2) — for the ring symmetric with respect to horizontal axis, as obtained by symmetrization of the effective potential shown in Fig. 1b. The period of AB oscillations corresponds to $r_{\rm eff} \approx 85$ nm.

However symmetrization of the effective potential at least doubles the amplitude of ABOs (Fig. 4).

This result and the previous studies [9] shows that suppressed ABOs are not necessarily caused by disruption of coherence or approach to the tunneling regime in an arm of the ring, but geometric imperfection of the devices may be sufficient for this. It is worth noticing that agreement of background conductance, amplitude and period of ABOs in experiment and computation (Figs. 2–4) was not full because microscopic disorder in the sample was not taken into account in our models.

Acknowledgements

This work was supported by RFBR (grant 05-02-16591-a) and programs "Quantum nanostructures" of RAS, and "Russian Scientific School" Grant No. 8401.2006.8.

References

[1] A. A. Bykov, D. G. Baksheev, L. V. Litvin *et al*, *JETP Lett.* **71**, 255 (2000); K. A. Cheng, C. H. Yang, M. J. Yang, *J. Appl. Phys.* **88**, 5272 (2000); A. A. Bykov, O. Estibals, I. V. Marchishin *et al*, *Physica E* **12**, 778 (2002).

[2] D. Kähler, U. Kunze, D. Reuter and A. D. Weick, *Physica E* **17**, 284 (2003).

[3] A. Fuhrer, S. Lüsher, T. Ihn *et al*, *Nature* **413**, 822 (2001); U. F. Keyser, S. Bock, R. J. Haug *et al*, *Semicond. Sci. Technol.* **17**, L22 (2002).

[4] T. Ihn, A. Fuhrer, M. Sigrist *et al*, in *Advances in Solid State Physics* (Springer–Verlag) Vol. 43 / 2003, pp. 139–154, Heidelberg, 2003.

[5] V. A. Tkachenko, Z. D. Kvon, D. V. Sheglov *et al*, *JETP Lett.* **79**, 136 (2004).

[6] D. V. Sheglov, A. V. Latyshev, A. L. Aseev, *Appl. Surf. Sci.* **243**, 138 (2005).

[7] E. B. Olshanetsky, Z. D. Kvon, D. V. Sheglov *et al*, *Int. J. Mod. Phys. B* **18**, 3505 (2004).

[8] T. Ando, *Phys. Rev. B* **44**, 8017 (1991).

[9] O. A. Tkachenko, V. A. Tkachenko, D. G. Baksheev and J. C. Portal, Proc. 13th Int. Symp. Nanostructures Physics and Technology, St Petersburg, 2005, p. 205.

14th Int. Symp. "Nanostructures: Physics and Technology"
St Petersburg, Russia, June 26–30, 2006

Gate-controlled spin filter and quantum splitter

I. A. Shelykh[1], N. G. Galkin[2] and N. T. Bagraev[3]

[1] St Petersburg State Polytechnical University, St Petersburg, Russia
[2] Algodign LLC, Force Field Lab, 123379, Moscow, Russia
[3] Ioffe Physico-Technical Institute, St Petersburg, Russia

Abstract. We propose the mesoscopic device based on the Rashba spin orbit interaction (SOI) that contains a gated ballistic Aharonov–Bohm (AB) ring with incoming lead and two asymmetrically situated outgoing leads. The variations of the Rashba spin- orbit coupling parameter induced by the gate voltage applied to the AB ring is shown to cause the redistribution of the carrier flux between the outgoing leads and spin polarization of the outgoing currents, thus allowing the system to manifest the properties of the quantum splitter and spin filter.

Introduction

The role of the spin in the processes of the quantum transport has been in focus of both experimental and theoretical investigations in the last decade. The studies of the Rashba spin-orbit interaction (SOI) in semiconductor heterostructures have specifically attracted much interest as it can form a basis of the spintronic devices in which the the spins of single electrons become an object of the precise manipulation and control (for review see [1]). Importantly, the structure inversion asymmetry needed for Rashba SOI can be lifted by the external gate voltage V_g applied perpendicular to the structure interface thereby leading to the controllable variations of the Rashba SOI coupling parameter α.

The first spintronic device known as spin field effect transistor (FET) proposed in the pioneering work of Datta and Das [2] needed the efficient spin injection from ferromagnetic contacts into semiconductors. However, the reported experimental values of the polarization degree of the injected electrons were several percents only, so that the expected modulation of the conductance of the spin-FET is very small [3]. The version of the the spin-interference device working without any ferromagnetic electrodes and external magnetic field was later proposed in the work of Aronov and Lyanda–Geller [4]. It consists of the ballistic Aharonov–Bohm (AB) ring covered by the gate electrode. In addition to the Berry phase, the Rashba SOI in the AB ring induces the Aharonov–Casher phaseshift between the spin waves propagating in the clockwise and anticlockwise directions, which results in the large conductance modulation due to the interference of the spin wave functions [5].

1. The structure

Here we propose the modified version of the spin interference device which does not need the spin-polarized carrier injection. It represents a ballistic AB ring with one ingoing electrode 0, and two asymmetrically placed outgoing electrodes, 1 and 2, shown in Fig. 1 [6]. The spin-dependent conductances $G_{01,\pm}$ and $G_{02,\pm}$ of this three-terminal device can be experimentally measured; the index $\pm$ corresponds to the spin projection of the carrier on its wavevector in the outgoing leads. It should be noted that in the two-terminal devices with single propagating mode in zero magnetic field the outgoing current is unpolarized being due to the time-inversion symmetry [7]. However, using the multi-terminal structures where the electrons with opposite spins can be redistributed unequally between the outgoing leads, the effect of the spin filtering can be achieved [8].

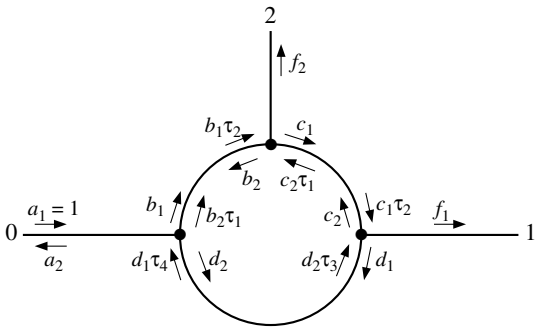

Fig. 1. Schematic view of a spin-interference device based on the AB ring connected with three one-dimensional leads and covered by the gate electrode that controls the amplitudes of travelling electronic waves via Rashba SOI.

In the ballistic regime the conductances are determined by the phase relations between the waves propagating in the AB ring in clockwise and anticlockwise directions which are controlled by tuning the Rashba parameter which redistributes the current between the outgoing leads and induces nonzero polarization degree of the outgoing currents.

$$P_j = \frac{G_{0j,+} - G_{0j,-}}{G_{0j,+} - G_{0j,-}}\,. \qquad (1)$$

2. The model

For the reasons of simplicity we consider the AB ring and the leads as being purely one-dimensional and ballistic. The preparation of the single channel devices is now experimentally achievable and they are always preferable as compare to the multichannel because of much less effective spin relaxation. The conjunctions between the AB ring and leads are modelled by the identic spin- conservative quantum point contacts (QPCs) which provide the elastic scattering of the carriers and can be characterised by the amplitude of the elastic backscattering σ of the carrier propagating in the leads. Constructing the scattering matrices of the contacts [6] one obtains the system of the linear algebraic equations connecting the ingoing and outgoing amplitudes on each of the QPCs. This permits the finding of the transmission amplitudes of the structure $f_{1,2}$ if the phaseshifts τ_j of the waves travelling inside the ring are known. Within the framework of the adiabatic approximation

the latter are given by the following expressions

$$\tau_1 = \exp\left[i\frac{\pi}{2}\left(k_{\pm}a - \frac{\Phi}{\Phi_0} \pm \frac{1}{2}\right)\right], \quad (2)$$

$$\tau_2 = \exp\left[i\frac{\pi}{2}\left(k_{\mp}a + \frac{\Phi}{\Phi_0} \mp \frac{1}{2}\right)\right], \quad (3)$$

$$\tau_1 = \exp\left[i\pi\left(k_{\pm}a - \frac{\Phi}{\Phi_0} \pm \frac{1}{2}\right)\right], \quad (4)$$

$$\tau_2 = \exp\left[i\pi\left(k_{\mp}a + \frac{\Phi}{\Phi_0} \mp \frac{1}{2}\right)\right], \quad (5)$$

where the upper sign corresponds to the spin orientation towards the center of the ring, the lower sign to the spin orientation from the center, Φ is the magnetic flux through the AB ring, Φ_0 is an elementary flux quantum. The first term at the argument of the exponent corresponds to the Aharonov–Casher phase, the second to the the Aaronov–Bohm phase, the third to the geometrical Berry phase [4]. The values of $k_{\pm}$ can be found as

$$k_{\pm} = \pm\frac{m\alpha}{\hbar^2} + \frac{1}{\hbar}\sqrt{m\left(\frac{m\alpha^2}{\hbar^2} + 2E_{\mathrm{F}}\right)}, \quad (6)$$

where m is an effective mass of the electron.

It is seen, that in presence of the Rashba SOI the electrons with a given spin projrection travelling in the clockwise and anticlockwise directions have different values of k. This result is easily understandable from the classical point of view. Indeed, neglecting the AB ring curvature, the effective magnetic field created by the Rashba SOI is given by the vector product of the external electric field and the carrier wavevector, $\mathbf{B}_{\mathrm{eff}} \sim [\mathbf{k}\times\mathbf{E}]$ and have only the radial component, which can be positive or negative depending on the direction of the carrier motion. In the adiabatic approximation the spin of the carrier moving inside the AB ring is either parallel or antiparallel to the effective magnetic field, so that the carriers with the same radial component of the spin propagating in opposite directions have different mutual orientations of the spin and the effective magnetic field. Since the carrier energy should be equal to Fermi energy in both cases, the wave numbers and of the electron propagating in the clockwise and anticlockwise should differ.

3. Numerical results

The dependence of the conductances of the structure considered on the Rashba parameter is shown in Fig. 2. The value of the external magnetic field was taken zero, and the backscattering on the QPCs was neglected, $\sigma = 0$. The total conductances of both outgoing leads, $G_{0j} = G_{0j,+} + G_{0j,-}$ are seen to reveal the AC-type oscillations. The AC oscillations of the G_{01} and G_{02} are phaseshifted, and thus tuning of the Rashba parameter allows the control of the preferential direction of the carrier's motion after passing the gated AB ring. Besides, the conductances become to be spin-dependent, and the outgoing currents are spin-polarized. Their polarization degree as a function of the Rashba parameter is shown at the lower part of the Fig. 2. It turns that the amplitude and the form of the AC oscillations of the conductance strongly depend on the backscattering amplitude. With increasing of the σ each conductance peak doubles due to the increase of the probability of the round trips in the system (not shown). The increase of the backscattering amplitude is also seen to decrease the difference of the conductances of two spin components, thus suppressing the spin filtering effect.

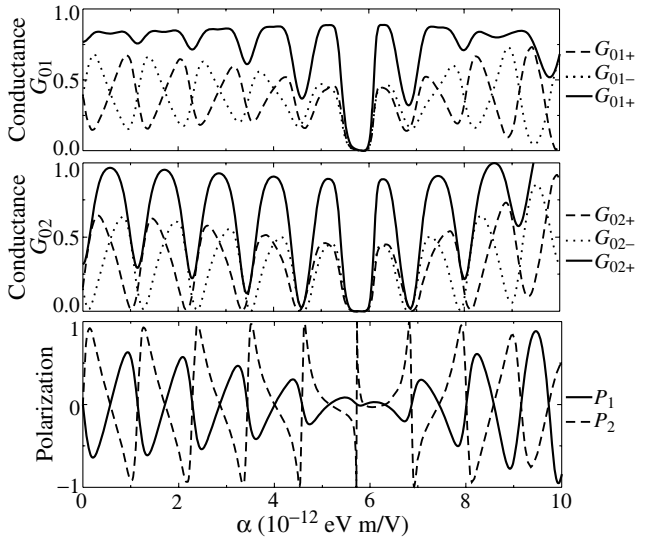

Fig. 2. From Ref. [6]. The conductances $G_{01,\pm}$, $G_{02,\pm}$, and the spin polarization degree of the outgoing currents $P_{1,2}$ as functions of the Rashba coupling parameter.

4. Conclusions

In conclusion, we have shown that the gated ballistic AB ring with three asymmetrically situated electrodes is the spintronic device that is able to demonstrate the properties of both the quantum splitter and spin filter. The conductances and spin polarization degrees of the outgoing currents in this three-terminal device are predicted to be dependent on the external gate voltage. Consequently, tuning of V_{g} allows the efficient control of the redistribution of the current between the two outgoing leads and its spin polarization.

Acknowledgements

This work has been supported by SNSF in frameworks of the programme "Scientific Cooperation" between Eastern Europe and Switzerland, Grant. IB7320-110970/1.

References

[1] I. Zutic, J. Fabian, *Rev. Mod. Phys.* **76**, 323 (2004).
[2] S. Datta, B. Das, *Appl. Phys. Lett.* **56**, 665 (1990).
[3] S. Gardelis, C. G. Smith, C. H. W. Barnes, E. H. Linfield and D. A. Ritchie, *Phys. Rev. B* **60**, 7764 (1999).
[4] A. G. Aronov and Y. B. Lyanda-Geller, *Phys. Rev. Lett* **70**, 343 (1993).
[5] I. A. Shelykh, N. T. Bagraev, N. G. Galkin, L. E. Klyachkin, *Phys. Rev. B* **71**, 113311 (2005).
[6] I. A. Shelykh, N. G. Galkin, N. T. Bagraev, *Phys. Rev. B* **72**, 235316 (2005).
[7] E. N. Bulgakov, A. F. Sadreev, *Phys. Rev. B* **66**, 075331 (2002).
[8] A. A. Kiselev, K. W. Kim, *Appl. Phys. Lett.* **78**, 775 (2001).

14th Int. Symp. "Nanostructures: Physics and Technology"
St Petersburg, Russia, June 26–30, 2006

Evolution of the photoresponse time of GaAs/AlGaAs QHE device

K. E. Spirin[1], S. V. Morozov[1], V. I. Gavrilenko[1], Y. Kawaguchi[2] and S. Komiyama[2]

[1] Institute for Physics of Microstructures, 603950 N. Novgorod, Russia
[2] Department of Basic Science, The University of Tokyo, Komaba, Meguro-ku, Tokyo 153-8902, Japan

Abstract. The characteristic time of far IR response of a quantum Hall effect (QHE) detector in GaAs/AlGaAs heterostructure has been investigated versus the magnetic field around the even values of the Landau level filling factor $\nu = 2,\ 4$. The response time is shown to have a dip minimum in the center of QHE plateau and two sharp maxima at both sides of the plateau. Outside the QHE plateau the response time drop seems to result from the rise of the equilibrium population of the Landau level over/below the Fermi energy with electrons/holes that increases the probability of photoexcited carrier recombination. The minimum at the QHE plateau center is due to the vanishing of screening of the random potential. The length scale of the potential fluctuations has been estimated.

Introduction

The quantum Hall effect based detectors operating at cyclotron resonance (CR) of 2D electrons in GaAs/AlGaAs heterostructures are known to be sensitive ($S \sim 10^7$ V/W, $NEP \leq 10^{-14}$ W/Hz$^{1/2}$) and selective detectors of far infrared (FIR) radiation [1–5]. In the QHE the longitudinal resistance R_{xx} vanishes. The finite R_{xx} emerges when electrons and holes are excited by FIR radiation at the cyclotron resonance (CR) in the delocalized (extended) states near the Landau level centers above and below the Fermi level E_F. The key role of a random potential in the mechanism of FIR-photoresponse was demonstrated in [5]. The length scale of the random potential has been shown to determine the photoresponse time constant τ that increases exponentially with the magnetic field [6]. At the same time a characteristic minimum of τ was observed in the center of the QHE plateau corresposponding to the filling factor $\nu = 2$ [5]. The present paper deals with detailed study of the detector response time evolution nearby a QHE plateau that proved to be highly nonmonotonic.

Experimental

The samples under study were Hall bars fabricated on a selectively doped GaAs/$Al_{0.3}Ga_{0.7}As$ heterostructure with high mobility 2DEG: ($\mu_{4.2K} = 4.65\times10^5$ cm^2/V s, $n_s = 3.65\times10^{11}$ cm^{-2}). They had a long 2DEG channel 50 mm × 170 mm in size patterned in a zigzag shape and fitted into an area of 4×4 mm^2 [1, 5]. All measurements were carried out either at $T = 4.2$ or at $T = 2.4$ K. A sample placed in a liquid helium in the center of a superconducting solenoid was biased by a d.c. current 2 to 4 mA. As a broad band FIR emitter we used a bulk p-Ge crystal ($N_A - N_D = 10^{13}$cm^{-3}) of 12×4×2 mm^3 in size, the ohmic contacts being deposited onto 12×4 mm^2 opposite faces. Throughout the measurements the emitter was excited with current pulses of 300 mA, 160 ms in duration and repetition rate of 16 Hz. The emitter was placed in liquid helium in the same cryostat, the distance between the emitter and the sample being 30 cm. The emitter radiation was guided to the sample through a metallic light pipe of 7 mm in diameter. The response from the detector was analyzed using either digital oscilloscope or lock-in amplifier.

Results and discussion

Typical magnetic field dependences of the longitudinal resistance R_{xx} (dotted line) and the photoresponse on the broad band radiation from the p-Ge emitter (solid line) of the QHE device as well the response time τ versus the magnetic field are shown in Fig. 1, 2. It is clearly seen that the response occurs near the $R_{xx}(H)$ minimums at the even values of the filling factor $\nu = 4$ and $\nu = 2$ corresponding to quantum Hall plateaus. At $\nu = 2$ there are two pronounced peaks in the response dependences on the magnetic field that a general trend if QHE plateaus are well developed [5]. If the "quality" of an R_{xx} minimum becomes worse (e.g. at $\nu = 4$), the two peaks merge to form a single peak structure. A typical signal oscillogram in semilogarithmic scale is given in the insert to Fig. 1. As easy to see in Fig. 1, 2 the detector time constant τ (determined as the response decay time after switching off the voltage applied to the emitter) varies over one order of magnitude with the magnetic field. It is known that there is a long-range random potential in 2DEG systems at high magnetic fields, the amplitude of the fluctuation potential reaching the order of $\hbar w_c$ in close vicinity of a QHE state due to the vanishing of the

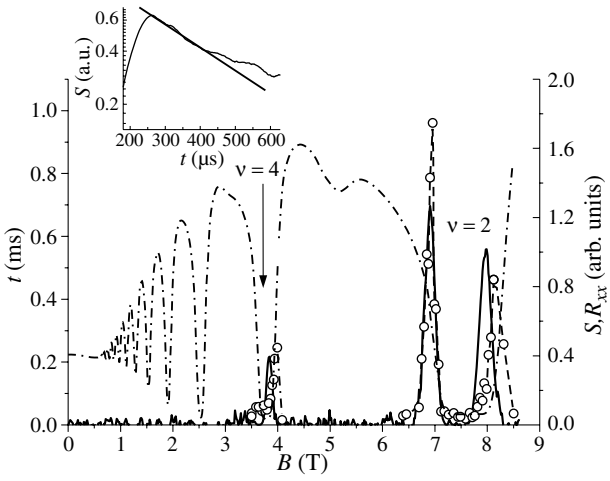

Fig. 1. Magnetic field dependences of the longitudinal resistance R_{xx} (dotted line), of the photoresponse (solid line) and the response time t versus the magnetic field (symbols connected with dashed line); $T = 2.4$ K. In the insert: typical signal oscillogram in semilogarithmic scale recorded at the left signal maximum at $\nu = 2$.

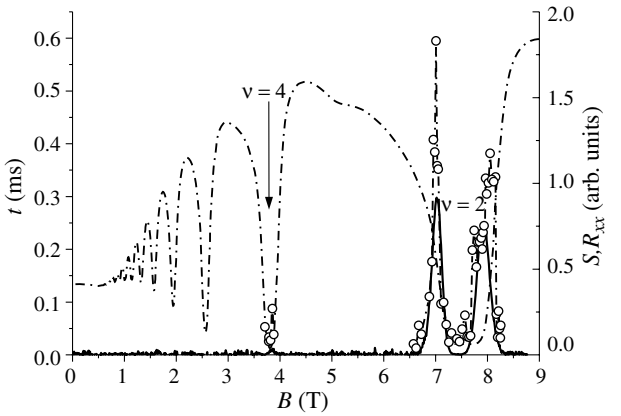

Fig. 2. Magnetic field dependences of the longitudinal resistance R_{xx} (dotted line), of the photoresponse (solid line) and the response time t versus the magnetic field (symbols connected with dashed line); $T = 4.2$ K.

screening effect [7]. This random potential results in the spatial separation of photoexcited electron and hole at the Landau levels above and below E_F, respectively, thus preventing the excited carriers from quick recombination. A localized electron (hole) can be excited occasionally to a delocalized state formed around the Landau level center thus participating in the longitudinal conductivity and giving rise to the photoresponse. The time constant of FIR response is closely related to the recombination lifetime of localized carriers separated by the characteristic distance ΔY. In strong magnetic fields in high mobility samples ΔY could exceed significantly the magnetic length $l_B = (hc/eH)^{1/2}$ that is the extension of a carrier wavefunction.

If the QHE plateau (where the longitudinal resistance practically vanishes) is well developed, the lifetime is mini-mal at the plateau center because the random potentials are not screened by the 2D electron gas thus resulting in small-scale random potential and strong overlap of the electron and hole wavefunctions. This is just the case at $\nu = 2$ in Fig. 1, 2 (cf. [5]). The lifetime increases as B departs from the plateau center within the Hall plateau because the screening becomes effective due to an increasing finite longitudinal conductance. The screening decreases randomness, and thereby causes the separation between electrons and holes to increase. This is reminiscent of the fact that τ is longer in higher-mobility samples because of smaller randomness. When B goes out of the QHE plateau region, the longitudinal conductivity does not longer increase the screening effects. At the same time, outside the QHE plateau, the number of electrons/holes that exist at the thermal equilibrium (i.e. in the "dark") increases as B increasingly departs to the left/right from the plateau center. This works to increase the recombination probability of excited carriers and leads to a decrease of the lifetime thus resulting in the observed two sharp maxima of τ versus B at $\nu = 4$ in Fig. 1, 2. The similar picture is observed at $\nu = 4$, $T = 2.4$ K (Fig. 1). Though in this case the QHE plateau is less developed and there is only one pronounced peak of the photoresponse (on right hand side of the plateau), the response time dependence on the magnetic field exhibits two-peak structure with the minimum at the plateau center. In strong magnetic fields the response time increases exponentially with the field [5, 6]:

$$\tau = A \exp\left(\Delta Y/2l_B\right)^2 = A \exp\left(H/H^*\right) , \qquad (1)$$

where the magnetic field H^* is related to the characteristic distance ΔY as $\Delta Y = 2(hc/eH^*)^{1/2}$. From the increase of the response time at $\nu = 2$ (right peak) if compared with that at $\nu = 4$ (Fig. 1, 2) one can determine the characteristic magnetic fields H^* and obtain the following data for ΔY:

$$T = 2.4\ \text{K}\,, \quad H^* = 6.55\ \text{T}\,, \quad \Delta Y = 200\ \text{A}\,,$$
$$T = 4.2\ \text{K}\,, \quad H^* = 3.12\ \text{T}\,, \quad \Delta Y = 300\ \text{A}\,. \qquad (2)$$

These values are two times less than those obtained for the sample with higher mobility [6] that corresponds to the proposed mechanism of the photoresponse of the QHE detector [5].

References

[1] S. Komiayma *et al*, *Proc. 21st Int. Conf. on Infrared and Millimeter Waves (Berlin)*, BT2 (1996).
[2] Y. Kawano and S. Komiyama, *Phys. Rev. B* **61**, 2931 (2000).
[3] A. V. Antonov *et al*, *Ins. Phys. Conf. Ser.* **N162**, 111 (1999).
[4] B. A. Andreev *et al*, *Semicond. Sci. Technol.* **16**, 300 (2001).
[5] Y. Kawano *et al*, *Journ. Appl. Phys.* **89**, 4037 (2001).
[6] I. V. Erofeeva *et al*, *Nanotechnology* **12**, 453 (2001).
[7] D. B. Chklovskii *et al*, *Phys. Rev. B* **46**, 4026 (1992).

14th Int. Symp. "Nanostructures: Physics and Technology"
St Petersburg, Russia, June 26–30, 2006

Quantum point contacts in inversion p-channel Si-MOS mesoscopic structures: Non-linear conductance and percolation path locality

A. S. Vedeneev and M. A. Feklisov
Institute of Radioengineering and Electronics, RAS, Fryazino, Moscow District.,141190, Russia

Abstract. The e^2/h and non-linear longitudinal conductance behavior in disordered Si-MOS structures with inversion p-channel at 10 μm gate length is studied. The structure disorder had been stimulated with the ion (Na^+) replacement in the insulating (under-gate) SiO_2 layer onto the Si-SiO_2 interface by the ion thermo-electric activation. The ion formed a random built-in charge ensemble, thus shown, promises both the strong fluctuation potential at the Si-SiO_2 interface and the conductance percolation character promoting the non-coherent mesoscopic effects and quantum point contact formation. The conductance G to be $< e^2/h$ is discussed vs. the gate and longitudinal voltage at the built-in charge concentration up to 10^{13} cm^{-2} and temperatures $\geq$ 77 K.

FET-applied MIS structures are presently disordered due to a high built-in charge concentration N_t at the semi- conductor-insulator interface. In practical FETs the impurity formed built-in charge random ensemble ($N_t \geq 10^{12}$ cm^{-2}) causes the surface fluctuation potential (FP), $\Delta \geq 20$ meV $> kT$ [1] even at temperatures $\geq$ 77 K. The electron transport there is carried out by a charge carrier transition in-between chaotic potential wells and restricted with the FP saddle-point constrictions thereon [2]. When the constriction sizes are comparable to the electron wave-length, the constrictions act themselves as the quantum point contacts and the e^2/h conductance quanization is followed by [3]. A broad distribution of these random contacts at the energy scale $\approx \Delta$ also causes the percolation conductance properties and non-coherent mesoscopic behavior [4]. When the structure length is comparable with the percolation cluster correlation radius L_c, the electron transport is seen to be mainly carried along a most conducting percolation path out and thus controlled by the quantum-point contacts as resistive elements of the path [5].

In the paper the e^2/h — and non-linear conductance are studied vs. the gate V_g and longitudinal V_d voltage for the case of model Si-MOS structures with inversion p-channel. The structures with the gate length $L = 10$ μm and SiO_2 under-gate layer thickness $d = 200$ nm have been fabricated on (100) low-doped n-Si substrates. The structure disorder has been stimulated with the thermo-electric ion (Na^+) activation in the SiO_2 layer and the ion replacement onto the Si-SiO_2 interface at temperatures up to 250 °C and $V_g \leq +40$ V during a time up to 30 min [5].

Fig.1 illustrates the G vs. V_g field effect curves for the temperature $T = 77$ K and different N_t. At $N_t \geq 10^{12}$ cm^{-2} the curves show a quasi-plateau appearance at $G \approx 2e^2/h$ evident as dG/dV_g maximum and minimum at $G \approx e^2/h$ and $\approx 2e^2/h$ respectively (the insert). The peculiarity means the FP formed saddle-point constrictions to act as the quantum point contacts [2] and the sample conductance G to be restricted with a most resistive contact along the only resistive path [5, 6]. The case provides an estimation of the quantum point contact characteristics in frames of the Landauer–Buttiker model [3]. The $\hbar\omega_x$ and $\hbar\omega_y$ energy parameters here correspond to the saddle-point constriction curvatures along the transport x-axis and in plane transverse the y-axis [3].

The $\hbar\omega_y$ estimation has been previously shown to be less then an order close to the $\hbar\omega_x$ value for the case (see [5, 6]).

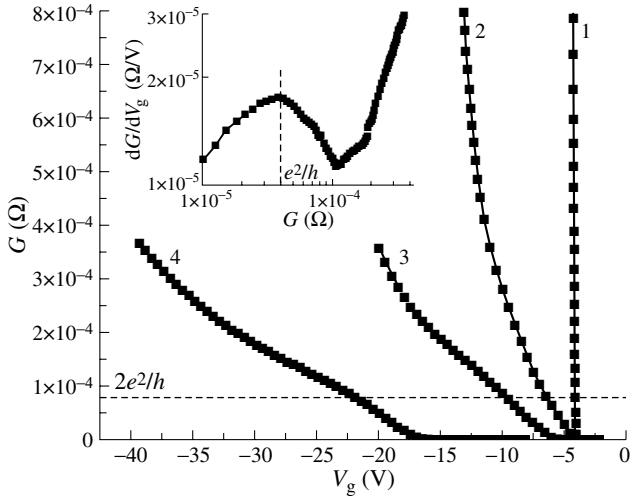

Fig. 1. G vs. V_g ($T = 77$ K) for $N_t \sim 10^{11}$ (1) and $N_t = 6\times10^{11}$ (2), 1×10^{12} (3), 2.5×10^{12} cm^{-2} (4). The insert: dG/dV_g for $N_t = 2.5\times10^{12}$ cm^{-2}.

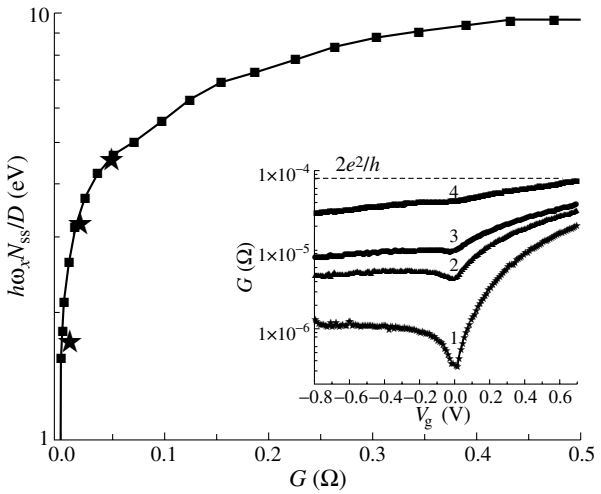

Fig. 2. $\hbar\omega_x$ vs. G obtaind by the field-effect data (■) and $G(V_d)$ dependence (⋆). The insert: G vs. V_d ($N_t = 2.5\times10^{12}$ cm^{-2}) for $V_g = 6.1$ (1), 6.7 (2), 7.1 (3) and 8.9 V (4).

Fig. 2 shows the $\hbar\omega_x$ vs. G behavior obtained by the data of Fig. 1. The estimated $\hbar\omega_x \approx 10$ meV well corresponds to the calculated values, while the following $\hbar\omega_x$ decreasing at $G < 0.1 \times e^2/h$ was previously explained as a non-parabolic local potential distribution at the saddle-point constriction (see [6]).

The observed G minimum at $V_d \approx 0$ and following it rising at $|Vd| \leq 100$ mV (the insert to Fig. 2) confirm the case when the structure conductance is restricted with the quantum contacts along the percolation path. Estimated by [7] the $\hbar\omega_x$ values for different V_g and $V_d \approx 0$ well coincide the field-effect results for $G < e^2/h$. Meanwhile, then estimated $\hbar\omega_x$ for $|Vd| > 100$ mV shows an anomaly rising with V_d up to $\hbar\omega_x \geq 200$ meV $> \Delta$. We consider the anomaly cause as the percolation path reconstruction. The V_d rise causes a quantum contact conductance rise [7] and the following V_d redistribution along the percolation path when other less resistive quantum contacts come similar conductance rise. Thus estimated the number of quantum contacts along the percolation path, $N \leq 10$, well corresponds to the N value variation at the field effect, the $N \leq L/2d \approx 25$, and the longitudinal voltage experiment, the $N \leq 20$ [5].

Acknowledgement

The work has been supported by the RFBR and ISTC (#2503).

References

[1] V. A. Gergel and R. A. Suris, *Sov. Phys. JETP* **57**, 415 (1983).
[2] Y. Meir, *Phys. Rev. Lett.* **83**, 3506 (1999).
[3] M. Buttiker, *Phys. Rev. B* **41**, 7906 (1990).
[4] Y. Imry, *Introduction to mesoscopic physics*, (Oxford: University press) 2002.
[5] A. S. Vedeneev, M. A. Feklisov, *Semiconductors* **40**, (to be published at 2006).
[6] B. A. Aronzon, A. S. Vedeneev *et al*, *Semiconductors* **35**, 448 (2001), **36**, 1241 (2002).
[7] T. Ouchterlony and K.-F. Berggren, *Phys. Rev. B* **52**, 16329 (1995).

14th Int. Symp. "Nanostructures: Physics and Technology"
St Petersburg, Russia, June 26–30, 2006

Silicon nanocrystals: photosensitizers for oxygen molecules

Dmitry Kovalev
Department of Physics, University of Bath, Bath BA2 7AY, United Kingdom

Abstract. The e^2/h and non-linear longitudinal conductance behavior in disordered Si-MOS structures with inversion p-channel at 10 μm gate length is studied. The structure disorder had been stimulated with the ion (Na^+) replacement in the insulating (under-gate) SiO_2 layer onto the Si-SiO_2 interface by the ion thermo-electric activation. The ion formed a random built-in charge ensemble, thus shown, promises both the strong fluctuation potential at the Si-SiO_2 interface and the conductance percolation character promoting the non-coherent mesoscopic effects and quantum point contact formation. The conductance G to be $< e^2/h$ is discussed vs. the gate and longitudinal voltage at the built-in charge concentration up to 10^{13} cm^{-2} and temperatures $\geq$ 77 K.

Photosensitization is an important process employed for the excitation of molecules exhibiting optically forbidden electronic transitions. Of particular interest is molecular oxygen (MO), since it is the most common oxidant and is involved in a variety of biochemical reactions. The ground triplet state of MO is chemically inert and the high reactivity of MO results from its energy-rich excited singlet states. However, spin selection rules prevent the direct excitation of MO by light.

We report on efficient resonant energy transfer from excitons confined in silicon nanocrystals to MO. We will demonstrate that silicon at nanoscale has entirely new properties due to morphological and quantum size effects: large accessible surface area and variable energies of excitons having well-defined spin structures. These features result in new emerging functionality of nanosilicon: it is a very efficient spin-flip activator of oxygen molecules and, therefore, is a chemically- and biologically-relevant material. The whole effect is based on the energy transfer from long-lived triplet excitons, confined in Si nanocrystals, to surrounding oxygen molecules via exchange of single electrons having opposite spins.

We present experimental proof for the efficient generation of singlet MO in the gas phase and in liquids. Spectroscopic analysis of the emission band of Si nanocrystals evidences that for nonresonant energy transfer the energy is conserved via multi-phonon emission process. From time-resolved measurements the characteristic time of energy transfer is found to be in the range of microseconds. The dependence of photoluminescence quenching efficiency on the surface termination of nanocrystals is consistent with short-range resonant electron exchange mechanism of the energy transfer. We will demonstrate that very small magnetic energy ($\sim$ 1 meV) can efficiently control the energy exchange processes at the scale of eV by aligning the spins of the interacting species.

Further, we will discuss implications of these findings for physics, chemistry, biology and medicine.

14th Int. Symp. "Nanostructures: Physics and Technology"
St Petersburg, Russia, June 26–30, 2006

Functionalization of semiconductor quantum dots with biomedical structures for biophotonics applications

Bakhysh Bairamov[1], Vladimir Toporov[1], Farid Bayramov[1,2], Michael Petukhov[2], Evgenyi A. Glazunov[2], Boris Shchegolev[3], Gert Irmer[4], Yang Li[5], Dinakar Ramadurai[6], Peng Shi[6], Mitra Dutta[5,7] and Michael A. Stroscio[5,6,7]

[1] Ioffe Physico-Technical Institute, St Petersburg, Russia
[2] Petersburg Nuclear Physics Institute, RAS, Gatchina, 188300, Russia
[3] Pavlov Institute of Physiology, RAS, St Petersburg, 199034, Russia
[4] Institute of Theoretical Physics, University of Mining and Technology, D-09596 Freiberg, Germany
[5] Department of Electrical and Computer Engineering, University of Illinois, Chicago, IL 60607 USA
[6] Department of Bioengineering, University of Illinois, Chicago, IL 60607 USA
[7] Department of Physics, University of Illinois, Chicago, IL 60607 USA

Abstract. We will discuss our results on study of structural properties of the nanoscale integrated colloidal semiconductor quantum dots (SQDs) such as ZnS-capped CdSe and TiO_2 conjugated with biomolecules such as short peptides and dopamine for biomedical applications.

The applications of the nanoscale integration of colloidal semiconductor quantum dots (SQDs) with biomolecules have been highlighted recently by a broad variety of applications [1–3] in the study of subcellular processes of fundamental importance in biology. These applications include the use quantum dots as a new type of fluorescent probes as well as their use as active electronic and optical components in nanostructure — biomolecules complexes of potential utility in influencing biomolecular processes in cells (Rajh *et al* 2004). Note that fluorescence microscopy is a well established, sensitive, high-resolution method for biological research, and has become one of the foundation of real-time and powerful imaging of living cells. Though they have been used for many years, these so called fluorophores usually have one or more deficiencies, including sensitivity to environmental pH changes, susceptibility to photobleaching, fixed emission spectra. In recent years, advances in nanomaterials have produced a new class of fluorescent probes by conjugating SQDs, with biomolecules that have affinities for binding with selected biological structures. These inorganic dyes have great advantages [4] over conventional organic dyes; such advantages include the option for continuously and precisely tuning the emission wavelength, and extreme stability of coated quantum dots against photobleaching as well as changes in the pH of the biological electrolytes that are ubiquitous in biological environments. These novel optical properties render quantum dots ideal fluorophores for ultra sensitive, multicolour, and multiplexing applications in cell and molecular biology.

One specific strategy for functionalizing SQDs involves conjugating CdS QDs or ZnS-capped CdSe QDs with peptide sequences with certain motifs. To determine whether the conjugation of peptides has any effects on the optical properties of the carboxyl-CdSe-ZnS dots, absorption spectra before and after attachment of peptides were measured; based on these results, it appears that attaching the peptide to the surface of the QDs does not affect the absorption spectra of the dots significantly. As shown in Fig. 1, a distinct absorption peak of the same wavelength is observed.

In order to study the incorporation of quantum dots into the internal cytoplasm of a cell, CdSe-ZnS QDs were functionalized with transferrin. We will show that the a fluorescence image of HeLa cells that were incubated with transferrin-functionalized CdSe-ZnS quantum dots reveal presence of the quantum dots inside or on the surface of the cell.

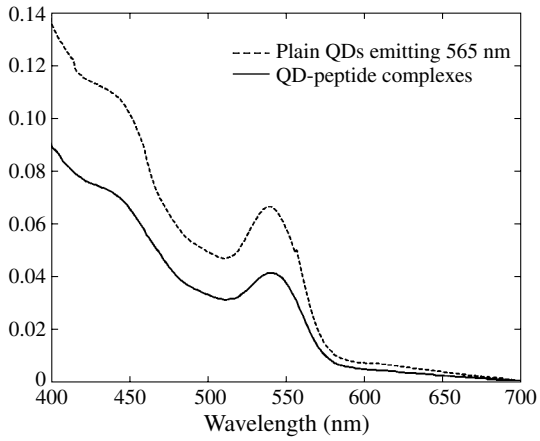

Fig. 1. Absorption spectra of the yellow CdSe-ZnS QDs before and after conjugation with peptide GGGGLDV.

Unlike these SQDs considered in this paper, titanium dioxide is not a direct bandgap semiconductor. It has been [5] demonstrated that these nanocomposites retain the intrinsic photocatalytic capacity of titanium dioxide and the bioreactivity of oligonucleotide DNA. However, these nanocomposites also possess the biologically and chemically unique property of a light-inducible nucleic acid endonuclease, which could provide a new means of using nanocomposites and photon-excited transitions in semiconductor nanoparticles for gene therapy.

Figure 2 demonstrates the inelastic light scattering spectrum of the TiO_2 nanocrystals suspended in high-purity water. The spectrum is obtained in a backscattering geometry using 532 nm excitation laser line and spectral resolution 1 cm^{-1}. We find that the spectrum is similar to that of the bulk phase anatase with an exception of the observed frequency blueshift and linewidth increase. Observed high intensity and narrow lines indicate on formation of the long-range order and high crystallinity of the TiO_2 nanocrystals. The most intense line at 158 cm^{-1} exhibited approximately 15 cm^{-1} blueshift in com-

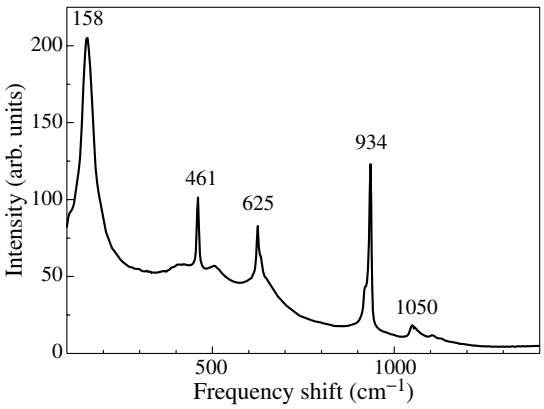

Fig. 2. Inelastic light scattering spectrum of the TiO_2 nanocrystals suspended in high-purity water. The spectrum is obtained in a backscattering geometry using 532 nm excitation laser line.

parison to the bulk anatase and can be definitely prescribed to the E_g optical phonon of the anatase phase.

We will show that the blueshift observed can be explained as a direct result of phonon confinement. This influence of the phonon confinement is quantitatively estimated in terms of spatial correlation model [6] and show that the crystalline size of the TiO_2 nanocrystals is approximately 4 nm. Theoretically calculated value of the confined phonon linewidth for the 4 nm crystalline size of the TiO_2 nanocrystals of approximately 26 cm^{-1} is smaller then the measured one of 32 cm^{-1} indicating contribution of the non-stoichiometry effect. We note that additional contribution to the observed broadening of the confined phonon line can be caused by interfacial vibrations [7].

New features in the vibrational spectra of TiO_2 nanocrystals conjugated with dopamine will be also discussed.

Acknowledgements

The work at the Ioffe institute was supported by the grant No. 06-02-16304 of the Russian Foundation for Basic Research.

References

[1] B. H. Bairamov, V. V. Toporov, F. B. Bayramov, M. Petukhov, E. A. Glazunov, B. Shchegolev, Y. Li, D. Ramadurai, P. Shi, M. Dutta and M. A. Stroscio, *International Journal of Nanoscience* **5**, (2006).

[2] M. A. Stroscio and M. Dutta, Advances in Quantum Dot Research and Technology: The Path to Applications in Biology, in Advanced Semiconductor Heterostructures, World Scientific Publ. Co., Singapore, 2003; S. Rufo, M. Dutta and M. A. Stroscio, *J. Appl. Phys.* **93**, 2900 (2003).

[3] M. A. Stroscio and M. Dutta, Biological Nanostructures and Applications of Nanostructures in Biology: Electrical Mechanical and Optical Properties (New York: Kluwer–Academic), 2004.

[4] A. P. Alivisatos, *J. Phys. Chem.* **100**, 13226 (1996).

[5] T. Paunesku, T. Rajh, G. Wiederrecht, J. Maser, S. Vogt, N. Stojicevic, M. Protic, B. Lai, J. Oryhon, M. Thurnauer and G. Woloschak, *Nat. Mater.* **2**, 343 (2003).

[6] H. Shen and F. H. Pollak, *Appl. Phys. Lett.* **45**, 692, 1984.

[7] W. F. Zhang, Y. L. He, M. S. Zhang, Z. Yin and Q. Chen, *J. Phys. D: App. Phys.* **33**, 912 (2000).

14th Int. Symp. "Nanostructures: Physics and Technology"
St Petersburg, Russia, June 26–30, 2006

GaAs nanowhiskers: MBE growth optimization and observation of space-ordered biological structures

G. E. Cirlin[1,2,3], A. A. Evstrapov[1], A. L. Bulyanitsa[1], V. G. Dubrovkii[2,3], I. P. Soshnikov[2,3], A. A. Tonkikh[1,2,3], Yu. B. Samsonenko[1,2,3], N. K. Polyakov[1,2], N. V. Sibirev[1] and V. M. Ustinov[2,3]

[1] Institute for Analytical Instrumentation RAS, Rizhsky 26, 190103, St Petersburg, Russia
[2] Ioffe Physico-Technical Institute, St Petersburg, Russia
[3] Saint Petersburg Physico-Technical Centre of the Russian Academy of Sciences for Research and Education, Khlopina 8/3, 195220 St Petersburg, Russia

Abstract. We report on the molecular beam epitaxial growth of GaAs nanowhiskers on the GaAs (111)B substrates catalyzed by gold particles using the vapor-liquid-solid growth. Optimized structures embedded in nanobiochips have demonstrated space-ordering phenomena of biological substance when fluorescein was introduced into a chip.

Introduction

Nanowhiskers, or vertical nanowires (NWs), having a high (10–100) length/diameter ratio and a diameter of several tens of nanometers, are a new attractive object in modern nanotechnology due to an interesting physics of quasi-1D systems and their potential applications in electronics, biology, field-emission devices etc. [1]. In most cases, NWs are fabricated by epitaxial techniques by exploring the so-called vapor-liquid-solid (VLS) growth with different metal seed particles as the growth catalyst. Recently, we have shown that molecular beam epitaxy (MBE) has several advantages in NW formation, in particular due to the diffusion origin of NW growth [2, 3]. Concerning biological applications, the "lab-on-a-chip" technology seems to be one of the most promising directions where semiconductor NWs can be monolithically integrated within the chip. To fully realize the advantages of biological nanochips based on NWs, such as a high degree of flux stabilization, well reproducible hydro-dynamical properties and the possibility for the control of nanofluxes streaming, we require the NWs arrays with appropriate properties, including their height, diameter, surface density and, in some cases, selective doping possibility.

In this work, we report on the experimental and theoretical studies of MBE growth of GaAs NWs, optimization of their properties, and finally demonstrate that a specially injected chemical or biological substance (in our case, a fluorescein) can produce regular arrangement of species within an array of NWs.

1. Experimental details

In our growth experiments, the NW formation procedure consisted of three stages [2]. First, GaAs(111)B substrates were placed in the growth chamber of the EP1203 MBE setup, where the oxide was removed from the substrates and the GaAs buffer layer was deposited. The GaAs buffer layer thickness was kept about 300 nm in all growth runs. In comparison with our previous study, we put the Au source into the growth chamber of our MBE setup and deposited gold at the second stage under the ultra-high vacuum conditions. The Au film thickness was amounted to 0.1–1 nm for different samples studied. At the third stage, the samples were heated up in order to form the eutectic Au-Ga seed drops on the GaAs surface. After that, the GaAs layers with the effective thickness H from 300 to 1500 nm were deposited. The deposition rate of GaAs $V = 1$ ML/s and As/Ga fluxes ratio $F = 1$ were kept constant in all growth runs and the substrate temperature T was varied from 500 to 630 °C for different samples. The structures were n-type doped to the concentration $\sim 5 \cdot 10^{17}$ cm^{-3}. The visualization of surface morphology was performed by applying the CamScan S4-90FE scanning electron microscope (SEM) with a field emission gun, operating in the regime of secondary electron emission. To fabricate nanobiochips, the NWs samples were cut into pieces and integrated in polymethylmethacrylate (PMMA) matrices having 100 μm size cross-shaped channels. Leica TCS SL confocal scanning microscope (CSM) with excitation by 488 nm laser was used to visualize the static fluorescein patterns. We note that our nanobiochips design is different from that proposed in [4], where NWs were first cut down and only then horizontally placed on the substrate. In our case, we used NW arrays as they were grown and incorporate them into a monolithic NW — substrate base.

2. Optimization of MBE growth parameters (theory and experiment)

To understand the effect of growth conditions influence on the NW structural properties, we have developed a kinetic model of NWs formation taking into account (i) adsorption of atoms on the drop surface from the material flux of rate V; (ii) desorption from the drop surface; (iii) diffusion flux of adatoms from

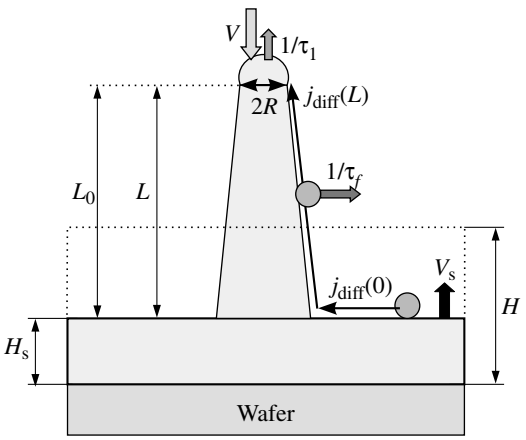

Fig. 1. Schematics of NW growth during MBE: (a) — adsorption, desorption and the ad-atom diffusion to the drop and the growth of substrate surface; the NW length $L = L_0 - H_s$.

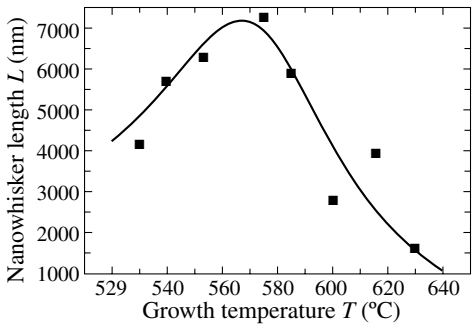

Fig. 2. Experimental (dots) and calculated temperature dependences of NW length.

the surface towards the NW top $j_{\text{diff}}(L)$ and (iv) growth of non-activated surface with rate Vs. The complete description of the model can be found in Refs. [3, 5] and schematically presented in Fig. 1. The model allows one to predict theoretically the dependence of NW length L on the growth parameters V, T and the NW radius R (at fixed fluxes ratio F and deposition thickness H). As shown in Ref. [6], the growth of NWs during MBE is mainly controlled by the adatom diffusion from the substrate surface to NW tops along their sidewalls while the adsorption-desorption contribution on the drop surface is less important and can often be neglected. It has been also shown theoretically that in the diffusion-induced mode of NW formation during MBE (i) NW length decreases with increasing the growth rate; (ii) the $L(T)$ dependence at otherwise same conditions has the maximum within the range from 550 to 600 °C (the position of the maximum depends mainly on R) and (iii) the $L(R)$ dependence is decreasing. As an example, Fig. 2 demonstrates the comparison of theoretical $L(T)$ dependence with our experimental data for the GaAs NWs. The both curves show that the longest NWs are obtained within the interval from 560 to 600 °C. Qualitative explanation of this effect is the following. At sufficiently low temperatures, the increase in surface temperature fastens the adatom diffusion on the surface and also increases the surface concentration of adatoms. These two effects increase the outgoing diffusion flux of adatoms to the NW bases $j_{\text{diff}}(0)$, while the diffusion-induced growth rate $j_{\text{diff}}(L)$ remains approximately equal to $j_{\text{diff}}(0)$ due to the low desorption rate from the sidewalls. Therefore, at low temperatures the $L(T)$ dependence must be increasing. When, however, the temperature becomes too high, the fast desorption from the sidewalls takes place. In this case adatoms will mainly evaporate before they reach the NW tip and the diffusion-induced contribution to the overall growth rate will decrease. Theoretical curve provides a good fit with the experimental data. Additionally, we have found that an increase of Au portion leads to the decrease of NWs length and to the increase of their diameter together with larger variation in lateral sizes.

3. Observation of fluorescein regular arrangement using integrated NWs in a chip

The CSM image of biochip NWs sample containing the pumped fluorescein is presented in Fig. 3. Usually, fluorescein is used for labeling different biological particles. In Fig. 3 one can clearly see self-ordered chemical clusters having a fractal-like shape. In order to describe theoretically the observed structures, we use a simple model taking into account the Coulomb interaction between negatively charged

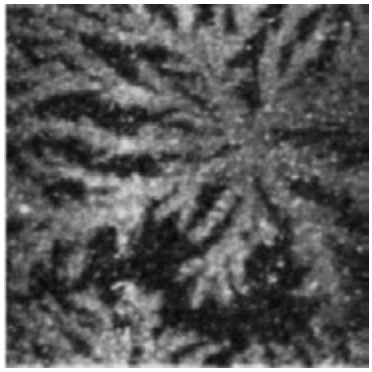

Fig. 3. Steady-state CSM image after fluorescein solution was embedded in NW-based nanochip. Size of the image is 100×100 μm.

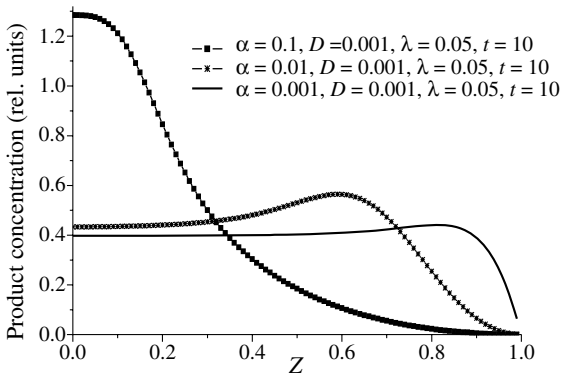

Fig. 4. Results of numerical calculations of product concentration profiles on normalized coordinate calculated with different α.

(due to the doping) NWs and the biological species. Within the frame of this model, NW is described as a vertical homogeneously charged rod with electrostatic field $\overline{E} \cong \overline{r}/r^2$. The convective velocity along the normalized coordinate Z, where $Z = \pm 1$ are the two symmetric NW positions in a specie, can be now written as $V(Z) = \frac{2Z}{1-Z^2}\alpha$, with α being the parameter describing the specie mobility. The profile concentration C (in the liquid phase) and P (in the solid phase) can be obtained as solutions to the two differential equations $\frac{\partial C}{\partial t} = -\lambda C + D\frac{\partial^2 C}{\partial z^2} + \frac{\partial}{\partial z}\left(\frac{2\alpha z}{1-z^2}C\right)$ and $\frac{dP}{dt} = \lambda C$ with boundary conditions of the second type $\frac{\partial C}{\partial z}\,|_{z=0} = 0$; $\frac{\partial C}{\partial z}\,|_{z=1} = 0$. In Fig. 4 we present the calculated profiles $P(Z)$. The main conclusions of the model are the following: i) increase of α leads to the increase of velocity gradient and, therefore, of the concentration gradient near the NW boundaries, ii) increase of D and λ leads to blurring the product concentration. These two factors stimulate the formation of space-ordered clusters.

Acknowledgements

The authors are grateful to the financial support received from SANDiE program, RFBR grants No. 05-02-16495 and No. 05-02-08090-OFI, scientific grant of St Petersburg Scientific Center and different scientific programs of RAS.

References

[1] M. S. Gudiksen, *et al*, *Nature* **415**, 617 (2002).
[2] G. E. Cirlin, *et al*, *Semiconductors* **39**, 557 (2005).
[3] V. G. Dubrovskii, *et al*, *Phys. Rev. B* **71**, 205325 (2005).
[4] G. Zheng, *et al*, *Nature Biotechnology* **23**, 1294 (2005).
[5] V. G. Dubrovskii, *et al*, *Phys. Rev. E* **73**, 021603 (2006).

14th Int. Symp. "Nanostructures: Physics and Technology"
St Petersburg, Russia, June 26–30, 2006

Raman study of bio-conjugated CdSe/ZnS core-shell quantum dots

T. V. Torchynska[1], A. Diaz Cano[1], S. Ostapenko[2], *Yu. V. Vorobiev*[3], S. Jimenez-Sandoval[3], J. Gonzalez-Hernandez[4] and T. Zhukov[5]

[1] SEPI Nacional Polytechnic Institute, Mexico D.F. 07738; Mexico
[2] University of South Florida, 4202 E Fowler Ave, Tampa, FL, USA
[3] CINVESTAV, Unidad Queretaro, 76230 Queretaro, Mexico
[4] CIMAV, 31109 Chihuahua, Mexico (on sabbatical leave from CINVESTAV-Queretaro)
[5] Lee Moffitt Cancer Center, Tampa, FL, USA

Abstract. Core-shell CdSe/ZnS quantum dots (QDs) are promising as bio-luminescent markers: being coupled to bio molecules (proteins), they change the photoluminescence (PL) intensity which presents the possibility to detect the variation of a number of these proteins (antibodies) in blood to make a diagnosis of a particular disease. We studied the effect of bio molecules conjugated to QDs upon the Raman spectra, and found that in some cases the conjugation leads to marked changes of the spectra, so that the detection of bio molecules could be done more precisely than using PL measurements. An explanation of the effect is proposed.

Introduction

The nanometer-scale II–VI semiconductors (quantum dots QDs) have unique optical characteristics such as photoluminescence (PL) with sufficiently high quantum efficiency in surface passivated core-shell structures [1]. A particularly interesting case is the CdSe/ZnS core/shell coupling, where a large band-gap material (ZnS) serves as a surface passivating layer and as a barrier assisting the electron-hole confinement in the CdSe core [2].

It has been reported [3] that these QDs can be used as bio-luminescent markers varying the PL intensity when coupled to different bio molecules and thus indicating changes in quantity of these molecules. The attempts were made to employ this effect for diagnosis of diseases, like ovarian cancer or pulmonary fibrosis giving rise to specific antibodies in living tissue whose detection is a method of detection of a particular disease.

However, the study of QDs PL intensity is not a very reliable test since this intensity can vary for other reasons (like photo-chemical bond restructure or trap recharging [4]). It is of interest to look for other effect of QDs bio-conjugation that could be of qualitative, not just quantitative character.

Here we present the results of investigation of Raman light scattering in CdSe/ZnS QDs coupled to different bio molecules. It is shown that at least in two cases the coupling leads to appearance of new lines in the Raman spectra thus giving an opportunity to error free detection of the conjugation. We explain the result in terms of SERS (Surface Enhanced Raman Scattering).

1. Results and discussion

The commercially available CdSe/ZnS polymer coated quantum dots from Quantum Dot Corp. were used in a form of colloidal particles diluted with phosphate buffer (PBS) in a 1:200 volumetric ratio [5]. Samples of QDs (bio conjugated and non-conjugated) in the form of an mm-size spot were dried on a polished surface of crystalline Si substrate to ensure a low level of light scattering background. The proteins used for conjugation were Osteopontin, Interleukin, PSA (Prostate-Specific Antigen) and OC125 (antigen used for detection of ovarian cancer). The quantitative effect of conjugation was found in the first two cases.

Raman scattering spectra were measured at room temperature in a Lab Ram–Dilor micro Raman spectrometer using a He-Ne laser (632.8 nm) as an excitation source with a power of 20 mW in backscattering configuration.

Figure 1 presents the Raman spectra of QDs designed for luminescence with the PL wavelength peak at 605 nm, conjugated (curve 1) and non-conjugated (2) with Osteopontin molecule. The sharp peak around 521 cm^{-1} belongs to the Si substrate and that at 114 cm^{-1} is of instrumental origin. As can be seen, the spectrum of pure QDs has no other features. However, the spectrum of bio-conjugated QDs has three additional bands at 206.8, 273.1 and 414.6 cm^{-1}. Figure 2 shows similar data for another type of QDs (PL wavelength 655 nm) and another bio molecule (Interleukin, or interferon-beta 2). In the spectrum of bio conjugated QDs we see again 3 additional bands slightly shifted compared to the previous case (208.6, 278.4 and 419.9 cm^{-1}).

It seems surprising that the Raman bands appearing in spectra of conjugated QDs practically do not depend neither on the molecule type (although, some molecules produce the effect of appearance of these bands, and others not) nor on the QDs elec-

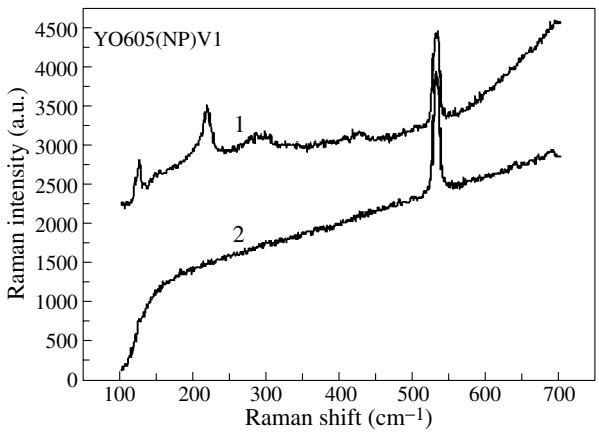

Fig. 1. Raman spectrum of conjugated with Osteopontin molecule (1) and non-conjugated (2) Quantum Dots.

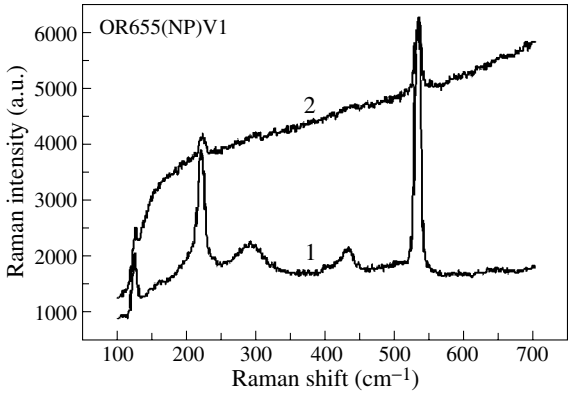

Fig. 2. Raman spectrum of conjugated with Interleukin molecule (1) and non-conjugated (2) Quantum Dots.

tronic structure. The strongest band at 207 cm^{-1} corresponds to the QDs core material CdSe and its overtone is observed at 414 cm^{-1}, while the band at 273 cm^{-1} agrees well with the TO mode of ZnS. Thus, we could state that in pure QDs we do not observe Raman lines of the dots material (most probably, due to the very small volume of nanosized particles) whereas the presence of certain bio molecules greatly enhances the corresponding signal. In this sense, the effect observed is similar to the well known Surface Enhanced Raman Scattering (SERS) effect usually caused by the presence of metal particles or interfaces in the studied material. A small difference in the Raman peak positions in two cases discussed can be attributed to the difference in size of the corresponding QDs.

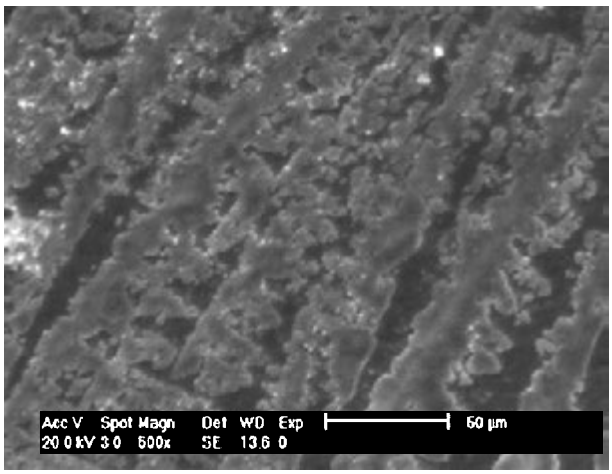

Fig. 3. SEM images of Si substrate covered with conjugated Quantum Dots.

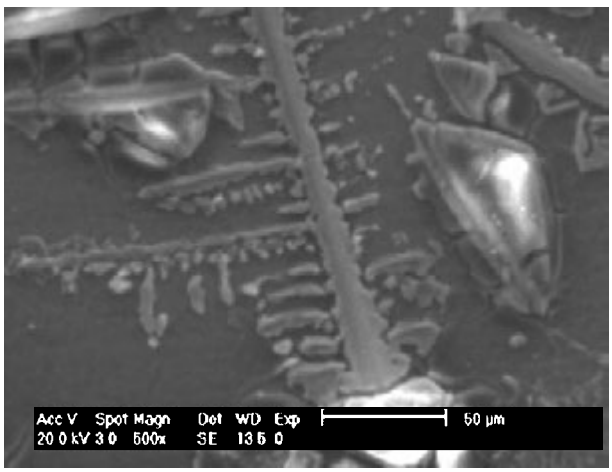

Fig. 4. SEM images of Si substrate covered with non-conjugated Quantum Dots.

A simple model for SERS was developed in [6]. The model is based on the assumption that near the interface of a base material with a metal, amplitude of the atomic vibrations giving rise to Raman light scattering could greatly increase due to the effect of electrostatic interaction of an ionized atom with the charge induced in metal (mirror image charge with opposite sign). Estimations made in [6] show that the effect could be quite large (hundreds-fold increase of amplitude).

The interaction between the core material of the QDs and the bio molecules is, most probably, based on Van der Vaals forces that actually result from the interaction due to induced dipole moments. This interaction is practically equivalent to the electrostatic interaction between a charged atom and its image charge induced in the metal. Therefore, we consider that this model is applicable to the case studied here, and can explain the obtained results. The actual mechanism of interaction between QDs and different bio molecules needs further investigation, which will be able to answer the question why some molecules produce the effect and others do not.

Figures 3 and 4 present the images of the Si substrate having QDs with the conjugated proteins (Fig. 3) and without them (4) obtained with Scanning Electron Microscopy. One could see that even in micron scale the two pictures are quite different: the percentage of area covered with conjugated QDs is much larger than that corresponding to pure QDs. The corresponding protein molecules are quite large (thousands of atoms) and are capable of providing strong enough interactions with the QDs (which actually starts from the conjugation itself); this is all it would take to observe the SERS effect.

2. Conclusion

We observed the marked effect of two types of bio molecules (that of Osteopontin and of Interleukin) upon the Raman spectra of CdSe/ZnS core-shell Quantum Dots: the band belonging to core material appeared in the spectra of bio-conjugated quantum dots. The effect is attributed to the enhancement of core material atoms vibrations caused by interaction with protein molecules (a kind of SERS effect). The results obtained could be useful in the application of Quantum Dots mentioned as bio markers for diagnostic purposes.

References

[1] M. A. Hines *et al*, *J. Phys. Chem.* **100**, 468 (1996).
[2] M. Bruchez *et al*, *Science* **281**, 2013 (1998).
[3] E. R. Goldman *et al*, *J. Phys. Stat. Sol. b* **229**, 407 (2002).
[4] N. E. Korsunska*et al*, *Semicond. Sci. Tech.* **20**, 876 (2005).
[5] www.qdots.com
[6] F. J. Garc'a-Rodriguez *et al*, *J. of Raman Spectroscopy* **29**, 763 (1998).

14th Int. Symp. "Nanostructures: Physics and Technology"
St Petersburg, Russia, June 26–30, 2006

Interaction of isolated semiconductor quantum dots with charged amino acids

G. G. Zegrya, N. L. Bazhenov and K. D. Mynbaev
Ioffe Physico-Technical Institute, St Petersburg, Russia

Abstract. Advantages of semiconductor quantum dots (QDs) for study and diagnostics of biological systems are discussed. A new method for amino acid diagnostics using semiconductor QDs is proposed. Interaction of isolated QDs with charged amino acids is studied in detail. It is shown that such interaction results in a shift of the QD luminescence spectra by several dozens of meV. This effect provides new possibilities for identification of biological objects using QDs.

Introduction

Semiconductor quantum dots (QDs) are used effectively in opto- and nanoelectronics. For example, infrared (IR) lasers have been fabricated on the basis of semiconductor QD heterostructures. Such devices have improved characteristics as compared with those of quantum well lasers.

Recently, QDs found new applications in biology and medicine [1]. First of all, QDs are studied as new tools for obtaining an image of living cells and their diagnostics *in vivo*. As shown elsewhere [2–5], QDs have considerably better properties than fluorescent chromophores which are currently used in biology and medicine, namely: (i) higher quantum yield; (ii) optical activity in the long-wave range of the spectrum; (iii) and significantly greater photochemical stability.

Optical properties of QDs strongly depend on their dimensions. The emission wavelength is increased from 400 to 1000 nanometers with increasing the QD radius from 50 to 200 Å.

Unlike other fluorescent systems, semiconductor QDs have a threshold excitation energy; i.e., they can be excited by such and greater energies. Thus, the threshold energy must not be equal to the energy of transition within the QDs. Therefore, many QDs can be excited by the light with the same wavelength, whereas each QD emits the light with a different wavelength. Thus, unique spectral properties of QDs are very promising for biological and medicine studies.

In a number of papers (e.g., [5]) a study of multipurpose semiconductor QD samples for detection of cancer cells in living organisms and for creating images of these cells was described. A study of cancer cell growth in animals demonstrated that QDs were accumulated in tumors due to both improved transmittivity and binding to the biomarker surface of cancer bodies according to the antibody mechanism. High-sensitivity color images of cancer cells have been obtained directly in living organism. Thus, new methods of obtaining high-sensitive images of molecular objects in a living organism using QDs were demonstrated.

Due to their narrow and symmetrical peaks in emitting spectra, semiconductor QDs can be used for optical diagnostics where different colors (wavelengths) and different intensities of the spectral peaks can be used for identification of genes, amino acids, proteins and the molecular chains.

This paper presents a new prospective method of amino acid diagnostics using semiconductor QDs. The main topic is an effect of the amino acid-QD interaction on the emission spectrum of QDs.

1. Energy shift of QDs in the presence of amino acids

It is known that all 20 amino acids fall into four groups: ones with negative charge; with positive charge; polar and nonpolar. Each amino acid type interacts with QDs in a different way and, thus, differently affects energy levels of charge carriers in QDs and, consequently, the QD emission spectrum. We have carried out detailed microscopic calculation of electron and hole spectra in QDs, which interact with charged amino acids.

Let us consider an interaction of QD with charged amino acid (AA). For the sake of simplicity we shall approximate AA with a uniformly charged sphere. The electrical field on the surface of such sphere is:

$$E = \frac{Q}{\varepsilon_1 R^2}, \tag{1}$$

where R is the sphere radius; Q is the charge, wherein $Q = \frac{4}{3}\pi\rho R^3$ and ρ is the charge density; ε_1 is the dielectric constant.

Since the energy gap of QD is less than that of the surrounding material, the charge carrier motion in QD is confined by its volume. Thus, optical properties of QD are determined by the electronic structure of a spatially confined electron-hole pair (exciton). The QD–AA interaction can be considered as effect of the electric field of AA on QD. The case is that under an external electric field a shift of dimensional quantization energy levels for an electron-hole pair in QD in the band-to-band absorption range is determined by the quadratic quantum-dimensional Stark effect [6, 7]. It should be noted, that such shift is caused not only by the quadratic quantum-dimensional Stark effect but also by the linear Stark effect. There can exist certain conditions in low-dimensional structures when the linear Stark effect dominates. In the present publication, we shall consider solely a contribution resulted from the quadratic quantum-dimensional Stark effect. A detailed comparative analysis of the contributions due to both Stark effects will be carried out in a more extended publication.

As in [6, 7], let us consider a spherical QD with the radius a, the dielectric constant of QD being $\varepsilon_2 \gg \varepsilon_1$. Let us study the effect of the electric field E on the electron-hole pair spectrum. The electron-hole pair Hamiltonian for QD exposed to the electric field includes, in addition to the kinetic energies of the electron and hole, the following: the energy of the Coulomb interaction of the electron and hole; the energy of the electron and hole interaction with their own images; the energies of interactions with "foreign" images, and the energy of electron and hole interaction with the field. The Hamiltonian can be

significantly simplified when $\varepsilon_2 \gg \varepsilon_1$.

We shall consider a case when the QD dimension is confined by the condition:

$$a_{\rm h} \ll a \le a_{\rm e}\,, \tag{2}$$

where $a_{\rm e} = \frac{\varepsilon_2\hbar^2}{m_{\rm e}e^2}$, $a_{\rm h} = \frac{\varepsilon_2\hbar^2}{m_h e^2}$ are Bohr's radii of electron and hole, respectively; e is the electron charge; $m_{\rm e}$ and $m_{\rm h}$ are the effective masses of electron and hole, respectively. If condition (2) is satisfied, the polarization interaction provides the main contribution to the potential energy of electron and hole [7]. Furthermore, when $m_{\rm e} \ll m_{\rm h}$, condition (2) allows us to consider the heavy hole motion in the fields with the electron potential averaged over the total electron path (the so called adiabatic approximation). The electronic structure of an electron-hole pair within the adiabatic approximation can be easily calculated; see, for example [7]. After averaging the potential energy of the electron-hole pair over electron wave functions (in the case of a spherical potential well), we have an expression for the potential energy of a heavy hole moving in the adiabatic potential field of an electron:

$$U = \frac{\hbar^2}{2m_{\rm h}a_{\rm h}a}\left[\frac{1}{1-r_{\rm n}^2/a^2} + 2{\rm Ci}(2\pi n_{\rm e}) - 2{\rm Ci}(2\pi n_{\rm e}r_{\rm n}/a) + \frac{\sin(2\pi n_{\rm e}r_{\rm n}/a)}{\pi n_{\rm e}r_{\rm n}/a} + 2\ln(r_{\rm n}/a) + \frac{\varepsilon_2}{\varepsilon_1} - 4\right] - eEr, \tag{3}$$

where $n_{\rm e}$ is the electron principal quantum number; $r_{\rm n}$ is the distance between the hole and the centre of QD; ${\rm Ci}(y)$ is the integral cosine. The last term in (3) results in shifting the potential well bottom for the hole in QD by a value:

$$\Delta x = \frac{\varepsilon_2/e}{1 + \frac{2}{3}\pi^2 n_{\rm e}^2} Ea^2 \tag{4}$$

as well as in shifting the dimensional quantization energy levels by a value:

$$\Delta E_{\rm h} = -\frac{\varepsilon_2}{2\left[1 + \frac{2}{3}\pi^2 n_{\rm e}^2\right]} E^2 a^3\,, \tag{5}$$

where $x = r_{\rm n}/a$. From (5) it follows that the energy shifts for electron and hole do not depend on the hole principal quantum number $n_{\rm h}$ and are determined solely by $n_{\rm e}$. Under the electron field E the shift of dimensional quantization energy levels ΔE_c will be about:

$$\Delta E_c \approx \varepsilon_2 \left(\frac{a_{\rm e}}{a}\right) E^2 a^3\,.$$

For the ground electron state $n_{\rm e} = 1$ and if $(a_{\rm e}/a) \le 1/3$, $E_{\rm e} \ll E_{\rm h}$. Thus, expression (5) describes the quantum-dimensional quadratic Stark effect, when quantum-dimensional energy levels shift under the electric field by a value proportional to a^3E^2. Figure 1 shows an emission spectrum of InAs QD without and with an account for interaction with AA. For calculation, we took the following parameters of InAs: $a = 5\times10^{-7}$ cm, $\varepsilon_2 = 14.9$, $Q = 5e$, $R = 10^{-7}$ cm, $\varepsilon_1 = 4$. The resulting shift of the emission peak was approximately 50 meV.

2. Conclusion

A case was considered when polarization interaction of an electron and hole with the QD environment contributes to rearrangement of the spectrum. It is shown that when QD interacts with charged amino acids, a shift of dimensional quantization energy levels for an electron-hole pair in QD in the band-to-band absorption range is determined by the quadratic quantum-dimensional Stark effect. An analytical expression for the energy shift for electron and hole levels has been obtained as a function of the electric intensity and QD radius. A case was considered when dielectric constants of QDs and their environment are essentially different. This approach allows us to significantly simplify the expression for the polarized interaction energy of electron and hole with the QD environment.

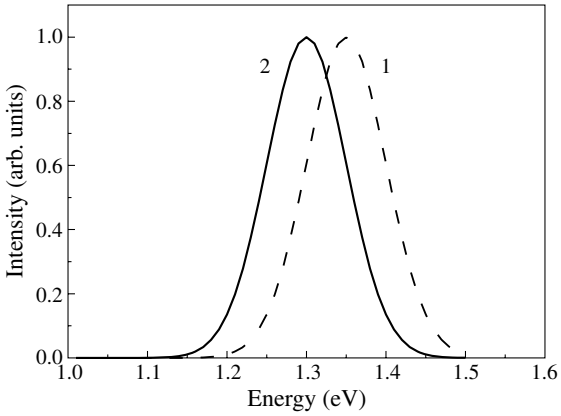

Fig. 1. Emission spectrum of InAs QD without (curve 1) and with an account for interaction (curve 2) with charged amino acid.

The energy shift of electron and hole levels defining the shift of the QD luminescence peak has been calculated.

Thus, a good method for using semiconductor QDs for experimental detection of charged amino acid presence with high accuracy is provided.

Acknowledgements

This work was supported in part by Russian Foundation for Basic Research (grants No. 04-02-16786, 04-07-90148, 05-02-16679) and program of the Russian Academy of Sciences for supporting scientific schools.

References

[1] C. W. Warren *et al*, *Science* **281**, 2016 (1998).
[2] X. Michalet *et al*, *Science* **307**, 538 (2005).
[3] Xiaohu Gao *et al*, *Nature Biotechnology* **22**, 969 (2004).
[4] Zh. Zhelev *et al*, *Anal. Chem.* **78**, 321 (2006).
[5] A. Aharoni *et al*, *J. Am. Chem. Soc.* **128**, 264 (2006).
[6] S. I. Pokutnii, *Semiconductors* **34**, 1079 (2000).
[7] S. I. Pokutnii *et al*, *J. Appl. Phys.* **96**, 1115 (2004).

14th Int. Symp. "Nanostructures: Physics and Technology"
St Petersburg, Russia, June 26–30, 2006

Effective radiative recombination of electron and hole Tamm-like interface states in ZnSe/BeTe heterostructures

A. N. Litvinov[1], *A. S. Gurevich*[1], V. P. Kochereshko[1], A. V. Platonov[1], B. A. Zyakin[1], A. Waag[2] and G. Landwehr[3]

[1] Ioffe Physico-Technical Institute, St Petersburg, Russia
[2] Braunschweig Technical University, 38106 Braunschweig, Germany
[3] Physikalisches Institut, Universität Würzburg, 97074 Würzburg, Germany

Abstract. We present an experimental data, which demonstrate a basically new mechanism of carrier radiative recombination in semiconductor heterostructures — recombination via Tamm-like interface states. Bright line was observed in photoluminescence spectra of MQW ZnSe/BeTe heterostructures at the energies, which correspond to the optical transitions between electron and hole Tamm-like interface states in studied heterosystem. It was found that for short-period ZnSe/BeTe heterostructures the intensity of photoluminescence via Tamm-like interface states is at least ten times higher than the intensity of emission caused by conventional interband recombination.

Recently, it was reported about the direct experimental evidence of the existence of the Tamm-like interface states (TIS) in semiconductor heterostructures [1]. Spectral dependencies of the natural in-plane optical anisotropy of periodical undoped ZnSe/BeTe heterostructures with non-equivalent interfaces have been studied using a spectroscopic ellipsometry. A set of structures with different period was studied. For each heterostructure, the peculiarities were observed in the spectra within the bandgap of the structure. The analysis of the spectral position of the peculiarities depending on the period of the structure have allowed us to conclude about the existence TIS. The state of this type is a satellite of the conduction or valence band and can be considered as an electron or a hole interface state, respectively.

In this work we studied low-temperature photoluminescence (PL) spectra of periodical type-II ZnSe/BeTe heterostructures with non-equivalent Zn-Te:Be-Se interfaces. Fig. 1 represents the band diagram of studied structures. Each sample contained 20 periods of ZnSe/BeTe. The thickness of layers was 30/15, 40/20 and 100/50 Å. The samples were grown by MBE on (100)-oriented GaAs semi-insulating substrates. No intentional doping of the samples was undertaken.

There are two types of interband optical transitions typical for ZnSe/BeTe heterostructures (see for example [2]). They are: spatially direct transitions (DT) in ZnSe layers connecting electron localized in QW and above barrier hole state, and spatially indirect transitions (IT) connecting an electron localized in ZnSe and a hole localized in BeTe (Fig. 1). But as it was mentioned above, our resent low-temperature ellipsometric studies have revealed another one type of optical transitions in the studied heterostructures [1]. This transitions connect an electron and a hole TIS and marked as (RL) at Fig. 1.

PL spectra of studied heterostructures registered at samples temperature 80 K are presented on Fig. 2. Photoluminescence was excited using pulsed solid-state laser emitting at the wavelengh 355 nm. Solid curves correspond to relatively low excitation density (100 W/sm^2); dotted curves correspond to high excitation density (6000 W/sm^2).

Fig. 2(a) represents the spectra obtained of structure with thickness of ZnSe/BeTe layers 100/50 Å. The PL bands correspond to spatially direct optical transition (DT) as well as spatially indirect ones (IT) are clearly seen.

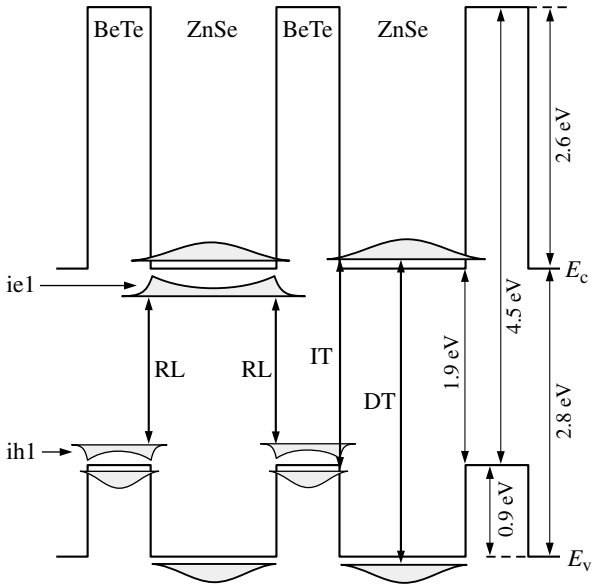

Fig. 1. Band diagram and optical transitions in periodical type-II ZnSe/BeTe heterostructures. Electron and hole Tamm-like interface states marked as ie1 and ih1 correspondingly.

Figures 2(b) and 2(c) represent PL spectra for short period heterostructures with thickness of layers 40/20 and 30/15 Å correspondingly. The bright PL band (RL) was observed for this structures in the range of the bandgap with energy being lower than the energy of spatially indirect transitions (IT). The spectral position of this band ($E_{RL} \sim 1.75$ eV) is in excellent agreement with the energy of optical transition connecting electron and hole TIS (RL, Fig. 1) measured previously by spectroscopic ellipsometry for the same structures and at the same temperatures [1]. Thus we attribute this PL band to radiative recombination of an electron and a hole TIS.

One can see that at low excitation densities the intensity of PL caused by recombination via TIS is much more higher compared to PL caused by conventional interband recombination (Fig. 2(b) and 2(c), solid curves). For short period heterostructures PL via TIS was observed at the temperature range from 12 to 100 K and at the excitation density range from 100 to 6000 W/sm^2. It should be also noticed that at the studied ranges of temperatures and excitation densities now noticeable photo-

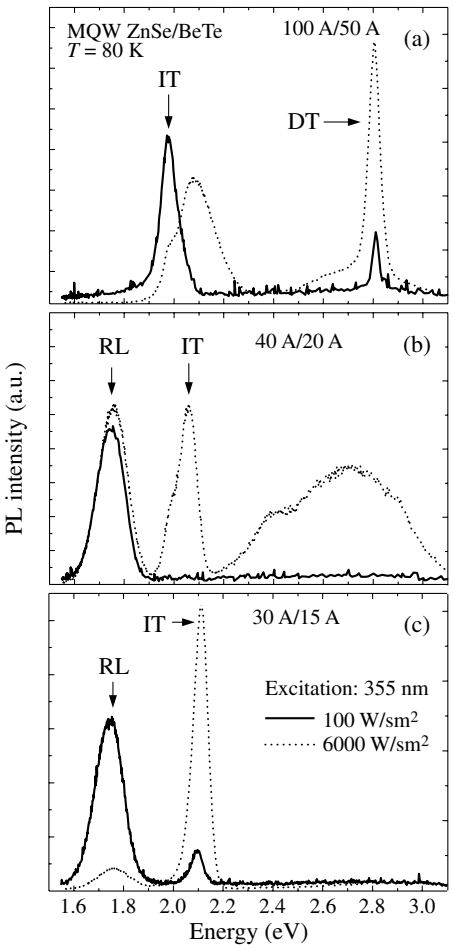

Fig. 2. Photoluminescence spectra of periodical type-II ZnSe/BeTe heterostructures with different value of period. RL-emission band corresponding to recombination of electron and hole Tamm-like interface states.

luminescence via TIS was observed for ZnSe/BeTe heterostructures with layer thickness 100/50 Å and higher. It allows us to conclude that the probability of carrier being captured into TIS dramatically depends on the period of heterostructure.

Acknowledgements

This work was supported in part: by the grant No. 06-02-17246-p of Russian Foundation for Basic Research, Program of Presidium RAS, and by the grant No. 2006-RI-19.0/001/529 of Russian Federal Agency of the Science and Innovations.

References

[1] A. S. Gurevich, V. P. Kochereshko, A. V. Platonov, B. A. Zhyakin, A. Waag and G. Landwehr, *Phys. Solid State* **47**, 10 1964 (2005).

[2] A. S. Gurevich, V. P. Kochereshko, A. V. Platonov, A. Waag, D. R. Yakovlev and G. Landwehr, *Phys. Solid State* **46**, 4 780 (2004).

14th Int. Symp. "Nanostructures: Physics and Technology"
St Petersburg, Russia, June 26–30, 2006

Phonon replica fine structure in CdSe/ZnSe quantum dots

T. Kiessling[1], A. V. Platonov[2], G. V. Astakhov[1,2], S. Mahapatra[1], T. Slobodskyy[1], W. Ossau[1], G. Schmidt[1], K. Brunner[1] and L. W. Molenkamp[1]

[1] Physikalisches Institut, Universität Würzburg, 97074 Würzburg, Germany
[2] Ioffe Physico-Technical Institute, St Petersburg, Russia

Abstract. We report on resonant photoluminescence and photoluminescence excitation spectroscopy of CdSe/ZnSe quantum dots. The studied samples have been tailored such that the energetic spacing of the quantized levels is close to the optical phonon energy of the host lattice. The observed phonon bands clearly yield fine structure, which is well resolved by polarization sensitive spectroscopy and assigned to optical phonons of different symmetry points of the Brillouin zone.

Introduction

Quantum Dots (QDs), often designated as artificial atoms attract huge interest for both basic research as well as applications, e.g. QD lasers. Detailed understanding of the coupling of phonons and carriers is a key feature for the description of energy relaxation in QDs, which plays a vital role in any technological application. Especially for the II–VIs, which are highly polar materials, the electron-phonon interaction can be significant due to Fröhlich interaction.

Two general cases are considered in the literature, the weak and the strong coupling regime. The latter is met when the energetic distance between electronic levels in QDs coincides with the LO phonon energy [1, 2, 3]. In this case the formation of polarons occurs and the quantum dot can no longer be described by a pure electronic state. We show that this leads to massive reconstruction of the photoluminescence and to the formation of a phonon replica band, displaying fine structure rather than a single sharp peak.

Experimental

The experiments presented here were performed on self-assembled CdSe/ZnSe QDs grown on (001) GaAs substrate by molecular beam epitaxy. To avoid unwanted photocarrier diffusion into the substrate a 300 nm $Zn_{0.97}Be_{0.03}Se$ buffer was grown between the dotlayer and the substrate. The QDs were formed by depositing one monolayer of CdSe on a ZnSe surface and subsequently capped with ZnSe. For details of the growth see [4]. In such small sized QDs the energy level of the exciton ground state is relativly close to the ZnSe barrier, being just 200 meV below. Furthermore, the samples for our study were selected such that the energetic splitting between exciton ground and excited states matches an integral multiple of the LO phonon energy of the host material ZnSe, so that the above condition for strong coupling was met.

Photoluminescence (PL) and photoluminescence excitation (PLE) measurements were performed using a dye-laser charged with Stilbene-3 for excitation, which allowed for continuous tuning of the excitation energy from the ZnSe barrier to the exciton ground state in the QD. The optical spectra were recorded by a LN_2 cooled CCD camera mounted to a one meter spectrometer with 1200 mm^{-1} grating. In addition, the optical alignment was probed using a photoelastic modulator, an avalanche photo diode and a two channel photon counter as detection scheme. All data were taken at $T = 1.6$ K.

Results

First, PL measurements were performed on the QD ensemble with the linearly polarized excitation set parallel to the [110] crystalline axis of the sample. The results are summarized in Figure 1. When exciting above the ZnSe barrier one probes the inhomogenously broadened PL band of the QD ensemble, which peaks at $E = 2.649$ eV and has a full width at half maximum (FWHM) of 35 meV. It is a direct display of the size distribution of the QDs adding up the narrow lines that are emitted by individual QDs. Furthermore, the energetic position of the QD ensemble luminescence shows the small size of the QDs [4].

As the excitation is tuned below the ZnSe barrier and close to the energetic position of the PL band, a sharp peak arises and the ensemble peak luminescence is blueshifted by $\Delta E = 11$ meV accompanied by a narrowing of the PL band. It is well established that the sharp peak is a phonon replica [ZnSe LO(Γ)] of the laser line, quasi-resonantly exciting photocarriers into the QDs, which then relax into energetically lower states of QDs and thus give rise to the reformation of the PL band.

The PL undergoes a massive reconstruction when the excitation is tuned into excited states of the QDs (whose energetic position is known form previous work, see [5]). The FWHM

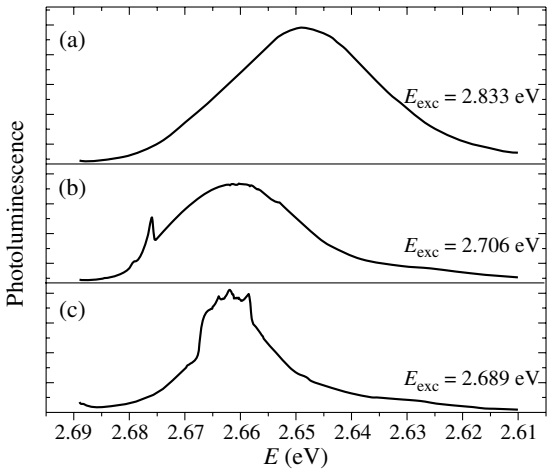

Fig. 1. Evolution of the PL signal as a function of excition energy E_{exc} at $T = 1.6$ K. (a) QD ensemble luminescence with excitation above the ZnSe barrier. (b) Appearance of the phonon replica with excitation below the ZnSe barrier. (c) Resonant excitation into higher QD states. The phonon replica no longer appears as a narrow peak, but rather as a broad band revealing fine structure.

of the PL is reduced to 14 meV and the phonon replica no longer appears as a narrow line but instead manifests as a broad band that clearly yields fine structure. At least three peaks are resolved out of which only the lowest energetic one can be ascribed to the ZnSe LO(Γ) phonon.

For a more detailed description of the phonon replica fine structure, polarization-sensitive PLE was performed on the QDs. Assuming that the optical polarization is conserved during the fast phonon relaxation process, only the PL polarized parallel to exciting polarization (thus, parallel to the [110] crystalline direction) should contain information on the phonon band. Therefore we recorded PLE for polarization parallel and perpendicular to the excitation polarization direction and took the difference of the normalized spectra for background removal. The result can be depicted from Figure 2.

From the background corrected PLE four phonon bands are obtained, out of which the three lower energetic ones restore with high accuracy the fine structure that was previously observed in the PL spectra. The intensities of the phonon band are changing because of decreased signal-to-noise ratio as the energy rises, which is also the reason no fine structure is resolved in the fourth peak. This can easily be understood, as increased dephasing occurs as more phonons are involved in the relaxation process. Again, the outmost peak situated 31.7 meV above E_{det} can be ascribed to LO(Γ)-ZnSe phonon. Three additional marks are noticable: First, the energetic width of 10 meV is conserved for all four phonon bands in the spectrum, as is their energetic spacing of 31 meV suggesting a correlation to the ZnSe LO(Γ) phonon. Second, the energetic position of the fine structure peaks within the phonon band reproduce for all phonon bands. Finally, the intensities of the fine structure peaks relative to each other apparently change within the PLE spectrum, but no clear trend can be extracted throughout the development of the phonon band in the spectrum.

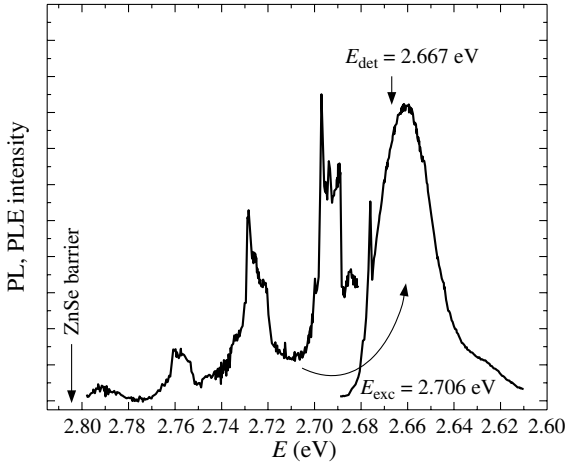

Fig. 2. PL and PLE spectrum at $T = 1.6$ K, background corrected by taking the difference in intensity of PL polarized parallel and perpendicular to the excitation polarization. The PLE, detected at $E_{\mathrm{det}} = 2.667$ eV, reveals four phonon bands, out of which the first three resolve fine structure.

Discussion

It appears to be unlikely that these peaks can be explained as additional ternary alloy $Zn_{1-x}Cd_xSe$ phonon modes arising from interdiffusion of Zn and Cd within the dots. Such modes should be statistically distributed and therefore result in broad bands without defined structure when probing over the ensemble. Furthermore, they can hardly be interpreted in terms of interface (IF) phonons, since these additional modes should appear at integral multiples of one distinct energy in the PLE spectrum. This then would lead to an increase of the overall width of the phonon band as the excitation energy is increased and should also result in an increase of the energetic spacing of the various peaks within the band, which both is not observed in our data.

However, our findings can be explained assuming that the strong three dimensional confinement of the excitons enables interaction with phonons of any wave vector. It appears to be possible that for QDs the k-vector conservation is relaxed in the case of strong coupling [3,6]. In this scenario the width of the polaron band reflects the difference of the minimal and the maximal energy of the LO-phonon branch, which for our data corresponds well with LO-phonon dispersion in ZnSe [7]. The resonance fine structure then relates to specific points of the LO-branch. Especially the lowest energetic peak within the polaron band corresponds nicely to the LO-phonon at the X-point of the Brillouin zone with an energy of $E = 24.2$ meV. On balance, we are then able to reconstruct the LO phonon dispersion within the Brillouin zone from our experimental data.

As of now it is not completly clear whether or not the middle peak of the polaron band arises from the LO(L) phonon. In this picture, it is also surprising that phonons with large k-vectors couple almost as strong as the LO(Γ) phonon. Furthermore, it remains uncertain, how the coupling strength depends on the excitation. These questions appear to be perspective for future studies.

Acknowledgement

This work has been supported by the Deutsche Forschungsgemeinschaft (SFB 410) and RFBR.

References

[1] T. A. Nguyen, S. Mackowski, H. E. Jackson *et al*, *Phys. Rev. B* **70**, 125306 (2004).
[2] H. Rho, H. E. Jackson, S. Lee *et al*, *Phys. Rev. B* **61**, 15641 (2000).
[3] U. Woggon, D. Miller, F. Kalina *et al*, *Phys. Rev. B* **67**, 045204 (2003).
[4] S. Mahapatra, C. Schumacher, T. Kiessling *et al*, *Acta Phys. Pol. A* **108**, 769 (2005).
[5] A. V. Platonov, T. Kiessling, G. V. Astakhov *et al*, *phys. stat. sol. (c)* **3**, 924 (2006).
[6] A. Reznitsky, A. Klochikhin, S. Permogorov *et al*, *phys. stat. sol. (b)* **229**, 509 (2002).
[7] B. Hennon, F. Moussa, G. Pepy *et al*, *Phys. Lett.* **36A**, 376 (1971).

14th Int. Symp. "Nanostructures: Physics and Technology"
St Petersburg, Russia, June 26–30, 2006

Nonequilibrium carrier statistics in deep InGaN quantum dots

D. S. Sizov[1], W. V. Lundin[1], E. E. Zavarin[1], V. S. Sizov[1], A. F. Tsatsul'nikov[1], A. M. Mintairov[1,2], R. A. Suris[1], N. N. Ledentsov[1] and J. Merz[2]

[1] Ioffe Physico-Technical Institute, St Petersburg, Russia
[2] University of Notre Dame, Notre Dame, IN 46556 USA

Abstract. We studied optical properties of quantum dot (QD) structures with different carrier activation energy from QD ground states to continuous spectrum edge. As it is shown experimentally and theoretically using rate equation model, in case of high value of the activation energy (0.4–0.5 eV for electrons and holes in sum) the nonequilibrium carrier population in QD states takes place even at room temperature. Influence of this carrier population on the QD optical properties such as peak position of QD ensemble luminescence and its quantum efficiency is also studied.

Introduction

Strong carrier confinement in semiconductor quantum dots (QDs) leads to improvement of the quantum efficiency and thermal stability of light emitting devices. In this case, however, nonequilibrium carrier statistics in QD levels is expected that makes description of QD optical properties more complex as compared with quasiequilibrium case [1, 2]. Theoretical approaches of different carrier population in QDs are being developed, and the future development as well verification on certain semiconductor systems is of importance for both fundamental and applied purposes.

Studies of InGaN QDs are motivated by opportunity to create and develop visible range light emitting devices. Owing to strong values of band offsets, deeply localizing InGaN QDs are now commonly used in active area of highly efficient GaN based LEDs and are also promising for high temperature operation of emerging types of devices such as single photon sources [3]. Indeed, as we have previously shown, progress in growth technology of QD arrays allowed us to increase activation energy from QD ground states to continuous spectrum edge up to the value of 0.8 eV [4], i.e. much more than value of $k_B T$ at room temperature.

In this work we discuss the rate equation model and its application for this system. We demonstrate influence of the activation energy value on emission wavelength peak position and quantum efficiency depending on temperature and excitation power.

1. Experimental structures

The studied LED structures contained multiple QD epitaxial layers separated by 7 nm GaN barriers. QDs are formed by a phase separation leading to formation of 3–5 nm wide In-rich areas with narrower bandgap where carriers are confined [4]. In order to increase the phase separation we used special growth method described in [5]. The structures were studied experimentally using photoluminescence (PL), electroluminescence (EL) and X-ray difractometry. Quantum dot origin of luminescence was revealed using near field spectroscopy. Details of the structure growth and characterization can be found in [5]. The schemes of bandgap along QD layer for two samples with different degree of phase separation are presented in Fig. 1a. In the first sample the phase separation was stimulated while the average InN concentration was decreased. EL results of these structures are shown in Fig. 2. The structures demonstrate almost equal peak position and almost equal linewidth at low pumping power indicating that InN fraction in QDs as well the QD ensemble inhomogeniety is almost the same for both the structures. By X-ray diffraction and calculations in spherical QD shape assumptions we were able to evaluate average In composition and estimate InN concentration inside QDs. We found that, InN concentration inside QDs is $\sim 30\%$ while InN concentration between QDs is $\sim 4\%$ and $\sim 9\%$ for the structure with the stimulated phase separation (SPS) and without it correspondingly. The difference in In content between

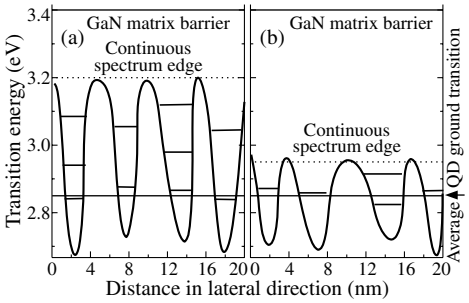

Fig. 1. Schematic diagram of bandgap in InGaN QD layer for (a) Deep QDs grown with SPS, (b) shallow QDs grown without SPS.

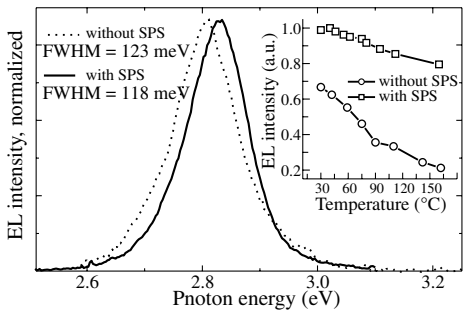

Fig. 2. Electroluminescence spectra of the QD structures. Insert shows temperature dependences of intensity.

QDs means that the total electron and hole activation energy from QD ground states to continous spectrum $\Delta E = \Delta E_n + \Delta E_p$ is 400–500 meV for the first structure and below 200 meV in the second structure that is in agreement with our previous optical studies [5].

2. Theoretical approach

General model description. In our theoretical approach we used the model developed in ref [1]. We consider carrier capture to QD levels, escape to continuous spectrum where they can move in lateral directions and the recombination of electron–hole pairs by the following set of rate equations:

$$\sigma = \frac{4}{3}\pi r_T^2 \frac{r_T}{l},\ f_e'^i = \gamma_n^i \left[n(1-f_e^i) - n_1^i f_e\right] - \frac{1}{\tau_r^i} f_e^i f_h^i,$$
$$f_h'^i = \gamma_p^i \left[p(1-f_h^i) - p_1^i f_h^i\right] - \frac{1}{\tau_r^i} f_e^i f_h^i,$$
$$J_r = \frac{e}{S\tau_r} \sum_i^{N_{QD}} f_h^i f_e^i \qquad (1)$$

that have zero left part in stationary case. The charge neutrality equation must also be satisfied:

$$\frac{1}{S} \sum^{N_{QD}} \left[f_h^i - f_e^i\right] + n - p = N_0, \qquad (2)$$

here $f_{e,h}^i$ — electron and hole populations in i-th QD ground states, $\gamma_{p,n}^i$ — parameters of electron and hole capture from continous spectrum where their planar density is n and p correspondingly, S — ensemble area and τ_r — carrier radiative lifetime. Carrier escape parameters n_1, p_1 play a key role in carrier statistics and depend on

activation energy $\Delta E = E_{\rm mob} - E$ ($E_{\rm mob}$ — electron-hole transition energy at continous spectrum edge and QD ground state transition energy E) in the following way:

$$n_1^i = N_{\rm c} \exp\Big(\frac{\Delta E_n^i}{k_{\rm B}T}\Big), \quad p_1^i = N_{\rm v} \exp\Big(\frac{\Delta E_p^i}{k_{\rm B}T}\Big), \qquad (3)$$

here $k_{\rm B}$ — Boltzmann constant, $N_{\rm c,v}$ — effective density of states in continuous spectrum.

Application to InGaN QDs. We assumed $\Delta E_n = \beta \Delta E$, $\Delta E_p = (1-\beta)\Delta E$, $\beta = 0.7$ according to band offset ratio. We also assumed Gaussian distribution of QD ground state transitions depending on E. Here we named this funcion $\rho(E)$ and normalized it to total planar QD density $N_{\rm sQD}$. The Gauss linewidth parameter $\sigma \sim 100$ meV. Spontaneous luminescence emission spectra is expressed as following:

$$R_{\rm sp} = \rho(E) f_{\rm h}(E) f_{\rm e}(E)\,. \qquad (4)$$

The following condition is sufficient for the quasiequilibrium carrier population with any pumping: $\gamma_n n_1 \tau_{\rm r} > 1$ and $\gamma_p p_1 \tau_{\rm r} > 1$. We take into account only ground states because their recombination dominates in considered pumping power range. Using time resolved data [4] and the data concerning QD density we estimated $\gamma_{n,p}$ to be ~ 0.1 cm^2/s and $\tau_{\rm r} \sim 10^{-9}$ s. Our calculations of $f_{\rm e,h}(E)$, and $R_{\rm sp}(E)$ by derivation (1)–(4) show that in the case of InGaN QDs the carrier statistics is qualitatively different at different $E_{\rm mob}$. In case of shallow QDs (when $E_{\rm mob}$ is near E_0 that is maximum of $\rho(E)$, the quasiequilibrium population for both electrons and holes is observed at 300 K as it is shown in Fig. 3b. In this case emission peak position is equal E_0–$\sigma^2/k_{\rm B}T$ that was shown by P. G. Eliseev in [6]. However, if $E_{\rm mob} - E_0 \geq 400$ meV no Boltzmann carrier statistics of electrons in most QD ground states takes place even when, $f_{\rm e,h} \ll 1$. Holes distribution remains still near Boltzmann's so there is no influence of random population effects described in [2]. One can see in Fig. 3a that the nonequilibrium electron population takes place in QDs with transition energy E below some value $E_{\rm d}$ that we called demarcation transition (DT). We found that in this case the DT determines the emission peak position. We also derived dependence of $E_{\rm d}$ and the quantum efficiency η on the product $f_{\rm e}(E) f_{\rm h}(E)$ as the following:

$$E_{\rm d} \approx E_{\rm mob} + \frac{k_{\rm B}T}{2\beta} \ln\Big(\frac{\alpha \cdot f_{\rm h}(E_{\rm d}) f_{\rm e}(E_{\rm d})}{(\gamma_n \tau_{\rm r})^2 N_{\rm c}^2}\Big), \qquad (5)$$

$$\eta \approx (f_{\rm h}(E_{\rm d}) f_{\rm e}(E_{\rm d}))^{1/2} \left(\xi^{1/2}\tau_n + \xi^{-1/2}\tau_p\right) \times \frac{\rho(E_{\rm d}) N_{\rm QD}}{\tau_{\rm r}(N_{\rm c}N_{\rm v})^{1/2}} \exp\Big(\frac{\Delta E_{\rm a}}{2k_{\rm B}T}\Big), \qquad (6)$$

where e — electron charge, $\xi = n/p = N_{\rm c}/(\alpha N_{\rm v}) \exp((1 - 2\beta)\Delta E_{\rm a}/(k_{\rm B}T))$, τ_n, τ_p — electron and hole nonradiaive lifetimes [7], $\alpha = \gamma_n/\gamma_{\rm h}$ $\Delta E_{\rm a} = \min(E_{\rm mob} - E_0 - \sigma^2/k_{\rm B}T,\ E_{\rm mob} - E_{\rm d})$.

The dependences (5) and (6) are of interest because they represent dependence of emission peak position and quantum efficiency on the intensity in spectrum maximum through $f_{\rm h}(E_{\rm d}) f_{\rm e}(E_{\rm d})$ using (4). A consequence of (5) is that in strongly inhomogeneous system the dependence of peak position on intensity obeys logarithmic law. A consequence of (6) is that activation energy $\delta E_{\rm a}$ determines the efficiency thermal stability also in this nonequilibrium case. In case of stable peak position η is proportional to a square root of intensity.

3. Experimental results and comparision with the theory

As it is shown in the insertions in Fig. 2 the structure grown using SPS with higher $E_{\rm mob}$ demonstrates ~ 2.5 times better thermal stability of quantum efficiency that is in agreement with (6) since $\Delta E_{\rm a}$ for this structure is ~ 2.5 time larger. We also studied emission peak position and $\Delta E_{\rm a}$. We can see in Fig. 4b that for the structure grown without SPS with $\Delta E_{\rm a} < 200$ meV PL peak position is stable and corresponds to $\sigma^2/(k_{\rm B}T)$ law of Boltzmann population and so $\Delta E_{\rm a} = E_{\rm mob} - E_0 - \sigma^2/(k_{\rm B}T)$ unless the pumping power

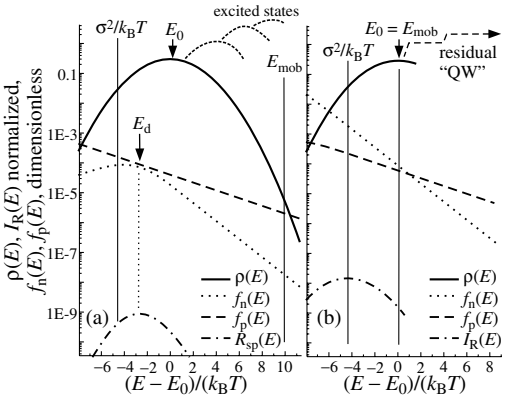

Fig. 3. Calculated spectral dependences of carrier populations and emission spectra.

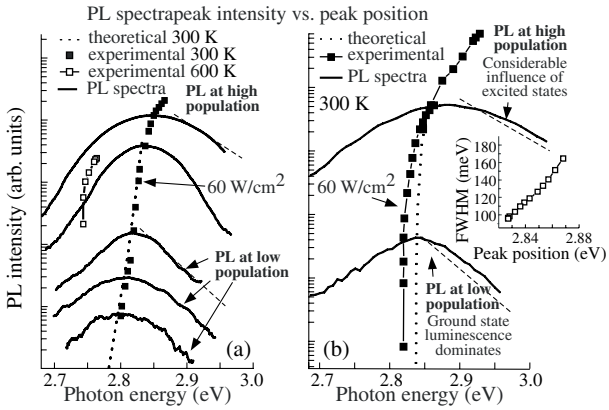

Fig. 4. Experimental PL data and comparison with theory.

is higher than 60 W/cm^2 when strong shift to high energy side and increase of linewith is observed due to transition to no Boltzmann population [6] and considerable population of excited states. In the case of stable peak position we observed square root dependence of η on PL and EL intensity (not shown here).

At the same time as it is shown in Fig. 4a for the structure with $\Delta E \approx 500$ meV steady shift of PL peak position is observed even at pumping power below 60 W/cm^2 due to change of Ed according to (5). This situation takes place when $E_{\rm d} > E_0 - \sigma^2/(k_{\rm B}T)$ and so $\Delta E_{\rm a} = E_{\rm mob} - E_{\rm d}$. It is however important to note that stable peak position at low population is observed in this structrure at higher temperature of 600 K when the quasiequilibrium carrier population takes place even in this structure (Fig. 4a). Good agreement with calculation is observed in both structures in low population case. We believe that the strong shift at power above 60 W/cm^2 is caused by filling of states and considerable population of excited states. We can see in this case deviation from theoreticcal dependence because we considered here only ground state transitions. The influence of the excited states in this system which is also accompanied by decrease in η will be considered in our further works.

Acknowledgements

This work has been supported by RFBR and by NATO linkage grant CBP.NR.CLG 981516.

References

[1] L. V. Asryan and R. A. Suris, *Sem. Sci. Technol.* **11**, 554 (1996).
[2] M. Grundmann and D. Bimberg, *Phys. Rew. B.*, **44**, 9740 (1997).
[3] C. Santori *et al*, *Letters to nature* **419**, (10) (2002).
[4] I. L. Krestnikov *et al*, *Phys. Rev. B* **66**, 155310 (2002).
[5] D. S. Sizov *et al*, Proc. 13th Int. Symp. "Nanostructures: Physics and Technologies", St Petersburg, 296–297, 2005.
[6] P. G. Eliseev *et al*, *J. of Appl. Phys.* **93**, 5404 (2003).
[7] B. E. Larson *et al*, *Phys. Rev. B* **37**, 4137 (1988).
[8] S. Yu. Karpov and Yu. N. Makarov, *Appl. Phys. Lett.* **81**, 4721 (2002).

14th Int. Symp. "Nanostructures: Physics and Technology"
St Petersburg, Russia, June 26–30, 2006

The band gap composition dependence of InGaN alloys

V. Yu. Davydov[1], A. A. Klochikhin[1,2], A. V. Sakharov[1], E. E. Zavarin[1], M. A. Sinitsyn[1], A. N. Smirnov[1], A. P. Skvortsov[1], M. A. Yagovkina[1], Hai Lu[3] and William J. Schaff[3]

[1] Ioffe Physico-Technical Institute, St Petersburg, Russia
[2] Nuclear Physics Institute, 188350, St Petersburg, Russia
[3] Department of Electrical and Computer Engineering, Cornell University, Ithaca, New York 14853, USA

Abstract. We present the results of investigations of the photoluminescence and absorption spectra of InGaN alloys in the entire range of compositions. The crystal structure and the alloy compositions were controlled by X-ray, Raman scattering, and Rutherford back-scattering techniques. It is shown that the behavior of the band gap as a function of composition is characterized by large bowing parameter of 2.5 eV.

Introduction

InGaN alloys are direct gap semiconductors whith band gap changing from near IR to near UV spectral regions at varying the composition. As a result, these compounds are very promising for fabrication of heterostructures and nanostructures suitable for different applications. The basic physical properties of these alloys have been investigated only recently [1]. The composition dependence of the InGaN band gap is one of the most important characteristics of these alloys. However, the information on this fundamental parameter is still scanty and contradictory. For example, the estimates of the band gap bowing parameter of InGaN alloys, which characterizes the deviation from the linearity, range from 1.4 eV to 2.7 eV [2–6]. All previous studies were concerned with the alloys in a limited range of compositions. The present study has been performed to study the band gap of InGaN alloys as a function of the composition for a large set of the samples covering all compositional range from InN to GaN.

Samples

The samples studied in this work were hexagonal $In_xGa_{1-x}N$ epilayers grown on (0001) sapphire substrates. Alloy films in the composition range of ($0.35 < x < 0.95$) were grown by plasma-assisted molecular-beam epitaxy [7]. The films in the compositional range of ($0.05 < x < 0.30$) were grown by using metalorganic vapor phase epitaxy. The film thickness ranged from 0.2 to 0.5 μm in the MBE grown samples and was around 0.5 μm in the MOVPE grown films. All alloys were nominally undoped films of the n-type with a Hall carrier concentration in the range from 1×10^{18} to 1×10^{19} cm^{-3}. X-ray and Raman scattering were used to characterize the crystal structure.

Experimental results

Figure 1a shows typical X-ray data for alloys studied in this work. It is seen that the Bragg reflections shift monotonically with the increase of Ga content from their position for InN toward those for GaN. It has been found that FWHM for $\theta-2\theta$ scan for alloys to be considerably larger than similar characteristics for the binary compounds. This indicates that alloys are more inhomogeneous than GaN or InN crystals. However no macroscopic phase separation was revealed in alloys, since their X-ray profiles are single-mode and near symmetrically shaped in all cases. The compositions of alloys were determined by Rutherford back-scattering of deuterons. This technique gives more precise composition values than X-ray technique because it is independent, for example, on the lattice strain.

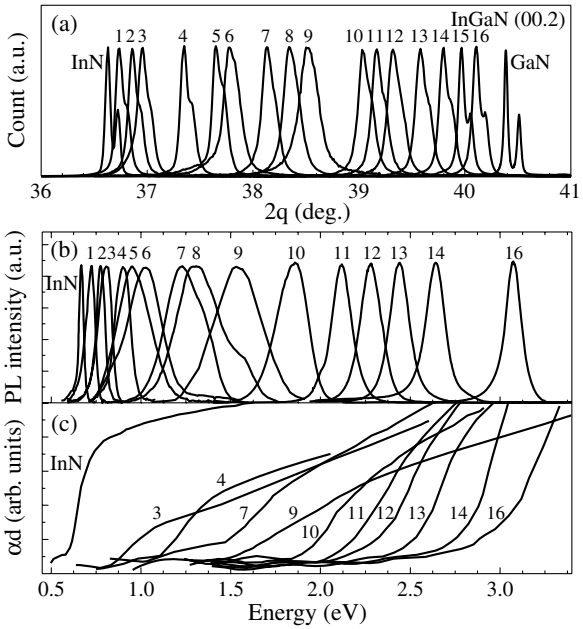

Fig. 1. X-ray data (a), PL (b) and absorption (c) spectra for InN, GaN and $In_xGa_{1-x}N$ alloys: 1 — $x = 0.86$, 2 — 0.82, 3 — 0.80, 4 — 0.68, 5 — 0.63, 6 — 0.60, 7 — 0.50, 8 — 0.46, 9 — 0.42, 10 — 0.35, 11 — 0.28, 12 — 0.23, 13 — 0.17, 14 — 0.13, 15 — 0.09, 16 — 0.06.

The photoluminescence (PL) and absorption spectra of InGaN were investigated in entire composition range (see Figs. 1b and 1c). These studies were followed by the analysis of the spectra that allow one to establish the composition dependence of the band gap.

The details of the band gap analysis

The InGaN samples demonstrate the PL bands with the tails formed by donor-acceptor annihilation of localized electron and holes. Tails of this kind are known to appear in the disordered systems, such as alloys and amorphous semiconductors, as a result of the random distribution of atoms over the lattice sites or the structural imperfections randomly scattered over the crystal. One can expect that the localized hole states of acceptor-type impurities and tail states of the conduction band will play a noticeable role in the formation of the interband PL. These bands must be red-shifted as compared with the band-to-band PL and can coexist with Urbach tails of the band-to-band PL.

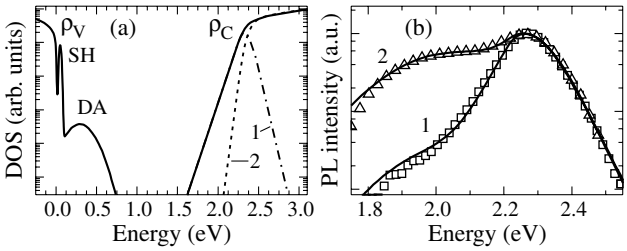

Fig. 2. (a) The model DOS of valence and conduction bands ρ_v and ρ_c, respectively, used in calculations. SH and DA denote the positions of shallow and deep acceptor states. Curves 1 and 2 present the filled and empty states of the conduction band. (b) The PL spectra of $In_{28}Ga_{72}N$ at liquid nitrogen (1) and room (2) temperatures. Symbols are the experimental data and the solid lines are the results of calculations.

We consider a model description of the density of states (DOS) of the valence bands taking into account both the Urbach tail and the acceptor states of different localization depths. The behavior of the density of states in the Urbach tail is commonly well described in a wide energy range by the exponential law [8]. Taking the density of acceptor states in the Gaussian form we present the model density of states for holes as it shown in Fig. 2a. It can be expected that the concentration of the localized valence band states is smaller than the electron concentration. If the localized states are spread over a wide energy range then the dependence on the filling of these states at relatively low excitation powers can influence the PL band.

In the limit of weak excitation of samples in presence of a tail of localized states and a fast relaxation rate, we can expect that only the holes localized by the deepest states will influence the PL band shape. The PL mechanism of this kind was observed in the spectra of disordered systems under weak excitation, when the recombining excitons are captured by localized states of the tail [9].

We present the density of states of the conduction band (Fig. 2a) in the similar form taking into account the Urbach tail. The origin of localized states that lie below the bottom of the conduction band may be associated with, e.g., the spatial fluctuations. The states of conduction band filled by electrons are responsible for the PL process, while the band-to-band transitions into the empty states of conduction band (Fig. 2a) define the absorption.

Interband PL spectra of InGaN

The PL spectrum of $In_{28}Ga_{72}N$ at liquid nitrogen and room temperatures and the model calculations are presented in Fig. 2b. The high-energy band of the interband PL arises due to annihilation of the photo-excited holes and electrons. The luminescence bands formed by recombination of electrons and deeply localized holes are red-shifted, as in the case of GaAs and GaN. The PL spectrum exhibits a strong transformation in the range between nitrogen and room temperatures. The sensitivity of the PL spectrum to the temperature shows that the population of one of two types of the carriers participating in PL is strongly influenced by temperature. On the other hand, the Hall data evidence that the electrons are still degenerate. Then, the relative decrease in the high-energy peak with temperature can be assigned to the redistribution of the population between deeply localized and delocalized states of holes.

The similar approach was used in the model calculations of the PL and absorption spectra in entire interval of concentrations. As an example the typical PL and absorption spectra, their model fit and the positions of the band gap for four samples are shown in Fig. 3. Figure 4 compares the results of this work with other literature data. We have found that the best fit of our results on the InGaN band gap composition dependence $E_G = 3.49 - 2.84x - bx(1-x)$ is provided by the bowing parameter of $b = 2.5$ eV.

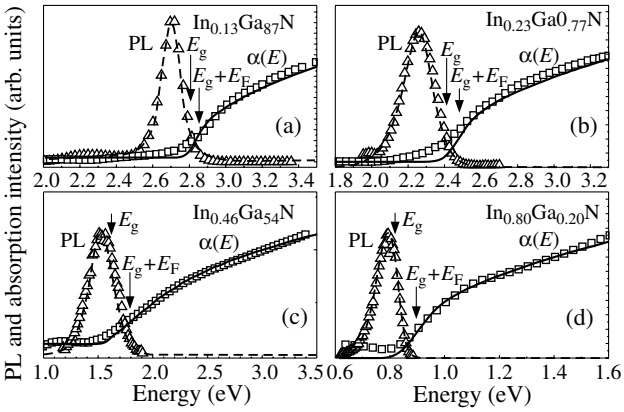

Fig. 3. Experimental room-temperature absorption and PL spectra, of $In_xGa_{1-x}N$: (a) $x = 0.13$, (b) 0.23, (c) 0.46, (d) 0.80. Solid and dashed lines give results of model calculations for absorption and PL spectra, respectevely.

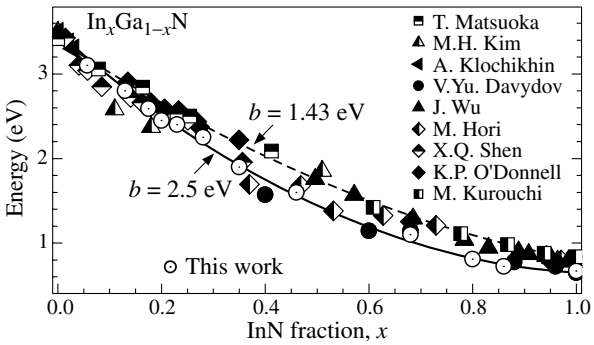

Fig. 4. Band gap of $In_xGa_{1-x}N$ alloys vs composition x.

Conclusions

We have performed the detailed investigation of the band gap of InGaN alloys as a function of the concentration of the constituents in the entire compositional range. It has been found that this fundamental parameter is characterized by the strongly nonlinear behavior with the large bowing parameter of 2.5 eV.

Acknowledgements

This work is supported by the Programs of RAS "Quantum nanostructures" and "New materials and structures", and RFBR (grant 06-02-17240).

References

[1] Abstracts of The 6th Int. Conf. on Nitride Semiconductors, August 28–September 2, 2005, Bremen, Germany.
[2] V. Yu. Davydov *et al*, *phys. stat. sol. (b)* **234**, 787 (2002).
[3] J. Wu *et al*, Appl. Phys. Lett. **80**, 4741 (2002).
[4] M. Hori *et al*, *phys. stat. sol. (b)* **234**, 750 (2002).
[5] M. Kurouchi *et al*, *phys. stat. sol. (b)* **241**, 2843 (2004).
[6] K. P. O'Donnell *et al*, *J. Cryst. Growth* **269**, 100 (2004).
[7] Hai Lu *et al*, *Appl. Phys. Lett.* **82**, 1736 (2003).
[8] A. A. Klochikhin *et al*, *Phys. Rev. B* **48**, 3100 (1993).
[9] A. Klochikhin *et al*, *Phys. Rev. B* **59**, 12947 (1999).

14th Int. Symp. "Nanostructures: Physics and Technology"
St Petersburg, Russia, June 26–30, 2006

Effect of the band bending on the optical spectra of thin epilayers and nano-size samples of n-InN

A. A. Klochikhin[1,2], V. Yu. Davydov[1], V. V. Emtsev[1], A. N. Smirnov[1], C.-H. Shen[3], H.-Y. Chen[3] and S. Gwo[3]

[1] Ioffe Physico-Technical Institute, St Petersburg, Russia
[2] Nuclear Physics Institute, 188350, St Petersburg, Russia
[3] Department of Physics, National Tsing-Hua University, Hsinchu 300, Taiwan, Republic of China

Abstract. It is shown that the band bending caused by the surface accumulation layers strongly affect the optical characteristics of thin epilayers and nano-size samples of n-InN. We present the model calculations and experimental data demonstrating that optical absorption, the shape and the temperature variation of PL band are sensitive to the presence of the accumulation layers.

Introduction

Absorption and photoluminescence (PL) spectra near the band gap of heavily doped InN samples governed by interband transitions are influenced by the Burstein–Moss filling factor [1]. It is established now that the considerable band bending induced by the surface accumulation layers in n-InN samples [2,3,4,5] results in an inhomogeneous spatial distribution of the carrier concentration. We investigate the influence of the spatial inhomogeneity of the carrier distribution on the absorption and PL spectra in thin epilayers and in nano-size samples of n-InN.

Samples

The vertically aligned wurztie-InN nano-rods were grown on 3-inch Si(111) substrates by plasma-assisted molecule beam epitaxy. The InN nanorods were grown at sample temperatures of 330 °C (LT) and 520 °C (HT) under nitrogen-rich growth conditions. For the LT-InN nanorods, the average rod diameter is quite uniform and varies from few tens of nm to 100 nm (height/diameter ratio $\approx$ 10). On the other hand, for the HT-InN nanorods we have found that the diameter distribution shows a bimodal behavior. Additionally, the InN epilayers grown on Si(111) [6] with thicknesses from 0.22 to 2.36 μm and with Hall concentrations of 5×10^{18} cm^{-3} and of 8×10^{18} cm^{-3} were also studied.

Influence of accumulation layers on absorption

Figure 1a presents the variation of the absorption coefficient in three epilayers with different thickness. The monotonous decrease of the slope from curve 1 to curve 3 can be attributed to the increasing influence of accumulation layers with the sample thickness decrease. The mechanism of this effect is demonstrated schematically in Fig. 1b where, as an example, the band bending created by two accumulation layers for the epilayer with thickness of 100 nm is presented. In calculations the potential energy $\phi(\mathbf{r})$ with the maximum amplitudes of 0.6 eV near the surfaces and with the half-width of 1.4 nm has been assumed. This leads to the decrease of the chemical potential from the value $\mu_0^{\rm e}$ without accumulation layers to $\mu^{\rm e}$ at the same averaged electron density and to the inhomogeneous distribution of the electron density. The electron density reaches the maximum values near the both surfaces of the sample. Its spatial distribution is characterized by the half-width of about 0.4 nm. The parameters of the accumulation layer

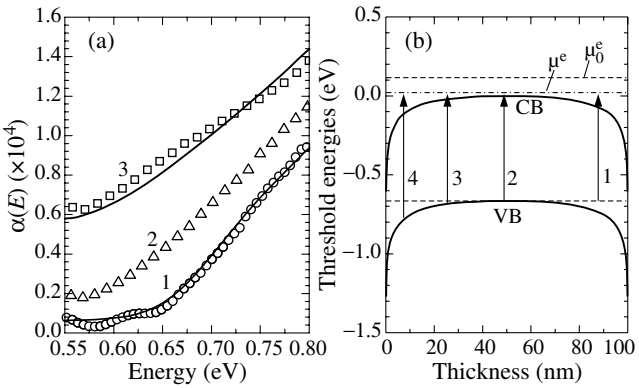

Fig. 1. (a) Absorption coefficient of epilayers (symbols). The sample thicknesses are 2.36 (curve 1), 0.51 (curve 2), and 0.22 (curve 3) μm. Solid lines are the calculated absorption coefficients without (1) and with (3) accumulation layer. (b) The band bending of conduction CB and valence VB bands induced by the accumulation layers, $\mu_0^{\rm e}$ and $\mu^{\rm e}$ are the chemical potentials without and with accumulation layers. Arrow 1, and arrows from 2 to 4 show the Burstein–Moss threshold of the interband transition without and with accumulation layer, respectively.

are in agreement with the data of Refs. [2,3,4,5]. The absorption coefficients calculated for this model with and without the accumulation layers are presented in Fig. 1a. The accumulation layer leads to the smearing of the Burstein–Moss threshold and to the decrease of the slope of the absorption coefficient. The obtained agreement with experimental data shows that the optical absorption allows to estimate the parameters of the accumulation layers for thin samples.

Influence of the accumulation layer on the PL spectra

The influence of the accumulation layer on the PL spectra can be established by studying the shape of PL band and its temperature dependence.

Figures 2a and 2b demonstrates the PL spectra of nano-rods of two types at different temperatures. The PL bands of both types of samples experience a considerable broadening with the temperature increase. The PL band maximum of the HT sample does not shift with the temperature while the maximum of the PL band of the LT sample shifts toward the high energies with the increase of the temperature. These results differ from the PL maximum behavior typically observed for InN epilayers. For comparison, the temperature variations of PL spectra of

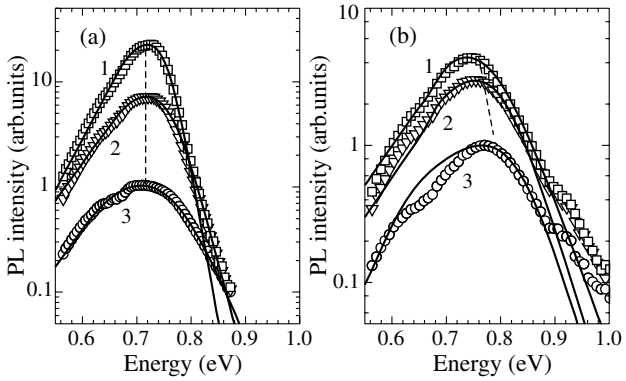

Fig. 2. The PL spectra of HT nano-rods (a) and LT nano-rods (b) at 12, 100 and 300 K, curves 1, 2 and 3, respectively. Symbols are the experimental data and solid lines are the results of calculations.

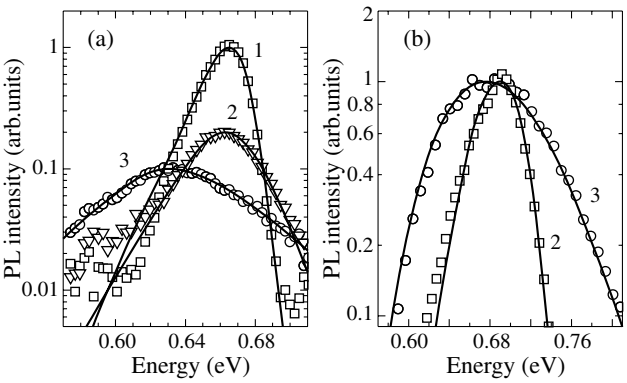

Fig. 3. The PL spectra of InN epilayers with the thicknesses of 0.65 μm (a) and 2.36 μm (b). Curves 1, 2, and 3 correspond to temperatures of 4, 77, and 300 K. Symbols are the experimental data and solid lines are the results of calculations.

two types of epilayers are presented in Figs. 3a and 3b.

The temperature shift and broadening of the interband PL band in epilayers are governed by three factors. These factors are the temperature shrinkage of the band gap, the temperature broadening of the free electron distribution and the temperature change of the photohole distribution. The hole distribution is of great importance because the increase of the hole kinetic energy with temperature shifts the PL maximum in the direction opposite to the band gap shrinkage. The difference in temperature shifts (see Fig. 3) of the PL maxima in different samples can be explained by the different role of the momentum conservation law in interband transitions. If the momentum conservation law is violated and the indirect interband transitions dominate in the PL process, a considerable compensation of the band gap shrinkage takes place (see Fig. 3a and 3b) that decreases the low-energy shift of the PL band.

In case of the low-dimensional samples like nano-rods an additional factor can play an important role, namely, an inhomogeneous distribution of the carrier concentration over the cross-section of the sample. As a result of energy relaxation the photoholes populate the different spatial states in the sample at different temperatures. At low temperatures the photoholes populate the narrow central part of the rod where the states of the valence band have the uppermost energies, and PL is formed by transitions in this region where the electron concentration is minimal (Fig. 4a). At room temperature the holes are distributed within a larger central area where the hole potential energy has the order of the thermal energy kT. In this case the

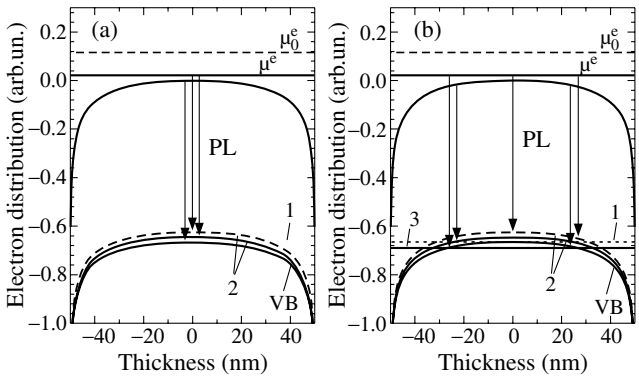

Fig. 4. The schematic presentation of the transformation of the PL process from the low (a) to the room (b) temperatures. Line 1 is the position of the valence band top, lines 2 denotes the hole localized states, and line 3 in Fig. 2b shows the hole kinetic energy kT at room temperatures. Arrows in Figs. 2a and 2b show the interband PL transitions at low and room temperatures. Other notations are the same as in Fig. 1b.

PL transitions involve the larger area of the sample with larger electron content larger (Fig. 4b) which leads to the high-energy shift and broadening of the PL band.

It was demonsrated in Ref. [1] that the electron concentration in doped n-InN samples can be estimated independently from the PL experimantal data. These estimations are of great importance for nano-rods for which the Hall measurements are complicated. The free carrier concentration was found to increase in the case of the HT sample from 3.75×10^{18} at 12 K to 7.75×10^{18} cm^{-3} at 300 K, and in the case of LT sample from 4.75×10^{18} at 12 K to 1.5×10^{19} cm^{-3} at 300 K. These data give the evidence that the sample region where the PL band is formed is varying with temperature. This process can be effective due to the small transverse size of nano-rods and due to the trapping of the relatively large fraction of free electrons by the surface accumulation layer at low temperatures.

Conclusions

The influence of an accumulation layer on the optical absorption of thin InN epilayers and on the PL spectra of InN nano-rods is demonstrated. It is shown that the important parameters of the accumulation layer can be deduced from the optical spectra.

Acknowledgements

This work is supported by NSC-RFBR (grant 94WFA0400 128) and the Programs of RAS "Quantum nanostructures" and "New materials and structures".

References

[1] A. A. Klochikhin, V. Yu. Davydov, V. V. Emtsev, A. V. Sakharov *et al*, *Phys. Rev. B* **71**, 195207 (2005).
[2] Hai Lu, William J. Schaff, Lester F. Eastman and C. E. Stutz, *Appl. Phys. Lett.* **82**, 1736 (2003).
[3] I. Mahboob, T. D. Veal, C. F. McConville, H. Lu and W. J. Schaff, *Phys. Rev. Let.* **92**, 036804 (2004).
[4] L. F. J. Piper, T. D. Veal, I. Mahboob, C. F. McConville, H. Lu and W. J. Schaff, *Phys. Rev. B* **70**, 115333 (2004).
[5] C. H. Swartz *et al*, *J. Cryst. Growth* **269**, 29 (2004).
[6] S. Gwo, C.-L. Wu, C.-H. Shen, W.-H. Chang, T. M. Hsu, J.-S. Wang and J.-T. Hsu, *Appl. Phys. Lett.* **84**, 3765 (2004).

14th Int. Symp. "Nanostructures: Physics and Technology"
St Petersburg, Russia, June 26–30, 2006

InGaN layers and InGaN/GaN quantum wells with intense room-temperature photoluminescence in a visible spectral range

P. S. Kop'ev[1], V. N. Jmerik[1], A. M. Mizerov[1], T. V. Shubina[1], S. B. Listoshin[1], M. G. Tkachman[1], A. A. Sitnikova[1], R. V. Zolatareva[1], Ya. Domracheva[1], M. Yagovkina[1], M. V. Zamoryanskaya[1], Min-Ho Kim[2], Masayoshi Koike[2], Bum-Joon Kim[2] and S. V. Ivanov[1]

[1] Ioffe Physico-Technical Institute, St Petersburg, Russia
[2] Samsung Electro-Mechanics Co., Ltd, Korea

Abstract. The results on the plasma-assisted molecular beam epitaxy growth of InGaN layers and InGaN/GaN quantum-well structures with high In-content are reported. The intense room-temperature photoluminescence with peak wavelength within a 470–830 nm (2.6–1.5 eV) range was observed in the InGaN layers and related structures showing inhomogeneous distribution of In with the average content of 20–65%.

Introduction

High-efficiency InGaN/GaN based light-emitting devices for the long wavelength range (500–600 nm) still remains an actual problem despite the significant progress in III-nitrides technology. Different phenomena, such as phase separation, both surface and bulk In segregation, strain relaxation, morphology variation from nano-columnar to atomically-flat, obscure manufacture of such structures. This paper reports on the successful fabrication by plasma-assisted molecular beam epitaxy (PA MBE) of both InGaN layers and InGaN/GaN quantum-well (QW) structures with high In-content, which demonstrate bright room-temperature photoluminescence (PL) with the wavelengths well beyond 470 nm.

Experiment

InGaN layers with a thickness of 50–700 nm were grown at a growth rate of 0.1–0.4 m/h in a wide compositional range up to pure InN, using Compact 21T setup. All InGaN epilayers were grown on c-sapphire atop of a thick GaN buffer layer deposited either *in situ* by PA MBE or *ex situ* by metal-organic vapor phase epitaxy (MOVPE) growth techniques. Different growth temperatures ($T_S = 500-670$ °C), III/N and In/Ga flux ratios, growth rates were employed. *In-situ* monitoring of the growth rate, surface morphology and strain relaxation give rich opportunities to control In-incorporation into the layers and QWs with rather high accuracy. The structural and optical properties of the structures were analyzed using scanning electron microscopy (SEM), X-ray diffraction (XRD), PL and PL excitation (PLE) spectroscopy, energy dispersive x-ray analysis, cathodoluminescence (CL), and transmission electron microscopy.

Results and discussion

Study of InGaN growth kinetics during PA MBE revealed that T_S is the main factor governing the efficiency of In-incorporation into InGaN (α_{In}), which is defined as a ratio of the incorporated In flux to the incident one. Increase in T_S in the 590-670°C range reduces steeply In down to 0.15, while rising the incident flux ratio $F_{N^*}/(F_{Ga} + F_{In})$ enhances In, although the latter effect is much weaker. Knowing the efficiency of In-incorporation α_{In}, it is possible to change the composition of $In_xGa_{1-x}N$ layers within a wide range from minimum $x \cong 0$ at $F_{N^*}/F_{Ga} = 1 : 1$ (stoichiometric mode) up to $x = 1 - F_{Ga}/F_{N^*}$ at $F_{N^*}/(\alpha_{In}F_{In} + F_{Ga}) < 1$ (the group III-rich mode) or $x = \alpha_{In}F_{In}/(\alpha_{In}F_{In} + F_{Ga})$ at $F_{N^*}/(\alpha_{In}F_{In} + F_{Ga}) \geq 1$ (the N-rich mode). The latter ratio also governs a surface stoichiometry of the InGaN layer.

Usage of the stoichiometric mode results in In incorporation into GaN layer at a level of several percents and at the relatively high $T_S(> 600$ °C) practically whole In flux re-evaporates from the growth surface, just influencing the surface kinetics of Ga atoms through segregation effects and, thus, improving the GaN:In quality. It was confirmed by *in situ* observation of the relatively bright and streaky RHEED pattern during growth of the layer, as well as by *ex situ* finding by SEM of the droplet-free layer surface.

InGaN epilayers grown under group-III rich conditions with relatively low In content (at least $x < 0.14$, as estimated by XRD) exhibit atomically smooth surface and no traces of phase separation. It was confirmed by observation of a single symmetrical peak in XRD $\omega/2\theta$ scan with well pronounced interference fringes that allowed us to determine the thickness and In content independently. However, the intensity of RT PL peak at 470 nm, observed for this layer, was rather low. An increase in the In flux until appearance of metallic In droplets resulted in rising the In content in the 2D InGaN layers (up to $x = 0.35$, according to XRD data). They demonstrate rather long wavelength PL maximum ($\sim$ 570 nm) detectable at 20 K only.

Contrary to that, the $In_xGa_{1-x}N$/GaN heterostructures grown under the N-rich conditions and possessing 3D nanocolumnar surface morphology exhibit the relatively intense PL. Room temperature PL with peak wavelength within a 470–830 nm (2.6–1.5 eV) range was observed in the InGaN layers with average In content of 20–65%, as it has been determined by XRD and using growth dependences. It has been found that the increase of T_S higher than 600 °C causes significant enhancement of room temperature PL intensity in InGaN layers with any In content. An increase of the In-content in InGaN alloy and corresponding red shift of the PL energy maximum at constant T_S (640 °C) can be achieved by reduction of the Ga flux intensity or raising the activated N flux intensity. Figure 1 shows variation of the PL spectra shape and intensity of

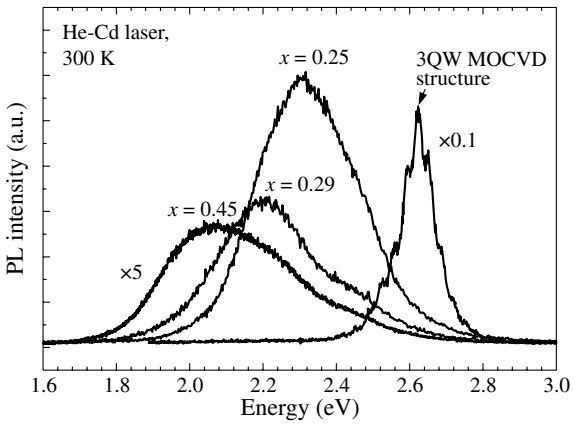

Fig. 1. PL spectra of the InGaN layers grown at the N-rich conditions with constant N-flux, different In/Ga ratios and Ts in comparison with a reference 3QW MOCVD structure.

PA MBE InGaN layers with the wavelength shift from green to red. The PL peak intensity of the layers drops 10 times from 550 to 600 nm, and just 100 times with respect to a reference MOCVD grown MQW structure emitting at 470 nm.

We suppose that the columnar growth usually observed in PA MBE of III-N under the N-rich conditions stimulates the formation of defect free InN-rich InGaN clusters resulting in the PL enhancement, despite the relatively high total threading dislocation density ($\sim 10^{10}$ cm^{-2}). Pronounced excitonic peaks have been registered below the principal edge in PLE spectra recorded in these layers. The shift of the PLE peak at different registration wavelengths indicates certain non-homogeneity of the emitting sites. One should note that some layers with highest In content exhibit two-bands PL emission, with the lower-energy band being within the 1.8–2 μm range characteristic for pure InN. This evidences an onset of phase separation in the In-rich InGaN layers.

Using these data the InGaN/GaN QW structures were grown. The key point of these growth runs is a modulation of stoichiometric conditions to grow barrier and QW layers. It has been shown that the nitrogen-rich conditions are preferable for growth of QW layers, whereas group-III rich ones should be used during the barrier layer growth. The intensity of the 480 nm emission in the InGaN/GaN QW structure with the nominal well thickness of 3 nm is comparable with that in 230-nm-thick bulk InGaN layers grown at the same conditions. Figure 2 gives the PA MBE single QW PL spectrum in comparison with the PL of MOCVD 3QW structure, demonstrating the great potential of the employed PA MBE growth technique in fabricating high emission efficiency InGaN QWs in the visible spectral region.

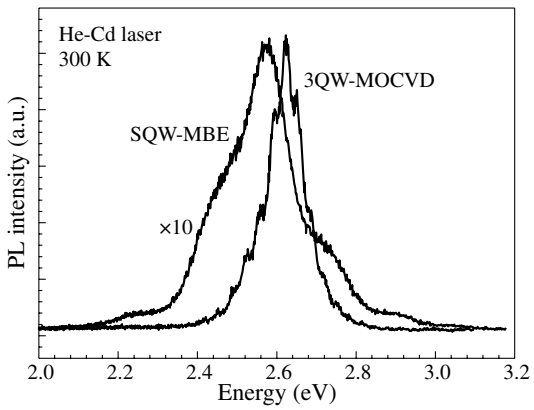

Fig. 2. PL spectra of single QW structure InGaN/GaN grown by PA MBE in comparison with a reference 3QW MOCVD structure.

Conclusions

These results indicate that MBE-grown InGaN structures are promising as active regions of green-red-emitting LEDs. Inhomogeneous spatial distribution of In plays a key role in luminescence properties at high In content.

Acknowledgement

The work is supported partly by a Samsung Electro-Mechanics Co., Ltd., cont. #75/1, RFBR and Program of PSD of RAS.

14th Int. Symp. "Nanostructures: Physics and Technology"
St Petersburg, Russia, June 26–30, 2006

Lattice dynamics and Raman spectra of InGaN alloys and InN/GaN superlattices

M. B. Smirnov[1], V. Yu. Davydov[2] and A. N. Smirnov[2]

[1] Fock Institute of Physics, St Petersburg State University, 198504, St Petersburg, Russia
[2] Ioffe Physico-Technical Institute, St Petersburg, Russia

Abstract. Composition effect on the Raman spectra of InGaN alloys is theoretically studied with a rigid-ion model within a finite super-cell and a random-element isodisplacement approximations. Complex structure arising from the vibrations localized on different structural clusters is predicted for A_1(TO) and E_1(TO) Raman spectra. The results obtained for InGaN alloys are compared with those for InN/GaN superlattices.

Introduction

III-nitride ternary alloys $A_xB_{1-x}N$ (A, B = Al, Ga, In) have recently attracted much attention as very promising materials for the fabrications of optoelectronic devices operating from the near IR to ultraviolet spectral regions. It was demonstrated that one of the most efficient, sensitive, and direct techniques for the quantitative characterization of these compounds is the Raman spectroscopy [1, 2]. The analytical ability of this technique is much higher if the observed spectral features are reliably interpreted and assigned to particular kinds of atomic vibrations. In this case, it is possible not only to determine the alloy composition but also to draw some conclusions about local structures and mechanisms of atomic interactions.

Theoretical studies of the composition dependences of Raman spectra of III-nitride alloys are few in number [2, 3, 4]. The results of the most comprehensive studies of wurtzite AlGaN, InGaN and AlInN are preseted in Ref. [2]. The composition dependence of phonon spectra for these compounds was described within a random-element isodisplacement (REI) model. The model involves the averaging over disordered configurations and, therefore, such analysis did not offer a microscopic interpretation for particular spectral features. The goal of our work is a numerical simulation of the lattice dynamics and Raman spectra of wurtzite InGaN alloys in order to create a basis for the quantitative characterization of related heterostuctures and nanostructures.

Model

Our approach is based on the rigid ion model (RIM) and the polarizable bond model which were successfully used in our recent studies of GaN and AlN [5], and related superlattices [6]. Structural disorder is treated by using a super-cell which obeys the composition homogeneity condition.
Potential model used in the study was including the terms corresponding to the Coulomb interaction and the pair-wise short-range repulsion interactions described within Born–Karman scheme. Thus, the parameter set includes two effective charges $Z(\mathrm{Ga}) = 1.14e$ and $Z(\mathrm{In}) = 1.06e$. Effective charges of nitrogen atoms were defined depending on their actual positions in a tetrahedrons $NGa_{n1}In_{n2}$ as

$$Z(N) = 1/4\,(n_1 Z(\mathrm{Ga}) + n_2 Z(\mathrm{In}))\ .$$

The Born–Karman parameters,

$$A = d^2E/dR^2 \quad \text{and} \quad B = (1/R)(dE/dR)$$

represent the second and the first derivatives of the energy with respect to bond length. Their values are listed in Table 1.

Table 1. Values of Born–Karman parameters (in N/m) for GaN and InN crystals.

	Ga-N	In-N	N-N (in GaN)	N-N (in InN)	Ga-Ga	In-In
A	23	16	1	0.45	2	1.5
B	−1.7	−1.085	0	0	0	0

Raman intensities were calculated by using the polarizable bond model. More details and the definitions of the model parameters can be found in Refs. [5] and [6].

The model used in the study represents the structure of InGaN alloy as an infinite periodic structure with unit cell built up as $3 \times 3 \times 2$ super-cell of wurtzite lattices inherent to the pure nitride crystals. The super-cell contains 36 cation positions which are randomly occupied by Ga and In atoms correspondingly to a given composition parameter x.
Selecting the cation positions occupied by 'admixture' atoms, we were trying to obey the homogeneity condition which means that the relative numbers of the tetrahedrons NGa_4, NGa_3In, NGa_2In_2, $NGaIn_3$ and NIn_4 in the finite super-cell system must coincide with those calculated for an infinite absolutely homogenous mixture of corresponding composition.

Results

In order to simulate the composition dependence of the frequencies of zone-center optical modes, the dynamic matrix of a disordered lattice was represented as a combination of matrixes of pure lattices with weighting coefficients proportional to given concentrations. The results of these calculations are shown in Fig. 1. It is seen that the model predicts an one-mode behavior for all high frequency modes. This conclusion is in line with the results of Ref. [2]. The calculated dependence of the phonon frequencies on the composition parameter x agree well with the experimental data from Refs. [7, 8]. Fig. 1 presents also the results of the calculations for InN/GaN superlattices within the dielectric continuum approximation (the details of calculations will be given in a separate paper). One-mode type behavior was found also for A_1(TO) and E_1(LO) modes in these nanostructures. However, the dependence of the phonon frequencies on the composition parameter x in InN/GaN superlattices is different from that in InGaN alloys.

The lattice dynamics simulations within REI approximation have predicted a pure one-mode behavior for the A_1(TO)

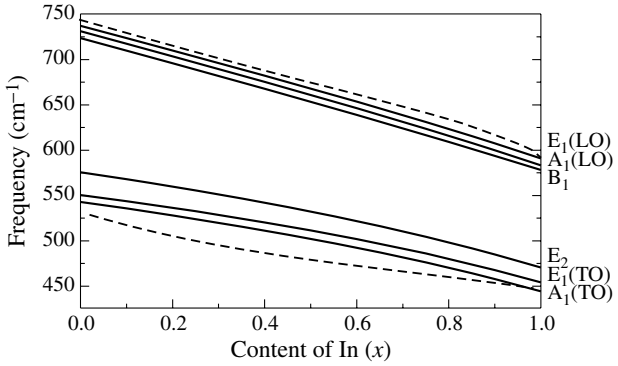

Fig. 1. Frequencies of optical modes versus InGaN composition calculated by RIM model within REI approximation (solid lines) and similar dependences for InN/GaN superlattices calculated within the dielectric continuum approximation (dashed lines).

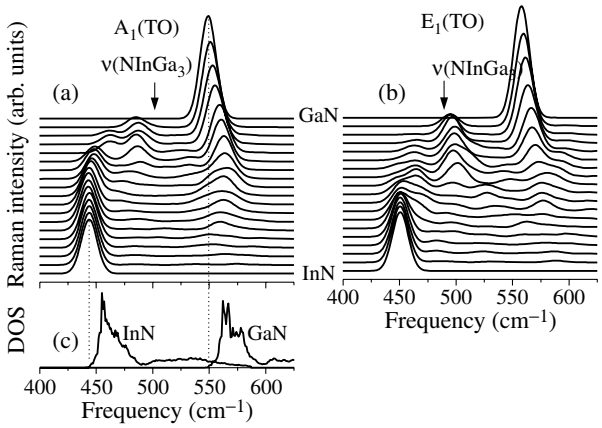

Fig. 2. Calculated Raman spectra of InGaN alloys at different compositions: (a) A_1(TO) and (b) E_1(TO). (c) Calculated density of phonon states for wurtzite GaN and InN crystals. Frequency positions of A_1(TO) and E_1(TO) lines in pure crystals are shown by vertical dotted lines.

mode in AlGaN alloys in the whole compositional range [2]. However, it has been found that the Raman spectra of Al-rich AlGaN exhibit a complex structure caused by the statistical Ga clusters in the cation sublattice [9].

It should be noted that the REI approximation does not allow to detect the spectral manifestation of the local modes of different statistical clusters. To overcome the shortcomings of the REI approximation, we have simulated the Raman spectra of InGaN alloys within the super-cell approach. The A_1(TO) and E_1(TO) spectra, calculated for $x(zz)x$ and $z(xz)z$ polarization condition, respectively, are shown in Figs. 2(a) and 2(b). Their composition dependences are quite similar and indicate a two-mode behavior. The InN-like branch is clearly seen up to $x = 0.8$. At decreasing the In content, this branch monotonously declines towards the position of the GaN-like mode. At lower In content, the frequency of this branch exhibit a step-wise behavior. Frequency positions of the "step" modes are shown by arrows in Figs. 2(a) and 2(b). By analyzing the calculated eigenvectors, we have revealed that these intermediate modes correspond to the vibrations localized in the NInGa$_3$.

It can be seen that at decreasing the Ga content, the GaN-like A_1(TO) and E_1(TO) modes shift towards the high-er frequencies. This effect is similar to those revealed in AlGaN al-

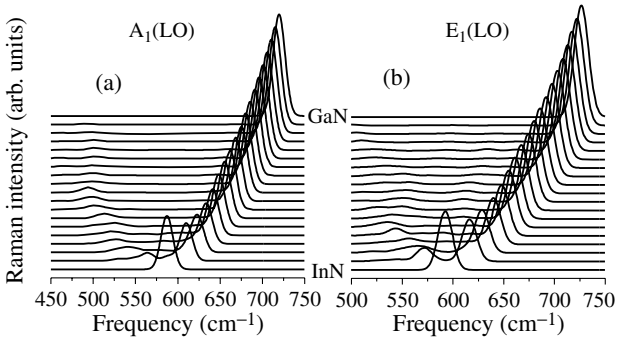

Fig. 3. Calculated Raman spectra of $In_xGa_{1-x}N$ alloys in dependence on composition: (a) A_1(LO) and (b) E_1(LO).

loys [9]. It can be explained by the violation of the wave-vector conservation law and manifestation of the whole phonon DOS as a result of the considerable difference in masses of heavy In atoms substituting the lighter Ga. In order to illustrate this effect, the DOS for pure GaN and InN wurtzite crystals are shown in Fig. 2(c).

The A_1(LO) and E_1(LO) spectra calculated for $x(zz)x$ and $y(xz)x$ polarization conditions, respectively, are shown in Figs. 3(a) and 3(b). Their composition dependences are quite similar and indicate a one-mode behavior. The dependences of frequencies of these modes on x agree well with those presented in Fig. 1. Typically, the one-mode behavior of the longitudinal polar phonons is explained by the influence of the long-range dipole-dipole interaction which is not sensitive to the local microscopic structure and can be adequately taken into account by the macroscopic models such as REI approximation.

Conclusions

Theoretical study of InGaN alloys shows that the Raman spectra of these compounds should exhibit the trends inherent to others nitrides ternary alloys. These are the one-mode behavior of longitudinal optic modes and the two-mode behavior of the transverse optic modes. Complex structure arising from the vibrations localized on the different structural clusters is predicted for A_1(TO) and E_1(TO) symmetry Raman spectra. Two approaches used in the study — the macroscopic REI approximation and the microscopic finite super-cell model — provide the complementary descriptions of the composition dependence of Raman spectra of the InGaN alloys.

Acknowledgements

This work is supported by the Programs of RAS "Quantum nanostructures" and "New materials and structures", and RFBR (grant 06-02-17240).

References

[1] V. Yu. Davydov *et al*, *Phys. Rev. B* **65**, 125203 (2002).
[2] H. Grille *et al*, *Phys. Rev. B* **61**, 6091 (2000).
[3] C. Bungaro *et al*, *Appl. Phys. Letters* **76**, 2101 (2000).
[4] R. Zheng *et al*, *Phys. Rev. B* **66**, 075327 (2002).
[5] V. Yu. Davydov *et al*, *Phys. Rev. B* **58**, 12899 (1998).
[6] M. B. Smirnov *et al*, *Phys. Sol. State* **47**, 742 (2005).
[7] K. Osamura *et al*, *J. Appl. Phys.* **46**, 3432 (1975).
[8] D. Behr *et al*, *Mater. Res. Soc. Symp. Proc.* **468**, 213 (1997).
[9] A. A. Klochikhin *et al*, *Phys. Rev. B* **62**, 2522 (2000).

14th Int. Symp. "Nanostructures: Physics and Technology"
St Petersburg, Russia, June 26–30, 2006

Investigations of a local indium composition in an ultrathin InGaN layers

S. O. Usov, A. F. Tsatsulnikov, V. V. Lundin, A. V. Sakharov, E. E. Zavarin, D. S. Sizov, Yu. G. Musikhin, N. A. Bert, E. M. Arakcheeva and N. N. Ledentsov
Ioffe Physico-Technical Institute, St Petersburg, Russia

Abstract. Optical and structural properties of the ultrathin InGaN insertions in a GaN and AlGaN matrices grown both on sapphire and SiC substrates were investigated. The method of the estimation of the local indium composition in indium-rich areas in the InGaN ultra thin insertions, using experimental spectra of photoluminescence (PL), was suggested.

Introduction

InGaN based structures are widely used in modern optoelectronics of a visible and ultra-violet range as active medium for light-emitting diodes and lasers. The band-gap of the solid solution $In_xGa_{1-x}N$ is varied in a wide range from 0.7 to 3.4 eV [1] that depends on In concentration. It permits to creation of light emitting devices in wide wavelength interval.

The emission intensity of such optoelectronic devices is defined by nonhomogeneous distribution of In and formation of indium-rich areas (QDs) due to large lattice mismatch (about 11%) between InN and GaN. The InGaN alloys are unstable over most of the composition range, desirable for both photonic and electronic devices, at the temperatures commonly used for epitaxial growth which leads to phase separation in the InGaN system [2]. QD formation due to phase decomposition are observed even at small In concentration. Diameters of the QDs are usually known to be 1–10 nm in accordance with high resolution transmission electronic microscopy [2].

The InGaN QDs is supposed to be significant increase of radiation recombination efficiency due to carrier confinement that reduces nonradiative recombination. A number of mechanisms such as formation of islands due to deformation, spinodal decomposition and surface impurity segregation affect on formation of such QDs during growth process and subsequent heat treatment.

For estimation of local In composition in the QDs using experimental spectra of photoluminescence, the generalized theoretical model and the program were developed. This model permits calculating of transition energy as a function of In composition in QDs, taking into account confinement energy and effects of spontaneous and piezoelectric fields.

1. Experimental

Three samples (A, B, C) containing multiple InGaN insertions in an AlGaN matrix were grown on sapphire substrates by the MOCVD method. Samples consist of 5 periods of InGaN insertions separated by AlGaN barriers.

Two samples (D, E) containing multiple InGaN insertions separated by GaN barriers were grown on sapphire and SiC substrates, respectively.

These samples were investigated by the photoluminescence method in the spectral range from 360 to 600 nm. Spectral characteristics of these samples were measured in the flowing cryostat in temperature range from 80 to 300 K. Photoluminescence was excited by ultraviolet He-Cd laser with wavelength 325 nm.

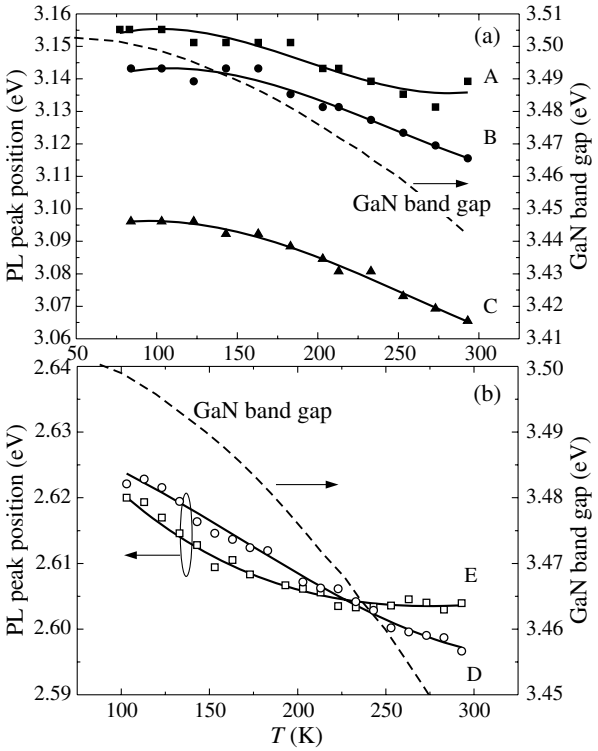

Fig. 1. Temperature dependence of the photoluminescence peak positions for the investigated samples.

The position of peaks were obtained at 3.14, 3.12 and 3.06 eV for samples A, B, and C, respectively (Fig. 1a). For the samples D and E the peak positions at 2.596 and 2.604 eV (Fig. 1b).

These results demonstrate that for all samples temperature shift of the QD emission is less than renormalization of the GaN band gap. This can be due to QD formation in the InGaN layers. Moreover, temperature dependence of the QD emission for the sample grown on SiC substrate differs from such dependence for the samples grown on sapphire substrates. These effects will be investigated elsewhere.

The HRTEM image of the InGaN insertions in the GaN matrix, shown in Fig. 2, displays the regions corresponding to the QDs that marked with arrows.

2. Results and discussion

In order to obtain the electron transition energy in the $In_xGa_{1-x}N$ quantum wells as a function of local In compo-

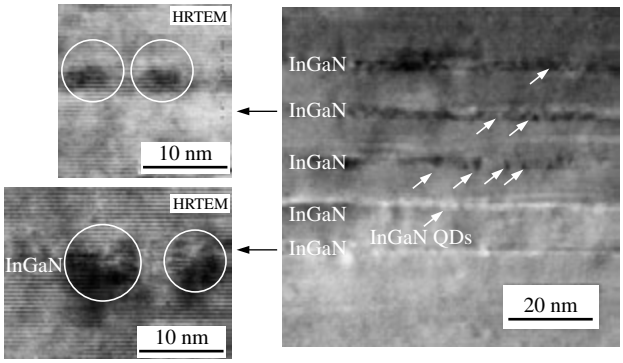

Fig. 2. HRTEM image of specific sample. The regions marked with arrows corresponds the QDs. b) and c) are enlarged view of a) image.

sition the following expression for energy is used [2]:

$$E_t = E_g + E_{conf} - E_p\,, \qquad (1)$$

where E_g is the band-gap energy for the bulk InGaN, E_p is the energy of polarization field and E_{conf} is the confinement energy. Confinement energy for the samples A, B and C was calculated in accordance with Brus model [3], believing that localization of carriers inside QDs is high due to AlGaN barriers. In this model the shape of QDs is supposed to be spherically symmetric, and the confinement energy is defined as:

$$E_{conf} \cong \frac{\hbar^2\pi^2}{2m^*r^2} - \frac{1.8e^2}{4\pi\varepsilon\varepsilon_0 r} - \frac{0.124e^4}{\hbar^2 m^*(4\pi\varepsilon\varepsilon_0)^2}\,, \qquad (2)$$

where $m^* = (m_e^{-1} + m_h^{-1})^{-1}$ is the reduced effective mass, r is the QDs radius, $\hbar$ is the Planck's constant, ε_0 is the dielectric permittivity of vacuum, e — elementary charge.

The effective masses of electron m_e and heavy hole m_h, and the permittivity constant ε of $In_xGa_{1-x}N$ in the expression (2), were obtained by linear extrapolation according to Vegard's law. Dependence of band-gap energy as a function of indium composition in the solid solution $In_xGa_{1-x}N$ is defined as:

$$E_g^{InGaN} = xE_g^{InN} + (1-x)E_g^{GaN} - b(1-x)x\,, \qquad (3)$$

where $b = 1.9$ eV is the bowing parameter.

The total polarization energy E_p, consists of spontaneous $P^{sp}_{In_xGa_{1-x}N}$ and piezoelectric $P^{pz}_{In_xGa_{1-x}N}$ polarizations along c axis were used in accordance to Fiorentini model as follows [4]:

$$E_p = \frac{eL_W^{InGaN}}{\varepsilon_0}(P^{pz}_{InGaN} + P^{sp}_{InGaN})\,, \qquad (4)$$

where L_W^{InGaN} is the $In_xGa_{1-x}N$ quantum well width. The polarization energy was calculated using reduced layer approach that equivalent to nonuniform distribution of QDs [5].

The calculated dependences of transition energies as a function of indium composition of $In_xGa_{1-x}N$ solid solution is shown in Fig. 3. for QDs, the diameters being changed from 2.5 to 6 nm. The accuracy of electronic transitions energy dependence on In composition were checked by comparing the calculated and well-known experimental data for the same InGaN multilayer structures [6,7] (Fig. 3, points 6 and 7).

As shown in the Fig. 3, the results of Ref. [7] are in accordance with calculated curve corresponding to QDs having diameter of 3 nm, and the results of Ref. [6] demonstrate good agreement between calculated and experimental data.

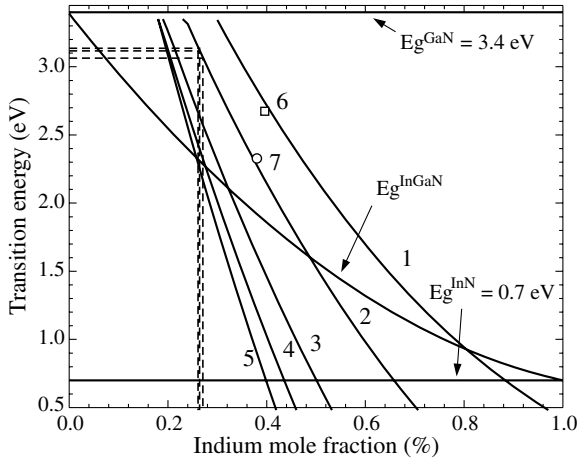

Fig. 3. The calculated dependences of transition energies as a function of indium composition of $In_xGa_{1-x}N$ solid solution for QDs having various diameters (nm): 2.5 — *1*, 3 — *2*, 4 — *3*, 5 — *4*, 6 — *5*. Points 6 and 7 are the experimental data from Refs. [6,7] at $x = 39.6\%$, $E = 2.67$ eV and $x = 38\%$, $E = 2.33$ eV, respectively.

The local indium compositions in the QDs for the samples A, B, C, prepared by MOCVD and measured by PL, were calculated using this theoretical model.

The analysis of obtained experimental data shows that more probable QD diameters are in the range from 2 to 6 nm. For diameter of the QDs of 3 nm, local indium composition for samples A and B is $\sim$ 26%, for sample C is $\sim$ 27% (Fig. 3, dash lines). The variation of the QD diameter from 3 to 6 nm changes the value of composition about 3%.

The suggested model are supposed to be useful to obtain the indium compositions of $In_xGa_{1-x}N$ solid solutions, using photoluminescence experimental data and will apply for growth parameters and characteristics of light-emitting devices.

Acknowledgements

This work was supported by Russia Foundation for Basic Research and Joint research center "Material science and characterization in high technology".

References

[1] V. Yu. Davydov, A. A. Klochikhin, V. V. Emtsev *et al*, *phys. stat. sol. (b)* **230**, No. 2, R4–R6 (2002).
[2] Yen-Lin and Chau-Pu Liu, *Appl. Phys. Lett.* **86**, 121915 (2005).
[3] L. E. Bruce, *J. Chem. Phys.* **80** (9), 4403–4409, 1 May 1984.
[4] Vincenzo Fiorentini, Fabio Bernardini, Oliver Ambacher, *Appl. Phys. Lett.* **80** No. 7, 1204–1206, 18 February 2002.
[5] N. A. Shapiro, Piotr Perlin, Christian Kisielowski, L. S. Mattos, J. W. Yang and R. Eicke *Weber, MRS Internet J. Nitride Semicond.* **Res. 5** 1–6 (2000).
[6] H. K. Cho, J. Y. Lee, N. Sharma and C. J. Humphreys, *Appl. Phys. Lett.* **79**, 2594–2596 (2001).
[7] Yen-Shen Lin, Kung-Jen Ma, C. C. Yang, Tomas E. Weirich, *Journal of Crystal Growth* **242** 35–40 (2002).

14th Int. Symp. "Nanostructures: Physics and Technology"
St Petersburg, Russia, June 26–30, 2006

Radiative and non-radiative recombination and peculiarities of photoluminescence kinetics in type-II ZnSe/BeTe superlattices

S. V. Zaitsev[1], A. A. Maksimov[1], I. I. Tartakovskii[1], D. R. Yakovlev[2] and A. Waag[3]

[1] Institute of Solid State Physics, Russian Academy of Sciences, 142432 Chernogolovka, Russia
[2] Experimentelle Physik II, University of Dortmund, D-44227 Dortmund, Germany
[3] Institute of Semiconductor Technology, Braunschweig Technical University, D-38106 Braunschweig, Germany

Abstract. Detailed investigation of radiative recombination intensity and its kinetics on photoexcitation density have been performed in type-II ZnSe/BeTe superlattices. Excitation power dependence of the intensity demonstrates typical saturation of non-radiative recombination channels at high excitation levels. Above the saturation region strong shortening of the emission time with increasing density of spatially separated electrons and holes is found and attributed to the band bending effect. Surprisingly, very long recombination times (> 10 ns) are observed at low excitation levels, contrary to the expected short times usual at dominating non-radiative processes. The observed peculiarities of photoluminescence and its kinetics are explained by strong lateral inhomogeneity that is a specific feature of the investigated heterosystem with no-common atom at interfaces.

Introduction

Wide gap II–VI and III–V semiconductors like ZnSe and GaN are usually considered as promising candidates for different sort of devices such as UV/blue/green light-emitting diodes (LED) and lasers. Despite of great progress and commercialization of III–V nitride-based LEDs, mostly appropriate to blue and UV spectral range, strong interest still remains to ZnCdSe-based heterostructures, emitting in green-blue range.

First detailed investigations have shown quite low efficiency of ZnSe/BeTe heterostructures, which is also different for different interface configurations, possible in this heteropair with no-common atoms at the interface [1]. Thus, knowledge of the influence of non-radiative centers on the optical properties in ZnSe/BeTe LED heterostructures is very important for improving their performance.

In this contribution we present results of investigations of the radiative efficiency and photoluminescence (PL) kinetics depending on the photoexcitation density in symmetric ZnSe/BeTe SLs. Investigations of power dependencies of radiative characteristics are known as a powerful tool for studying of non-radiative centers in semiconductors [2]. Unusual behavior of PL is observed pointing to a peculiarity of non-radiative recombination in this heteropair.

1. Experimental

ZnSe/BeTe SLs were grown by molecular beam epitaxy on (001)-oriented GaAs substrates. Structures contain 5 monolayer (ML) BeTe buffer layer and 5 periods of alternating 5 nm-thick BeTe and 10 nm-thick ZnSe layers with ZnSe layer at the top.

PL was excited by a pulsed N_2-laser (3371 Å) with a pulse width of ~ 0.3 ns. The laser emission is absorbed in the ZnSe layers only, as the BeTe direct band gap is ≈ 4.5 eV [1]. Time-resolved spectra and PL decay curves, emitted perpendicular to the SL plane, were recorded by a photomultiplier with a temporal resolution of ~ 1 ns. Samples were measured in a He-flow cryostat at temperature $T = 5$ K.

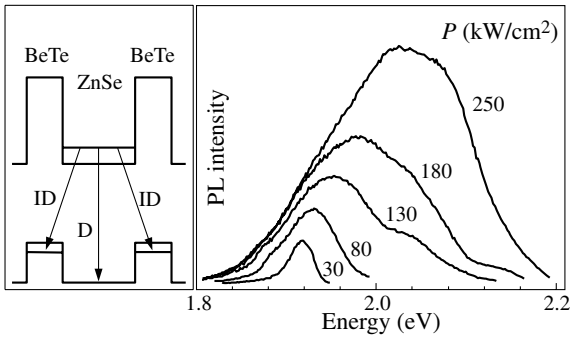

Fig. 1. PL spectra of ZnSe/BeTe SL (10 nm/5 nm) at different excitation densities (depicted in figure) at $T = 5$ K. Left panel displays SL band alignment and D and ID transitions.

2. Evolution of PL spectra and kinetics with photoexcitation density

Fig. 1 displays time-integrated PL spectra of a sample with symmetric Te–Zn interfaces and different densities of optical excitation P_{exc}. Spectra show two bands: direct transition (D) at ≈ 2.8 eV (not shown in Fig. 1) in the ZnSe layer and a wide band in the energy range 1.8–2.2 eV, corresponding to indirect (ID) transition of photoexcited electrons in the ZnSe layers and holes, relaxed to the BeTe layers [4]. As a result of increasing P_{exc}, an appreciable modification of the ID spectral band occurs: its blue-shift is more than 0.1 eV and both the intensity and spectral width strongly increase.

Time-resolved PL decays for different P_{exc} are presented in Fig. 2a. Direct transition is very short at any P_{exc} and corresponds to our temporal resolution. On the other hand, ID recombination decay is very long at low excitation levels becomes shorter with increasing P_{exc} and comparable with D decay at the highest P_{exc}. Integrated ID intensity and decay times τ at different excitation levels are demonstrated in Fig. 2b.

3. Discussion

ZnSe/BeTe is a novel semiconductor system with a type-II band alignment [1] and large band offsets, leading to localizing po-

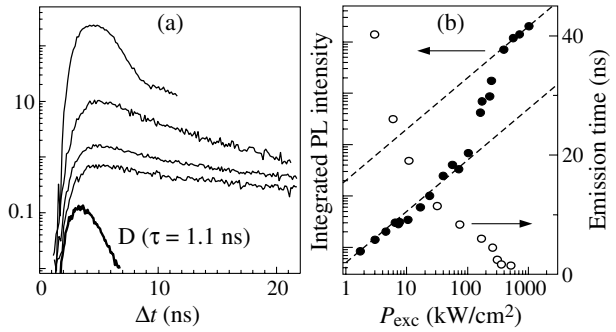

Fig. 2. (a) PL decay as a function of excitation density (520, 170, 32 and 11 kW/cm^2) at the PL maximum of ID band. D (thick line) represents direct transition decay. (b) Integrated ID intensity (closed circles, left scale) and PL decay times τ_{rec} (open circles, right scale) vs excitation density. Dashed lines are linear dependencies.

tentials of ≥ 2.0 eV for electrons in ZnSe layers and ≈ 0.9 eV for holes in BeTe layers. Deep potential wells result in a very small penetration of the carrier wavefunctions into the adjacent layers. Holes, initially excited in ZnSe layers, quickly (less than direct recombination time ~ 0.1 ns) relax to the BeTe layers [3] and radiative recombination is mostly spatially indirect. The ID transition matrix element is very small because of the electron and hole wavefunctions overlap within very narrow region ($\approx 1-2$ ML) at the interface [4], that makes spatially indirect optical transition also extremely sensitive to the interface quality. Consequently, the transition oscillator strength is very small that results in very long radiative recombination times (10–100 ns) and allows to accumulate spatially separated electrons and holes with huge densities exceeding 10^{13} cm^{-2} [4].

At high photoexcitation levels spatially separated electrons and holes with high density in ZnSe and BeTe layers, respectively, induce strong electric fields inside SL, which, in turn, give rise to a strong bending of the conduction and valence bands. This leads to a large blue shift of the carrier energy levels, as well as to a strong change of electron and hole wavefunctions with increasing of their overlap at the interface at high $P_{\rm exc}$ [4]. As a result, radiative time $\tau_{\rm r}$ shortens and ID band intensity increases. That is observed in Fig. 1. Large spectral width of the ID band (150 meV at 250 kW/cm^2) and its spectral shift corresponds to degenerate e-h plasma with density $\sim 1\times10^{13}$ cm^{-2}, according to calculations [4].

The most interesting and intriguing result is a developing of ID band kinetics. A specific behavior of PL intensity vs $P_{\rm exc}$ (like that demonstrated in Fig. 2b) in materials with initially short non-radiative recombination time $\tau_{\rm nr}$, much shorter than radiative time $\tau_{\rm r}$, at low $P_{\rm exc}$ usually corresponds to saturation of such non-radiative channels [2]. Transition region with superlinear intensity dependence separates two different regimes: nonsaturated one with lifetime $\tau = \tau_{\rm nr}$ at low $P_{\rm exc}$ and saturated regime with $\tau = \tau_{\rm r}$ at high $P_{\rm exc}$ when all the non-radiative recombination channels are saturated.

In our experiments opposite picture is observed. While shortening of τ with increasing $P_{\rm exc}$ is explained by the band bending effect at high density of spatially separated electrons and holes, investigated by now in details [4], behavior at low $P_{\rm exc}$ is completely unclear. On one hand, long τ corresponds to flat-band limit with low carrier density and absence of non-radiative recombination channels [1]. On the other hand, the ID band intensity dependence and low total quantum yield η evidence about very strong non-radiative recombination processes in investigated SLs.

To explain the observed unusual behavior of PL intensity and its kinetics we suggest that it is due to strong in-plane inhomogeneity of the SLs, laterally separated on microscopic regions with different η values. In this case the regions with high η magnitudes are responsible for long τ observed at low $P_{\rm exc}$. Places with intermediate value of η contribute to superlinear intensity dependence and saturate at high $P_{\rm exc}$ when quantum yield η approaches $\eta \approx 1$. However due to low total quantum yield a lot of regions remain still completely "dark" with very low quantum yield $\eta \sim 0$ even at the highest $P_{\rm exc}$ until mechanical destruction (at $\simeq 10$ MW/cm^2).

As to a physical origin of the presence of such regions with $\eta \to 0$ there is good reason to think that it could be due to specific property of the ZnSe/BeTe heteropair with no-common atom at the interface. Actually in the case of that sort of interfaces one ML thickness fluctuation results in a change of chemical bond Te–Zn to the bond Be–Se at the interface. As the band gap of BeSe $E_{\rm g} \approx 5.4$ eV is huge as compared to the $E_{\rm g}$ (ZnTe) ≈ 2.4 eV, interface fluctuations would act as a strong static scatterers and, possibly, also contain different centers of non-radiative recombination. There are some evidences of such assumptions. Firstly, structural properties of ZnSe/BeTe interfaces have been investigated in details by high-resolution transmission electron microscopy [5]. It has been found that strain state in ZnSe/BeTe SLs is strongly influenced by their different shear modules, and that the bond configuration at the interface plays an important role for its quality. Thus, both direct and inverted Te–Zn interfaces are very sharp (of ~ 1 ML) while Be–Se interfaces are broader (of ~ 3 MLs) [5]. Secondly, X-ray photoemission spectroscopy, that yielded large value of the valence-band offsets ≥ 0.8 eV, revealed also the effect of the strain and interface chemical content on the electronic properties [6]. Further investigations are required to clarify the situation.

Acknowledgements

This work is supported by RFBR grant No. 04-02016852 and 05-02-17288.

References

[1] S. V. Zaitsev *et al*, *J. Appl. Phys.* **91**, 652 (2002).
[2] K. Zeeger, *Semiconductor Physics*, Springer–Verlag (New York), ch. 12, (1973).
[3] A. A. Maksimov *et al*, *JETP Lett.* **83**, 1 (2006).
[4] A. A. Maksimov *et al*, *Phys. Stat. Sol. (b)* **221**, 523 (2000).
[5] T. Walter *et al*, *Phys. Rev. B* **59**, 8114 (1999).
[6] M. Nagelstraßer *et al*, *J. Appl. Phys.* **83**, 4253 (1998).

14th Int. Symp. "Nanostructures: Physics and Technology"
St Petersburg, Russia, June 26–30, 2006

Effect of cavity mode excitation on emission spectra from pillar microcavity with quantum dots in the active layer

V. D. Kulakovskii[1], G. Sek[2], C. Hofmann[2], M. N. Makhonin[1], R. Krebs[2], A. Loeffler[2], J. P. Reithmaier[2], M. Kamp[2], L. V. Keldysh[2,3], T. L. Reinecke[4] and A. Forchel[2]

[1] Institute of Solid State Physics RAS, 142432 Chernogolovka, Russia
[2] Technische Physik, Würzburg University, Würzburg, Germany
[3] Lebedev Physical Institute, Moscow, Russia
[4] Naval Research Institute, Washington DC, USA

Abstract. By comparing measured PL spectra with theory we show that the spectra depend sensitively on the primary excitation mechanism via QD excitons or the cavity mode. Both cases can be distinguished by the relative intensities of QD and cavity mode. In the latter case a dip in the emission spectrum appears already in the weak coupling regime (due to interference effect between the cavity and QD oscillators).

Introduction

One of the major trends of current semiconductor research is towards achieving a strong coupling between electronic and photonic states of low dimensionality. The simplest system is a quantum dot (QD) in the active layer of a 3D confined microcavity (MC) [1]. The 3D confined pillar MC represents the "ultimate" system, where both electrons and photons are confined in all dimensions. Such a system should exhibit peculiar effects characteristic of a two-level atom in interaction with an optical cavity, e.g. an enhancement or inhibition of the spontaneous emission rate in the weak coupling regime (Purcell effect) [2] and vacuum-field Rabi splitting in the strong coupling regime. In semiconductor MCs, the optical modes C are coupled to electron-hole excitations in the QD, X forming a coupled exciton-photon states [1]. The splitting and the decay of these modes provide important insight into their couplings to their environment, and they also play a critical role in applications of the optical systems.

In a simple approximation, for interacting X and C modes at a resonance ($E_X = E_C = E_0$) the energies of interacting modes are [3]

$$E_{1,2} = E_0 - i\,(\gamma_C + \gamma_X)/2 \pm \left[g^2 - (\gamma_C - \gamma_X)^2/4\right]^{1/2}, \quad (1)$$

where $\gamma_{C,X}$ is the FWHM of the cavity (exciton) mode, $\gamma_C = E_C/2Q \gg \gamma_C$, Q is the cavity finesse, and g is the "vacuum Rabi splitting". The criterion for the strong coupling regime of the QD exciton and MC modes ($\gamma_C \gg \gamma_X$) can be determined as $g > \gamma_C/2$.

The strong coupling regime is fixed as an anticrossing of coupled QD exciton and cavity modes. In a simplified analysis one assumes a similar filling of two coupling modes. However that is definitely not the case especially when the detuning of the cavity and QD exciton mode becomes comparable or exceeds Rabi splitting.

We analyze PL from MCs with QDs for various excitation conditions, namely, under the primary excitation of (i) QD exciton, (ii) cavity mode and (iii) exciton and cavity mode.

1. Experiment

The samples studied are single λ GaAs MC structures with an array of $In_xGa_{1-x}As$ QDs placed at the antinode of the resonant mode. The pillars with a circular cross-section have been processed by ECR and ICP reactive ion-etching of planar MC structures through the Bragg reflector mirrors. PL of single pillars has been measured using a micro PL setup. The excitation was carried out by second harmonics of Nd:YAG laser with wavelength of 532 nm.

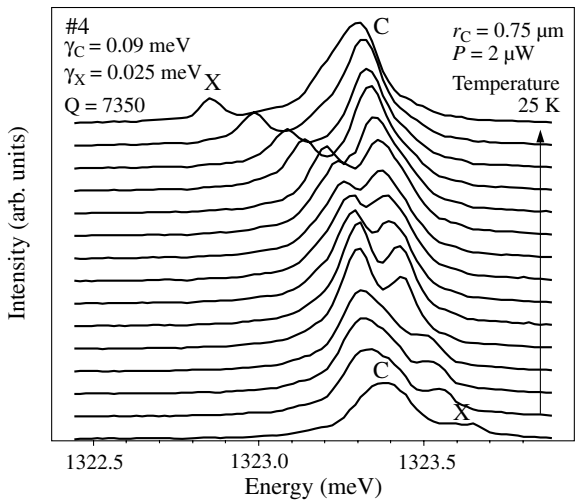

Fig. 1. PL spectra from MC recorded for various temperatures.

2. PL spectra

Figure 1 displays PL from a single pillar MC with the radius of 0.75 μm containing a set of InGaAs QDs in the range of 10–25 K. The spectra at the lowest and highest temperatures consist of a narrow line corresponding to the exciton emission of single QD with γ_X within 0.055 meV and a markedly thicker line with $\gamma_C = 0.18$ meV corresponding to the cavity mode with $Q = 7350$. The variation of the temperature allows one to tune the QD emission on and off the resonance with cavity mode.

Figure 1 shows that with approaching the resonance the PL spectra demonstrate (i) strong broadening of the X line, (ii) narrowing of the MC line, and (iii) well pronounced anticrossing behavior with splitting $\Delta_0 = 0.14$ meV characteristic to the strong coupling regime. It is also seen that the cavity line displays a rather high intensity far from the resonance. That means that one has to take into account the contribution from the primary excitation through the cavity mode [4].

3. MC emission: theory

Depending on the excitation mechanism the spectral density of the electromagnetic field in the cavity may be represented in terms of two functions

$$I_{\rm C} = \omega / \left[(\omega - \Omega_{\rm C} - P(\omega))^2 + (\gamma_{\rm C} + Q(\omega))^2 \right] , \qquad (2)$$

$$I_{\rm X} = g^2 \omega / \left\{ \left[(\omega - \Omega_{\rm C} - P(\omega))\,(\omega - \Omega_{\rm X}) - (\gamma_{\rm C} + Q(\omega))\,\gamma_{\rm X} \right]^2 + \left[\gamma_{\rm X}\,(\omega - \Omega_{\rm C} - P(\omega)) + (\gamma_{\rm C} + Q(\omega))\,(\omega - \Omega_{\rm X}) \right]^2 \right\} . \qquad (3)$$

Here Ω_j are the corresponding resonant frequencies, $P(\omega)$ and $-Q(\omega)$ are the real and imaginary parts of the polarizability of the QD. In the linear regime

$$P(\omega) - i\,Q(\omega) = g^2 / (\omega - \omega_{\rm X} + i\gamma_{\rm X}) . \qquad (4)$$

Both functions $I_{\rm C}(\omega)$ and $I_{\rm X}(\omega)$ describe the radiation of the cavity mode, hybridized with QD resonances but refer to two different mechanisms of the primary excitation. The distinction is in the fact, which of participating in the hybridization partners — cavity mode or QD exciton — is pumped directly by the primary excitation. The function $I_{\rm X}(\omega)$ corresponds to the process of the primary excitation of QDs (photoexcited exciton is trapped by the QD, then being relaxed to the ground QD state, which is resonant and therefore hybridized with the cavity mode). Hybridization itself corresponds to the partial transfer of the excitation into the electromagnetic field. Unlike that the function $I_{\rm C}(\omega)$ refers to the process of the primary excitation coming into the cavity mode, and then becoming hybridized. Both $I_{\rm C}(\omega)$ and $I_{\rm X}(\omega)$ have exactly the same set of poles in the complex plane. However, the shape of spectra may be different drastically due to the difference in residue values. Surely, in any case both freedom degrees become excited, however, with amplitude and phase relations essentially depending on the excitation path. The mathematical manifestation of that is clearly seen in the analytical structure of spectral functions and illustrated in Fig. 2 displaying spectra calculated for primary excitation of the QD and cavity modes for two cases, $g \ll \gamma_{\rm C}$ and $g \sim \gamma_{\rm C}$. Figure shows that the plots of $I_{\rm C}(\omega)$ and $I_{\rm X}(\omega)$ look like mutually complementary. As expected, the behavior of spectra under the excitation of slowly decaying QD, $I_{\rm X}(\omega)$ is very similar to one expected from the simple model (Eq. 1). For the parameter range $\gamma_{\rm X} \ll |g| \ll \gamma_{\rm C}$, the dominating feature in the plot is the Purcell effect. The MC mode itself is practically invisible until some dots approach the resonance. Unlike that the plot $I_{\rm C}(\omega)$ is dominated by the strong and broad MC emission, cut, however, by narrow dip — precursors of the Rabi splitting — at the resonant QD frequency. The dip results from the mode interference and exists already for $g^2 > \gamma_{\rm X}^3/(2\gamma_{\rm C})$. Nothing like that can be seen in the $I_{\rm X}(\omega)$) plot, until the usual strong coupling condition becomes fulfilled.

Generally both types of excitation channels may be effective. Then the luminescence spectrum can be described as a sum

$$I(\omega) = a I_{\rm C}(\omega) + b I_{\rm C}(\omega) , \qquad (5)$$

where a and b are the partial excitation rates in corresponding channels. Then peaks of the second term overlap deeps of the first one, which makes the plot more complicated. The use of formulas (2, 3, 5) allows one to describe the experimental spectra and determine Rabi splitting with a high accuracy. In particular, the spectra in Fig. 1 are well described with the set of parameters $a/b \sim 1$ and $g = 0.055$ meV. The latter differs markedly from Rabi splitting determined with the use of simplified model: $g = \Delta/2 = 0.07$ meV.

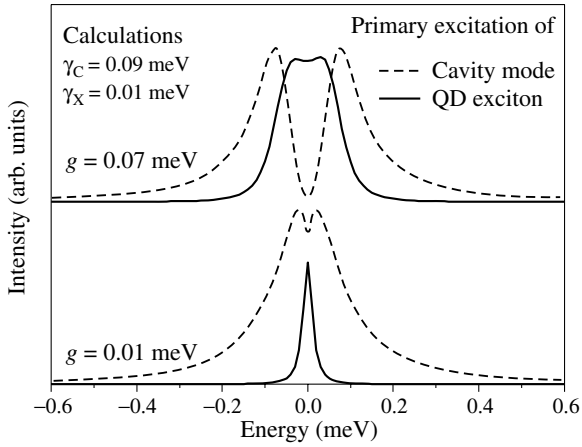

Fig. 2. PL spectra from MCs with $g \ll \gamma_{\rm C}$ (low) and $g \sim \gamma_{\rm C}$ (upper) calculated for primary excitation of the QD and cavity modes, respectively.

In conclusion, by comparing measured PL spectra with theory we have shown that the spectra depend strongly on the primary excitation mechanism via QD excitons or the cavity mode. In the case of primary QD excitation the PL spectra demonstrate (i) extremely weak cavity emission, (ii) strong Purcell effect, and (iii) the appearance of the line splitting only in the strong coupling regime. In contrast, under the excitation of the cavity mode the spectra demonstrate (i) strong cavity emission and (ii) appearance of a well pronounced dip in the cavity peak instead of Purcell enhancement. The latter appears at a very weak coupling, well before the strong coupling regime, and the dip halfwidth exceeds strongly the exciton-photon coupling constant g.

Acknowledgements

Financial support of RFBR, INTAS and the State of Bavaria is gratefully acknowledged.

References

[1] See, e.g., *Confined Excitons and Photons: New Physics and Devices*, ed. by E. Burstein and C. Weisbuch, Plenum, New York, (1995).
[2] E. M. Purcell, *Phys. Rev.* **69**, 681 (1946).
[3] L. C. Andreani *et al*, *Phys. Rev.* **60**, 13276 (1999).
[4] S. Rudin and T. L. Reinecke, *Phys. Rev. A* **62**, 053806 (2000).

14th Int. Symp. "Nanostructures: Physics and Technology"
St Petersburg, Russia, June 26–30, 2006

Evidence of a collapse of the TM photonic stop bands in high-contrast photonic crystals

A. V. Baryshev[1,2], R. Fujikawa[1], A. B. Khanikaev[1], H. Uchida[1] and M. Inoue[1,3]

[1] Toyohashi University of Technology, Toyohashi, Aichi 441-8580, Japan
[2] Ioffe Physico-Technical Institute, St Petersburg, Russia
[3] CREST, Japan Science and Technology Corporation, Tokyo 113-0033, Japan

Abstract. We fabricated three-dimensional a-SiO_2 opaline films of various thicknesses and studied coupling of differently polarized light to their crystalline structure. Photonic stop bands were observed and attributed to the $\{111\}$ family of crystallographic planes. Polarization resolved transmission data show strong anisotropy of light coupling to opaline films. Our studies confirm a collapse of stop bands for TM waves in opaline films, which are representatives of high-contrast photonic crystals.

Introduction

During the past decade a number of groups demonstrated that the appearance of band gaps in the energy spectra of photonic crystals (PCs) [1] is associated with the Bragg diffraction of electromagnetic waves on a periodic variation of dielectric constant. Of special interest is obtaining a complete photonic band gap, i.e. the situation when the photonic band gaps overlap in all directions and form an energy range for electromagnetic waves which propagation is prohibited irrespective of both the state of polarization and direction of waves in a 3D PC. It was theoretically shown that the creation of a complete photonic bandgap is possible for a sufficiently large dielectric contrast in the PC having the face-centered-cubic (fcc) lattice — inverted opals [2], and also in binary titania colloidal structures [3]. A pseudogap in low frequency range was found to exist in an inverted fcc structure [2]. In Ref. [2] the possibility of opening pseudogap of fcc structure into complete photonic band gap was considered via reduction of symmetry. However, the pseudogap does not convert into a complete band gap at the reduction of symmetry from cubic to tetragonal [2].

From the experimental point of view, it is of great interest to observe both a pseudogap and a complete band gap, and also understand their origin. Therefore, experimental studies on polarized light coupling to high-contrast 3D PCs are required. It is worth mentioning that there is the only report on scanning a photonic band structure (PBS) of such structures [4]. In 2005, W. Man *et al* presented a PBS of 3D photonic quasicrystals, high-contrast PCs made from cells and roads and consisted of 17.3 (and 7.36) vol.% polymer. An effective Brillouin zone of a sample having complicated icosahedral symmetry was determined for one chosen state of polarization of microwaves, however, features of the PBS of icosahedral quasicrystals for differently polarized light, especially for TM waves, remain uncertain.

The available experimental data on the polarization-resolved study of 3D PCs at low dielectric contrast conditions are incomplete and their interpretation is still ambiguous. Note that experimentally measured PBS of 3D opal based PCs for non-polarized light was demonstrated but once [5].The polarization- and angle-resolved transmissivity of an fcc colloidal crystals was studied along the directions between the L point and the W point [6]. The results were analyzed in Ref. [7] showing a disagreement between the experimental and calculated photonic stop gaps. The polarization-resolved reflectivity of the opal-based photonic crystals in the vicinity of the L point of the BZ was studied in Ref. [8]. The limited angular range of the incident light could provide only the response of the (111) planes. Recently, experimental results on coupling of differently polarized light to synthetic opals (bulk samples) have been reported [9]. It was demonstrated that transmissivity and reflectivity (diffraction patterns) change with the state of polarization of incident light, indicating a strong polarization dependence of photonic stop bands in synthetic opals. In a sharp contrast with propagation of the TE modes, it was shown that there exists a critical angle of incidence on the (hkl) crystal plane, at which no the TM modes are reflected from crystal planes, the resonance contribution to Bragg diffraction vanishes and the related (hkl) stop band does not open.

Here we present polarization resolved transmissivity of a representative of high-contrast PCs, opaline films. We found a complete collapse of the TM photonic stop bands, when illuminating the samples along certain directions. The TM modes are shown to propagate in films without coupling, which means that photonic crystals are transparent for them. Our studies provide quantitative information on light interaction with opaline films and their structural characteristics.

1. Experimental

Monodisperse colloidal a-SiO_2 spheres with a diameter of 290 nm were assembled on a glass substrate using the vertical deposition method to form an opaline film. The grown films consist of two-dimensional hexagonal layers, (111) layers in the terms of the fcc lattice, which are parallel to the substrate. Our previous studies show that opaline films grown using vertical deposition are divided by through-thickness cracks into domains of different size (10–50 μm); note that in the experiment the preferential orientation of cracks coincides with the axis of rotation [10]. In Ref. [10] the opaline film structure is found to be the twinned fcc, in which domains are fcc-type twins. Diameter of a-SiO_2 spheres and orientation of the (111) hexagonal layers on the glass substrate was checked using field emission scanning electron microscopy.

Transmission measurements were carried out by using polarized collimated beams from a spectrophotometer (Shimadzu UV-3100), cross-sectional size of the light beam was about 4 mm^2. When measuring angle resolved transmissivity $T_{\mathbf{k}}(\lambda)$

along the $L_g \to K \to L$ path, the films under study were rotated about a vertical axis along which a-SiO_2 spheres packed into dense chains. Note that in our experiments the sample was aligned so that that the beam fell on the film at the external angle of incidence, θ, and after that entered the glass substrate. The linearly polarized electric fields were chosen to be normal $\mathbf{E}_\perp$ (TE wave) and parallel $\mathbf{E}_\parallel$ (TM wave) to the scanning plane $L_g \Gamma L$.

2. Results

The series of transmission spectra for the opaline film of $\approx$ 20 layers in thickness are shown in Fig. 1. Plots (a) and (b) present the spectra, when scanning the film with the $\mathbf{E}_\perp$- and $\mathbf{E}_\parallel$-polarized light along $L_g \to K \to L$ path. At normal incidence on the film ($\theta = 0$, the L_g point) transmission spectra ($T_\perp$- and $T_\parallel$) for both polarizations, show one deep of equal intensity, which is the (111) stop band.

In scanning form the L_g point to L point ($\theta > 0$), we find the following results. First, the (111) stop band shifts to the short wavelength spectral range and another deep, which is determined as the $(\bar{1}11)$stop band, experiences shift to the long wavelengths. The mentioned spectral shifts are fairly seen in plot (a), for the $\mathbf{E}_\perp$-polarized light. Note that for the TE modes the spectral width of the (111) stop band is of 50 nm and does not experience significant change with the angle of incidence, while the width of the $(\bar{1}11)$stop band changes to be of about 20 nm at intermediate angles $\theta \in [34^\circ;\ 44^\circ]$ and of about 35 nm at other angles. Second, the $T_\perp(\lambda_B^{(111)})$ transmissivity for the Bragg wavelengths, $\lambda_B^{(111)}(\theta)$ is a spectral position the (111) stop band at the angle θ, gradually decreases as the angle θ rises. Third, which is a key result for high-contrast 3D PCs,

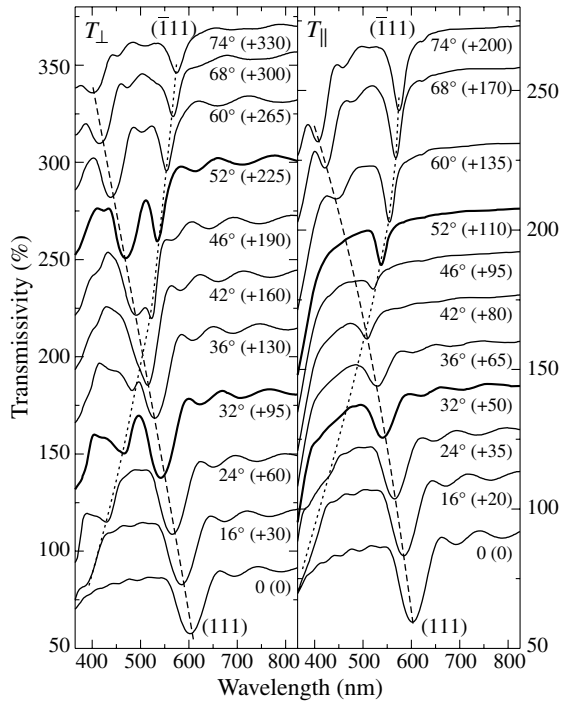

Fig. 1. Transmission spectra of an opaline film taken along the $L_g \to K \to L$ path on the BZ surface of fcc lattice: illumination with the $\mathbf{E}_\perp$-polarized (a) and $\mathbf{E}_\parallel$-polarized light (b). The external angle of incidence θ and vertical shifts of transmission spectra are given.

the $T_\parallel$ transmissivity for $\lambda_B^{(111)}(\theta)$ behaves in a sharp contrast to the $T_\perp(\lambda_B^{(111)})$ transmissivity, namely $T_\parallel(\lambda_B^{(111)}$ rises as the angle of incidence reaches and gains its maximum at $\theta = 52^\circ$, a situation when the (111) stop band does not exist and the TM wave does not couple to the film [see plot (b), thick line]; at angles $\theta > 52^\circ$ we see that the (111) stop band opens and becomes more intensive as θ rises. As for the $(\bar{1}11)$ stop band, one can see that it does not open for a wide range of incident angles but maximum transmissivity of the TM wave $\lambda_B^{(\bar{1}11)}(\theta)$ is observed at about $\theta = 32^\circ$. These transmission spectra ($\theta = 32^\circ,\ 52^\circ$) directly give us the effective refractive index of the film, which is found to be of ≈ 1.28. Also, our data show that the spectral positions of the (111) stop band is described well by the simple Bragg diffraction taking into account refraction on the film surface, whereas shifts of the $(\bar{1}11)$ stop band is not fitted with the Bragg low. These can be explained by different length of the planes — the (111) planes are rather extended but the $(\bar{1}11)$ planes are short.

Main features of transmission spectra can be qualitatively understood by analogy with the Fresnel theory and Brewster effect. However, to fit experimental data quantitatively we used *ab initio* layered Korringa–Kohn–Rostoker (LKKR) method [11] and found both the measured and calculated spectra to be in a good agreement. From our results, it became evident that the vectorial nature of electromagnetic waves prevents formation of a complete photonic band gap for high-contrast 3D PCs in low frequency range and only a pseudogap can appear [2].

In this work, we have demonstrated experimentally a strong polarization dependence of transmissivity and the disappearance of stop bands for TM waves in high-contrast 3D PCs. Our estimations based on *ab initio* LKKR numerical simulation confirm that the TM modes propagate through the high-contrast 3D PC slab without coupling irrespective of the slab thickness, i.e. number of the (111) hexagonal layers.

Acknowledgements

We are grateful to A. B. Granovsky for helpful discussion. This work was supported by Grant-in-Aid for Scientific Research (S) No. 17106004 from Japan Society for the Promotion of Science.

References

[1] J. D. Joannopoulos, R. D. Meade, J. N. Winn, *Photonic Crystals*, Princeton Univ. Press (1995).
[2] K. Busch and S. John, *Phys. Rev. E* **58**, 3896 (1998).
[3] R. Biswas, M. M. Sigalas, G. Subramania, K.-M. Ho, *Phys. Rev. B* **57**, 3701 (1998).
[4] W. Man, M. Menges, P. J. Steinhard, P. M. Chaikin, *Nature* **436**, 993 (2005).
[5] A. V. Baryshev, *et al*, *Phys. Rev. B* **70**, 113104 (2004).
[6] I. I. Tarhan and G. H. Watson, *Phys. Rev. Lett.* **76**, 315 (1996).
[7] V. Yannopapas, N. Stefanou, A. Modinos, *J. Phys.: Condens. Matter* **9**, 10261 (1997).
[8] J. F. Galisteo-Lopez, *et al*, *Appl. Phys. Lett.* **82**, 4068 (2003).
[9] A.V. Baryshev, *et al*, *Phys. Rev. B* **73**, 033103 (2006); M.V. Rybin, *et al*, (in press).
[10] R. Fujikawa, *et al*, *J. Porous Materials* (in press).
[11] A. Modinos, *et al*, *Physica B* **296**, 167 (2001).

14th Int. Symp. "Nanostructures: Physics and Technology"
St Petersburg, Russia, June 26–30, 2006

Membrane photonic crystal defect cavities for quantum wire lasers and 1D polariton

K. A. Atlasov, K. F. Karlsson, E. Deichsel, B. Dwir, A. Rudra and E. Kapon
Ecole Polytechnique Federale de Lausanne (EPFL), Laboratory of Physics of Nanostructures
CH-1015 Lausanne, Switzerland

Abstract. Two-dimensional semiconductor photonic-crystal (PhC) membrane-based microcavities have been considered for integration with V-groove quantum wires (QWR). Single-QWR laser in a high-Q PhC-cavity is discussed. Numerical modelling and optimization of L-type PhC-cavities based on 2D finite-differences and 3D finite-differences time-domain methods is performed, and experimental PhC-samples are fabricated and tested by the internal light source technique.

Introduction

The two-dimensional confinement of the electron wave function in a semiconductor quantum wire (QWR) results in strong modification of the density-of-states distribution exhibiting singularities. As a consequence, the luminescence spectrum of a QWR is expected to show a linewidth sharpening at low excitation powers, which should lead to an increased material gain coefficient for a specific spectral range. Therefore, lasers based on such a structure were predicted to have significantly reduced threshold operation [1]. In practice however, in order to overcome the lasing threshold the laser cavity must have minimized losses while on the other side, the optical confinement factor should be maximized. Regarding the scientifically interesting case of a single-QWR laser, this would imply implementing a cavity that possesses both sufficiently high finesse (Q-factor) and small modal volume.

Semiconductor photonic crystal (PhC) membrane-based microcavities provide strong confinement for the electromagnetic field of certain resonant frequencies attaining very high Qs together with extremely small modal volumes [2]. Moreover, such a cavity allows for efficient control of the spontaneous emission (SE) of the incorporated source, significantly increasing the SE-into-lasing-mode factor β, which lowers further the lasing threshold and may lead even to a thresholdless lasing phenomenon [3]. Additionally, as a result of PhC-QWR integration, other phenomena may be observed such as 1D-polariton when a QWR is incorporated into a PhC-cavity extended in one dimension.

In the present paper we study both theoretically and experimentally the L_n-cavity type (n missing holes in a row) in a hexagonal photonic lattice with the aim of the integration of such cavities with V-groove QWRs [4].

1. Modelling

Our numerical analysis is based on fast 2D finite-difference (FD) eigenvalue computation with effective-index approximation. Cavity resonances as well as mode distributions are thus extracted and further analyzed with respect to their potential Q-values and primary polarization. The latter is also important for efficient coupling with the QWR due to its polarization anisotropic gain spectrum [5]. As an illustrative example, Figure 1 shows the near-field distribution of the E_x-component of a potentially high-Q mode of the L_6 cavity polarized mainly along the QWR (x-direction). In order to determine the Q of a given mode and deduce the cavity resonance spectrum, analysis in k-space [6] is performed relying on calculations of the out-of-plane losses. Since this analysis is done using a 2D model where the electro-magnetic field is described by TE-like modes in the center of the slab, only qualitative data on cavity losses can be extracted. However, it is sufficient for making a prediction of the general trend and for finding a relative relationship between modes with lower and higher Qs.

The selected modes of potential interest are further analyzed by using full 3D finite-difference time-domain (FDTD) simulation. It is found that, by modifying the cavity geometry with respect to the given mode distribution symmetry, extremely high Q-values may be obtained for this specific resonant frequency while the modal volume undergoes only minor changes. $Q > 2\times10^5$ can be, for example, attained on a modified L_6 cavity by introducing a certain shift of first upper and lower rows of the holes (Fig. 2). Following further this example, the confinement factor Γ for a single V-groove QWR of effective cross-sectional area of $\sim$ 80 nm^2 was estimated using the 3D electric-field distribution. The value $\Gamma \sim 0.001$ was obtained. A rough estimation based on the exponential field decay assumption in a general lossy cavity suggests that in order to reach lasing threshold (at threshold material gain of $\sim 10^4$) a Q-factor of $\sim 2\times10^4$ is required. Thus in principle it seems feasible to attain lasing threshold even with a single short QWR.

Considering a QWR as a 1D electronic system embedded into a PhC cavity, it is very interesting to study the case when the photonic system becomes 1D. The coupling between excitons and photons that both have 1D-like density of states may lead to the observation 1D polaritons. By extending the L_n-type PhC cavity in one dimension (i.e. by increasing n) we were able to model the mode evolution during such a transition. As n is increased, more and more photonic states come into scene to form two very dense subbands separated by a gap. The density of states bears a clear signature of 1D photonic wire formation

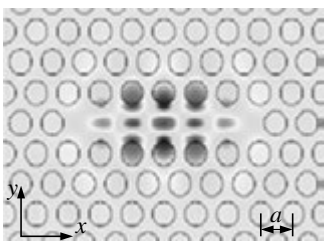

Fig. 1. Computed E_x-distribution of a x-polarized potentially high-Q mode of the L_6 PhC membrane defect cavity.

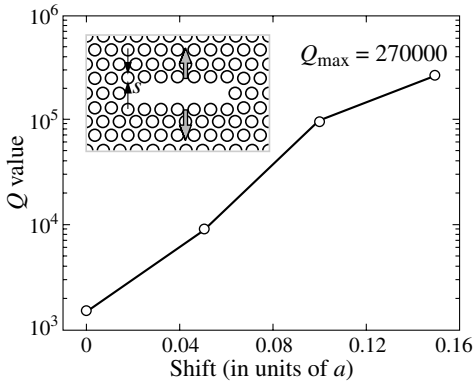

Fig. 2. Geometrical optimization of the L_6 PhC cavity for attaining high Q for a selected resonant frequency. First upper and lower rows of the holes are shifted by $s = 0 - 0.15a$. The simulation predicts that starting from $Q \simeq 1500$ for $s = 0$, values of $Q > 2\times10^5$ may be attained.

representing in the extreme case of an infinitely long cavity the dispersion diagram of a PhC waveguide.

2. Experimental

The fabrication technology for PhC-membrane realization, being fully based on e-beam lithography, employs clorine-based reactive ion etching (RIE) and highly selective wet underetching of the sacrificial $Al_xGa_{1-x}As$ layer. The RIE may be done either directly through the PMMA (electron resist) or through an additional SiO-layer involving in the latter case an additional pattern transfer step. Best results were however obtained with SiO. Figure 3 shows an example of one of our samples: 200 nm thick free-hanging GaAs PhC-membrane (SEM oblique view – cross-section through the membrane).

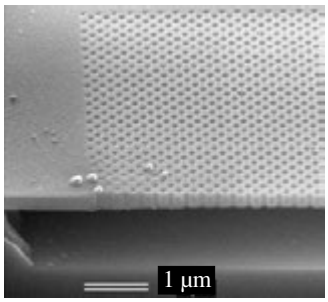

Fig. 3. SEM oblique view of the sectioned free-hanging GaAs PhC-membrane.

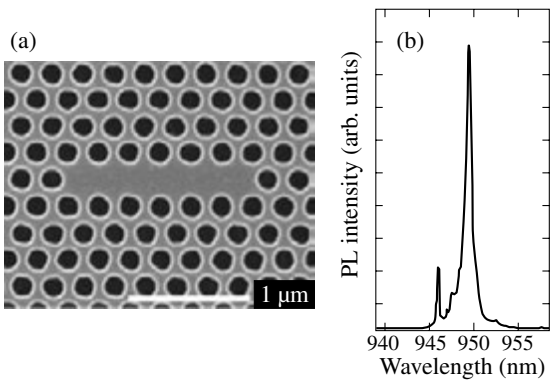

Fig. 4. (a) SEM top view on a 260 nm pitch PhC-membrane with a L_6 defect cavity in the center and (b) 10 K PL spectrum showing its dominating mode.

A top SEM view is presented in Fig. 4a where the cavity is formed by omitting 6 holes in a row. The crystal's pitch a and the r/a ratio (r being the opening's radius) are chosen to match the 900–1000 nm working spectral range. The characterization of such cavities is performed by the well-known internal light source technique [7]. A layer of InAs self-assembled quantum dots (QDs) incorporated into the membrane during OMCVD growth is used as a relatively broad-band light source which at the same time ensures carrier capture and efficient radiative recombination. Low temperature (10 K) PL measurements showed that such a cavity has a relatively high finesse ($Q \sim$ 1300 was found, Fig. 4b) and is indeed promising for further optimization toward the integration with the QWR.

3. Conclusion

L_n-type of PhC membrane-based cavity was numerically studied, fabricated and tested with a perspective on its integration with a QWR. Performed numerical calculations have resulted in a design of PhC cavities appropriate for QWR integration. In order to attain lasing in the considered PhC-QWR system relatively high cavity Q values are required, which can be reached by means of optimization of the cavity geometry. Vertical stacking of QWRs may be also regarded as an efficient solution to increase the confinement factor and therefore lower the required cavity finesse. Additionally, the potential phenomenon of 1D polariton was discussed indicating the perspective of 1D exciton-photon system formation.

References

[1] A. Yariv, *Appl. Phys. Lett.* **53**, 1033 (1988).
[2] Y. Akahane *et al*, *Nature* **425**, 944 (2003).
[3] F. De Martini and G. R. Jacobovitz, *Phys. Rev. Lett.* **60**, 1711 (1988).
[4] E. Kapon *et al*, *Superlattices and Microstructures* **12**, 491 (1992).
[5] D. S. Citrin and Y.-C. Chang, *IEEE J. of Quant. Electron.* **29**, 97 (1993).
[6] D. Englund *et al*, *Optics Express* **13**, 5961 (2005).
[7] H. Benisty *et al*, *J. Lightwave Technol.* **17**, 2063 (1999).

14th Int. Symp. "Nanostructures: Physics and Technology"
St Petersburg, Russia, June 26–30, 2006

Photonic properties of a nanoporous metal: Rayleigh anomalies versus Mie plasmons

T. V. Teperik[1], V. V. Popov[1], Yu. A. Avetisyan[2], F. J. García de Abajo[3], T. Kelf[4], Y. Sugawara[4] and J. J. Baumberg[4]

[1] Institute of Radio Engineering and Electronics (Saratov Division), Russian Academy of Sciences, 410019 Saratov, Russia
[2] Institute of Precision Mechanics and Control, Russian Academy of Sciences, 410028 Saratov, Russia
[3] Donostia International Physics Center, Aptdo. 1072, 20080 San Sebastian, Spain
[4] Department of Physics and Astronomy, University of Southampton, Southampton, SO17 1BJ, United Kingdom

Abstract. We study the plasmonic and photonic properties of metal surfaces, which have a periodic lattice of close-packed voids buried immediately beneath their surface. There are three type of anomalies that are observed in the reflectivity spectra of these nanoporous metal surfaces: surface plasmon-polariton resonances, Mie plasmons in voids, and Rayleigh anomalies. We focus on the interaction between two latter type of the anomalies and show that the Rayleigh anomalies are drastically enhanced by Mie plasmons in voids. Diffraction spectra are measured and calculated to support these conclusions, showing good quantitative agreement.

Introduction

Considerable advances having been made recently in template-assisted assembly of microporous and nanoporous metal structures with peridocally arranged pores [1–3] prompted the investigation of their optical properties. There are three type of anomalies that can be observed in the optical spectra of such structures: surface plasmon-polariton resonances, Mie plasmons in voids, and diffractive Rayleigh anomalies. On one hand, the lattice of voids beneath the flat metal surface acts as a coupling element, which couples incoming light to the surface plasmon-polaritons and diffracted beams. On the other hand, in this specific type of a resonant grating coupler the inherent confined resonances in the voids (Mie plasmon resonances) can be excited. Therefore, one can expect a complex optical response associated with different type of plasmon excitations in periodic porous metal structures. The role of surface plasmon-polaritons and Mie plasmons in molding the optical spectra of nanoporous metals has been discussed in recent publications [3–5]. In particular, the interaction between the surface-plasmon polaritons and Mie plasmons localized in the buried voids have been observed in reflectivity spectra of nanoporous metal surfaces [3] and theoretically explained in [5]. However, the diffractive Rayleigh anomalies on the surface of nanoporous metals, which are associated with opening the diffraction orders into surrounding medium, have not been studied neither experimentally nor theoretically.

In this paper, we study the plasmonic and photonic properties of a hexagonal two-dimensional (2D) lattice of close-packed spherical nanovoids buried inside metal below a flat metal surface both experimentally and theoretically. The experimental sample was prepared using a nanoscale casting technique with the electrochemical deposition of metal through a self-assembled latex template [1–3]. To calculate the reflectivity spectra of such a nanoporous metal surface we use a self-consistent electromagnetic multiple-scattering layer-Korringa–Kohn–Rostoker (KKR) approach [4,6]. This approach allows us to elucidate the behavior of localized Mie plasmons in voids, delocalized surface plasmon-polaritons, and diffracted photons. We focus on the investigation of diffracted beams (Rayleigh anomalies) and their interaction with Mie plasmons in voids.

Results and discussion

Incoming light is incident at an angle θ to the surface normal on a flat surface of metal that contains a 2D lattice of voids just beneath the metal surface (Fig. 1a). The incident light has p-polarization with its plane of incidence along the $\Gamma - M$ direction of the first Brillouin zone (see Fig. 1b). The lattice of voids has primitive vectors $\mathbf{a}$ and $\mathbf{b}$, where $|\mathbf{a}| = |\mathbf{b}|$ and $\mathbf{a} \cdot \mathbf{b} = |\mathbf{a}|^2 \cos 60^\circ$.

The frequencies of grazing photons can be estimated in the 'empty lattice approximation' as $\omega = c|\mathbf{q}_{pq}|$, where $\mathbf{q}_{pq} = \mathbf{k}_\parallel + \mathbf{g}_{pq}$ are the wavevectors of grazing photons, $\mathbf{g}_{pq} = p\mathbf{A} + q\mathbf{B}$ are the reciprocal lattice vectors, $\mathbf{A} = 2\pi(\mathbf{b}\times\mathbf{n})/|\mathbf{a}\times\mathbf{b}|$ and

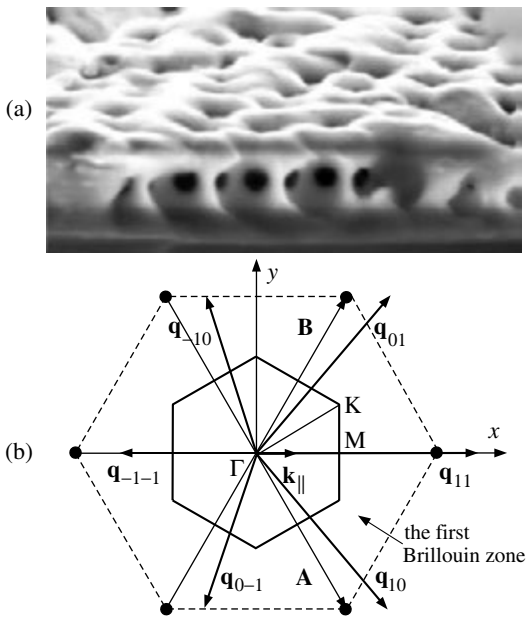

Fig. 1. (a) Experimental sample and (b) the first Brillouin zone and the wavevectors of grazing photons $\mathbf{q}_{pq}$ in the lowest frequency subband with $\mathbf{k}_\parallel$ along the $\Gamma - M$ directions.

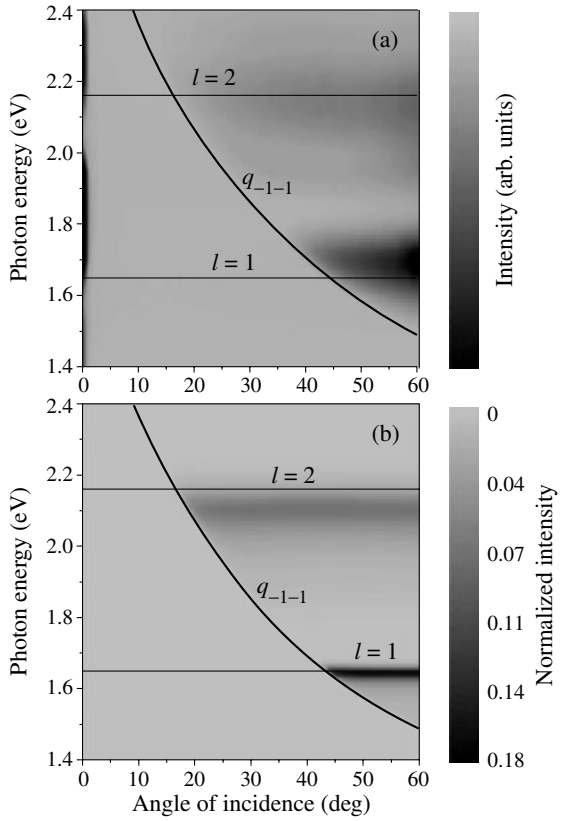

Fig. 2. (a) The measured and (b) calculated intensity of diffractive beam with in-plane wavevector $\mathbf{q}_{-1,-1}$ as a function of the photon energy $\hbar\omega$ and angle of incidence θ for a surface of nanoporous gold formed by a hexagonal arrangement of close-packed spherical voids of diameter 500 nm buried just beneath the metal surface. Curves labeled with q_{-1-1} mark the dispersion of grazing photons estimated in the 'empty lattice approximation'. The horizontal straight lines mark the energy of the fundamental ($l = 1$) and second ($l = 2$) Mie-plasmon mode of a single void in bulk gold. The calculated intensity of the diffracted beam is normalized to the intensity of the incident light.

$\mathbf{B} = 2\pi(\mathbf{n}\times\mathbf{a})/|\mathbf{a}\times\mathbf{b}|$ are the primitive vectors of the reciprocal 2D lattice, p and q are integers, and $k_{\parallel} = (\omega\sin\theta)/c$ is the in-plane component of the incident light wavevector (see Fig. 1b), which is equal to zero in the case of normal incidence. The frequencies of void plasmons can be approximated in the framework of a simple model of the plasmon modes supported by a spherical void in an infinite metallic medium [1].

Results of both measurements and calculations of intensity of the specularly reflected beam (not shown here) demonstrate that the Mie plasmon resonances quench abruptly starting with the onset of the respective Rayleigh anomaly that corresponds to the emergence of a grazing photon (diffracted beam). The reason for this is that the diffracted beam consumes a certain amount of energy of the specularly reflected beam.

Figure 2 shows the measured and calculated intensity of the first-order diffracted beam with in-plane wavevector $\mathbf{q}_{-1,-1}$ as a function of the photon energy $\hbar\omega$ and angle of incidence θ for a nanoporous gold surface formed by the hexagonal arrangement of close-packed spherical nanovoids with diameter 500 nm buried just beneath a continuous surface of gold. Naturally, the diffracted beam appears only in the frequency/angle-of-incidence region to the right of the dispersion curve for grazing photons with wavevector $\mathbf{q}_{-1,-1}$. However, the intensity of the diffracted beam becomes strong only at the frequency of the Mie plasmon resonances. Obviously, the polar angle of diffraction decreases with increasing angle of incidence. Note that in the case under consideration the diffracted beam with in-plane wavevector $\mathbf{q}_{-1,-1}$ preserves the polarization of the incident wave (p-polarization). The theoretical results agree quantitatively with experimental data, demonstrating that the diffracted beam gains a significant intensity only at the Mie plasmon resonance frequency. However, the width of plasmon resonances in the experimental plot is broader than predicted by the theory (cf. Fig. 2a and Fig. 2b). One possible reason for such broadening of the plasmon resonances may be the scattering of electrons from the void boundaries [7] in thin membrane-like metal regions between the close-packed voids, although the role of additional inhomogeneous plasmon broadening caused by imperfections in the experimental sample also cannot be ruled out.

The Mie plasmon resonance in voids is characterized by enormous Q-factor, huge local field enhancement and also can be tuned in frequency by variation of dielectric properties of a void-infiltrating material [4]. Because of that the frequency-selective excitation of intensive diffracted beams can be achieved in nanoporous metal structures.

In conclusion, the Rayleigh anomalies on nanoporous metal surfaces have been shown to be hugely enhanced due to the excitation of Mie plasmons localized in the voids. The effect can be used for characterization of nanoporous metal structures as well as in optoelectronics for designing various photonic devices.

Acknowledgements

This work was supported by the Russian Academy of Sciences, Russian Foundation for Basic Research (Grant 05-02-17513) and UK EPSRC EP/ C511786/1. Y.S. was supported by a *JSPS* Fellowship for Research Abroad, HEISEI 15. T.V.T. acknowledges the support from the President of Russia through the grant for young scientists MK-1802.2005.2. F.J.G.A. acknowledges support from the Spanish MECD (contract No. FIS2004-06490-C03-02) and from the EU (*Metamorphose* No. E NMP3-CT-2004-500252).

References

[1] S. Coyle *et al*, *Phys. Rev. Lett.* **87**, 176801 (2001).
[2] M. E. Abdelsalem *et al*, *Adv. Mater.* **16**, 90 (2004).
[3] T. A. Kelf *et al*, *Phys. Rev. Lett.* **95**, 116802 (2005).
[4] T. V. Teperik *et al*, *Phys. Rev. B* **71**, 085408 (2005).
[5] T. V. Teperik *et al*, *phys. stat. sol. (c)* **202**, 362 (2005).
[6] N. Stefanou *et al*, *Comput. Phys. Commun.* **113** 49 (1998); **132** 189 (2000).
[7] T. V. Teperik *et al*, *Phys. Rev. B* **69**, 155402 (2004).

14th Int. Symp. "Nanostructures: Physics and Technology"
St Petersburg, Russia, June 26–30, 2006

Polarization dependent stop-band collapse in 1D photonic crystal

A. A. Dukin, N. A. Feoktistov, A. V. Medvedev, A. B. Pevtsov, A. V. Sel'kin and V. G. Golubev
Ioffe Physico-Technical Institute, St Petersburg, Russia

Abstract. Bragg reflection spectra of high-contrast silicon-based 1D photonic crystals were measured at oblique incidence of light. The angular behavior of stop-band width has been investigated in the vicinity of the critical angle of incidence θ_c (an analogue of Brewster angle) at which the stop-band for TM-mode disappears. The stop-band inhibition is experimentally observed against the background of pronounced Fabry–Perot interference due to the finite thickness of a photonic crystal slab. The conditions for the stop-band collapsing are considered theoretically and shown to be in good agreement with the experimental data presented.

Introduction

The interaction of electromagnetic radiation with a photonic crystal representing a periodic dielectric structure with a spatial period of modulation comparable with the light wavelength strongly modifies the photon energy spectrum. It exhibits, in particular, the presence of photonic band gaps and well-defined effects of resonance Bragg light diffraction [1]. The energy band structure of photons is determined by their polarization state and varies with the crystal symmetry and the ratio of the dielectric constants of materials comprising the periodic medium [2].

Optical effects due to the propagation of polarized light through a periodic structure are of special interest (see, e.g., [3]). It is predicted [3], when the oblique incidence of light from a high-density optical medium approaches a critical angle θ_c (an analogue of the Brewster angle), the TM stop-band width (in p-polarization) has to tend to zero, leading to the stop-band collapse: the resonance Bragg diffraction is inhibited in p-polarization. On the other hand, there is a TE stop-band (in s-polarization), producing a noticeable Bragg diffraction effect. Experimental studies in this area were limited by angular measurements of Bragg reflection peak intensity from low-contrast 1D holographic gratings [4, 5].

In the present work high dielectric-contrast silicon-based 1D photonic crystals with finite number (14) of layers were selected as objects for the study. This photonic crystals possessed rather wide stop-band, whose width is noticeably larger than the broadening due to the inhomogeneity and radiative decay of the eigenmodes. The choice of appropriate samples enabled us to measure the angular dependence of Bragg reflectance contour in detail and to establish behavior pecularities of the stop-band width near the critical angle. The experimental data were compared with model computations.

1. Sample parameters: evaluation and fabrication

We synthesized a 1D photonic crystal representing a 14-layer Bragg structure made up of alternating quarter-wave a-Si:O:H and a-Si:C:H layers deposited on a quartz substrate [6, 7]. The thicknesses (a-Si:C:H, $a = 190.8$ nm; a-Si:O:H, $b = 273.6$ nm) and dielectric constants of individual layers ($\varepsilon_a = 4.4$, $\varepsilon_b = 2.14$) were chosen such that the structure possessed a noticeable dielectric contrast determining the stop-band width. In order to achieve critical angle of incidence the sample was placed in a glass vessel filled with liquid CCl_4 with $\varepsilon_v = 2.01$.

We used the above values of ε_a, ε_b, a, b, and period $L = a + b$ to simulate the band structure of an infinite 1D photonic crystal which is depicted in Fig. 1 (the gray regions are propagating states and the white regions are evanescent states). The computations show that the TM stop-band disappears (the dotted circle) at the angle $\theta = \theta_c = 57.82^\circ$ for light coming from the liquid CCl_4 ambient.

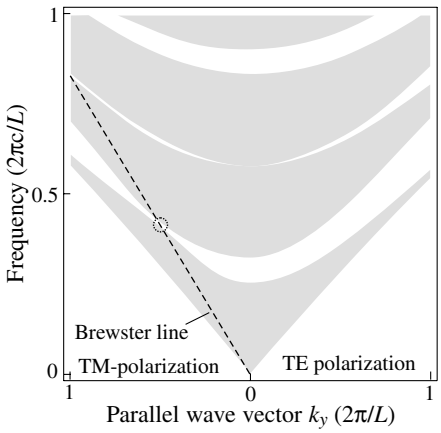

Fig. 1. The calculated band structure of an infinite 1D photonic crystal studied in present work. The dashed circle shows the site of the first stop-band collapse.

2. Results and discussion

The reflection spectra were registered by an automatic grating monochromator in a lock-in mode. The radiation detector was an InGaAs photodiode. The model calculations were made using the transfer matrix method for a structure of 14 alternating a-Si:O:H/a-Si:C:H layers, accounting for the characteristics of the quartz substrate $\varepsilon_{\text{substrate}} = 2.14$ and the ambient (CCl_4, $\varepsilon_v = 2.01$).

The experimental reflectance spectra shown by solid lines in Fig. 2 were normalized to the theoretical spectra (dashed lines) for the TM mode and the angles of 40–69°. Far from θ_c the spectra have a wide (~ 200 meV) contour of nearly 100% reflectance. The stop-band width ΔE_{SB} can be estimated from the experimental data (Fig. 2) as the width ΔE (FWHM) of the Bragg reflectance contour. As the incidence angle becomes larger, the reflected signal intensity decreases, reaching a minimum in the vicinity of the critical angle, and then it rises again. The width ΔE behaves similarly. The insert to Fig. 2 shows magnified reflectance spectra registered at $\theta = 58.5^\circ$, close to the critical angle. Of importance is the fact that the resonance contour corresponding to the stop-band is then strongly masked by the Fabry–Perot interference structure.

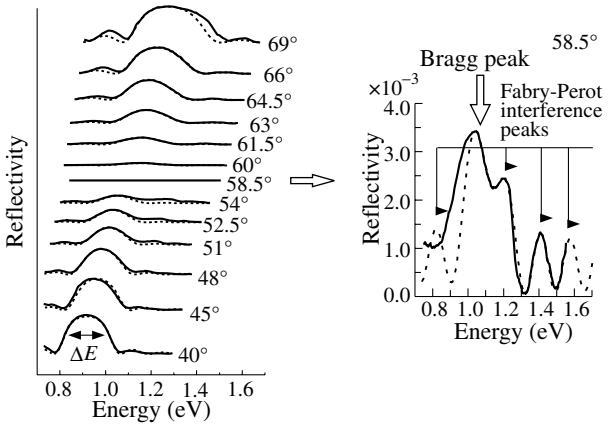

Fig. 2. Experimental (solid lines) and theoretical (dashed lines) reflection spectra in p-polarization of light for a 1D photonic crystal consisting of periodic quarter-wave a-Si:O:H and a-Si:C:H layers at various incidence angles from the ambient (liquid CCl_4). The experimental spectra are normalized to the calculated ones. For convenience of comparison, the spectra are shifted along the Y-axis. The insert on the right shows the reflection spectra at $\theta = 58.5^\circ$, close to the critical incidence angle in the experimental structure.

Let us discuss in more detail the behavior of reflection spectra in the immediate vicinity of the critical angle. To analyze their transformation, it is convenient to consider the relative width $\Delta E/E_c$, where E_c is the position of the reflection peak maximum. Figure 3 illustrates the experimental (black circles) angular dependences of the peak intensities of the Bragg reflection contour (Fig. 3a) and its relative width $\Delta E/E_c$ (Fig. 3b). One can see that the reflection intensity of the 14-layer structure drops by about two orders of magnitude (Fig. 3a), whereas the relative width $\Delta E/E_c$ decreases only by 50% (curve 1 in Fig. 3b). Thus TM stop-band collapse has been not observed experimentally for the 1D photonic crystal of finite thickness.

For comparison, Fig. 3b presents the calculated angular dependence of $\Delta E/E_c$ for a model 40-layer structure possessing the same parameters (curve 2). It is seen that the relative width

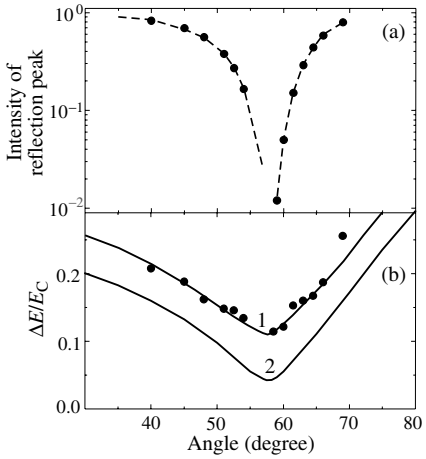

Fig. 3. (a) The angular dependence (black points) of the Bragg reflection peak intensity in p-polarized light for a 1D photonic crystal consisting of periodic quarter-wave a-Si:O:H and a-Si:C:H layers. For clarity, the points are connected with a dashed line. (b) The angular dependences of the relative width $\Delta E/E_c$ of the Bragg reflection contour for the experimental 14-layer (1) and a model 40-layer (2) structures. Black points — experiment, solid lines — calculations.

of the Bragg reflectance band decreases with increasing the number of layers, as compared with the experimental 14-layer structure. However, the width $\Delta E/E_c$ still has a rather large finite value of $\sim 5\%$ (curve 2).

The latter circumstance is directly related to the specific of light propagation in the vicinity of the critical incidence in a bounded spatially periodic structure. At the angles $\theta \approx \theta_c$, the attenuation length $\xi = -NL/\ln T$ ($L = a + b$ is the period of the structure, N is the number of periods and T is the transmittance) of the TM mode becomes comparable with the periodic structure thickness, so light propagates practically without being scattered by the layer interfaces. Therefore, the periodic structure can be considered as a quasi-homogeneous film of thickness NL, located on a semi-infinite substrate.

In this case the experimental FWHM of the reflectance contour (ΔE_{min}) is defined by the width of equidistant bands arising from Fabry–Perot light interference in a film of finite thickness. The value of ΔE_{min} varies with the number of layers in the structure and the dielectric constants of adjacent (ambient and substrate) media. Our transfer matrix calculations of the reflection spectra at various incidence angles agree with the experimental data.

In conclusion, a pronounced supression of stop-band in 1D photonic crystal for p-polarization has been demonstrated. The experimentally measured width of Bragg reflectance contour is limited from below by the Fabry–Perot interference peak width, which depends on thickness of the structure investigated. The value of the critical angle found from the Bloch wave equation fits well the results of numerical simulation and experiments for bounded 1D photonic crystals.

Acknowledgements

The work was supported by the Russian Foundation for Basic Research (Grants # 05-02-17776, 05-02-17803), and the EC-funded Contract PHOREMOST (FP6/2003/IST-2-511616).

References

[1] J. D. Joannopoulos, R. D. Meade, and J. N. Winn, *Photonic Crystals: Molding the Flow of Light*, Princeton, NJ: Princeton University Press, 1995.

[2] J. Rarity and C. Weisbuch, *Microcavities and Photonic Bandgaps: Physics and Applications*, Dordrecht-Amsterdam: Kluwer, 1996.

[3] A. Yariv and P. Yeh, *Optical Waves in Crystals*, New York: Wiley, 1984.

[4] K. Ren *et al*, *Optics Communic.* **241**, 357 (2004).

[5] V. Kimberg *et al*, *J. Opt. A: Pure Appl. Opt.* **6**, 991 (2004).

[6] A. B. Pevtsov *et al*, *Int. J. Electronics* **78**, 289 (1995).

[7] A. A. Dukin *et al*, *Appl. Phys. Lett.* **77**, 3009 (2000).

14th Int. Symp. "Nanostructures: Physics and Technology"
St Petersburg, Russia, June 26–30, 2006

Second-harmonic generation spectroscopy of 3D gallium nitride photonic crystals

A. A. Fedyanin[1], O. A. Aktsipetrov[1], D. A. Kurdyukov[2], V. G. Golubev[2] and M. Inoue[3]

[1] Department of Physics, M. V. Lomonosov Moscow State University, 119992 Moscow, Russia
[2] Ioffe Physico-Technical Institute, St Petersburg, Russia
[3] Toyohashi University of Technology, 441-8580 Toyohashi, Japan

Abstract. Intensity of second-harmonic generation from 3D photonic crystals fabricated from opal templates impregnated by gallium nitride and silicon shows pronounce enhancement for wavelength and angles of incidence corresponding to efficient nonlinear diffraction along the Λ direction.

Introduction

Impregnation of three-dimensional (3D) photonic crystals of opals by functional semiconductors, metals or dielectric (magnetic) opens new functionalities of photonic crystals including modification of photonic band structure by external impacts [1]. The dielectric function periodicity imposed by initial opal matrix is utilized for the control of the optical field propagation inside such composite photonic crystals. However, the even-order nonlinear-optical processes such as second-harmonic generation (SHG) are forbidden in the bulk of amorphous silica microspheres due to their inversion symmetry. Effective nonlinear diffraction in SHG can be observed in opal photonic crystals after impregnation of opal voids by noncentrosymmetric semiconductors.

The III-nitrides, including GaN, InN, and AlN, have proven to be robust materials for the development of blue or green LEDs and violet lasers lasers [2]. The detector sensitivity can be increased in photodetector applications since the wide band gap of the nitrides aids to minimize the dark current. The transparency to visible light will reduce the need for the extensive external filters. One-dimensional photonic crystals, such as multilayered Bragg mirrors and filters fabricated from these materials also have applications for lasers and photodetectors. In this way, fabrication of 3D photonic crystals based on nitrides is an important topic both from fundamental and practical reasons.

In this paper, realization of enhancement of second — harmonic generation in 3D photonic crystals utilizing nonlinear diffraction is demonstrated. The second-harmonic (SH) intensity is increased significantly if the fundamental wavelength is close to the Bragg reflection condition. Spectral dependence of the intensity of the SH light generated in reflection from the (111) faces of the fcc opal lattice demonstrates the pronounce enhancement when the fundamental wavelength is tuned across the photonic band gap (PBG).

1. Experimental

The samples are composed from close-packed silicon oxide spheres with diameter of 250 to 300 nm in each sample forming an ordered fcc opal matrix. The opal voids are filled by noncentrosymmetric gallium nitride and centrosymmetric silicon with filling factor close to unit by the thermal chemical vapor deposition. The photonic band gap is obtained for light reflected from the (111) face and localized in the spectral region from 800 to 950 nm for different samples. The PBG is blue-shifted by approximately 100 nm in comparison with unfilled opals. Scanning electron microscope images show that the size of a single domain ranges from 30 to 100 microns. The reflection spectra measured for small angles of incidence upon the (111) faces of photonic crystals shows maximum of reflectance achieved at the wavelength corresponding to the photonic band gap for this light direction. The PBG center wavelength is monotonous blue-shifted with the increase of the incident angle.

SHG spectroscopy is realized by tuning the fundamental wavelength, λ_ω, at the small angle of incidence, $\theta \simeq 12^\circ$. The output of a nanosecond OPO laser system tunable from 720 nm to 1000 nm is used as the fundamental radiation. Laser energy is approximately 10 mJ per pulse, pulse width is below 2 ns and laser spot area is below 0.5 mm^2. The second-harmonic radiation reflected from the (111) photonic crystal surface is separated by a set of appropriate color filters and detected by a photomultiplier tube. A monochromator is used to check the spectral background. The reference channel is used to normalize the SH intensity spectrum over the laser fluence and the spectral sensitivity of the optical detection system. A z-cut quartz plate is used as a source of the reference SH signal and the detection system is identical to the system in the sample channel.

2. Enhancement of SHG in GaN — opal photonic crystals

Figure 1 shows the spectral dependence of the SH intensity when the fundamental wavelength is tuned in the spectral region of the PBG. For comparison, Figure 1 shows also the linear reflection spectrum. Maximum of reflectance is achieved at the wavelength of $\lambda_{\mathrm{PBG}} \simeq 770$ nm and $\lambda_{\mathrm{PBG}} \simeq 790$ nm and corresponds to the PBG for this light direction for each sample. FWHM of the reflection peak is approximately from 60 to 70 nm. The PBG center wavelength λ_{PBG} is monotonous blue-shifted with the increase of the incident angle θ. Both waves in the experimental, fundamental and second-harmonic, are polarized perpendicular to the plane of incidence corresponding to the s-in, s-out polarization configuration. The SH intensity peaks at 800 nm and 840 nm for each sample that is red-shifted from the PBG wavelength measured at the same angle of incidence. The magnitude and the spectral shape of the SHG peak are checked to be almost the same for other polarization combinations of the fundamental and SH waves. The SHG growth at the blue edge of the spectra is due to the quadratic susceptibility resonance associated with the direct electron transitions

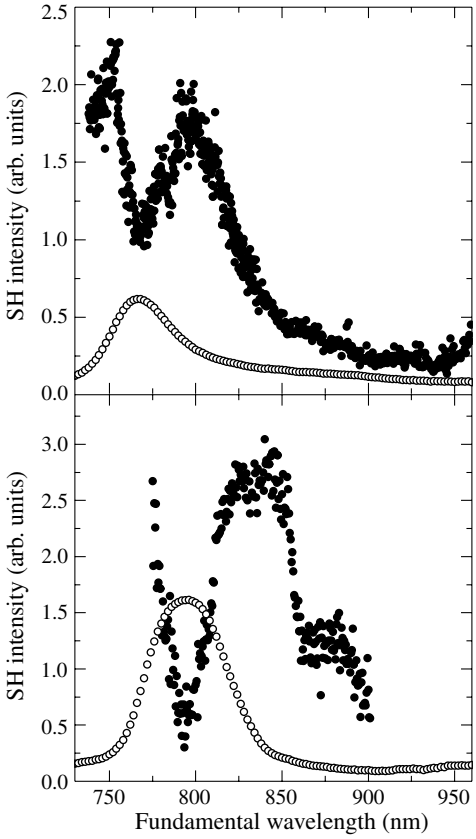

Fig. 1. Second-harmonic intensity (filled circles) and linear reflection (open circles) spectra for two opal — GaN photonic crystals.

in gallium nitride in the vicinity of 3.2 eV.

The SHG enhancement is attributed to combination of linear diffraction of the fundamental radiation from the (111) opal layers and nonlinear diffraction utilizing the 3D periodicity of the quadratic susceptibility of gallium nitride nanocrystals in opal voids [3]. In medium with spatial periodicity of the second-order susceptibility, efficient SHG is achieved as the scattered SH wave vector $\mathbf{k}_{2\omega}$ satisfies the condition of nonlinear diffraction [4], $\mathbf{k}_{2\omega} = 2\mathbf{k}_{\omega} + \mathbf{G}^{\mathrm{NL}}$, with the reciprocal vector $\mathbf{G}^{\mathrm{NL}}$ characterizing the spatial lattice of the second-order susceptibility. The condition of nonlinear diffraction of the SH wave from the series of the (111) opal layers has a form

$$\mathbf{k}_{2\omega} = 2\mathbf{k}_{\omega} + 2\mathbf{G}^{\mathrm{NL}}_{111} \,. \qquad (1)$$

In GaN-opal photonic crystals, 3D lattices of dielectric function and effective quadratic susceptibility are equivalent and reciprocal vectors $\mathbf{G}^{\mathrm{NL}}_{111} = \mathbf{G}^{\mathrm{L}}_{111} \equiv \mathbf{G}_{111}$. Here $\mathbf{G}_{111}$ is the reciprocal vector of the fcc opal lattice directed along the Λ direction of the photonic Brillouin zone. Spectral position of the maximal SHG achieves at the fundamental wavelength in the vicinity of the long-wavelength-edge of the PBG, where group velocity of the fundamental radiation takes the minimum. Small value of group velocity is equivalent to the enhancement of the photonic mode density in this spectral region and the SH intensity is increased significantly at the PBG edge [5].

Acknowledgement

This work has been supported in part by Russian Foundation of Basic Research.

References

[1] A. Blanco *et al*, *Nature* **405**, 437 (2000).
[2] S. Nakamura *et al*, *Jpn. J. Appl. Phys.* **35**, L74 (1996).
[3] A. A. Fedyanin *et al*, *Appl. Phys. Lett.* **87**, 151111 (2005).
[4] V. Berger, *Phys. Rev. Lett.* **81**, 4136 (1998).
[5] K. Sakoda and K. Ohtaka, *Phys. Rev. B* **54**, 5742 (1996).

14th Int. Symp. "Nanostructures: Physics and Technology"
St Petersburg, Russia, June 26–30, 2006

Collective threshold phenomena in microcavity exciton polariton system

S. S. Gavrilov[1], N. A. Gippius[2], V. D. Kulakovskii[1] and S. G. Tikhodeev[2]

[1] Institute of Solid State Physics, RAS, 142432 Chernogolovka, Russia
[2] A. M. Prokhorov General Physics Institute, RAS, Moscow, Russia

Abstract. We report a full two-dimensional numerical model of the polariton-polariton scattering in a semiconductor microcavity (i.e., accounting for *any* angular orientation of the scattered polariton planes of incidence). In this model, we investigate the threshold behavior of the polariton parametric scattering for the situation when the pump energy is above the resonant polariton energy (corresponding to the pump angle). Then, the system becomes bistable, and the time evolution of the angular scattering diagrams shows dramatic changes with the jump of the internal cavity field. Polariton density fluctuations result in considerable Rayleigh scattering of the pumped mode.

Introduction

Effect of parametric instability in the system of microcavity (MC) exciton polaritons was investigated in a number of recent studies [1–5]. We consider a strongly coupled exciton-photon system that contains a single source of *nonlinearity*, namely, a contact exciton-exciton interaction. Numeric simulations allow to take into account a *multi-mode* structure of the studied system: it is crucial for understanding the nature of sharp transitions caused by instabilities in the pumped polaritonic system. Recently there was described the so-called rigid regime of stimulated parametric polariton scattering [1], which happens in systems with bistable response of the pumped mode. The bistability occurs if the pump frequency is above the resonant one (i.e., for *positive* pump detuning). Then, on reaching the threshold value of the pump intensity, the amplitude of the pumped mode rises very quickly, and such a transition may deliver the system into the region of very strong instability in regard to polariton-polariton scattering. The numerical model developed in [1, 2] was a quasi-one-dimensional one; it helped to understand the essence of the studied effects. Two-dimensionality (that corresponds to the cavity plane) brings several distinctive features, those are presented here. Two-dimensional model for similar system was developed ([5]) only for the case of *negative* pump detuning, when bistability does not occur.

1. Theoretical model

The initial point of our study is a system of semi-classical equations [1] for $\mathcal{E}_{\rm QW}(\mathbf{k},t)$, the quantum well electric field in a microcavity, and $\mathcal{P}(\mathbf{k},t)$, exciton polarization (integrated over the QW width):

$$\left[i\frac{d}{dt}-E_{\rm C}(\mathbf{k})\right]\mathcal{E}_{\rm QW}(\mathbf{k},t)=\alpha(\mathbf{k})\mathcal{E}_{\rm ext}(\mathbf{k},t)+\beta(\mathbf{k})\mathcal{P}(\mathbf{k},t)\,,$$

$$\left[i\frac{d}{dt}-E_{\rm X}\right]\mathcal{P}(\mathbf{k},t)=A(\mathbf{k})\mathcal{E}_{\rm QW}(\mathbf{k},t)$$
$$+F\sum_{\mathbf{q},\mathbf{q}'}\mathcal{P}(\mathbf{q}',t)\mathcal{P}^*(\mathbf{q}+\mathbf{q}'-\mathbf{k},t)\mathcal{P}(\mathbf{q},t)+\xi(\mathbf{k},t)\,.$$

Here, $\mathcal{E}_{\rm ext}(\mathbf{k},t)=\delta_{\mathbf{k},\mathbf{k}_{\rm p}}\mathcal{E}(t)\exp(-iE_{\rm p}t)$ is the external electric field of the incident pump wave far from the MC, which is assumed to be a macro-occupied photonic mode with a fixed frequency $E_{\rm p}$, the wave number $\mathbf{k}_{\rm p}$ and the time-variable amplitude $\mathcal{E}(t)$. $\xi(k,t)$ is the stochastic Langevin force, which allows to model the quantum fluctuations of the scattered signals. Let us consider a solution of the above equations in the form

$$\mathcal{E}_{\rm QW}(\mathbf{k},t)=\tilde{\mathcal{E}}(\mathbf{k},t)+\delta_{\mathbf{k},\mathbf{k}_{\rm p}}\mathcal{E}_0e^{-iE_{\rm p}t}\,,$$
$$\mathcal{P}(\mathbf{k},t)=\tilde{\mathcal{P}}(\mathbf{k},t)+\delta_{\mathbf{k},\mathbf{k}_{\rm p}}\mathcal{P}_0e^{-iE_{\rm p}t}\,,$$

here, $\tilde{\mathcal{P}}$ and $\tilde{\mathcal{E}}$ are assumed to be small deviations from the solution with the single macro-occupied mode ($|\tilde{\mathcal{P}}/\mathcal{P}_0|\ll 1$, $|\tilde{\mathcal{E}}/\mathcal{E}_0|\ll 1$).

In the zeroth order approximation over $\tilde{\mathcal{P}}$ and $\tilde{\mathcal{E}}$, it's easy [2] to find the response of the pumped polaritonic mode itself, i.e. the dependence of $|\mathcal{P}_0^2|$ on $|\mathcal{E}_{\rm ext}^2|$. Starting with certain positive values of pump detuning [$\Delta\equiv E_{\rm p}-E_{\rm LP}(\mathbf{k}_{\rm p})$], this dependence has an *S*-shape type as shown in Fig. 1; it means the bistability of the response ([1–4]).

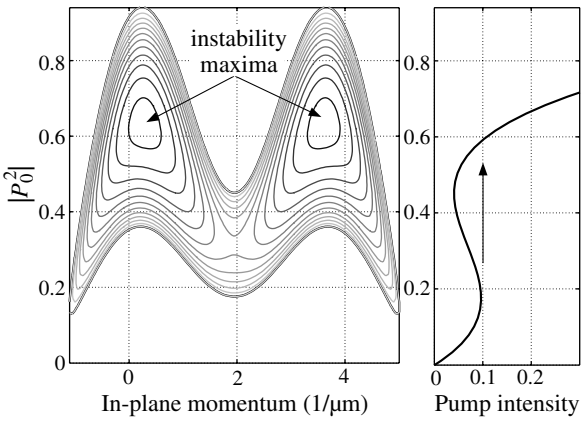

Fig. 1. *Right panel*: The response of the pumped polaritonic mode, $|\mathcal{P}_0|^2$ vs. $|\mathcal{E}_{\rm ext}|^2$ (arbitrary units). The vertical arrow symbolizes a jump through the region of the pumped mode self-instability. *Left panel*: k-space distribution of increment $\Gamma(k;\mathcal{P}_0)$ (quasi-1D model). It is symmetrical relative to $k=k_{\rm pump}$. The shown contours correspond to the set of positive values from 0 to 0.22 meV with the step of 0.02 meV. Note that the vertical scales in both panels coincide.

In order to analyse the stability of the system in regard to the scattering process $(\mathbf{k}_{\rm p},\mathbf{k}_{\rm p})\rightarrow(\mathbf{k}_{\rm s},2\mathbf{k}_{\rm p}-\mathbf{k}_{\rm s})$ (the pumped state breaks-up onto the "signal" and the "idler" states, [3]), one must linearize it [2] over small deviations of "signal" and

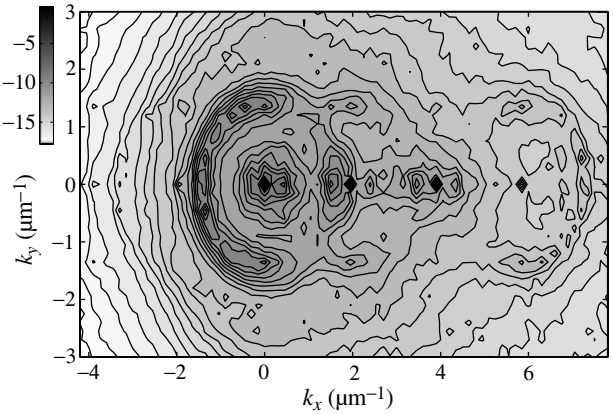

Fig. 2. Momentum-space distribution of scattered intensity, $\log\langle|\mathcal{E}_{\rm QW}(k_x,k_y)|^2\rangle$, arbitrary units. Here, $\langle\ldots\rangle$ means averaging over the last 300 ps of the pump pulse. The gray (logarithmic) scale is explained in the gray vertical bar, left hand side.

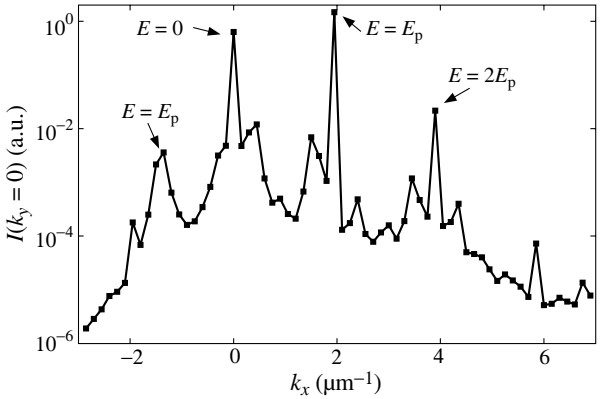

Fig. 3. Momentum-space distribution of intensity scattered in the direction of pump pulse, i.e. $\langle|\mathcal{E}_{\rm QW}(k_x,0)|^2\rangle$ (a.u.). The shown energies of main peaks are counted off from the bottom of renormalized lower polariton branch, $E_{\rm LP}(0)$.

"idler" amplitudes. Such procedure allows to write an "effective Hamiltonian" $H_{\rm eff}(\mathbf{k};\mathcal{P}_0)$ in the form of 4×4 matrix for each mode $\mathbf{k}\equiv\mathbf{k}_{\rm s}$. It is convenient to define an increment $\Gamma(\mathbf{k};\mathcal{P}_0)$ of the $\mathbf{k}$-th state as the greatest value among imaginary parts of 4 eigenvalues of $H_{\rm eff}(\mathbf{k};\mathcal{P}_0)$. As soon as the increment $\Gamma(\mathbf{k};\mathcal{P}_0)$ becomes positive for some $\mathbf{k}$ (e.g. because of increasing of the pump intensity and corresponding growth of $\mathcal{P}_0$, see in Fig. 1), the system loses its stability, so the mentioned linear model breaks up. The scenario of a further evolution depends strongly on excitation conditions, and can be only modelled numerically.

2. Numerical simulation

In the considered system, the cavity photon and the free exciton states are detuned by $\delta\equiv E_{\rm C}(0)-E_{\rm X}=-1$ meV and Rabi splitting amounts to 6.4 meV (this corresponds roughly to the experiments in [3]). Free exciton level $E_{\rm X}=1454$ meV, the pump frequency exceeds the resonant one on $\Delta=0.35$ meV. The pump angle corresponds to $|\mathbf{k}_{\rm p}|=k_{px}=1.95\ \mu{\rm m}^{-1}$, while the inflection point of the LP branch (the so-called "magic angle") is $k_{\rm infl}=1.6\ \mu{\rm m}^{-1}$. The calculations are made on a rectangular mesh in the momentum-space (with a step $0.15\ \mu{\rm m}^{-1}$.

In the numerical model discussed below, the pump firstly rises up to $|\mathcal{E}^{(0)}_{\rm ext}|^2=0.275$ (a.u.) within 50 ps, and then remains steady during next 1000 ps. As a result, the amplitude of the pumped mode rises up to $\mathcal{P}_0(\mathcal{E}^{(0)}_{\rm ext})$, in accordance with the one-mode approximation. However, at the same time the system enters the region of sharp instability (see in Fig. 1). About 20 ps later an explosion-like occupancy of the states with $k\neq k_{\rm p}$ develops, so the linear model breaks up and $|\mathcal{P}(\mathbf{k}_{\rm p})|^2$ decreases drastically. Thus the computation like that represented in the Fig. 1 reveals only an "entry point" to the regime of rigid scattering. Nevertheless, in this case it allows a correct prediction for locations of the main maxima of scattered intensity [$\mathbf{k}_1=(0,0)$ and $\mathbf{k}_2=(2k_{\rm p},0)$] (Fig. 2, 3). Note that the diagram of scattered intensity reveals the two separate modes occupied sufficiently greater than all others (Fig. 3), though the distribution of increment $\Gamma\left(k;\mathcal{P}_0(\mathcal{E}^{(0)}_{\rm ext})\right)$ has the maxima with the certain width of about $1\ \mu{\rm m}^{-1}$ (Fig. 1). Thus, macro-occupation of the states with $\mathbf{k}_1=0$ and $\mathbf{k}_2=2\mathbf{k}_{\rm p}$ results in formation of a new quasi-stationary regime.

It is significant to note that the resulting distribution develops via a self-organization of scattered signals. The initial stochastic populating of states in a wide range of k-space (happened at the time of the breaking-up of the "unperturbed solution") makes possible an appearance of an elastic (Rayleigh) scattering within the lower polariton branch (LPB). Namely, the semicircle-shaped structure (clearly visible in Fig. 2 to the left from the peak at $\mathbf{k}=0$) corresponds to the states with the frequencies approximately equal to the pump one ($E_{\rm p}$). This circle can be defined as an intersection of LPB surface by the plane of $E=E_{\rm p}$.

3. Discussion

The considered model of parametric polariton scattering shows a good qualitative correlation with the experiments [3]. The mentioned case of rigid scattering in systems with positive pump detuning implies the "jump" of the pumped mode amplitude through the region of its self-instability. This transition results in predominant instability of the states with $\mathbf{k}\approx0$ and $\mathbf{k}\approx2\mathbf{k}_{\rm p}$, for sufficiently wide range of pump frequencies. Such a behavior is considerably different from the case of a scattering in a stable system (when the quasi-momenta of the main maxima depend essentially on the pump frequency, [3]).

Acknowledgements

The work is supported in part by RFFI and INTAS grants.

References

[1] N. A. Gippius *et al*, *Europhys. Lett.* **67**, 997–1003 (2004).
[2] N. A. Gippius *et al*, *J. Phys.-Condensed Matter* **16**, S3653–S3664 (2004).
[3] V. D. Kulakovskii *et al*, *PHYSICS-USPEKHI* **48(3)**, 334–340 (2005).
[4] D. M. Whittaker *Phys. Rev. B* **71**, 115301 (2005).
[5] I. Carusotto and C. Ciuti *Phys. Rev. B* **72**, 125335 (2005).

14th Int. Symp. "Nanostructures: Physics and Technology"
St Petersburg, Russia, June 26–30, 2006

Stability of the photonic band-gap in the presence of disorder

M. A. Kaliteevski[1], V. V. Nikolaev[1], D. M. Beggs[2], S. Brand[2] and R. A. Abram[2]

[1] Ioffe Physico-Technical Institute, St Petersburg, Russia
[2] Department of Physics, University of Durham, Durham, DH1 3LE, UK

Abstract. The photonic eigenmodes near a band gap of a type of one-dimensional disordered photonic crystal have been investigated statistically. For the system considered, it is found that the tail of the density of states entering the band gap is characterized by a certain penetration depth, which is proportional to the disorder parameter. A quantitative relation between the relative penetration depth, the relative width of the photonic band gap and the disorder has been found. It is apparent that there is a certain level of disorder below which the probability of the appearance of photonic eigenstates at the centre of the photonic band gap essentially vanishes. Below the threshold, the ensemble-averaged transmission at the centre of the photonic band gap does not change significantly with increasing disorder, but above threshold it increases much more rapidly.

Introduction

At present it is impossible to produce an ideal photonic crystal (PC) for use at optical wavelengths [1, 2]. Imperfections in PCs can damage the photonic band gap (PBG) significantly and result in a finite value of the density of states across the whole of the intended gap [3]. In 1987 John stated, that the "photonic band gap is filled with localized photonic states even in the case of weak disorder" [8], but no quantitative estimate of the density of states or other characteristics of the gap states were provided. However, in 1999 Vlasov and co-authors [9] found that as long as the disorder does not exceed a certain threshold value, the attenuation length within the PBG does not change significantly with increasing disorder. As a result, they suggested that, in contrast to John's statement, localized states do not appear in the PBG for disorder below threshold, but they did not demonstrate that explicitly by calculating the mode spectrum.

Therefore, in an effort to clarify the physical picture of light localization in disordered photonic crystals we have conducted *ab inito* calculations of both the mode structure of the electromagnetic field and the photon transport properties of 1D disordered photonic crystals.

1. Results and discussion

We consider a one-dimensional periodic structure, which is a sequence of a pair of layers A and B of the same thickness $D/2$, whose refractive indices are $n^{(0)}_{\mathrm{A,B}} = n_0 \pm g$ where g is the modulation of the refractive index, and n_0 is the average refractive index. An infinite structure possesses PBGs, and the centre of the first PBG is at $\omega_0 = \pi c/n_0 D$, and the relative width of the gap is $\Delta\omega/\omega_0 \approx 4g/\pi n_0$. In the case of a structure of finite size, the mode spectrum is discrete and the eigenfrequencies can be obtained by setting outgoing wave boundary conditions, corresponding to light not being incident on the structure, using the equation

$$A \begin{pmatrix} 1 \\ -n_f \end{pmatrix} = \hat{\mathbf{M}} \begin{pmatrix} 1 \\ n_l \end{pmatrix} . \qquad (1)$$

Here n_f and n_l are the refractive indices of the semi-infinite media surrounding the structure, $\hat{\mathbf{M}}$ is the transfer matrix through the whole structure, and A is a constant.

For the study of the properties of disordered structures we introduce random fluctuations of the refractive indices: for each pair of layers A and B in the unit cell, the refractive indices are defined by the formula $n_{\mathrm{A,B}} = n_0 \pm g + n_0 \delta P$, where P takes random values in the interval from -1/2 to 1/2 and δ is the constant for a particular structure that specifies the level of disorder. Thus the optical lengths D_i of the unit cells in a particular disordered structure are given by

$$D_i = D\,(n_{\mathrm{A}} + n_{\mathrm{B}})\,/2 = Dn_0\,(1 + \delta P) = D_0\,(1 + \delta P)\ , \qquad (2)$$

where $D_0 = n_0 D$ and the range of the random fluctuations in D_i/D_0 is given by δ.

Circles in Fig. 1 shows the density of states averaged over 10^4 random configurations of disorder obtained using equation (2) and characterized by different values of δ. For $\delta = 0.035$, the eigenfrequencies fluctuate near the values corresponding to the eigenmodes of the ideal structure. Some of the modes penetrate into the PBG but there is no qualitative change of mode spectrum.

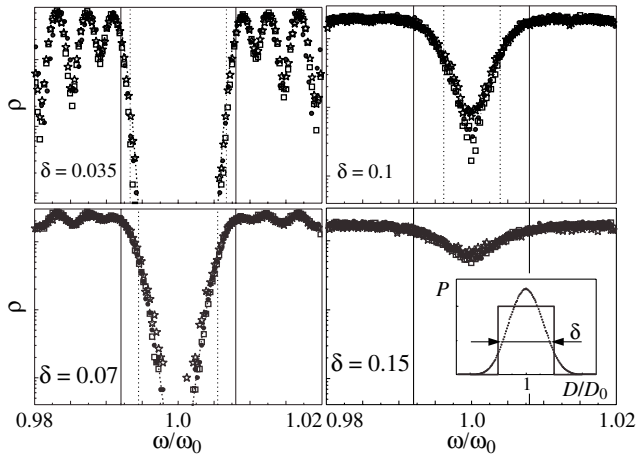

Fig. 1. Density of states averaged over ensembles of 10^4 structures with $\delta = 0.035$, 0.07, 0.1, and 0.15, plotted on a logarithmic scale. Circles (squares) correspond to the case of fluctuation of the optical length of the periods D_i with a square distribution function, shown in the inset of the lower graph by the solid line, due to fluctuations of the refractive indices (widths) of the layers. Stars correspond to the near Guassian distribution of D_i shown in the inset by the dotted line. Vertical solid lines show the boundaries of the PBG for the ideal structure. Dashed lines show the fit for the density of states within the PBG using equation (3). Vertical dotted lines indicate the penetration depth Ω for each case.

The fluctuation of D_i can also be obtained by varying the thicknesses as described above for the refractive index, and for this case the resulting DOS is shown by squares in Fig. 1.

When the refractive indices and thicknesses of the layers are taken to fluctuate simultaneously and independently, and the fluctuation of each quantity is characterized by a top-hat distribution of relative width δ, the distribution function of the optical length D_i of a period of the structure will be almost a Gaussian with width close to δ, as shown in the inset to Fig. 1 by the dotted line. The resulting DOS is shown in Fig. 1 by stars. Note that due to similar widths of the top-hat and Gaussian distributions of D_i, the densities of states are practically identical for all the types of disorder considered. Thus we conclude that the density of modes in a disordered photonic crystal is defined by the relative fluctuation of the optical length of one period of the structure.

The shape of the tails in the density of modes within the PBG is described with very high accuracy by the formula

$$\rho \sim \exp\left(-\frac{(\omega - \omega_e)^2}{\Omega^2}\right) , \qquad (3)$$

where ω_e is the angular frequency of the relevant band edge in the crystal and Ω is penetration depth. The penetration depth Ω is found to be proportional to δ but does not depend on the length of the structure (as is to be expected since the density of states is a self-averaging quantity).

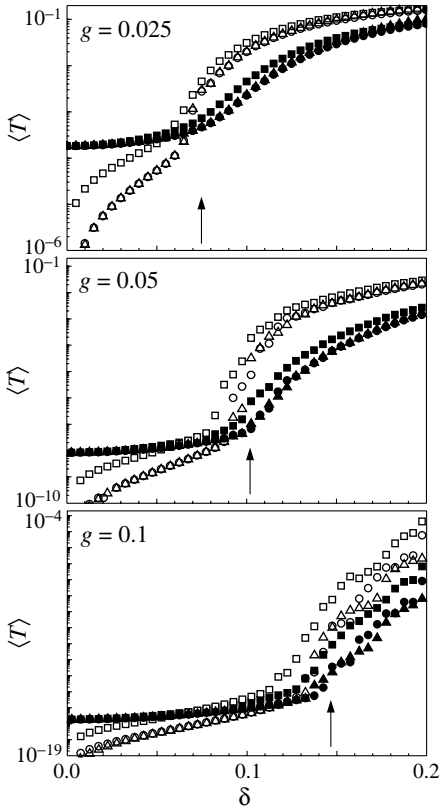

Fig. 2. Transmission coefficient averaged over 10^6 structures (solid symbols) and its standard deviation (open symbols) as a function of the disorder parameter δ for the photonic crystals with $n_0 = 2.0$ and different levels of modulation of the refractive index: $g = 0.025$; 0.05; and 0.1. Circles and triangles corresponds to the "refractive index" and "thickness" disorder with top-hat distribution of D_i; squares corresponds to the "Gaussian" distribution. Vertical arrows indicate the threshold levels of disorder predicted by the formula $\delta_{\rm th} = \sqrt{(\Delta\omega/\omega_0)/3}$.

When δ is increased to 0.07, the edge states penetrate further into the PBG and the fluctuations of the lifetime of the modes increase. The width of the PBG is reduced but nevertheless remains substantial. Eventually, when δ is increased to 0.1 the probability of the appearance of eigenmodes in any part of the original PBG becomes substantial and the fluctuations in the lifetimes of the eigenstates are greater.

An increase of δ to 0.15 leads to a decrease in the dip of the density of states, an increase of the fluctuations of the lifetime, and a slight decrease of its mean value. Further increase of δ leads to the disappearance of the effects associated with the periodic modulation of the refractive index, and the system becomes completely disordered. We believe that the filling of the PBG with states is the reason for the transition from anomalous to normal behaviour of the Lyapunov exponent observed in Deych *et al* [12].

For all the structures considered the penetration depth Ω is proportional to the square root of the relative band width $\Delta\omega/\omega_0$.

Analysis of the density of states for the structures with different parameters n_0, g and L indicate that the dimensionless quantity $(\Omega/\delta\omega_0)\sqrt{\omega_0/\Delta\omega}$ is approximately constant. The latter leads us to conclude that the penetration depth is decribed by the formula

$$\frac{\Omega}{\omega_0} \approx \frac{\delta}{5}\sqrt{\frac{\Delta\omega}{\omega_0}} \tag{4}$$

i.e. the relative penetration depth exhibits a universal dependence on the relative gap width.

Equation 4 provides a means to specify a practical criterion for the resilience of the PBG to the presence of disorder. Assuming that for a particular application there is a certain acceptable level of the density of states at the centre of the gap described by a suppression factor $S_{\rm th}$, which is defined as the ratio of the densities of states at the centre and the edge of the PBG, the threshold value of the disorder $\delta_{\rm th}$ is

$$\delta_{\rm th} \approx \frac{5}{2\sqrt{-\ln S_{\rm th}}}\sqrt{\frac{\Delta\omega}{\omega_0}}\,. \tag{5}$$

For example, suppression of the density of states at the centre of the PBG by a factor 10^{-8}, would correspond to $\Omega \approx \Delta\omega/9$, and a threshold disorder parameter given by $\delta_{\rm th} \approx \sqrt{(\Delta\omega/\omega_0)/3}$. Note that the square root of the logarithm in equation (5) varies very slowly with the change of the argument, and the above estimate can be considered as an almost universal criterion for the stability of the PBG in one-dimensional photonic crystals in the presence of disorder.

The existence of a threshold level of disorder is illustrated in Fig. 1, where the dependences on disorder parameter δ of the transmission coefficient $\langle T\rangle$ and its standard deviation at the centre of the band gap for structures, characterized by different refractive index modulation g are shown for the three models of disorder. For all the cases considered the dependences are characterized by a threshold; when $\delta < \delta_{\rm th}$, $\langle T\rangle$ grows slowly with increasing δ, and the attenuation length ξ virtually does not change. When δ reaches $\delta_{\rm th}$, $\langle T\rangle$ grows much faster with increasing δ. The threshold in the dependence of $\langle T\rangle$ on δ is accompanied by a crossing of $\langle T\rangle$ and its standard deviation; below threshold $\langle T\rangle$ is larger than its standard deviation, but smaller for $\delta > \delta_{\rm th}$. For all cases the position of threshold is well described by the formula $\delta_{\rm th} \approx \sqrt{(\Delta\omega/\omega_0)/3}$.

Such behaviour can be easily explained. The increase of $\langle T\rangle$ is a consequence of the appearance of sharp spikes, corresponding to localized eigenmodes, in the transmission spectrum of individual structures [13]. When $\delta < \delta_{\rm th}$, the increase of the transmission coefficient is provided by the tails of such spikes and therefore is very small. When $\delta > \delta_{\rm th}$, localised states and corresponding peaks in the transmission spectra can appear in the centre of the PBG, and $\langle T\rangle$ starts to grow faster with increasing δ. Note, that for an individual structure in the ensemble, when $\delta > \delta_{\rm th}$ the transmission coefficient at a given frequency can be any value from zero to one, and the standard deviation of $\langle T\rangle$ exceeds its mean value.

For the "refractive index" and "thickness" disorder, the dependences of $\langle T\rangle$ and its standard deviation on δ are identical, but for the Gaussian distribution the threshold is achieved at a slightly smaller value of δ. This is further confirmation that the relative fluctuation of the optical length of the unit cell is an appropriate parameter to describe the disorder.

Conclusion

To conclude, we have analyzed quantitatively the penetration of states into the band gap of a type of one-dimensional disordered photonic crystal. We have shown that the tail of the density of states in the band gap has a Gaussian form characterized by a penetration depth parameter and there is an allowed level of disorder below which the probability of the appearance of photonic eigenstates at the centre of photonic band gap essentially vanishes. A relationship between the relative penetration depth, relative gap width and disorder parameter has been found and a scaling formula relating the attenuation length to the gap width and disorder has also been obtained.

Acknowledgements

The work was supported by an EPSRC grant.

References

[1] D. R. Vlasov *et al*, *Phys. Rev. E* **61**, 5784 (2000).
[2] T. F. Krauss *et al*, *Nature* **383**, 699 (1996).
[3] Z. Y. Li *et al*, *Phys. Rev. B* **62**, 1516 (2000).
[4] C. M. Soukoulis ed., *Photonic Band Gap and Localization*, NATO ASI Series B, vol 308 (Plenum, New York, 1993).
[5] A. P. Vinogradov *et al*, *Phys. Rev. E* **70**, 026610 (2004).
[6] D. J. Thouless *et al*, *Phys. Lett.* **13**, 142 (1974).
[7] P. Cheng, *Introduction to Wave Scattering Localization and Mesoscopic*, (Academic, London 1995).
[8] S. John, *Phys. Rev. Lett.* **58**, 2486 (1987).
[9] Y. A. Vlasov *et al*, *Phys. Rev. B* **60**, 1555 (1999).
[10] D. J. Thouless *et al*, *Phys. Rev. Lett.* **39**, 1167 (1977).
[11] H. Kogelnick *et al*, *J. Appl. Phys.* **43**, 2327 (1972).
[12] L. I. Deych *et al*, *Phys. Rev. Lett.* **81**, 5390 (1998).
[13] M. A. Kaliteevski *et al*, *Phys. Rev. E*, in print (2006).
[14] M. A. Kaliteevski *et al*, *Phys. Rev. B* **66**, 113101 (2002).
[15] M. A. Kaliteevski *et al*, *Phys. Status Solidi A* **195**, 612 (2003).
[16] D. M. Beggs *et al*, *J. Phys.: Condens. Matter* **17**, 1781 (2005).

14th Int. Symp. "Nanostructures: Physics and Technology"
St Petersburg, Russia, June 26–30, 2006

Propagation of circularly polarized light waves in magneto-photonic crystals

V. A. Kosobukin
Ioffe Physico-Technical Institute, St Petersburg, Russia

Abstract. A theory is presented for propagation of circularly polarized electromagnetic waves through magneto-photonic crystals at normal incidence. For Bragg structures consisting of alternating magnetic and dielectric layers two models are treated with the magnetic layers being (I) atomically thin and (II) macroscopically thick. In the spectral ranges of photonic stop-bands, the Faraday rotation and the magnetization-induced modulation of in-plane intensity are shown to change considerably, the latter being enhanced.

Introduction

Optical properties of photonic crystals, i.e. solid-state structures with periodically modulated dielectric permittivity, are extensively studied. Recently, the magneto-photonic crystals were fabricated by layer-by-layer growth of periodic magnetic structure with dielectric spacers [1] and by filling the voids of three-dimensional opal lattice with magnetic substances [2]. Magneto-optical spectroscopy revealed significant changes in the Faraday rotation near the stop-bands of such materials [1, 2]. In this work, a theory is proposed for propagation of circularly polarized electromagnetic waves through one-dimensional magnetic Bragg structures (magneto-photonic crystals). Within a self-consistent propagator (the Green function) formalism [3] the transfer matrices of circularly polarized waves and magneto-optical observable quantities are analytically derived, and preliminary results are presented.

1. Models of magneto-photonic crystals

Consider an array of N magnetic layers surrounded by a dielectric and having the identity period d along the z-axis. The magnetization $\mathbf{M}||\mathbf{e}_z$ is assumed to be along the layer normal (the z-axis). The dielectric permittivity tensor has the non-zero components $\varepsilon_{\alpha\alpha} = \varepsilon$ and $\varepsilon_{xy} = -\varepsilon_{yx} = ig$ in magnetic layers with $g \sim |\mathbf{M}|$, while it is isotropic with the diagonal components ε_1 in surrounding dielectric. Two circularly polarized waves

$$E_\pm = E_x \pm i E_y \tag{1}$$

can be excited by a normally incident wave with linear polarization to propagate along the magnetization direction (Faraday's geometry). Difference in the propagation constants of the two waves (1) results in the Faraday rotation and other magneto-optical effects that are of most interest for us near the stop-bands of magneto-photonic crystal.

On passing the nth ($1 \le n \le N$) magnetic layer centered at $z = z_n = d\,(n - 1/2)$ the electric fields (1) in the dielectric spacer are

$$E_\pm(z) = a_\pm^{(n)} e^{ik_1(z-nd)} + b_\pm^{(n)} e^{-ik_1(z-nd)}. \tag{2}$$

Here, $k_1 = k_0\sqrt{\varepsilon_1}$, $k_0 = \omega/c$, ω is the frequency and c is the speed of light in vacuum. The amplitudes entering Eq. (2) on the left and on the right of the nth magnetic layer are related as follows

$$\begin{pmatrix} a_\pm^{(n)} \\ b_\pm^{(n)} \end{pmatrix} = \frac{1}{t_\pm} \begin{pmatrix} \left(t_\pm^2 - r_\pm^2\right) e^{ik_1 d} & r_\pm \\ -r_\pm & e^{-ik_1 d} \end{pmatrix} \begin{pmatrix} a_\pm^{(n-1)} \\ b_\pm^{(n-1)} \end{pmatrix}. \tag{3}$$

Here, the transfer matrix of circularly polarized waves is expressed through the reflectivity $r_\pm$ and transmissivity $t_\pm$ of single magnetic layer centered at $z = 0$. We calculated the coefficients $r_\pm$ and $t_\pm$ for two models referred to as I and II below. The model I is that with microscopically thin magnetic layers described within the quasi-microscopic (non-local) electrodynamics [3]. The model II treats thick magnetic layers within the macroscopic (Fresnel-type) approximation.

(I) *Ultrathin magnetic layers*. For such layers as metallic monatomic layers or semiconductor quantum wells a non-local dielectric permittivity continuous at interfaces is necessary [3] rather than a macroscopic (local) one. Starting from the macroscopic electrodynamics with the uniform permittivity ε_1 as the zeroth-order approximation, one can introduce the non-local dielectric $\Delta\varepsilon\left(z - z_n, z' - z_n\right)$ and gyrotropic $ig\left(z - z_n, z' - z_n\right)$ perturbations due to the response of the nth magnetic layer [3]. Self-consistent solution of the resulting non-local electrodynamics problem gives $t_\pm = (1 - \alpha_\pm)^{-1}$ and $r_\pm = \alpha_\pm t_\pm$ in Eq. (3). Here,

$$\alpha_\pm = \frac{ik_0\sqrt{\varepsilon_1}}{2} \frac{\langle\Delta\varepsilon\rangle \pm \langle g\rangle}{\varepsilon_1} \tag{4}$$

is expressed via the constants $\langle\Delta\varepsilon\rangle$ and $\langle g\rangle$ obtained by integrating the non-local perturbations over z and z'.

(II) *Thick magnetic layers*. For the magnetic layer whose thickness a exceeds the atomic size considerably, one obtains that in Eq. (3)

$$\begin{aligned} \widetilde{r}_\pm &= e^{-ik_1 a} s_\pm \left(1 - e^{2ik_\pm a}\right) \Delta_\pm^{-1}, \\ \widetilde{t}_\pm &= e^{-i(k_1 - k_\pm)a} \left(1 - s_\pm^2\right) \Delta_\pm^{-1}, \\ \Delta_\pm &= 1 - s_\pm^2 e^{2ik_\pm a}. \end{aligned}$$

Here

$$\begin{aligned} k_\pm &= \sqrt{\varepsilon_\pm} k_0, \quad \varepsilon_\pm = \varepsilon \pm g, \\ s_\pm &= \left(\sqrt{\varepsilon_1} - \sqrt{\varepsilon_\pm}\right) / \left(\sqrt{\varepsilon_1} + \sqrt{\varepsilon_\pm}\right). \end{aligned}$$

2. Magneto-optical observable quantities

If the circularly polarized waves (1) are excited by the linearly polarized incident wave $\mathbf{E}^{\rm inc} = \mathbf{e}_x a^{(0)} e^{ik_1 z}$, one gets

$a_{\pm}^{(0)} = a^{(0)}$ in Eq. (2). Then, the amplitude reflectivities $\rho_{\pm} = b_{\pm}^{(0)}/a_{\pm}^{(0)}$ and transmissivities $\tau_{\pm} = a_{\pm}^{(N)}/a_{\pm}^{(0)}$ of the whole crystal are calculated following [4] under the conditions $b_{\pm}^{(N)} = 0$. This gives

$$(\rho_{\pm}, \tau_{\pm}) = \left(\frac{r_{\pm}}{t_{\pm}} Q_{\pm}^{(N)}, 1\right) \left(P_{\pm}^{(N)} - L_{\pm} Q_{\pm}^{(N)}\right)^{-1}, \quad (5)$$

where $P_{\pm}^{(N)} = \cos(q_{\pm} N d)$, $Q = \sin(q_{\pm} N d) / \sin(q_{\pm} d)$,

$$L_{\pm} = (2t_{\pm})^{-1}\left[\left(t_{\pm}^2 - r_{\pm}^2\right) e^{ik_1 d} - e^{-ik_1 d}\right] = K_{\pm} - t_{\pm}^{-1} e^{-ik_1 d}. \quad (6)$$

The dispersion equation

$$\cos(q_{\pm} d) = K_{\pm} \quad (7)$$

gives the eigenvalues $\lambda_{\pm} = \exp(i q_{\pm} d)$ of the transfer matrix entering Eq. (3) with $q_{\pm}$ being the quasi-wavenumbers of Bloch-type circularly polarized waves in an infinite ($N \to \infty$) crystal.

For the transmitted wave, the Faraday rotation angle is expressed in terms of (5) as follows

$$\Psi = \frac{1}{2} \arg\left(\frac{\tau_+}{\tau_-}\right). \quad (8)$$

The magneto-optical modulation of the power reflectivity $\Delta R(g) = R(g) - R(0)$ in the analyzer plane making an angle of Ω with the incidence polarization plane is

$$\Delta R(g) = \frac{1}{4}\left|\rho_+ e^{-i\Omega} + \rho_- e^{i\Omega}\right|^2 - |\rho_0|^2 \cos^2\Omega, \quad (9)$$

with $\rho_0 = \rho_{\pm}|_{\mathbf{M}=0}$ from Eq. (5).

3. Discussion

For the non-local model I, explicit Eq. (7), i.e.

$$\cos(q_{\pm} d) = \cos k_1 d + i\alpha_{\pm} \sin k_1 d \quad (10)$$

gives the dispersion relation $q_{\pm}(\omega)$ of circularly polarized waves. The condition $k_1 d = m\pi$ in Eq. (10) corresponds to Bragg diffraction of the mth-order. Under this condition, using Eq. (4) for $\alpha_{\pm} = \alpha_0 \pm \Delta\alpha$ with $\alpha_0 = \alpha_{\pm}|_{\langle g\rangle = 0}$ one obtains from Eq. (5)

$$\{\rho_{\pm} - \rho_0, \tau_{\pm} - \tau_0\} = \pm \frac{\Delta\alpha}{\alpha_0} \frac{N\alpha_0}{(1 - N\alpha_0)^2} \left\{(-1)^m, (-1)^{mN}\right\}$$

to the lowest-order terms in $|\Delta\alpha/\alpha_0| = |\langle g\rangle / \langle \Delta\varepsilon\rangle| \ll 1$. Here, τ_0 is given by Eq. (5) with $\langle g\rangle = 0$.

For the model II with thick magnetic layers, Fig. 1 shows the spectra of transmissivity $|\tau_0|^2$, normalized rotation angle $\Psi/(|g|N)$, Eq. (8), and magneto-optical reflectivity modulation $\Delta R(g)$, Eq. (9). The spectrum of ΔR evaluated at the optimum angle of $\Omega = 45^\circ$ is the magneto-optical correction to the in-plane reflectivity $|\varrho_0|^2/2 = (1 - |\tau_0|^2)/2$ in the absence of dielectric loss. The minima of transmissivity (a) in Fig. 1 correspond to the photonic stop-bands caused by the Bragg diffraction with the reciprocal lattice vectors $\mathbf{b}_m = -2\pi m \mathbf{e}_z/d$ in the orders $m = 1$ and 2, the Bragg conditions being $2k_1 = |\mathbf{b}_m|$.

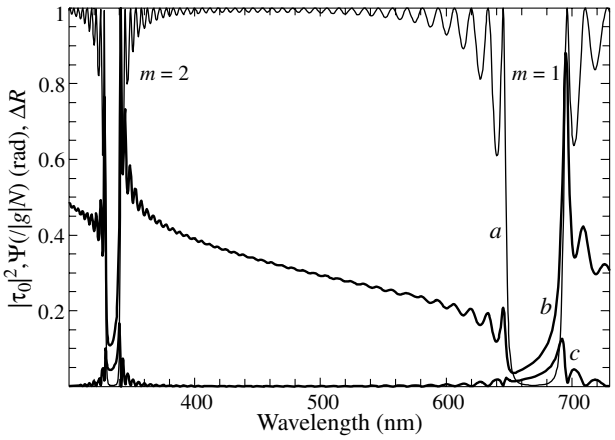

Fig. 1. Transmissivity $|\tau_0|^2$ (a), normalized Faraday rotation angle $\Psi/(|g|N)$ (b) and magneto-optical reflectivity modulation ΔR in the $\Omega = 45^\circ$ analyzer plane (c) vs. wavelength. Calculated for model II in the range of the stop-bands $m = 1$ and $m = 2$ of a magneto-photonic crystal with $N = 40$, $d = 240$ nm, $a = 0.3d$, $\varepsilon = 1.5^2$, $g = 10^{-2}$, $\varepsilon_1 = 1.35^2$.

It is seen from Fig. 1 that the spectra of magneto-optical responses (b) and (c) change substantially in the range of the stop-bands, where the modulus of the in-plane reflectivity correction (c) increases. Physically, the enhancement of $|\Delta R|$ is associated with increasing the number of reflected photons in each of the two orthogonal linear polarizations under the Bragg resonance conditions.

Conclusion

In conclusion, a theory is developed for propagation of circularly polarized light waves undergoing the Bragg diffraction from a one-dimensional dielectric lattice of a magneto-photonic crystal. The magneto-optical characteristics are found to change significantly in the spectral ranges of photonic stop-bands, the intensity modulation being strongly enhanced. One may expect the results to be qualitatively valid for both 1D magneto-photonic crystals and 3D opal-based photonic crystals with magnetic filling near their long-wavelength diffraction edge where the only diffraction $m = 1$ from the planes (111) occurs [5].

Acknowledgements

This work was supported by the Russian Foundation for Basic Research, grants 04-02-17592 and 05-02-17809.

References

[1] M. Inoue, *Magneto-Optical Materials for Photonics and Recording, Proc. MRS, Symp. J.* Boston, 2004.

[2] A. V. Baryshev, T. Kodama, K. Nishimura, H. Uchida, M. Inoue, *J. Appl. Phys*, **95**, 7336 (2004); *Trans. Magn. Soc. Japan* **4**, 290 (2004).

[3] V. A. Kosobukin, *J. Magn. Magn. Mater* **153**, 397 (1996); *Phys. Solid State* **38**, 3461 (1996).

[4] V. A. Kosobukin, *Physica Status Solidi (b)* **208**, 271 (1998).

[5] A. V. Baryshev, A. A. Kaplyanskii, V. A. Kosobukin, K. B. Samusev, D. E. Usvyat, M. F. Limonov, *Phys. Rev. B* **70**, 113104 (2004).

14th Int. Symp. "Nanostructures: Physics and Technology"
St Petersburg, Russia, June 26–30, 2006

Giant magnetic nonlinear-optical effects in magnetophotonic microcavities

T. V. Murzina[1], O. A. Aktsipetrov[1], R. V. Kapra[1], I. E. Razdolskii[1] and M. Inoue[2]

[1] Depertment of Physics, Moscow State University, 119992 Moscow, Russia
[2] Toyohashi University of Technology, Toyohashi, Aichi 441-8580, Japan

Abstract. Experimental studies of quadratic and cubic nonlinear magneto-optical effects in planar magnetophotonic microcavities (MPMC) are presented. It is shown that for the case of MPMC the magnetization-induced contribution to optical second harmonic generation exceeds the non-magnetic one. Nonlinear third-order Faraday effect is observed.

Introduction

Photonic crystals (PhC) and microcavities have been a subject of intensive studies over recent years [1]. Tremendous progress in fabrication techniques of these photonic band-gap (PBG) materials brought about the observation of new phenomena in contemporary optics related to the interaction between the radiation field and matter. These studies also generate a lot of technological applications of photonic crystals in microelectronics and optical and microwave communications.

Magneto-photonic crystals and microcavities (MPMC), i.e. PBG materials partially consisting from magnetic materials or microcavity with a magnetic spacer, exhibit unique optical and magneto-optical responses that is due to a strong confinement of light in these structures. For the case of MPMC, the electromagnetic wave is localized in the magnetic defect layer that brings about many-fold enhancement of magneto-optical and nonlinear magneto-optical effects in these materials. Large values of magneto-optical Faraday effects, both in linear- and nonlinear-optical response, have been demonstrated in one-dimensional MPMC composed of a Bi:YIG half-wavelength thick film sandwiched between dielectric Bragg reflectors [2]. Significant nonlinear magneto-optical Kerr effect (NOMOKE) rotation of the second-harmonic (SH) wave polarization and magnetization-induced variations of the SHG intensity were detected in the vicinity of the localized photonic state. At the same time, important questions remained to be unclear, one being connected with the relative values of the magnetization-induced components of the quadratic response. Another question that is of interest for the case of MPMC is the search of new, higher-order, nonlinear-optical effects which can be expected in such structures due to high concentration of electromagnetic field in the MC spacer.

In this work the results of the experiental studies of quadratic and cubic nonlinear-optical effects at SH and fundamental frequencies are reported.

The samples under study are MPMC composed by $\lambda/2$ thick $Bi_1Y_2Fe_5O_x$ layer squeezed between two Bragg mirrors, each of them being of the composition $(SiO_2/Ta_2O_5)^5$. The samples are grown on a glass substrate by rf sputtering of corresponding targets in an Ar^+ atmosphere. Prior to the fabrication of the top Bragg reflector, the sample with Bi:YIG layer is annealed in air at 700 °C for 20 min for the residual oxidation and crystallization of the Bi:YIG spacer. For the composed MPMC with 245 nm-thick spacer the wavelength of 1064 nm was in resonance with the MC mode at $\sim 30^\circ$ angle of incidence.

As a fundamental beam, the output of a Nd^{3+}:YAG nanosecond laser operating at 1064-nm wavelength is used. The SH or the fundamental radiation reflected from MPMC is selected by appropriate filters and detected by a photomultiplier tube or a photodiode, respectively. The resonant angle of incidence of the pump radiation $\approx 30^\circ$ is chosen for the experiments. The saturating magnetic field of 2 kOe is applied in the plane of the sample using the permanent FeNdB magnets.

1. Nonlinear magneto-optical Kerr effect in MPMC

Figure 1 shows the dependence of the SHG intensity reflected from the MPMC as a function of the azimuthal angle of the applied magnetic field, $I_{2\omega}(\phi)$. The rotation of the magnetic field in the plane of the sample is achieved by azimuthal rotation of the housing with permanent magnets, $\phi = 0$ corresponds to the transversal (i.e. perpendicular to the plane of incidence) configuration of the magnetic field. The $p-$polarization of the fundamental wave is used and the SH wave polarization is kept to be p or s. Filled circles in Fig. 1 show the dependence $I_{2\omega}(\phi)$ obtained for $p - p$ combination of polarizations. It is known that in this case variations of the *transversal* component of the magnetic field can change the intensity of the SH wave due to the contribution of magnetization-induced components of quadratic susceptibility which are *odd* with respect to magnetization [3]. Interference between non-magnetic (crystallographic), $\chi^{\rm cr}$ and magnetization-induced, $\chi^{\rm M}$, components of quadratic susceptibility brings about *odd* in magnetization changes in the SH intensity.

It can be seen in Fig. 1 that for the opposite directions of the transversal magnetic field achieved at $\phi = 0^\circ$, 180° the values SH intensity are different, the magnetic contrast commonly

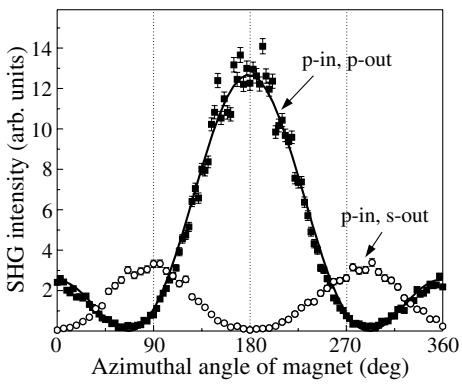

Fig. 1. Dependencies of the SHG intensity on the azimuthal angle of the applied magnetic field for p-in, p-out combination of polarizations; zero angle corresponds to the transversal magnetic field.

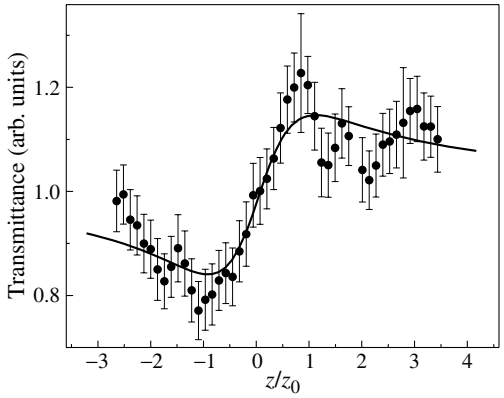

Fig. 2. Transmittance of MPMC as a function of its position with respect to the focusing plane of the lens.

introduced as

$$\frac{I_{2\omega}(0^\circ) - I_{2\omega}(180^\circ)}{I_{2\omega}(0^\circ) + I_{2\omega}(180^\circ)},$$

reaches the value of about 0.6. Zero values of SH intensity attained in the vicinity of $\phi = 70^\circ$, 290° are the result of the destructive interference between non-magnetic and magnetization-induced components of the SH field and are a direct proof that magnetization-induced contribution to the SH wave is larger than non-magnetic one. The approximation of the experimental $I_{2\omega}(\phi)$ dependencies gives the ratio of these components $\chi^{\mathrm{M}}/\chi^{\mathrm{cr}} \approx 3$.

In order to visualize the pure magnetization-induced SH radiation, $I_{2\omega}(\phi)$ dependence is measured for the $p - s$ combination of polarizations shown by open circles in Fig. 1. It is well known that for isotropic nonlinear medium s-polarized SHG is absent for nonmagnetized samples and can appear only if longitudinal or polar magnetic field is applied [3]. Maxima of the SH intensity observed for $\phi = 90^\circ$, 270° correspond to the longitudinal magnetic field and are caused by pure magnetic SH components.

2. Nonlinear Faraday effect in MPMC

Third-order nonlinear-optical effect which we intended to observe in MPMC is nonlinear Faraday rotation at the fundamental wavelength, governed by the imaginary part of third-order optical nonlinearity $\chi^{(3)}$ ($\omega = \omega + \omega - \omega$). To study this effect, the polarization-sensitive Z-scan technique is developed. The MPMC was translated in the direction parallel to the laser beam that was focused by a lens. The angle between the plane of the MPMC surface and the fundamental beam corresponds to the excitation of the microcavity mode. Transmitted through the MPMC beam passed through a Glan analyzer fixed at $+45^\circ$, 0° or -45° with respect to the input polarization. The nonlinear Faraday angle, ϑ_{Z}, was estimated from the expression:

$$\sin(2\vartheta_{\mathrm{Z}}) = \frac{I_\omega(Z, -45^\circ) - I_\omega(Z, +45^\circ)}{I_\omega(Z, 0^\circ)},$$

where $I_\omega(Z)$ is the intensity of the detected signal of the fundamental frequency measured as a function of position of the translator, Z, for the orientation of the analyzer $+45^\circ$, 0° and -45°. Such experimental procedure allows for the highest detection sensitivity of the polarization plane rotation.

The results obtained show the existence of the nonlinear contribution to the Faraday rotation due to the increase of the intensity of the fundamental beam in the vicinity of the beam waist. The maximum values of the nonlinear Faraday rotation observed in MPMC is about $6^\circ \pm 1^\circ$. The angle of the nonlinear Faraday rotation is obtained for the intensity of the fundamental beam in the waist region of about 10 MW/cm^2. It should be noted that the magnitude of the nonlinear Faraday effect for the case of Bi:YIG MPMC in the transparency spectral region exceeds the linear magneto-optical Faraday effect under the same experimental conditions.

References

[1] J. D. Joannopoulos *et al*, *Photonic Crystals.* Princeton University Press, Princeton NJ, (1995).
[2] O. A. Aktsipetrov *et al*, *JOSA B* **22**, 176 (2005).
[3] R. P. Pan *et al*, *Phys. Rev. B* **175/176**, 619 (1997).

14th Int. Symp. "Nanostructures: Physics and Technology"
St Petersburg, Russia, June 26–30, 2006

Exciton polaritons in three- and two-dimensional photonic crystals

A. N. Poddubny and E. L. Ivchenko
Ioffe Physico-Technical Institute, St Petersburg, Russia

Abstract. We have developed a theory of exciton polaritons in resonant three- and two-dimensional photonic crystals for arbitrary dielectric contrast and effective mass of the exciton that is excited in one of the compositional materials. The calculation has been carried out for a periodic array of spheres or parallel cylinders embedded in a dielectric matrix. It has been shown that the position of the lower branches of the polariton dispersion curve monotonously depends on the exciton effective mass and is determined by the coupling of light with the first few states of the mechanical exciton quantum-confined inside each sphere or cylinder. We have also calculated the optical reflection spectra from the finite array of cylinders and compared the spectral features with the arrangement of exciton-polariton branches.

1. Introduction

The concept of photonic crystals was put forward by Yablonovich [1] and John [2] in 1987. Since then this term is used for media with the dielectric susceptibility varying periodically in the space and allowing the Bragg diffraction of the light. The simplest model realization of a three-dimensional (3D) or two-dimensional (2D) photonic crystal is a periodic array of spheres or cylinders of the material A embedded in a dielectric matrix B. Periodic structures where the dielectric susceptibility of one of the compositional materials, as a function of the frequency ω, has a pole at a certain resonance frequency are grouped into a special class of resonant photonic crystals where the normal light waves are polaritons.

In Refs. [3, 4] the dispersion of light waves has been calculated taking into consideration the frequency dependence of the dielectric susceptibility in the frame of the local material relation between the electric displacement and the electric field. In Ref. [5] the dispersion of exciton polaritons in a resonant 3D photonic crystal has been calculated taking into account only one level of the quantum-confined exciton in a sphere A and neglecting the difference between the dielectric constant $\varepsilon_{\rm B}$ and the background dielectric constant $\varepsilon_{\rm A}$ of the material A. In the present work we have studied theoretically the dispersion of exciton polaritons in a resonant 3D and 2D photonic crystals making allowance for all available exciton quantum-confinement levels as well as for the dielectric contrast, i.e., for $\varepsilon_{\rm A} \neq \varepsilon_{\rm B}$.

2. Face-centered cubic photonic crystal

The structure under consideration is characterized by seven parameters: R, a, $\varepsilon_{\rm B}$, $\varepsilon_{\rm A}$, $\omega_{\rm LT}$, ω_0 and M. Here R is the radius of the spheres A, a is the lattice constant for the FCC lattice, $\varepsilon_{\rm B}$ is the dielectric constant of the matrix, ω_0, $\omega_{\rm LT}$ and M are the resonance frequency, longitudinal-transverse splitting and translational effective mass of the triplet $1s$ exciton excited inside the spheres A, $\varepsilon_{\rm A}$ is the background dielectric constant. Thus, we take into account both the frequency and spatial dispersion of the material A. The radius R is chosen so that, on the one hand, the spheres A do not overlap, i.e. $R < a/\sqrt{8}$, but, on the other hand, R should exceed the Bohr radius of the $1s$-exciton in the material A and, hence, the exciton can be considered as a single particle with the mass M. It follows then that the problem is reduced to the solution of a system of two vector equations, namely, the wave equation

$$\text{rot rot}\, \boldsymbol{E}(\boldsymbol{r}) = (\omega/c)^2 \left[\varepsilon(\boldsymbol{r})\boldsymbol{E}(\boldsymbol{r}) + 4\pi \boldsymbol{P}_{\rm exc}(\boldsymbol{r})\right] \quad (1)$$

and the material equation for the $1s$-exciton contribution to the dielectric polarization

$$\left[-\hbar/(2M)\ \Delta + \omega_0 - \omega\right] \boldsymbol{P}_{\rm exc}(\boldsymbol{r}) = \varepsilon_a \omega_{\rm LT} \boldsymbol{E}(\boldsymbol{r})/4\pi\,, \quad (2)$$

where $\varepsilon(\boldsymbol{r}) = \varepsilon_{\rm A}$ inside the spheres and $\varepsilon(\boldsymbol{r}) = \varepsilon_{\rm B}$ outside the spheres, $\boldsymbol{E}(\boldsymbol{r})$ and $\boldsymbol{P}_{\rm exc}(\boldsymbol{r})$ are the electric field and the exciton polarization at the frequency ω. On a surface separating materials A and B we impose the standard Maxwell boundary conditions: continuity of the tangential components of the electric and magnetic fields, and the Pekar additional boundary condition for the exciton polarization: the vanishing vector $\boldsymbol{P}_{\rm exc}(\boldsymbol{r})$ at $|\boldsymbol{r}-\boldsymbol{a}| = R$, where the translational vectors $\boldsymbol{a}$ define the centers of the spheres A.

Below we present the results of calculation of the exciton-polariton dispersion $\omega_{n\boldsymbol{k}}$, where n is the branch index. The computation has been performed by using a photonic analogue of the Korringa–Kohn–Rostoker (KKR) method [6, 7, 8]. In this method (i) the electric field is decomposed in the spherical waves, and (ii) following the consideration of the light scattering by a single sphere and the introduction of a structural factor the dispersion equation is transformed to

$$\left|\hat{1} - \hat{t}(\omega)\hat{G}(\omega, \boldsymbol{k})\right| = 0\,. \quad (3)$$

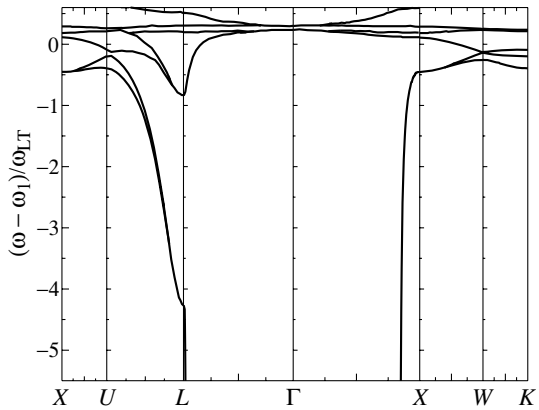

Fig. 1. Exciton-polariton band structure of a photonic crystal with a FCC lattice of spheres A inserted into the matrix B. The calculation is performed neglecting the dielectric contrast and for the set of parameters indicated in the text.

Here $\hat{t}$ is a single-scatterer T matrix and $\hat{G}(\omega, \boldsymbol{k})$ is the matrix of structure constants [8]. Both $\hat{t}$ and $\hat{G}$ are considered as matrices with matrix elements labelled by pairs of angular momentum numbers and a vector-wave polarization index.

Ajiki *et al* [9] have calculated elements of $\hat{t}(\omega)$ taking into account the exciton resonance in the spheres A and the finite exciton effective mass M.

Fig. 1 presents the dispersion of exciton-polaritons calculated for a FCC lattice and the following set of structure parameters: $\varepsilon_A = \varepsilon_B = 10$, $R = a/4$, $\hbar\omega_1 = 2$ eV, $\hbar\omega_{LT} = 1$ meV, $P \equiv (\sqrt{3}\pi c/\omega_1 n_B a)^3 = 1.1$, $M = 0.5m_0$. Here m_0 is the free electron mass in vacuum and, instead of the bulk exciton resonance frequency ω_0, we introduced the resonance frequency $\omega_1 = \omega_0 + \hbar\pi^2/(2MR^2)$ of the ground state of the exciton quantum-confined in a sphere of the radius R. For $P = 1.1$, the anticrossing between the horizontal line $\omega = \omega_1$ ("bare" exciton branch) and the line $\omega = ck/\sqrt{\varepsilon_B}$ ("bare" photon branch) occurs inside the Brillouin zone at k amounting approximately 97% of k_L and 84% of k_X.

3. 2D quadratic photonic crystal

Fig. 2 presents the dispersion of exciton-polaritons in a resonant 2D photonic crystal with the dielectric contrast. We have studied exciton polaritons propagating perpendicularly to the cylinder axis and polarized along this axis (TE-polarization).

In Fig. 3a the solid curves show the same dispersion branches as in the previous figure but in an increased scale and in the vicinity of the X point. The resonance frequency of the exciton quantum-confined in a cylinder of the radius R is given by $\omega_1 = \omega_0 + \hbar\gamma^2/(2MR^2)$, where $\gamma \approx 2.40$ is the first zero of the Bessel function J_0. Parameters of the structure were chosen in such way that it lies inside the stop-band of the analogous photonic crystal without excitons.

It is instructive to analyze the polariton dispersion in two opposite limiting cases, namely, for $M \to 0$ and $M \to \infty$. The lower polariton branch is formed as a result of "repulsion" of the photon branch towards the longwavelength side because of the interaction with the exciton quantum-confinement levels. For $M \to 0$ but $\omega_1 = \text{const}$, this branch is remarkably affected by the lower level only. For $M \to \infty$, other levels act upon this branch to the maximum since in this limit their resonance frequencies coincide and are equal to ω_0. We conclude then that

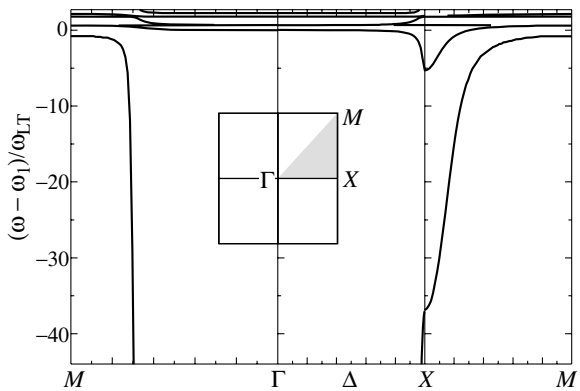

Fig. 2. Dispersion of TE-polarized exciton-polaritons in a 2D resonant photonic crystal. The calculation is carried out for the following set of parameters: $\varepsilon_A = 11, a = 0.99c\pi/(\omega_1\sqrt{\varepsilon_B})$, $R = 0.3a$. Here a is the lattice constant for a 2D square lattice, and R is the radius of the cylinders. Other parameters are the same as in Fig. 1.

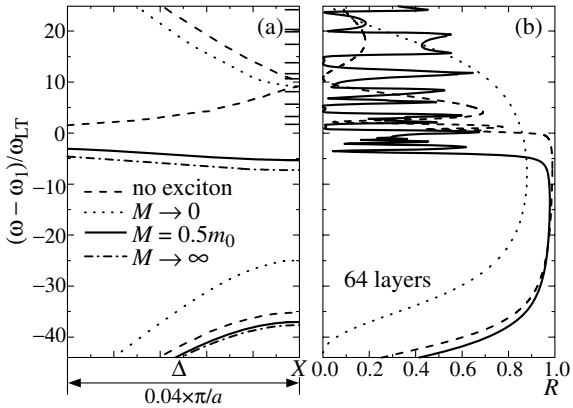

Fig. 3. (a) Dispersion of TE polarized exciton-polaritons in an array of parallel cylinders. Only two lower branches of the dispersion curve are shown for the system with the exciton effective mass $M = 0.5\ m_0$. Instead of presenting a dense network of upper polariton branches, only the exciton-polariton eigenfrequencies at the X point are indicated by short horizontal lines touching the vertical line X. Dotted, dashed, solid and dashed-and-dotted lines represent the branches of the dispersion curve calculated neglecting and taking into account exciton-photon coupling for the exciton effective mass $M \to 0$, $M = 0.5m_0$ and $M \to \infty$. (b) The reflection spectra for the TE-polarized light incident from the material B upon 64 layers of cylinders. The spectrum for $M = \infty$ is omitted in order not to overload the figure. Spectra were calculated with exciton nonradiative damping $\hbar\Gamma = 0.1$ meV.

the lower polariton branch corresponding to the finite mass M must always lie between the dashed-and-dotted and dashed lines, in agreement with the results of calculation shown in Fig. 3a.

The optical reflection spectra presented in Fig. 3b are calculated by using the 2D layer KKR method [6]. In this method electromagnetic field is decomposed in cylindrical waves in order to perform the calculation of light scattering by a single cylinder and in plane waves in order to describe field propagation between neighboring layers of cylinders. Comparing Figs. 3a and 3b one can see, that the reflection coefficient R reaches a maximum inside the forbidden gaps and rapidly decreases in the adjoining allowed bands. In a frequency region $\omega > \omega_1$ the reflection spectra calculated for the exciton mass $M = 0.5m_0$ has a series of sharp maxima at frequencies corresponding to the horizontal lines in Fig. 3a.

Acknowledgements

This work has been supported in part by the Russian Foundation for Basic Research and the programme of the Russian Academy of Sciences.

References

[1] E. Yablonovitch, *Phys. Rev. Lett.* **58**, 2059 (1987).
[2] S. John, *Phys. Rev. Lett.* **58**, 2486 (1987).
[3] O. Toader and S. John, *Phys. Rev. E* **70**, 46605 (2004).
[4] K. C. Huang *et al*, *Phys. Rev. B* **69**, 195111 (2004).
[5] E. L. Ivchenko *et al*, *Phys. Solid State* **42**, 1756 (2000).
[6] X. Wang *et al*, *Phys. Rev. B* **47**, 4161 (1993).
[7] A. Moroz, *Phys. Rev. B* **51**, 2068 (1995).
[8] Kazuo Ohtaka *et al*, *Phys. Rev. B* **57**, 2550 (1998).
[9] H. Ajiki *et al*, *Phys. Rev. B* **66**, 245322 (2002).

14th Int. Symp. "Nanostructures: Physics and Technology"
St Petersburg, Russia, June 26–30, 2006

Light scattering in hetero-opals

S. G. Romanov[1], C. M. Sotomayor Torres[2], J. Ye[3] and R. Zentel[3]

[1] Ioffe Physico-Technical Institute, St Petersburg, Russia
[2] Tyndall National Institute, University College Cork, Cork, Ireland
[3] Institute of Organic Chemistry, University of Mainz, 55099 Mainz, Germany

Abstract. Light scattering in hetero-opals consisting of two thin opal films with different lattice constants has been compared to scattering in single opal films. It has been shown that the reversing of angles of the incidence and detection changes the scattering spectra of hetero-opals, in contrast to spectra of single opal films, which remains unchanged. Squeezing of the scattering diagram of hetero-opals compared to single opal films has been also observed. These effects have been assigned to anisotropy of scattering at the photonic bandgap interface.

Introduction

An important step to realise potential of photonic crystals (PhCs) is to tailor-design the inhomogeneities in a periodic structure to perform waveguiding, lasing or wave division multiplexing. Among functionalised structures, the interface between two PhCs with different properties can be considered as a basic component. Photonic devices for light transport are usually characterised with respect to light losses. There are two kinds of scattering in non-absorbing PhCs: the coherent one, which opens the photonic band gap (PBG), and the incoherent scattering, which deteriorates the PBG. The scattered light carries more comprehensive information about conditions of light propagation, compared to transmitted/reflected one, owing to its inherent coupling to all optical modes of the PhC. The light transport can be either diffusive or ballistic depending on the correlation between the mean free path of photons and the optical path length. In bulk opals with the diffusive propagation, the PBG structure, which is resolved in the spectra of the scattered light, is associated with the last portion of the photon trajectory [1, 2]. In thin opal films with the ballistic transverse propagation, the weakly scattered light retains the memory about propagation along both the incident and exit directions [3, 4]. Multiple-film opals consisting of films with different lattice constants [5] contain PBG interfaces. Group velocity mismatch of optical modes at interfaces gives rise to specific losses. We studied two configurations of angle-resolved collection of forward scattered (FS) light to underpin the effect of the interface upon the light scattering. Directionality diagrams of scattering light were extracted to quantify the scattering directionality. Comparing single- and double-film opals, we showed that the PBG interface induces the scattering anisotropy but does not destroy the ballistic propagation.

1. Experimental

Hetero-opals were prepared by convective crystallisation from a colloidal suspension of PMMA spheres of 349 nm and 290 nm in diameter beads. Angle-resolved transmission spectra were compared to angle-resolved forward scattered (FS) light spectra. The FS1 (FS2) configurations correspond to fixing either the incidence angle $\theta = 0^\circ$ (variable α) or the scattering angle $\alpha = 0^\circ$ and scanning over another angle. Angle diagrams were extracted from angle-resolved spectra of the FS1 light.

2. Results and discussion

FS1 and FS2 scattering spectra of a single opal film look alike, although they differ in spectral positions of minima. These minima refer to the diffractive attenuation of the weakly scattered light along directions of incidence (E) and detection (X) as follows from comparison with transmission spectra (Fig. 1a) The FS1 and FS2 spectra contain non-directional and one directional minima associated with one constant and one variable angle.

At $\theta = 0^\circ$ and $\theta = 40^\circ$ the transmission spectra of the double film opal contain (111) and minima for each of films (Fig. 1b). Both FS1 and FS2 spectra differ from transmission spectra because they show different number of minima. Angle dispersions of FS1 and FS2 minima of the single film opal are the same, thus reflecting the reciprocity of the scattering. On contrary, angle dispersions of attenuation minima in the hetero-opal differ from each other (Fig. 2a, b).

The illuminated film retains the non-directional E1 minimum and, partly, the directional X1 minimum in FS1 spectra, while the next film demonstrates directional X2 and non-directional E2 minima. FS2 spectra demonstrate a splitting of the directional E1 minimum into two branches due to attenuation by (111) and planes and non-directional X2 minimum. This observation permits the assessment of the PBG interface. In the FS1 configuration the incident beam suffers

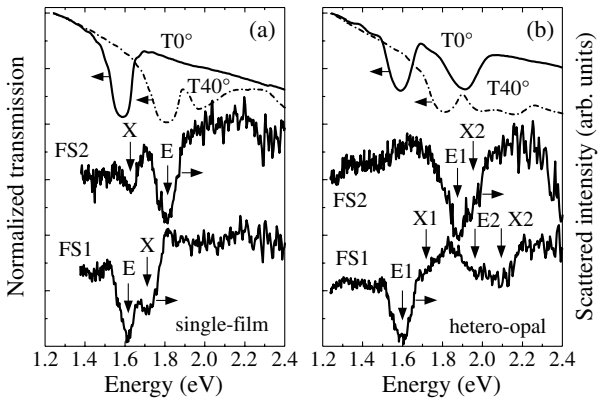

Fig. 1. (a) FS1 and FS2 spectra of the single opal film from 349 nm beads at $\theta = 0^\circ$, $\alpha = 40^\circ$ and at $\theta = 40^\circ$, $\alpha = 0^\circ$, respectively, and transmission spectra at $\theta = 0^\circ$ and $\theta = 40^\circ$. Spectra are shifted for clarity. (b) The same for the hetero-opal. E1 (E2) and X1 (X2) minima correspond to entry and exist photon trajectories in the bottom (top) films.

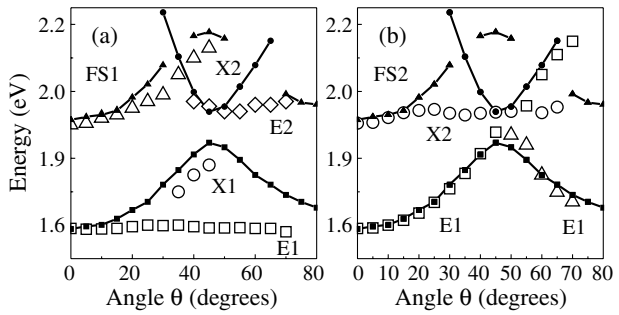

Fig. 2. (a) Angle dispersions of transmission minima of the bottom and the top opal films (2) compared to dispersion of E1, E2 and X1, X2 minima in FS1 spectra (open symbols). (b) The same for FS2 spectra of the hetero-opal.

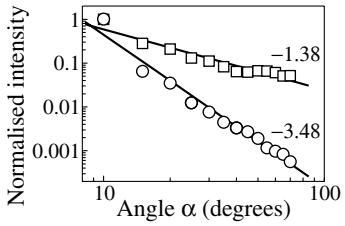

Fig. 3. (a) FS1 scattered light diagrams of double (dots) and single opal films (squares) of the same thickness at 1.745 eV. Numbers are the k exponents obtained in the fit.

scattering either in the second film or at the interface. Because the X2 minimum appears irrespectively to the scattering regime, the observation of non-directional E1 and E2 minima suggests that photons approaching the interface along the film normal can be then scattered only once before being detected, whereas photons approaching the interface at oblique angles are deemed to undergo the multiple scattering.

In the case of the off-normal incidence, the photons scattered in the first film have no chance to reach detector ballistically, i.e., FS2 scattering is dominated by the interface. The transport remains to be ballistic, because the E1 minimum would be lost otherwise.

The angle diagram of the scattered light in the FS1 configuration reflects the probability of a photon to be scattered to a given angle. The intensity of scattered light decreases as $I_{\mathrm{FS1}}(\alpha) \propto I_{\mathrm{inc}}\alpha^{-1}$ with increasing angle α, where I_{inc} is the incident light intensity. Remarkably, squeezing of the scattering diagram along the direction of the incident light occurs in the hetero-opal (Fig. 4).

The diffraction attenuation of the scattered light is about

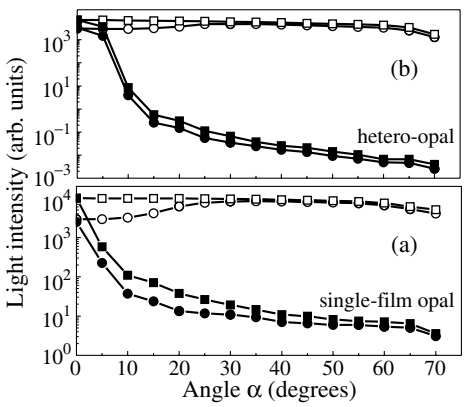

Fig. 4. Squeezing of the scattering diagram in the double-film opal.

30–50% of the transmission suppression. This is not sufficient for the hyperbolic drop of the scattered light intensity.

Summarizing, we showed that the PBG interface becomes the place of major scattering, especially for oblique light incidence. Squeezing of the scattering diagram in the hetero-opal as compared to single opal films is a consequence of the anisotropy of the interface scattering. Fortunately, the regime of weak scattering, which is characterised by a large contribution of single scattered photons in the flux propagating off the direction of the incident light beam, is preserved in hetero-opals.

Acknowledgements

This work was supported in part by the EU IST project "PHAT" and the NoE "Phoremost", the SFI and the RFBR 05-02-16975 grant.

References

[1] V. N. Astratov *et al*, *Phys. Rev. B* **66**, 165215 (2002).
[2] A. F. Koenderink *et al*, *Phys. Rev. Lett.* **91**, 213902 (2003).
[3] S. G. Romanov *et al*, *Phys. Rev. E* **69**, 046611–1 (2004).
[4] S. G. Romanov, *JETP Letters* **79**, 614 (2004).
[5] R. Rengarajan *et al*, *Phys. Rev. B* **64**, 205103 (2001).

14th Int. Symp. "Nanostructures: Physics and Technology"
St Petersburg, Russia, June 26–30, 2006

CdTe nanocrystal emission in the vicinity to 2D Langmuir–Blodgett colloidal photonic crystal

S. G. Romanov[1,2], M. Bardosova[2], C. M. Sotomayor Torres[2], M. Pemble[2], N. Gaponik[3] and A. Eychmüller[3]

[1] Ioffe Physico-Technical Institute, St Petersburg, Russia
[2] Tyndall National Institute, University College Cork, Cork, Ireland
[3] Institute of Physical Chemistry and Electrochemistry, Technical University of Dresden, Dresden, Germany

Abstract. Spontaneous emission (Em) of CdTe nanocrystals has been modified by the local field of the 2D colloidal photonic crystal in the photonic bandgap frequency range. The spectrum broadens as compared to the bare emitting film, the Em diagram becomes wider and the Em extraction increases at the photonic bandgap.

Introduction

Recently, semiconductor LEDs were realised via an all-chemical approach using colloidal semiconductor nanocrystals (NCs) encapsulated in polyelectrolyte films [1]. To improve the external quantum efficiency, photonic crystals (PhCs) can be prepared on the surface of such light emitting film. In spite the fact that only a fraction of the Em can be coupled to PhC eigenmodes due to spatial separation of the emitter, the interaction of PhC and NCs in the near field zone of the PhC remains high enough to affect the NC emission.

We report the preparation of the thin polyelectrolyte film embedded with size-selected colloidal CdTe NCs coated by colloidal PhC deposited using the Langmuir–Blodgett (LB) technique [2]. This method offers large area coating and deposition of several sphere monolayers. Comparison of emission from bare and coated NC films revealed flattening of the Em spectrum, broadening of the Em diagram and frequency dependence of the Em extraction efficiency. In spite of the simplicity of the examined architecture and weakness of the effects, the underlying physics is very interesting.

1. Experimental

Thin films of CdTe NCs [3] were prepared by layer-by-layer (LbL) infiltrating NCs assembling in polyelectrolytes (PE). 20 bi-layers consisting of a polymer/NC composite were deposited with the total thickness ca. 60 nm. 2 nm NCs were used with an emission maximum around 530 nm. SiO_2 spheres of 519 nm in diameter were deposited on the LbL PE-CdTe films using LB technique, which will be referred further as PhC coatings.

Angle-resolved transmission spectra were acquired at different angles of incidence, θ, with respect to the film normal. The photoluminescence (PL) spectra were excited by 457.9 nm line of the Ag-ion laser. The spot size was 5 mm in diameter to mimic the emission from a large-area display. The illumination conditions — the laser power and the spot size, were maintained constant at all angles of the emission detection. Emission and transmission spectra were obtained at angles between 0 and 50° with a step of 5°.

2. Results and discussion

The transmission minimum for the light traversing the 2D hexagonal grating assembled from 519 nm spheres is centred at ∼ 535 nm (Fig. 1a). This PBG survives in the case of 5L coating. The PBG structure of a 2D lattice of dielectric spheres [4] explains reasonably well the minimum and its angle dispersion. Another minimum is observed at 441 nm. PL spectra of the bare CdTe-LbL film are shown in Fig. 1b. At $\theta = 0°$ the PL spectrum consists of overlapping 508 nm and 535 nm bands. The PL intensity at a given wavelength, $I(\lambda, \theta)$, rapidly decreases with increasing the angle of detection. The angle diagram of the emission intensity at 535 nm (Fig. 1b) shows that two-fold decrease occurs at $\theta \approx 15°$.

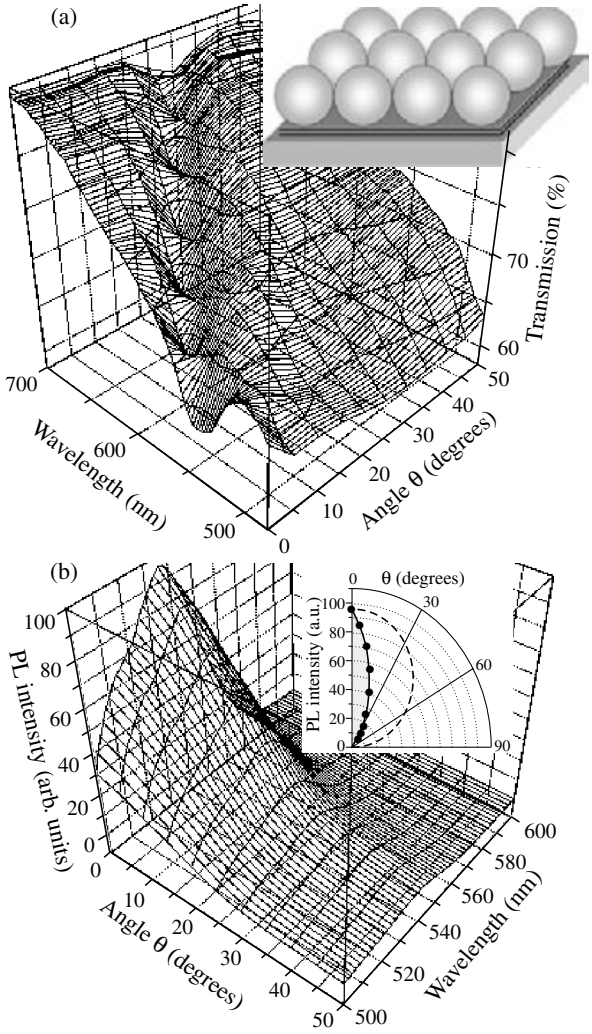

Fig. 1. (a) transmission spectrum of 1L LB film. Inset — schematics of the sample. (b) emission spectrum of bare CdTe film. Inset — the angle diagram of emission and the Lambert law (dash).

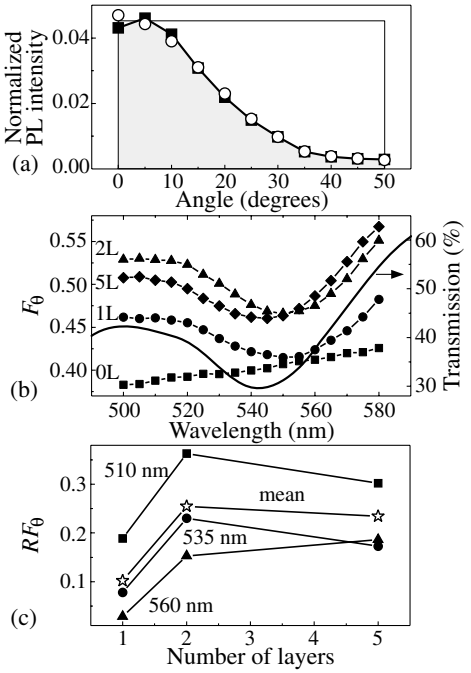

Fig. 2. (a) Normalised angle diagrams of the PL intensity of 1L coated NC film at 505 and 535 nm. Rectangle is the maximum possible diagram area. (b) Spectra of the relative diagram area for different number of coatings. (c) Broadening, RF_θ of the angle diagram at different wavelength and its mean value over the whole spectrum range (stars).

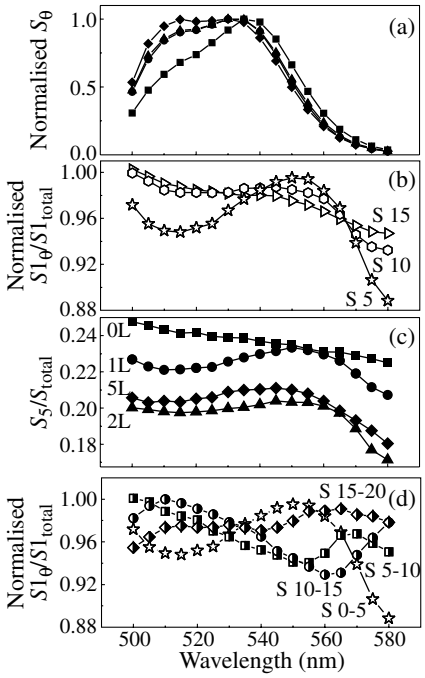

Fig. 3. (a) Normalised spectra of angle diagram areas for bare NC film (squares) and 1L (circles), 2L (triangles) and 5L (diamonds) coated NC films. (b) Spectra of emission extraction from 1L coated NC film for different angle intervals from 0 to 5 (stars), to 10 (hexagons) and to 15° (triangles) normalized to their maximum value. (c) Spectra of emission extraction from 0 to 5° for different coating thickness. (d) Spectra of emission extraction from 1L coated NC film at different angle intervals from 5 to 10 (squares), from 10 to 15 (circles) and from 15 to 20° (diamonds).

To evaluate the angle width of the Em diagram $\mathrm{I}(\lambda, \theta, N)$, the fraction occupied by the diagram area, $S_\theta(\lambda, N)$, in the rectangle of dimensions $I_{\max}(\lambda, \theta, N)$ and the angle interval, $\Delta\lambda$, from 0° to 50°, $F_\theta(\lambda, N) = S(\lambda, N)/I_{\max}(\lambda, \theta, N)\Delta\theta$, (Fig. 2a) was calculated. The spectra of this fraction for the coated NC films differ from that of the bare film by a well-defined minimum (Fig. 2b). With the increase of the number of coating layers, the magnitude of the diagram fraction saturates at two layers.

$RF_\theta(\lambda, N) = (F_\theta(\theta, N) - F_\theta(\theta, 0))/F_\theta(\theta, 0)$-the relative fraction, characterises the increase of the emission diagram width after coating. This quantity increases by 10 to 30% depending on the wavelength. Averaging over all wavelengths shows that the diagram broadening achieves 25% for the 2L PhC coating (Fig. 2c).

By construction, the minimum in the $F_\theta(\lambda, N)$ spectra can appear either due to a decrease of the diagram area or an increase of the emission intensity along the film normal. Because the area spectrum $S_\theta(N)$ does not show the minimum in the wavelength range of the transmission minimum (Fig. 3a), this minimum should relate to an increase in the out-of-plane emission intensity. We compared for 1L-NC film in Fig. 3b the ratio spectra of the diagram areas corresponded to the first 5, 10 and 15° to the total diagram area, $S1_\theta/S1_{\text{total}}$: the broad maximum of $S1_5/S1_{\text{total}}$ spectrum is centred at 551 nm, i.e., at the transmission minimum (Fig. 3b). This maximum degrades with increasing the angle interval, indicating its angular selectivity. Hence, the emission extraction increases towards the PBG of 2D PhC.

Since ratio spectra in Fig. 3c are superimposed on the same decreasing background, the extraction maximum can be assign solely to the PhC coating. With increasing the number of coating layers, this effect saturates at 2L coating. Apparently, the deviations of the diagram broadening and light extraction in a sample with 5L coating (Fig. 2b, 3c) can be associated with the higher dimensionality of the PhC.

The scenario of emission in the vicinity of the 2D PhC is following. The emission is generated in a NC film and emitted primarily in the substrate. If the light emitting film is in the near-field region of the 2D PhC coating, two processes take place. On the one hand, the PBG reflected radiation is partly recycled, that leads to broadening of the emission spectrum. On the other hand, emission is coupled to in-plane leaky PhC eigenmodes. These modes are responsible for broadening of the light emission diagram.

Model [5] suggests a 5–100 times increase of the local field at the surface of PhC coating. Since this effect is a property of evanescent waves, it decays on a scale of a lattice constant. The local field enhances the radiative properties of NCs. Thus, instead of PBG shadow the diagram displays the maximum.

Acknowledgements

This work was supported in part by the EU IST project "PHAT" and the NoE Phoremost, the Science Foundation of Ireland and the RFBR 05-02-16975 grant.

References

[1] A. Shavel *et al*, *Eur. J. Inorg. Chem.* 3613 (2005).
[2] M. Bardosova *et al*, *Thin Sol. Films* **437**, 276 (2003).
[3] N. P. Gaponik *et al*, *J. Phys. Chem. B* **106**, 7177 (2002).
[4] H. T. Miyazaki *et al*, *J. Appl. Phys.* **87**, 7152 (2000).
[5] H. Miyazaki and K. Ohtaka, *Phys. Rev. B* **58**, 6920 (1998).

14th Int. Symp. "Nanostructures: Physics and Technology"
St Petersburg, Russia, June 26–30, 2006

Superfluid transition and propagation of spinor polariton condensates

I. A. Shelykh[1,2], Yu. G Rubo[3], G. Malpuech[4], D. Solnyshkov[4] and A. V. Kavokin[2]

[1] St Petersburg State Polytechnical University, St Petersburg, Russia
[2] School of Physics & Astronomy, University of Southampton, SO17 1BJ, Southampton, UK
[3] Centro de Investigación en Energía, Universidad Nacional Autonóma de México, 62580, Mexico
[4] LASMEA, UMR 6602 CNRS, Université Blaise Pascal, 63177 Aubière, France

Abstract. With use of the generalized Gross–Pitaevskii equation it is shown that the polaritons in semiconductor microcavity form a linearly polarized condensate with two anisotropic co- and cross-linearly polarized branches of the excitation spectrum. The formalism is applied to describe the real-space dynamics of a polarized polariton superfluid.

Introduction

Exciton-polaritons in planar microcavities with embedded quantum wells (QWs) are composite bosons which retain the properties of both excitons and cavity phonons. Due to the excitonic component polaritons can efficiently interact with each other, while the photonic component makes their effective mass extremely small. Consequently, they are expected to condense at unusually high temperatures (up to room temperature) [1].

The exciton polaritons have only two allowed spin projections on the QW axis: +1 and -1. The projection 0 is forbidden for the polaritons formed by heavy-hole excitons. This represents an important peculiarity of the polariton condensates with respect to the Bose-condensates of cold atoms having usually 0 spin projection allowed. Interactions mix linearly polarized polariton states, moreover, additional mixing comes from the longitudinal-transverse (LT) splitting of exciton-polaritons [2].

All this makes the polariton condensates behave differently from the atomic condensates or superfluids even in the thermodynamic limit. In particular, the real-space dynamics of polariton droplets is expected to be qualitatively different from the superfluid dynamics and to reveal strong polarization effects. While theoretical simulations of the real-space propagation of polariton condensates have been reported recently [3], neither dispersion nor the real-space dynamics of polarized exciton-polaritons have been addressed till now.

In this work we show that a dramatic dependence of the renormalized exciton-polariton dispersion on the polarization strongly affects the real-space dynamics of the condensed polaritons.

1. Renormalization of the polariton dispersion

The spectrum of excitations of the polariton condensate at equilibrium can be studied on the basis of Gross–Pitaevskii equation

$$\mathrm{i}\frac{\partial\psi_i}{\partial t}=\left[T_{ij}(-\mathrm{i}\nabla)-\mu\delta_{ij}\right]\psi_j+U_0\psi_j^*\psi_j\psi_i-U_1\psi_j\psi_j\psi_i^*, \quad (1)$$

with the liner term given by

$$T_{ij}(\mathbf{k})=\omega_t(k)\delta_{ij}+[\omega_l(k)-\omega_t(k)]\frac{k_ik_j}{k^2}. \quad (2)$$

Here $i, j = x, y$ and $\omega_{l(t)}(k)$ is the dispersion of the noninteracting longitudinal(transverse) polaritons in the lower polariton branch. In terms of nonlinear optics, the U_0-term describes polarization independent properties of the condensate, while the U_1-term defines so-called linear-circular dichroism. he equilibrium properties of polariton condensates depend crucially on the presence and the sign of the dichroic U_1-term. For $U_1 > 0$ the condensate with linear polarization is formed, while in the case $U_1 < 0$ the circular polarization of the condensate becomes energetically favourable. The realistic polaritonic system ciorresponds to the former case.

To obtain the renormalized dispersion, we follow the method of Ref. [4] and look for the solutions of Eq. (1) in the form

$$\psi(\mathbf{r},t)=\sqrt{n}\,\mathbf{e}+\mathbf{A}e^{\mathrm{i}(\mathbf{k}\cdot\mathbf{r}-\omega t)}+\mathbf{B}^*e^{-\mathrm{i}(\mathbf{k}\cdot\mathbf{r}-\omega t)}. \quad (3)$$

Linearizing Eq. (1) with respect to the small amplitudes A_i and B_i we obtain the dispersion equation

$$\omega^4-\left[\omega_l^2+\omega_t^2+2(u_0-u_1)\omega_++2u_1\omega_-\right]\omega^2 +\left[\omega_l\omega_t+2(u_0-u_1)\omega_-\right]\left[\omega_l\omega_t+2u_1\omega_+\right]=0, \quad (4)$$

where $\omega_\pm=[\omega_l+\omega_t\pm(\omega_l-\omega_t)\cos(2\varphi)]/2$ and φ is the angle between the condensate polarization $\mathbf{e}$ and the wave vector $\mathbf{k}$. As in the case of two-component atomic condensates in the region of small wave vectors, where $\omega_{l,t}\ll\min\{(u_0-u_1),\,u_1\}$, the solutions of (4) give two sound-like branches of excitation spectrum. In the case of polariton condensates, however, these branches are anisotropic. This anisotropy is both due to the cylindrical-symmetry breaking due to the presence of condensate and the existence of LT-splitting. The dispersion becomes isotropic and more simple if one neglects the LT-splitting of noninteracting polariton band by putting $\omega_l=\omega_t=\omega_0$. In this case one obtains the co-polarized with the condensate

$$\omega^2\simeq\omega_0^2+2(u_0-u_1)\omega_0=\omega_0^2+2\mu\omega_0, \quad (\mathbf{A}\parallel\mathbf{B}\parallel\mathbf{e}), \quad (5)$$

and cross-polarized

$$\omega^2\simeq\omega_0^2+2u_1\omega_0, \quad (\mathbf{A}\parallel\mathbf{B}\perp\mathbf{e}). \quad (6)$$

Bogolyubov-like polariton branches. The linear character of the dispersion at small k is a signature of the superfluid transition in the system.

2. Propagation of the polariton superfluid

The anisotropic splitting of the two branches has a remarkable impact on the dynamics of the polariton superfluid. The coherent dynamics of the nonequilibrium condensate created by

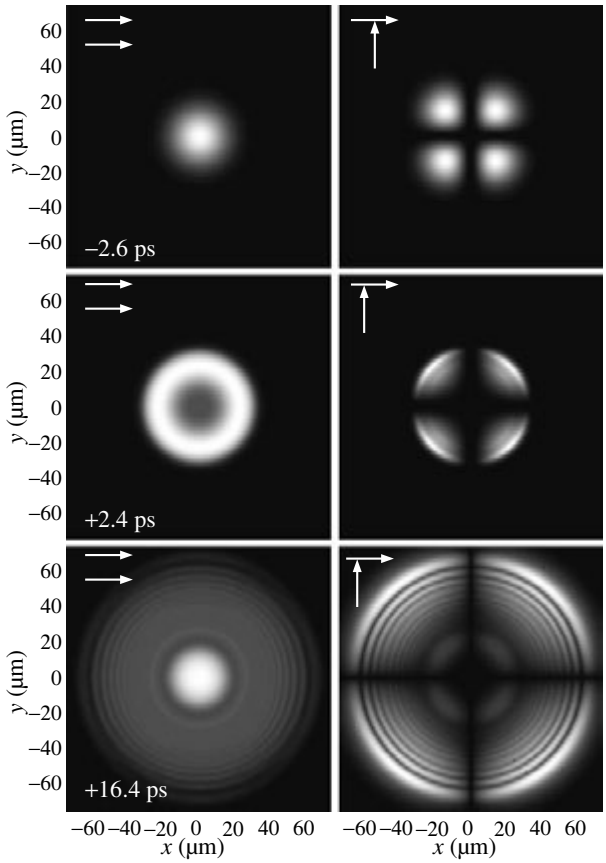

Fig. 1. Real-space image of the polariton the wave function, showing evolution of a Gaussian shape pulse in non-linear regime in X and Y polarizations. Zero time corresponds to the peak intensity of the pulse.

a pumping pulse within a limited spot and propagating in the real space can be written as

$$\mathrm{i}\left(\frac{\partial}{\partial t}-\frac{1}{\tau}\right)\psi_i=\left[T_{ij}(-\mathrm{i}\nabla)-\mu\delta_{ij}\right]\psi_j+ \\ +U_0\psi_j^*\psi_j\psi_i-U_1\psi_j\psi_j\psi_i^*\,, \qquad (7)$$

It is just Gross–Pitaevskii equation with finite polariton lifetime added. We consider a CdTe microcavity showing a Rabi splitting of 10 meV at zero detuning between exciton and photon modes at $k=0$. The constant U_0 is approximately given by [5]:

$$U_0=6xa_\mathrm{B}^2E_\mathrm{b}\,, \qquad (8)$$

where a_B is the exciton Bohr radius, E_b is the exciton binding energy, x is the exciton fraction in the polariton wave function. In what follows we take $U_1=0.55U_0$ in accordance with the estimation of Ref. [6] and $x=0.5$. We consider a 1.8 ps exciting pulse of light having a lateral size of 15 μm. It resonantly excites the ground state of the lower polariton branch as well as some of the excited states because of its finite broadening. It is polarized horizontally (along the X-axis). We assume zero temperature, the polariton life time of 3.5 ps. Fig. 1 shows the 2D plot of the absolute value of the polariton wave function at different times for both horizontal and vertical polarizations. One clearly sees the appearence of the Y-polarized component in the diagonal directions, which are the directions where the horizontal and vertical polarizations are no more eigenstates because of the anisotropic LT splitting. 2.4 ps after the maximum of the pulse, the X-polarized component forms a ring having the same width as the initial Gaussian pulse. This way of motion is characteristic of a linear dispersion and strongly contrasts with the normal spreading of a wave packet moving in a parabolic dispersion. We believe that the observation of such a ring would be a clear experimental evidence of polariton superfluidity. It is also interesting to notice that in the same time the quarter rings formed by the cross-linear polarization become sharper. These rings propagate without deformations, new rings forming from the center while the external ones are expanding. The velocity of sound can be directly extracted measuring the speed of propagation of these rings (about 5×10^6 m/s in our case, which corresponds to the value given by $c^2=\mu n/m$). This velocity is linked with the density n of the polariton condensate and it changes with time because of the radiative decay of the polariton population.

Recently W. Langbein [7] reported observation of cross-like dynamics of polarization propagation in microcavities showing remarkable similarities to our Figure 2. However, this result cannot be associated with the superfluidity since it was obtained exciting resonantly polariton excited states and not the ground state like in our work. We believe that spatial disorder in realistic cavities may have a strong impact on the spatial structure of polariton condensates and may substantially affect the motion of the polariton superfluid. Observation of the superfluid behavior remains an important challenge to the experimentalists.

Acknowledgements

This work has been supported in part by EPSRC and the project IN116402 of DGAPA-UNAM.

References

[1] A. Imamoglu, J. R. Ram, *Phys. Lett. A* **214**, 193 (1996).
[2] G. Panzarini *et al*, *Phys. Rev. B* **59**, 5082 (1999).
[3] I. Carussoto and C. Ciuti, *Phys. Rev. Lett.* **93**, 166401 (2004).
[4] E. M. Lifshitz and L. P. Pitaevskii, *Statistical Physics II*, the problem to S30.
[5] F. Tassone and Y. Yamamoto, *Phys. Rev. B* **59**, 10830 (1999).
[6] P. Renucci *et al*, *Phys. Rev. B* **72**, 075317 (2005).
[7] W. Langbein in *Proceedings of 26th International Conference on Physics of Semiconductors*, (Institute of Physics, Bristol, 2003), p. 112.
[8] M. Richard *et al*, *Phys. Rev. B* **72**, 201301 (2005).

14th Int. Symp. "Nanostructures: Physics and Technology"
St Petersburg, Russia, June 26–30, 2006

Design, dispersion analysis and fabrication of a photonic microcavity resonant structures

O. A. Usov, A. V. Nashchekin, S. A. Blokhin, E. M. Arakcheeva and E. M. Tanklevskaya
Ioffe Physico-Technical Institute, St Petersburg, Russia

Abstract. A two-dimensional (2D) hexagonal lattice photonic crystal (PhC) with different type defect superlattices such as coupled-cavity resonator array (CCRA) with In(Ga)As/GaAs quantum dots as active region were fabricated by standard nanotechnology methods [1]. The numerical calculations by transfer matrix plane wave and finite element methods showed that the designed CCRA structures with different coupling strength have a quasiflat impurity band with reduced group velocity over all range of wave vectors.

Introduction

The problem of slowing light down is very attractive now since both of fundamental understanding of light-matter interaction and possible applications such as controllable optical delay lines, data storage, optical memories, and other optical components for photonic integrated circuits. There have many demonstrations of slowing the speed of light in different optical resonant media [2, 3]. But one of the most prominent candidates for the control of the propagation of electromagnetic waves and slowing light is supposed to be a photonic crystals (PhCs), which are periodic structures of two or more materials with different refractive indices. Interference of optical waves scattered at different lattice planes of the PhCs determines their optical properties. For instance, if the scattering is strong enough, e.g. at strong index contrast, a photonic band gap (PBG) can be created. The resonant photon scattering gives a significant dispersion and a strong reduction of the group velocity at the band edges of the gap. However it is limited to a very narrow range of wave vectors in a particular direction and therefore an optical pulse propagating through the structure implies a significant distortion. A microcavity array of high-Q resonators in PhCs with opening impurity bands in PBG which is known as coupled-cavity resonator array (CCRA) or coupled-resonator optical waveguide (CROW) [4, 5] are supposed to have wide frequency range. Besides it has wholesome features since based on the structural dispersion and fabricated using standard technology [1]. Their optical properties depend on the configuration of the CCRA, mainly on transmission properties of single defect and also its coupling. The properly designed and fabricated CCRA structures exhibit quasiflat bands with reduced group velocity, which minimizes the distortion and attenuation of an optical pulse propagating.

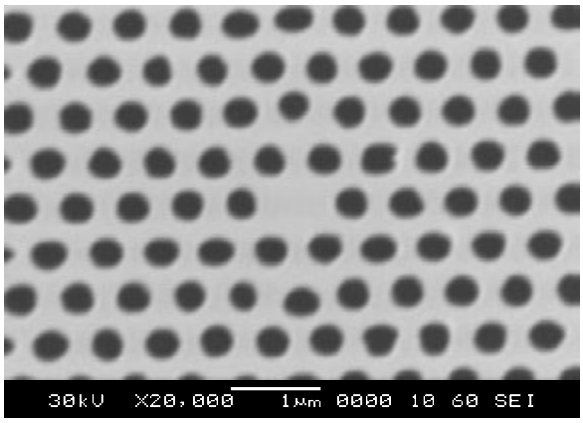

Fig. 1. Single air hole defect in a 2D PhC, the air holes being arranged in a triangular lattice in GaAs background.

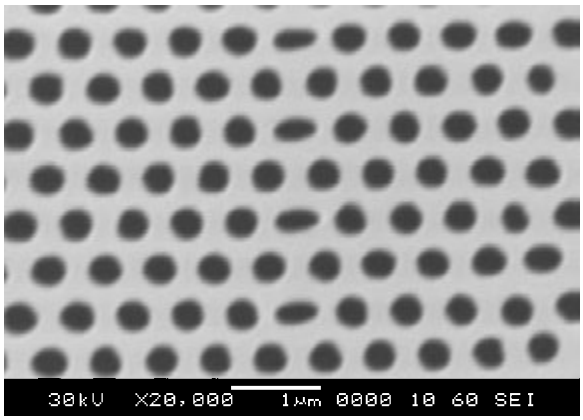

Fig. 2. The CCRA structure consists of defect superlattice created by periodically remove or change size or shape of holes.

1. Technology and fabrication

The PhCs and CCRAs were fabricated using technology of the optical and electron lithography, chemical and reactive ion etching (RIE). As electron resist was used positive resist polymethylmethacrylate (PMMA) with thickness as large as 300 nm spinned on the surface of the grown waveguide structure. The 20 nm Ni layer as a mask for RIE was deposited before PMMA. The direct electron lithography was applied using regime of scanning optimization along longitudinal axis and proximity effect correction to reach the correct shape of the assigned geometry of 2D PhC. The Ni layer argon etching was applied after PMMA development. Further, RIE was used for drilling the active region in GaAs waveguide through the Ni pattern. Thus, 2D photonic hexagonal lattice with the air-holes size as large as 300–400 nm and period 600 nm were obtained. The etching depth was about 1000 nm with a good vertically aligned smooth surface walls. The air-hole radius was selected about 0.25–0.3 times of the lattice period. The samples of prepared single hexapole defect and CCRA of such defects in Γ-M direction of 2D PhC structure are shown in Fig. 1, 2.

2. Results and discussion

The ordered superlattice defect structure in 2D PhC shown in Fig. 2 can be used for variety of passive and active optical devices. In such structures, light is confined within the defect

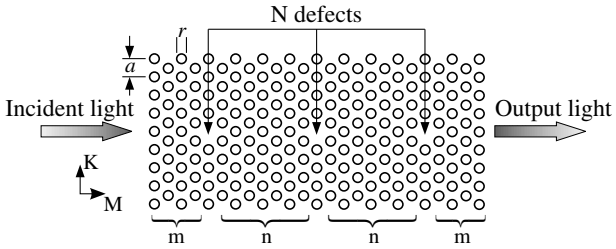

Fig. 3. The equivalent 1D PhC scheme, used for calculations dispersion, group velocity and time delay. The total number of defects is N, number periods between two neighboring defects is n, and the number of periods at both ends is m.

regions by the combined action of distributed Bragg reflection and internal reflection. The most significant loss in such slabs is radiative loss for mode lies above the light line. But designing defects with multi-nodal modes such as quadrupole or hexapole, i.e. whispering gallery (WG) type modes in which radiation in the vertical direction is reduced due to destructive interference, permits to realize an small-V_m and high-Q resonators and also resonator arrays in 2D PhC slabs [5]. The CCRA structure and its 1D model used for calculation are also shown in Fig. 3. The photonic dispersion of TE type modes of 2D PhC calculated by plane wave transfer matrix method are shown in Fig. 4, where points with low group velocity and partial PBG in Γ-M direction being marked. The CCRA based on evanescent field coupling between high-Q hexapole WG modes of defect microcavities which designed such that the resonant frequency falls within PBG of 2D PhCs and creates impurity band. In the tight-binding (TB) approximation the group velocity and band dispersion were determined such as:

$$v_g(k) = d\omega(k)/dk = \Omega\Lambda\kappa \sin(k\Lambda)\,, \quad (1)$$

$$\omega/\Omega = 1 - \kappa\cos(k\Lambda)\,, \quad (2)$$

where k — wave vector, Λ — period superlattice, Ω — frequency of single resonator, κ — coupling strength parameter calculated numerically in the TB nearest neighbor approximation. The impurity band formed by the coupling of N defect modes contain N resonances in the transmission spectrum. The coupling strength depends on defect mode Q-factor and confinement or defect separation, which assign as n in Fig. 3. The coupling strength is reduced with increasing confinement. For 1D PhC transmission coefficient of CCRA $T_N(\omega)$ which characterizes impurity band can be calculated analytically as follows: $1/T_N(\omega) = (1/T_1(\omega))\sin^2(N\beta)/\sin^2(\beta)$, where $T_1(\omega)$ is a transmission coefficient of unit cell, the Bloch phase β is determined as $\cos\beta = \mathrm{Re}(1/T_1(\omega))$.

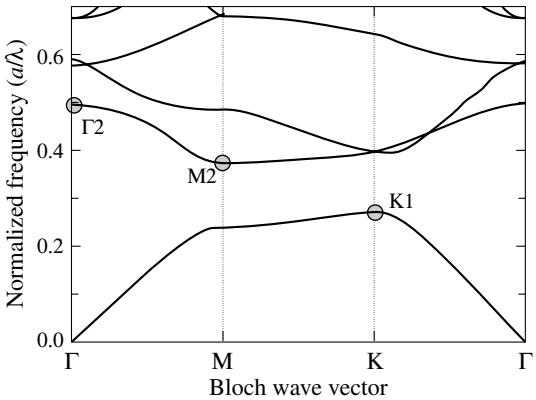

Fig. 4. Band structure of 2D triangular lattice PhC. The air-hole radius is $0.30a$, where a is a lattice period. Three band-edge points (M2, K2 and G2) with low group velocity are shown.

The optimized the CCRA structures of 2D PhCs in accordance with calculations were fabricated. The experimental photonic band (PB) structure will be determined by variable-angle reflectivity spectroscopy. The angle-resolved photoluminescence which permits tracing of the photonic dispersion and revealing the PB structure of leaky modes will be also used. Application of quantum dots (QDs) as active material promising due to reduced diffusion in QD layer and so reduced surface nonradiative recombination for PhCs. Another important feature of QDs is a wide spectral bandwidth for emission which results from QD size fluctuations and helps for probing PB structure over a wide wavelength range. The transmission measurements will be also used to obtain the group velocity dispersion and slowing light due to quasiflat impurity band of the CCRA superlattice structures.

3. Conclusions

The technology of fabrication of 2D PhCs with coupled-cavity resonator array (CCRA) that is patterned into an active planar waveguide containing In(Ga)As/GaAs quantum dots has been developed and the samples with different coupling strength were prepared. The numerical calculations with transfer matrix and finite element methods confirmed that the photonic structure can be optimized to achieve impurity band with reduced group velocity. The optical characterization and experimental analysis slowing light and group velocity dispersions of the CCRA are in progress now.

Acknowledgements

This work is partially supported by the program of Physical Science department of RAS "Novel materials and structures", State contract No. 02.442.11.7566 "Realization of the Science investigations by young Scientists" and Grant SSch-5920.2006.2. Authors are grateful to V. Nevedomskij for help in the SEM analysis.

References

[1] E. M. Arakcheeva *et al*, *Zh. Tech. Phys.* **75**, 78 (2005).
[2] M. S. Bigel *et al*, *Phys. Rev. Lett.* **90**, 113903 (2003).
[3] Robert W. Boyd *et al*, *Phys. Rev. A* **71**, 023801 (2005).
[4] S. Mookherjea *et al*, *Phys. Rev. E* **66**, 046610 (2002).
[5] M. Notomi *et al*, *Phys. Rev. Lett.* **87**, 253902 (2001).

14th Int. Symp. "Nanostructures: Physics and Technology"
St Petersburg, Russia, June 26–30, 2006

Special frequencies in optical spectra of resonant Bragg structures

M. M. Voronov, E. L. Ivchenko, A. N. Poddubny and V. V. Chaldyshev
Ioffe Physico-Technical Institute, St Petersburg, Russia

Abstract. We demonstrate theoretically that there exist two special frequencies in the optical reflection spectra from the resonant Bragg quantum-well structures at which the absolute value of reflection coefficient $r(N)$ is almost independent of the quantum well number N. We give an analytical explanation of this effect in terms of a linear-fractional transformation $r(N)$ sending points N on the real axis to a circle in the complex plane. It has been shown that allowance for the dielectric contrast gives rise to a third special frequency at which the contributions to the reflectivity related to the dielectric contrast and the exciton resonance compensate one another. The absorption spectra are shown to have special frequencies as well; however the latter lie not outside the polariton band gap as in the case of reflection spectra but inside the gap.

1. Introduction

In resonant Bragg structures without the dielectric contrast, i.e., with coinciding the dielectric constant n_b^2 of the barrier material and the background dielectric constant n_a^2 of the quantum well (QW), the reflection spectrum for small enough number N of wells is described by a Lorentzian with the halfwidth $N\Gamma_0 + \Gamma$, where Γ_0 and Γ are exciton radiative and nonradiative damping rates [1]. For a very large number of wells the reflection coefficient is close to unity within the forbidden gap for exciton polaritons and rapidly decreases near the gap edges $\omega_0 - \Delta$ and $\omega_0 + \Delta$, where ω_0 is the exciton resonance frequency and $\Delta = \sqrt{2\omega_0\Gamma_0/\pi}$ [2,3,4]. In Refs. [4,5] the reflection spectra are calculated for arbitrary values of N. The calculations have demonstrated an existence of two special frequencies at which the reflection coefficient from the resonant Bragg structure is practically independent of the QW number and very close to that for reflection from a semi-infinite homogeneous medium with the refractive index n_b. In the present paper we give for the first time an analytical interpretation of this effect and question its existence in the absorption spectra. Moreover, we analyze the role of dielectric contrast and the detuning from the exact Bragg condition $n_b(\omega_0/c)d = \pi$ in the formation of the special frequencies (d is the structure period).

2. Reflection spectra

The structure under consideration contains a cap layer of the thickness b' (material B), N QWs (material A), each of the width a, separated by the barriers B of the thickness b and the semi-infinite medium B. Under normal incidence of the light wave of the frequency ω, the amplitude reflection coefficient can be written as [1]

$$r(N) = \frac{r_{01} + \tilde{r}_N e^{2i\phi}}{1 + r_{01}\tilde{r}_N e^{2i\phi}} . \qquad (1)$$

Here $r_{01} = (1-n_b)/(1+n_b)$, $\phi = k_b(b'-b/2)$, $k_b = n_b(\omega/c)$, $\tilde{r}_N$ is the reflection coefficient from the structure with N QWs placed between the infinite barriers. It is given by [6]

$$\tilde{r}_N = \frac{\tilde{r}_1}{1 - \tilde{t}_1 \frac{\sin(N-1)Kd}{\sin NKd}} , \qquad (2)$$

where the complex coefficients $\tilde{r}_1$, $\tilde{t}_1$ describe the reflection from and transmission through the layer of the thickness $d = a + b$ containing a QW in its center, K is the wave vector of an exciton polariton at the frequency ω in an infinite regular QW structure.

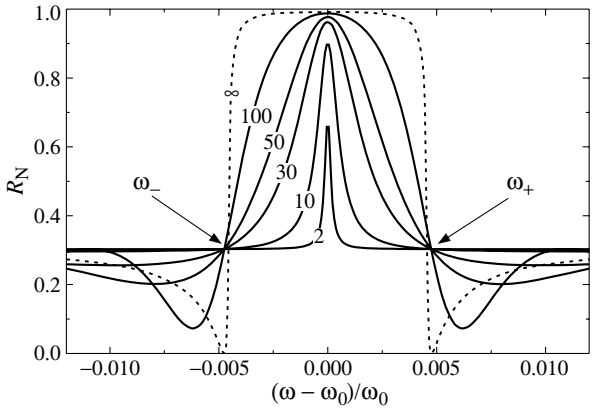

Fig. 1. The reflection spectra $R_N(\omega)$ from N-QW structure with the matched dielectric constants of compositional materials A and B. The calculation is performed for the background refractive index $n_b = 3.45$, the exciton resonance frequency, radiative and nonradiative damping rates defined by $\hbar\omega_0 = 1.533$ eV, $\hbar\Gamma_0 = 50$ μeV, $\hbar\Gamma = 100$ μeV and $b' = (a/2) + b$. Curves correspond to six structures with different number of QWs indicated at each curve.

Fig. 1 shows the reflection spectra from the resonant Bragg structures with matched dielectric constants. Parameters of the structures are indicated in the figure caption. In agreement with [4,5], one can see that for two frequencies labelled ω_+ and ω_- the reflection coefficient $R_N = |r(N)|^2$ is indeed close to r_{01}^2 and almost independent of N, at least for $N < 100$. The special frequencies are tied to the exciton-polariton forbidden-gap edges $\omega_0 \pm \Delta$ in such a way that $\omega_+ - (\omega_0 + \Delta) \ll \Delta$ and $(\omega_0 - \Delta) - \omega_- \ll \Delta$. On the other hand, the reflection coefficient R_∞ from the semi-infinite structure (curve ∞ in Fig. 1) shows an abrupt fall from values close to unity at $\Gamma \neq 0$ (or equal unity at $\Gamma \to +0$) inside the forbidden gap to values $R_\infty < r_{01}^2$ in the adjoining allowed bands.

An existence of the special frequencies $\omega_\pm$ in the reflection spectra can be understood if one notices that in the vicinity of the edge frequencies $\omega_0 \pm \Delta$, where $|N(Kd - \pi)|$ is small, the ratio of the sine functions in (2) can be approximated by

$$\sin[(N-1)Kd]/\sin(NKd) \approx -(N-1)/N . \qquad (3)$$

Therefore, the reflection coefficient $\tilde{r}_N$ and, hence, the reflec-

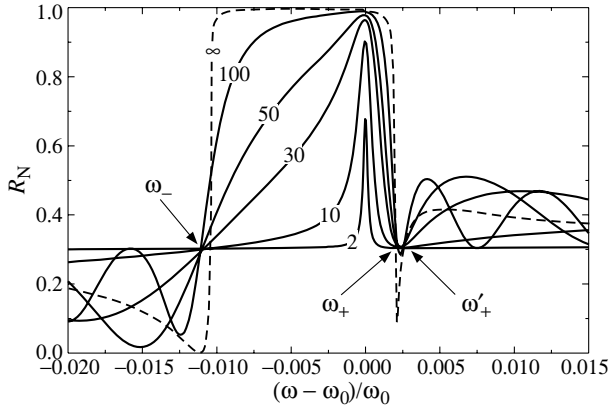

Fig. 2. The reflection spectra from Bragg QW structures with the dielectric contrast. The calculation is performed for $\hbar\Gamma = 100\ \mu$eV, $a = 120$ Å, $n_a = 3.59$ and $n_b = 3.45$. Curves are calculated for six structures containing different number, N, of wells indicated at each curve.

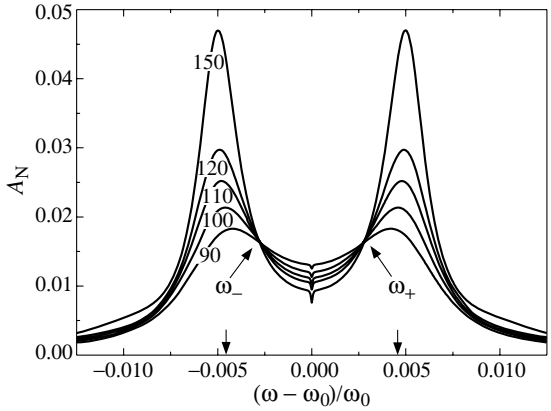

Fig. 3. The absorbance spectra from Bragg QW structures with the matched dielectric constants. The parameters of the structures coincide with those indicated in the caption to Fig. 1. Inclined lines point to the special frequencies ω_+ and ω_-, vertical arrows touching the abscissa indicate the polariton-gap edges in the infinite Bragg structure.

tion coefficient (1) can be presented as the Möbius or linear-fractional transformation

$$r(N) = (\alpha N + \beta)/(\gamma N + \delta) \tag{4}$$

with $\alpha = r_{01}(1 + \tilde{t}_1) + e^{2i\phi}\tilde{r}_1$, $\beta = -r_{01}\tilde{t}_1$, $\gamma = 1 + \tilde{t}_1 + e^{2i\phi}r_{01}\tilde{r}_1$ and $\delta = -\tilde{t}_1$. Let us continue analytically the dependence $r(N)$ to the whole complex plane $z = z' + iz''$ and take into account that the linear-fractional transformation $r(z)$ sends a circle to a circle, a straight line can be considered as a circle of the infinite radius, and the points $z = 1, 2, \ldots, N, \ldots$ lie on the real axis. It follows then that the complex values $r(N)$ lie on the circle of some radius ρ centered at some point w_0 so that one has $r(N) = w_0 + \rho e^{i\phi_N}$, where only the phase ϕ_N is N-dependent. The values of w_0 and ρ are related to α, β, γ and δ by [7]

$$w_0 = \frac{i}{2}\,\frac{\alpha\delta^* - \beta\gamma^*}{\mathrm{Im}(\gamma^*\delta)}\,, \quad \rho = \left|\frac{\alpha}{\gamma} - w_0\right|\,. \tag{5}$$

If there exists a frequency ω where w_0 vanishes (or is very close to zero) then the reflection coefficient R_N at this frequency is independent of N and equal to $|\alpha/\gamma|^2$. We see that the approximation of $r(N)$ by a linear-fractional transformation (4) and a smallness of the minimal value of the function $|w_0(\omega)|$ allows us to explain the existence of special frequencies $\omega_\pm$.

Fig. 2 shows the N-dependence of reflection spectra from the resonant Bragg structures with the different refractive indices n_a and n_b. The values of parameters are indicated in the figure caption. One can see that, instead of two, there are three special frequencies in the reflection spectra. They are labelled as ω_-, ω_+ and ω'_+. An appearance of the special frequencies $\omega_\pm$ can be explained in terms of the linear-fractional transformation as well as for the structures without the dielectric contrast. Unlike the frequencies $\omega_\pm$, at the frequency ω'_+ both the absolute value and the phase of the reflection coefficient $r(N)$ are practically independent of N. This happens because the contributions to the reflectivity due to the dielectric contrast and the exciton resonance compensate one another [8]. As a result, the amplitude reflection coefficient from the whole structure $r(N, \omega'_+)$ equals r_{01} and is independent of N.

3. Absorption spectra

In Fig. 3 we depict the absorbance spectra, $A_N(\omega)$, of QW structures with the same parameters as in the caption to Fig. 1 but for different numbers of wells (indicated at each curve). The absorbance is defined as $A_N = 1 - R_N - T_N$, where T_N is the transmission coefficient. It determines the fraction of the incident photon flux absorbed in the QWs and is nonzero only for nonvanishing exciton nonradiative damping. In agreement with Ref. [5], the spectra are also characterized by special frequencies similar to those in the reflection spectra. A crucial difference between the special frequencies in the reflection and absorption spectra is that the former and latter lie, respectively, outside and inside the polariton band gap. Moreover, in the case of absorption spectra the special frequencies are formed beginning from a rather large number of wells, $N \geq 90$. It is worthwhile to notice a narrow dip in the absorbance spectra at the resonant frequency ω_0 which is absent for few QWs and becomes pronounced with the increase in N. The origin of this dip will be explained elsewhere.

The calculation shows that allowance for a small dielectric contrast or the slightest detuning from the resonant Bragg condition strongly modifies the reflection and absorption spectra and remarkably shifts the special frequencies.

Acknowledgements

This work is supported by the programme of the Russian Academy of Sci. and Russian Foundation for Basic Research.

References

[1] E. L. Ivchenko *et al*, *Sov. Phys. Solid State* **36**, 1156 (1994).
[2] E. L. Ivchenko *et al*, *phys. stat. sol. (b)* **215**, 199 (1999).
[3] L. I. Deych *et al*, *Phys. Rev. B* **62**, 4242 (2000).
[4] T. Ikawa *et al*, *Phys. Rev. B* **66**, 85338 (2002).
[5] L. Pilozzi *et al*, *Phys. Rev. B* **69**, 205311 (2004).
[6] E. L. Ivchenko, *Optical spectroscopy of semiconductor nanostructures*, Alpha Science International, Harrow, UK, 2005.
[7] M. A. Lavrentyev *et al*, *Methods of function theory of a complex variable*, Nauka, Moscow, 1987 (in Russian).
[8] M. V. Erementchouk *et al*, *Phys. Rev. B* **71**, 235335 (2005).

14th Int. Symp. "Nanostructures: Physics and Technology"
St Petersburg, Russia, June 26–30, 2006

Low frequency noise in monodispersed platinum nanostructures close to the percolation threshold

S. L. Rumyantsev[1,2], *M. E. Levinshtein*[1], S. A. Gurevich[1], V. M. Kozhevin[1], D. A. Yavsin[1], M. S. Shur[2], N. Pala[2] and A. Khanna[2]

[1] Ioffe Physico-Technical Institute, St Petersburg, Russia
[2] Department of Electrical, Computer, and Systems Engineering, CII 9017, Troy NY 12180-3590, USA

Abstract. We report, for the first time, on the low frequency noise in monodispersed nanostructures. The platinum (Pt) spheres of 1.8 nm in diameter were deposited on a dielectric substrate using the laser ablation technique. The low-frequency noise was studied in the frequency range 1 Hz–50 kHz at temperatures from 9 to 300 K. Noise processes have been investigated both above and below the percolation threshold. The level of the $1/f$ noise in "metallic phase" (above the threshold) indicates a strikingly high level of the Pt structure quality in the spheres. In the "dielectric phase" (below the threshold), the noise spectral density S_I is proportional to the squared current only at very small currents I. Deviation from the conventional $S_I \propto I^2$ law occurs in these samples at current densities which are 5–6 orders smaller than that in metallic phase.

Introduction

Investigation of the granular nanostructures transport properties is in the forefront of solid state physics. Such structures have an excellent potential for applications in nanoelecronics and single electron devices [1, 2]. One of the most promising technologies for fabrication of these structures is the laser ablation technique [3]. This technique allows obtaining spherical metallic nanoparticles with extremely small dispersion of the particles sizes. The dispersion in the diameters of Pt and Ni spherical nanoparticles does not exceed, for example, the thickness of a single atomic layer. Investigations of the low frequency noise in such systems can provide important information about the character of the current percolation. In addition, the level and character of the low frequency noise is one of the most important characteristics of nano-devices, which can be potentially used in microwave and optical communication systems (see, e.g. [4]). However, to the best of our knowledge, the low frequency noise in metallic monodispersed nanostructures has not been investigated until now.

1. Experimental

In this work we studied the low frequency noise in monodispersed nanostructures of Pt spheres with the 1.8 nm diameter deposited as a monolayer on a dielectric substrate by the laser ablation technique. The spectral noise density of the current fluctuations S_I was measured in the frequency range 1 Hz–50 kHz in the temperature interval 9–300 K. Temperature measurements were made in the LTS-22 cryostat. Low frequency noise was measured using the low noise Signal Recovery 5184 amplifier and SR770 spectrum analyzer.

2. Result and discussion

The percolation threshold, p_0, for the monolayer of the Pt particles in question corresponds to the condition $0.51 < \vartheta < 0.76$, where ϑ is the part of the area occupied by the Pt spheres.

At $\vartheta = 0.76$ (quasi metal phase), the level of the noise as well as its temperature dependence are very close to those of thick pure metallic layers of platinum. The conductivity of such samples is also very close to the conductivity of bulk platinum.

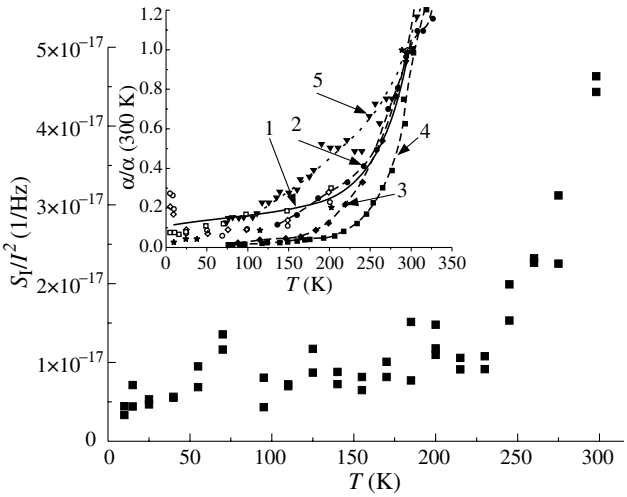

Fig. 1. Typical temperature dependences of the relative spectral noise density for "metallic" samples ($\theta = 0.76$, above percolation threshold). Inset shows the temperature dependences of relative Hooge parameter (normalized to (300 K) for different metals and alloys with different level of the structural perfection. Curve 1 represents the data obtained in this work for nanospheres of amorphous Pt. Curves 2 and 3 show the data for the 70 nm thick Au and Ag films. Curves 4 and 5 show the data for $Au_{60}Pd_{40}$ films subjected to different temperature treatments.

This result is quite unexpected one, because even in the layers of a much larger thickness than the diameter of nanospheres under investigation, the conductivity is appreciably smaller and the level of the $1/f$ noise is much higher than those in bulk platinum.

The frequency dependence of the relative spectral noise density S_I/I^2 has the form $S_I/I^2 \propto 1/f$, where γ is close to unity across all temperature range 9–300 K (flicker noise).

The Hooge constant, α, is about 10^{-2} at room temperature and decreases monotonically with temperature decrease in the region from 300 to 60 K (Fig. 1).

At current density $j < 10^7$ A/cm^2, the spectral noise density, S_I, is approximately proportional to I^2. With a further increase in j, the $S_I(I)$ dependence becomes noticeably steeper due to generation of excess defects by the flowing current [5].

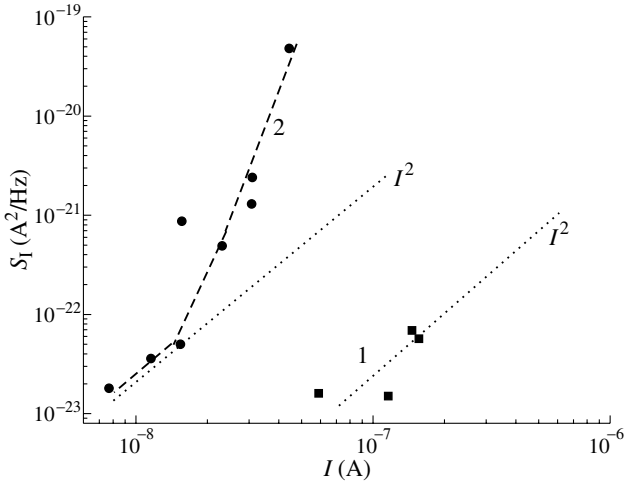

Fig. 2. The current dependences of the noise spectral density for "dielectric" samples. 1 — typical dependence; 2 — the dependence for a sample with maximum noise level. 300 K. Dashed lines correspond to the law $S_I \propto I^2$. 300 K. Frequency of analysis $f = 10$ Hz.

At $\theta = 0.51$ (below the percolation threshold), the temperature dependence of the conductivity, σ, follows the well known law $\sigma \exp[-(T_0/T)^{1/2}]$. The relative noise spectral density S_I/I^2 exceeds by many orders the corresponding value of S_I/I^2 for the quasi metallic structure ($\theta = 0.76$). The value of S_I is approximately proportional to I^2 only at very small currents and increases very sharply with a further increase in current (Fig. 2).

In dielectric samples a deviation from the $S_I \propto I^2$ law takes place at current densities 5–6 orders smaller than those for quasi metallic samples. One can assume that in dielectric samples, close to the percolation threshold, the voltage applied to the sample drops across several tunnel junctions between "metallic filaments" of conducting clusters. In this case, even at a small applied voltage, the electric field in these junctions is very high.

Acknowledgements

At Ioffe Institute this work was supported by Russian Foundation for Basic Research (grants 05-02-1774, 05-02-1772) and Civilian Research and Development Foundation (CRDF 2681). At RPI, this work was supported by National Science Foundation (Project Monitor Dr. James Mink).

References

[1] S. V. Vyshenski, *Phys. Low-Dim. Structures* **11/12**, 9 (1994).
[2] R. H. Chen *et al*, *Appl. Phys. Lett.* **72**, 61 (1998).
[3] V. M. Kozhevin *et al*, *JVST B* **18**, 1402 (2000).
[4] M. E. Levinshtein *et al*, in: *"Noise and Fluctuations Control in Electronic Devices"*, A. Balandin, ed., American Scientific Publishers (2002).
[5] G. P. Zhigalskii, *Phisics Uspekhi* **173**, (5) 466–490 (2003).

14th Int. Symp. "Nanostructures: Physics and Technology"
St Petersburg, Russia, June 26–30, 2006

Low-temperature magnetic properties of In-opal nanocomposites

D. Kaczorowski[1], *M. S. Kononchuk*[2], R. V. Parfeniev[2], S. G. Romanov[2] and D. V. Shamshur[2]

[1] Institute of Low Temperature and Structure Research, PAS, Wroclaw, Poland
[2] Ioffe Physico-Technical Institute, St Petersburg, Russia

Abstract. The method of production of superconducting (SC) nanoparticles ensembles inside a regular porous dielectric opal matrix with spatially modulated electrical and magnetic properties was applied. Magnetic properties of In-opal nanocomposite materials were investigated in SC state. Size and collective effects in magnetic properties of nanoscale superconductor ensembles in SC state with grain sizes comparable to the coherence length ξ are discussed.

Introduction

Superconductivity of three-dimensional regular ensembles of metallic nanoparticles was studied much less extensively than SC of two-dimensional systems, mainly because of technological difficulties. The recent finding of size and collective effects in such nanoscale superconductor ensembles [1] stimulated interest in studying the magnetic properties of these systems.

1. Samples and their characterization

3-dimensional regular ensembles of SC nanosize In grains were prepared using porous opals as templates [2]. The voids between contacting SiO_2 spheres of diameter $D = 230 - 290$ nm were filled by molten In under pressure (sample 60.1). The method [3] of molecular layer-by-layer deposition of TiO_2 oxide on inner surfaces of the voids and channels interconnecting the voids was used to prepare several samples with different numbers of TiO_2 monolayers (up to 60 for the samples 60.2, 60.3, 34). This method of changing the opal inner surface allows to vary the geometric parameters of the In grain lattice down to the limit when the size of octahedral voids d_O, tetrahedral voids d_T, which are interconnected by narrow bridges db (Table 1), are less than the coherence length ($\xi_0 = 640$ nm in bulk In) and the London penetration depth ($\lambda_L = 64$ nm in bulk In).

Table 1. Geometric characteristics and superconducting parameters of the In-opal nanocomposites.

Sample	60.1	60.2	60.3	34
k_{In}	0.26	0.22	0.19	0.08
D (nm)	290	290	290	230
d_O (nm)	120	115	109	69
d_T (nm)	66	60	55	26
d_b (nm)	45	40	34	10
H_{c1} (Oe)	52	280	320	1250
$\xi_{0\,eff}$ (nm) [4]	208	147	130	< 48
λ_{eff} (4.2 K) (nm) [4]	94	47	36	< 5

The dc magnetic properties were studied in the temperature interval 1.72–10 K and in magnetic fields up to 10 kOe using a commercial SQUID magnetometer. Before each measurement near-surface region of the samples was etched in hydrochloric acid in order to remove thin In layers possibly deposited on the surfaces.

2. Results and discussion

Fig. 1 shows for all the composite In-opal samples studied that with increasing magnetic field the Meissner state is followed by the "mixed state" and eventually the normal state, as for type-II superconductors. The observed numerous magnetization jumps manifest first-order phase transitions $L \to L + 1$ inside the SC state, associated with the subsequent vortex entering into minimal In contours with four Josephson junctions in the (110) plane. For the sample No. 34 the jumps on increasing field occur at $H_{0\to1} = 1.45$ kOe, $H_{1\to2} = 2.5$ kOe, $H_{2\to3} = 3.2$ kOe, $H_{3\to4} = 3.7$ kOe, $H_{4\to5} = 4.15$ kOe and $H_{5\to6} = 4.45$ kOe. For sweeping down the magnetic field only the transition into $L = 1$ state was observed for the samples No. 60.2 and No. 60.3 ($H_{2\to1} \approx 0.3$ kOe for both composites), yet no such effect was observed for the sample No. 34. Instead, a similar series of magnetizations jumps as given above appeared on the negative side of the magnetization loop (see Fig. 2). Apparently, pinning of vortices brings about a substantial magnetic hysteresis that increases with decreasing the In grain sizes (cf. Fig. 1). Such a hysteresis is associated with the existence of the critical current, which can be estimated using the Bean model that predicts $J_c(H, T) = a\Delta\sigma(H, T)/R$ (J_c in units of A/cm^2, in Gs, R in cm), with the coefficient $a = 16.97$ for a sphere of radius R [6] and $a = 15$ for a cylinder.

The observed screening is produced by Josephson supercurrents flowing between the SC grains through the bridges in response to the applied magnetic field. The magnetic field generated by these supercurrents screens the interactions between the fractionally charged vortices in the array. In most cases the screening length was proven to be larger than the size of the sample itself.

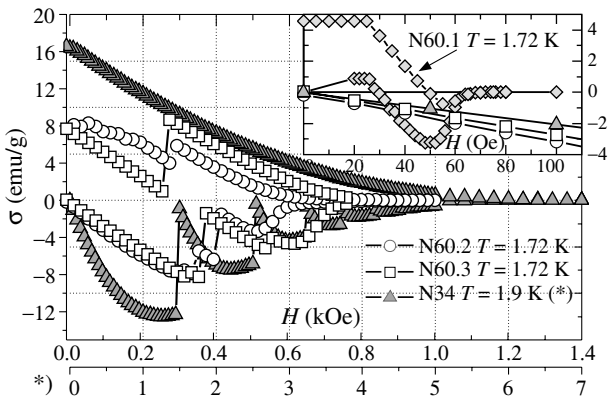

Fig. 1. Magnetic field variations of the low-temperature dc magnetization in a few samples of In-opal nanocomposites having different values of In-volume fractions k_{In} and bridge sizes d_b (Table 1). The inset shows the magnetization in the Meissner state ($L = 0$) for the samples No. 60.2, 60.3 and 34, as well as the first-order SC transition in the sample No. 60.1 with maximal k_{In}.

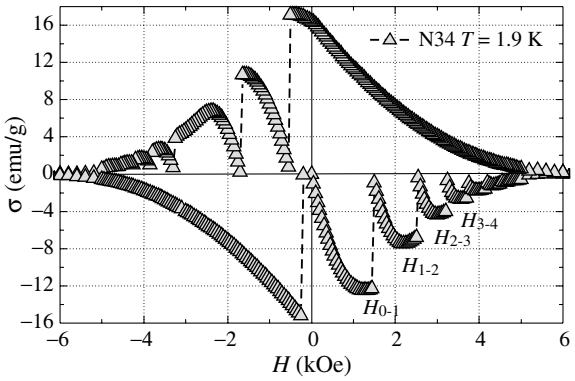

Fig. 2. Magnetization hysteresis loop measured for the sample No. 34 at 1.9 K.

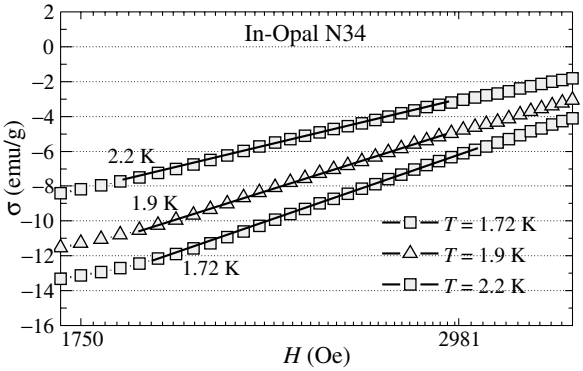

Fig. 3. The magnetization isotherms of the sample No. 34, plotted as a function of ln H in the region between the first and second critical magnetic fields.

Markedly, the shielding fraction of the sample No. 34, calculated from the low-field data, was about 80% of that predicted for an ideal diamagnet, in spite of the volume fraction of In grains in this sample was only 8%. In order to estimate the penetration depth the magnetization isotherms were analyzed in terms of the relation $d\sigma/d(\ln H) \sim 1/\lambda^2(T) \sim n_S(T)$, valid in intermediate-field region, as displayed in Fig. 3. Some deviation of ($\ln H$) curves from a straight-line behavior seen in stronger magnetic fields may be due to contribution of the vortex core energy to the magnetization [5], because the volume of vortex cores (SiO_2 spheres) is in the sample studied much larger than the overall volume of In insertions.

The temperature variations of the magnetization in the sample No.34, measured in a few different magnetic fields upon cooling the specimen in zero field, are shown in Fig. 4. Evident from this data is a paramagnetic response that occurs when flux enters inside a unit cell of the Josephson-junction array. In such a case the screening SC current changes from a negative value that compensates the external magnetic field to a positive one, which gives rise to an additional flux density generating the fluxoid equal to 0 (the phase difference around the cell changes by 2). This circular SC current gradually diminishes with increasing H and reaches zero for $\phi_{\text{int}} = \phi_{\text{ext}} = \phi_0$. For the sample No. 34 it happens for $H \approx 1.4$ kOe (cf. Fig. 4).

3. Conclusions

The present study revealed the key role of SiO_2 spheres in In-opal composites (with TiO_2 layers deposited on the inner surfaces of the voids) in controlling the magnetic hysteresis and

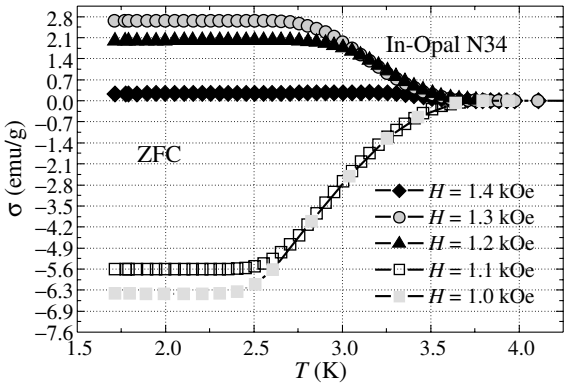

Fig. 4. Temperature dependencies of the magnetization in the sample No. 34, taken in different fields in ZFC regime.

flux capture processes inside the SC nanoparticle regular ensembles. The systems studied were characterized by the size of the nanoparticles being less than the London penetration depth and the magnetic vortices being unable to form in the grains via the regular Abrikosov mechanism. It was clearly demonstrated that the magnetic dynamics in such three-dimensional Josephson-junction arrays significantly differs from that characteristic of homogeneous superconductors.

Acknowledgements

Supports of the Russian Foundation for Basic Research (project No. 05-02-16975-a), the Presidium of the Russian Academy of Sciences, and the Foundation for Support of Leading Scientific Schools is gratefully acknowledged.

References

[1] A. V. Chernyaev, D. V. Shamshur, R. V. Parfeniev, A. V. Fokin and S. G. Romanov, *Proc. of 11th Int. Symp. "Nanostructures: Physics and Technology" (St Petersburg, 2003)*, 398 (2003).

[2] V. G. Balakirev, V. N. Bogomolov, V. V. Zhuravlev, Y. A. Kumzerov, V. P. Petranovskii, S. G. Romanov and L. A. Samoilovich, *Cryst. Rep.* **38**, 348 (1993).

[3] V. B. Aleskovskii, *Chemistry of the Solid State*, (Moscow: Vysshaya Shkola) 1978.

[4] D. V. Shamshur, A. V. Chernyaev, A. V. Fokin and S. G. Romanov, *Phys. Solid State* **47**, (2005).

[5] Z. Hao and J. R. Clem, *Phys. Rev. Lett.* **67**, 17 (1991).

[6] J. R. Clem and V. G. Kogan, *Jpn. J. Appl. Phys.* **26**, 1162 (1987).

14th Int. Symp. "Nanostructures: Physics and Technology"
St Petersburg, Russia, June 26–30, 2006

Nanomagnetism and nonlinear magneto-optics: magnetization-induced third-harmonic generation in Co nanostructures

O. A. Aktsipetrov[1], E. M. Kim[1], T. V. Murzina[1] and A. F. Kravets[2]

[1] Physics Department, Moscow State University, 119992 Moscow, Russia
[2] Institute of Magnetism, National Academy of Sciences of Ukraine, Kiev, 03680 Ukraine

Abstract. Magnetization-induced optical third-harmonic generation (MTHG) is observed in magnetic nanostructures: Co nanolayers and granular films containing Co nanoparticles. Magnetization-induced variations of the MTHG characteristics in these nanostructures exceed the typical values of linear magneto-optical Kerr effect by at least an order of magnitude. Correlation between the concentration dependencies of magnetic contrast of MTHG intensity and coefficient of giant magnetoresistance is observed in nanogranular films below the percolation threshold. This points out the obvious relations between nanomagnetism and nonlinear magneto-optical phenomena.

Introduction

Magneto-optics, with its more than century-long history, remains one of the most important experimental methods in studies of magnetism. Recently, significant attention has been directed exclusively towards nonlinear magneto-optics: first magnetization-induced second harmonic generation (MSHG) was observed experimentally in yttrium-iron garnet films [1], then at surfaces of magnetic metals [2], in magnetic multilayers [3] and nanogranules [4]. For the period of MSHG studies it was well recognized that MSHG is a powerful probe of surface and interface magnetism. These magnetization-induced effects in MSHG overshadowed third-order nonlinear magneto-optical effects because of their small expected value. Moreover, the pessimism in observation of the third-order magneto-optical effects increased when authors of [5] failed in observation of MTHG in thin magnetic films. Meanwhile, experimental extension of nonlinear magneto-optics from MSHG to the MTHG probe is desirable as can provide complementary information about magnetic contribution related to the bulk of nanostructures whereas MSHG probes the surface and interfacial contributions to nanomagntism.

In this paper, considerable magnetization-induced THG is experimentally observed in the magnetic nanostructures: Co nanolayers and granular films containing Co nanoparticles. The correlation between giant magnetoresistance and magnetization-induced THG is observed in magnetic nanogranular films.

1. Experimental

The samples of magnetic nanostructures studied in this work are: (1) magnetic nanogranular films of the composition Co_xAg_{1-x} and (2) thin homogeneous Co films. The Co_xAg_{1-x} films are prepared by the co-evaporation of Co and Ag from two electron-beam sources onto glass-ceramic substrates. The structure of Co_xAg_{1-x} films is characterized by X-ray diffraction and reveals the existence of nanogranules with the diameter ranging from 3 nm to 6 nm for the composition $x < 0.4$. The fabricated granular films exhibit giant magnetoresistance (GMR) effects that are characterized by the GMR coefficient: $\rho_{GMR} = -[R(0) - R(M)]/R(0)$, where $R(M)$ and $R(0)$ is Ohmic resistance measured in magnetized and demagnetized material. ρ_{GMR} is measured by the four-probe method at room temperature in a magnetic field up to 8 kOe. Homogeneous Co films 400 nm thick are deposited in similar conditions using a single Co source.

The output of an OPO laser system "Spectra-Physics MOPO 710" at 800 nm wavelength, pulse duration of 4 ns, pulse intensity of 2 MW/cm^2, and a Q-switched YAG:Nd^{3+} laser at 1064 nm wavelength, pulse duration of 15 ns and pulse intensity of 1 MW/cm^2 are used as the fundamental radiation. The THG radiation is filtered out by appropriate glass bandpass and is detected by a PMT and gated electronics. To normalize the THG signal over the OPO and YAG:Nd^{3+} laser fluency and the spectral sensitivity of the optical detection system, an independent reference arm is used with a Z-cut quartz plate as a reference and a detection system identical to that in the "sample" arm. The THG interferometry is performed by translating a 30 nm thick indium-tin-oxide (ITO) film on a glass substrate in the direction parallel to the laser beam. An in-plane dc-magnetic field up to 2 kOe is applied in nonlinear magneto-optical measurements at the magnetic samples by permanent Fe-Nd magnets.

2. Magnetization-induced third-harmonic generation

Figure 1 shows the THG interference patterns for Co film for the opposite directions of magnetization. These interference patterns demonstrate considerable magnetization-induced effect in THG intensity and the magnetization-induced phase shift of $\varphi_{3\omega}(M) = 70^\circ$ between optical fields of magnetic and

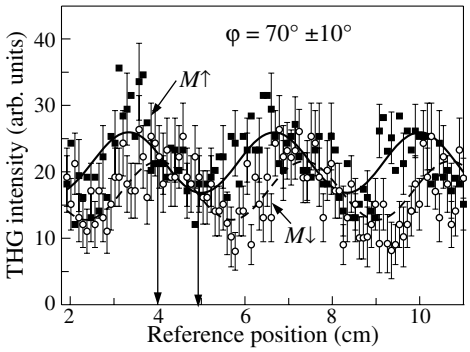

Fig. 1. The MTHG interferometry patterns in Co film for the opposite directions of the magnetization, $M \uparrow\downarrow$.

crystallographic (nonmagnetic) contributions. The MTHG interferometric measurements allow to get both relative contribution of MTHG in the total THG intensity, relative phase shift between magnetic and crystallographic THG fields and, as a consequence, a ratio of magnetic and crystallographic (nonmagnetic) third-order susceptibilities. Results of these complex measurements of the magnetic contrast in the THG intensity, the relative phase shift of magnetization-induced THG field and the ratio of the magnetic and crystallographic components of the third-order susceptibility are summarized in Table 1 for homogenous Co nanolayer and $Co_{0.31}Ag_{0.69}$ nanogranular film.

Table 1.

	$\rho_{3\omega}$	$\varphi_{3\omega}(M)$	$\chi_{\rm eff}^{(3){\rm odd}}(M)/\chi_{\rm eff}^{(3){\rm cryst}}$
Co	0.09 ± 0.03	$70^\circ \pm 10^\circ$	0.55 ± 0.1
$Co_{0.31}Ag_{0.69}$	0.09 ± 0.03	$17^\circ \pm 5^\circ$	0.16 ± 0.05

These magnetization-induced variations of the MTHG characteristics exceed the typical values of linear magneto-optical Kerr effect (MOKE) by more an order of magnitude.

3. Correlation between GMR and nonlinear magneto-optical Kerr effect

The observation of magnetization-induced effects in THG from Co_xAg_{1-x} nanogranular films allows one to perform a comparative analysis of MTHG and GMR effects. Figure 2 shows the dependence of $\rho_{3\omega}$ on the concentration of Co in Co_xAg_{1-x} films, which reveals a monotonic increase for $x > 0.4$ and a local maximum in the vicinity of $x \approx 0.3$. The monotonic increase corresponds to a straightforward monotonic enlargement of the ferromagnetic phase in the Co fraction of the composite material as the concentration of Co exceeds the percolation threshold. As a result of this general relation between Co concentration and magnetic contrast the latter is reduced in the granular materials relative to the continuous films. A local maximum corresponds to the specific magnetic properties of nanogranules: $\rho_{3\omega}(x)$ attains a local maximum at the same region of Co concentration (0.3–0.35) as the concentration dependence of $\rho_{\rm GMR}$. It is worth noting that correlation between

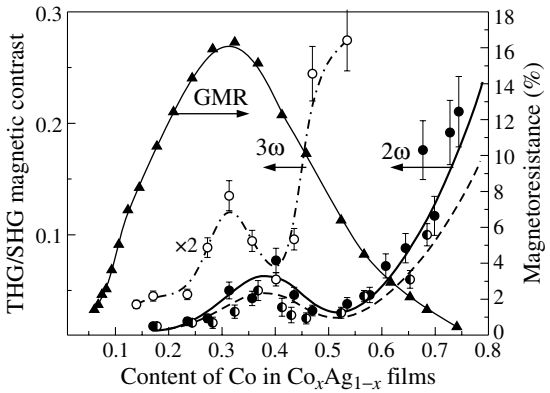

Fig. 2. Magnetic contrast of the THG intensity for Co_xAg_{1-x} nanogranular films at the fundamental wavelength of 1064 nm as a function of Co content x (shown with open circles). The SHG magnetic contrast at the fundamental wavelength of 1064 nm (closed circles), and 800 nm (half-closed circles), respectively. Magnetoresistance as a function of x in the Co_xAg_{1-x} films (triangles).

$\rho_{3\omega}(x)$ and $\rho_{\rm GMR}(x)$ is almost the same as for $\rho_{2\omega}(x)$ for the MSHG intensity as it is shown in Fig. 2 and is recently observed in [4]. GMR in Co_xAg_{1-x} nanogranular films is attributed to the spin-dependent electron scattering and is highly sensitive to the quality of nanoparticle structure and interface that can become apparent in correlations between GMR and both MSHG and MTHG.

In conclusion, magnetization-induced optical third-harmonic generation is observed in magnetic homogeneous Co nanolayers and magnetic films containing Co nanogranules. Magnetization-induced variations of the THG parameters exceed the typical values of the linear MOKE by at least an order of magnitude. Correlation between the dependencies of $\rho_{3\omega/2\omega}(x)$ and $\rho_{\rm GMR}(x)$ is observed below the percolation threshold in Co_xAg_{1-x} films, which reveals the spin-dependent *scattering* GMR mechanism. The general conclusion about correlation between MTHG and GMR in Co_xAg_{1-x} films demands further detailed studies.

References

[1] O. A. Aktsipetrov, O. V. Braginskii and D. A. Esikov, *Sov. J. Quantum Electron.* **20**, 259 (1990).
[2] J. Reif, J. C. Zink, C.-M. Schneider and J. Kirschner, *Phys. Rev. Lett.* **67**, 2878 (1991).
[3] B. Koopmans, M. G. Koerkamp, Th. Rasing and H. van den Berg, *Phys. Rev. Lett.* **74**, 3692 (1995).
[4] T. V. Murzina *et al*, *Surf. Sci.* **482–485**, 1101 (2001).
[5] V. V. Pavlov, R. V. Pisarev, M. Fiebig, D. Frohlich, *Physics of the Solid State* **45**, 630 (2003).

14th Int. Symp. "Nanostructures: Physics and Technology"
St Petersburg, Russia, June 26–30, 2006

Giant optical third-harmonic generation in Ag nanoparticles: nonlinear-optical spectroscopy of local fields in nanostructures

O. A. Aktsipetrov, E. M. Kim, S. S. Elovikov and T. V. Murzina
Physics Department, Moscow State University, 119992 Moscow, Russia

Abstract. Surface-enhanced optical third-harmonic generation (THG) is observed in silver island films. The THG intensity from Ag nanoparticles is enhanced by more than two orders of magnitude with respect to the THG intensity from a smooth and homogeneous silver surface. This enhancement is attributed to local plasmon excitation and plasmon resonance of the local field at the third-harmonic wavelength.

Introduction

Observation of surface-enhanced nonlinear optical effects in silver island films dates back to paper by Wokaun *et al* [1], where surface-enhanced optical second-harmonic generation (SHG) and surface-enhanced Raman scattering were observed in silver island films. The enhancement of the SHG intensity was attributed to the resonant enhancement of the local field at the SHG wavelength, mediated by the excitation of the local surface plasmons in silver nanoparticles.

According to this approach, the third-order nonlinear polarization of a rough metal surface or an array of small metal particles is given by: $P_{3\omega} = L_{3\omega}\chi^{(3)}(3\omega)L_{\omega}^{3}E_{\omega}^{3}$ at the third-harmonic generation (THG) wavelength, where $\chi^{(3)}(3\omega)$ is the third-order susceptibility of metal; E_{ω} is the optical field at fundamental wavelength; and L_{ω} and $L_{3\omega}$ are the local field factors at the corresponding wavelengths. The spectral dependence of the local field factor of an array of small metal spheroids embedded in a dielectric matrix within the simple approach in dipole and effective media approximations, is given by:

$$L(\lambda) = \frac{\varepsilon_{\mathrm{d}}(\lambda)}{\varepsilon_{\mathrm{d}}(\lambda) + [\varepsilon_{\mathrm{m}}(\lambda) - \varepsilon_{\mathrm{d}}(\lambda)]\,(N - q/3)}\,, \qquad (1)$$

where $\varepsilon_{\mathrm{d}}(\lambda)$ and $\varepsilon_{\mathrm{m}}(\lambda)$ are the dielectric constants of the dielectric matrix and of the metal, respectively; N is the shape-dependent depolarization factor of the spheroids; and q is the filling factor, i.e., the relative fraction of the metal in a composite material. The resonant wavelength of the local field factor, λ_{res}, corresponds to setting the real part of the denominator in Eq. 1 to zero:

$$\mathrm{Re}\,[\varepsilon_{\mathrm{d}}(\lambda_{\mathrm{res}}) + [\varepsilon_{\mathrm{m}}(\lambda_{\mathrm{res}}) - \varepsilon_{\mathrm{d}}(\lambda_{\mathrm{res}})]\,(N - q/3)] = 0\,.$$

For an isolated small Ag sphere in vacuum $\lambda_{\mathrm{res}} \approx 200$ nm. Three factors result in the red-shift of λ_{res} up to the visible range for an array of particles: (1) the distortion of the particle shape, (2) the dipole-dipole interaction between particles and (3) an increase in the dielectric constant of the matrix material. The resonant increase of the local field factor at λ_{res} results in a many-fold increase of the nonlinear-optical response from a nanoparticle array.

In this paper, surface-enhanced THG and third-order hyper-Rayleigh scattering is observed in Ag island films. The resonant plasmon mechanism of the THG enhancement is proved.

1. Experimental

The films were prepared by thermal evaporation of silver onto the substrates of silicon Si(001) wafers at a rate of 3–4 Å/s and residual pressure of 10^{-5} Torr. The silicon wafers were chosen as substrates because of, first, the flatness and homogeneity of the surface, and, second, the simplicity of the chemical etching procedure that is used for the preparation of a step-like SiO_2 wedge. Three types of Ag films are studied: Ag island film with a mass thickness of $d_{\mathrm{M}} \approx 1$ nm and expected plasmon resonance at $\lambda_{\mathrm{res}} \sim 355$ nm, Ag island film with plasmon resonance in the vicinity of $\lambda_{\mathrm{res}} \sim 270$ nm on the silicon oxide step-like wedge, and a thick homogeneous Ag reference film with a thickness of $d_{\mathrm{R}} \approx 40$ nm. The thick homogeneous Ag film is used as a reference source of non-enhanced bulk THG for the measurement of the THG enhancement from island films. An atomic force microscopy with a height resolution of 1 nm and lateral resolution of approximately 10 nm, shows that the average lateral size and height of silver nanoparticles is about 40 and 3 nm, respectively. The outputs of two laser systems are used as the fundamental radiation in the THG experiments: (1) an OPO laser system, "Spectra-Physics MOPO 710", with a wavelength which is tunable in the spectral range from 490 nm to 680 nm, a pulse duration of 4 ns, and a pulse intensity of 2 MW/cm^2; and (2) a Q-switched YAG:Nd^{3+} laser at a 1064 nm wavelength, a pulse duration of 15 ns, and a pulse intensity of about 1 MW/cm^2. The THG radiation is filtered out by appropriate UV and bandpass filters and detected by a PMT and gated electronics.

2. Surface-enhanced third-harmonic generation

The black circles in Fig. 1 show the azimuthal dependence of the THG intensity from the sample of Ag island film in the specular direction for the s-in, s-out combination of polarizations of the fundamental and TH waves. The anisotropic component of the THG signal is related to the nonlinear response of Si(001) substrate, whereas the isotropic THG is attributed to both Ag nanoparticles and Si substrate. To distinguish the THG contribution of Ag island film from that of the substrate, the azimuthal dependence of the THG intensity from Si(001) is measured in the same s-in, s-out geometry (open triangles in Fig. 1). The ratio of the anisotropic components of THG from silver island film on Si(001), $I_{\mathrm{IF+Si}}^{\mathrm{anis}}(3\omega)$, and silver-free Si(001) substrate, $I_{\mathrm{Si}}^{\mathrm{anis}}(3\omega)$, gives an attenuation coefficient of the THG response from substrate due to the absorption and scattering in the silver coverage: $\alpha_{3\omega} = I_{\mathrm{IF+Si}}^{\mathrm{anis}}(3\omega)/I_{\mathrm{Si}}^{\mathrm{anis}}(3\omega) = 0.46$. The estimation of the $\alpha_{3\omega}$ coefficient is the first step in the determination of the THG enhancement for Ag island films. The relative value of the THG intensity from Ag nanoparticles in the specular direction is $I_{\mathrm{IF}}^{\mathrm{spec}}(3\omega) = I_{\mathrm{IF+Si}}^{\mathrm{is}}(3\omega) - \alpha_{3\omega}I_{\mathrm{Si}}^{\mathrm{is}}(3\omega)$, where

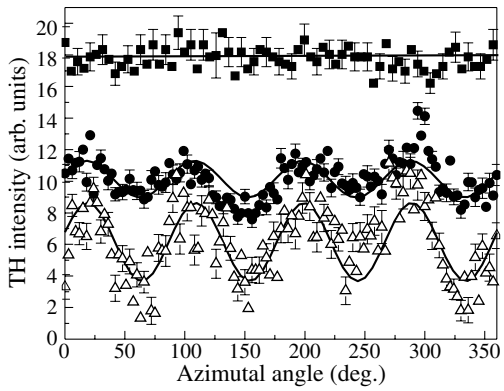

Fig. 1. The THG intensity as a function of the azimuthal angle from: (black circles) silver island film with $d_M \approx 1$ nm on Si(001) substrate, (open triangles) silver-free Si(001) substrate, (black squares) thick homogeneous reference Ag film with a thickness of $d_R \approx 40$ nm; the solid lines are results of approximations.

$I^{is}_{IF+Si}(3\omega)$ and $I^{is}_{Si}(3\omega)$ are the isotropic components of THG from the island film on Si(001) and from silver-free substrate, respectively. Obtaining the total intensity of the diffuse THG from Ag nanoparticles demands the measurement of the THG scattering pattern or depends of the THG intensity on the polar scattering angle. Inset in Fig. 2 shows the experimental scattering pattern of diffuse THG from silver island films where the angular width of the normalized form-factor is approximately $3^\circ \pm 0.5^\circ$. This sufficiently exceeds the angular width of $1^\circ \pm 0.5^\circ$ of the scattering pattern of linear Rayleigh scattering. The total intensity of the diffuse THG can be obtained by angular integration of the THG scattering pattern and in the case of the small angular width of $S_{3\omega}(\theta)$, is given by:

$$I_{IF}(3\omega) = I^{spec}_{IF}(3\omega)\left(\frac{1}{\Omega}\int\limits_{\Delta\theta} S_{3\omega}(\theta)d\theta\right)^2 \approx 0.6{\cdot}10^2 I^{spec}_{IF}(3\omega)\,,$$

where Ω is an angular aperture of the THG detection system and $\Delta\theta$ is the angular interval of integration. To estimate quantitatively the THG enhancement, we consider the total THG intensity of the specular THG from a model homogeneous film with an equivalent thickness of $d_H = 1$ nm and compare this with the THG intensity from a thick homogeneous reference film with a thickness of $d_R \approx 40$ nm. The THG intensity detected from the reference film comes from the Ag layer corresponding to the escape depth L_{Esc} of the THG wave (black squares in Fig. 1). In our experimental conditions, $L_{Esc} \sim 7$ nm for $\lambda_{3\omega} = 355$ nm. Thus, the enhancement of the THG intensity from Ag island film with respect to a thick homogeneous Ag film is given by:

$$G = \frac{I_{IF}(3\omega)}{I_{HF}(3\omega)} \approx \frac{I_{IF}(3\omega)}{I_{Ref}(3\omega)}\left[\frac{L_{Esc}}{d_H}\right]^2 \approx 1.2\cdot 10^2\,, \qquad (2)$$

where $I_{HF}(3\omega)$ and $I_{Ref}(3\omega)$ are the THG intensity from the model homogeneous film with the thickness of $d_H \equiv d_M$ and thick homogeneous reference Ag film, respectively.

3. Spectroscopy of third-harmonic generation: local plasmon mechanism of enhancement

The main panel in Fig. 2 shows a set of THG spectra for d_{ox} increasing in the range from 2 nm to 100 nm. The observed

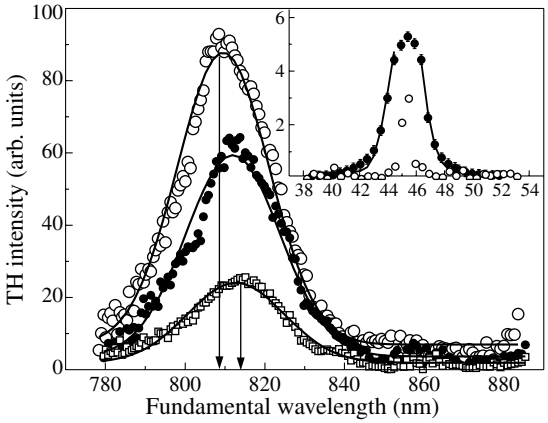

Fig. 2. Main panel: dependencies of the THG intensity on the fundamental wavelength for Ag island films deposited on the SiO_2 step-like wedge for $d_{ox} = 2$ nm (open squares), 70 nm (black circles) and 100 nm (open circles). Inset: THG scattering pattern, the THG intensity from the island film as a function of polar scattering angle (angular width is $3^\circ \pm 0.5^\circ$) and the linear Rayleigh scattering pattern with angular width of $1^\circ \pm 0.5^\circ$.

effects of d_{ox} on the THG spectra as SiO_2 thickness increases from 2 nm to 100 nm is two-fold: (1) an apparent blue-shift of approximately 6 nm of the THG resonance and, (2) a more than four-fold increase of the THG resonant intensity. These changes correspond to the decrease of the effective dielectric constant of Ag islands situated at different steps of the SiO_2 wedge. The impact of the dielectric constant of the substrate on the resonant properties of surface-enhanced THG proves the plasmon-assisted mechanism of the enhancement.

Normalized form-factors of scattering pattern at the THG wavelengths is given by:

$$S_{3\omega}(\theta) \sim \exp\left[-M_{3\omega}k^2_{3\omega}l^2_{cor}(3\omega)\right]\,, \qquad (3)$$

where $l_{cor}(3\omega)$ is the correlation length at the THG wavelength, $k_{3\omega} = 2\pi(\sin\theta - \sin\theta_0)/\lambda_{3\omega}$ and $M_{3\omega}$ is an adjustable parameter at the THG wavelength, respectively; and θ_0 is the angle of incidence. The approximation of the diffuse THG scattering patterns (inset in Fig. 2, solid line) corresponds to the correlation lengths of $l_{cor}(3\omega) \approx 42$ nm. This probably corresponds to the average Ag particle size of 40 nm obtained from the AFM measurements.

In conclusion, surface-enhanced THG is observed in Ag island films with an enhancement of $1.2{\cdot}10^2$, which is attributed to the local surface plasmon excitation in Ag nanoparticles at the THG wavelength.

References

[1] A. Wokaun, J. G. Bergman, J. P. Heritage, A. M. Glass, P. F. Liao and D. H. Olson, *Phys. Rev. B* **24**, 849 (1981).

14th Int. Symp. "Nanostructures: Physics and Technology"
St Petersburg, Russia, June 26–30, 2006

Effect of increase of conductivity in nanometer island metallic films under the influence of weak electric field

A. P. Boltaev and F. A. Pudonin
P. N. Lebedev Physical Institute, RAS, 119991 Moscow, Russia

Abstract. The variation of differential conductivity in island Ti-films were studied.

A study of the conductivity of ultrathin Ti films in weak electric fields is presented here. Thin Ti films were grown by RF sputtering onto glassceramic substrates; a thin dielectric layer (Al_2O_3, $d = 8$ Å) was sputtered on top of each metallic film as a protective layer. The electric-field dependences of the specific surface conductivity at $T = 77$ K and $T = 300$ K were measured for three samples of this type, differing by the thickness of the Ti film ($d = 7$, 8.7, and 11 Å). In addition, the surface morphology of the structures was investigated by atomic-force microscopy. AFM experiments show that Ti films with $d \sim 7$ Å consist of islands with dimensions of $\sim 150-300$ Å. The distance between the islands is 15–100 Å. As the film thickness increases, the island size grows and the distance between them decreases.

In Fig. 1, the relative change of the conductivity of these three films (d = (1) 7, (2) 8,7 and (3) 11 Å) is plotted as a function of the applied electric field (F). The specific conductivity at $F = 0$ was $\sigma_1 = 7.5 \cdot 10^{-8}\ \Omega^{-1}$ for sample 1, $\sigma_2 = 8.2 \cdot 10^{-6}\ \Omega^{-1}$ for sample 2, and $\sigma_3 = 9.3 \cdot 10^{-5}\ \Omega^{-1}$ for sample 3. The dependences of relative change of specific surface differential conductivity for titanium films in depend on applied electric field and measured at temperature $T = 77$ (curve a) and 300 K (curve b) are presented on Fig. 2 for structures with thickness $d = 7$ Å.

One can see from Fig. 1, that considerable changes and complex behavior of σ are observed for thinner sample, which has lower conductivity (sample 1). Thus, a steep rise of σ in electric fields up to 20 V/cm is observed in Ti films with $d = 7$ Å and 8,7 Å; for $F > 20$ V/cm, σ increases linearly with the field. The conductivity of the Ti film with $d = 11$ Å has linear character at $F > 5$ V/cm.

The shape of the electric-field dependences of $\Delta\sigma$ in the structures under study can be explained in the framework of the well-known mechanism of the current flow in island and granular films [1, 2]. The current flow in the island films is related with two processes. First, thermodynamic equilibrium is established in the system via electron tunneling between the islands. As a result, a number of positively and negatively charged islands appear (due to electron tunneling from one initially neutral island to another) in addition to neutral islands. As an electron passes from one neutral island to another, the energy of the system changes by $E \sim e^2/\varepsilon R$ (R is the island size and ε is the permittivity). The number of such islands $N_{+-} \sim T\exp(-E/kT)$ for $E \gg kT$. Second, formation of charged islands results in the possibility of the current flow via tunneling of electrons between charged and neutral islands, which does not require considerable energy changes. Indeed, in such tunneling process the energy can be changed by $\Delta E \sim e^2/\varepsilon(1/R_1 - 1/R_2)$ (where R_1 and R_2 are the sizes of the two islands), if the islands have different dimensions. The probability of such transition $W \sim T\exp(-\Delta E/kT)$ for $\Delta E \gg kT$; note that $E \gg \Delta E$. Ultimately, the conductivity of a such metallic structure $\sigma \sim N_{+-}W \sim \exp(-E/kT) \cdot \exp(-\Delta E/kT)$ [2].

Apparently, the variation of σ with the electric field orig-

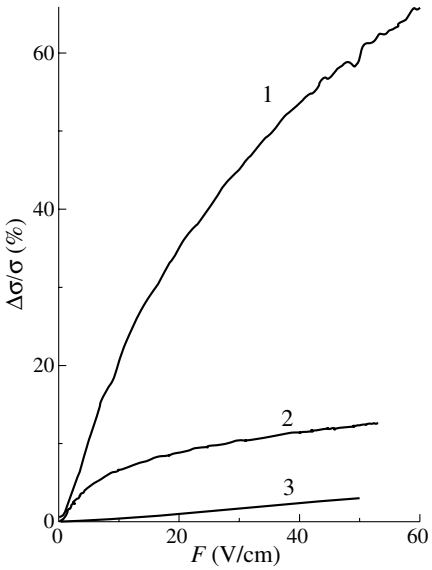

Fig. 1. Dependence of relative change of specific surface conductivity of Ti — films on electric field (1 — $d = 7$ Å; 2 — 8.7 Å; 3 — 11 Å).

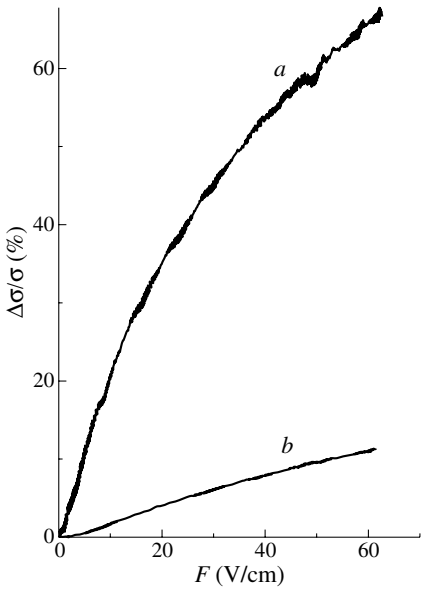

Fig. 2. Dependence of relative change of specific surface conductivity of Ti — films on electric field ($d = 7$ Å; a — $T = 77$ K, b — $T = 300$ K).

inates from the fact that, upon electron transitions between the islands, the energy of the system changes (a) by the value eU (where U is the potential difference between positive and negative islands) in the case of tunneling from one neutral island to another and (b) by the value eU_1 (where U_1 is the potential difference between charged and neutral islands) in the case of transitions between charged and neutral islands. Since $E \gg \Delta E$, the increase of σ in the low-field region is determined by the increase in the transition probability of electron tunneling between charged and neutral islands; this probability finally approaches some saturation value when $U_1 \approx \Delta E/e$. When the potential difference between the islands becomes still higher, the only effect is an increase in the number of positively and negatively charged islands; it is this process that determines the increase of the film conductivity in this regime. As the film thickness increases, the energy ΔE is reduced due to the growth of the island size. When the island size becomes sufficiently large, the energy $\Delta E \ll kT$; therefore, the contribution to $\Delta\sigma$ related to the variation of the probability of electron transition between charged and neutral islands with the electric field disappears. Really, the dependence of conductivity for film with thickness $d = 7$ Å at temperature $T = 77$ K on electric field has difficult character as follow from Fig. 2. As mention above, in this case the growth of film conductivity at increasing of electric fields determine by increasing of charged island number and increasing of probability of electron tunneling between charged and neutral islands in electric field direction. When the relation $\Delta E/kT$ decrease approximately in four times at temperature $T = 300$ K, the contribution in growth of conductivity at increase of electric field from probability of electron tunneling between charged and neutral islands is decreased as can see from approximately linear dependence of film conductivity (Fig. 2, curve b).

Acknowledgements

This study was supported by the Russian Foundation for Basic Research, Program in Support of Leading Scientific Schools, and Scientific Program "Physics of the Solid-State Nanostructures".

References

[1] H. R. Zeller and I. Giaever, *Phys. Rev.* **181**, 789 (1969).
[2] A. P. Boltaev *et al*, *JETP* **99**, 827 (2004).

14th Int. Symp. "Nanostructures: Physics and Technology"
St Petersburg, Russia, June 26–30, 2006

Ferromagnetic clusters and transport in Mn and Mg co-implanted GaAs

V. A. Kulbachinskii[1], P. S. Gurin[1], R. A. Lunin[1], Yu. A. Danilov[2], E. I. Malysheva[2], Y. Horikoshi[3] and K. Onomitsu[3]

[1] M. V. Lomonosov Moscow State University, Low Temperature Physics Dept, 119992, GSP-2, Moscow, Russia
[2] Physico-Technical Research Institute, University of Nizhny Novgorod, 603950, Nizhny Novgorod, Russia
[3] School of science and engineering, Waseda university, 3-4-1, Okubo, Shinjuku-ku, Tokyo 169-8555, Japan

Abstract. Ferromagnetic clusters were incorporated into GaAs samples by Mn implantation and subsequent annealing. Additional Mg implantation was used to provide the enhancement of p-type doping in GaAs:Mn layer. We characterized the samples with SQUID magnetometry and magnetotransport measurements in the temperature interval 4.2 K $< T <$ 400 K. Magnetization measurements reveal ferromagnetism up to 400 K (limited by the experimental setup). The anomalous Hall effect elucidates the interaction the Mn spins and the itinerant holes. Negative magnetoresistance was observed at low temperatures which changes to enchanced positive magnetoresistance effect at higher temperature.

Introduction

Mn-doped GaAs is an attractive diluted magnetic semiconductor (DMS) for a new spin-based electronics. It has been shown that the Curie temperature (T_c) in $Ga_{1-x}Mn_xAs$ can be raised by increasing the hole concentration as well as Mn concentration [1]. Although Mn acts as an acceptor in GaAs, the hole activation ratio is much less than unity and the hole concentration tends to saturate due to the compensation of Mn acceptors by the defects [2, 3]. Therefore, some additional doping of acceptor impurity is needed to achieve a high hole concentration. It has been theoretically shown that the formation of Mn interstitials and Mn-related clusters are enhanced with increasing the hole concentration due to the Fermi energy effect [4]. A significant reduction of Mn interstitials is achieved by the spatially separated doping of Mn and Be in GaAs applying the migration-enchanced epitaxy (MEE) method [5, 6]. The other method is the molecular beam epitaxy (MBE) growth of the GaAs based heterostructures followed by low-temperature annealing. Such procedure leads to the value of $T_c = 250$ K [7].

Ion implantation of Mn is also one of methods to fabricate samples with carrier-mediated ferromagnetism. This method was used to produce ferromagnetic hole-doped (Ga,Mn)As [8–10].

In the present study we investigated the influence of Mn and Mg ion implantation accompined by rapid thermal annealing on magnetic and galvanomagnetic properties of p-GaAs.

1. Samples and experimental

Investigated structures were fabricated on semi-insulating GaAs (100) substrate by ion implantation by Mn+ with the energy of 100 keV and dose of 10^{16} cm^{-2}. To stimulate an enhancement of hole concentration in implanted layers, additional acceptor doping by Mg^+ ion implantation was performed. The energy of Mg^+ ions (45 keV) was selected for coincidence of peaks for Mg^+ and Mn^+ ion distributions. Dose of Mg^+ ion implantation was varied from 1×10^{14} to 1×10^{15} cm^{-2}. Thus p-type conductivity layer in GaAs was formed by double implantation. All implantations were performed in conditions to avoid a canalization of incident ions. The implanted samples were submitted to rapid (10 s) thermal annealing (RTA). Temperature T_a of RTA was varied in the range from 700 to 800 °C. Some parameters of samples are listed in Table 1. Annealing forms in the samples clusters of solid solution $Ga_{1-x}Mn_xAs$ and MnAs [8–10]. Surface mor-

Table 1. Mg dose, annealing temperature T_a and sheet resistivity ρ.

Sample	Mg ion dose (10^{14}/cm^2)	T_a (°C)	ρ (kΩ/□) T=300 K	T=77 K	T=4.2 K
#3	3	800	1.27	9.1	—
#4	10	700	5.07	29.5	—
#5	10	725	2.90	8.7	—
#6	10	750	2.38	20.5	29.5

phology (AFM) and magnetic imaging (MFM) of implanted and annealed samples were investigated at room temperature by microscope "Solver Pro", fabricated by NT-MDT company (Zelenograd, Russia). According to AFM, clusters with height up to 50 nm and diameter up to 300 nm are visible on the surface. Some of them reveal magnetic contrast, principally, of single-domain type. For measurements of the magnetization in the temperature interval 4.2–400 K in magnetic fields up to 7 T, a SQUID magnetometer Quantum Design Co. Ltd. MPMS-7 was used. The measurements were perfomed by applying the magnetic field parallel to the surface of samples. Temperature dependences of resistance have been measured in the temperature range $4.2 \le T \le 300$ K. Magnetoresistance and Hall effect have been measured by a conventional four probe technique in the temperature range $4.2 \le T \le 300$ K in magnetic field B up to 6 T applied perpendicular to the sample surface.

2. Results and discussion

All samples had p-type conductivity. When temperature decreased resistivity ρ of Mn and Mg co-implanted samples increased. In the temperature range between 50 and 110 K a kink is visible in $\rho(T)$, which is a characteristic of the ferromagnetic transition [11]. At $T < T_c$ the spin flip scattering disappears [12], mobility increases and resistance decreases. This effect results in a kink for an activation type of the experimental dependence of $\rho(T)$ as we have observed. All samples showed ferromagnetism, as indicated by hysteresis loop in the magnetization (all samples studied showed qualitatively similar magnetic behavior). The hysteresis loops show clear temperature dependence over the entire range of temperatures studied, as

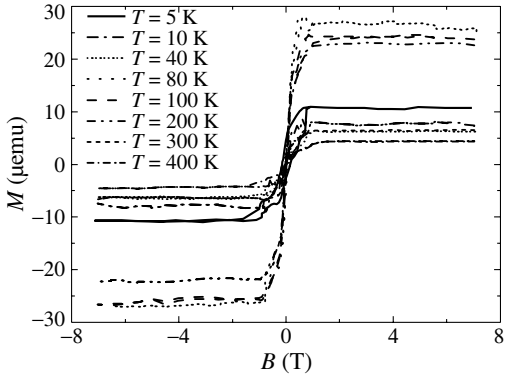

Fig. 1. Magnetization loops at different temperatures for sample 5 (diamagnetic background was subtracted).

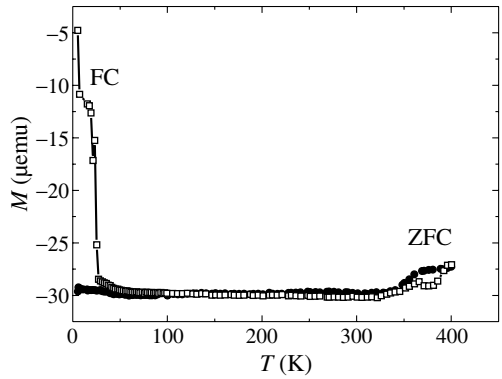

Fig. 2. Zero field cooling (ZFC) and field cooling (FC) data for sample 6.

can be seen in Fig. 1. The coercive field at $T = 400$ K is nearly identical to that at $T = 40$ K. In Fig. 2 we plot ZFC and FC data for one of the sample. Due to diamagnetic matrix the value of M is negative. As it is seen in Fig. 1 and Fig. 2 there are at least two different magnetic phases in the samples, one with T_c about 50 K and second with T_c above room temperature. The first value of T_c is very typical for hole mediated ferromagnetism in $Ga_{1-x}Mn_xAs$ solid solutions and the second one is due to formation of MnAs clusters. The Curie temperature for bulk MnAs is about 310–320 K. The enhancement of T_c in the Mn containing layer may be due to quasi-2D character of MnAs clusters, their size and stehiometry as it was observed in digital alloys GaSb/Mn [13].

One of the methods to detect the spin-polarized carriers is the anomalous Hall effect. The anomalous Hall effect is measurable up to 195 K and shows the hole-mediated ferromagnetism of $Ga_{1-x}Mn_xAs$ solid solution formed after Mn implantation and rapid thermal annealing. Above this temperature, ferromagnetism survives due to the MnAs clusters. The interaction between these clusters and holes in the semiconducting matrix should be very small because of the Schottky barriers at the boundaries.

The magnetoresistance shown in Fig. 3 for one of the samples changes from negative to positive with increasing temperature near $T = 35$ K. The high value of positive magnetoresistance can be explained by the enhanced geometric magnetoresistance effect in inhomogeneous semiconductors [14].

Thus the ferromagnetic clusters were embedded into GaAs by Mn ion implantation and rapid thermal annealing. A detailed theoretical study is needed to fully understand the mechanisms involved to the observed ferromagnetism at higher temperature.

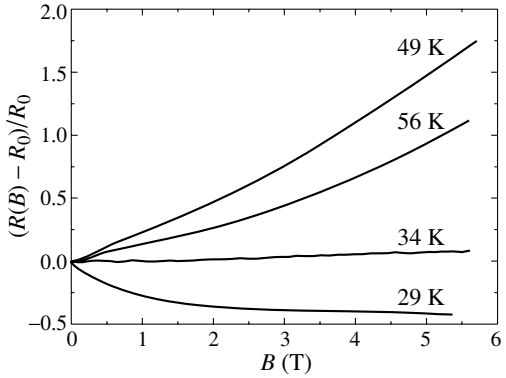

Fig. 3. Relative magnetoresistance of sample 3 at different temperatures.

Acknowledgements

The work was supported by RFBR, grants 05.02.17029a and 05-02-16624.

References

[1] T. Dietl, H. Ohno *et al*, *Science* **287**, 1019 (2000).
[2] H. Shimizu, T. Hayashi, T. Nishinaga, M. Tanaka, *Appl. Phys. Lett.* **74**, 398 (1999).
[3] P. A. Korzhavyi, I. A. Abrikosov, E. A. Smirnova *et al*, *Phys. Rev. Lett.* **88**, 187202 (2002).
[4] P. Manadevan, A. Zunger, *Phys. Rev. B* **68**, 075202 (2003).
[5] K. Onomitsu, H. Fukui, T. Maeda, Y. Hirayama, Y. Horikoshi, *J. Cryst. Growth* **278**, 699 (2005).
[6] K. Onomitsu, H. Fukui, T. Maeda, Y. Hirayama, Y. Horikoshi, *J. Vac. Sci. Technol. B* **22**(4), 1746 (2004).
[7] A. M. Nazmul, T. Amemiya, Y. Shuto, S. Sugahara and M. Tanaka, *Phys. Rev. Lett.* **95**, 017201 (2005).
[8] O. D. D. Couto, M. J. S. P. Brasil, F. Iikawa *et al*, *Apll. Phys. Lett.* **86**, 071906 (2005).
[9] C. Chen, M. Cai, X. Wang, S. Xu, M. Zhang, X. Ding and Y. Sun, *J. Appl. Phys.* **87**, 5636 (2000).
[10] Y. Shon, Y. S. Park, K. J. Chung *et al*, *J. Appl. Phys.* **96**, 7022 (2004).
[11] F. Matsukura, H. Ohno, A. Shen and Y. Sugawara, *Phys. Rev. B* **57**, R2037 (1998).
[12] M. N. Baibich, J. M. Broto, A. Fert *et al*, *Phys. Rev. Lett.* **61**, 2472 (1988).
[13] X. Chen, M. Na, M. Cheon *et al*, *Appl. Phys. Lett.* **81**, 511 (2002).
[14] Sh. U. Yuldashev, Y. Shon *et al*, *J. Appl. Phys.* **90**, 3004 (2001).

14th Int. Symp. "Nanostructures: Physics and Technology"
St Petersburg, Russia, June 26–30, 2006

Current driven magnetization switching and resistance hysteresis in ferromagnetic nanojunctions

E. M. Epshtein, Yu. V. Gulyaev and *P. E. Zilberman*
Institute of Radio Engineering and Electronics of the Russian Academy of Sciences,
Fryazino, Moscow District, 141190, Russia

Abstract. Current flowing through a spin-valve type magnetic nanojunction is considered. Two current-induced effects take into account, namely, the longitudinal spin injection and transverse spin-transfer torque. It is shown that the prevailing mechanism is determined by lattice magnetization viscosity constant. Switching between parallel and antiparallel configurations under current cycling leads to hysteretic behavior of the junction resistance. The hysteresis is possible only in presence of spin injection.

Introduction

The current driven exchange switching effect in magnetic junctions attracts great attention of theorists and experimentalists since it was predicted in [1, 2]. Switching from high resistive antiparallel configuration of the magnetic layers to low resistive parallel one occurs when the current density through the junction exceeds certain threshold value. The switched junction remains in the parallel state under current lowering below the threshold value. Switching to the initial antiparallel state occurs, when the current density reaches certain negative value, so that the back current switching takes place. Therefore, a hysteresis appears under current cycling. Such a hysteresis has been observed repeatedly in experiments (see [3, 4], for example).

Theoretical study of the switching effect was carried out, usually, in scope of the spin-transfer torque approach. It was considered, that this mechanism was able to describe the hysteresis effect. Meanwhile, there is another mechanism of current effect on the magnetic junction state, namely, the nonequilibrium longitudinal spin injection [5]. In general, both mechanisms coexist and can dominate each other depending on the experimental conditions [6]. As to the back current switching and subsequent hysteresis effect, it will be shown here for the first time that only the spin injection causes these effects.

1. Model, equations, and boundary conditions

We consider a spin-valve type magnetic junction, containing a ferromagnetic layer **1** with pinned lattice magnetization, free ferromagnetic layer **2** and nonmagnetic contact layer **3**. A very thin spacer is placed between layers **1** and **2** to prevent direct exchange interaction between the layers. The current flows perpendicular to the layers (CPP mode).

The equations used include Landau–Lifshitz–Gilbert (LLG) equations for the free layer **2** lattice magnetization vector $\mathbf{M_2}$ and continuity equations for mobile electron magnetization vectors $\mathbf{m}_1, \mathbf{m}_2, \mathbf{m}_3$ of the corresponding layers. External magnetic field, anisotropy field, demagnetization field and *sd* exchange between the mobile electron and lattice magnetizations are taken into account. We assume that the external magnetic field is less than the anisotropy field, and the latter is much less than the demagnetization field. The initial orientation of $\mathbf{M}_2$ vector is assumed to be parallel to the external magnetic field, while the layer **1** magnetization $\mathbf{M}_1$ is antiparallel to it.

The boundary conditions at the layer interfaces include continuity conditions for total magnetization flux and spin-polarized electron chemical potentials. It is shown that the current can be excluded from LLG equations and taken into account in the boundary conditions only. Two mechanisms mentioned play different role in the boundary conditions. The spin injection and spin-transfer torque mechanisms are determined by the longitudinal and transverse (with respect to the collector layer lattice magnetization vector) electron spin current components, respectively. The spin injection produces nonequilibrium spin-state populations near the interfaces and thereby modifies the electron *sd* exchange interaction with the lattice, while the spin torque transfers to the lattice within a very small ($\sim \lambda_F$, the Fermi wavelength) distance from the boundary. When the current flows from the pinned layer to the free one (forward direction, **1** $\rightarrow$ **2**), both mechanisms act simultaneously. On the other hand, spin-transfer torque mechanism does not work under the back current direction (from the free layer to the pinned one, **2** $\rightarrow$ **1**), because the transferred transverse magnetization flux is lost in the pinned lattice.

2. Instability conditions and hysteresis

Using the equations of motion and boundary conditions mentioned, the spectrum and damping have been found for the magnetization fluctuations in the free layer **2**. We consider antiparallel and parallel magnetizations of layers **1** and **2** (upper and lower signs in Eq. (1)), the current being in **1** $\rightarrow$ **2** direction. In the case of thin layer **2**, so that its thickness L is small compared to the longitudinal spin diffusion length l, the fluctuation spectrum is described by the following expression:

$$\frac{\omega}{\omega_0}=\sqrt{\left[\left(1\pm\frac{h}{h_a}\right)-\frac{|j|}{j_0}\right]-\left(\frac{\kappa_0}{2\sqrt{h_a}}\right)^2\left(\frac{\kappa}{\kappa_0}\mp\frac{j}{j_0}\right)^2} -i\left(\frac{\kappa_0}{2\sqrt{h_a}}\right)\left(\frac{\kappa}{\kappa_0}\mp\frac{j}{j_0}\right). \quad (1)$$

Here ω is fluctuation frequency, ω_0 is spin wave frequency in absence of the current and external magnetic field, $h_a = H_a/4\pi M_2$, H_a is anisotropy field, M_2 is saturation magnetization, j is current density through the junction, κ is dimensionless damping (viscosity) constant in LLG equation,

$$\kappa_0 = \frac{2h_a\nu}{\alpha\gamma M_2\tau\lambda}, \quad j_0 = \frac{4\pi e M_2 h_a l\nu}{\alpha\mu_B Q_1\tau},$$

α is dimensionless *sd* exchange constant, γ is gyromagnetic ratio, τ is longitudinal spin relaxation time, $\lambda = L/l$, ν is

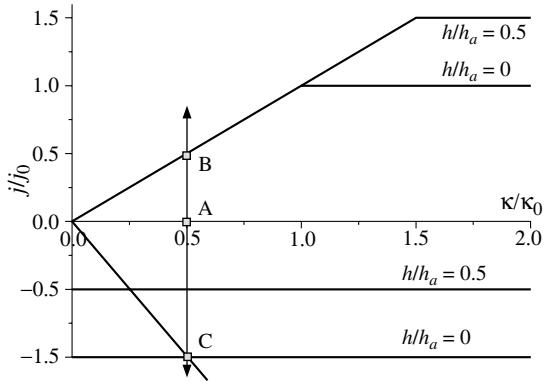

Fig. 1. Threshold current density as a function of the damping constant under forward and back current conditions. The arrows correspond to current cycling.

matching parameter between the layers **2** and **3**, μ_B is Bohr magneton, Q_1 is conductivity polarization degree in layer **1**.

The fluctuations become unstable under $\mathrm{Im}\omega > 0$ condition. The threshold current density j_{th} is determined by

$$\frac{j_{th}}{j_0} = \frac{\kappa}{\kappa_0} \quad \text{at} \quad \frac{\kappa}{\kappa_0} < 1 \pm \frac{h}{h_a} \tag{2}$$

and

$$\frac{j_{th}}{j_0} = 1 \pm \frac{h}{h_a} \quad \text{at} \quad \frac{\kappa}{\kappa_0} > 1 \pm \frac{h}{h_a}\,. \tag{3}$$

At low damping (see Eq. (2)), the threshold current density is proportional to the damping constant and does not depend on the external magnetic field. This case corresponds to the spin-transfer torque mechanism. On the contrary, at high damping (Eq. (3)) the threshold depends on the magnetic field and does not depend on the damping constant. In this range the spin-injection mechanism dominates. The parameter κ_0 has a meaning of a characteristic damping constant that determines the instability mechanism. At typical parameter values ($\alpha \sim 2\times10^4$, $\lambda \sim 0.1$, $h_a \sim 0.1$, $\nu \sim 1$, $\gamma M \sim 10^{10}$ c^{-1}, $\tau \sim 3\times10^{-13}$ c) we have $\kappa_0 \sim 3\times10^{-2}$. The aforementioned parameter j_0 has a clear sense also: it is the threshold current density in absence of external magnetic field and spin-transfer torque mechanism. At parameter values cited, $j_0 \sim 10^7$ A/cm^2.

The imaginary part of the fluctuation frequency becomes negative at all values of the current density. Therefore, a parallel state remains stable under the any current in forward direction. In particular, the switching of initially antiparallel state to parallel one remains stable too.

There is a specific situation under the back current (**2** → **1**). Only the longitudinal (with respect to $\mathbf{M}_2$ vector) electron spin current exists in layer **2**. The spin current passed to layer **1** has both longitudinal and transverse components with respect to $\mathbf{M}_1$ vector. The first creates nonequilibrium spin-state population in that layer, while the second transfers to the lattice and is lost there because of its pinning. As to the lattice magnetization flux from layer **2**, it vanishes at the interface, because the spacer is not transparent to the lattice magnetization flux. As a result, only the injection mechanism works under back current flowing. The threshold current density as a function of the damping constant under forward and back current conditions is shown in Fig. 1.

Note, the two mechanisms that are spin-transfer torque and spin-injection field, should be considered together. Spin injection creates spatial nonuniformity in the layer **2** near the interface. This nonuniformity turns on the spin-transfer mechanism of switching. To consider the switched parallel state behavior under back current, the following modifications in aforementioned formulae should be done. First, only the injection mechanism is to be considered. This corresponds to a limit $\kappa_0 \to 0$. Second, the current density sign is to inverted in Eq. (1). Finally, the sign of the external magnetic field (h) should be inverted too, because the vector $\mathbf{M}_2$ becomes antiparallel to the field in the switched state. As a result, the switched parallel state appears to become unstable under back current conditions at the current density

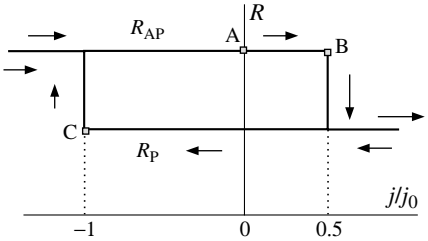

Fig. 2. Resistance hysteresis. R_{AP} and R_P are the junction resistances in antiparallel and parallel states, respectively. The arrows indicate the current change directions. The marked points A, B, C correspond to the points of the same name in Fig. 1.

$$|j| > j_0 \frac{\kappa}{\kappa_0}\,. \tag{4}$$

As to the antiparallel state, it remains stable at back current densities. Hence the back switching remains stable as well. Thus, the hysteresis behavior takes place under current cycling, because of different junction resistance in initial and switched states (Fig. 2). Note one more, that such a behavior would be impossible if only the spin-transfer torque mechanism (without injection) is present.

Acknowledgements

The work was supported by RFBR (Grant No. 06-02-16197).

References

[1] J. C. Slonczewski, *J. Magn. Magn. Mater.* **159**, L1 (1996).
[2] L. Berger, *Phys. Rev. B* **54**, 9353 (1996).
[3] T. Y. Chen, Y. Ji and C. L. Chien, *Appl. Phys. Lett.* **84**, 380 (2004).
[4] Y. Huai, F. Albert, P. Nguyen, M. Pakala and T. Valet, *Appl. Phys. Lett.* **84**, 3118 (2004).
[5] Yu. V. Gulyaev, P. E. Zilberman, E. M. Epshtein and R. J. Elliott, *JETP Lett.* **76**, 155 (2002).
[6] Yu. V. Gulyaev, P. E. Zilberman, E. M. Epshtein and R. J. Elliott, *JETP* **100**, 1005 (2005).

14th Int. Symp. "Nanostructures: Physics and Technology"
St Petersburg, Russia, June 26–30, 2006

Detection and emission of terahertz radiation by nanometer-size InGaAs and GaN field-effect-transistors

D. B. Veksler[1], A. El Fatimy[2], N. Dyakonova[2], F. Teppe[2], W. Knap[2], N. Pala[1,3], S. Rumyantsev[1,4], M. S. Shur[1], D. Seliuta[5], G. Valusis[5], S. Bollaert[6], A. Shchepetov[6], Y. Roelens[6], C. Gaquiere[6], D. Theron[6] and A. Cappy[6]

[1] Rensselaer Polytechnic Institute, Troy, 12180 New York, USA
[2] GES CNRS-Universite Montpellier 2 UMR 5650 34900 Montpellier, France
[3] Sensor Electronic Technology, Inc. Columbia, South Carolina 29209, USA
[4] Ioffe Physico-Technical Institute, St Petersburg, Russia
[5] Semiconductor Physics Institute, A. Gostauto Street 11, LT-01108 Vilnius, Lithuania
[6] Institut d'Electronique et de Microélectronique du Nord, UMR CNRS, 59652 Villeneuve d'Acsq, France

Abstract. Current flowing through a spin-valve type magnetic nanojunction is considered. Two current-induced effects take into account, namely, the longitudinal spin injection and transverse spin-transfer torque. It is shown that the prevailing mechanism is determined by lattice magnetization viscosity constant. Switching between parallel and antiparallel configurations under current cycling leads to hysteretic behavior of the junction resistance. The hysteresis is possible only in presence of spin injection.

Introduction

The terahertz (THz) range of frequencies is often referred to as the "terahertz gap", since it lies in between the frequency ranges of electronic and photonic devices and it is difficult to achieve from both sides. Therefore, the development of the THz emitters and detectors is of the high importance. Dyakonov and Shur, proposed to use the nonlinear properties of plasma excitations in a 2D gated electron gas for terahertz detectors, mixers, and THz radiation sources [1, 2]. A short FET channel of a given length, L, acts as a resonant "cavity" for the plasma waves with the eigen frequencies given by $\omega_N = \omega_0(1+2N)$, where $N = 1, 2, \ldots$ and the fundamental plasma frequency $\omega_0 = \pi/2L\sqrt{e(U_{\rm gs} - U_{\rm th})/m}$ can be easily tuned by changing the gate voltage, $U_{\rm gs}$. Here $U_{\rm th}$ is the threshold voltage, e is the electronic charge and m is the electron effective mass.

The basic idea of detection can be formulated as follows: An electromagnetic radiation with the frequency ω excites plasma waves in the channel. The nonlinear properties of such waves and asymmetric boundary conditions at source and drain lead to the radiation-induced constant voltage drop along the channel ΔU [1, 2], which is the detector response. When $\omega_0\tau \ll 1$, (τ is the momentum relaxation time), the detector response is a smooth function of radiation frequency and the gate voltage (broadband detector). When $\omega_0\tau \gg 1$, the FET can operate as a resonant detector. For submicron gate lengths, the resonant detection frequency $f = \omega_0/2\pi$ can reach the THz range [1]. If the quality factor of the resonant cavity, $\omega_0\tau \gg 1$, the electron flow in the channel may become unstable (at certain boundary conditions) with respect to the growth of the resonant plasma oscillations. Due to the coupling with electro-magnetic waves, the instability should lead to generation of radiation with the same frequency ω_0. In this paper, we review our recent experimental results for the detection and generation of terahertz and subterahertz radiation by submicron heterostructure field effect transistors.

1. Detection

The experimental exploration of the subject has begun long time ago, starting from the observation of the non-resonant detection in high mobility transistors [3, 4]. A new boost to the research in this direction was given by a series of publications [5–7], reporting observation of the far-infrared detection in short channel high-electron-mobility transistors (HEMTs) fabricated from different materials and in Si MOSFETs. The publications reporting non-resonant detection were followed by the demonstration of the resonant detection in GaAs HEMTs [8, 9] and gated double quantum well heterostructures [10, 11]. In all these devices, the 2D plasmons were tuned to the frequency of subterahertz radiation by varying the gate bias. In our recent papers [12, 13], we have demonstrated that the detection might be strongly affected by a dc drain current. We found that driving a transistor into the saturation region enhances the non-resonant detection and can lead to the resonant detection even if the condition $\omega_0\tau \gg 1$ is not satisfied, since the effective decay time for plasma oscillations becomes $1/\tau_{\rm eff} = 1/\tau - 2v/L$, where v is the electron drift velocity. However, most of the experiments described above were performed with the sub-THz radiation sources. Reference [8] reported on the THz detection, but the resonant character of the response was only weakly pronounced.

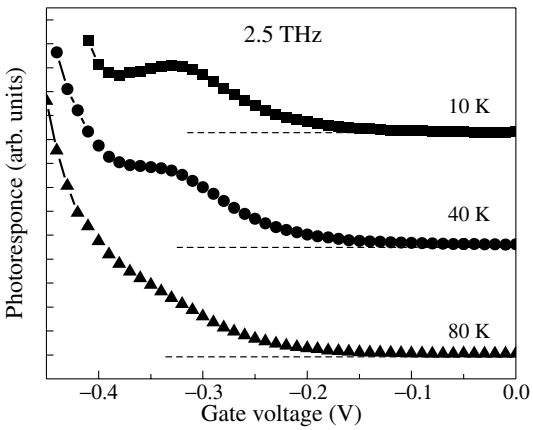

Fig. 1. Photoresponse of InGaAs device vs. the gate voltage at different device temperatures at 2.5 THz. Curves are shifted vertically. Dashed lines show zero levels. (After Ref. [14]).

Recently, we observed the resonant detection using THz

sources in the range from 0.7 to 3.1 THz [14]. The experiment was performed using a InGaAs/AlInAs HEMT with a 50 nm gate, employing the CO_2 pumped FIR gas laser as a source of THz radiation. Figure 1 presents the results of the photoresponse measured in InGaAs/AlInAs-based devices. At the device temperature below 100 K, the shoulder becomes pronounced in the lower gate voltage side, in between $-0.4-\,-\,0.3$ V, in addition to the temperature-independent non-resonant detection peak near the transistor threshold voltage. The shoulder further evolves to the clearly resolved temperature-sensitive spike nicely visible below 40 K. We attribute these peaks to the resonance detection of THz frequencies by plasma waves. Since the electron mobility at 60 K is about 36.000 cm^2/Vs, which corresponds to the momentum relaxation time of 800 fs, we should expect the quality factor at 2.5 THz to be $\omega_0\tau \approx 13$. However, even at 10 K, the resonance peak still remains very broad, about 60 mV (about 1.5 THz in the frequency domain). The corresponding relaxation time and the quality factor determined from the resonance half width are $\tau = 1/\pi\Delta f = 212$ fs corresponding to $\omega_0\tau \approx 3$. This resonance peak broadening shows that additional mechanisms of the plasma waves damping must be involved. These mechanisms might include the effect of ballistic transport [15], viscosity of the electron fluid due to the electron-electron collisions [1], and a possible effect of oblique plasma modes [16].

The relaxation time due to ballistic contact effects can be estimated as $\tau = \mu_{\rm bal} m/e$, where $\mu_{\rm bal} = 2eL/\pi\hbar\sqrt{2\pi n_{\rm ch}}$ is the ballistic mobility. This time is about 150 ns (assuming the electron concentration in the channel, $n_{\rm ch}$, to be 10^{11} cm^{-2}). The viscosity causes an additional damping of plasma waves with the decrement $a = \eta k^2 = \eta(\pi/4L)^2$ [1]. The viscosity of the 2D electronic fluid in the InP matched InGaAs channel is of the order of $\eta = \hbar/m \approx 2.7\times10^{-3}$ m^2/s. Then for plasma oscillations at fundamental frequency the relaxation time, $\tau = 1/2a \approx 740$ fs. Hence, the resonance width might be explained by taking into account the effects discussed above, even without involving the oblique plasma modes. Figure 2

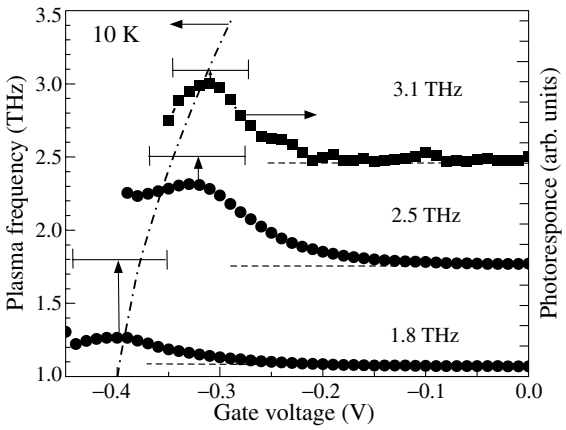

Fig. 2. Photoresponse in InGaAs device vs. gate voltage at three different excitation frequencies (1.8 THz, 2.5 THz and 3.1 THz) at 10 K (right axis). Curves are shifted vertically. Dashed lines indicate zero photoresponse. Arrows indicate resonance positions. Calculated plasmon frequency as a function of the gate voltage for $U_{\rm th} = -0.41$ V is shown by the dash-doted line (left axis). The error bars correspond to the linewidth of the experimental resonance peaks. (After Ref. [14]).

shows the photoresponse at different excitation frequencies at 10 K. One can see, that with the increase of the excitation frequency from 1.8 THz to 3.1 THz, the plasmon resonance moves to higher gate voltages in a decent agreement with the calculated dependence of fundamental plasma frequency vs. $U_{\rm gs}$.

The responsivity of the device was estimated to be of the order of (0.1–1) V/W. Such a low value is due to a weak coupling of the THz radiation to the channel plasma, and to a small area of the device. According to the recent theoretical calculations [17], the coupling could be dramatically improved by using large area multi-finger design or employing THz antennas. Operating temperature required for the resonant detection, could be increased by driving transistor into the saturation mode [18] and, ideally, the resonant detection can be reached at 300 K.

2. Emission

While the experiments on non-resonant and resonant detection seem to be in agreement with the theory, for emission measurements, the situation is more subtle. The first evidence of the sub-THz emission from GaN/AlGaN HEMT was reported in Ref. [19]. Later tunable THz emission was demonstrated using an InGaAs HEMT with a 60 nm long gate [20] (see Fig. 3). These emission experiments were performed in the cyclotron emission spectrometer [21]. Figure 3 shows the measured spectra. The emission had a threshold behavior vs. drain bias, in a good agreement with the theory [1]. The observed radiation power was in the nW range. These measurements were done on device with the merged source and gate contacts, to better meet the boundary conditions required for the Dyakonov–Shur instability [1]. Therefore, the emission was tuned by the drain bias. The resonant frequency value did shift from 0.42 THz up to 1 THz with increasing source-to-drain voltage in a reasonable agreement with the theory.

Recently the THz emission was observed from the transistors with gate and source separated, which allowed for the investigation of the gate bias dependence [22]. The experiments using 60 nm gate InAlAs/InGaAs/InP and 150 nm AlGaN/GaN HEMTs with gate and source separated were performed not only at cryogenic, but also at room temperature. The emission signal was excited by square source-drain voltage pulses with amplitude $U_{\rm ds} = 0-0.5$ V and $U_{\rm ds} = 0-12$ V for InGaAs

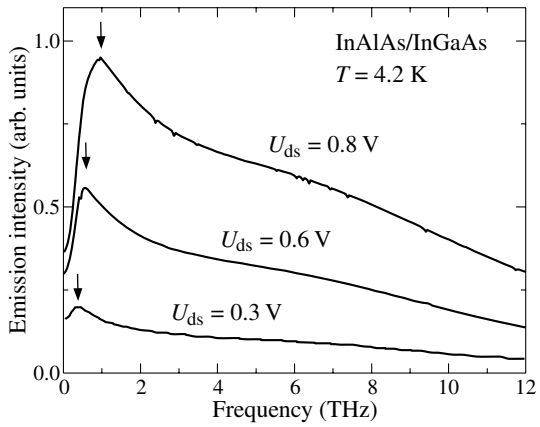

Fig. 3. Spectra of emission from an InGaAs HEMT for different source-drain voltages, $U_{\rm ds}$. The arrows mark emission maxima at 0.42, 0.56 and 1.0 THz for $U_{\rm ds}$ equal to 0.3, 0.6 and 0.8 V. (After Ref. [20]).

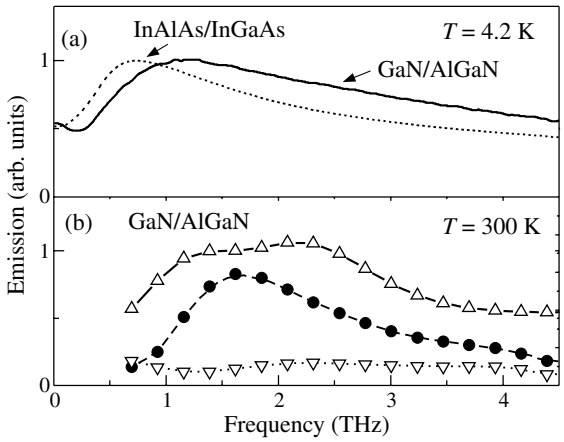

Fig. 4. (a) Normalized emission spectra at 4.2 K for InAlAs/InGaAs-HEMT ($U_{ds} = 0.3$ V, $U_{gs} = -0.1$ V) and for AlGaN/GaN-HEMT, $U_{ds} = 3$ V $U_{gs} = -1$ V). The emission from InGaAs based device is several times lower than that from the GaN based device. (b) Emission spectra at 300 K for AlGaN/GaN-HEMT at $U_{ds} = 8$ V, △ — $U_{gs} = 0$, • — $U_{gs} = -1.1$ V, ▽ — $U_{gs} = -4$ V. (After Ref. [22]).

and GaN HEMTs, respectively. The emission spectra for both structures at 4.2 K are presented in Fig. 4a. The most powerful single device integrated (in the entire range of the detector sensitivity, which was from 0.2 to 4.5 THz) emission at 300 K was observed from GaN HEMT. Its value was on the order of 0.1 μW.

At room temperature, only the emission spectra for the GaN transistor were measured (Fig. 4b), since the radiation intensity in the InGaAs device, observed at 300 K, was not high enough to allow such measurements. One can see that, the maximum of the emission from GaN-based device depends on temperature and that the form of the emission spectrum noticeably changes depending on the gate voltage. The emission went to zero for $U_{gs} = -4$ V, near the channel pinch-off. We observed (both at 4.2 and at 300 K and for both transistors), that the THz emission existed in a certain interval of U_{gs} values, between a negative value corresponding to the channel pinch-off and an upper limit, which increased at higher U_{ds}. The emission power differed from one sample to another within several times.

The radiation frequencies were in a reasonable agreement with the estimates for fundamental plasma modes either in the gated or ungated regions [23]. However, other features predicted in Ref. [1] (such as the tunability of the radiation frequency by the gate bias) were not observed. We would like to note, that the emission was observed close to the velocity saturation regime or even in the saturation regime. Therefore, we feel, that the mechanisms other than the plasma instability predicted in [1] can not be excluded. In particular, different instabilities caused by electron "run-away" phenomena [24, 25], transit time effects [26, 27], enhanced emission of optical phonons [28], and stratification of electron flow [29] might lead to the terahertz excitation.

To conclude, both resonant and non-resonant detection of sub-THz and THz radiation exploiting plasma waves have been observed in transistors of different materials including Si, GaAs, and GaN. The emission of THz radiation from InGaAs and GaN HEMTs was demonstrated at room and cryogenic temperatures. However, the additional experiments and theoretical investigations should be carried out to understand the underlying physics of the observed emission.

Acknowledgements

The authors acknowledge the financial support provided by the Russian Fund of Basic Re-search (Grant 05-02-1774) and Civilian Research and Development Foundation (CRDF 2681). The work at RPI was supported by the NSF under the IGERT (Grant No. 0333314) and by the STTR contract by ARO (subcontract from SET, Inc.).

References

[1] M. Dyakonov and M. S. Shur, *Phys. Rev. Lett.* **71**, 2465 (1993).
[2] M. Dyakonov and M. S. Shur, *IEEE Trans. Electron Devices* **43**, 380 (1996).
[3] R. Weikle *et al*, *Electronics Letters* **32**, 2148 (1996).
[4] J. Lu *et al*, *IEEE Electron Device Letters* **19**, 373 (1998).
[5] W. Knap *et al*, *J. Appl. Phys.* **91**, 9346 (2002).
[6] W. Knap *et al*, *Appl. Phys. Lett.* **80**, 3433 (2002).
[7] W. Knap *et al*, *Appl. Phys. Lett.* **85**, 675 (2004).
[8] J.-Q. Lu *et al*, *IEDM '98 Technical Digest*, San Francisco, CA, December (1998).
[9] W. Knap *et al*, *Appl. Phys. Lett.* **81**, 4637 (2002).
[10] X. G. Peralta *et al*, *Appl. Phys. Lett.* **81**, 1627 (2002).
[11] X. G. Peralta *et al*, in Proc. *ICPS-26*, Edinburgh, UC, (2002), Institute of Physics (2003).
[12] F. Teppe *et al*, *Appl. Phys. Lett.* **87**, 022102 (2005).
[13] F. Teppe *et al*, *Appl. Phys. Lett.* **87**, 052107 (2005).
[14] A. El Fatimy *et al*, "Resonant terahertz detection in InGaAs/AlInAs and AlGaN/GaN — based nanometric transistors", *Appl. Phys. Lett.*, submitted.
[15] M. S. Shur, *IEEE Electron Device Letters* **23**, 511 (2002).
[16] M. Dyakonov. *Private communications* (2005).
[17] V. V. Popov *et al*, Proc. *SPIE* **5772**, 63 (2005).
[18] D. Veksler *et al*, *Phys. Rev. B* **73**, 125328 (2006).
[19] Y. Deng *et al*, *Appl. Phys. Lett.* **84**, 70 (2004).
[20] W. Knap *et al*, *Appl. Phys. Lett.* **84**, 2331 (2004).
[21] W. Knap *et al*, *Review of Scientific Instruments*, **63**, 3293 (1992).
[22] N. Dyakonova *et al*, "Room-temperature terahertz emission from nanometer field-effect transistors", *Appl. Phys. Lett.* 2006 (accepted).
[23] M. Dyakonov and M. S. Shur, *Appl. Phys. Lett.* **87**, 111501 (2005); V. Ryzhii *et al*, "Plasma oscillations in high-electron-mobility transistors with recessed gate", *J. Appl. Phys.* 2006 (accepted).
[24] V. Dienys and J. Pozhela, *Hot electrons*, (Mintis, Vilnius, USSR) 1971.
[25] E. M. Conwell, *High Field Transport in Semiconductors* (Academic, New York) 1967.
[26] A. Satou *et al*, *Semicond. Sci. Technol.* **18**, 460, (2003).
[27] V. Ryzhii *et al*, *Physica Status Solidi (a)*, **202**, R113 (2005).
[28] V. L. Kustov *et al*, *Sov. Phys. JETP* **52**, 1207 (1980).
[29] V. Yu. Kachorovskii *et al*, *Phys. Rev. B* **68**, 033308 (2003).

14th Int. Symp. "Nanostructures: Physics and Technology"
St Petersburg, Russia, June 26–30, 2006

Rectification of microwave radiation by asymmetric ballistic dot

Sergey A. Vitkalov[1], Jing-qiao Zhang[1], Z. D. Kvon[1,2], J. C. Portal[3,4,5] and A. Wieck[6]

[1] Physics Department, City College of the City University of New York, New York 10031, USA
[2] Institute of Semiconductor Physics, 630090 Novosibirsk, Russia
[3] GHMFL, CNRS/MPI-FKF, BP 166, Grenoble Cedex 9, F-38042, France
[4] INSA, Toulouse Cedex 4, 31077 France
[5] Institut Universitaire de France
[6] Angewandte Festkorperphysik D-44780, Bochum, Germany

Abstract. Rectification of microwave radiation by asymmetric, ballistic dot is observed. The directed transport is studied at different frequency (1–40 GHz) temperatures (0.3 K–6 K) and magnetic field. Dramatic reduction of the rectification is found in magnetic fields at which the cyclotron (Larmor) radius of the electron orbits at Fermi level is less than the size of the dot. It indicates toward ballistic origin of the observed nonlinear phenomena. Both symmetric and asymmetric with respect to the magnetic field contributions to the directed transport are presented. We have found that the behavior of the symmetric part of the rectified voltage with the magnetic field is different significantly for microwaves with different frequencies. A ballistic model of the directed transport is proposed.

Introduction

Nonlinear directed transport in mesoscopic quantum objects has been investigated both theoretically and experimentally in different regimes. At high frequency photovoltaic effects demonstrating an unavoidable break of the inverse symmetry of small quantum systems by an impurity potential have been studied [1,2,3]. Since then different competing mechanisms of the rectification in quantum dots have been predicted [4,5] and found experimentally [6]. Most efforts have been focused on nonlinear properties of mesoscopic objects in the regime, in which the electron transport is governed by the electron quantum interference. Here we present results of experimental study of the directed electron transport in a regime, at which the classical ballistic trajectories appear to provide a dominant contribution to the rectification effect. The dot with a lateral size $d \approx 1\ \mu$ is studied. The size is significantly shorter than the mean free path $l_p = 8\ \mu$ of the 2D electrons in a complementary bulk system. We have observed a *gigantic* reduction of the directed electron transport through the ballistic dot by external magnetic field.

1. Experiment

The sample is fabricated from high mobility GaAs/AlGaAs heterostructures using electron beam lithography and consecutive plasma etching. A schematic view of the sample is presented in Fig. 1a. The dot is restricted by boundaries of three insulating disks of diameter 5 μ etched inside 2D conducting layer (see Fig. 1b). Two narrow conducting channels (the left and right channels in the figures) with a width approximately 0.3 μ and one channel with width 0.2 μ (the top, vertical channel) are formed between the disks. These channels provide electrical connections between the dot and three electrically isolated macroscopic 2D electron systems. A semitransparent metal gate was placed on the top of the structure at the distance 86 nm above the 2D electron gas (2DEG). Application of a voltage to the top gate changed resistance of the channels. The density of the 2DEG $n = 3.08\times10^{11}$ cm^2 and the 2D bulk mobility $\mu = 0.91\times10^6$ cm^2/V s were changed less than 10%

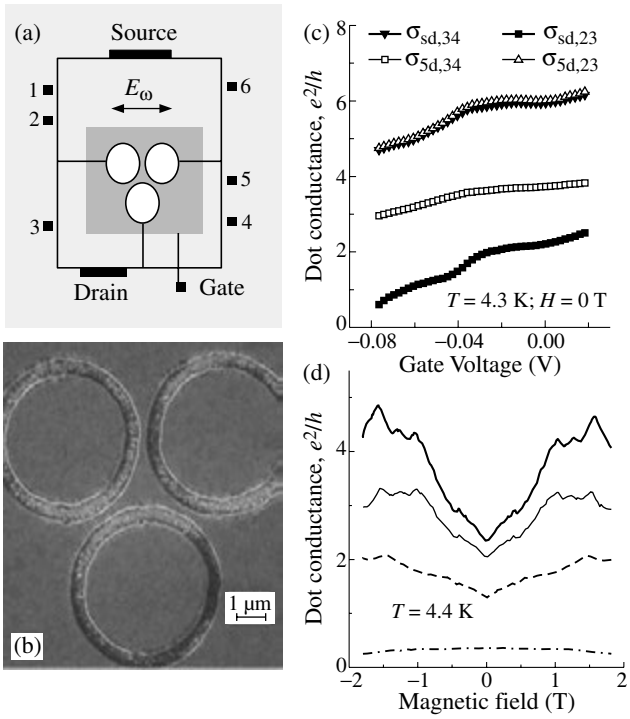

Fig. 1. (a) Schematic view of experimental setup. Different numbers correspond to different contacts to the sample. (b) SEM image of the sample before the gate deposition. (c) Dependence of the dot conductance on gate voltage at $H = 0$ T. Different curves correspond to different current-voltage configurations as labeled. Conductance $\sigma_{sd,34} = I/V$ is ratio of electrical current I flowing between source (s) and drain (d) to voltage V measured between contacts 3 and 4. (d) Dependence of the dot conductance $G_{sd,23}$ on perpendicular magnetic field. Different curves correspond to different gate voltages (from bottom to top in mV): −80.8, −49.1, −20.3, 11.

with the gate voltages used in the experiments. Measurements were done at temperature 0.3–6 K and magnetic field up to 2 T. The microwave radiation (1–40 GHz) was applied through a semi-rigid coax. The longitudinal resistance of bulk 2D parts

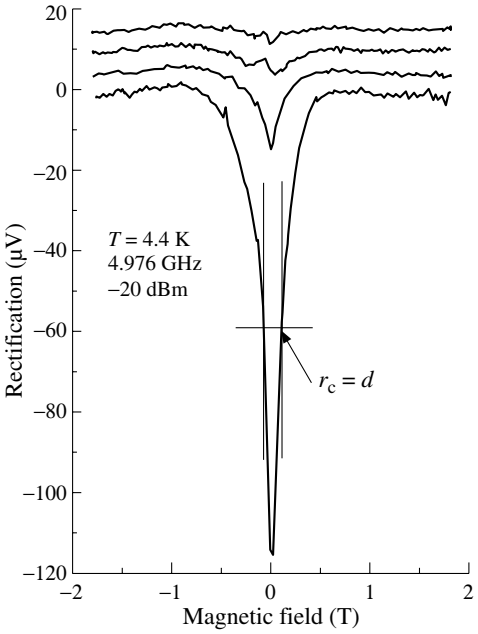

Fig. 2. Dependence of the rectified voltage V_{2-3} on magnetic field. Different curves correspond to different gate voltages(from bottom to top in mV): −80.8, −49.1, −20.3, 11. Three upper curves ($n = 1, 2, 3$) are shifted up on $5\times n$ μV for clarity. Sign of the rectified voltage corresponds to an electron pumping into the 2D area connected to contact 2.

and the dot conductance were determined by a standard 4-points method at frequency 10 Hz in the linear regime. The rectified voltage was measured using high impedance digital multimeters.

2. Results

Figure 1c presents a dependence of the dot conductance on the top gate voltage at different current-voltage configurations at temperature $T = 4.3$ K. The data in Fig. 1c demonstrate that the dot is well conducting through horizontal channels ($\sigma_{5d,34}$), whereas conductance through vertical channel ($\sigma_{sd,23}$) is small especially at low gate voltages $V_g \approx -0.08$ V. At the low gate voltages conductance $\sigma_{sd,23}$ demonstrates an activation behavior with temperature indicating an electron tunneling through the vertical channel. The conductance $\sigma_{5d,34}(-0.08\ \text{V}) \approx 3e^2/h$ through the horizontal channels is less sensitive to the temperature remaining to be roughly the same between $T = 0.3$ and 5 K. At temperature below 1 K a reproducible oscillations of the conductances with gate voltage are observed (not shown) similar to reported earlier for ballistic dots [7].

Magnetic field dependence of the conductance $G_{sd,23}$ is presented in Fig. 1d at different gate voltages. The conductance increases by 1.5–2 times with the magnetic field up to 2 Tesla. Reproducible oscillations of the conductance accompany the conductance increase and have been observed earlier [7].

The rectification of the microwave radiation by the dot is shown in Fig. 2. The rectified voltage V_{2-3} is measured between contacts 2 and 3 (see Fig. 1a). The main and drastic property of the rectification is very strong dependence on the magnetic field. The reduction of the rectification by two order of magnitude is observed for the dot with the conductance $G_{sd,23}$ below e^2/h. This is considerably stronger than the variation of the dot conductance $G_{sd,23}$ with the magnetic field (see Fig. 1d). At higher dot conductance the variation of the rectified voltage V_{2-3} with the magnetic field becomes to be weaker (upper curves on Fig. 2a). Substantially smaller (one-two order of magnitude less) rectified voltage V_{4-3} arises between contacts 4 and 3 (not shown).

To estimate a scale of the magnetic field, which is important for the observed dependence, we measure the width W of the first curve in Fig. 2a at half of it's height. This level is marked by a horizontal line in the Figure. The half width $W/2 = 0.088$ T is close to field $H = 0.085$ T at which the cyclotron radius r_C is equal to the dot size d. Thus the directed transport through the dot is reduced by half of it's zero field value at the magnetic field corresponding to condition $r_C \approx d$. This is strong indication toward a ballistic origin of the directed transport of electrons through the dot.

The rectification is not perfectly symmetric with respect to magnetic field (see Fig. 2). Significant variation of the symmetric part of the rectification with the microwave frequency is observed at frequencies above 10 GHz. An additional structure occurs at the high microwave frequencies, changing the direction of the rectified transport at zero magnetic field. The physical parameters relevant to the temporal behavior of the quantum dot are level spacing: $\Delta = 2\pi\hbar^2/(m^*A) = 28$ mK, bulk momentum relaxation time: $\tau_p = 34$ ps, dot crossing time $\tau_{cross} \approx 2d/V_F = 10$ (ps). The dot crossing time appears to be the closest time at which the frequency variations of the directed transport begins to appear: $\omega\tau_{cross} \approx 1$ at $\omega/2\pi \approx 10$ GHz.

In conclusion, an unexpected gigantic reduction of directed electron transport through asymmetric ballistic dot under microwave radiation is observed. The magnetic field at which the reduction occurs satisfies condition $r_C \approx d$, indicating ballistic origin of the observed phenomena. A ballistic model based on bending of electron trajectories by electric field inside the dot is proposed.

Acknowledgements

The work is supported by NSF: DMR 0349049, by DOE: DOE-FG02-84-ER45153, PICS, programs "Low-dimensional quantum structures" and "Quantum macrophysics" of RAS.

References

[1] V. I. Falko *et al*, *Zh. Eksp. Teor. Fiz.* **95**, 328 (1989).
[2] A. A. Bykov *et al*, *Pis'ma Zh. Eksp. Teor. Fiz.* **49**, 13 (1989).
[3] J. Liu *et al*, *Phys. Rev. B* **45**, 1267 (1992).
[4] B. Spivak *et al*, *Phys. Rev. B* **51**, 13226 (1995).
[5] M. G. Vavilov *et al*, *Phys. Rev. B* 63, 195313 (2001).
[6] L. DiCarlo *et al*, *Phys. Rev. Lett* **91**, 246804 (2003).
[7] J. P. Bird *et al*, *Rep. Prog. Phys.* **66**, 583 (2003).

14th Int. Symp. "Nanostructures: Physics and Technology"
St Petersburg, Russia, June 26–30, 2006

Emission of terahertz radiation from new grating-bicoupled HEMT device

Y. M. Meziani[1], T. Otsuji[1], M. Hanabe[1], T. Ishibashi[1], T. Uno[1] and E. Sano[2]

[1] Research Institute of Electrical Communication, Tohoku University, 980-8577 Sendai, Japan
[2] Research Center for Integrated Quantum Electronics, Hokkaido University, 060-8628 Sapporo, Japan

Abstract. A doubly interdigitated grating gate structure was incorporated into a GaAs-based HEMT device. When two-dimensional electrons were periodically confined to form a plasmonic grating, plasma instability was intensively promoted by photoexcitation, leading to the first emission of terahertz radiation at room temperature.

Introduction

Two dimensional (2D) plasma-wave instabilities in submicron transistors have attracted much attention the last ten years due to their nature of promoting emission of electromagnetic radiation, which is expected to realize frequency tunable sources/detectors in the terahertz range [1–5]. 2D plasmon itself is a non-radiative mode so that a metal-wired grating coupler structure is frequently utilized to yield terahertz electromagnetic-wave emission [6–9]. Wilkinson, *et al*, studied far infrared response of plasmon excitation from bi-periodically modulated 2D electron gas coupled with doubly interdigitated grating gates [6]. We have recently proposed a terahertz photomixer incorporating similar grating-bicoupled periodic plasmon-resonant cavities into a high-electron mobility transistor (HEMT) structure [7].

1. Grating-bicoupled HEMTs

Figure 1 illustrates the cross section and plan view of the grating bi-coupled plasmon-resonant terahertz emitter. The device structure is based on a high-electron mobility transistor (HEMT) and incorporates doubly interdigitated grating gates (G1 and G2) that periodically localize the 2D plasmon in 100-nm regions with a submicron interval. We fabricated two types of samples with different length for gate 2 (Sample 1: $L_{g2} = 300$ nm and sample 2: $L_{g2} = 1800$ nm). When an appropriate 2D electronic charge ($10^{11} - 10^{12}$ cm^{-2}) is induced in the plasmon cavities under the gate grating G1 while the regions under G2 are depleted, a strong electric field of the order of 1–10 kV/cm arises at the plasmon cavity boundaries. When the device is photoexcited by laser irradiation, photoelectrons are dominantly generated in the regions under G2 and then are injected to the plasmon cavities under G1. If a specific drain-to-source bias potential is applied to promote a uniform slope along the source-to-drain direction on the energy band in the depleted regions under G2, photoelectrons in each depleted region under G2 are unidirectionally injected to one side of the adjacent plasmon cavity. This may lead to excitation of plasmon instability.

According to the Mikhailov formulae [9] for the conditions of amplification of far-infrared radiation by means of instability of grating-coupled 2D-plasmons, the threshold velocity is still too high to perform room-temperature operation where electron drift mobility of the order of 10^5 cm^2/Vs is required even for idealistic III–V material systems. The periodically confined 2D-plasmon grating structure of our proposal is expected to accelerate the instability leading to room-temperature operation. It is noted that the feature size of the grating is by two orders of magnitude smaller than the wavelength of terahertz electromagnetic waves under consideration.

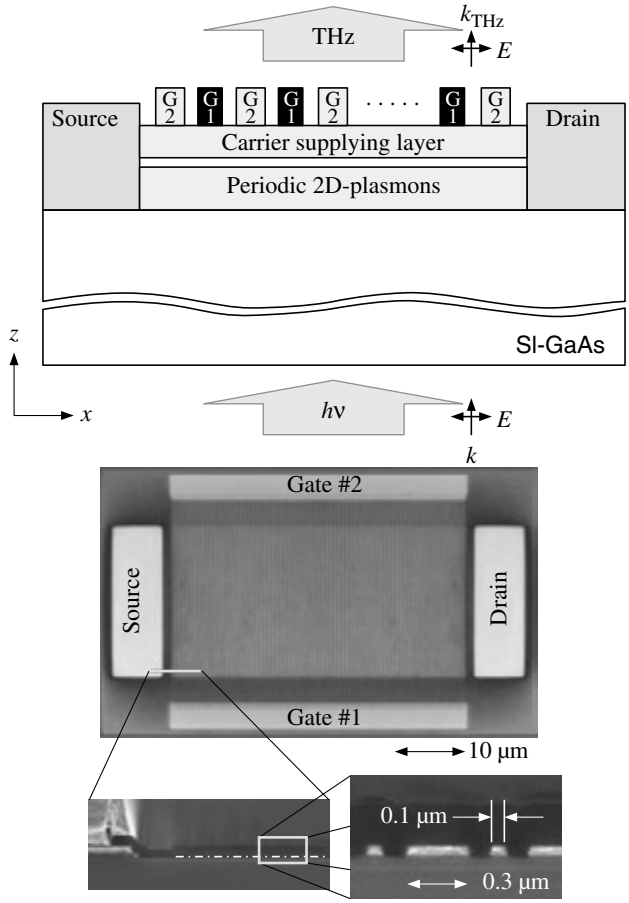

Fig. 1. Device cross section and plan view; k is the wave vector of irradiated photons, E — the electric field (linear polarization), k_{THz} — the wave vector of electromagnetic radiation.

2. Results and discussion

Figure 2 shows the photoresponse, obtained at room temperature, of our samples as function of G1, at $V_{g1} = 0$ V and for different drain biases (1, 2 and 3 V). The fundamental resonance frequency is observed for two grating samples ($L_{g2} = 300$ and 1800 nm). By increasing drain bias, the peaks are shifted to high values of gate biases (G2). In case of sample 1 at $V_{ds} = 3$ V, the second harmonic is also observed at $V_{g2} = -3$ V (Fig. 2b). The observed response is interpreted as excitation of plasmon resonance [10]: it's completely different from that of

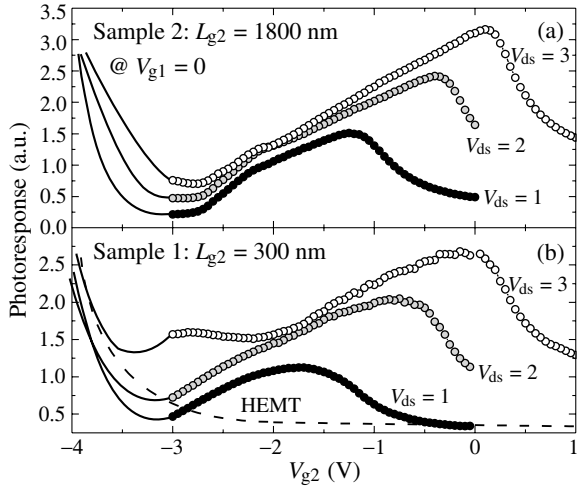

Fig. 2. Photoresponse signal showing excitation of plasmon instability for two samples and normal HEMT (dashed line).

standard HEMT's fabricated on the same wafer showing monotonic dependence on gate bias V_{gs} (dashed line). This clearly shows manifestation of plasmon instability in our devices.

In order to verify the electromagnetic radiation from the device due to photo-induced plasmon instability, temporal electromagnetic response to impulsive photoexcitation was measured at room temperature by using a reflective electrooptic sampling (REOS) system. 1.5 μm, fiber laser pulse with a FWHM of 70 fs and a 20-MHz repetition was used as pump and probe beams. The lineally polarized pump beam illuminated the device from the back surface. The Fourier spectrum exhibited resonant-like peaks around 1 and 4 THz (0.7 and 3 THz) for sample 2 (sample 1)(Fig. 3). It is inferred that the result is attributed to the emission of electromagnetic radiation

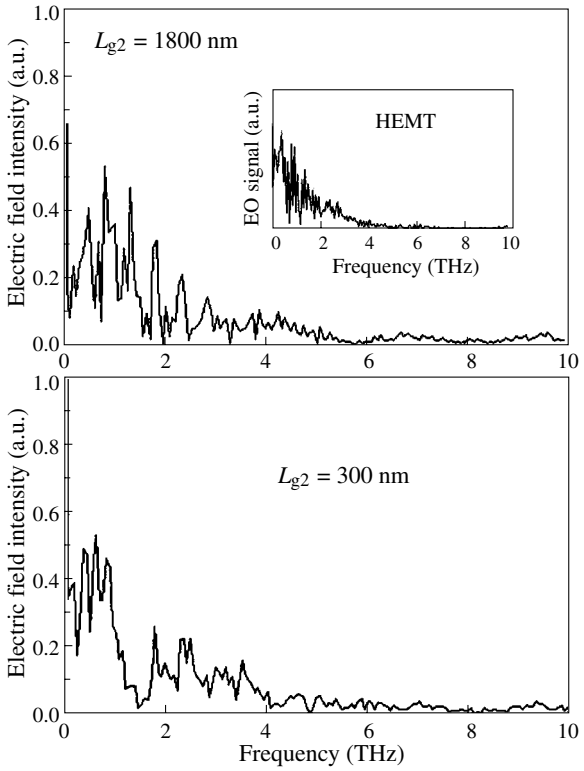

Fig. 3. Fourier spectrum of samples when 1.5-μm, 70-fs laser pulse irradiated the device. $V_{g1} = 0.0$ V, $V_{g2} = -2.5$ V, $V_{ds} = 3.0$ V.

produced by photo-induced plasmon instability.

3. Conclusion

Two dimensional electrons are periodically confined in grating bicoupled HEMTs. This type of devices can enhance the plasma instability leading to the first observation of emission of THz radiation at room temperature.

Acknowledgements

This work was financially supported in part by the SCOPE program from the Ministry of Internal Affairs and Communications, Japan. We also thanks JSPS for financial supporting of author to do this work. The authors thank Prof. M. Dyakonov, Prof. V. Ryzhii, Prof. S. Mikhailov and Prof. T. Asano for their valuable discussion and Dr. T. Nagatsuma for his supporting electrooptic sampling instrumentation.

References

[1] M. Dyakonov and M. Shur, *Phys. Rev. Lett.* **71**, 2465–2468 (1993).

[2] W. Knap, Y. Deng, S. Rumyantsev, J.-Q. Lü, M. S. Shur, C. A. Saylor and L. C. Brunel, *Appl. Phys. Lett.* **80**, 3433 (2002).

[3] W. Knap, F. Teppe, Y. M. Meziani, N. Dyakonova, J. Lusakowski, F. Boeuf, T. Skotnicki, D. Maude, S. Rumyantsev and M. S. Shur, *Appl. Phys. Lett.* **85**, 675 (2004).

[4] T. Otsuji, M. Hanabe and O. Ogawara, *Appl. Phys. Lett.* **85**, 2119 (2004).

[5] S. J. Allen, Jr., D. C. Tsui and R. A. Logan, *Phys. Rev. B* **38**, 980–983 (1977).

[6] R. J. Wilkinson, C. D. Ager, T. Duffield, H. P. Hughes, D. G. Hasko, H. Armed, J. E. F. Frost, D. C. Peacock, D. A. Ritchie, A. C. Jones, C. R. Whitehouse and N. Apsley, *J. Appl. Phys.* **71**, 6049–6061 (1992).

[7] T. Otsuji, M. Hanabe, J. Shigenobu, S. Takahashi and E. Sano, *12th Int. Conf. on Terahertz Electron. (IEEE, New York, 2004)*, 331–332 2004.

[8] K. Hirakawa, K. Yamanaka, M. Grayson and D. C. Tsui, *Appl. Phys. Lett.* **67**, 2326–2328 (2004).

[9] S. A. Mikhailov, *Phys. Rev. B* **58**, 1517–1532 (1998).

[10] Y. M. Meziani, J. Lusakowski, N. Dyakonova, W. Knap, D. Seliuta, E. Sirmulis, J. Devenson, G. Valusis, F. Boeuf, T. Skotnicki, *IEICE*, in Press, 2006.

14th Int. Symp. "Nanostructures: Physics and Technology"
St Petersburg, Russia, June 26–30, 2006

Nitride-based quantum-well lasers on InAs substrate for midwave-infrared emission.

M. Debbichi[1], A. Ben Fredj[1], A. Bhouri[1], M. Saïd[1], J.-L. Lazzari[2], P. Christol[3], Y. Cuminal[3], *A. Joullié*[3] and V. K. Kononenko[4]

[1] Unité de recherche de Physique des Solides, Département de Physique, Faculté des Sciences de Monastir, 5019 Monastir, Tunisia
[2] Centre de Recherche en Matière Condensée et Nanosciences, CRMC-N, UPR-CNRS 725, Campus de Luminy, 13288 Marseille cedex 9, France
[3] CEM2-UMR CNRS 5507, Université Montpellier 2, 34095 Montpellier, France
[4] Stepanov Institute of Physics NASB, Fr. Scorina Pr., 70, 220072 Minsk, Belarus

Abstract. We propose and simulate a new "W" laser structure, whose type-II broken gap active region, based on InAsN/GaAsSb/InAsN system, is designed for growth on InAs substrate. Combining the "W" configuration with the coulombic interaction, this nitride-based structure ensures high electron and hole wavefunction overlap, that can exceed 0.70 under injected carrier density of 2×10^{12} cm^{-2}. By slightly varying the thickness of the InAsN QWs and GaAsSb barriers, the emitted wavelength could be tuned between 3 μm and 4 μm.

Introduction

Semiconductor laser diodes emitting in the midwave infrared region (MWIR: 3–5 μm) are in great interest due to their prospect in various optoelectronic applications, especially for gas analysis by tuneable diode laser absorption spectroscopy. For such application, MWIR laser diodes operating at room temperature (RT) in continuous wave (cw) mode are required with single optical mode emission and laser wavelength tuning in a wide spectral domain. In the past few years, significant progress has been achieved in MWIR laser devices but the objective of RT operation in cw regime still remains to be reached above 3 μm. In this communication, we simulate a new class of dilute-nitride InAsN/GaAsSb multi-quantum well (MQW) laser structures to be grown on InAs substrate for RT emission in the MWIR domain.

1. Design of the Nitride-based laser structure for MWIR emission

By using an accurate **k–p** model with a self consistently Schrödinger–Poisson solver [1], the Nitride-based laser structure was designed to exhibit a RT laser emission at 3.3 μm that is suitable for methane detection. The numerical values used in the calculations were extracted from the literature [2]. The conduction and valence band-offset DEc and DEv of the InAsN/GaAsSb heterostructure were calculated by interpolating binary heterointerface values [3] followed by calculation of shifts due to strain. Like the most MWIR Sb-based structures, the InAsN/GaAsSb heterostructure presents an indirect type-II band alignment [4] where the electrons are confined in one layer while the holes are gathered in the other. In this configuration, the overlap of electron and hole wavefunctions, which governs the interband optical coupling, tends to be weak, resulting in a dramatic increase of current threshold and limiting the device performances. Fortunately, this overlap can be largely improved by wavefunction engineering of heterostructures having smart geometry [5] compared to conventional multi-quantum well lasers.

Firstly, the proposed structure for MWIR laser emission is considered without electrostatic consideration. Fig. 1 displays the conduction and valence band profiles of the laser structure, with the two fundamental electron and hole levels and probability densities.

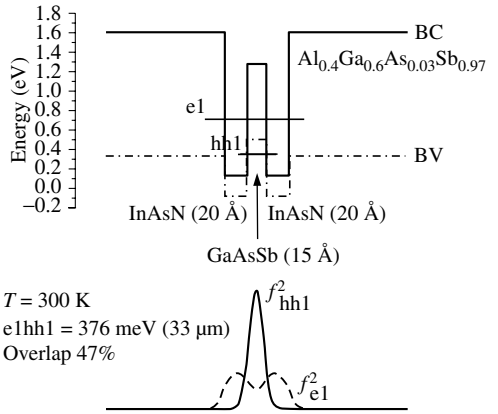

Fig. 1. RT band diagram of $InAs_{1-x}N_x$ ($x = 0.034$) / $GaAs_{1-y}Sb_y$ ($y = 1$) / $InAs_{1-x}N_x$ ($x = 0.034$) "W" laser structure on InAs substrate and fundamental electron (e1) and heavy hole (hh1) presence probability densities. Without carrier injection at thermodynamic equilibrium, the fundamental e1-hh1 optical transition is expected at 3.3 μm with a wavefunction overlap of 47%.

The designed active zone is composed of several strain-compensated dilute-nitride InAsN(2 nm)/GaAsSb(1.5 nm)/InAsN(2 nm) type-II broken gap QWs having the "W" geometry [4] and each "W" period is separated by AlGaAsSb quaternary alloy lattice-matched to the InAs substrate in order to ensure a two-dimensional behaviour for both electrons and holes. We can note that, this particular band diagram without carrier injection, where the GaAsSb "hole" QW is sandwiched between the two InAsN "electron" QWs, already provides a sufficient electron-hole wavefunction overlap to ensure a good radiative efficiency, while keeping the advantage of type-II MQWs concerning the reduction of Auger recombinaison rate [6].

Next, under carrier injection, the holes in the GaAsSb barriers are strongly attracted by the electrons localised in the deep InAsN QWs. Consequently, we have to solve self-consistently the well-known Schrödinger (eq. 1 and eq. 2) and Poisson equa-

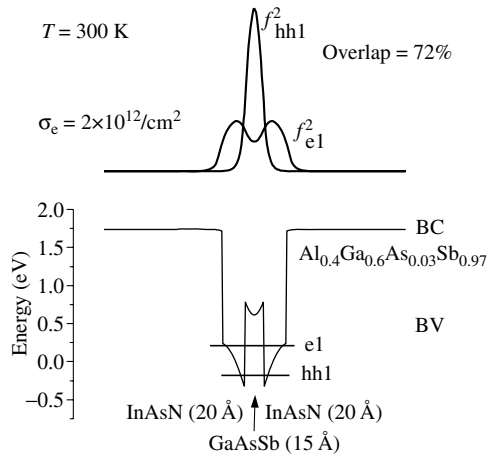

Fig. 2. The same as Fig. 1 but under carrier injection ($\sigma_e = 2\times10^{12}$ cm^{-2}). The coulombic attraction enhances the overlap value that exceed 70%.

tions (eq. 3):

$$\left(-\frac{\hbar^2}{2m_e}\frac{d^2}{dz^2} + U_e(z) + V(z)\right)\Psi_e(z) = E_e\Psi_e\,, \qquad (1)$$

$$\left(-\frac{\hbar^2}{2m_h}\frac{d^2}{dz^2} + U_h(z) - V(z)\right)\Psi_h(z) = E_h\Psi_h\,, \qquad (2)$$

$$\frac{d^2}{dz^2}V(z) = \frac{e^2}{\varepsilon}\left(\sigma_h\,|\Psi_h(z)|^2 - (\sigma_e\,|\Psi_e(z)|^2\right)\,, \qquad (3)$$

where $U_e(z)$ and $U_h(z)$ are the conduction and valence band discontinuities, $V(z)$ being the potential induced by Coulombic attraction. $\Psi_e(\Psi_h)$ is the first quantum level envelope function for the electron (the hole) and $E_e(E_h)$ is the associated energy; ε stands for the dielectric constant; σ_e and σ_h are, respectively, the electron and hole charge densities t hat we considered constant across the whole structure. For a given σ_e, σ_h is determined by charge neutrality.

Fig. 2 shows the effect of coulomb attraction, induced by carrier injection, on band diagram and wavefunction overlap.

Taking into account the electrostratic interaction in such *pseudo-indirect* MQW structure, the overlap value can exceed 70% for a typical carrier densities of 2×10^{12} cm^{-2}.

To complete, we report in Fig. 3 the influence of the InAsN QW thickness on the expected laser emission peak with carrier injection $\sigma_e = 2\times10^{12}$ cm^{-2}.

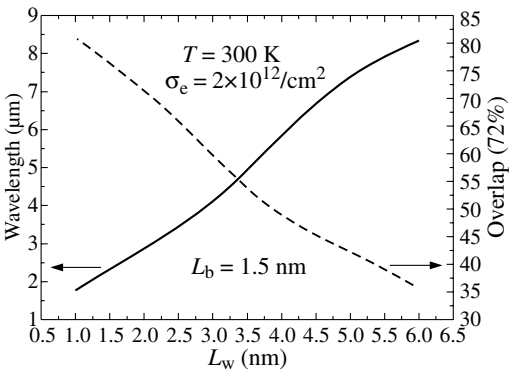

Fig. 3. Influence of InAsN quantum well width with carrier injection of 2×10^{12} cm^{-2} on calculated emission wavelength (solid line) and on wavefunction overlap (dashed line) for InAsN/GaAsSb/InAsN "W" laser structure.

By slightly varying the thickness of the InAsN QW at GaAsSb barriers fixed ($L_B = 1.5$ nm), the active region could be easily designed for emission in the 3–4 μm wavelength range with wavefunction overlap always superior than 60%. If the predicted suppression of Auger recombination in dilute nitrogen III–V compounds [7] is confirmed, a laser structure, using this active "W" region and AlGaAsSb cladding layers, has a strong potential for RT operation with small threshold current.

Acknowledgements

This work is partially supported by CMCU project No. 05S/1122 and by a cooperation project CNRS/NASB 2005-06 No. 18086.

References

[1] P. Christol *et al*, *IEE Proc-Optoelectron.* **146**, 3 (1999).
[2] I. Vurgaftman *et al*, *J. Appl. Phys.* **89**, 5815 (2001).
[3] A. Joullié *et al*, *Topics Appl. Phys.* **89**, 1 (2003).
[4] I. Vurgaftman *et al*, *Appl. Phys. Lett.* **96**, 4653 (2004).
[5] J. R. Meyer *et al*, *Appl. Phys. Lett.* **67**, 757 (1995).
[6] J. R. Meyer *et al*, *Appl. Phys. Lett.* **73**, 2857 (1998).
[7] B. N. Murdin *et al*, *Phil. Trans. R. Soc. London* **A359**, 459 (2001).

14th Int. Symp. "Nanostructures: Physics and Technology"
St Petersburg, Russia, June 26–30, 2006

The generation of terahertz radiation in GaP-based semiconductor waveguide

A. A. Dubinov[1], A. A. Afonenko[2] and V. Ya. Aleshkin[1]

[1] Institute for Physics of Microstructures of RAS, 603950 Nizhny Novgorod, Russia
[2] Belarusian State University, 220050 Minsk, Belarus

Abstract. A design of a semiconductor waveguide based on an AlP/GaP/AlP heterostructure for parametric generation of the difference mode is proposed; this design provides for the presence of two modes in the 1 μm region and for initiation of the difference mode of waveguide in the terahertz range. It is shown that the power of the difference mode in the 1–8 THz range generated by 10-W short-wavelength modes in a 100-μm-wide waveguide at room temperature can be $\sim$ 300 μW, and $\sim$ 5 mW for using Si substrate and 10–14 THz difference mode range.

Introduction

Semiconductor lasers operating in the terahertz region attract considerable interest in view of their high potential for different applications. Cascade medium-infrared lasers capable of room-temperature operation have been successfully implemented [1], whereas with terahertz lasers based on cascade structures generation has been achieved only at cryogenic temperatures [2]. However, an extremely complicated band diagram of cascade structures and high requirements for control of parameters restrict their application. Owing to the optical nonlinearity of A_3B_5 semiconductors there is a possibility for parametric generation of radiation in this range in A_3B_5 based waveguides when two near-infrared modes propagate there.

The nature of the second order nonlinear susceptibility of GaP is anharmonicity of the optical vibrations. Therefore, there is a nonlinear susceptibility resonance when the difference frequency corresponds to the transverse optical phonon frequency. In zinc blend structure semiconductors the nonlinear susceptibility tensor components $\varepsilon^{(2)}_{ijk}$ are not zero, if $i \neq j \neq k$ only. All nonzero components are equal.

In order to attain effective parametric generation, the phase-matching condition should be satisfied that means that the phase velocities of the polarization wave and the propagating mode at the difference frequency must be the same. It was shown that the phase matching condition can be satisfied using simple GaP-based semiconductor waveguide in contrast to complex GaAs-based waveguide [3]. The reason of these is little GaP frequency dispersion of refractive index in the 1 μm region because of substantial interval to bandgap absorption edge. Therefore GaP effective refractive index of the polarization wave is substantial below that GaAs effective refractive index of such wave. Second possibility is the use Si substrate for growth of the AlP/GaP/AlP heterostructure [4].

According to our calculations, the maximum power is achieved for Si substrate based structure, when the frequency of generated radiation falls into the region of the phonon absorption peak GaP. In this case the nonlinear susceptibility of semiconductor increases greatly. The results of our calculations indicate that at the near infrared modes generated with a power of 10 W in a 1-μm region, the difference mode can be generated with a power of $\sim$ 5 mW in the range of optical phonon frequency in GaP (10–14 THz) in a 100-μm-wide waveguide at room temperature.

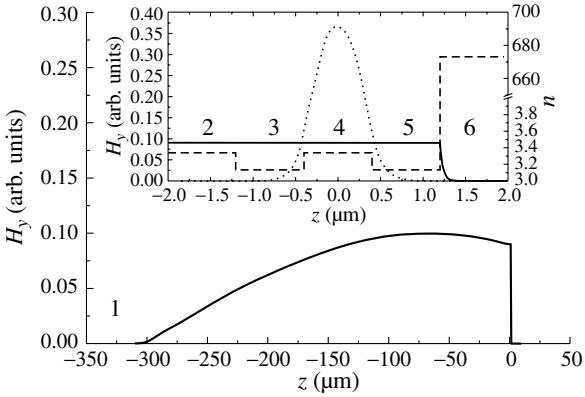

Fig. 1. Spatial profiles of the absolute value of the magnetic field strength in the difference mode (full curve). At inset of the figure the amplitude of high-frequency modes is shown in arbitrary units by dotted line, and the real part of the refractive index n at the frequency 1.8 THz is shown by dashed line. The layer #1 is air, layers #2 and #4 are GaP, layers #3 and #5 are AlP, layer #6 is Au. Thicknesses of the layers: #2 — 300 μm, #3, #4 and #5 — in 0.8 μm.

1. Calculation of the difference mode power

In the case when the semiconductor waveguide is grown on the (001)-plane substrate and the high-frequency modes have TE polarization and propagate along the [110] direction, the nonlinear polarization in GaP is normal to the plane of layers and the TM mode is generated at the difference frequency [3]. The Z-axis is directed along the crystallographic direction [001] (see Fig. 1). The TM mode propagating along the X-axis has one magnetic field component directed along the Y-axis. The coordinate dependence of the magnetic field strength H_y in the mode of difference frequency ω can be determined from the equation:

$$\varepsilon(z,\omega)\frac{d}{dz}\left[\frac{1}{\varepsilon(z,\omega)}\frac{dH_y}{dz}\right]+\left(\varepsilon(z,\omega)\frac{\omega^2}{c^2}-k_x^2\right)H_y = -2\varepsilon^{(2)}_{xyz}\frac{k_x\omega}{c}A_1^*(z)A_2(z)\,, \quad (1)$$

where $\varepsilon(z,\omega)$ is permittivity and c is vacuum light velocity. The coordinate dependences of the electric field amplitudes in high-frequency modes A_1 and A_2, as well as the difference between their propagation constants $k_x = k_2 - k_1$, are determined by solving the wave equation with a particular refractive-index profile. The electric field component of the difference mode E_z

and its power P are defined by expressions:

$$E_z = -\frac{1}{\varepsilon(z,\omega)}\left(\frac{ck_x}{\omega}H_y + 2\varepsilon^{(2)}_{xyz}\frac{k_x\omega}{c}A_1^*(z)A_2(z)\right), \quad (2)$$

$$P = -\frac{cL_y}{2\pi}\int\limits_{-\infty}^{\infty}\mathrm{Re}\left(H_y E_z^*\right)dz, \quad (3)$$

where L_y is the width of the waveguide.

Sandwiching a narrow-gap GaP between wide-gap AlP emitter layers with a lower refractive index one can form the waveguide for near-infrared radiation. Waveguide for a terahertz radiation is wide GaP or Si substrate.

2. Results

The dependence of nonlinear susceptibility of GaP on frequencies of the waves which are influenced by the medium in semiconductors A_3B_5 was considered in [5]. The nonlinear susceptibility dependence on the difference frequency is shown in Fig. 2 and Fig. 3. From the figure one can see that there is a maximum of susceptibility near the transverse optical-phonon frequency, and then the susceptibility tends to constant $\varepsilon^{(2)}_{xyz}$ with a frequency growth. At maximum the value of nonlinear susceptibility is more than 40 times higher than that at high frequencies. Therefore, the output power of the difference frequency wave largely increases near the transverse optical-phonon frequency, in spite of a high absorption in this region.

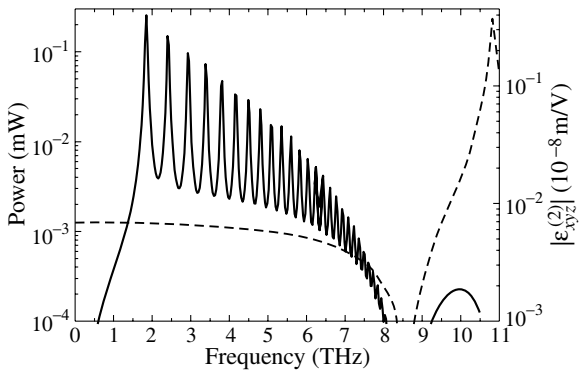

Fig. 2. The difference mode power versus the difference mode frequency in a GaP substrate based waveguide at room temperature (full curve, $\lambda_1 = 0.95\ \mu$m). Broken curve corresponds to the dependence of the $\varepsilon^{(2)}_{xyz}$ component in GaP on the difference mode frequency.

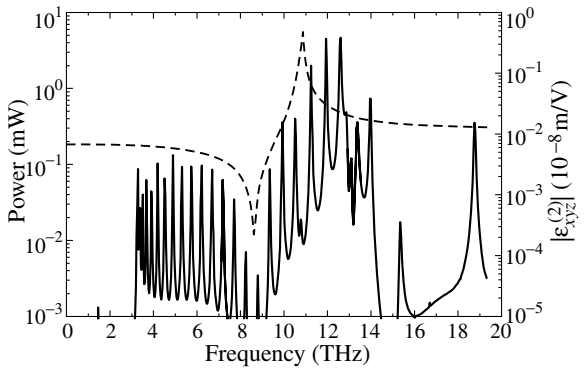

Fig. 3. The difference mode power versus the difference mode frequency in a Si substrate based waveguide at room temperature (full curve, $\lambda_1 = 0.97\ \mu$m). Broken curve corresponds to the dependence of the $\varepsilon^{(2)}_{xyz}$ component in GaP on the difference mode frequency.

The contribution of the optical phonons to permittivity is accounted for by correct definition of the refractive index for the difference mode. A simple estimate of the contribution of the optical phonons to permittivity is provided by formula (26) from the paper [6], which is applicable to semiconductor materials.

The calculated difference-mode powers for GaP- and Si-substrate based waveguides are shown in Fig. 2 and Fig. 3 correspondingly. The longest wavelength for a near-infrared mode λ_1 is fixed in our calculation. The wavelength of the difference mode is changed by variation of the wavelength of another near-infrared mode. The spectral dependence of power features great number of resonance peaks. Each peak corresponds to waveguide mode. Great number of resonance peaks involves with big width of the waveguide ($\sim 300\ \mu$m).

The results of our calculations indicate that given phase-match and high-frequency modes generation 10 W power in a 1-μm region, the difference mode can be generated with a power of $\sim 300\ \mu$W in the ranges 1–8 THz for GaP-substrate based structure and ~ 5 mW in the ranges 10–14 THz, ~ 0.5 mW around 19 THz for Si-substrate based structure with a 100-μm-wide waveguide at room temperature.

Acknowledgements

This work was supported by CRDF # RUE1-2657-NN-05; the RFBR # 04-02-17432; the RFBR–BRFFR # 06-02-81020; the RAS Physical Sciences Division "Semiconductor Lasers" Program; Programs "Low-Dimensional Quantum Structures" and "Electromagnetic waves of terahertz region" of RAS.

References

[1] F. Capasso *et al*, *IEEE J. Sel. Top. Quantum Electron.* **5**, 792 (1999).
[2] M. Rochat *et al*, *Appl. Phys. Lett.* **81**, 1381 (2002).
[3] A. A. Afonenko *et al*, *Semicond. Sci. Technol.* **20**, 357 (2005).
[4] T. Soga *et al*, *J. Crystal Growth.* **132**, 414 (1993).
[5] C. Flytzanis, *Phys. Rev. B* **6**, 1264 (1972).
[6] J. S. Blakemore, *J. Appl. Phys.* **53**, R123 (1982).

14th Int. Symp. "Nanostructures: Physics and Technology"
St Petersburg, Russia, June 26–30, 2006

Spontaneous terahertz emission from stressed GaAsN/GaAs heterostructures

D. A. Firsov[1], L. E. Vorobjev[1], V. A. Shalygin[1], V. Yu. Panevin[1], A. N. Sofronov[1], D. V. Tsoy[1], A. Yu. Egorov[2], A. G. Gladyshev[2] and O. V. Bondarenko[2]

[1] St Petersburg State Polytechnic University, 195251 St Petersburg, Russia
[2] Ioffe Physico-Technical Institute, St Petersburg, Russia

Abstract. Terahertz radiation at lateral electric field from stressed GaAs/GaAsN/GaAs structures doped with Be was observed for the first time. The observed radiation is attributed to hole transitions between resonant and localized acceptor states. This is proved with comparative studies of terahertz radiation from unstressed p-GaAs/GaAs structures where no resonant states exist.

Introduction

The radiation of terahertz (THz) spectral range can be used in various scientific and technical fields but wide application of THz techniques is still limited because of the lack of compact effective solid state emitters. Optical carrier transitions between impurity states in semiconductors are very perspective from the point of view of the development of such solid state THz emitters. Of particular interest is the use of impurity resonant states arising for example in p-Ge in the conditions of valence subband splitting under uniaxial stress. THz lasers based on intracenter hole transitions in uniaxially stressed germanium had been already created [1]. Harnessing the nanoheterostructures opens the new prospects of the development of THz sources because the possibility to afford the internal strain allows do not to use the external pressure. This simplifies significantly the design of the emitter. It was reported in Ref. [2] about the observation of the stimulated THz emission from strained structures with $Si/Si_{1-x}Ge_x/Si$ quantum wells doped with boron. It was also shown that this THz radiation is connected with population inversion arising between resonant and localized acceptor states under impurity electrical breakdown. In the present paper we report the first data on the observation of spontaneous THz emission from stressed GaAs/GaAsN/GaAs structures doped with beryllium.

1. Layers of $GaAs_{1-x}N_x$ as a basis for THz sources

Thin $GaAs_{1-x}N_x$ layers with small nitrogen content ($x = 1 - 2\%$) grown on GaAs substrate are stretched in the plane of the structure. This corresponds to uniaxial stress applied along the structure growth axis. In these conditions the degeneracy of light and heavy hole subbands is lifted that leads to splitting the acceptor states too. The split value is determined with nitrogen content. The variation of quantum well width allows additionally to change the split value. Under definite value of split the acceptor states bound to heavy hole subband fall within the energy interval corresponding to light hole subband, that is, they became resonant ones (Fig. 1). There is a possibility of population inversion between resonant and localized acceptor levels in this system in accordance with mechanism described, for example in Ref. [3]. Excitation of free holes may be realized with the help of lateral electric field applied in the plane of the structure.

It should be noted that GaAs/GaAsN/GaAs structures match more adequate to intracenter population inversion mechanism [3] in comparison to $Si/Si_{1-x}Ge_x/Si$ structures because in the latter case the mechanical stress corresponds to tensile strain but not to compressive strain. Besides, structures based on III–V compounds are preferable for the fabrication of optical resonator because they can be easy cleft along of crystallographic planes producing the parallel sides.

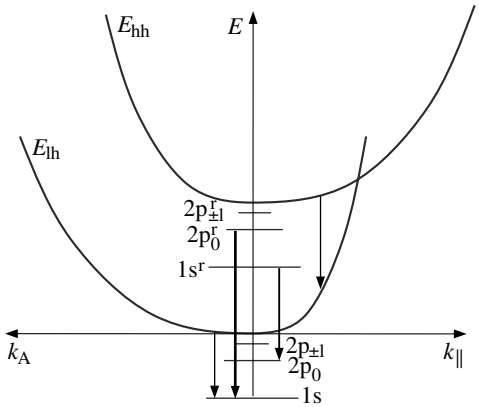

Fig. 1. Heavy (E_{hh}) and light (E_{lh}) hole energy bands and the schematic diagram of optical hole transitions in GaAs/GaAsN/GaAs structure. Indexes "$\parallel$" and "$\perp$" relate to the direction of mechanical stress.

In Ref. [1] THz stimulated emission was observed from p-Ge at parallel directions of external mechanic pressure and electric field. In case of GaAsN layers grown on GaAs substrate it is more convenient to use another configuration with perpendicular directions of lateral electric field and stress (the same configuration was used in experiments with $Si/Si_{1-x}Ge_x/Si$ quantum wells [2]). As it was shown in Ref. [4], perpendicular directions of electric field and pressure are preferable from the viewpoint of the observation of THz emission.

2. Experimental results

The present paper is devoted to the first investigations aimed at the study of spontaneous THz emission from stressed GaAs/GaAsN/GaAs structures. The structures under investigations contained rather thick 0.1 μm $GaAs_{1-x}N_x$ layers ($x = 0.018$) grown by MBE on semiinsulating GaAs substrate. In order to increase the emitting volume, ten such layers separated with 0.5 μm GaAs layers were grown. GaAsN layers were doped with beryllium, acceptor concentration was $3 \cdot 10^{17}$ cm^{-3}. For comparison, p-GaAs/GaAs structures do not containing nitrogen were grown and studied too. In these

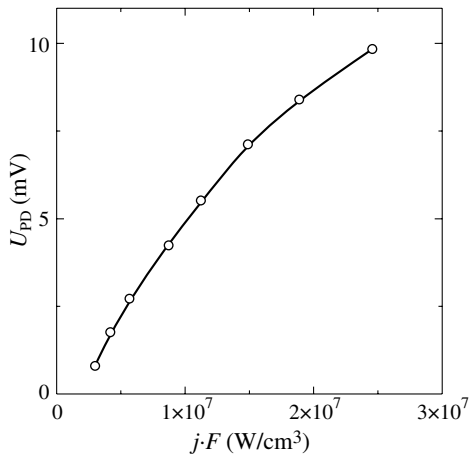

Fig. 2. The signal of Ge⟨Ga⟩ photodetector as a function of specific power of electric current in doped GaAs/GaAsN/GaAs structures (j is a density of current, F is electric field).

structures no effects related to resonant impurity states have to be observed. THz radiation was registered with Ge⟨Ga⟩ photodetector with a set of filters limiting the spectral range of detector sensitivity to 70 . . . 200 μm. Measurements were made in pulse regime.

In order to determine the range of electric fields corresponding to impurity breakdown the current-voltage characteristics were studied. It was shown that in sub-breakdown fields ($E < 100$ V/cm) the hopping mechanism is responsible for hole transport. At temperature $T = 4.2$ K and electric fields exceeding 2000 V/cm the main part of acceptors is ionized.

According to our calculations emission wavelength corresponding to intracenter hole transitions is close to 80–100 μm. Results of electroluminescence studies are presented in Fig. 2. The integral signal from photodetector U_{PD} is presented as a function of specific power released in the sample under electric current flow. The observed THz emission can be of different nature. Together with hole transitions between resonant and localized acceptor states it can be related to lattice heating, direct intersubband hole transitions and band-acceptor transitions. The comparison of electroluminescence data obtained in GaAs/GaAsN/GaAs structures with resonant states and in p-GaAs/GaAs structures where no resonant states exist, allowed to make conclusion that the radiation observed in the present studies from GaAs/GaAsN/GaAs structures is connected mainly with intracenter hole transitions. Measurements of emission spectra are in progress.

Acknowledgements

This work was supported by grants of RFBR, ISTC and Russian Ministry of Education and Science.

References

[1] I. V. Altukhov, M. S. Kagan, K. A. Korolev, V. P. Sinis, *JETP Letters* **59** (7), 476 (1994).

[2] I. V. Altukhov, E. G. Chirkova, V. P. Sinis, M. S. Kagan, Yu. P. Gousev, S. G. Thomas, K. L. Wang, M. A. Odnoblyudov, I. N. Yassievich, *Appl. Phys. Lett.* **79** (24), 3909 (2001).

[3] M. A. Odnoblyudov, I. N. Yassievich, M. S. Kagan, Yu. M. Galperin, K. A. Chao, *Phys. Rev. Lett.* **83** (3), 644 (1999).

[4] V. N. Bondar, A. T. Dalakyan, L. E. Vorob'ev, D. A. Firsov, V. N. Tulupenko, *JETP Letters* **70** (4), 265 (1999).

14th Int. Symp. "Nanostructures: Physics and Technology"
St Petersburg, Russia, June 26–30, 2006

Electron transport and detection of terahertz radiations by GaN/AlGaN submicronic field effect transistor

S. V. Morozov[1], K. V. Maremyanin[1], E. V. Demidov[1], V. I. Gavrilenko[1], W. Knap[2], J. Lusakowski[2], M. A. Poisson[3], E. Moran[3], C. Dua[3],C. Caquiere[4] and D. Ducatteau[4]

[1] Institute for Physics of Microstructures RAS, 603950 Nizhniy Novgorod, Russia
[2] GES–UMR, CNRS — Universite Montpellier 2, Place E. Bataillon 34950 Montpellier, France
[3] Thales Research Technology/TIGER, Domaine de Corbeville, 91404 Orsay Cedex, France
[4] IEMN/TIGER, 59655 Villeneuve d'Ascq, France

Abstract. We report on the resonant detection of THz ($f = 0.58$ THz) radiation by plasma waves in submicron GaN/AlGaN HEMT with two-dimentional electronic gas.

Introduction

Recently there has been considerable interest in terahertz (THz) radiation detection by two-dimensional (2D) electron plasma in field effect transistors. THz range (0.3–10 THz) corresponds to different type excitation energies in condensed matters, such as phonons, binding energy of shallow impurities, rotational and oscillatory excitation in liquids, as well as in gases and biological objects. THz technology is of particular interest for nondestructive control and visualization in medicine, environment monitoring, food industry, struggle against terrorism, etc. [1]. For many applications it is desirable to use a fast selective detector tunable by voltage. Such detection mode can be realized in field effect transistor with 2D electronic gas in the channel [2–4]. In a usual operating mode the upper limiting frequency of the transistor is restricted by the electron transit time. Using the plasma effects allows to raise the working frequency of submicronic field effect transistors up to THz range [2] because characteristic velocities of plasma waves of 10^8 cm/sec are essentially higher than electron drift velocities in the channel of the transistor. Resonant frequency of plasma oscillations in the gated 2D electron gas is determined by the gate length L and electron concentration n that is in the first approximation described by the simple expression of the flat capacitor $n = CU_0/e$. Here C is the capacity between the gate and the channel per unit area, $U_0 = U_{\rm GS} - U_{\rm th}$ is the swing voltage (a difference between gate voltage and the cut-off voltage), e is the electron charge. For large U_0 the simple expression for resonant frequency

$$f_0 = \frac{1}{4L} \cdot \sqrt{\frac{eU_0}{m}} \qquad (1)$$

is valid. In the present work the electron transport and the photoresponse in the THz-range in GaN/AlGaN HEMT with submicronic gate with 2D electron gas (Fig. 1) was investigated.

1. Results and discussion

Transistors under study were fabricated from MBE grown GaN/AlGaN heterostructure with high mobility 2D electronic gas. The gate length was $L = 0.25$ μm and the channel width was 30 μm. The chip with transistors was mounted in the holder that was inserted into the reciprocal module placed in waveguide insert into storage liquid helium vessel; all measurements were carried out at $T = 4.2$ K. Backward wave tube was used as a source of THz radiation, the radiation being chopped with the frequency of 200 Hz. Measurements were carried out at fixed frequency of radiation $f = 580$ GHz sweeping the gate voltage. The photoinduced e.m.f was measured between source and drain versus the gate voltage $U_{\rm GS}$. The standard lock-in amplifier was used to recover the signal. The mobility of 2D carriers in the channel was estimated from the measured dependence of conductivity on the magnetic field (solid line in Fig. 2). As easy to see, after substracting the "parallel" conductivity (that is assumed to be independent on the magnetic field) the dependence can be approximated by the Lorentz curve (dotted line in Fig. 2). Therefore the mobility can be estimated from the relation $\mu H_{1/2}/c = 1$ where $H_{1/2} \approx 28$ kOe is the magnetic field in which the conductivity decreases two times. This estimation gives $\mu \approx 3600$ cm^2/Vs that corresponds to condition $\omega\tau \geq 1$ be fulfilled at frequen-

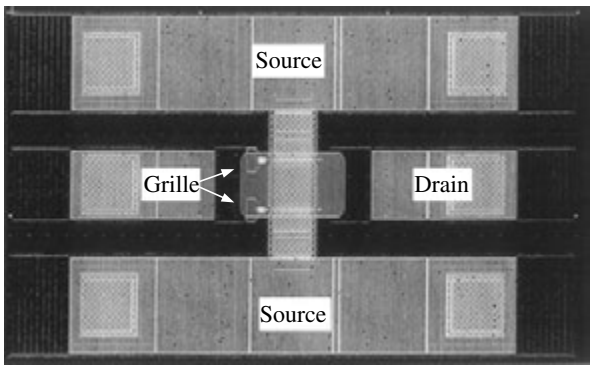

Fig. 1. Photo of the GaN/AlGaN transistor.

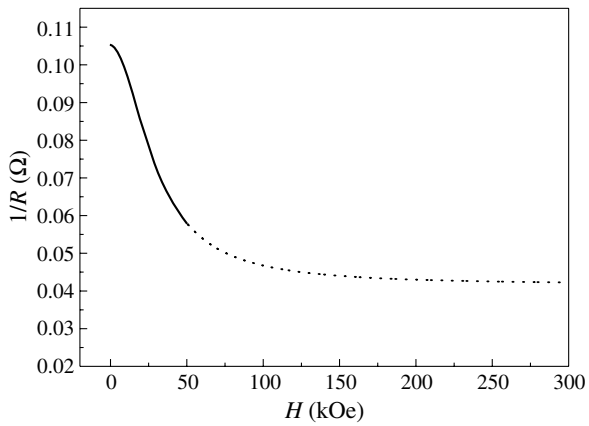

Fig. 2. The magnetoconductivity measurements.

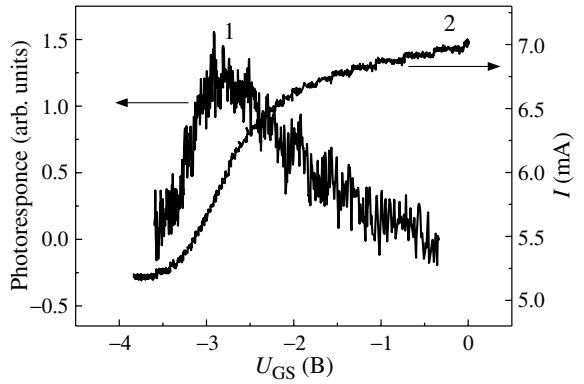

Fig. 3. The dependence the transistor photoresponse by the gate voltage (1), and the measured transfer characteristic (2).

cies over 380 GHz. Fig. 3 presents the measured transistor photoresponse at $f = 580$ GHz versus the gate voltage as well as the transfer characteristics. The observed cut-off voltage $U_{\rm th} = -3.5$ V corresponds according to the formula (1) to the resonant frequency $f_0 = 1.5$ THz at zero gate voltage which should decrease down to the zero at $U_{\rm GS}$ approaching $U_{\rm th}$. The distinct maximum of the photoresponse in Fig. 2 observed at the gate voltage $U_{\rm GS} = -3$ V corresponds according to relation (1) to the frequency of plasma oscillations $f_{\rm r} = 580$ GHz that just coincides with the frequency of the backward wave tube radiation. From the above mobility estimation one can get the $\omega\tau$ factor of 1.8. Thus the observed photoresponse maximum can be related with resonant detection by plasma waves in gated 2D electron gas.

Acknowledgement

The work has been financially supported by RFBR (# 05-02-17374) and RFBR-CNRS (# 05-02-22001) projects and by Russian Academy of Sciences.

References

[1] B. Ferguson *et al*, *Nature Materials* **1**, 26 (2002).
[2] M. Dyakonov *et al*, *Phys. Rev. Lett.* **71**, 2465 (1993).
[3] M. Dyakonov *et al*, *IEEE Trans. on Electr. Dev* **43**, 380 (1996).
[4] W. Knap *et al*, *Appl. Phys. Lett.* **30**, 3433 (2002).

14th Int. Symp. "Nanostructures: Physics and Technology"
St Petersburg, Russia, June 26–30, 2006

Slit-grating gate field-effect transistor: a plasmonic device for high terahertz frequencies

V. V. Popov[1], G. M. Tsymbalov[1], D. V. Fateev[1] and M. S. Shur[2]

[1] Institute of Radio Engineering and Electronics (Saratov Branch), Russian Academy of Sciences, 410019 Saratov, Russia
[2] Department of Electrical, Computer, and System Engineering and RPI/IBM Center for Broadband Data Transfer, CII9015, Rensselaer Polytechnic Institute, Troy, 12180 New York, USA

Abstract. Our computer simulations show that higher plasmon modes in a slit-grating gate field-effect transistor with two-dimensional electron channel effectively couple to terahertz radiation, which makes it possible to design terahertz plasmonic devices with operating frequencies up to 10 THz or even higher.

Introduction

High-frequency response of field-effect transistors (FET's) with two-dimensional (2D) electron channels is strongly affected by plasma oscillations exited in the channel under the gate electrode. This phenomenon in its various manifestations can be used for the detection, frequency multiplication and generation of terahertz (THz) radiation [1–4]. Plasmon modes excited under the gate electrode (gated plasmons) are the most attractive for practical applications because their frequency can be effectively tuned by variation of the gate voltage. However, the gated plasmons in a single-gate FET are weakly coupled to THz radiation [5] because they are: (i) strongly screened by the metal gate electrode and (ii) have a vanishingly small net dipole moment due to their acoustic nature. If the length of the gated channel W is much longer than the gate-to-channel distance, the frequency of the gated plasmons coupled to THz radiation can be estimated as [1]

$$\omega = k_n \sqrt{\frac{eU_0}{m^*}}\,, \qquad (1)$$

where $k_n = \pi(2n-1)/W$ ($n = 1, 2, 3, \ldots$) are the wavevectors of the gated plasmons, $U_0 = U_g - U_{th}$ is the difference between the gate voltage U_g and channel depletion (i.e., threshold) voltage U_{th}, e and m^* are the electron charge and mass, respectively. Simple estimations show that the frequency of the fundamental plasmon mode ($n = 1$) may exceed 5 THz only in a FET with the gate shorter than 100 nm, which sets a limitation for designing the single-gate FET plasmon devices in the high-frequency THz range. Although higher gated plasmon modes ($n > 1$) have greater frequencies, they can hardly be used for increasing the operation frequency of a single-gate THz plasmonic transistor because of a weaker coupling of higher plasmon modes to THz radiation [6].

It was suggested in [5] that the coupling efficiency of gated plasmons to THz radiation can be dramatically enhanced due to their interaction with the ungated portions of the electron channel. In this paper, we calculate the THz plasmon absorption spectra of a grating-gate FET with 2D electron channel in frame of the fist principle electrodynamic approach and show that the the gated-plasmon resonances in such a structure increase by several orders of magnitude due to excitation of plasma oscillations in ungated portions of the channel. We also show that intensive higher plasmon resonances (up to 9th order) can be effectively excited in a slit-grating gate FET.

1. Results and discussion

Based on the first principle electrodynamic approach, using the full system of the Maxwell equations, we have calculated the THz plasmon absorption spectra of a grating-gate FET shown schematically in Fig. 1. Theoretical approach is based on the integral equation method developed by us earlier in [7]. We describe the THz response of the 2D electron channel by the sheet conductivity in the local Drude model as

$$\sigma(\omega) = \frac{e^2 N_{1,2}\tau}{m^*(1 - i\omega\tau)}\,,$$

where τ is the characteristic electron scattering time and N_1 and N_2 are the sheet electron densities in the gated and ungated regions of the channel, respectively (see Fig. 1). The sheet electron density under the gate strips is calculated in the parallel-plate capacitor model as

$$N_1 = \epsilon\epsilon_0 U_0/ed\,,$$

where ϵ is the dielectric constant of the barrier layer material, ϵ_0 is the dielectric permittivity of vacuum, d is the gate-to-channel distance (the barrier layer thickness). Calculations were performed for the characteristic parameters of AlGaN/GaN HEMT: $\epsilon = 9$, $U_{th} = -3$ V, $d = 8$ nm. Surface conductivity of Au gate strips was assumed to be 2.5 S. Numerical calculations showed that the plasmon absorption spectra do not change noticeably depending on realistic variation of a DC current through the channel (if one neglects the effect of the channel length modulation by the drain bias). Because of that all numerical results below are presented for zero DC drain current in the FET structure. Note that the effect of the channel length modulation by the drain bias can be easily accounted for by corresponding variation of the channel length L in Eq. 1.

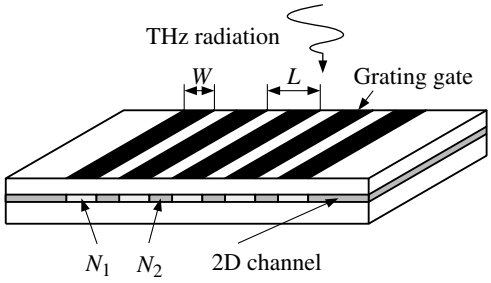

Fig. 1. The schematic of a grating-gate FET.

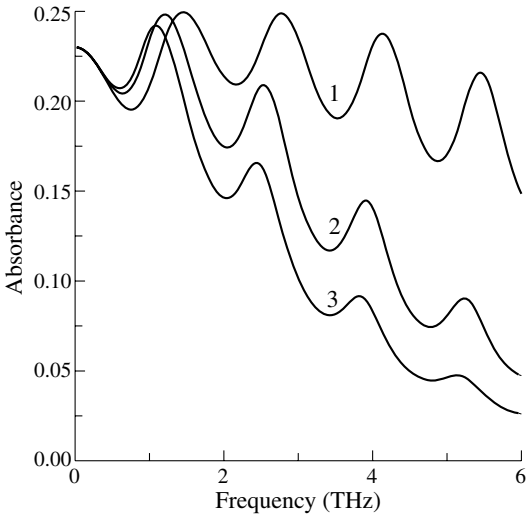

Fig. 2. Absorption spectra of AlGaN/GaN HEMT with 1-μm-wide grating-gate strips for three different slit widths: 0.1 μm (curve 1), 0.3 μm (curve 2) and 0.5 μm (curve 3) at room temperature ($\tau = 2.27\times10^{-13}$ s) for zero gate voltage.

Figure 2 shows the THz absorption spectra of AlGaN/GaN HEMT with 1-μm-wide grating-gate strips for three different grating-gate slit widths and zero gate voltage. These results demonstrate that one is able to observe quite pronounced and well-resolved higher plasmon resonances even at room temperature in the structure with sub-micron slits. For narrow slits (narrower than 0.2 μm) all higher resonances are excited with comparable (large) amplitudes because narrow grating-gate slits generate strong higher Fourier harmonics of the incident THz wave. As a result, intensive higher plasmon resonances may be excited at high THz frequencies up to 7th resonance at about 10 THz (not shown in Fig. 2). Radiative damping of plasmon oscillations grows significantly with decreasing the slit width, thus the radiative damping and dissipation of plasmon oscillations contribute comparably to the total linewidth

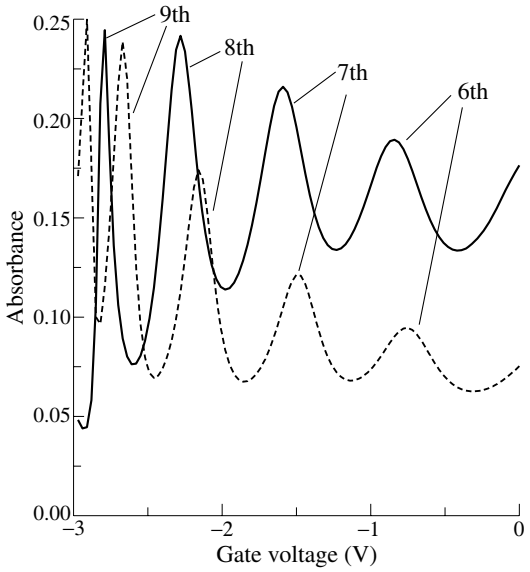

Fig. 3. The same as in Fig. 2 as a function of the gate voltage for two different slit widths: 0.1 μm (solid curve), 0.2 μm (dashed curve) at frequency 6.86 THz. Numbers mark the high-order gated-plasmon resonances.

of the plasmon resonance in the FET with a narrow-slit grating-gate, which makes all plasmon resonances stronger. Note that the maximum absorbance of 0.5 at the plasmon resonance is reached when the radiative and dissipative contributions to the resonance linewidth become equal [7]. The calculations also show that all plasma resonances become weaker by two orders of magnitude when the electron density under the grating-gate openings tends to zero. This fact demonstrates a crucial role of the ungated portions of the channel in excitation of the gated plasmons.

Figure 3 shows the terahertz absorption of AlGaN/GaN HEMT with 1-μm-wide grating-gate strips and sub-micron grating-gate slits as a function of the gate voltage. The most intriguing result here is that the intensity of higher plasmon resonances (up to 9th order) increases at more negative gate voltage. It happens because the radiative damping of higher plasmon modes increases with increasing the electron density modulation along the electron channel [6]. Notice also that the plasmon resonances excited at more negative gate voltages exhibit a narrower linewidth, $\Delta U_{\rm g}$, of the resonance. The more negative the resonant value of $U_{\rm g}$, the narrower the resonance is. One can easily understand this fact by performing the differentiation of Eq. (1):

$$\Delta U_0 = \frac{2W}{\pi(2n-1)}\sqrt{\frac{m^*U_0}{e}}(\Delta\omega)\,,$$

where $\Delta\omega$ is the linewidth of the resonance in the frequency domain. Obviously, for a given $\Delta\omega$, ΔU_0 tends to zero when $U_{\rm g}$ approaches the threshold voltage $U_{\rm th}$.

2. Conclusions

It is shown that a slit-grating gate acts as an effective coupling element between THz radiation and plasmon modes in the 2D channel. Strong plasmon resonances up to 9th order can be excited in such a structure in the high-frequency THz range. The intensity of higher plasmon resonances increases with increasing the electron density modulation in the channel by applying the negative gate voltage. These results open a gateway to designing the FET plasmon devices in the high-frequency THz range (up to 10 THz).

Acknowledgements

This work was supported by the Russian Foundation for Basic Research, Russian Academy of Sciences Program "Novel Materials and Structures", and the U. S. Army Research Office under STTR subcontract from Sensor Electronics Technology.

References

[1] M. S. Shur *et al*, *IEEE Trans. Microwave Theory and Techniques* **48**, 750 (2000).
[2] W. Knap *et al*, *Appl. Phys. Lett.* **84**, 2331 (2004).
[3] A. Satou *et al*, *Semicond. Sci. Technol.* **18**, 460 (2003).
[4] F. Teppe *et al*, *Appl. Phys. Lett.* **87**, Art. No. 052107/3 (2005).
[5] V. V. Popov *et al*, *J. Appl. Phys.* **98**, Art. No. 033510/7 (2005).
[6] V. V. Popov *et al*, *Semiconductors* **39**, 142 (2005).
[7] V. V. Popov *et al*, *J. Appl. Phys.* **94**, 3556 (2003).

14th Int. Symp. "Nanostructures: Physics and Technology"
St Petersburg, Russia, June 26–30, 2006

Effect of dc and ac excitations on the longitudinal resistance of a 2D electron gas in highly doped GaAs quantum wells

A. A. Bykov[1,2], Jing-qiao Zhang[2], S. Vitkalov[2], A. K. Kalagin[1], D. R. Islamov[1] and A. K. Bakarov[1]

[1] Institute of Semiconductor Physics, 630090 Novosibirsk, Russia
[2] Physics Department, City College of the City University of New York, New York 10031, USA

Abstract. Linear ac resistance of highly mobile two-dimensional electrons in GaAs heavily doped quantum wells is studied at different magnitudes of dc and ac (10 kHz and 100 kHz) excitations. In the dc excitation regime the differential resistance oscillates with the dc current and external magnetic field similar to that observed earlier in AlGaAs/GaAs heterostructures [C. L. Yang *et al*, *Phys. Rev. Lett.* **89**, 076801 (2002)]. At external ac excitations the resistance is also found to be oscillating with the magnetic field. However the form of the oscillations is considerably different from the dc case. We show that at frequency below 100 kHz the difference is the result of a specific average of the dc differential resistance during the period of the external acexcitations.

Introduction

Nonlinear properties of highly mobile two-dimensional electrons in AlGaAs/GaAs heterojunctions is a subject of considerable current interest. Several new transport phenomena have been observed in these systems recently [1–7]. In the pioneer work [1] strong oscillations of the longitudinal resistance induced by microwave radiation have been observed at magnetic fields, which satisfy the condition $\omega = n\omega_c$, where ω is the microwave frequency and ω_c is the cyclotron frequency.

Another interesting nonlinear phenomenon has been observed in the response of the 2D highly mobile electrons to dc excitations [2]. Oscillations of the longitudinal resistance, which are periodic in inverse magnetic field, have been found at dc biases, satisfying the condition $h\omega_c/2\pi = 2R_cE_H$, where R_c is Larmor radius of electrons at Fermi level and Hall electric field, induced by the dc bias in the magnetic field. The effect has been attributed to Zener tunneling between Landau orbits, tilted by the Hall electric field [2].

In this paper we report an observation of the resistance oscillations with magnetic field in dc biased GaAs quantum well with 2D electron density of an order of magnitude higher than reported earlier [2]. Moreover we have found similar resistance oscillations with magnetic field in response to low frequency (10 and 100 kHz) ac excitations. The particular form of the resistance oscillations at the ac excitations is considerably different from the dc case. We show experimentally that for the low frequencies the difference is the result of an average of the dc differential resistance during a period of ac excitations.

1. Experimental

Our samples were cleaved from a wafer of a high-mobility GaAs quantum well grown by MBE on GaAs substrates. The width of the GaAs quantum well was 13 nm. AlAs/GaAs type-II superlattices served as barriers, which made it possible to obtain a high-mobility 2D electron gas with high electron density. In dark, the electron density and mobility of the 2D electron gas in our samples were $n_e = 1.18\times10^{16}$ m^{-2} and $\mu = 91$ m^2/Vs, respectively. After brief light illumination, the electron density and mobility of the 2D electron gas in our samples were $n_e = 1.28\times10^{16}$ m^{-2} and $\mu = 111$ m^2/Vs, respectively. Measurements were carried out at $T = 4.2$ K in magnetic field up to 1 T on 50 μm wide Hall bars with distance of 250 μm between potential contacts. The resistance was measured using 1 μA current at frequency of 888 Hz.

2. Results and discussion

Dependence of the longitudinal resistance r_{xx} of the 2D electron gas is presented in Fig. 1 at different values of the dc bias. With an increase of the dc current through the sample an oscillating behavior of the longitudinal resistance is found, similar to that reported earlier [2].

A dependence of the longitudinal resistance on magnetic field at different level of ac excitation (100 kHz) is presented in Fig. 2. Recognizable oscillations of the linear resistance with magnetic field are detected.

The ac voltage V_{ac} at frequency 888 Hz were measured using standard lockin amplifier synchronized with the testing current I_{ac}. Since at frequency 888 Hz the response is found to be linear with respect to the testing current I_{ac} we approximated the responseby Ohm's law:

$$V_{ac} = R_{xx}(I_F)I_{ac}\,, \qquad (1)$$

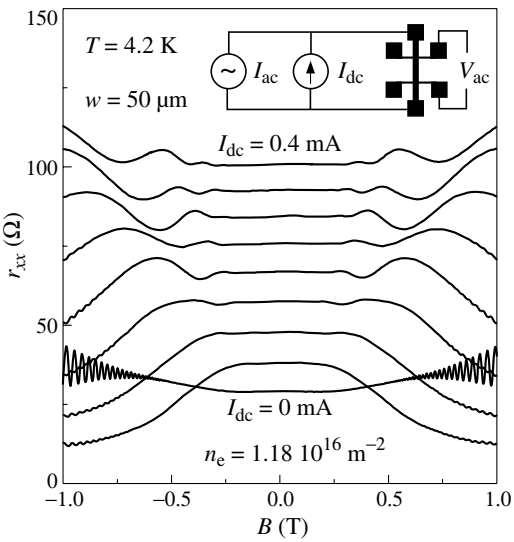

Fig. 1. Dependence of differential resistance r_{xx} on magnetic field at different dc current from 0 to 0.4 mA in steps of 0.05 mA. For clarity, the curves are shifted vertically by $n \times 8$ Ω, where $n = 0, 1, \ldots, 8$. The experimental setup is shown on the top.

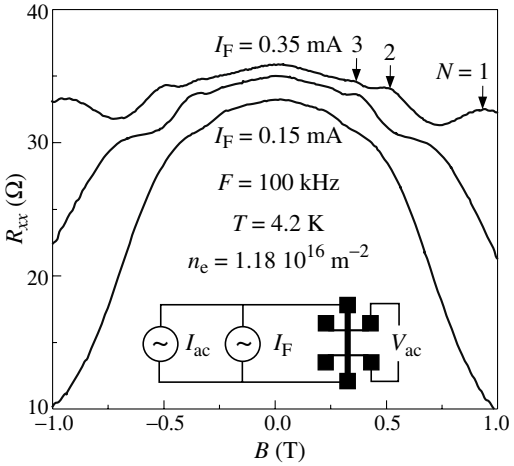

Fig. 2. Magnetoresistance R_{xx} at different amplitudes of ac excitation. Maximums of the resistance oscillations are marked by arrows. Positions of the maxima are approximately periodic in $1/B$. A diagram for the electrical measurement is presented at the bottom of the figure.

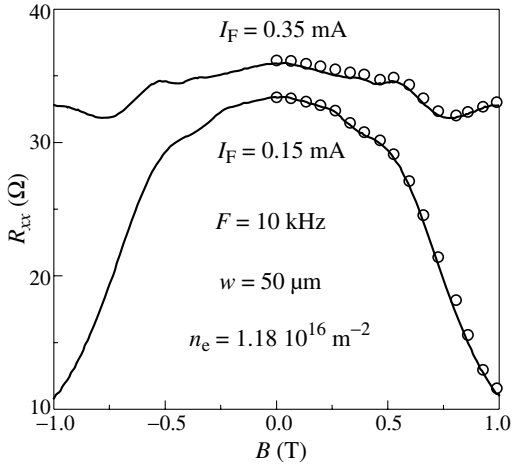

Fig. 3. Measured magnetoresistance R_{xx} at two different levels of ac excitations as labeled (solid lines). Calculated magnetoresistance obtained from the dc biased measurements (opendots).

where $R_{xx}(I_F)$ is a resistance of the sample, which depends on the external ac current $I_F = I_0 \cos(2\pi Ft)$, where I_0 is amplitude of the acexcitation. One can expand the resistance $R_{xx}(I_F)$ in a sum of all possible harmonics (iF) of the external ac current:

$$R_{xx}(I_F) = \sum_i R_i(I_0) \cos(i 2\pi Ft) \,, \qquad (2)$$

where $R_i(I_0)$ is a Fourier component of the $R_{xx}(I_F)$ at a frequency iF and $i = 0,\ 1,\ 2,\ \ldots$ is an integer.

The lockin amplifier locked at frequency 888 Hz measures exclusively the zero frequency ($i = 0$) harmonic R_0, because only the R_0 provides a term oscillating at frequency 888 Hz in Eq. (1). Thus to find the resistance $R_{xx}(B)$ at magnetic field B one has to obtain the zero frequency harmonic of the $R_{xx}(I_0, B)$:

$$R_0(B) = \frac{1}{T} \int R_{xx} \left[I_0 \cos(2\pi Ft) dt \right] \,, \qquad (3)$$

where $T = 1/F$ is a period of the ac excitation.

In order to perform the integration in Eq. (3), we need to know the dependence of the resistance R_{xx} on the driving current I. This is done at zero frequency (dc case). Calculated resistance R_{xx} is presented in Fig. 3 (circles) as a function of the magnetic field at two different amplitudes of the acexcitation. Measured dependencies of the resistance R_{xx} on magnetic field at two different amplitudes of the external ac excitations are also shown in the figure for comparison (solid lines). We note that there are no adjusting parameters between measured and calculated curves.

Similar results are obtained at 100 kHz frequency. The agreement indicates a valid approach for interpretation of the ac induced oscillations of the longitudinal conductivity at low frequency of the ac excitations.

Summary

Effect of dc and low frequency ac excitations on longitudinal resistance of the two-dimensional electron gas in highly doped GaAs quantum wells is studied. A strong, periodic (in inverse magnetic field oscillations) of the resistance is found in the dc biased samples. The position of the oscillation maximums is found to be proportional to the dc density. Similar oscillations are observed with ac excitations applied to the samples at the frequencies 10 kHz and 100 kHz. We have shown that the resistance oscillations observed at frequency below 100 kHz are due to the nonlinear response of the dc biased 2D electron systems.

Acknowledgements

This work was supported by NSF Grants No. DMR 0349049, No. DOE-FG02-84-ER45153, INTAS Project No. 03-51-6453, and RFBR Projects No. 04-02-16789, No. 06-02-16869.

References

[1] M. A. Zudov *et al*, *Phys. Rev. B* **64**, 201311(R) (2001).
[2] C. L. Yang *et al*, *Phys. Rev. Lett.* **89**, 076801 (2002).
[3] R. G. Mani *et al*, *Nature (London)* **420**, 646 (2002).
[4] M. A. Zudov *et al*, *Phys. Rev. Lett.* **90**, 046807 (2003).
[5] S. I. Dorozhkin, *Pis'ma v ZhETF* **77**, 681 (2003).
[6] A. A. Bykov *et al*, *Pis'ma v ZhETF* **81**, 357 (2005).
[7] J. H. Smet *et al*, *Phys. Rev. Lett.* **95**, 116804 (2005).

14th Int. Symp. "Nanostructures: Physics and Technology"
St Petersburg, Russia, June 26–30, 2006

Interaction correction to the conductivity of 2D electron gas in the diffusion regime

A. V. Germanenko[1], G. M. Minkov[2], O. E. Rut[1], A. A. Sherstobitov[2], V. A. Larionova[1], A. K. Bakarov[3] and B. N. Zvonkov[4]

[1] Institute of Physics and Applied Mathematics, Ural State University, 620083 Ekaterinburg, Russia
[2] Institute of Metal Physics RAS, 620219 Ekaterinburg, Russia
[3] Institute of Semiconductor Physics RAS, 630090 Novosibirsk, Russia
[4] Physical-Technical Research Institute, University of Nizhni Novgorod, 603600 Nizhni Novgorod, Russia

Abstract. An electron-electron ($e-e$) interaction correction to the conductivity of two-dimensional (2D) electron gas in $Al_xGa_{1-x}As/GaAs/Al_xGa_{1-x}As$ and $GaAs/In_x\ Ga_{1-x}As/GaAs$ single-quantum-well heterostructures is studied. We have shown that the $e-e$ interaction contributes to σ_{xx} only, while the contribution to σ_{xy} is equal zero. The experimental value of the diffusion correction is equal to $-K_{ee}\,G_0\,\ln\left[1/(T\tau)+1\right]$. It is shown that the interaction correction does not include the temperature independent term $-K_{ee}G_0\ln(E_F\tau)$.

The temperature and magnetic field dependences of the resistivity of the degenerated two dimensional gas at low temperatures are determined by the quantum corrections to the conductivity. They are the interference correction and the correction caused by the electron-electron interaction. As a rule, the interaction correction is the main in classically strong magnetic field, $\mu B \geq 1$ (μ is the mobility).

In the diffusion regime, $T\tau \ll 1$, where τ is the transport relaxation time, the $e-e$ interaction contributes to σ_{xx} and does not to σ_{xy} [1]:

$$\sigma_{xx} = \frac{en\mu}{1+\mu^2B^2} + \delta\sigma_{ee}\,, \quad \sigma_{xy} = \frac{en\mu^2B}{1+\mu^2B^2}\,, \qquad (1)$$

where n stands for the electron density. The interaction correction $\delta\sigma_{ee}$ logarithmically depends on the temperature and does not depend on the magnetic field. In [1,2,3] this correction is written as

$$\delta\sigma_{ee} = K_{ee}G_0\ln T\tau\,, \qquad (2)$$

where $G_0 = e^2/2\pi^2\hbar$, and $K_{ee} = 1+3\left(1-\ln(1+F_0^\sigma)/F_0^\sigma\right)$, F_0^σ is the Fermi-liquid constant. In the same time the authors of [4] underlined that the argument in the logarithm should include the Fermi energy, E_F:

$$\delta\sigma_{ee} = K_{ee}G_0\ln\frac{T}{E_F}\,. \qquad (3)$$

It is easy to see that the difference between Eqs. (2) and (3) is equal to $K_{ee}G_0\ln(E_F\tau) = K_{ee}G_0\ln(k_Fl/2)$, that for systems with $k_Fl \gg 1$ can be not so very small.

The aim of this paper is to study the interaction correction in the diffusion regime experimentally and to clarify how the $\ln(E_F\tau)$-terms contributes to the conductivity.

We investigated the conductivity and the Hall effect in single-quantum-well heterostructures with δ-doped barriers of two types, $Al_{0.3}Ga_{0.7}As/GaAs/Al_{0.3}Ga_{0.7}As$ (structure T1520) and $GaAs/In_{0.2}Ga_{0.8}As/GaAs$ (structure 3510), up to $B = 5$ T within the temperature range from 0.4 to 25 K. The samples were mesa etched into standard Hall bars. To change the electron density in the structure T1520, an Al gate electrode was deposited by thermal evaporation onto the cap layer. The electron density in the structure 3510 was controlled through the illumination due to the persistent photoconductivity effect.

Figure 1 shows typical magnetic field dependences of ρ_{xx} and ρ_{xy} measured at different temperatures for the structure T1520. One can see that following the sharp magnetoresistance in low magnetic field evident at $B < 0.05$ T, which results from the suppression of the interference quantum correction, the parabolic-like negative magnetoresistance against the background of the Shubnikov–de Haas oscillations is observed [Fig. 1(a)]. The parabolic-like behavior of ρ_{xx} weakens with the increasing temperature. The transverse magnetoresistance ρ_{xy} slightly decreases in magnitude with the increasing temperature [Fig. 1(b)].

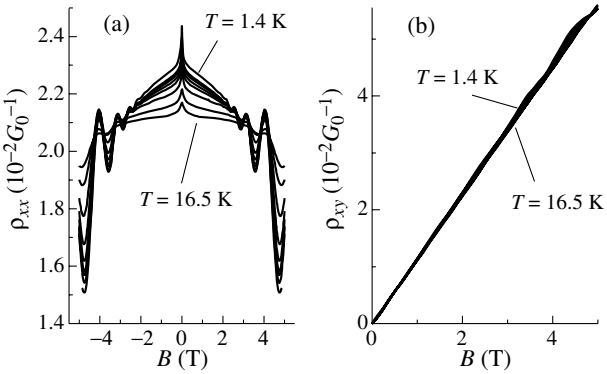

Fig. 1. The magnetic field dependences of ρ_{xx} (a) and ρ_{xy} (b) measured for different temperatures for $V_g = -3.7$ V, $n = 7.15\times10^{11}$ cm^{-2}. Structure T1520. The temperature for curves are: 1.4, 2.0, 2.5, 3.0, 4.2, 6.2, 9.0, 13.0, 16.5.

First of all, we have ascertained that Eqs. (1) work in our situation. We have inverted the resistivity tensor and analyzed the experimental temperature dependence of σ_{xx} and σ_{xy} at high enough magnetic field where the interference correction is significantly suppressed. It has been really found that the σ_{xx} component logarithmically depends on the temperature while σ_{xy} is practically constant. The slope of the σ_{xx}-vs-ln T dependence corresponds to $K_{ee} = 0.4-0.5$ for different gate voltages.

The absolute value of $\delta\sigma_{ee}$ has been obtained from analysis of the curvature of the parabolic-like negative magnetoresistance. It follows from Eq. (1) that the longitudinal magnetoresistance should have the form

$$\rho_{xx}(B,T) \simeq \frac{1}{en\mu} - \frac{1}{(en\mu)^2}\left(1-\mu^2B^2\right)\delta\sigma_{ee}\,. \qquad (4)$$

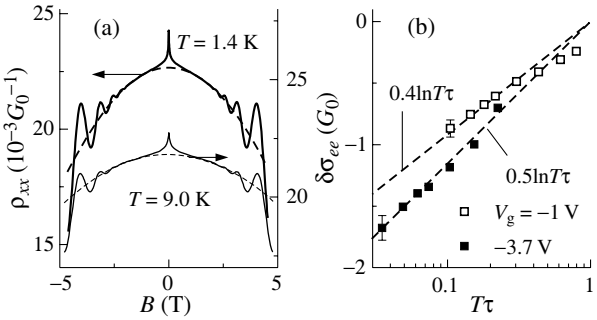

Fig. 2. (a) — The parabolic-like magnetoresistance for different temperatures for $V_g = -3.7$ V, structure T1520. Solid curves are the experimental data. Dashed curves are the fit by Eq. (4). (b) — The temperature dependences of $\delta\sigma_{ee}$. Symbols are the experimental results obtained from treating of ρ_{xx}-vs-B curves. Dashed lines are Eq. (2).

Thus, fitting the experimental ρ_{xx}-vs-B curve for a given temperature by Eq. (4) one can find the value of interaction correction $\delta\sigma_{ee}$. As Fig. 2(a) shows Eq. (4) excellently describes the experimental data. The temperature dependences of $\delta\sigma_{ee}$ found for two gate voltages in such a way are presented in Fig. 2(b). One can see that they are really close to the logarithmic one in accordance with Eqs. (1) and (2). The slopes of these dependences correspond to $K_{ee} \simeq 0.4$ and 0.5 for $V_g = -3.7$ V and -1 V, that coincides with the K_{ee}-values obtained from the temperature dependence of σ_{xx}.

Let us compare experimental results with theoretical predictions [1, 2, 3] and [4] (see Fig. 3). Dashed and dotted lines in this figure are drown according to Eqs. (2) and (3), respectively. Obviously, it is not needed to involve the $\ln(E_F\tau)$-term to describe the experimental results. Taking into account the experimental error, one can conclude that any temperature independent contribution that might exist in $\delta\sigma_{ee}$ is lower than $(0.1-0.2)\,G_0$.

Although the accordance between the experimental results and Eq. (2) is good on the whole, the divergence is clearly seen at $T\tau > 0.3$ (see Figs. 2(a) and 3). We have found that the agreement can be improved if one replaces the argument $1/(T\tau)$ in logarithm in Eq. (2) by $1/(T\tau)+1$ that removes the divergence of diffusion contribution with $T\tau$-increase:

$$\delta\sigma_{ee} = -K_{ee}G_0 \ln\left(\frac{1}{T\tau} + 1\right). \qquad (5)$$

After such modification the agreement with the experimental data becomes excellent within entire $T\tau$-range (see solid lines in Fig. 3).

Thus, the experimental value and the temperature dependence of the interaction correction in the diffusion regime is well described by Eq. (2). This correction does not include the temperature independent term $-K_{ee}G_0 \ln(E_F\tau)$. Just the correction given by Eq. (2) contributes to σ_{xx} and does not to σ_{xy} and namely this term is figured experimentally out. The term $-K_{ee}G_0 \ln(E_F\tau)$ contributes both to σ_{xx} and to σ_{xy}. In fact, it renormalizes the mobility, and, thus, does not influences the curvature of the parabolic-like negative magnetoresistance. The good accordance between the theory and experiment in the entire $T\tau$-range including non-diffusion regime $T\tau \sim 1$ is achieved with the use of modified expression, Eq. (5).

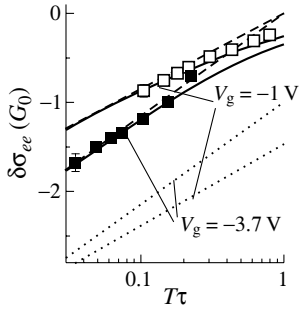

Fig. 3. The $T\tau$-dependence of $\delta\sigma_{ee}$. Symbols are the experimental data. Dashed and dotted lines correspond to Eqs. (2) and (3), respectively. Solid lines are the improved formula for $\delta\sigma_{ee}$, Eq. (5).

Acknowledgements

This work was supported in part by the RFBR (grants 04-02-16626, 05-02-16413, and 06-02-16292) and the CRDF (grant Y1-P-05-11).

References

[1] B. L. Altshuler and A. G. Aronov in *Electron-Electron Interaction in Disordered Systems*, Edited by A. L. Efros and M. Pollak (North Holland, Amsterdam), 1985.

[2] A. M. Finkelstein, *Zh. Eksp. Teor. Fiz.* **84**, 168 (1983).

[3] C. Castellani, C. Di Castro, P. A. Lee and M. Ma, *Phys. Rev. B* **30**, 527 (1984); **30**, 1596 (1984); C. Castellani, C. Di Castro and P. A. Lee, *ibid*, **57**, 9381(R) (1998).

[4] G. Zala, B. N. Narozhny and I. L. Aleiner, *Phys. Rev. B* **64**, 214204 2001.

14th Int. Symp. "Nanostructures: Physics and Technology"
St Petersburg, Russia, June 26–30, 2006

Tunnel density of states at the Fermi level in the two-dimensional electron system of the delta-doped layer in GaAs

I. N. Kotel'nikov[1], E. M. Dizhur[2], A. N. Voronovskii[2] and S. E. Dizhur[1]

[1] Institute of Radioengineering and Electronics of the RAS, Moscow 125009, Mokhovaya St. 11/7, Russia
[2] Institute for High Pressure Physics of the RAS, Troitsk, Moscow Region 142190, Russia

Abstract. Tunnel junctions Al/delta-GaAs were studies of different electron concentration in the two-dimensional electron system of the delta-layer. The amplitude of the zero bias anomaly was shown to increase substantially as the concentration decreases. This behavior may be attributed to decreasing density of states at the Fermi level due to the enhancement of the interelectron interaction in the diffusion channel of the delta-layer as soon as the latter approaches to the state of metal-insulator transition.

Introduction

Delta-doping of GaAs with Si donors of $> 10^{12}$ cm^{-2} area density enables to realise a two-dimensional electron system (2DES) in which metallic type of conductivity at low temperatures is defined by relatively high Fermi energy (scores of meV) and by the momentum scattering at charged impurities in the δ-layer (h/τ of 1 meV order). As the δ-layer approaches the metal-GaAs interface, the electrons transfer to the surface states and the concentration n_{2D} of the free carriers decreases, conditioning the carrier localization in the self-consistent potential well of the δ-layer. Due to this the transition from the weak localization to the strong one was observed in the δ-layer GaAs structures at lowering temperature below $T_0 \simeq 2.6$ K [1] as well as pressure induced metal-insulator transition in a tunnel structure Al/δ-GaAs [2] at $T = 4.2$ K. The latter structure allowed not only to measure the lateral transport in the δ-layer but also to analyse the effects of density of states (DOS) and many-body effects in the 2DES using tunnelling spectroscopy technique. For the case when dephasing time constant τ_φ for the electrons in a diffusion channel of a 2DES is defined, say, by interelectron collisions the theory [3] predicts the drop of the DOS at the Fermi level. As n_{2D} decreases and the localization increases (change to the hopping regime of conductivity in the 2DES occurs), a weak singularity at the Fermi level may transform to the "soft" Coulomb gap [4]. Tunnelling is one of rare experimental techniques that allows to reveal singularities in the DOS at the Fermi-level. Here we present the variation of the tunnelling DOS in the 2DES of the near-to-surface δ-layer with n_{2D} decrease due to the technological parameters change during the fabrication of the Al/δ-GaAs structures as well as by high pressure tuning of n_{2D}. The latter case is concerned with the n_{2D} variation in the same sample as a consequence of the pressure induced barrier growth at the Al/GaAs interface and electron trapping by the DX-centers.

Experiment and Results

The samples of Al/δ-GaAs structure under study were fabricated in IRE of the RAS using MBE technique described elsewhere [5]. The separation of the interface from the Si δ-doped layer was about $\sim$ 20 nm. The tunnelling spectra of the Al/δ-GaAs structures were held at 4.2 K. As a representation of the tunnelling spectrum (TS) the dependence of the logarithmic derivative $S = d\ln\sigma/dU$ of the tunnelling conductivity $\sigma = dI/dU$ with respect to the bias voltage U was used. As is known [6], the tunnelling conductivity in the case of tunnelling from 3D to 2D states is proportional to the DOS $\rho_i(E)$ of the 2DES, $\sigma(U) \propto \sum_i D_i(U)\rho_i(U)$, $D_i(U)$ being the tunnelling transparency for the level E_i. High quality of the tunnel junction Al/δ-GaAs is well seen on Fig. 1a, where the nearest to the Fermi level $E_{F\delta}$ ($U = 0$) filled ($E_{0F} < 0$) and empty ($E_{1F} > 0$) quantum confinement subbands are revealed. These subbands $E_{iF} = E_i - E_{F\delta}$ may be retrieved from the TS [5] while $|E_{0F}| = 21$ meV is the Fermi energy of the 2DES. The features due to the LO-phonons and the Zero Bias Anomaly (ZBA), corresponding to the dip in σ at $U = 0$, are also well resolved. Non-parametric smoothing cubic spline approximation was used to extract background S_{bkg} and ZBA and phonon lines from the tunnelling spectra S. The procedure implied the background extraction from the spectrum $S(U)$ suppressing the contribution of the bias regions containing the ZBA and the phonon singularities, by the weight matrix, and correspondingly promoting the singularities to be extracted [7]. The ZBA line ΔS_{zba} accepted to be the difference $\Delta S = S - S_{bkg} = d(\ln\sigma - \ln\sigma_{bkg})/dU$.

Assuming that $\sigma = \Delta\sigma_{zba} + \sigma_{bkg}$ near $U = 0$, where $\Delta\sigma_{zba}$ reflects the change of the DOS at the Fermi level due to the diffusion character of electron movement within the δ-layer plane, one obtains $\Delta S = d(\ln(1 + \Delta\sigma_{zba}/\sigma_{bkg}))/dU$. Therefore, integrating ΔS over dU gives the dependence of $\ln(1 + \Delta\sigma_{zba}/\sigma_{bkg}) = \ln(1 + \Delta\rho_0/\rho_{bkg})$ on U. Following this assumption, the value of $\Delta\rho_0/\rho_{bkg}$ at $U = 0$ corresponds to the dip in the DOS at the Fermi level. It is worth mentioning that tunnelling measurements for sample #4 in Table at $T = 0.3$ K, presented on insert in Fig. 1, show the superconducting gap in the Al gate. The TS were obtained for 7 different samples

Table 1.

Sample	E_{0F} (meV)	E_{1F} (meV)	E_{2F} (meV)	$R_0 s$ (Ω cm^2)
#1	−61	−7.5	28	13
#2	−35	18	54	123
#3	−33	12	45	55
#4/4*	−21/−24	18/11.5	44/24.5	25
#5	−21	36	76	308
#6/6*	−11/−13	19/8.6	40/21	6300
#7*	20	52	?	900

enlisted in Table at normal pressure and (sample #3) at hydrostatic pressure up to $\sim$ 2.0 GPa [2]. The energies of three

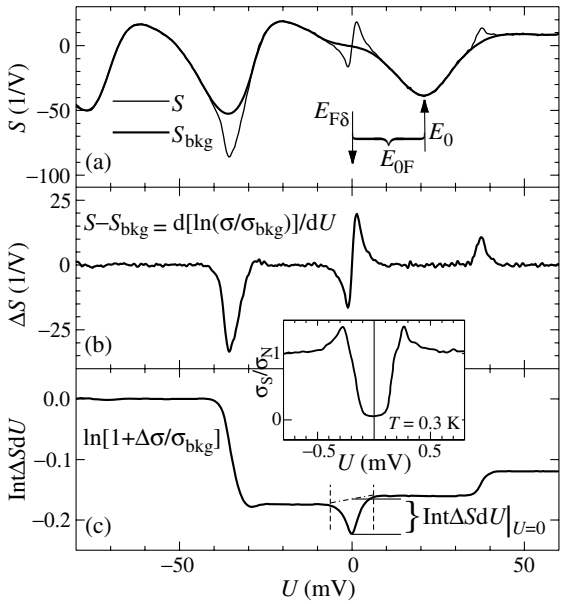

Fig. 1. a) The tunnelling spectra $S(U)$ and background $S_{\rm bkg}(U)$ for Al/δ-GaAs sample; b) the result of background extraction $\Delta S(U)$ and c) the integral of $\Delta S(U)$ over dU gives the dependence of $\ln(1+\Delta\rho_0/\rho_{\rm bkg})$ on U. The insert shows the dependence $\sigma_{\rm S}/\sigma_{\rm N}$ on U, where $\sigma_{\rm N}$ and $\sigma_{\rm S}$ are tunnelling conductances in normal and superconducting states of Al-electrode, respectively.

low levels $E_{i\rm F}$ of these samples, found from the TS [5], are cited in Table. The energies of 2D-subbands in δ-layer can be changed by persistent tunnelling photoconductivity (PTPC) effect (marked "*") [8].

Fig. 2 shows the dependence of $\ln(1+\Delta\rho_0/\rho_{\rm bkg})_{U=0}$, representing the dip in the DOS at the Fermi level, on the energy position $E_{0\rm F}$ for all the samples from Table together with the high pressure data (sample #3). The both dependencies show substantial deepening of the dip in DOS ($(\Delta\rho_0/\rho_{\rm bkg})_{U=0} \simeq -0.3$) when approaching metal-insulator transition. In high pressure experiments it corresponds to the pressure value $P \approx 2$ GPa ($E_{0\rm F} \simeq 25$ meV) [2], and for set of samples studied at ambient pressure, — to the rightest point corresponding to sample #7*, for which the lateral resistance of the δ-layer R_δ cooled in the dark exceeded 10^8 Ω. We could measure its TS

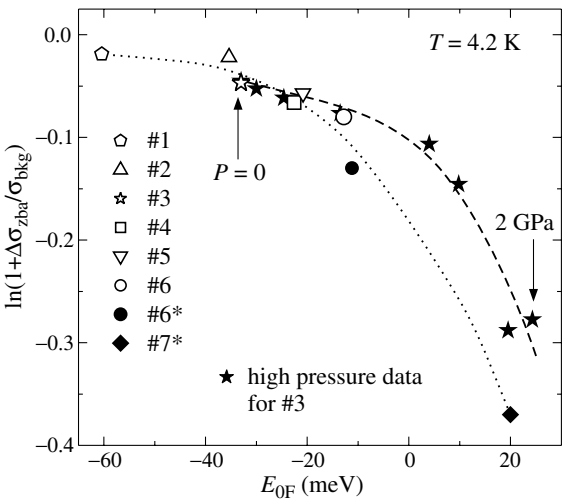

Fig. 2. The dependence of tunnel DOS $(\Delta\rho_0/\rho_{\rm bkg})_{U=0}$ at Fermi level on the lowest subband position $E_{0\rm F}$ in 2DES.

only in PTPC regime, when R_δ dropped down to 0.5×10^6 Ω per square and became comparable with R_δ of sample #3 at 2 GPa which presumably corresponds to the hopping regime of conductivity along the δ-layer [2]. For that high resistivity, the Fermi level in the potential well formed by the δ-doping should fall down to the region of the lower tail in the DOS of quantum confinement level E_0, whose halfwidth ΔE_0 in our samples is in the range from 5 meV (sample #5) to 10 meV (#3) [9]. This is indicated by positive values of $E_{0\rm F}$, obtained for sample #7 and for #3 under pressures above ~ 1.6 GPa. So, $E_{0\rm F}$ must not to be proportional to $n_{2\rm D}$ when $0 < E_{0\rm F} < \Delta E_0$.

Conclusion

To our knowledge, the data presented on Fig. 2 show that in the proximity of the metal-insulator transition in near-to-surface δ-doped layer, the dip in the tunnelling DOS at the Fermi level of 2DES reaches considerable value $(\Delta\rho_0/\rho_{\rm bkg})_{U=0} \simeq -0.3$ even at as high temperature as $T = 4.2$ K. The measurements of TS of samples ##1, 2, 5 at $T = 1.6$ K show additional deepening of the drop by 20… 30% in comparison with 4.2 K. It allows to hope for the possibility to observe a soft Coulomb gap in the samples of structure similar to sample #7 at $T < 1.6$ K. A weak dependence of the singularity (ZBA) at the Fermi level on magnetic field seen in our samples [10], may indicate an interaction between the electrons as the most probable origin of this singularity in the tunnelling DOS of the 2DES in the δ-doped layer.

Acknowledgements

This work is supported by RFBR, Presidential program of State support of leading Scientific Schools and by programs of RAS. The authors thank V. N. Trofimov for his help in low-temperature measurements, Yu. V. Fedorov and A. S. Bugaev for preparation of the samples and M. N. Feiginov.

References

[1] Yu. Havin *et al*, *Phys. Rev. B.* **58**, 8009 (1998).
[2] E. M. Dizhur *et al*, *JETP Lett.* **80**, 433 (2004).
[3] B. I. Altshuler, A. G. Aronov, *Electron-electron interaction in disordered conductors, in Electron-electron interaction in disordered systems* (North-Holland), 1985.
[4] A. L. Efros *et al*, *J. Phys.* **C12**, 1023 (1979).
[5] I. N. Kotel'nikov *et al*, *JETP Lett.* **71**, 387 (2000).
[6] E. L. Wolf, *Principles of Electron Tunneling Spectroscopy* (Oxford Univ. Press, Oxford), 1985.
[7] E. M. Dizhur and A. V. Fedorov, *Instr. and Exp. Tech.* **48**, N4 455 (2005).
[8] S. E. Dizhur *et al*, *PLDS* **11/12**, 233 (2001).
[9] I. N. Kotel'nikov *et al*, *Semicond.* **40**, N7 (2006), to be published.
[10] S. E. Dizhur *et al*, *Proc. of 26th Int. Conf. of Phys. and Semicond. (Edinburgh, Scotland, UK, 2002)*, IOP Publishing, IOP Series 171, P158, 2002.

14th Int. Symp. "Nanostructures: Physics and Technology"
St Petersburg, Russia, June 26–30, 2006

The transparent case of the metallic-like temperature dependence of the conductivity in 2D system

G. M. Minkov[1], A. V. Germanenko[2], O. E. Rut[2], A. A. Sherstobitov[1], L. E. Golub[3] and B. N. Zvonkov[3]

[1] Institute of Metal Physics RAS, 620219 Ekaterinburg, Russia
[2] Ural State University, 620083 Ekaterinburg, Russia
[3] Ioffe Physico-Technical Institute, St Petersburg, Russia
[4] Physical-Technical Research Institute, University of Nizhni Novgorod, 603600 Nizhni Novgorod, Russia

Abstract. The temperature and magnetic field dependences of the conductivity of the p-type InGaAs quantum well structures with In gradient are studied. We have shown that metallic-like temperature dependence of the conductivity observed in the structures investigated is understandable quantitatively within whole temperature range. At $0.4 < T < 1.5$ K it is due to weak localization at fast spin relaxation, at $1.5 < T < 4$ K it is due to *e-e* interaction in ballistic regime and at $T > 5$ K it is due to the phonon scattering.

The transport properties of two dimensional (2D) systems reveal the intriguing features. One of the feature is a metallic-like temperature dependence of the resistivity at low temperature for some kind of 2D systems: $\partial\sigma/\partial T < 0$. It is strange because the quantum correction to the conductivity (the weak localization (WL) and the interaction corrections) lead to dielectric ($\partial\sigma/\partial T > 0$) temperature dependence of the conductivity of 2D systems. As a rule metallic-like behavior is observed in the structures with strong hole-hole (*h-h*) interaction characterized by large value of the parameter $r_s = \sqrt{2}/(a_B k_F)$, where a_B and k_F are the Bohr radius and Fermi quasimomentum, respectively. Up to now there is not conventional opinion whether the metallic-like temperature dependence of the conductivity attests on quantum phase transition or it results from the quantum corrections to the conductivity.

From other hand, the conventional theories of the quantum corrections predict that the sign of the $(d\sigma/dT^{WL})$ depends on interrelation between the spin relaxation rate $1/\tau_s$ and the phase relaxation rate $1/\tau_\phi$. At $\tau_s/\tau_\phi < 1$ the sign of $\partial\sigma/\partial T^{WL}$ is negative. The *e-e* correction may change sign also at transition to the ballistic regime. Thus, in the framework of the conventional theories $\sigma - vs - T$ dependence may reveals the metallic-like behavior in the 2D systems with strong spin-orbit interaction at $T\tau \simeq 1$.

In this report we have experimentally study the transport in the hole 2D system GaAs/InGaAs/GaAs with asymmetric doping which leads to fast spin relaxation due to Bichkov–Rashba mechanism. The heterostructures were grown by metal-organic vapor phase epitaxy on semi-insulator GaAs substrate. The structures consist of a 0.2 μm-thick undoped GaAs buffer layer, a 7 nm $In_{0.2}Ga_{0.8}As$ well, a (6–7) nm spacer of undoped GaAs, a C δ-layer and 200 nm cap layer of undoped GaAs. The samples were mesa etched into standard Hall bars and then an Al gate electrode was deposited by thermal evaporation onto the cap layer through a mask. The hole density was $(7.5-4)\times10^{11}$ cm^{-2} and mobility was (8000–4000) cm^2/V s for different structures and gate voltages.

At high hole density the structures investigated show the metallic-like temperature dependence of the conductivity at $B = 0$ which changes to dielectric one ar decreasing the hole density. The studies of low- and high magnetic field dependences of the conductivity show that in structure investigate there is not universal mechanism which leads to metallic-like temperature dependence of the conductivity. There are tree different mechanisms, namely: weak localization, interaction and phonon scattering, each give main contribution within different temperature ranges.

Acknowledgements

This work was supported in part by the RFBR Grants and Grant of the President of RF MK-1778.2005.2.

14th Int. Symp. "Nanostructures: Physics and Technology"
St Petersburg, Russia, June 26–30, 2006

Magnetotransport properties of high-mobility two-dimensional electron gas on cylindrical surface

A. B. Vorob'ev[1,2], K.-J. Friedland[1], H. Kostial[1], R. Hey[1], Ju. S. Yukecheva[2], U. Jahn[1], E. Wiebicke[1] and V. Ya. Prinz[2]

[1] Paul-Drude-Institut für Festkörperelektronik, D-10117 Berlin, Germany
[2] Institute of Semiconductor Physics, 630090 Novosibirsk, Russia

Abstract. Structures with a high-mobility two-dimensional electron gas (2DEG) on cylindrical surface were fabricated. A strong asymmetry of the longitudinal magnetoresistance of the cylindrical 2DEG was revealed in the case of diffusive transport regime in perpendicular magnetic field. A ballistic electron waveguide uniformly bent in the confinement direction was realized.

Introduction

Two-dimensional electron gas (2DEG) in planar heterostructures has been under a great deal of investigations finally resulting in the discovery of a number of remarkable quantum phenomena. Non-planar low-dimensional systems are fundamentally new physical objects that have attracted considerable attention in recent years. The energy spectrum of 2D systems on cylindrical surfaces and their magnetotransport properties in ballistic regime were theoretically predicted [1]. Spin polarization of electrons was predicted to arise in nanotubes containing 2DEG placed in a perpendicular magnetic field [2]. Experimentally, non-planar surfaces with 2DEG were fabricated by means of molecular-beam epitaxy (MBE) on prepatterned substrates [see, e.g., 3]. A disadvantageous feature of such structures is that the surface curvature in them fluctuates considerably, making the effect of surface curvature on the magnetotransport phenomena in such structures too difficult to examine. Lorke *et al* studied magnetotransport in curved 2DEG of 1.1 mm radius [4]; in this study, a sample fully processed in Hall-bar geometry was released from the "native" GaAs substrate using the "epitaxial lift-off" method and then manually transferred on a glass tube. This manual preparation technique hardly allows decreasing curvature radius of the 2DEG below 1 mm.

The problem of fabrication of contacted 2DEG on cylindrical surface of small curvature radius is the main obstacle for experimental studies in this promising field. The strain-induced, three-dimensional micro- and nanostructuring [5] allowed us to fabricate free-standing objects of cylindrical shape with a constant radius of curvature, including modulation-doped GaAs/AlGaAs [6–8] and InAs/InGaAs [9] quantum wells (QW) rolled up in microtubes and containing cylindrical 2DEG of good spatial uniformity.

A method for directional rolling of lithographically-patterned multi-layered strained film was developed to fabricate three-dimensional free-standing objects of complicated shapes [10], which was necessary for obtaining contacted 2DEG on cylindrical surface. The directional rolling method was used to obtain cylindrical 2DEG contacted in two-probe [6, 7] and Hall-bar [8] configurations. Mendach *et al* later used similar technique to prepare contacted curved 2DEG [11]. The common draw back of the free-standing structures based on (Al,Ga,In)As is the additional surface located close to the 2DEG, usually resulting in depletion of carriers and degradation of the mobility. Here, we present the fabrication of a high-mobility cylindrical 2DEG, based on GaAs quantum wells with spacers consisting of AlAs/GaAs short-period superlattices (SPSL), where heavy-mass X-electrons gather in the direct vicinity of dopant atoms, which screening the fluctuating potential of randomly distributed ionized Si donors, thus effectively reducing the remote impurity scattering of electrons in the high-mobility 2DEG [12]. These X-electrons also screen the free-standing 2DEG from surface states.

1. Fabrication of the high-mobility cylindrical 2DEG

The multi-layered heterostructure was pseudomorphically grown on a GaAs (100) substrate by MBE; it included a 50-nm thick AlAs sacrificial layer and a strained multi-layered film with a nominal thickness of 192 nm to be released from the substrate. The multi-layered film contained a 20-nm-thick $In_{0.15}Ga_{0.85}As$ stressor and a central 13-nm-thick GaAs QW cladded with δ-doped AlAs/Gas SPSL-spacers that contained the 2DEG. In the initial flat structure the electron mobility along the $[01\bar{1}]$ direction was 118 $m^2/V\,s$ and the sheet density was 7.1×10^{15} m^{-2}. Being detached from the substrate by selective etching of the sacrificial layer in the preset direction, the lithographically prepatterned film rolled up in tubes with a visible outer curvature radius of 24 μm. The resulting structure allowed us to obtain an appropriate system for studying the magnetotransport of high mobility 2DEG on cylindrical surfaces (Fig. 1).

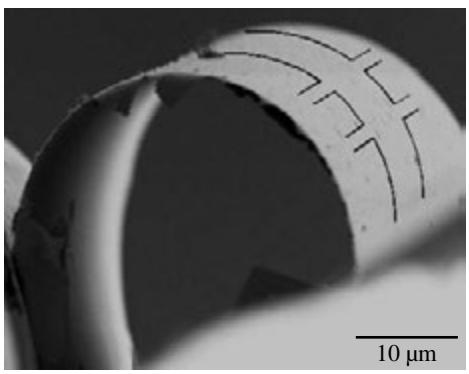

Fig. 1. Cross-sectional SEM image of the rolled-up film. The position of the Hall-bar for magnetotransport measurements is shown schematically.

2. Asymmetric magnetoresistance and ballistic transport

The local motion of electrons in a cylindrical 2DEG is governed by the normal-to-surface component of the magnetic field vector. As a result, cylindrical 2DEGs enable a 2D electron system in an effectively inhomogeneous magnetic field with a spatial dependence defined by the angle φ between the surface normal and the field: $B = B_0 \cos(\varphi)$. A strongly asymmetric longitudinal magnetoresistivity in the diffusive transport regime has been revealed in the cylindrical 2DEG placed in the perpendicular magnetic field. Longitudinal magnetoresistivities for different directions of the magnetic field was found to differ by a factor of 1000. This asymmetric longitudinal magnetoresistance was recognized as a manifestation of the recently predicted static skin effect for a 2DEG placed in an inhomogeneous magnetic field due to an exponential dependence of current density on the transverse coordinate [13].

Interesting features of this asymmetry in the longitudinal magnetoresistance are: (1) high sensitivity of this asymmetry to even slightest misalignments of the rolled-up sample from the symmetric position with respect to the magnetic field vector; (2) zero (within the experimental inaccuracy) value of the longitudinal magnetoresistance in classical magnetic fields. A clear indication for the ballistic transport in the rolled-up 2DEG was observed [14]; thus, a two-dimensional ballistic electron waveguide uniformly bent in the confinement direction was realized. On the length of mean free path the deflection of the waveguide from the planar position is approximately 20 times more than the width of the QW.

In summary, we fabricated high-mobility 2DEG on cylindrical surface and studied its magneto-transport properties for azimuthal direction of the current. A strong magnetoresistance asymmetry was observed and explained as a manifestation of the static skin effect. A ballistic electron waveguide uniformly bent in the confinement direction was realized.

Acknowledgements

One of the authors (A. V.) appreciates the support provided by INTAS (Grant No. 04-83-2575) and by the Russian Science Support Foundation.

References

[1] L. I. Magarill *et al*, *Jpn. J. Appl. Phys.* **78**, 1870 (2001).
[2] A. Kleiner, *Phys. Rev. B*, **67**, 155311 (2003).
[3] M. L. Leadbeater *et al*, *Phys. Rev. B* **52**, R8629 (1995).
[4] A. Lorke *et al*, *Superlatt. and Microstruct.* **33**, 347 (2003).
[5] V. Ya. Prinz *et al*, *Physica E* **6**, 828 (2000).
[6] A. B. Vorob'ev *et al*, *26th ICPS*, Edinburgh, UK 2002, H 118.
[7] A. B. Vorob'ev *et al*, *Physica E* **23**, 171 (2004).
[8] A. B. Vorob'ev *et al*, *12th Int. Symp. "Nanostructures: Physics and Technology", St Petersburg, Russia*, 360 (2004).
[9] A. B. Vorob'ev *et al*, *Jpn. J. Appl. Phys.* **42**, L7 (2003).
[10] A. B. Vorob'ev, V. Ya. Prinz, *Semicond. Sci. Technol.* **17**, 614 (2002).
[11] S. Mendach *et al*, *Physica E* **23**, 274 (2004).
[12] K.-J. Friedland *et al*, *Phys. Rev. Lett.* **77**, 4616 (1996).
[13] A. V. Chaplik, *JETP Lett.* **72**, 503 (2000).
[14] K.-J. Friedland, A. Vorob'ev *et al*, *MS+S2006*, Atsugi, Japan 2006, PMo-13.

14th Int. Symp. "Nanostructures: Physics and Technology"
St Petersburg, Russia, June 26–30, 2006

Bound states in a 2D short range potential induced by spin-orbit interaction

A. V. Chaplik and *L. I. Magarill*

Institute of Semiconductor Physics, Siberian Branch of Russian Academy of Sciences, Novosibirsk, 630090, Russia

Abstract. We have discovered an unexpected and surprising fact: a 2D axially symmetric short-range potential contains an *infinite* number of the levels of negative energy *if one takes into account the spin-orbit (SO) interaction.* For a shallow well ($m_e U_0 R^2/\hbar^2 \ll 1$, where m_e is the effective mass, U_0 and R are the depth and the radius of the well, respectively) and weak SO coupling ($|\alpha| m_e R/\hbar \ll 1$, where α is the SO coupling constant) exactly one twofold degenerate bound state exists for each value of the half-integer moment $j = m + 1/2$, and the corresponding binding energy E_m extremely rapidly decreases with increasing m.

As is well known from any textbook on quantum mechanics a very shallow potential well ($m_e U_0 R^2/\hbar^2 \ll 1$) cannot capture a particle with the mass m_e in 3D case and does this in 2D and 1D situations provided the wells are symmetric: even potential in 1D, axially symmetric well in 2D. In the latter case *the only* negative level corresponds to the s-state ($m = 0$). These statements relate to spinless particles.

During the past few years various effects depending on the spin degree of freedom of electrons have been intensively discussed in literature in connection with a spin transistor, quantum computer and some other applications. Therefore the problem of localized states of charge carriers with accounting for SO interaction becomes quite topical. In the present paper we show that SO interaction in 2D electron gas drastically changes the picture of the bound states formation for a short range axially symmetric potential well $U(r)$: in contrast with the spinless case mentioned above the number of the levels of negative energy becomes infinite.

Consider a 2D electron accounting for the SO interaction in the Bychkov-Rashba form [1]. The Hamiltonian reads:

$$\hat{H} = \frac{\hat{p}^2}{2m_e} + \alpha\left(\boldsymbol{\sigma}\left[\hat{\mathbf{p}} \times \mathbf{n}\right]\right) + U(r)\,, \qquad (1)$$

where r and $\hat{\mathbf{p}}$ are the radius in cylindrical coordinates and the 2D electron momentum operator, respectively, $\boldsymbol{\sigma}$ are Pauli matrices, and $\mathbf{n}$ is the normal to the plane of 2D system.

It is convenient to write down the Schrödinger equation in the $\mathbf{p}$-representation:

$$\left[\frac{p^2}{2m_e} + \alpha\left(\boldsymbol{\sigma}\left[\mathbf{p}\times\mathbf{n}\right]\right)\right]\Psi(\mathbf{p}) + \int \frac{d\mathbf{p}'}{4\pi^2}\mathcal{U}\left(\mathbf{p}-\mathbf{p}'\right)\Psi\left(\mathbf{p}'\right) = \mathcal{E}\Psi(\mathbf{p})\,. \qquad (2)$$

Here $\mathcal{U}(\mathbf{p}) = \int d\mathbf{r} e^{-i\mathbf{pr}} U(r) = 2\pi \int_0^\infty dr\, r U(r) J_0(pr)$ is the Fourier-transform of the potential ($J_0(z)$ is the Bessel function). Because of the axial symmetry of the problem it is possible to separate the cylindrical harmonics of the spinor wave function and search for the solution in the form

$$\Psi^{(m)}(\mathbf{p}) = \begin{pmatrix} \psi_1^{(m)}(p) e^{im\varphi} \\ \psi_2^{(m)}(p) e^{i(m+1)\varphi} \end{pmatrix} \qquad (3)$$

(φ is the azimuthal angle of the vector $\mathbf{p}$). If the conditions $2m_e U_0 R^2/\hbar^2 \equiv \xi \ll 1$ and $|E| \ll m_e\alpha^2$ are fulfilled (U_0, R are the characteristic depth and radius of the well, E is the energy counted from the bottom of continuum, $E = \mathcal{E} + m_e\alpha^2/2$), one can solve Eq. (2) assuming that all the actual momenta are closed to p_0 ("pole" approximation); $p_0 = m_e|\alpha|$ is the radius of the loop of extrema. After rather cumbersome calculations one can get

$$\begin{aligned} E_m &= -(\chi_m + \chi_{m+1})^2/2 \\ &= -\frac{\pi^2 p_0^2 m_e}{2}\left(\int_0^\infty dr r U(r)\left[J_m^2(p_0 r) + J_{m+1}^2(p_0 r)\right]\right)^2 \\ &= -\frac{\pi^2 p_0^2 m_e}{2}\left(\int_0^\infty dr r U(r)\left[J_{j-1/2}^2(p_0 r) + J_{j+1/2}^2(p_0 r)\right]\right)^2, \qquad (4) \end{aligned}$$

where $j = m + 1/2 = \pm 1/2, \pm 3/2, \ldots$ is the z-projection of the total moment. As it is seen from Eq. (4) all levels are two-fold degenerate: E_m is even function of j. If the SO interaction is small ($p_0 R \ll 1$) we can get the asymptotic behavior of the binding energy by expanding the Bessel functions in Eq. (4). For a rectangular well $U(r) = -U_0\theta(R-r)$ we have $|E_m| \propto \alpha^{4|j|}/(2^{4|j|}((|j|-1/2)!)^4(2|j|+1)^2)$. For an exponential well $U(r) = -U_0\exp(-r/R)$ one can find: $|E_m| \propto \alpha^{4|j|}((2|j|)!)^2/(2^{4|j|}((|j|-1/2)!)^4)$.

Thus, we see that in an arbitrary axially symmetric short-range (the integral in Eq. (4) converges) potential well there exists at least one bound state for each cylindrical harmonic with the energy level below the bottom of continuum ($-m_e\alpha^2/2$). The energy of this state E counted from $-m_e\alpha^2/2$ in the regime $|E| \ll m_e\alpha^2$ is proportional to U_0^2, where U_0 is the characteristic depth of the well. Such a dependence is typical for a shallow level in a symmetric 1D potential well. The one-dimensional character of the motion results from the so called "loop of extrema" (see [2]). In a small vicinity of the bottom of continuum the dispersion law of 2D electrons has a form $\mathcal{E}(p) = -m_e\alpha^2/2 + (p-p_0)^2/2m_e$ and corresponds to a 1D particle at least in the sense of the density of states: one may formally consider the problem as the motion of a particle with anisotropic effective mass; in the $\mathbf{p}$-space the radial component of the mass equals m_e, while its azimuthal component is infinitely large (the dispersion law is independent of the angle in $\mathbf{p}$-plane) [3].

We realize that our conclusion looks paradoxical: for a sufficiently large value of m the centrifugal barrier (CB) can

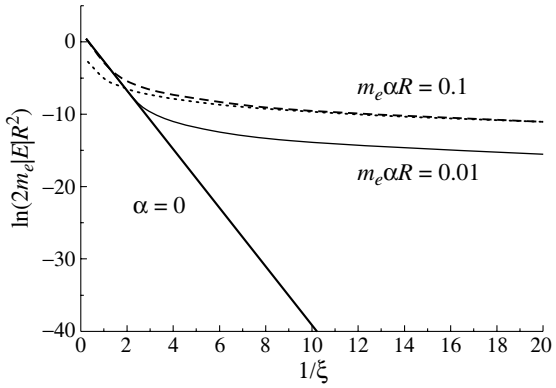

Fig. 1. The behavior of the s-level versus the well depth. The curves demonstrate the transition between 2D and 1D regimes. At $\alpha = 0$ we have an exponentially shallow level (2D result), while for finite α at small enough $\xi \equiv 2m_eU_0R^2$ the binding energy parabolically depends on U_0 (1D regime). The dotted line represents the results of our "pole" approximation (Eq.(4)).

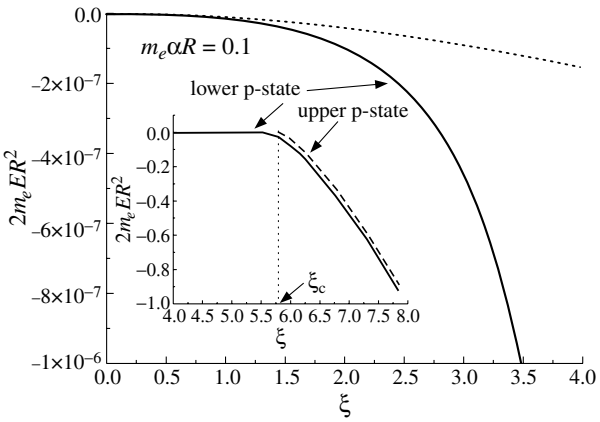

Fig. 2. p-states. Comparison of the exact solution for the square well with Eq. (4) (dotted line). Inset: spin split states of the p-level: the upper curve terminates at $U_0 = U_0^{(c)}$ — the level merges with continuum.

make the effective potential energy $U(r) + U_{CB}$ positive all over the space. How can a bound state with *negative* energy be formed in such a situation? Our arguments are as follows: for a particle with dispersion relation $(p - p_0)^2/2m_e$ there exists no CB; the azimuthal effective mass tends to infinity and CB vanishes.

To check our results, we have numerically analyzed the square well potential $U(r) = -U_0\theta(R - r)$ where θ is the Heaviside function. We seek a solution of the Schrödinger equation in the form

$$\Psi(r, \varphi) = \begin{pmatrix} \psi_1(r)\, e^{im\varphi} \\ \psi_2(r)\, e^{i(m+1)\phi} \end{pmatrix}, \qquad (5)$$

where now φ is the azimuthal angle of the vector $\mathbf{r}$. Spinor components $\psi_{1,2}(r)$ are given by linear combinations of the Bessel functions $J_m(\tilde{\kappa}_\pm r)$, $J_{m+1}(\tilde{\kappa}_\pm r)$ for $r < R$ or $K_m(\kappa_\pm r)$, $K_{m+1}(\kappa_\pm r)$ for $r > R$, where

$$\tilde{\kappa}_\pm = \sqrt{2m_e(E + U_0)} \pm m_e\alpha\,, \quad \kappa_\pm = \sqrt{2m_e|E|} \pm im_e\alpha\,. \qquad (6)$$

Expressions (6) are valid when the condition $E < 0$ is satisfied. Now we have to meet the matching conditions for the wave function and its derivative at $r = R$. After rather cumbersome algebra we arrive at the determinants, zeros of which give the required spectrum of localized states. The energy levels have been estimated numerically for s- and p-states ($m = 0, 1$). The results totaly coincide with the ones given above for $|E| \ll m_e\alpha^2$. Fig. 1 demonstrates this for s-state. The exited p-state at zero SO interaction appears when U_0 exceeds a certain critical value $U_0^{(c)}$, namely, when $\xi > \xi_c = x_1^2$, where x_1 is the first root of the Bessel function $J_0(x)$. Taking SO interaction into account results in the splitting of the p-level and lowering the critical value $U_0^{(c)}$ for the upper of spin-split sublevels. The lower sublevel exists at any value of the parameter ξ (see Fig. 2).

In conclusion, we have shown that 2D electrons interact with impurities by a very special way if one takes into account SO coupling: because of the loop of extrema, the system behaves as 1D one for negative energies close to the bottom of continuum. This results in the infinite number of bound states even for a short-range potential.

Acknowledgements

We thank M. V. Entin for numerous valuable comments and useful discussions. This work has been supported by the RFBR grant No. 05-02-16939, by the Council of the President of the Russian Federation for Support of Leading Scientific Schools (project No. NSh-593.2003.2), and by the Programs of the Russian Academy of Sciences.

References

[1] Yu. A. Bychkov and E. I. Rashba, *JETP Lett.* **39**, 78 (1984).
[2] E. I. Rashba and V. I. Sheka, in *Landau Level Spectroscopy*, ed. by G. Landwehr and E. I. Rashba (Elsevier, 1991), p. 178.
[3] For s-level such a transition to 1D regime has been mentioned by A. G. Galstyan and M. E. Raikh, *Phys. Rev. B* **58**, 6736 (1998).

14th Int. Symp. "Nanostructures: Physics and Technology"
St Petersburg, Russia, June 26–30, 2006

Effect of tensile-strained Si layer on photoluminescence of Ge(Si) self-assembled islands grown on relaxed SiGe/Si(001) buffer layer

M. V. Shaleev[1], *A. V. Novikov*[1], A. N. Yablonskiy[1], O. A. Kuznetsov[2], Yu. N. Drozdov[1], D. N. Lobanov[1] and Z. F. Krasilnik[1]

[1] Institute for Physics of Microstructures RAS, Nizhny Novgorod, Russia
[2] Physical-Technical Research Institute at Nizhny Novgorod State University, Nizhny Novgorod, Russia

Abstract. Photoluminescence (PL) of Ge(Si) self-assembled islands embedding in a tensile-strained Si layer grown on relaxed SiGe/Si(001) buffer layers has been studied. The redshift of the PL peak position from Ge(Si) islands with an increase in thickness of the strained Si layer confirms the model for real-space indirect optical transition between the electrons confined in Si layer and the holes localized in Ge-rich islands. The considerable increase in the intensity of the PL signal from Ge(Si) islands embedding in a strained Si layer as compared to the PL signal from Ge(Si) islands grown on unstrained Si(001) substrates was demonstrated.

Introduction

Due to the effective hole confinement an electro and photoluminescence (PL) signal from Ge(Si)/Si(001) self-assembled islands was observed up to room temperature [1,2]. However, only holes are effectively localized in Ge(Si) islands, while electrons are only weakly confined in Si on the heterojunction with an island [3]. A weak confinement of electrons is one of the possible reasons for rather a low intensity of PL signal from islands. The embedding of Ge(Si) islands in a tensile-strained Si layer (ϵ-Si layer) grown on a relaxed SiGe/Si(001) buffer can essentially improve the localization of electrons on the heterojunction with an island [4] (Fig. 1) which can result in the increase of PL signal from islands. In this paper we study the photoluminescence of structures with Ge(Si) self-assembled islands embedding between (ϵ-Si layer) layers.

1. Experimental

The structures under study were grown by MBE on smooth (root mean square roughness less 0.5 nm), graded relaxed $Si_{1-x}Ge_x$/Si(001) ($x = 20-30\%$) buffer layers fabricated by atmospheric pressure CVD with a subsequent chemical-mechanical polishing [5]. The schematic cross-section of heterostructures used in our PL experiments is shown in Fig. 2. It was shown by AFM [6,7], that the growth of Ge(Si) islands on the ϵ-Si layer deposited on a smooth relaxed SiGe buffer layer (Ge(Si)/ϵ-Si islands) is qualitatively similar to the growth of Ge(Si) islands on Si(001) substrates (Ge(Si)/Si(001) islands). The structures with Ge(Si)/ϵ-Si dome islands grown at 650 °C

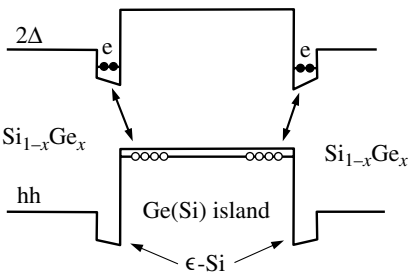

Fig. 1. Schematic band alignment is structures with Ge(Si) islands embedded in ϵ-Si layer. Position of 2Δ electron valleys and heavy holes band are shown. Arrows show real-space indirect optical transition on top and bottom island heterojunctions.

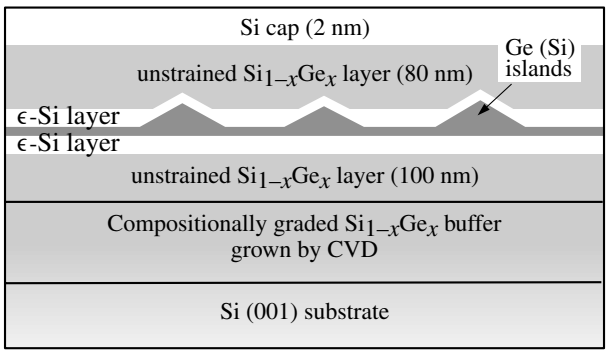

Fig. 2. Schematic cross-section of studied structures with Ge(Si) islands embedded in ϵ-Si layer.

and having a narrow size distribution (dispersion of islands sizes $< 10\%$) were used for PL study [6]. The PL spectra were recorded at 77 K using a cooled Ge and InSb detectors. PL was excited by HeCd laser ($\lambda = 325$ nm).

2. Results and discussion

The only one PL peak from structures with Ge(Si)/ϵ-Si islands was observed in spectra exited by UV HeCd laser (Fig. 3). This peak is associated with the real-space indirect optical transition between the holes confined in Ge-rich islands and the electrons localized in the ϵ-Si layer on the heterojunction with an island (Fig. 1) [6]. The PL peak from Ge(Si)/ϵ-Si islands is redshifted with an increase in the ϵ-Si layer thickness (Fig. 3). This redshift is caused by a change of the electron energy level in the thin ϵ-Si layers under and above islands due to quantum confinement effects. The increase in the ϵ-Si layer thickness reduces the energy levels of electrons in the ϵ-Si layer and results in the decrease of energy of the real-space indirect optical transition (Fig. 1). Thus, the position of PL signal from Ge(Si)/ϵ-Si islands can be controlled by changing the thickness of the ϵ-Si layer.

The width of the observed PL peak is increased in the structures with different thicknesses of the ϵ-Si layer under and above islands (Fig. 3). This increase in PL peak width is caused by two peaks in PL spectra, which related to the optical transition of holes on the base and on the top of an island (Fig. 1). The discrepancy between these PL peaks is defined by the discrepancy in the electron energy level in the ϵ-Si layer under

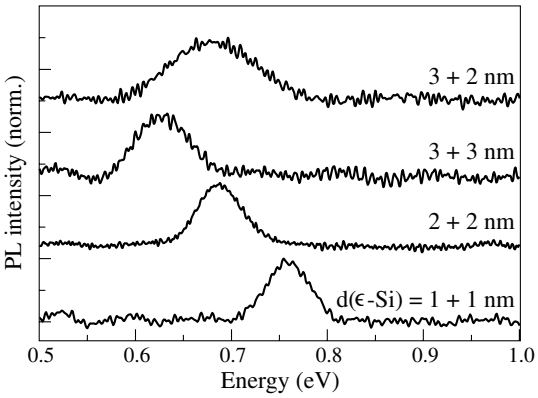

Fig. 3. PL spectra of structures with Ge(Si)/ϵ-Si islands. The numbers on graphs indicate the thickness of ϵ-Si layers under and above islands respectively. The PL spectra were recorded at 77 K using a low-sensitivity InSb detector.

and above islands.

Due to the real-space indirect nature of an optical transition and large band offsets at heterojunctions the PL signal from Ge(Si)/ϵ-Si islands was obtained at the energies significantly less than the energy of a band gap of bulk Ge (down to 0.59 eV (2.1 μm)) (Fig. 3). The low-sensitivity InSb detector having a cutoff energy smaller than that one of the high-sensitivity Ge detector was used for the registration of a PL signal in order to avoid a modification of the PL spectra by the spectral characteristics of the detector. The intensity of a PL signal from Ge(Si)/Si islands in spectra excited by HeCd laser and recorded by InSb detector is very low that makes the comparison of PL signal from Ge(Si)/ϵ-Si and Ge(Si)/Si islands difficult. But the most part of PL signal from Ge(Si)/ϵ-Si islands with the thinnest ϵ-Si layer (1 nm) falls in the region of Ge detector sensitivity (Fig. 3). It is shown that the intensity of PL peak from Ge(Si)/ϵ-Si islands is more than an order higher than the intensity of PL signal from Ge(Si)/Si(001) islands (Fig. 4). The significant increase in the PL intensity is associated with the efficient confinement of electrons in the ϵ-Si layer on the heterojunction with islands (Fig. 1).

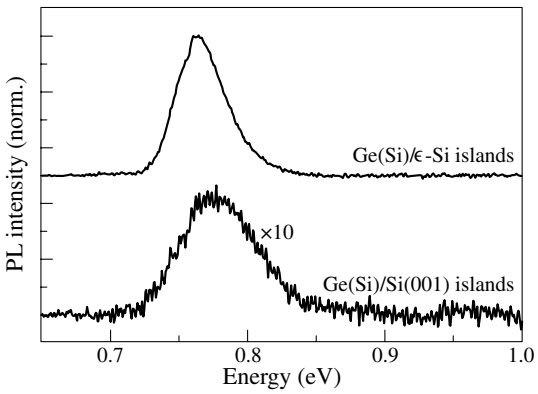

Fig. 4. PL spectra of Ge(Si)/ϵ-Si islands (thickness of ϵ-Si layers under and above islands equals 1 nm) and Ge(Si) islands grown on Si(001) substrate (Ge(Si)/Si(001) islands). The PL spectra were recorded at 77 K using a Ge detector.

Acknowledgements

This work was supported by RFBR (grants # 05-02-17336), BRHE program (Project # Y1 P-01-05) and Ministry of Education and Science of Russian Federation.

References

[1] L. Vescan and T. Stoica, *J. Lumin.* **80**, 485 (1999).
[2] K. Eberl, O. G. Schmidt, R. Duschl, O. Kienzle, F. Ernst and Y. Rau, *Thin Solid Films* **369**, 33 (2000).
[3] V. Ya. Aleshkin, N. A. Bekin, N. G. Kalugin, Z. F. Krasilnik *et al*, *JETP Lett.* **67**, 48 (1998).
[4] A. Beyer, E. Muller, H. Sigg, S. Stutz, C. David, K. Ensslin and D. Grutzmacher, *Microelectron J.* **33**, 525 (2002).
[5] N. V. Vostokov, Yu. N. Drozdov *et al*, *Russian Microelectronics* **34**, 203 (2005).
[6] M. V. Shaleev, A. V. Novikov, A. N. Yablonskiy *et al*, *Appl. Phys. Lett.* **88**, 011914 (2006).
[7] N. V. Vostokov, Yu. N. Drozdov, Z. F. Krasil'nik *et al*, *Semiconductors* **40**, 229 (2006).

14th Int. Symp. "Nanostructures: Physics and Technology"
St Petersburg, Russia, June 26–30, 2006

Strain mapping at the surface of nanometric Ge/Si(100) 3D islands

V. A. Zinovyev[1,2], G. Vastola[2], F. Montalenti[2] and Leo Miglio[2]

[1] Institute of Semiconductor Physics, 630090 Novosibirsk, Russia
[2] L-NESS and Dipartimento di Scienza dei Materiali, Universita di Milano Biccoca, via R. Cozzi, I-20125 Milano, Italy

Abstract. We have employed the projection force density method and the Green's function for isotropic semi-infinite solid to obtain analytical solution for the surface strain in vicinity of the nanometric Ge islands on Si(100) substrate. We demonstrated, that obtained solution well reproduces the main results of atomistic simulations based on Tersoff potential and it is convenient for the high aspect ratio islands.

Introduction

In order to get more insight in the morphological evolution of Ge/Si heteroepitaxial systems composed by three dimensional (3D) islands with characteristic size of 20–200 nm, it is very useful to have a surface mapping of the strain components. In fact, the changes in shape and arrangement of the 3D islands at typical experimental temperatures (400–600 °C) are essentially driven by a fully thermodynamic flow of surface atoms according the difference in chemical potential. The latter is mainly modulated by the in-plane strain components.

The most straight forward method to obtain detail information about surface strains is an atomistic simulation which gives a full strain tensor at each surface site. However, the size and complexity of the real system prevents an extensive use of the method. Analytic continuum theory in the framework of a Green's function approach [1] has provided a simple and useful tool in prediction the surface in-plain strain generation.

In this work we focus on the comparison of the two methods, namely, continuum elasticity theory and atomistic simulation based on the Tersoff potential. The nanometric-size Ge islands on Si(100) substrate are used as a model system. We have employed the projection force density method and the surface Green's function to obtain the analytical expression for the surface strain profiles in vicinity of 3D islands. Our analytical model includes two essential mechanisms of the 3D island relaxation. The first is the strain release at the island top due to free surface of the island facets, the second is the strain relaxation at the island bottom by distortion of the substrate. It has been shown, that obtained solution well reproduces main results of atomistic simulations and it can be used to describe strain evolution of nanoscale islands during heteroepitaxial growth.

1. Theoretical approach

For the some physically relevant cases strain field at the surface can be evaluated analytically in framework "flat island" approximation. The "flatness" of the island implies that the lattice constant a and the characteristic island size L and island height H are related via the inequality $a \ll H \ll L$. In fact, this approximation replaces the island by the effective force density distribution applied to the flat surface. To simplify problem we reduce the dimentionality of the system in two dimensions that is physically relevant to elongated faceted islands in three dimensions. Then, by using the projection force density method [1] and surface Green tensor of isotropic solid, in-plain strain field produced by the infinitely elongated (along [010] direction (y)) island can be evaluated as follows:

$$\varepsilon_{xx}(x) = \varepsilon_0 + 2\frac{1-\nu}{\pi Y}\int_0^L \frac{P_x(x')}{|x-x'|}dx', \qquad (1)$$

where x is the position along surface (x being the along [100] direction), is the base size of the island, ε_0 is the lattice mismatch strain, ν is the Poisson ratio, Y is the Young modulus, $P_x(x)$ is the surface force density along [100] direction.

In contrast to other works we used here a high order approximation of the projection force density which accounts for a lattice misfit relaxation at the island top:

$$P_x(x) = \sigma_0\left(1-\frac{\Lambda}{L}h(x)\right)\exp\left\{-\frac{\Lambda}{L}h(x)\right\}\frac{\partial h(x)}{\partial x}. \qquad (2)$$

Here σ_0 is the xx component of bulk stress in planar Ge film (wetting layer) coherently strained to Si(100) substrate, $h(x)$ is the local island height (island profile function) at the x position, Λ is the material dependent parameter, which characterizes efficiency of the relaxation process. According to atomistic model of Ratsch and Zangwill [2] this parameter can be defined as the average number of atoms in every atomic layer of the island which are completely relaxed. It was found, that for typical semiconductors $\Lambda \approx 3\pi/2$.

2. Results of simulations

First, we consider isolated Ge island with {105} facets, that physically relevant to dilute array of the islands. In Fig. 1 strain component ε_{xx} along island facets are shown. Solid circles represent ε_{xx} at the surface calculated by molecular dynamic (MD) simulation, while curves correspond to analytical calculations by using Eq. (1). Elastic constants in analytical treatment are ones of Tersoff potential. The solid line is the results of analytical calculation which take into account both mechanism of the elastic relaxation: at the island top and at the island bottom. While dashed line corresponds to the limit case when the elastic relaxation at the island apex can be omitted ($\Lambda = 0$). It is clear visible, that former analytical solution provides better agreement between atomistic and continuum approaches (solid line 1, Fig. 1). It is apparent also, that it is more suitable to describe higher aspect ratio islands (such as Ge dome-like islands in the Ge/Si system) than another one

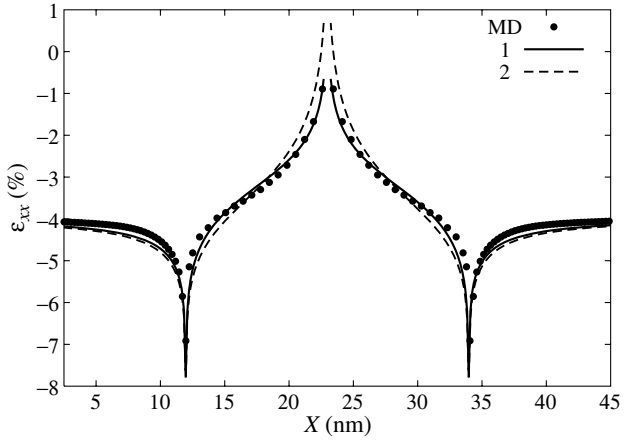

Fig. 1. The strain components ε_{xx} at the surface of Ge island bounded by {105} facets. The base length of the island $L = 22$ nm, the height $H = 2.2$ nm. The solid circles correspond to the results of MD calculation. The solid line 1 represents results of the analytic calculation by using Eqs. (1), (2) which takes into accounts the strain relaxation at the island top ($\Lambda = 3\pi/4$), while dash line 2 does not include this process ($\Lambda = 0$).

at $\Lambda = 0$ (dashed line 2, Fig. 1). From our simulations, it turns out, that largest quantitative discrepancies between MD results and analytical profiles reside mainly in the vicinity the island edges and apex. This discrepancy between atomistic and continuum elasticities is attributed to the deviation from linearity assumed in continuum elastic theory (Hooke's law), i.e. anharmonicity in the Tersoff potential. In order to verify that our analytical solution is more convenient for higher aspect ratio islands, we performed calculations for {102} faceted island. The results of verification is shown on Fig. 2. It is clear visible, that analytical solution which include both mechanism gives more realistic strain at the island apex (solid line 1 Fig. 2), than another one (dashed line 2, Fig. 2).

The dense array of coherently strained islands is a very interesting object for the practical application, because the elastic interaction between islands apparently is the main driving force for the lateral island motion, and eventually for the ordering process [3]. In the further consideration, we focus on the case of two strongly elastically interacted islands. We investi-

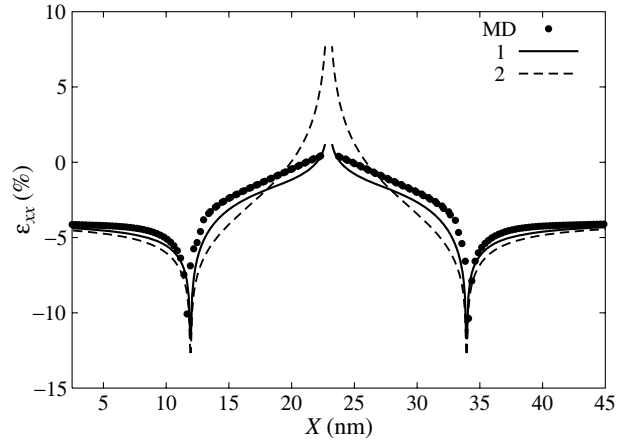

Fig. 2. The surface stain distribution for {102} faceted Ge island. The base length of the island $L = 22$ nm, the height $H = 5.5$ nm. The relaxation parameter $\Lambda = 3\pi/4$. The correspondence between symbols and lines is the same as in Fig. 2.

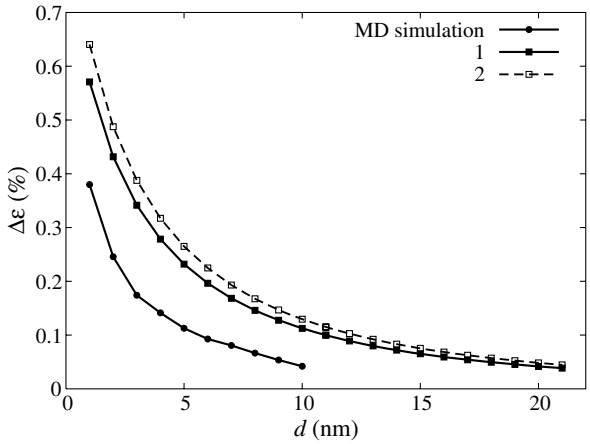

Fig. 3. The strain difference $\Delta\varepsilon_{xx}$ between the opposite edges of an island vs distance between islands d. Solid circles represent MD results, while the solid squares were calculated by using Eqs. (1), (2) at $\Lambda = 3\pi/4$, while the open circles at Λ=0.

gate the effect of elastic interaction by looking the difference between strains on the inner facets of the islands and those on the outer facet. In Fig. 3 the strain difference $\Delta\varepsilon_{xx}$ between opposite facets is plotted as a function of the distance d between two pure-Ge dots, for the atoms closer to the base. The predictions of continuum theory can verify by a comparison of $\Delta\varepsilon$ in pure-Ge pyramid calculated by means of Eq. (1) against the results obtained by MD simulations. We found that the continuum-theory curves and the MD results predict the same general trends. But the continuum approach shows a general tendency in overestimating. This discrepancy between two methods can be attributed to the departure from the linearity regime continuum elasticity.

Acknowledgement

This work has been supported from the Cariplo Foundation by project TESEO.

References

[1] V. A. Shchukin and D. Bimberg, *Rev. Mod. Phys.* **71**, 1125 (1999).

[2] C. Ratsch and A. Zangwill, *Surf. Sci.* **293**, 123 (1993).

[3] G. Capellini, M. De Seta, F. Evangelisti, V. A. Zinovyev, G. Vastola, F. Montalenti and Leo Miglio, *Phys. Rev. Lett.* (2006) (submitted to publication).

14th Int. Symp. "Nanostructures: Physics and Technology"
St Petersburg, Russia, June 26–30, 2006

Fluctuation-stimulated spin relaxation in array of Ge quantum dots

A. F. Zinovieva, A. V. Nenashev and A. V. Dvurechenskii
Institute of Semiconductor Physics, 630090 Novosibirsk, Russia

Abstract. Spin relaxation of hole localized in the Ge quantum dot due to fluctuations of electric field in the environment were studied theoretically. It was found that the time of spin relaxation has exponentially broad distribution and can reach the value $\sim 10^{-6}$ s in the typical array of Ge quantum dots in magnetic field $B = 1$ T.

Introduction

A spin degree of freedom of carrier localized in a quantum dot can be considered as a useful tool for the realization of nanoscale devices. The spin-orbit (SO) coupling in quantum dots plays a crucial role for spin manipulation and lifetime of prepared spin states. For example, the SO coupling allows the effective manipulation of spins by an external electric field. It becomes possible because the electric field changes the orbital part of wave function, and, through SO coupling, the spin states.

Recently it was found that in the Ge/Si heterostuctures with quantum dots (QDs) the SO coupling leads to turning of spin during tunneling of carrier between QDs [1]. The source of spin turning is the structure-inversion asymmetry (SIA) of Ge QDs. This asymmetry leads to appearance of effective magnetic field, which affects the spin of hole. This magnetic field can be considered as an analog of Rashba field for two-dimensional systems. This effect can be used also for spin manipulation during transition between coupled QDs.

But the SO coupling makes possible the spin relaxation caused by fluctuations of electric field in the environment. This mechanism can be actual in Ge QD arrays at low temperatures ($T \leq 4$ K). The disorder in real arrays of QDs leads to dispersion in energy levels. Some QDs have high tunneling coupling and high transition probability between them. The fast electron hops within such pairs of QDs produce the fluctuations of electric field. These fluctuations in the environment can assist the transitions between spin states in one QD as well as they assist the hopping between QDs. And because in this temperature range ($T \leq 4$ K) the phonon-assisted spin relaxation became less efficient [2], it is actual to consider the fluctuation mechanism of spin relaxation. In this paper we propose the method of calculation of spin relaxation rate due to fluctuation in the environment and give some numerical estimations for typical parameters of Ge QDs arrays.

1. Theoretical approach

We start by considering a single hole localized in the ground state in any Ge quantum dot in a dense Ge QD array, which is subject to a homogeneous magnetic field **B**. We restrict ourselves to simple situation when the average occupation number of QDs in array is $\nu \sim 1/2$. So, the effects of Coulomb and spin blocade do not affect the transitions between QDs.

Our main idea is the following. We assume that the fluctuations of electric field produced by transitions within some pair j can affect the spin of hole localized in the quantum dot i. This dipole excitation changes the orbital part of wave function and disturbs the spin of hole by means of SO interaction. The interaction that can lead to the spin relaxation is described by

$$\hat{V}_E = qE\hat{\rho}\,,$$

where $\hat{E}$ is the electric field, produced by the fluctuators, $q = |e|$ is the hole charge, $\hat{\boldsymbol{\rho}}$ is the in-plane position vector. In magnetic field the Kramers degeneracy of hole level in Ge QD is lifted. The time reversal invariance can not apply in an interaction involving a magnetic field. Consequently the matrix element $\langle\uparrow|\hat{V}_E|\downarrow\rangle$ is not zero. Its calculation is reduced to calculation of matrix element $\langle\uparrow|\rho|\downarrow\rangle$. We obtain this value in the tight-binding approach, based on the our previous study of electronic structure of Ge QDs [3]. According to the results of this calculation the matrix element $\langle\uparrow|\rho|\downarrow\rangle \sim 10^{-2}$ Å in magnetic field $B = 1$ T, which is parallel to the principal axis of symmetry of Ge QD, $B \| Z$.

According to Fermi Golden Rule the perturbation $\hat{V}_E$ produces transitions at the rate

$$\Gamma = (2\pi/\hbar^2)|\langle\uparrow|\hat{\rho}|\downarrow\rangle|^2 e^2 \langle\hat{E}\hat{E}\rangle_{\omega_z}\,.$$

Here ω_z is the Zeeman frequency, $\langle\hat{E}\hat{E}\rangle_w$ is the spectrum function of fluctuations of hole energy in chosen quantum dot due to Coulomb potentials of holes in surrounding QDs:

$$\langle\hat{E}_i\hat{E}_i\rangle_\omega = \frac{1}{\omega}\sum_j (\delta E(R_{ij}))^2 \frac{n_j(1-n_j)\omega\tau_j}{1+(\omega\tau_j)^2}\,.$$

Here δE is a change of the electric field in the quantum dot i related to a transition within the fluctuator j, τ_j is a relaxation time corresponding to the fluctuator while $n_j = n(\Delta\epsilon_j)$ is the occupation number of fluctuator upper level, $\Delta\epsilon_j = \epsilon_j^{(2)} - \epsilon_j^{(1)}$ is the fluctuator energy splitting.

The time of spin relaxation has exponentially broad distribution depended on the position of chosen QD. Each QD has a special set of fluctuators that strongly affect the spin orientation of hole in this QD. In some QDs the spin relaxation will be very intensive, while in another ones the spin relaxation is suppressed. Not all fluctuators make the contribution to spin flip process. This contribution is determined by three main factors. The first factor depends on the relative positions of fluctuator parts ($j^{(1)}$ QD and $j^{(2)}$ QD) and chosen i QD with considered spin, $\mathbf{R}_{ij}^{(1)}$ and $\mathbf{R}_{ij}^{(2)}$ correspondingly. This factor determines the electric field amplitude, we named it geometric factor:

$$\left(\delta E(R_{ij})\right)^2 = \left(\frac{e}{4\pi\varepsilon_0\varepsilon}\right)^2 \left(\frac{\mathbf{R}_{ij}^{(1)}}{(R_{ij}^{(1)})^3} - \frac{\mathbf{R}_{ij}^{(2)}}{(R_{ij}^{(2)})^3}\right)^2 .$$

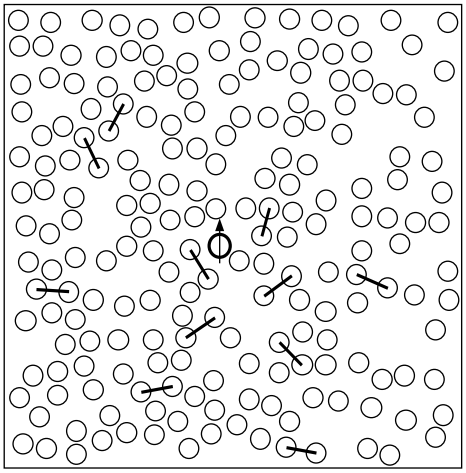

Fig. 1. An example of the fluctuator distribution in the array of quantum dots. Fluctuators are indicated by thick lines. The arrow in one of quantum dots denotes the spin.

Second factor, the energy factor $n_j(1-n_j)$, determines the probability of transitions within fluctuators. The fluctuators are represented by compact pairs of sites, each pairs having one hole with high transition rate between the sites of the pair. Such pairs play the role of electronic two-level systems and can be characterized by one energy parameter $\Delta\epsilon_j$. The probability of transitions depends on the $n_j(1-n_j) = \exp(-\Delta\epsilon_j/kT$. The most efficient fluctuators have $\Delta\epsilon_j \sim kT$.

Third factor is the frequency factor $\omega_z\tau_j/(1+(\omega_z\tau_j)^2)$. The frequency factor reflects the closeness of the fluctuator frequency $1/\tau_j$ to Zeeman frequency ω_z. The time τ_j is defined by exponential dependence of the intersite transition rate Γ on the intersite distance l, $\tau_j \sim \Gamma^{-1} \sim I^{-2}$, where $I \sim \exp(-l/\xi)$ is the overlapping integral, ξ is the localization length.

Now we can estimate the rate of spin relaxation due to electric field produced by neighboring fluctuator with optimal geometric factor $(\delta E(R_{ij}))^2 \sim (e/4\pi\varepsilon_0\varepsilon d^2)^2$, where d is the average distance between QDs. The value of this optimal factor is $(\delta E(d))^2 = 1.3\times10^{11}$ (V/m)^2. For $\omega_z = 10^{12}$ s^{-1} (corresponding to $B = 1$ T and hole g-factor $g \sim 10$) and matrix element $\langle\uparrow|\rho|\downarrow\rangle = 10^{-2}$ Å the rate of spin relaxation is $\Gamma = 2\times10^6$ s^{-1}.

The energy and frequency factors lead to suppression of spin relaxation. For optimal fluctuator, which provides the maximal transitions rate, their values are $n(n-1) = 1/4$ and $\omega_z\tau_j/(1+(\omega_z\tau_j)^2) = 1/2$. Consequently the rate of spin relaxation reduces down to $\Gamma = 2.5\times10^5$ s^{-1}.

In order to obtain the average value of spin relaxation rate in the real array of Ge QDs one should know the spatial distribution of fluctuators for each QD and their frequency characteristics and then average over all QDs in the array. A simple averaging of spin relaxation rate over QD array gives a wrong value, because it is determined by the fastest rates in the QDs with the most efficient set of fluctuators. That is why we turn to numerical simulation of spin relaxation rate in the typical QD array.

2. Results of numerical simulations

In order to model the array of QDs with random distribution of dots in the plane of array we apply the solution of the billiard problem. We allow QDs to take the random positions as billiard-balls. Only one restriction on the distance between QDs was applied, $d \geq 0.7\cdot\langle d_{QD}\rangle$, where $\langle d_{QD}\rangle$ is the average distance between QDs. For typical Ge QD array with density of QDs $N_{QD} \approx 3\times10^{11}$ cm^{-2} the average distance is $\langle d_{QD}\rangle = 1/\sqrt{N_{QD}} \approx 18$ nm. In this way we found the different realizations of QD array (see Fig. 1). In each realization we took the set of the quite good fluctuators and calculated the rate of spin relaxation in arbitrarily chosen QD.

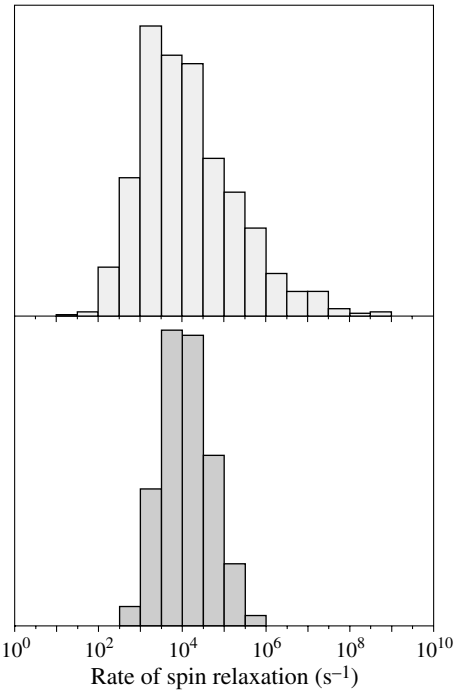

Fig. 2. The distribution of spin relaxation rate in the array of Ge QDs (a) — without restrictions on positions of quantum dots, (b) — with restriction on the distance between QDs, $d \geq 0.7\cdot\langle d_{QD}\rangle$.

We accumulated the statistics and plotted the histogram, that shows the distribution of spin relaxation rates in the typical Ge QD array. In the Fig. 2 one can see that the most probable rate of spin relaxation is $\Gamma \sim 10^4$ s^{-1}. The calculations were performed for $kT/\Delta\epsilon \sim 0.1$, where ϵ is the energy levels dispersion in Ge QD array.

The increasing of magnetic field up to $B = 10$ T leads to one order of magnitude more intensive spin relaxation. It is related to increasing of matrix element $\langle\uparrow|\hat{\rho}|\downarrow\rangle \sim 0.1$ Å (square dependence on magnetic field). As the rate is $\Gamma \sim 1/\omega_z$, the resulting rate dependence on the magnetic field is linear.

Acknowledgements

This work has been supported by RFBR (Grants No. 05-02-16285, 06-02-16988, 05-02-39006-GFEN), by "Dynasty" Foundation and SB RAS (Lavrentiev project No. 57).

References

[1] A. F. Zinovieva, A. F. Nenashev and A. V. Dvurechenskii, *Phys. Rev. B* **71**, 033310 (2005).

[2] A. F. Zinovieva, A. F. Nenashev and A. V. Dvurechenskii, *JETP Letters* **82**, 302 (2005).

[3] A. V. Nenashev, A. V. Dvurechenskii and A. F. Zinovieva, *Phys. Rev. B* **67**, 205301 (2003).

14th Int. Symp. "Nanostructures: Physics and Technology"
St Petersburg, Russia, June 26–30, 2006

Inverted resonant tunneling heterostructures

A. A. Gorbatsevich[1], *V. V. Kapaev*[2] and M. N. Zhuravlev[1]

[1] Moscow Institute of Electronic Technology (Technical University), Moscow, Russia
[2] P. N. Lebedev Physical Institute, Moscow, Russia

Abstract. Single barrier heterostructures are proposed which demonstrate under-barrier resonant tunneling and whose potential relief is inverted in respect to an ordinary double-barrier heterostructures. It is shown that under-barrier resonance results from the entrance of bound state into the continuum and has no relation with Ramsauer–Townsend-like interference of electrons scattered from the potential discontinuities. Under-barrier resonance is not accompanied by charge build-up which improves its dynamical characteristics. Optical analog of the considered phenomenon is electromagnetic wave transmission through the metallic layer covered on both sides with dielectric films due to the excitation of interface plasmons or waveguide modes.

Introduction

Electronic resonances in semiconductor heterostructures are of great interest both for fundamental physics and device applications. The possibility of a new type of resonance was recently forecasted in [1] — resonant tunnelling on a single barrier with complex heterointerfaces described by generalized boundary conditions [2] with off-diagonal elements in the transfer matrix. The off-diagonal elements in the transfer matrix result in the appearance of localized interfacial states. Under-barrier resonance takes place when bound state is pushed into the continuum due to the tunneling splitting of interfacial states localized at opposite heterointerfaces of the barrier. Analogous effect occurs in heterostructures with standard boundary conditions (such as well-studied GaAs/AlGaAs hetrostructures) if quantum wells are located at the barrier boundaries (see insert in Fig. 1). In fact this structure is the inverted structure of an ordinary double-barrier resonant tunneling diode with barriers being replaced by quantum wells and vice versa. Such single-barrier resonant tunneling heterostructures are studied in the present report. In the first section interaction of resonances in inverted tunneling structure is studied and the existence of a novel phenomenon — collapse of resonances in single-mode regime is demonstrated. In the second section analytical solution of the scattering problem is presented for a system with smooth quantum well potential and is shown that under-barrier resonance still exists when Ramsauer–Townsend-like interference of electrons scattered from the potential discontinuities is abscent.

1. Rectangular quantum wells and barrier

The numerical solution of the Schroedinger equation was performed for the system consisting of two quantum wells (widths h_{w1} and h_{w2}, depth U_w) separated by a barrier (width h_b, height U_b). Transmission T and reflection R coefficients were calculated as a function of an incident particle energy E (at $E > 0$) as well as localized states energies (at $E < 0$). The results are presented in the diagrams where the energy locations of transmission coefficient T maximum E_max and minimum E_min are plotted as functions of quantum well depth at fixed well width and barrier height. Such diagrams are presented in Fig. 1 for the structure with $h_{w1} = h_{w2} = 50$ Å, $h_\mathrm{b} = 20$ Å, $U_\mathrm{b} = 0.2$ eV, $m = 0.067m_0$. Plots at $E < 0$ are size-quantized energies of localized states. Notations ε_3, ε_4 correspond to well depths at which size-quantized levels 3 and 4 enter the continuum.

Under-barrier resonance with unit transparency in this system takes place in the interval of quantum well depths where odd states are localized while even states are in continuum. Two types of resonance behavior can be emphasized. As well depth or width is changed resonance curve starts at the point where one localized state originates (disappears) and ends at the point where the next localized state originates (states 1 and 2). Another type of behavior (states 3 and 4, 5 and 6) takes place when resonance curves extend localized state curves into the continuum. These resonance curves with unit transparency attract each other in pairs and finally merge into one resonance curve with transparency smaller than unity (point U_2). Consequently we have collapse of resonances in single mode transmission — the phenomenon which has not been described in heterostructures yet. The positions of scattering matrix poles in the complex plain were calculated which are usually related to continuum states resonances. However pole curves vary almost linearly with well width variation and don't cross. Points $U_{1,3}$ correspond to the disappearance maximum in transmission coefficients.

The structure of the diagram near the (localized sate ↔ resonance) transformation point appears to be quite universal. At this point three curves meet always: localized state curve (LS), resonance state curve with unit transparency (T1) and resonance state curve with transparency smaller than unity (T2) (e.g. solid line to the right of point ε_4 is T1 and to the left — T2). The latter two always belong to different regions of well depth

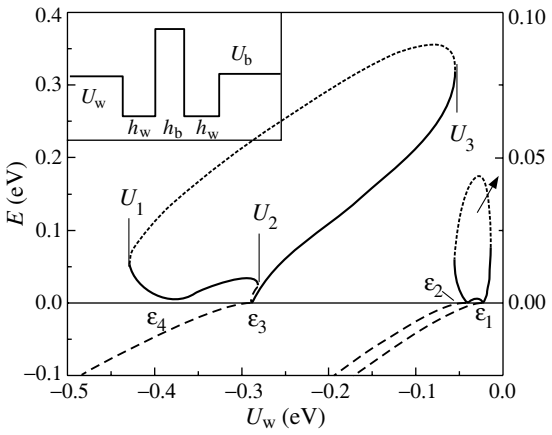

Fig. 1. The location of transmission extrema (solid line — E_max, dotted — E_min) and size-quantized energies (dashed) as a function quantum well depth U_w for $h_w = 50$ Å, $h_\mathrm{b} = 20$ Å.

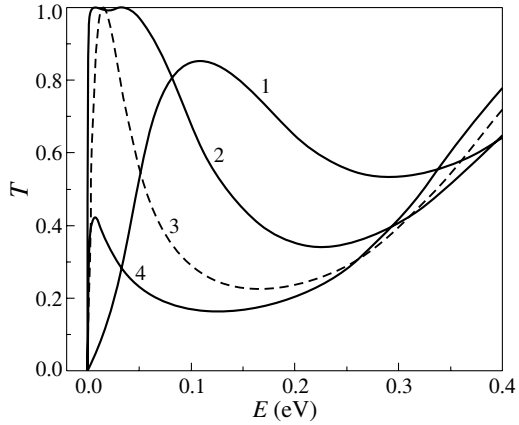

Fig. 2. Dependance of the transmission coefficient T on the incident electron energy E for $-U_w$, (eV): 1 — 0.2; 2 — 0.285; 3 — 0.350; 4 — 0.390.

variation while LS can belong either to the same region as T1 or as T2. It can be shown that analogous situation takes place for a single quantum well where T1 resonance is Ramsauer–Townsend-like resonances. In this case T2 curve also exists and LS curve is located in the same parameter region as T2. It is well known that Ramsauer–Townsend-like resonance can be interpreted as the result of the interference of waves scattered from potential discontinuities. In the next section we consider a system with smooth potential relief and show that physical origin of under-barrier resonance is related directly to (localized state $\leftrightarrow$ continuum resonance) transformation. As the resonance number grows under-barrier resonances become more pronounced, range of well depths corresponding to unit transparency and $E_{\max}$ variation range grow. It is desirable for the experimental observation that both the difference between a maximum and a minimum of a transmission coefficient and separation of $E_{\max}$ from the top of the barrier be the maximum.

In Fig. 2 the dependence of the transmission coefficient on energy is presented for a set of U_w corresponding to the under-barrier resonance caused by the exit of 3th and 4th states into the continuum. Wave-function distribution in the resonance was calculated. Wave-function amplitude doesn't grow at resonance contrary to double-barrier resonant tunnelling structures. Its maximum is of the order of a unity and minimum approaches zero. Hence there is no charge accumulation in the structure under consideration which is favorable for its dynamical properties.

2. Smooth quantum well and δ-function potential

Consider the system with smooth quantum well potential

$$U(x) = -\frac{U_0}{ch^2(\alpha x)} + \beta\delta(x) \ .$$

The first term in the r.h.s is the potential which at certain values of the parameters can become reflectionless [3]. The solution of the Schroedinger equation with this potential at $x \neq 0$ can be expressed in hypergeometric functions. Using connection rules obtained by integration of Schroedinger equation at $x = 0$ one can find transmission and reflection amplitudes and obtain for the transmission coefficient the following expression

$$T = \left| \frac{\varepsilon}{\varepsilon+s} \frac{\Gamma^2(\varepsilon)}{\Gamma(\varepsilon+s)\,\Gamma(\varepsilon-s)} C_1(\varepsilon, s) + \frac{\sin(\pi s)}{\sin(\pi\varepsilon)} C_2(\varepsilon, s) \right|^{-2} .$$

Here $C_{1,2}$ - are the coefficients obtained from the boundary condition and

$$\varepsilon = -\frac{i}{\hbar\alpha}\sqrt{2mE} \ , \quad s = \frac{1}{2}\left(-1 + \sqrt{1 + \frac{8mU_0}{\alpha^2\hbar^2}}\right) .$$

The analysis of this expression shows that qualitative modification of the transmission coefficient curve as a function of an energy takes place at the value of the well depth corresponding the origin (disappearance) of new localized state. Origin of localized state as U_0 is increased is accompanied by the appearance of the resonance maximum of unit transparency in the continuum. With further decrease of well depth localized state energy and position of under-barrier resonance first shift on energy scale in opposite directions but then the position of resonance starts to decrease and finally passes zero and turns into second localized state. This type of resonance behavior is analogous to the transformation of first two localized states in Fig. 1.

3. Conclusion

A novel phenomenon — under-barrier resonance in inverted resonant-tunneling structure was described. Physically it can be considered as the manifestation of localized states passing into the continuum. Because of similarity of Schroedinger and wave equations and unique nature of electron and electromagnetic field propagation all the known electron resonances possess optical (or microwave) analogs. Thus resonant tunneling is analogous to Fabri–Perro resonances, Ramsauer–Townsend-like resonances — to the resonances in light transmission through thin refracting plates, Fano resonaces — to the resonances in multimode microwave waveguides. It can be shown that a direct analog of under-barrier resonance in optics is resonant transmission of an S-polarized (vector **H** in the plane of incidence) electromagnetic wave through thin metallic layer (which plays the role of a barrier) covered with dielectric films (analogs of quantum wells). Optical resonance in such structure of a P-polarized wave (vector **E** in the plane of incidence) described in Ref. [4] corresponds to inverted resonant tunneling structure with negative effective mass in the barrier.

References

[1] I. V. Tokatly, A. G. Tsibizov and A. A. Gorbatsevich, *Phys. Rev. B* **65**, 165328 (2002).

[2] T. Ando and S. Mori, *Surf. Sci.* **113**, 124 (1982); T. Ando, S. Wakahara and H. Akera, *Phys. Rev. B* **40**, 11609 (1989).

[3] L. D. Landau and E. M. Lifshitz, *Quantum Mechanics* (Pergamon Press, Oxford, 1977).

[4] R. Dragila, B. Luther-Davies, S. Vukovic, *Phys. Rev. Lett.* **55**, 1117 (1985).

14th Int. Symp. "Nanostructures: Physics and Technology"
St Petersburg, Russia, June 26–30, 2006

Elastic 2D-2D tunnelling and the zero-bias anomaly in an in-plane magnetic field

V. G. Popov[1], Yu. V. Dubrovskii[1], L. Eaves[2] and M. Henini[2]

[1] Institute of Microelectronis Technology of RAS, Chernogolovka 142432, Russia
[2] The School of Physics and Astronomy, University of Nottingham, Nottingham NG7 2RD, UK

Abstract. Electron tunnelling between identical δ-doped layers is studied in an in-plane magnetic field. A new symmetrical conductance-peaks series has been revealed near zero voltage in strong in-plane magnetic fields. The origin of the peaks is discussed as a manifestation of electron tunnelling between magnetically hybridized states assisted by the elastic electron-impurities scattering. It is interesting to note that formation of the peaks is accompanied by the zero-bias-anomaly transformation from the conductance peak into the gap.

Introduction

Tunnelling between two-dimensional systems is well known to be very sensitive to the alignment of subband levels in the systems, namely, the tunnelling probability is high when the levels are align. In the case of identical systems this leads to a strong conductance peak at zero voltage. Applied an in-plane magnetic field changes the tunnel probability drastically. The conductance peak splits into two peaks with smaller amplitudes those diminish further so as the field is risen. This gradual peak suppression was successfully explained in terms of the additional momentum shift gained by a tunnelling electron due to the Lorentz force [1]. However the model described in Ref. [1] takes into account only the first-order term of the magnetic perturbation. Hence it is applicable at low fields. To consider high fields it is more relevant to say about the spectrum change that is about so-called magneto-electric hybridized states [2]. There are two types of the states. These are the skipping and traverse orbits. Both of them can take part in resonant tunnelling at high bias voltages that was observed as pronounced peaks of the conductance derivative. In this paper we report observation of new conductance peaks near zero voltage in high in-plane magnetic fields.

Recently Dubrovskii *et al* had discovered a new type of zero-bias anomaly in electron tunnelling between disordered two-dimensional systems (2DESs) [3]. A very narrow conductance peak was observed exactly at zero bias voltage. This peak was smeared at 2 K that indicates on its many-body origin. The high magnetic field normal to the 2DES planes suppresses the peak and induces a dip that had also been thoroughly investigated by Dubrovskii *et al* [3]. Here we report similar the peak-dip transformation induced by a high in-plane magnetic field. Moreover the thorough consideration shows that this transformation is accompanied by formation of the conductance peaks near zero voltage.

1. Experiment

The vertical tunnel diodes were made of a single-barrier δ-GaAs/$Al_{0.4}Ga_{0.6}As$/δ-GaAs heterostructure. The disordered 2DESs were located in the Si δ-doped GaAs layers that were separated from the n^+-GaAs regions by slightly doped GaAs spacers of 100 nm thickness. The 2D electron concentrations $n_{1,2}$ are equal to $3 \cdot 10^{11}$ cm^{-2}. The tunnel diodes represented cylinders of 100 μm diameter prepared by the conventional photolithography and chemical wet-etching techniques. All the measurements carried out at the liquid helium ($T = 4.2$ K) and lower temperatures ($T = 0.3$ K).

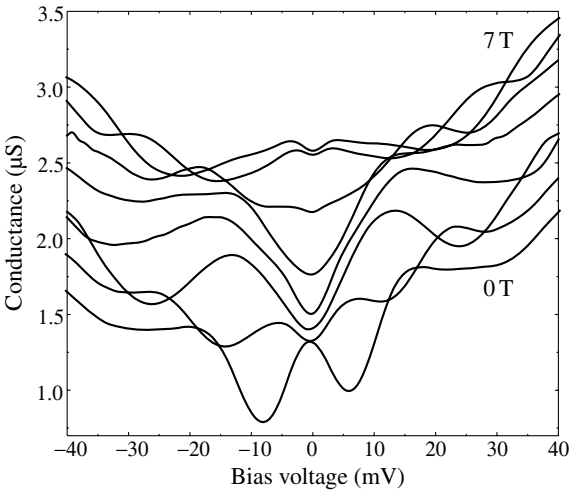

Fig. 1. Conductance versus bias voltage at the different in-plane magnetic fields and $T = 4.2$ K.

The conductance-voltage characteristics are shown in Figure 1. At zero magnetic field one can see a broad conductance peak originated from the resonant coherent tunnelling with energy and in-plane momentum conservation. This peak is splitted and suppressed by the in-plane magnetic field like that was observed early [1]. However at the fields higher 5 T a new pair of conductance peaks appears near the zero voltage. The other interesting finding is observed at the lower temperatures. At $T = 0.3$ K the peak-type anomaly has been observed in the zero field (see Fig. 2). At the field $B = 5$ T the peak is suppressed and the narrow dip appears at the higher fields.

2. Discussion

To clarify the origin of the observed features it is necessary to consider thoroughly the spectrum change caused by the in-plane magnetic field. This task requires self-consistent calculations of the Poisson and Shrödinger equations. Such kind of calculations had been performed early for example in Ref. [4]. Here we only pay attention to the qualitative results of the calculations. First of all the Hamiltonian of the 2DES in the Landau gauge allow to draw the Shrödinger equation to the one-dimensional one. In this an additional magnetic potential $U_m = 1/2m\omega_c^2(z - z_0)^2$ is added to the zero-field confined one

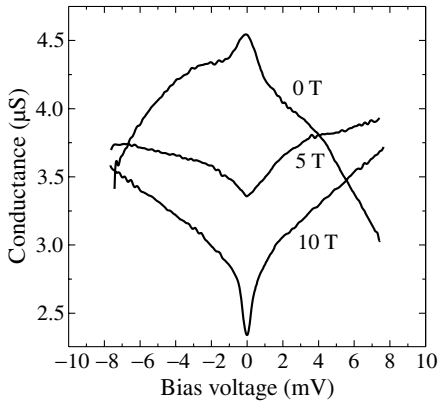

Fig. 2. Conductance versus bias voltage at the different in-plane magnetic fields and $T = 0.3$ K.

$U_{\rm conf}(z)$, where $z_0 = p_x/(eB)$; p_x is the momentum component along in-plane direction x perpendicular to the field B. Such potential leads to the z_0 dependency of the confined-state energies $E_{01,2}(z_0)$ shown in Fig. 3. Since the coherent tunnelling conserves the full energy and in-plane momentum component of an electron this tunnelling is allowed only for states in the crossing point of the $E_{01,2}(z_0)$ curves. This means that at the zero voltage the coherent tunnelling is possible if the crossing energy $E_{01}(0) = E_{02}(0) = E_0$ is lower than the Fermi energy $E_{\rm F}$. At the high field E_0 exceeds $E_{\rm F}$ and the coherent tunnelling is possible only at the finite voltages (see Fig. 3). This leads to the conductance suppression at the zero voltage and to the appearance of the conductance peaks at the finite voltages. This model is adequately describe the data for the fields lower than 3 T.

One can see from Fig. 1 that at the high fields new conductance peaks appear near zero voltage. Moreover the zero-conductance has a maximum at high fields (see the curve with the filled squares in Fig. 4). Since the coherent model falls to describe the high field features one should consider incoherent processes. We propose to take into account the tunnelling assisted by the elastic electron-impurities scattering. Since the process is elastic the full energy of electron is conserved and the conductance near the zero voltage is proportional to the 2DESs densities of states (DOS) product. To calculate these DOSs is not simple task but one can expect that at the very high magnetic field the magnetically hybridized states can be considered as the inhomogeneously broadened Landau levels.

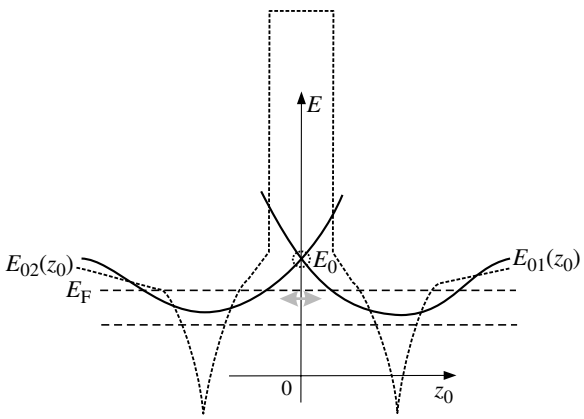

Fig. 3. Energy spectrum of the 2DESs in the tunnel junction in an in-plane magnetic field. The dotted curve represents a schematic conduction-band-bottom diagram of the structure.

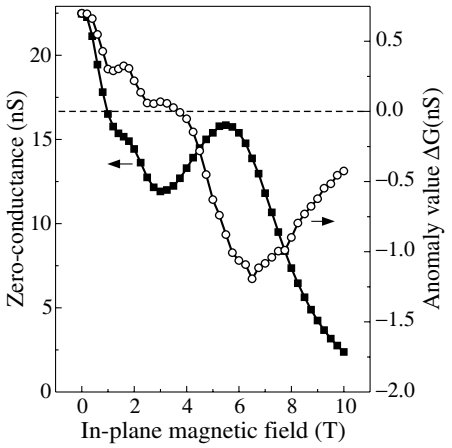

Fig. 4. Zero-conductance and zero-anomaly-value field dependencies.

As for the Landau levels they are well known to be able to produce the modulation of DOS and the oscillations in the conductance-field and conductance-voltage dependencies. In particularly, the zero-conductance is proportional to the Fermi DOS in square and reaches the maximum when the Landau level is almost half-populated.

The most exciting finding comes from the zero-anomaly analysis. To determine its field dependence we have used the conductance-voltage curve smoothing to smear the zero-bias anomaly. After that the anomaly value was determined as a difference between the measured zero-conductance and smoothed one. The field dependence of the anomaly value is shown in Fig. 4 by the curve with the empty circles. First of all one can see that anomaly value changes sign or transforms from the peak into the dip in the zero-conductance minimum where the coherent resonant tunnelling is suppressed. Secondly the anomaly-value field dependence resembles that of the zero-conductance. This resemblance indicates that the absolute value of the anomaly is proportional to the Fermi DOS.

Acknowledgements

This work has been supported in part by the RFBR (grant 04-02-16870), INTAS (grant YSF 05-109-4786), "Russian Science Support Foundation" and RAS program "Quantum nanostructures".

References

[1] W. Demmerle *et al*, *Phys. Rev. B* **44**, 3090 (1991).
[2] M. L. Leadbeater *et al*, *J. Phys.: Cond. Matt.* **1**, 4865 (1989).
[3] Yu. V. Dubrovskii *et al*, *Physica E* **12**, 300 (2002).
[4] T. Jungwirth *et al*, *J. Phys.: Cond. Matt.* **5**, L217 (1993).

14th Int. Symp. "Nanostructures: Physics and Technology"
St Petersburg, Russia, June 26–30, 2006

The inter-subband interaction effect on the electron transport in quantum contacts

V. A. Sablikov
Institute of Radio Engineering and Electronics, RAS, Fryazino, Russia

Abstract. We show that Friedel oscillations of the electron density exist in junctions between quasi-one-dimensional and two-dimensional systems. The backscattering of electrons by the Friedel oscillations can qualitatively explain a number of transport features observed in recent experiments.

In recent years a lot of experiments appears revealing new features of the electron transport through quantum point contacts and quantum wires, which are not satisfactory explained as yet. They can be classed into three groups. First, the electron localization was observed in quantum contacts formed by a rather smooth potential of gates [1]. The analysis of the $0.7 \cdot 2e^2/h$ plateau and the nonlinear conductance at low voltage shows convincingly that the electron spin is localized in the contact [2], though this seems to be strange, since a potential hump is the contact rather than a well. Nevertheless, the Kondo model describes the experiment adequately [3]. Other group of experiments relates to nonlinear transport. An increase of the differential conductance with an applied voltage was observed on the clean semiconductor wires whereas the decrease in the ballistic conductance is expected from existing theory. Moreover, the differential conductance exceeds the standard value $2e^2/h$ [4]. This seems to be very astonishing since e^2/h corresponds to the maximum conductance per spin channel. The third group includes the works studying the series resistance, which is usually found in the structures when analyzing the conductance quantization. It was found that there is a specific resistance of the junctions between 1D and 2D electron systems [5]. This resistance is of the order of 1 kΩ, i.e. about $0.1 \cdot 2e^2/h$. In addition, the very recent experiments clearly show that the conductance depends not only on the chemical potential but on the potential step in the junction between the wire and the reservoir [6], and the electron localization occurs in a wire between two junctions to electron systems of higher dimensionality [7].

In this paper we show that these experiments can be explained, at least qualitatively, taking into account the interaction of electrons traveling through the contact with electrons of closed subbands, which can not pass the contact. This interaction occurs in the junctions between quasi-1D and 2D systems even if the shape of the transition region is smooth on the Fermi-wavelength scale.

The interaction is caused by Friedel oscillations of the electron density which appear in the junction as a consequence of the reflection of electrons of higher subbands. A large number of electrons in the reservoirs strike on the contact but only few of them, belonging to the lower open subbands, are able to pass through it. The electrons of higher (closed) subbands are reflected giving rise to Friedel oscillations. Though the oscillation phases in various subbands are different, the resulting oscillation amplitude is not vanishing since the reflecting surface is regular. The density oscillations contain a clearly defined component with the wave vector $2k_F$. This supposition is supported by the experiment [8], in which $2k_F$ oscillations of the electron density were observed far from the contact. These oscillations affect essentially the electron transport through the contact.

We have studied the Friedel oscillations in quantum junctions and their effect on the scattering of electrons in open and closed subbands. The theory is developed for smooth junction shape using the quasicllassic approximation for the calculation of the density matrix and Born approximation for scattering processes. General expressions are obtained and two specific types of contacts are investigated in detail:
(i) a smooth junction between a quasi-1D wire and a half plane of 2D electron gas in the form

$$d(x) = d/\sqrt{1 - x^2/R^2}\,.$$

This is a case of a 'separate' quantum contact.
(ii) a smooth constriction in a 2D stripe in the form

$$d(x) = D - (D - d)\exp\left[-x^2/R^2\right],$$

which corresponds to a more realistic structure of the junction where flat edges of the 2D system are absent. In both cases the 2D region is supposed to be a stripe of the width $D \gg d$.

The Friedel oscillation amplitude and its dependence on the distance are determined by the geometric form of the contact, which is characterized by the wire width $d(x)$ as a function of the distance x. This is because the dispersion of the phases of the reflected waves with different wave vectors and subband indexes depends on the shape of the junction.

The effective 1D electron density contains an oscillating component

$$\tilde{\rho}(x) = \frac{2k_F}{\pi} A(x)\cos\left[2k_F x + \phi(x)\right],$$

the amplitude $A(x)$ of which decreases along x direction from the quasi-1D system to the 2D reservoir. The amplitude $A(x)$ and phase $\phi(x)$ are slow varying functions. In the case of a separate contact

$$A(x) \sim \frac{D}{8}\frac{\exp\left\{-2k_F\delta\sqrt{2R(x-R)}\right\}}{(x-R)\sqrt{k_F(x-R)}},$$

where $\delta = d/D$. The power-type dependence dependence $\sim x^{-3/2}$ is caused by the reflection from the nearly flat parts of the junction (similar to the Friedel oscillations at the edge of 2D gas [9]), the exponential factor with a characteristic length $\sim D^2/(4Rk_F^2d^2)$ originates directly from the junction. This factor is not important if $\delta 1$ is low enough.

In the case of smooth constriction a new characteristic length $l_c = (cR)^4 k_F^3/2$ appears, $c \sim 1$ being a characteristic parameter of the junction shape. The amplitude $A(x)$ decreases asymptotically as $x^{-1}(x + l_c)^{-1/2}$ and turns out to be noticeably smaller than in the 'separate' contact because the phase dispersion is larger there.

The interaction of electrons with the Friedel oscillations is determined by both the direct interaction and the exchange interaction. The effectively one-dimensional potential of pair interaction $V_{nm}(x)$ is obtained by integration over the transverse coordinate and describes the interaction of transverse cords of electron density in n-th and m-th subbands. The resulting potential of direct interaction $V_H(x)$ and the potential, which determines exchange interaction, $V_{ex}(x)$ are different. In particular, the the exchange interaction potential more strongly decreases with x and depends on the subband number. The screening of the interaction by 2D electrons is taken into account within the RPA approximation.

The Friedel oscillations act on the electron system by producing the backscattering of electrons in open subbands and inter-subband transitions, which include particularly the electron transitions from closed subbands into the open subband. These processes are characterized quantitatively by a reflection coefficient r. The direct and exchange interaction both contribute to r. The role of the direct interaction is determined by the $2k_F$ Fourier component of the interaction potential $V_H(q = 2k_F)$. The contribution of the exchange interaction is determined by an integral of $V_{ex}(x)$ multiplied by a power function of x, i.e. roughly speaking, by the Fourier component with zero wave number, $V_{ex}(q = 0)$. This is why the exchange interaction dominates despite the screening effect is more essential for Fourier component with $q = 0$. The Friedel oscillation effect on the reflection is illustrated qualitatively by Fig. 1. The calculation shows that the reflection coefficient and its dependence on the Fermi energy is sensitive to the shape of the junction and to the interaction potential. In the case of a separate contact with Coulomb interaction, $|r|$ varies with k_F as $(a_B k_F)^{-1/2} \exp[-c_1 \delta (R k_F)^{1/2}]$ (with k_F being the Fermi wave vector in the 2D electron gas, a_B Bohr radius, $c_1 \sim 1$). Numerically the $|r|^2$ can be as high as 0.5. In the case of a constriction in 2D stripe, $|r| \sim \ln(2l_c/R)/(cRk_F)^2$. Here Rk_F is a large parameter of the smooth junction. For realistic conditions ($Rk_F \sim 10$ and $c \sim 0.2$) the reflection coefficient $|r|^2$ is estimated as about 0.1. With increasing the Fermi energy the reflection coefficient changes as a power of Rk_F depending on the contact shape details. This contrasts with the usual notion that the transmission of adiabatic contacts depends exponentially on the energy.

The interaction of electrons with the Friedel oscillations causes the following effects in quantum contacts:

1. A specific resistance appears in 1D/2D junctions as a result of the backscattering of electrons by the Friedel oscillations. The resistance depends on the Rk_F parameter and the junction shape and can be estimated as $0.1 \cdot 2e^2/h$ in qualitative agreement with the experiment.

2. The conductance becomes nonlinear at a low applied voltage (depending on the interaction potential) because of the strong dependence of the backscattering probability on the electron energy. Increasing the energy causes the decrease in the scattering probability, hence the conductance increases with an applied voltage.

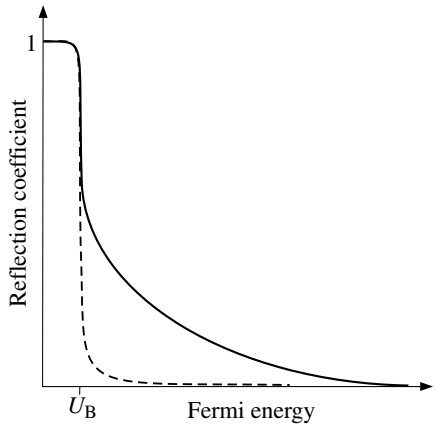

Fig. 1. Reflection coefficient of the junction versus the Fermi energy for the cases with (full line) and without (dashed line) the Friedel oscillation effect.

3. The differential conductance of a biased contact can exceed the $2e^2/h$ quantum because the interaction with the Friedel oscillations makes it possible to transfer the electrons of closed subbands into the open subbands. This is caused by the fact that the potential of the Friedel oscillations in each subband oscillates not only along x direction, but in the transverse y-direction as well. Hence the inter-subband transitions become possible.

4. Quasibound states can arise in the quantum point contacts as a result of the backscattering of electrons by Friedel oscillations in the opposed slopes of the potential barrier forming the contact. The electron waves reflected from both junctions interfere giving rise to resonances.

5. The Friedel oscillation effect can be extracted experimentally by comparing two kinds of measurements, in which the conductance is determined (i) as a function of the Fermi energy with the fixed barrier in the contact and (ii) as a function of the barrier height in the contact with the fixed Fermi energy.

Acknowledgements

This work was supported by RFBR (05-02-16854) and the Programs of RAS 'Quantum nanostructures' and 'Strongly correlated electrons'.

References

[1] S. M. Cronenwett *et al*, *Phys. Rev. Lett.* **88**, 226805 (2002).
[2] Y. Meir *et al*, *Phys. Rev. Lett.* **89**, 196802 (2002).
[3] K. Hirose *et al*, *Phys. Rev. Lett.* **90**, 026804 (2003).
[4] R. de Picciotto *et al*, *Phys. Rev. Lett.* **92**, 036805 (2004).
[5] A. E. Hansen, A. Kristensen, H. Bruus, cond-mat/0208452, *Proc. 26th ICPS*, Edinburgh, UK 2002, publication on CD.
[6] D. J. Reilly, *Phys. Rev. B* **92**, 036805 (2005).
[7] O. M. Auslaender *et al*, *Science* **308**, 88 (2005); cond-mat/0507065.
[8] M. A. Topinka *et al*, *Nature* **410**, 183 (2001).
[9] L. Shekhtman and L. I. Glazman, *Phys. Rev. B* **52**, R2297 (1995).

14th Int. Symp. "Nanostructures: Physics and Technology"
St Petersburg, Russia, June 26–30, 2006

Bose–Einstein condensation of microcavity polaritons — myth or reality?

J. Kasprzak[1], M. Richard[2], S. Kundermann[2], A. Baas[2], P. Jeambrun[2], J. Keeling[3], F. M. Marchetti[4], M. H. Szymanska[5], R. André[1], J. L. Staehli[2], P. B. Littlewood[4], B. Deveaud[2] and *Le Si Dang*[1]

[1] Laboratoire de Spectrométrie Physique, CNRS-Université J. Fourier-Grenoble, France
[2] Ecole Polytechnique Fédérale de Lausanne, Lausanne, Switzerland
[3] M.I.T., Cambridge (Ma.), USA
[4] Cavendish Laboratory, University of Cambridge, Cambridge, United Kingdom
[5] Clarendon Laboratory, University of Oxford, Oxford, United Kingdom

Abstract. We show that Friedel oscillations of the electron density exist in junctions between quasi-one-dimensional and two-dimensional systems. The backscattering of electrons by the Friedel oscillations can qualitatively explain a number of transport features observed in recent experiments.

Bose–Einstein condensation (BEC) of bosons, i.e. particles with an integer spin, is one of the most fascinating expressions of quantum degeneracy. This thermodynamic phase transition takes place when the de Broglie thermal wavelength $\lambda_{\mathrm{dB}} = (2\pi h^2/mk_{\mathrm{B}}T)^{0.5}$ becomes comparable to the mean separation between particles. For dilute atomic gases, this critical situation has been recently achieved by lowering the temperature below 10^{-6} K. In solids, the quest for BEC has been mostly focused on semiconductor excitons for the past three decades. Excitons are composite bosons, consisting of bound electron-hole pairs akin to positronium, but with an effective mass on the order of the free electron mass. They are expected to undergo BEC at temperatures of a few Kelvin, but in spite of intense studies, no conclusive evidence has been reported up to now [1].

To realize BEC in a solid state system, we have concentrated our efforts on 2D exciton polaritons in semiconductor microcavities. These devices are planar Fabry–Perot cavities with embedded quantum wells. Their optical length is a half-integer multiple of the emission wavelength of quantum well excitons. Polaritons are eigenstates of such a microcavity system which result from the strong coupling between cavity optical modes and quantum well excitons [2]. With respect to excitons, polariton mass and density of state are much smaller, typically by four orders of magnitude, which should favour quantum degeneracy at higher temperature and smaller density. This is a key advantage for polariton BEC since both excitons and polaritons are composite bosons, and behave as bosons only in the dilute density limit. On the other hand, the polariton lifetime is extremely short, on the picosecond time scale, as compared to microseconds measured for "indirect" excitons in coupled quantum wells, and several hundreds of picoseconds for acoustic phonon relaxation times. Thus polaritons cannot be in thermal equilibrium with the host lattice by phonon interaction.

In this presentation we will discuss a recent spectroscopic study at 5 K of a CdTe-based microcavity, using non-resonant and quasi-cw laser excitation. Various observations suggesting BEC of polaritons will be examined: thermalization and condensation, spontaneous linear polarization, temporal and spatial first order correlations.

We gratefully acknowledge support from EU Network HPRN-CT-2002-00298 "Photon-mediated phenomena in semiconductor nanostructures".

References

[1] D.W. Snoke, *When should we say we have observed Bose condensation of excitons? Phys. Stat. Sol. (b)* **238**, 389 (2003).
[2] C. Weisbuch *et al*, *Observation of the coupled exciton-photon mode splitting in a semiconductor quantum microcavity*, *Phys. Rev. Lett.* **69**, 3314 (1992);
A. Kavokin and G. Malpuech, *Cavity Polaritons*, Elsevier, Amsterdam (2003).

Author Index

Abram R. A., 299
Adell M., 91
Adelmann C., 39
Adolph D., 89
Afanasiev M. M., 59, 158
Afanasiev N. N., 236
Afonenko A. A., 176, 340
Agekyan V. F., 202
Ajayan P., 218
Akai I., 202
Akimov A. V., 69
Aktsipetrov O. A., 295, 303, 321, 323
Aleksandrov S. B., 246
Alekseev A. N., 246
Alekseev P. S., 47
Aleshkin V. Ya., 17, 51, 164, 166, 172, 340
Amand T., 33
André R., 371
Andronikov D., 208
Andronov A. A., 214
Ankudinov A. V., 160
Antonov A. V., 164
Arakcheeva E. M., 15, 281, 313
Arapov Yu. G., 77
Armbrister V. A., 101
Arseev P. I., 188
Aseev A. L., 82, 250
Asryan L. V., 7
Astakhov G. V., 146, 269
Atlasov K. A., 289
Averkiev N. S., 21, 53, 136, 224

Baas A., 371
Bacher G., 206
Bagraev N. T., 252
Bahir G., 234
Baidus' N. V., 51
Bairamov B., 259
Bakarov A. K., 212, 230, 348, 350
Baltz R. v., 196
Banshchikov A. G., 178
Bao M., 232
Baranov A. N., 156, 160
Bardosova M., 309
Barrick T., 208
Baryshev A. V., 287
Bauman D. M., 192, 242
Baumberg J. J., 291
Bayer M., 31, 37, 61, 65, 67, 69, 129
Bayramov F., 259
Bazarov K. V., 184
Bazhenov N. L., 265
Becker C. R., 206
Beggs D. M., 299
Bel'kov V. V., 29, 42, 75
Belyanin A., 11
Belyanin A. A., 17
Ben Fredj A., 338
Benemanskaya G. V., 93, 162
Ber B. Y., 242
Berezovets V. A., 53
Bernard R., 98
Bert N. A., 281
Besombes L., 36
Bhattacharya P., 4
Bhouri A., 338
Bimberg D., 15, 121, 125, 152
Biryukov A. A., 17
Bisti V. E., 61
Blokhin S. A., 9, 15, 105, 313
Boer-Duchemin E., 98
Bogomolov V. N., 53
Boiko A. M., 95
Bollaert S., 331
Boltaev A. P., 325
Bondarenko O. V., 342
Borisov A. G., 170
Bouravleuv A. D., 96
Bracker A., 194
Brand S., 299
Brudnyi V. N., 101
Brunner K., 146, 269
Budantsev M. V., 212, 230
Bulyanitsa A. L., 261
Burbaev T. M., 132
Burlakov A. A., 240
Bykov A. A., 348
Byrnaz A. E., 246

Cappy A., 331
Caquiere C., 344
Carlberg P., 89
Cataluna M. A., 25
Chaldyshev V. V., 315
Chaly V. P., 246
Chan Yi-Ci, 238
Chang Chia-Fu, 238
Chaplik A. V., 357
Charar S., 91
Chen H.-Y., 275
Cherbunin R. V., 31, 129
Cherkov A. G., 170
Chernyakov A. E., 242
Chernyuk A. A., 204
Chi J. Y., 9
Chistyakov V. M., 47
Cho Hyun-Ick, 75
Choi Yeon-Shik, 244
Christol P., 176, 338
Cirlin G., 117
Cirlin G. E., 84, 99, 150, 261
Clendenin J. E., 248
Comtet G., 98
Cosma D. A., 200
Crooker S. A., 39, 208
Crowell P. A., 39
Cuminal Y., 176, 338

Danilov S. N., 29, 42, 75
Danilov Yu. A., 51, 327
Davydov V. Yu., 273, 275, 279
Debbichi M., 338
Deichsel E., 289
Dem C., 23
Demidov E. V., 344
Demikhovskii V. Ya., 49
Demina P. B., 51
Deryagin A. G., 25
Deveaud B., 371
Diaz Cano A., 263
Dizhur E. M., 352
Dizhur S. E., 352
Dmitriev A. P., 57
Dneprovskii V. S., 134, 142
Dobinde I. I., 134
Dodin E. P., 214
Domagałai J. Z., 91
Domracheva Ya., 277
Doorn S. K., 198
Dorokhin M. V., 51
Doty M. F., 194
Doyennette L., 234
Drozdov Yu. N., 359
Dua C., 344
Dubinov A. A., 17, 340
Dubonos S. V., 156, 216, 240
Dubrovskii V. G., 84, 99, 261
Dubrovskii Yu. V., 367
Ducatteau D., 344
Dudinov K., 111
Dujardin G., 98
Dukin A. A., 293
Dutta M., 259
Dvurechenskii A. V., 101, 363
Dwir B., 289
Dyakonova N., 331
Dzyubenko A. B., 200

Eaves L., 367
Eble E., 33
Efimov Yu. P., 31
Efros Al. L., 37
Egorov A. Yu., 59, 158, 342
Eguchi T., 178
El Fatimy A., 331
Eliseev S. A., 31
Elovikov S. S., 323
Emtsev V. V., 275
Entin M. V., 138, 220
Epshtein E. M., 329

Erkhov D. N., 236
Evans C. A., 13
Evstrapov A. A., 261
Evtikhiev V. P., 160
Eychmüller A., 309

Farbstein I. I., 53
Fateev D. V., 346
Fathpour S., 4
Fedyanin A. A., 295
Fehr M., 208
Feklisov M. A., 256
Feoktistov N. A., 293
Ferrand D., 36
Filippov A. V., 166
Filosofov N. G., 202
Firsov D. A., 342
Fokina L., 31
Forchel A., 206, 285
Frank-Kamenetskaya G. E., 93, 162
Friedland K.-J., 355
Froberg L. E., 228
Fujikawa R., 287
Furis M., 39

Galatsis K., 232
Galkin N. G., 252
Gammon D., 194
Gamov N. A., 27
Ganichev S. D., 29, 42, 75
Gaponik N., 309
Gaquiere C., 331
García de Abajo F. J., 291
García G., 148
Gavrilenko L. V., 164
Gavrilenko V. I., 17, 164, 166, 172, 254, 344
Gavrilov S. S., 297
Gavrilova T. A., 82
Geller M., 125, 152
Gerchikov L. G., 248
Gerl C., 42
Gerlovin I. Ya., 31
Germanenko A. V., 350, 354
Ghatnekar-Nilsson S., 89
Giglberger S., 42
Gippius N. A., 297
Gladyshev A. G., 15, 168, 342
Glas F., 79
Glazov M. M., 43
Glazunov E. A., 259
Gobsch G., 150
Golod S. V., 107, 170
Golub L. E., 43, 63, 75, 354
Golubev V. G., 293, 295
Gonzalez-Hernandez J., 263
Gorbatsevich A. A., 365
Gorbenko V., 84
Gorokhov E. B., 170
Goupalov S. V., 198
Gösele U., 150
Graczyk M., 89
Greilich A., 31, 37, 65, 129
Greshnov A. A., 242
Gridnev V. N., 55
Gubenko A. E., 21
Guillot F., 234
Gulyaev Yu. V., 329
Gurevich A. S., 267
Gurevich S. A., 317
Gurin P. S., 327
Gurtovoi V. L., 216, 240
Gutakovskii A. K., 101
Gutakovskiy A. K., 119
Gwo S., 275

Hahn Cheol-Koo, 244
Hai Lu, 273
Hanabe M., 336
Hansel S., 166
Hansen L., 23
Harada J., 190
Harmand J. C., 84
Harmand J. H., 117
Harrison P., 13, 140
Harus G. I., 77
Härkönen A., 19
Henini M., 367
Hernandez C., 91
Hessman D., 89
Hey R., 355
Hoffmann Ch., 29, 42
Hofmann C., 285
Horikoshi Y., 327
Huc V., 98
Hvam J., 61

Ignatiev I. V., 31, 65, 73, 129
Ikezawa M., 73, 158
Ikonić Z., 13, 140
Ikonnikov A. V., 172
Ilver L., 91
Indjin D., 13, 140
Inoue M., 287, 295, 303
Irmer G., 259
Ishibashi T., 96, 336
Islamov D. R., 348
Ivanov S. V., 27, 99, 115, 277
Ivanov Yu. L., 136
Ivchenko E. L., 29, 42, 59, 63, 305, 315

Jahn U., 355
Jancu J.-M., 45, 174
Jeambrun P., 371
Jimenez-Sandoval S., 263
Jmerik V. N., 277
Johnson S. R., 172
Joullié A., 176, 338
Jovanović V. D., 13
Julien F. H., 234

Kabanin D. A., 142
Kachorovskii V. Yu., 57
Kaczorowski D., 319
Kalagin A. K., 348
Kalevich V. K., 59, 158
Kaliteevski M. A., 299
Kalt H., 196
Kaminski B., 67
Kamp M., 285
Kang T. W., 156
Kanski J., 91
Kapaev V. V., 365
Kapon E., 289
Kapra R. V., 303
Kar S., 218
Karasawa T., 202
Karczewski G., 67, 202, 208
Karlsson K. F., 289
Karlsson L. S., 228
Kasprzak J., 371
Kaveev A. K., 178
Kavokin A. V., 311
Kawaguchi Y., 254
Keeling J., 371
Keldysh L. V., 285
Kelf T., 291
Kelly II T. D., 200
Kesler V. G., 101
Khanikaev A. B., 287
Khanna A., 317
Khanna S., 218
Khitun A., 232
Khodos I. I., 156
Khomitsky D. V., 49
Kiessling T., 146, 269
Kim B.-J., 277
Kim Dong Ho, 244
Kim E. M., 321, 323
Kim Hoon, 244
Kim M.-H., 277
Kim Tae Geun, 244
Kiwi M., 148
Klimov A. Yu., 214
Klingshirn C., 196
Klochikhin A., 196
Klochikhin A. A., 273, 275
Knap W., 172, 331, 344
Kocharovsky V. V., 17
Kocharovsky Vl. V., 17
Kochereshko V., 208
Kochereshko V. P., 267
Koike M., 277
Kokurin I. A., 222
Komiyama S., 254
Komkov O. S., 184
Kononchuk M. S., 319
Kononenko O. V., 156
Kononenko V. K., 176, 338
Kop'ev P. S., 27, 277
Kopylov A. V., 103
Korenev V. L., 194
Korovin L. I., 144

Kosobukin V. A., 301
Kossut J., 67
Kostial H., 355
Kotel'nikov I. N., 352
Kovalchuk A., 111
Kovalev D., 258
Kovarskyi A. P., 242
Kovsh A. R., 9, 21
Kovtunovich A. M., 242
Kowalik K., 33
Kozhevin V. M., 317
Kozlov D. V., 166
Krasilnik Z. F., 359
Krasnik V., 111
Krasovitskiy D. M., 246
Kravets A. F., 321
Krebs O., 33
Krebs R., 285
Krishtopenko S. S., 172
Krupenin V. A., 236
Kryzanivskii A. K., 162
Kryzhanovskaya N. V., 15, 168
Kuchinskii V. I., 25
Kudelski A., 33
Kulagina M. M., 9
Kulakovskii V. D., 51, 285, 297
Kulbachinskii V. A., 327
Kundermann S., 371
Kurbatov V. A., 132
Kurdyukov D. A., 295
Kuzmenkov A. G., 9, 15, 105
Kuznetsov O. A., 359
Kvon Z. D., 75, 250, 334
Kyutt R. N., 178, 190

La Rocca G. C., 174
Ladutenko K. S., 160
Lagunova T. S., 180
Landwehr G., 23, 267
Lang I. G., 144
Larionov A. V., 61
Larionova V. A., 350
Latyshev A. V., 250
Lavrov R. A., 230
Lazzari J.-L., 338
Le Si Dang, 27, 371
Ledentsov N. N., 9, 15, 123, 271, 281
Lee J.-Y., 232
Lee Jung-Hee, 75
Leinonen T., 19
Lemaître A., 33
Letvinov A. N., 267
Levinshtein M. E., 317
Léger Y., 36
Li Y., 259
Lin G., 9
Lipaev A. F., 180
Listoshin S. B., 277
Littlewood P. B., 371
Liu Z. F., 89
Lobanov D. N., 359
Loeffler A., 285
Lou X., 39
Loyola C., 148
Luh D.-A., 248
Lundin V., 111, 123
Lundin V. V., 281
Lundin W. V., 271
Lunin R. A., 327
Luo G., 89
Lupu L., 234
Lusakowski J., 344
Lyaskovskii V. L., 142
Lyubinskiy I. S., 57
Lyublinskaya O. G., 115
L'vova T. V., 115

Magarill L. I., 138, 357
Mahapatra S., 146, 269
Mahmoodian M. M., 220
Maingault L., 36
Makhonin M. N., 285
Maksimov A. A., 283
Maleev N. A., 9, 15, 105, 168
Malpuech G., 311
Malysheva E.I., 327
Mamaev Yu. A., 248
Mancevich V. N., 154
Marchetti F. M., 371
Marem'yanin K. V., 17
Maremyanin K. V., 344
Marent A., 125, 152
Margulis V. A., 222
Marie X., 33
Mariette H., 36
Marin D. V., 170
Markevtsev I. M., 166
Marmalyuk A. A., 214
Maruyama T., 248
Maslova N. S., 109, 154, 188
Masumoto Y., 59, 73, 158
Maude D., 91
Maximov I., 89, 228
Maximov M. V., 9, 15, 25, 168
Mayne A. J., 98
Medvedev A. V., 293
Merkulov I. A., 37, 69
Merz J., 271
Merz J. L., 123
Meziani Y. M., 336
Mi Z., 4
Miglio L., 361
Mikhailova M. P., 180
Mikhrin S. S., 9
Mikhrin V. S., 168
Minami K., 96
Minkov G. M., 350, 354
Mintairov A. M., 123, 271
Mizerov A. M., 277
Moiseenko A. N., 166
Moiseev K. D., 180
Molenkamp L. W., 23, 69, 146, 206, 269
Monroy E., 234
Montalenti F., 361
Montelius L., 89
Moran E., 344
Morozov M. Yu., 19
Morozov S. V., 17, 166, 254, 344
Morozov Yu. A., 19
Murzina T. V., 303, 321, 323
Musikhin Yu. G., 99, 281
Muzychenko D. A., 154
Mynbaev K. D., 265

Nadtochy A. M., 15
Nalamasu O., 218
Nashchekin A. V., 313
Nastaushev Yu. V., 82
Naumova E. V., 107
Naumova O. V., 82
Neizvestny I. G., 113
Nekorkin S. M., 17
Nenashev A. V., 363
Nestoklon M. O., 63
Neverov V. N., 77
Nevou L., 234
Nguyen-Quang T., 45
Nicoluk V. A., 65
Nikolaev V. V., 21, 299
Nikulov A. V., 216, 240
Novikov A. V., 359
Novikov B. V., 150
Novikov I. I., 9, 25
Novikov P. L., 101
Nozdrin Yu. N., 214

Ohtake Y., 178
Olshanetsky E. B., 250
Onomitsu K., 327
Orellana W., 148
Oreshkin A. I., 109, 154
Oreshkin S. I., 109, 154
Ortenberg M. von, 166
Osinniyi V., 91
Osipov N. N., 216
Ossau W., 23, 146, 269
Ostapenko S., 263
Otsuji T., 336
Oulton R., 37, 129

Padalitsa A. A., 214
Pal B., 59, 73
Pala N., 218, 317, 331
Palmstrøm C. J., 39
Panevin V. Yu., 342
Panin G. N., 156
Panov V. I., 109, 154, 188
Parfeniev R. V., 319
Patriarche G., 79, 117
Pavlenko M. V., 246
Pavlov K. M., 190
Pavlov S. T., 144
Pavlov V. V., 67
Pemble M., 309

Peregoudov D. V., 27
Permogorov S., 196
Pessa M., 19
Petrov P. V., 136
Petrov S. I., 246
Petukhov M., 259
Pevtsov A. B., 293
Pikhtin A. N., 184, 246
Pisarev R. V., 67
Platonov A., 208
Platonov A. V., 23, 146, 267, 269
Platonov V. V., 166
Plotnikov A. E., 212
Plotnikov A. Ye., 230
Poddubny A. N., 305, 315
Podgornyh S. M., 77
Pogorelsky M. Yu., 246
Pogosov A. G., 212, 230
Pohl U. W., 121
Poisson M. A., 344
Polianski M. L., 210
Polyakov N. K., 99, 261
Ponomarev I. V., 194
Popov V. G., 367
Popov V. V., 291, 346
Portal J. C., 212, 230, 250, 334
Portnoi E. L., 21
Pötschke K., 121
Preobrazhenskii V. V., 119
Presnov D. E., 236
Prettl W., 42, 75
Prinz A. V., 103
Prinz V. Ya., 86, 103, 107, 119, 355
Pudonin F. A., 325
Putyato M. A., 119

Radchenko I. V., 109, 154
Rafailov E. U., 25
Ramadurai D., 259
Ramírez R., 148
Rastegaeva M. G., 160
Razdolskii I. E., 303
Reinecke T. L., 194, 285
Reithmaier J. P., 285
Reuter D., 37, 65
Reznitsky A., 196
Richard M., 371
Roberts J. S., 248
Rodriguez J. B., 176
Rodt S., 121
Roelens Y., 331
Rogan J., 148
Rogov V. V., 214
Roh Cheong Hyun, 244
Romanov K. S., 53, 136
Romanov S. G., 307, 309, 319
Rozhansky I. V., 224
Rubo Yu. G., 311
Rudra A., 289
Rumyantsev S., 218, 331
Rumyantsev S. L., 317
Rut O. E., 350, 354
Rzaev M. M., 132

Sablikov V. A., 369
Sadovyev Yu. G., 172
Sadowski J., 91
Sadowski M. L., 172
Saïd M., 338
Sakata O., 190
Sakharov A., 111
Sakharov A. V., 9, 273, 281
Samsonenko Yu. B., 99, 261
Samuelson L., 228
Sankin V. I., 186
Sano E., 336
Santalov A. N., 134
Satishkumar B. C., 198
Sato K., 96
Sato Y., 96
Savinov S. V., 109, 154, 188
Sänger I., 67
Schaff W. J., 273
Schäffler F., 132
Scheibner M., 194
Scherbakov A. V., 69
Schliwa A., 121
Schmidt G., 146, 269
Schuh D., 29, 42
Sedova I. V., 27, 99, 115
Seguin R., 121
Seidl S., 75
Seifert W., 1
Sek G., 285
Sel'kin A. V., 293
Selemir V. D., 166
Seleznev V. A., 107
Seliuta D., 331
Semenov A. N., 115
Semenova E. S., 15, 125
Serov A. Yu., 202
Shabaev A., 37
Shaleev M. V., 359
Shalygin V. A., 29, 342
Shamshur D. V., 319
Shapoval S., 111
Shchegolev B., 259
Shchepetov A., 331
Sheglov D. V., 250
Shelushinina N. G., 77
Shelykh I. A., 252, 311
Shen C.-H., 275
Shernyakov Yu. M., 9
Sherstobitov A. A., 350, 354
Shi P., 259
Shimura T., 190
Shiryaev A. Yu., 59, 158
Shkrebiy P. P., 186
Shkurko A. P., 246
Shmidt N. M., 192, 242
Shubina T. V., 277
Shulgunova I. S., 152
Shur M., 218
Shur M. S., 317, 331, 346
Shwartz N. L., 113
Sibbett W., 25
Sibeldin N. N., 132
Sibirev N. V., 84, 261
Sinitsyn M. A., 273
Sirotkin V., 111
Sitnikova A. A., 277
Sitnikova A. M., 99
Sivachenko A. Yu., 200
Sizov D., 123
Sizov D. S., 271, 281
Sizov V., 123
Sizov V. S., 271
Skvortsov A. P., 273
Slobodskyy T., 146, 269
Smagina Zh. V., 101
Smirnov A. N., 273, 275, 279
Smirnov M. B., 279
Smith D., 11
Smith D. L., 39
Soerensen K., 61
Sofronov A. N., 342
Sokolov A. S., 150
Sokolov I. A., 246
Sokolov L. V., 82
Sokolov M. A., 246
Sokolov N. S., 178, 190
Sokolovskii G. S., 25
Soldano C., 218
Solnyshkov D., 311
Solomonov A. V., 152
Solov'ev V. A., 115
Song Hong Joo, 244
Sorokin S. V., 27, 99, 115
Soshnikov I. P., 84, 261
Sotomayor Torres C. M., 307, 309
Spirin K. E., 254
Staehli J. L., 371
Stavarache V., 37, 65
Stepanov M. V., 246
Stepina N. P., 101
Stinaff E. A., 194
Stock E., 15
Stroscio M. A., 259
Studionov V. B., 27
Sugakov V. I., 204
Sugawara Y., 291
Sumetani K., 190
Suris R. A., 84, 95, 271
Suturin S. M., 190
Suyatin D. B., 228
Svitasheva S. N., 82
Syperek M., 31
Szymanska M. H., 371

Tabuchi M., 178, 190
Takeda Y., 178, 190
Talalaev V. G., 150
Tanklevskaya E. M., 15, 313

Tarasenko S. A., 29, 42, 71
Tartakovskii I. I., 283
Tatsenko O. M., 166
Tchernycheva M., 84, 117, 234
Teperik T. V., 291
Teppe F., 331
Terki F., 91
Teys S. A., 113
Theron D., 331
Tikhodeev S. G, 297
Tikhomirov V. G., 168
Timoshnev S. N., 93
Titkov A. N., 160
Tkachenko A. G., 246
Tkachenko O. A., 250
Tkachenko V. A., 250
Tkachman M. G., 277
Todd A. R., 200
Tomm J. W., 150
Tonkih A. A., 261
Tonkikh A. A., 99, 136, 150
Toporov V., 259
Torchynska T. V., 263
Toropov A. I., 212, 230, 250
Travers L., 117
Tsatsul'nikov A., 123
Tsatsul'nikov A. F., 271
Tsatsulnikov A., 111
Tsatsulnikov A. F., 281
Tsiper E. V., 127
Tsitsishvili E., 196
Tsoy D. V., 342
Tsvetkov V. A., 132
Tsymbalov G. M., 346
Tulin V. A., 216, 240

Uchida H., 287
Ulin V. P., 190
Uno T., 336
Urbaszek B., 33
Ushakov D. V., 176
Usikova A. A., 115
Uskova E. A., 51, 77
Usov O. A., 313
Usov S. O., 281
Ustinov V., 111
Ustinov V. M., 9, 15, 25, 59, 84, 99, 105, 125, 158, 168, 261

Vajtai R., 218
Valusis G., 331
Van Haesendonck C., 188
Vardi A., 234
Vasil'ev A. P., 15, 105, 125, 168
Vasilyev Yu. B., 172
Vassiliev N. N., 202
Vastola G., 361
Vedeneev A. S., 256
Veksler D. B., 331
Velikovskiy I. E., 246
Velikovskiy L. E., 246
Verbin S. Yu., 73
Vergeles P. S., 192
Vershinin A. V., 113
Vijayaraghavan A., 218
Vikhnin V. S., 93
Vitkalov S., 348
Vitkalov S. A., 334
Vlasenko V. S., 236
Vlasov A., 123
Voisin P., 33, 45, 174
Volodin V. A., 170
Vorob'ev A. B., 119, 355
Vorobiev Yu. V., 263
Vorobjev L. E., 342
Voronina T. I., 180
Voronov M. M., 315
Voronovskii A. N., 352
Vukmirović N., 140

Waag A., 23, 69, 267, 283
Wallenberg L. R., 228
Wallin D., 228
Wan Zou-ni, 238
Wang K. L., 232
Warde E., 234
Ware M. E., 194
Weber W., 75
Wegscheider W., 29, 42
Weiss D., 42, 75
Welsch M. K., 206
Werner P., 82, 150
Wiebicke E., 355
Wieck A., 37, 65, 334
Winzer A., 150
Wojtowicz T., 67
Wumaier T., 142

Xie F., 11
Xu H. Q., 89, 228

Yablonskiy A. N., 359
Yagovkina M., 277
Yagovkina M. A., 273
Yakimov E. B., 192
Yakimova R., 186
Yakovlev D. R., 23, 31, 37, 65, 67, 69, 129, 283
Yakovlev Yu. P., 180
Yakunin M. V., 77
Yang J., 4
Yanovitskaya Z. Sh., 113
Yashin Yu. P., 248
Yassievich I. N., 47
Yavich B. S., 192, 242
Yavsin D. A., 317
Ye J., 307
Yugova I. A., 31, 37, 65
Yukecheva Ju. S., 355
Yukecheva Yu. S., 119

Zaitsev S. V., 206, 283
Zakgeim A. L., 242
Zakharov N. D., 82, 150
Zakrevskii N. V., 166
Zamoryanskaya M. V., 277
Zavarin E., 111, 123
Zavarin E. E., 271, 273, 281
Zaytsev S. V., 51
Zdanova E. V., 27
Zegrya G. G., 265
Zemlyakov V., 111
Zentel R., 307
Zhang J.-G., 334
Zhang Jing-qiao, 348
Zhang Y.-H., 172
Zhu T., 89
Zhukov A. E., 15, 25, 105, 125, 168
Zhukov E. A., 37, 134, 142
Zhukov T., 263
Zhuravlev M. N., 365
Zilberman P. E., 329
Zinchenko D. I., 214
Zinovieva A. F., 363
Zinovyev V. A., 361
Zolatareva R. V., 277
Zubkov V. I., 152
Zverev A. V., 113
Zverev M. M., 27
Zvonkov B. N., 17, 51, 77, 166, 350
Zvonkov G. M., 354
Zvyagin I. P., 226
Zyakin B. A., 267